2018 European Frequency and Time Forum (EFTF)

Torino, Italy
April 10-12, 2018

ISBN: 978-1-5386-4077-7

2018 European Frequency and Time Forum (EFTF)

Copyright and Reprint Permission: Abstracting is permitted with credit to the source. Libraries are permitted to photocopy beyond the limit of U.S. copyright law for private use of patrons those articles in this volume that carry a code at the bottom of the first page, provided the per-copy fee indicated in the code is paid through Copyright Clearance Center, 222 Rosewood Drive, Danvers, MA 01923. For reprint or republication permission, email to IEEE Copyrights Manager at pubs-permissions@ieee.org. All rights reserved. Copyright ©2018 by IEEE.

ISBN: 978-1-5386-4077-7

EFTF 2018 TABLE OF CONTENTS

GROUP 1 Materials, Resonators, & Resonator Circuits

Microwave Acoustic Properties of Diamond Based HBAR at Low Temperatures 1
Boris Sorokin[2], Gennady Kvashnin[1], Andrey Novoselov[2], Anton Shipilov[2]
[1]Technological Institute for Superhard and Novel Carbon Materials, Russia;
[2]Technological Institute for Superhard and Novel Carbon Materials / Moscow Institute of Physics and T, Russia

Hysteresis in Phononic Frequency Combs 6
Adarsh Ganesan, Ashwin Seshia
University of Cambridge, United Kingdom

Inkjet Printing of Thin Electrodes for Quartz Resonators.....10
Amina Saadani[3], Pierre Lavenus[3], Olivier Le Traon[3], Gilgueng Hwang[1], Fabrice Sthal[2]
[1]C2N-CNRS/Université Paris-Sud, France; [2]FEMTO-ST Institute/ENSMM, France;
[3]ONERA, France

Reactive Sputtering of AlScN Thin Films with Variable Sc Content on 200 mm Wafers 13
Marta Clement[2], Valeriy Felmetsger[1], Teona Mirea[2], Enrique Iborra[2]
[1]OEM Group LLC, United States; [2]Universidad Politécnica de Madrid, Spain

Finding the Upper Mass Limit Until Which Gravimetric Sensors Preserve Their Original TCF and Sensitivity 17
Teona Mirea, Marta Clement, Jimena Olivares, Enrique Iborra
Universidad Politécnica de Madrid, Spain

A High Q Length-Extension Mode Quartz Resonator for MEMS Oscillator and Time-Frequency Applications 20
Paul Chapellier[2], Olivier Le Traon[2], Pierre Lavenus[2], Bernard Dulmet[1]
[1]FEMTO-ST Institute, France; [2]ONERA, France

Consideration and Implementation of Inherent Losses in SAW Devices 24
Marianne Sagnard, Thierry Laroche, Sylvain Ballandras
Frec'n'sys, France

GROUP 2 Oscillators, Synthesizers, Noise, & Circuit Techniques

INVITED: Above 100-GHz Low Phase Noise Frequency Generation in Silicon Integrated Technologies 32
Alexandre Siligaris, Zyad Iskandar, Jose Moron Guerra
CEA-LETI, France

Study of the Phase Noise of Langatate Crystal Resonators.....37
Alok Pokharel[2], Fabrice Sthal[3], Etienne Vaillant[2], Joel Imbaud[2], Jean-Jacques Boy[2], François-Xavier Esnault[1], Gilles Cibiel[1]
[1]CNES, France; [2]FEMTO-ST Institute, France; [3]FEMTO-ST Institute/ENSMM, France

Direct Measurement of Cryogenic Sapphire Oscillators with Tracking DDSs and 2-Sample Covariance.....41
Claudio Eligio Calosso[3], François Vernotte[1], Vincent Giordano[2], Christophe Fluhr[2], Benoit Dubois[2], Enrico Rubiola[2]
[1]Besancon Observatory, France; [2]FEMTO-ST Institute, France; [3]INRIM, Italy

Measuring Small Propagation Frequency Shifts and Fluctuations by Phase to Avoid Cross-Correlation Errors 45
Michael Underhill
Underhill Research Limited, United Kingdom

GROUP 3 Microwave Frequency Standards

Design of Mercury Lamp for Trapped Ion Frequency Standards 50
Nuan-Rang Wang, Xing Chen, Huan Zhao, Renfu Yang
Beijing Institute of Radio Metrology and Measurement, China

Fountain Equation and Frequency Calculation 53
Yury Domnin, Olga Kupalova
VNIIFTRI, Russia

Towards a Quantum-Enhanced Atomic Clock on a Chip 56
Tommaso Mazzoni[2], Meng-Zi Huang[1], Théo Laudat[1], Carlos L. Garrido Alzar[2], Jakob Reichel[1]
[1]Laboratoire Kastler Brossel, France; [2]Observatoire de Paris, France

Raman-Ramsey CPT with a Grating Magneto-Optical Trap 61
Rachel Elvin, Gregory W. Hoth, Michael W. Wright, James P. McGilligan, Aidan S. Arnold, Paul F. Griffin, Erling Riis
University of Strathclyde, United Kingdom

INVITED: Microsemi Chip Scale Atomic Clock (CSAC) Technical Status, Applications, and Future Plans 65
Peter Cash, Will Krzewick, Paul Machado, K. Richard Overstreet, Mike Silveira, Matt Stanczyk, Dwayne Taylor, Xianli Zhang
Microsemi Corporation, United Kingdom; Microsemi Corporation, United States

Development Status of the Rb Pop Space Clock for GNSS Applications 72
Pier Giorgio Arpesi[5], Jacopo Belfi[2], Marina Gioia[5], Nicholas Marzoli[2], Romano Romani[5], Adalberto Sapia[5], Michele Gozzelino[6], Claudio Eligio Calosso[4], Filippo Levi[4], Salvatore Micalizio[4], Alberto Tuozzi[1], Marco Belloni[3]
[1]Agenzia Spaziale Italiana, Italy; [2]Alten Italia - Milano, Italy; [3]European Space Agency/ESTEC, Netherlands; [4]INRIM, Italy; [5]Leonardo SpA, Italy; [6]Politecnico di Torino & INRIM, Italy

Ramsey-Mode Rb Cell Clock Demonstration with a 3D-Printed Microwave Cavity 75
William Moreno[3], Christoph Affolderbach[3], Matthieu Pellaton[3], Gaetano Mileti[3], Anton Ivanov[1], Anja Skrivervik[1], Tomislav Debogovic[2], Santiago Capdevila[2], Diane Hoerni[2], Emile deRijk[2]
[1]École Polytechnique Fédérale de Lausanne, Switzerland; [2]SWISSto12 SA, Switzerland; [3]University of Neuchâtel, Switzerland

Microwave Field Amplitude Stabilization Using Ramsey Spectroscopy Signal 80
Michele Gozzelino[2], Salvatore Micalizio[1], Aldo Godone[1], Filippo Levi[1], Claudio Eligio Calosso[1]
[1]INRIM, Italy; [2]Politecnico di Torino & INRIM, Italy

CPT Atomic Clock Based on an Antirelaxation-Coated Cell and Quadrature-Signal Method of the Light Shift Cancellation 83
Stepan Ignatovich[2], Vladislav Vishnyakov[2], Anton Makarov[2], Mikhail Skvortsov[2], Nikolai Kvashnin[2], Vadim Vasiliev[2], Sergei Atutov[1], Denis Brazhnikov[3], Valeriy I. Yudin[3], Alexey V. Taichenachev[3], Sergei Bagayev[3]
[1]Institute of Automation and Electronics SB RAS, Novosibirsk, Russia; [2]Institute of Laser Physics SB RAS, Russia; [3]Novosibirsk State University / Institute of Laser Physics SB RAS, Russia

Influence of an Optical Dense Medium at the Ramsey Method of CPT Resonance Detection 87
Konstantin Barantsev, Gavriil Voloshin, Andrey Litvinov, Evgeniy Popov
Peter the Great St. Petersburg Polytechnic University, Russia

Gold Microdiscs As Alkali Preferential Condensation Spots for Cell Clock Long-Term Frequency Improvement 91
Sylvain Karlen, Thomas Overstolz, Jean Gobet, Jacques Haesler, Fabien Droz, Steve Lecomte
CSEM SA, Switzerland

Recent Progress of Development of Cesium Fountain Primary Frequency Standard NMIJ-F2 94
Akifumi Takamizawa, Shinya Yanagimachi, Ken Hagimoto, Iku Hirano, Takeshi Ikegami
National Metrology Institute of Japan, Japan

Contributions to the Mid-term Frequency Noise of the Pulsed CPT Clock at SYRTE 98
Francois Tricot, Stephane Guérandel, Emeric De Clercq
Observatoire de Paris, France

GROUP 4 Sensors & Transducers

SAW Temperature Sensor with Mirror Topology 101
Ivan Antcev[1], Sergey Bogoslovsky[1], Gennadiy Sapozhnikov[1], Sergei Zhgoon[2], Alexander Shvetsov[2]
[1]JSC "Radar-mms", Russia; [2]National Research University MPEI, Russia

Choice of SAW Humidity Sensor Coatings 105
Ivan Antcev[1], Sergey Bogoslovsky[1], Mikhail Derkach[1], Gennadiy Sapozhnikov[1], Sergei Zhgoon[2]
[1]JSC "Radar-mms", Russia; [2]National Research University MPEI, Russia

Nonlinear Enhancement of Locking Range of Mutually Injection-Locked Oscillators for Resonant Sensing Applications 109
Jérôme Juillard, Ali Mostafa, Pietro Maris Ferreira
CentraleSupélec / GEEPS, France

Analysis of Resonant Sensors Based on Mutually Injection-Locked Oscillators Beyond the Critical Duffing Amplitude 114
Jérôme Juillard, Ali Mostafa, Pietro Maris Ferreira
CentraleSupélec / GEEPS, France

Long Term Stabilization of Large Frame Laser Gyroscopes 119
Fabio Stefani[2], Nicolo Beverini[2], Giorgio Carelli[2], D. Ciampini[3], Angela Di Virgilio[1], F. Fuso[3], Umberto Giacomelli[2], Enrico Maccioni[2]
[1]INFN, Italy; [2]INFN / Università di Pisa, Italy; [3]Università di Pisa, Italy

Optimization of Low-Power Oscillator Topology for Frequency Modulated MEMS Inertial Sensors 122
Cristiano Rocco Marra[2], Alessia Maria Ruggieri[2], Paolo Minotti[2], Giorgio Mussi[1], Andrea Giovanni Bonfanti[2], Andrea Leonardo Lacaita[2], Giacomo Langfelder[2]
[1]Politecnico di Mialno, Italy; [2]Politecnico di Milano, Italy

Influence of the Acoustic Energy Distribution on the in-Liquid Sensitivity of Thin Film Electroacoustic Resonators 126
Teona Mirea, Jimena Olivares, Marta Clement, Enrique Iborra
Universidad Politécnica de Madrid, Spain

GROUP 5 Timekeeping, Time and Frequency Transfer, GNSS Applications

Measuring the Mitigation of a Jamming Attack on a GPS Server at the National Physical Laboratory of Israel 130
Nadya Goldovsky[2], Omer Sharar[1]
[1]GPSdome Ltd., Israel; [2]INPL, Israel

Carrier-Phase Two-Way Satellite Frequency Transfer Between BIRMM and NIM 135
Shuwei Wang[1], Xueyun Wang[1], Haifeng Wang[1], Zhiqiang Yang[2], Wenzhe Yang[1], Hongbo Wang[1], Shengkang Zhang[1]
[1]Beijing Institute of Radio Metrology and Measurement, China; [2]National Institute of Metrology, China

Time Synchronization Performance Using the Network Time Security Protocol 138
Martin Langer[1], Kristof Teichel[2], Dieter Sibold[2], Rainer Bermbach[1]
[1]Ostfalia University of Applied Sciences, Germany; [2]Physikalisch-Technische Bundesanstalt, Germany

The Study of Using Hydrogen Maser Ensemble to Steer UTC(TL) 145
Shinn Yan Lin
Chunghwa Telecom Co. Ltd., Taiwan

Automatic Calibration of the Actively Stabilized Fiber-Optic Time Transfer 149
Przemysław Krehlik, Jacek Kołodziej, Łukasz Śliwczyński
AGH University of Science and Technology, Poland

On-Line Optimization of Time and Frequency Fiber Optic Links Exploiting Bi-Directional Amplifiers 152
Łukasz Śliwczyński, Przemysław Krehlik, Karol Salwik, Jacek Kołodziej
AGH University of Science and Technology, Poland

An Anti-Jamming System for GNSS Timing Applications 155
Jorge Querol[3], Adriano Camps[2], Esteban Garbin Manfredini[1], Ricardo Píriz[1]
[1]GMV, Spain; [2]UPC-BarcelonaTech, Spain; [3]UPC-BarcelonaTech / MITICS, Spain

Evaluation of CGGTTS Time Transfer Software Using Multiple GNSS Constellations 159
Kenneth Jaldehag, Carsten Rieck, Per Jarlemark
RISE Research Institues of Sweden, Sweden

Evaluation and Development of Optical Time Transfer (OTT) Links Between PTB and Deutsche Telekom 167
Łukasz Śliwczyński[1], Przemysław Krehlik[1], Jacek Kołodziej[1], Helmut Imlau[2], Horst Ender[2], Harald Schnatz[3], Dirk Piester[3], Andreas Bauch[3]
[1]AGH University of Science and Technology, Poland; [2]Deutsche Telekom Technik GmbH, Germany; [3]Physikalisch-Technische Bundesanstalt, Germany

Study on BeiDou All-in-View Time Transfer 170
Jihai Zhang[1], Wenjun Wu[1], Wei Guang[1], Lulu Yan[2], Wei Li[1], Haibo Yuan[1], Shaowu Dong[1]
[1]National Time Service Center Chinese Academy of Sciences, China; [2]NTSC / School of Astronomy and Space Science, University of Chinese Academy of Sciences, China

Study on the Relation Between Laser Noise and Optical Frequency Transmission 175
Xi Zhang, Fei Yang, Zitong Feng, Youzhen Gui, Haiwen Cai, Ronghui Qu
Shanghai Institute of Optics and Fine Mechanics Chinese Academy of Sciences, China

Stabilized Optical-Frequency Transfer Using Optical Injection Locking Amplifier 178
Zitong Feng, Fei Yang, Xi Zhang, Dijun Chen, Nan Cheng, Youzhen Gui, Haiwen Cai
Shanghai Institute of Optics and Fine Mechanics Chinese Academy of Sciences, China

Analysis of GNSS Time Scales 181
Petr Bogdanov, Andrei Druzhin, Tatiana Primakina, Arkadii Tiuliakov
Russian Institute of Radionavigation and Time, Russia

Optimal Traceability to the SI Second Through TAI 185
Gérard Petit, Gianna Panfilo
International Bureau of Weights and Measures, France

Improvements on the UTC(IT) Timescale at INRIM 188
Marco Sellone[1], Roberto Costa[1], Alberto Mura[1], Giancarlo Cerretto[1], Filippo Levi[1], Marco Siccardi[2]
[1]INRIM, Italy; [2]SKK Electronics, Italy

Phase Synchronization for 5G Using Mass Market GNSS Receivers 192
Zdenek Chaloupka[3], Lionel Ries[2], Andrea Samperi[2], Pierre Waller[1], Massimo Crisci[2]
[1]European Space Agency, Netherlands; [2]European Space Agency/ESTEC, Netherlands; [3]European Space Agency/European Space Research and Technology Centre, Netherlands

Joint Time Scale Algorithm of UTC(NTSC) and UTC(SU) 197
Shanshan Bai[1], Shuhong Zhao[1], Shaowu Dong[1], Lulu Yan[2], Lili Qu[1]
[1]National Time Service Center Chinese Academy of Sciences, China; [2]NTSC / School of Astronomy and Space Science, University of Chinese Academy of Sciences, China

Comparison of Highly-Stable Optical Frequency Transfer in a Single Bidirectional and Double Unidirectional Fibers 202
Przemysław Włodarczyk, Przemysław Krehlik, Łukasz Śliwczyński
AGH University of Science and Technology, Poland

Timing Jitter Characterization of Dual-Comb System via TWTFT Method 205
Honglei Yang, Shengkang Zhang, Huan Zhao, Hongbo Wang, Xueyun Wang, Haifeng Wang, Hang Yi, Wenzhe Yang, Shuwei Wang
Beijing Institute of Radio Metrology and Measurement, China

GNSS Antenna Multipath Effects 208
Giovanni Daniele Rovera[1], Michel Abgrall[1], Pierre Uhrich[1], Pascale Defraigne[2], Bruno Bertrand[2]
[1]Observatoire de Paris, France; [2]Royal Observatory of Belgium, Belgium

DWDM Stabilized Optics for White Rabbit 213
Paul Boven
Joint Institute for VLBI ERIC (JIVE), Netherlands

Study on Time Scale Algorithm of Hydrogen Maser Based on Minimum Error Theory 217
Meng Jiang, Shaowu Dong, Mojuan Yin, Wenjun Wu, Huijie Song, Lili Qu, Weixiong Wang
National Time Service Center Chinese Academy of Sciences, China

Comparison of Two Methods of Time-Interval Measurement Based on SAWF and SAWDDL 221
Haifeng Wang, Shengkang Zhang, Xie Yong, Xueyun Wang, Hongbo Wang, Hang Yi, Honglei Yang, Wenzhe Yang, Shuwei Wang
Beijing Institute of Radio Metrology and Measurement, China

Long Term Simulations for Bi-Static Radar and Test Bench Design 225
Ricardo Granados Alfaro, Alain Herique, Sylvain Rochat, Etienne Le-Coarer
Institut de Planetologie et d'Astrophysique de Grenoble, France

Final Characterization of InLambda Delay Standards for Supplementary Time Interval Comparison 231
Albin Czubla[1], Piotr Szterk[1], Roman Osmyk[1], Borut Pinter[4], Rado Lapuh[3], Uros Dragonja[2], Jurij Tratnik[2]
[1]Central Office of Measures, Poland; [2]InLambda Company, Slovenia; [3]Metrology Institute of the Republic of Slovenia, Slovenia; [4]Slovenian Institute of Quality and Metrology, Slovenia

Preprocessing for Fast Synchronization of High-Stability Oscillators Disciplined by GNSS 1 PPS Signal 234
Paweł Kubczak, Michał Kasznia, Mieczysław Jessa
Poznan University of Technology, Poland

Relativistic Corrections for Intersatellite Frequency Transfer 240
Bethany Kroese, Gabriele Giorgi, Christoph Günther
German Aerospace Center, Germany

A Recursive Clock Anomalies Detector with Double Exponential Smoothing 245
Valerio Formichella[1], Patrizia Tavella[2]
[1]INRIM, Italy; [2]INRIM / BIPM, Italy

High Accuracy Continuous Time Transfer with GPS IPPP and T2L2 249
Julia Leute[2], Gérard Petit[2], Pierre Exertier[1], Etienne Samain[1], Giovanni Daniele Rovera[3], Pierre Uhrich[3]
[1]Géoazur, Observatoire de la Côte d'Azur, France; [2]International Bureau of Weights and Measures, France; [3]Observatoire de Paris, France

Analysis and Compensation of Polarization in an Optical Frequency Transfer Through a Fiber Communication Network 253
Per Olof Hedekvist, Ludwig Weddig, Sven-Christian Ebenhag
RISE Research Institues of Sweden, Sweden

First Experiments on Application of Rb Fountain Frequency Standards for TA(SU) Time Scale Maintenance 257
Igor Blinov[1], Alexander Boiko[2], Nikolai Kosheliaevskii[2], Olga Kupalova[2], O. Sokolova[2]
[1]FGUP VNIIFTRI, Russia; [2]VNIIFTRI, Russia

Passive Utilization of the TWSTFT Technique 263
Carsten Rieck, Per Jarlemark, Kenneth Jaldehag
RISE Research Institues of Sweden, Sweden

Multi-GNSS Time Transfer with CGGTTS-V2E 270
Pascale Defraigne, Katrijn Verhasselt
Royal Observatory of Belgium, Belgium

Galileo and GNSS Time Offsets 276
Giovanna Signorile[1], Ilaria Sesia[1], Thanh Tùng Thai[1], Pascale Defraigne[3], Patrizia Tavella[2]
[1]INRIM, Italy; [2]INRIM / BIPM, Italy; [3]Royal Observatory of Belgium, Belgium

Time-Frequency Analysis of Atomic Clock Anomalies 281
Lorenzo Galleani
Politecnico di Torino, Italy

The H2020 European Project CLONETS: Clock Services Over Optical-Fibre Networks in Europe 285
Davide Calonico[4], Filippo Levi[4], Łukasz Śliwczyński[1], Josef Vojtěch[2], Vladimir Smotlacha[2], Alwyn Seeds[19], Alessandro Galardini[18], Mauro Campanella[3], Nicolas Quintin[7], Ondřej Číp[5], Ronald Holzwarth[8], Maurice Lessing[8], Bruno Desruelle[9], Jean Lautier Gaud[9], Elizabeth Laier English[10], Jochen Kronjäger[10], Harald Schnatz[14], Jiří Štefl[13], Robert Urbaniak[15], Wojbor Bogacki[16], Anne Amy-Klein[6], Trinidad García[17], Eva Bookjans[11], Paul-Eric Pottie[12], Philip Tuckey[11]
[1]AGH University of Science and Technology, Poland; [2]CESNET, Czech Rep.; [3]GARR, Italy; [4]INRIM, Italy; [5]Institute of Scientific Instruments of the CAS, v. v. i., Czech Rep.; [6]Laboratoire de Physique des Lasers, Université Paris 13, France; [7]Laboratoire de Physique des Lasers, Université Paris 13, GIP-RENATER, France; [8]Menlo Systems GmbH, Germany; [9]Muquans, France; [10]National Physical Laboratory, United Kingdom; [11]Observatoire de Paris, France; [12]Observatoire de Paris / Université Paris 13, France; [13]OPTOKON, Czech Rep.; [14]Physikalisch-Technische Bundesanstalt, Germany; [15]PIKTIME, Poland; [16]Poznań Supercomputing and Networking Center, Poland; [17]SEVENSOL, Spain; [18]TOPIX, Italy; [19]University College London, United Kingdom

Two-Way Optical Phase Comparison at 10^-21 Level 290
Qi Zang[1], Xue Deng[1], Jie Liu[1], Dongdong Jiao[1], Jing Gao[1], Xiang Zhang[1], Dan Wang[1], Guanjun Xu[2], Ruifang Dong[1], Tao Liu[1], Shougang Zhang[1]
[1]National Time Service Center Chinese Academy of Sciences, China; [2]Northwestern Polytechnical University & National Time Service Center, China

Phase-Coherent Transfer of Optical Frequency Between ISI CAS and CESNET 293
Martin Čížek[2], Lenka Pravdova[2], Václav Hucl[2], Simon Rerucha[2], Jan Hrabina[2], Michal Jelinek[2], Bretislav Mikel[2], Josef Lazar[2], Ondřej Číp[2], Vladimir Smotlacha[1], Ondrej Havlis[1], Josef Vojtěch[1]
[1]CESNET, Czech Rep.; [2]Institute of Scientific Instruments of the CAS, v. v. i., Czech Rep.

Kalman Filter Simulation and Characterization of BDS Satellite Clock 296
Bin Wang[2], Junping Chen[1], Binghao Wang[3]
[1]Shanghai Astronomical Observatory, CAS and School of Astronomy and Space Science, UCAS, China; [2]Shanghai Astronomical Observatory, Chinese Academy of Sciences, China; [3]Zhengzhou Institute of Surveying and Mapping, China

Real Like Transmission Lines for Sagnac Correction Study 300
Martin Šlapák, Josef Vojtěch
CESNET, Czech Rep.

Bidirectional Optical Amplifier Delivering High Gain 303
Ondrej Havlis, Josef Vojtěch, Radek Velc, Martin Šlapák, Miloslav Hula, Jan Radil, Vladimir Smotlacha, Martin Kolbe
CESNET, Czech Rep.

Remote Atomic Clock Contribution to UTC(TP) 308
Vladimir Smotlacha[1], Alexander Kuna[2]
[1]CESNET, Czech Rep.; [2]Institute of Photonics and Electronics of the AS CR, v. v. i., Czech Rep.

GROUP 6 Optical Frequency Standards and Applications

Absolute Frequency Measurement of the Ytterbium Ion E3 Optical Clock Transition Using International Atomic Time 312
Rachel M. Godun[2], Charles F. A. Baynham[2], Jonathan M. Jones[5], Steven A. King[3], Peter B. R. Nisbet-Jones[2], Fred Baynes[2], Antoine Rolland[2], Patrick E. G. Baird[6], Kai Bongs[4], Patrick Gill[2], Gérard Petit[1], Helen S. Margolis[2]
[1]International Bureau of Weights and Measures, France; [2]National Physical Laboratory, United Kingdom; [3]Physikalisch-Technische Bundesanstalt / National Physical Laboratory, United Kingdom; [4]University of Birmingham, United Kingdom; [5]University of Birmingham / National Physical Laboratory, United Kingdom; [6]University of Oxford, France

Advances in the Uncertainty Evaluation of a 88Sr+ Single Ion Optical Clock 315
Pierre Dubé[1], Bin Jian[1], Amar Vutha[2]
[1]National Research Council Canada, Canada; [2]University of Toronto, Canada

Effect of Pulse Duration Fluctuation on the Photodetection of a Train of Pulses from an Optical Frequency Comb 318
Xiaopeng Xie[3], Romain Bouchand[3], Michele Giunta[2], Wolfgang Hänsel[2], Matthias Lezius[2], Ronald Holzwarth[2], Giorgio Santarelli[1], Yann Le Coq[3]
[1]LP2N, CNRS, Institut d'Optique d'Aquitaine, Université de Bordeaux - CNRS, IOGS, France; [2]Menlo Systems GmbH, Germany; [3]Observatoire de Paris, PSL Research University, CNRS, Sorbone Université, France

Dark Matter Searches Within the Intercontinental Optical Atomic Clock Network 322
Piotr Wcisło[4], Piotr Ablewski[4], Kyle Beloy[2], Sławomir Bilicki[5], Marcin Bober[4], Roger Brown[2], Robert Fasano[2], Roman Ciuryło[4], Hidekazu Hachisu[1], Tetsuya Ido[1], Jérôme Lodewyck[6], Andrew Ludlow[2], William McGrew[2], Piotr Morzyński[4], Daniele Nicolodi[2], Marco Schioppo[3], Mamoru Sekido[1], Rodolphe Le Targat[6], Peter Wolf[6], Xiaogang Zhang[2], Beata Zjawin[4], Michał Zawada[4]
[1]National Institute of Information and Communications Technology, Japan; [2]National Institute of Standards and Technology, United States; [3]National Physical Laboratory / National Institute of Standards and Technology, United States; [4]Nicolaus Copernicus University in Toruń, Poland; [5]Nicolaus Copernicus University in Toruń / LNE-SYRTE, Poland; [6]Observatoire de Paris, PSL Research University, CNRS, Sorbone Université, France

Photoassociation Measurements to Evaluate Collisional Shifts in Strontium and Prospects for Clock Spectroscopy with Ytterbium Molecules 326
Marcin Bober[2], Mateusz Borkowski[1], Piotr Morzyński[2], Sławomir Bilicki[3], Piotr Ablewski[2], Roman Ciuryło[2], Michał Zawada[2]
[1]Nicolaus Copernicus University, Poland; [2]Nicolaus Copernicus University in Toruń, Poland; [3]Nicolaus Copernicus University in Toruń / LNE-SYRTE, Poland

Two-Photon Spectroscopy of Hydrogen Molecular Ions for Precision Measurements of Fundamental Constants 330
Florin Lucian Constantin
Laboratoire PhLAM, CNRS UMR 8523, France

Thermal Noise Further Reduced Ultrastable Laser with Frequency Instability of 5×10^-16 338
Lulu Yan[2], Zhaoyang Tai[1], Yanyan Zhang[3], Pan Zhang[1], Wenyu Zhao[1], Xiaofei Zhang[1], Wenge Guo[1], Shougang Zhang[1], Haifeng Jiang[1]
[1]National Time Service Center Chinese Academy of Sciences, China; [2]NTSC / School of Astronomy and Space Science, University of Chinese Academy of Sciences, China; [3]School of Astronomy and Space Science, University of Chinese Academy of Sciences, China

Progress on Development of Optical Frequency Combs at NTSC 341
Yanyan Zhang[4], Lulu Yan[3], Pan Zhang[2], Songtao Fan[2], Bingjie Rao[1], Xiaofei Zhang[2], Wenge Guo[2], Shougang Zhang[2], Haifeng Jiang[2]
[1]Key Laboratory of Time and Frequency Primary Standards of Chinese Academy of Sciences, China; [2]National Time Service Center Chinese Academy of Sciences, China; [3]NTSC / School of Astronomy and Space Science, University of Chinese Academy of Sciences, China; [4]School of Astronomy and Space Science, University of Chinese Academy of Sciences, China

Towards Compact Transportable Optical Clock Based on 171Yb+ 344
Ilia Zalivako[3], Ksenia Khabarova[3], Ilya Semerikov[3], Alexander Borisenko[3], Nikolay Kolachevsky[3], Ivan Sherstov[4], Sergei Bagaev[1], Alexey Lugovoy[1], Alexey V. Taichenachev[2], Sergei Chepurov[1]
[1]Institute of Laser Physics, Russian Academy of Sciences, Russia; [2]Novosibirsk State University / Institute of Laser Physics SB RAS, Russia; [3]P.N. Lebedev Physical Institute of the Russian Academy of Sciences / Russian Quantum Center, Russia; [4]Skolkovo Institute of Science and Technology, Russia

Two-Loop Frequency Stabilization Using Concomitant Parameter 348
Valeriy I. Yudin[4], Alexey V. Taichenachev[4], Maxim Yu. Basalaev[3], Thomas Zanon-Willette[1], James Wesley Pollock[2], Moshe Shuker[2], Elizabeth A. Donley[2], John Kitching[2]
[1]LERMA, Observatoire de Paris, France; [2]National Institute of Standards and Technology, United States; [3]Novosibirsk State University, Russia; [4]Novosibirsk State University / Institute of Laser Physics SB RAS, Russia

Reducing Blackbody Radiation Shift Uncertainty in Optical Lattice Clocks 352
Piotr Ablewski, Marcin Bober, Michał Zawada
Nicolaus Copernicus University in Toruń, Poland

Analysis of Optical Atomic Clocks Readouts Aimed on Searches for Dark-Matter Signatures 356
Beata Zjawin[4], Piotr Ablewski[4], Kyle Beloy[2], Sławomir Bilicki[5], Marcin Bober[4], Roger Brown[2], Roman Ciuryło[4], Robert Fasano[2], Hidekazu Hachisu[1], Tetsuya Ido[1], Jérôme Lodewyck[6], Andrew Ludlow[2], William McGrew[2], Piotr Morzyński[4], Daniele Nicolodi[2], Marco Schioppo[3], Mamoru Sekido[1], Rodolphe Le Targat[6], Piotr Wcisło[4], Peter Wolf[6], Xiaogang Zhang[2], Michał Zawada[4]
[1]National Institute of Information and Communications Technology, Japan; [2]National Institute of Standards and Technology, United States; [3]National Physical Laboratory / National Institute of Standards and Technology, United States; [4]Nicolaus Copernicus University in Toruń, Poland; [5]Nicolaus Copernicus University in Toruń / LNE-SYRTE, Poland; [6]Observatoire de Paris, PSL Research University, CNRS, Sorbone Université, France

Telecom Laser Standard for Time and Frequency Transfer 361
Jan Hrabina, Lenka Pravdova, Martin Čížek, Ondřej Číp
Institute of Scientific Instruments of the CAS, v. v. i., Czech Rep.

Kinetics of Atoms Cooled on Clock Transitions: Behavior of Energy and Momentum 364
Roman Ya Il'enkov[1], Alexey V. Taichenachev[2], Valeriy I. Yudin[2], Oleg Prudnikov[1]
[1]Institute of Laser Physics SB RAS, Russia; [2]Novosibirsk State University / Institute of Laser Physics SB RAS, Russia

The Features of Collective Level Shift and Line Broadening in a Fabry-Perot Microcavity and Near the Conducting Surface 369
Alexey Kuraptsev, Igor M. Sokolov
Peter the Great St. Petersburg Polytechnic University, Russia

Development of the Strontium Optical Lattice Clock at National Time Service Center 374
Mojuan Yin[1], Qinfang Xu[1], Yebing Wang[1], Jie Ren[1], Yang Guo[2], Hong Chang[1]
[1]National Time Service Center Chinese Academy of Sciences, China; [2]School of Astronomy and Space Science, University of Chinese Academy of Sciences, China

Towards an 27Al+ Based Optical Clock 377
Ksenia Khabarova, Ilia Zalivako, Ilya Semerikov, Alexander Borisenko, Nikolay Kolachevsky
P.N. Lebedev Physical Institute of the Russian Academy of Sciences / Russian Quantum Center, Russia

Characterization of the Gravity Gradiometer Based on the Sr Optical Clock Transition 381
Liang Hu, Leonardo Salvi, Enlong Wang, Guglielmo Tino, Nicola Poli
Università degli Studi di Firenze, Italy

Two-Stage Stabilization Setup of the Laser Working on 729 nm for Spectroscopy with Cold 40Ca+ Ion 386
Tuan Minh Pham, Martin Čížek, Adam Lesundak, Václav Hucl, Josef Lazar, Ondřej Číp
Institute of Scientific Instruments of the CAS, v. v. i., Czech Rep.

Study on the Effect of ULE Rings on the Vibration Sensitivity of Horizontal Ultra-Stable Optical Cavities 389
Guanjun Xu[2], L. Zhang[1], L. Chen[1], Dongdong Jiao[1], Jie Liu[1], C. Jiang[1], X. Zhang[1], Qi Zang[1], X. Wang[1], Ruifang Dong[1], Tao Liu[1]
[1]National Time Service Center Chinese Academy of Sciences, China; [2]Northwestern Polytechnical University & National Time Service Center, China

The Compact Setup for Laser Cooling and High-Resolution Spectroscopy with Cold 40Ca+ Ions.....392
Ondřej Číp[1], Adam Lešundák[1], Tuan Minh Pham[1], Václav Hucl[1], Martin Čížek[1], Jan Hrabina[1], Šimon Řeřucha[1], Josef Lazar[1], Petr Obšil[2], Radim Filip[2], Lukáš Slodička[2]
[1]Institute of Scientific Instruments of the CAS, v. v. i., Czech Rep.; [2]Palacký University, Czech Rep.

Active Isolator Development of Ultra-Stable Narrow Linewidth Laser of Atomic Clock.....395
Min Xiong[2], Qing Li[2], Lei Liu[2], Guanjun Xu[3], Qicheng Shi[1], Tao Liu[1]
[1]National Time Service Center Chinese Academy of Sciences, China; [2]Northwestern Polytechnical University, China; [3]Northwestern Polytechnical University & National Time Service Center, China

Microwave Acoustic Properties of Diamond Based HBAR at Low Temperatures

Boris P. Sorokin[*†], Gennady M. Kvashnin[*], Andrey S. Novoselov[*†], and Anton B. Shipilov[*†]

Email: bpsorokin1953@yandex.ru genmih@yandex.ru diver841@gmail.com hair_boom@mail.ru

*Diamond electronics department, Technological Institute for Superhard and Novel Carbon Materials, Troitsk, Moscow, Russian Federation

[†]Moscow Institute of Physics and Technology (State University), Dolgoprudny, Moscow region, Russian Federation

***Abstract* — Original technique for low-temperature microwave acoustic investigations of single crystalline diamond by HBAR operating on bulk acoustic wave has been developed for the first time. Study of the temperature and frequency dependences for HBAR's quality factor in experimental samples as Al/AlN/Mo/diamond was carried out in a wide frequency range 0.5-10 GHz and temperatures of 4 - 400 K. The transition between Akhiezer's and Landau-Rumer's acoustic attenuation modes in diamond has been investigated in details.**

Keywords — HBAR; diamond; aluminum nitride; low temperature investigation; microwave acoustic attenuation

I. INTRODUCTION

One of the main trends in physical acoustics, actual both in a fundamental and practical sense, is an achievement of the maximal possible frequencies of excitation and propagation acoustic waves in solids. However, known piezoelectric materials (crystalline quartz, lithium niobate, etc.) successfully used in acoustoelectronic devices on bulk (BAW) and surface (SAW) acoustic waves, at frequencies ~ 1 GHz already show an unacceptable high acoustic attenuation, which increases as a quadratic frequency function (according to the Akhiezer's attenuation regime).

In recent decades, including the beginning of the XXI century, a great attention in acoustics and acoustoelectronics has been paid on composite acoustoelectronic devices based on the piezoelectric layered structures (PLS), consisting of thin-film piezoelectric transducer (TFPT), deposited on the substrate material with low UHF acoustic losses. High-overtone Bulk Resonator (HBAR) differs from conventional piezoelectric resonator due to a small size and high quality factor Q at microwave operational frequencies [1]. Note that HBARs have certain advantages over SAW devices due to less UHF acoustic attenuation, and also because of lower processing requirements in a device production. PLS based composite acoustoelectronic devices do not only increase the operating frequencies but also extend a number of possible applications, such as highly sensitive physical, chemical and microbiological sensors.

A lot of materials have been successfully used as the HBAR substrates: crystalline quartz, fused silica, silicon [2], sapphire [2, 3], and yttrium aluminum garnet [4]. But the highest frequencies of the acoustic overtone excitation didn't exceed 10 GHz. Recently a distinctive progress in the achievement of record resonance frequencies up to 20 GHz has been emphasized by the development of HBAR involved the single crystalline diamond substrate and AlN-based TFPT [5].

High Q is an essential characteristic of any resonator defined its successful practical application of the technique. But the data on Q temperature dependences of diamond-based HBAR are unknown at present time.

The main goal of this paper is to present the results on temperature and frequency dependences of quality factor for diamond-based HBARs and to investigate the peculiarity of the transition from Akhiezer's attenuation mode to Landau-Rumer's one.

II. MICROWAVE INVESTIGATION TOOLS AND LOW TEMPERATRURE MEASUREMENT METHODS

Method of low-temperature (LT) microwave studies of PLS acoustic properties was developed on the vector network analyzer E5071C-2K5 (300 kHz – 20 GHz), the probe station M150, the automated low-temperature system for measuring material properties Quantum Design Physical Property Measurement System EverCool 2 (4 – 400 K), and the non-standard LT adapter (Fig. 1).

To carry out the microwave measurements with HBARs as experimental samples, due to a weak level of the useful signal against the noise, and to obtain the correct quantitative value of the impedance, it must to calibrate the whole measuring circuit consisting of a probe, a microwave cable and a vector network analyzer. Typically, this procedure is performed near the room temperature at the probe station using a special calibration plate. However, for cryogenic temperatures, the use of a probe station was impossible. We have developed the LT measuring adapter that made possible to measure the complex reflection coefficient $\hat{S}_{11}(f)$ of microwave signal obtained by HBAR conjugated with the possibility of calibration procedure starting from cryogenic temperatures up to 400 K. Since all measurements were carried out using a reflected signal, a single-port connection scheme with OPEN-SHORT-LOAD calibration options was selected for measurement and calibration. The calibration elements corresponding to these options were located on the operational disk made of corundum ceramics with contact pads from Au/Pt/Ti produced by the photolithography method. Connection of a measured sample to the contact pads on the operational disk was executed by adhering with a silver paste SPI # 5001-AB Silver Paint,

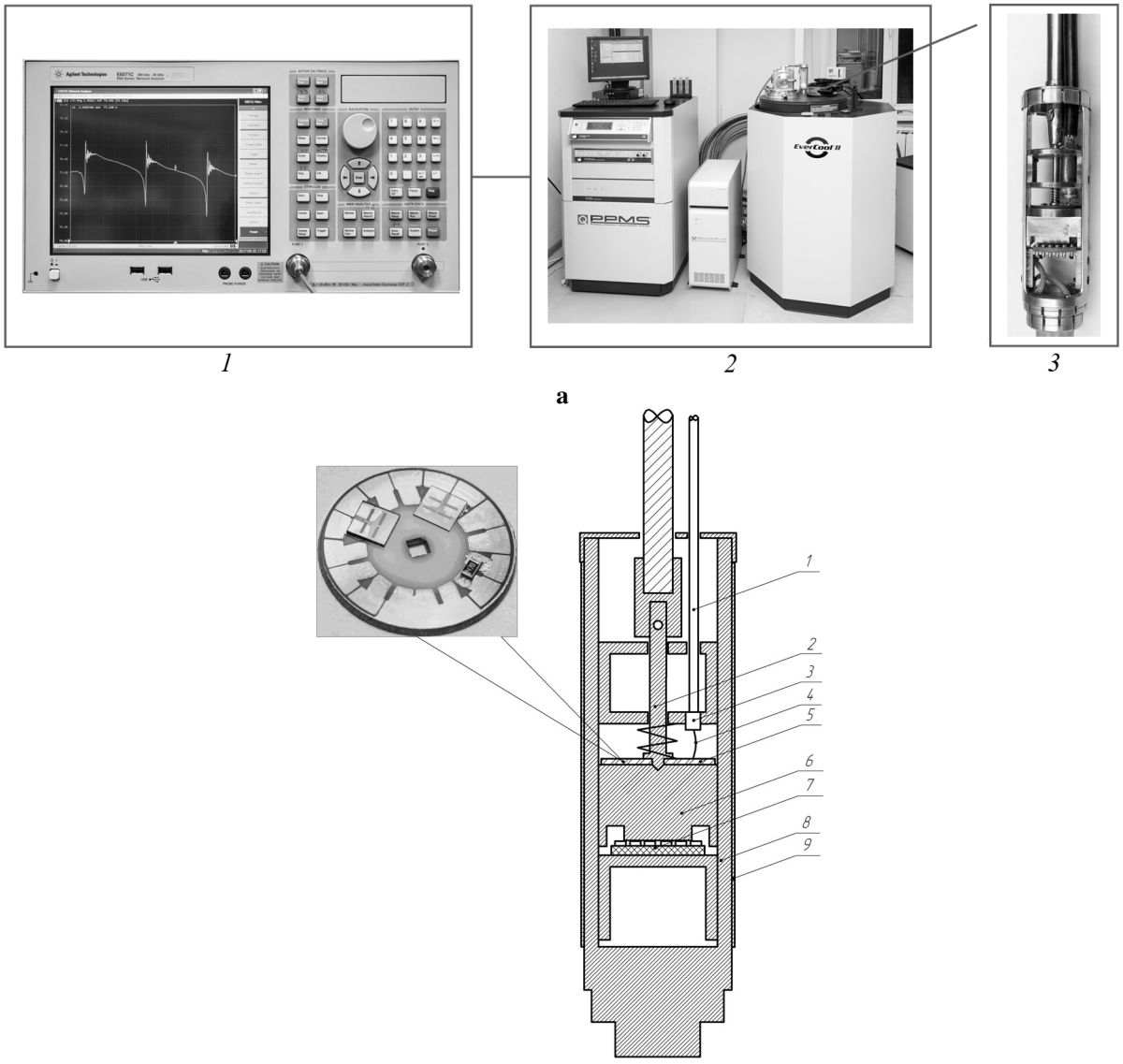

Fig. 1. (a) Block diagram of low-temperature microwave measurements: *1* – vector network analyzer E5071C, *2* – cryogenic control and temperature stabilization system PPMS EverCool II Quantum Design, *3* – LT measuring adapter. (b) Sketch of LT adapter: *1* – microwave cable, *2* – rod, *3* – SMA connector, *4* – sliding contacts, *5* – operational disk with calibration elements and two samples, *6* – disk support, *7* – Pt thermistor, *8* – carcass, *9* – protective screen.

resistant to both low and high temperatures. Simultaneously, two measured samples could be placed on the operational disk. Control measurements on the same sample, carried out at room temperature by M150 probe station or using a low-temperature measuring adapter, were in a good agreement. Method for measuring the sound phase velocity in a substrate was based on the determination of the HBAR's eigen frequencies taking into account the frequency and temperature dependences of the complex reflection coefficient $\hat{S}_{11}(f)$ in the composite resonator. Then, the complex impedance $\hat{Z}_{11}(f)$ of the measuring circuit along with the sample was calculated with the help of vector analyzer software in accordance with the relation:

$$\hat{Z}_{11}(f) = Z_0 \frac{1+\hat{S}_{11}(f)}{1-\hat{S}_{11}(f)} \tag{1}$$

where Z_0 is the input impedance of the microwave circuit equal to 50 Ω. The full impedance $\hat{Z}_{11}(f)$ included the quantity $\hat{Z}_{11t}$ of the microwave cable together with the contacts and HBAR's "pure" impedance $\hat{Z}_{11e}$ as

$$\hat{Z}_{11}(f) = \hat{Z}_{11t}(f) + \hat{Z}_{11e}(f). \tag{2}$$

Required impedance $\hat{Z}_{11e}(f)$ was determined by (2) where the value $\hat{Z}_{11t}$ was experimentally determined at the frequency outside the resonance of one of a given overtone. Taking the $\hat{Z}_{11e}(f)$ values by the vector analyzer software, the frequency dependence of HBAR's loaded quality factor $Q(f)$ was calculated at -3 dB level about the maximum of the $\mathrm{Re}\,\hat{Z}_{11e}$ module, as well as the values of $\mathrm{Re}\,\hat{Z}_{11e}$, $\mathrm{Im}\,\hat{Z}_{11e}$, the phase angle $\varphi(f)$, the group delay time $\tau(f)$, and the Smith diagram. All these parameters quite allowed to evaluate HBAR's resonant processes both in a qualitatively and quantitatively sense in the frequency range from 0.5 up to 20 GHz together with a temperature change within 4 … 400 K.

To determine an absolute value of the BAW phase velocity V in a substrate, first the anti-resonance frequencies $f_{a,n}$, was determined about the maxima of $\mathrm{Re}\,\hat{Z}_{11e}$ module in the vicinity of an odd half-wave resonance of the thin-film piezoelectric transducer, for example designated as $f_{p,k}$. The reason was that the near such frequency, within the substrate thickness approximately an integer $(n - 1)$ of half-waves should be fitted at HBAR's excitation on anti-resonance points $f_{a,n}$. In this case, the HBAR's quality factor tends to a maximum value. So, the phase velocity in the substrate can be calculated by the formula:

$$V \approx \frac{2df_{a,n}}{n-k} \tag{3}$$

where d is the substrate's thickness, and k = 1, 2, 3, ... is the number of the TFPT half-wave resonance. But an accuracy of the this way determination of the phase velocity was strongly depended on the correct definition of an overtone number n in the vicinity of the frequency $f_{p,k}$. In the real experiment it was far from always possible to track all anti-resonances, especially in the low frequency band and bands with high ultrasonic attenuation.

III. Results and Discussion

Temperature and frequency dependences of Q factor are in close connection with phonon-phonon interaction between acoustic wave and assembly of thermal phonons in crystalline lattice. So, a phonon-phonon interaction should be of minimal magnitude at low temperatures. Taking into account the results about so-called quality parameter $Q{\cdot}f$ obtained by authors [6], one can write the relations in Akhieser's and Landau-Rumer's approximation, respectively:

$$Q \times f = \frac{\rho V_a^2 \left[1 + \left(2\pi f\tau\right)^2\right]}{C_v T \gamma^2 \tau} = const,\ \omega\tau << 1, \tag{4}$$

$$Q \times f = \frac{30\rho V_a^5 h^3}{\pi^4 \gamma^2 \left(kT\right)^4} f,\ \omega\tau >> 1, \tag{5}$$

where ρ is the density, V_a is the BAW phase velocity, γ is the anharmonic Grünaisen constant, k is the Boltzmann constant, τ is the time of phonon relaxation, and C_v is the heat capacity. As one can see from (4) and (5), in the Akhieser's mode there is an independence of a quality parameter on the frequency variation, but the quality parameter should increase as a linearly proportional function of the frequency in Landau-Rumer's approximation. Earlier we have obtained the confirmation of such behavior for diamond-based HBAR at room temperature [5].

Further development of a given work was associated with detailed investigation of temperature and frequency dependences of Q factor in a number of diamond-based HBARs placed on substrates of (100), (110), and (111) crystalline orientation (fig. 2). An experimental technique used is described above in the Section II. As a material of substrates the synthetic IIa type diamond single crystal prepared in Technological Institute for Superhard and Novel Carbon Materials has been used. TFPT as sandwich structure Al/AlN/Mo was deposited on the diamond substrate by means of magnetron sputtering equipment AJA ORION 8. Control of preferred crystallite orientation (00·2) in the AlN film was provided by X-ray diffraction equipment Empyrean Panalytic. For example, in "Al/AlN/Mo/(100) diamond" PLS sample there were the thicknesses of layers (in nm) as 135/4350/140, respectively, and the thickness of diamond substrate was equal to 137 microns. Two independent HBARs on a single substrate were differed by aperture, and the squares of top Al electrodes were equal to 20,000 and 80,000 square microns, respectively. Configuration of a top electrode was chosen as pentagon with different length of sides in order to damp the influence of inharmonics.

Measured Q values were changed from 5,000 at low frequencies and higher temperatures up to 40,000 at low temperatures and higher frequencies for the HBAR with (100) substrate orientation. It should be emphasized a general conclusion, that the results on the temperature dependence of diamond's Q-factor obtained at relatively low frequencies below 1 GHz were quite different in comparison with ones measured at the frequencies up to 5 GHz. Note, that such behavior was observed for all the samples regardless the substrate's orientation.

Taking into account the HBAR's acoustic overtones of maximal Q factor only, the temperature and frequency dependences of quality parameter for the acoustic wave propagated along [100] direction can be represented in more convenient form (fig. 3). Here one can see that below 1 GHz the frequency dependences of the $Q{\cdot}f$ are essentially distinctive in comparison with the similar ones measured at higher frequency band, and such difference takes place for all the temperature points. Above ~1 GHz the quality parameter increased as a linearly proportional function of the frequency in accordance with the relation (5) for a number of temperature points. One can assume that above mentioned difference could be explained in terms of changing mechanism of acoustic attenuation from the Akhiezer's type at the frequencies below 1 GHz to the Landau-Rumer's one at a higher frequency band in the single crystalline diamond. Appropriate bands were marked on the fig. 3.

As a result one can estimate by (4) the temperature dependence of the time of phonon relaxation τ in diamond (fig. 4).

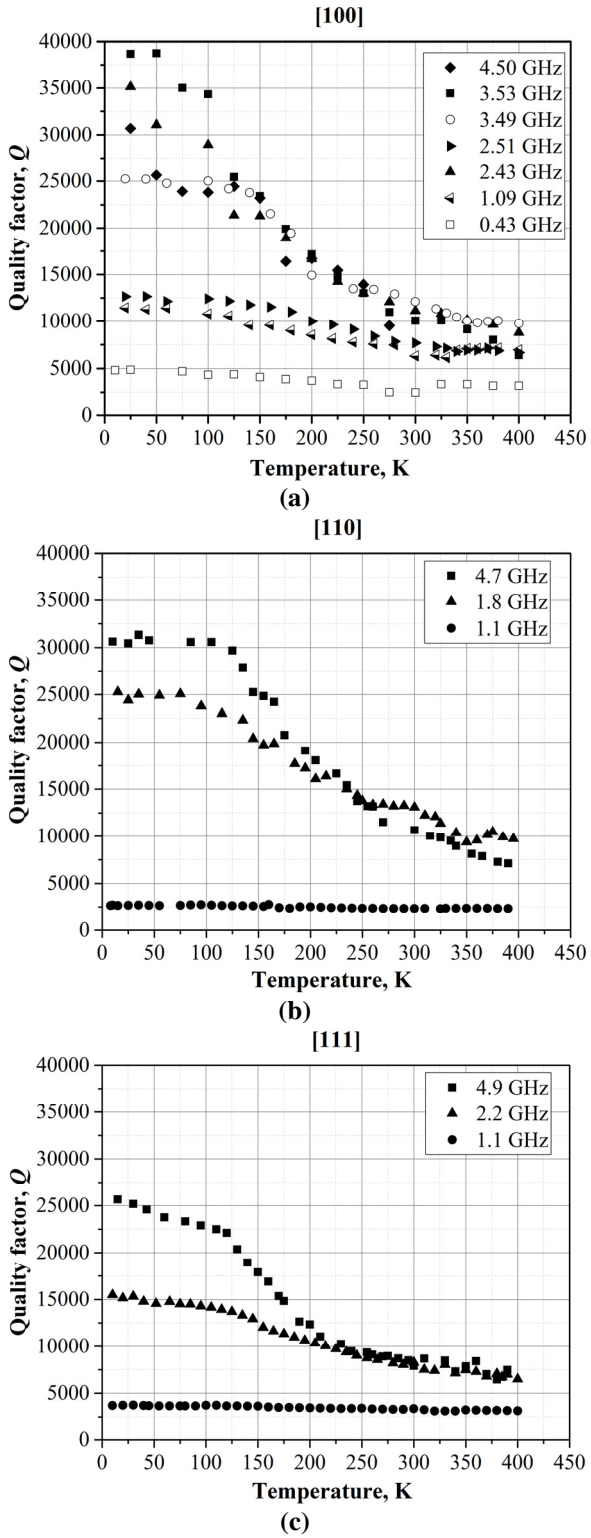

Fig. 2. Temperature and frequency dependences of Q factor in a number of diamond-based HBARs where the longitudinal bulk acoustic wave was propagated along the [100] (a), [110] (b), and [111] (c) diamond's crystalline direction.

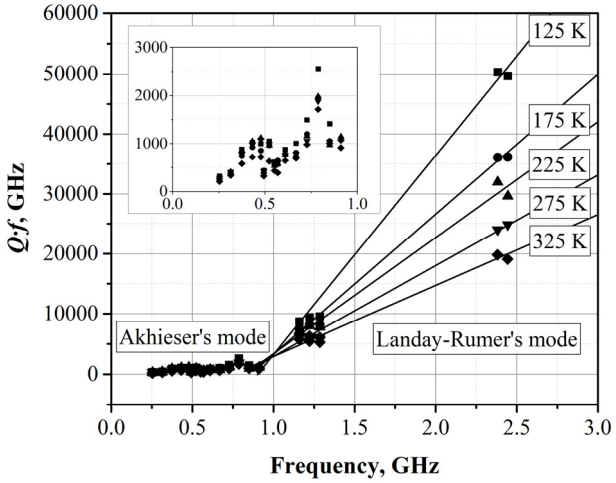

Fig. 3. Temperature and frequency dependences of $Q{\cdot}f$ quality parameter of diamond-based HBAR where the longitudinal bulk acoustic wave was propagated along the [100] diamond's crystalline direction.

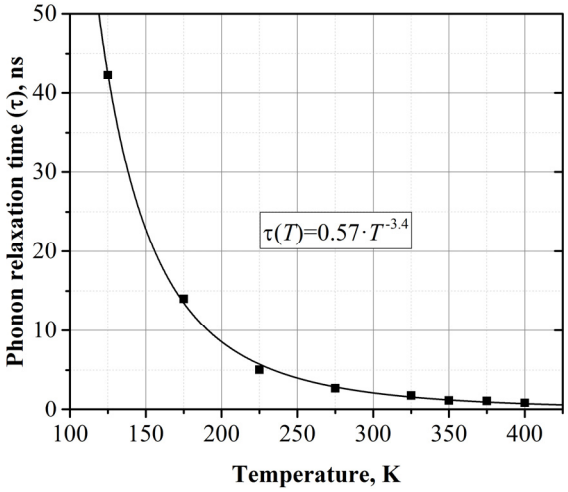

Fig. 4. Estimation of temperature dependence of the phonon relaxation time τ in diamond for the longitudinal bulk acoustic wave propagated along the [100] diamond's crystalline direction.

In the τ calculation the partial Grünaisen constant in diamond for the longitudinal bulk acoustic wave propagated along the [100] crystalline direction was approximately taken as $\gamma \approx 0.85$ [7], and the data on diamond's heat capacity and thermal expansion were taken from the handbook [8].

Note, that the further improvement of such results will be closely concerned with an accuracy increasing of a Q magnitude measurement, especially in the low frequency band below 0.5 GHz and at high temperatures, where the Akhiezer's type of acoustic attenuation in diamond will be predominant. Decreasing of HBAR's operational frequency down to said band is a complicated task now.

But one can emphasize that the threshold between Akhiezer's and Landau-Rumer's modes in diamond should really exist below 1 GHz at room temperature. This fact has an important meaning in the terms of applied application of diamond as a substrate of acoustoelectronic devices, because in

Landau-Rumer's approximation above the said threshold the quality parameter will be increased as a linearly proportional function of the frequency as $Q \cdot f \sim f$, and as a consequence the quality factor Q will be constant at a given condition.

IV. Conclusion

Method of HBAR microwave studies of temperature dependences of such acoustic properties as BAW phase velocity and quality factor in the temperature region 4 – 400 K and frequency band 0.5 – 5 GHz has been developed. It should be emphasized a general conclusion, that the results on the temperature dependence of diamond's Q-factor obtained at relatively low frequencies below 1 GHz were quite different in comparison with ones measured at the frequencies up to 5 GHz. Such behavior was observed for all the samples regardless the substrate's orientation. One can assume that that difference could be explained in terms of changing mechanism of acoustic attenuation from the Akhiezer's type at the frequencies below 1 GHz to the Landau-Rumer's one at a higher frequency band in the single crystalline diamond. In the last case, if taking a given point close to room temperature, the quality parameter $Q \cdot f$ with the frequency variation must change as a linearly proportional function in a manner of $Q \cdot f \sim f$, i.e. the quality factor must not depend on the frequency in that approximation in accordance with (4). That result has earlier been proved for operational frequencies up to 20 GHz at room temperature [5]. Also, this fact is of great practical importance, as it allows realizing acoustoelectronic devices on diamond substrates at microwave frequencies with an acceptable level of acoustic attenuation.

Acknowledgment

This work was supported by a grant of the Russian Science Foundation (project #16-12-10293).

References

[1] K.M. Lakin, "Thin film resonator technology," IEEE Trans. Ultrason. Ferroelectr. Freq. Control, vol. 52, pp. 707–716, 2005.

[2] H. Zhang, W. Pang, H. Yu, and E.S. Kim, "High-tone bulk acoustic resonators on sapphire, crystal quartz, fused silica, and silicon substrates," J. Appl. Phys., vol. 99, pp. 124911, 2006.

[3] L. Baumgartel, and E.S. Kim, "Experimental optimization of electrodes for high Q, high frequency HBAR," in: Proc. 2009 IEEE Intl Ultrasonics Symp. (Rome, Italy), pp. 2107-2110, 2009.

[4] G.D. Mansfel'd, S.G. Alekseev, and N.I. Polzikova, "Unique properties of HBAR characteristics." in: Proc. of the 2008 IEEE Intl Ultrasonics Symp. (Beijing, China), pp. 439-442, 2008.

[5] B.P. Sorokin, G.M. Kvashnin, A.S. Novoselov, V.S. Bormashov, A.V. Golovanov, S.I. Burkov, and V.D. Blank, "Excitation of hypersonic acoustic waves in diamond-based piezoelectric layered structure on the microwave frequencies up to 20 GHz," Ultrasonics, vol. 78, pp. 162–165, 2017.

[6] R. Tabrizian, M. Rais-Zadeh, and F Ayazi, "Effect of phonon interactions on limiting the f·Q product of micromechanical resonators," in Proc. 15 Intl Conf. on Solid-State Structures, Actuators and Microsyst. (Denver, USA), pp. 2131–2134, 2009.

[7] B.P. Sorokin, G.M. Kvashnin, A.V. Telichko, S.I. Burkov, and V.D. Blank, "Piezoelectric layered structure based on the synthetic diamond," in: T. Ogawa (Ed.), Piezoelectric Materials, InTech, pp. 161–199, 2016.

[8] N.B. Novikov (Ed.), "Physical properties of diamond," (in Russian). Handbook, Kyiv, Naukova dumka, 1987, 188 p.

Hysteresis in Phononic Frequency Combs

Adarsh Ganesan
Nanoscience Centre
University of Cambridge
Cambridge, United Kingdom, CB39JJ
ag815@cam.ac.uk

Ashwin Seshia
Nanoscience Centre
University of Cambridge
Cambridge, United Kingdom, CB39JJ
aas41@cam.ac.uk

***Abstract*—This paper reports the experimental observations for hysteresis in phononic frequency combs. The systematic control of drive conditions in different paths presents evidence for non-unique frequency comb solutions for specific drive conditions. These results can thus present an opportunity to tailor frequency comb spectra with desired frequencies and stabilities, utilizing the hysteretic operation.**

Keywords—MEMS Resonator; Nonlinear Dynamics; Phononic Frequency Combs; Time and Frequency Metrology

I. INTRODUCTION

Hysteresis is a feature that is often evidenced in nonlinear mechanisms [1]. Specifically, in this paper, we present the experimental evidence of hysteresis in a nonlinear process leading to phononic frequency combs. The phononic frequency comb represents an array of precisely positioned equidistant frequencies and is generated through the interactions among phonon modes and the drive frequency [2-4]. Such underlying interactions related to the generation of phononic frequency combs are only existent under very specific drive conditions. Now, when hysteresis is also operative, the existence and uniqueness of such frequency combs at a nominally favorable drive condition is lost. This paper demonstrates this specific aspect through the systematic control of drive conditions along different paths. For this study, an experimental device of two mechanically coupled micromechanical resonators is considered. The existence proof of frequency combs in such a device model is experimentally validated in [3]. Now, using the same device structure, the evidence of hysteresis associated with phononic frequency combs is demonstrated in this paper.

II. DYNAMICS

For the demonstration of hysteresis, we consider a system described by the following dynamics.

$$\ddot{Q}_i = -\omega_i^2 Q_i - 2\zeta_i \omega_i \dot{Q}_i + \sum_{\tau_1=1}^{3}\sum_{\tau_2=1}^{3} \alpha_{\tau_1\tau_2} Q_{\tau_1} Q_{\tau_2} + \sum_{\tau_1=1}^{3}\sum_{\tau_2=1}^{3}\sum_{\tau_3=1}^{3} \beta_{\tau_1\tau_2\tau_3} Q_{\tau_1} Q_{\tau_2} Q_{\tau_3} + P\cos(\omega_d t)\,; i = 1,2,3 \quad (1)$$

Here, Q_i, ω_i and ζ_i are the displacement, natural frequency and damping ratio of mode $i = 1,2,3$ respectively. The interactions among modes 1, 2 and 3 are captured by quadratic and cubic terms. Such a coupled dynamical system is then driven by a signal $P\cos(\omega_d t)$. Here, the drive frequency ω_d is such that $\omega_d \cong \omega_1 \cong \omega_2 \cong 2\omega_3$. Since $\omega_d \cong \omega_1 \cong \omega_2$, modes 1 and 2 can be simultaneously excited if ω_d is specified within both of their resonant bandwidths. Now, for high-enough values of P, the strengths of interactions modelled by Q_1Q_3 and Q_2Q_3 nonlinearities can cross the threshold for parametric excitation as set by the damping coefficients ζ_i. Henceforth, the parametric excitation of mode 3 occurs and the frequency corresponding to this excitation is $\frac{\omega_d}{2}$. Hence, the motion of the dynamical system modelled by equation 1 can be captured by ω_d and $\frac{\omega_d}{2}$. However, based on our recently discovered nonlinear process, an array of equidistant frequencies termed 'phononic frequency comb' gets generated instead of mere ω_d and $\frac{\omega_d}{2}$. Such frequencies can be either $\frac{\omega_1}{2} \pm n(\omega_d - \omega_1), \omega_d \pm n(\omega_d - \omega_1)$; $\frac{\omega_d}{2} \pm n(\omega_d - \omega_1), \omega_d \pm n(\omega_d - \omega_1)$ or $\frac{\omega_2}{2} \pm n(\omega_d - \omega_2), \omega_d \pm n(\omega_d - \omega_2)$ and $\frac{\omega_d}{2} \pm n(\omega_d - \omega_2), \omega_d \pm n(\omega_d - \omega_2)$. Here, the spacing of frequency comb is controlled by the resonant frequency of one of the driven modes. In [3], we had experimentally mapped the regimes of these solutions of frequency combs. In this paper, we show that such regimes are hysteretic. In other words, the frequency comb solution at a specific drive condition is dependent on the prior solutions of the dynamical system.

III. EXPERIMENTAL SETUP

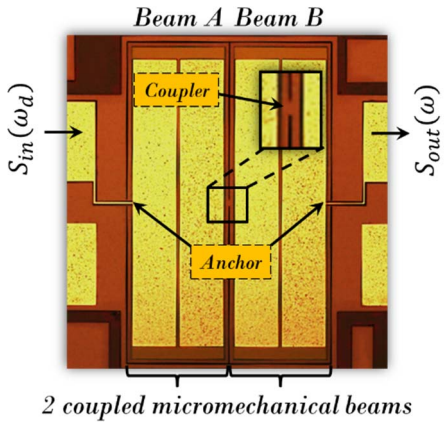

Fig. 1: Two mechanically coupled free-free beam microstructures of dimensions 1100 μm × 350 μm × 11 μm

For the demonstration of hysteresis associated with phononic frequency combs, an experimental system which allows for the frequency matching condition $\omega_d \cong \omega_1 \cong \omega_2 \cong 2\omega_3$ should be considered. The two nearly identical coupled mechanical structures can lead to nearly degenerate eigenmode solutions. Hence, the first part of the condition i.e., $\omega_d \cong \omega_1 \cong \omega_2$ can be satisfied. In this specific device, this initial frequency matching condition is achieved in higher order bulk modes and the modal density is high enough to meet the other half of the frequency matching condition $\omega_d \cong 2\omega_3$. Therefore, two mechanically coupled micromechanical free-free beam structures of dimensions $1100\ \mu m \times 350\ \mu m \times 11\ \mu m$ are considered. The mechanical coupler has the dimensions $20\ \mu m \times 2\ \mu m \times 11\ \mu m$ (Figure 1A). In this predominantly Si-based micromechanical device, $0.5\ \mu m$ thick AlN and $1\ \mu m$ thick Al layers are also patterned for the piezoelectric excitation and electrical interfacing respectively. The AlN and Al patterns on each beam are identical to preserve the symmetry of the coupled device. The length-extensional modes of this coupled device with the component beams moving in-phase and out-of-phase corresponds to the modes 1 and 2 in the equation (1). To excite these modes, the synthesized electrical signal from an arbitrary waveform generator (Agilent 335ARB1U), with the frequency closer to their resonant frequencies, is applied to the Al electrodes and the resulting response of the device is characterized using an oscilloscope (Keysight infiniium 54830B DSO).

IV. Results and Discussion

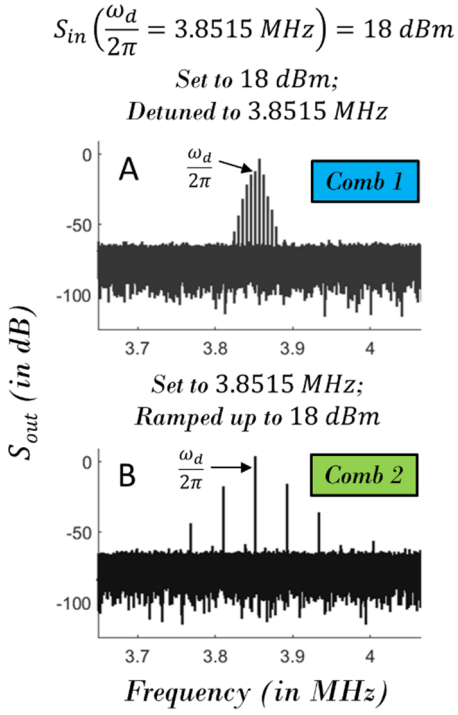

Fig. 2: Two different frequency comb solutions at a specific drive conditions due to hysteresis

When the drive signal is first set to the drive condition – drive power level $S_{in} = 18\ dBm$ and drive frequency $\omega_d = 3.88\ MHz$ and then detuned to $\omega_d = 3.8515\ MHz$, the response corresponds to a frequency comb with small frequency spacing (Fig. 2A). However, when the drive signal is first set to the drive condition – $S_{in} = 0\ dBm$; $\omega_d = 3.8515\ MHz$ and the drive level is increased to $S_{in} = 18\ dBm$, the response corresponds to a frequency comb with large frequency spacing (Fig. 2B). Despite the drive conditions (corresponding to Fig. 2A and Fig. 2B) being the same, the resulting responses are different and are heavily dependent on the prior history of the device. For the ease of discussion, we term the frequency comb with small frequency spacing as 'comb-1' and the one with large frequency spacing as 'comb-2'. As evidenced by Fig. 2A and Fig. 2B, it is possible to visually distinguish the nature of 'comb-1' and 'comb-2' by simply examining the response about the frequency range of $3.61\ MHz$ to $4.11\ MHz$.

To investigate this further, the experiments were systematically conducted in four different ways. In the first run, ω_d is set to a value of $3.82\ MHz$; S_{in} is continuously increased from $-10\ dBm$ to $23\ dBm$ and the electrical responses are probed at the intervals of $1\ dBm$. Once this round is complete, the electrical signal is switched off, then ω_d is increased by $500\ Hz$ and S_{in} is reset to $-10\ dBm$, then the electrical signal is switched on again and the responses for the increasing values of S_{in} are probed. This process is continued until ω_d is incremented to $3.88\ MHz$. At the end of this run, the electrical signal is switched off.

Now, in the second run, ω_d is set to a value of $3.82\ MHz$; S_{in} is continuously decreased from $23\ dBm$ to $-10\ dBm$ and the electrical responses are probed at the intervals of $1\ dBm$. Once this round is complete, the electrical signal is switched off, then ω_d is increased by $500\ Hz$ and S_{in} is reset to $23\ dBm$, then the electrical signal is switched on again and the responses for the decreasing values of S_{in} are probed. This process is continued until ω_d is incremented to $3.88\ MHz$. At the end of this run, the electrical signal is switched off.

In the third run, S_{in} is set to a value of $-10\ dBm$; ω_d is continuously increased from $3.82\ MHz$ to $3.88\ MHz$ and the electrical responses are probed at frequency intervals of $500\ Hz$. Once this round is complete, the electrical signal is switched off, then S_{in} is increased by $1\ dBm$ and ω_d is reset to $3.82\ MHz$, then the electrical signal is switched on again and the responses for the increasing values of S_{in} are probed. This process is continued until S_{in} is incremented to $23\ dBm$. At the end of this run, the electrical signal is switched off.

In the fourth run, S_{in} is set to a value of $-10\ dBm$; ω_d is continuously decreased from $3.88\ MHz$ to $3.82\ MHz$ and the electrical responses are probed at intervals of $500\ Hz$. Once this round is complete, the electrical signal is switched off, then S_{in} is increased by $1\ dBm$ and ω_d is reset to $3.88\ MHz$, then the electrical signal is switched on again and the responses for

the decreasing values of S_{in} are probed. This process is continued until S_{in} is incrementally varied upto 23 dBm. At the end of this run, the electrical signal is switched off.

The nature of spectra observed in each of these runs is classified as 'comb-1', 'comb-2' and 'ill-defined'. While the spectra of 'comb-1' and 'comb-2' are like the ones in Fig. 2A and 2B respectively, a representative 'ill-defined' spectrum is presented in Fig. 3E. We have visually inspected all the spectra corresponding to the four runs and have placed those under the three categories of 'comb-1', 'comb-2' and 'ill-defined'. Figs. 3A-3D show the respective maps. The dotted yellow line in these figures correspond to the parametric resonance threshold. In the region enclosed by this dotted line, self-excitation of mode 3 (equation(1)) takes place. While the comb regimes always feature above the dotted line in Figs. 3A-3D, the regimes need not cover the entire parameter space above the dotted line.

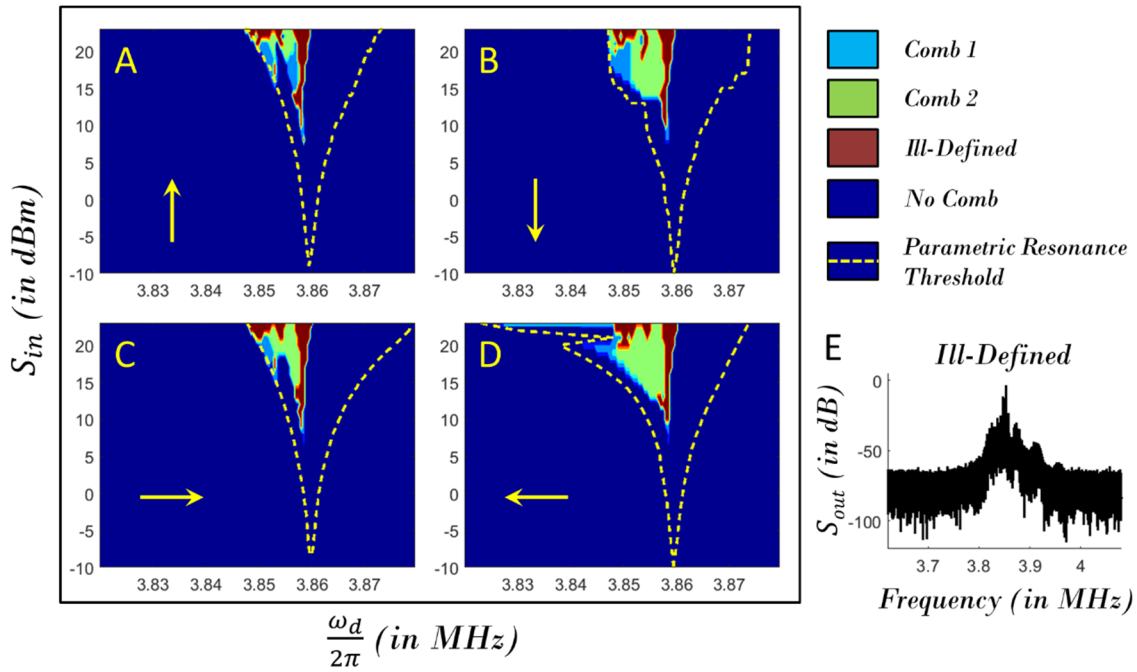

Fig. 3: The operational regimes of frequency combs when the electrical drive level S_{in} and drive frequency ω_d are varied along different paths – A: S_{in} is increased from -10 dBm to 23 dBm for each ω_d; B: S_{in} is decreased from 23 dBm to -10 dBm for each ω_d; C: ω_d is increased from 3.82 MHz to 3.88 MHz for each S_{in}; D: ω_d is decreased from 3.88 MHz to 3.82 MHz for each S_{in}; E: A representative ill-defined spectrum.

To start with, we discuss the hysteretic behavior associated with the parametric resonance threshold lines (Figs. 3A-3D). A large S_{in} and low detuning from parametric resonance is required for crossing the parametric resonance threshold. However, to switch the parametric resonance off, S_{in} should be decreased to a value which is lower than what is required to switch the same on and the level of detuning should be larger than what is required to switch the same on [1]. This aspect can be evidenced by comparing the dotted lines in Figs. 3A and 3B and the dotted lines in Figs. 3C and 3D. The dotted line of Fig. 3B is lower than that of the dotted line of Fig. 3A. Hence, the switch-off threshold value of S_{in} is lower than the switch-on threshold value. The right dotted line of Fig. 3C is shifted towards the right as compared to that of Fig. 3D. Similarly, the left dotted line of Fig. 3D is shifted towards the left compared to that of Fig. 3C. This means that, for switching the parametric resonance off, ω_d should be detuned to a level more than the level for switching the same on. Despite this discussion, the aspects presented in this paragraph are well-known. However, the interesting aspect is the non-monotonous threshold line in Fig. 3D. Within a specific band of S_{in}: $19 - 22$ dBm, the parametric resonance threshold shifts towards the right side. This non-monotonous behavior points to the possible unestablished interplay among the parameters of equation (1) and should also be established in the future through systematic experimental and numerical studies.

The hysteretic behavior associated with parametric resonance can thus present the context for the discussion of hysteresis in phononic frequency combs. Figs. 3A-3D show that the right-bound of comb region is roughly fixed at around $\omega_d = 3.86\ MHz$. However, the left-bound is variable with the parametric resonance threshold. This means that the frequency comb solution is forbidden in the right side of the $\omega_d - S_{in}$ parameter space above the parametric resonance threshold.

For the drive conditions: $\omega_d = 3.852 - 3.858\ MHz$ and $S_{in} = 10 - 20\ dBm$, the frequency combs are only excited when the drive condition is approached from the top (Fig. 3B) or from the right side (Fig. 3D). This means that there also exists

specific ‘on’ and ‘off’ thresholds for frequency combs, which are different from those associated with parametric resonance. Fig. 3D also shows that the transition from ‘comb-2’ to ‘comb-1’ only happens when ω_d is decreased to a value lower than the values which are typically associated with the other runs (Figs. 3A-3C). This can be due to varying ‘on’ and ‘off’ threshold values associated with the ‘comb-2’ process. On the other hand, Fig. 3B shows that the transition from ‘comb-1’ to ‘comb-2’ only happens when ω_d is increased to a value higher than the values which are typically associated with the other runs (Figs. 3A, 3C and 3D).

V. Conclusions

This paper thus validates the hysteretic feature of phononic frequency combs. The hysteresis of frequency combs reveals striking characteristics in comparison to the hysteresis of parametric resonance. The hysteretic operation may also provide additional opportunities to tailor comb spectra with requisite frequencies and stabilities. Like our present work and [2-3,5-12], the micromechanical resonator presents an exemplar experimental platform to study phononic frequency combs and related nonlinear processes. Such experiments can also be relevant to phononic frequency combs based resonant frequency tracking [13].

Acknowledgment

Funding from the Cambridge Trusts is gratefully acknowledged.

References

[1] B. E. DeMartini, J. F. Rhoads, K. L. Turner, S. W. Shaw, and J. Moehlis, “Linear and nonlinear tuning of parametrically excited MEMS oscillators,” Journal of Microelectromechanical Systems 16(2), pp.310-318 (2007).

[2] A. Ganesan, C. Do, and A. Seshia, “Phononic frequency comb via intrinsic three-wave mixing,” Phys. Rev. Lett. 118, 033903 (2017).

[3] A. Ganesan, C. Do, and A. Seshia, “Excitation of coupled phononic frequency combs via two-mode parametric three-wave mixing,” Phys. Rev. B 97(1), 014302 (2018).

[4] L. S. Cao, D. X. Qi, R. W. Peng, M. Wang, and P. Schmelcher, Phononic Frequency Combs through Nonlinear Resonances, Phys. Rev. Lett. 112, 075505 (2014).

[5] A. Ganesan, C. Do, and A. Seshia, “Observation of three-mode parametric instability in a micromechanical resonator,” Appl. Phys. Lett. 109, 193501 (2016).

[6] A. Ganesan, C. Do, and A. A. Seshia, “Phononic four-wave mixing,” preprint arXiv:1610.08008 (2016).

[7] A. Ganesan, C. Do, and A. Seshia, “Excitation of multiple 2-mode parametric resonances by a single driven mode,” Europhys. Lett. 119(1), 10002 (2017).

[8] A. Ganesan, C. Do, and A. Seshia, “Towards N-mode parametric electromechanical resonances,” preprint arXiv:1708.01660 (2017).

[9] A. Ganesan, C. Do, and A. Seshia, “Phononic frequency comb via three-mode parametric resonance,” Appl. Phys. Lett. 112(2), 021906 (2018).

[10] A. Ganesan, C. Do, and A. Seshia, “Frequency transitions in phononic four-wave mixing,” Appl. Phys. Lett. 111, 064101 (2017).

[11] A. Ganesan, C. Do, and A. Seshia, “Observation of phononic frequency combs in a micromechanical resonator,” in 2017 Joint Conference of the European Frequency and Time Forum and IEEE International Frequency Control Symposium (IEEE, 2017), pp. 148–152.

[12] A. Ganesan, C. Do, and A. Seshia, “Coexistence of multiple multimode nonlinear mixing regimes in a microelectromechanical device,” Appl. Phys. Lett. 112(2), 084102 (2018).

[13] A. Ganesan and A. Seshia, “Tracking the resonant frequency of a micromechanical resonator using phononic frequency combs,” preprint arXiv:1710.07058 (2017).

Inkjet printing of thin electrodes for quartz resonators

A. Saadani, P. Lavenus, O. Le Traon
Physics, Intrumentation, Environment, Space department
ONERA
Châtillon, France
amina.saadani@onera.fr

G. Hwang
Department of Microsystems and Nanobiofluidics
C2N-CNRS Univ. Paris-Saclay
Marcoussis, France

F. Sthal
Time and Frequency department
FEMTO-ST, Univ. Bourgogne Franche-Comté, CNRS, ENSMM
Besançon, France

***Abstract*—A first vibrating inertial quartz gyrometer with gold nanoparticles electrodes is presented in this paper. Electrical measurements have shown enhancement of the quality factor compared to standard gyrometers with 200 nm evaporated gold electrodes.**

Keywords—Quartz resonator; Viscoelactic losses; Quality factor; Inkjet printing; Nanoparticles

I. INTRODUCTION

Microelectromechanical systems (MEMS) are used to develop different kinds of sensors: accelerometers, gyrometers, gas sensors… They can be actuated by three means: optical, electrostatic and piezoelectric [1-3] actuation. For the piezoelectric actuation, electrodes are deposited on a piezoelectric material, as quartz. For many years, ONERA has developed monolithic quartz vibrating inertial sensors for vehicle attitude control and navigation. Compared to other piezoelectric materials, quartz has many advantages: high mechanical stability, temperature and pressure stability, collective machining through a wet etching process and low cost fabrication process, easy actuation. For quartz sensors working on flexural vibration modes, with small dimensions and a very high intrinsic quality factor, it has been demonstrated that the quality factor is limited by the viscoelastic behavior of the metallic electrodes needed for the piezoelectric actuation [4]. The viscoelastic losses of the vibrating inertial quartz sensors are proportional to the electrode thickness. This suggests that ideal electrodes have to be very thin but still conductive in order to increase the quality factor and improve the performances of the resonators. A monolayer of graphene has been used as a massless electrode for aluminum nitride resonators and has shown significant improvement of the resonators quality factor [5].

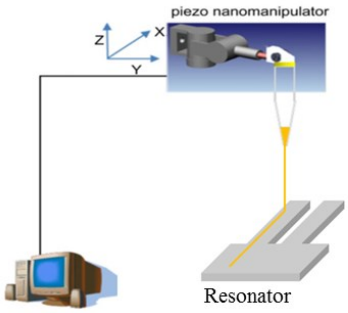

Fig. 1. Conductive ink deposition setup.

Conventional electrodes for the vibrating inertial sensors developed at ONERA are made of evaporated gold by standard photolithography techniques. Electrodes thickness is about 200 nm to assure a good electrical conductivity and charge collect. To reduce this thickness, metallic nanoparticles and low dimensional materials as graphene or carbon nanotubes (CNT) seem suitable for reducing the electrode thickness below 200 nm. With the rise of flexible electronics and the development of inkjet printing techniques [6-7], metallic nanoparticles are widely used to create thin conductive films. Inkjet printing is a rapid, low cost and low waste fabrication technique for patterning two dimensional structures onto a substrate. Droplets of conductive ink are deposited onto a substrate without the need of patterning the substrate by lithographic steps. The wettability of the target substrate has to be controlled to assure a strong adhesion of the deposited ink onto the substrate. Wettability also monitors the resolution of the patterns. The electronic properties of the thin layers are tunable by annealing, by controlling the thickness or by changing the properties of the nanostructures (size, shape, surface chemistry…) [8].

In this paper, a vibrating inertial gyrometer with gold nanoparticles electrodes deposited by an inkjet printing technique on the active part of the resonator is presented. Electrical characterization of this resonator has been conducted and the performances have been compared to the ones with evaporated gold electrodes.

II. FABRICATION PROCESS

The setup [9] used to deposit thin conductive films on a target substrate is presented in Fig. 1. A micropipette with a 6 µm inner diameter is filled with a conductive ink. The substrate is fixed and a piezoelectric manipulator is used to move the micropipette. In this study, commercial ink (ULVAC) of gold

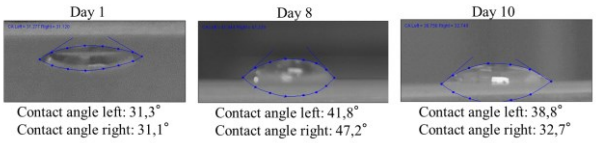

Fig. 2. Contact angles of deionized water droplets onto quartz.

TABLE I. SHEET RESISTANCES OF GOLD NANOPARTICLES.

	Width (µm)	Thickness (µm)	R_s (Ω/□)
TLM1	120	72	4,7
TLM2	134	96	1,6

nanoparticles with a diameter between 2 and 4 nm suspended in toluene are used.

Standard quartz resonators with full evaporated gold electrodes are chemically etched by hydrofluoric acid through a metallic mask. To obtain thin electrodes by inkjet printing of metallic nanoparticles, quartz resonators are chemically etched without evaporated gold layers on the vibrating parts of the gyrometers (i.e. the tuning fork). Afterword, thin electrodes are created by deposition of gold nanoink. An annealing step is required to allow the coalescence and percolation of the nanoparticles in order to create a dense, continuous and conductive film.

The wettability of the target substrates, here quartz resonators, has to be controlled. Once a droplet is ejected from the nozzle, it spreads onto the substrate. The contact angle of the droplet on the substrate is dependent of numerous parameters and defines the hydrophilicity or the hydrophobicity of the substrate. The wettability of the quartz resonators after hydrofluoric etching has been studied. Droplets of deionized water are spread onto the quartz and contact angle measurements are performed with ImageJ. Fig. 2 shows contact angles below 90°. This suggests that quartz resonators have a high surface energy after the resonators fabrication process, allowing the ink droplets to spread along the surface substrate. Furthermore, quartz remains hydrophilic even after several days. Gold nanoink deposition on quartz substrates has been realized and has shown the formation of continuous films with a fine lateral resolution, below 20 µm, which is enough for the realization of electrodes onto quartz gyrometers or accelerometers.

III. RESULTS AND DISCUSSION

A. *Electrical resistance of gold nanoparticles layers*

Transmission Line Measurements (TLM) devices have been realized to determine the electrical resistance of the deposited layers. Current-voltage measurements have been performed with a source meter (Keithley Series 2600B) on two devices with gold nanoparticles films. Table I resumes the width, the thickness and the sheet resistance of the two devices. The resulted films are thinner than the 200 nm obtained by evaporation and the thickness can be monitored by the number of passages, i.e. the number of layers deposited on each other. Low sheet resistances show that the films realized are conductive, suggesting a strong adhesion with the substrate and the formation of dense nanostructures. Sheet resistances are only one order of magnitude higher than a bulk gold layer, which is enough for conductive electrodes.

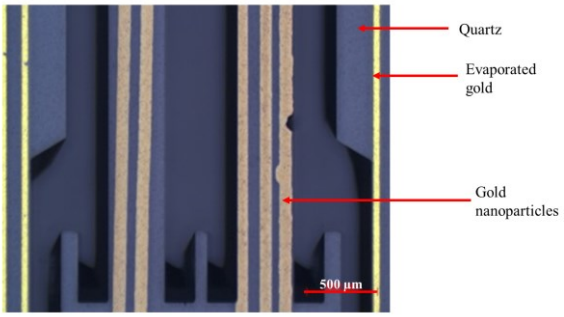

Fig. 3. Gyrometer with gold nanoparticles electrodes.

B. *Experimental results on a gyrometer with gold nanoparticles electrodes*

A first vibrating inertial quartz gyrometer with gold nanoparticles electrodes deposited by inkjet printing onto the vibrating element of the sensor has been realized. The sensing element is a tuning fork which has two flexural modes that are interesting for the vibrating inertial gyrometers: the drive (in-plane) and the sense (out of plane) modes [10]. Both modes have a resonance frequency around 22 kHz. For the piezoelectric actuation and detection of the vibration modes of the gyrometer, three electrodes on both sides of each arms of the tuning fork are needed to optimize the charge collect. Nevertheless, the gold nanoparticles electrodes have been realized only on one side of the resonator and the electrode configuration is not optimal on the left beam (Fig. 4). Electrical measurements have been performed at ambient temperature and under vacuum with an impedance analyzer (Keysight EA990A) on this resonator and a gyrometer with full evaporated gold electrodes for comparison.

Table II resumes the electrical parameters obtained for both resonators when the drive mode is excited. Both modes are measured because of mechanical coupling. Quality factors of the resonator with gold nanoparticles electrodes are enhanced compared to standard resonators for both vibration modes. The drive mode is increased by 26% and the sense mode by 6%. This suggests that the deposited layers induce less damping and energy dissipation than the evaporated gold layers. The partially broken decoupling frame of the resonator may explain the lower enhancement of the sense mode, which is more sensitive to the thermoelastic damping. The drive mode is less sensitive because it is highly isolated from the frame. In terms of resonance frequency, there is no significant shift and the slight difference may be attributed to differences of final geometry after the fabrication process. The thickness of the gold nanoparticles electrodes has still to be determined but

TABLE II. ELECTRICAL PARAMETERS OF GYROMETERS WITH GOLD NANOPARTICLES ELECTRODES AND EVAPORATED GOLD ELECTRODES.

	Gold nanoparticles electrodes		Evaporated gold electrodes	
	Frequency (Hz)	**Quality factor**	**Frequency (Hz)**	**Quality factor**
Drive mode	21825	144640	22429	114820
Sense mode	22889	146850	22945	138460

these results seem promising to get higher quality factors.

IV. Conclusion

A first vibrating inertial gyrometer with gold nanoparticles electrodes has been realized. Compared to standard resonators, with 200 nm evaporated gold electrodes, electrical measurements have shown significant enhancement of the quality factor of the two vibrating modes, despite the poor electrode configuration.

Future work to confirm these results will be conducted. Other materials, as graphene or CNT inks will also be experimented as thin electrodes on gyrometers and accelerometers and the resulted performances will be compared to standard electrodes and gold nanoparticles.

Acknowledgment

This work was supported by the LABEX Cluster of Excellence FIRST-TF (ANR-10-LABX-48-01), within the Program "Investissements d'Avenir" operated by the French National Research Agency (ANR).

References

[1] A. G. Krause, M. Winger, T. D. Blasius, Q. Lin and O. Painter, "A microchip optomechanical accelerometer", Nature Photonics 6, pp. 768–772, 2012.

[2] T. Murakoshi, Y. Endo, K. Fukatsu, S. Nakamura and M. Esashi, "Electrostatically levitated ring-shaped rotational-gyro/accelerometer", Japanese Journal of Applied Physics 42, pp. 2468–2472, 2003.

[3] N. Yazdi, F. Ayazi and K. Najafi, "Micromachined inertial sensors", Proceedings of the IEEE, Vol. 86, No. 8, 1998.

[4] O. Le Traon, S. Masson, C. Chartier and D. Janiaud, "LGS and $GaPO_4$ piezoelectric crystals: New results", Solid State Sciences 12, pp. 318–324, 2010.

[5] Z. Quian, F. Liu, Y. Hui, S. Kar and M. Rinaldi, "Graphene as a massless electrode for ultrahigh-frequency piezoelectric nanoelectromechanical systems", Nano Letters 15, pp. 4599-4604, 2015.

[6] F. Torrisi, T. Hasan, W. Wu, Z. Sun, A. Lombardo, T. Kulmala, G. W. Hshieh, S. J. Jung, F. Bonaccorso, P. J. Paul, D. P. Chu and A. C. Ferrari, "Ink-Jet Printed Graphene Electronics", ACS Nano 6, pp. 2992–3006, 2012.

[7] K. Kordás, T. Mustonen, G. Tóth, H. Jantunen, M. Lajunen, C. Soldano, S. Talapatra, S. Kar, R. Vajtai and P. M. Ajayan, "Inkjet Printing of Electrically Conductive Patterns of Carbon Nanotubes", Small 2, No. 8-9, pp. 1021–1025, 2006.

[8] M.-C. Daniel and D. Astruc, "Gold Nanoparticles: Assembly, Supramolecular Chemistry, Quantum-Size-Related Properties, and Applications toward Biology, Catalysis, and Nanotechnology", Chemical Reviews 104, pp. 293–346, 2012.

[9] G. Hwang, S. Haliyo, S. Régnier, "Infrared-photovoltaic properties of graphene revealed by electro-osmotic spray direct patterning of electrodes", Micro & Nano Letters, Vol. 5, Iss. 2, pp. 140–145, 2010.

[10] A. Parent, O. Le Traon, S. Masson and B. Le Foulgoc, "A Coriolis Vibrating Gyro Made of a Strong Piezoelectric Material", Proceedings of the IEEE Sensors, 2007.

Reactive sputtering of AlScN thin films with variable Sc content on 200 mm wafers

Marta Clement+, Valeriy Felmetsger*, Teona Mirea+, and Enrique Iborra+
+GMME-CEMDATIC ETSI de Telecomunicación. Universidad Politécnica de Madrid, Spain
*OEM Group LLC. Gilbert, AZ, USA
Email: eiborra@etsit.upm.es

***Abstract*— Sc-doped AlN polycrystalline films are attractive active layers for high frequency (GHz range) acoustic resonators owing to the significant enlargement of the AlN piezoelectric activity with the increasing Sc content. To sputter homogenously doped AlScN films on 200 mm Si wafers we use a configurable cathode containing a variable number of embedded Sc pellets to fine tuning the Sc content in the films. The method was implemented in an Endeavor-AT™ cluster tool from OEM Group, adapted for sputtering on 200 mm wafers. 1 µm thick AlScN films with uniform Sc content (around 7 at.%), high crystal quality and good piezoelectric response have been sputtered over 200 mm production-level wafers.**

Keywords—AlScN films; 200 mm silicon sustrates; variation of Sc content.

I. INTRODUCTION

5G technologies require wider bandwidths and higher communication speeds for the new era systems. Part of the bands will be allocated below 6 GHz where electroacoustic filters based on piezoelectric thin films can play an important role. Other bands of higher frequencies (27–40 GHz, and 64–71 GHz) will require the use of microstrip or cavity microwave filters, which size is being reduced for application in mobile devices [1]. Although most of the tools needed for implanting the 5G technology are already mature, significant amount of work is still required in the filter side in order to fulfill the demanding specifications. To tackle the lower frequency bands resonators based on Sc-doped AlN films are being increasingly considered owing to the significant increase of their electromechanical coupling, which can double that achievable with pure AlN mature technology. But not only does future communication electronics require significantly improving the performance of the piezoelectric active films; other applications in the microelectromechanical devices area demand increasing the piezoelectric activity of thin film piezoelectric materials [2].

Since Akiyama [3] first synthesized Sc-doped AlN thin films in 2009, much effort has been devoted to the in-depth understanding of the actual properties of the new active material. Presently, manufacturers are trying to develop reliable deposition processes to bring the new material to production and incorporate it to the actual technology. Alloying Al and Sc presents some difficulties, which precludes the use of compound targets with high Sc contents [4]. However, reactive sputtering of alloyed Al-Sc targets with moderate Sc contents is still the best choice so far to achieve good quality AlScN films of controlled composition. The possibility of varying the Sc content to modulate the piezoelectric response of the films would be very desirable for small volume production of microelectromechanical devices. This would require using alloyed targets of different compositions, which is not economically viable. Co-sputtering from two independent Al and Sc targets is a possible alternative technique although homogeneity over large substrates areas is hardly achieved.

In this paper we present the study of the AlScN thin films with around 7 at.% of Sc atoms obtained from a special target arrangement formed by two concentric ac-powered aluminum targets containing a variable and easily removable number of embedded Sc pellets. This method allows obtaining films with homogeneous and controllable composition on 200 mm silicon production wafers. The film properties were assessed by Rutherford back-scattering spectrometry, X ray diffraction, infrared reflectance and electrical impedance spectrometry.

II. METHODS

A. Sputter deposition method

The deposition system used in this work was an Endeavor-FX sputter tool recently introduced by OEM Group LLC. The tool contains a load-lock module, a transfer module equipped with a vacuum high-speed robot, a pre-cleaning process module equipped with a planarization rf module (PRF) plasma source, which allows substrate pre-cleaning, and up to four sputter modules equipped with S-gun magnetrons.

A special characteristic of the S-Gun magnetron is its dual concentric target arrangement shown in figure 1 [5]. Two independently controlled ring-shaped sputtering targets (diameters 7” and 11”) are arranged so that both targets sit on the same vertical axis being, and the larger outer target is positioned above and outside the smaller inner target. A dc powered S-gun is typically employed for metal and alloy film sputtering, while an ac powered magnetron provides an ideal solution for reactive sputtering of non-conductive films such as nitrides, oxides, and oxynitrides. In the ac version, a 40 kHz alternating current power supply with a floating output is connected directly to the 7” inner and the 11” outer targets (Fig. 1). This cathode arrangement allows stable and arcing-free operation along with the ability to control intrinsic stress in

reactively sputtered films independently from other film properties [5]. The S-gun's capability to deposit highly c-axis oriented AlN films without wafer heating and biasing has been already demonstrated even with very thin thickness [6].

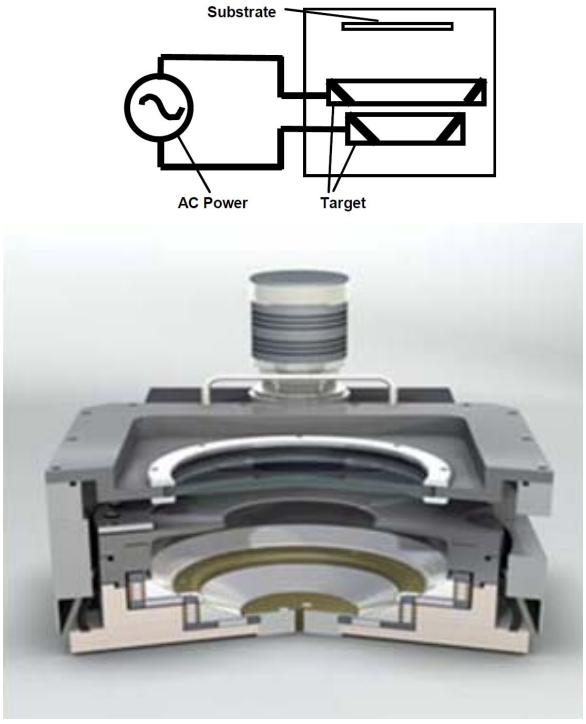

Fig. 1. The dual-target S-gun magnetron: (a) ac-powering schematic diagram and (b) process module arrangement.

The partial substitution of some Al atoms in the wurtzite AlN network by other metal atoms is a conventionally used method for the improvement of some material properties. Alloyed targets allow obtaining such types of films although it is not easy to study composition variations. The dual cathode arrangement of S-gun allows depositing ternary compounds by co-sputtering two single-element targets. However, this method does not succeed in achieving radial homogeneity in the film compositions. In this paper we describe a procedure that enables achieving radial homogeneity along the substrate and offers the possibility of changing the composition of the films in an easy way. This method consists in embedding pellets of the Sc doping material in the two concentric Al targets, as shown in figure 2. The number of pellets allows setting the composition of the film in a certain range whereas their spatial distribution between the inner and outer targets allows controlling the composition radial homogeneity in of the deposited film. With the current arrangement, films with up to 14 at.% of Sc can be deposited. By substituting the Sc pellets by Al ones, the Sc content can be reduced to zero. Higher Sc concentration could be achieved by using denser pellet distributions.

B. Material charcaterization

The structure of deposited films was characterized by x-ray diffraction measurements to explore the preferred orientation of the films (theta-2theta measurements) and the degree of alignment of the microcrystals along the 00·2 direction (rocking curve around the wurtzite c-axis).

Fig. 2. The S-gun magnetron equipped with pure Al targets containing inserted Sc pellets

Intrinsic stress and in-wafer thickness distribution were routinely derived for all wafers by profilometry measurements.

The atomic composition of the films was assessed by Rutherford Back-Scattering (RBS) spectrometry. A 2.3 MeV beam of 4He+ particles with a 5 μC dose was used for the analysis, measuring backscattered particles with a scattering angle of 170º and using 20 keV resolution detector. Figure 3 shows the typical RBS spectra across a wafer radius, indicating the signals corresponding to the different elements. RBS spectra reveal that the composition of the AlScN film is roughly homogenous across the thickness of the films.

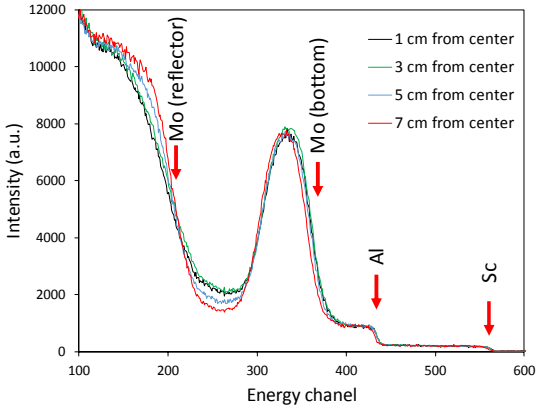

Fig. 3. RBS spectra of a wafer along its radius. Al and Sc arrows point out to the signals corresponding to the surface of the AlScN film. The signal corresponding to the Mo bottom electrode is superimposed to the Al signal. The signal corresponding to the first Mo layer of the reflector appears at lower backscatered energies

Additionally, infrared absorption measurements in the reflectance mode (IRR) were carried out to analyze the fine structure of the longitudinal optical (LO) region of the reststrahlen band [7]. Figure 4 shows a typical IR reflectance spectrum of a 1 μm-thick AlScN film, showing the interference

fringes from which the film thickness was derived, and the reststrahlen band region (around 700 cm^{-1}) showing the characteristic LO absorption band at its edge.

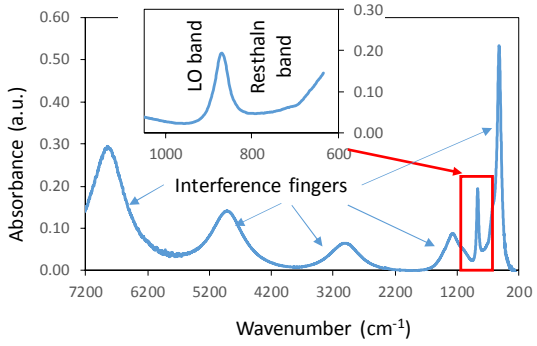

Fig. 4. FTIR spectrum showing the interference fingers due to the multiple reflections in the film. The inset show a detailed view of the reststrahlen band with th LO band in its edge.

Finally, for electroacoustic characterization, we manufactured test bulk acoustic wave (BAW) resonators over simple acoustic mirrors made of five alternating layers of Al and Mo, which provided sufficient acoustic isolation. The quality factor, the material electromechanical coupling factor, the longitudinal sound velocity and the dielectric constant were derived by fitting the electrical measurements with Mason's model [8]. Electrical measurements consisted in the measurement of the reflection scattering parameter S_{11} by using a network analyzer, from which the electrical impedance spectrum was derived. In figure 5 a typical electrical impedance spectrum is shown.

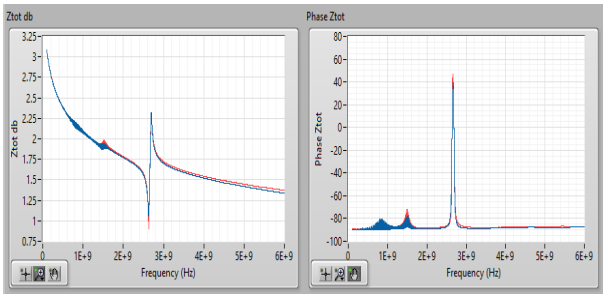

Fig. 5. Electrical impedance spectrum of a typical resonator.

III. RESULTS AND DISCUSSION

The targeted composition of our films was around 7 at.% Sc films. To achieve it, we used 10 out of the 20 possible Sc pellets in the inner target and 14 out of the 28 possible Sc pellets in the outer target. Before the deposition of the films, the substrates were etched in PRF module (Ar plasma at rf power) and then pre-heated to about 350ºC in the sputter module. In addition, the wafers were intentionally heated during the first stage of the deposition process (from 50 nm to 600 nm) to improve the structure of the growing films.

The structure of all analyzed films is wurtzite highly c-axis oriented. The plane spacing of the AlScN films, obtained from the (00·2) diffraction angle, was around 5.00 Å ±0.005 Å, which is a value 5% higher than pure AlN. This indicates that the increase in the piezoelectric activity, which will be commented below, is due to the deformation of the wurtzite structure. The full width at half maximum (FWHM) of the θ/2θ diffraction peak of around 0.15º reveals large size microcrystals and uniformly distributed Sc atoms into the material crystal network. The FWHM of the rocking curve around the (00·2) reflection varies from 1.6˚ to 2˚ in all analyzed samples, indicating a very good crystal quality. Some AlScN films, deposited on the wafers with roughest Al/Mo acoustic reflectors, are those showing the widest rocking curves. Probably the roughness of the substrate is responsible of these high rocking curve widths.

RBS compositional analysis shows an atomic Sc content ranging from 6 at.% to 7.5 at.%, wafer to wafer, which is close to the targeted composition (7 at.%). This content is higher in samples deposited at the highest substrate temperature indicating better Sc incorporation to the films. Homogeneity across the 200 mm diameter of the wafer was always below the 10% of the nominal value, being the Sc content always slightly higher at the edges of the wafer. To avoid this, a restructuration of the Sc pellets into the targets described above should be undertaken.

Infrared absorption in the reflection mode was chosen as a sensitive and nondestructive method to determine the Sc content in the film. Usually the presence of different neighbor atoms induces slight variations in the bond energy between two atoms, which modifies the wavenumber of the associated vibrational modes appearing in the absorbance spectra. Sometimes, these variations are used to determine the amount of doping in the material but the wavenumber shift may also account for other effects, such as stress-induced deformation. In the case of AlScN films we found that there are two different absorption bands with close absorption wavenumbers, which can be attributed to Al-N and Sc-N bonds.

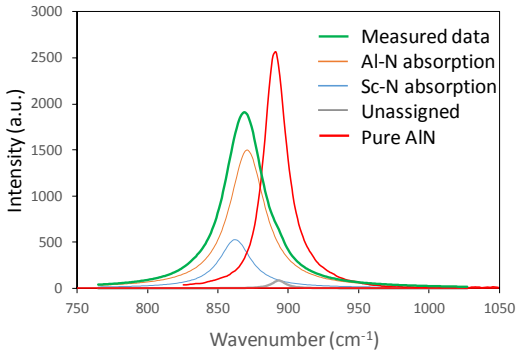

Fig. 6. IR reflectance spectrum of a tipical AlScN layer and its decomposition in gaussian bands associated to Al-N and Sc-N bonds. A small non-assigned band is also present.

The position of these absorption bands varies with the Sc content in the films. This situation is not usual and for this material we can take advantage from it. Figure 6 shows the LO region of the reflection spectrum (depicted as absorbance) is shown for a pure AlN film and for an AlScN films together with their best fits with a combination of Gaussian funtions. Pure AlN spectrum can be fitted with a single one Gaussian

band at 890.89 cm^{-1} while AlScN requires two bands at 862.11 cm^{-1} and 869.4 cm^{-1}, respectively.

The first one is assigned to the Sc-N bonds and the second one to the Al-N bonds. As in many other materials, their particular position in photon energy depends on the neighbors and then, if Sc content varies, these band positions also vary. This effect can be observed in figure 7 that highlights the shift in the position of these bands as a function of the atomic percentage of Sc atoms in the narrow range obtained in this work.

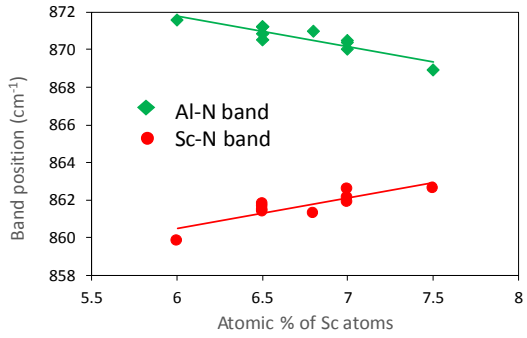

Fig. 7. Al-N and Sc-N associated absorption band positions as a function of the Sc at% in the films. Variations in Sc content is due to differences in deposition conditions and inhomogeneity inside each wafer.

Piezoelectric response of the material was estimated through the measurement of the electromechanical coupling factor (k^2) of BAW resonators derived from the fitting of the electrical impedance spectrum to the Mason's model [8]. This method allows obtaining a value of k^2 characteristic of the material and not of the geometry of the particular resonators if their quality factors (at resonant and antiresonant frequencies) are high enough (> 20). Although the acoustic reflectors used in this work were not optimized, the quality factor of the devices fabricated fulfill this requirement (Q> 50 in all cases) allowing achieving reliable values of material k^2. In all measured wafers, the values of k^2 were greater at the edge of the wafer than at the center. This is not clearly related with the radial variation of the Sc content, nor to the variation of any other accessible parameter of the sputtering system. We attribute this variation to a difference in the ionic bombardment of the surface of the wafer during the deposition process. The use of the independent control of stress and other film parameters [5] make this possibility very likely. Ionic bombardment has other effects in the material like the growth of misaligned grains that lower the piezoelectric response [7,9]. Additional experiments were carried out to obtain films with uniform values of the k^2, as shown in figure 8. The sound velocity of the longitudinal mode for AlScN films resulted to be slightly lower than that of pure AlN. Values ranging between 9200 m/s and 10800 m/s were estimated from the fittings of the resonator response. Similarly, we also found values of the material dielectric constant higher than that of pure AlN. The estimated values were ranged between the pure AlN value of 82 pF/m to 90 pF/m. The estimated values of these parameters (sound velocity and dielectric constant) are very dependent on the thickness of the AlScN layer. Thickness determination by optical profilometry show a variation of around 2 % into the wafer by using a refractive index of 2.088. The thickness obtained by this method can be affected by other parameters making the estimated values of the sound velocity and dielectric constant to be affected by a significant error.

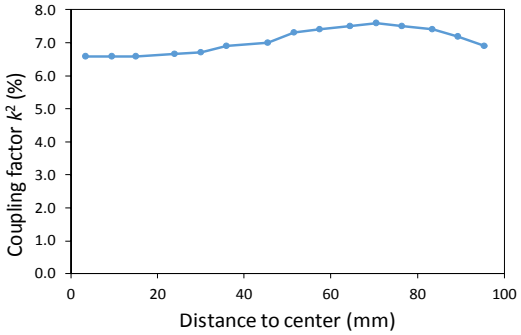

Fig. 8. In wafer radial variation of k^2 of a representative sample.

CONCLUSIONS

AlScN films were deposited by an original PVD method consisting in an AC excited double cathode containing variable number of pure scandium pellets embedded in a pure Al matrix. The number and distribution of pellets in the cathodes allow controlling the film Sc content and the composition uniformity in 200 mm in diameter production wafers. As an example 7 at.% Sc films were deposited under different deposition conditions, yielding reasonably good uniform distribution of Sc in each wafer (within 10% of variation) and a slight variation from 6 at.% to 7.5 at.% of Sc from wafer to wafer. Properties of the films are excellent under a structural point of view and can be improved by making more uniform the ionic bombardment, in their piezoelectric response.

REFERENCES

[1] S. Mahon, "*The 5G Effect on RF Filter Technologies*", IEEE Trans. Semicon. Manufac. 30 (2017) 494-499.

[2] "*Advanced Piezoelectric Materials (Second Edition)*" Edited by Kenji Uchino. (2017). Chapter 14 (*Piezoelectric MEMS Technologies*) pp. 533–574

[3] M. Akiyama, K. Kano, and A. Teshigahara. "*Influence of growth temperature and scandium concentration on piezoelectric response of scandium aluminum nitride alloy thin films*" Appl. Phys. Lett. 95 (2009) 162107.

[4] J. Royset and N. Ryum, *"Scandium in aluminium alloys"*. International Material Reviews, 50 (2005) 19-44

[5] V.V. Felmetsger, P.N. Laptev, and S.M. Tanner, "Design, operation mode, and stress control capability of S-Gun magnetron for ac reactive sputtering", Surf. Coat. Technol., 204 (2009) 840-844.

[6] E. Iborra, M. Clement, J. Capilla, J. Olivares, V. Felmetsger. "Low-thickness high-quality aluminum nitride films for super high frequency solidly mounted resonators". Thin Solid Films, 520 (2012) 3060–3063.

[7] J. Olivares, S. González-Castilla, M. Clement, A. Sanz-Hervás, L. Vergara, J. Sangrador, E. Iborra, "Combined assessment of piezoelectric AlN films using X-ray diffraction, infrared absorption and atomic force microscopy". Diamond & Related Materials 16 (2007) 1421–1424.

[8] J. F. Rosenbaum, Bulk Acoustic Wave Theory and Devices (Artech House, New York, 1945).

[9] Y. Lu, M. Reusch, N. Kurz, A. Ding, T. Christoph, L. Kirste, V. Lebedev, and A. Zukauskaitė. Phys. Status Solidi A 2017, 1700559

Finding the upper mass limit until which gravimetric sensors preserve their original TCF and sensitivity

Teona Mirea, Marta Clement, Jimena Olivares, Enrique Iborra
GMME-CEMDATIC-ETSIT,
Universidad Politécnica de Madrid, Madrid, Spain
Email: teona@etsit.upm.es

***Abstract*—Thin film bulk acoustic wave resonators (FBARs) have undoubtedly overcome the mass sensitivity of their predecessors quartz crystal microbalances. However, the mass sensitivity of FBARs strongly depends on all layers composing their complex structure. It has been proved that the addition of materials with different acoustic impedances at the sensing surface of the device can vary their sensitivity by energy redistribution effects. Such materials have been also used for temperature coefficient (TCF) compensation. Here we aim at studying up to which thickness of an added specific material on AlN-based solidly mounted resonators (SMRs), the initial mass sensitivity and TCF are still preserved. We prove that the sensitivity can be considered lineal up to the deposition of around 100 nm of SiO_2, not affecting the detection of small masses in the pg range. On the contrary, TCF variation with few nm of SiO_2 needs to be accurately controlled since it affects the detection in the pg range. For the detection of heavy masses, these effects can be considered negligible. This study should be performed for each particular case depending on the material accumulated on the device.**

Keywords—AlN-based SMR; mass sensitivity; temperature coefficient of frequency.

I. INTRODUCTION

Thin film acoustic wave resonators working in the GHz range of frequency, particularly the ones based on bulk waves (FBARs), have overcome the mass sensitivity of their quartz crystal microbalance predecessors [1]. However, in contrast to the QCM sensitivity, which only depends on the thick quartz plate characteristics and the ones of the sensed (or deposited) material [2], the sensitivity of FBARs depends on the characteristics of all the films composing the multilayered structure including the one formed by the sensed material [3]. To accurately use FBARs as gravimetric sensors, either in liquid or gaseous media, factors such as the temperature coefficient of frequency (TCF) that accounts for the influence of the ambient temperature on the sensor frequency shifts, needs to be considered. If the TCF value is well-known, it can be used for measurements correction. Numerous studies on the TCF analysis of FBARs have been carried out, most particularly on their zero TCF compensation, which can be achieved by adding a SiO_2 film to the device structure [4]–[6]. Most of them investigate the appropriate SiO_2 thickness to get the full compensation, however none of them discuss the maximum SiO_2 (or other material) thickness up to which the initial TCF does not vary. Another important issue is the variation of the device sensitivity due to the energy trapping effect, i.e. the sensitivity variation with the increased deposited material [3]. Both effects need to be considered in biosensors with complex functionalization or in mass sensors that do not recover the initial state (mass accumulation).

In this work we adopt a reverse view, compared to the existing studies, and we aim at finding the thickness limit of a given film deposited on solidly mounted resonators (SMRs), up to which the initial TCF and sensitivity values of the device are still preserved in a given range. We study both the shear and longitudinal modes, which are typically used for biosensing (liquid) and gas phase sensing applications, respectively. We used both theoretical predictions based on Mason's model, and experimental results. Based on the obtained results we will discuss if SMR gravimetric sensors can be reused or not in different mass sensing applications.

A. Devices

We use SMRs based on fully-insulating acoustic reflectors made of seven alternating layers of SiO_2/AlN, on which we deposit a tilted piezoelectric AlN film sandwiched between two electrodes, Ir and Mo as bottom and top electrodes, respectively (Fig. 1a). The acoustic reflector was designed to properly confine (reflect) the acoustic energy of the shear mode operating at around 1.5 GHz and the longitudinal mode at around 2.5 GHz (Fig. 1b).

B. Characterization

As testing film deposited on the surface of our SMRs we used SiO_2 sputtered sequentially up to 300 nm, which corresponds to 66 µg/cm^2 (0.22 µg/nm·cm^2 considering a density of 2.2 g/cm^3). The mass sensitivity (S_m) and TCF values were tested after each deposition, allowing us to determine if the previous deposited film had an influence on the new structure characteristics. Their values were calculated according to:

$$S_m = (\Delta f) / (\Delta t \cdot \rho_{SiO2}) \quad (1)$$

$$TCF = (\Delta f/f_0) / (\Delta T) \quad (2)$$

where Δt and ρ_{SiO2} stand for the deposited thickness and density of the SiO_2 layer (i.e. the mass of Δt per unit of area), and Δf

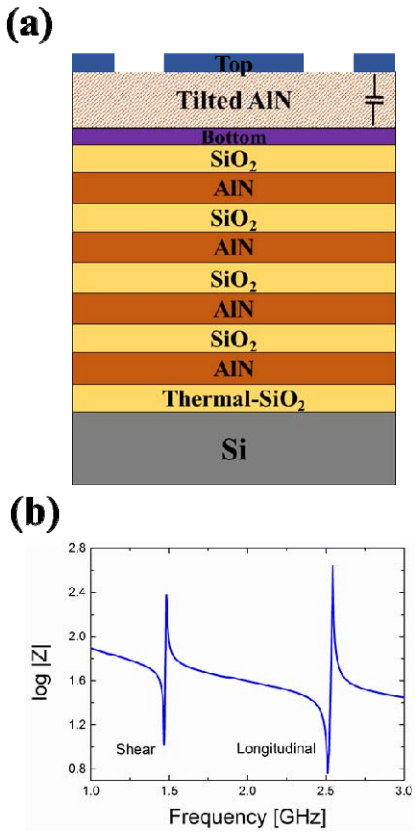

Fig. 1. Cross sectional sketch of the AlN-based SMR used (a) and its electrical impedance response showing the presence of both shear and longitudinal modes.

and ΔT for the frequency and temperature shifts; f_0 is the starting frequency.

For the TCF assessment we subjected the devices to temperatures ranging from 20°C to 100°C using a Peltier cell (Fig. 2) and monitored the device response by tracking the frequency of the admittance real part (Re(Y)) maximum through a specifically designed LabView® application. This procedure is based on acquiring the Re(Y) maximum around the resonant frequency with a bandwidth of 20 MHz and fitting it to a rational function. Floor-noise levels under 500 Hz as a function of time were systematically achieved.

II. RESULTS AND DISCUSSION

Fig. 3 shows the simulated and experimental results of both the longitudinal and shear sensitivities against the previously deposited SiO_2 thickness. That is, x axis values are the thickness of the SiO_2 film that the device had on the top electrode prior to a new sensing event, while Δx values between each point correspond to the sensed thickness, i.e. Δt in Eq. 2. As expected, we observe that the mass sensitivity of the longitudinal mode is higher than for the shear mode, and while the experimental values for the shear mode fit pretty well the simulated results, the experimental measurements for the longitudinal mode have a considerable deviation at lower thicknesses of SiO_2. We attribute this to a possible difference in

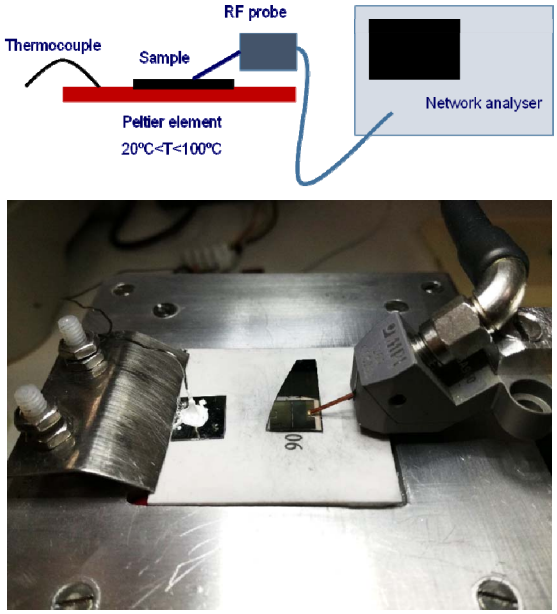

Fig. 2. Measurment set-up for the TCF characterization.

the longitudinal acoustic characteristic of real and simulated SiO_2 films. It is evident that the mass sensitivity starts deviating from its initial value (i.e. without SiO_2) with very few nm of deposited SiO_2. It is reduced up to around 100 nm, value after which starts having a considerable increase (curves decay). For the shear mode, up to approximately 100 nm of deposited SiO_2, the sensitivity moves between $-2.55 \cdot 10^{12}$ Hz·cm^2/g and $-2.7 \cdot 10^{12}$ Hz·cm^2/g, which means an average deviation of around $-0.15 \cdot 10^{12}$ Hz·cm^2/g. Considering that our target would be the detection of $\Delta m = 1$ ng/cm^2, that would imply a shift in frequency of around 2.6. In this case the error in detection $\Delta f_2 - \Delta f_1 = 0.15$ kHz is much lower than our resolution, hence allowing us to consider a constant sensitivity of $S_m = -2.7 \cdot 10^{12}$ Hz·cm^2/g for devices with up to 100 nm of deposited SiO_2. Of course, SiO_2 is just a particular case here and the study should be extended for each material case. The same conclusion could be applied for the longitudinal case, where the sensitivity seems to keep a relatively small variation (according to the simulation) compared to its pronounced variation after 100 nm of deposited SiO_2.

As for the TCF, Fig. 4 reveals that it follows the same tendency as the mass sensitivity. Both the longitudinal and shear TCFs start to deviate from their initial values with few nm of SiO_2. This influence is more pronounced for the longitudinal than for the shear mode. Up to around 120 nm of deposited SiO_2 we move around a relative constant deviation of 2 ppm/°C in both cases. This means variations of 2.8 kHz and 5 kHz for the shear and longitudinal modes, respectively. Considering the values of our sensitivities 2.8 kHz and 5 kHz are already in the range of $\Delta m = 1$ ng/cm^2 detection, hence for accurate small weight detection the temperature of the device should be kept constant to avoid errors. On the contrary, if the target are bigger masses, then this error arising from TCFs variation could be negligible.

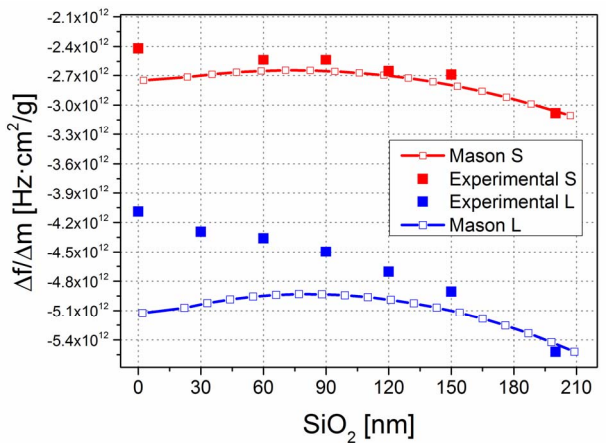

Fig. 3. Sensitivity evolution of the shear and longitudinal mode with deposited SiO_2.

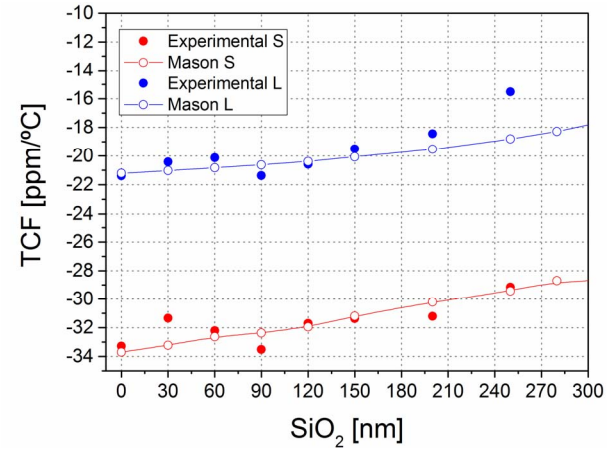

Fig. 4. TCF evolution of the shear and longitudinal mode with deposited SiO_2.

CONCLUSIONS

The mass sensitivity of AlN-based SMRs varies with only few nm of deposited SiO_2 on their active surface. This is in agreement with previous studies where they proved the mass sensitivity of FBARs is increased by adding low acoustic impedance materials as SiO_2. Nevertheless, for a SiO_2 deposition of up to approximately 100 nm the sensitivity can be considered constant even when the target are low masses in the ng/cm^2 range, since the error is less than the detection resolution. The TCF follows the same tendency, with a constant deviation of 2 ppm/°C up to around 150 nm of SiO_2. In this case, this deviation is in the range of the sensitivity resolution, hence for very accurate sensing applications (i.e. detection of very light masses in the ng range) these effects should be taken into account. Depending on the characteristics of the deposited materials, these effects could vary. Hence they should be studied for each particular case. In all cases, if large masses or heavy species are to be detected, these effects can be disregarded, being the sensor available for reuse up to a certain limit.

ACKNOWLEDGMENT

This work was partially supported by Ministerio de Economía y Competitividad del Gobierno de España through project MAT2013-45957-R.

REFERENCES

[1] S. Rey-Mermet, R. Lanz, and P. Muralt, "Bulk acoustic wave resonator operating at 8 GHz for gravimetric sensing of organic films," *Sensors Actuators B Chem.*, vol. 114, no. 2, pp. 681–686, Apr. 2006.

[2] G. Sauerbrey, "Verwendung von Schwingquarzen zur Wagungdiinner Schichten und zur Mikrowagung," *Zeitschrift fur Phys.*, vol. 155, pp. 206–222, 1959.

[3] G. Wingqvist, V. Yantchev, and I. Katardjiev, "Mass sensitivity of multilayer thin film resonant BAW sensors," *Sensors Actuators A Phys.*, vol. 148, no. 1, pp. 88–95, 2008.

[4] B. Ivira, P. Benech, R. Fillit, F. Ndagijimana, P. Ancey, and G. Parat, "Modeling for temperature compensation and temperature characterizations of BAW resonators at GHz frequencies," *IEEE Trans. Ultrason. Ferroelectr. Freq. Control*, vol. 55, no. 2, pp. 421–430, Feb. 2008.

[5] J. Bjurström, G. Wingqvist, V. Yantchev, and I. Katardjiev, "Temperature compensation of liquid FBAR sensors," *J. Micromechanics Microengineering*, vol. 17, no. 3, pp. 651–658, Mar. 2007.

[6] K. M. Lakin, K. T. McCarron, and J. F. McDonald, "Temperature compensated bulk acoustic thin film resonators," in *2000 IEEE Ultrasonics Symposium. Proceedings. An International Symposium (Cat. No.00CH37121)*, vol. 1, pp. 855–858.

A high Q length-Extension Mode Quartz Resonator for MEMS Oscillator and Time-Frequency Applications

Chapellier Paul,
Physics, Instrumentation, Environment,
Space Department (DPHY)
ONERA
Châtillon, France
paul.chapellier@onera.fr

Lavenus Pierre
DPHY
ONERA
Châtillon, France
pierre.lavenus@onera.fr

Dulmet Bernard
Time and Frequency Department
FEMTO-ST, UMR CNRS 6174
Besançon, France
bdulmet@ens2m.fr

Le Traon Olivier
DPHY
ONERA
Châtillon, France
olivier.le_traon@onera.fr

***Abstract*—This paper presents recent advances on two-dimensional Length-Extensional Modes (LEM) quartz micro-resonators providing high quality factor (Q) on resonances at a fewMHz. The resonators have been manufactured with a two teps Deep Reactive Ion Etching (DRIE) in a wafer level process reducing costs for collective realization. Samples vibrating at 2.2 and 3.0 MHz on the fundamental mode have shown promising results with very high Q exceeding 200,000. Best result obtained so far were obtained on a partial mode vibrating at 6.6 MHz reaching a Q of 250,000. The collective process, advantages of quartz and high Q make these resonators a promising candidate for Time & Frequency applications.**

Keywords—Quartz resonator, Time & Frequency, MEMS, DRIE.

I. Introduction

In order to reach the quantum limit, ONERA developed a resonator exploiting a three dimensional length extension mode during a previous research [ref]. The resonator showed an extremely high Q of 2x106 at 4.0 MHz reaching a Q.f product of 8x1012 Hz [1] near the quantum limit of quartz which is estimated around 3,2x1012 Hz in the Akhiezer losses regime [2]. This resonator is shown in Fig.1, its extremely high Q made it a potential candidate for Time-Frequency applications, but the resonator was bulky (10x10x0.5mm3) and used optical detection involving a relatively complex mode of operation.

To aim a reduction in size, weight and power consumption, ONERA developed a new design of resonator based on two dimensional (2D) LEM.

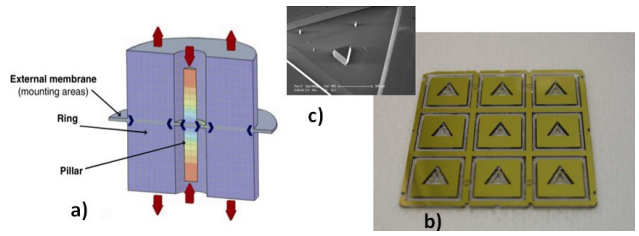

Fig. 1. a) Concept of the 3D-LEM: a ring around the pillar with an out of phase length-extension vibration, b) 1.5-inches square quartz wafer including 9 3D-LEM made using wet etching, c) detail of the micro-pillar.

II. 2D-LEM Design, Quality Factor and Process Flow

A. 2D-LEM design

The 2D-LEM consists of a beam vibrating in extension-compression in the Y-axis due to an electric field along the X-axis as illustrated in Fig.2. Gold electrodes are patterned along the Y-axis and are deposited only on one face due to the ease of manufacturing process: better coupling would be obtained with electrodes on both faces and the best coupling occurs with full electrodes in the Y-Z plane, creating the most intense electric field along X-axis. The design is optimized to reduce Poisson effects in order to trap the strain energy inside the vibrating part and thereby reduce energy losses through tethers to ensure the best intrinsic quality factor.

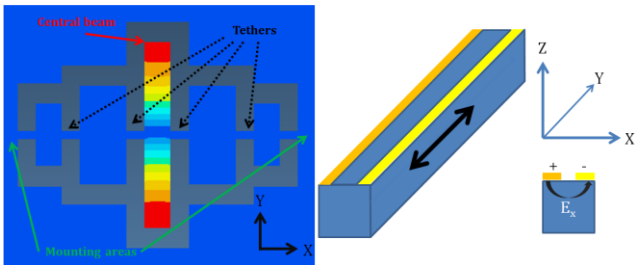

Fig. 2. Left: amplified nodal displacements of the central beam during its length-extension mode vibration, right: practical array of electrodes realized.

The relation between resonant frequency, modes and length of the beam is given by equation (1)[3]:

$$f_{2n+1} = 2{,}72.(2n+1)/L \text{ MHz} \quad (1)$$

Where n is mode number n=1,2,3… and L is the total length of the central beam in mm. The product $f_n.L$ is theoretically constant, which is in agreement with simulations using the Finite Elements Method (FEM) for several sizes of resonators vibrating at 2.21, 2.96 and 4.42 MHz. It is possible to use higher frequencies thanks to partial modes, but these modes should exhibit higher motional resistance (R_m) because the electrodes array is optimized for the fundamental mode (n=0), however first harmonic (n=1) has shown promising results.

B. *Expected quality factor*

The quality factor of a resonator is defined as the ratio of stored energy over the energy dissipated per cycle via several damping mechanisms.

$$Q^{-1} = \sum Q_i^{-1} \qquad (2)$$

Thanks to the vibration mode, the specific decoupling and the vacuum environment, only the damping due to the viscosity of the gold electrodes, noted Q_{visc} is expected to limit Q. In previous work [4] Q_{visc} has been estimated around $6{,}0.10^5$ for a 90 µm-thick 2D-LEM with a slight frequency dependency.

C. *Process flow*

As the dimensions of the 2D-LEM shrink, standard wet etching of quartz using hydrofluoric acid (HF) and ammonium fluoride (NH_4F) is not suitable due to the strong anisotropy and faceting [5]. A process using two steps of DRIE of quartz has been developed. The patterns of resonators are made during the first step while etching through cavities permits to release the structures during the second step. The process is summarized on Fig. 3.

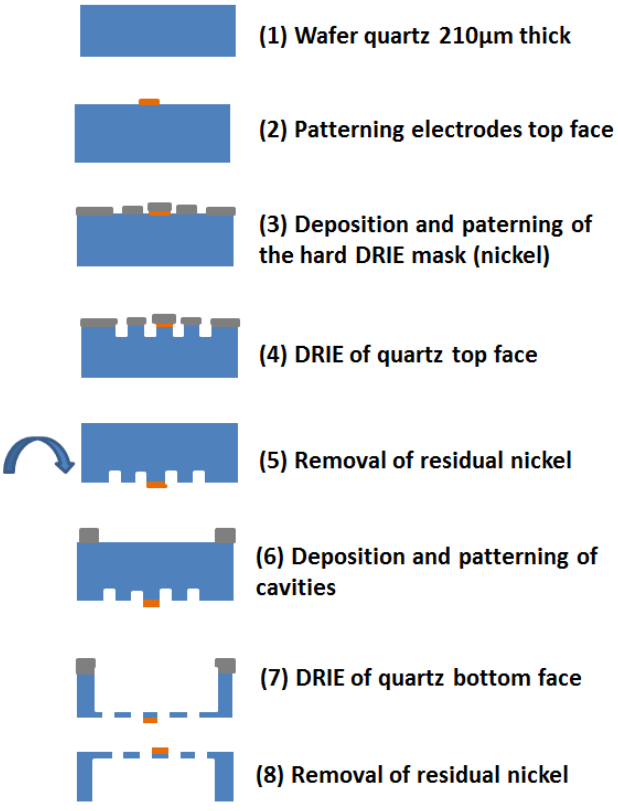

Fig. 3. Process flow using two DRIE steps.

A thick sputtered nickel mask of 3µm is used; achieving selectivity around 45 in the fluorocarbon based assisted plasma etching. One must note that the resonators with different lengths (and different resonant frequencies) will have the same thickness modulated to some microns by the Aspect Ratio Dependent Etching effect [6].

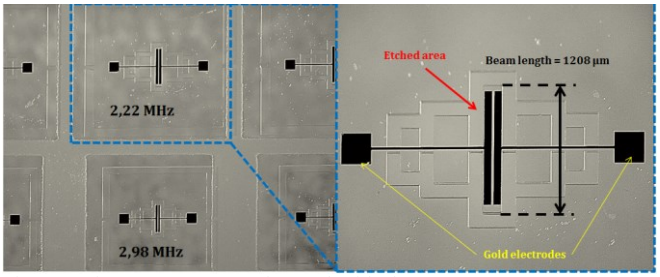

Fig. 4. Left: resonators manufactured with the two DRIE steps process, top resonators vibrating at 2.22 MHz and bottom at 2.98 MHz for the fundamental mode. Right: focus on a 2.22 MHz resonator.

III. Results and Discussion

A. *Product $f_1.L$*

Resonators vibrating at 2.22 and 2.98 MHz have been successfully manufactured using the process described above, as illustrated in Fig.4, which pertains to a Z-cut 210 µm thick quartz wafer thinned down to 90 µm. Average products $f_1.L$ of 2.68±0.01 MHz.mm for the 2.22 MHz resonators and 2.72±0.01 MHz.mm for the 2.98 MHz resonators have been found, which is in good agreement with analytical model and simulations.

B. *Mechanical parameters*

Measurements of equivalent electrical parameters using a standard Butterworth-Van Dyke (BVD) model have been performed with impedance analyzer (Keysight EA990A) under atmospheric pressure and vacuum (10^{-4} mbar).

1) *Fundamental mode*

The best resonators have shown high Q of 250,000 at 2.2 MHz and 210,000 at 3.0 MHz. Fig. 5 shows experimental data of the impedance module and phase of a 2.2 MHz vibrating resonator under atmospheric pressure and under vacuum with corresponding fits.

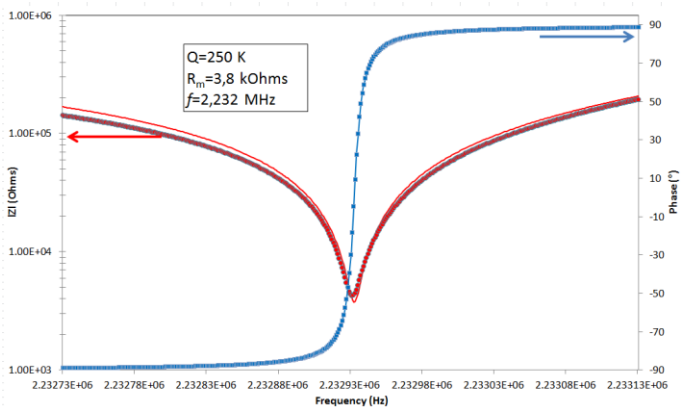

Fig. 5. Experimental data of 2.2 MHz LEM resonator for fundamental mode: in blue squares phase of impedance, in red circles impedance module. Straight lines are the corresponding fit using standard BVD model.

These results show improved *Q.f* product of 20 % in comparison with previous works on similar design, reaching $6.3.10^{12}$ Hz. As it was found in previous work, the quality factor seems to decrease with increasing frequency as shown in Fig. 6.

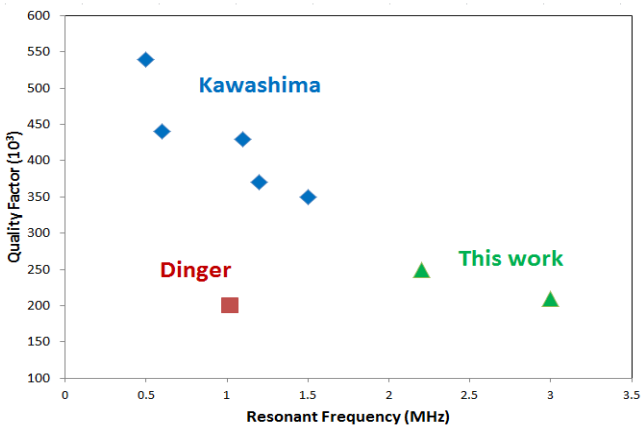

Fig. 6. Quality factor versus resonant frequency of previous works on similar devices, square: data from [3], diamond data from [8], triangles: this work.

2) Partial mode

First harmonic has been also characterized, it has shown high Q even at atmospheric pressure exceeding 60,000 at 6.6 MHz and a very high Q of 250,000 under vacuum, exhibiting a motional resistance of 12 kOhms, reaching a *Q.f* product of $1,7.10^{12}$ Hz. Impedance module and phase are shown in the Fig. 7. Resonators vibrating at 3.0 MHz, first harmonic around 8.9 MHz, did not show such good performances with Q around 40,000 at atmospheric pressure and only 70,000 under vacuum.

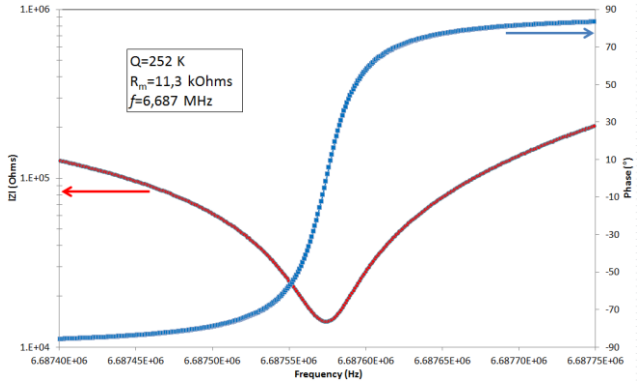

Fig. 7. Experimental data of 2.2 MHz LEM resonator for first harmonic mode: in blue squares phase of impedance, in red circles impedance module. Straight lines are the corresponding fit using standard BWD model.

It should be noted that the electrode array has been optimized for the fundamental mode. An adapted electrode array would reduce R_m.

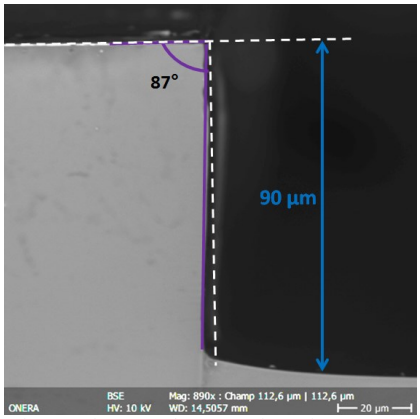

Fig. 8. SEM picture of a cross beam section of test pattern etched with current quartz DRIE used for 2D-LEM resonators. A deviation of 3° has been measured.

C. Analysis

Experimental quality factors of the fundamental mode are half of the expected values, meaning that there exists at least another limiting damping mechanism. It appears that the current used DRIE of quartz recipe cannot realize the perfect verticality of the sidewalls as illustrated in the scanning electron microscopy (SEM) of a beam section Fig. 8 on which it can be seen a deviation of the vertical angle close to 3°, best result in term of verticality known is 89° or 1° deviation [7].

Taking into account this imperfection due to the manufacturing process in the simulations, the quality factor Q_{anchor} which is the ratio between the strain energy and the energy leakage through the mounting areas decays quickly as the flank angle increases. As illustrated in Fig.9, Q_{anchor} is greater than 10^{10} for an ideal structure and decreases to reach around 550,000 for a resonator vibrating at 2.2 MHz and 430,000 at 3 MHZ.

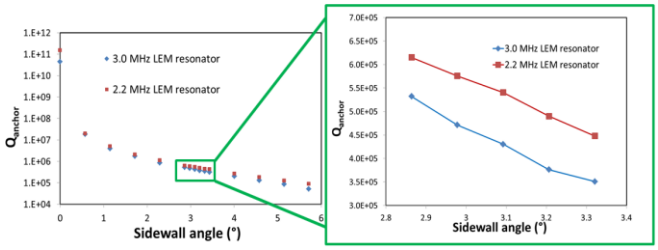

Fig. 9. Simulation using FEM of the Q_{anchor} vs sidewall angle for 2.2 and 3.0 MHz 2D-LEM resonators and a focus on the 3° region on the right.

In the simulations, the value of the sidewall angle is framed by measurement uncertainties. Values from analytical model, simulations and measurements are reported in Table 1.

Table 1. Summary of the expected quality factor values of the main dissipation mechanism and experimental measurements.

Resonator frequency (MHz)	**Q_{anchor} (10^3) for 3° (FEM)**	**Q_{visc} (10^3)** [4]	**$Q_{expected}$ (10^3)**	**$Q_{experimental}$ (10^3)**
2.2	**490-576**	**607**	**263-286**	**250**
3.0	**376-471**	**571**	**232-265**	**210**

The values expected by taking into account the flank angle are in good agreement, somehow 10 % lower with the experimental values and reflect the decrease of the quality factor with the increase of the resonant frequency.

IV. Conclusion

2D-LEM resonators vibrating at 2.2 and 3.0 MHz have been successfully manufactured using a two DRIE steps process exhibiting high quality factors exceeding 200,000 for the fundamental mode and 250,000 for the first harmonic at 6.6 MHz. Major damping mechanisms have been identified and quantified. Future work will be focused on optimizing the etching recipe to increase Q_{anchor} and adapting electrodes technology as well as the characterization of temperature sensitivity and phase noise measurement.

Acknowledgment

This work is supported by the Centre National d'Etudes Spatiales (CNES).

References

[1] O. Le Traon, M. Bahriz, O. Ducloux, S. Masson, and D. Janiaud, "A Micro-Resonator for Fundamental Physics Experiments and its Possible Interest for Time and Frequency Applications," *Jt. Conf. IEEE Int. Freq. Control Eur. Freq. Time Forum Proc.*, 2011.

[2] S. Ghaffari *et al.*, "Quantum limit of quality factor in silicon micro and nano mechanical resonators.," *Sci. Rep.*, vol. 3, p. 3244, 2013.

[3] R. J. Dinger, "A minature quartz resonator vibrating at 1 MHz," *Proc. 35 th Ann. Freq Control Symp.*, pp. 144–148, 1981.

[4] B. Bourgeteau-verlhac, R. Lévy, T. Perrier, P. Lavenus, J. Guérard, and O. Le Traon, "Gold Thin Film Viscoelastic Losses of a Length Extension Mode Resonator."

[5] R. Pelle, H. Christer, V. K. Ilia, and B. Ylva, "Etch rates of crystallographic planes in Z -cut quartz - experiments and simulation," *J. Micromechanics Microengineering*, vol. 8, no. 1, p. 1, 1998.

[6] P. Chapellier, P. Lavenus, C. Gageant, and O. Le Traon, "Aspect ratio dependent etching in advanced Deep Reactive Ion Etching of quartz," *2017 Symp. Des. Test, Intergation Packag. MEMS MOEMS*, pp. 4–9, 2011.

[7] A. Kamijo, S. Monoe, N. Murayama, T. Saito, and N. Kimura, "Wafer-level quartz dry etching technology," *IFCS 2014 - 2014 IEEE Int. Freq. Control Symp. Proc.*, vol. 1035, pp. 6–9, 2014.

[8] H. Kawashima and M. Nakazato, "Variational analysis of new shape length extensional mode quartz crystal resonator taking account of lateral motion," *Proc. 35 th Ann. Symp. Freq. Control*, pp. 378–386, 1981.

Consideration and implementation of inherent losses in SAW devices

Marianne Sagnard*†, Thierry Laroche†, Sylvain Ballandras†
*Femto-St, Time and Frequency department, Besançon, France
†Frec|n|sys, Besançon, France
Emails: marianne.sagnard@frecnsys.fr, thierry.laroche@frecnsys.fr, sylvain.ballandras@frecnsys.fr

***Abstract*—In the past decades, numerical simulation tools have been improved to allow more efficient designs of surface acoustic wave (SAW) devices. Indeed, many phenomena are now taken into account to most closely evaluate the behaviour of the system in real environment. In keeping with these previous works, this paper is devoted to the raising of three current approximations that lead to imprecisions in the computations. As a consequence, this study uses a physical model (Kelvin-Voigt internal damping) to take into account the internal behaviour of the material under stress or strain. Furthermore, losses related to the polarization of the material and to the residual conductivity in the piezoelectric are no more considered as null. After a software implementation of these phenomena, numerical simulations are conducted and calculation/test correlations are carried out.**

I. Introduction

Surface acoustic wave (SAW) devices are often used in various industry sectors, such as defense, aeronautics, telecommunications. Nowadays, highly reliable sensors and filters can be manufactured using SAW technologies [1], [2], [3]. Among the numerous advantages they provide, we can notice their small sizes, their sustainability in harsh environments due to the absence of batteries and wires and to the remote monitoring of physical quantities such as pressure, temperature or strain.

In the past decades, numerical simulation tools have been improved to allow more efficient designs of SAW devices [4], [5]. Indeed, many phenomena can now be taken into account such as the electrical resistance due to the device probing, the electrode resistivity [6], the transverse modes [7] etc to most closely evaluate the behavior of the system in real environment.

In keeping with these previous works, this paper is dedicated to the raising of three current approximations :

1) The wave propagates without any loss at the surface of the material ;
2) Piezoelectric materials are perfectly dielectric (conductivity $\sigma = 0\ S.m^{-1}$)
3) Polarization of the material is performed without any loss (the effective permittivity ε is real).

Because they are approximations, considering these statements as true involves imprecisions in the computations. For instance, the gap between current numerical analysis and the effective frequency response of a delay line can be notice on figure 1.

As a consequence, this study uses a physical model (Kelvin-Voigt internal damping [8]) to describe the internal behavior of the material under stress or strain. Here, the strain is imposed by the passing of the SAW. Furthermore, losses related to the polarization of the material and to the residual conductivity in the piezoelectric are no more considered as null.

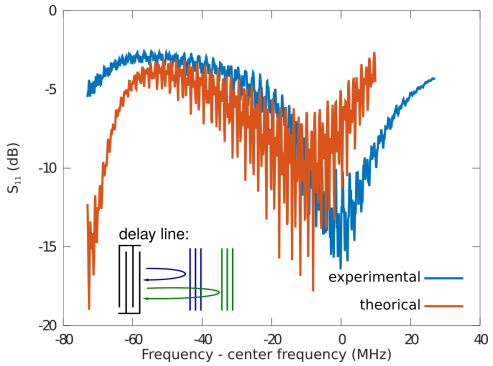

Fig. 1. Highlighting of the difference between the numerical analysis of SAW devices when the model doesn't take into account propagation, dielectric and polarization losses and the measure of the manufactured device

Once the equations allowing to take the "non perfect" character of the material into account are implemented in the software, numeral simulations are conducted. Then, calculation/test correlations based on a very well known piezoeletric material, the Quartz, are carried out.

II. Losses due to viscoelasticity

In the first place, loss phenomena are briefly reminded and equations which describe the behavior of the system are set down.

Surface acoustic wave propagation causes a displacement of the material which consequently undergoes both stress and strain. Therefore, frictional forces of the material on itself come out inside the substrate. This phenomenon appears through losses and, as a consequence, a decrease in the quality factor Q of the device.

Kelvin-Voigt internal damping model (figure 2) provides a good approximation for the internal friction. In fact, it highlights that the behavior of the material is no more ruled only by its Young modulus ξ but both by this constant and by a viscoelasticity coefficient η.

This model is valid for an isotropic, homogeneous material on which a stress T is applied in one direction. The mathe-

978-1-5386-5620-4/18/$31.00 ©2018 IEEE

matical relationship between stress, strain S and deformation rate $\dot{S}$ can be written as follow :

$$T(t) = \xi S(t) + \eta \dot{S}(t) \tag{1}$$

Using the Fourier transform (with ω, the angular frequency) and because ξ and η don't depend on time, (1) becomes:

$$\begin{aligned} \widetilde{T}(\omega) &= \xi \widetilde{S}(\omega) + j\omega\eta \widetilde{S}(\omega) \\ &= (\xi + j\omega\eta)\widetilde{S}(\omega) \\ &= c^* \widetilde{S}(\omega) \end{aligned} \tag{2}$$

In this equation, $c^* = \xi + j\omega\eta$ is the complex elastic coefficient of the material. ξ is still related to the elastic behaviour of the material and the added imaginary part $\omega\eta$ corresponds to the losses due to the strain. These losses are frequency dependant.

Equation (2) is then generalised to 3D structures :

$$\begin{aligned} \widetilde{T}_{ij}(\omega) &= c^*_{ijkl} \widetilde{S}_{kl}(\omega) \\ &= (c^{\mathbb{R}}_{ijkl} + j\omega\eta_{ijkl})\widetilde{S}_{kl}(\omega) \end{aligned} \tag{3}$$

where $\widetilde{T}_{ij}$ and $\widetilde{S}_{kl}$ are rank 2 tensors ; c^*_{ijkl}, complex stiffness elastic constants (rank 4 tensor), is composed of a real part $c^{\mathbb{R}}_{ijkl}$ (tensor of elastic constants) and of an imaginary part $\omega\eta_{ijkl}$ in which the viscoelasticity tensor η_{ijkl} (rank 4) is multiplied by the angular frequency ω.

The components of elastic tensor $c^{\mathbb{R}}_{ijkl}$ according to the material symmetry classes are given in the book indexed [9], chapter 3 "Elasticity and Piezoelasticity". The tensor η_{ijkl} is filled following the same rules as $c^{\mathbb{R}}_{ijkl}$.

Previous equations are given for a non-piezoelectric material. Yet, the behaviour of a piezoelectric solid is ruled by the following equations [9] :

$$\begin{cases} D_i = \varepsilon_{ij} E_j + e_{ijk} S_{jk} \\ T_{jk} = c^E_{jklm} S_{lm} - e_{ijk} E_i \end{cases} \quad \text{i, j, k, l, m} \in 1,2,3 \tag{4}$$

With D_i the electrical induction tensor, ε_{ij} the material permittivity which translates the electrical polarization, e_{ijk} piezoelectric modulus.

Elastic constants are only present in the first term of the second equation of the equation system (4). As a consequence, the model proposed for non-piezoelectric material is still available for piezolectric substrates: losses due to internal friction can be taken into account by the addition of an imaginary part, frequency dependant, on the real elastic constants. At last, piezoelectricity equations (4) read:

$$\begin{cases} D_i = \varepsilon_{ij} E_j + e_{ijk} S_{jk} \\ T_{jk} = (c^{\mathbb{R}}_{ijkl} S_{lm} - e_{ijk} E_i) + j\omega\eta_{ijkl} S_{lm} \end{cases} \tag{5}$$

The second line of this last equation clearly displays two terms. The first one, between brackets is consistent with the standard piezoelectric equations (4). The sescond one is an imaginary term that depends on the viscoelasticity η and involves losses in the material.

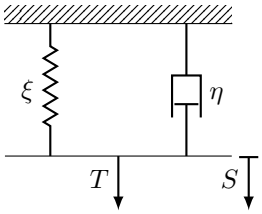

Fig. 2. Kelvin-Voigt internal damping model

III. Losses due to the dielectric character of piezoelectric materials

In this part, dielectric approximation is relaxed. For this, two differences are brought in piezoelectric [9] and Maxwell equations [10]. At first, the conductivity is no more considered as null. That has a direct impact on local Ohm's law. Secondly, losses due to the polarization of the material are usually indexed thanks to the loss tangent $tant(\delta)$. In standard analysis, $tan(\delta)$ is equaled to 0. This term is now set to a non zero value.

As a result of electrical current, free electrons can move in solid materials. Therefore, local Ohm's law can be written :

$$\vec{J} = \sigma \vec{E} \tag{6}$$

where $\vec{J}$ is the density of current, σ is the conductivity and $\vec{E}$ is the electric field vector.

We can make two points:

- If the solid is conductor, $\sigma \neq 0$: current can cross the material ;
- If the solid is an electric insulator (also called dielectric material), current can't go through the material and $\sigma = 0$. In this case, the material is assumed to be a perfect insulator: it does not contain any free electron.

But, even in insulators, a few free electrons can be detected inside real materials. As a consequence, σ remains different from zero. However, the better the insulator, the smaller σ.

Piezoelectric electric materials are known as good electrical insulator, so $\sigma \ll 1$. Until now, they were assumed to be perfect insulating materials and σ was taken to zero.

To take the residual σ into account, Maxwell-Ampere equation has to be reconsidered. Indeed, it links the magnetic field $\vec{H}$ to $\vec{J}$ and to the electric induction $\vec{D}$:

$$\vec{rot}\vec{H} = \vec{J} + \frac{\partial \vec{D}}{\partial t} \tag{7}$$

D_i, which are $\vec{D}$ components, follow (4). In the following developments, $\vec{E}$ has E_i as components, ε_{ij} are the components of the dielectric tensor ε, etc. Now, using eq. 4 and 6, Maxwell-Ampere equation (7) becomes :

$$\vec{rot}\vec{H} = \sigma \vec{E} + e\frac{\partial \vec{S}}{\partial t} + \varepsilon \frac{\partial \vec{E}}{\partial t} \tag{8}$$

A harmonic time dependency ($e^{j\omega t}$) is assumed. The previous equation is then written in the Fourier domain :

$$\begin{aligned} \vec{rot}\vec{H} &= \sigma\vec{E} + e \times j\omega\vec{S} + \varepsilon \times j\omega\vec{E} \\ &= (\frac{\sigma}{j\omega} + \varepsilon) \times j\omega\vec{E} + e \times j\omega\vec{S} \\ &= \varepsilon_{eff} \times j\omega\vec{E} + e \times j\omega\vec{S} \end{aligned} \tag{9}$$

Then, by coming back to time domain:

$$\begin{aligned} \vec{rot}\vec{H} &= \varepsilon_{eff}\frac{\partial\vec{E}}{\partial t} + e\frac{\partial\vec{S}}{\partial t} \\ &= \frac{\partial}{\partial t}(\varepsilon_{eff}\vec{E} + e\vec{S}) \\ &= \frac{\partial\vec{D}}{\partial t}^{\text{losses}} \end{aligned} \tag{10}$$

The exponent "losses" indicates that the new $\vec{D}$ is now composed of the usual electrical displacement $\vec{D}$ and of losses. ε_{eff} is defined such as the first piezoelectric equation is now:

$$\vec{D} = \varepsilon_{eff}\vec{E} + e\vec{S} \tag{11}$$

with :

$$\varepsilon_{eff} = \varepsilon - j\frac{\sigma}{\omega} \tag{12}$$

Moreover, ε can be decomposed into two terms : a real one (ε') describing the polarization of the material and an imaginary one (ε'') takes into account energy losses due to charge carrier movements.

As a consequence, ε_{eff} becomes :

$$\varepsilon_{eff} = \varepsilon' + j(\varepsilon'' - \frac{\sigma}{\omega}) \tag{13}$$

Imaginary part of effective permittivity ε_{eff} is known as dielectric losses. It can be deduced from material datasheet : the loss tangent $tan(\delta)$ is defined such as :

$$tan(\delta) = \frac{\varepsilon''}{\varepsilon'} \tag{14}$$

IV. Software implementation

In practice, the behavior of SAW structures is calculated using finite element analysis (FEA) software [11], [12]. This section is consequently dedicated to the description of the implementation of viscoelastic and dielectric losses in dedicated software. Indeed, an imaginary part, dependent on the pulsation ω must now be added to material properties in order to compute the intrinsic losses. Therefore, this part reminds the working principles of FE software and the way new material properties are inserted in computation programs.

A. Basics of the finite element method

In the context of the study of SAW devices, finite elements aim at determining the deformed shape of the structure when the wave propagates. In concrete terms, it consists in solving partial differential equations associated to boundary conditions. In the particular case of this paper, piezoelectric equations, linked to the periodicity of the structure and to the nature of the environment at the top of the structure are considered.

In more general words, the studied system is known as the domain Ω whose boundary if Γ. This domain Ω is divided into subdomains Ω^e (boundary Γ^e) further in this work (see figure 3).

The behavior of the system is defined thanks to the equilibrium equations, the boundary and the initial conditions, and the constitutive relations of the problem.

The most common formulation of finite element problems, in which the displacements (and the electrical potential) are the unknowns rest on the three following basis :

1) the writing under an integral formulation of a variational principle;
2) the decomposition of these integrals in subdomains Ω^e. These subdomains are, strictly speaking, the finite elements;
3) the discretization of the continuous problem by nodal interpolation inside each element.

As part of piezoelectricity, the use of the first principle of thermodynamics and the addition of a term to include the work per unit of time provided by the electric field on the crystal lattice involves the rewriting of the constitutive equations of the problem in a integral formulation called *variational equation* :

$$\int_\Omega ({}^T\delta u\rho\ddot{u} + {}^T\delta\varepsilon T - {}^T\delta u b)\,\mathrm{d}\Omega - \int_\Gamma {}^T\delta u\bar{t}\mathrm{d}\Gamma = 0 \tag{15}$$

In the previous equation (15), ^{T} stands for the transpose of the matrix that follows this sign, δu is the variational unknown, ρ the density, $\ddot{u}$ the second derivative in time of the displacement u. In the same way, $\delta\varepsilon$ is the virtual strain related to δu:

$$\delta\varepsilon_{ij} = \frac{1}{2}(\delta u_{i,j} + \delta u_{j,i}) \tag{16}$$

$\delta u_{i,j}$ is the j^{th} derivative of the i^{th} term of the variational unknown δu. In the same way, $\delta u_{j,i}$ is the i^{th} derivative of the j^{th} term δu as follows.

Finally, T are the stresses applied on the structure, b the body forces and $\bar{t}$ the stress applied on the boundary.

In many cases, (15) cannot be solved directly. That's why the domain Ω is divided into a finite number of subdomains Ω^e. The exponent e stands for each element, namely each subdomain. The variational equation of the system can thus be approximated by:

$$\sum_e \left\{ \int_{\Omega^e} {}^T\delta u\rho\ddot{u}\,\mathrm{d}\Omega + \int_{\Omega^e} {}^T\delta\varepsilon T\,\mathrm{d}\Omega - \int_{\Omega^e} {}^T\delta u b\,\mathrm{d}\Omega - \int_{\Gamma^e} {}^T\delta u\bar{t}\mathrm{d}\Gamma \right\} \tag{17}$$

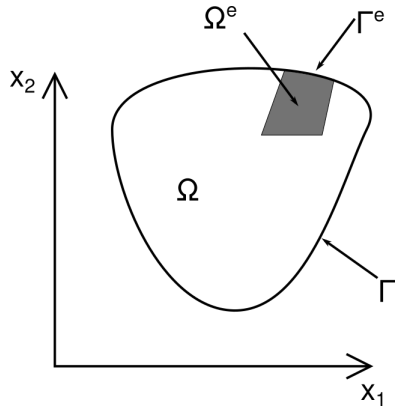

Fig. 3. Problem Ω and boundary Γ

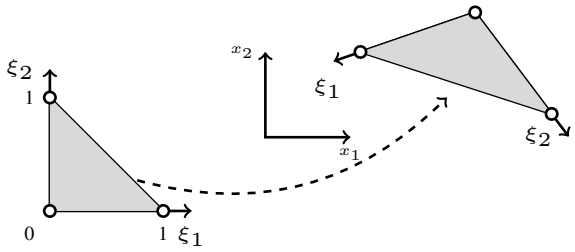

Fig. 4. Reference finite element in its local coordinate system (ξ_1, ξ_2)(on the left) and one element of a structure on the global coordinate system (x_1, x_2) (on the right)

The resolution of this finite element problem is now possible by approximating the displacements $u(x,t)$ by:

$$u(x,t) \simeq \widehat{u} = N(x)a(t) \tag{18}$$

in the global coordinate where N is the matrix of element shape functions. It corresponds to the interpolation of the displacements at the nodes of the subdomains. a is the time dependent nodal displacements in the element. In isoparametric forms, that is to say, in the coordinate of the element of reference, nodal displacements are approximated by:

$$u(\xi,t) \simeq \widehat{u}(\xi,t) = N(\xi)a(t) \tag{19}$$

Figure 4 clarifies the difference between the two types of coordinates (local and global). In the left side of the figure, a triangular reference element with three nodes is drawn. Local coordinates (ξ_1, ξ_2) are associated to this element. On the right side, the element is assumed to be inserted in a domain Ω. Nodal coordinates are consequently given relatively to the global coordinate system (x_1, x_2). However, the nodes are still indexed in the local system (ξ_1, ξ_2) too. Moreover, the coordinates of the element can be expressed either in one or another coordinate system. By this way, an approximation of the virtual displacement is given by :

$$\delta u(\xi) = N(\xi)\delta a \tag{20}$$

Pursuant to the relations between the different parameters that are developed in [11], [12], the weak form of the problem for one element becomes :

$$\delta\widehat{\prod}_{eq}^{e} = {}^T\,\delta a \left\{ \int_{\Omega^e} {}^T N\rho N\ddot{a}\,\mathrm{d}\Omega + \int_{\Omega^e} {}^T BT\,\mathrm{d}\Omega - \int_{\Omega^e} {}^T Nb\,\mathrm{d}\Omega - \int_{\Gamma^e} {}^T N\bar{t}\mathrm{d}\Gamma \right\} = 0 \tag{21}$$

The motion equation can be recognized from 21:

$$M\ddot{a} + Ka = f \tag{22}$$

with :

$$\begin{aligned} M &= \sum_e \int_{\Omega^e} {}^T N\rho N\,\mathrm{d}\Omega \\ K &= \sum_e \int_{\Omega^e} {}^T BCB\,\mathrm{d}\Omega \\ f &= \sum_e \left\{ \int_{\Omega^e} {}^T Nb\,\mathrm{d}\Omega + \int_{\Gamma^e} {}^T N\bar{t}\,\mathrm{d}\Gamma \right\} \end{aligned} \tag{23}$$

where M is the mass matrix. M is related to the shape functions N and to the density ρ. K, the stiffness matrix, is composed of the strain-displacement matrix B and of the usual elastic moduli in matrix form C. Finally, the forces applied on the system f are related to the body forces b and to the stress boundary conditions $\bar{t}$.

Because it is written in this particular form which contains as many unknowns than differential equations, the system can now be solved and an approximate solution of the displacement u can be defined. As the purpose of this paper is the implementation of viscoelasticity phenomenon and dielectric losses, problem-solving method and model reduction techniques are not developed in this paper. Nevertheless, they can be found in some books of reference [11], [12]. Instead, we will glance at the procedures to finally explain the way viscoelasticity and dielectric losses can be numerically taken into account.

B. FEA computer procedures

The principles we saw in the previous paragraph have to be programmed to allow a fast numerical resolution of the problem. That's why this section is devoted to the description of the major steps needed to build a FEA software.

The general algorithm diagram is represented figure 5. Three main stages are required :

1) The data input module. This first step aims at defining the finite element problem. This part will be developed in more details in the next paragraph;

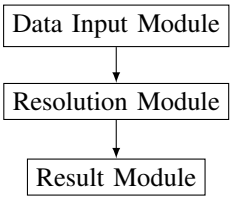

Fig. 5. General algorithm of finite element software

2) The solution module that gathers algorithms dedicated to the resolution of FE problems. This module is designed for the specific kind of problem it addresses (steady-state, fluid dynamics etc.). Consequently, it should be programmed in order to allow its own improvement and to be able to solve simultaneously different types of problems.
3) The result module. This last stage involves the printing of the results in a dedicated file and eventually in their drawing.

The combination of all these steps might allow an efficient computation of the finite element problem.

In order to be able to take into account the viscoelasticity of the materials and the dielectric losses, our attention has to be focused on the first step.

C. Focus on the prepocessing step

The preprocessing step is the first stage mentioned in the previous paragraph. It also corresponds to three points :

1) the definition of the mesh layout. Namely, the coordinates of each node of each element are identified as well as the boundary and continuity conditions, the stresses, forces and nodal displacements ;
2) then, material properties are linked to the elements ;
3) finally, the matrices $[M]$, $[K]$ and $[f]$ are written.

After these stages, the FE software goes to the solution module and performs a loop on frequency to solve the equations in the wanted frequency interval.

Figure 6a schematically represents these stages. It can be seen that, in the standard finite element computation, material properties are linked to the mesh layout once and for all. They remain unchanged for the entire duration of the computation.

Figure 6b corresponds to the algorithm in which frequency dependent losses are added to the model. It displays some differences with the previous diagram. Indeed, the link between material properties and the elements is made inside the frequency loop. As a consequence, $[K]$, $[M]$ and $[f]$ matrices are recomputed at each frequency point. This change in the FE software is imposed by the imaginary parts $\omega\eta$ and $(\varepsilon'' - \frac{\sigma}{\omega})$. These terms involve different material matrices at each point of the loop and thus, different $[M]$,$[K]$ and $[f]$.

Afterwards, the resolution of the problem remains unchanged.

V. Validation of the model

In order to confirm the validity of the previous developments, two tests are performed. In the first one, a infinite periodic structure is considered. The product *quality factor* Q $\times$ *frequency* f of the structure is compared to the $Q \times f$ product of the considered material. Then, a SAW filter is designed and manufactured. The comparison is now based on the experimental measurements versus numerical analysis results with and without the consideration of viscoelasticy phenomenon.

A. Validation of viscoelasticity phenomenon on an infinite structure

This paragraph tests the model previously developed in this article for viscoelasticity losses. Unfortunately losses related to relative permittivity cannot be evaluated at the moment because of a lack of information regarding the conductivity. To validate the model, two cases are studied and compared to the knowledge of men of the art.

Overview of the process:

The system proposed figure 7 is considered. It is composed of a semi infinite piezoelectric material along $\vec{z}$ and of an aluminum layer (the electrodes). The system is infinitely periodic along $\vec{y}$. Because the electrodes are much longer than the wavelength, the device is assumed to be infinite in the $\vec{x}$ direction. The electrode grating is made with an alternated polarity to generate a potential difference (succession of + and -, so the electrical period λ is twice the mechanical period p).

Two kinds of numerical simulations are conducted:

1) In the first one, only the electrodes are meshed. The piezoelectric substrate and its semi-infinite character are expressed through a radiation condition [13]. This computation is based both on the finite element method and on the boundary element method [14] ;
2) The second numerical simulation consists in meshing a large thickness of Quartz. The computation is now only based on the FEA. Indeed, substrate thickness is 150 μm (50 λ). As the propagation of a Rayleigh wave is considered, this thick mesh is big enough to contain all the energy of the wave in the $\vec{z}$ direction [15]. Moreover, it provides a system whose behavior along $\vec{z}$ axis is close to the behavior of the device with a radiation condition.

The validation of the viscoelastic model is conducted using Quartz AT crystal. A conclusion is then drawn further to the numerical results.

Validation:

Quartz is chosen to conduct this study because its elastic and viscoelastic constants ($C^{\mathbb{R}}$ in 10^{11} Pa and η in 10^{11} Pa/MHz) are well known:

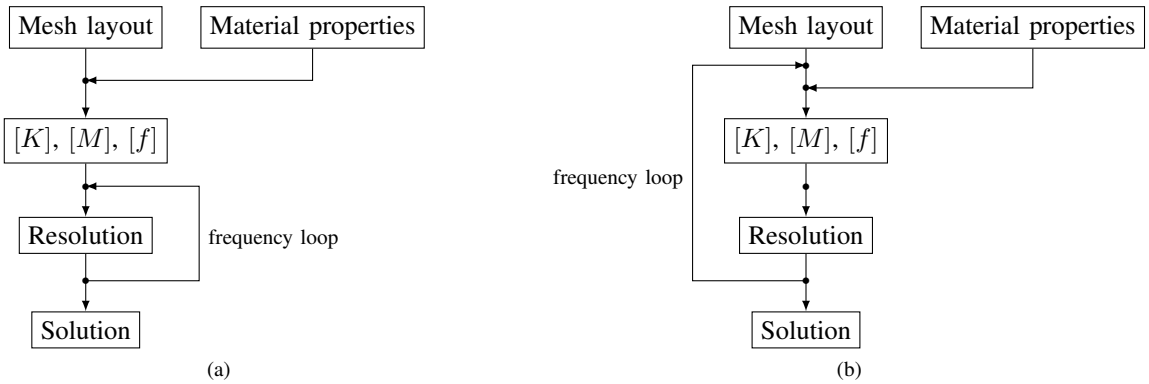

Fig. 6. Diagram of the finite element algorithm - (a) usual case, (b) when viscoelastic and dielectric losses are included

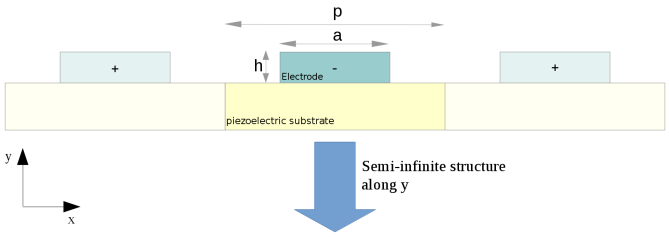

Fig. 7. Schematic of the piezoelectric device

$$C^{\mathbb{R}} = \begin{pmatrix} 0.8674 & 0.07 & 0.1191 & -0.1797 & 0 & 0 \\ 0.07 & 0.8674 & 0.1191 & 0.1791 & 0 & 0 \\ 0.1191 & 0.1191 & 0.01072 & 0 & 0 & 0 \\ -0.1791 & 0.1791 & 0 & 0.5794 & 0 & 0 \\ 0 & 0 & 0 & 0 & -0.1791 & 0.3987 \\ 0 & 0 & 0 & 0 & 0 & -0.1710 \end{pmatrix}$$

$$\eta = \begin{pmatrix} 1.37 & 0.73 & 0.71 & 0.01 & 0 & 0 \\ 0.73 & 1.37 & 0.71 & -0.01 & 0 & 0 \\ 0.71 & 0.71 & 0.96 & 0 & 0 & 0 \\ 0.01 & -0.01 & 0 & 0.36 & 0 & 0 \\ 0 & 0 & 0 & 0 & 0.01 & 0 \\ 0 & 0 & 0 & 0 & 0 & 0.32 \end{pmatrix}$$

The results of both computations are summarized on figures 8a, 8b and in table I. We can notice the good correlation between both calculation methods: indeed, the resonance arises at the same frequency (1.04676 GHz) and the admittance equals 9.23163 S/m when a radiation condition is considered and 9.22158 S/m if the domain is meshed. The two computations lead to a relative gap of about 0.1 % of the bandwidth. The Q factor is calculated using the resonant frequency and the bandwidth. In both cases, the Q factor is closed from 12200, leading to a $Q \times f$ of about 10^{13} Hz, which is consistent with the $Q \times f$ of Quartz devices [16], [17], [18].

This first result obtained in the particular case of an infinitely periodic structure on Quartz leaves the door wide open to a deeper analysis of the viscoelastic phenomena in solid materials. In fact, as the $Q \times f$ product of the simulated structure corresponds to the $Q \times f$ of real Quartz, the consistency of the result on a SAW filter designed and manufactured can now be verified.

TABLE I
RECAP OF THE CELL DIMENSIONS

	With radiation	Without radiation
Resonant frequency f_r (GHz)	1.04676	1.04676
Quality factor Q	12249	12194
$Q \times f_r$ (Hz)	$1.28 \cdot 10^{13}$	$1.27 \cdot 10^{13}$

A last remark can be made on these results: the computation time of the meshed structure is about 120 hours using one chore whereas it took 1h20 with the radiation condition and considering a fine meshed structure.

B. Application and validation on an actual device

A Quartz SAW filter is now designed as a double port (LCRF - longitudinally coupled resonator filter). Its dimensions and working frequency are hidden for confidentiality reasons. The response function of the device is simulated in two different ways :

- in the usual way, without taking into account the effect of viscoelasticity ;
- with the addition of viscoelasticity phenomenon to the numerical model.

Finally, a foresaid device is manufactured.

The transfer functions corresponding to the three cases (the two numerical simulations and the measure) are plotted figure 9. The first element to notice is the difference between numerical simulations and measure between the normalized frequencies 0.9951 and 0.99756: the disparity is not due to a wrong simulation of the behavior of the system but to contingencies of the production process. Then, regarding the resonance, the remarks that can be drawn are the following:

- the insertion losses (IL) are slightly underestimated with the usual simulation (without viscoelasticity). However, when internal damping is taken into account in the model, the IL of the simulated system become closer to the actual IL;
- The viscoelasticity is for now a little overestimated and a more precise material characterization should be performed to improve the numerical simulation;

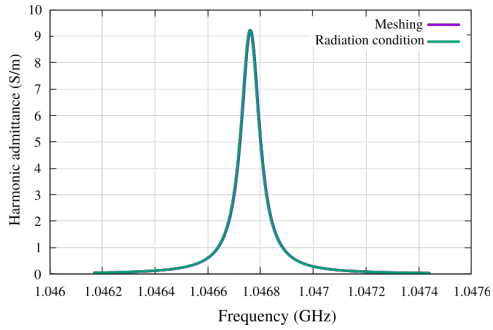

(a) Response function (admittance)

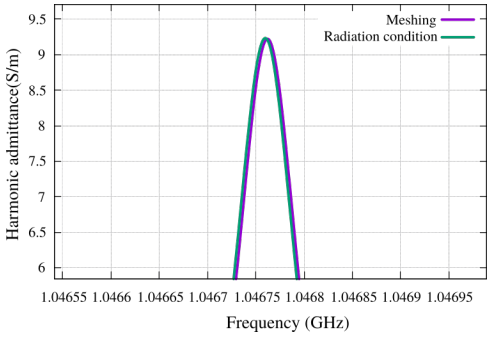

(b) zoom at the resonance

Fig. 8. Frequency response of an infinitely periodic Quartz structure on which an electrode grating is deposited

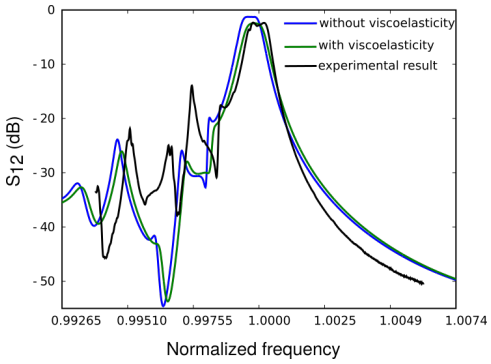

Fig. 9. Transfer function of a manufactured SAW device (black curve) whose frequency response was simulated first with (green) and without (blue) taking account the viscoelasticity phenomenon

- moreover, the center frequency f_c of the system is also underestimated in the case without losses compared to the measure whereas f_c and the bandwidth are closer to the measure when viscoelasticity is considered in the numerical model.

In the light of these results; the design of a Quartz SAW filter and the simulation of its behavior with and without the addition of a viscoelastic condition displayed that the response function is closer to the reality when a Kelvin-Voigt model generalized to three dimensions to take into account the internal damping of the substrate is added to the numerical simulation.

C. Validation of the dielectric losses

The next step should have been the validation of the dielectric losses (that includes the ε'' term and σ). However, as written previously in this document, the so low level of information on the residual conductivity σ of piezoelectric materials makes currently difficult the implementation of the data needed the complete the computation.

VI. Conclusion and perspectives

This study was conducted to address the needs of both academics and industrials regarding the design of SAW devices. Actually, gaps between simulated and measured insertion losses have been noticed, leading to the necessity to redesign the devices. It has been determined that this error during the numerical computation was due to neglected loss phenomena. Consequently, these losses have been identified and implemented in FEA software for validation purpose. Three types of losses are modeled :

- losses due to internal friction of the piezoelectric material on itself when the wave passes. A Kelvin-Voigt internal damping model is included in the finite element software ;
- losses due to relative permittivity of the material. Suppliers are used to providing the loss tangent of the material which is the ratio between imaginary and real parts of ε_r. This quantity transcribes the existence of losses in ε_r and is inserted in the constitutive equations of the system ;
- losses related to the leakage of the electrical charges in the piezoelectric material: the conductivity is close but different from zero.

The two last kind of losses lead to an imaginary part added to the real term of ε_r.

These phenomena have consequently been modeled and implemented if a FEA software. Numerical tests have been performed and compared to experimental measures. By this way, we saw that taking into account the viscoelasticity losses through a Kelvin-Voigt model allows a better estimation of the central frequency and of the insertion losses than the same computation without this module. However, the impact of η on the bandwidth is a little overestimated. Therefore, the next step regarding viscoelasticity losses is to know the origin of this limitation : it could come from the model itself or from a bad estimation of the matrix η.

Furthermore, ε'' and σ couldn't be implemented and tested in the FEA software due to a lack of knowledge on the materials. This point will be raised thanks to new material characterizations.

In any cases, for now, taking into account viscoelastic losses allows a more precise computation of the central frequency and insertion losses than when losses are neglected or when an empirical Q factor is added to the numerical simulation.

ACKNOWLEDGMENT

We are grateful to the DGA and to the ANRT for their financial backings.

REFERENCES

[1] G. Bruckner, J. Bardong, M. Postl, and A. Klug. Experimental investigations of the acousto-electric effect in high temperature SAW gas sensing. In *2016 IEEE International Ultrasonics Symposium (IUS)*, pages 1–4, Sept 2016.

[2] I. D. Avramov. Design of Rayleigh SAW Resonators for Applications as Gas Sensors in Highly Reactive Chemical Environments. In *2006 IEEE International Frequency Control Symposium and Exposition*, pages 381–388, June 2006.

[3] M. Mimura, D. Ajima, C. Konoma, and T. Murase. Small sized band 20 SAW duplexer using low acoustic velocity Rayleigh SAW on LiNbO3 substrate. In *2017 IEEE International Ultrasonics Symposium (IUS)*, pages 1–4, Sept 2017.

[4] X. Li, J. Bao, Y. Huang, B. Zhang, T. Omori, and K. y. Hashimoto. Traveling wave excitation for FEM simulation of RF SAW/BAW devices. In *2017 IEEE International Ultrasonics Symposium (IUS)*, pages 1–4, Sept 2017.

[5] V. Laude, A. Reinhardt, M. Wilm, A. Khelif, and S. Ballandras. Fast FEM/BEM simulation of SAW devices via asymptotic waveform evaluation. *IEEE Transactions on Ultrasonics, Ferroelectrics, and Frequency Control*, 51(3):359–363, March 2004.

[6] O. Manner and G. Visinitini. Analysis and compensation of metal resistivity effects in apodized SAW transducers. In *Proceedings., IEEE Ultrasonics Symposium,*, pages 1–6 vol.1, Oct 1989.

[7] C. K. Campbell. Modelling the transverse-mode response of a two-port SAW resonator. *IEEE Transactions on Ultrasonics, Ferroelectrics, and Frequency Control*, 38(3):237–242, May 1991.

[8] Krzystof Marynowski and Tomasz Kapitaniak. Kelvin-Voigt versus Bürgers internal damping in modeling of axially moving viscoelastic web. *International journal of non-lienar mechanics*, 37:1147–1161, 2002.

[9] D. ROYER, D.P. Morgan, and E. Dieulesaint. *Elastic Waves in Solids I: Free and Guided Propagation*. Advanced Texts in Physics. Springer Berlin Heidelberg, 1999.

[10] Paul G. Huray. *Foundations of Maxwell #39;s Equations*, pages 275–. Wiley-IEEE Press, 2010.

[11] O.C. Zienkiewicz and R.L. Taylor. *The Finite Element Method: Solid mechanics*. Referex collection.Mecánica y materiales. Butterworth-Heinemann, 2000.

[12] O.C. Zienkiewicz, R.L. Taylor, and J.Z. Zhu. *The Finite Element Method: Its Basis and Fundamentals*. Elsevier Science, 2005.

[13] P. Ventura, J. M. Hode, M. Solal, J. Desbois, and J. Ribbe. Numerical methods for SAW propagation characterization. In *1998 IEEE Ultrasonics Symposium. Proceedings (Cat. No. 98CH36102)*, volume 1, pages 175–186 vol.1, 1998.

[14] Ke Yabing, Li Honglang, and He Shitang. Fast FEM/BEM Simulation of non-periodic SAW structures. In *2012 IEEE International Ultrasonics Symposium*, pages 815–818, Oct 2012.

[15] D. ROYER, S.N. Lyle, and E. Dieulesaint. *Elastic Waves in Solids II: Generation, Acousto-optic Interaction, Applications*. Advanced Texts in Physics. Springer Berlin Heidelberg, 1999.

[16] S. Galliou, P. Abbé, R. Bourquin, M. Goryachev, M. E. Tobar, and E. N. Ivanov. Properties related to Q-factors and noise of quartz resonator-based systems at 4K. In *2014 European Frequency and Time Forum (EFTF)*, pages 33–35, June 2014.

[17] S. Galliou, M. Goryachev, P. Abbé, X. Vacheret, M. E. Tobar, and R. Bourquin. Quality Factor Measurements of Various Types of Quartz Crystal Resonators Operating Near 4 #x00A0;K. *IEEE Transactions on Ultrasonics, Ferroelectrics, and Frequency Control*, 63(7):975–980, July 2016.

[18] I. Antcev, S. Bogoslovsky, G. Sapozhnikov, S. Zhgoon, and A. Shvetsov. Comparative analysis of the experience obtained from the use of SAW and BAW wireless resonator temperature sensors for surgery. In *2015 IEEE International Ultrasonics Symposium (IUS)*, pages 1–4, Oct 2015.

Above 100-GHz Low Phase Noise Frequency Generation in Silicon Integrated Technologies

Alexandre Siligaris, Zyad Iskandar and Jose Moron Guerra
CEA, LETI, Grenoble F-38054, France and the University of Grenoble Alpes, France

***Abstract*—This paper summarizes the design techniques in integrated Silicon technologies for oscillator signal generation above f_{max}. It describes the general schematics using N-push techniques in oscillators and their theoretical operating principle. Furthermore, sub-harmonic injection locking is discussed as a solution for low phase noise. Finally, some examples of CMOS and BiCMOS fabricated circuits are given as a proof of concept that demonstrate the feasibility of low phase noise frequency generation around 300 GHz.**

Keywords—CMOS, BiCMOS, THz, oscillator, phase noise, push-push, triple-push, mmW, harmonics.

I. INTRODUCTION

Sub-THZ frequency bands (>100-GHz) are gaining interest among the scientific community for RF system development. As a matter of fact, the THz bands are more and more explored in Silicon CMOS and BiCMOS technologies since 7 years with a multitude of circuits published in recent literature. There are three main reasons that push the scientific community towards exploring these frequency bands. First, the development of RF wireless communications at sub-THz bands offer ultra large bandwidth (many tens of GHz) that enables ultra-high data rate (>100 Gbps). The other two interesting fields of application are radar and sensing, and imaging due to small wave length (mm) and thus high imaging resolution. Wireless communication systems need high performance local oscillators (LO) in terms of frequency stability and phase noise (PhN) [1]. Indeed, first aimed applications are mostly point-to-point wireless links that require very low phase noise when using high order modulation schemes. As an example, for a 16-QAM modulated signal the required phase noise must be lower than -92 dBc/Hz at 1 MHz offset from the carrier.

Figure 1 illustrates the PhN of recent frequency synthesizers at 1 MHz offset, as a function of the LO frequency in the synthesizer. We observe that increasing the LO frequency in the synthesizer leads to higher PhN than the ideal 20·log(N) when extrapolating the phase noise from lower LO circuits. N is the multiplication factor when a lower frequency LO is used followed by a frequency multiplication by N. Thus, in order to obtain high frequency LO with outstanding PhN it is preferable to use a lower frequency synthesizer combined to a high order frequency multiplication factor.

This paper summarizes the various techniques for generating above 100 GHz signal on chip in Silicon technologies. The second section explains the operating principle and gives some schematic examples. The third section details some fabricated circuits in CMOS and BiCMOS technologies from the LETI institute that operate near 300 GHz. An emphasis is given on the architectures that allow obtaining low phase noise.

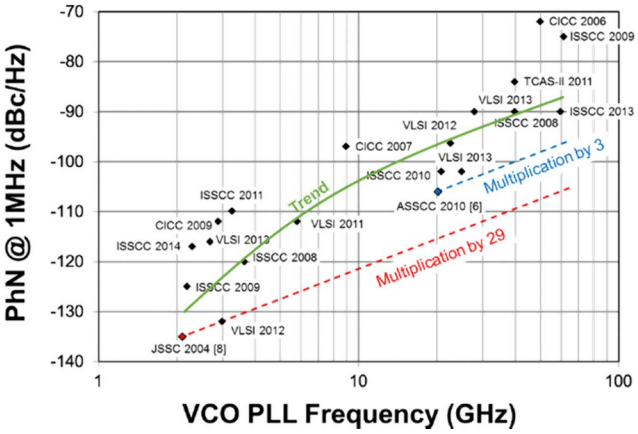

Fig. 1. Synthesizers with LO operating in the 2 – 60 GHz range. Trend is the green line.

II. DESIGN TECHNIQUES FOR SILICON THZ OSCILLATORS

In the THz bands, the main challenge in CMOS and BiCMOS technologies is to generate an LO signal on chip. Around 300 GHz, most of the technologies must operate above the f_{max} of the transistor. To face this issue many design techniques have been developed in recent literature. Most of such design techniques that enable to generate a signal above transistor's f_{max} combine a lower frequency oscillator to an in-situ frequency multiplication operation. This is done essentially by the use of harmonic recombination inside the oscillator core. The recent literature shows a multitude of THz sources in which the oscillators are operating well above the f_{max}. Whatever being the author's approach and aim, the general applied technique is the N-Push [2-8]. N-push technique consists in generating a signal at a lower frequency in multiple nodes of a circuit with a different phase at each one. The phase difference between each node is fixed by design and must be determined by the N^{th} desired multiplication order. A common node is used to recombine all phase shifted signals on which the impedance at the N^{th} harmonic is set in order to maximize the signal.

More specifically, the most popular N-push designs use a 2, 3 or 4 value for N. For N=2 in the well-known push-push technique, two 180° phased signals are recombined on the

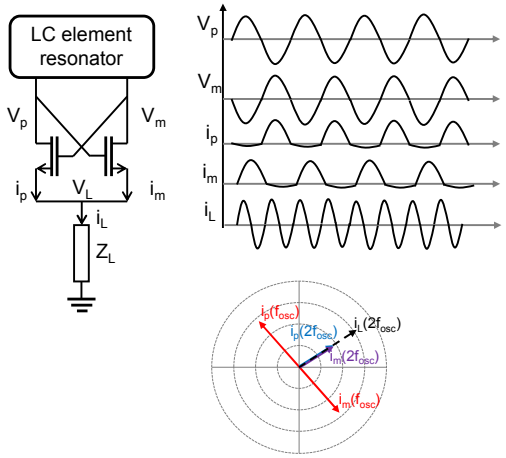

Fig. 2. Signals in a differential pair on the differential nodes and the common node.

common node. For N=3, three 120° phase shifted signals are recombined to boost the third harmonic (triple-push). The four-push technique is similar to the push-push (even number), but the 4th harmonic is privileged. Higher order phase-shifted recombination has not been explored as it is not efficient in terms of output signal level. Finally, another less popular technique, the so-called push-push and mix, is detailed at the end of this section.

A. Push-Push and four-push (N even)

The most common multiplying in-situ technique is the push-push. It is based on a differential pair in which two signals are phased by 180° at the fundamental frequency f_{osc}. This mechanism is illustrated in figure 2. Let us consider a differential cross coupled pair with its resonator. It is tuned to oscillate at f_{osc} (fundamental harmonic). The sum of the i_p and i_m currents is performed on the V_L node. The currents in each branch are positive only one half of the cycle of the fundamental frequency f_{osc}. The currents i_p and i_m can be written as the sum of Fourrier series as follows:

$$i_p(\omega) = I_{oscp}^{(1)} e^{j\left(\omega_{osc}t+\varphi_p^{(1)}\right)} + I_{oscp}^{(2)} e^{j\left(2\omega_{osc}t+\varphi_p^{(2)}\right)} + I_{oscp}^{(3)} e^{j\left(3\omega_{osc}t+\varphi_p^{(3)}\right)} + \cdots \quad (1)$$

$$i_m(\omega) = I_{oscm}^{(1)} e^{j\left(\omega_{osc}t+\varphi_m^{(1)}\right)} + I_{oscm}^{(2)} e^{j\left(2\omega_{osc}t+\varphi_m^{(2)}\right)} + I_{oscm}^{(3)} e^{j\left(3\omega_{osc}t+\varphi_m^{(3)}\right)} + \cdots \quad (2)$$

Where, $I_{oscp}^{(i)}$ is the amplitude of the i_{th} harmonic of the positive branch current and $\varphi_p^{(i)}$ its respective phase. Considering a symmetric balanced structure, $I_{oscp}^{(i)} = I_{oscm}^{(i)}$. Moreover, the current phases fulfill the following conditions: $\left|\varphi_p^{(i)} - \varphi_m^{(i)}\right| = 180°$, when i is odd and $\left|\varphi_p^{(i)} - \varphi_m^{(i)}\right| = 0°$ when i is even. The vectorial sum of each harmonics results to a total current at the common node (i_L) in which the even harmonics are summed constructively and the odd harmonics are summed destructively resulting to a total i_L current:

$$i_L \approx I_{DC} + 2I_{oscp}^{(2)} e^{j\left(2\omega_{osc}t+\varphi^{(2)}\right)} + 2I_{oscp}^{(4)} e^{j\left(4\omega_{osc}t+\varphi^{(4)}\right)} + \cdots \quad (3)$$

The resulting i_L signal includes all the even harmonics (N=2, 4, 6 …). The odd harmonics (N=1, 3, 5 …) are out of phase and their sum is null. In figure 2, the currents are also shown as vectors at the fundamental f_{osc} frequency and the second harmonic ($2f_{osc}$). The fundamental harmonic currents are recombined with 180° of relative phase at the common node V_L.

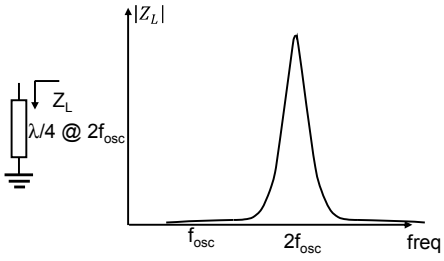

Fig. 3. Load impedance at amplitude when using a quarter wave length stub (shorted) at the 2nd harmonic: at $2f_{osc}$ the imaginary part of the impedance becomes zero and the magnitude is maximized. At f_{osc}, .the signal is shorted.

The Z_L impedance is employed for optimal signal swing at the even harmonic of interest (here N=2) in order to maximize only the signal at the 2nd harmonic. For that, one can use, for example, a transmission line stub that is tuned at λ/4 at $2f_{osc}$. Thus the impedance is maximized at $2f_{osc}$ and is minimized at the other non-desired harmonics (f_{osc}) to filter out signal residues.

By extending the above design technique, one can extrapolate at the fourth harmonic and operate an in-situ multiplication by four. However, it is much more efficient instead to generate four signal phases at the fundamental (0°, 90°, 180° and 270°) before operating the sum. Indeed, extracting the 4th harmonic by a 4-push structure is more efficient in terms of signal amplitude.

B. Triple-Push (N odd)

The triple-push technique follows the same principle as the push-push. However, here the oscillator, from which we want to extract the 3rd harmonic, must have three stages that generate signals phased by 120° between each other. The usual circuit architecture is the so called triple-push oscillator. It is shown in figure 4 and consists in a three-stage ring oscillator that uses transmission lines, or inductances (L_P and L_S in figure 4) as reactive loads in order to tune frequency at the fundamental harmonic f_{osc}. The sum of the i_1, i_2 and i_3 currents is done at the V_L node. The currents in each branch are positive only one half of the cycle of the fundamental frequency f_{osc}. The currents i_1, i_2 and i_3 can be written as the sum of Fourrier series as follows:

$$i_1(\omega) = I_{osc1}^{(1)} e^{j\left(\omega_{osc}t+\varphi_1^{(1)}\right)} + I_{osc1}^{(2)} e^{j\left(2\omega_{osc}t+\varphi_1^{(2)}\right)} + I_{osc1}^{(3)} e^{j\left(3\omega_{osc}t+\varphi_1^{(3)}\right)} + \cdots \quad (4)$$

$$i_2(\omega) = I_{osc2}^{(1)} e^{j\left(\omega_{osc}t+\varphi_2^{(1)}\right)} + I_{osc2}^{(2)} e^{j\left(2\omega_{osc}t+\varphi_2^{(2)}\right)} + I_{osc2}^{(3)} e^{j\left(3\omega_{osc}t+\varphi_2^{(3)}\right)} + \cdots \quad (5)$$

$$i_3(\omega) = I_{osc3}^{(1)} e^{j\left(\omega_{osc}t+\varphi_3^{(1)}\right)} + I_{osc3}^{(2)} e^{j\left(2\omega_{osc}t+\varphi_3^{(2)}\right)} + I_{osc3}^{(3)} e^{j\left(3\omega_{osc}t+\varphi_3^{(3)}\right)} + \cdots \quad (6)$$

Where, $I_{oscк}^{(i)}$ is the amplitude of the i_{th} harmonic of the k[th] branch current and $\varphi_k^{(i)}$ its respective phase. A symmetric designed structure gives: $I_{osc1}^{(i)} = I_{osc2}^{(i)} = I_{osc3}^{(i)}$. Moreover, the current phases fulfill the following conditions: $\left|\varphi_k^{(i)} - \varphi_{k+1}^{(i)}\right| = 120°$, when the i^{th} harmonic is 1, 2, 4, 5 … The phase for the i^{th} harmonics 3, 6, 9 … is $\left|\varphi_k^{(i)} - \varphi_{k+1}^{(i)}\right| = 0°$. The vectorial sum of each harmonics results to a total current at the common node (i_L) in which the 3, 6, 9 …

harmonics are summed constructively and the 1, 2, 5, 7 … harmonics are summed destructively resulting to a total i_L current:

$$i_L \approx I_{DC} + I_{osctot_3} e^{j(3\omega_{osc}t)} + I_{osctot_6} e^{j(6\omega_{osc}t)} + I_{osctot_9} e^{j(9\omega_{osc}t)} + \cdots \quad (7)$$

The resulting i_L signal includes the harmonics N=3, 6, 9 …. The other harmonics (N=1, 2, 4, 5 …) are out of phase and their sum is null. Figure 5 depicts the complex current vectors in a polar graph for harmonics 1, 2, 3, 4, 5 and 6. To maximize and extract the third harmonic signal at the common node V_L, a similar technique to the push-push oscillator is applied, but the stub line is tuned to $3f_{osc}$ (figure 6).

C. *Push-push and Mix (third harmonic extraction)*

The following technique is a hybrid circuit design that uses a double-push oscillator core combined to a mixer that adds the fundamental harmonic to the second harmonic. Figure 7 illustrates the schematic view that implements the push-push and mix. The oscillator core analysis is the same than the double-push, but it is loaded to a single balanced mixer core. The resulting output differential signal (Vout in figure 7) includes the mixing product harmonics $N \cdot \omega_{osc} + 2K\omega_{osc}$. The Z_L impedance at the common node is tuned to resonate at $2f_{osc}$ with the input capacitance of the mixer stage C_{inmix}:

$$Z_L = {}^{1}/_{(4\pi f_{osc} C_{inmix})} \quad (8)$$

Thus, the second harmonic voltage swing is maximized at $2f_{osc}$ on the common node. Note that using a single balanced mixer as shown here, the first harmonic leakage (f_{osc}) is not negligible. A more complex circuit is needed to reject the first harmonic using a double balanced mixer like a Gilbert cell.

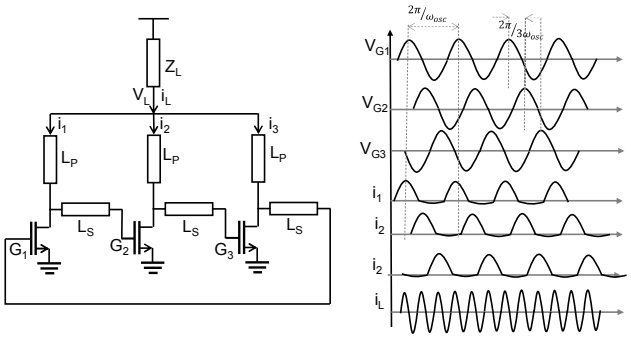

Fig. 4. Triple-push oscillator architecture. Time domain gate voltages and drain currents resulting to a high harmonic load current.

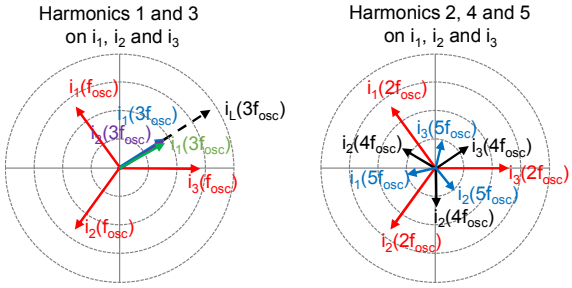

Fig. 5. Polar representation of the Fourrier harmonics (1 to 6) of each branch currents in a triple-push oscillator

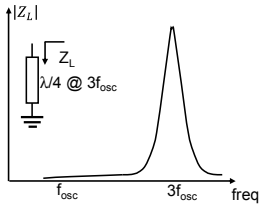

Fig. 6. Triple-push oscillator load for maximum signal swing on the load at the third harmonic .

D. *Low phase noise: sub-harmonic injection locking*

The above proposed circuits use free running oscillators. For frequency generation around 300 GHz, the fundamental oscillation frequency should be around 100 GHz for the triple-push and the push-push and mix approaches. For the double-push structure f_{osc} must be around 150 GHz. This implies inherently very high free running phase noise, not suitable for wireless communication systems.

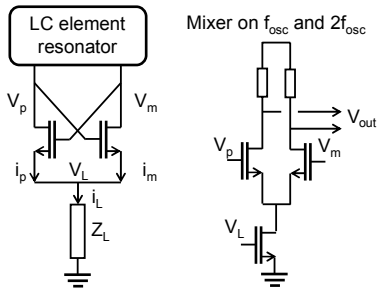

Fig. 7. Push-push and Mix technique schematic.

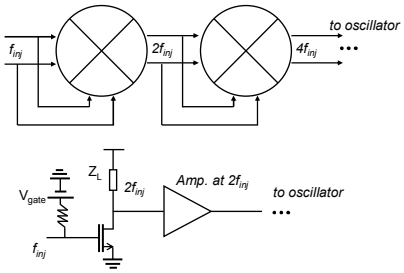

Fig. 8. Frequency multiplier techniques for low frequency (< 50 GHz).

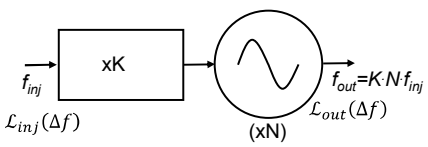

Fig. 9. Hybrid high order injection locked frequency generator combining simple multipliers to injection locked multi-push oscillator.

In order to mitigate phase noise, sub-harmonic injection locking is proposed. The direct consequence of injection locking is that the oscillator's output signal copies the phase and frequency characteristics of the injected signal. Indeed according to Adler's theory, the steady state phase φ_{SS} when the oscillator is locked is given by:

$$\varphi_{SS} = \arcsin\left(\frac{\omega_{osc} - \omega_{INJ}}{\omega_L}\right) \quad (9)$$

with:

$$\omega_L = \frac{\omega_{osc}}{2Q}\frac{I_{INJ}}{I_{osc}} \quad (10)$$

ω_L is the locking bandwidth, I_{INJ} is the injection current, Q the quality factor of the oscillator's resonator and I_{osc} the oscillator's current. As a matter of fact, the locking occurs around the free running oscillator's frequency. To lock the oscillator using a lower frequency signal, it is needed to first multiply the injected signal. For that, additional circuitry is designed. Nevertheless, the operating frequency being lower, simple schemes like self-mixing Gilbert cell is easy to implement. Another approach for frequency multiplication is the use of a high-class biased transistor that generates high order harmonics (distortion).

Figure 8 shows schematically both techniques for multiplying efficiently the injected frequency at injection frequencies lower than 50 GHz. The final phase noise of a system combining a frequency multiplier (xK) and an injection locked N-push oscillator (xN) as shown in figure 9, is given by:

$$\mathcal{L}_{out}(\Delta f) = \mathcal{L}_{inj}(\Delta f) + 20 \cdot log(K \cdot N) \quad (11)$$

This is the minimum theoretical achievable phase noise in an injection locked system. Note that this minimum phase noise depends on frequency offset Δf and the output phase noise tends to approach the free running oscillator's phase noise for high Δf.

Next section describes fabricated circuits in CMOS as well as in BiCMOS technologies integrating the above described functionalities.

III. Silicon 300-GHz Sub-harmonic Injection Locked Oscillators

A. Push-push and mix in CMOS 65nm

The first fabricated circuit is a push-push and mix type oscillator. It also implements sub-harmonic (/2) injection locking circuitry. Figure 10 shows the schematic of the circuit including the biasing parts. The injection locking multiplier uses two transistors driving the injection signal directly into the oscillator's core. They are biased near the threshold voltage to maximize 2nd order distortion. The oscillator is designed to operate around 96 GHz and it is loaded to a single balanced mixer to up-convert the signal around 288 GHz. The power consumption is 50 mW. Figure 11 shows the output power on 50 Ohm load versus the output frequency. On the right of figure 11 is shown the output spectrum of the circuit. It is locked on an injection signal at 47.39 GHz.

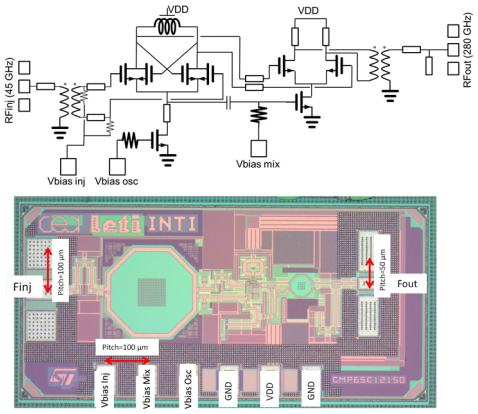

Fig. 10. Injection locked Push-push and Mix oscillator schematic in CMOS 65nm technology. Micrograph of the chip.

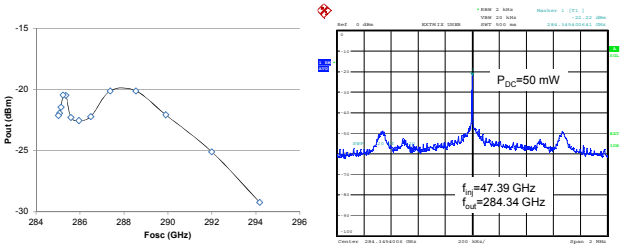

Fig. 11. Output power versus free running frequency and output spectrum locked at 284.34 GHz.

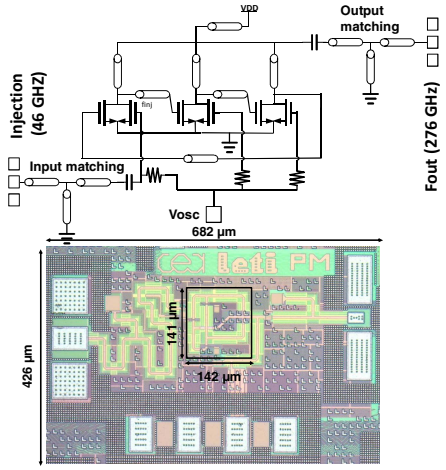

Fig. 12. Injection triple-push oscillator schematic in CMOS 65nm technology and micrograph of the chip.

B. Triple-push in CMOS 65nm

The next circuit implements a triple-push oscillator that includes a similar sub-harmonic injection locking circuit. Figure 12 shows the schematic of the circuit. The core oscillator operates around 92 GHz the output frequency is 276 GHz. The free running oscillation tuning range covers from 271 GHz to 278 GHz. The oscillator locking range spans the whole band as illustrated in figure 13. The output phase noise when locked to a

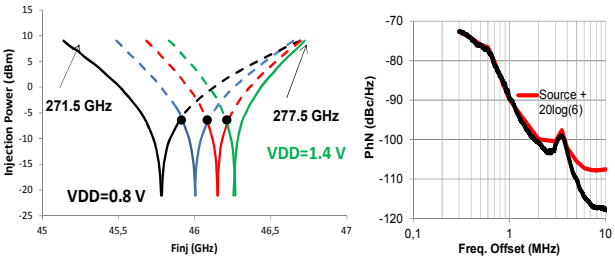

Fig. 13. Locking sensitivity curve of the sub-harmonic injection locked triple-push oscillator. Locked output phase noise at 276 GHz compared to the injection phase noise adding 20·log(6).

46 GHz injection signal reproduces exactly the injected signal value augmented by the theoretical multiplication factor of 20·log(6). The total power consumption is 40 mW. The fabricated circuit demonstrates the potentiality of such architecture for low power, low phase noise for 300 GHz frequency generator in standard CMOS technology. Indeed, the f_{max} of the CMOS 65nm technology is 210 GHz.

C. *Triple-push in BiCMOS 55nm*

The same architecture has been implemented also in a BiCMOS 55nm technology that offers higher active performances. That helps for example to obtain larger tuning range and higher level output signal around 300 GHz compared to a CMOS technology. The circuit schematic is depicted in figure 14. For injection locking, a Gilbert cell is designed for more efficiency. The oscillator core frequency covers the 90-to-100 GHz frequency (>10 %). Thanks to improved injection locking, the locking range covers the global oscillation frequency band with low injection power (<0 dBm). Figure 14.d and 14.e show the output locked spectrum at 297 GHz and the output phase noise respectively. We observe an outstanding phase noise of -105 dBc/Hz at 297 GHz. The circuit power consumption is 52 mW.

CONCLUSION

This paper shows the basic design techniques that enable to implement above f_{max} frequency generators in standard Silicon technologies. It describes the so called N-push techniques that are used to boost high order harmonics from oscillators operating at lower frequency. Combining the N-push design to sub-harmonic injection locking it is shown that low phase noise can be achieved around 300 GHz from Silicon based technologies. The theoretical discussion is followed by on-chip measurements on various implemented circuits operating from 270-to-300 GHz.

REFERENCES

[1] K. Katayama, et al., "A 300GHz 40nm CMOS Transmitter with 32-QAM 17.5Gb/s/ch Capa-bility over 6 Channels," *ISSCC*, pp. 342–343, 2016.

[2] K. Sengupta and A. Hajimiri, "A 0.28 THz Power-Generation and Beam-Steering Array in CMOS Based on Distributed Active Radiators," *IEEE JSSC*, vol. 47, no. 12, pp. 3013-3031, Dec. 2012.

[3] T. Chi, Jet al., "A Multi-Phase Sub-Harmonic Injection Locking Technique for Bandwidth Extension in Silicon-Based THz Signal Generation," *IEEE JSSC*, vol. 50, no. 8, pp. 1861-1873, Aug. 2015..

[4] J. Grzyb, Y. Zhao and U. R. Pfeiffer, "A 288-GHz Lens-Integrated Balanced Triple-Push Source in a 65-nm CMOS Technology," *IEEE JSSC*, vol. 48, no. 7, pp. 1751-1761, July 2013.

[5] L. Wu, S. Liao and Q. Xue, "A 312-GHz CMOS Injection-Locked Radiator With Chip-and-Package Distributed Antenna," *IEEE JSSC*, vol. 52, no. 11, pp. 2920-2933, Nov. 2017.

[6] R. Han and E. Afshari, "A CMOS High-Power Broadband 260-GHz Radiator Array for Spectroscopy," *IEEE JSSC*, vol. 48, no. 12, pp. 3090-3104, Dec. 2013.

[7] P. Y. Chiang, et al., "A Silicon-Based 0.3 THz Frequency Synthesizer With Wide Locking Range," *IEEE JSSC*, vol. 49, no. 12, pp. 2951-2963, Dec. 2014.

[8] A. Siligaris et al., "A 270-to-300 GHz Sub-Harmonic Injection Locked Oscillator for Fre-quency Synthesis in Sub-mmW Systems," *IEEE MWCL*, vol. 25, pp. 259-261, April 2015.

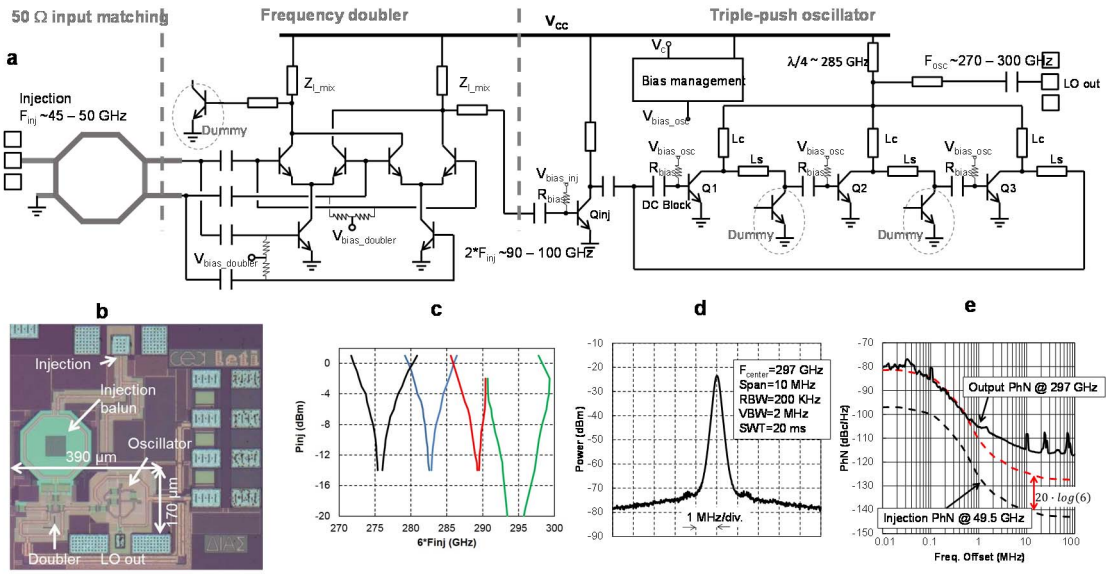

Fig. 14. a. Injection locked triple-push oscillator in CMOS 65nm technology. b. Micorgraph of the chip. c. Locking sensivtivity curve. Injection signal 45.3 – 50 GHz. d. Output spectrum at 297 GHz locked on an input signal at 49.5 GHz. e. Output Phase Noise at 297 GHz locked on an input signal at 49.5 GHz.

Study of the phase noise of Langatate crystal resonators

A. Pokharel, F. Sthal, E. Vaillant,
J. Imbaud, J.J Boy
FEMTO-ST Institute,
Univ. Bourgogne Franche-Comté, CNRS, ENSMM
Besançon, France
fsthal@ens2m.fr

F. X . Esnault, G. Cibiel
Microwave, Digital & Optic Dept.
Centre National d'Etudes Spatiales (CNES)
Toulouse, France

***Abstract*— In this paper, the intrinsic study on Langatate (LGT) crystal resonators has been carried out at 10 MHz resonant frequency. Among the crystals belonging to the Langasite family, the Langatate ($La_3Ga_{5.5}Ta_{0.5}O_{14}$) also called LGT seems to be an alternative option to substitute the quartz crystal resonators for frequency and time applications. The intrinsic properties like electromechanical coupling coefficients, product of quality factor and frequency are normally seen higher than in quartz crystal resonators. Moreover, the amplitude- frequency effect and the force-frequency coefficient are lower. The characterization of these resonators is given in terms of impedance, Q-factors, turnover temperature, amplitude-frequency effect and phase noise. The short-term stability of some resonator pairs has been measured about $3 \cdot 10^{-13}$ in terms of Allan standard deviation.**

Keywords—LGT resonators; Y-cut; Q-factor; phase noise; carrier suppression

I. INTRODUCTION

Ten years back, the first 10 MHz Ultra Stable LGT Oscillators whose fractional frequency stability and noise almost similar to quartz oscillators i.e. 10^{-13} and -110 dBc/Hz at 1 Hz were built in FEMTO-ST [1]. However, the disadvantageous behavior in frequency-temperature characteristics in comparison to quartz crystal resonators still exists. In this paper, very high quality LGT crystal resonator pairs at 10 MHz have been measured on an advanced phase noise measurement system setup in collaboration with Centre National d'Etudes Spatiales (CNES). The noise measurement system is equipped with carrier suppression technic and allows a passive characterization of the resonator pair in Fourier frequencies. Because of the very small value of impedance, lower than 10 Ω, special adaptation was done using transformers in order to maximize the loaded Q-factor in the measurement system. The impedance bridge had been simulated in Pspice using an advance optimization process. The resonators have been named *a*, *b* and *c* and characterized in terms of impedance, turnover temperature, amplitude-frequency effect and phase noise. The resulting short-term stability of the resonators measured on their metrological vibrating C-mode at 10 MHz is reported.

II. RESONATOR PARAMETERS

The LGT resonators were achieved in Y-1° cut in order to achieve a turnover temperature point near 80°C. The applied power to measure the motional parameters is around 60 µW. Fig. 1 shows the amplitude and phase of the impedance in reference to the resonant frequencies of the resonators *a*, *b* and *c*.

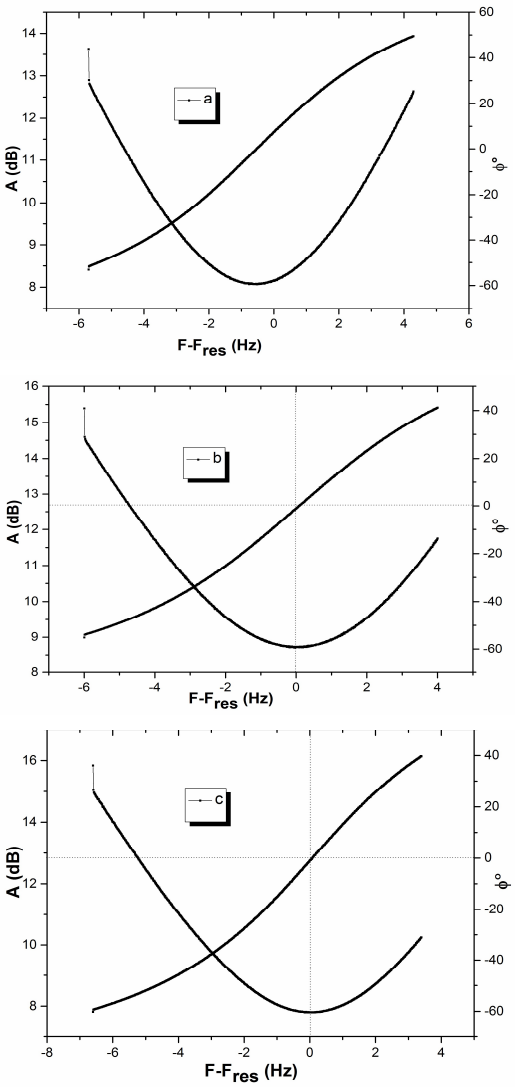

Fig. 1. Amplitude and phase of the resonators *a*, *b* and *c,* at approximately 60 µW excitation power respectively.

Table I enlists the experimental values of the resonant frequencies at turnover temperatures, the turnover temperatures *PI*, the motional parameters *R* and *L*, the static capacitances C_0 and the unloaded quality factor *Q* of the three resonators *a*, *b* and *c* respectively. The motional resistance is given by minimum of the impedance amplitude. The quality factor is measured from the inverted slope of ±1° phase shift in Fig. 1. Values of internal impedances were found to be around 8 Ω on average. The unloaded quality factors Q were seen to be around $1.1 \cdot 10^6$.

TABLE I. EXPERIMENTAL VALUES OF MOTIONAL PARAMETERS, TURNOVER TEMPERATURE (PI) AND QUALITY FACTOR.

Res.	f_{res} - 10 MHz (Hz)	PI (°C)	β (ppb/°C²)	R (Ω)	L (mH)	C_0 (pF)	Q (10^6)
a	44.8	85.3	-67.7	8.1	153	17.3	1.19
b	34.4	83.7	-59.4	8.7	150	17.0	1.08
c	29.4	83.6	-72.6	7.8	158	17.2	1.27

About the thermal behavior, a parabolic effect has been observed using a fitting curve given by the following equation:

$$\frac{\delta f}{f_0} = \frac{f_{T_r} - f_{T_0}}{f_{T_0}} = \beta \cdot (T_r - T_0)^2$$

Here, T_0 is the turnover temperature f_{T_r} is the value of frequency obtained at temperature T_r and β is the parabolic constant whose value strictly depends on the cut of the resonator. There was similarity on the turn-over temperatures for all the three resonators. The turnover temperatures were found around 84 °C. The ppb values of β of the resonators deviated in almost same magnitude. Unlike discussions in [2], there were no high range of frequency fluctuations in these LGT resonators but the parabolic nature of turnover temperature curve questions the elevated temperature sensitivity effect still prevailing in the LGT resonators. β values are around six times more sensitive than of the SC-cut quartz cut. About the applied power, the resonator's excitation power was varied from few tens µW to few mW. A relative frequency variation value of around $-3.2 \cdot 10^{-10}$/µW has been observed for the resonators [3].

III. PHASE NOISE MEASUREMENT BY PASSIVE METHOD

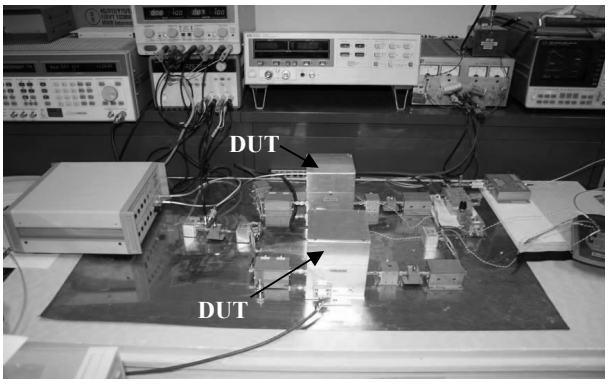

Fig. 2. Phase noise measurement bench.

Figure 2 shows the experimental setup used to measure phase noise [4]. This is a carrier suppression bench that has an equivalent flicker floor in terms of Allan deviation till 8.10^{-15}. All the components of the bench are optimized to do measurements at 10 MHz frequency. The bench has three most vital sections those are; the excitation source, the Device Under Test (DUT) and the output analyzer. It is a double arm bench, the input power from the excitation source is split in such a way to deliver equal amount of power in both arms. Both the arms have similar arrangement of components. Each arm has a tuning capacitor and an attenuator to adjust the frequency shift and loaded quality factor. The signals from both the arms are 180° shifted to the complete suppression of the carrier. The two signals are then combined and amplified by a RF amplifier and then fed to the mixer. Now that the influence of carrier source is highly reduced, the only remaining fluctuations in output signal would be the noise from the DUT's. Finally, after mixing the baseband and amplifying, the output signal is fed to the FFT analyzer to observe the power spectral density of phase fluctuations. All the components of the bench have been matched at 50 Ω. Classically, the measured resonators are matched to 50 Ω using a half π-bridge in the case of the motional resistance of LGT resonator (Fig. 3).

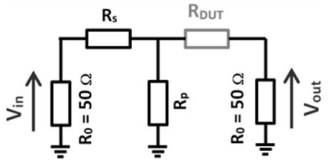

Fig. 3. Classical impedance matching circuit (50 Ω).

Using the classical circuit, the loaded Q of the resonator was around 100 k, and it was too small to have a sufficient output signal for the noise measurement.

IV. PSPICE SIMULATION

Transformer matching is proposed in order to improve the loaded Q factor of the resonator. Fig. 4 shows the special matching circuit arrangement.

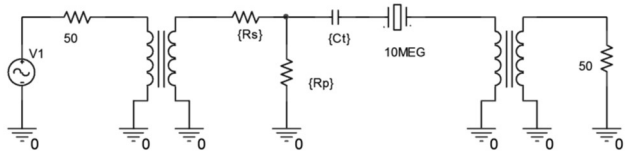

Fig. 4. Special impedance matching circuit with transformers.

Simulation with Pspice has been investigated. Fig. 5 are the magnitude and phase of the resonators using special adaptation circuit with transformers along with the resonators. The impedance ratio of the used transformer was increased from 1 to 16. Then, the loaded Q factor of the resonators increases from 10 % to 70 %, respectively. The experimental and simulated values of magnitude and phase were almost same but with minor shift in frequency and phase. This shift can be induced by the uncertainty about the values of oven in-built tuning capacitor.

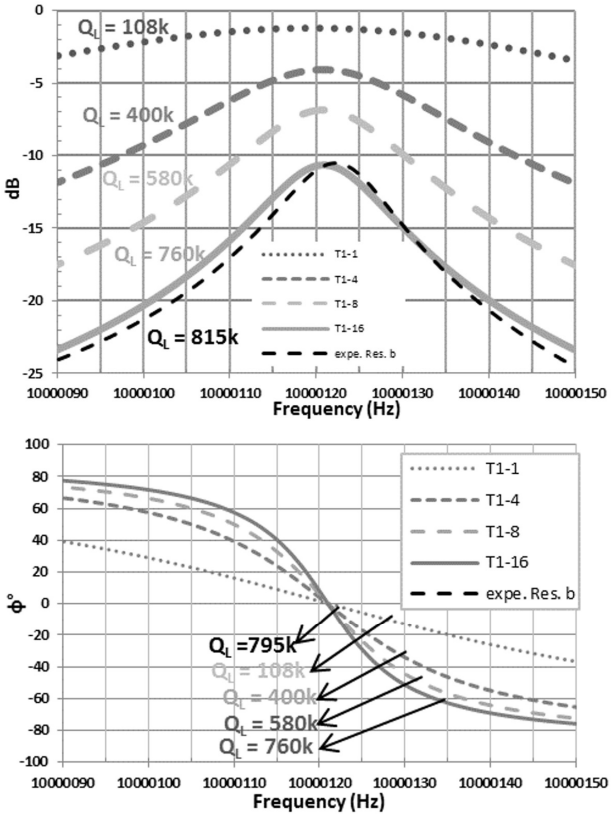

Fig. 5. Amplitude and phase of the transfer function simulated with some transformer ratios compared to experimental results.

V. PHASE NOISE RESULTS

A. Noise floor of the measurement system

Fig. 6 presents the noise floor of the system. It has been measured at 10.000121 MHz that corresponds to the tuned frequency of the resonators.

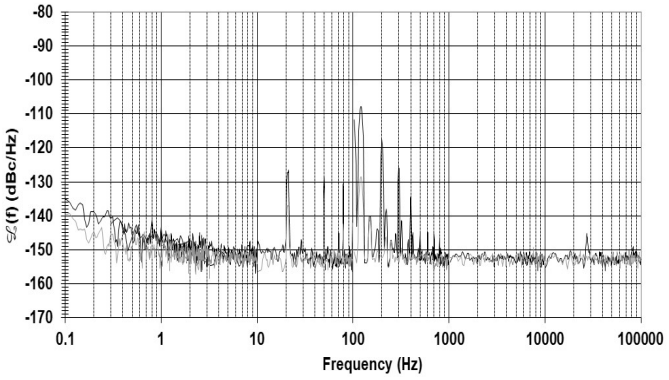

Fig. 6. Phase noise of the floor with oven turned on (dark) and off (light). The source frequnecy is 10.000121 MHz.

The phase noise measurement of the floor was achieved by inserting an equivalent resistor replacing the resonator. The result showed in Fig 6 that the transformers introduced for optimization had no effect on the phase noise floor.

Spurs on the curves above 10 Hz can be explained by the mixing between the reference at 10 MHz of the synthesizer and its output signal at 10.000121 MHz. In that case, a spur at 121 Hz can be generated. Also, the 50, 100, 150 ...Hz spurs from power supply which were fed-in the oven and with the resonators being inside, produced other spurs. For example, mixing between the frequencies at 100 Hz and 121 Hz leads to 21 Hz spur.

B. Phase noise measurement results of LGT resonators

Figure 7 shows the typical one sided power spectral density of phase fluctuations graph measured for the resonators. The power dissipated by resonators was around 120 µW. The $\mathcal{L}(f)$ at 1 Hz bandwidth was at -128dBc/Hz. The phase noise floor was around -156 dBc/Hz at 1 kHz offset frequency for the resonator pair. The short-term stability σ_{y_floor} was calculated around $3{\cdot}10^{-13}$. This result was achieved by using the transformers with T1-16 impedance ratio which optimized the loaded quality factor. The optimization of the quality factor can be easily visualized by value of PSD and its asymptotic approach to determine F_L.

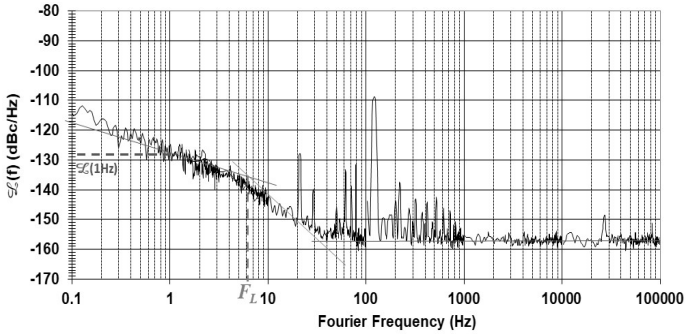

Fig. 7. Example of Phase noise of the resonator pair (*a* and *b*) with T1-16 transformer

Table II sums up the measured phase noise of the resonators and the flicker floor of the short-term stability obtained from measurements of $\mathcal{L}$(1 Hz) computed from the cut off frequency F_L [5].

TABLE II. SHORT-TERM STABILITY OF THE LGT RESONTORS.

Res. pairs	***a-b***	***a-c***	***b-c***
F_L **(Hz)**	6.3	5.7	6.3
$\mathcal{L}$**(1 Hz) (dBc/Hz)**	-128	-127	-129
σ_{y_floor}	$2.99{\cdot}10^{-13}$	$3.04{\cdot}10^{-13}$	$2.66{\cdot}10^{-13}$

VI. CONCLUSION

Phase noise of bulk acoustic wave (BAW) Langatate crystal resonator has been explored using a passive measurement system based on carrier suppression. It has been measured through impedance matching using transformer to improve the loaded quality factor of the resonators. With this conditioning, the phase noise is increased above the noise floor of measurement system. Measurements show that transformers do not degrade the noise floor of the measuring bench. The level of the short term stability of the LGT resonators computed from the phase noise measurement is around 2 to $3{\cdot}10^{-13}$.

ACKNOWLEDGMENT

This work was supported by the LABEX Cluster of Excellence FIRST-TF (ANR-10-LABX-48-01), within the Program "Investissements d'Avenir" operated by the French National Research Agency (ANR) and Region Bourgogne-Franche-Comté.

REFERENCES

[1] J. Imbaud, S. Galliou, J.P. Romand, P. Abbe, R. Bourquin, "Development of a 10 MHz oscillator working with an LGT crystal resonator: Preliminary results," IEEE Trans. Ultrason. Ferroelec. Freq. Contr., vol. 55, Issue 9, pp. 1913-1920, September 2008.

[2] J. Imbaud, J. J. Boy, F. Sthal, "LGT alternative quartz materials for Ultra-stable Oscillators," Proc.IEEE Int. Freq. Contr. Symp. , DOI 10.1109/FCS.2014.6859848, 2014.

[3] Y. Kim, "Amplitude-Frequency Effect of Y-cut Langanite and Langatate," IEEE Trans. on Ultrason., Ferroelect. and Freq. Contr., vol. 50, pp. 1683-1688, December. 2003.

[4] F. Sthal, M. Devel, J. Imbaud, R. Bourquin, S. Ghosh, G. Cibiel, "Study on the origin of 1/f noise in quartz resonators," J. Stat. Mech., n° 6, May, 054025, 2016.

[5] F. Sthal, M. Devel, S. Ghosh, J. Imbaud, G. Cibiel, R. Bourquin, "Volume dependence in Handel's model of quartz crystal resonator noise," IEEE Transactions on Ultrasonics, Ferroelectrics and Frequency Control, vol. 60, no. 9, November, pp. 1971-1977, 2013.

Direct Measurement of Cryogenic Sapphire Oscillators with Tracking DDSs and 2-Sample Covariance

Claudio E. Calosso♥, François Vernotte♦, Vincent Giordano♣, Christophe Fluhr♠, Benoit Dubois♠, Enrico Rubiola♣
♥Division of Physics Metrology, Istituto Nazionale di Ricerca Metrologica (INRIM), Torino, Italy
♦Observatoire de Besançon, Besançon, France
♣Department of Time and Frequency, FEMTO-ST Institute, Besançon, France,
♠FEMTO Engineering, Besançon, France.
Email: c.calosso@inrim.it

***Abstract*—Cryogenic Sapphire Oscillators have very good frequency stability and their measurement is possible only by comparing three similar units. The task is challenging because the short-term instability is significantly lower than the background noise of commercial phasemeters and counters. In this work, we demonstrate the direct ADEV measurement of each CSO at 100 MHz. We use a 6-channel phasemeter based on tracking DDS and then we take advantage of the two-sample covariance that reduces the contribution of the instrument noise for large averaging size. The result is in the low 10^{-15} at 1 s.**

Keywords—ultra stable oscillators; phasemeter, 2-sample covariance, 3-cornered hat

I. Introduction

Cryogenic Sapphire Oscillators (CSOs) provide microwave signals, and also HF-VHF signals via dedicated frequency synthesis, with short-term stability of parts in 10^{-16} [1]. This exceeds by two orders of magnitude the stability of masers and other commercial atomic standards. The measurement of such CSOs is possible only by comparing three similar units, and the task is challenging because the short-term instability is significantly lower than the background noise of commercial phasemeters and counters. For this reason, the measurement was until now done by beating the microwave outputs of the bare CSOs, with no synthesizer [2]. The beat notes of a few MHz provide a leverage factor of >60 dB. In this work, we remove the limitation of the beat note method, and we demonstrate the direct ADEV measurement of each CSO at 100 MHz. We use a 6-channel tracking DDS which exhibits a background noise in the low 10^{-14} in single channel [3]. Each CSO output is split into two channels. Thus, we collect two data streams per CSO, with statistically independent background noise. We use the two-sample covariance [4], in order to make the contribution of the instrument background converges to zero for large averaging size.

II. Notation

A. Time and Frequency quantities

In this paper we refer to time and frequency quantities such as phase φ, phase time x, fractional frequency y… of oscillators, time interval counters (TIC) and phasemeters. We indicate the signals from oscillators with capital letters (A, B, C…) that are used as subscript of the related quantities, i.e. φ_A is the absolute phase noise of oscillator A. Quantities related to instruments are indicated with numbers. In particular, we use n_j and m_j for the residual noise and for the measure of j-channel respectively. When used as subscript, the letter "m" can be dropped, i.e. x_{m1} and x_1 indicate the phase time measured by channel 1. Two indexes are used when the instrument gives the difference of two channels: $x_{12} = x_1 - x_2$ is the difference of the phase times measured by channels 1 and 2, while: $x_{n12} = x_{n2} - x_{n2}$ is the residual noise of the instrument in that configuration.

B. Allan Variance and 2-Sample Covariance (GCOV)

Time and frequency quantities are related each other: the phase is proportional to the phase time through the carrier frequency ν_0 [$\varphi(t) = 2\pi\nu_0 x(t)$] and the fractional frequency is the time derivative of the phase time [$y(t) = \mathrm{d}x(t)/\mathrm{d}t$]. For convenience, we introduce a new quantity z

$$z(t,\tau) \equiv \frac{\bar{y}(t) - \bar{y}(t-\tau)}{\sqrt{2}} \tag{1}$$

where $\bar{y}$ is the fractional frequency y averaged over the measurement time τ. Thanks to (1) the definition of AVAR and GCOV became respectively

$$\sigma_y^2(\tau) = \mathbb{E}[z^2(t,\tau)] = \mathbb{E}[z^2] \tag{2}$$

$$\sigma_{y_A,y_B}(\tau) = \mathbb{E}[z_A(t,\tau) z_B(t,\tau)] = \mathbb{E}[z_A z_B] \tag{3}$$

($\mathbb{E}[\cdot]$ is the expectation) while their estimators, based on the measures $z_i = z(i\tau,\tau)$, $i = 1 \ldots M$, are

$$\hat{\sigma}_y^2(\tau) = \frac{1}{M-1}\sum_{i=1}^{M-1} z_i^2 \tag{4}$$

$$\hat{\sigma}_{y_A,y_B}(\tau) = \frac{1}{M-1}\sum_{i=1}^{M-1} z_{Ai} z_{Bi} \tag{5}$$

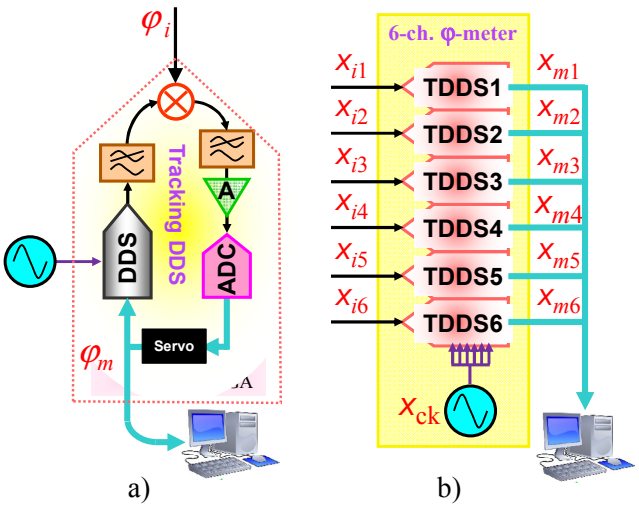

Fig. 1: block diagram of the Tracking DDS a) and of the 6-channel phasemeter used for characterizing the CSOs.

Two-sample variance and covariance are in general referred to the fractional frequency y and, for simplicity, the subscript y can be dropped so that $\sigma^2_{y_A}(\tau)$ and $\sigma^2_A(\tau)$ are the same quantity. Finally, in this paper we consider only 2-sample (co)variance, and, for compactness, in some formulae the dependency versus averaging time (τ) is not explicitly indicated.

III. Tracking DDS

The instrument used in this work is a multi-channel synchronous and real-time phasemeter based on Tracking Direct Digital Synthesizer (TDDS) technique [5]. For each channel, a controller maintains the DDS aligned with the signal at the input, by continuously updating the DDS numerical phase. Within the bandwidth of the controller, the latter is the measure of the channel, since it is representative of the input phase. Fig. 1.a shows in more detail that the DDS output is compared with the signal at the input by means of a single side band mixer used as phase discriminator. Its output, the phase error, is low-pass filtered, amplified and acquired by an Analog to Digital Converter (ADC) and read by a Field Programmable Gate Array (FPGA) that implements the servo. The servo calculates the frequency correction by means of a proportional-integrative controller and then the phase correction to the DDS through an accumulator. This closes the loop. The measures, i.e. the phase corrections, are sent to external PC where they are stored and analyzed.

As shown in Fig. 1.b, the phasemeter is composed of six TDDSs driven by the same FPGA that guarantees synchronous measures. Each channel k measures the phase time of the input x_{ik} with respect to the local oscillator (LO) x_{LO} with a residual noise x_{nk}

$$x_{mk} = x_{ik} + x_{nk} (-x_{LO}) \qquad k = 1 \ldots 6 \qquad (6)$$

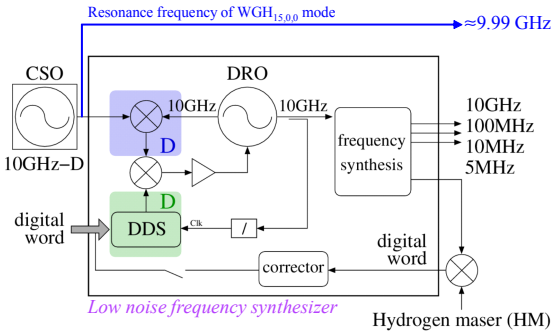

Fig. 2: The CSO oscillates slightly below 10 GHz. A low noise frequency synthesizer allows generating the frequencies commonly used in T&F laboratories.

The noise of the local oscillator x_{LO} can be dropped from (6), since it is in common mode and cancels out by considering, as we do in this work, differences of two channels or of weighed combinations of them. The residual noise of each channel coincides with the one of the DDS used (Analog Devices AD9912), since mixer, ADC, and amplifier noises do not degrade the performance of the channel [6]. Each channel has a residual frequency stability $\sigma_{nk}(\tau) = 1.5\times10^{-14}/\tau^{0.9}$ (flicker phase noise) for ν_0 = 100 MHz and a measurement bandwidth f_H = 5 Hz. The temperature sensitivity is of the order of 1 ps/K. The instrument accepts any frequency from 5 to 400 MHz.

IV. Cryogenic Sapphire Oscillators

The goal of this work is the characterization of the Cryogenic Sapphire Oscillators (CSO) named ULISS [1]. They offer an unprecedented frequency stability that is below 10^{-15} for averaging time from 1 to 10000 s. It comes from the exceptional stability provided by a high-purity Al_2O_3 crystal placed at liquid helium temperature in a well-controlled environment. The sapphire crystal has the shape of a cylinder: approximately 5 cm diameter, 3 cm high. It constitutes a Whispering Gallery Microwave Resonator with a quality factor Q of $\approx10^9$ at 10 GHz. Beside low dielectric losses, the cryogenic sapphire resonator presents a low sensitivity to temperature fluctuations and to mechanical vibrations. A turning point at about 6 K is provided by a controlled amount of Mo^{3+}, Ti^{3+}, Cr^{3+} that substitute Al^{+3} in the crystal. The working temperature is maintained by a Closed Cycle Cryocooler specially designed to limit mechanical vibrations and thermal fluctuations.

The oscillator is based on the Pound-Galani scheme [7], where a voltage-controlled oscillator is frequency locked to the resonator using the reflected microwave. In the Pound-Galani scheme, the same resonator is used also as the reference of the locked oscillator. In this implementation, the resonator power is stabilized by a second control. Two tunnel diodes near the resonator input detect forward and reflected power.

ULISS CSOs are complemented with a low noise frequency synthesizer generating useful ultra-stable signals at round frequencies. The sapphire resonators are designed to operate on the $WGH_{15,0,0}$ whispering gallery mode at 9.99 GHz

±5 MHz. The uncertainty is due to machinery tolerance and, incidentally, this avoids injection locking from other CSOs. The intentional 13-7 MHz frequency offset from the 10 GHz round frequency was chosen to permit compensating for the resonator frequency uncertainty by using a low noise Direct Digital Synthesizer (DDS). The DDS is inside the phase locked loop that locks the DRO to the CSO and provides the frequency offset that is necessary to obtain the desired frequency. The DDS allows to adjust the output frequency in a wide range (more than 100 ppm) with a resolution as low as 1×10^{-16}. The system is completed by frequency dividers that generate 100, 10 and 5 MHz from the 10 GHz signal. The frequency dividers have residual noise that is not negligible at 1 s. In the case of 100 MHz, the frequency measured in this work, it contributes at the level of $1\div2\times10^{-15}$ / τ.

V. Measurement Methods

The CSO provides several outputs at very different frequencies to fulfil the main applications: with the 10 GHz output, it's possible to drive directly the frequency comb and synthesize ultra-low noise local oscillators for atomic fountains. The range of applications is limited to few meters by the attenuation in microwave cables or by the necessity of frequency combs, for the optical domain. On the other hand, the 100 MHz output can be distributed at longer distance and can be directly compared with the 100 MHz output of hydrogen masers. Many schemes of comparisons are possible. In all cases presented here, we assume that all the noises (oscillators and instruments) are uncorrelated.

A. Indirect measure (beat-note method)

The tolerance in manufacturing the sapphire crystal induces the CSOs to oscillate at its own frequency that is spread in a range of few megahertz. Disposing of three CSOs, as required by the 3-cornered hat method, it's possible to beat each oscillator with the other two by means of power splitters and double side band frequency mixers. The specifications in terms of phase time of the counters is relaxed by more than 60 dB, i.e. by 10 GHz / ν_{BN}, where ν_{BN} is the frequency of the beat note. In this regard, the instrument can be considered noiseless and the 3-cornered-hat method can be used without any problem.

B. Direct measure

The direct measure of the CSOs is more challenging, since there is no leverage factor that reduces the contribution of the instrument. Best frequency counters, even in Λ or Ω mode [8], hardly behaves better than $10^{-13}/\tau$ and cannot be used. Phasemeters have better frequency resolution, in the low 10^{-14} at 1 s, but their use with three-cornered-hat method is problematic, since the noise of the instruments appears in the estimation of the oscillator stability [4] and needs to be estimated and subtracted. Equation (7) is related to Fig. 3.a and reports the case of oscillator *B*. For the CSO *A* and *C*, analogous equations hold.

$$\frac{1}{2}\mathbb{E}[z_{12}^2+z_{34}^2-z_{56}^2]=\sigma_B^2(\tau)+\frac{1}{2}[\sigma_{n12}^2+\sigma_{n34}^2-\sigma_{n56}^2] \quad (7)$$

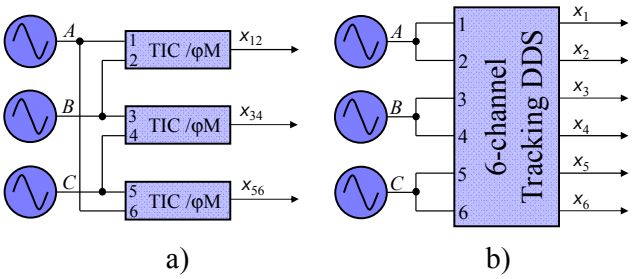

Fig. 3: Direct measure of the CSOs by means of three independent instruments (a) and of a 6-channel phasemeter based on Tracking DDS (b).

On the other hand, for the 2-sample covariance, in analogy of what happens for the cross-spectrum with phase noise power spectral density, the contribution of the instrument noise converges to zero (8) for a large number of measures *M*, without the necessity of any particular compensation for the instrument noise.

$$\mathbb{E}[z_{12}z_{34}]=\sigma_B^2(\tau) \quad (8)$$

In our particular case, it's convenient to connect the Tracking-DDS phasemeter as shown in Fig. 2.b. The CSO outputs *A*, *B* and *C* are splitted in order to feed a couple of channels: *A* is measured by (1, 2), *B* by (3, 4), and *C* by (5, 6). In this configuration, (8) translates to (9)

$$\sigma_B^2(\tau)=\mathbb{E}[z_{32}z_{45}] \quad (9)$$

Equation (9) is the simplest way to take advantage of the 2-sample covariance, but it is not the best way to use the information contained in the set of data, in particular for what concerns the noise of the instrument. A better way to combine the measures is described by (10)

$$\sigma_B^2(\tau)=\frac{1}{2}\mathbb{E}[z_{3\langle12\rangle}z_{4\langle56\rangle}+z_{4\langle12\rangle}z_{3\langle56\rangle}] \quad (10)$$

where $z_{i\langle jk\rangle}=z_i-(z_j+z_k)/2$ indicates that the channel *i* is compared to the average of channels *j* and *k*. In addition, the two possible combinations: $z_{3\langle12\rangle}z_{4\langle56\rangle}$ and $z_{4\langle12\rangle}z_{3\langle56\rangle}$ are exploited.

VI. Results

The test bench used during this campaign implemented the indirect and the direct (Fig. 3.b) measures. The test bench and the CSOs were placed in a room with controlled temperature (22 ± 0.5 °C) and humidity (50 ± 10 %). The measure lasted about 6 days. During this campaign, CSO *B* operated with power stabilization off, due to the failure of the tunnel diode

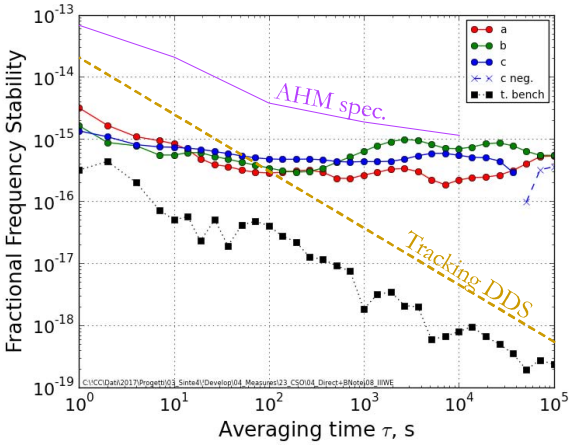

Fig. 4: frequency stability of the three CSOs is reported in red, green, and blue. CSO *C* presents negative covariance, reported with crosses and dashed line. In violet it's reported the frequency stability of state-of-the-art active hydrogen masers and in brown, the residual noise of the Tracking-DDS (difference of two channels).

used as probe. As a result, a drift of 3.7×10^{-13}/day is present in the measures. Despite it is a factor 30 higher with respect to the typical CSO drift, it is very stable and, once removed, the quality of the set of data is comparable with the other two.

For what concerns the direct method, the measure was done at 99.999, 100.001 and 356.7 MHz. The first two frequencies are close to 100 MHz and are at the output of the first two CSO synthesizers. The third frequency is obtained by direct division by a factor 4×7 of the third CSO output, since its frequency synthesizer was not available. Measuring at different frequencies was useful to avoid the effect of crosstalk among the channels. In addition, each TDDS was tuned in order to minimize AM-PM conversion that, as in the case of cross-spectrum [9], may lead to the collapse of the measure. Then (10) was applied to the measured data. The result is shown in Fig. 4. The direct method furnishes the same results for $\tau > 10$ s with respect to the beat-note method, used as a term of comparison. The difference for lower averaging time is due to the residual noise of synthesizer used to generate the 100 MHz outputs. The stability measured at 1 s is well below the residual noise of the Tracking DDS, that in case 2-sample covariance is not used, becomes negligible only for $\tau > 100$ s.

VII. Conclusion

We reported on the direct characterization of three Cryogenic Sapphire Oscillators at FEMTO-ST, by means of a 6-channel synchronous phasemeter based on the Tracking DDS technique. That was possible thanks to the 2-sample covariance that allowed to average down the residual noise of the instrument by more than one order of magnitude at 1 s in few days of measure. With this work, we extend the possibility for characterizing ultra-stable sources, by removing the limitations of the beat-note method. The CSOs confirmed to have very high stability and very low drift even in this unfortunate case, where the power stabilization of one oscillator was off.

Acknowledgment

The work has been realized in the frame of the ANR project: Equipex Oscillator-Imp. The authors would like to thank the Council of the Région de Franche-Comté for its support to the Projets d'Investissements d'Avenir and the FEDER for funding one CSO. This work has been funded by the EMRP program (IND55 Mclocks). A special thank to the European Space Agency, for supporting this activity.

References

[1] V. Giordano, S. Grop, C. Fluhr, B. Dubois, Y. Kersale, E Rubiola, J. Physics: Conf. Series 723 (2016), article no. 012030.

[2] C. Fluhr, S. Grop, B. Dubois, Y. Kersale, E. Rubiola, V. Giordano, IEEE Transact UFFC 63(6) pp. 915-921, June 2016.

[3] M. Caligaris, G. Costanzo, C. E. Calosso, Proc. 2015 IFCS-EFTF pp. 681-683.

[4] F. Vernotte, C. E. Calosso, E. Rubiola, Proc. 2016 IFCS, pp. 282-287.

[5] C. E. Calosso, "Tracking DDSs in time and frequency metrology," Proc. Joint IFCS / EFTF Symposium (Prague, 2013).

[6] C. E. Calosso et al., "Phase noise and amplitude noise in DDS", Proc. IFCS.

[7] Z. Galani, M. Bianchini, R. Waterman, R. Dibiase, R. La- ton, and J. Cole, "Analysis and design of a single- resonator GaAs FET oscillator with noise degeneration," IEEE Transactions on Microwave Theory and Technques, vol. 32, no. 12, pp. 1556–1565, Dec. 1984.

[8] E. Rubiola, M. Lenczner, P.Y. Bourgeois, F. Vernotte, The Ω Counter, a Frequency Counter Based on the Linear Regression, IEEE Transact. Ultrason., Ferroelec. Freq. Control Special Issue of the 2015 Int'l Freq. Control Symp. vol.63 no.7 p.961-969, July 2016.

[9] C. W. Nelson et al. "A collapse of the cross-spectral function in phase noise metrology". Review of Scientific Instruments, vol. 85, 024705 (2014); doi: http://dx.doi.org/10.1063/1.4865715niques, vol. 32, no. 12, pp. 1556–1565, Dec. 1984.

Measuring Small Propagation Frequency Shifts and Fluctuations by Phase to Avoid Cross-Correlation Errors

Michael J Underhill
Underhill Research Limited, Lingfield, UK
Email: mike@underhill.co.uk

***Abstract*—This paper investigates the practicality of measuring microhertz to millihertz frequency differences by phase differences using an off-the-shelf SDR receiver. The phase difference method is two orders of magnitude faster if the phase can be measured to 3.6^0. The method has been used to confirm the discovery of a 16.2 (±1) µHz red-shift of the frequency over a 190 km ground wave path. The estimate by extrapolation from previous ionospheric HF measurements is 15-20 µHz on a transmitter absolute frequency error of ~1 mHz. The mechanism now assumed is that the frequency red-shift is proportional to the curvature angle of the path, and also proportional to the square root of frequency. The new Propagation-Phase/Frequency-Shift (PPFS) theory is now being analysed using a new Coupling-Graph technique. It is based on the 'Filamentary Model of Electromagnetism' originally announced in 2011. It further supports the concept of EM detection and generation of gravity-potential-waves. The phase-difference method is found to be impervious self- and cross-correlation random 'spurs' and 'spectrum-collapse' that can bedevil phase noise measurements.**

Keywords— Frequency measurement by Phase, SDR, gravity-waves, propagation red-shift frequency errors, spurs and spectrum collapse.

I. Introduction and Aim

Research has continued into the measurement of propagation frequency shifts and fluctuations of off-air frequency standards at frequencies from 25MHz now down to 60 kHz. The ionospheric frequency shifts down to about 1.5MHz can easily be observed and measured on the spectrum displays of an SDR receiver supplied with a high-quality reference source. Measurements so far have been made on the RFSpace SDR-IP clocked at 10MHz by a SpectraTime LCR 900 Rubidium Source [1-2]. (These references are based on the fundamental physics of reference [3]).

Ionospheric frequency shifts vary from about 50mH to 1Hz and can be multi-path with several components. All these can be seen and measured on a SpectraVue display on an SDR receiver with a resolution of <10 mHz. However, the absolute accuracy of these measurements depends on accurate calibration and setting of the Rubidium Clock for the SDR. For calibration the SDR Kits GPS phase locked 10MHz source is used. Although the GPS signal is not phase stable when switching from one satellite to another this occurs infrequently, about two or three times a day, an calibration can easily be retained over one or two hours on a single satellite source.

This paper shows that the final measurement accuracy is improved by up to two orders by measuring phase to $\pm 1.8^0$ rather than frequency differences over this time. A 1000s measurement can thereby give a10µHz accuracy on a 10MHz comparison, corresponding to an accuracy of 1 in 10^{12}.

Some additional advantages of measuring frequency and phase noise by phase were pointed out by S. Stein in [4]. Spectrum collapse and unwanted spurs thendo not occur. And then there are no 'mixers' as a possible cause of these effects.

Previous measurements show that 'off-air' frequency-standards propagated by ground-waves can be used to set the frequency of a local rubidium oscillator to a few parts-per-trillion (10^{12} =ppt). For example, to achieve 1ppt with the AM frequency standard signal at 198kHz, R4 at Droitwich, UK over a path length of 190km to Lingfield in Surrey, the phase should not change by more than six degrees over 24 hours.

Thus the aims of this paper are:

1. To show that small frequency differences can be measured faster and more accurately from a phase difference plot taken over a reasonable time. We can estimate a reduction of measurement time typically of two orders of magnitude.

2. To find whether the Hubble type red-shift of frequency previously discovered for ionospheric propagation of frequency standards still holds for low frequency (LF) round wave propagation over relative short paths of a few hundred kilometers. A mysterious 'red-shift' of frequency of about 5 ppb (5 in 10^9), or 1 mHz, had been found for the Droitwich 198 kHz signal over the 190 km path to Lingfield. This is much larger than the estimated refraction-shift of about 17 µHz, predicted from measurements of higher frequency ionospheric frequency shifts.

3. To demonstrate that cross-correlation digitization errors in spectrum analysis can be reduced but not sufficiently to compete with direct-phase measurement of small frequency differences

II. First Measurements

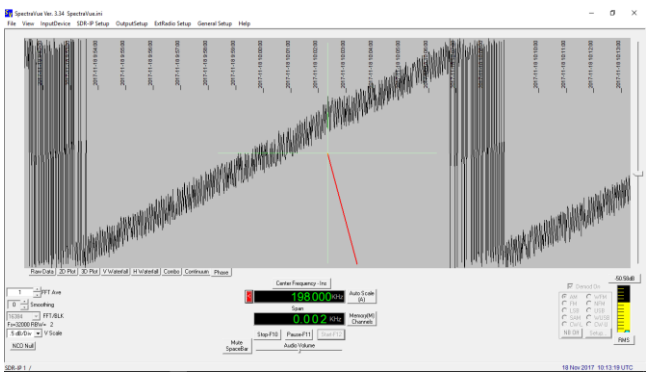

Fig. 1. Measurement of phase of BBC R4 Droitwich transmitter at 190 km. One cycle in 930s is 1.075mHz or 1/(930×198000) =5.43 parts in 10^9 frequency error.

The initial research focus has been the measurement of standard frequency sources available by groundwave propagation at LF. The first two successful measurements at Lingfield, 30km south of the Thames in London, were (a) from the 198kHz signal from the BBC Radio 4 500kW transmitter at Wychbold, near Droitwich at a distance of 190 km and 312^0 bearing, and (b) the 2MW 162 kHz RTF standard frequency transmission at Allouis, France at a distance of 475 km and 160^0 bearing. These are shown in Figs 1 and 2 respectively.

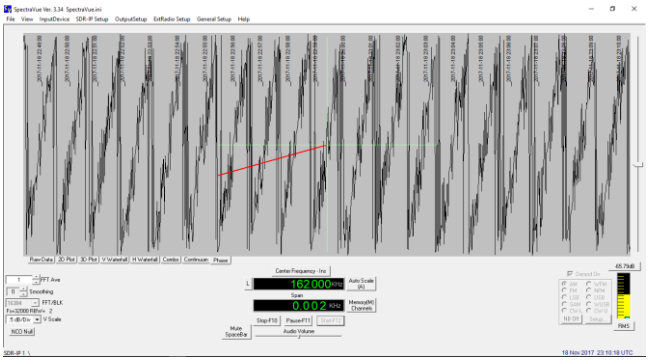

Fig. 2. Measurement of phase of Allouis RTF transmitter at 475 km. 18 cycles in 20min 45s =14 46mHz which in 162kHz is 89 parts in 109.

The first measurements shown in Figs 1 and 2 respectively show that both transmitters have small frequency errors relative to the local LCR-900 rubidium source. which has been phase synchronised to the GPS derived SDR-kits source during an observed time of GPS frequency/phase stability.

III. The 198 kHz Red-Shift Experiment

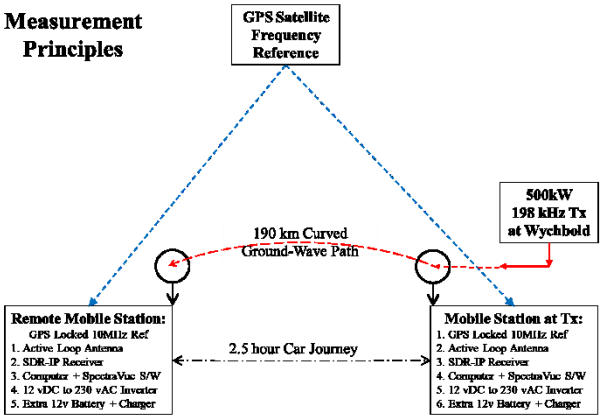

Fig. 3. Measurement pinciples for 198 kHz red-shift experiment. Ideally duplicate equipment is used at both ends of the radio path. Second best is one set of equipment driven fromone enf to the other.

The safe way to measure the expected red-shift of 17-25 µHz of the 198 kHz R4 standard frequency rubidium-locked signal over the 190 km Droitwich to Lingfield path is with simultaneous frequency measurements made at each end using a common frequency reference, such as a GPS reference from the same satellite. (20 µHz in 200 kHz is 1 in 10^{10} and 20 µHz has a period of 50,000 s = 833 min =13.88 hours.)

The next best, more cost effective, method was chosen. The same measurement equipment was used at both ends of the path, within the 12 hours of a typical GPS satellite visibility. The measuring equipment was made portable by car. Figure 3 illustrates the principles of both methods.

The mobile equipment is shown in Fig. 4 operating in a car park about 600 m from the R4 LW antenna which is also pictured in Fig. 4. The S

Fig. 4. Mobile Measurement Equipment: (a) Wychbold car park 600 m from antenna, (b) operation at Wychbold, (c) BBC Droitwich antenna (d) at Lingield

Figure 5 shows the RFSpace SDR-IP used for the measurements.

Fig. 5. RFSpace SDR-IP used for measurements. RFSpace SDR-IP isat bottom of four SDR receivers stack

IV. The Experimental Results

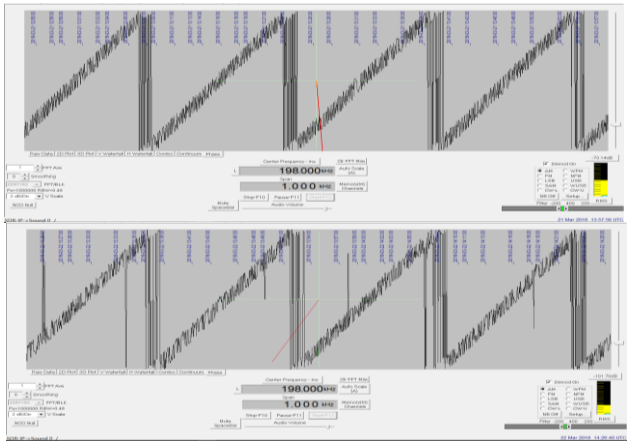

Fig. 6. 198 kHz red-shift for 190 km path = 16.2 µHz (±1), or 16.2×10^{-6} /198,000 = 82 ppt ($\times 10^{-12}$). Top plot is at tx at Wychbold and bottom is 190 km distant at Lingfield. Phase difference is measured at starts and finishes of plots.

Fig. 6 is the key red shift result that confirms the predicted result of 15 to 20 µHz. The basis for this prediction

is that a single ionospheric reflection gives a fractional red-shift frequency proportional to the final angle of reflection.

For measurements of the Issoudun, France DRM test tone at 3965.752 kHz the reflection angles estimated for single and triple (two-hop) reflections are about 270^0 to 320^0. The measured red shift per reflection is about 0.08 Hz. This times a frequency ratio of 1/200 and an angle ratio of 190/40000 gives 15 to 17 µHz predicted red-shift.

V. Additional Wychbold Frequency-Shift Results

At Wychbold more measurements were made at the additional frequencies of 909 kHz, 1215 kHz, 693 kHz, 162 kHz, 77.5 kHz and 60kHz for comparison with Lingfield measurements at the same frequency.

Of these, Fig. 7 for 909kHz shows that interference makes it impossible to measure accurately enough for detection of any redshift.

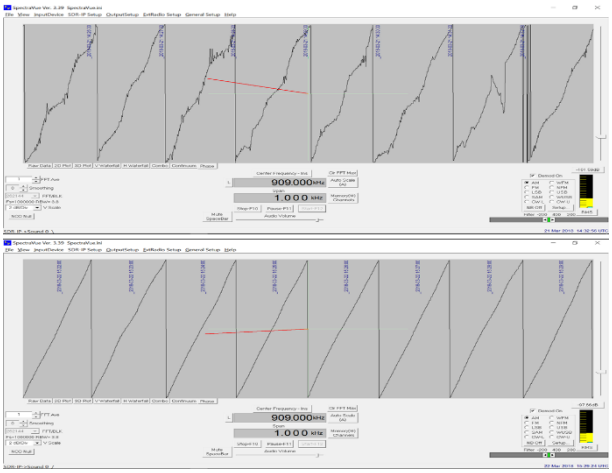

Fig. 7. 909 kHz Phase Measurements at Wychbold (top) and Lingfield (bottom). Transmitter at Brookman's Park just north of London.No significant frequency shift measurable in this case. At Wychbold note the presence of interference at about four times the main sawtooth frequency presumably from the Moorside Edge transmitter in North Yorkshire nominally on the same frequency.

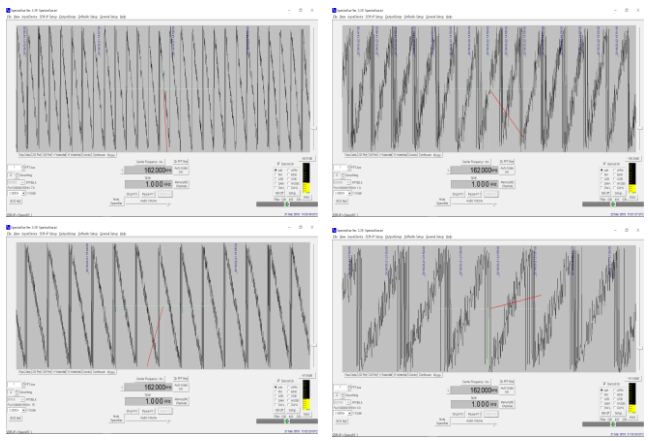

Fig. 8. Allouis, France, 162 kHz measurements at: Wychbold (l) and Lingfield (r). Top and bottom left both give 'blue-shift' of +113 mHz at 1500 and 1515 at Wychbold. At Lingfield top right at 2200 = -14.3mHz, and at bottom right next day 1500 =-14.5 mHz, 'red-shifts'. But why? – it's a mystery! Could it be local 'parametric' pumping of the 162 kHz weak signal from Allouis by the very strong local 198 kHz signal at Wychbold? (NB Allouis also has phase modulated data signal on its carrier.)

Some new theory of 'parametric' coupling of electromagnetic and gravity waves is presented in the form of a 'coupling-graph'(CG) in section VII below.

This indicates that the ''blue-shift' shown in Fig. 8 may be 'parametric-pumping' of the incoming distant weak 162 kHz signal from Allouis in central France, by the very strong 198 kHz signal present for some distance from the Wychbold antenna.

It is therefore perhaps a General-Relativity outcome where the permittivity and permittivity of space are locally being modulated by the very strong signal at 198 kHz?

More measurements of this effect at distances not so close to Wychbold will be necessary to establish or refute this explanation. A fuller explanation of these results is needed in any case.

VI. Local Phase Variations of Common GPS Reference

Fig. 9 shows the typical magnitude of the local variations in phase of the common GPS clock. The assumption is that the local variations are similar statistically at the two measurement locations but are not correlated.

The phase variations are best considered as path length variations. It is then easy to convert them in phase variations at any measurement frequency.

Note that local aircraft typically cause path errors of a few metres, normally less than ten, over typically 3 to 5 minutes.

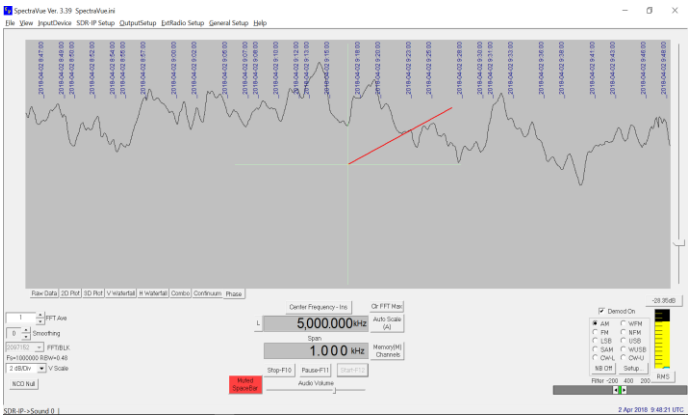

Fig. 9. GPS Phase Variations Referenced to 5 MHz. GPS Variations plotted over 63 min 10sec = 3790 sec. This corresponds to $\pm 3.5^0$ at 200kHz. Fast 3 min 'blips' are aircraft induced because near Gatwick Airport. Full vertical scale is 360^0. At 5MHz full-scale is thus 60 m.

The plot in Fig. 9 was obtained by comparing the 5MHz output of the SDR Kits GPS reference with th SDR-IP being supplied with the SpectraTime 10 MHz Rubidium source. This was fine

tune by a voltage input until the long term drift was minimised before taking any measurements

VII. Propagation-Phase/Frequency-Shift (PPFS) Concept and Model

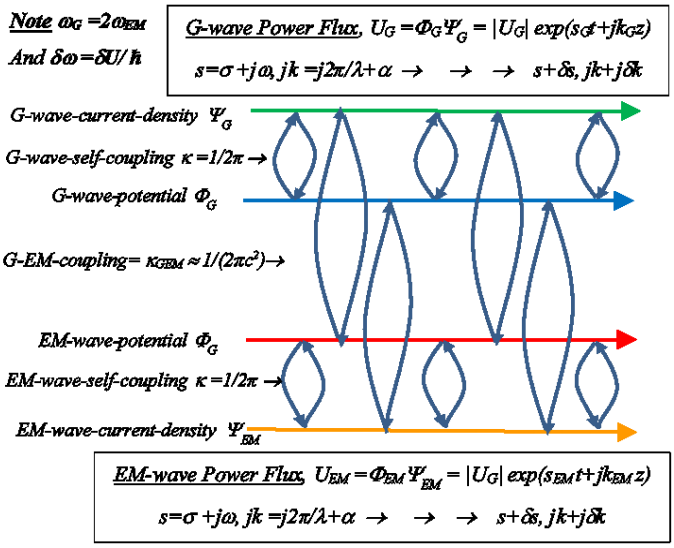

Fig. 10. Coupling Graph Model for the Parametric Interaction of Electromagnetic and Gravity Waves.

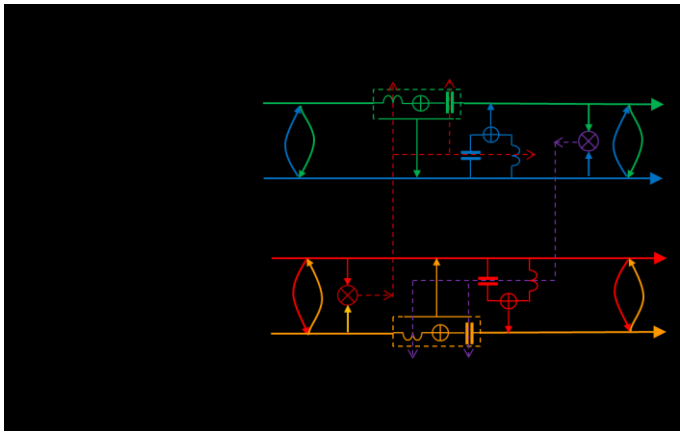

Fig. 11. The Model for PPFS Theory consists of Electromagnetic (EM-) and Gravitational (G-) waves travelling from left to right, both mildly self-coupled, with coupling coefficient κ = 1/2π, and weakly coupled to each other, with parametric inter-coupling coefficient κGEM ≈1/2πc2. The G-wave is at twice the frequency of the EM-wave and has a quarter-power dc component. All coupling has a fixed fundamental time delay which is a function of root frequency$\tau(\sqrt{f})$ where f=ω /2π. Because of this, energy is progressively lost from the EM-wave and transferred to the G-wave until equilibrium is reached. A discovery is that the frequency red-shift δf is proportional to the loss of energy δU with Planck's Constant h as the constant of proportionality. We have δf = δU/h.

The Coupling-Graph model in Fig. 11 is based on The Filamentary Model of Electromagnetism[3]. Electromagnetic (EM-) and Gravitational (G-) waves travelling from left to right, both mildly self-coupled, with coupling coefficient $\kappa = 1/2\pi$, and weakly coupled to each other, with parametric inter-coupling coefficient $\kappa_{GEM} \approx 1/2\pi c^2$. The G-wave is at twice the frequency of the EM-wave and has a quarter-power dc component. All coupling has a fixed fundamental time delay which is a function of root frequency $\tau(\sqrt{f})$ where $f = \omega/2\pi$. Because of this, energy is progressively lost from the EM-wave and transferred to the G-wave until equilibrium is reached. A discovery is that the frequency red-shift δf is proportional to the loss of energy δU with Planck's Constant h as the constant of proportionality. We have $\delta f = \delta U/h$.

VIII. Solvling The Problems of Spur and Spectrum Collapse by SDR Techniques

Unwanted close-to-carrier-spurs and spectrum-collapse further away from the carrier are well known problems in cross-correlation methods of phase noise measurement. Two animations of off-the-shelf spectrum measurement have been produced showing how these problems may be solved. The solution is based on a combination of appropriate FFT windowing and spectrum averaging. Figures 12 and 13 show the opening frame of each animation (as presented at the conference). This solution will be explained further in a forthcoming paper [5].

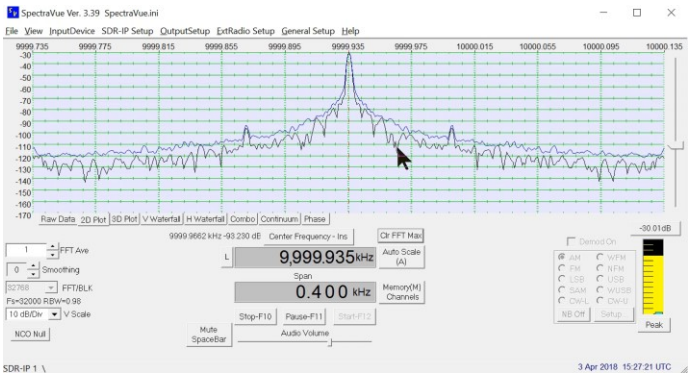

Fig. 12. SDR Spectrum animation showing removal of both Spectrum-Collapse and Close-in-Spurs using Blackman-Harris windowing and FFT-averaging

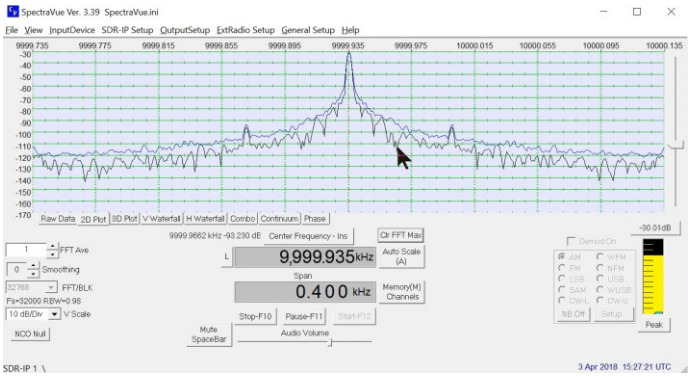

Fig. 13. SDR Spectrum Animation Showing Removal of both Spectrum-Collapse and Close-in Spurs using Blackman-Harris Windowing and FFT-Averaging.

IX. Conclusion(s)

1. 'Off-air' frequency-standards propagated by ground-waves can be used to set the frequency of a local rubidium oscillator to a few parts in a trillion (10^{12} = ppt) and nearly two

orders of magnitude faster by using fractional-cycle phase measurements on an SDR.

2. A fundamental red-shift in frequency proportional to distance has been measured for the BBC Radio 4 Droitwich transmitter on 198 kHz. At a distance of 190km the frequency was measured to be lower by 16.2 μHz (±1). This is 82 ppt.

3. GPS clock carrier phase variations from weather and local aircraft effects have been measured as corresponding to path length changes typically less than ten metres over 3 to 5 minutes.

4. A significant 'blue-shift' in a 162 kHz signal in the strong near-field of a 198kHz has been found. 'Parametric-pumping' is thought to be a possible explanation. More measurements are needed.

5. In summary, the advantages of measuring small frequency differences by phase are pointed out and have been demonstrated for the measurement of LF off-air frequency standards. Theory and explanation for these errors has been presented.

References

[1] M. J. Underhill, "The two-edge anti-jitter circuit for phase noise reduction on received frequency standards", Joint Conf. EFTF/IFCS 2017, Besancon, France, pp. 117 - 120.

[2] M. J. Underhill "Observed propagation-phase/frequency-shift theory with impact on time/frequency transfer and GNSS", Joint Conf. EFTF/IFCS 20177, Besancon, France, pp. 733 – 735.

[3] M. J Underhill, "A Physical Model of Electro-magnetism for a Theory of Everything", *PIERS Online*, Vol.7, No. 2, 2011, pp. 196 -200. Also in *Proc. PIERS 2011*, March 20-23, Marrakesh, Morocco, pp. 1665 – 1669.

[4] S. Stein; slide showing that "Phase Measurements of Oscillator Noise Avoid Spectrum Collapse and Unwanted Spurs" presented in Cross Spectrum Workshop, Joint Conf. EFTF/IFCS 2017, Besancon, France.

[5] M. J. Underhill, "SDR Measurement of Phase and Noise and Frequency Shifts for Enhanced Dynamic Range without Random Spurs or Spectrum Collapse", accepted for presentation at IFCS2018 in Olympic Valley, CA, USA in May 2018.

Design of Mercury lamp for trapped ion frequency standards

Nuan-rang Wang，Xing Chen，Huan Zhao，Ren-fu Yang
(1. Science and Technology on Metrology and Calibration Laboratory, Beijing 100854, China;
2. Beijing Institute of Radio Metrology & Measurement, Beijing 100854, China)
Email:lorious@163.com

***Abstract*—the mercury ion trapped microwave frequency standard has the potential applications for the future satellite, deep space explorations, time keeping and broadcasting for its great advantages in the total volume, stability and lifetime. The high frequency spectrum of mercury ion trapped microwave frequency standard is pumped by the mercury lamp which has small volume and long lifetime, as the base of superiority of mercury ion trapped microwave frequency standard. However, the mercury RF discharge lamp used for optical pumping and state detection may limit the ultimate stability performance of the clock. So we have carried out many experiments to enhance the light stability and the ratio of useful light at 194nm and unwanted background light at 254nm (194/254). Finally, the stability of light power is about 3% in 3 days, the 194/254 ratio is about 1/45, and with filter bulb the ratio is about 1/3. The experimental system of mercury ion trapped microwave frequency standard will be introduced and the Hg lamp device is presented with the radiation regime.**

Keywords—Mercury ion trapped microwave frequency standard, Mercury lamp, Buffer gas, Optical pumping.

I. INTRODUCTION

The mercury ion trapped microwave frequency standard has multiple applications. The outstanding long-term stability has attracted significant interest for time-keeping and metrology [1~3]. Now in the world, only in JPL, the mercury ion trapped microwave frequency standard has been investigated deeply and good results have been achieved [4]. In China, the features of mercury ion trapped microwave frequency standard of small volume, nice stability, and environmental adaptation make it attractive to many research groups.

To achieve a mercury ion trapped microwave frequency standard with good performance, the most crucial technology is the mercury lamp which is used for optical pump and limits the performance of the clock.

We optically pump the $^{199}Hg^+$ ions with a $^{202}Hg^+$ lamp. This is because that the transition in $^{202}Hg^+$ which is 194.2 nm is fortuitously resonant with the transition from the upper ground hyperfine state ($6^2S_{1/2}$, F = 1) in $^{199}Hg^+$ to the first excited state $6^2P_{1/2}$ shown in Fig. 1. The ions decay from the $6^2P_{1/2}$ state to both hyperfine states ($6^2S_{1/2}$, F = 0 or $6^2S_{1/2}$, F = 1), but the effect of continued illumination with 194.2 nm populates the lower hyperfine state ($6^2S_{1/2}$, F = 0) in $^{199}Hg^+$ at the expense of the upper. This is called state selection. Applying resonance radiation at the hyperfine frequency 40.5 GHz restores the population of the upper state ($6^2S_{1/2}$, F = 1).

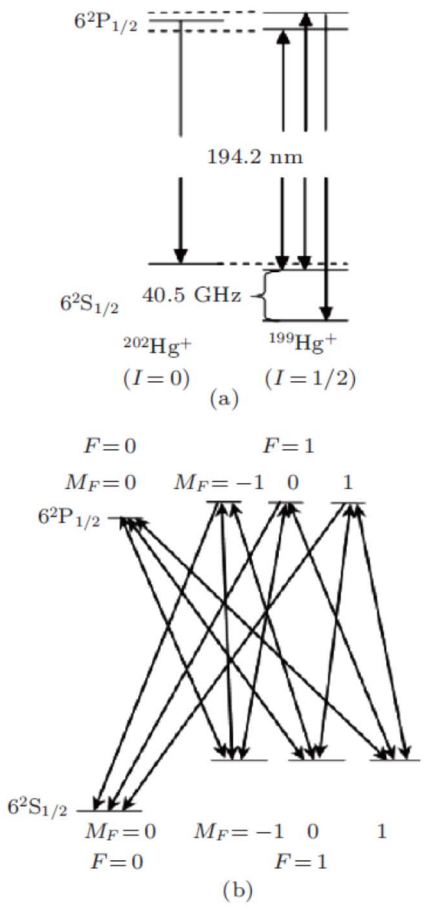

Fig.1 (a) Energy levels of $^{202}Hg^+$ and $^{199}Hg^+$ showing the hyperfine splitting and isotope shifts. (b) Optical pumping transition in $^{199}Hg^+$ leading to preferential population of the F = 0 sublevel.

II. EXPERIMENTS AND RESULTS

A. Theory analysis

In plasma with low pressure, Doppler effect may increase the spectrum width which is related to the temperature of atoms. So the speed of atoms is yield to Maxwell distributing, and the shape is Gauss type.

$$G(\nu-\nu_0) = I_0 \exp\left[-4\ln 2\left(\frac{\nu-\nu_0}{\Delta\nu_G}\right)^2\right] \qquad (1)$$

$$\Delta\nu_G = 7.16 \times 10^{-7}\nu_0\sqrt{\frac{T}{\mu}}$$

Where, $\Delta\nu_G$ is FWHM. ν is frequency. ν_0 is center frequency. T is the temperature of atoms. m is mass quality 。

When T=333K and m=199, the Doppler width is as shown in the following expression.

$$\Delta\nu_G = 1.67\text{GHz} \quad (2)$$

Where, $\nu_0 = \frac{c}{\lambda} = 1.5 \times 10^{15}\text{Hz}$。

$\Delta\nu_{int}$ is the width brought by natural width $\Delta\nu_{nat}$ and resonance width and effect from among particles .

$$L(\nu - \nu_0) = \frac{\Delta\nu_L/\pi}{4(\nu-\nu_0)^2+\Delta\nu_L^2} \quad (3)$$

Where, $\Delta\nu_L = \Delta\nu_{nat} + \Delta\nu_{res} + \Delta\nu_{int}$. The Lorenz width of 194.2nm spectrum is about 0.002cm^{-1}. Based on $1/\delta = \Delta\nu/c$, So the Lorenz width is

$$\Delta\nu = 3 \times 10^8 \times 0.2\text{Hz} = 0.06\text{GHz} \quad (4)$$

So, the width brought by Gauss and Lorenz can be shown by Voigt function.

$$V(a,\omega) = a/\pi\int_{-\infty}^{\infty}\frac{\exp(-z^2)dz}{a^2+(\omega-z)^2} \quad (5)$$

And $a = \frac{\Delta\nu_L}{\Delta\nu_G}\sqrt{\ln 2}$, $\omega = \frac{2(\nu-\nu_0)\sqrt{\ln 2}}{\Delta\nu_G}$, $z = \frac{(\nu-\nu\prime)\sqrt{\ln 2}}{\Delta\nu_G}$.

B. Design of the lamp

Mercury lamp includes bulb, RF circuits and temperature control circuits. The design of bulb includes the material, the shape, argon pressure and the mass of mercury. The model of bulb material is JGS1. The bulb we designed is shown in Fig.2. The equipment is used to fill the bulb with mercury and argon and the picture is shown in Fig.4.

Fig.2 the picture of bulb

Fig.3. the picture of equipment

We have carried out many experiments to confirm the best argon pressure. Finally, for our bulb (d=8mm), we achieved the results and the curve is shown in Fig3.

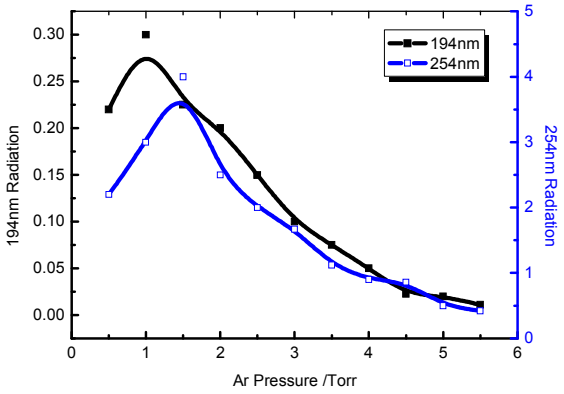

Fig.3. the light power of 194nm (black) and 254nm (blue) changes with argon pressure.

The frequency and power of RF circuits is very important to the power of 194.2nm spectrum. Through analysis and experiment, when the frequency is 196MHz, the power of 194nm spectrum is better. The changing between the intensity of 194nm with the power of RF circuits is shown in Fig.4.

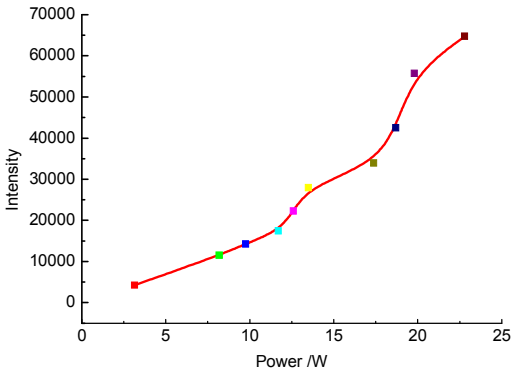

Fig.4 the intensity of 194nm changes with the power of RF circuits

The temperature of bulb is also relating with the intensity of 194nm spectrum as is shown in Fig.5.

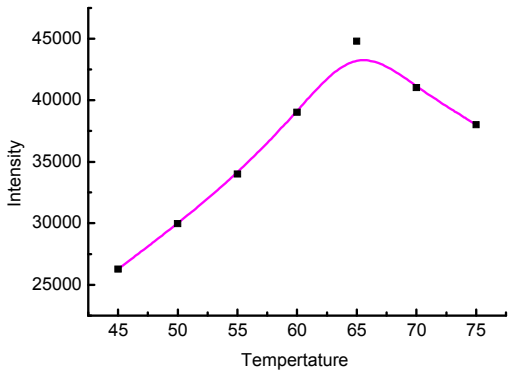

Fig.5 the intensity of 194nm changes with the bulb temperature

When the temperature is 65, the intensity of the wanted spectrum is higher.

C. The performances of the lamp

After designed and optimized, the lamp is done. The performances have achieved our aim. The diameter is 8mm. The power is 10W. The ratio between 254nm and 194nm is about 45. We test the lamp for 2 months. The short and long stability is shown in Fig.6 (a) and Fig.6 (b), respectively. The 3 day stability is about ±2.5%.

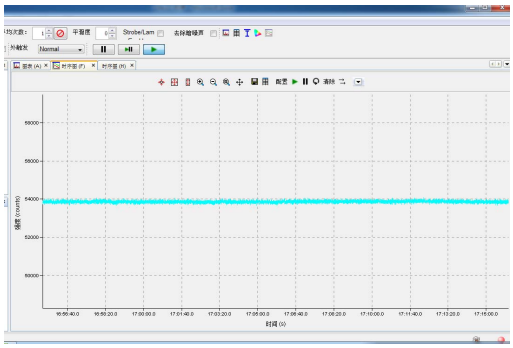

(a)

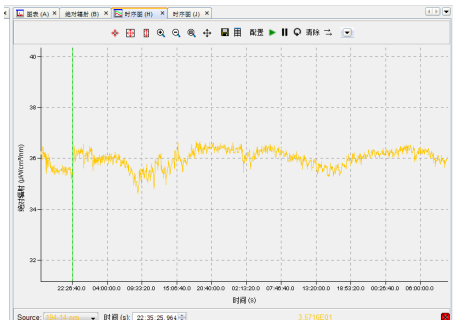

(b)

Fig.6 the power stability of 194nm

III. CONCLUSIONS

As an on-going effort to improve mercury discharge lamp, many relationships are studied. Although the performances of mercury lamp now can satisfy our demand, there are still many problems to be solved. The discharge plasma is very complex, there are still several unknowns. First, how can increase the lifetime of lamp? Now, when it works for about 6 months, the bulb will be polluted and the bulb will become dark. Second, how discharge plasma evolve over time which is invisible and immeasurable. There are no useful theories that can guide the research direction. Third, how to measure the power of 194nm exactly. There are no instruments which can do that and there are no institutions that can calibrate the deep ultra-violet spectrum in China. So there are still long ways to go.

REFERENCES

[1] Douglas D J, Frank A J, Mao D. Linear ion traps in mass spectrometry[J]. Mass Spectrometry Reviews, 2005, 24:1-29.

[2] Olver F, Lozier D, Boisvert R. NIST handbook of mathematical functions[M]. Cambridge: Cambridge University Press, 2010.

[3] Prestage J, Tjoelker R, Maleki L. Recent Developments in Microwave Ion Clocks, in: Luiten A[C], (eds.). Proceedings of Frequency Measurement and Control. Springer Berlin Heidelberg, 2001, 195-211.

[4] L. Yi et al., "Sub-mm Scale Fiber Guided Deep/Vacuum Ultra-Violet Optical Source for Trapped Mercury Ion Clocks," Proc. Of the Precise Time and Time Interval Systems and Applications(2013), Dec 2-5, Bellevue,WA

Fountain Equation and Frequency Calculation

Yu. S. Domnin, O. Kupalova

Department of Metrology for Time and Space
VNIIFTRI
Mendeleevo, 141570, Russia
Email: ydomnin@vniiftri.ru

***Abstract* — An algorithm of data processing, based on fountain equation noise model is presented. Calculation of fountain frequency measurement for two years demonstrate a coincidence with 'international' fountain within 1×10^{-16}.**

Keywords — fountain; equation; algorithm; data processing.

INTRODUCTION

An application of time and frequency standards concerns practically any human activity. The most striking effect from the time and frequency measurement accuracy is in the directions of communication, navigation, geodesy and dynamics etc.

For new level of accuracy it is necessary to implement new approach in the measurements and data processing. Par example spin exchange shift in fountains standards leads to changing of modes of measurements. One should have to measure the frequency with different density of atoms in cloud and so on [1, 2]. In the work [3] the model of atomic fountain noises is proposed. The noises are separated by their dependence from number of atoms in cloud. According to this model it is necessary to carry out the frequency measurements at five different fluxes of atoms.

I. GUESS

Recently we have passed an époque of continuous measurements. Before atomic fountains era all quantum standards were operating continuously. People were do not bother about a phase of the measurement intervals because a frequency shift, par example, for one day was far beyond of an accuracy of these standards. Atomic fountains and optical frequency standards on cooled atoms operated in a pulsed manner. An accuracy of measurement increased hundreds times. And what is changed? It was Dick, who first pointed out that pulsed manner of the standard operation causes some phenomena, which restrict the accuracy of measurement [4]. The main idea is that, due to finite intervals, one may have an influence on a stability due to Fourier components in a probing signal.

Let us consider the influence of the finite intervals of measurement from another point of view. When we start to measure the frequency at a given intervals of time we should take into account that our measurable duration of the wave train has initial and final phase. And theses phases cause a frequency shift, which turns to zero with indefinite time. But it has a meaning for finite time intervals the rather than accuracy of measurements have increased manifold times.

May we write a "dispersion" for finite time intervals as $(\sigma+i\phi/\tau)^2$, where σ is a standard deviation, ϕ is a residual phase of measurement sample and τ is a duration of measurement session?

It is evident that for the indefinite time of measurements the expression turns to the real dispersion.

Let us postulate that any noise leads to frequency scattering σ and frequency shift δ due to random walk of a residual phase. Par example, what are typical noises in case of atomic fountain They are technical noises - photodetector noise, synthesizer noise and, of course, electronic component noise. And there are noises produced by fountain itself – quantum projection noise and spin-exchange noise.

So when one measured the fountain frequency during some session one may have an algebraic sum of frequency shifts due to various noises.

If it so the question is – can one separate different noise in order to evaluate their frequency shifts and extract them properly for final frequency meaning.

II. FOUNTAIN EQUATION

In atomic fountain one may control a number of atoms in any shot. According to [3] atomic fountain noises may be separated by their dependence from number of atoms in a cloud. In the fountain one may have a limited maximum of atoms and one may control number of atoms by only decreasing them from their maximum value. Let introduce the coefficient α, which shoes how many times we decreased number of atoms in the cloud.

Next stage is the "dispersion". What is the dispersion really. In its essence it is a ratio of the signal power to the noise power. In this case we will have operate with the "dispersions" F^2, Φ^2, N^2, C^2 and S^2. When we have maximum of atoms in the atomic fountain α will be equal 1. Then we may write the following system of equations:

$$\left.\begin{array}{c} F^2+\Phi^2+N^2+C^2+S^2=\sigma^2 \\ \alpha^2F^2+\lambda\Phi^2+N^2+\alpha^{-1}C^2+\alpha^{-2}S^2=\sigma_\alpha^2 \\ \beta^2F^2+\beta\Phi^2+N^2+\beta^{-1}C^2+\beta^{-2}S^2=\sigma_\beta^2 \\ \gamma^2F^2+\gamma\Phi^2+N^2+\gamma^{-1}C^2+\gamma^{-2}S^2=\sigma_\gamma^2 \\ \delta^2F^2+\delta\Phi^2+N^2+\delta^{-1}C^2+\delta^{-2}S^2=\sigma_\delta^2 \end{array}\right\} \quad (1)$$

where α, β, γ, δ shows how many times we decreased the number of atoms.

So we may wright the final equation for fountain as

$$\alpha^2F^2+\lambda\Phi^2+N^2+\alpha^{-1}C^2+\alpha^{-2}S^2=\sigma_\alpha^2 \quad (2)$$

In the above equations F^2 denote the dispersion due to photodetector noise. Φ^2 - is the dispersion due to quantum projection noise, N^2 - nyquist noise, C^2 - probing signal (synthesizer) noise, and S^2 - spin-exchange noise.

Let us consider the term α^2F^2. It is proportional to the signal power because α reflects the signal change, F^2 is a noise equivalent noise power of photo detector, so the term α^2F^2 is linked with the dispersion due to photo detector noise.

The character of dependence from α shows that $\alpha\Phi^2$ is a part of dispersion due to shot noise of fountain. The signal to noise ratio is equal to $N/\sqrt{N}$, where N is number of atoms so the calculation of Φ^2 enables to evaluate a number of working atoms in the fountain. The income from N^2 is due to noise of electronics component which is really does not dependent from the atoms number. Why the term $\alpha^{-1}C^2$ is reflects an income to the noise from a probing signal? If we have one atom there would not be an influence of probing signal. If have an infinite number of atoms we will have only noise from a probing signal. So we have reciprocal dependence of this term from α.

Finally, the term $\alpha^{-2}S^2$ reflects the influence of the spin-exchange process.

Now we have five equations and we may find five "dispersion" (F^2, Φ^2, N^2, C^2 and S^2).

III. Algorithm for shifts calculations

Before creating an algorithm for frequency calculations it worse to stress, that the equations solutions does not have any relations to measured frequency, but they may determine the squares of different noise shifts.

The solutions of equations let us to find F^2, Φ^2, N^2, C^2 and S^2 for different numbers of atoms in the cloud. According to solutions in was shown, that any dispersion in the solution may have positive or negative sign. It does not means, that one does have negative dispersion. It means only that one have to use this value with negative sign.

Let us consider the result of system solution, for example, for equation with α=1. In left part of equation we will have the sum like, $(\sigma^2_F+\delta^2_F+\sigma^2_\Phi-\delta^2_\Phi+\sigma^2_N-\delta^2_N+\sigma^2_C\delta^2_C+\sigma^2_S-\delta^2_S)$.

It is the meanings of this private solutions (they are not bold). The signs we choose arbitrary only for example. It is actually the sum of square of frequency shifts and standard deviations for different kind of noises. One may summarized that in the left part, actually, we have total dispersion and total frequency shift square. How ca we separate them?

In the right part equation of we have $\sigma^2-\delta^2$, where δ^2 is a total frequency shift square. The value of σ^2 must be positive.

Let us derive an algebraic sum of dispersions by their sum of absolute values. We will get a coefficient k^2, which equal to the result of division positive part of the sum by absolute values in the left part of equation. This is the part of the dispersion in the right part of equation. If we multiply the total value of the right part by the coefficient k^2 we will get the dispersion. We may extract this value from the sum of the left part of equation and we get the total frequency shift in the rest The square of frequency shift is equal to $F^2+\Phi^2+N^2+C^2+S^2-k^2(\sigma^2-\delta^2)$ for α=1.

From the other hand the square of frequency shift in the right part of equation is equal to $(1-k^2)\times(\sigma^2-\delta^2)$.

After extracting the square root of left part of algebraic sum or square root of right part we should divide the result by √2 to get the frequency correction. Why we divide the expression by √2. We should remember that we used the expression $(\sigma+i\phi/\tau)^2$. That means that σ and $i\phi/\tau$ are mutually perpendicular and we should use projection only. We have also the square of frequency shift correction from the right part of equation, which is also should be divided by √2.

We need five equations to find all noises dispersion. In the process of operation our fountain changes the number of atoms five times periodically. The results of launching atoms with different fluxes of atoms are grouped in blocks, containing one hundred launching in one grope. The coefficients α, β, γ and δ are determined from division of maximum full signal by the full signals with decreased number of atoms. Full signals include in itself the signals from atoms in state F=3, m=0 and F=4, m=0. Where F=3, m=0 and F=4, m=0 denotes quantum states of atoms. The frequency correction are determined for all five fluxes of atoms and mean weighted frequency is determined.

It is important, that we have to use the square roots from algebraic sum of all components but not from the components individual.

NOTE

- From practical calculation it was shown that $F^2+\Phi^2+N^2+C^2+S^2-k^2(\sigma^2-\delta^2)$ is strictly equal $(1-k^2)\times(\sigma^2-\delta^2)$ in case of a proper operation of a fountain.
- Any individual noise behaves itself with time as white phase noise.
- The total noise behaves itself with time as white frequency noise.
- It is possible to find an income to shift by any noise separately. For this one may recalculate the results for four dispersions by neglecting some individual shift. The difference between five and four dispersions will show the income from excluded noise. For example we evaluated the frequency shift income from the Nyquist noise as $\sim 4\times10^{-17}$.

IV. FREQUENCY CALCULATION

Our fountain is always measure the frequency of H-maser and the data of this H-maser are send to BIPM.

According to algorithm from fountain equation, the results of data processing for two years of H-maser frequency measurements were presented. There are H-maser frequency meaning according to the BIPM data, and this data were published in BIPM bulletin of "rates relative to TAI of clocks participating in the computation of TAI". The frequency of this H-maser for the same time was measured by our SUFO2. So we may find the position of SUFO2 against TAI.

In the circular T there are the data about frequencies of national fountains and pfs – mean weighted frequency all of these fountains relative to TAI. And we know the position of SUFO2 relative to TAI due to the measurement of H-maser frequency by SUFO2. The results are presented on fig 1. We have determined the difference TAI - SUFO2 by measuring via SUFO2 the frequency of H-maser.

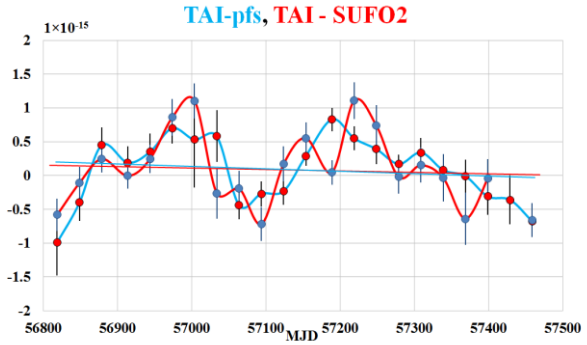

Fig. 1. Frequency difference between TAI and pfs (blue) and TAI and SUFO2 (red). Duration campaign is two years.

When we find equations solutions from atomic fountain formulae we introduce corrections for the shifts produced by photodetector noise, quantum projection noise, temperature noise, synthesizer noise and spin exchange noise. For two years of observation a mean frequency difference between pfs and SUFO2 is equal ($2\times10^{-17}\pm9.6\times10^{-17}$).

On Fig.2 TAI - SUFO2 (physical frequency is calculated without any corrections) is added.

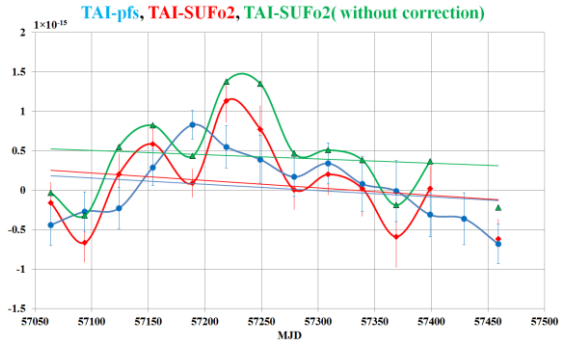

Fig. 2. The difference between TAI - pfs and TAI - SUFO2 and TAI - SUFO2 without corrections. Mean difference between pfs - SUFO2 is equal -0.37±0.1.

CONCLUSION

Results of frequency calculation via fountain equation are in a good agreement with BIPM determination of pfs frequency. (Discrepancy is $2\times10^{-17} \pm 1\times10^{-16}$).

All shifts are variable for every session of measurements. Uncertainity uB is become free from spin-exchange, microwave shift etc.

Fountain uncertainity uB for SUFO2 at present has decreased till 1×10^{-16} and may be diminished to a few units of 10^{-17}. Note that the so called spin-exchange shift (actually the resulting shift due to the action of all possible noises) for our fountain is 3.7×10^{-16} and it is included in uncertainty uA.

An application of the algorithm developed enable as to increase of accuracy to the level below 1×10^{-16} and find the parameters of a given set-up.

The income to the frequency shift may be determined for any noise separately.

It worth to note, that an algorithm is applicable to any quantum frequency standard.

From above-stated it is crystal clear that we never determine the exact value of spin-exchange shift from finite measurements.

REFERENCES

[1] S. Weyers, U. Hübner, R. Schröder, Chr. Tamm, A. Bauch, Metrologia 38 (4), pp. 343–352 (2001)

[2] S.R. Jefferts, J. Shirley, T. E. Parker, T.P. Heavner, D.M. Meekhof, C. Nelson, F. Levi, G. Costanzo, A. DeMarchi, R. Drullinger, L. Hollberg, W.D. Lee and F.L. Walls, "Accuracy Evaluation of NIST-F1," Metrologia, vol. 39, pp 321-336, 2002.

[3] Yu.S.Domnin "Atomic Fountain Equation" Measurement Techniques, 58(10), 1135-1138 DOI 10.1007/s11018-015-0854-4

[4] G. Dick, "Local oscillator induced instabilities in trapped ion frequency standards," in Proc. of Precise Time and Time Interval, Redendo Beach, 1987, pp. 133–147.

Towards a Quantum-Enhanced Atomic Clock on a Chip

Tommaso Mazzoni*, Meng-Zi Huang†, Théo Laudat*†, Carlos L. Garrido Alzar* and Jakob Reichel†
*SYRTE, Observatoire de Paris, Université PSL, CNRS, Sorbonne Université, LNE,
61 Avenue de l'Observatoire, 75014 Paris, France
†Laboratoire Kastler Brossel, ENS–Université PSL, CNRS, Sorbonne Université, Collège de France,
24 rue Lhomond, 75005 Paris, France
Email: tommaso.mazzoni@obspm.fr

***Abstract*—The Dick effect and quantum projection noise (QPN) are among the most stringent limiting factors for state-of-the-art atomic frequency standards, including both primary and secondary standards, as well as compact clocks. A possible solution to the Dick effect relies on Quantum Non-Destructive (QND) detection, which allows multiple interrogations with weak measurements on the same atomic ensemble. Furthermore, spin-squeezed states, which can also be prepared by such QND detection, have the potential to enable clock measurements beyond the standard quantum limit, by employing quantum correlations. Our experimental platform is a Trapped-Atom Clock on a Chip (TACC) that uses ultracold Rb atoms, having demonstrated metrological stability. In the second generation of this experiment, we target quantum enhancement by using QND detection and spin-squeezed ultra-cold atoms generated by cavity QED interactions. To reach this goal, we have integrated two fiber Fabry-Perot cavities on the clock chip, realizing a platform for cavity QED in the strong coupling and weak coupling regimes. With this new device we aim to explore spin squeezing at a metrologically relevant level of stability. Here, we report on the current status and perspectives of this project.**

***Index Terms*—Spin squeezing; QND measurements; compact clock; atom chip; cavity-QED; quantum metrology**

I. Introduction

The Dick effect and quantum projection noise are among the most stringent limiting factors for state-of-the-art atomic frequency standards [1]. They also play a crucial role for compact (liter-sized) microwave clocks currently under development, which target a stability down to 10^{-13} at 1s [2]. The Dick effect limits the frequency stability due to the phase noise of the local oscillator during the dead time, while quantum projection noise is responsible for the standard quantum limit (SQL), which universally affects quantum measurements with uncorrelated atoms. A possible solution [3] to the Dick effect relies on quantum non-destructive detection, which allows multiple interrogations with weak measurements on the same atomic ensemble, drastically reducing the time between successive interrogations. Another solution to overcome the SQL relies on the use of spin-squeezed states, a type of highly entangled states that are known to improve the measurement precisions. With their use, the fundamental quantum uncertainty can be redistributed away from the atomic phase to enable clock measurement beyond the SQL [4]. Cavity-based spin squeezing and QND-based locking of a local oscillator have both been demonstrated in proof-of-principle experiments [5]–[9], but the stability of these experiments did not yet reach a metrologically relevant level.

On the technological side, atom chips [10] provide a robust, miniature platform which has been used to realize compact atomic clocks, atom interferometers, and a fast sources of BECs. In particular, we have developed a Trapped Atom Clock on a Chip (TACC) that reached a stability of 5.8×10^{-13} $\mathrm{s}^{-1/2}$ [11]. With this system we have recently demonstrated that spin squeezing can be generated spontaneously in a rubidium BEC [12]. In the next generation of this experiment, we target quantum enhancement by using QND detection and spin squeezing generated by cavity-QED interactions in ultra-cold thermal atoms. To reach this goal, we have integrated two fiber Fabry-Perot cavities [13] on the clock chip (Fig. 1), realizing a platform for cavity QED in the strong-coupling and weak-coupling regime, respectively.

In this paper we summarize the basic idea of spin squeezing and QND detection in optical cavities that we are implementing in our system. We describe the experimental setup and report on the preliminary clock measurements realized at the cavity position, which will set a reference for the quantum enhanced measurements that we want to achieve with cavity QED interactions.

II. Spin squeezing and QND detection in optical cavities

QPN is a fundamental limit for uncorrelated atoms that we want to overcome with entanglement, such as spin squeezing. Its contribution comes from the fact that the detection is a projective measurement that makes the atomic superposition collapse on one of the two clock states in a Poissonian distribution whose standard deviation depends on the number of atoms N. The shot-to-shot noise on the transition probability for an equally populated superposition is $\sigma_{\mathrm{QPN}} = 1/(2\sqrt{N})$. Two possible approaches to produce spin squeezed states in an atomic ensemble are QND measurements and squeezing by cavity feedback, both relying on the use of optical cavities (Fig. 1a).

Cavity feedback squeezing [14] has the advantage of not requiring the detection of the probe light and produces unconditionally squeezed states. The shearing of the atomic noise

978-1-5386-5620-4/18/$31.00 ©2018 IEEE

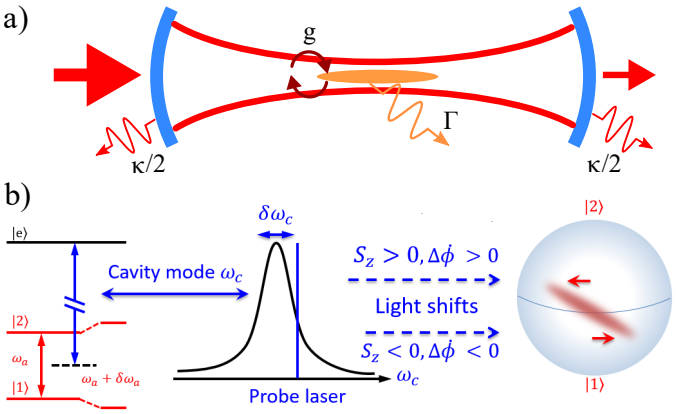

Fig. 1. (a) Sketch of atom-cavity interaction. (b) Spin squeezing by cavity feedback. A probe laser is tuned at the slope of the cavity resonance and halfway the two clock states. The cavity light is responsible for the shift of the atomic level via as-Stark effect and the atoms act as a medium of refractive index which shifts the cavity resonance depending on the population difference S_z. This double role leads to the squeezing of the atomic noise distribution, allowing reduction below the SQL.

distribution is a result of the double role of the atom-cavity interaction. On one hand, the atoms act as a medium of variable index of refraction depending on the atom number difference between the clock states. This shifts the cavity resonance, while the cavity light shifts the energy levels of the atoms because of the ac-Stark effect. In the Bloch sphere representation, the population difference of the clock states $|1\rangle$ and $|2\rangle$ is depicted by the projection S_z of the collective spin vector. If the light is tuned to the slope of the cavity resonance ω_c ($\delta\omega_c = \kappa/2$, with κ the cavity decay rate) and equally detuned from the optical transitions of the two clock states, the intra-cavity intensity I will depend on the collective atomic state, and it will change the precession speed of each single atom via the Stark shift. The linear dependence of I on S_z leads the precession speed of each individual spin to depend on the overall spin state through S_z, conjugating the transverse components S_y and S_z of the collective spin. The system is then described by a one-axis twisting Hamiltonian [15], which is proportional to S_z^2. For a collective spin state prepared on the equator (by a $\pi/2$ pulse), this leads to a linear shearing of the uncertainty region, as depicted in Fig. 1b. As a result, the reduced variance of S_z can reach a minimum value $\Delta S_z^2 = 2/\sqrt{3S_0C}$ [14], which depends on the collective spin length S_0 and the cooperativity $C = 4g/\kappa\Gamma$, with g the atom-cavity coupling and Γ the atomic decay rate. In order not to exit the linear region of the cavity resonance one requires $\delta\omega_c \ll \kappa$, which in our case leads to a weak-coupling regime.

QND measurements rely on weak detection of the spin S_z, without destroying the atomic ensemble. Similar to cavity feedback squeezing, the cavity resonance depends on S_z, which can be therefore measured nondestructively by measuring the cavity shift. Such non-destructive probing also projects the atomic ensemble into a subspace with squeezed spin distribution. The measurement can be accomplished either by counting the number of photons transmitted through the cavity, or a phase measurement in a Pound-Drever-Hall scheme. One can show that the maximum reduction of the spin variance is $\Delta S_z^2 = 1/\sqrt{6S_0C}$ [14], which has the same scaling as squeezing with cavity feedback. The highest amount of spin squeezing reported so far [8] was achieved by a combination of cavity feedback squeezing with subsequent squeezing by QND measurement. One goal of our experiment is to investigate both types of spin squeezing implementations at a stability level in the $10^{-13}\,\mathrm{s}^{-1/2}$ range.

The aforementioned QND measurement can also be beneficial for mitigating the Dick effect, which is often more severe than the SQL, especially for long cycle times. The Dick effect is a result of the local oscillator phase noise entering through the sensitivity function which depends on the interrogation time and the dead time between consecutive measurements. Alternative to the challenging task of improving the local oscillator phase noise, the Dick effect can be reduced by minimizing the dead time in the clock cycle. QND measurements enable multiple weak measurements during the interferometric time, alleviating the requirement on the local oscillator quality (which is extremely desirable for compact clocks), without increasing the dead time. In comparison with a demonstrated QND measurement protocol [16], which was carried out with a free-space probe beam using frequency modulation spectroscopy techniques, our scheme with cavities would enhance the sensitivity of the phase measurement and suppress certain technical noise sources [7], [9]. The SNR of the dispersive cavity detection system is only proportional to the square root of the finesse $\mathcal{F}$, preferring a strong-coupling regime.

III. Experimental Setup

The second generation of the TACC experiment takes advantage of experience gained with the first-generation setup, which already demonstrated a well-characterized stability, described in [11]. A cold ^{87}Rb ensemble is magnetically trapped close to the chip surface in a cigar-shaped trap. The two clock states are the two magnetic trappable hyperfine ground state sublevels $|1\rangle \equiv |F = 1, m_F = -1\rangle$ and $|2\rangle \equiv |F = 2, m_F = 1\rangle$. The transition frequency is measured with a Ramsey sequence. The transition is driven by two photons, radiofrequency (RF) plus microwave (MW) pulses, detuned from the intermediate state $|F = 2, m_F = 0\rangle$ by ~ 500 kHz. The MW photon is applied through an on-chip coplanar waveguide and the RF photon through an adjacent chip wire.

To achieve strong cavity-QED interactions and be compatible with the compactness of our atom chip based clock, fiber-based Fabry-Perot cavities [17] are a natural choice. We implemented two pairs of optical fiber cavities, which are glued side by side (about 500 μm separation) on a pair of piezoelectric transducers (PZT) held by a fused silica bridge, at a distance of about 400 μm from the chip surface (Fig. 2). As the cavity length must be long enough to accommodate the elongated atomic cloud, a new technique based on multi-pulse CO_2 laser milling was used for the cavity mirror fabrication [13]. This method allows the realization of millimeter-size

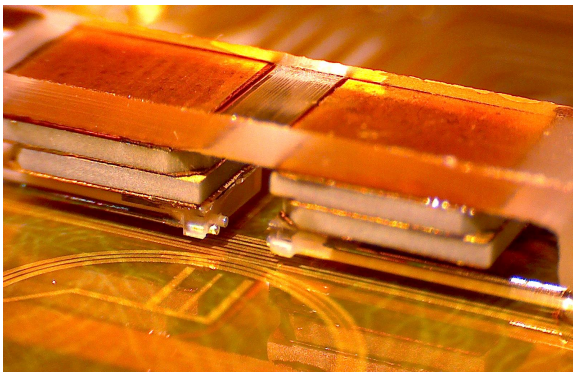

Fig. 2. A pair of optical fiber cavities integrated on the clock atom chip.

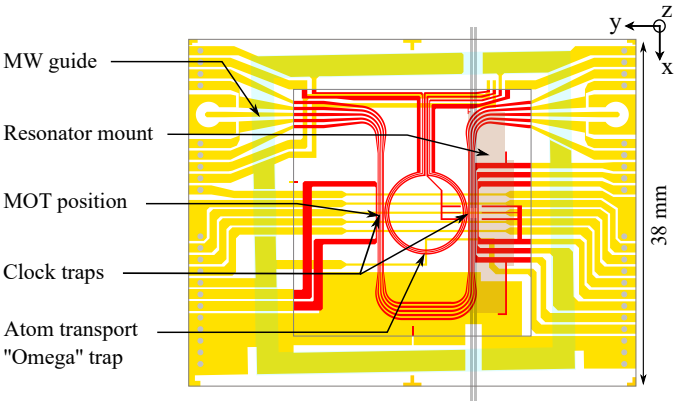

Fig. 3. Layout of the atom chip. Yellow wires denote the base layer, red wires correspond to the top layer. Gray shadow denotes the cavity mount bridge and fibers. Adapted from [18].

fiber cavities previously unavailable. Based on the previous cloud size for clock measurements, we have chosen confocal cavities with length $L = 1.2$ mm and radius of curvature $R = 1.5$ mm, giving a waist of $w_0 = 13.5$ μm for wavelength $\lambda = 780$ nm. Both cavity mirrors are high-refection coated at 780 and 1560 nm. The former wavelength for the cavity-QED interaction, while the 1560 nm light for cavity locking. The finesses of the 780 nm modes in the two cavities differ by an order of magnitude, $\mathcal{F}_{\mathrm{LF}} = 3000$ and $\mathcal{F}_{\mathrm{HF}} = 38000$, giving the single-atom cooperativity of 0.6 and 8.4 (taking into account the imperfect overlap between the atomic cloud and the cavity mode) to tackle squeezing by cavity feedback and QND measurement, respectively. Moreover, the choice of mounting the two cavities on the same PZT potentially allows to stabilize the length of one cavity by sending the locking light only to the other one. In this way, the clock measurements would not be affected by the locking light, which could otherwise be a source of light shift and decoherence.

The fiber cavities blocks optical access for the magneto-optical trap (mirror MOT configuration), rendering the preparation of cold atoms directly at the cavity position impossible. In the new design (Fig. 3) the MOT is formed in one half of the chip while the cavity experiments are carried out on the opposite half. We could then perform clock measurement both at the MOT position and near the cavity modes. The atom transport from the MOT zone to the optical cavities can be performed thanks to a central "Omega" wire and a series of parallel wires which allow a lateral displacement of the cigar-shaped trap. The coplanar waveguide for the MW photon is bent to pass through both trap sites.

An additional improvement with respect to the first generation consists in the addition of a 2D-MOT for fast loading of the 3D-MOT. In the previous experiment, the MOT was loaded from thermal vapor in a single cell, limiting the number of atoms in the MOT to 4×10^6 in 6 s. With the increased flux we can reach the same number of atoms in 200 ms and the MOT saturates at about 6×10^7 atoms around 6 s. Lifetime in the new setup is 2.8 s, probably limited by diffusion through an epoxy sealant that was used to fix a small leak.

IV. Preparation sequence and atoms detection

We load 2×10^7 atoms in 1 s in the 3D-mirror-MOT, where they reach a temperature of about 1 mK. The atoms are successively brought closer to the chip surface in a compressed MOT in 20 ms, which also increases the phase-space density. To further reduce the atomic temperature, a 5 ms molasses stage, in which the quadrupole field is switched off and the cooling beams further red-detuned, is performed. Here the atoms reach a temperature of about 5 μK. The cooling light is switched off and an optical pumping pulse prepares the atoms in the magnetic trappable clock state $|1\rangle$. Atoms are then loaded into a first quadrupole magnetic trap realized by the combination of the gradient generated by the current running in "omega" wire and a bias field B_y. The transport towards the cavity is achieved by rotating the bias field by 180°, using a dynamic combination of the bias fields B_y and B_x. The atoms are then parked into the clock trap by ramping up and down the current in the adjacent parallel wires. This procedure takes 260 ms and currently has a transport efficiency of about 50%. The atoms are then transferred into a tight Ioffe-Pritchard trap with non-vanishing magnetic field B_0 in the trap center, where RF evaporation is performed, reaching the BEC state if desired. After 1.25 s, we get 4×10^4 atoms slightly above the condensation threshold. Finally, we adiabatically transfer the atoms in the elongated clock trap in about 650 ms. The trap frequencies are $\omega_{x,y,z} = 2\pi \times (4.5, 102, 90)$ Hz and the trap center is located about 400 μm below the chip surface and inside the low-finesse cavity mode. Here we measure a final temperature of $T_z = 225$ nK along the tight axis and $T_x = 58$ nK along the shallow one. In the clock trap, the atoms have a lifetime of 2.8 s. We verified that the trap position corresponds to the cavity mode position by looking at the trap losses when a light pulse, resonant with the atomic transition, was sent inside the cavity. We initially align the trap position by maximizing the losses.

The atoms can be detected along the two horizontal directions by absorption imaging. The probe along x direction, parallel to the fiber cavities and to the elongated direction

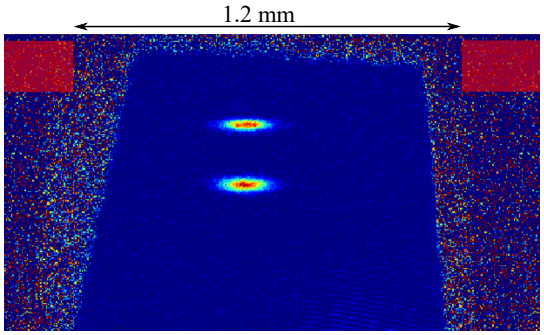

Fig. 4. A typical absorption imaging picture of the two clock states after a $\pi/2$-pulse. The image is taken after 5 ms the cavity trap was released and after 8 ms the ARP pulse was applied. The red regions represent the fibers of the low-finesse cavity mirrors. We applied a mask to the imaging laser beam in order to avoid scattering from the fiber tips and the holding bridge. The noisy region corresponds to the area not illuminated by the probe beam.

of the trap, is used for monitoring all the preparation steps and can be used to perform clock measurements in the MOT loading site. Along the y direction, we can image the atoms trapped inside the cavities with a magnification of 3.8 on a back-illuminated deep depletion CCD camera with $> 90\%$ quantum efficiency (Andor iKon M 934-BRDD). After the Ramsey sequence, the two clock states are detected simultaneously after an adiabatic-rapid-passage (ARP) pulse. This consists of a 3-ms-long MW pulse and a ramped magnetic field B_x, which ensures that atoms in state $|1\rangle$ are adiabatically transfered into the untrapped $|F = 2, m_F = 0\rangle$ state. A typical image after a $\pi/2$-pulse is shown in Fig. 4. The picture is taken 5 ms after the trap for state $|2\rangle$ (upper cloud) was released, and 7.5 ms after the ARP pulse was applied, which released the state $|1\rangle$ (lower cloud).

V. Preliminary clock results

In this section we present preliminary clock stability measurements in the trap aligned with the cavity mode. The bottom field of the trap is chosen close to the "magic" magnetic field ~ 3.229 G [19], where the clock frequency exhibits a minimum, but offset by -35 mG, for which the fluctuations of magnetic field and atomic temperature are minimized [11]. We set a Ramsey time of $T_R = 3$ s. The contrast is 90%, measured in a Ramsey spectroscopy by scanning the RF frequency around the central fringe.

In every cycle we measure the transition probability $P = N_2/(N_1 + N_2)$, where N_1 and N_2 are the measured atom number of the two clock states. We measure close to half transition probability $P \sim 0.5$, alternating between both sides of the central fringe, and compute the difference of P every two shots in order to remove long-term drifts of detection or MW power. Figure 5 shows the fractional frequency Allan deviation for a set of data acquired for 2.5 h. The data are corrected for the frequency noise induced by atom number fluctuation, based on the measured correlation between the frequency deviation and the detected atom number. [11]. The clock frequency fluctuation roughly follows a white noise

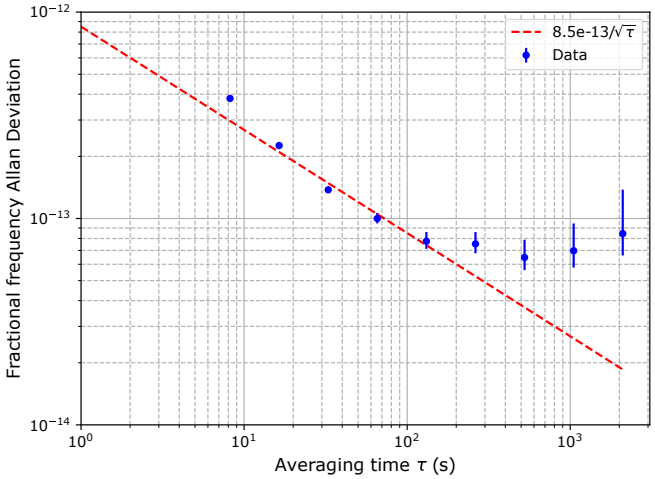

Fig. 5. Allan deviation of the preliminary measurements of clock frequency in the trap aligned with the cavity mode (blue points). The short term stability of 8.5×10^{-13} at 1 s is extracted from the $\tau^{-1/2}$ behavior (red line).

behavior up to ~ 100 s, showing a short term stability of 8.5×10^{-13} at 1 s (red line). The long term drift has still to be characterized and understood. While not far from the short term stability of the first generation of the TACC experiment, we are still in the process of finding the best working point (Ramsey time in particular) for the new setup.

VI. Conclusion and outlook

The stability shown above is a preliminary result, where many parameters have not yet been optimized, making it reasonable to expect the best stability approaching the targeted $10^{-13}\mathrm{s}^{-1/2}$ regime. Even the present stability level, however, is an unexplored territory for spin squeezing experiments. In particular, we will study how spin squeezing interacts with spin self-rephasing [20], another effect due to spin interactions that is known to be relevant to the performance of trapped-atom clocks at this stability level.

Acknowledgments

Work funded by the Délégation Générale de l'Armement (DGA) via the ANR ASTRID program (Contract No. ANR-14-ASTR-0010).

References

[1] G. Santarelli, Ph. Laurent, P. Lemonde, A. Clairon, A. G. Mann, S. Chang, A. N. Luiten, and C. Salomon, *Quantum Projection Noise in an Atomic Fountain: A High Stability Cesium Frequency Standard*, Phys. Rev. Lett. **82**, 461, 1999.

[2] S. Micalizio, C. E. Calosso, A. Godone and F. Levi, *Metrological characterization of the pulsed Rb clock with optical detection*, Metrologia **49**, 425, 2012.

[3] T. Vanderbruggen, R. Kohlhaas, A. Bertoldi, S. Bernon, A. Aspect, A. Landragin, and P. Bouyer, *Feedback Control of Trapped Coherent Atomic Ensembles*, Phys. Rev. Lett. **110**, 210503, 2013.

[4] C. Gross, *Spin squeezing, entanglement and quantum metrology with Bose-Einstein condensates*, J. Phys. B: A. Mol. Opt. Phys. **45**, 103001, 2012.

[5] I. D. Leroux, M. H. Schleier-Smith, and V. Vuletić, *Implementation of Cavity Squeezing of a Collective Atomic Spin*, Phys. Rev. Lett. **104**, 073602, 2010.

[6] J. G. Bohnet, K. C. Cox, M. A. Norcia, J. M. Weiner, Z. Chen, and J. K. Thompson, *Reduced spin measurement back-action for a phase sensitivity ten times beyond the standard quantum limit*, Nature Photonics **8**, 731, 2014.
[7] R. Kohlhaas, A. Bertoldi, E. Cantin, A. Aspect, A. Landragin, and P. Bouyer, *Phase Locking a Clock Oscillator to a Coherent Atomic Ensemble*, Phys. Rev. X **5**, 021011, 2015.
[8] O. Hosten, N. J. Engelsen, R. Krishnakumar, and M. A. Kasevich, *Measurement noise 100 times lower than the quantum-projection limit using entangled atoms*, Nature **529**, 505, 2016.
[9] G. Vallet, E. Bookjans, U. Eismann, S. Bilicki, R. Le Targat and J. Lodewyck, *A noise-immune cavity-assisted non-destructive detection for an optical lattice clock in the quantum regime*, New J. Phys. **19** 083002, 2017.
[10] J. Reichel and V. Vuletic (eds.), *Atom Chips*, Wiley-VCH, 2011.
[11] R. Szmuk, V. Dugrain, W. Maineult, J. Reichel, and P. Rosenbusch, *Stability of a trapped-atom clock on a chip*, Phys. Rev. A **92**, 012106, 2015.
[12] T. Laudat, V. Dugrain, T. Mazzoni, M. Huang, C. L. Garrido Alzar, A. Sinatra, P. Rosenbusch, and J. Reichel, *Spontanous spin squezing in a rubidium BEC*, in preparation.
[13] K. Ott, S. Garcia, R. Kohlhaas, K. Schüppert, P. Rosenbusch, R. Long, and J. Reichel, *Millimeter-long fiber Fabry-Perot cavities*, Optics Express Vol. **24**, 9839, 2016.
[14] M. H. Schleier-Smith, I. D. Leroux, and V. Vuletić, *Squeezing the collective spin of a dilute atomic ensemble by cavity feedback*, Phys. Rev. A **81**, 021804(R), 2010.
[15] M. Kitagawa and M. Ueda, *Squeezed spin states*, Phys. Rev. A **47**, 5138, 1993.
[16] J. Lodewyck, P. G. Westergaard, and P. Lemonde, *Nondestructive measurement of the transition probability in a Sr optical lattice clock*, Phys. Rev. A **79**, 061401(R), 2009.
[17] D. Hunger, T. Steinmetz, Y. Colombe, C. Deutsch, T. W. Hänsch, and J. Reichel, *A fiber Fabry-Perot cavity with high finesse,* New J. Phys. **12**, 065038, 2010.
[18] K. Ott, *Towards a squeezing-enhanced atomic clock on a chip*, PhD thesis, Université Pierre et Marie Curie, 2016.
[19] M. R. Matthews, B. P. Anderson, P. C. Haljan, D. S. Hall, M. J. Holland, J. E. Williams, C. E. Wieman, and E. A. Cornell, *Watching a Superfluid Untwist Itself: Recurrence of Rabi Oscillations in a Bose-Einstein Condensate*, Phys. Rev. Lett. **83**, 3358, 1999.
[20] C. Deutsch, F. Ramirez-Martinez, C. Lacroûte, F. Reinhard, T. Schneider, J. N. Fuchs, F. Piéchon, F. Laloë, J. Reichel, and P. Rosenbusch, *Spin Self-Rephasing and Very Long Coherence Times in a Trapped Atomic Ensemble*, Phys. Rev. Lett. **105**, 020401, 2010.

Raman-Ramsey CPT with a Grating Magneto-Optical Trap

Rachel Elvin, Gregory W. Hoth, Michael W. Wright,
James P. McGilligan, Aidan S. Arnold, Paul F. Griffin and Erling Riis
Experimental Quantum Optics and Photonics Group
SUPA, Dept. of Physics
University of Strathclyde
Glasgow, United Kingdom
Email: rachel.elvin@strath.ac.uk

***Abstract*—We describe an experiment which combines cold ^{87}Rb atoms from a grating magneto-optical trap (GMOT) with Lin⊥Lin coherent population trapping (CPT) and pulsed Ramsey interrogation. The bichromatic fields required for Lin⊥Lin are generated by combining light from a single external cavity diode laser (ECDL) with an electro-optic modulator (EOM) and an acousto-optic modulator (AOM). With this laser system and the GMOT, we are able to produce Raman-Ramsey fringes using either the $F' = 1$ or the $F' = 2$ excited states of the ^{87}Rb D_1 line. As a step towards realising a frequency standard based on the GMOT, we measure the Ramsey fringe amplitude as a function of the magnetic bias field and the excited state. We observe dark state interference with $F' = 1$ and show that this interference is suppressed with $F' = 2$, as expected from prior work on CPT with ^{87}Rb in thermal vapour cells.**

I. Introduction

Laser cooling is responsible for many innovations in quantum sensing and atomic metrology [1]. While the pursuit of better performance leads to exciting possibilities [2], it is also important to reduce the complexity of the apparatus in order to bring the benefits of cold atoms to more applications. The majority of compact atomic clocks are based on room temperature systems; however, the long-term stability is limited by collisional shifts from buffer gases. This can be overcome through the use of cold atoms, which provide long interaction times for better sensitivity. The grating magneto-optical trap (GMOT) is a favourable candidate for a compact cold-atom clock, due to its relative simplicity and potential for further miniaturisation [3]–[5].

Optical interrogation of the hyperfine ground state splitting can be done using the coherent population trapping (CPT) technique [6], [7]. In CPT, a bichromatic laser field is used to pump atoms into a non-interacting superposition of the clock states via one excited state. By monitoring the transmission of the laser field through an atomic sample, one can use these 'dark' resonances as narrow linewidth frequency references without the need for cm-scale microwave cavities.

The frequency resolution of the CPT resonances can be further improved through the use of a two pulse Raman-Ramsey sequence [8]. In the first pulse, the atoms are pumped into a dark state. Then, the atoms are left to freely precess for a time T. During this free evolution time, the phase builds up between the driving CPT field and the atomic coherence. A second pulse of the CPT light maps the accumulated phase into absorption, and interference fringes with a width of $1/T$ are observed inside a Lorentzian envelope when the transmission of the readout pulse is measured.

For a high-performance frequency reference, it is desirable to maximise the contrast of the CPT resonance while minimising its sensitivity to external influences. Through extensive studies, several techniques have been developed to satisfy this requirement, including Lin∥Lin [9]–[11], Lin⊥Lin [8], [12], and Push-Pull Optical Pumping [13]–[15]. With these methods, high-contrast CPT resonances are realised by arranging for the constructive interference of multiple dark resonances. However, this can also introduce unwanted magnetic sensitivities. With Raman-Ramsey interrogation, this can manifest as oscillations in the fringe amplitude as a function of the magnetic field used to define the quantisation axis [10], [16], [17]. In the case of the D_1 line of ^{87}Rb, these interference effects depend strongly on the excited state chosen to drive the CPT resonance [18]. With $F' = 1$, three dark resonances are expected to be present leading to large interference in the Ramsey fringe amplitude. With $F' = 2$, two of these dark resonances are suppressed by couplings to the $|F' = 2, m_F = \pm 2\rangle$ states and so the magnetic sensitivity of the Ramsey fringe amplitude will also be reduced [18]. These dark state interference effects can degrade the performance of the CPT resonance as a frequency standard, and so it is important to characterise them experimentally [16], [17].

Here, we describe our apparatus and an initial characterisation of these dark state interference effects in our system. In section II, we describe the laser system used for Lin⊥Lin CPT. In section III, we review the three dark resonances that arise in Lin⊥Lin CPT with $F' = 1$. In section IV, we describe the Ramsey fringes produced in our apparatus with an interrogation time $T = 9$ ms as a function of the excited state and the bias field. The paper concludes with section V.

II. Laser system for Lin⊥Lin CPT

This section describes the laser system in the clock side of the experiment and details the preparation of a laser spectrum

978-1-5386-5620-4/18/$31.00 ©2018 IEEE

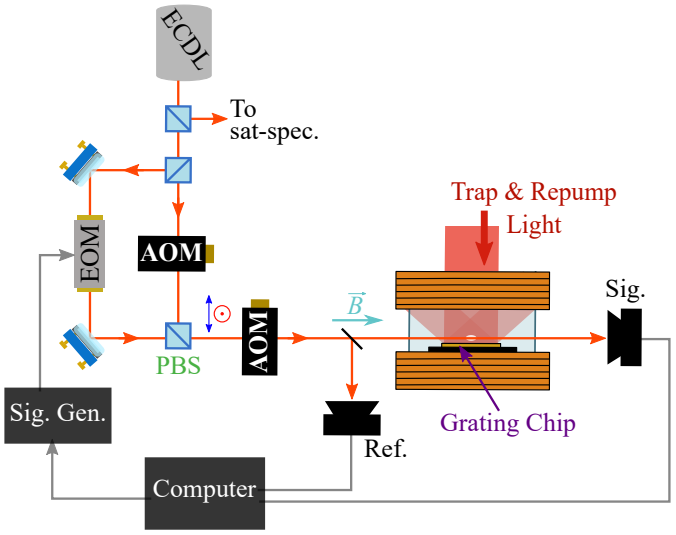

Fig. 1. Laser system and simplified optical layout for the clock side of the experiment. ECDL: external cavity diode laser. EOM: electro-optical modulator. AOM: acousto-optical modulator. PBS: polarising beam splitter. Magnetic bias field direction is denoted by $\vec{B}$. Two photodetectors, 'Ref.' and 'Sig.', measure the laser intensity before and after the atoms respectively.

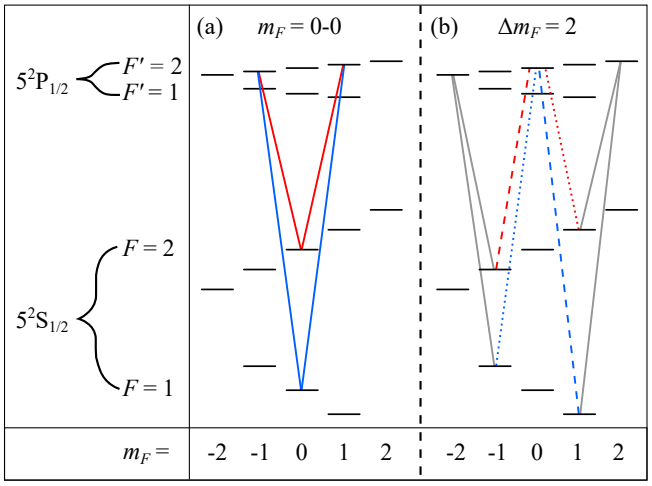

Fig. 2. CPT resonances present in the Lin⊥Lin scheme for the ^{87}Rb D_1 line. The solid red and blue lines in (a) show the transitions that pump atoms into the coherent dark state with m_F = 0-0. The red and blue lines in (b) show the (-1) - (+1) and (+1) - (-1) transitions, as dashed and dotted lines respectively. These latter transitions pump atoms into coherent dark states referred to as $\Delta m_F = 2$. The outer grey lines in (b) highlight the transitions which suppress the $\Delta m_F = 2$ dark states.

appropriate for Lin⊥Lin CPT with light from one external cavity diode laser (ECDL).

In the cooling and trapping side of the experiment, home-built ECDLs are used to generate trap and re-pump light on the ^{87}Rb D_2 (780 nm) line. The combined light is then fibre-coupled onto the grating chip which is held outside the glass cell of the vacuum chamber. With the GMOT, we are able to load more than 10^7 atoms with one beam coupled to a 2×2 cm grating chip [19]. The GMOT has also recently realised atom temperatures as low as 3 μK [20].

A simplified diagram of our CPT experiment is shown in Fig. 1. We use a 795 nm ECDL and a fibre-coupled electro-optical phase modulator (EOM) to address the D_1 line of ^{87}Rb. The orthogonal linearly polarised components for Lin⊥Lin CPT originate from one laser, and are therefore inherently phase-coherent. The D_1 ECDL is locked using saturated absorption spectroscopy, and the frequency of the locked laser is made tunable by use of an AOM in the spectroscopy path (not shown in Fig. 1).

The primary beam path is split into two arms using a polarising beam splitter (PBS). The light through one of the arms is passed through the EOM which is driven by a microwave signal with a frequency of $f_0 + \delta$, where $f_0 \approx 6.834$ GHz is tunable about the ground-state hyperfine splitting of ^{87}Rb and $\delta \approx 200$ MHz is a fixed frequency offset. In the second arm the light is passed through an acousto-optical modulator (AOM) operating at $f = \delta$. The beams are then recombined on a PBS. At this point, the light that passed through the AOM and a single sideband of the light that passed through the EOM are now in two-photon resonance with the atoms, in addition to being orthogonally polarised. A second AOM is used for temporal control of pulses and to bring light from both arms onto the single photon resonance. With the appropriate choice of AOM offset frequencies and lock-points, we are able to operate the system with the CPT pair resonant with either $F' = 1$ or $F' = 2$.

The use of the EOM results in additional off-resonant light, with components that are detuned by δ and by $f_{\rm hfs} + \delta$ from the clock resonance. We plan to investigate the light shifts caused by these off-resonant components in future work.

A magnetic bias of ∼100 mG along the direction of the laser propagation, generated by a Helmholtz coil pair, is used to set the quantisation axis and to lift the degeneracy on the magnetic (Zeeman) sub-levels. The transmission of the laser light is measured by two photodetectors, one before and one after the atoms. A computer records both signals from the probe pulse, which enables normalisation of the signal to minimise the effect of intensity fluctuations.

III. Dark State Structure in Lin⊥Lin

In this section, we review the dark resonances that play an important role in a Lin⊥Lin CPT frequency reference [16], [17]. First, a dark resonance can be formed with the $m_F = 0$ ground states. These states are simultaneously addressed by both circular components of the bi-chromatic CPT beam as shown in Fig. 2 (a). In the Lin⊥Lin configuration, the phases of the polarisation components and the Clebsch-Gordan coefficients are such that the coherent dark state formed by the σ^+ pair and the σ^- pair are the same. As a result, a high contrast dark resonance is formed [7], [8]. Since this dark resonance involves only the m_F = 0 ground states, it experience a quadratic Zeeman shift. For ^{87}Rb, the shift is given by $\Delta f = 575$ Hz/G^2 [21].

Two other dark resonances can be formed between the states $|F = 1, m_F = \pm 1\rangle$ and $|F = 2, m_F = \mp 1\rangle$, as shown in Fig. 2 (b). These $\Delta m_F = 2$ resonances have a small linear

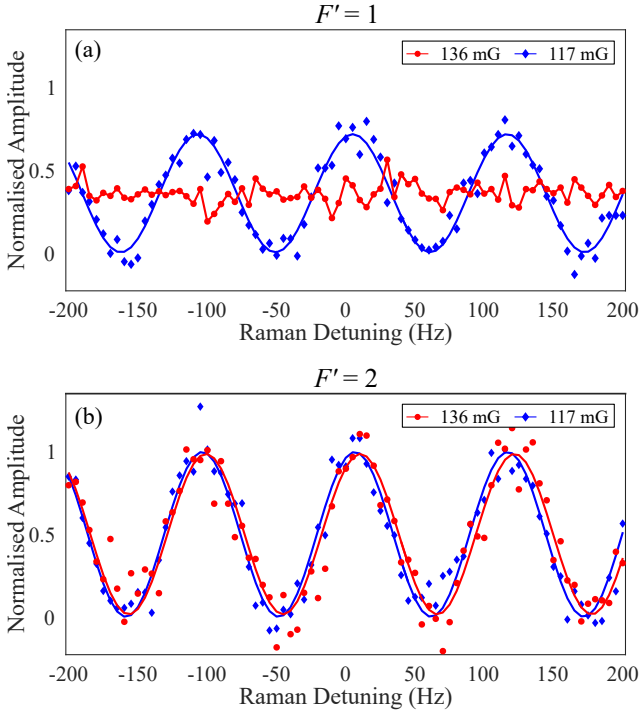

Fig. 3. Ramsey fringes for Lin⊥Lin CPT when driven via $F' = 1$ (a) and $F' = 2$ (b), for magnetic bias fields of B =136 mG and B =117 mG. In both cases, the first CPT pulse was 200 μs long and the free evolution time was $T = 9$ ms. The fringe amplitude was normalised to the average amplitude observed with $F' = 2$.

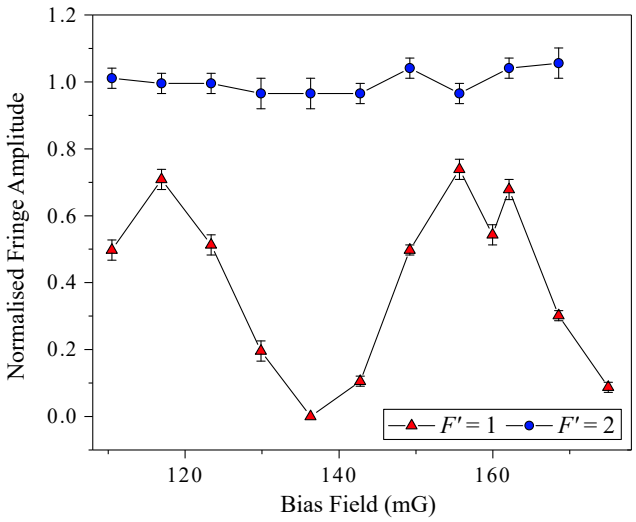

Fig. 4. Ramsey fringe amplitude as a function of the magnetic bias field for $F' = 1$ (red triangles) and $F' = 2$ (blue circles). The bias field was calibrated by spectroscopy of the magnetically sensitive CPT resonances. The free evolution time is $T = 9$ ms. The fringe amplitude was normalised to the average amplitude observed with $F' = 2$.

Zeeman shift due to the nuclear part of the Landé g-factor [9]. For ^{87}Rb, the shift of the $\Delta m_F = 2$ resonances is given by $\Delta f = 432$ Hz/G^2 $\pm$ 2786 Hz/G [10].

The Δm_F = 2 resonances are truly dark states only when $F' = 1$ [9]. When $F' = 2$, they are suppressed by the coupling to the $|F' = 2, m_F = \pm 2\rangle$ states as illustrated by the grey lines in Fig. 2 (b) [18]. However, it is possible to produce a coherence associated with the $\Delta m_F = 2$ dark resonances even when $F' > 1$ [16]–[18]. Therefore, it is important to characterise the dark state population experimentally.

IV. Experiment: Dark State Interference

In order to explore the dark state interference effects in our apparatus, we measured CPT Ramsey fringes as a function of the magnetic field for both $F' = 1$ and $F' = 2$. Ramsey fringes with $T = 9$ ms and two different magnetic fields are shown in Fig. 3. With $F' = 1$, shown in Fig. 3 (a), the fringe pattern washes out when the field changes by approximately 20 mG. In the case of $F' = 2$, this change in the bias field has almost no effect on the fringes.

The variation of fringe amplitude is shown over a wider range of magnetic fields in Fig. 4. The data are consistent with our expectations in that we see high contrast interference with $F' = 1$, and this interference is suppressed with $F' = 2$. With the three dark states described in section III, one expects a full cycle of the interference pattern to correspond to a magnetic field change $\Delta B = 1/TZ$ where Z is the residual linear Zeeman shift of the $\Delta m_F = 2$ resonances. For ^{87}Rb and $T = 9$ ms, $\Delta B \approx 40$ mG, which is in good agreement with the data shown in Fig. 4. The nearly complete extinction of the fringes with $F' = 1$ indicates that roughly half of the population is in the 0-0 dark state with the other half divided between the two $\Delta m_F = 2$ dark states, but this simple analysis does not account for the different quadratic Zeeman shifts of the 0-0 and the $\Delta m_F = 2$ resonances or an imbalance in the population of the $\Delta m_F = 2$ dark states.

In the case of $F' = 2$, one can see that the maximum fringe amplitude is larger by a factor of 1.3 in Fig. 4. A larger contrast enhancement for $F' = 2$ compared to $F' = 1$ has been observed for Lin⊥Lin CPT on the D_1 line of ^{87}Rb using continuous interrogation in a thermal vapour [18]. The strong suppression of the interference with $F' = 2$ is also of interest in its own right. Simulations of Lin⊥Lin CPT in a thermal vapour of ^{87}Rb show that residual excitation of the $\Delta m_F = 2$ resonances is expected for $F' = 2$ [18], and it is possible that this could be detected in our apparatus with an improved signal to noise ratio.

V. Conclusion

We have shown that GMOT technology can be used as a compact source of cold atoms for CPT interrogation. We have also made an initial study of the magnetic field dependence of the Ramsey fringes in our apparatus with $F' = 1$ and $F' = 2$. As expected, with $F' = 1$, we see significant interference between the three dark states. With $F' = 2$, the Ramsey fringes are significantly less sensitive to the bias field and the fringe contrast is also increased. Thus, the $F' = 2$ excited state is a more favorable candidate for realising a frequency reference based on Lin⊥Lin CPT and cold ^{87}Rb atoms. In future work, we plan to investigate the distribution of the dark

state populations in more detail. Cold ^{87}Rb is a promising system for this study due to its relative simplicity and the availability of an excited state with $F' = 1$. In the long term, our goal is to demonstrate a frequency reference with good long-term stability based on the GMOT technology.

ACKNOWLEDGMENT

We acknowledge financial support from EPSRC (EP/M013294/1), DSTL (DSTLX-100095636R), the UK Quantum Technology Hub for Sensors and Metrology and the National Physical Laboratory. We would also like to thank Elizabeth Donley for helpful technical discussions.

REFERENCES

[1] G. K. Campbell and W. D. Phillips, "Ultracold atoms and precise time standards," *Phil. Trans. R. Soc. A*, vol. 369, no. 1953, p. 4078, 2011.

[2] A. D. Ludlow, M. M. Boyd, J. Ye, E. Peik, and P. Schmidt, "Optical atomic clocks," *Rev. of Mod. Phys.*, vol. 87, no. 2, pp. 637–701, 2015.

[3] J. P. McGilligan, P. F. Griffin, E. Riis, and A. S. Arnold, "Phase-space properties of magneto-optical traps utilising micro-fabricated gratings," *Opt. Express*, vol. 23, no. 7, p. 8948, 2015.

[4] J. P. McGilligan, P. F. Griffin., E. Riis, and A. S. Arnold, "Diffraction-grating characterization for cold-atom experiments," *J. Opt. Soc. Am. B*, vol. 33, no. 6, p. 1271, 2016.

[5] J. P. McGilligan, R. Elvin, P. F. Griffin, E. Riis, and A. S. Arnold, "Utilising diffractive optics towards a compact, cold atom clock," in *2016 European Frequency and Time Forum (EFTF)*, 2016, pp. 1–2.

[6] J. Vanier, "Atomic clocks based on coherent population trapping: a review," *Appl. Phys. B*, vol. 81, no. 4, pp. 421–442, Aug 2005.

[7] V. Shah and J. Kitching, "Chapter 2 - advances in coherent population trapping for atomic clocks," in *Advances in Atomic, Molecular, and Optical Physics*. Academic Press, 2010, vol. 59, pp. 21 – 74.

[8] T. Zanon, S. Guerandel, E. de Clercq, D. Holleville, N. Dimarcq, and A. Clairon, "High contrast Ramsey fringes with coherent-population-trapping pulses in a double lambda atomic system," *Phys. Rev. Lett.*, vol. 94, no. 19, p. 193002, 2005.

[9] A. V. Taichenachev, V. I. Yudin, V. L. Velichansky, and S. A. Zibrov, "On the unique possibility of significantly increasing the contrast of dark resonances on the D_1 line of ^{87}Rb," *J. Exp. Theor. Phys.*, vol. 82, no. 7, pp. 398–403, 2005.

[10] F.-X. Esnault, E. Blanshan, E. N. Ivanov, R. E. Scholten, J. Kitching, and E. A. Donley, "Cold-atom double-Λ coherent population trapping clock," *Phys. Rev. A*, vol. 88, no. 4, p. 042120, 2013.

[11] X. Liu, E. Ivanov, V. I. Yudin, J. Kitching, and E. A. Donley, "Low-drift coherent population trapping clock based on laser-cooled atoms and high-coherence excitation fields," *Phys. Rev. Appl.*, vol. 8, no. 5, p. 054001, 2017.

[12] C. Xi, Y. Guo-Qing, W. Jin, and Z. Ming-Sheng, "Coherent population trapping-ramsey interference in cold atoms," *Chinese Phys. Lett.*, vol. 27, no. 11, p. 113201, 2010.

[13] Y.-Y. Jau, E. Miron, A. B. Post, N. N. Kuzma, and W. Happer, "Push-pull optical pumping of pure superposition states," *Phys. Rev. Lett.*, vol. 93, no. 16, p. 160802, 2004.

[14] M. Abdel Hafiz and R. Boudot, "A coherent population trapping Cs vapor cell atomic clock based on push-pull optical pumping," *J. Appl. Phys.*, vol. 118, no. 12, p. 124903, 2015.

[15] M. Abdel Hafiz, G. Coget, P. Yun, S. Guerandel, E. de Clercq, and R. Boudot, "A high-performance raman-ramsey Cs vapor cell atomic clock," *J. Appl. Phys.*, vol. 121, no. 10, p. 104903, 2017.

[16] R. Boudot, S. Guerandel, E. de Clercq, N. Dimarcq, and A. Clairon, "Current status of a pulsed CPT Cs cell clock," *IEEE Trans. Instr. Meas.*, vol. 58, no. 4, pp. 1217–1222, April 2009.

[17] O. Kozlova, J. M. Danet, S. Gurandel, and E. de Clercq, "Limitations of long-term stability in a coherent population trapping Cs clock," *IEEE Trans. Instr. Meas.*, vol. 63, no. 7, pp. 1863–1870, July 2014.

[18] Z. Warren, M. S. Shahriar, R. Tripathi, and G. S. Pati, "Experimental and theoretical comparison of different optical excitation schemes for a compact coherent population trapping Rb vapor clock," *Metrologia*, vol. 54, no. 4, pp. 418–431, 2017.

[19] C. C. Nshii, M. Vangeleyn, J. P. Cotter, P. F. Griffin, E. A. Hinds, C. N. Ironside, P. See, A. G. Sinclair, E. Riis, and A. S. Arnold, "A surface-patterned chip as a strong source of ultracold atoms for quantum technologies," *Nat. Nanotechnol.*, vol. 8, no. 5, pp. 321–324, 2013.

[20] J. P. McGilligan, P. F. Griffin, R. Elvin, S. J. Ingleby, E. Riis, and A. S. Arnold, "Grating chips for quantum technologies," *Sci. Reports*, vol. 7, no. 1, 2017.

[21] D. A. Steck, "Alkali D line data," 2015. [Online]. Available: http://steck.us/alkalidata

Microsemi Chip Scale Atomic Clock (CSAC) Technical Status, Applications, and Future Plans

Peter Cash, Will Krzewick, Paul Machado, K. Richard Overstreet, Mike Silveira, Matt Stanczyk, Dwayne Taylor, Xianli Zhang
Microsemi Frequency and Time Division

Microsemi's CSAC was developed from 2001 to 2011 and represented revolutionary technology for atomic clocks. The use of Coherent Population Trapping, pioneered at NIST, enabled a significant reduction in size, weight, and power compared to conventional gas cell clocks. Last year, Microsemi released an updated version of CSAC that improved the operating temperature range and reliability. Development of the technology continues at Microsemi to meet the current and future applications. This paper provides some historical background, design description, a detailed technical status of CSAC including performance data from production testing. Also, the paper will contain a description of both the original and future applications. Finally, a description of the future development plans with the goals of increased performance, further reliability improvements, and wider environmental tolerances. The improvements include wider temperature range from -40°C to 80 °C, improved drift and temperature stability, radiation tolerance and RoHS 6/6 compliance.

Figure 1 Microsemi CSAC

Nearly all the current commercial atomic clocks were developed in the 1950's and 1960's with updates over the past twenty years. The clocks included Cesium Beam Tube, Rubidium Gas Cells, and Hydrogen Masers. Innovative laboratory clocks based on cold atoms, ions, lattice and optical clocks have been demonstrated in laboratories. Although these clocks demonstrated exceptional performance, commercialization has not taken place. Developing and manufacturing clocks capable of high volume production along with reliability and long lifetime is a technical and manufacturing challenge.

Microsemi's CSAC represents the first new high volume commercial atomic clock in many years. There have been challenges during the development, transition to manufacturing and product release. This paper will provide some historical background, describe our design and manufacturing approach, provide performance information and look to the future of the technology.

Coherent Population Trapping (CPT) and Initial Developments

Low power and high-performance atomic clocks have been an area of academic, government and industry focus for the past 30 years. CPT clocks utilize a different physics package configuration that provides opportunities for technology evolution. This topology allows for the use of a laser in place of a lamp to interrogate the atoms, typically Cesium or Rubidium. Northrop Grumman, formerly Westinghouse, pioneered the first VCSEL based clocks in the 1990's that contained vapor cells in a microwave cavity. The Northrop Grumman team demonstrated Allan Deviation of $< 2 \times 10^{-11} / \sqrt{\tau}$ and long-term drift of 3×10^{-12} at 10^4 seconds. The clock was approximately 16 cm^3 and required 200-300 mW of operating power. The United States National Institute of Standards (NIST) continued the leadership of CPT technology by research and driving collaboration between Universities, National Laboratories, and Industry. NIST developed candidate physics packages which included anodic bonding to contain the Rubidium, and a stacked vertical assemble more suitable for manufacturing.

Figure 2 NIST Physics Package

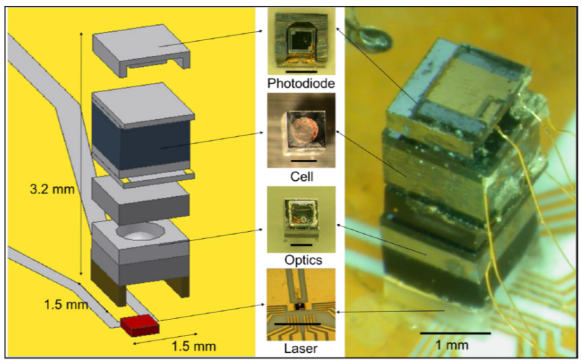

DARPA CSAC Program and Microsemi Approach

In 2001, the US Defense Advanced Research Project Agency (DARPA) funded a multi-team program to develop a commercial CSAC in support of critical needs for the US military for secure communication and jam-resistant GPS receivers. The performance goals of the contract were a volume of fewer than 1 cm^3, power consumption of less than 30 mW and Allan Deviation of $\sigma_y(\tau) < 6x10^{-10}\ \tau^{-1/2}$. Microsemi participation in the program began in 2002. Our partners were Draper Laboratories and the Sandia National Laboratory. The Draper and Microsemi team focused initially on the physics package development and allocated 15 mW of the budget for the operation. Key technology choices included the anodic bonding process and the use of polyimide tethers in a vacuum package. Microsemi focused on the electronics and firmware development. Sandia developed the 895 nm VCSEL diode.

The low power physics package is based on a suspended VCSEL/Resonance Cell/Photodetector using polyimide tethers in a vacuum. The vacuum is maintained in a Leadless Ceramic Chip Carrier (LCCC) and Cover. This Design technique provides a thermal resistance of 7000ºC/W from the environment to the physics assembly. The mechanical design has been modeled and confirmed with testing to survive above 2000 gs shock and 20 grms random vibration. The power consumption of physics package is 12mW to 15 mW. Vacuum integrity for greater than ten years of operation has been validated. Figure two shows a photograph and three-dimensional model of the physics package. The integrity of the design has been established using Krypton fine leak measurement techniques and high-temperature testing that predicts the length of time the physics package would remain operating.

Figure 3 CSAC Physics Package

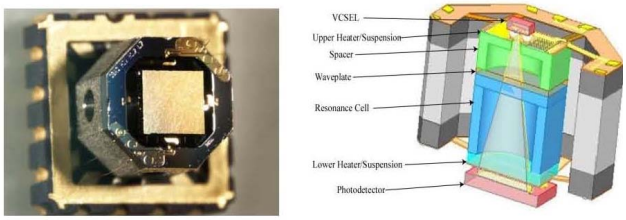

VCSEL (Vertical Cavity Surface Emitting Laser) Diode

The 895 nm VCSEL diode is a critical element in the clock that determines the signal to noise ratio and is an important factor in frequency drift and stability. VCSEL diodes are used in low power CPT clocks because of their high efficiency and reliability, low power (~3 mW) compared to DFBs and Fabry Perot lasers, coherent light source and symmetry. The diodes are tested in wafers for performance parameters and the correct devices selected. Key attributes of VSEL diodes include line width, reliability (validated with long-term reliability testing), single mode and polarization determination and operating temperature.

The Cesium gas cell and suspensions are manufactured using MEMs processing. The Cesium cells are created using anodic bonding of glass to deep reactive ion etch(ed) DRIE silicon wafers. Cesium is introduced into the assembly along with optimized buffer gas. Anodic bonding is used to enclose the cavity hermetically.

Figure 4 MEMS Cesium Cell Fabrication

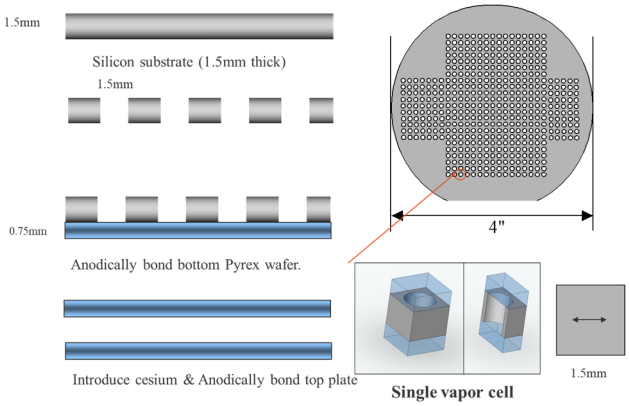

The MEMS suspensions are fabricated using conventional processing along with the introduction of polyimide.

CSAC manufacturing has a number of unique challenges that need to overcome for satisfactory yields and reliability. These include:

- Precision assembly and alignment of components of the physics package
- Reliable vacuum operation that can be compromised by internal outgassing and vacuum integrity of the physics package
- Vacuum requirements are < 1 x 10^{-11} atm-cc/sec
- Cleanliness of all processes due to outgassing risks
- Tracking of material and clock data using automation to monitor and optimize processes
- Testing capability to support high volume atomic clock manufacturing

The CSAC control electronics use architectures similar to previous Rubidium and Cesium atomic clocks developed at Microsemi. The component selection is on lowest power possible, trading off performance in some instances. The control servos are based primarily on software, in comparison to heritage clocks. The control electronics also provide the capability of 1 pulse per second steering of the clock to an external source.

Figure 5 CSAC Block Diagram

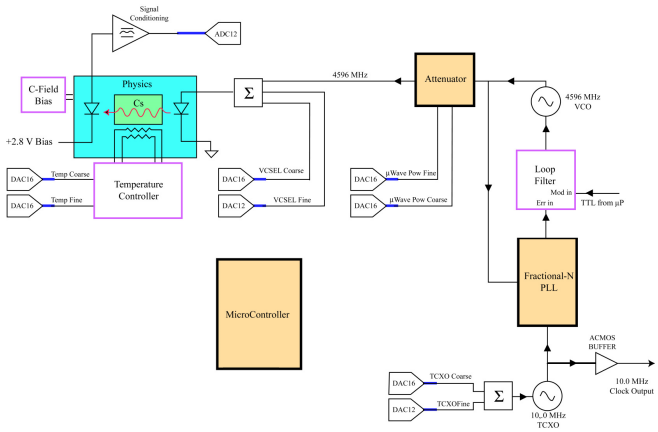

The principal servos in the CSAC include:

- Laser Servo - Lock laser wavelength to optical absorption resonance via DC Bias
- Temperature Servo - Optimize optical power via temperature
- Clock Servo – Lock local oscillator to CPT resonance
- Power Servo - Optimize CPT signal amplitude via µWave power

Market Overview

Revolutionary products such as CSAC has been adopted for applications for which it was intended, and others that were not originally considered.

Key features depend on the specific application. Power is typically the defining parameter. Other critical requirements include:

- Height for VPx Chassis
- Warm-up time/Lock time
- Temperature Stability
- Drift
- 1 Pulse per Second (PPS) functionality
- Timing functionality
- Vibration and Orientation insensitivity

Ocean Bottom Seismic (OBS)

OBS provides extremely accurate information about new and existing oil and gas reserves to maximize the probability of finding new fields and maximum utilization of existing locations. Conventional Oil and Gas exploration used surface vessels to map underwater sub-terrain regions. The resulting surveys often have inadequate information which produced poor results once drilling operations preceded. Often at the cost of hundreds of millions of dollars. OBS provides a precise mapping that determines reservoir complexity and geological structures. The process creates accurate three-dimensional mapping shows pre and subsalt basins, allowing for access around and under infrastructures. The use of pressure and shear data results in full azimuth data of the highest quality. Companies such as Magseis can place sensors on the bottom of the ocean in large arrays. These sensors operate for periods of months using CSACs to data time stamp measurements of seismic response to sounds waves starting near the ocean surface to depths of 3000m. Precise timing is required to get high-quality seismic images of the reservoirs. The arrays are becoming larger and can now contain more than 10,000 nodes. The plans for longer-term deployment of larger array drive efforts to further reduce the power requirements for CSAC which represent an appreciable amount of the node power. The advantages of OBS continue to be validated by many customers throughout the world. As a result, more explorations are moving away from surface mapping to OBS. The low power and low drift from CSAC have been an enabling technology. Figure six shows a highly automated system that places the nodes on the Ocean bottom with minimal labor.

Figure 6 Marine Autonomous Seismic Systems

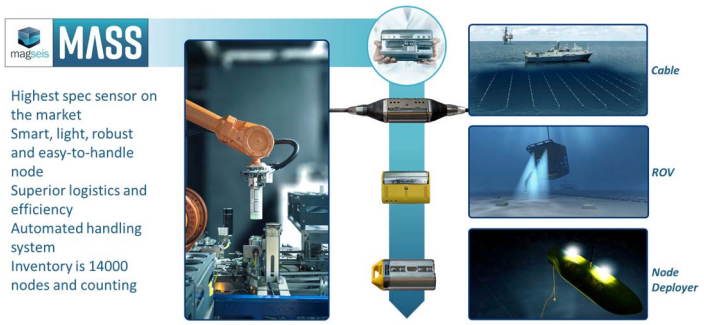

Military Applications

CSAC provides unique capabilities for operation in harsh environments such as military operations. Crystal oscillators have been used in such missions previously. However, the combination of intrinsic accuracy, fast warmup, low power, low sensitivity to orientation and vibration, temperature changes, magnetic field, and shock

are compelling. Jam resistant GPS receivers were an initial intended use for CSAC. CSAC adds capabilities such as fast warm-up and GPS lock and using to time-keeping to validate incoming GPS signals and operate in their absence. CSAC provides the ability to encrypt communications and operate in dangerous environments. Figure 7 below shows effective use of a CSAC that enables the placement of the Jackson Laboratories GPS transcoder to add SAASM/M-Code capabilities to a standard GPS receiver by using the timing and low power capabilities of CSAC. The acronym SAASM stands for Selective Availability Anti-Spoofing Module. This is an upgraded feature for a military GPS receiver that is nearly impossible to spoof and difficult to Jam.

Figure 7 Jackson Laboratories GPS Transcoder

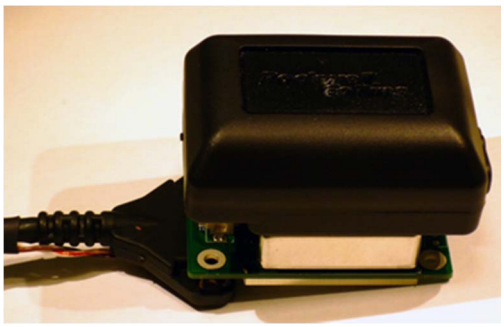

Although power consumption is critical in portable applications, the reduced height of 10mm (0.45") is ideal for board mounting in the industry standard PCx chassis used in vehicles, avionics, and spacecraft. CSAC's low sensitivity to orientation, vibration, and shock are differentiating characteristics. This mechanical insensitivity is due to the rigid construction of the VCSEL diode, Cesium Cell, and Photodetector. Under various operations, the three frequency determining component move together. For this reason, the performance of CSAC degrades minimally at high levels of random vibration and shock. A real-world example is a soldier with a timing device in a backpack. If the backpack were laid down horizontally and then put on the soldiers back, the orientation change would produce a one us time error. A CSAC would exhibit no change. Timing devices in non-linear motion would have similar degradation in performance. Holdover is another method to characterize the timing accuracy of a clock under various conditions, usually time and temperature. CSAC has good performance for holdover, particularly in the context of the power required. Figure 8 shows measured holdover of two CSAC under constant temperature.

Figure 8 CSAC Holdover Measurements

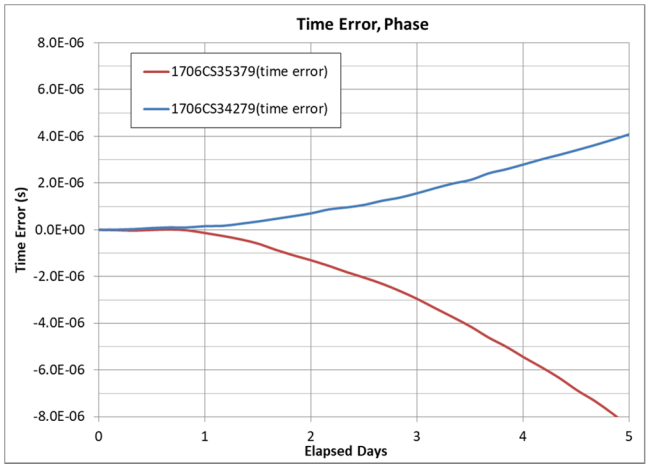

CSAC Production Current State

Microsemi has experience delivering atomic clocks in high volumes. However, the CSAC technology did require the development of specialized equipment and processing. Manufacturing areas with cleanrooms are dedicated to the assembly of the physics packages. Cleanliness is a priority and precision robotic assembly is necessary to properly align the VCSEL diode, Cesium cell, photodetector, and suspensions within the LCCC.

The need to maintain a near-perfect vacuum inside the physics package has been a challenge during the development and production release. Over the past four years, improvements to the materials and processes have been implemented to increase the reliability of CSAC. Before these improvements, CSAC had restrictions on upper operation temperatures. The improvements included:

- Updates to manufacturing baseline including added visual inspections, vacuum bake and selection of material increased reliability
- Implementation of 100% high-temperature screening of the physics package
- Rigorous evaluation of materials at incoming inspection
- Qualification testing process that confirms the long-term reliability of changes
    - Temperature cycling
    - High-temperature bakeout of physics packages for extended lengths of time
    - Random vibration and Shock testing
    - Long-term frequency drift
- Operating Temperature increased to -10ºC to 70ºC, and the early return rate is <0.2%

Microsemi introduced a new part number in September of 2016 that included these improvements.

Another important best practice is the evaluation of long-term operation for the units. Figure 9 shows long-term drift measurements of CSACs for the past eighteen months. The data helps to validate the improvement made to the product.

Figure 9 Long-Term Frequency Drift

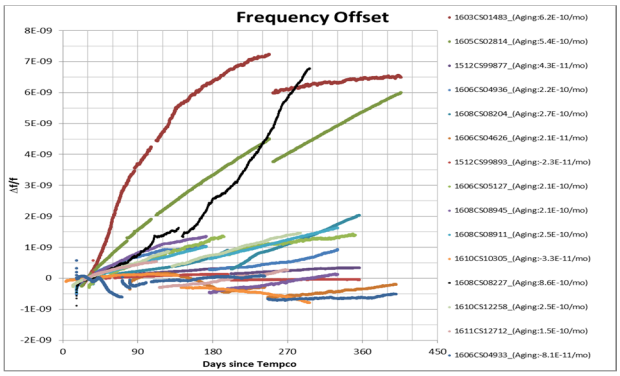

Typical frequency drift of CSAC is 3 x 10^{-10} per month. The data does show a few outliers as well as units that behave similarly to conventional Rubidium clocks with drifts of less than 1 x 10^{-10} per month.

Production Test Data

Microsemi has delivered more the 95,000 CSACs to customers over the past seven years. Sophisticated data storage is utilized, so that information for every production device is maintained. The following charts show production measurements for total power consumption (25º), Allan Deviation at 1 second, Temperature coefficient, along with phase noise and Allan Deviation Plots. In all these characteristics, CSAC performs better than the published data sheet. Margin compared to specification limits is important to consistent production flow. Similarly, the production test and qualification results show margin for warm-up time and magnetic field sensitivity.

Figure 10 Power Consumption 25 degrees C

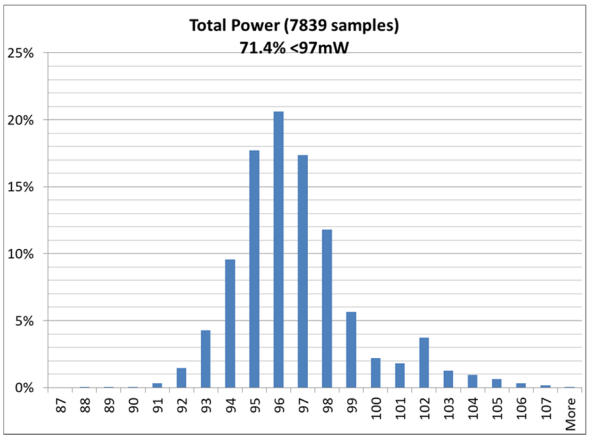

Figure 11 Allan Deviation, 1 second

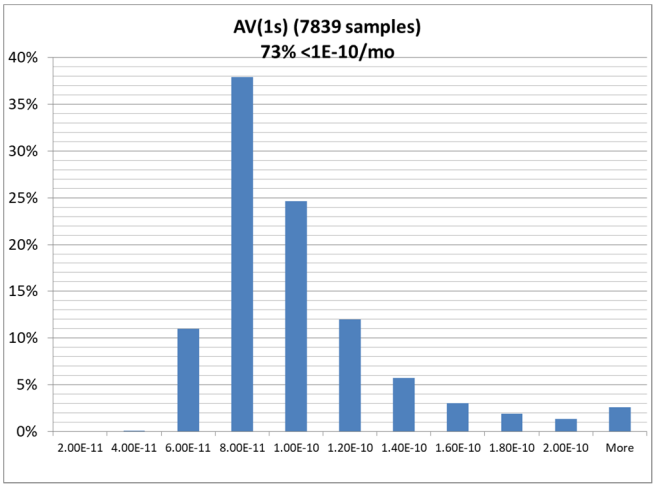

Figure 12 Temperatue Stability -10 to 70 deg C

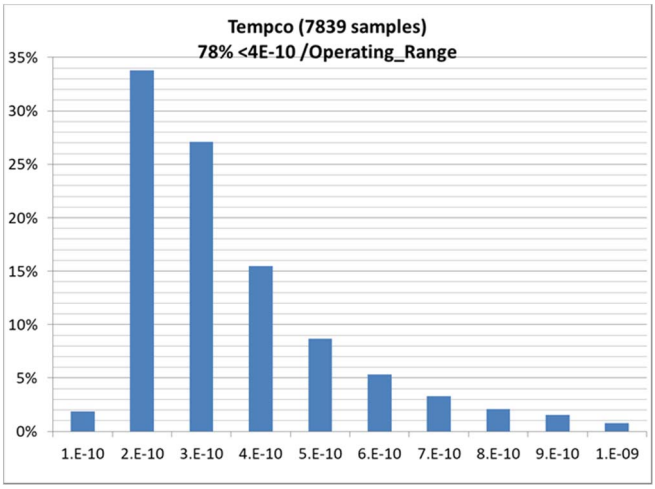

Figure 13 Phase Noise Measurements

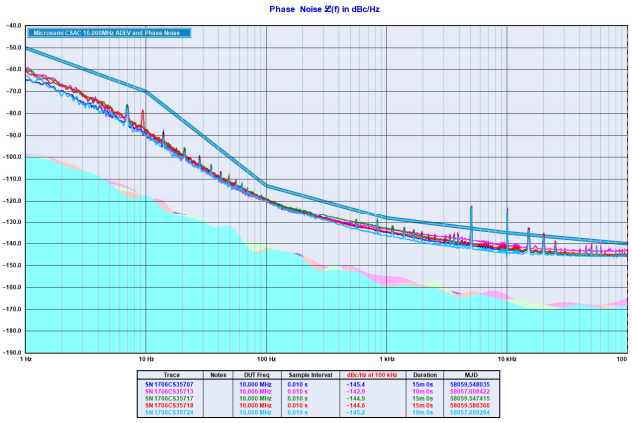

Figure 14 Allan Deviation 1 to 1000 seconds

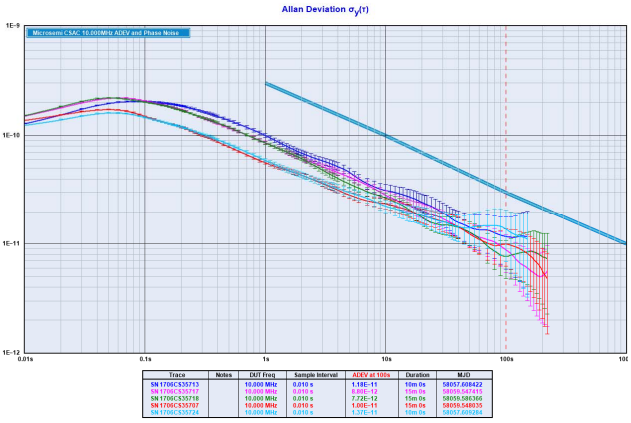

LNCSAC

Many applications require precision timing and low phase noise. These include communications, radar, and measurement. CSAC uses a conventional TCXO as part of the frequency synthesis chain. However, the oscillator can be replaced by a low power low phase noise OCXO. This design provides a lower noise version of CSAC in a slightly larger enclosure. The table below shows a comparison of the standard CSAC performance vs. the LNCSAC. A photograph is shown in figure 15.

Figure 15 CSAC vs. LNCSAC

	CSAC -10 MHz	LNCSAC - 10 MHz
Allan Deviation @ 1 sec. @ 10 sec.	 < 2e-10 < 7e-11	 < 2e-11 < 5e-11
Phase Noise @ 1 Hz @ 10 Hz @ 100 Hz @ 1 kHz @ 10 kHz @100 kHz	 - 50 dBc/Hz - 70 dBc/Hz - 113 dBc/Hz - 128 dBc/Hz - 135 dBc/Hz - 140 dBc/Hz	 - 85 dBc/Hz - 120 dBc/Hz - 140 dBc/Hz - 145 dBc/Hz - 150 dBc/Hz - 150 dBc/Hz

Figure 16 LNCSAC

LNCSAC like CSAC provides timing capabilities such as 1 pps in/out and steering, time of day (TOD).

Space CSAC

Many attributes of CSAC are ideal for space applications in which size, weight, and power (SWaP) are at a premium. Traditional space applications in high altitude orbits with extreme radiation conditions are not suited for the commercial electronics used in CSAC. However, the recent trend towards smaller satellites with lower orbits (LEO) that require state of the art technology and rapid design and deployment is perfectly suited for CSAC. The space CSAC is characterized by a total ionizing dose of 20 krad (Si), Single Event Effects (SEE) to 64 MeVcm2/gm and Neutron environments. The space CSAC utilizes a different commercial TCXO more resilient to radiation and has the electronics lot qualified for total dose performance. CSAC's precision frequency and timing keeping may be used in several scenarios in orbit including crosslinking, earth science, data collection, and communication. CSAC and Space CSAC are already utilized in space and are deployed for critical government space missions.

Future CSAC Development Plans

Microsemi along with assistance from the US government continues to improve the performance of CSAC. An updated version of the clock, CSAC B, is currently in Engineering qualification testing. The updated design will include performance from -40 to 80 ºC. Improvements in lifetime, reduced sensitivity to temperature and voltage changes, better phase noise, and Allan Deviation and warm-up time are anticipated. CSAC B has an option to provide additional power to the physics package which improves the time to lock and maintains lock in the event of a reduced vacuum inside of the physics package. The form, fit and function of

CSAC B is identical to the current version. As a result, the design will be a drop in replacement with improved performance. The CSAC B is expected to be ready for delivery by the end of 2018.

Microsemi is developing a more significant design improvement to the current CSAC. The design is referred to as the "Next Generation" CSAC. The effort is a multi-year project and is investigating improvements to the physics package and changes to the electronics and firmware. The goals of this design are to improve the temperature stability and drift rate by a factor of five or more. Power reduction design updates are being explored. Breadboard versions of the updated physics packages have shown daily drift rates of less than 1 x 10^{-11} per day. The photograph below shows the prototype version being evaluated.

Figure 17 Next Generation CSAC Prototype

The roadmap shown below represents Microsemi's current roadmap for the CSAC platform.

Product	CY17	CY18	CY19	CY20	CY21	Comment
CSAC A		MD				
CSAC A+	Release		MD			-10 to 70°C
CSAC B		Release				-40 to 80°C
CSAC Next Generation	Breadboard	Pilot			Release	Improved Temperature Performance and Drift, ASIC, reduced power
LNCSAC	Commercial Release 10 MHz					Low profile option being evaluated

Conclusions

Coherent Population Trapping technology has lead to a new generation of atomic clocks. In particular, commercial portable clock technology with the capabilities of atomic clocks able to operate at extremely low power such as Microsemi's CSAC. CSAC has changed the manner in which time and frequency are utilized in low power applications. Key markets such and Oil and Gas exploration, and Military time and frequency generation have been changed dramatically, and new capabilities and missions enabled.

REFERENCES

[1] John Kitching, "Chip-Scale Atomic Clocks" Johns Hopkins Applied Physics Laboratory Journal, 2018

[2] R. Lutwak, A. Rashed, M. Varghese, G. Tepolt, J. Leblanc, M. Mescher, D.K. Serklan and G.M Peaske, "The Miniature Atomic Clock - Preproduction Results," *Proceedings*, 2007 IEEE Frequency Control Symp., Geneva, Switzerland, May 29-June 1, 2007

ACKOWLEDGEMENTS

The authors would like to thank the following individuals for support of this paper and the oral presentation.

A. John Kitching from the US National Institute of Standards
B. Nils Heieren and Nils Gateman of Magseis
C. Said Jackson of Jackson Laboratories

Development status of the Rb POP space clock for GNSS applications

P. Arpesi[1], J. Belfi[2], M. Gioia[1], N. Marzoli[3], R. Romani[1], A. Sapia[1],
M. Gozzelino[4], C. Calosso[4], F. Levi[4] , S. Micalizio[4], A. Tuozzi[5], M. Belloni[6]

[1] Atomic Clocks, Leonardo SpA, Milan, Italy, [2] Altran c/o Leonardo , Milan, Italy
[3] Positech, Alten group, c/o Leonardo , Milan, Italy
[4] Physics Metrology Division , INRIM, Torino, Italy, [5]Agenzia Spaziale Italiana, Rome, Italy
[6]European Space Research and Technology Centre – Noordwijk, NL

***Abstract*— We present the status of the industrialization activity of a Rubidium POP (Pulsed Optically Pumped) clock Physics Package (PP) designed to meet the harsh space environment and more than 12 years of life-time. Leonardo completed the design phase including thermal, mechanical and magnetic analyses. PP manufacturing started at the beginning of 2018. The vibration test on the full microwave cavity assembly prototype including the Rb cell is foreseen by the first half of the year. The target for the Rb POP industrialization activity is to achieve a space qualification of the full clock by 2020 and the readiness for experimental flight by 2022.**

I. INTRODUCTION

Next generation Global Navigation Satellite Systems require atomic clocks with improved frequency stability with respect to the rubidium atomic frequency standard (RAFS) presently flying on GPS and Galileo satellites. Galileo's Passive Hydrogen Maser (PHM) surpasses the RAFS performance by one order of magnitude in terms of both short term stability and integration time. This is however at the cost of higher mass and complexity. A simpler technology with comparable performances and smaller impact on the satellite in terms of volume, mass and power consumption is desirable. The Rb POP clock technology, developed by the Italian National Institute of Metrology is presently considered one of the best candidates [1].

II. RB POP WORKING PRINCIPLE

The ^{87}Rb POP clock is a vapor cell clock based on a Ramsey interrogation scheme. The clock transition is excited by means of microwaves pulses at 6.834 GHz while pulsed optical radiation at 780.2 nm is used to prepare the rubidium atoms ground state for the microwave interrogation and for the detection phase. Microwave pulses, obtained by fast switching of the microwave synthesis chain output signal, excite the TE_{011} mode of the cavity containing the vapour-cell. High contrast optical pulses are obtained by means of an AOM.

Since atoms never interact simultaneously with microwave and optical radiation, a strong reduction of the light shift effect is obtained with respect to continuously operating vapour-cell frequency standards [2]. The optical detection of the atomic reference signal allows the usage of microwave cavities with a quality factor below 200. This strongly reduces the cavity pulling with respect to the case where the detection is performed on the microwave signal for which higher cavity quality factors are required [4]. A frequency stability of $1.7\text{x}10^{-13}$ at 1s and $5\text{x}10^{-15}$ up to 50000 s, (drift $<10^{-14}$/day) has been demonstrated in [2]. Such performances are fully compliant with the modern GNSS on-board clock requirements..

III. RB POP DESIGN FOR SPACE

Leonardo, in collaboration with INRIM, is developing a space version of the Rb POP clock. The system shall provide high frequency stability, low failure rate over 12 years mission time, low sensitivity to temperature and magnetic field, low mass and power consumption. Space environment requires the clock to sustain vibration and shocks experienced during the launch, extreme non-operating temperature, long term exposure to space radiation, in orbit micro-vibration and vacuum conditions.
In addition, the clock shall comply with satellite's electromagnetic compatibility requirements.
The architecture of the space clock is sketched in Figure 1, where the main functional blocks are represented.

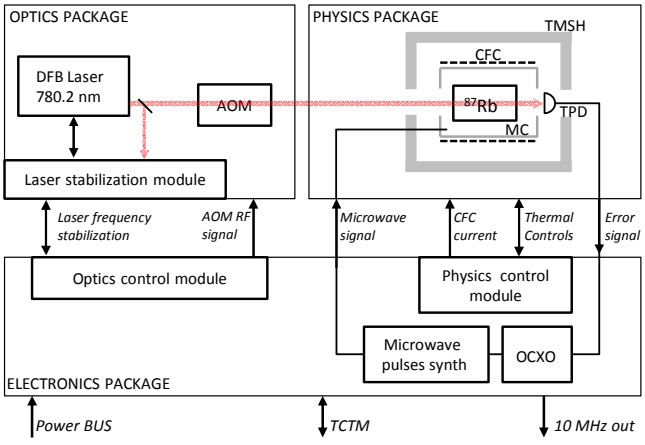

Figure 1 Block scheme. CFC: C-Field Coil; TMSH: Thermal and Magnetic Shielding; MC: Microwave Cavity; TPD: Transimpedance Photo Diode; TCTM: TeleCommand TeleMetry.

Leonardo and INRIM design study [3] demonstrated the feasibility of a compact device with reduced mass, power

consumption and without maintenance needs. Design target performance are summarized in Table 1.

Allan deviation ($1s<t<10^4s$)	$< 4x10^{-13} \times t^{-1/2}$ (Threshold) $< 2x10^{-13} \times t^{-1/2}$ (Goal)
Frequency Drift (/Day)	$\leq 1x10^{-14}$ after 1 week stabiliz.
Freq. sensitivity to temperature	$< 1 \times 10^{-15}$/°C
Freq. sensitivity to Magnetic Field	$< 3x10^{-13}$/Gauss
Freq. sensitivity to Main Bus Voltage	$\leq 3x10^{-15}$/V
Dimensions	200 x 350 x 240 mm
Mass	9 Kg
Power consumption	< 50 W

Table 1:Target design performance for the Rb POP clock version for space .

In this paper we will focus on the development status of the PP. The current development phase follows an extensive analysis of the main critical aspects of the Rb POP for space, including the Electronics and the Optics package (ref. to [5]).

IV. PHYSICS PACKAGE INDUSTRIALIZATION

The PP main components are represented schematically in Figure 1. The most critical items identified toward PP industrialization is the system composed by the microwave cavity+cell assembly and the Rb cell production. The first phase of the industrialization plan is organized in two tasks which have been developing in parallel.

Task A: the construction and test of two PP engineering models (EMs);

Task B: installation and validation of the glass cell filling facility for the buffered ^{87}Rb vapour-cells preparation.

The roadmap for Task A is summarized in the flowchart of Figure 2.

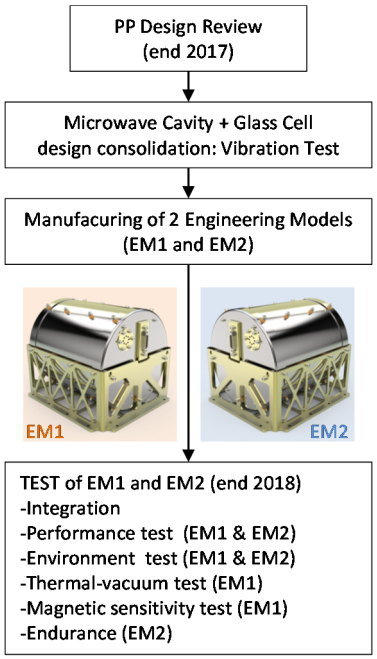

Figure 2 Ongoing development activity for the PP engineering model industrialization (Task A). Completion of this activity is expected by the end of 2018.

The PP industrialization will go through the construction of two identical prototypes (EM1 and EM2). This will allow us to conduct some of the tests in parallel and also to verify the reproducibility of the construction process. In addition, having two identical PPs opens up the possibility for INRIM to evaluate the microwave and laser noise contribution to the clock noise by implementing a "zero dead time" operation of two interleaved clocks [6].

Before testing the two EMs performances at clock level using the well consolidated INRIM setup, a vibration test (scheduled by May 2018) of the cavity+cell assembly will be performed to validate the design assumptions.

Task B development plan is reported in Figure 3. The apparatus for vacuum pumping and glass cleaning will be installed in a dedicated room in Leonardo plant by April 2018. A laboratory activity dedicated to the acquisition of the experimental skills for producing high quality buffered Rb cells will follow. The validation of the filled cells quality will be conducted by Leonardo as well by means of an optical spectroscopy setup which is already available in Leonardo. Main parameters under evaluation are the pressure shift and pressure broadening of the D2 absorption line with respect to a reference cell containing Rb only. In order to define proper pass-fail criteria of the filled cell, the two-photon transition relaxation parameters will be characterized taking advantage of the INRIM recognized know-how.

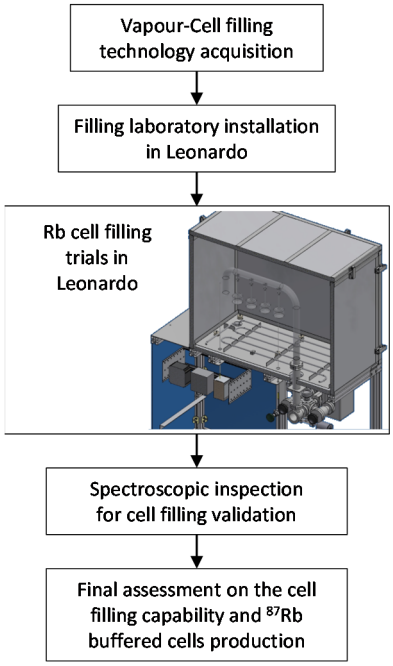

Figure 3 Roadmap toward the industrialization of the Rb POP buffered cell production (Task B).

V CONCLUSIONS

We presented the status of the Rb POP space industrialization activity. The construction of the clock's PP started in the beginning of 2018. We expect to complete a vibration test of the cavity+cell assembly by the first half of the year. The vibration test will validate the design and open the way to the of two complete PP EMs. The full characterization tests of the two PP EMs, including a clock's performance test using the

INRIM optics and electronics setup, is planned by the end of 2018 (Task A). The technology transfer, from INRIM to Leonardo, of the Rb cell filling process and cells characterization (Task B) plays a central role for the success of this activity and runs in parallel to Task A. It is expected to have the first in house filled and validated cells by July 2018. The final assessment on the Physics Package development together with the kick-off of the Optics and Electronics packages design, is expected by the end of 2018.

AKNOWLEDGMENTS

This work is funded by GSTP 6.2 Contract N. 4000118182/16/NL/GLC/fk for Rubidium POP Atomic Clock Physics Package and by Leonardo and INRIM. In addition it was supported by the European Metrology Research Program (EMRP project IND55-Mclocks). The EMRP is jointly funded by the EMRP participating countries within EURAMET and the European Union.

REFERENCES

[1] J. Camparo "The Mercury-Ion Clock and the Pulsed-Laser Rubidium Clock: Near-Term Candidates for Future GPS Deployment", Aerospace Report NO. TOR-2015-03893S, 2015.

[2] Micalizio et al, "Metrological characterization of the pulsed Rb clock with optical detecton", Metrologia vol. 49, pp. 425-436, 2012.

[3] M. Belloni et al., "A space rubidium pulsed optical pumped clock-Current status and future activities," PTTI 2009.

[4] A. Godone et al., "The Pulsed Rubidium Clock", IEEE transactions on ultrasonics, ferroelectrics, and frequency control, vol. 53, no. 3, march 2006.

[5] A. Battisti et al, "Industrialisation approach of the POP atomic clock for application to GNSS"., Proceedings of the EFTF2014 (Neuchatel, Switzerland) p.423-426, 2014.

[6] G.W. Biedermann et al., "Zero-Dead-Time Operation of Interleaved Atomic Clocks" Phys. Rev. Lett 111, 170802, 2013.

Ramsey-mode Rb cell clock demonstration with a 3D-printed microwave cavity

W. Moreno, C. Affolderbach, M. Pellaton, G. Mileti
Laboratoire Temps-Fréquence (LTF)
University of Neuchâtel
Neuchâtel, Switzerland
Christoph.affolderbach@unine.ch

A. E. Ivanov, A. Skrivervik
Microwave and Antennas Group
Ecole Polytechnique Fédérale de Lausanne EPFL-MAG
Lausanne, Switzerland
Anja.skrivervik@epfl.ch

T. Debogovic, S. Capdevila, D. Hoerni, E. deRijk
SWISSto12 SA
Ecublens, Switzerland
T.debogovic@swissto12.ch

We demonstrate operation of a Ramey-mode Rb vapor-cell atomic clock based on a microwave cavity realized by additive manufacturing (3D-printing). The cavity design is based on a loop-gap approach and its critical electrode structure is realized in one monolithic piece by stereolithography of a polymer which simplifies the assembly of the cavity. The microwave magnetic field in the cavity shows excellent uniformity and high homogeneity across the Rb cell, which results in high-contrast Ramsey fringes observed on the clock transition. A measured clock stability of $2.2\times10^{-13}\ \tau^{-1/2}$ demonstrates the feasibility of the approach. We discuss aging studies performed on 3D-printed test samples that are of relevance for long-term operation of the clock.

Keywords—Rb atomic clock; Ramsey scheme; microwave cavity; additive manufacturing.

I. INTRODUCTION

Atomic clocks based on alkali vapor cells cover the majority of mobile clock applications, ranging from the chip scale atomic clocks (CSAC), dedicated to highly portable applications such as GNSS receivers or dismounted military applications, to the high performance and compact rubidium atomic frequency standards (RAFS) equipping the global navigation satellite systems (GNSS). Their performances as well as size, weight, power consumption and cost (SWaP-C) have been drastically improved thanks to technological advances either in terms of interrogation schemes, pumping light sources, or manufacturing techniques. During the past years, significant effort and progress have been made in the development of next generation compact and high-performance Rb-type atomic frequency standards, notably using the Pulsed Optically Pumped (POP) Ramsey scheme [1]. Recently our team showed that state-of-the-art clock stabilities can also be achieved with POP clocks based on highly compact microwave cavities using a loop-gap-type electrode configuration [2, 3]. Another revolution has come with the advent of additive manufacturing (AM), commonly known as 3D printing. In the microwave domain, AM previously served for fabrication of waveguides and antennas [4] as well as metallic high Q-factor cryogenic resonators [5]. Recently, AM was proven to be suitable also for atomic clock applications [6]. Potentially, this technology presents strong advantages in terms of weight and fabrication cost, while maintaining the same clock performances.

Here we present a summary of our studies on a high performance compact atomic clock based on a 3D printed microwave cavity. We demonstrate the feasibility of this innovative approach and present studies on accelerated aging of the employed technology and the realization of a monolithic version of the cavity.

II. 3D-PRINTED MICROWAVE CAVITIES

The cavity design used in this work is based on the loop-gap resonator approach, employing a cylindrical cavity geometry with six electrodes as presented in [3]. This electrode structure allows to achieve a highly homogeneous microwave magnetic field across a large portion of the cavity volume occupied by a 25 mm diameter Rb vapor cell. It also results in a field aligned parallel to the cavity's axis of symmetry (z-axis). Furthermore, this approach also reduces the cavity size well below the one of a simple cylindrical cavity. In the following we demonstrate the feasibility of using AM for producing the cavity's critical electrode structure, whose precise dimensions are among the main parameters controlling the cavity's field mode and resonance frequency.

A. Cavity Fabrication

The realized cavities feature an outer cavity cylinder and six electrodes manufactured in one single component using AM, see inset of Fig. 1. The manufacturing process uses stereolithography (SLA), i.e. selective laser-activated polymerization of a liquid polymer [7] followed by adding a copper coating for achieving RF functionality as well as a thin silver passivation layer, as described in [6]. This SLA approach has previously been shown to be suitable for manufacturing

This work was supported by the Space Positioning Measures of the Swiss Space Office of the State Secretariat for Education, Research and Innovation of the Swiss Confederation (SERI/SSO), call 2016, and the Swiss National Science Foundation (grants 156621 and 162346). The authors also acknowledge previous support from the European Space Agency (ESA) and the European Metrology Research Programme (EMRP Project IND55 Mclocks). The EMRP is jointly funded by the EMRP participating countries within EURAMET and the European Union.

high-performance microwave waveguides and antennas up to 110 GHz [4]. The use of the polymer material results in a mass reduction by around 40% compared to using e.g. aluminum. For performance evaluation, the cavity is completed by a cavity bottom with coupling loop and a Rb vapor-cell holder, both realized by conventional machining.

B. RF performance

Fig. 1 shows the measured S_{11} parameter measured for the AM cavity. The resonance of the desired TE_{011} mode is tuned to the required 6.835 GHz frequency of the Rb clock transition and is well separated from the closest unwanted mode (at ≈ 7.1 GHz), in agreement with numerical simulations. Typical resonance linewidths are about 100 MHz, corresponding to a loaded quality factor of Q ≈ 60.

III. Clock Operation

For further evaluation and clock operation, the AM cavity was integrated into the physics package (PP) of an experimental atomic clock as described in [2]. The clock setup is completed by a compact laser head emitting at the 780 nm Rb D2 wavelength which includes laser frequency stabilization as well as an acousto-optical modulator serving as optical switch [8]. The microwave Local Oscillator (LO) and clock loop electronics are similar to the one described in [9]. The clock can be operated in either continuous-wave double-resonance (CW-DR) or pulsed Ramsey mode.

A. Preliminary evaluation

A first preliminary evaluation of the 3D-printed microwave cavity in atomic clock mode was carried out using the CW-DR scheme [10] as reported in [6]. The recorded spectrum of all the seven Zeeman transitions (see Fig. 2) allows us to evaluate the quality of the field orientation, or in other words, the field orientation factor (FOF) [11]. The obtained value of FOF=0.98 indicates a highly uniform microwave magnetic field, oriented highly parallel to the z-axis. In terms of clock performances, we measured a CW clock signal with a linewidth below 500 Hz and a contrast of nearly 20%. Taking also into account the detection noise, such signal would allow a fractional clock frequency stability of $4.2 \cdot 10^{-13} \cdot \tau^{-1/2}$ [6].

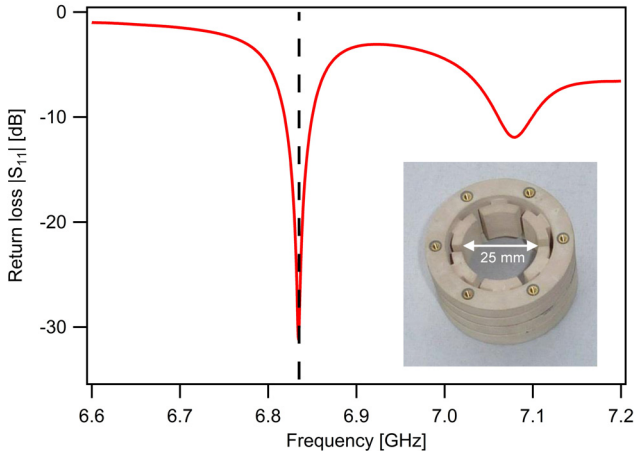

Figure 1: example of measured S_{11} for the AM cavity. The vertical dashed line shows the 6.835 GHz Rb frequency. Inset: photograph of the AM cavity structure.

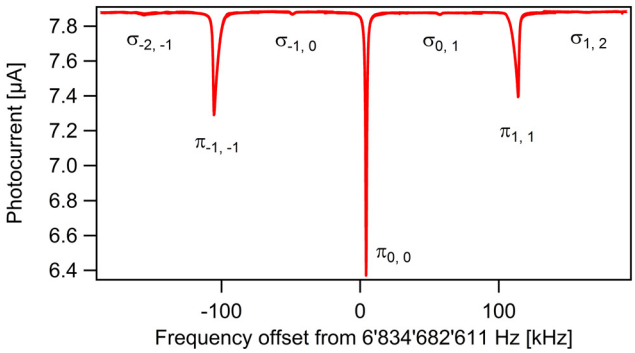

Figure 2: CW-DR spectrum of the seven Zeeman transitions within the ground state of the 87 Rb using the SLA cavity. Note the very weak sigma transitions.

B. Ramsey clock results

A second evaluation was performed using the POP scheme [12]. The optically detected Ramsey fringes (see Fig. 3) present a contrast of the central fringe of 34%. Rabi oscillations of the atomic population (see Fig. 4), measured by varying the power of the microwave pulses employed in the Ramsey sequence, are impacted by the residual inhomogeneity of the magnetic field inside the vapor cell [2]. The low damping of the Rabi oscillations indicates a good homogeneity of the relevant microwave magnetic field inside the vapor cell, comparable to the one achieved in conventionally manufactured cavities.

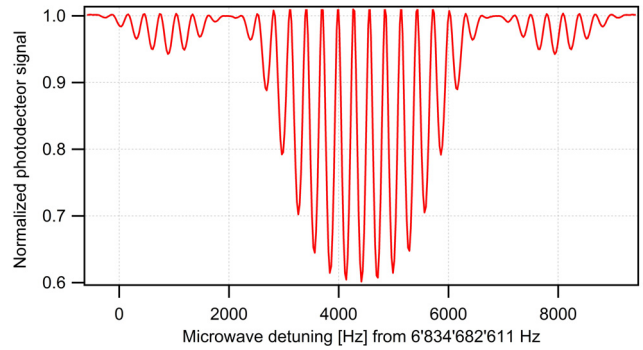

Figure 3: Ramsey signal of the 87 Rb clock transition observed using the SLA cavity.

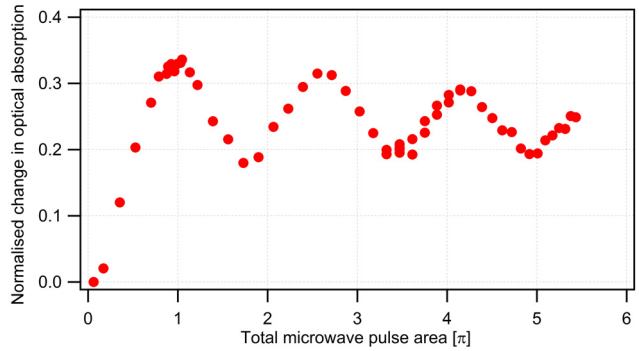

Figure 4: Rabi oscillations observed using the AM cavity.

TABLE I. MAIN SHORT-TERM INSTABILITY CONTRIBUTIONS

Effect	Instability contribution @ 1s
Signal-to-noise	$1.1 \cdot 10^{-13}$
Dick effect	$7 \cdot 10^{-14}$
Shot-noise	$2.7 \cdot 10^{-14}$
Total predicted short-term stabiltiy	$1.3 \cdot 10^{-13}$

For clock operation, the LO is frequency stabilized to the central fringe of the Ramsey pattern of Fig. 3. We measured a short-term stability of $2.2 \times 10^{-13}\ \tau^{-1/2}$ up to 30 s (see Fig. 5). This short-term frequency instability is close to the expected stability and mainly dominated by the signal-to-noise ratio of the optical detection, see Table 1.

IV. ADVANCED 3D-PRINTED CAVITIES

In the following we analyze the potential of AM for simplifying further the manufacture of our compact loop-gap cavity for Rb clocks. We also discuss aging studies of the cavity material that could affect the long-term performances.

A. Monolithic integration

Fig. 6a shows a cavity bottom realized by SLA that features a 2 mm-wide coupling loop monolithically integrated onto the cavity bottom during the AM process. The loop is electrically closed by connecting the center conductor of the RF coaxial cable with a conductive glue. In contrast to conventional assembly of coupling loops from discrete parts, this approach allows for improved reproducibility of the loop geometry. We observed good reproducibility of the S_{11} performance for three samples tested that all allowed tuning a test cavity to 6.835 GHz. A somewhat degraded return loss on resonance ($|S_{11}| \approx$ - 7 dB) is still acceptable for clock operation and is expected to be optimized by refined loop design. We also manufactured a more radically integrated version of the AM cavity, see Fig. 6b, where all the loop and bottom part (Fig. 6a) together with the electrodes and cylinder (shown in Fig. 1a) were manufactured in one single piece using SLA. This approach has the advantages of further reducing assembly steps and allows omitting the screw inserts (see Fig. 1) for mounting the cavity bottom. It thus demonstrates the potential of AM for the realization of complex microwave cavity structures.

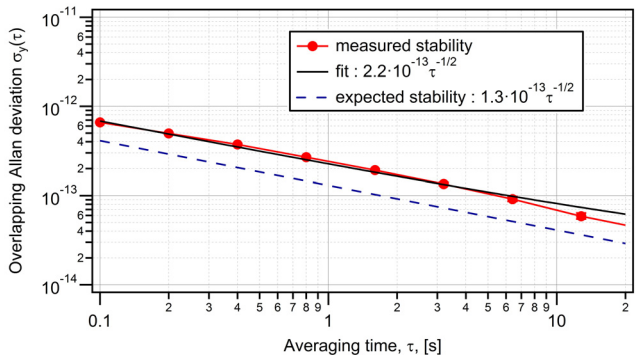

Figure 5: Measured clock stability with the AM cavity in Ramsey scheme.

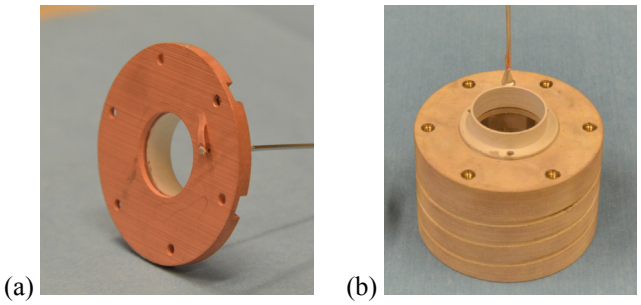

Figure 6: photographs of (a) coupling loop realized by AM monolithically onto the cavity bottom; (b) drastically monolithic microwave cavity manufactured by AM. The screw inserts visible serve only for mounting the cavity into the clock physics package.

B. Long-term performance assessment

To assess the long-term performance of the SLA approach, an accelerated thermal ageing test procedure was carried-out on representative test specimens. Physical properties measurement, dimensional control, check of copper adhesion on the substrate and RF performance were performed before and after the test procedure. We applied the following test procedure:

- 400 thermal cycles between -55°C and +85°C on dedicated samples as per ASTM D638 and ASTM D790 standards to perform tensile and bending properties measurement.
- 800 thermal cycles between 0°C and +85°C to generate internal constraints into the material. The following measurements were performed every 200 cycles:
  - Dimensional control
  - Adhesion check
  - SEM analysis of the material surface
  - RF performance

The test specimen shown in Fig. 7 was used to assess dimensions before and after thermal ageing. To check copper adhesion and perform SEM images, we used the coupons shown in Fig. 8. Fig. 9 shows the resonator test specimens used for RF performance assessment, whose specifications are representative of the cavity resonator for the Rb atomic clock.

C. Long-term assessment results

Tensile and bending measurements showed that the ageing process does not lead to significant degradations of material properties. On the contrary, ageing seems to improve its tensile and flexural properties. SWISSto12 material behavior to thermal aging process is promising for future applications.

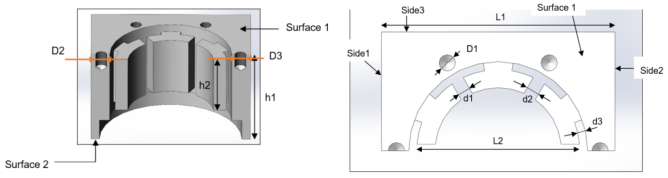

Figure 7: Test samples for dimension control.

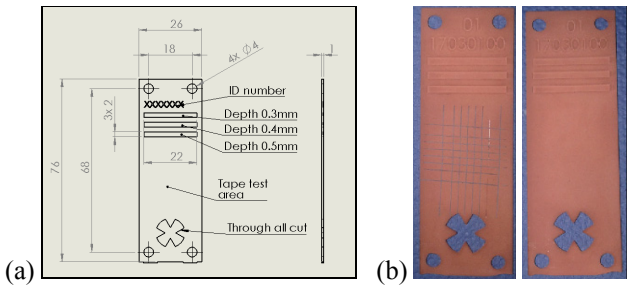

Figure 8: (a) design and (b) photographs of the test coupons for Cu adhesion tests and SEM images.

Dimensional control has shown changes of 20 µm maximum measured on critical cavity dimensions (with digital caliper). These slight differences cannot be attributed to thermal ageing but rather to measurement uncertainties, showing that the material is stable throughout the ageing procedure.

Copper adhesion test, performed with cross-cut and tape test method following ISO 2409, has shown excellent results with 100% of adhesion all along the ageing procedure. No degradation of adhesion has been noticed.

Images of the surface done with SEM equipment (magnified 300 times) on coupons show no evolution of the surface nor any appearance of cracks.

RF performance measurement before and after the ageing procedure show that the RF properties of the test specimens are maintained throughout the test procedure, see Fig. 10. No considerable changes in RF performance were detected throughout this campaign. This is clearly observed in Fig. 11 that shows the evolution of the resonant frequency (< 2 MHz variation), *Q*-factor and the resonant insertion loss (S_{21} parameter) for each of the RF test specimens. All these parameters remain essentially constant with time (cycles). Minor variations observed are caused by the measurement uncertainty rather than the variation of the RF performance itself.

As a conclusion, measurements performed before and after the thermal ageing procedure show that the test specimens and the copper layer have not been damaged or modified in terms of physical properties of the material, geometry, surface integrity, plating, nor in terms of RF performance. The SLA components manufactured by SWISSto12 prove to be reliable and promising for RF applications at elevated temperatures.

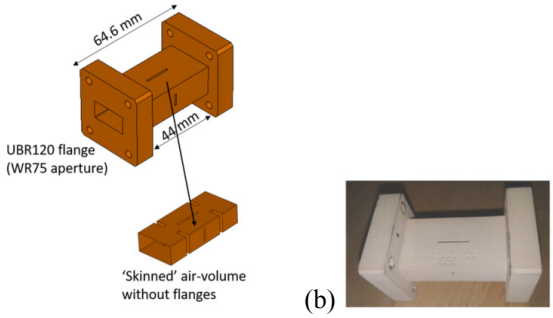

Figure 9: (a) design and (b) photograph of the WR75 waveguide resonator test specimens employed for RF tests.

CONCLUSIONS

We reported on microwave cavities for atomic clock applications, manufactured by stereolithography of a polymer followed by metal coating. We analyzed the cavity performance in a compact Rb-cell atomic clock setup, operated in both CW as well as pulsed optically pumped (Ramsey mode) scheme. The short-term clock stability in Ramsey mode is $2.2\times10^{-13}\ \tau^{-1/2}$ which is comparable to reported state-of-the-art stabilities of other compact high-performance clocks. Extended accelerated aging tests performed on SLA test specimens indicate that degradation of the cavities over long-term time scales may be expected to be very small. This study demonstrates the feasibility of compact atomic clocks based on AM (3D printed) microwave cavities.

ACKNOWLEDGMENT

C.A., W.M., M.P., and G.M. thank C. E. Calosso (INRIM, Italy) for providing and support on the microwave local oscillator and F. Gruet and P. Scherler (both University of Neuchâtel, Switzerland) for technical support.

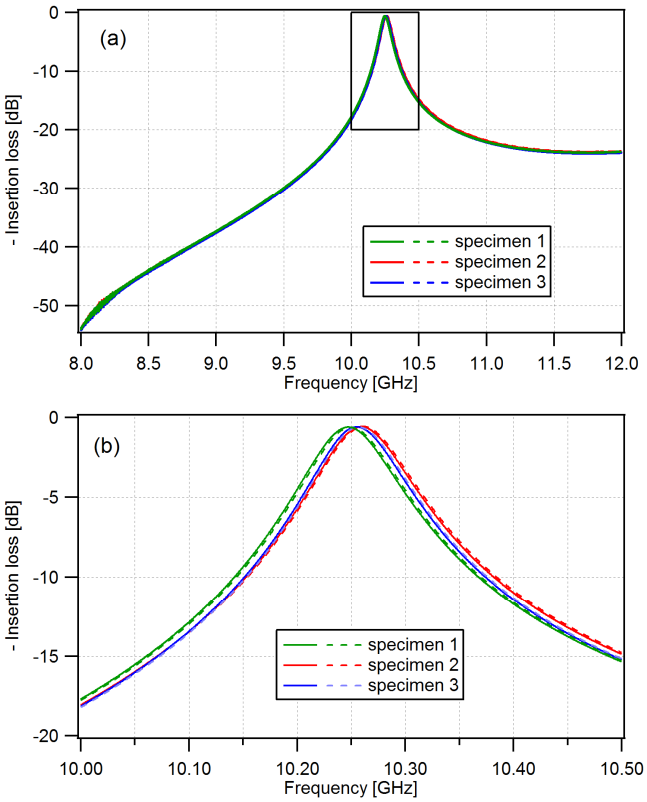

Figure 10: Insertion loss measured before (solid lines) and after (dashed lines) the 800 thermal cycles, for the three test specimens. (a) full span. (b) zoom on the resonance peak indicated by the box in sub-panel (a). The small shifts observed from before to after aging are mostly due to the measurement uncertainty.

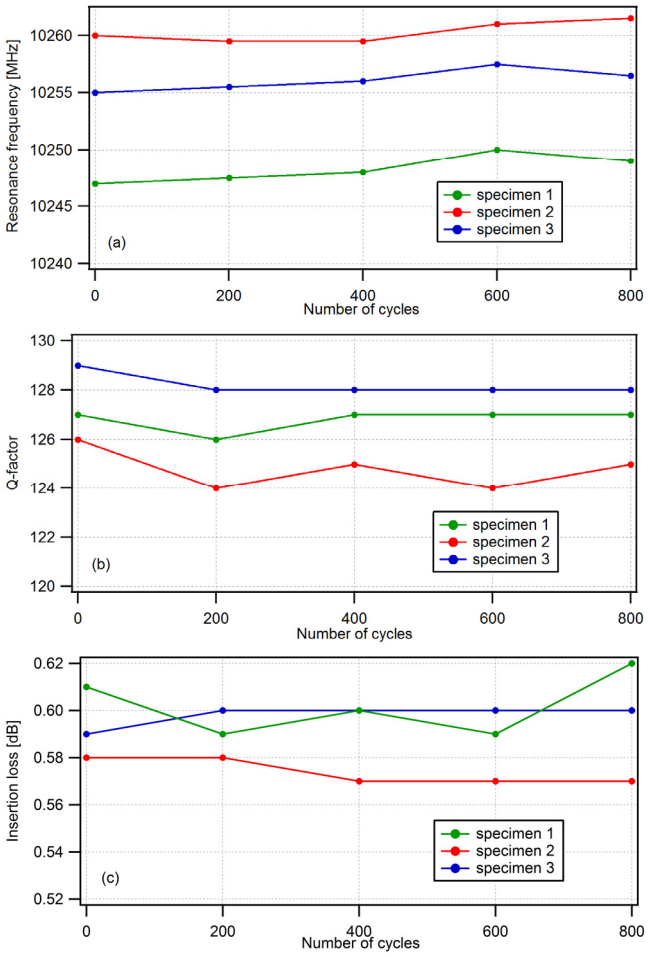

Figure 11: development of (a) resonance frequency, (b) Q-factor, and (c) insertion loss at resonance results for three RF test specimens over the 800 thermal cycles.

REFERENCES

[1] S. Micalizio, C.E. Calosso, A. Godone, F. Levi, "Metrological characterization of the pulsed Rb clock with optical detection," Metrologia, 49, pp. 425-436 (2012).

[2] S. Kang, M. Gharavipour, C. Affolderbach, F. Gruet, G. Mileti, "Demonstration of a high-performance pulsed optically pumped Rb clock based on a compact magnetron-type microwave cavity," J. Appl. Phys., vol. 117, 104510 (2015).

[3] C. Stefanucci, T. Bandi, F. Merli, M. Pellaton, C. Affolderbach, G. Mileti, A.K. Skrivervik, "Compact microwave cavity for high performance rubidium frequency standards," Rev. Sci. Instrum., vol. 83, 104706 (2012).

[4] A.I. Dimitriadis, T. Debogovic, M. Favre, M. Billod, L. Barloggio, J.P. Ansermet, E. de Rijk, "Polymer-Based Additive Manufacturing of High Performance Waveguide and Antenna Components," in Proc. IEEE, vol. 105 (4), pp. 668–676 (2017).

[5] D.L. Creedon, M. Goryachev, N. Kostylev, T.B. Sercombe, M.E. Tobar, "A 3D printed superconducting aluminium microwave cavity," Appl. Phys. Lett., vol. 109, 032601 (2016).

[6] M. Pellaton, C. Affolderbach, A.K. Skrivervik, A.E. Ivanov, T. Debogovic, E. de Rijk, G. Mileti, "3D printed microwave cavity for atomic clock applications: proof of concept," accepted for publication in Electron. Lett., 2018. Doi 10.1049/el.2017.4176

[7] F. Calignano, D. Manfredi, E.P. Ambrosio, S. Biamino, M. Lombardi, E. Atzeni, A. Salmi, P. Minetola, L. Iuliano, and P. Fino, "Overview on additive manufacturing technologies," in Proc. IEEE, vol. 105 (4), pp. 593–612 (2017).

[8] S. Kang, M. Gharavipour, F. Gruet, C. Affolderbach, G. Mileti, "Compact and high-performance Rb clock based on pulsed optical pumping for industrial applications," in Proc. of the 2015 joint Conference of the IEEE International Frequency Control Symposium & the European Frequency and Time Forum, Denver, USA, April 12-16, 2015, (IEEE, New York, 2015), pp. 800-803.

[9] C.E. Calosso, S. Micalizio, A. Godone, E.K. Bertacco, F. Levi, "Electronics for the Pulsed Rubidium Clock: Design and Characterization," IEEE Trans. Ultrason. Ferroelectr. Freq. Control, vol. 54, pp. 1731–1740 (2007).

[10] T. Bandi, C. Affolderbach, C. Stefanucci, F., Merli, A.K. Skrivervik, G. Mileti, "Compact high-performance continuous-wave double-resonance rubidium standard with $1.4\times10^{-13}\ \tau^{-1/2}$ stability," IEEE Trans. Ultrason. Ferroelectr. Freq. Control, vol. 61, pp. 1769–1778 (2014).

[11] M. Violetti, M. Pellaton, C. Affolderbach, F. Merli, J.F. Zürcher, G. Mileti, and A.K. Skrivervik, "The Microloop-Gap Resonator: A Novel Miniaturized Microwave Cavity for Double-Resonance Rubidium Atomic Clocks," IEEE Sens. J., vol. 14, pp. 3193-3200 (2014).

[12] C. Affolderbach, W. Moreno, A. E. Ivanov, T. Debogovic, M. Pellaton, A.K. Skrivervik, E. de Rijk, G. Mileti, "Study of additive manufactured microwave cavities for pulsed optically pumped atomic clock applications," Appl. Phys. Lett., vol. 112, 113502 (2018).

Microwave field amplitude stabilization using Ramsey spectroscopy signal

Michele Gozzelino[1, 2]
[1]Physics Metrology Division
Istituto Nazionale di Ricerca Metrologica, INRIM
Torino, Italy
m.gozzelino@inrim.it
[2]Politecnico di Torino
Torino, Italy

Salvatore Micalizio
Physics Metrology Division
Istituto Nazionale di Ricerca Metrologica, INRIM
Torino, Italy
s.micalizio@inrim.it

Aldo Godone
Physics Metrology Division
Istituto Nazionale di Ricerca Metrologica, INRIM
Torino, Italy
a.godone@inrim.it

Filippo Levi
Physics Metrology Division
Istituto Nazionale di Ricerca Metrologica, INRIM
Torino, Italy
a.godone@inrim.it

Claudio Calosso
Physics Metrology Division
Istituto Nazionale di Ricerca Metrologica, INRIM
Torino, Italy
c.calosso@inrim.it

***Abstract*—We present a method to actively stabilize the amplitude of the microwave field which constitutes the probe for many state-of-the-art compact atomic clocks. The method applies to clocks working in pulsed operation, specifically with a Ramsey scheme. The proposed technique relies on information directly extracted from the clock atomic signal, as it computes the gradient in the two variables (amplitude and frequency) characterizing the probe field, instead of differentiating solely the frequency response, as in usual operation. Magnetic field sensing based on spectroscopy has proven to be a valuable tool for metrology and precise measurement field. We demonstrate the advantage of using the spectroscopic signal to stabilize the microwave field amplitude, in order to reach 10^{-15} stability with compact clocks, by mitigating cavity-pulling shift effects.**

Keywords—atomic frequency standards; vapor cell clocks; compact cold atom clocks; frequency instability: microwave fluctuations.

I. INTRODUCTION

Compact and high performing frequency standards are based on two well established technologies. In the first approach, the atoms are cooled by isotropic laser cooling in an integrating sphere/cylinder which is also used as a resonant microwave cavity [1, 2].

In the other approach, a hot sample of atoms is contained in a cell which in turn is placed in either a traditional microwave cavity [3, 4] or a magnetron cavity [5].

Cold and hot atoms techniques demonstrated very effective in terms of metrological performances. The measured frequency stability is at the level of $2\times10^{-13}\ \tau^{-1/2}$ (τ being the integration time) up to 10000 s [1, 3] and in the case of cold atom devices an accuracy below 10^{-15} is claimed [6].

Two important characteristics are shared by compact clocks working with either hot or cold atoms: 1) all the operation phases take place inside the cavity and 2) the clock transition is probed through the Ramsey interaction scheme.

The first point implies that the clock frequency is affected by cavity pulling: the atomic coherence excited by the interrogating microwave field acts as a source of magnetic field. This magnetization excites the main cavity mode that in turn reacts back on the atoms, as shown in Fig. 1. This feedback mechanism affects the atom's wave function and causes cavity pulling shift $\Delta\omega_{cp}$ when the cavity is detuned from the atomic frequency [7]:

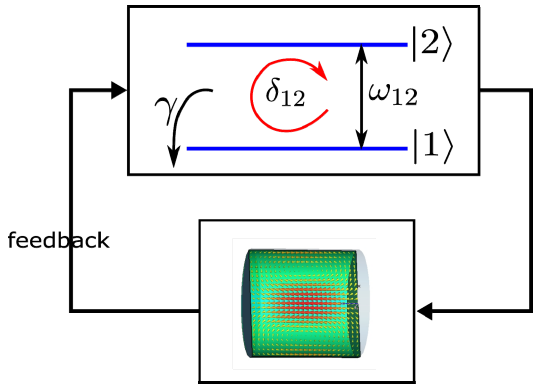

Fig. 1. Explanation of the feedback mechanism of the cavity on the atoms at the basis of the cavity pulling effect; δ_{12} is the atomic ground state coherence; ω_{12} is the ground state angular frequency; γ is the coherence relaxation.

$$\Delta\omega_{cp} = -\frac{2Q_L\Delta\omega_C}{\pi Q_a}\ln\{\cosh A(T) + \cos\theta\sinh A(T)\} \quad (1)$$

where Q_L is the loaded cavity quality factor, Q_a is the atomic quality factor $\Delta\omega_C = \omega_C - \omega_{12}$ is the cavity detuning (ω_C being the cavity resonance frequency), θ is the microwave pulse area and $A(T)$ is a function of the Ramsey time.

We notice that the pulsed operation allows to make negligible the cavity pulling. In fact, around $\theta = \pi/2$ the previous equation is zero. On the other hand, the cavity pulling shift is sensitive to residual microwave field amplitude fluctuations, affecting the clock frequency stability.

We devised a technique to lock the microwave amplitude on the atomic signal itself. This allows to improve the medium term stability of the clock

II. Active Amplitude Stabilization Using Ramsey Signal

We remind that the central fringe of the Ramsey signal can be written as:

$$S(\omega_0,\theta) \propto \sin^2\theta\,[1-\cos(\omega_0-\omega_{12})T] \quad (2)$$

where ω_0 is the (angular) microwave frequency. Equation (2) holds for any clocks working in Ramsey operation, in the following we often will refer to the pulsed optically pumped (POP) Rb clock described in detail in [3]. Around the desired working point ($\theta \approx \pi/2$) there is a minimum with respect to:

1) frequency;
2) microwave field amplitude (at fixed pulse duration).

In other words, we can use the signal expressed by (2) to discriminate both the frequency and the microwave field amplitude (see Fig. 2). This is an atom based approach: there is no need to finely scan the resonance for calibration and it is intrinsically robust against environmental perturbations.

Therefore, we implemented a two-loop stabilization algorithm, modulating frequency and amplitude of the microwave field at the same time.

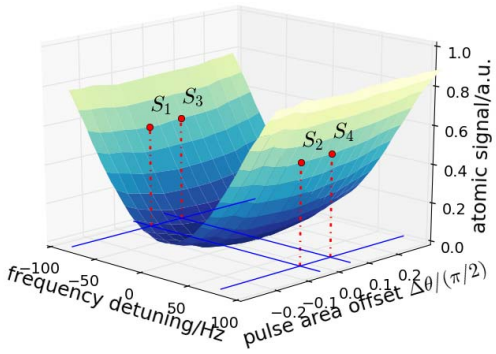

Fig. 2. Atomic signal as a function of both the frequency detuning $(\omega_0-\omega_{12})/2\pi$ and the pulse area θ. The experimental data used to draw the plot are the result of several frequency scans at different fixed power levels. They have been obtained for the pulsed optically pumped Rb clock.

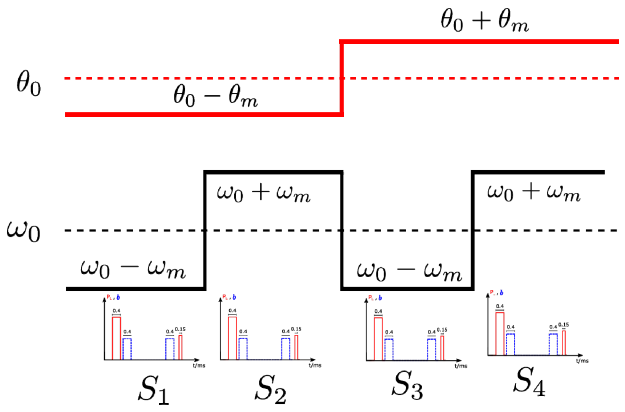

Fig. 3. Modulation sequence of both microwave amplitude and frequency: θ_0 (ω_m) is the nominal locking value and θ_m (ω_m) is the modulation depth. In this way it is possible to obtain four signal values that can be used to build up two different error signal as explained in the text.

The lock algorithm consists of four-point probing of the atomic resonance to get the atomic signal. Specifically, the microwave field amplitude and frequency are modulated in four subsequent basic clock sequences, as explained in Fig. 3. Two independent error signals E_θ and E_ω are fed to their respective control loops:

$$E_\theta = S_4 + S_3 - (S_2 + S_1) \quad (3)$$

to the microwave field amplitude control loop and:

$$E_\omega = S_4 - S_3 + S_2 - S_1 \quad (4)$$

to the microwave field frequency control loop.

III. Implementation for the POP Clock

The basic scheme of the clock components is presented in Fig.4 and we address the reader to the literature for a complete description of the device [3].

The parameters of the controllers are set in order to minimally perturb the classical operation of the clock. As usual, ω_m kept at HWHM, whereas b_m is a trade-off for having a sufficient sensitivity to amplitude variations without significant degradation of the frequency sensitivity.

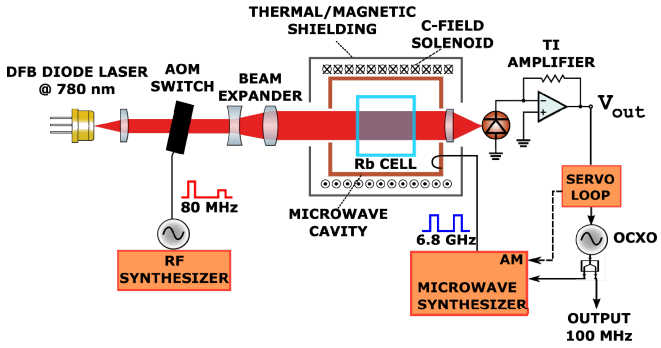

Fig. 4. POP clock experimental setup.

In more detail, the frequency modulation depth is ω_m = 80 Hz (the FWHM of the central Ramsey fringe is 160 Hz) and the microwave amplitude modulation depth is b_m = 0.05 b_0. The loop actuator is implemented by operating on the amplitude modulation input of the DDS which constitutes one of the fundamental steps of the synthesis chain.

The POP clock frequency is measured against a reference oscillator, which is a composed of a BVA option 08 phase-locked to an active hydrogen maser (Kvarz ch1-75). Between the two measures, we reduced the time constant of the phase-lock loop (from 3 s to 100 ms), to improve the frequency stability of the reference. All other experimental parameters are the same in the two configurations.

From Fig. 5, we observe a factor of two of improvement in the medium term stability (τ>10^4 s) when the microwave amplitude stabilization loop is on. The ultimate performance is limited by other sources of instabilities (e.g. thermal environment fluctuations).

In addition, we measured an improvement of the long term drift which is reduced from 4×10^{-14}/day (no amplitude loop) to 8×10^{-15}/day when the microwave amplitude stabilization loop is on.

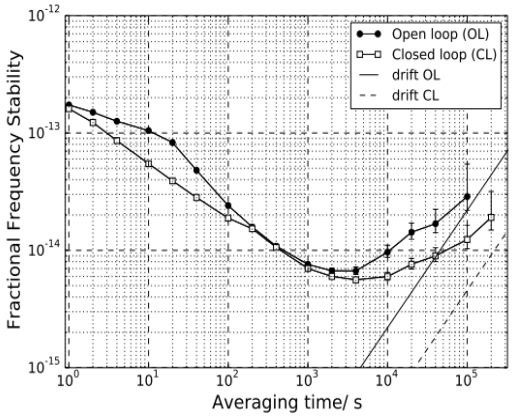

Fig. 5. POP clock frequency stability without (black circles) and with (white squared) amplitude active stabilization loop. The figure also shows the drifts in the two cases.

IV. CONCLUSIONS

We have implemented an active microwave amplitude stabilization loop to reduce cavity pulling in compact atomic clocks. The method uses the atoms themselves to discriminate the set point for the value of the microwave field amplitude, analogously to the common frequency loop used to discriminate the atomic frequency.

The technique does not impact the Dick effect, since the duty cycle is not affected. For the POP clock, we demonstrated a frequency stability improvement both in the medium and in the long term period.

The microwave amplitude stabilization loop can be also useful in compact clocks working with cold atoms. Cavity pulling is indeed recognized as one of the main source of frequency instability in the medium-long term.

REFERENCES

[1] Esnault et al., "High-stability compact atomic clock based on isotropic laser cooling, "Phys. Rev. A, vol. 82, p. 033436, Sep 2010.

[2] Liu et al., "Scheme for a compact cold-atom clock based on diffuse laser cooling in a cylindrical cavity," Phys. Rev. A, vol. 92, p. 062101, Dec 2015.

[3] Micalizio et al., ''Metrological characterization of the pulsed Rb clock with optical detection'', Metrologia, vol. 49, no. 4, p. 425, 2012.

[4] Lin et al., "Detection of ultrahigh resonance contrast in vapor-cell atomic clocks", Optics Letters, Volume 37, p. 5036, 2012.

[5] Kang et al., "Stability limitations from optical detection in Ramsey-type vapour-cell atomic clocks", Electron. Lett., Volume: 51, Pages: 1767 – 1769, 2015.

[6] Data sheet of Muclock from Muquans website

[7] Godone et al., "Physics characterization and frequency stability of the pulsed rubidium maser", Phys. Rev. A 74, 043401 (2006)

CPT Atomic Clock Based on an Antirelaxation-Coated Cell and Quadrature-Signal Method of the Light Shift Cancellation

S.M. Ignatovich[1], V.I. Vishnyakov[1], A.O. Makarov[1], M.N. Skvortsov[1*], N.L. Kvashnin[1], V.A. Vasiliev[1], S.N. Atutov[1,2], D.V. Brazhnikov[1,3], V.I. Yudin[1,3,4], A.V. Taichenachev[1,3] and S.N. Bagayev[1,3]

[1]Institute of Laser Physics SB RAS, Novosibirsk, Russia
[2]Institute of Automation and Electrometry SB RAS, Novosibirsk, Russia
[3]Novosibirsk State University, Novosibirsk, Russia
[4]Novosibirsk State Technical University, Novosibirsk, Russia

***Abstract*—High-stability and compact clocks are in great demand for many applications, for example, such as global navigation satellite systems (GNSS), broadband communication networks and high-secret lines, smart electricity grids, etc. Many applications of the clocks require small size and weight (V < 50 cm^3, m < 50 g), low power consumption (P << 1 W) and high long-term frequency stability (≤ 5×10^{-12} per a day). The most promising technology involves approach based on the coherent populations trapping (CPT) phenomenon, because it can combine all the features listed. Here we present the recent progress of development a version of CPT atomic clocks, which involves an antirelaxation-coated cell and the quadrature-signal method for the light shift cancellation.**

Keywords—coherent population trapping; Pound–Drever–Hall technique; antirelaxation coating; light shift cancellation; atomic clocks

I. INTRODUCTION

The buffer-gas-filled vapor cells are usually used to achieve narrow dark resonances caused by the coherent population trapping (CPT) [1,2]. The resonances are required for obtaining the good error signals for feedback frequency stabilization loop in atomic clocks (e.g. see [3-5]). However, the buffer-gas approach leads to very strict requirements to thermostabilization system and other problems. The vapor cells with antirelaxation coating of walls are less sensitive to temperature variations than the buffer-gas-filled ones. Moreover, the coated cells can be made pretty small by means of glass-blown [6] as well as MEMS technologies [7]. Another serious issue that should be solved to reach the high long-term stability consists in the light-induced shift of "clock" transition in the atom (so-called "0–0" transition). CPT-based atom clocks represent the all-optical technology, the microwave frequency is used to frequency modulate laser radiation. This feature is an important advantage of CPT clocks in comparison with, for example, the double-resonance-based clocks where a relatively bulky microwave cavity is needed.

In the CPT clocks, the high-frequency modulation is stabilized by means of the narrow dark resonance in an alkali-metal vapor cell. The clock parameters can be monitored by atoms themselves, rather than using conventional control systems [8].

The authors thank the Russian Science Foundation (grant no. 17-72-20089).

II. EXPERIMENTAL SETUP

To create atomic clock we designed a setup depicted in Fig. 1. As a laser source we used Ulm Vertical-Cavity Surface-Emitting Laser (VCSEL) emitting at λ=795 nm. The VCSEL lasers are enabling technology for using in various miniature devices. They have proven to be almost ideal in such applications. Their minimal size and power consumption together with well-developed low-cost technology make them useful in the chip-scale clock production [4]. We are using laser with thermoelectric cooler (TEC) inside, which is used to control temperature of the laser and, thus, tune wavelength. The VCSEL beam is divergent. In order to compensate this, lens were added to scheme to collimate the beam.

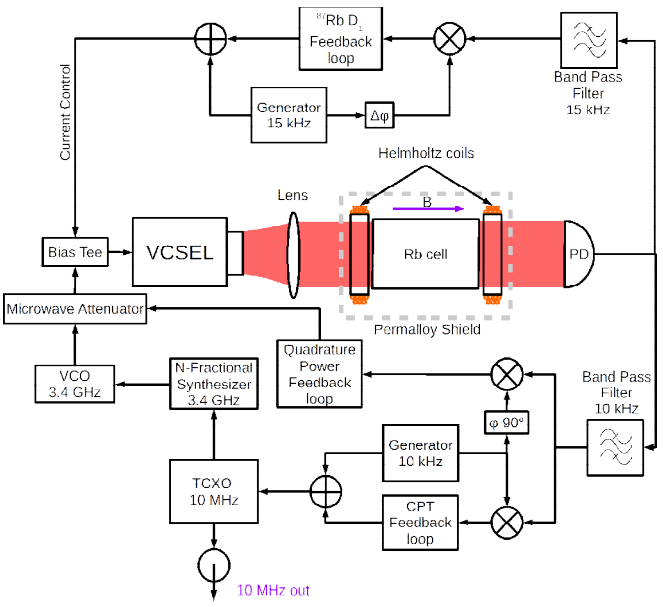

Fig. 1. The experimental setup.

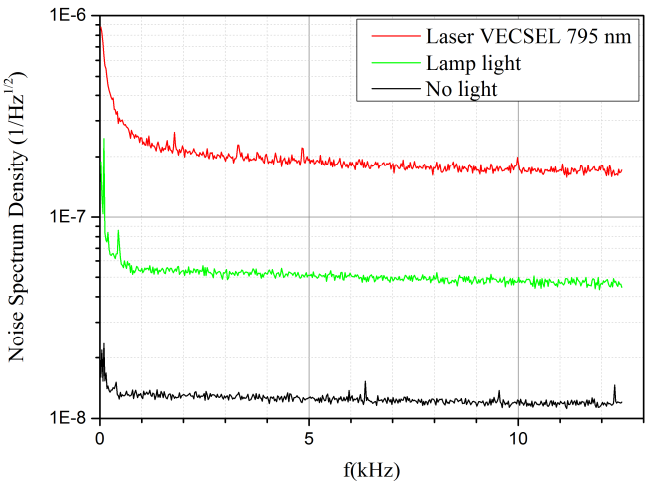

Fig. 2. Noise spectrum density measured without light (black curve) and with a bulb light with the same optical power (green curve).

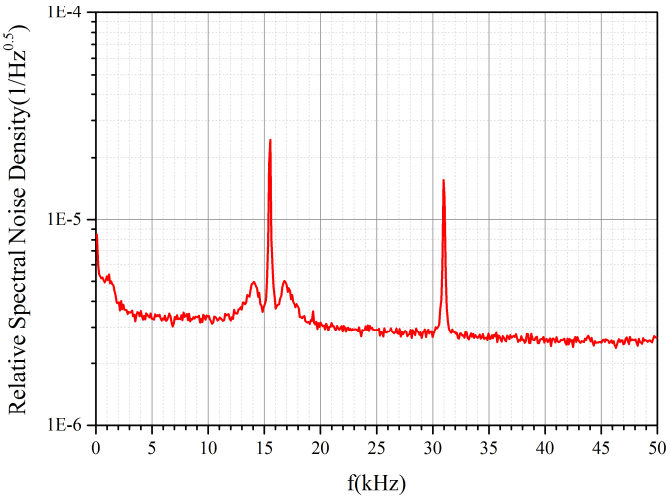

Fig. 3. Relative spectral noise density when all feedback loops are active.

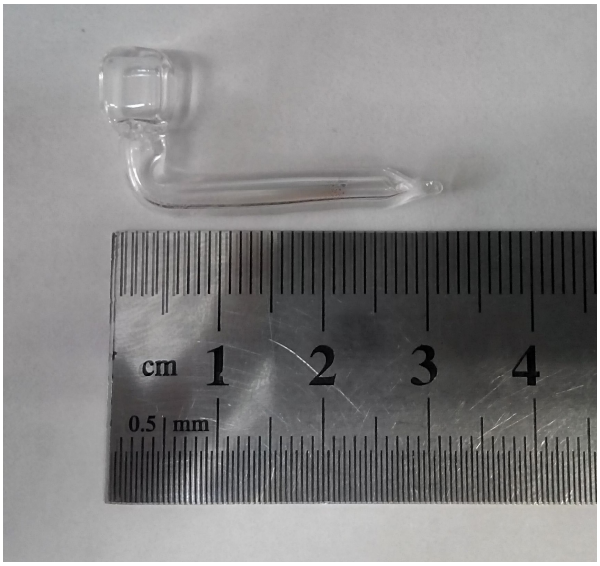

Fig. 4. Glass-blown ^{87}Rb vapor cell with antirelaxation coating.

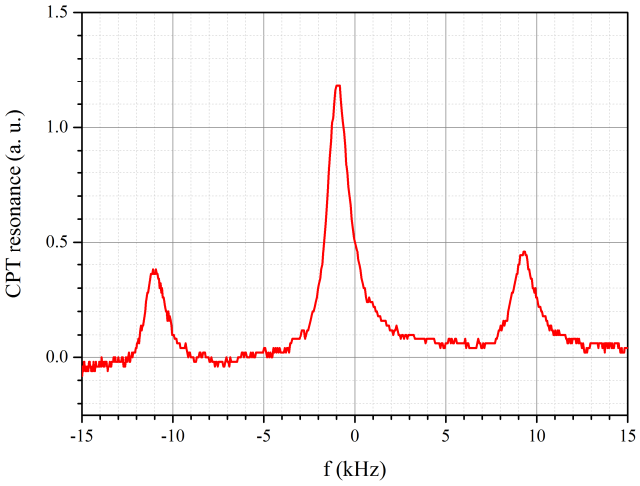

Fig. 5. CPT resonance under the 0.3 dBm UHF power applied and cell temperature stabilized at 52.5 °C.

The microwave current modulation can be supplied to the VCSEL for fast scanning the wavelength. To achieve high efficiency of microwave modulation and mixing, the bias tee was involved. To validate level of frequency noise in this particular VCSEL we measured noise spectrum density in three conditions: electronics noise only (black line); bulb equivalent noise floor resulting in similar photodetector voltage (green line) comparing to laser; laser itself (red line) (see Fig. 2). The relative spectral noise density was also measured when all feedback loops was active and system was in locked mode (Fig. 3). Let us focus on the peaks at 15 kHz and 30 kHz. 15 kHz is working frequency of ^{87}Rb D_1 line feedback loop (see Fig. 1). 30 kHz is just the second harmonic of 15 kHz signal.

To create homogenous controllable magnetic field we used Helmholtz coils and stabilized current control circuit. Magnetic field was varied in the range from –300 to 300 mG. To defend the cell from large ambient magnetic fields, several permalloy magnetic shields were constructed. Our cell is made by glass-blowing technique and is of an approximately 5×5 mm cubic shape with a 3 cm stem (Fig. 4). The wall thickness is about 0.2 – 0.3 mm. In our experiment we used ^{87}Rb isotope filled cell with paraffin coating.

In order to get high absorption contrast ratio we increased cell temperature up to 52.5 °C. To ensure linear polarization of the light, polarizing beam splitter (PBS) and λ/2 wave plate were added (not shown in scheme in Fig. 1). It is worth noting that VCSELs are sensitive to returning residual light beams. After supplying 0.33 dBm of microwave modulation at ≈ 3.4 GHz to the laser current, two sidebands can be observed (Fig. 5). Stabilization can be divided into several stages. First, laser wavelength need to be locked against ^{87}Rb D_1 line (Fig. 1). Then the feedback signal goes to the VCSEL current controller. Second, it is important to note that CPT feedback loop output connected to 10 MHz Temperature Compensated Crystal Oscillator (TCXO), which in turn connected to 3.4 GHz synthesizer. The synthesizer is controlled by the 3.4 GHz Voltage-Controlled Oscillator (VCO). So this 3.4 GHz frequency is applied to the laser current through

microwave attenuator and diplexer (bias tee). Quadrature signal comes from a mixer with phase shifted to 90°. To create required feedback stabilization loop, the error signal is generated (Fig. 6). The stabilization loops include D_1 line loop for absorption profile stabilizing scheme, CPT loop and quadrature loops. To generate the feedback signal for ^{87}Rb D_1 loop 15 kHz generator was used. As for CPT loop, the carrier microwave frequency is modulated at a rate 10 kHz (Pound-Drever-Hall technique). The first harmonic component of 15 kHz modulation is detected synchronously with a lock-in amplifier and can be used as an error signal for the ^{87}Rb D_1 stabilization loop. While 10 kHz modulation is also synchronously detected and used for CPT feedback loop. It is essential that, in general, the error signal significantly depends on the lock-in amplifier phase. This means that one can use "in-phase" and "out-of-phase" (quadrature) signals to suppress the light shift of the atomic microwave transition just by use of electronics [9].

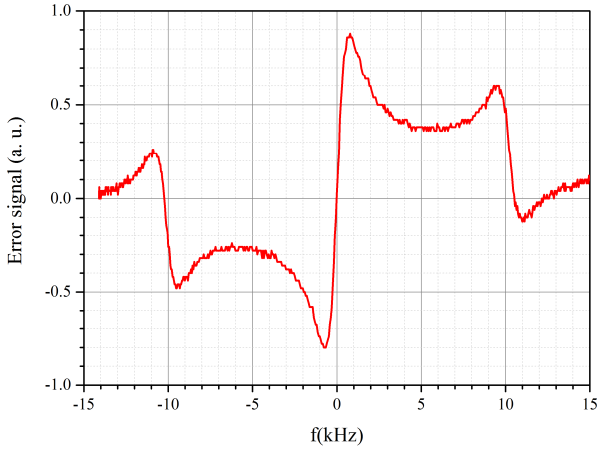

Fig. 6. Error signal after the synchronous detector.

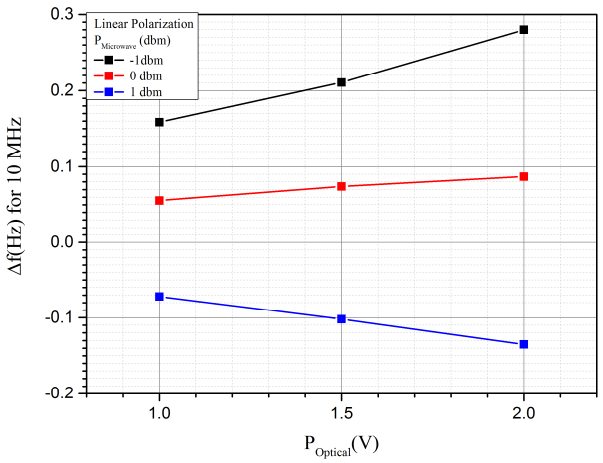

Fig. 7. Shift of the microwave transition vs. light field power for three different microwave powers.

We also studied the light-field-induced shift and its dependence on various microwave-modulation power values. 10 MHz clock signal was measured by a frequency meter, which external reference was the hydrogen frequency standard. As it is seen in Fig. 7, there is the optimal microwave power when output frequency of the standard almost insensitive to the light power variation. The experimentally found dependence of the quadrature channel variation on the light-field-induced shift is shown in Fig. 8.

Allan deviation depicted in Fig. 9 shows that application of the quadrature method of stabilization allow us to achieve frequency instability 4×10^{-11} at $\tau=10^3$ s. While Allan deviation *with* quadrature method enabled has worse short-term stability, same equipment *without* quadrature method leads to degrading stability at $\tau=60$ s and further. Cause of such results can be found in imperfect configuration of feedback loops parameters.

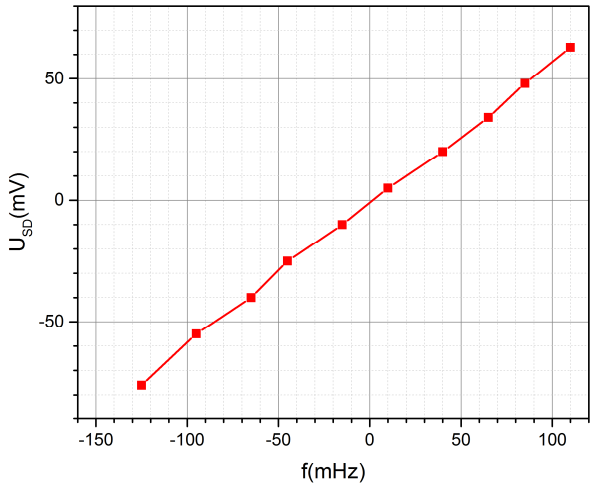

Fig. 8. Quadrature channel dependence on the light-field-induced shift.

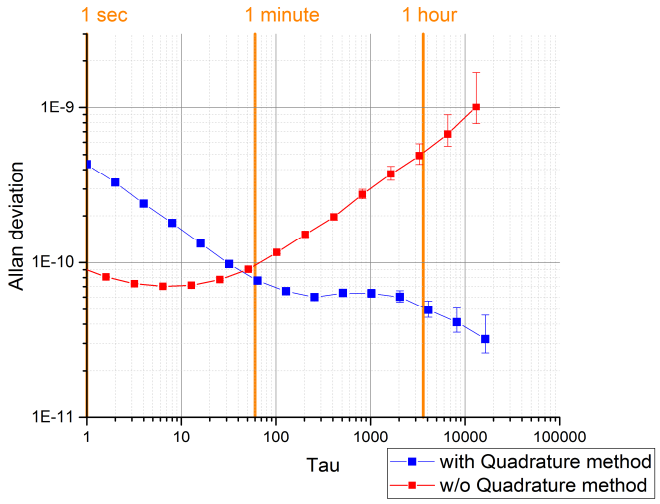

Fig. 9. Allan deviation versus time in seconds for measurements assisted by the quadrature-signal light-shift-cancellation method and without it.

III. Results

The paper presents the preliminary results of the microwave frequency standard, which is being developed in our group. Novelty of the work consists in combination of the antirelaxation coated-cell approach and the quadrature-signal method of the light shift suppression. We used a glass-blown

compact ^{87}Rb vapor cell with antirelaxation coating of walls. The dark resonance linewidth was typically about 1 kHz under the linearly polarized light excitation (D_1 line, *lin*||*lin* configuration). The Pound-Drever-Hall technique was exploited for microwave frequency stabilization. The preliminary tests showed a medium-term stability $\sigma_y \leq 5\times10^{-11}$ at $\tau=10^3$ s and it continued goes down with τ increase. We can expect that realization of physical package evacuation and some other improvements will lead to the long-term stability at the level better than 5×10^{-12} per a day.

REFERENCES

[1] G. Alzetta, A. Gozzini, L. Moi, and G. Orriols, "An experimental method for the observation of r.f. transitions and laser beat resonances in oriented Na vapour", Nuovo Cimento B, vol. 36, pp. 5–20, 1976.

[2] E. Arimondo, "Coherent population trapping in laser spectroscopy", Progress in Optics, vol. 35, pp. 257-354, 1996.

[3] M. Merimaa, Th. Lindvall, I. Tittonen, and E. Ikonen, "All-optical atomic clock based on coherent population trapping in ^{85}Rb", J. Opt. Soc. Am. B, vol. 20, pp. 273-279, 2003.

[4] S. Knappe, P.D.D. Schwindt, V. Shah, L. Hollberg, J. Kitching, L. Liew, and J. Moreland, "A chip-scale atomic clock based on ^{87}Rb with improved frequency stability", Opt. Express, vol. 13, pp. 1249-1253, 2005.

[5] S.A. Zibrov, I. Novikova, D.F. Phillips, R.L. Walsworth, A.S. Zibrov, V.L. Velichansky, A.V. Taichenachev, and V.I. Yudin, "Coherent-population-trapping resonances with linearly polarized light for all-optical miniature atomic clocks", Phys. Rev. A, vol. 81, 013833, 2010.

[6] M. V. Balabas, D. Budker, J. Kitching, P. D. D. Schwindt, and J. E. Stalnaker, "Magnetometry with millimeter-scale antirelaxation-coated alkali-metal vapor cells", J. Opt. Soc. Am. B, vol. 23, pp. 1001-1006, 2006.

[7] R. Straessle, M. Pellaton, C. Affolderbach, Y. Pétremand, D. Briand, G. Mileti, and N. F. de Rooij, "Microfabricated alkali vapor cell with anti-relaxation wall coating", Appl. Phys. Lett., vol. 105, 043502, 2014.

[8] V. Gerginov, V. Shah, S. Knappe, L. Hollberg, and J. Kitching, "Atomic-based stabilization for laser-pumped atomic clocks", Opt. Lett., vol. 31, pp. 1851-1853, June 2006.

[9] B. H. McGuyer, Y.-Y. Jau, and W. Happer, "Simple method of light-shift suppression in optical pumping systems", Appl. Phys. Lett., vol. 94, 251110, 2009.

Influence of an optical dense medium at the Ramsey method of CPT resonance detection

Konstantin Barantsev, Gavriil Voloshin, Andrey Litvinov, Evgeniy Popov
Dept. of Theoretical Physics
Peter the Great St.Petersburg Polytechnic University
Saint-Petersburg, Russia
kostmann@yandex.ru

***Abstract*—In this paper we investigate the effects observed in optical dense medium when detecting the coherent population trapping resonance by the Ramsey method. The cloud of cold atoms interacts with two laser pulses one of which excites the coherent population trapping resonance and the second detects it. The signal of radiation passed through the medium and signal of fluorescence were analyzed. Shifts of the side peaks of the Ramsey fringes are observed with increasing optical density of the medium.**

Keywords—coherent population trapping, Ramsey method, cold atomic cloud, optically dense medium

I. INTRODUCTION

The Ramsey method [1] of detection the resonance of a physical system allows us to significantly narrow down the line width of this resonance. So this method can be used in the metrological areas, such as frequency standards, magnetometers, high-resolution spectroscopy. The main idea of this method for detecting atomic resonance by an external coherent electromagnetic wave is use two separated interaction regions between which an atomic beam flies.

On the other hand, one of the effects providing a narrow resonance line is the coherent population trapping (CPT) [2-5] effect. It is known that the interaction of the bichromatic radiation with a three-level quantum system can lead to the appearance of so-called dark state. In this case the quantum system stops to interact with the radiation and the transparency window appears in experiment. The idea of using two-frequency optical radiation to stabilize the frequency of microwave range was expressed. The idea's value lies in the fact that there is no need to use bulky waveguides and microwave cavities, which can significantly reduce the size and power consumption of the device. The width of CPT resonance can be much narrower than the natural line width of atoms [6-8]. It makes it possible to use this effect in wide range of practical applications such as quantum frequency standards [9-12], optical magnetometers [13,14], laser generation without inversion [15,16], optical communications [17-19], recording and processing of quantum information [20-22].

The CPT effect has been investigated for more than forty years. During this time, a wide range of questions has been studied both on the various conditions for observing the CPT effect, and on the influence of various factors on the shape of the CPT resonance. So, it is known that the presence of absorption in a medium can lead to the appearance of light shifts [23,24], ellipticity of polarization upon pumping of alkali atoms [25], an increase in the degree of correlation between the modes of laser radiation [26]. With a further increase in the optical thickness the effects of the weak light localization and coherent backscattering of light occur [27-29].

Detection of the CPT resonance by the Ramsey method allows us to further narrow the resonance line. One of the possible modifications is the original scheme based on the atomic beam. It was realized in the beam of sodium atoms in [30]. The theoretical investigation of the CPT resonance in the Rb-87 beam was done in [31]. The other way of narrowing the resonance is using zone pumping which leads to analog of the Ramsey scheme [32]. In such geometry of excitation the diffusion of atoms in the direction perpendicular to laser beam leads to limitation of the time of interaction between atom and field. This makes it possible to observe the narrowing of the CPT resonance in the gas cells both with buffer gas and in cells with antirelaxation wall coating [33,34].

In [35] it is proposed the Ramsey method of registration with separation of the interaction regions of atoms with field not in space, as in original Ramsey method, but in time domain, that is, the use of pulse pumping. In this variant it is not necessary to create a collimated atomic beam and fly-through base, which makes it possible to significantly reduce the dimensions of the device. This method allows to narrow the resonance and suppress the light shifts [36-39].

This work is devoted to investigation of the CPT resonance which is excited by the pulsed radiation in an optically dense cold atomic cloud and detected by Ramsey method. Despite the large number of modern works on the investigation of Ramsey detection method, there remain some open questions related to the influence of an optical density of the medium at the shape of Ramsey fringes, which is the main subject of our work. We compared the signal of radiation passed through the medium and fluorescence signal, also dependence of the Ramsey fringes on intensities was analyzed.

978-1-5386-5620-4/18/$31.00 ©2018 IEEE

II. STATEMENT OF THE PROBLEM

Let's consider the cold atomic cloud at the temperature when Doppler and collision broadening of the absorption line is close to zero. The atoms have three energy states, two of them 1 and 2 are metastable ground states and 3 is excited state (Fig.1(a)). The transitions 1-3 and 2-3 lie in the optical range and the transition 1-2 belongs to the microwave range. The cloud is optically dense along z axis (Fig.1(b)) for resonant optical radiation. It means that the mean free path of a photon is much smaller than the length L of the cloud ($n_a\lambda^2 L >> 1$, where n_a is the atomic concentration, λ is the resonant wavelength). However, we assume that the cloud is dilute enough and there is not collective effects and the dipole-dipole interaction [40-43] between atoms ($n_a\lambda^3 < 1$).

According to Ramsey method of detection the atomic cloud interacts with the sequence of two laser pulses. The pulses contain two carrier frequencies ν_1 and ν_2 which are quasiresonant to transitions 1-3 and 2-3. Electric field can be written as

$$\mathbf{E}(z,t) = \mathbf{E}_1^0(z,t)e^{-i(\nu_1 t - k_1 z)} + \mathbf{E}_2^0(z,t)e^{-i(\nu_2 t - k_2 z)} + c.c., \quad (1)$$

where $E_j^0(z,t)$, j=1,2 are the complex amplitudes, k_j are the wave numbers. So, the Λ-scheme of interaction takes place (Fig.1(a)).

The interaction between atoms and laser pulses can be described by the Maxwell-Bloch equations:

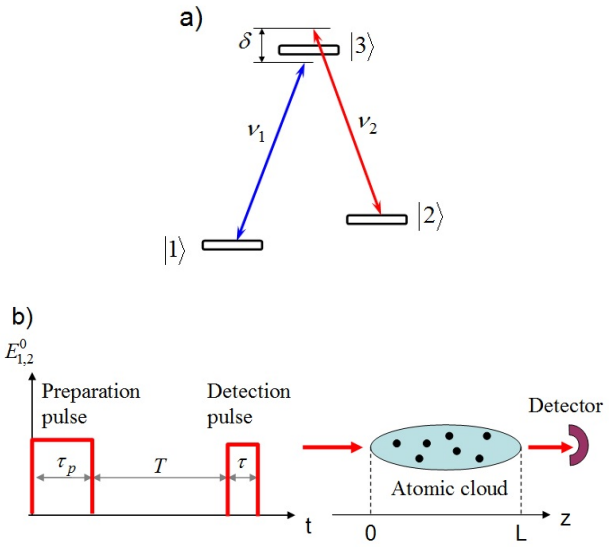

Fig. 1. a) - Level structure of the atoms interacting with two-frequency radiation. b) - Geometry of the problem.

$$\begin{cases} \dfrac{\partial \tilde{\rho}_{mn}(z,t)}{\partial t} = \dfrac{i}{\hbar}\left[\tilde{\rho}(z,t), \hat{H}\right]_{mn} + \Gamma_{mn}\{\tilde{\rho}(z,t)\} \\ \left(\dfrac{\partial}{\partial z} + \dfrac{1}{c}\dfrac{\partial}{\partial t}\right) E_j^0(z,t) = iq_j \rho_{3j}(z,t) \end{cases}, \quad (2)$$

where $\tilde{\rho}_{mn}(z,t)$ is the one-particle density matrix of the atoms, m,n=1,2,3, $q_j = 4\pi k_j n_a$, j=1,2. Γ describes the spontaneous decay of the atoms. The Hamiltonian can be written as the sum $\hat{H} = \hat{H}_0 + \hat{V}$. The Hamiltonian of atoms without electromagnetic field is

$$\hat{H}_0 = \sum_{n=1}^{3} \varepsilon_n |n\rangle\langle n|, \quad (3)$$

where ε_n are the energies of atomic levels $|n\rangle$. The Hamiltonian of interaction in dipole approximation is

$$\hat{V} = -\hat{\mathbf{d}}\mathbf{E} = -d_{31}E_1^0(z,t)e^{-i(\nu_1 t - k_1 z)}|3\rangle\langle 1| - \\ -d_{32}E_2^0(z,t)e^{-i(\nu_2 t - k_2 z)}|3\rangle\langle 2| + \text{H.c.} \quad (4)$$

In the expression (4) we assume that the vector $\mathbf{E}$ is co-directed with the vector of dipole momentum $\hat{\mathbf{d}}$ (d_{mn} are its matrix elements), therefore $\hat{\mathbf{d}}\mathbf{E} = \hat{d}E$. The system (2) is written in one dimension approximation, when the electromagnetic wave propagates along z axis and has a plane wave front.

The set of equations (2) for atomic density matrix is solved with equations for field transport and gives the information about atomic population, atomic coherences and field distribution along z axis.

III. DISCUSSION OF RESULTS

On the Fig.2(a) one can see the Ramsey signal of the radiation passed through the medium. The vertical axis represents the energy of the detection pulse

$$W = \int_0^\infty I(L,t)dt \quad (5)$$

in normalized units, where I is the intensity. The intensity on the detector $I(z=L,t)$ is found from the set of equations (2) as

$$I(z,t) \sim \left\langle E(z,t)^2 \right\rangle = \left|E_1^0(z,t)\right|^2 + \left|E_2^0(z,t)\right|^2, \quad (6)$$

where $E(z,t)$ is the magnitude of the electric field vector (1), brackets $\langle \ldots \rangle$ mean time averaging over the period of beats with the frequency $\nu_1 - \nu_2$, so the cross terms in Eq. (6) disappear. The period of beats is ~ 1 ns for the frequency of the transition 1-2 in microwave range and it is much smaller than γ^{-1}~100 ns.

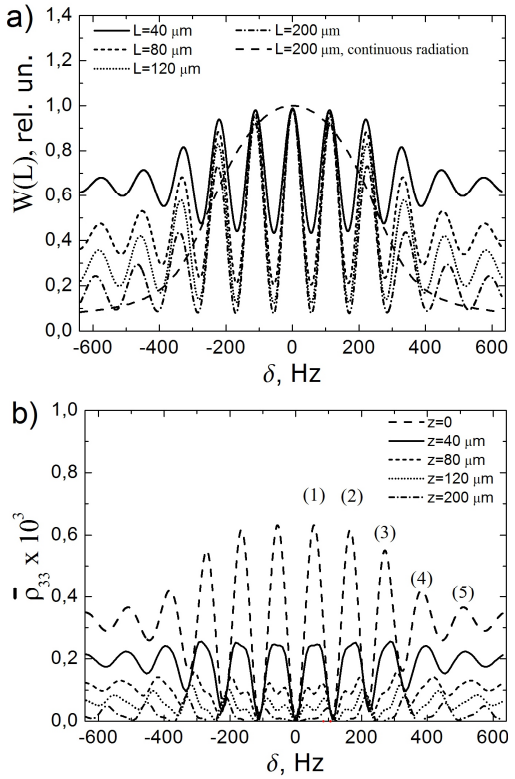

Fig. 2. a) - Signal of the radiation passed through the medium for different lengths L of the atomic cloud. b) - Population of the excited level for different cross-section z of the medium. Duration of the detection pulse is $\tau=10\gamma^{-1}$, duration of the dark pause is T=8 ms, Rabi fequencies $\Omega_1=\Omega_2=0.01\gamma$, atomic concentration is $n_a=5*10^{10}$ cm^{-3}, length of the medium is L=200 μm, optical density is $n_a\lambda^2 L\sim 5$, decay rate of the excited level is $\gamma=10^7$ s^{-1}.

The different curves correspond to different length L of the medium. Dashed envelope curve corresponds to the CPT signal in continuous radiation. The influence of the optically dense medium consists in two factors: increasing of the contrast of the Ramsey fringes with growth of the length L and in the shift of the side resonances. This shift is related to derivative of the CPT-resonance contour (dashed envelope curve) and reaches the maximum where the steepness of the contour has the greatest value.

The effect of shift is better seen in the dependence of the population of the excited level 3 on the two-photon detuning (Fig.2(b)). This population is proportional to the signal of fluorescence. In this figure one can see distortion and shift of the Ramsey fringes with growth of the length L. The maximal shift and distortion correspond to peaks (3) and (4).

The absolute values of the shifts are shown in Fig.3. The curve for the minimum (3) lies above the others, since the maximum of the envelope derivative is reached for it (Fig.3(a)). For the position of the maximum, the situation is similar, as can be seen in Fig.3(b) - the greatest shift for the maximums (3) and (4).

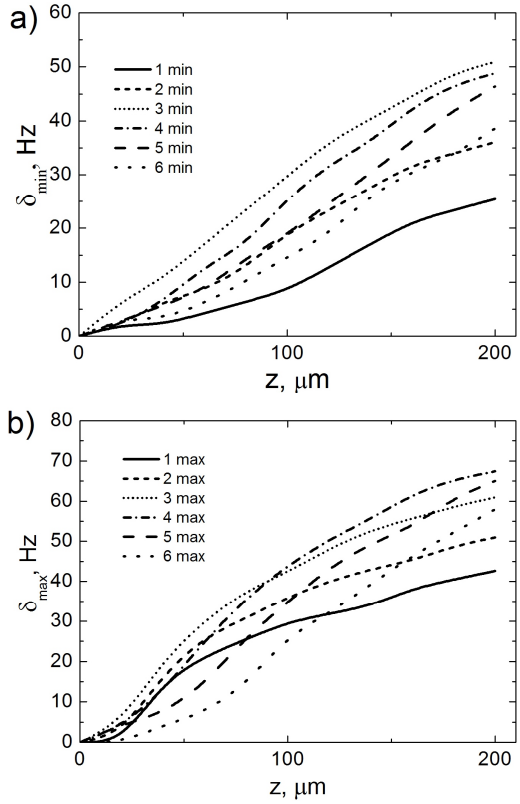

Fig. 3. Absolute value of the shifts of the minimums (a) and maximums (b) of the Ramsey resonance in the Fig.2(b) depending on the longitudinal coordinate z.

The Fig. 4 shows the dependence of the Ramsey signal on the Rabi frequencies of the laser field in the input of the medium. Envelope of the signal has the different shape with growing of the Rabi frequencies. Therefore changes in the shifts of the peaks are observed.

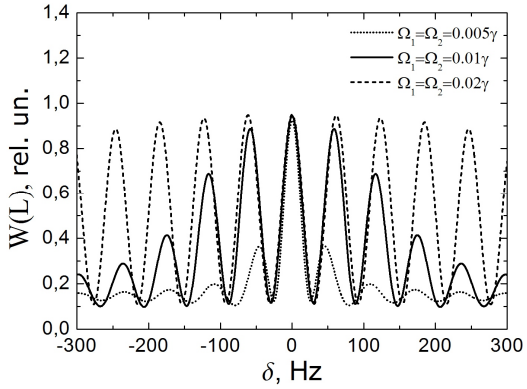

Fig. 4. Dependence of the form of Ramsey resonance on the Rabi frequencies of the pulses (their amplitudes). Parameters are the same as in the Fig. 2.

The central peak always remains in place of zero two-photon detuning in the case of three-level scheme. But in a real alkaline atom there is a multiplet of excited levels that can lead to the shift of the central peak.

IV. CONCLUSIONS

In this work we applied the semi-classical theory of interaction between the laser pulses and atomic medium to describe the detection of the coherent population trapping resonance by the Ramsey method in the case of optically dense medium. It is shown that when the optical density of the medium is increased, the Ramsey fringes are modified.

The dependences of the energy of the transmitted pulse and the population of the excited level on two-photon detuning are analyzed. It is found that there is a shift of the peaks of Ramsey resonance as the optical thickness of the medium increases. This shift is different for different peaks. The maximum value it reaches in the region of two-photon detuning, where the envelope has the greatest gradient to the horizontal.

This results can be applied in the quantum frequency standards, rotation sensors, magnetometers and high-resolution spectroscopy.

ACKNOWLEDGMENT

This work is supported by Ministry of Education and Science of the Russian Federation in terms of FTP "Research and development on priority trends of Russian scientific-technological complex evolvement in 2014-2020 years (agreement 14.578.21.0211, agreement unique identifier RFMEFI57816X0211)".

REFERENCES

[1] N. F. Ramsey, Phys. Rev., vol. 78, 1950, pp. 695-699.

[2] G. Alzetta, A. Gozzini, L. Moi, et al., Nuovo Cimento B, vol. 36, no.5, 1976.

[3] E. Arimondo, G. Orriols, Nuovo Cimento Lett., vol. 17, 1976, p. 333–338.

[4] H. R. Gray, R. M. Whitley, and C. R. Stroud, Opt. Lett., vol. 3, 1978, p. 218.

[5] B.D. Agap'ev, M.B. Gornyi, B.G. Matisov, Yu. V. Rozhdestvenskii, Physics Uspekhi, vol. 36, 1993, p.763.

[6] R. Wynands and A. Nagel, Appl. Phys. B, vol. 68, 1999, 1.

[7] V.M. Datsyuk, I.M. Sokolov, D.V. Kupriyanov, and M.D. Havey, Phys. Rev. A, vol. 77, 2008, 033823.

[8] D. V. Brazhnikov, A. V. Taihenahev, A. M. Tumaikin, and V. I. Yudin, Las. Phys. Lett., vol. 11, 2014, 125702.

[9] J. Vanier, Appl.Phys. B, vol. 81, 2005, p.421.

[10] G. Kazakov, B. Matisov, I. Mazets, et. al., Phys. Rev. A, vol. **72**, 2005, 063408.

[11] S. A. Zibrov, I. Novikova, D. F. Phillips, et. al., Phys. Rev. A, vol. 81, 2010, 013833.

[12] S. Khripunov, D. Radnatarov, S. Kobtsev, Proc. SPIE, vol. 93780A 2015.

[13] A. Akulshin, A. Celikov and V. Velichansky, Opt.Commun vol. 84, 1991, p.139.

[14] M. Stahler, R. Wynands, S. Knappe et al., Opt.Lett., vol. 27, 2002, p.1472.

[15] O. Kocharovskaya and Ya. I. Khanin, Pis'ma Zh. Eksp. Teor. Fiz., vol. 48, 1988, p.581.

[16] S. Harris, Phys. Rev. Lett., vol. 62, 1989, p.1022.

[17] L. V. Hau et al., Nature, vol. 397, 1999, p.594.

[18] A. M. Akulshin, A. Cimmino, A. I. Sidorov, P. Hannaford, and G. I. Opat, Phys. Rev. A, vol. 67, 2003, 011801(R).

[19] E. E. Mikhailov, V. A. Sautenkov, I. Novikova, and G. R. Welh, Phys. Rev. A, vol. 69, 2004, 063808.

[20] M. Fleishhauer and M. D. Lukin, Phys. Rev. Lett., vol. 84, 2000, p.5094.

[21] C. Liu, Z. Dutton, C. H. Behroozi, and L. V. Hau, Nature (London), vol. 409, 2001, p.490.

[22] M. D. Lukin, Reviews of Modern Physics, vol. **75**, 2003, p.457.

[23] K.A. Barantsev, A.N. Litvinov, E.N. Popov, I.M. Sokolov, IEEE Xplore, European Frequency and Time Forum, 2016, doi: 10.1109/EFTF.2016.7477818

[24] K.A. Barantsev, E.N. Popov, A.N. Litvinov, V.M. Petrov, Radiotechnika, no. 12, 2016, pp.164-170.

[25] K.A. Barantsev, E.N. Popov, A.N. Litvinov, Quantum Electronics, vol. 47(9), 2017, pp. 812-817.

[26] K.A. Barantsev, A.N. Litvinov, E.N. Popov, JETP, vol. 125, No.6, 2017, pp.993-1004.

[27] V.M. Datsyuk, I.M. Sokolov, D.V. Kupriyanov, and M.D. Havey, Phys. Rev. A, vol. 74, 2006, 043812.

[28] I.M. Sokolov, D.V. Kupriyanov, and M.D. Havey, Optics Communications, vol. 243, 2004, pp.165-173.

[29] D. V. Kupriyanov, I. M. Sokolov, N. V. Larionov, et. al., Physical Review A, vol. 69, 2004, 033801.

[30] J. E. Thomas, P. R. Hemmer, S. Ezekiel, et al., Phys. Rev. Lett., vol. 48, 1982, p.867.

[31] I.M. Sokolov, Quantum Electronics, vol. 45, 2015, pp.947-952.

[32] Y. Xiao, I. Novikova, D. F. Phillips, and R. L. Walsworth, Phys. Rev. Lett., vol. 96, 2006, 043601.

[33] E. Breschi, G.Kazakov, C. Schori, et.al., Phys.Rev. A, vol. 82, 2010, 063810.

[34] G. A. Kazakov, A. N. Litvinov, B. G. Matisov, et.al., Journal of Physics B, vol. 44, 2011, 235401.

[35] G. Pati, K. Salit, R. Tripathi, et al., Opt. Commun., vol. 281, 2008, p.4676.

[36] Y. Yano, W. Gao, S. Goka, and M. Kajita, Phys. Rev. A, vol. 90, 2014, 013826.

[37] G. S. Pati, Z. Warren, N. Yu, and M. S. Shahriar, JOSA B, vol. 32, 2015, p.388.

[38] P. Yun, F. Tricot, C. E. Calosso, S. Micalizio, B. François, R. Boudot, S. Guérandel, and E. de Clercq, Phys. Rev. Applied, vol. 7, 2017, 014018.

[39] V. I. Yudin, A. V. Taichenachev, M. Yu. Basalaev, Phys. Rev. A, vol. 93, 2016, 013820.

[40] A. S. Kuraptsev, I. M. Sokolov, and M. D. Havey, Phys. Rev. A, vol. 96, 2017, 023830.

[41] A. S. Kuraptsev and I. M. Sokolov, Phys. Rev. A, vol. 90, 2014, 012511.

[42] S. Roof, K. Kemp, M.D. Havey, I.M. Sokolov, and D.V. Kupriyanov, Opt. Lett., vol. 40, 2015, p.1137.

[43] Ya. A. Fofanov, A. S. Kuraptsev, I. M. Sokolov, and M. D. Havey, Phys. Rev. A, vol. 84, 2011, 053811.

Gold microdiscs as alkali preferential condensation spots for cell clock long-term frequency improvement

Sylvain Karlen, Thomas Overstolz, Jean Gobet, Jacques Haesler, Fabien Droz and Steve Lecomte
CSEM SA, Systems, Time & Frequency
Neuchâtel, Switzerland
sylvain.karlen@csem.ch

***Abstract*— One of the main source of long-term frequency instabilities in MEMS cell clocks is the light-shift induced by optical intensity changes which can be caused by the presence of condensed alkali droplets within the light-path of the interrogation laser. We report here on the use of patent pending gold micro-discs as alkali preferential condensation spots in order to concentrate the alkali droplets outside of the laser light-path. Evidenced of preferential condensation of Rb on Au micro-discs is reported and the effect on the long-term frequency stability of a CPT clock setup are assessed.**

Keywords—MEMS atomic vapor cells, chip-scale atomic clock (CSAC), Au microdiscs, long-term frequency stability, light-shift

I. INTRODUCTION

MEMS atomic vapor cells have a large variety of applications in atomic devices such as chip-scale atomic clocks (CSACs) [1], atomic magnetometers [2] and atomic gyroscopes [3]. They consist of hermetically sealed cavities having an optical access, filled with a metallic alkali and a buffer gas. One of the main source of long-term frequency instabilities in cell clocks is the light-shift induced by changes of the optical intensity. These variation can, among other effects, be due to the presence of condensed alkali droplets within the light-path of the interrogation laser, at the input window of the cell, and changes in their size, shape or location. A common solution to avoid this issue is to generate a thermal gradient in order to create a cold spot and condensate the alkali on a preferential zone out of the light-path. This solution is however hard to implement in MEMS cells, due to their small dimensions, and it does not prevent alkali migration during storage of the clock in off mode. As an alternative, we report here on the use of CSEM patent pending gold micro-discs as alkali preferential condensation spots.

II. CELLS FABRICATION

Two different wafer-level cell fabrication technologies are used in the experiment reported here. The first fabrication technology is shown on Fig. 1 – left and was previously described in [4]. Cells fabricate according to this technology are used to evidence the effect of the instabilities due to Rb migration (see below). First a 2 mm diameter single cavity is etched in a 1 mm thick silicon wafer. After that, a first borosilicate glass window is anodically bonded to the bottom of the cavity. The resulting preform and the top borosilicate glass window are then coated with Al_2O_3 by molecular vapor deposition (MVD). The cavity is then filled by the dispensing of an aqueous solution of $^{87}RbN_3$ [5]. After drying of the solution, the top borosilicate wafer is anodically bonded to the top of the cavity under Ar atmosphere. After dicing of the cells into individual pieces, the RbN_3 is decomposed with UV light in order to create metallic Rb and an Ar-N_2 buffer gas mixture.

The second MEMS cell fabrication technology presented here uses natural rubidium dispensing micropills for the filling of the cells. It is presented in Fig. 1 – right. This technology is used here in combination with Au microdiscs in order to evidence the effects of the preferential condensation spots on the long-term frequency stability (see below). In that case, a two cavities design inspired from [6] is etched in a 1 mm thick silicon wafer: a 2 mm diameter measurement cavity is connected to a second filling cavity by micro-channels. As before, a first borosilicate glass window is bonded to the bottom of the wafer and an Al_2O_3 MVD deposition is realized. The dispensing cavity is then filled with a commercially available dispensing micropill (SAES getters). After anodic bonding of the top borosilicate wafer under Ar-Ne buffer gas atmosphere, the micropill is activated by heating with a focalized laser. Ar-Ne buffer gas is used in that case because the conventional Ar-N_2 buffer gas mixture cannot be used due to the reaction of N_2 with the Zr compound [7].

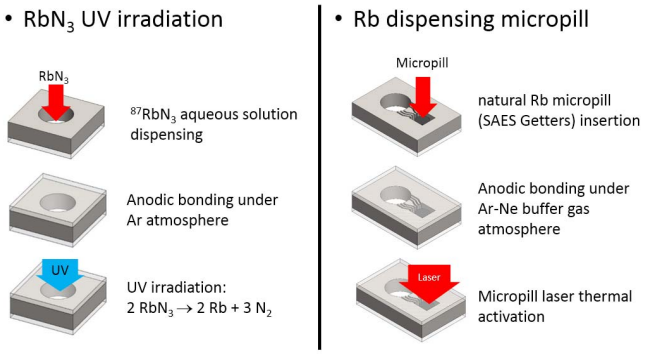

Fig. 1. Microfabrication processes for the two cells types: left – single cavity cell filled with $^{87}RbN_3$ UV decomposition ; right – double cavity cell filled with natural Rb dispensing micropill. Both cells were coated with Al_2O_3 prior to the filling.

III. Instabilities due to Rb migration: evidence of the phenomenon

The long-term frequency stability of a CPT atomic clock mostly relies of the stability of the different atomic frequency shifts of the clock, that is to say, the AC Stark shift, the buffer gas shift and the 2nd order Zeeman shift. Each of these shifts induces a sensitivity of the clock frequency to interrogation parameters: The AC Stark shift induces a sensitivity to changes in the interrogation light frequency and intensity and to the laser RF modulation intensity through changes in the relative intensity of the modulation sidebands. The buffer gas shift induces a sensitivity to changes in the cell buffer gas pressure and temperature and the 2nd order Zeeman shift induces a sensitivity to changes in the magnetic field.

In order to investigate the long-term frequency stability performances of MEMS atomic vapor cells, a measurement setup was therefore developed. It is presented in details in [8]. The clock interrogation parameters linked the frequency shift sources that influence the long-term frequency stability are individually monitored. That is to say, the cell temperature, the laser RF modulation intensity, the laser optical intensity and the C-field intensity. Exception is made of the interrogation light frequency stability which is not measured but estimated.

The Allan variance of a measurement made on a vapor cell without Au microdiscs is presented in Fig. 2. The cell is filled via RbN_3 UV-decomposition (see above). The long-term frequency stability of such a cell is not explained by variation of the clock interrogation parameters. However, changes in the input window transmission due to Rb droplets migration directly influence the clock frequency through light intensity variations. The cell output power is also influenced by changes in the window transmission. Therefore, by recording this parameter it is possible to extrapolate the induced instabilities. The effect of these variations on the Allan variance is also shown in Fig. 2 (black line). As it can be seen from the figure, the variations due to Rb droplets explain to a large extent the observed frequency instability.

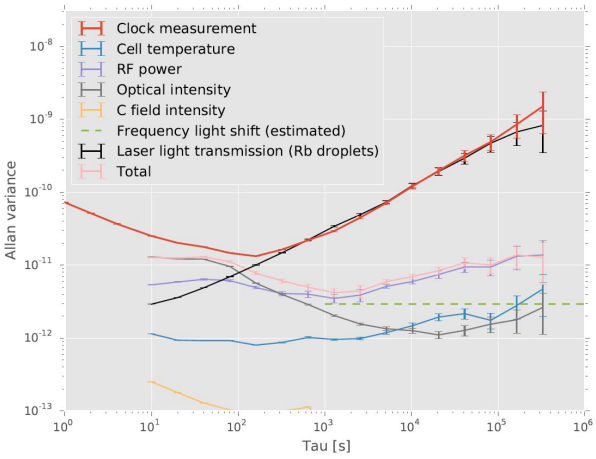

Fig. 2. Allan variance measurement made on a MEMS atomic vapor cell without Au microdiscs (red). The instabilies due to the monitored clock parameters are summed up in the "Total" curve (rosa). The extrapolation of the instabilities due to light transmission instabilities (black) are not summed up in the "Total" curve.

IV. Au microdiscs: Working principle

In order to reduce the effect of Rb droplets migration evidenced above, CSEM patent pending [9] gold microdiscs were proposed. They work on the following principle. The Au-Rb system (as well as the Au-Cs system) are known to form intermetallic compounds [10]. The enthalpy of mixing and excess Gibbs energy of the liquid alloys are said to be expected to be large, negative, and "V-shaped", with a sharp minimum at 50 atomic % of Rb. Therefore, if Rb is present in a sufficient excess as compared to Au in a cell, and if the Au spots are sufficiently big to neglect the effect of the drop size, the Rb vapor is expected to preferentially condensate on the Au gold surface and to create an AuRb - Rb liquid mixture at the equilibrium state.

MEMS atomic vapor cells comprising Au microdiscs were therefore fabricated (see Fig. 3). The fabrication process is described above and illustrated in Fig. 1 – right. The additional microdiscs were structured by lift-off on the top borosilicate glass window of the cell after Al_2O_3 MVD coating of the wafer. These cells differ from the previous one (measured in Fig. 2), not only by the presence of the Au discs in the inside of the measurement cavity, but also by the filling method and the buffer gas mixture. These double-cavity cells were nevertheless measured thanks to the same setup as above (Fig. 2).

Fig. 3. Double-cavity MEMS atomic vapor cell filled with an Rb dispensing micropill. Au micro-discs have been added to the output glass window.

V. Results

The Allan variance of measurements made on the double-cavity cell with Au microdiscs is presented in Fig. 4 and compared with the previous measurement made on single-cavity cells (Fig. 2). A clear improvement of the long-term frequency stability can be seen, the instabilities being now dominated by RF and input light fluctuations (see [8] for details).

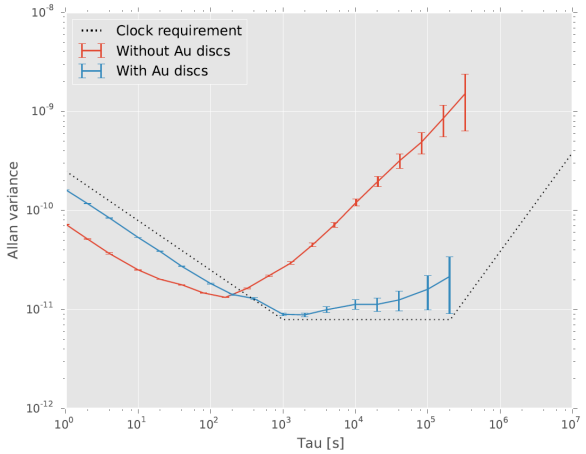

Fig. 4. Allan variance of a cell with Au microdiscs compared with the a cell without Au microdiscs. The clock requirements shown here are typical requirements for a chip-scale atomic clock.

VI. Conclusion

The potential of Au microdiscs for improvement of the long-term frequency stability of MEMS atomic vapor cells through reduction of internal light shift effects due to alkali droplet migration was demonstrated. Indeed, the long-term frequency stability of a laboratory clock based on MEMS cells was drastically improved thanks to cells using this novel technology. This result paves the way for improvement of all type of cell clocks long-term frequency stability, including chip-scale atomic clock. However, for a formal proof of the effect of Au micro-discs, a direct comparison between identical cells with and without this technology is required. Work going in that direction is currently being performed.

Acknowledgments

We gratefully acknowledge G. Mileti (Université de Neuchâtel, Switzerland), for the fruitful discussions on the subject as well as G. Bergonzi, A. Bionaz, M. Amine, and P.-A. Clerc (CSEM SA) for their participation in the MEMS cell manufacturing.

This work was funded by CSEM's R&D activity (financed by the canton of Neuchâtel) and supported by the European Space Agency (ESA) under the Networking and Partnering Initiative (NPI) (ESA Contract No. 4000112650/14/NL/GLC).

References

[1] L. Liew, S. Knappe, J. Moreland, H. Robinson, L. Hollberg, and J. Kitching, "Microfabricated alkali atom vapor cells," *Appl. Phys. Lett.*, vol. 84, no. 14, pp. 2694–2696, 2004.

[2] P. Schwindt, S. Knappe, V. Shah, L. Hollberg, J. Kitching, L. Liew, and J. Moreland, "Chip-scale atomic magnetometer," *Appl. Phys. Lett.*, vol. 85, no. 26, pp. 6409–6411, 2004.

[3] E. Donley, "Nuclear magnetic resonance gyroscopes," in *SENSORS*, 2010.

[4] S. Karlen, J. Gobet, T. Overstolz, J. Haesler, and S. Lecomte, "Lifetime assessment of RbN3-filled MEMS atomic vapor cells with Al2O3 coating," *Opt. Express*, vol. 25, no. 3, pp. 2187–2194, 2017.

[5] T. Overstolz and J. Haesler, "Micro-machined vapor cell," US9461659 (B2), 2016.

[6] M. Hasegawa, R. Chutani, C. Gorecki, R. Boudot, P. Dziuban, V. Giordano, S. Clatot, and L. Mauri, "Microfabrication of cesium vapor cells with buffer gas for MEMS atomic clocks," *Sensors Actuators A Phys.*, vol. 167, no. 2, pp. 594–601, 2011.

[7] S. Karlen, J. Haesler, T. Overstolz, G. Bergonzi, and S. Lecomte, "MEMS atomic vapor cells sealed by Cu-Cu thermocompression bonding," in *International Frequency Control Symposium (IFCS), Joint with the 31st European Frequency and Time Forum (EFTF)*, 2017.

[8] S. Karlen, "Fabrication and characterization of MEMS alkali vapor cells used in chip-scale atomic clocks and other atomic devices," University of Neuchâtel, 2017.

[9] J. Gobet, T. Overstolz, and F. Droz, "Alkali vapor cell," US2017331485 (A1), 2017.

[10] A. Pelton, "The Au-Rb (Gold-Rubidium) system," *Bull. Alloy Phase Diagrams*, vol. 7, no. 2, pp. 139–142, Apr. 1986.

Recent Progress of Development of Cesium Fountain Primary Frequency Standard NMIJ-F2

AKIFUMI TAKAMIZAWA, SHINYA YANAGIMACHI, KEN HAGIMOTO, IKU HIRANO, TAKESHI IKEGAMI
National Metrology Institute of Japan, AIST, 1-1-1 Umezono, Tsukuba, Ibaraki, Japan
e-mail: akifumi.takamizawa@aist.go.jp

***Abstract*—For our cesium fountain primary frequency standard, NMIJ-F2, uncertainty for most of the dominant physical effects such as the second-order Zeeman shift, the blackbody radiation shift, and the collisional shift has been evaluated. As for the microwave power dependence shift, when continuous microwave is fed into the Ramsey cavity, a frequency shift of $+5\times10^{-15}$ is caused. The shift is greatly reduced to $(+0.1\pm0.1)\times10^{-15}$ by turning off the microwave only for 10 ms after Ramsey interrogation. Instead, the phase transient of the microwave due to the switch may cause a frequency shift but has not been evaluated yet. Excluding the shift due to the microwave switch and the generally non-dominant shifts such as the light shift and the Ramsey pulling, the tentative type B uncertainty is evaluated to be 0.59×10^{-15}. However, the frequency of NMIJ-F2 is different from International Atomic Time by 3 times the tentative uncertainty for the moment. We are considering that the problem will be solved by evaluating the phase transient due to the microwave switch.**

Keywords—cesium fountain; primary frequency standard; uncertainty evaluation

I. INTRODUCTION

In National Metrology Institute of Japan (NMIJ), we have been developing the second cesium fountain primary frequency standard (PFS), NMIJ-F2, since 2007. Because reports for calibration of International Atomic Time (TAI) to BIPM by cesium fountain PFSs have decreased recently, we want to complete uncertainty evaluation and contribute to calibration of TAI as soon as possible. Because we have not reported calibration data since operation of the first fountain, NMIJ-F1 [1], stopped due to troubles caused by the huge earthquake in 2011, the restart of contribution to TAI using NMIJ-F2 is very important for us. For this purpose, we plan to complete evaluation with uncertainty of $< 1\times10^{-15}$ as an immediate goal and start contribution to calibration of TAI. Afterward we will pursue lower uncertainty.

Now we are close to completion of uncertainty evaluation. The frequency stability reaches $7\times10^{-14}\tau^{-1/2}$ (τ: averaging time(s)) at the maximal atomic density. Experiments to estimate large frequency shifts such as the second-order Zeeman shift and the collisional shift have been done. We take calculation in our previous study for evaluation of the distributed cavity phase shift [2] while recently frequency is measured as a function of a tilt of a fountain for its evaluation in the other atomic fountains [3]. In addition, the frequency measurement at several microwave powers for evaluation of the microwave power dependence shift has been conducted, and the data has been well fitted to the theoretical function.

However, we look at an unexpected problem; the microwave power dependence shift is estimated to be $+5\times10^{-15}$, which is much larger than that in the other fountains. Although frequency correction for the quite large shift with uncertainty of 10^{-16} order may be possible, it may be necessary to measure the shift frequently in a frequency measurement campaign. Therefore, reducing the shift is better.

We found that the large shift was greatly reduced to $+1\times10^{-16}$ when the Ramsey microwave was turned off with a common voltage variable attenuator for only 10 ms after the interrogation. Nevertheless, instead of reduction of the shift, the phase transient of the microwave due to the switch must be evaluated in the low 10^{-16}. That is not easy, and the switch might not be possible to be used to obtain uncertainty of 10^{-16} order by the result.

In this proceeding, we describe the current status of the development of NMIJ-F2. In §II, the apparatus and the operation of NMIJ-F2 are explained. In §III, uncertainty evaluation at present is described, especially on the collisional shift, the second-order Zeeman shift, and the microwave power dependence shift. In §IV, frequency comparison between NMIJ-F2 and TAI is represented. Finally, we give a summary.

II. APPARATUS AND OPERATION

The experimental apparatus of NMIJ-F2 is basically the same as that represented in the proceeding of EFTF 2014 [4]. There are optical molasses with (001) configuration, optical pumping to the Zeeman sublevel of $m_F = 0$, two microwave cavities for Ramsey $\pi/2$-pulses and state-selection, a pipe for Ramsey interrogation, and detection of fluorescence from atoms. Cold atoms with a temperature of around 1 μK are launched upward by moving molasses with a launching velocity of 4.6 m/s. The apogee reaches 36 cm above the Ramsey cavity and the interrogation time is 0.55 s. Cold atoms of 6×10^5 are observed at the detection region at maximal atom density.

A local oscillator for the Ramsey $\pi/2$-pulses is a cryogenic sapphire oscillator using a pulse-tube cryocooler (cryoCSO) with frequency stability of 10^{-15} at 1 s, which is good enough for removal of the Dick effects. 10.8-GHz microwave

generated from the cryoCSO is converted to 9.2-GHz microwave by synthesizers, and then rf wave with approximately 7.4 MHz generated from a direct digital synthesizer (DDS) is mixed to obtain microwave resonant with cesium. The cryoCSO is locked to a hydrogen maser at a time constant of 300 s. The frequency of NMIJ-F2 can be compared with TAI via the hydrogen maser and UTC(NMIJ).

The Ramsey cavity is identical to the state-selection cavity with a Q factor of 17 000. They are combined to each other (not discrete) and are the part of the vacuum chamber. The Ramsey cavity is connected to the state-selection cavity via a hole with a diameter of 1 cm and a length of 7 cm. The interrogation region including the cavities is surrounded with three-layer magnetic shielding for suppressing environmental magnetic fields. In the magnetic shielding, a vertical magnetic C-field is applied with a 1-m solenoid coil. To obtain a homogeneous magnetic field, additional compensation coils at the bottom, the middle, and the top of the C-field coil are used.

The chamber is located in a room where the temperature is stabilized with air conditioning. Three platinum resistance thermometers are put on the wall of the top, the middle, and the bottom of the interrogation region. The temperature is measured every 10 minutes with the thermometers. The cavities and the pipe are made of copper with high thermal conductivity and combined each other, so that they are suitable to get homogeneous temperature.

III. Uncertainty Evaluation

A. *Frequency stability and collisional shift*

To evaluate a frequency shift due to collision between cold atoms, the frequency at zero atom density is extrapolated from frequencies at high and low densities. In NMIJ-F2, the extrapolation is done during frequency measurement by alternating the atom number by changing the microwave power fed into the state-selection cavity. In our case, the ratio between high and low numbers is nominally 4. 10 cycles of the fountain sequence (165 s) at high number and 40 cycles (660 s) at low number are repeated.

The Allan deviation of the frequency as a function of averaging time is shown in Fig. 1. Frequency stability at high atom density is somewhat improved from $8.3\times10^{-14}\tau^{-1/2}$ in 2014 [5] to $7.0\times10^{-14}\tau^{-1/2}$ due to improvement of laser cooling of atoms. In operation with extrapolation to zero density, the frequency stability is degraded from that at high atom density. In our case, the effective frequency stability is $2.6\times10^{-13}\tau^{-1/2}$, which gives stability of 0.20×10^{-15} when τ = 20 days. This is good enough to obtain total uncertainty of $< 1\times10^{-15}$.

The collisional shift at low density is typically -2×10^{-15}. We take 10% of the collisional shift, 0.2×10^{-15}, as type B uncertainty, which is resulted from difference in the density distribution of atoms between high and low densities.

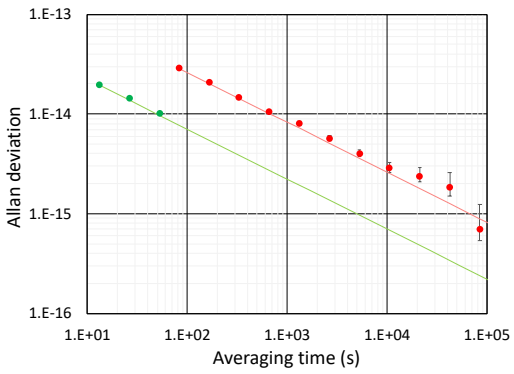

Fig. 1. Frequency stability as a function of averaging time. The red dots and the green dots show the frequency stability at extrapolation to zero density and the one at high atom density, respectively.

B. *Second-order Zeeman shift*

The second-order Zeeman shift is estimated from the first-order Zeeman shift of $m_F = +1 \leftrightarrow +1$ transition, which is measured from Ramsey fringes. From a set of measurements for various launching heights, the first-order Zeeman shift at a particular height (not averaged over interrogation time) is derived. Fig. 2 shows the magnetic field calculated from the first-order Zeeman shift as a function of the height from the center of the optical molasses. The magnetic field is homogeneous within 1.5 nT. From the map of the magnetic field, the second-order Zeeman shift averaged over interrogation time at the launching height in operation (1.07 m from the optical molasses) is evaluated to be -165.5×10^{-15}.

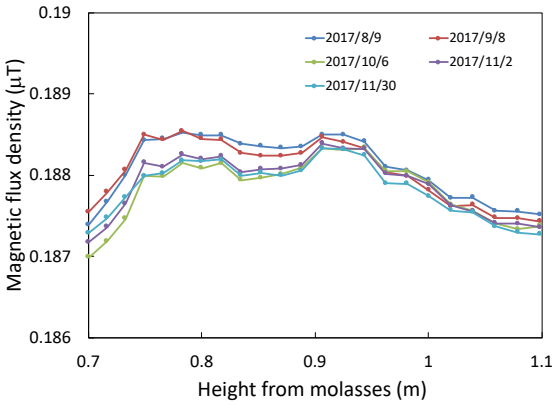

Fig. 2. Magnetic field above the Ramsey cavity. Five measurements with an interval of 1 month are represented.

The measurements were performed 5 times with an interval of 1 month. The variation in the second-order Zeeman shift during one month is less than 0.2×10^{-15}.

In frequency measurement campaigns for about 1 month, the second-order Zeeman shift will be estimated at the beginning and the end. The frequency correction for the shift will be derived from their average. The uncertainty is resulted from the long-term variation, and given as a half of the difference between the two measurements, typically 0.1×10^{-15}, where the accuracy of the measurement is much better than the long-term variation.

C. *Microwave power dependence shift*

The microwave power dependence shift is estimated from the frequency measurement at microwave pulse areas of $n\pi/2$ (n = 1, 3, 5,…). A function $An\sin(n\pi/2)$ is fitted [6], and the frequency at zero power is extrapolated. One of the causes of the shift is microwave leakage from the Ramsey cavity, so that some groups uses an interference switch to turn on/off microwave without phase transient [7]. On the other hand, a shift of $< 1\times10^{-17}$ is reported even when using continuous microwave [8]. Therefore, we initially used no microwave switches and expected a shift of the low 10^{-16} level or less.

However, in the case of continuous microwave, we obtain a frequency shift of $+5\times10^{-15}$ at $\pi/2$ pulses as shown by the black dots in Fig 3(a). This large shift is greatly reduced to $(+0.1\pm0.1)\times10^{-15}$ as shown in Fig. 3(b) by turning off the Ramsey microwave for only 10 ms while atoms pass downward through the state-selection cavity. The large shift at the continuous feed should attribute to so-called the after-Ramsey interaction; the microwave leaks from the Ramsey cavity into the state-selection cavity and is enhanced.

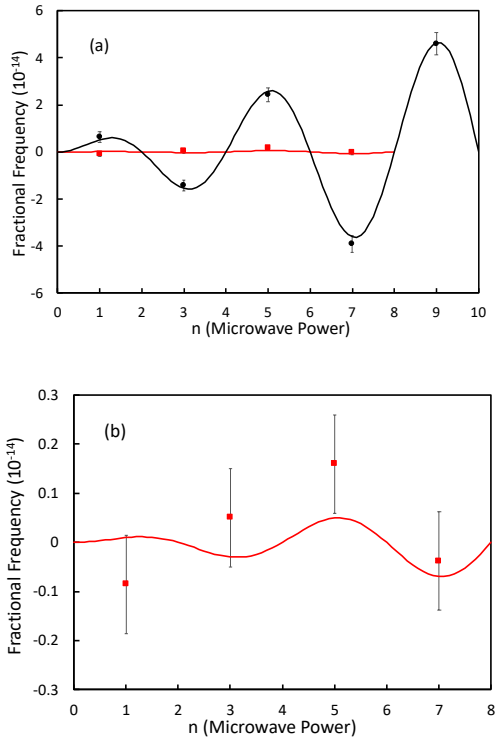

Fig. 3. Fractional frequency as a function of n, where the Ramsey pulse areas are $n\pi/2$. (a) The black dots and the red squares show the case without and with the microwave switching, respectively. (b) The case with the microwave switching (magnified from (a)).

In our case, it takes long time of 1 s from the switching to the beginning of the next interrogation. Therefore, we use not an interference switch but a common voltage variable attenuator, which turns on/off the 7.4-MHz rf wave and consequently the microwave resonant with cesium. The phase transient has not been evaluated in 10^{-16} order yet.

For the moment, our main plan is evaluating the phase transient due to the switch. However, if the phase transient is not negligible, another method will be taken. One of the methods is precisely evaluating the frequency shift with no switches. The frequency shift might be reduced to several times smaller by detunimg the resonance frequencies of the cavities with temperature even with no switches. Another method is making and evaluating an interference switch without phase transient.

D. *Others*

The blackbody radiation shift is evaluated from the temperature of the material with which the interrogation region is surrounded. Substituting the temperature averaged over the thermometers into the equation given in [9], the frequency correction for the blackbody radiation shift is estimated to be typically -16.7×10^{-15}. The uncertainty is evaluated to be 0.1×10^{-15} from inhomogeneity of the temperature.

The distributed cavity phase shift is calculated in our previous study [2] to be within $\pm0.5\times10^{-15}$ when power imbalance between microwave fed into the two ports of the Ramsey cavity is less than 20%.

The frequency correction for the gravitational red shift is evaluated to be $(-1.6\pm0.1)\times10^{-15}$ similarly with NMIJ-F1.

As for the microwave lensing effect, we take frequency correction of 0 and uncertainty of 0.15×10^{-15} as the upper-limit.

Uncertainty evaluation for the other effects such as the light shift, the background gas collision, and Ramsey pulling has not been completed yet, but they generally make only negligible frequency shifts. We will describe the uncertainty when a full-evaluation paper is submitted to somewhere.

The root mean square of the type B uncertainty excluding the unevaluated effects is 0.59×10^{-15} (Here we call it tentative uncertainty).

IV. Frequency Comparison with TAI

We have compared the frequency of NMIJ-F2 with TAI for 60 days (MJD58029-58064, 58069-58094) with fractional operation time of 84%. The difference y(NMIJF2 – TAI) = -1.7×10^{-15}, which exceeds the tentative uncertainty of NMIJ-F2 and the uncertainty of frequency transfer by a factor of about 3. That might result from the phase transient due to the microwave switching. Further uncertainty evaluation is necessary. Moreover, comparison with TAI in longer terms is also needed for confirmation.

V. Summary

Uncertainty for most of the dominant physical effects has been evaluated for NMIJ-F2. Nevertheless, the frequency of NMIJ-F2 has not been agreed with TAI within the tentative uncertainty yet. The most important unevaluated effect should be the phase transient due to microwave switching, which is necessary for reduction of the microwave power dependence shift. Although there are some remaining works, we consider that the current status is good to anticipate completion of uncertainty evaluation and calibration of TAI in the near-future.

ACKNOWLEDGMENT

This work was supported by JSPS KAKENHI Grant Number 15K21669.

REFERENCES

[1] T. Kurosu, Y. Fukuyama, Y. Koga, and K. Abe, "Preliminary evaluation of the Cs atomic fountain frequency standard at NMIJ/AIST," *IEEE Trans. Instrum. Meas.*, vol. 53, no. 2, pp. 466-471, 2004.

[2] S. Yanagimachi, Y. Fukuyama, T. Ikegami, and T. Kurosu, "Numerical simulation of distributed cavity phase shift in atomic fountain frequency standard," *Jpn. J. Appl. Phys., vol.* 44, no. 3, pp. 1468-1475, 2005.

[3] J. Guéna, J., R. Li, K. Gibble, S. Bize, and A. Clairon, "Evaluation of Doppler Shifts to Improve the Accuracy of Primary Atomic Fountain Clocks," *Phys. Rev. Lett.*, vol. 106, no. 13, art. no. 130801, 2011.

[4] A. Takamizawa, S. Yanagimachi, T. Tanabe, K. Hagimoto, I. Hirano, K. Watabe, T. Ikegami, and J. G. Hartnett, "Development of the Cesium Fountain Frequency Standard, NMIJ-F2," in *Proc. European Frequency and Time Forum*, 2014, pp. 394-397.

[5] A. Takamizawa, S. Yanagimachi, T. Tanabe, K. Hagimoto, I. Hirano, K. Watabe, T. Ikegami, and J. G. Hartnett, "Atomic fountain clock with very high frequency stability employing a pulse-tube-cryocooled sapphire oscillator," *IEEE Trans. Ultrason. Ferroelectr. Freq. Control*, vol. 61, no. 9, pp. 1463-1469, 2014.

[6] J. H. Shirley, F. Levi, T. P. Heavner, D. Calonico, D.-H. Yu, and S. R. Jefferts, "Microwave leakage-induced frequency shifts in the primary frequency standards NIST-F1 and IEN-CSF1," *IEEE Trans. Ultrason. Ferroelectr. Freq. Control*, vol. 53, no. 12, pp. 2376-2385, 2006.

[7] G. Santarelli, G. Governatori, D. Chambon, M. Lours, P. Rosenbusch, J. Guéna, F. Chapelet, S. Bize, M. E. Tobar, P. Laurent, T. Potier, and A. Clairon, "Switching atomic fountain clock microwave interrogation signal and high-resolution phase measurements," *IEEE Trans. Ultrason. Ferroelectr. Freq. Control*, vol. 56, no. 7, pp. 1319-1326, 2009.

[8] T. P. Heavner, E. A. Donley, F. Levi, G. Costanzo, T. E. Parker, J. H. Shirley, N. Ashby, S. Barlow, S. R. Jefferts, "First accuracy evaluation of NIST-F2," *Metrologia*, vol. 51, pp. 174-182, 2014.

[9] K. Beloy, U. I. Safronova, A. Derevianko, "High-accuracy calculation of the blackbody radiation shift in the ^{133}Cs primary frequency standard," Phys. Rev. Lett., vol. 97, no. 4, article number 040801, 2006.

Contributions to the mid-term frequency noise of the pulsed CPT clock at SYRTE

F. Tricot, S. Guerandel, E. de Clercq
LNE-SYRTE, Observatoire de Paris, PSL Research University, CNRS, Sorbonne Universités, UPMC Univ. Paris 06
61 avenue de l'Observatoire, 75014 Paris, France
francois.tricot@obsmp.fr

***Abstract*— We report here the performance obtained with a laboratory compact caesium clock based on coherent population trapping (CPT). The clock is working with two orthogonal linear polarizations made by two phase-locked continuous lasers tuned to 895 nm and separated by 9.192 GHz. Here we focus on the laser power and magnetic field fluctuations which mainly contribute to the mid-term frequency stability of the CPT clock.**

Keywords—atomic clock, vapour cell, frequency stability, coherent population trapping, power laser fluctuations.

I. INTRODUCTION

On-board applications (GNSS) need compact and high stability clocks. The vapour cell atomic clock used in Galileo system has a frequency stability at the level of 5×10^{-12} at 1 s [1]. The next generations of compact atomic clock based on CPT phenomenon offer a good alternative and a promising candidate for this application [2] since they have a simple scheme and a high performance frequency stability.

II. EXPERIMENTAL SETUP

The CPT signal of the SYRTE lin-perp-lin clock is observed on the Cs D1 line transmission, using a double Λ scheme and a Ramsey interrogation technique [3]. For this purpose we use two extended cavity diode lasers (ECDL) tuned at 895 nm. The laser beams are orthogonally linearly polarized. The Master laser is frequency locked thanks to a saturated absorption scheme. The Slave laser is phase-locked to the Master thanks to the optical phase lock loop (OPLL) as follows: the beat-note at 9.192 GHz detected by the fast photodiode PD1 is compared to the synthesis chain frequency (Fig. 1). This comparison give an error signal which is integrated by the OPLL circuit.

The two laser beams are sent through the acousto-optic modulator (AOM_R). The zero order is blocked and only the first order pass through the cell where atoms can experience the Ramsey interrogation. The transmitted signal is detected by the photodiode PD2 and processed by the computer in order to frequency-lock the synthesis chain on the atomic response.

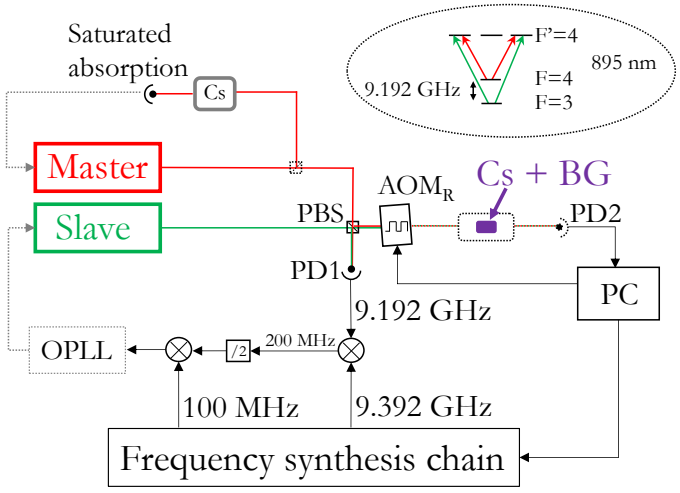

Fig. 1. The Master laser is frequency locked by a saturated absorption scheme. The Slave laser is phase-locked on the Master by comparing the optical beat-note with the synthesis chain. The Cs cell is also filled with a buffer gas (BG) mixture. The power lock scheme is not drawn.

To reduce the short-term and mid-term laser power contributions, we use an AOM (3080-122, Crystal technology) to control the laser power (Fig. 2). A few amount of laser power is detected thanks to a half-wave plate and a polarising beam splitter (PBS). The voltage is compared with a low noise and low drift reference voltage (LT1021, Linear technology) Thanks to the new power-lock circuit and the reduction of the phase noise of the synthesis chain, we reduced the short-term frequency stability to $2.3\times10^{-13}\,\tau^{-1/2}$ up to 100 s [4].

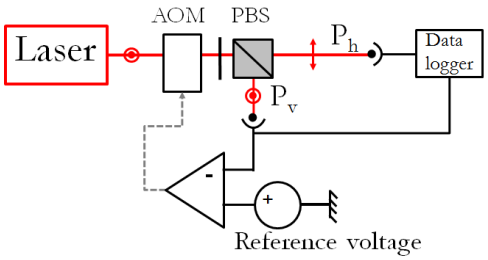

Fig. 2. Setup of the power lock A half-wave plate is set before the PBS to detect the verticaly polarisation and compare it to the reference voltage. The circuit, not drown here, controls the radio frequency of the signal driving the AOM.

F. Tricot is supported by Thales Electron Devices and DGA.

In this proceeding, we are interested in the mid-term laser power fluctuations. By the mean of a Data logger (Agilent 34970A) we measured the laser power and calculate the Allan deviation of the relative laser power stability.

III. MID-TERM CONTRIBUTIONS

A. *Frequency instability*

We measured the frequency stability of the clock up to 2000 s. In Fig. 3, we see that the magnetic field and the laser power fluctuations are contributing at the level of 10^{-14} at 2000 s. These contributions limit the frequency stability at the level of 2×10^{-14}, from 400 s to 2000 s integration time.

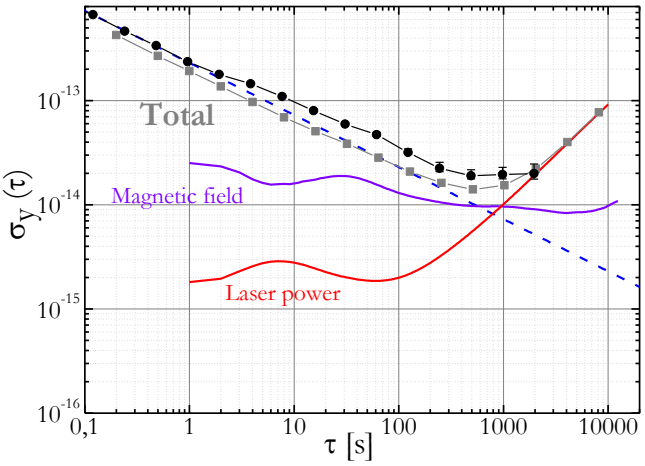

Fig. 3. Frequency instability of the clock (black). Magnetic field contributions (purple), laser power contribition (red). Quatradatic sum of the noise, including the short-term contributions (grey). The blue dashed line is a white noise asymptote at the level of $2.3\times10^{-13}\,\tau^{-1/2}$, this is the frequency stability we want to achieve.

In Fig 3, we also show the quadratic sum of all frequency noise sources: short-term contributions $1.9\times10^{-13}\,\tau^{-1/2}$ [4] , and the mid-term contributions. The calculated frequency stability is quite close to the measured frequency stability (Table I).

Frequency noise source	σ_y (2000 s)×10^{14}
Laser power	2
Magnetic field	0.9
Short-term	0.42
Total	**2.2**
Measured	**2.1**

TABLE I. FREQUENCY NOISE SOURCE AND ITS CONTRIBUTION

To understand why a laser power drift is visible, starting from 300 s integration time, we also measured the temperature inside the box containing the experiment. We present the result in the next section.

B. *Laser power fluctuations*

The Fig. 4 presents the useful laser power (horizontally polarised) when the power-lock circuit is ON. We see that the laser power fluctuations are correlated to the temperature fluctuations of the box.

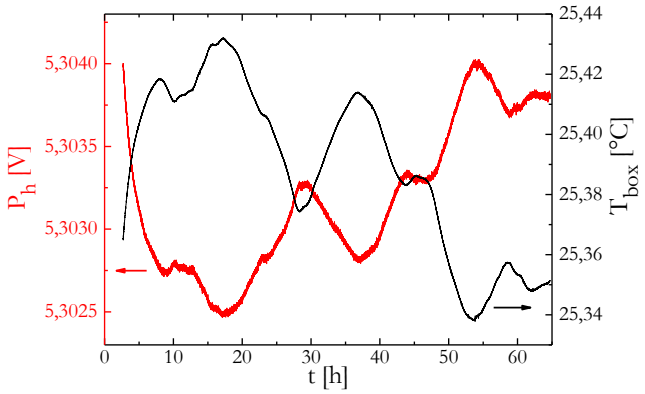

Fig. 4. Laser power fluctuations (red) and the temparature of the experiment measured during 60 h.

In the power-lock setup, we checked the influence of the temperature of the AOM used to lock the laser power fluctuations. Since we detected the laser power after a PBS, the Fig. 5 shows that the AOM temperature is rotating the linear polarisation. Around 25.4 °C (the box temperature), the laser power fluctuations is the most sensitive to temperature fluctuations. If the box temperature fluctuated with a $+\delta T$ quantity from 25.4 °C, the in-loop voltage is decreasing with a $-\delta P_v$ quantity while the out-loop voltage is increasing. If the in-loop voltage is decreasing, the power-lock circuit is counterbalancing this fluctuation by increasing the laser power before the PBS. Therefore, the out-loop voltage will increase while it was already increasing because of the $+\delta T$ fluctuation.

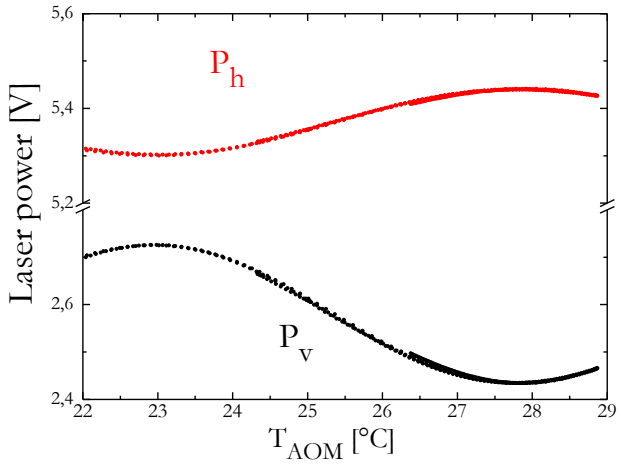

Fig. 5. Verticaly (in-loop) and horizontaly (out-loop) polarisation fluctuation as a function of the AOM temparature.

To avoid this inter-connected effect of the temperature fluctuations, one can chose to control the AOM temperature around 23 °C or 27.8 °C, where the sensitivity is cancelled. We did another measurement of the relative power stability laser while the AOM temperature is regulated at 27.8 °C to confirm this sensitivity. We show the results on the next part.

C. *Laser power stability*

The Fig. 6 shows the relative laser power stability out of the loop when the AOM temperature is not controlled and also when the AOM temperature is controlled at 27.8 °C.

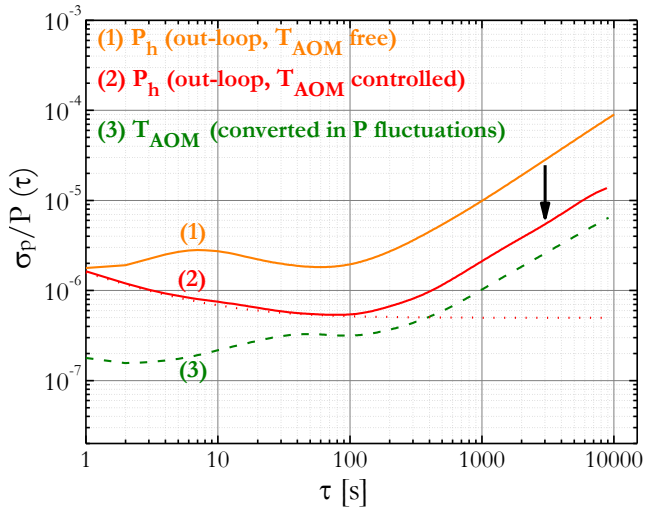

Fig. 6. Relative laser power stability of the power laser. (1) The AOM temparature is free. (2) The AOM temparature is regulated at 27.8 °C. (3) Temparature fluctuations of the AOM converted in laser power fluctuations. The red and the black dashed lines are the relative laser power stability we should measured if there were no drif but only flicker noise and the noise of the data logger (white noise from 1 s to 50 s interrogation time).

The relative laser power stability is improved by a factor 5 from 100 s to 10000 s integration time when the AOM temperature is controlled. Below 70 s, the power stability is limited by the data logger noise. This noise corresponds to a white noise, this is why the flicker noise of the laser power is not visible from 1 s to 70 s. Thanks to the AOM temperature regulation, the relative laser power stability is closed to what we should measure. The drift is propably due to residual temperature of the AOM. In the future, we will investigate more about the temperature effect of the AOM on the linear polarization.

D. *Expected frequency stability*

With the control of the AOM temperature and thanks to a low noise current supply, the mid-term contributions of our clock is at the level of 6×10^{-15} at 2000 s integration time. In Fig. 7 we show the expected frequency stability of the clock. The relative laser power stability contributions is lower by a factor 5 and the magnetic field contributions is also lower by a factor of 10 from 1000 s to 10000 s integration time. With this upgrade, we should measure a frequency stability of about $2\times10^{-13}\,\tau^{-1/2}$ up to 2000 s.

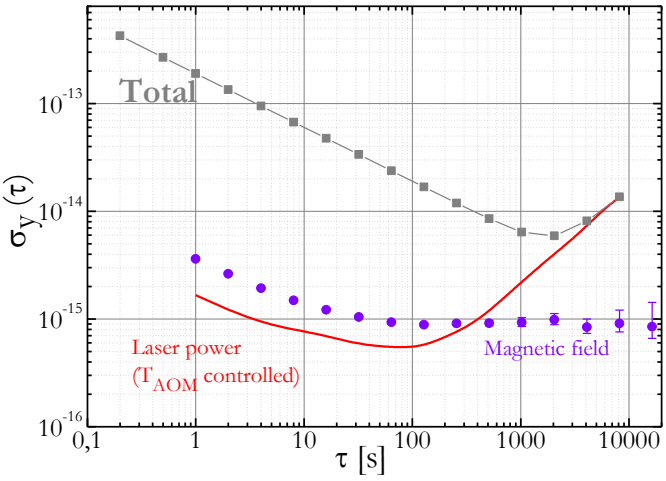

Fig. 7. Expected frequency instability of the clock (grey). Magnetic field contributions (purple), laser power contribition when the AOM temperature is controlled (red). Quatradatic sum of the noise with short-term contributions (grey).

IV. CONCLUSION

In this proceeding, we show the mid-term works of the CPT clock experiment. We show that the box temperature fluctuations had an effect on the relative laser power stability. By controlling the AOM temperature of the power lock set up, the laser power stability has been improved. With this necessary precautions and the use of a lower noise current supply, we should improve the frequency stability of the clock. With the short and mid-term improvements, we should measure a frequency stability of about $2\times10^{-13}\,\tau^{-1/2}$ up to 2000 s.

ACKNOWLEDGMENT

We are very grateful for the electronic and mechanical assistance at SYRTE. We thank Pierre Bonnay for manufacturing Cs cells.

REFERENCES

[1] P. Waller *et al.*, "The in-orbit performances of GIOVE clocks", IEEE Trans. Ultrason., Ferroelect., Freq. Contr. **57**, 738 (2010)

[2] J. Vanier, "Atomic clocks based on coherente population trapping: a review", Appl. Phys. B **81**, 421-442 (2005)

[3] T. Zanon, S. Guérandel, E. de Clercq, D. Holleville, N. Dimarcq, and A. Clairon, "High Contrast Ramsey Fringes with Coherent Population Trapping Pulses in a Double Lambda Atomic System", Phys. Rev. Lett. **94**, 193002 (2005)

[4] F. Tricot, P. Yun, S. Guerandel, E de Clercq, "Latest achievements on the pulsed CPT clock", IEEE, EFTF/IFCS (2017)

SAW Temperature Sensor with Mirror Topology

Ivan Antcev, Sergey Bogoslovsky,
Gennadiy Sapozhnikov
JSC "Radar-mms"
St Petersburg, Russian Federation
bogoslovsky_sv@radar-mms.com

Sergei Zhgoon, Alexander Shvetsov
Department of Radio Engineering Fundamentals
National Research University "MPEI"
Moscow, Russian Federation
zhgoon@ieee.org

***Abstract*—One of the main directions for improving surface acoustic wave (SAW) sensors is to increase the range of operation. Besides achieving greater interrogation distances, the aim of this work is to increase the amount of information that can be obtained from the sensor. The design of the sensors with mirror topology assumes that there is a significant difference in variation of SAW propagation velocity with temperature in two different substrates. The search for optimum piezoelectric materials showed that it is preferable to use two different cuts of lithium niobate (Y-Z-cut and 128°Y-X-cut). The achieved measurement distance with a 1.8 µs long interrogation pulse and 10 mW average power exceeded 30 m at 433 MHz. Measurement accuracy in the range of -50 to 50 °C was better than ±5°C.**

Keywords— surface acoustic waves; temperature sensor; delay line

I. INTRODUCTION

Passive wireless surface acoustic wave (SAW) sensors find applications in monitoring equipment for various purposes [1, 2]. In the conditions of practical application, the echo signals reflected from nearby buildings and other obstacles have a significant effect on the receiving channel of the reader. This justifies the need to provide an initial signal delay of at least 2-3µs. This is reason for using delay lines as sensitive elements of SAW based sensors. The design of the sensor in the form of a delay line with reflective structures also gives following advantages: good matching to the antenna and minimum mismatch loss; the ability to realize different kinds of impulse response; the adjustable reflectance from each reflector (by changing the thickness of the metal or the depth of the grooves) and the possibility to choose its optimum value to obtain the desired impulse response. The temperature sensor presented here is implemented in accordance with the principles of mirror topology that were successfully used in force SAW sensors [3].

II. TEMPERATURE SENSOR BASED ON THE PRINCIPLES OF MIRROR TOPOLOGY

In case of temperature measuring, the mirror topology is realized on two different piezoelectric substrates with different temperature coefficients of delay (TCD). On each of them interdigital transducer (IDT) is formed and two reflecting structures placed on both sides of each IDT. The IDTs of these two delay lines are connected in parallel and this pair of delay lines (sensitive element) is connected to the antenna. Remote temperature monitoring is realized by sending interrogation signals from the interrogation unit and receiving response signals from the sensor (Fig. 1). The measured temperature is estimated by processing of the received sensor response.

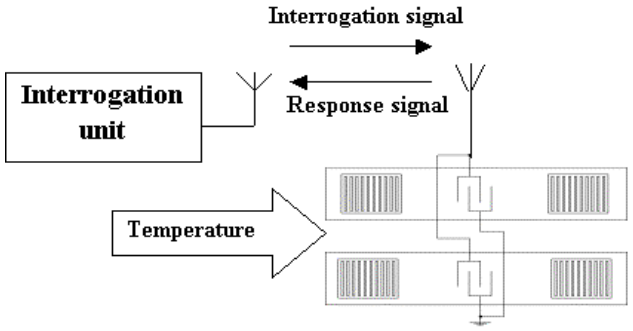

Fig. 1. Temperature sensor design and its interaction with interrogation unit.

When the interrogation radio signal arrives from antenna of the interrogation unit to the antenna of the SAW sensor, an RF electrical signal is applied to the IDTs. Each IDT generates SAW propagating to the reflecting structures. When reflected SAW returns to the IDT, it generates an RF electrical signal applied to the sensor antenna. The sensor antenna radiates a response RF signal into the space and it is received by the interrogation unit. The difference in the delay times of the interrogation signal on different substrates is determined by SAW velocities and distances of SAW propagation and it is proportional to the difference in TCD.

The reflecting structures realize the required type of the sensor impulse response. An example of impulse responses of individual delay lines is shown in Fig. 2, left. As shown in Fig. 2 the impulse characteristics of the delay lines are different, and the minimums of the impulse response of one delay line correspond to the maxima of the impulse response of another delay line in time domain. An example of the combined impulse response is shown in Fig. 2, right.

The change in the temperature changes the geometric dimensions of the IDT, the acoustical propagation length, and the parameters of the reflecting structures on both substrates. The change in the geometric dimensions and in SAW velocities on each of the piezoelectric substrates leads to a change in the delay times of the response signals. Since in time domain the minimum values of the impulse response of one substrate correspond to the maximum values of the impulse response of

This work was partially supported by the Ministry of Education and Science of the Russian Federation, grant 8.6108.2017/6.7.

the other substrate, with different SAW velocity variations on different substrates, the response signal (convolution of the interrogating signal and of the combined impulse response) will be different at different temperatures. Thus, a change in SAW velocity will not only lead to a change in the delay time, but also to a change in the envelope and internal structure of the response signal. Thus, the response signal will have a different shape at different temperatures. The change in the shape of the response signal can be attributed to the temperature value and the calibration dependence "form-temperature" is used for measurements processing.

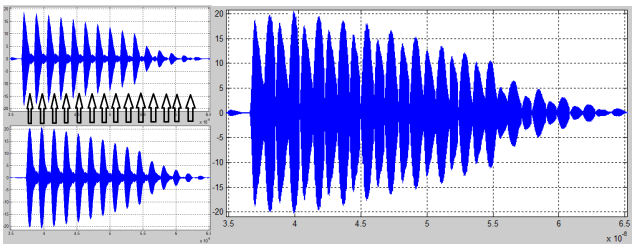

Fig. 2. Impulse responses of individual delay lines (left) and combined impulse response of two different delay lines (right).

The information signal is a response signal that provides the maximum amplitude value of the temperature sensor response. The sensor realizes the convolution of the received interrogation signal with the impulse response of the device, which depends on the current temperature. Obviously, in order to synthesize the optimal interrogation signal (or a set of interrogation signals), as well as for efficient processing of the received response in the interrogating device, it is necessary to know the correspondence between the shape of the impulse response and the response signal at specific temperature. This correspondence can be established experimentally by successively reaching each value from the set of reference temperature values and recording the corresponding impulse responses and the sensor responses (convolution of the impulse response and of the interrogation signal).

III. Choice of Substrates for the Pair of Delay Lines

The sensor based on the delay line requires a high value of the electromechanical coupling factor K^2 and low SAW propagation attenuation. Therefore, lithium niobate was chosen as the material for manufacturing the long-range temperature sensor. This material is characterized by a low value of the acoustical loss, a high value of K^2, and a high value of the temperature coefficient of frequency (TCF) or TCD. Using of mirror topology requires also a significant value of TCD difference for SAWs propagating on two different substrates.

Therefore, simulation of the propagation of SAW in lithium niobate and analysis of its results in the context of temperature sensitivity were carried out. SAW parameters strongly depend on substrate orientation that is described by the Euler angles (φ, θ, ψ). The results of the calculation of the TCD for SAW (the velocity of which is lower than the velocity of all bulk acoustic waves (BAW) propagating at same direction) propagating in different directions on all cuts of lithium niobate are shown in Fig. 3. Freeware software VCAL [4] modified by us for calculation of temperature behavior was used for these calculations, lithium niobate constants were taken from [5 – 7].

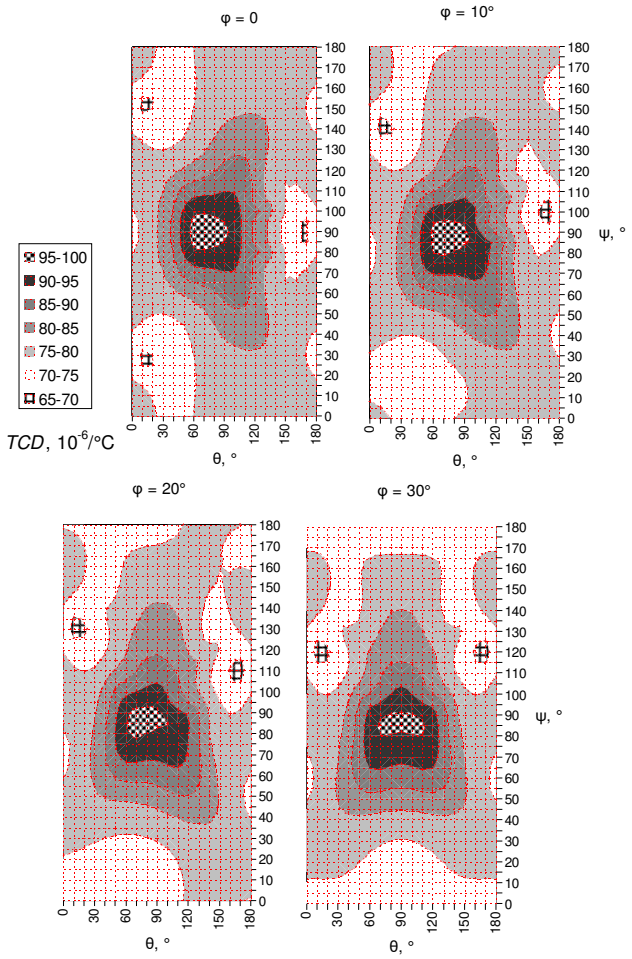

Fig. 3. The dependence of TCD on the second Euler angle θ and the third Euler angle ψ for 4 fixed values of the first Euler angle φ.

The maximum TCD, according to the calculation, is 98 ppm/°C and it is reached when the SAW propagates perpendicular to the X axis at -20°Y-cut. This propagation direction corresponds to the K^2 value of about 4.6% (which is close to the local maximum and slightly lower than the global one for non-leaky SAW) and the zero value of power flow angle (PFA). The SAW on the YZ-cut has similar properties (TCD is lower by 2 ppm/°C and slightly smaller than K^2).

The minimum TCD among non-leaky SAW, according to the calculation, is 67 ppm/°C and is reached when the SAW propagates perpendicular to the X axis on the 66°Y-cut. This propagation direction corresponds to the K^2 value of about 1.7% and the zero value of PFA. Almost the same calculated TCD and slightly smaller K^2 has a SAW propagating perpendicular to the X axis at 64°Y-cut. By choosing a cut with a slightly larger rotation angle, one can get a higher K^2 with a slight increase in TCD. Thus, for the 69°Y-cut the calculated TCD is higher by about 0.25 ppm/°C and K^2 reaches a value of 2%; while for a local maximum (at about 80°Y-cut) K^2 reaches a value of 2.6% and TCD a value of 70 ppm/°C. Chosen orientations have SAW velocities that are higher than the

velocities of bulk acoustic waves (BAW) propagating in same direction. Such SAWs are non-leaky only when propagating strictly perpendicular to the X axis.

The local minimum of the TCD also exists in the region of the substrate orientations determined by the Euler angles (φ, 5..25°, 110..160°), the minimum value of the TCD in this region is about 69 ppm/°C. At the same time, the corresponding values of K^2 do not exceed 1.5% in this region for smallest TCD values (not exceeding 71 ppm/°C). Another local minimum of TCD is near the global maximum of K^2, which is achieved when the SAW propagates along the X axis on the 128°Y-cut (TCD is about 71 ppm/°C, K^2 is about 5.5%).

Thus, the use of a pair of delay lines from different cuts (using non-leaky SAW only) makes it possible to obtain a difference of TCD up to 27 ppm/°C with K^2 over 4% for each of them. If the K^2 is assumed to exceed 2%, it is possible to reach 31 ppm/°C TCD difference. Using SAW with only lowest velocities restricts the possibility of obtaining high TCD difference and high K^2 (it is possible to reach up to 29 ppm/°C if the K^2 is assumed to exceed 0.5%).

The maximum of TCD difference for two SAW propagating in two different directions on single cut Δ_{TCD} exists in the region of substrate orientations, determined by the Euler angles (φ, 60..90°, ψ). SAW with a high TCD (95..98 ppm/°C) propagates in directions corresponding to ψ from 75° to 95°. SAW with low TCD (72..75 ppm/°C) propagates in directions corresponding to ψ from 0 to 25°. The maximum value of Δ_{TCD} is about 24 ppm/°C. The K^2 of SAW with a high TCD is close to 4%; the K^2 of SAW with a low TCD is close to 2..2.3%. The difference in TCD over 20 ppm/°C can be obtained at the condition that the minimum acceptable value of K^2 is 2.5..3%.

A useful value of Δ_{TCD} (that is closer to the maximum value) in combination with close to 2% K^2 and moderate values of PFA can be obtained by using the X-cut. By using the Y-cut, it is possible to obtain a value of Δ_{TCD}, approximately 20% below the global maximum value in combination with a lower K^2 of the SAW with low TCD and zero values of PFA. The global maximum of Δ_{TCD} is achieved with the use of double rotated cuts with nonzero values of PFA, sometimes exceeding 10°. This Δ_{TCD} value is only about 2 ppm/°C greater than the one achievable on X-cut. Thus, it looks reasonable to use the cuts that are common or simplest for fabrication. The calculated properties of these cuts are summarized in Table I.

The use of a pair of delay lines made on two different cuts using non-leaky SAW (where one of them is a Y-cut with wave propagation along the Z axis, or an X-cut with propagation at an angle of 92° to the Y axis, while the other is a 128°Y-cut with propagation along the X axis) allows to obtain a TCD difference of 25 ppm/°C for K^2 exceeding 4% for each of the combinations. The variant using the YZ-cut seems preferable because of zero PFA and closer to optimal diffraction parameter value, although the SAW with the maximum TCD on the X-cut is characterized by a slightly higher K^2.

The use of another pair of delay lines on different cuts (where one of them is a Y-cut with propagation of a wave along the Z axis, or an X-cut with propagation at an angle of 92° to the Y axis, while the other is a 64°Y-cut with propagation perpendicular to the X axis) allows to obtain a TCD difference of 29 ppm/°C. The SAW velocity on the 64°Y- may exceed the BAW velocity (this SAW is non-leaky only when propagating strictly perpendicular to the X axis).

TABLE I. PROPERTIES OF SAW ON SELECTED CUTS

Cut	ψ	Velocity (m/s)	PFA	K^2 (%)	TCD (ppm/°C)	Δ_{TCD} (ppm/°C)
Y	90°	3487	0	4.2	96	20
	0	3718	0	0.74	76	
128°Y	90°	3673	0	1	85	14
	0	3979	0	5.5	71	
41°Y	-	-	-	< 0.45[a]	78..83[a]	< 7[b]
	90°	4076[c]	0	0.04[c]	76[c]	
	0	4752[d]	0	3.3[d]	61[d]	< 22[e]
64°Y	-	-	-	< 1.4[a]	71..78[a]	< 11[b]
	90°	4428[c]	0	1.5[c]	67[c]	
	0	4450[f]	0	11[f]	74[f]	< 7[e]
X	92°	3479	-3°	4.4	96	23
	168°	3631	6°	1.9	73	

[a.] Range of values for SAW with lowest velocity propagating in all directions on the cut.

[b.] Range of values for all non-leaky SAW propagating in all directions on the cut.

[c.] Velocity value of non-leaky SAW exceeding BAW velocity.

[d.] Velocity value of leaky SAW propagating along free surface.

[e.] Range of values for specified leaky SAW in combination with any non-leaky SAW on specified cut.

[f.] Value for the leaky SAW propagating over a metallized surface.

If a single wafer is used the X-cut makes it possible to obtain the greatest Δ_{TCD} among the considered cuts, as well as the greatest value of the K^2 with small difference in a pair of directions. The non-leaky SAWs on 41°Y-cut and the leaky SAW on 64°Y-X-cut (propagating with a relatively low loss on the metallized surface) are not interesting in comparison with other considered SAWs.

The greatest difference in TCD among the considered variants, about 35 ppm/°C, can be obtained by using a leaky SAW on the 41°Y-X-cut (propagating with a relatively low loss on the free surface) in combination with a non-leaky SAW with a high TCD propagating on the other cut (YZ-cut or X-cut with propagation at an angle of 92° to the Y axis). But it is quite possible that even relatively low loss in leaky waves will be not acceptable for the discussed purpose, especially in a range of temperatures, consequently the use of leaky waves requires additional studies.

Note that all considered variants of a pair of delay lines on a single substrate assume perpendicular (or almost perpendicular) placement of delay lines. They do not allow to minimize the device size and two separate substrates assembly is smaller. Thus, using of non-leaky waves on commonly used cuts for two delay lines on separate substrates was chosen for sensor design.

IV. EXPERIMENTAL

The delay lines were made with the following widely used piezoelectric materials: lithium niobate YZ-cut and lithium niobate 128°Y-X-cut.

In order to minimize the acoustic losses introduced by metal the reflecting structures were made with etched grooves.

To achieve amplitude equality of the impulse responses on different substrates of lithium niobate, different depths of the grooves in the reflecting structures were used. For the formation of the test samples vacuum deposition of aluminum thin film, photolithography and chemical etching were used. Grooves for reflecting structures were formed by plasma etching through aluminum mask. The test sample assembly for electrical parameters testing is shown in Fig. 4.

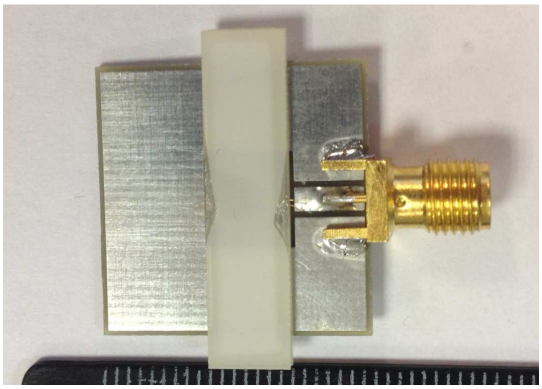

Fig. 4. Test assembly of delay line.

Main characteristics of the first delay line topology (YZ-cut): velocity – 3487 m/s; number of IDT electrodes – 60; the width of the electrode – 2.013 microns; the width of the gap - 2.013 microns, the aperture of the IDT – 238 microns; the interval between the center of the IDT and the inner edge of the reflecting structure – 6.6 mm; number of grooves in one section of the reflecting structure – 10; the depth of the grooves – 450 Å; the distance between the outer edges of the reflecting structures – 19.08 mm.

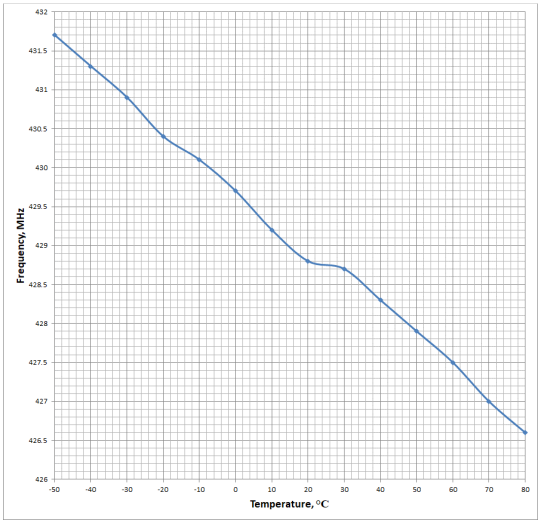

Fig. 5. The dependence on temperature of the interrogation signal frequency resulting in maximum response signal amplitude.

Main characteristics of the second delay line topology (128°Y-X-cut): velocity – 3975.7 m/s; number of IDT electrodes – 51; the width of the electrode – 2.295 microns; the width of the gap – 2.295 microns, the aperture of the IDT – 246 microns; the interval between the center of the IDT and the inner edge of the reflecting structure – 7.35 mm; number of grooves in one section of the reflecting structure – 10; the depth of the grooves – 210-230 Å; the distance between the outer edges of the reflecting structures – 21.39 mm.

In order to determine the impulse response of the device, the complex impedance frequency response was directly measured by a vector network analyzer and further transformed into impulse response by means of embedded software. The sample under investigation was exposed to interrogation signal with amplitude 1 V in a range of temperature. To ensure maximum operation range, it is necessary to obtain the maximum amplitude response from the sensor. Fig. 5 shows the temperature dependence of interrogation signal frequency resulting in maximum response signal for first delay line. The maximum frequency change, as expected, was about 5 MHz. Measured insertion loss of sensor not exceed 15 dB.

Testing of sensor in condition of wireless interrogation with a 1.8 μs long and 10 mW average power interrogation signal shows that 30 m operation range can be reached together with 5°C measurement accuracy in the range of -50 to 50 °C.

V. CONCLUSION

The principles of mirror topology were successfully applied to wireless temperature sensor. The choice of optimum substrates for such sensor was discussed in details and pair of lithium niobate substrates (Y-Z-cut and 128°Y-X-cut) was suggested. Measurement distance 30 m was reached with 5°C measurement accuracy in the range of -50 to 50 °C.

ACKNOWLEDGMENT

The use of Ken-ya Hashimoto software is gratefully acknowledged.

REFERENCES

[1] N. Kozlovski, D. Malocha, and A. Weeks, “A 915 MHz SAW sensor correlator system,” IEEE Sensors Journal, vol. 11, No. 12, 2011, pp. 3426-3432.

[2] A. Pohl, “A low-cost high-definition wireless sensor system utilizing intersymbol interference,” IEEE Transactions on UFFC, vol. 45, No. 5, 1998, pp. 1355-1362.

[3] I. Antcev, S. Bogoslovsky, G. Sapozhnikov, and S. Zhgoon. “SAW force sensor based on reflective delay line quasi-mirror topology,” IEEE Int. Ultrasonics Symp. Proc., 2015, pp. 53-56.

[4] K. Hashimoto and M. Yamaguchi, “Free software products for simulation and design of surface acoustic wave and surface transverse wave devices,” IEEE Int. Freq. Control Symp., 1996, pp. 300-306.

[5] G. Kovacs, M. Anhorn, H. E. Engan, G. Visintini, and C. C. W. Ruppel, “Improved material constants for $LiNbO_3$ and $LiTaO_3$,” IEEE Ultrasonics Symp., 1990, pp. 435-438.

[6] R. T. Smith and F. S. Welsh, “Temperature dependence of the elastic, piezoelectric and dielectric constants of lithium tantalate and lithium niobate,” J.A.P., vol. 42, No. 6, 1971, pp. 2219-2230.

[7] S. Kim and R. T. Smith, “Thermal expansion of lithium tantalate and lithium niobate single crystals,” J.A.P., vol. 40, No. 11, 1969, pp. 4637-4641

Choice of SAW Humidity Sensor Coatings

Ivan Antcev, Sergey Bogoslovsky, Mikhail Derkach, Gennadiy Sapozhnikov
JSC "Radar-mms"
St Petersburg, Russian Federation
bogoslovsky_sv@radar-mms.com

Sergei Zhgoon
Department of Radio Engineering Fundamentals
National Research University "MPEI"
Moscow, Russia
zhgoon@ieee.org

***Abstract*—Very thin sensitive layers deposited on the surface of SAW resonators were investigated (ST-Quartz was used as substrate). The thickness of the layers did not exceed several percent of the wavelength at the operating frequency of the device. The humidity sensitivity and hysteresis of several organic and inorganic sensitive coatings were studied at different temperatures, the reproducibility and stability of the results were analyzed. The following materials were applied by centrifugation and subjected to heat treatment: Nafion® polymer (Nafion®); polybenzoxazole polymer; silicate films of the general composition nP2O5 * SiO2; single-layer and multilayered carbon nanotubes (CNTs); polymethyl methacrylate (PMMA); PMMA with CNT; polymer Nafion® with CNT. Comparing resonators with three different thicknesses of the deposited Nafion® polymer film (50, 100 and 150 nm) has shown that the larger is the thickness, the higher is the initial frequency offset from the initial frequency of the resonator at 434 MHz. This required topology modifications to compensate for the frequency change due to film deposition. It was found that the resonance frequency sensitivity to humidity increases with decreasing coating thickness. It was also found that the hysteresis and the sensitivity of the relative humidity measurement varied with temperature - with the increase in air temperature the hysteresis decreased from ± 2 % RH at 0 °C to ± 1% RH at 60 °C, and the sensitivity to relative humidity increased from 4.5-5.0 kHz /% RH at 0 °C to 6.5-7.0 kHz /% RH at 60 °C for 434 MHz resonators. Measurements with Nafion® films thinner than 150 nm revealed that the change of the resonator S_{11} magnitude induced by humidity moderate increase started to return to its initial value with further humidity increase towards the values approaching 100%. This experimental feature has proven to be very useful for wireless sensor interrogation setup operation, as it allowed to maintain the impedance matching conditions in the electrical circuit of the antenna connection to the sensor and thus to reduce the readout and interrogation distance sensibility on the potential impedance mismatch induced by humidity changes. A conclusion was made that for Nafion® polymer, the recommended layer thickness should not exceed 100 nm for operation at 434 MHz**

Keywords—SAW sensor; humidity; coating thickness; Nafion®

I. INTRODUCTION

Among chemical gas sensors, humidity sensors are the simplest and the most demanded. Humidity sensors are the simplest example of chemical sorption sensors. They could be widely used in many approaches from industry to consumer electronics. Surface acoustic wave (SAW) devices have some advantages against semiconductor chip devices. These advantages make them attractive for sensor design especially for wireless sensors. A very perspective trend is to use sorption-type chemical sensors based on SAW with selective layers in biochemical and biological research, as well as in medicine. This kind of sensors could be used for example in medical hyperbaric chamber for outward breath composition control etc., when one need highs accuracy and simple sensor design together with wireless flexibility. This paper is focused on experimental studies of SAW resonators coated with selective thin films.

This work was partially supported by the Ministry of Education and Science of the Russian Federation, grant 8.6108.2017/6.7.

II. OPERATING PRINCIPLE AND DESIGN OF PROPOSED SENSOR

One-port SAW resonator device consists of a piezoelectric substrate with an interdigital transducer (IDT) and two reflecting arrays on the substrate surface. Studied selective thin layers are deposited on the entire surface of a proposed sensor, covering the reflectors and the IDT.

When creating sensors with coatings on SAW components, the applied film has both an initial static effect on the characteristics of the device, and the effect related to the measured property that dynamically influences the sensor response by changing the SAW velocity. The velocity change occurs when the mass (density) and/or the elastic properties of the applied film change.

The investigated humidity sensor consists of a SAW element chip, on which a humidity-sensitive film is applied. The contact pad areas are free from the film to ensure reliable connection. A SAW resonator sensing element was studied, onto which Nafion® or other polymer films were applied by spinning. The thickness of the deposited film was varied by diluting the polymer solution with isopropyl alcohol and increasing the spinning speed of the centrifuge up to the limit of 10,000 rpm. For these studies, single port SAW resonators were used with central frequencies of 200 and 434 MHz.

III. EXPERIMENTAL RESULTS

Inorganic coatings of the P_2O_5-SiO_2 system, that are often used in capacitive and resistive humidity sensors, were also studied. These films showed good sensitivity to humidity with two distinct areas: mass moisture sensitivity and viscoelastic moisture sensitivity. However, hysteresis and extremely strong change in properties during aging and annealing of such films

do not allow using them in a SAW humidity sensor. All resonators with films of the P_2O_5-SiO_2 system showed significant long-term instability.

Coatings made with carbon nanotubes (CNT) were also studied. CNTs were applied by centrifugation in vinyl alcohol and subsequent drying. The resonator has demonstrated an extremely high sensitivity to humidity, but the quality factor became very poor. The section of the viscoelastic sensitivity of the resonator terminates by 70%, since in this case the quality factor and the resonant response fall too low for practical use. In fact, at values of the air relative humidity (RH) more than 70%, the surface acoustic waves no longer propagate along the surface of the substrate.

More suitable for using in the humidity SAW sensor with are the results obtained with the polymer coating by Nafion®. Numerous studies of resonators with the frequencies of 200 and 434 MHz have been carried out with a film of this polymer deposited on their surface [1]. During the investigation, the film was applied by spinning of the polymer emulsion diluted in isopropyl alcohol. The thickness of the film was controlled through the rotational speed of the spinner. As a result of the experiments, coating regimes were selected which gave good uniformity over the substrate area and a sufficiently small thickness. The coating demonstrated excellent characteristics of the sensitivity to humidity up to 95% of relative humidity in the temperature range from 0 to 60 °C and a very good temporal stability.

The interesting results from the point of view of the sensitivity increase were demonstrated by the Nafion® polymer coating with dispersed single-layer carbon nanotubes. In addition to a sufficiently large overall frequency change, this film showed a good relative sensitivity over a wide range of relative humidity values. Besides, a uniform sensitivity pattern, is closer to linear than in samples with Nafion® without CNTs. But for this film the resulting film thickness and CNT content were not repeatable after each coating deposition.

As a result of numerous experiments, a Nafion® coating was chosen for the humidity sensor. Nafion® provides both high sensitivity to humidity and reproducibility of thickness from one sensor to another sensor in one batch and in different batches [1]. After selecting the sensitive layer, it was necessary to determine the optimum layer thickness for use in the SAW-based humidity sensor.

When comparing resonators with three different thicknesses of the deposited Nafion® film (50, 100 and 150 nm), it can be seen that the larger is the thickness, the higher is the initial frequency offset compared to the uncovered resonator (Fig. 1) [1]. According to the sensitivity to humidity criterion in the frequency dependencies on relative humidity, it becomes obvious that the sensitivity to humidity increases with decreasing the film thickness. To explain this fact, one has to return to theoretical explanations of the deposited film effect on the parameters of the surface acoustic wave and to the analysis of formulas (1) and (2), which relate the SAW velocity decrease and the frequency change to the film properties. The formulas are taken from [2].

$$\frac{\Delta V}{V_o} = -\rho \cdot k \cdot h \left\{ \left(1 - \frac{c_{44}}{\rho \cdot V^2} \right) \cdot U_y^2 + U_z^2 + \left(1 - \frac{4c_{44} \cdot (c_{13} + c_{44})}{\rho \cdot V^2 \cdot c_{33}} \right) U_x^2 \right\} \quad (1),$$

$$\frac{\Delta f}{f_o} = K_p \frac{\Delta V}{V_o} \quad (2).$$

In formulas (1) and (2), ρ is the film density, h is the thickness of the film, c_{ij} are the elastic constants of the film, k is the wave number, U_i is the displacement along the corresponding axes, V is the SAW velocity, ΔV is the deceleration, f is the resonance frequency, Δf – frequency change, K_p – coefficient of proportionality.

Due to the presence of two mechanisms of the sensitivity to humidity, called mass sensitive and viscous (viscoelastic), the sensitivity curves have a characteristic form, which is a combination of a straight line and of a polynomial curve [3]. At low values of relative humidity, the sensitivity to humidity and the nature of the frequency dependence on the relative humidity will be determined by the increment of the film mass due to the added moisture. In this case, the effect of moisture absorbed by the film on the elastic properties of the film will be negligible.

At high values of the relative humidity of the air, the elastic properties of the film will vary considerably. This will lead to a strong nonlinear change in the SAW velocity. Although the mass of the moisture added will substantially affect the speed, the mechanism of changes in the elastic properties is prevalent. It is also possible to expect that with a decrease in the thickness of the humidity-sensitive film, an appreciable change in the elastic properties will occur at lower values of the relative humidity of the air.

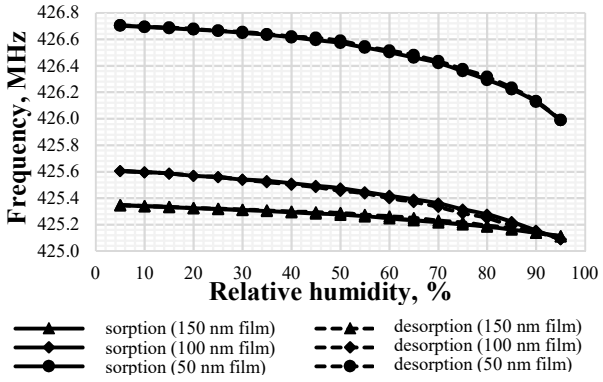

Fig. 1. Resonance frequency dependence on relative humidity for different film thicknesses.

The measurements were carried out using the Agilent E5071C vector network analyzer at a temperature of 23 ° C. Relative air humidity and temperature were accurately set using a HygroGen2 humidity calibration generator produced by Rotronic™. A characteristic feature of all the curves (Fig. 1) is the presence of an interval in which the frequency varies linearly with the variation of the relative humidity. This

interval is in the range of relative humidity values from 5 to 25% RH. A common feature for all the curves is the presence of an interval at which the frequency dependence is nonlinear, close to the parabolic law. It changes with the variation of the relative humidity. This interval corresponds to large values of relative humidity – more than 70%. Undoubtedly, both mechanisms coexist simultaneously for all values of relative humidity, but these two sections are areas of the characteristic prevalence of the mechanisms.

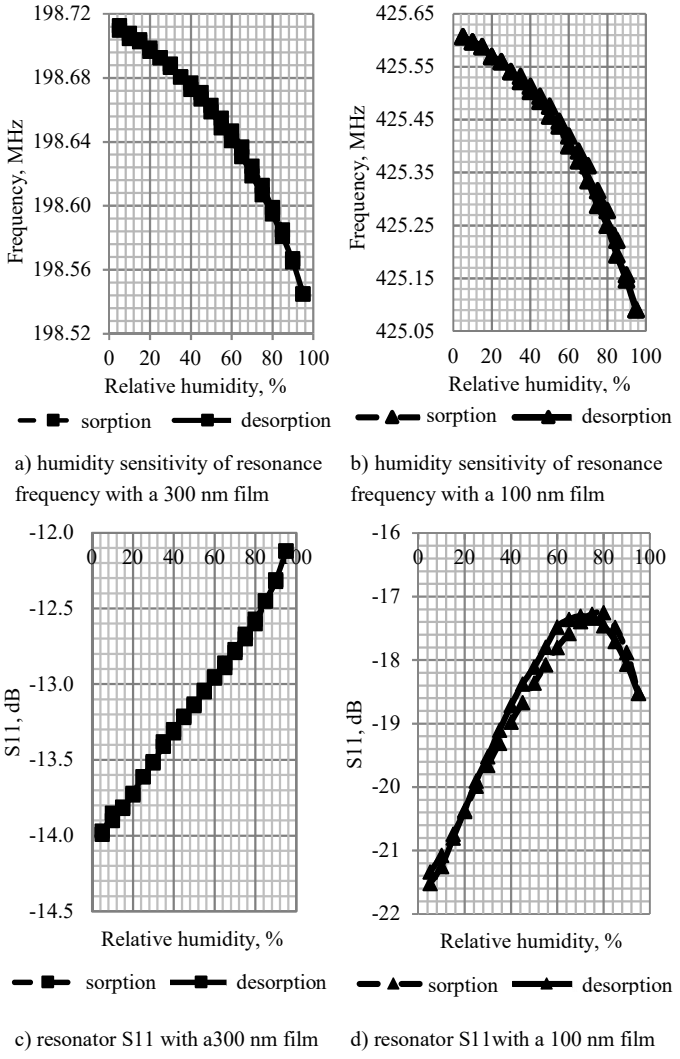

a) humidity sensitivity of resonance frequency with a 300 nm film

b) humidity sensitivity of resonance frequency with a 100 nm film

c) resonator S11 with a300 nm film

d) resonator S11with a 100 nm film

Fig. 2. Resonance frequency and S11 dependence on relative humidity.

Between 25 and 70% relative humidity, the effect of both of these regimes on the change in the resonance frequency has practically the same order of magnitude. It can be seen from the curves (Fig. 1) that the onset of the viscous mechanism of the sensitivity to humidity of the SAW resonator with the deposited film occurs earlier in thinner films. The hysteresis of the relative humidity dependence and the sensitivity of the sensor to humidity at different temperatures varied - the hysteresis is dependent on the air temperature and it decreased from ± 2% RH at 0 °C to ± 1% RH at 60 °C, while the relative sensitivity to humidity increased from 4.5-5.0 kHz / % RH at 0 °C to 6.5-7.0 kHz /% RH at 60 °C for 434 MHz resonators.

Thus, the sensitivity of the SAW resonator sensor to the relative humidity of air increases with decreasing film thickness up to the limiting technological value. In this work, the minimum thickness was 50 nm and it was limited by the capabilities of the spinning process. Also, reducing the thickness of the coating reduces the hysteresis frequency dependence on humidity of the sensor, which increases the accuracy of the readings.

After the deposition of films on the surface of the resonators, a drift of the parameters was observed, which was leveled by the use of an additional technological operation - aging. Also aging should reduce the effect aging of the sensing elements on the sensor long-term instability. The aging technique was developed on the basis of the generally accepted aging technique for sensitive to humidity resistive and capacitive elements, but with some modifications. Traditionally, the substrates and individual chips with the deposited film were annealed in air for several hours at a temperature of 120 °C. The adopted in this work process of aging consisted of several alternating cycles of 8 hours annealing time at a temperature of 80 °C and a humidity of 95% and the annealing cycles at same temperature and a humidity of 5%.

In the course of this work, the effect of compensation of the resonator impedance change with a change in the relative humidity in the region of high humidity values was observed leading to the transition of the S_{11} magnitude dependence on humidity from ascending to descending behavior [1]. This effect manifested itself in Nafion® films with a thickness of less than 150 nm. Fig. 2 shows the frequency dependence of the relative humidity and of the reflection coefficient S_{11} on the relative humidity for resonators with Nafion® film thicknesses of 300 and 100 nm. The measurements were carried out at a temperature of 23 °C.

The equivalent circuit of the SAW resonator is shown in Fig. 3 (from [4]).

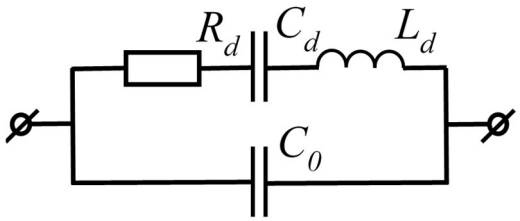

Fig. 3. Equivalent circuit of the SAW resonator.

Equations (3) - (6) from [5] relate the coefficient of electromechanical coupling (k^2) to resonance frequencies (f_r) and antiresonance (f_{ar}), and express the parameters of the equivalent circuit (dynamic capacitance C_d, inductance L_d, resistance R_d) through a link to the static capacitance of the resonator C_0 and to the Q-factor:

$$f_{ar} = \frac{f_r}{1 - \left(\frac{4 \cdot k^2}{\pi^2} \right)} \quad (3),$$

$$C_d = C_0 \cdot \left[\left(\frac{f_{ar}}{f_r} \right)^2 - 1 \right] \quad (4),$$

$$L_d = \frac{1}{(2\pi \cdot f_r)^2 \cdot C_d} \quad (5),$$

$$R_d = \frac{1}{2\pi \cdot f_r \cdot C_d \cdot Q} \quad (6).$$

The tentative explanation of the observed resonator impedance may be as follows: in the mass-sensitive regime of the sensitivity to humidity mechanism, the film becomes saturated with water vapor and its dielectric constant increases with increasing relative air humidity. With the increase of the dielectric permittivity of the film, the static capacitance of the high-frequency resonator increases, which causes an increase in the magnitude of S_{11} of the resonator from -21.5 dB to -17.4 dB (Fig. 2 d). With increasing film mass, as a consequence of moisture absorption, k^2 also decreases. But in the viscous regime, because of the interaction of the SAW with the water-saturated film, a decrease in the k^2 becomes more pronounced. This may partially compensate for the effect of the static capacitance increase and to move the magnitude of S_{11} back to -18.5 dB.

The observed S_{11} magnitude behavior and the associated effect of impedance variation at high relative humidity values in test samples with a small thickness of the humidity-sensitive film can result in full compensation of the humidity induced impedance mismatch. This experimentally observed feature is especially useful for wireless sensor interrogation, it allows to maintain the impedance matching conditions in the electrical circuit of the antenna connection to the sensor and thus to reduce the readout and interrogation distance susceptibility to the humidity level exposure.

IV. CONCLUSION

It is shown that, when creating chemical sensors based on SAW components, thinner selective coatings should be chosen to provide greater sensitivity to the targeted chemical, to reduce the attenuation of acoustic waves by the film, and to compensate for impedance mismatch. For Nafion® polymer, the recommended layer thickness should not exceed 100 nm.

REFERENCES

[1] Derkach M.M., Korlyakov A.V., “Study of relative humidity sensor based on surface acoustic waves”, Biotekhnosfera, 5 vol.47, pp. 23-26, 2016. *(In Russian)*.

[2] Malov V.V., Piezoelectric Resonance Sensors. 2nd ed. Moscow: Energoatomizdat, 1989, 272 p. *(In Russian)*.

[3] Wen Wang, Chunbae Lim, Keekeun Lee, Sangsik Yang, “Wireless surface acoustic wave chemical sensor for simultaneous measurement of CO_2 and humidity”. Journal of Micro/Nanolithography, MEMS and MOEMS 8, vol.3, p. 031306, 2009.

[4] Zelenka J. Piezoelectric Resonators and their Applications. Amsterdam: Elsevier Science, 1986, 301 p.

[5] Hashimoto K. Surface Acoustic Wave Devices in Telecommunications. Modelling and Simulation. Berlin: Springer, 2000, 330 p.

Nonlinear enhancement of locking range of mutually injection-locked oscillators for resonant sensing applications

Jérôme Juillard, Ali Mostafa, Pietro Maris Ferreira

GEEPS, UMR CNRS 8507, CentraleSupélec, UPSud, UPMC
Gif-sur-Yvette, France
jerome.juillard@centralesupelec.fr

***Abstract*— Sensor architectures based on coupled resonators are receiving increased interest from the resonant sensing community. Certain output metrics of such sensors have an increased sensitivity to the measurand, compared to conventional resonant sensors with frequency-modulated outputs. In the present paper, we investigate the properties of a differential architecture based on mutually injection-locked oscillators beyond the linear theoretical framework, by driving the resonators higher than the critical Duffing amplitude. Our results show that a trade-off must be made between sensitivity and measurement (locking) range. Experimental results obtained with our MILO architecture and the amplitude ratio output metric are also reported for the first time.**

Keywords—resonant sensors; coupled resonators; MEMS

I. INTRODUCTION

Recent years have seen the development of several sensor architectures based on coupled MEMS resonators, such as open-loop or closed-loop sensors based on mode-localization [1-4] or on mutually-injection locked oscillators (MILOs) [5-6]. Such sensors usually have output metrics whose sensitivity to the measurand is much greater than those of conventional resonant sensors with frequency-modulated outputs, although this does not necessarily entail a gain in sensor resolution, as was recently shown [7].

MILOs consist in two resonators with nominally identical resonance frequencies and quality factors, placed in a nonlinear feedback loop (Fig. 1) designed so that the resonators oscillate synchronously, typically in quadrature. When a stiffness mismatch ε is induced between the resonators (e.g. electrostatically), the resonance frequencies of the resonators are no longer identical. The nonlinear mixer then ensures that the system remains in a phase-locked state, but with a phase difference which deviates from 90°. The deviation of the phase-difference from its nominal value provides a high-sensitivity measurement of the stiffness mismatch between the resonators, and hence of the quantity of interest. In the particular case considered in this paper, the nonlinear mixer is designed to have maximal phase difference sensitivity to stiffness mismatch, as well as minimal fluctuations of the phase difference [7]. The mixer consists of two comparators, which ensure that the Barkhausen gain criterion is met in both loops, and of a digital coupling stage. Under the hypothesis that both resonators operate in the linear regime, one may show that the phase difference is an "optimal" output metric for this architecture, with maximal sensitivity to the measurand and minimal sensitivity to thermomechanical fluctuations [5].

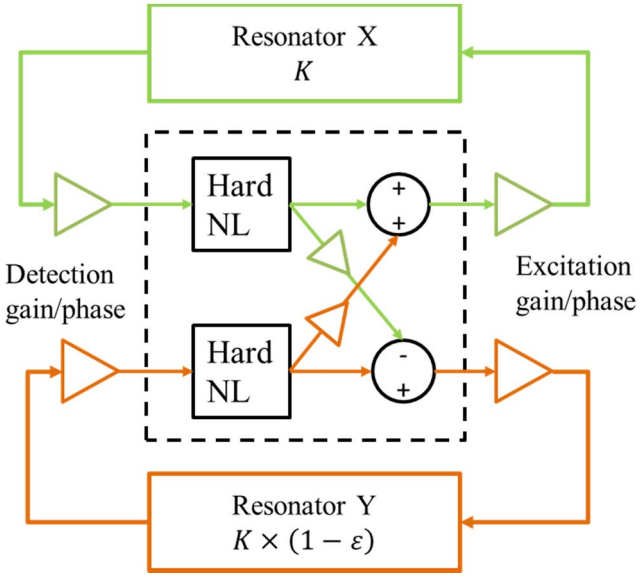

Fig. 1. High-level schematic of a MILO consisting of two resonators with a relative stiffness mismatch ε, a nonlinear mixer and gain/phase adaptation stages.

A key issue in MILOs is the measurement range, i.e. the range of values of ε for which the resonators remain synchronized. In the linear operation regime, this measurement range is inversely proportional to the quality factors of the resonators. Several recent studies [8-9] have pointed out the possibility of extending the synchronization domain of oscillators by operating them in the nonlinear regime. With the present paper and its companion [10], our aim is to investigate, theoretically and experimentally, some of the trade-offs that are entailed by nonlinearly-operated MILOs.

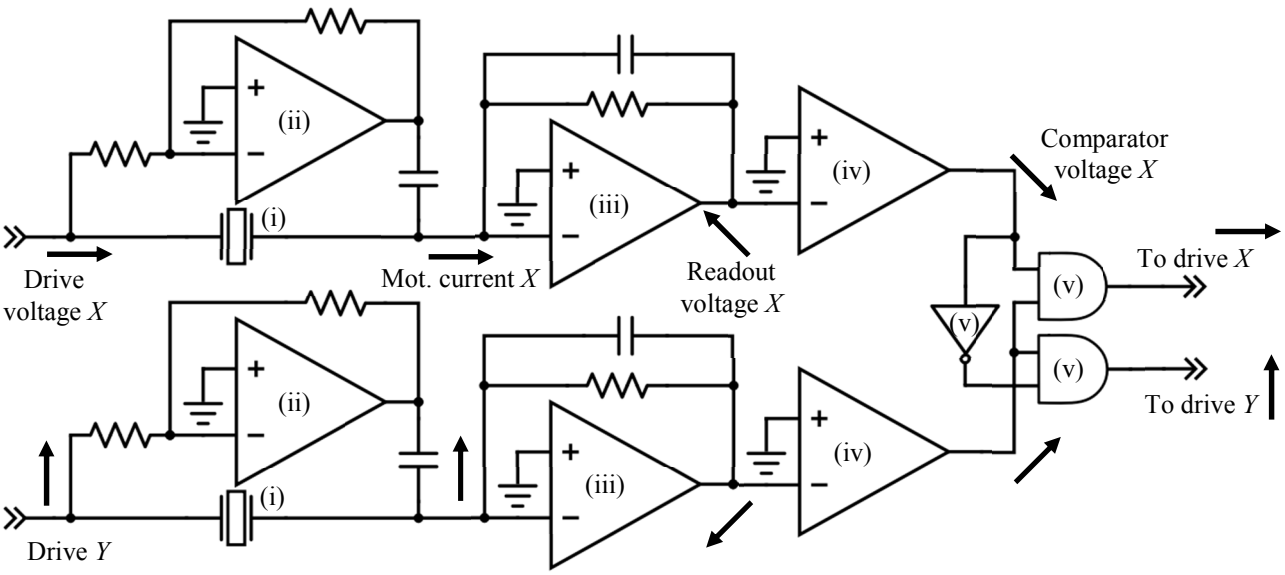

Fig. 2. Schematic of the studied MILO, consisting of resonators (i), feedthrough compensation stages (ii), readout stages (iii), comparators (iv) and logic gates (v). The resistive bridges used for setting drive voltage values have been omitted.The black arrows correspond to the phasor representation of the indicated electrical quantities.

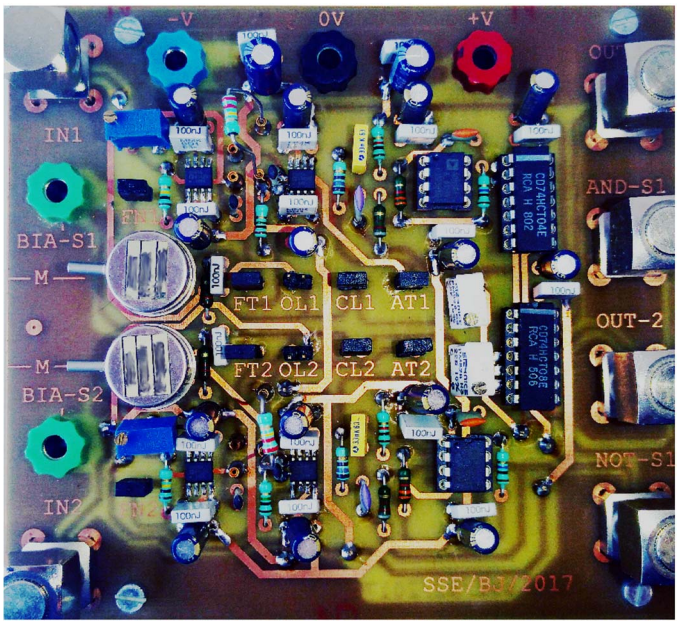

Fig. 3. PCB implementation of the MILO with discrete components.

Section II of this paper is dedicated to a description of our experimental setup. A simple model of the architecture is presented in section III. In section IV, we compare the experimental results to the ones derived from the model. In particular, we report for the first time measurements performed on MILOs with the amplitude ratio output metric. Section V is dedicated to concluding remarks.

EXPERIMENTAL SETUP

A schematic of the experimental setup is shown in Fig. 2, and a photograph of the corresponding printed circuit board (PCB) is shown in Fig. 3. The key elements here are (i) the resonators: these are high-Q (>10^4) capacitively-transduced resonant pressure sensors, with matched resonance frequencies around 70kHz, described at length in [11], (ii) an active feedthrough-cancellation stage, which effectively eliminates direct capacitive coupling between the input port and output port of the resonator, (iii) the analog readout stage, whose feedback impedance (half-resistive, half-capacitive) sets the phase in the loop and determines which oscillation mode is selected, and a digital mixer consisting of (iv) two comparators and (v) three logic gates. If feedthrough is correctly compensated, the current at the input of the readout stage is purely motional, and is thus in phase with the velocity of the resonator. The circuit is designed so that the voltage at the output of the comparator stage has a $-\pi/4$ phase-lag with respect to the motional current, or a $\pi/4$ phase-lead with respect to the mechanical motion. In the absence of mismatch between the resonators, this results in resonator Y oscillating with a $\pi/2$ phase-lead over resonator X, as illustrated in Fig. 2. Moreover, each resonator is then optimally driven at resonance, its drive voltage being in phase with its motional current, so that the influence of additive perturbations on frequency and phase difference stability is minimized, as shown in [5]. Note that the exact amount of delay introduced by each comparator is dependent on the relative amplitude of its input signal to the comparator hysteresis (a few mV).

The resonators can be finely tuned by adjusting their bias voltages. The (mechanical) oscillation amplitude can be adjusted independently by changing the ratio of the potentiometer bridge at the output of the mixer (not represented in Fig. 2). Here, we operate at a bias voltage close to 40V for both resonators, and an excitation signal varying between 250mV and 1.2V in peak amplitude, so that we span a range of

oscillation starting below the critical Duffing amplitude and finishing above.

The duty cycle of the mixer outputs (and hence the phase-difference between the resonators), and the RMS voltages at the output of the readout are measured with an MSO5204B oscilloscope. This lets us plot the evolution of the phase-difference and amplitude-ratio output metrics versus the detuning voltage, in the linear and nonlinear operation regimes. The results are reported in section IV.

II. MODELING

Provided the mechanical oscillation amplitude is small with respect to the electrostatic gap, the actuation nonlinearity can be neglected [11]. The system can then be modeled as two Duffing resonators, nonlinearly-coupled via the digital mixing stage. Following the harmonic balance approach of [5], a set of 4 (non-dimensionalized) equations is found:

$$\left(1+\frac{3}{4}\gamma X^2-\omega^2\right)X=\frac{F}{\pi}\left(\cos\psi+\cos\left(\psi+\phi\right)\right) \tag{1}$$

$$\frac{\omega}{Q}X=\frac{F}{\pi}\left(\sin\psi+\sin\left(\psi+\phi\right)\right) \tag{2}$$

$$\left(1-\varepsilon+\frac{3}{4}\gamma Y^2-\omega^2\right)Y=\frac{F}{\pi}\left(\cos\psi-\cos\left(\psi-\phi\right)\right) \tag{3}$$

$$\frac{\omega}{Q}Y=\frac{F}{\pi}\left(\sin\psi-\sin\left(\psi-\phi\right)\right) \tag{4}$$

where the state of the system consists in mechanical oscillation amplitudes X and Y, oscillation pulsation ω and phase difference ϕ, where F is the magnitude of the excitation force, proportional to the excitation voltage, Q is the quality factor of the resonators, ε is a detuning parameter, set by the bias voltage of the second resonator, γ is the *negative* Duffing coefficient, and $\psi=\pi/4$ is the phase difference between the comparator output and the mechanical motion of the resonator. For a given set of parameters, the state must usually be solved for with numerical methods.

When $\varepsilon=0$, the nominal state of the system verifies

$$\phi=\pi/2\,,\ X/Y=1\,. \tag{5}$$

The stability of the synchronized state can be assessed by a dynamic perturbation approach, as in [5]. This boils down to verifying that the roots of the characteristic polynomial

$$\begin{aligned}P(\lambda)=\lambda^2+\lambda\times\frac{1}{2Q}\left(3-\frac{1}{\sin\phi}\right)+\\ \frac{1}{4Q^2}\left(\frac{2}{1+\sin\phi}-\frac{3}{2}\gamma\frac{Q^3}{\omega^3}\frac{F^2}{\pi^2}\left(2\sin^2\phi+\sin\phi-1\right)\right)\end{aligned} \tag{6}$$

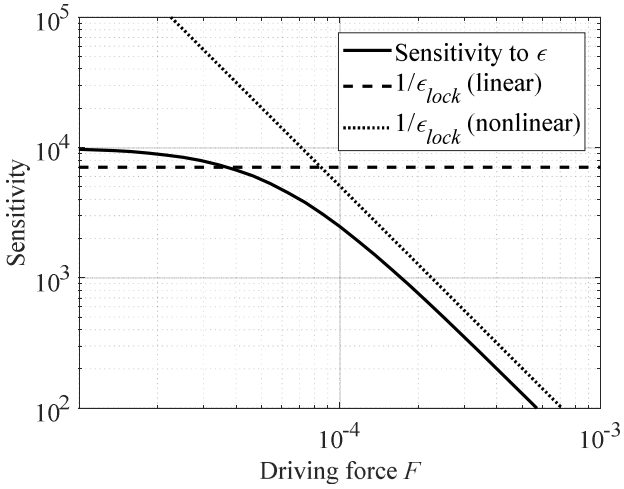

Fig. 4. Sensitivity to mismatch of the amplitude ratio and phase difference output metrics, versus driving force.

have negative real parts. From (6), it is plain that, for $\gamma=0$, the locking range (in terms of phase) is set by

$$\phi\in\left[\sin^{-1}\left(\frac{1}{3}\right),\pi-\sin^{-1}\left(\frac{1}{3}\right)\right]\approx\left[20°,160°\right]. \tag{7}$$

In the nonlinear regime, stability is governed by the sign of the term in factor of γ in (6), so that the synchronization range is then slightly reduced to:

$$\phi\in\left[\frac{\pi}{6},\frac{5\pi}{6}\right]=\left[30°,150°\right]. \tag{8}$$

Although the bounds on ϕ vary little from one regime to the other, those on ε are drastically changed. This is readily seen by subtracting (3) from (1), which yields:

$$\varepsilon=\frac{3}{4}\gamma\left(X^2-Y^2\right)+\frac{2}{Q}\frac{\cos\phi}{1+\sin\phi} \tag{9}$$

assuming $\omega\approx1$. In the linear regime, the first term on the right-hand side of (9) can be neglected, and (7) then corresponds to a measurement range

$$\left|\varepsilon\right|\le\varepsilon_{lock}=\frac{\sqrt{2}}{Q}. \tag{10}$$

whereas in the nonlinear regime, using (2) and (4) to express X and Y as functions of ϕ, (9) implies that

$$\left|\varepsilon\right|\le\varepsilon_{lock}=\frac{9\sqrt{3}}{8}\left|\gamma\right|\left(\frac{QF}{\pi}\right)^2. \tag{11}$$

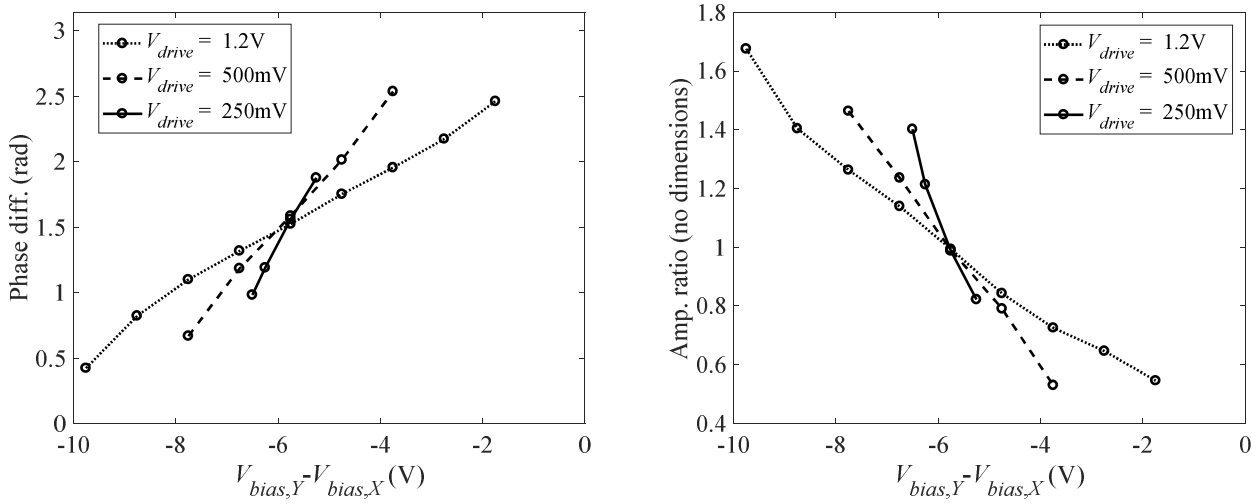

Fig. 5. Measured values of the phase difference (left) and amplitude ratio (right) output metrics vs. bias voltage difference for different values of the drive voltage.

These results, in agreement with [8-9], show that operating the MILO in the nonlinear regime is beneficial in terms of measurement range, with an obvious trade-off in terms of sensitivity to mismatch. Moreover, this is also true for the amplitude ratio output metric, which can be expressed simply as a function of ϕ by dividing (2) by (4). In particular, for the MILO considered here, the sensitivity to ε of the amplitude ratio close to $\varepsilon = 0$ is equal (in absolute value) to that of the phase difference. However, it should be noted that these output metrics have different sensitivities to additive random fluctuations, as shown in [10].

It is worth insisting that the nonlinear stability bounds established above are only valid when the Duffing coefficient γ is negative. In the case of a hardening Duffing nonlinearity, large-amplitude oscillation is not possible for the architecture considered here. This is readily seen by considering the $\varepsilon = 0$ case and letting $\phi = \pi/2$ in (6): for positive γ, the 0th-degree term of $P(\lambda)$ is cancelled out when

$$F \approx \pi / \sqrt{3\gamma Q^3} \ , \tag{12}$$

and the nominal steady-state solution (5) is unstable for larger values of the driving force. Thus, in order to operate beyond the critical Duffing amplitude, the parameters of a MILO should be chosen depending on the hardening or softening character of the nonlinearity. For example, the architecture described in section II with $\psi = \pi/4$ phase-shift in each branch is well-adapted to softening nonlinearities. But setting the phase-shift to $\psi = 3\pi/4$, so that the nominal state of the system is

$$\phi = -\pi/2 \, , \ X/Y = 1 \, , \tag{13}$$

leads to an architecture which is equally well-adapted to hardening nonlinearities.

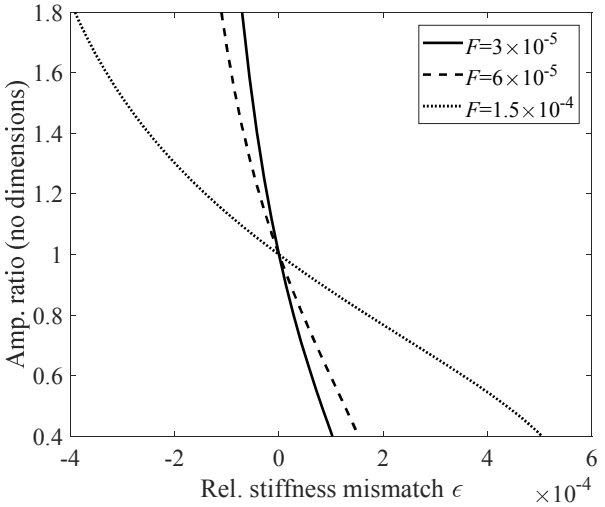

Fig. 6. Simulated value of the amplitude ratio vs. relative stiffness mismatch for different values of the driving force.

Illustrations of these theoretical results are given in the next section.

III. ILLUSTRATIONS AND RESULTS

We represent in Fig. 4 the sensitivity to ε of the phase difference and of the amplitude ratio output metrics, i.e.

$$\left.\frac{\partial \phi}{\partial \varepsilon}\right|_{\varepsilon=0} = -\left.\frac{\partial (X/Y)}{\partial \varepsilon}\right|_{\varepsilon=0} \tag{14}$$

versus the driving force F. System parameters are $Q = 10^4$, $\gamma = -10^{-3}$, which roughly corresponds to the parameters of the experimental setup at the chosen bias voltage [11]. One verifies that the sensitivity at $\varepsilon = 0$ is inversely proportional to the locking range ε_{lock} (10-11).

Similar results are obtained with the experimental setup of section II, as illustrated in Fig. 5. First of all, the bias voltage range over which the resonators remain synchronized clearly increases with the driving voltage. The nearly linear relation between the locking range and the drive amplitude indicates that the measurements correspond to a transition from the linear regime to the nonlinear regime, as Fig. 4 suggests. As a basis for comparison, the results obtained with our model and drive amplitudes $F = 3\times10^{-5}$, $F = 6\times10^{-5}$ and $F = 1.5\times10^{-4}$ are represented in Fig. 6, showing good qualitative agreement.

Discrepancies between our model and our measurements can be explained by several reasons. First of all, in this experiment, the bias voltage control was rather crude (100mV accuracy, controlled manually), which made it delicate to span the locking range, in particular when the sensitivity to mismatch is large, i.e. at small drive amplitudes. Furthermore, near the edges of the locking range, the amplitude of one of the motional signals decreases, so that the delay introduced by the comparator hysteresis becomes significant in that branch of the MILO, causing increased imbalance and reducing the locking range. This is also particularly true at smaller drive amplitudes. Finally, it should be pointed out that our idealized model assumes both resonators are identical (same quality factor, same Duffing coefficient, same actuation force) although this is not the case in the experimental setup: in particular several phenomena are neglected in the model, as the dependence of the Duffing coefficient and of the driving force on bias voltage (hence, on ε).

IV. CONCLUSION

We have presented in this paper a theoretical and experimental study of the properties of a MILO-based architecture, when the resonators are pushed into the nonlinear regime. It was shown that an increase of the synchronization range results from operating this architecture in the nonlinear regime.

Our experimental measurements are in good agreement with the idealized model results, showing the expected tradeoff between synchronization range and sensitivity [8-10]. Furthermore, the experimental results point out that operating at a larger amplitude makes it possible to relax the constraints of the electronic part of the system. Finally, our results confirmed that the amplitude ratio and phase difference output metrics are equivalent as far as sensitivity is concerned. However, it should be pointed out that these quantities are not equivalent as far as sensitivity to random fluctuations is concerned (e.g. thermomechanical noise), as shown in [10].

REFERENCES

[1] C. Zhao et al., "A review on coupled MEMS resonators for sensing applications utilizing mode localization," Sensors and Actuators A: Physical, vol. 249, pp. 93-111, 2016.

[2] P. Thiruvenkatanathan, J. Yan and A. A. Seshia, "Differential amplification of structural perturbations in weakly coupled MEMS resonators," IEEE Transactions on Ultrasonics, Ferroelectrics 9and Frequency Control, vol. 57, pp. 690-697, 2010.

[3] C. Zhao et al., "A closed-loop readout configuration for mode-localized resonant MEMS sensors" IEEE Journal of Microelectromechanical Systems, vol. 26, pp. 501-503, 2017.

[4] C. Zhao et al. "Experimental Observation of Noise Reduction in Weakly Coupled Nonlinear MEMS Resonators", IEEE Journal of Microelectromechanical Systems, vol. 26, pp. 1196-1203, 2017.

[5] J. Juillard, P. Prache and N. Barniol, "Analysis of mutually injection-locked oscillators for differential resonant sensing," IEEE Transactions on Circuits and Systems I: Regular Papers, vol. 63, pp. 1055-1066, 2016.

[6] P. Prache, et al., "Design and characterization of a monolithic CMOS-MEMS mutually injection-locked oscillator for differential resonant sensing", Sensors and Actuators A: Physical, vol. 269, pp. 160-170, 2017.

[7] J. Juillard, P. Prache, P.M. Ferreira, N. Barniol, "Ultimate limits of differential resonant MEMS sensors based on two coupled resonators", IEEE Transactions on Ultrasonics, Ferroelectrics and Frequency Control, 2018 (accepted).

[8] O. Shoshani, et al. "Phase noise reduction in a MEMS oscillator using a nonlinearly enhanced synchronization domain", IEEE Journal of Microelectromechanical Systems, vol. 25, pp. 870-876, 2016.

[9] P Taheri-Tehrani, M Defoort, DA Horsley, "Synchronization of a micromechanical oscillator in different regimes of electromechanical nonlinearity", Applied Physics Letters, vol. 111, pp. 183503, 2017.

[10] J. Juillard, A. Mostafa, P. M. Ferreira, "Analysis of resonant sensors based on mutually injection locked oscillators beyond the critical Duffing amplitude", European Frequency and Time Forum, 2018 (accepted).

[11] A. Brenes, J. Juillard, L. Bourgois, F. Vinci dos Santos, "Influence of the driving waveform on the open-loop frequency response of MEMS resonators with nonlinear actuation schemes", IEEE Journal of Microelectromechanical Systems, vol. 25, pp. 812-820, 2016.

Analysis of resonant sensors based on mutually injection-locked oscillators beyond the critical Duffing amplitude

Jérôme Juillard, Ali Mostafa, Pietro Maris Ferreira

GEEPS, UMR CNRS 8507, CentraleSupélec, UPSud, UPMC
Gif-sur-Yvette, France
jerome.juillard@centralesupelec.fr

***Abstract*— Sensor architectures based on coupled resonators are receiving increased interest from the resonant sensing community. Certain output metrics of such sensors have an increased sensitivity to the measurand, compared to conventional resonant sensors with frequency-modulated outputs. In the present paper, we extend our study of the properties of mutually injection-locked oscillators (MILOs) into the nonlinear domain, assuming the resonators are subject to cubic restoring forces. Our analysis shows that, depending on the softening or hardening character of the nonlinearity, some MILOs may be operated well above the critical Duffing amplitude. Moreover, it turns out that all the output metrics of such MILOs are not similarly affected by noise. A typical example is given, in which we show that, above the critical Duffing amplitude, phase difference measurements are limited by the A-f effect, whereas amplitude ratio measurements are not. These theoretical results are supported by transient simulations.**

Keywords—resonant sensors; coupled resonators; MEMS

I. INTRODUCTION

Recent years have seen the development of several sensor architectures based on coupled MEMS resonators, such as open-loop or closed-loop sensors based on mode-localization [1-4] or on mutually-injection locked oscillators (MILOs) [5-6]. So far, our study of coupled architectures has been confined to their operation in the linear regime, below the critical Duffing amplitude which marks the onset of the A-f effect in conventional resonant sensors based on a single resonator (with a cubic nonlinearity) [7]. In this framework, we have shown that the increased sensitivity to the quantity of interest of the output metrics of coupled architectures is always compensated by an increased sensitivity to external fluctuations [8], such as thermomechanical noise [9]. Thus, in the linear regime, there is little to be gained in terms of "ultimate" resolution when two coupled resonators are used instead of a single one.

With the present paper, we show that this conclusion is no longer valid in the nonlinear domain, as far as MILOs are concerned. MILOs consist in two resonators with nominally identical resonance frequencies and quality factors, placed in a nonlinear feedback loop designed so that the resonators oscillate in quadrature. When a stiffness or mass mismatch ε is induced between the resonators (e.g. electrostatically), the resonance frequencies of the resonators are no longer identical. The nonlinear mixer then ensures that the system remains in a phase-locked state, but with a phase difference which deviates from its nominal value. Within a certain measurement range, this deviation then provides a high-sensitivity measurement of the stiffness mismatch between the resonators, and hence of the quantity of interest. Depending on the parameters of the architecture, other output metrics may also be used, such as the ratio of the motional amplitudes of the resonators. It is shown in [10] that operation in the nonlinear regime of such MILOs may result in an increased measurement range, at the cost of a decreased sensitivity.

The theoretical framework of this paper, described in section II, is limited to a MILO consisting of two nominally identical, nonlinearly coupled resonators with cubic stiffness. In section III, we apply perturbation techniques to the governing equations of the system in order to perform sensitivity analysis. We show that the ultimate resolution that can be expected of the phase difference or pulsation output metrics is limited by the A-f effect. This is as opposed to the ultimate resolution of the amplitude ratio output metric, which is improved as the driving force and the oscillation amplitude are increased, even above the critical Duffing amplitude. These theoretical results, based on a quasi-static analysis, are validated by transient simulations. Section IV is dedicated to a discussion of our results, and section V to concluding remarks and perspectives.

II. THEORETICAL FRAMEWORK

We consider the MILO depicted in Fig. 1, which is almost the same as the one studied in [10]. It consists of two resonators with a softening Duffing nonlinearity (characterized by a Duffing coefficient $\gamma < 0$), a nonlinear mixer and a $\pi/4$ phase-shift in both branches. Following the harmonic balance approach of [5], in the absence of external perturbations, the system is governed by a set of 4 (non-dimensionalized) equations

$$\mathbf{g}(\mathbf{s}, \varepsilon) = \mathbf{0}, \tag{1}$$

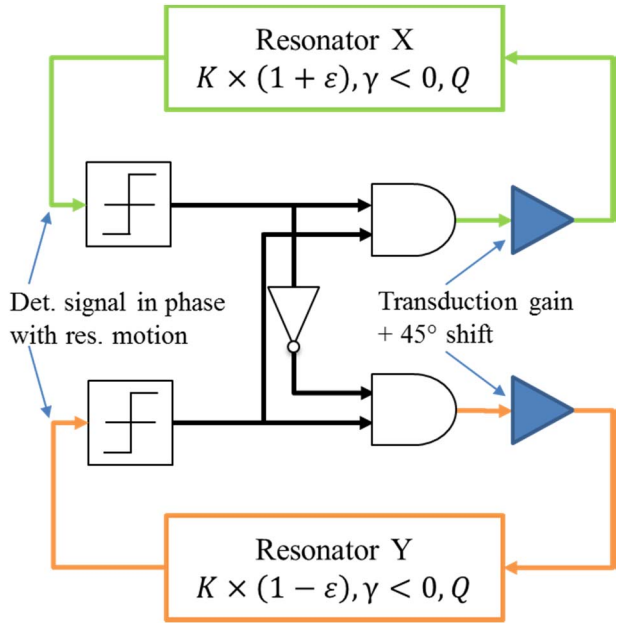

Fig. 1. High-level schematic of a MILO consisting of two nonlinear resonators with a relative stiffness mismatch 2ε, a digital nonlinear mixer and two gain/phase adaptation stages.

where

$$g_1 = \left(1+\varepsilon+\frac{3}{4}\gamma X^2-\omega^2\right)X - \frac{F}{\pi}\left(\cos\frac{\pi}{4}+\cos\left(\frac{\pi}{4}+\phi\right)\right) \quad (2)$$

$$g_2 = \frac{\omega}{Q}X - \frac{F}{\pi}\left(\sin\frac{\pi}{4}+\sin\left(\frac{\pi}{4}+\phi\right)\right) \quad (3)$$

$$g_3 = \left(1-\varepsilon+\frac{3}{4}\gamma Y^2-\omega^2\right)Y - \frac{F}{\pi}\left(\cos\frac{\pi}{4}-\cos\left(\frac{\pi}{4}-\phi\right)\right) \quad (4)$$

$$g_4 = \frac{\omega}{Q}Y - \frac{F}{\pi}\left(\sin\frac{\pi}{4}-\sin\left(\frac{\pi}{4}-\phi\right)\right) = 0 \quad (5)$$

where the state of the system

$$\mathbf{s} = \begin{bmatrix} X & Y & \omega & \phi \end{bmatrix}^T \quad (6)$$

consists in mechanical oscillation amplitudes X and Y, oscillation pulsation ω and phase difference ϕ, where F is the magnitude of the excitation force, Q is the quality factor of the resonators, and ε is a detuning parameter, corresponding to the physical quantity of interest one seeks to measure.

Note that this detuning parameter appears in (2) *and* in (4), with opposite signs, as opposed to [10] for example. Consequently, when $\varepsilon = 0$, the nominal state of the system verifies, as in [10]

$$\phi = \pi/2\,,\ X/Y = 1 \quad (7)$$

but the sensitivity to mismatch of the output metrics is multiplied by 2 compared to the cases studied in our previous studies, and the locking range of the MILO (in terms of mismatch) is also divided by 2.

III. Sensitivity Analysis of a Nonlinear MILO

A. Definition of a figure of merit

The performance of this architecture as a sensor can be studied with rather simple sensitivity analysis techniques. For example, the sensitivity of the system state $\mathbf{s}$ to ε may be derived from (1) as follows

$$\begin{aligned} &\mathbf{g}(\mathbf{s}+\delta\mathbf{s}, \varepsilon+\delta\varepsilon) = \mathbf{0} \Rightarrow \\ &\mathbf{g}(\mathbf{s}, \varepsilon) + \mathbf{J}_\mathbf{s} \times \delta\mathbf{s} + \begin{bmatrix} X & 0 & -Y & 0 \end{bmatrix}^T \delta\varepsilon \approx 0 \Rightarrow, \\ &\delta\mathbf{s} \approx -\mathbf{J}_\mathbf{s}^{-1} \times \begin{bmatrix} X & 0 & -Y & 0 \end{bmatrix}^T \delta\varepsilon \end{aligned} \quad (8)$$

where $\mathbf{J}_\mathbf{s}$ is the jacobian of $\mathbf{g}$ with respect to state $\mathbf{s}$. The sensitivity of any output metric $M(\mathbf{s})$ to ε can then be derived from (8) as

$$\frac{dM}{d\varepsilon} = -\frac{dM}{d\mathbf{s}} \times \mathbf{J}_\mathbf{s}^{-1} \times \begin{bmatrix} X & 0 & -Y & 0 \end{bmatrix}^T. \quad (9)$$

The sensitivity of $M(\mathbf{s})$ to other sorts of fluctuations may be established in a similar manner. In the case of thermomechanical fluctuations, which is of interest in order to determine the "ultimate" performance attainable with a given output metric, one must consider the perturbed system:

$$\mathbf{g}(\mathbf{s}+\delta\mathbf{s}, \varepsilon) = \mathbf{n} \quad (10)$$

where the components of $\mathbf{n}$ are independent, slowly-fluctuating "forces", with equal magnitudes. The sensitivity of $M(\mathbf{s})$ to these random fluctuations can be defined as the RMS value of the sensitivities to the independent noise components, i.e.

$$\frac{dM}{dn} = \sqrt{\sum_{i=1}^{4}\left(\frac{dM}{dn_i}\right)^2}\,. \quad (11)$$

A first-order expansion of (10) yields:

$$\delta\mathbf{s} \approx \mathbf{J}_\mathbf{s}^{-1} \times \mathbf{n}\,, \quad (12)$$

From (11) and (12), it follows that the sensitivity of $M(\mathbf{s})$ to random fluctuations is:

$$\frac{dM}{dn} = \left\| \frac{dM}{d\mathbf{s}} \times \mathbf{J}_\mathbf{s}^{-1} \right\|_2. \quad (13)$$

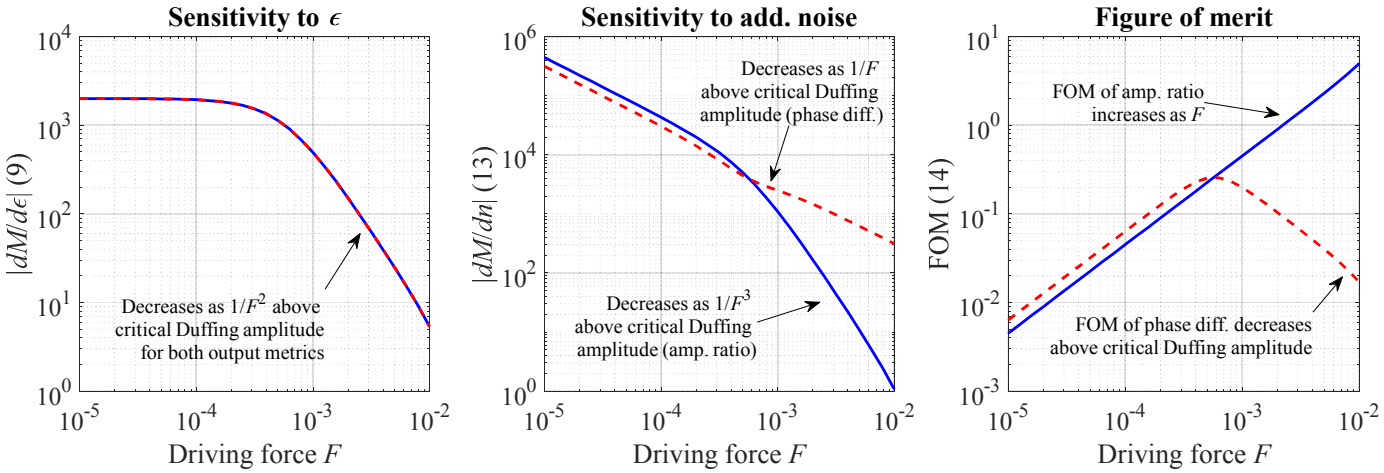

Fig. 2. Performance of amplitude ratio (solid blue line) and of phase difference (dashed red line) output metrics at ε=0 vs. driving force, for Q=10^3 and γ=-10^{-2}: sensitivity to ε (left), sensitivity to additive noise (center), and figure of merit (right).

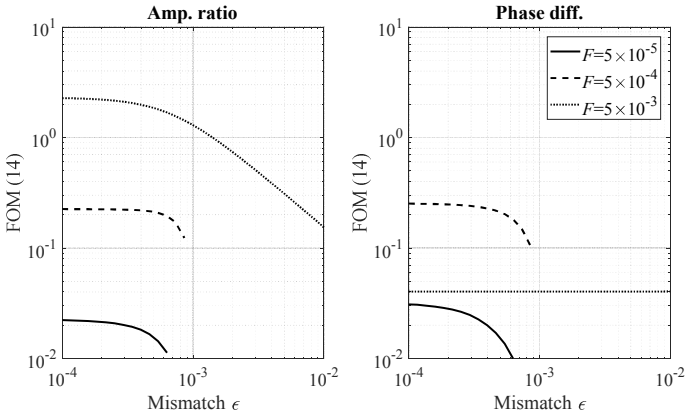

Fig. 3. Figure of merit of the amplitude ratio (left) and phase difference (right) output metrics vs. ε, for different values of the driving force, other system parameters as in Fig. 2.

Equations (9) and (13) may be used to define a figure of merit for $M(\mathbf{s})$, as the ratio of the sensitivity to ε to the sensitivity to noise, i.e. :

$$\mathrm{FOM}(M)=\frac{|dM/d\varepsilon|}{dM/dn} \tag{14}$$

which should be maximized in order to improve sensor performance, i.e. sensitivity to ε and immunity from noise.

B. Comparison of different output metrics

In the linear regime, close to $\varepsilon=0$ we find that

$$\mathrm{FOM}(\phi)=2\times\frac{QF}{\pi}=\sqrt{2}\times\mathrm{FOM}\left(\frac{X}{Y}\right), \tag{15}$$

so that, for the considered architecture phase difference is a slightly better output metric than amplitude ratio, although both have the same sensitivity to ε [10]. The figure of merit increases linearly with the amplitude of the drive, as can be expected [5,8], until the critical Duffing amplitude is neared.

Above the critical Duffing amplitude, the situation is almost dramatically different: while the figure of merit of the amplitude ratio output metric keeps increasing with the drive amplitude, that of the phase difference starts decreasing, a signature of the A-f effect (or A-ϕ in the present case). This is illustrated in Fig. 2.

More accurately, above the critical Duffing amplitude, the sensitivity to ε of both output metrics starts dropping as F^{-2}. From (13), one may show that the sensitivity to noise of the phase difference output metric decreases as F^{-1} in the nonlinear regime (as in the linear regime, in fact). Thus, the figure of merit for ϕ decreases as F^{-1}. On the other hand, the sensitivity to noise of the amplitude ratio output metric decreases as F^{-3} in the nonlinear regime (as opposed to F^{-1} in the linear regime). Thus, the figure of merit for the amplitude ratio keeps increasing proportionally to F, as it does below the critical Duffing amplitude. In fact, we have

$$\mathrm{FOM}\left(\frac{X}{Y}\right)\approx\sqrt{2}\times\frac{QF}{\pi} \tag{16}$$

regardless of the operating regime, as shown in Fig. 2.

It is worth noting that this remarkable property of the amplitude ratio output metric is valid only in a reduced range around $\varepsilon=0$, in spite of the nonlinear enhancement of the locking range of the MILO [10]. Although no closed-form formula has been derived for the range of validity of (16), our calculations suggest that this result holds only within the *linear* locking range of the architecture, as Fig. 3 indicates.

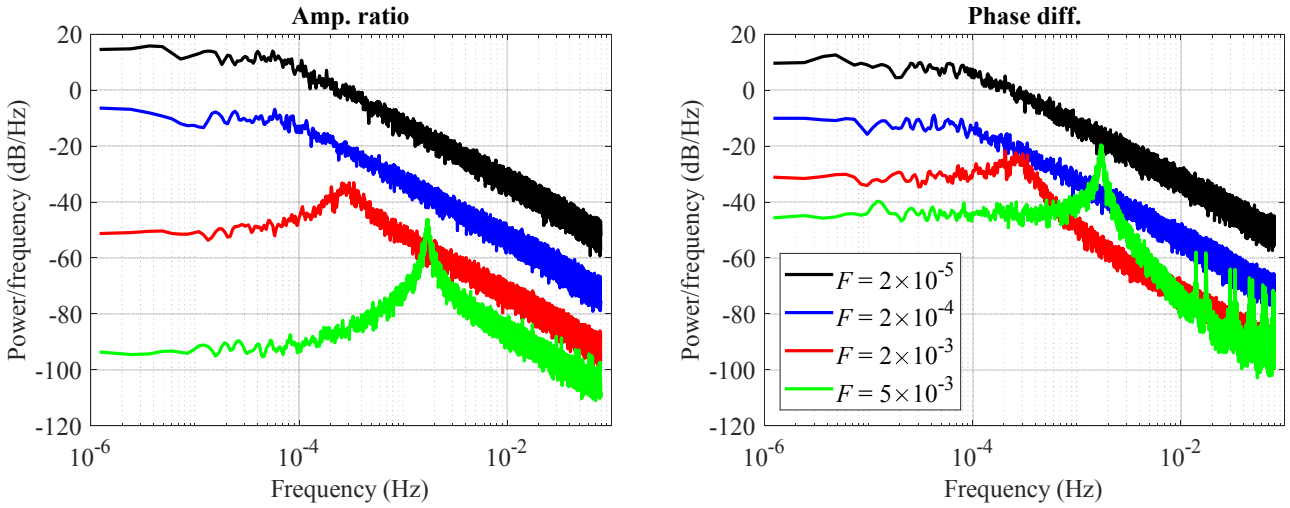

Fig. 4. Noise spectra obtained by transient simulation for the amplitude ratio (left) and phase difference (right) output metrics, with ε=0, Q=10^3 and γ=-10^{-2} and different values of the driving force.

C. *Transient simulation*

These theoretical results, based on a quasi-static analysis, are validated by transient simulations, with Simulink, of a MILO with parameters $Q=10^3$, $\gamma=-10^{-2}$ and $\varepsilon=0$. Independent white noise sources are placed at the inputs of the resonators to simulate the effect of thermomechanical forces. Four values of driving force are simulated: $F=2\times10^{-5}$, $F=2\times10^{-4}$, $F=2\times10^{-3}$, $F=5\times10^{-3}$, with the noise power kept constant. The power spectrum of the amplitude ratio and phase difference fluctuations are plotted in Fig. 4.

These simulated results are in very good agreement with our theory, which predicts that, in the last three simulations, the near-DC power of the phase difference should be 21dB, 41dB and 54dB below that of the linear case ($F=2\times10^{-5}$), whereas that of the amplitude ratio should be 21dB, 62dB and 106dB below the linear case.

It is also worth noting that a resonance peak appears at the cutoff frequency of the system at large driving forces. A quantitative analysis of this phenomenon would require a more involved dynamic perturbation analysis, as in [5].

IV. Discussion

It should be stressed that these results concerning MILO output metrics in the nonlinear regime can be extended to other MILO architectures than the one considered in this paper. For example, the previous results also apply when the nonlinearity is hardening ($\gamma>0$) and the phase-shift of the MILO is chosen to be $3\pi/4$ instead of $\pi/4$ (the only difference being that the nominal value of the phase difference in the absence of mismatch is then $\phi=-\pi/2$). Likewise, a phase-shift of $\pi/2$ (arguably easier to implement than $\pi/4$ or $3\pi/4$) results in an architecture with two possible oscillatory states [5]: one, with $\phi=\pi/2$, is stable above the critical Duffing amplitude when $\gamma<0$, the other, with $\phi=-\pi/2$, when $\gamma>0$. Both of these oscillatory states have qualitatively similar properties to the one studied in the previous sections. More generally, similar results hold provided the amplitude ratio is an output metric at all, i.e. provided its sensitivity to ε is non-zero, even when the resonators are not perfectly matched in terms of Duffing coefficient, quality factor or driving force. Finally, another point of interest is that (16) is independent of the value of γ: although this calls for a formal proof, this suggests that (16) may be valid for other types of static nonlinearities (e.g. non-polynomial).

Although such results seem to open the way for interesting new paradigms of resonant sensors, whose performance are not limited by nonlinear phenomena, one should also consider their practical limitations. First of all, the amplitude ratio is an analog quantity, as opposed to frequency or phase-difference: thus a sensor using amplitude ratio as an output metric will require analog-to-digital conversion (ADC) stages, with an added cost in terms of surface and power consumption compared to quasi-digital solutions. Moreover, the requirements on the ADC stage(s) are likely to become more stringent as the amplitude increases, because of the reduced sensitivity of such MILOs in the nonlinear regime [10]. In this respect, advantageous design tradeoffs can probably be scavenged from the field of (amplitude modulated) mode-matched gyroscopes [11-12], with which MILOs share many common points. Finally, note that our results are significant only for sensors that are limited by additive noise at the input of the resonator [7,9] and do not apply in the case of random parametric fluctuations, such as stiffness fluctuations [13].

V. Conclusion

We have presented in this paper a theoretical analysis of the properties of a MILO-based architecture, when the resonators are pushed into the nonlinear regime. A general figure of merit for the different output metrics used in coupled architectures was proposed. In the case of the framework defined in section II, it was shown that this figure of merit increases monotonically with drive amplitude, whether below or above the critical Duffing amplitude, when the amplitude ratio is used as an output metric. On the other hand, phase difference does not perform as well in the nonlinear regime, its figure of merit

decreasing with the drive amplitude once the A-f effect kicks in.

Our continuing work on this subject is dedicated to generalizing our formal approach to other architectures and other nonlinearities (e.g. damping, excitation and detection), deriving optimal output metrics, and obtaining an experimental validation of our results.

REFERENCES

[1] C. Zhao et al., "A review on coupled MEMS resonators for sensing applications utilizing mode localization," Sensors and Actuators A: Physical, vol. 249, pp. 93-111, 2016.

[2] P. Thiruvenkatanathan, J. Yan and A. A. Seshia, "Differential amplification of structural perturbations in weakly coupled MEMS resonators," IEEE Transactions on Ultrasonics, Ferroelectrics 9and Frequency Control, vol. 57, pp. 690-697, 2010.

[3] C. Zhao et al., "A closed-loop readout configuration for mode-localized resonant MEMS sensors" IEEE Journal of Microelectromechanical Systems, vol. 26, pp. 501-503, 2017.

[4] C. Zhao et al. "Experimental Observation of Noise Reduction in Weakly Coupled Nonlinear MEMS Resonators", IEEE Journal of Microelectromechanical Systems, vol. 26, pp. 1196-1203, 2017.

[5] J. Juillard, P. Prache and N. Barniol, "Analysis of mutually injection-locked oscillators for differential resonant sensing," IEEE Transactions on Circuits and Systems I: Regular Papers, vol. 63, pp. 1055-1066, 2016.

[6] P. Prache, et al., "Design and characterization of a monolithic CMOS-MEMS mutually injection-locked oscillator for differential resonant sensing", Sensors and Actuators A: Physical, vol. 269, pp. 160-170, 2017.

[7] D. K. Agrawal, A. A. Seshia, "An analytical formulation for phase noise in MEMS oscillators", IEEE Transactions on Ultrasonics, Ferroelectrics and Frequency Control, vol. 61, pp. 1938-1952, 2014.

[8] J. Juillard, P. Prache, P.M. Ferreira, N. Barniol, "Ultimate limits of differential resonant MEMS sensors based on two coupled resonators", IEEE Transactions on Ultrasonics, Ferroelectrics and Frequency Control, 2018 (accepted).

[9] A. N. Cleland, M. L. Roukes, "Noise processes in nanomechanical resonators", Journal of Applied Physics, vol. 92, pp. 2758-2769, 2002.

[10] J. Juillard, A. Mostafa, P. M. Ferreira, "Nonlinear enhancement of locking range of mutually injection-locked oscillators for resonant sensing applications", European Frequency and Time Forum, 2018 (accepted).

[11] I. Prikhodko et al. "Mode-matched MEMS Coriolis vibratory gyroscopes: myth or reality?", IEEE/ION Position, Location and Navigation Symposium, 4 pp., 2016.

[12] M. F. Zaman, A. Sharma, F. Ayazi, "High performance matched-mode tuning fork gyroscope", IEEE International Conference on MEMS, pp. 66-69, 2006.

[13] M. Sansa, et al. "Frequency fluctuations in silicon nanoresonators", Nature Nanotechnology, vol. 11, pp. 552-558, 2016.

Long term stabilization of large frame laser gyroscopes

F. Stefani[*†], N. Beverini[*†], G. Carelli[*†], D. Ciampini[†], A. Di Virgilio[*], F. Fuso[†], U. Giacomelli[*†], E. Maccioni[*†]

[†]Dipartimento di Fisica "E. Fermi"
Università di Pisa
Pisa, Italy
fabio.stefani@unipi.it

* INFN - Istituto Nazionale di Fisica Nucleare
Sezione di Pisa
Pisa, Italy

***Abstract*—The operation of a large frame ring laser gyroscope (RLG) with ultimate sensitivity requires the development of a very careful active control of the ring geometry. This can be obtained in a square ring by measuring against a reference laser the diagonals length and eventually implementing a procedure to equalize them. The technique to measure and to stabilize the diagonals has been tested on GP2, a RLG of reduced dimension installed in INFN laboratories in Pisa. A resolution better than 1 ppm, limited by the local anthropic noise, has been obtained.**

Keywords—Sagnac effect, Laser gyroscopes, Absolute length measurements.

I. INTRODUCTION

Large frame ring laser gyroscopes (RLG), which exploit Sagnac effect, are the more sensitive device for detecting angular motions in a very large range of frequency extending from kHz down to μHz and below. The beat note f_S between the frequencies of the two laser beams counter-propagating in the optical cavity is proportional to the rotational speed Ω of the apparatus against an inertial reference through a scale factor $k_S = \frac{4A}{\lambda P}\cos\vartheta$, where P is the perimeter, A the enclosed area, λ is the laser wavelength, and ϑ is the angle between the rotational axis and the normal to the ring plane.

GINGER (Gyroscopes IN General Relativity) is a proposal for a large-frame 3-dimensional array of ring laser gyroscopes that intended to be mounted inside the underground Gran Sasso Laboratories (LNGS), with the final aim of measuring in a ground laboratory the Lense-Thirring effect induced by the rotating Earth, as foreseen by General Relativity [1]. This requires achieving a resolution in angular velocity better than 10^{-14} rad/s, which is about a factor 10 below the present state-of-art performance obtained with "G" [2], the 4x4 m^2 square laser gyroscope active in the Geodetic Observatory of Wettzell (Bavaria). Enlarging the side of structure to 6-7 m would improve the shot noise limit and reduce the coupling by the backscattering between the two counter-rotating beams [3]. Long term stability will be also largely improved by a deep underground location, as the LNGS, that warrants isolation from meteorological noise. In order to validate the site, a gyroscope named Gingerino, with the side of 3.60 m, has been installed in LNGS. It has been working continuously unattended sinc more than six months with a duty factor better than 90%. In spite of the absence of active control of the geometry, it shows an excellent long-term stability.

G long-term stability is passively based on a monolithic structure in a zero-thermal dilatation glass (Zerodur) that cannot be replicated in an enlarged scale. For this reason, an active control of the geometry on an hetero-lithic structure becomes necessary. An advantage of active control is that it allows optimizing the laser cavity geometry. Indeed, the requirement of stability can be mitigated if the optical cavity is a regular polygon: in this case the ratio A/P in the gyroscope scale factor is only a quadratic function of the deviation from the perfect geometry [4].

In particular, in a ring square optical cavity the two mirrors placed in the opposite corners define two linear Fabry-Pérot (FP) resonators along the diagonals that can be interrogated and controlled by a laser beam referenced to a length standard, offering the opportunity to control the geometry. A procedure to measure and compare the absolute length of the two FP optical cavity through a three frequency modulation technique has been described in detail in [5]. In this way the absolute value of the FP lengths can be measured and the optical cavity can eventually brought close to the regular shape.

II. GP2 TEST RING LASER

The technique has been tested on GP2, a square RLG with the side of 1.60 m that is in operation in the INFN laboratory in Pisa (Fig.1). The laser cavity is mounted on a granite slab whose plane lies orthogonal to the Earth rotation axis. This orientation was chosen because it minimizes the sensitivity of the Sagnac frequency on tilting. The ring laser is operating on the He-Ne 632.8 nm transition.

As length reference we use a He-Ne iodine-stabilized laser provided by the Institute of Laser Physics of Novosibirsk, Russia. The available power was only a few hundred microwatt; then we transferred through optical injection locking its frequency stability to a diode laser. In this way the available output power of this master-slave laser system is about 5 mW, with a Full Width at Half Maximum linewidth (FWHM) of the order of 100 kHz. The radiation is coupled to a single mode polarization maintaining fiber and then split in two parts that are used to interrogate independently the two diagonals.

978-1-5386-5620-4/18/$31.00 ©2018 IEEE

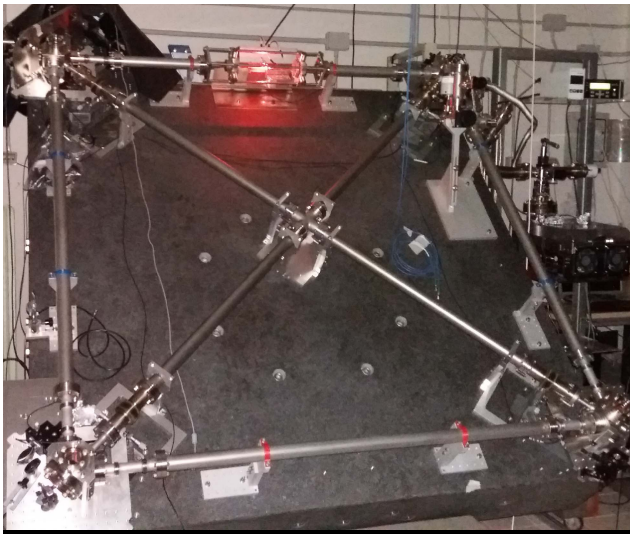

Fig. 1. GP2 laser gyroscope.

The experimental set up for each diagonal is shown in Fig. 2. It follows the general scheme of [5]. The laser radiation is launched into the FP cavity on the TEM00 mode. The reflected radiation is monitored through a fast PIN photodiode. Its signal is sent in parallel to the two input channels of a Zurich HF2LI high frequency lock-in amplifier. A second photodiode and a webcam observe the FP transmitted radiation in order to help the optical alignment. The laser frequency is controlled by an Acousto-Optical Modulator (AOM) and is modulated by an Electro-Optical Modulator (EOM).

The Zurich lock-in amplifier drives the whole control system with two independent servo loops; it has built-in digital PID controllers with fully customizable parameters in order to implement the required closed loop controls.

The first one is based on a Pound-Drever-Hall scheme (The first one is based on a Pound-Drever-Hall scheme (PDH) that locks the laser on the FP resonance. Channel 1 of the Zurich lock-in is devoted to this task. The laser radiation is modulated by the EOM at the frequency of OMEGA A = 23.3 MHz (mod OUT 1 of Zurich lock-in). GP2 was designed with the mirrors rigidly fixed to the corner towers of the vacuum chamber. To move the mirrors is necessary to move by PZT the whole tower mass. This limits the bandwidth of the correction dynamics at some Hz. Then, to keep the laser resonant with the FP in spite of mechanical and acoustic noise we act on the AOM, while the PZT corrects only the long term drift. For this purpose,the demodulated signal at OMEGA A, after being processed by an integrated digital PID controller (actuator 1 Zurich output) is sent to the Voltage Controlled Oscillator (VCO) that drives the AOM; the same control signal is sent in parallel through an analog integrator stage (with a time constant of 12.5 s) to the PZT driver.

The second circuit locks a second VCO to the 8th harmonic of the FP free spectral range (FSR) around 530.3 MHz and operates on Channel 2 of the lock-in amplifier. It has the task to give the order of interference of the interrogating laser radiation in TEM00*n* mode of FP, resolving the wavelength ambiguity. The VCO frequency is dithered at OMEGA C = 141 kHz by Zurich mod OUT 2 and the resulting signal is superimposed to the EOM driving signal. The component at OMEGA C of the photodiode signal is sent at the Zurich demod IN 2 input, processed by an integrated PID controller (actuator 2 output) and routed to the VCO. The FSR frequency is read by a frequency meter and stored and the optical length *l* of the FP is calculated

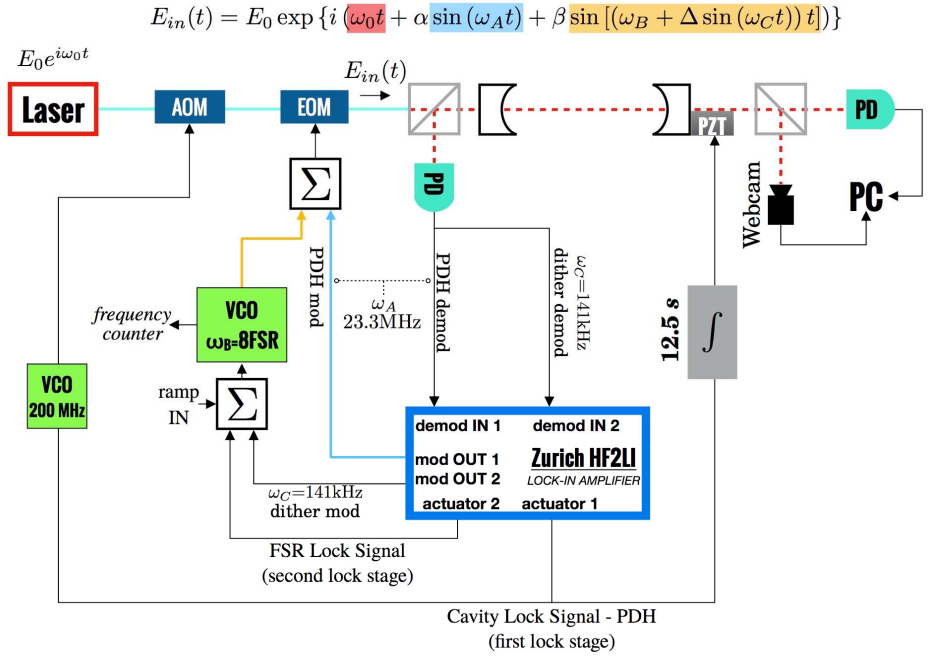

Fig. 2. Experimental apparatus for the absolute length measurement of one diagonal of GP2. The system was duplicated, starting from the same frequency stabilized laser, on the other diagonal in order to acquire both data in parallel.

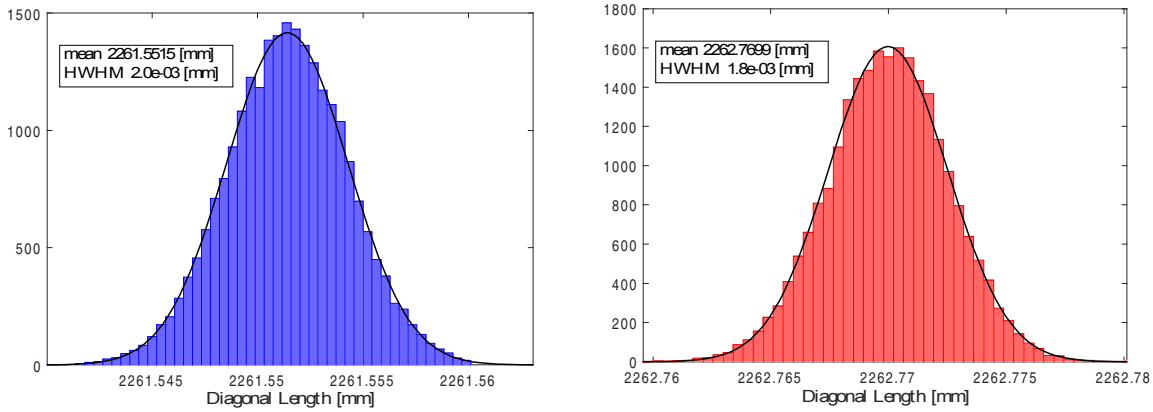

Fig. 3. Experimental measure of the two diagonal of GP2. Data was taken in parallel on the two diagonal over 14 hours. Black line is the best fit with a Gaussian profile.

as $l = \frac{c}{2\,FSR}$. An external ramp can be added in input to the VCO to manually find at the initial locking point.

As said before, this whole apparatus is duplicated in order to measure in parallel the two diagonals.

III. Results and Discussion

Fig. 3 shows the results of a run of data acquisition of the FSR of the two diagonal cavities taken over 14 hours. A single channel frequency meter read both the resonance frequencies at a rate of 1 s^{-1}, switching between the two VCOs every 30 s. The fit with a Gaussian profile of the data gives a value of the lengths of 2261.55154 mm and 2262.76985 mm, with a HWHM respectively of 2.0 µm and 1.8 µm. The accuracy of the diagonal length measurement is evaluated according to [6]. As previously stated, the length was inferred from the 8th harmonics of the FSR frequency, measured with a Keysight 53220A frequency counter with gate time of 1s and about 24000 points for each data set. We calculate the mean values of the red and blue diagonal lengths and their standard deviations for consecutive segments, averaging the data with averaging factors N from 1 to 1000. The resulting standard errors on the mean values, which corresponds to the standard deviation divided by the square root of the segments number, is almost constant with increasing N as expected for white frequency noise and is equal to 19 nm for the red cavity and 22 nm for the blue one. However, since for longer integration times the flicker noise starts dominating, we set a conservative estimate of the standard error as 84 nm for the red and 94 nm for the blue cavity, calculated from the last point of the corresponding Allan deviations of Fig. 4. The difference between the two diagonal is 1.21831 mm with a standard error over 1 hour of the order of 130 nm. This difference exceeds largely the PZT regulation range, and the present configuration of GP2 does not allow correcting it.

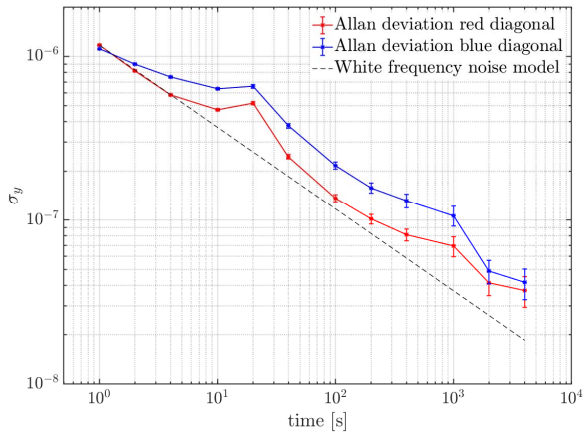

Fig. 4. Allan deviation of the measured length of the two diagonals.

For the applications it will be necessary increasing the short term stability of the length measurements. For this purpose, a first important improvement will be obtained by implementing as source for injecting the diagonal FP cavity a new Extended Cavity Diode Laser characterized by a better short term spectral purity, and slaving it to the iodine reference through a sideband frequency servo.

Acknowledgment

We thank dr. Primakov for his skill in keeping operative the iodine-stabilized reference laser.

References

[1] A. Tartaglia, A. V. Di Virgilio, J. Belfi, N. Beverini, M. L. Ruggiero: Testing general relativity by means of ring lasers, Eur. J. Phys. Plus , vol. 132: 73, 2017

[2] K. U. Schreber, private communication

[3] G.E. Stedman, "Ring-laser tests of fundamental physics and geo-physics", Rep. Prog. Phys. vol. 60, pp. 615–688, 1997

[4] R Santagata, et al., "Optimization of the geometrical stability in square ring laser gyroscopes" Class. Quantum Grav. vol. 32: 055013, 2015

[5] J Belfi, N Beverini, G Carelli, D Cuccato, A Di Virgilio, E Maccioni, A Ortolan, and R Santagata, "Interferometric length metrology for the dimensional control of ultra-stable Ring Laser Gyroscopes", Class. Quantum Grav. 31: 225003, 2014

[6] A.Bercy, F.Stefani, O. Lopez, C. Chardonnet, P.E. Pottie, and A. Amy-Klein, "Two-way optical frequency comparisons at 5× 10− 21 relative stability over 100-km telecommunication network fibers", Phys. Rev. A, vol. 90: 061802, 2014.

Optimization of low-power oscillator topology for frequency modulated MEMS inertial sensors

Cristiano R. Marra, Alessia M. Ruggieri, Paolo Minotti, Giorgio Mussi, Andrea G. Bonfanti, Andrea L. Lacaita, and Giacomo Langfelder
Dipartimento di Elettronica, Informazione e Bioingegneria
Politecnico di Milano
Milano, Italy
Email: cristianorocco.marra@polimi.it

***Abstract*—This work proposes two different feedback oscillator loops for MEMS frequency-modulated (FM) inertial sensors, identifying the optimum topology in terms of power-noise trade-off. More in detail, the focus is on the critical 90-degree shifter stage, realizable through either an analog integrator or a phase-locked-loop (PLL). After a theoretical analysis, the first option turns out to minimize noise-folding related issues, obtaining lower noise level at lower power consumption with respect to the PLL approach. In order to verify the theoretical model, the two loops are fabricated and coupled with a frequency modulated accelerometer measuring the oscillator loop phase noise at the system output.**

Keywords—MEMS; frequency-modulated; low-power, low-noise, oscillator.

I. INTRODUCTION

MEMS sensors next-generation applications as mixed reality and inertial pedestrian navigation demand extremely good performances in terms of bias and scale factor stability and repeatability, at low manufacturing cost. State of the art capacitive accelerometers and gyroscopes are affected by significative variations of offset and scale factor given by environmental perturbations (e.g. temperature, humidity) and piece-to-piece sensitivity fluctuations induced by unavoidable industrial process tolerances. High-stability levels are requested also to emerging technologies as MEMS magnetometers, in order to represent a real game-changing technology for the realization of multi degrees of freedom inertial measurement units (multi-DOF IMUs).

Resonant frequency sensing is currently in the limelight of the research community, thanks to its promising performance in terms of stability. This kind of solution indeed allows to bypass thermal and aging-dependent gain of electronic stages used to readout amplitude-modulated (AM) sensors; besides, a frequency modulation of the signal related to the quantity to detect, away from the region associated to slow environmental drifts, bypasses well-known thermal frequency drifts.

In the gyroscope case, a Lissajous FM gyroscope [1] is realized by letting a mechanical structure with two orthogonal vibration modes oscillate at each mode's resonance frequency. If an external rate orthogonal to both modes is present, it induces a resonance frequency variation. The device peculiarity is that the scale-factor depends only on a geometrical ratio between the two masses. Sub-0.5% part-to-part repeatability and sub-35 ppm/K temperature coefficients, even with no sensor calibration, were shown in recent works [2].

Quadrature-frequency-modulated (QFM) magnetometers, through the use of two identical resonators whose frequency is sensitive to the Lorentz force generated by an external magnetic field, reach a total thermal drift error of ~22 nT/K [3].

Time-switched frequency modulated accelerometers are based on a frequency differential readout performed on a single resonator biased in two opposite configurations in time. This enables offset thermal drift coefficients of 50 µg/K over the whole consumer temperature range [4].

All the described sensors are based on approaches where the FM signal sees a further amplitude-modulation (AM) at a frequency f_{mod} (typically of 100-200 Hz) from the carrier frequency f_0 (that usually falls in the 20-50 kHz range):

$$f = f_0 + X \cdot SF \cdot \sin(2\pi f_{mod} t) \qquad (1)$$

In Eq. (1) X is the generic physical quantity to measure and SF is the scale factor of the device. Note (i) how slow drifts of the rest frequency f_0 are bypassed with this approach; and (ii) that phase noise in the oscillator sustaining the resonant motion of these sensors needs to be analyzed at the mentioned split f_{mod} from the carrier.

II. ELECTRONIC OSCILLATOR

A. Proposed loops and folding issues

Due to the need for amplitude controlling circuits, feedback oscillators are the preferred choice for the described scenario. The electronic circuit, after converting into a voltage the current signal generated by the motion-induced capacitance variation of the MEMS resonator, has the task to clip the voltage signal to the power supply, in order to generate a square-wave that can be readout by a suitable frequency-to-digital converter (FDC). This hard-limiting is an intrinsically non-linear operation. Indeed, input noise perturbations affects the output only when the input signal is near the zero-crossings, while they do not affect the output when the input is far from this region, as it is clamped at one of the two supply rails. For high comparators gains, noise gain can be expressed as a Dirac comb function both in

frequency and time domains. Convolving this transfer function with the input noise power spectral density results in a down-folding of all noise tones around higher-order harmonics [5].

Thus, the noise shape at the non-linear component input determines the noise folding penalty in the overall noise floor. The two loops depicted in Fig. 1 and Fig. 2 are analyzed in detail, fabricated in AMS 0.35 µm technology and compared in terms of obtained resolution. The main difference in the two loops consists in the element used to obtain the 90-degrees phase shift needed to satisfy the Barkhausen criterion: an analog integrator or a phase-locked-loop. The current budget repartition of the two loops is schematized in the pie chart of Fig. 3.

B. Charge-to-voltage amplifier (C2V)

The output current of the resonant device has to be converted into a voltage before being processed further. The trans-capacitance configuration is preferred to the trans-resistance one because of its superior noise performances for the frequency range of interest. The feedback network is formed by a pseudo-resistor that has the role to fix the network pole at frequencies well below 25 kHz, while a feedback capacitance of 190 fF determines the gain of the stage. In order to maximize the current flowing in the input transistors (i.e. miniminzing the input referred noise), a single-stage telescopic cascode biased at 21 µA is used as the active element of this stage. It can be noted that the single-pole response of this configuration results in a 90-degrees phase delay of the signal, and thus the need for another phase shifter in the loop to satisfy the Barkhausen criterion on phase results evident.

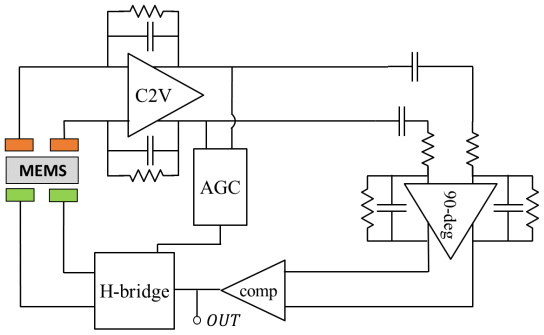

Fig. 1. Feedback oscillator loop with analog integrator used as a phase shifter block (90D loop).

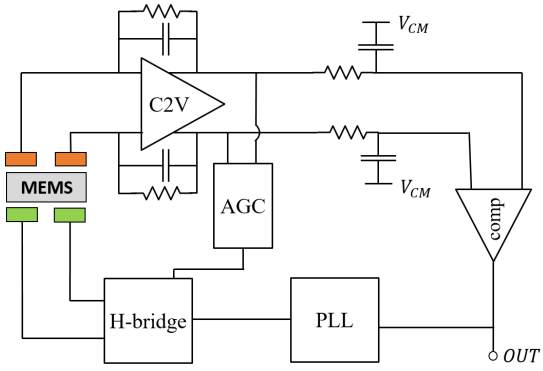

Fig. 2. Feedback oscillator loop with phase-locked-loop as a phase shifter block (PLL loop).

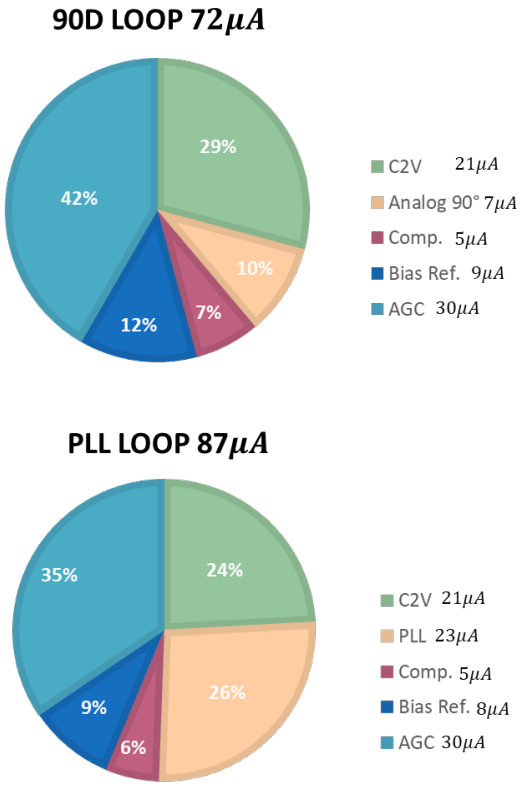

Fig. 3. Current consumption repartition in the analog 90D loop (top) and in the PLL based loop (bottom).

C. Automatic gain control (AGC) and driver

This secondary loop, through a negative feedback mechanism, controls the oscillation amplitude of the resonant device. The circuit takes as an input the sinusoidal output of the C2V, extracts the DC information about the displacement amplitude through a suitable butterfly switch, and finally compare it with an external user-selectable reference voltage. This negative control loop acts on the supply voltages of the H-Bridge used to provide at the MEMS resonator the push-pull driving square-waves, controlling in this way the resonator displacement.

D. Optimum phase shifter choice

The phase shifter block choice is the most critical part of the design. The first solution is an active integrator with a low-frequency zero and two poles well below the operating frequency. By carefully designing the input resistor and the feedback capacitor, the gain of the stage at 25 kHz can be fixed to unity. The OTA topology is the same of the C2V stage, but the current drained by this stage is considerably lower, given the less stringent noise constraints due to the pre-amplification of the signal by the previous block. This 90D stage provides simultaneously the needed phase shift and a reduction of wideband noise at the comparator input.

The second approach to phase shift involves a type II PLL. Its main building blocks are represented by a D-flip-flops phase-frequency detector (PFD), that controls the current flows of a

suitable charge pump (CP). The latter injects its current in an external loop filter (300 kΩ, 2 nF, 50 pF) that, in turn, drives a voltage-controlled-oscillator (VCO). The VCO is a ring oscillator, based on 7 current starved inverter cells, that oscillates at a frequency around 50 kHz, a factor 2 higher with respect to the device resonance: the subsequent digital division by 2 gives as an output both the in-phase and the quadrature signals, and the latter can be used to correctly close the loop. The current consumption of the PLL loop is higher with respect to the phase shifter one: this is mainly due to the circuital complexity of the whole block, and to the need to minimize the VCO noise injected in the oscillator main loop.

The effect of the two circuital topologies on phase noise can be derived starting from the considerations of section II.A. The noise at the comparator input in the analog shifter case, thanks to the active low-pass-filtering of the integrator, is limited in bandwidth, reducing the amplitude of noise components around higher harmonics and in turn almost nulling the noise folding penalty. The 1 MΩ resistance at the analog phase shifter input adds its own non-negligible thermal noise contribution which in the optimum case roughly equals the C2V noise, thus giving about a √2 overall noise worsening.

On the other hand, for the PLL approach, the wide-band noise at the C2V output is directly squared, resulting in worsened noise at the comparator output. This contribution is only partially mitigated by a passive low-pass filter at the C2V output, as the introduced pole should be more than one decade higher than the carrier frequency, to avoid undesired phase lags. The noise folding penalty factor, calculated as the ratio of the wideband noise filtering frequency and the carrier, is in the order of 10.

In conclusions, in terms of trade-off between consumption, noise folding and circuital area, the active integrator represents undoubtedly the optimum solution.

III. Experimental Results

A. FM Accelerometer

In order to perform the experimental measurements reported in this work, each of the two loops is coupled with a FM accelerometer, whose working principle is briefly described in this section. Classical approaches to resonant accelerometers relies on two different resonators that, in presence of an external acceleration, experience opposite frequency shifts, allowing differential sensing. This kind of approach is detrimental from the offset thermal drift point of view: indeed, if the rest frequencies of the two resonators are different due to process tolerances, they will drift in a different way in temperature, leading to a residual offset thermal drift contribution.

The time-switched approach, recently proposed in [4], performs a differential readout on a single resonator, allowing to erase mismatch-induced thermal drifts. This can be obtained with the structure represented in Fig. 4a. The anti-phase mode of the sensor is electronically sustained through sense and drive comb fingers, and its frequency is tracked. An external acceleration generates an in-phase motion that changes the gap between the proof mass and a suitable set of tuning ports. The blue and red tuning ports are turned on and off at a frequency of 100 Hz, modulating the acceleration-dependent contribution of electrostatic stiffness in time. The resulting behavior of the resonant frequency is exactly as the one described by Eq. 1, where X is now represented by the external acceleration.

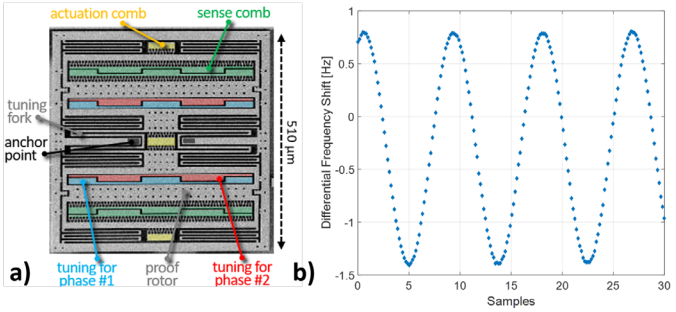

Fig. 4. Device SEM picture with highlighted electrodes and mechanical elements (a) and sensitivity measurements (b)

B. Experimental results

In order to verify the sensor and integrated circuit proper operation, the integrated system is glued on a ceramic carrier and inserted in suitably designed characterization PCB. The board is mounted on a rate table tilted in such a way to modulate the amount of gravitational acceleration applied to the sensor (Fig. 4b): the resulting scale-factor is about 1 Hz/g. From phase noise (Fig.5a) measured at the system output and input-referred in terms of acceleration noise density (Fig.5b), it can be evaluated how the analog shifter solution leads to 75 µg/√Hz, while the PLL solution leads to a slightly higher noise density (100 µg/√Hz), with an additional current consumption of 15 µA.

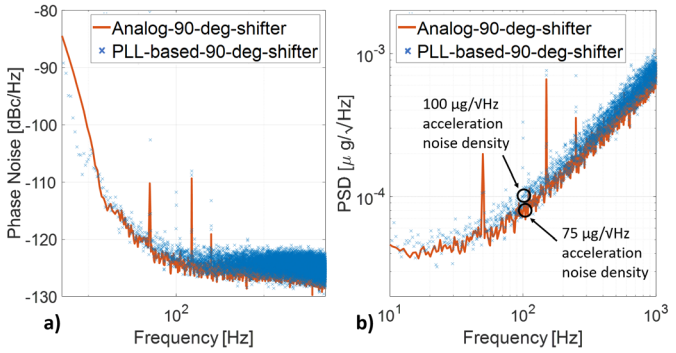

Fig. 5. Phase noise (a) measured at the output of the two electronic oscillators and corresponding input-referred acceleration density (b).

IV. Conclusions

The work theoretically and experimentally proves that, in a feedback oscillator for MEMS FM inertial sensors, the most convenient approach to close the loop in terms of phase shift is to use an analog integrator before converting the sinusoidal wave into a square-wave. This analog block indeed, while shifting the signal, performs a band-limiting action on noise, preventing folding issues at the comparator output.

As a result, a better resolution is obtained at a lower power consumption and with a lower area, compared to widely adopted, PLL-based approaches.

REFERENCES

[1] I. I. Izyumin et al., "*A 7ppm, 6 deg/hr frequency-output MEMS gyroscope*", IEEE 28th International Conference on Micro Electro Mechanical Systems (MEMS), Estoril, Jan.2015, pp. 33–36.

[2] P. Minotti, S. Dellea, G. Mussi, A.G. Bonfanti, S. Facchinetti, A. Tocchio, V. Zega, C. Comi, A.L. Lacaita, and G. Langfelder ., "*High Scale-Factor Stability Frequency-Modulated MEMS Gyroscope: 3-Axis Sensor and Integrated Electronics Design*", in IEEE Transactions on Industrial Electronics, vol. 65, no. 6, pp. 5040-5050.

[3] S. Sonmezoglu, I. B. Flader, Yunhan Chen, D. D. Shin, T. W. Kenny and D. A. Horsley, "*Dual-resonator MEMS Lorentz force magnetometer based on differential frequency modulation*", 2017 IEEE International Symposium on Inertial Sensors and Systems (INERTIAL), Kauai, HI, 2017, pp. 160-163.

[4] C. R. Marra, F. M. Ferrari, S. Karman, A. Tocchio, F. Rizzini, and G. Langfelder, "*Single-resonator, time-switched FM MEMS accelerometer with theoretical offset drift complete cancellation*", in IEEE 31th International Conference on Micro Electro Mechanical Systems (MEMS), Belfast, Jan 2018, pp. 117–120.

[5] C. Samori, A. L. Lacaita, F. Villa, and F. Zappa, "*Spectrum folding and phase noise in LC tuned oscillators*", IEEE Trans.Circuits Syst.II,Analog Digital Signal Process., vol. 45, no. 7, pp. 781–790, Jul. 1998

Influence of the acoustic energy distribution on the in-liquid sensitivity of thin film electroacoustic resonators

Teona Mirea, Jimena Olivares, Marta Clement, Enrique Iborra
GMME-CEMDATIC-ETSIT,
Universidad Politécnica de Madrid, Madrid, Spain
Email: teona@etsit.upm.es

***Abstract*—In contrast to quartz crystal microbalances, the sensitivity of thin film bulk acoustic wave resonators (FBARs) is strongly dependent on all layers composing the composite structure. Previous studies of the pure mass sensitivity of suspended FBARs, proved that placing low acoustic impedance materials at the sensing surface of the device can enhance their sensitivity by carefully controlling the energy trapping effects. Here we extend those studies by investigating if the in-liquid sensitivity of shear-mode AlN-based solidly mounted resonators (SMRs), working at 2 GHz, display a similar dependence on the device configuration (top electrode thickness and material). We use the finite element method (FEM) and experimental results to demonstrate that if one is restricted by the readout circuit to a certain resonant frequency, the sensitivity of the devices (particularly in-liquid sensors or biosensors) can be boosted by proper design while preserving the initial frequency. This is possible since the variations in sensitivity are strongly dependent on the energy distribution within the whole resonant structure.**

Keywords—AlN-based SMR; finite element method; in-liquid sensing.

I. INTRODUCTION

The sensitivity to mass attachment or liquid properties (density and viscosity) of single material electroacoustic resonators, like QCMs, can be derived from Sauerbrey's [1] or Kanazawa and Gordon's [2] equations, being in both cases directly dependent on the resonant frequency and influenced only by the quartz plate properties. Thin film resonators working in the GHz range can provide with a tremendous increase in sensitivity compared to their QCM antecessors [3]. However, in this type of resonators we cannot consider these simple equations anymore. In this case, to derive the sensitivity, we need to consider multilayered structures where the properties of all layers have an influence [4]. Particularly, the distribution of the acoustic energy within the structure strongly affects the sensitivity at the active surface. In thin film bulk acoustic wave resonators (FBARs) operating in air it has been proved that the addition of a low impedance material (e.g. SiO_2) on the sensing surface can increase their mass sensitivity [4], which can also be achieved by using low impedance electrodes of appropriate thicknesses [5]. In Ref. [4] it was studied in deep the mass sensitivity of suspended FBARs for both the fundamental and first harmonic modes, and envisaged that the addition of a low acoustic impedance material not only enhances the pure mass sensitivity by the energy trapping effect, but also affects the behavior of the devices in liquid by increasing their dissipation due to a larger portion of energy coupled to the liquid. However, their sensitivity towards liquid properties has not been studied.

Although FBARs working in the GHz range have overcome the sensitivity of QCMs, in practice the readout circuits can impose frequency restrictions. If such is the case and one cannot go further at higher frequencies, a proper design can increase the sensitivity while preserving the resonant frequency. Our aim here is to prove that the in-liquid sensitivity of solidly mounted resonators (SMRs) can be strongly affected by their design (i.e. electrodes materials and thicknesses) while working at roughly the same resonant frequencies. We assess the in-liquid sensitivity of shear mode SMRs with different structures, particularly towards density and viscosity, by employing the finite element method (FEM) and comparing the results with experimental ones. The study is extended to their mass sensitivity in liquid as an analogy to their biosensing application.

A. Devices

Our SMRs are based on fully-insulating acoustic reflectors made of seven alternating layers of SiO_2/AlN, on which we deposit a tilted piezoelectric AlN film sandwiched between two electrodes (Fig. 1a). The acoustic reflector was designed to properly confine (reflect) the acoustic energy of the shear mode operating at around 2 GHz. Since our purpose was to study the influence of the electrodes and AlN on the device in-liquid sensitivity, the bottom electrode/AlN/top electrode structure was varied keeping always similar frequencies.

To allow testing the response of the devices through a microfluidic system, the electrical contacts to the top electrode of the SMRs were extended to 1.7 mm far away from the resonator active area to ease contacting the devices outside the fluidic system with the RF probes (Fig. 1b). The bottom electrode located below the extensions of the top electrode was etched to avoid the presence of parasitic capacitances and inductances. For the same purpose, the fully-insulating reflector together with the high resistivity silicon wafer substrate are also pivotal; indeed, reflectors containing metallic or semi-metallic layers lead to the appearance of parasites due

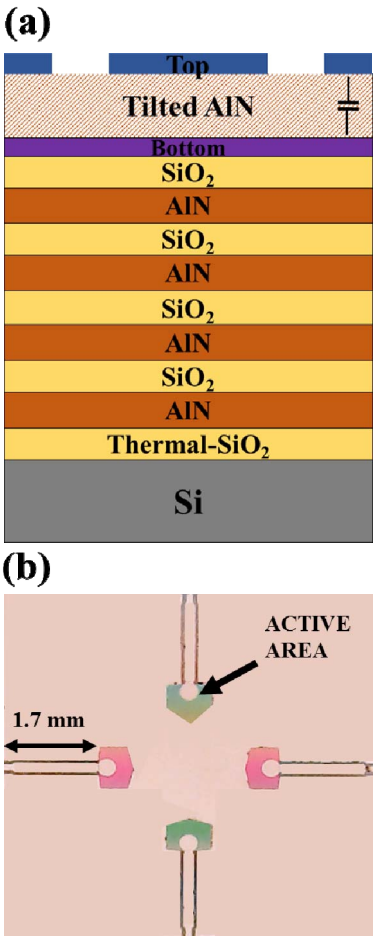

Fig. 1. AlN-based SMRs: (a) cross section sketch, and (b) optical top view of a chip containing 4 devices with extended top electrodes for the microfluidic testing.

to the capacitive coupling of the top electrode with the last layers of the reflector [6].

B. FEM Simulation

We used a 2D finite element analysis method to assess the in-liquid behavior of our devices. In this case, their response to varying density and viscosity of the contacting liquid as well as their mass sensitivity in liquid. The FEM model was a previously-designed one. A detailed description of this model and its validation can be found elsewhere [7]. It was designed to correctly account for the acoustic coupling to the liquid through shear stresses. The structures we employed for the simulations were single cells with applied lateral periodic conditions (Fig. 2), i.e. we applied periodic continuity on the lateral interfaces since we are not interested here on considering possible spurious modes in the structures but the physical interaction of the shear mode with the liquid interface. The cells include perfectly matched layers (PML) to simulate the absorption of outgoing waves in the liquid domain (liquid

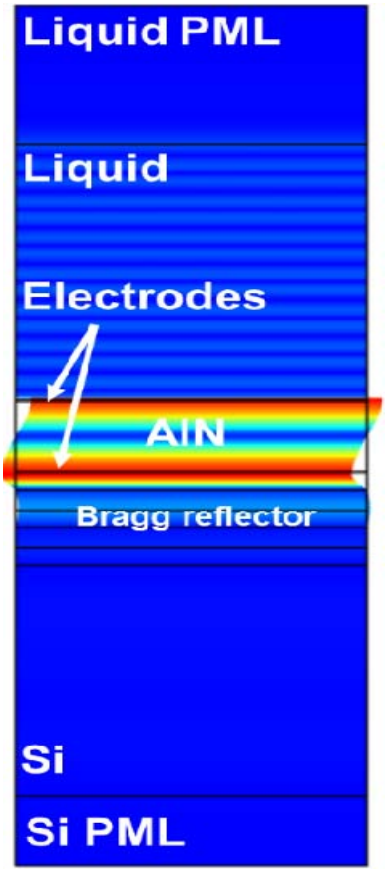

Fig. 2. FEM simulation: SMR single cell with lateral periodic conditions in contact with liquid on top. Liquid and Si PMLs are used to simulate to the complete absortion of the acoustic waves.

PML) and the Si substrate (Si PML) since, for efficiency, we did not consider an entire Si wafer.

C. Measurements Set-up

The devices were electrically evaluated with a network analyzer while integrated in a microfluidic system composed of a polydimethylsiloxane (PDMS) chamber where the liquids were recirculated with a peristaltic pump (Fig. 3). As mentioned, the SMR was electrically contacted through its 1.7 mm extensions through a 150 µm-pitch RF-probe connected to the network analyzer. The device response (variations of its resonant frequency) was monitored by tracking the maximum of the real part of the admittance (Re(Y)) curve through a specifically designed LabView® application. This procedure is based on acquiring the Re(Y) maximum around the resonant frequency with a bandwidth of 20 MHz (~1.5 kHz frequency spacing using 12000 data points) and fitting it to a rational function, which allows tracking the resonant frequency with a noise floor below 1 kHz. A typical response curve is shown in Fig. 4, where negative shifts in frequency were induced on the device upon introduction of solutions with different ethylene glycol concentrations in water. As observed, the solutions were sequentially fed starting with the less viscous and dense one. At the end, water was thoroughly flown to clean the device, which was confirmed by the recovery of its initial resonant frequency.

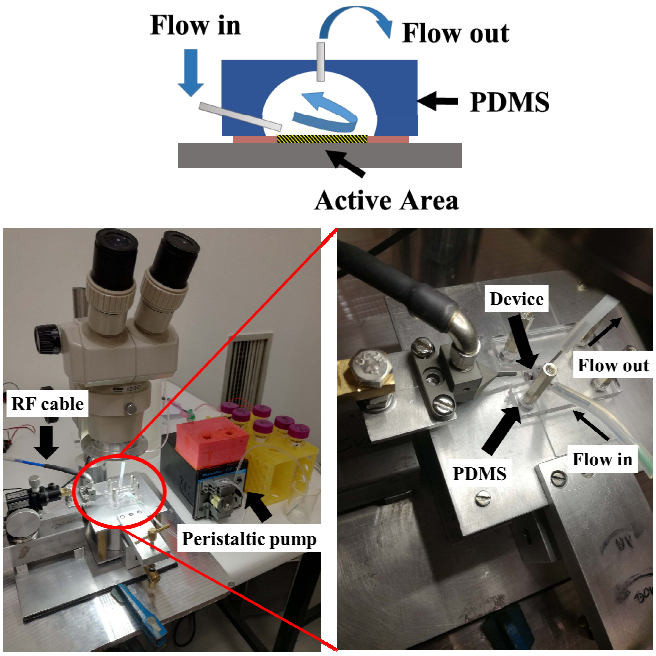

Fig. 3. Measurement set-up with a sketch on top an actual images below.

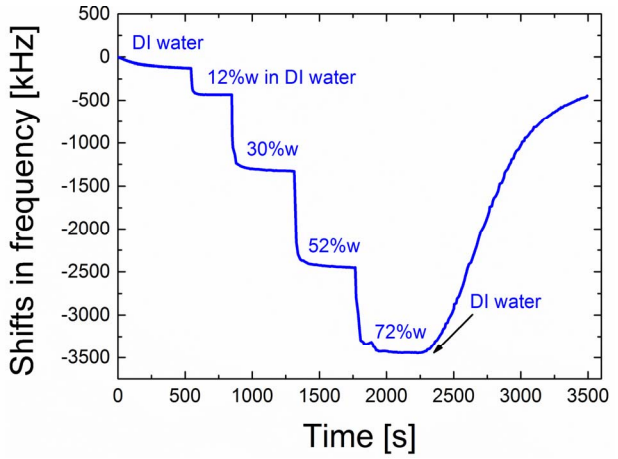

Fig. 4. Typical response of a device with increasing concentration of ethylene glycol % in pure water (%w stands for weigth percent of solute in water).

II. RESULTS AND DISCUSSION

Three different structures were simulated and experimentally tested. As mentioned, all of them contained the same acoustic reflector but differed on their bottom electrode/AlN/top electrode structure. The structures consisted of:

(a) 100 nm Mo / 900 nm AlN / 150 nm Mo

(b) 150 nm Mo / 900 nm AlN / 100 nm Mo

(c) 100 nm Mo / 1000 nm AlN / 100 nm Al

providing resonant frequencies of 2.007 GHz, 2.010 GHz and 2.261 GHz for a, b and c, respectively.

Fig. 5 shows the simulated and experimental results of all devices towards the different density and viscosity products of the ethylene glycol concentrations from Fig. 4. On one hand, we note a relatively good agreement between simulations and experiments. We attribute the small deviations to errors in the resonant peak tracking due to the presence of spurious modes in some cases. On the other hand, we observe that the sensitivity to density and viscosity is enhanced if (1) we interchange the electrodes thicknesses for cases (a) and (b), and (2) if we employ a lower acoustic impedance top electrode as Al. As for the first case, the reason of the sensitivity improvement at the top electrode surface is a redistribution of the energy within the acoustic cavity, which leads to an increased displacement field, or energy concentration, at the top 100 nm-thick electrode. Regarding the second case, the substitution of the Mo electrode with a lower impedance one (Al), redistributes again the energy within the cavity trapping a greater amount of energy at the Al top surface. This is in agreement with previously reported results where only pure mass sensitivity in air was considered [3]–[5]. Indeed, if one considers the transmission coefficient at the AlN//top electrode interface, which is defined as:

$$T = (2 \times Z_{AlN}) / (Z_{AlN} + Z_{top}) \quad (1)$$

being Z_{AlN} the specific acoustic impedance of AlN, and Z_{top} the one of the top electrode material, it is clear from Table I (acoustic impedance values) that the amplitude of the transmitted wave from AlN to the top electrode is increased when using Al (T = 1.42), while decreases when using Mo (T = 0.72). These values explain why we have a greater amount of energy involved in the sensing mechanism when using Al as top electrode.

Although we can achieve and enhanced sensitivity by properly designing the device, we need to take into account that this increased sensitivity carries also increased losses (lower quality factors) by coupling a greater amount of the energy to the liquid.

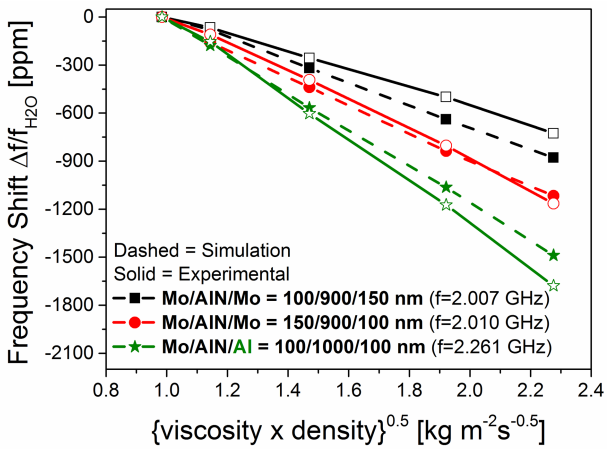

Fig. 5. Simulated and experimental normalized shifts in frequency of the three different structures towards increasing density and viscosity products.

TABLE I. SHEAR ACOUSTIC IMPEDANCES

Material	*Shear acoustic velocity [m/s]*	*Density [kg/m^3]*	*Z [Rayl]*
AlN	6170	10300	$2.03 \cdot 10^7$
Al	3040	3300	$8.21 \cdot 10^6$
Mo	3450	2700	$3.55 \cdot 10^7$

This is proved in Fig. 6 where we plot experimental values of the inverse of the normalized Re(Y) peak against density and viscosity for the extreme cases (a) and (c).

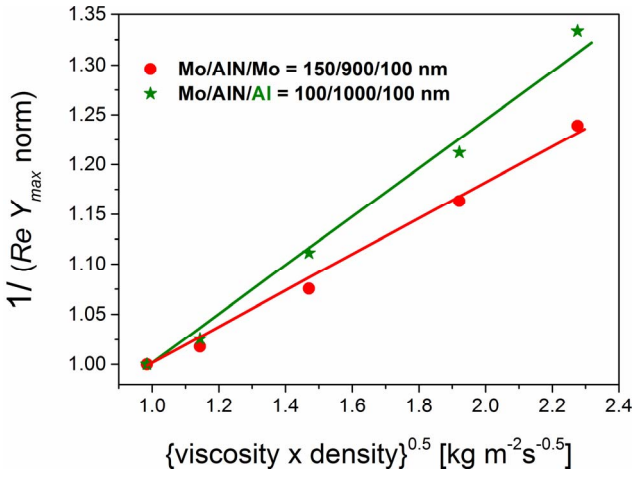

Fig. 6. Experimental measurements of the losses (inverse of the admittance peak normalized to its value in pure water) for structures (a) and (c).

To test the in-liquid mass sensitivity of the devices, experiments with BSA in buffer solutions are ongoing. Nevertheless, we used our model to predict the mass sensitivity results by computing the shift in resonant frequency for each structure towards the deposition of 50 nm of SiO_2 while operating in pure water. We obtained shifts in resonant frequency of -21.52 MHz, -27.05 MHz and -49.31 MHz, for cases (a), (b) and (c), respectively. Being, as expected, structure (c) more sensitive.

CONCLUSIONS

We have proved that, although working at the same frequencies, the in-liquid sensitivity of AlN-based shear mode resonators can be strongly affected by their structure. We showed that the sensitivity towards density and viscosity can be increased by reducing the thickness of the top electrode, in this case Mo, or by substituting it with a lower acoustic impedance one, for example Al. This phenomenon is explained by the energy distribution within the whole resonant structure, which gets to be more concentrated at the top sensing surface if the Mo top electrode is reduced or substituted by Al. Our results, obtained by FEM simulations and experimentally verified, are in good agreement with previous works that studied the pure mass sensitivity of suspended FBARs in air.

ACKNOWLEDGMENT

This work was partially supported by Ministerio de Economía y Competitividad del Gobierno de España through project MAT2013-45957-R.

REFERENCES

[1] G. Sauerbrey, "Verwendung von Schwingquarzen zur Wagungdiinner Schichten und zur Mikrowagung," *Zeitschrift fur Phys.*, vol. 155, pp. 206–222, 1959.

[2] K. K. Kanazawa and J. G. Gordon, "Frequency of a quartz microbalance in contact with liquid," *Anal. Chem.*, vol. 57, no. 8, pp. 1770–1771, Jul. 1985.

[3] S. Rey-Mermet, R. Lanz, and P. Muralt, "Bulk acoustic wave resonator operating at 8 GHz for gravimetric sensing of organic films," *Sensors Actuators B Chem.*, vol. 114, no. 2, pp. 681–686, Apr. 2006.

[4] G. Wingqvist, V. Yantchev, and I. Katardjiev, "Mass sensitivity of multilayer thin film resonant BAW sensors," *Sensors Actuators A Phys.*, vol. 148, no. 1, pp. 88–95, 2008.

[5] H. Liu, S. Ma, H. Wang, Q. Wang, and L. Qin, "Electrode effects on mass sensitivity of GaN thin film bulk acoustic wave resonator sensors," in *2015 Symposium on Piezoelectricity, Acoustic Waves, and Device Applications (SPAWDA)*, 2015, pp. 179–183.

[6] M. DeMiguel-Ramos, T. Mirea, J. Olivares, M. Clement, J. Sangrador, E. Iborra, and M. Barba, "Influence of the electrical extensions in AlN-BAW resonators for in-liquid biosensors," in *2014 European Frequency and Time Forum (EFTF)*, 2014, pp. 301–304.

[7] T. Mirea, V. Yantchev, J. Olivares, and E. Iborra, "Influence of liquid properties on the performance of S0□mode Lamb wave sensors II: Experimental validation," *Sensors Actuators B Chem.*, vol. 229, pp. 331–337, Jun. 2016.

Measuring the Mitigation of a Jamming Attack on a GPS Server at the National Physical Laboratory of Israel

Dr. Nadya Goldovsky
The National Physical Laboratory of Israel (INPL)
Jerusalem, Israel
Nadya.Goldovsky@Economy.gov.il

Omer Sharar
GPSdome Ltd.
Caesarea Industrial Park, Israel
Omer@gpsdome.com

Abstract— **Based in Israel, GPSdome, the GPS cyber company, develops and manufactures a GPS anti-jamming / anti-spoofing module protecting GPS-based systems against jamming and spoofing of the GPS signal which disrupts navigation and timing applications. The testing and calibration of this module is performed by the Time and Frequency Laboratory of INPL. Two GPSdome modules (Rev 1.0) were calibrated with two GPS-locked servers (Microsemi's SyncServer S650): one with an internal (basic) quartz oscillator OCXO and one with an internal Rb oscillator. The Unit Under Test (UUT) was compared against the time reference (the Cs-clock), which was calibrated at INPL versus Israeli Time Standard UTC (INPL). For each GPSdome module the internal time delay was evaluated and it was 57.9 ns for GPSdome #1 and 153.6 ns for GPSdome #2. The calibration results evidently show, that both servers with GPSdome protection save traceability to high performance time reference with standard deviation only 10-15 ns in the presence of jamming**.

Keywords—GPS signal protection; jamming; spoofing; calibration; time reference.

I. INTRODUCTION

In recent years, the threat of GNSS vulnerabilities has become real. Such events as signal anomalies, regional disruptions, loss of position and time in the presence of certain types of jammers had already occurred a multitude of times and affected critical applications all over the world. The solution of this problem for time-keeping, navigation, time and frequency synchronization which mitigated such threats is actual, and in the last several years many efforts are made for protection against jamming and spoofing.

Based in Israel, GPSdome, the GPS cyber company, develops and manufactures a GPS anti-jamming / anti-spoofing module protecting GPS-based systems against jamming and spoofing of the GPS signal [1, 2].

GPSdome implements a null-steering algorithm which significantly reduces the effect of a high-powered jamming/spoofing attack. The testing and calibration of this module is performed by the Time and Frequency Laboratory of INPL.

II. CALIBRATION SYSTEM

The calibration procedure consists of several stages: 1) calibration of GPSdome time reference (the high performance Cs-clock 5071A) versus Israeli National Time UTC (INPL) at the INPL; 2) calibration of time difference between the GPS controlled device (without and with GPSdome Rev 1.0 anti-jamming module) and the time reference in the absence of jamming; 3) calibration of time difference between the GPS controlled device (without and with GPSdome anti-jamming module) and the time reference in the presence of jamming.

A. Calibration of GPSdome time reference versus the national time scale of Israel UTC(INPL)

The calibration was performed against the Israeli National Time and Frequency Standard, using new time and frequency equipment, including new high performance Cs-clocks 5071A [3, 4], GNSS dual-frequency multi-channel Time Transfer System TTS5 [5, 6] and high performance Allan Deviation and phase noise test set 5120A [7]. The block diagram of the calibration system is shown in Fig.1, and the measurement results are shown in Fig.2.

Deviation of the time reference TR from the national time UTC(INPL) during 6 days (from 29.05.17 until 04.06.17) was in the range from -9.56 ns up to +1 ns (see Fig.2). The average value of time difference TR – UTC(INPL) was -5.25 ns and the standard deviation STDEV of measurement results was only STDEV = 1.62 ns.

The daily rate of reference time relatively to UTC(INPL) Y[TR-UTC(INPL)] was -1.5 ns/day. The daily rate of TR relatively to UTC Y[TR-UTC] was obtained by following formula:

$$Y[TR\text{-}UTC] = Y[TR\text{-}UTC(INPL)] + Y[UTC(INPL)\text{-}UTC] \quad (1)$$

Where Y[UTC(INPL)-UTC] is the daily rate of national time relatively to UTC obtained from the Key comparisons CCTF-K001.UTC [8, 9]. For measurement time interval it was -0.41 ns/day. Thus, the daily rate of TR relatively to UTC according to formula (1) was -1.99 ns/day.

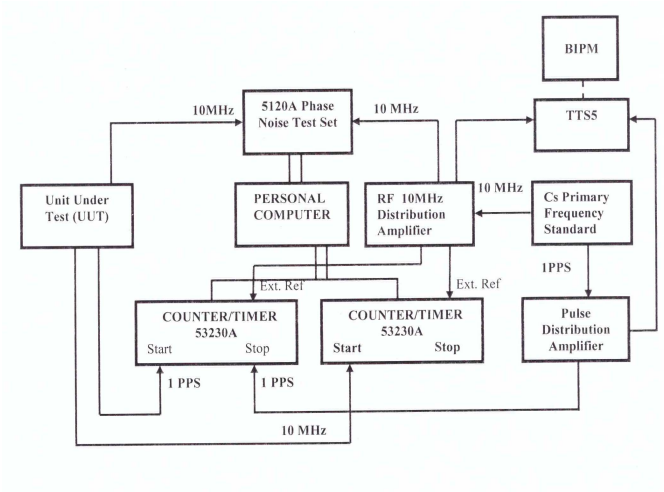

Fig.1. Block diagram of time reference calibration versus UTC(INPL).

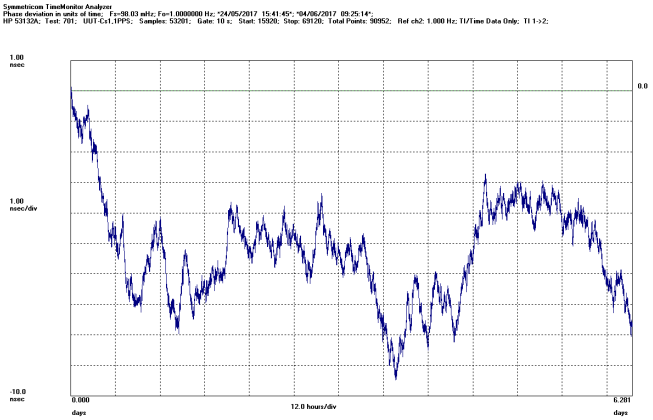

Fig.2. Time difference TR – UTC(INPL) during 6 days.

B. The measurement system for calibration of GPSdome module versus the time reference TR.

The testing of protection quality of two GPSdome modules was performed at the test laboratory of Focus-Telecom. The GPSdome module was compared against the time reference – 5071A Cs-clock which was calibrated at INPL.

The block diagram of calibration system is shown in Fig.3. The measurement system comprises: primary frequency standard – high performance Cs-clock 5071A-C001 [3, 4], Unit Under Test GPSdome (UUT) [2], two universal counters Agilent 53132A [10], two GPS locked SyncServers S650 [11, 12] #1 and #2, personal computer. SyncServer #1 operates with internal quartz oscillator OCXO, and SyncServer #2 operates with internal Rb oscillator.

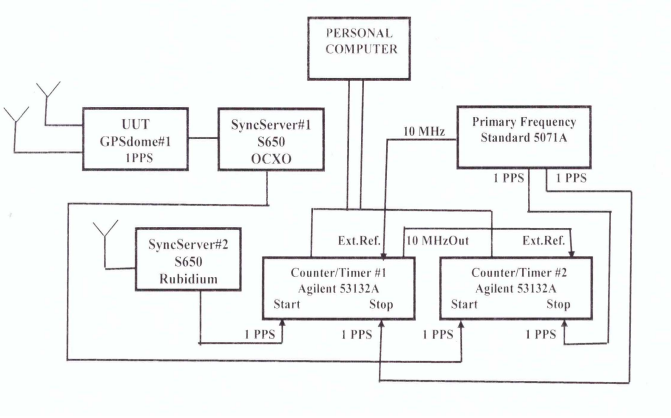

Fig.3. Block diagram of GPSdome module calibration versus time reference.

The measurements were performed simultaneously for two servers: one which operates with the protection module and the other without it. First, the measurements were carried out without jamming, and then in the presence of jamming. The GPSdome module was installed alternately for both servers #1 and #2 with internal quartz OCXO and Rb oscillator, and all measurement procedures were performed for these two options.

III. UNIT UNDER TEST GPSDOME MODULE

GPSdome (see Fig.4) is a compact light-weight GPS anti-jamming module [2], designed to prevent loss of position fix and time in the presence of a jammer. The unit may be installed on a range of installations that rely on GPS and connects between the antenna and the GPS receiver.

Two active GPS antennas are connected to the SMA RF connectors; the primary and auxiliary antenna inputs. The RF Output provides connection to the input of the GPS Receiver.

Figure 1: GPS Dome – General view

Fig.4. GPSdome – General view.

GPSdome ensures continuity of the navigation and timing signals used by emergency services, logistics, security, and commercial operations. No other device that offers the same level of performance is as small, light, affordable, or as easy to install and conceal as GPSdome.

GPSdome provides solutions for protection from the impact of GPS jammers which could easily be purchased online for as low as $20. GPSdome can be easily installed in any GPS-based system by simply replacing the current antenna with GPSdome and the two GPS antennas it comes with. GPSdome instantaneously makes any GPS-based system much more robust to jamming and spoofing.

IV. THE MEASUREMENT RESULTS AND DISCUSSION

Example of GPSdome module calibration results is presented in Fig. 5. The measurement without jamming were performed during 24 hours.

Table 1. Results of GPSdome #2 delay evaluation

Statistical Parameter	Server#2 without GPSdome #2, T_1	Server#1 with GPSdome #2, T_2
N points	43434	43434
Tmin, ns	139.8	-75.5
Tmax, ns	172.9	62.5
P-to-P, ns	33.1	138.0
T(average), ns	157.2	3.6
STDEV, ns	7.3	23.4
GPSdome#2 delay, $DT=T_1-T_2$, ns	153.6	
U, ns	24.5	

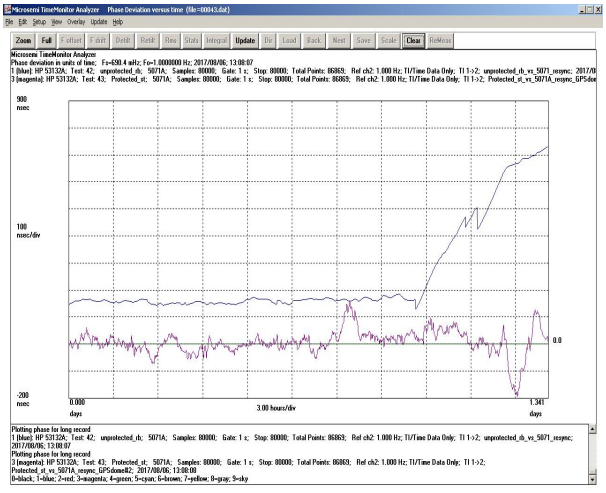

Fig.5. Results of GPSdome #2 testing without jamming during 24 hours and with jamming during 8.18 hours: Server #2 without protection versus Cs-clock TR (blue line); server #1 with GPSdome #2 versus Cs-clock (red line). The measurement were performed simultaneously for both servers.

It can be seen from Fig.5 that GPSdome #2 module introduce delay about 152.6 ns. This delay was evaluated from the time difference between the two lines: server without protection (blue line) and with protection (red line). Results of GPSdome #2 delay evaluation are presented in Tab. 1.

Mitigation of jamming effect can be clearly seen in Figure 5. Two servers were working with jamming for 8.18 hours. Server # 1 with an internal quartz oscillator and with the GPSdome #2 module retained its traceability to TR, the average time deviation from TR was only 13.7 ns. Server # 2 with an internal Rb oscillator and without a GPSdome module lost its traceability and drifted about 78 ns per hour.

The similar measurements were performed also for GPSdome #1 module. The time delay introduced by GPSdome #1 module was evaluated as 57.8 ns ± 10.1 ns.

Results of measurement of mitigation of a jamming attack on GPS signal using GPSdome #1 module are shown in Fig.6. In this case, Server #1 with quartz oscillator was protected by GPSdome #1 module, and Server #2 with Rb oscillator was without protection. Under jamming attack Server #2 has a drift about 201.5 ns/per hour (see Tab.2). Server #1 saved its traceability to Cs-clock TR with standard deviation STDEV about 13.5 ns (see Tab.2)

Results for second option, when Server #2 was protected by GPSdome #1 and Server #1 was not protected, are shown in Fig. 7 and Tab.3. From Fig. 7 it can be seen that Server #1 has drift about 1183. 9 ns/per hour (see also Tab.3). Server #2 saved its traceability to TR with STDEV about 14.2 ns (see Tab.3).

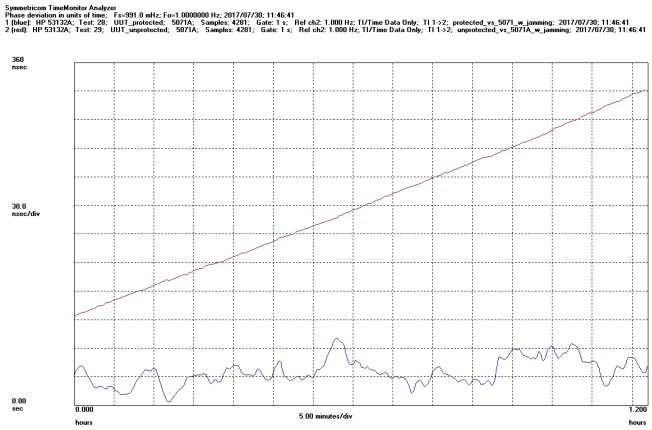

Fig 6. Results of GPSdome #1 testing in the presence of jamming during 1.2 hours. Server #1 with GPSdome #1 versus Cs-clock TR (blue line); server #2 without protection versus Cs-clock TR (red line). The measurement were performed simultaneously for both servers.

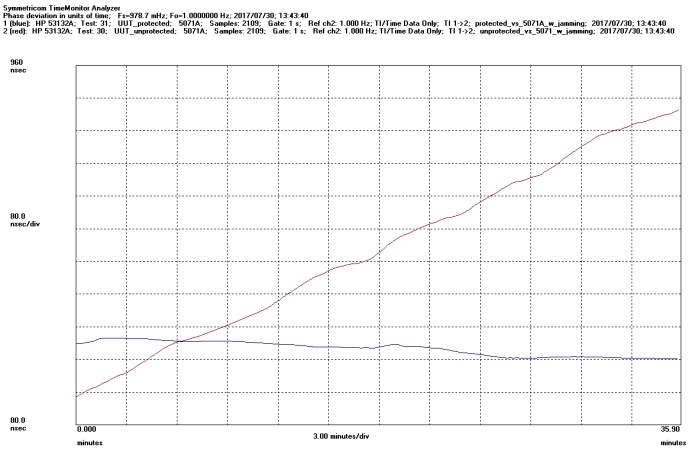

Fig.7. Results of GPSdome #1 testing in the presence of jamming during 35 minutes. Server #2 with GPSdome #1 versus Cs-clock TR (blue line); server #1 without protection versus Cs-clock TR (red line). The measurement were performed simultaneously for both servers.

Table 2. Results of GPSdome #1 testing in the presence of jamming.

Parameter	Server#1 with GPSdome #1	Server #2 without GPSdome#1
N	4281	4281
Tmin, ns	2.3	93.0
Tmax, ns	71.6	334.0
T(average), ns	35.2	-
STDEV, ns	13.5	-
Drift, ns/per hour	No	201.5

Table 3. Results of GPSdome #1 testing in the presence of jamming.

Parameter	Server#1 without GPSdome #1	Server #2 with GPSdome#1
N	2109	2109
Tmin, ns	147.7	241.1
Tmax, ns	856.1	293.3
T(average), ns	-	266.8
STDEV, ns	-	14.2
Drift, ns/per hour	1183.9	No

The time deviations of two servers #1 and #2 without jamming and without the GPSdome module are presented in Fig.8 for comparison. The measurements were performed simultaneously for both servers.

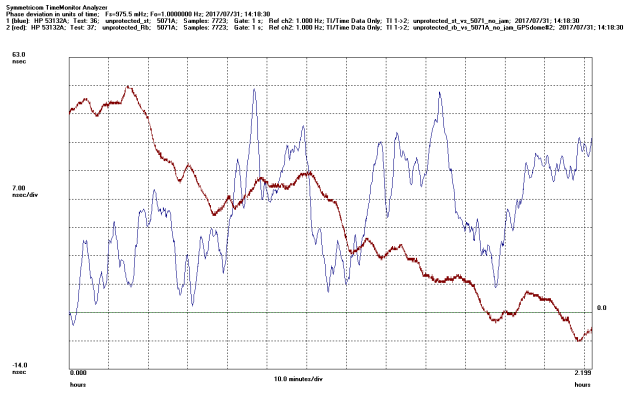

Fig. 8. The time deviations of two servers: #1 with quartz oscillator (blue line) and server #2 with rubidium oscillator (red line) without jamming and without GPSdome module during 2.19 hours.

Statistical parameters are given in Tab. 4.

Table 4. Statistical parameters of time deviation of two servers.

Parameter	Server #1 with quartz oscillator	Server #2 with Rb oscillator
N	7723	7723
Tmin, ns	-3.5	-7.1
Tmax, ns	55.9	58.9
T(average), ns	24.9	23.2
STDEV, ns	12.4	17.2

From the Fig.8 and Tab.4 it can be seen that the time deviation of both servers #1 and #2 versus Cs-clock has very close average value and standard deviation.

V. CONCLUSION

The measurements evidently show that both servers with GPSdome protection save traceability to high performance time reference with standard deviation only 10 – 15 ns in the presence of jamming. Without GPSdome protection, both servers (with internal quartz and Rb oscillator) have large drift. For quartz oscillator the drift is 1183.9 ns per hour. For rubidium oscillator the drift is less than for quartz but still is relatively large, about 201.2 ns per hour.

Our measurements showed the effectiveness of the GPSdome anti-jamming protection solution, provided by the Israel-based company, GPSdome Ltd.

REFERENCES

[1] http://www.gpsdome.com/

[2] http://www.gpsdome.com/installation-manual

[3] https://www.microsemi.com/product-directory/cesium-frequency-references/4115-5071a-cesium-primary-frequency-standard

[4] https://www.microsemi.com/product-directory/clocks-frequency-references/3832-cesium-frequency-references

[5] http://piktime.com/?sl=EN

[6] http://piktime.com/images/TTS-5.pdf

[7] https://www.microsemi.com/product-directory/phase-noise-and-allen-deviation-testers/4130-5120a

[8] BIPM Circular T 353, June 13, 2017.

[9] BIPM Circular T 354, July 11, 2017

[10] https://www.ebay.com/p/Agilent-53230a-350-MHz-Universal-Frequency-Counter-Timer-12-Digits-s-20ps/1137274548

[11] https://www.microsemi.com/product-directory/gps-instruments/4135-syncserver-s650

[12] https://www.microsemi.com/document-portal/doc_view/135737-datasheet-syncserver-s650

Carrier-Phase Two-Way Satellite Frequency Transfer between BIRMM and NIM

Shuwei Wang[1], Xueyun Wang[1], Haifeng Wang[1], Zhiqiang Yang[2],Wenzhe Yang[1], Hongbo Wang[1], Shengkang Zhang[1].
[1]Science and Technology and Metrology and Calibration Laboratory, Beijing Institute of Radio Metrology and Measurement, Beijing, China
[2]National Institute of Metrology, Beijing, China
Beijing, China
wsw_203@163.com

***Abstract*—Recently, after studying the carrier-phase two-way satellite frequency transfer principle, BIRMM constructed the experiment system and did some experiments through TWSTFT carrier phase link with NIM. The result showed that we reached the instability for frequency comparisons at short averaging times in the order of 4E-12 at 1s.**

Keywords—TWSTFT; Carrier-phase; Time transfer

I. INTRODUCTION

With the development of highly accurate atomic clock, there is an increasing requirement for time and frequency transfer with corresponding accuracy level to compare the clock in different sets. Two-way satellite time and frequency transfer (TWSTFT) is a commonly used method of comparing time and frequency over a long range. Due to it has the advantage of high accuracy and long transmission distance, it attracts more and more attention from lots of scientific research institutions.

TWSTFT can achieve the performance on the level 1ns in accuracy and about 3E-15/d in precision now. In order to further improve its accuracy and stability, and make it an optimal method for remote time transfer and synchronization, in recent years, a number of scientific institutions have carried out research on TWSTFT carrier phase experiments. According to the basic principle of carrier phase, TWSTFT will increase its precision by three orders of magnitude compared with pseudo-code ranging. M. Fujieda[1] et al have done a series of TWSTFT carrier phase experiments which showed a dramatic performance increase to the order of 2E-13/s in precision. In this paper, we will discuss the two-way satellite frequency transfer carrier phase system between BIRMM and NIM and make analysis and discussion of test results.

II. TWSTFT CARRIER PHASE LINK BETWEEN BIRMM AND NIM

We use UTC(BIRMM) as the reference of the TWSTFT station at BIRMM, and use UTC(NIM) as the reference of the station at NIM. The figure of the experiment system is as follows.

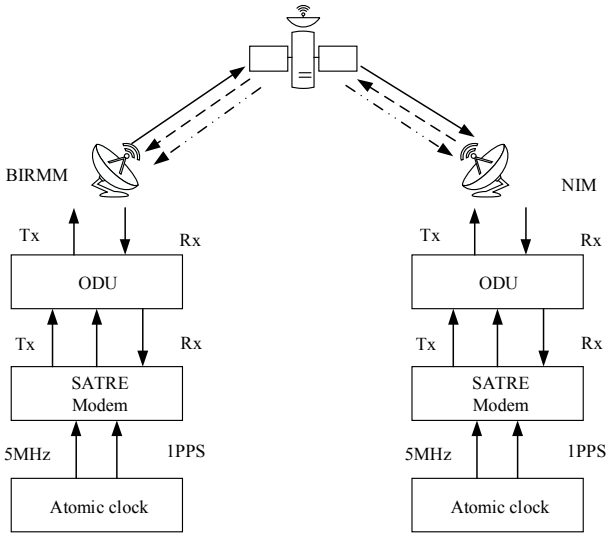

Fig. 1. The experiment system

Both stations have a two channels SATRE modem, one channel is used to receive the signal transmitted by satellite from the remote station, the other channel is used to receive the signal from its own. The modem is the core of the system, and we choose the SATRE modem to maintain the generality of the experiment and the consistency of the signal processing between the two sets. The signal transmission interval was determined by time interval counter (TIC). Two stations used different code signals in the transmit path. The signal was up-converter to 14GHz, then output to the feed port and transmitted through geosynchronous satellites at the same time. After the antenna receiver received and forwarded the signal, the signal passed through a low-noise amplifier and then was down-converted to 70MHz. The frequency of the received signal was then modulated and demodulated by the modem and recorded in real time by the computer. At the same time, the station also received and recorded the signal transmitted by itself via the satellite transponder. The process was the same as receiving the signal from the other station, and the two signal sequences were processed in parallel.

We use the receiving frequency measurements of the modem to obtain the carrier phase observations. The expressions used are the same as those used in previous USNO and PTB links [2].

$$\begin{bmatrix} F_{11}-f_{tx}+f_{SLO} \\ F_{22}-f_{tx}+f_{SLO} \\ F_{12}-f_{tx}+f_{SLO} \\ F_{21}-f_{tx}+f_{SLO} \end{bmatrix} = \begin{bmatrix} -f_{SLO} & 0 & 0 \\ 0 & -f_{SLO}+2f_{tx} & \frac{f_{SLO}}{f_{sys}} \\ f_{tx} & -f_{SLO}+f_{tx} & \frac{f_{SLO}-f_{tx}}{f_{sys}} \\ -f_{SLO}+f_{tx} & f_{tx} & \frac{f_{tx}}{f_{sys}} \end{bmatrix} \begin{bmatrix} k_1 \\ k_2 \\ df \end{bmatrix} \quad (1)$$

Where the notation F_{mn} is used to denote a frequency that has been transmitted by Station m and measured by Station n. Then it produces three lines with three different points of intersection.

$$df_{P1} = f_{sys}\left(\frac{(f_{tx}-f_{SLO})(F_{11}-F_{22})+(f_{SLO}-2f_{tx})(F_{11}-F_{12})}{-2f_{tx}(f_{tx}-f_{SLO})}\right)$$
$$df_{P2} = f_{sys}\left(\frac{(2f_{tx}-f_{SLO})(F_{11}-F_{21})-f_{tx}(F_{11}-F_{22})}{-2f_{tx}(f_{tx}-f_{SLO})}\right) \quad (2)$$
$$df_{P3} = f_{sys}\left(\frac{f_{tx}(F_{21}-F_{12})+f_{SLO}(F_{11}-F_{21})}{2f_{tx}(f_{tx}-f_{SLO})}\right)$$

To minimize the effect of noise, the three points may be averaged as

$$df_{AVG} = \frac{f_{sys}}{6}\left(\frac{f_{SLO}(F_{12}-F_{22})+2f_{SLO}(F_{11}-F_{21})-3f_{tx}(F_{12}-F_{21})}{f_{tx}(f_{tx}-f_{SLO})}\right) \quad (3)$$

III. ANALYSIS OF THE EXPERIMENTAL DATA

The signal to noise ratio was about 55dBHz during the experiment. Both station transmitted a signal with a frequency 14456MHz, which was defined with respect to the system frequency 5MHz. At the satellite, the frequency of the received signal mixed with the satellite's local oscillator frequency 1750MHz.

We chose an hour of sampling data and exchanged the data of two ground stations. Then the data was processed and the offset between the frequencies of two clock was obtained after processing. The result are as follows.

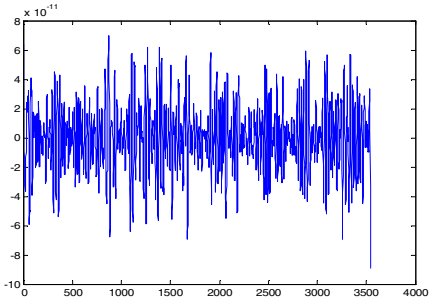

(a) Relative frequency difference

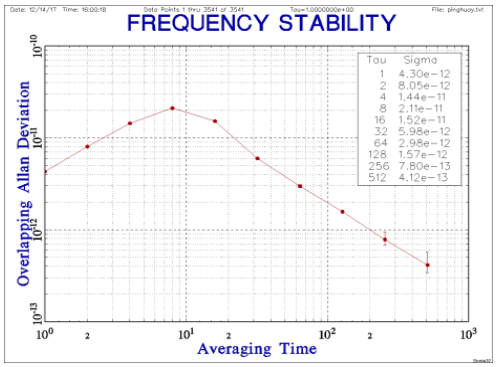

(b) Frequency stability of the link

Fig.2. Frequency differences between BIRMM and NIM measured by TWCP

There is a bump in the frequency stability curve at the integral time of 10s. The origin of the bump needs further analysis and demonstration, which may be due to the periodicity of the relative frequency difference curve. It is shown as follows.

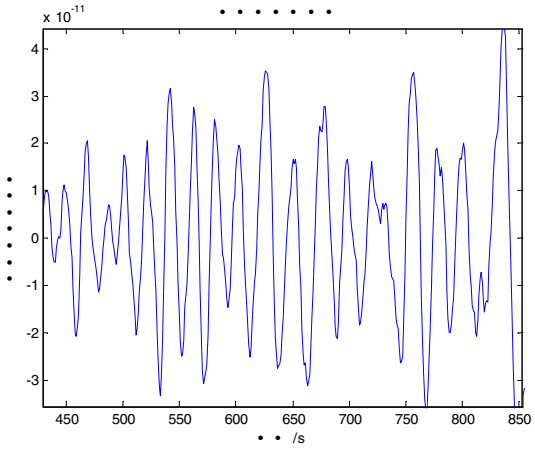

Fig.3. Periodicity in relative frequency deviation curve

IV. CONCLUSION

The result showed that we reached the instability for frequency comparisons at short averaging times in the order of 4E-12 at 1s. Although it showed that the accuracy and stability were improved with the traditional pseudo-code experiment, but the transmission accuracy was still different from that of the theory. This may come from the PLL noise in the frequency up/down converter. By constructing the system, we have found that the application of carrier phase to TWSTFT system is the development trend of TWSTFT technology, but there is still a lot of work to do.

REFERENCES

[1] M. Fujieda et al., " Carrier-phase two-way satellite frequency transfer over a very long baseline", Metrologia, vol. 51, p. 253-262, 2014.

[2] Blair Fonville, Demetrios Matsakis,“ Development of Carrier-phase-based two-way satellite time and frequency transfer(TWSTFT)”, 36th Annual Precise Time and Time Internal(PTTI) Meeting, 2005.

[3] M. Fujieda et al., “Carrier-Phase-Based Two-Way Satellite Time and Frequency Transfer,” IEEE Trans. Ultrason. Ferroelectr. Freq. Control, vol. 12, pp. 2625-2630, 2012.

[4] M. Fujieda, H. Maeno, D. Piester, A. Bauch, S. H. Yang, T. Suzuyama, W. H. Tseng, L. Huanxin, Y. Gao, J. Achkar, and D. Rovera, “Impact of the transponder configuration on the Asia-Europe TWSTFT network,” 2011 Joint Conference of the IEEE International Frequency Control and the European Frequency and Time Forum, 2011.

[5] Xueyun Wang, Hang Yi, Shengkang Zhang, Liang Wang et al., “Design of a new calibration device for Two-Way Satellite Time and Frequency Transfer station,” IEEE, pp. 180-183, 2016.

[6] Dieter Kirchner. “Two-Way Time Transfer Via Communication Satellites ,”IEEE,vol 7, pp. 983-990, 1991.

[7] D. Piester, H. Schnatz. “Novel techniques for remote time and frequency comparisons. PTB-Mitteilungen,” vol 119, pp. 33-44, 2009.

Time Synchronization Performance Using the Network Time Security Protocol

Martin Langer*, Kristof Teichel†, Dieter Sibold† and Rainer Bermbach*
Email: mart.langer@ostfalia.de, kristof.teichel@ptb.de, dieter.sibold@ptb.de, r.bermbach@ostfalia.de
*Ostfalia University of Applied Sciences, Wolfenbüttel, Germany
†Physikalisch-Technische Bundesanstalt, Braunschweig, Germany

***Abstract*—This paper compares the time synchronization performance of standard NTP versus NTP secured using the Network Time Security (NTS) protocol. The measurements were performed using the NTS software of Ostfalia University of Applied Science – the first implementation of NTS based on the IETF internet draft "draft-ietf-ntp-using-nts-for-ntp-06". The measurements quantify the impact of the security measures on the time synchronization performance and allow conclusions to be drawn regarding efficiency and potential improvements to the protocol.**

Keywords—Network Time Security (NTS); Network Time Protocol (NTP); security; authentication; integrity

I. INTRODUCTION

Time synchronization of networked computer systems is of paramount importance for the correct functioning and interoperability of many computer applications. The protection of time synchronization protocols is vital in order to both counter existing threats and comply with legal requirements. To date, time information has usually been disseminated in an unsecured form that creates opportunities for adversaries to maliciously alter time information [1]. An important and widely used example of a tool for disseminating time information is the Network Time Protocol (NTP) [2-4]. NTP meets the accuracy requirements of many application fields but offers only limited security measures. An analysis of security mechanisms specific to NTP demonstrated that they were either not secure or unsuitable for practical use [5]. This prompted the development of Network Time Security (NTS), which is currently in the final specification procedure. NTS was designed to solve the known security issues of NTP without sacrificing the accuracy and stability provided by the time synchronization process using standard NTP.

In this paper, we measure the impact of NTS concerning the efficiency and time synchronization performance of NTS-secured NTP. The measurements presented here are based on the NTS version defined by a set of three internet drafts: draft-ietf-ntp-using-nts-for-ntp-06 [6], draft-ietf-ntp-network-time-security-15 [7], and draft-ietf-ntp-cms-for-nts-message-06 [8]. These drafts were implemented by the Ostfalia University of Applied Sciences in cooperation with PTB [9] and refined in follow-up work, which has now been used to analyze the essential properties of this NTS version. Chapter II introduces the reader to the technical aspects of NTP and NTS. Chapter III describes the measurement setup, while the results of the measurements are presented and discussed in Chapter IV. This analysis also allows the inefficient steps in the NTS protocol to be identified; this information can be used to improve such protocol steps in the ongoing specification process.

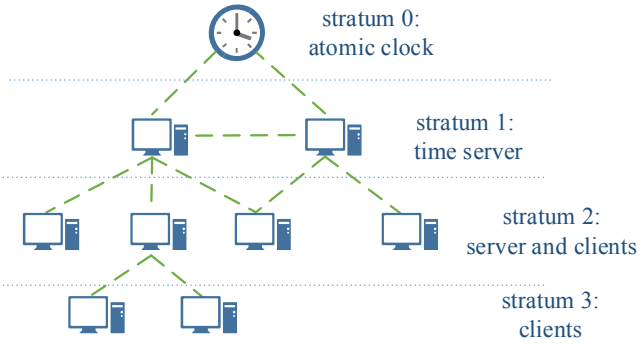

Fig. 1. Hierarchical structure of NTP time servers

II. PRELIMINARIES

This section gives an overview of the main aspects of NTP and NTS, to the extent to which they are relevant to the work presented.

A. The Network Time Protocol (NTP)

One of the most widely used protocols for clock synchronization worldwide is NTP, which is deployed on nearly every computer system in existence. Developed by David L. Mills in 1985 and presented in the IETF's RFC 958 [3], its Version 4 (NTPv4) has been available as RFC 5905 [4] since 2010. NTP communicates via packet-switched networks using the connectionless communication model of the UDP internet protocol to send and receive timestamps. What is most commonly used is a client/server model combined with a hierarchical structure as seen in Fig. 1. Available time servers are categorized according to their distances from the reference clock. Each level is called a *stratum* and given a number according to the distance. A reference clock would be stratum 0, the time server on the level below would be stratum 1 and so on. As the stratum number increases, the accuracy typically decreases.

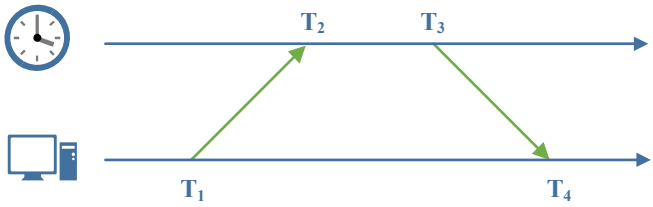

Fig. 2. Timestamps used in the NTPv4 Protocol

NTP uses different modes of operation that determine the kind of communication between NTP protocol objects. In *symmetric mode,* an NTP instance can distribute time information as well as receive it. It synchronizes its clock via calibration with servers of the same stratum. In *broadcast mode,* a server periodically transmits time information that can be used for clock synchronization by any NTP client that receives it. NTP's most prominent mode is the *client/server mode*, which applies a *unicast* communication model. In this mode, a client transmits time requests to an NTP server (once or periodically), whereupon the server responds by sending the time information required [2, 4]. In client/server mode, clock synchronization between an NTP client and an NTP server applies a two-way time transfer approach [10]: At time t_1, the client sends an NTP packet to the server containing the timestamp $T_1 = T(t = t_1)$. Upon arrival at time t_2, the server processes the packet, and at time t_3, it inserts the timestamps T_2 and T_3 and transmits the packet back to the client, where it is received at time t_4. This communication yields the four timestamps displayed in Fig. 2. Note that the clock at the client produces the timestamps T_1, T_4 and the clock at the server creates the timestamps T_2, T_3.

From these timestamps, the NTP client can derive the network delay δ and the time offset θ between the client and the server. Note that δ represents the packet round-trip time excluding the computing time at the server, indicating the time the packets have traveled in the network. Calculation of θ and δ is done according to the following equations [2, 4]:

$$\delta = (T_4 - T_1) - (T_3 - T_2) \quad (1)$$

$$\theta = ((T_2 - T_1) - (T_4 - T_3)) / 2 \quad (2)$$

Assuming that the propagation delay of the packets between the client and the server is the same in both directions, the offset θ quantifies the time difference between the clocks of the NTP client and its server. The NTP process continuously aims to minimize θ by adjusting the frequency of the client's system clock.

1) Issues of Previous Security Measures

In most cases, NTP transmits the time synchronization packets without any cryptographic protection. This allows an adversary to alter, replay or dismiss time synchronization packets, or to inject false packets. A comprehensive list of known threats to time synchronization protocols is compiled in RFC 7384 [1].

To increase security, the *symmetric key* method was introduced in 1992 as part of the NTPv3 protocol. It permits authentication of NTP participants and ensures the integrity of the transmitted time data by means of cryptographic hash functions. Although this method is still considered secure, it does not provide a key exchange mechanism or scale well for large network deployments or for the global internet. In order to address the scalability issue, the Autokey method was introduced with NTPv4 and specified in the informational RFC 5906 [11]. However, an in-depth analysis of Autokey [12, 13] exhibited severe security vulnerabilities. Therefore, Autokey is no longer considered secure or recommended for use [14].

Tunnel solutions such as TLS (Transport Layer Security) and IPSec offer another approach to adding security to time dissemination. Although they provide a secure connection for sending NTP packets, they entail two fundamental disadvantages. On the one hand, they require a permanent, stateful connection between the server and the client. Such a connection involves many resources, especially on the server side. On the other hand, tunnel solutions do not consider the unique requirements associated with the dissemination of time information, thus causing synchronization performance to decline. Consequently, they are of limited use.

B. *The Network Time Security Protocol*

Originally motivated by demand for cryptographically secured time synchronization mechanisms created within the scope of the Smart Grid Initiative of the German Federal Ministry of Economic Affairs and Energy, the Network Time Security (NTS) protocol offers a solution to the security problem. It extends existing time synchronization protocols and thus allows secure time synchronization in networks. NTS is currently under development, but is approaching finalization and publication as a standards track RFC of the IETF. The present draft version is draft-ietf-ntp-using-nts-for-ntp-11 [15].

The main goals of NTS are to enable NTP clients to cryptographically identify their NTP servers, ensure authenticity and integrity for exchanged time packets and ensure that the time synchronization quality is impacted as little as possible. To this end, an NTS-protected association between an NTP client and a server is established in a first phase, the so-called key exchange phase. In this stage, the client and server will negotiate the cryptographic algorithms, exchange certificates and generate cryptographic keys. In addition, the client will verify the authenticity of the server by means of a Public Key Infrastructure (PKI). In the subsequent phase, the participants exchange secured time synchronization packets protected by a Message Authentication Code (MAC), a digital fingerprint enabling the detection of any data manipulation. See [5] for further information. NTS does not require the NTP server to save the state of the client. Instead, it utilizes stateful clients and stateless servers. The server can process the requests of a client based solely on the information provided in the request packet.

III. Measurement Setup and Configuration

The goal of the measurements was to compare different implementations (unsecured and secured NTP) in terms of their performance, and to compare the resulting accuracy and stability of the synchronized clocks. Hence, the tests recorded the

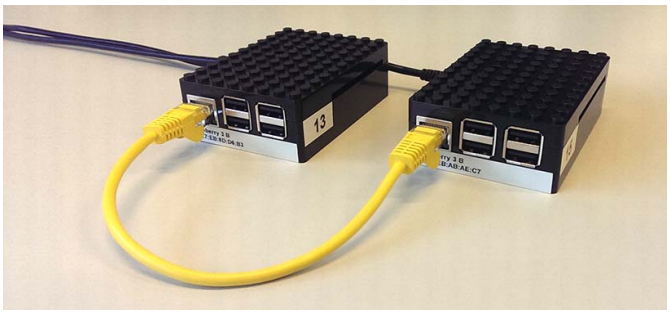

Fig. 3. Measurement setup with a direct client/server connection

Fig. 4. Composite of several measurement setups

time offset, the delay and the processing time of each implementation. The tests also considered the asymmetrical round-trip time of NTS. To obtain consistent and comparable results, identical conditions and simultaneous measurements were fixed for all measurement setups. The hardware was based on third-generation Raspberry Pi[1] devices, all of which were in closed standard boxes running identical software. They differed only in the individual configuration of the NTP implementation used and in their specific role in the communication process (NTP server or client). Data was exchanged between the client and the server via direct coupling using a Fast-Ethernet cable connection[2] (s. Fig. 3). In this way, one client always interacted with one server. All Raspberry Pis were operated in headless mode[3] and controlled via Wi-Fi, which is already integrated in these models. Thus, network traffic due to control messages had no impact on the measurements. Several of these units were assembled according to Fig. 4.

On the software side, the *Raspbian lite* operating system [16] formed the base of the measurements. All services needed by the system to synchronize the clock were set up manually using three different NTPv4 implementations or configurations. Two different realizations of NTP software were applied: the so-called reference implementation provided by the Network Time Foundation [17] (in the following referred to as **NTPD**[4]), and the implementation given in [18] and referred to throughout this paper as **NTP**. This realization offers an interface to plug in NTS functions, thus enabling secured time synchronization; we refer to this configuration as NTS or **NTP (NTS)**. The NTS service version employed [6] is operational in unicast client/server mode and is designed to ensure security by embedding additional security data into existing time transmission protocols without any further modification to those protocols. In the case of NTP, this is accomplished by encapsulating NTS-related content in NTP extension fields. Such fields are defined in RFC 7822 [19]. Both NTPD and our own NTS-secured NTP solution can each act as either a client or a server.

The timestamps that an NTS-enabled NTP server transmits during one measurement period are based upon its local time. Since this setup does not include any further network connectivity, there was no synchronization of the server's own clock to another party during the measurement. However, synchronization to external servers took place immediately before the measurements and was suppressed deliberately during the measurement periods in order to prevent potential fluctuations of the server's local time. In addition, the configuration regarding NTS took place in an identical way in order to increase comparability of the results.

NTS servers and clients each use local certification chains[5] with 2048-bit RSA keys and with sha256WithRSAEncryption as their signature algorithm. For authentication of the NTP time packets, the HMAC_SHA512 algorithm was used. Furthermore, the NTP poll interval was set to 16 seconds on all NTP clients. The typical duration of a measurement series in the data presented was 48 to 72 hours. Each dataset started at midnight and ended 24 hours later. The data was collected via the implementation itself, which saves the (raw) data as text files. Before a measurement series started, the devices went through several hours of warm-up time; here, the NTP clients became attuned to the same conditions as their servers. Additionally, this enabled temperature control and thereby minimized the quartz fluctuations that occur due to temperature differences. A fully temperature-stable environment was not available at the time of the measurement.

IV. Measurement Results

The measurements listed here observe the essential aspects of the NTS implementation and range from resource requirements and accuracy/stability achieved to non-correctible deviations in the time synchronization.

A. Computational Cost and Resource Requirements

The more complex processing chain and the employment of cryptographic functions[6] in NTS increase processing times and therefore the CPU power required. The values listed in Table 1 show the performance of the corresponding implementations for comparison, each differentiated by the different roles as client or server. Since the measurements were taken on relatively weak single-board computers, computation times are significantly higher than they would be in a desktop or server system. However, the relationship between the values can be expected to be preserved on a desktop computer. The processor time required daily was determined based upon the execution

[1] Raspberry Pi 3 Model B Rev 1.2

[2] 100 Mbit bandwidth using LAN9514-Chip

[3] No connection of other peripherals such as mouse, keyboard or monitor

[4] Network Time Protocol (NTP) Daemon v4.2.8p10

[5] In each case, the primary certificate, two intermediate and one root certificate

[6] The basis for this is the OpenSSL library in version 1.1.0

TABLE I. COMPARING THE REQUIRED PROCESSING TIME

Implementation	Role	CPU Time per Day [s]	Average CPU Usage [%]
NTPD	Client	7.18	0.008
NTPD	Server	6.57	0.008
NTP	Client	25.46	0.029
NTP	Server	11.28	0.013
NTP (NTS)	Client	41.33	0.048
NTP (NTS)	Server	22.85	0.026

time of the NTP daemon and the actual processing time of the CPU. To capture the values in Linux, the *top* and *htop* processor observation tools were used[7].

The data demonstrates that an NTS client generates approximately six times the computing load of an NTPD client for processing and transmitting the same number of NTP packets. However, the cryptography employed affects the values only marginally. A detailed analysis performed with the *KCachegrind* profiler tool [20] revealed that an NTP client with activated NTS functionality uses only 3 % of its required CPU time for the actual computation of the MAC, and only 8 % for the NTS service. The majority of the NTS-specific CPU time is consumed by the ASN.1[8] library (asn1c [21]), certificate processing, and debugging and logging functions employed. Furthermore, the direct comparison between NTPD and Ostfalia's NTP implementation indicates that there is potential for optimization. However, due to the *proof of concept* character of the implementation and the unfinished NTS specification, no effort to optimize this implementation has been made yet.

B. Obtainable Synchronization Accuracy

This section discusses the synchronization quality that an NTP/NTS client can achieve relative to its time server. Since the NTP protocol must work from the assumption of symmetric network delays, any asymmetry in packet transport times is hard to correct. However, symmetric packet delays can be assumed for the given measurement configuration because conditions are deliberately uniform on all devices, including identical hardware and software, and because unnecessary external devices such as routers in the network communication chain are eliminated wherever possible.

1) Determination of Minimum Packet Delays

To improve the measurability of the efficiency of the NTP/NTS service, assessment of the minimum possible packet round-trip delays is important. These are delays that not even a well-optimized implementation can go below. The necessary measurements were performed by *ping* commands on the corresponding Ethernet interfaces of the devices employed. For the fixed packet size chosen for this context, the payload (embedded in IPv4) matched the size of an NTS-secured NTP packet transported via UDP[9]. The diagram in Fig. 5 shows the

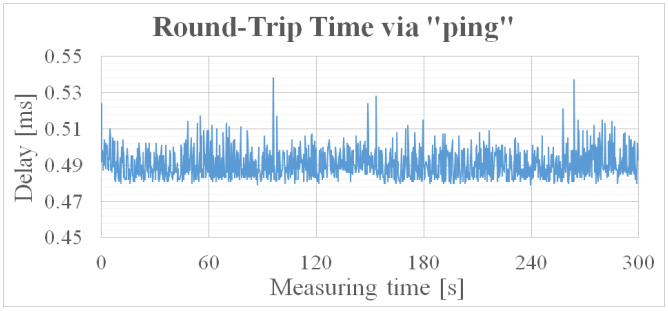

Fig. 5. Minimally achievable round-trip times

development of the measurement that involved firing such a *ping* four times per second. To minimize distortions during these experiments, the data was saved directly into RAM and console outputs were deactivated. The mean value detected of 0.49 ms and the standard deviation of 0.008 ms were consistently found for all measurement objects, even under variation of *ping* intervals during further tests.

2) Comparison of Delay and Time Offset between the Implementations

After ascertaining the minimum delay in IV.B.1, the comparison of the recorded delays can indicate the efficiency and the synchronization accuracy of the NTP services. The comparison of these measurements can be seen in Fig. 6. This diagram shows a 6-hour section of the various implementations. Each program calculates and stores its own delay values. Note that, in this case, the delay not only includes the round-trip time of the packets, but also contains implementation-dependent delays. As can be seen, the delay of NTPD is around 0.5 ms and very close to the minimum delay determined. Therefore, this service appears to be well optimized. By comparison, our own NTP service shows higher delays in the range of 0.9 ms, as well as a higher jitter. Hence, the missing optimizations and the debug functions presumably have a direct effect on the synchronization accuracies. Enabling NTS in this NTP service yields an increased mean and jitter of the network delay (approximately 1.5 µs larger than the NTPD implementation), due to the time needed for the ASN.1 encoding and the cryptographic operations. The latter accumulate completely to the delay, because the calculation of the MAC can only be performed after adding the timestamps T_1 or T_3, respectively, to the NTP packet.

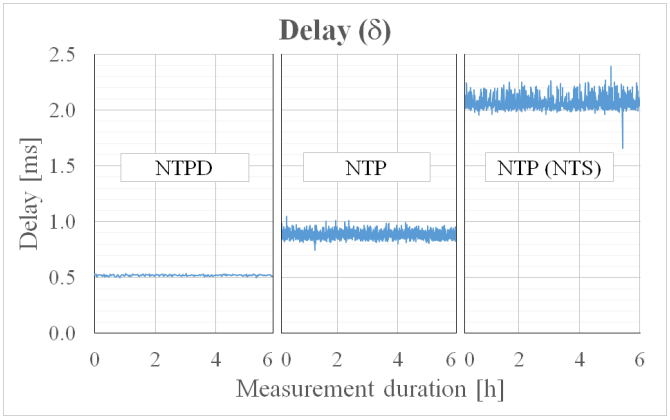

Fig. 6. Delay comparison between the different implementations

[7] Recording and evaluation of values: ELAPSED, TIME and TIME+

[8] Abstract Syntax Notation One

[9] Refers to the NTS server's TimeResponse message. The complete UDP frame thus has a total size of 152 Bytes.

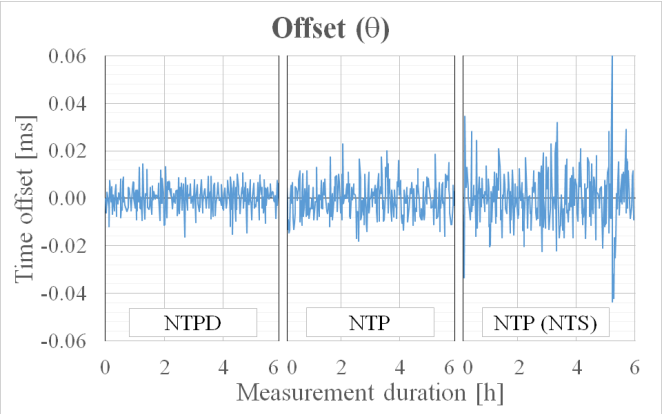

Fig. 7. Time offset comparison between the different implementations

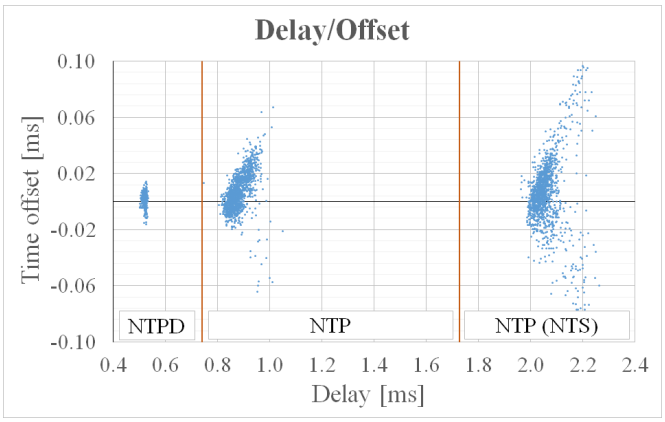

Fig. 8. Delay/offset scattering in comparison

Due to the higher delay and jitter caused by NTS, the jitter of the time offset also increases. The comparison in Fig. 7 shows the difference between the implementations in the same 6-hour measurement section. The standard deviation of the time offset of 4.7 µs in NTPD is smaller than that of 7.9 µs in NTP and much smaller than that of NTP (NTS), 11.6 µs. The combination of delay and offset in a scattering diagram (s. Fig. 8) additionally shows a positive bias of NTP and NTP (NTS) due to the implementation.

3) Time Stability

Fig. 9 compares the time deviation (TDEV) of the different measurements. The slope of the blue line (NTP/NTS) is approximately -0.5, which indicates a phase jitter with the character of white phase noise. The slope for NTP (orange) and NTPD (green) indicate that the noise processes are dominated by white phase noise. With increasing averaging time, the jitter (and thus, the instability) decreases. For averaging times larger than 2000 s, other noise processes such as flicker phase noise become dominant. As observed above, the NTPD implementation displays the best stability, followed by the NTP and NTS implementations.

C. Uncorrectable Time Offset When Using NTS

Due to NTS's applied cryptography, as well as the differently sized NTS-secured NTP packets, there is an inevitable asymmetry of the packet transmit delays. This is not correctable by NTP itself, and consequently causes a systematic error

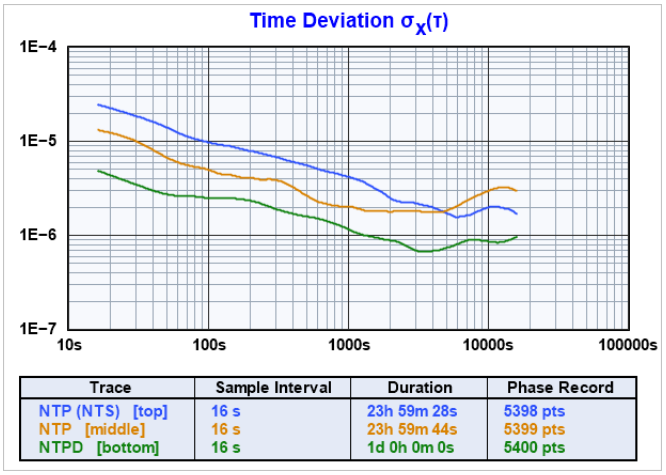

Fig. 9. Time deviation (TDEV) of the implementations

in the steering of the client's local clock. This section examines the causes and extent of the major errors in order to identify further areas of research and propose countermeasures.

1) Asymmetric Packet Sizes

The complete frame of an NTP network packet that has been sent can be divided into four parts: The Ethernet header (14 bytes), the IPv4 header (20 bytes), the UDP header (8 bytes) and the NTPv4 header (48 bytes). Using unsecured NTP, both the client request and the server response always have the same length (90 bytes). The transfer of this data via Fast-Ethernet (100 Mbit/s) takes 7.2 µs. If the NTP packet contains a *TimeRequest* message from the NTS client, then the size of the complete Ethernet frame with 214 bytes will be 124 bytes larger than that of an unprotected NTPv4 packet. This increases the transmit duration from client to server by an additional 9.92 µs. However, an NTP header (*TimeResponse*) from the server to the client that is 96 bytes larger needs 7.68 µs. Since NTP assumes symmetric packet transmission times, the difference of 2.24 µs leads to a permanent time offset at the client that is half of the packet round-trip time (1.12 µs). The data transfer over a gigabit Ethernet connection can be a temporary countermeasure to reduce the asymmetry of the packet delays. However, the asymmetry remains in this case, and the entire transmission path must have this bandwidth to achieve the desired effect. The alignment of the packet sizes is a better alternative in order to completely compensate for this systematic error. The resulting additional network load increases slightly to 28 bytes[10] per message exchange.

2) Cryptography and Performance Differences

Two critical issues related to the absolute synchronization quality are the use of cryptography and the performance differences between the client and the server. To measure this offset, the NTS software was provided with timestamps at the appropriate places in the implementation and decoupled from the NTP implementation. In this mode, the NTS service uses dummy NTP packets to prevent possible variations from being caused by the NTP implementation. Furthermore, in this test, the service works both as a server and as a client in the same program instance to avoid influences caused by communication between

[10] The size difference between TimeRequest and TimeResponse

two devices. This allows the time measurement of internal NTS processes that are included as delays in the packet round-trip time. The diagram in Fig. 10 shows measurement data obtained on a Raspberry Pi. In this measurement, 600 packages were produced and processed in direct succession. It can be shown that the weak hardware of the Raspberry Pis has a considerable influence on the delay. Due to the higher computational effort[11], the server's delay, at a mean value of 468 µs, is even higher than the client's, at 363 µs. The difference in the processing times represents the asymmetry, half of which results in an uncorrectable time offset during the synchronization of the client. Therefore, the measured difference of 105 µs leads to a permanent deviation of 52.5 µs. The frequent peaks are probably due to operating system-specific services that may affect the measurement but have not yet been determined. When comparing these results with the values on a desktop PC (s. Fig. 11), the delay on the client and server is reduced, but moves in the same proportion.

The results show two general problems. The interaction between the client and the server, where great differences exist in their performance, leads to a large asymmetry. Furthermore, correcting dynamic errors that occur as variations in the processing time for securing the time messages is virtually impossible. In addition, the measurements on the Raspberry Pi devices showed other cyclic increases in processing time in addition to the jitter. The origin of this behavior has not yet been clarified and presumably depends on the write access of the recorded measurement data to the storage medium or the internal Linux services.

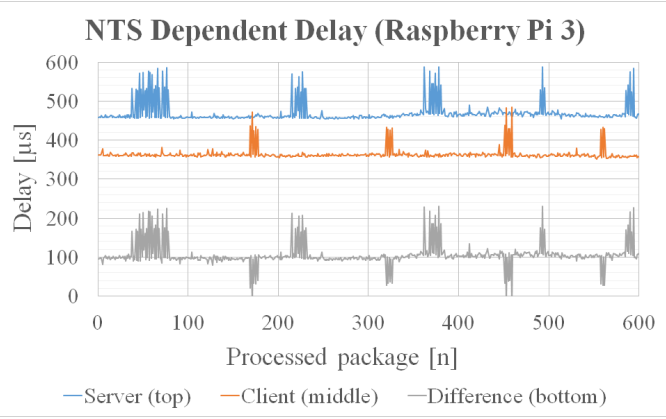

Fig. 10. Additional NTS-related delay on the Raspberry Pi 3

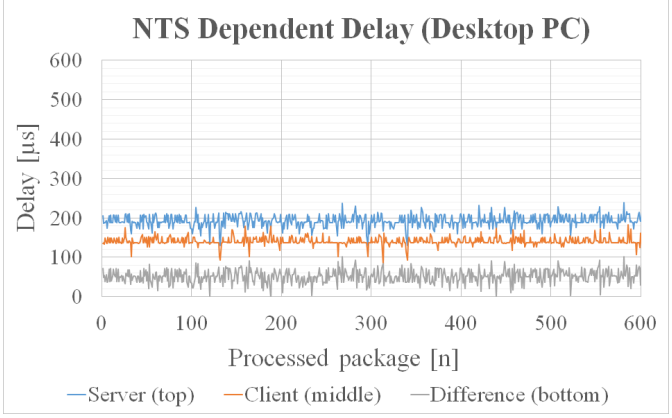

Fig. 11. Additional NTS-related delay on a desktop PC

Note that the measurement of these delays is distorted to some extent. The time measurements (as part of the implementation), the logging of information and the storage of measurement data during this critical processing time have a strong influence on the measurement results. With time recording activated, comparative measurements showed an increase in the delay of about 30-50 % (depending on the hardware). As mentioned in IV.A, the cryptography has shown little impact on processing time, which is currently 8 % of NTS. The optimization of the NTS service offers the possibility of reducing the delay, but cannot prevent it completely. A solution to compensate for these inaccuracies is currently unavailable and requires further research. For this reason, the optimization of the implementation is the best way to minimize the delays.

V. Conclusion and Further Work

The evaluation of the measurement results confirms that it is possible to secure time synchronization traffic with NTS, albeit at the cost of some precision. The relative accuracy that undergoes higher fluctuations due to NTS (and that is hard to correct for via NTP) can be significantly compensated for by optimizing the implementation code. A more problematic issue when securing time synchronization messages is that of performance differences caused by different hardware. Significant differences in processing time during time-critical phases of NTS can lead to a permanent systematic increase in the offset between the clocks of a client and its server. Additional fluctuations during these phases further impede potential solutions such as using correction data.

Since the current draft version of NTS, draft-ietf-ntp-using-nts-for-ntp-11, shows massive design changes from the basis of our implementation [6], it is critically important that new measurements be carried out after the update is fully implemented. Currently, the implementation of said current draft version is still in progress (parallel to the standardization process in the IETF). The changes relate to the communication sequence, the NTP modes supported and increased privacy protection. Furthermore, the current NTS draft does not use ASN.1, which contributes a significant part of the non-correctable asymmetries. Completion of the NTS specification is currently estimated for mid-2018.

Acknowledgment

We are especially grateful to Simon Häußler, Christian Jütte, Thorben Kompa, Silvan König and Thilo Tuschik, who provided Ostfalia's NTPv4 implementation. Special thanks to Dirk Piester who contributed to the analysis of time stability.

References

[1] T. Mizrahi, "Security Requirements of Time Protocols in Packet Switched Networks," RFC 7384, doi 10.17487/rfc7384, October 2014.

[2] D. L. Mills, "Computer network time synchronization: The Network Time Protocol," NY: CRC Press, 2006.

[3] D. L. Mills, "Network Time Protocol (NTP)," RFC 958, doi 10.17487/RFC0958, September 1985.

[4] D. L. Mills, J. Burbank, and W. Kasch, J. Martin, Ed., "Network Time Protocol Version 4: Protocol and Algorithms Specification," RFC 5905, doi 10.17487/rfc5905, June 2010.

[5] D. Sibold and K. Teichel, "Network Time Security Specification - Protecting Network-based Time Synchronization," in 2016 European Frequency and Time Forum (EFTF), York, UK, 2016.

[6] D. Sibold, S. Roettger, and K. Teichel, "Using the Network Time Security Specification to Secure the Network Time Protocol," Internet Draft, draft-ietf-ntp-using-nts-for-ntp-06, September 2016 (Work in Progress).

[7] K. Teichel, D. Sibold, and S. Roettger, "Network Time Security," Internet Draft, draft-ietf-ntp-network-time-security-15, September 2016 (Work in Progress).

[8] D. Sibold, S. Roettger, K. Teichel, and R. Housley, "Protecting Network Time Security Messages with the Cryptographic Message Syntax (CMS)," Internet Draft, draft-ietf-ntp-cms-for-nts-message-06, February 2016 (Work in Progress).

[9] M. Langer, "Implementierung des Network-Time-Security-Protokolls für den Unicast-Betrieb," Master Thesis, Elektrotechnik, Ostfalia University of Applied Science, 2016.

[10] J. Levine, "A review of time and frequency transfer methods," Metrologia, vol. 45, no. 6, pp. S162-S174, Dec 2008.

[11] D. L. Mills, B. Haberman, Ed., "Network Time Protocol Version 4: Autokey Specification," RFC 5906, doi 10.17487/rfc5906, June 2010.

[12] S. Röttger, "Analysis of the NTP Autokey Procedures," Project Thesis, Technische Universität Braunschweig, Institute of Theoretical Information Technology, Braunschweig, 2012.

[13] D. L. Mills, "NTP Security Analysis," [Online] Available (03/06/2018): https://www.eecis.udel.edu/~mills/security.html, May 2012

[14] D. Reilly, H. Stenn, and D. Sibold, "Network Time Protocol Best Current Practices," Internet Draft, draft-ietf-ntp-bcp-06, December 2017 (Work in Progress).

[15] D. F. Franke, D. Sibold, and K. Teichel, "Network Time Security for the Network Time Protocol," Internet Draft, draft-ietf-ntp-using-nts-for-ntp-11, March 2018 (Work in Progress).

[16] Raspberry Pi Foundation, "Raspbian Stretch Lite," [Online] Available (03/06/2018): http://downloads.raspberrypi.org/raspbian_lite/images/raspbian_lite-2017-09-08/, 2017

[17] Network Time Foundation, "Network Time Protocol (NTP) Daemon v4.2.8p10," [Online] Available (03/06/2018): https://www.eecis.udel.edu/~ntp/ntp_spool/ntp4/ntp-4.2, 2017

[18] S. Häußler, C. Jütte, T. Kompa, S. König, and T. Tuschik, "Entwicklung einer NTPv4-Implementation zur Unterstützung von NTS," Team Project, Ostfalia University of Applied Science, 2016.

[19] T. Mizrahi and D. Mayer, "Network Time Protocol Version 4 (NTPv4) Extension Fields," RFC 7822, doi 10.17487/RFC7822, March 2016.

[20] J. Weidendorfer, "KCachegrind v0.7.4," [Online] Available (03/06/2018): https://kcachegrind.github.io/html/Download.html, 2013

[21] L. Walkin, "The ASN.1 Compiler (asn1c v0.9.27)," [Online] Available (03/06/2018): https://github.com/vlm/asn1c/releases/tag/v0.9.27, 2014

The Study of Using Hydrogen Maser Ensemble to Steer UTC(TL)

Shinn-Yan Lin
Telecommunication Laboratories
Chunghwa Telecom Co., Ltd.
Taoyuan Taiwan
sylin@cht.com.tw

***Abstract*—For steering UTC(TL) during the latency period between UTC monthly announcements, we create a paper clock generated from a hydrogen maser ensemble according to the weekly published UTCr. The frequency of hydrogen masers are modeled and predicted as a linear function calculated from the linear regression of hydrogen masers vs. UTCr. The hydrogen masers with closer predictable frequency will be given more weight to constrain the paper clock follows the frequency trend of UTCr. In the paper clock simulation test, neglect the phase error accumulation affected by each frequency prediction error, the phase difference of 10 days prediction span between the paper clock prediction and official time scale are from -4 ns to 2 ns.**

Keywords—UTC; rapid UTC; time scale; clock ensemble;

I. INTRODUCTION

Currently, the national standard time and frequency of Taiwan, UTC(TL), is generated from a micro phase stepper which referenced by a hydrogen maser (h-maser) and steered according to the official time scale UTC (Coordinated Universal Time) which monthly announced by BIPM (Bureau international des poids et mesures) Circular T publication[1].

Since the windows period of the BIPM Circular T announcement can be as long as 45 days, and the free run atomic time scale of TL (Telecommunication Laboratories, Taiwan), TA(TL)[2-4], is not designed for short term accuracy, the cesium clock ensemble paper clock time scale, TA_1(TL)[5-6], which steered by UTC is used to be the mid-term prediction reference between monthly UTC publication. In the simulation test, the phase error of TA_1(TL) could reach the accuracy less than 10 ns in 45 days prediction span vs. UTC[6].

From 2014, following the new weighting algorithm introduced into UTC calculation [7], we gently changed the composition of clock ensemble from major cesium clocks into hydrogen masers (h-masers). In 2016, the composition of TL atomic clock ensemble is 12 cesium clocks and 3 h-masers and became 9 cesium clocks and 5 h-masers in 2018. Due to the TA_1(TL) will be getting less stable for its less numbers of cesium clocks in ensemble, we start to re-investigate the properties of atomic clocks and try to generate a new paper clock time scale reference based on limited numbers of h-masers and cesium clock ensemble.

In the atomic clock characteristics investigation, we find the minimum Hadamard deviations of h-masers vs. UTC are around 1×10^{-15} at the average time 5-10 days (Fig. 1), when average time > 10 days, the random walk, flicker walk, and random run FM noise would dominate[8-10]. By contrast, the Hadamard deviations of TL cesium clocks vs. UTC are around 9×10^{-15} at average time = 10 days (Fig. 2).

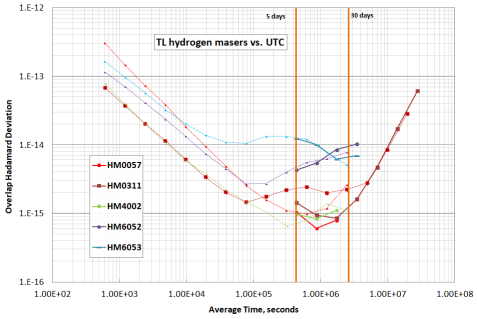

Fig. 1. The Hadamard deviations of h-masers with respect to UTC, the dash lines is the Hadamard devation of h-masers with respect to UTC(TL)

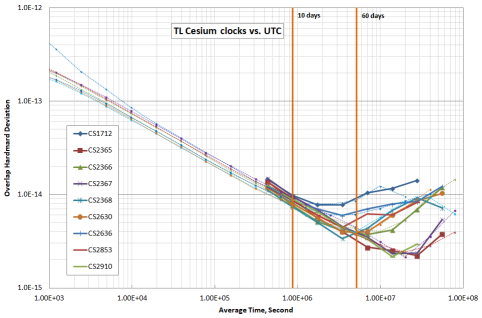

Fig. 2. The Hadamard deviations of cesium clocks with respect to UTC, the dash lines is the Hadamard devation of cesium clocks with respect to UTC(TL)

The Hadamard deviation is unaffected by linear frequency drift[8, 9], that is even we remove the frequency drifts of cesium clocks, the limited numbers of cesium-clock ensemble

is still too noisy to steer a h-maser referenced master clock during the windows periods of Circular T.

For better short term performance, instead of UTC, the quasi-official time scale, rapid UTC (UTCr) [11], is chosen to model and predict the h-masers. Every Wednesday, the BIPM publishes the daily values of [UTCr–UTC(k)] from last Monday to last Sunday. That is the window period of UTCr is less than 10 days, therefore we don't need to consider the noise types of h-masers dominate at long term (after the average time > 10 days), but simply keep focus on the more predictable properties of h-masers.

In section II, we first examine the phase and frequency difference between UTC and UTCr to confirm the accuracy and stability of UTCr, and then investigate the properties of h-masers vs. UTCr to model and predict the behavior of h-masers. The weighting procedure and the model of paper clock generated by h-maser ensemble are described in section III and IV. A simulation test is done for the inspection of the predictability of the paper clock. The result of simulation test will be discussed in section IV and V.

II. PREDICTION MODEL OF TL H-MASERS

Because UTCr is not the official time scale and we would like to steer UTC(TL) as close as the formal official reference UTC, before we build the prediction model of h-masers according to UTCr, we first examine the phase and frequency difference between UTCr and UTC.

Fig. 3 shows the comparison results of [UTCr(TL)-UTC(TL)] after MJD 57000. The typically phase difference of [UTCr(TL)-UTC(TL)] < ±2 ns, and occasionally > ±6 ns. It's obviously the UTCr is not continuous in phase domain. On the other hand, neglect the phase jump points, the difference of frequency offset between UTC(TL) and UTCr(TL) are less than 0.2 ns/day after MJD 57300 (Fig. 4), or the frequency of UTCr is quite coincident to UTC, we can model and predict the frequency of h-masers according to UTCr to indirectly obtain the results according to UTC.

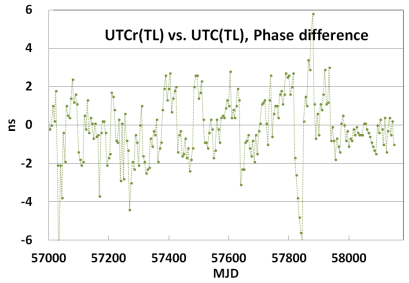

Fig. 3. The phase difference of UTCr(TL)-UTC(TL)

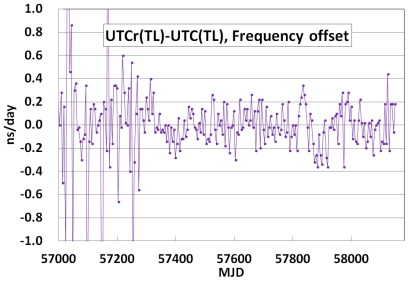

Fig. 4. The frequency difference between UTCr(TL) and UTC(TL)

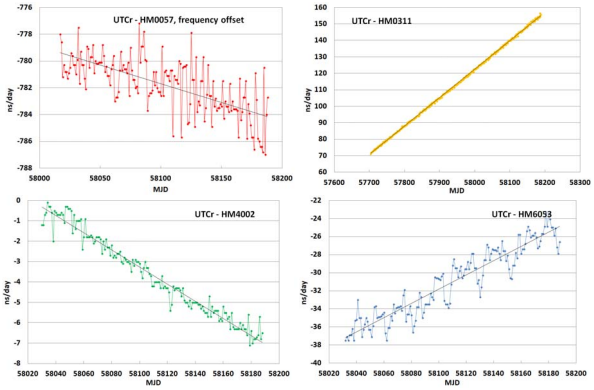

Fig. 5. The frequency drift of 4 TL h-masers HM0057, HM0311, HM4002, and HM6053 vs. UTCr.

Fig. 5 is the graphs of frequency offset of TL h-masers with respect to UTCr. In 150 days (HM0057, HM4002, and HM6053) and 450 days (HM0311) investigations, the frequency offsets of all h-masers are almost linear increase or decrease. We reasonably suppose the frequency offset of h-masers can be modeled by linear functions, and the linear function can be use to predict the frequency offset of h-masers at least in a certain span period.

Equation (1) is the prediction model for h-masers:

$$\begin{bmatrix} y_i(t+\tau_2) \\ y_i'(t+\tau_2) \end{bmatrix} = \begin{bmatrix} 1 & t+\tau_2 \\ 0 & 1 \end{bmatrix} \begin{bmatrix} b_i(t,\ t-\tau_1) \\ a_i(t,\ t-\tau_1) \end{bmatrix} + \begin{bmatrix} \Delta y_i(t+\tau_2) \\ \Delta y_i'(t+\tau_2) \end{bmatrix} \quad (1)$$

Where

τ_1: average period to get the linear functions

τ_2 : prediction span

$y_i(t+\tau_2)$: frequency offset at time $t+\tau_2$

$y_i'(t+\tau_2)$: frequency drift at time $t+\tau_2$

$a_i(t,\ t-\tau_2)$: slope of the linear function of frequency offset from time $t-\tau_2$ *to* time t

$b_i(t,\ t-\tau_2)$: intercept of linear function of frequency offset from time $t-\tau_2$ to time t

$\Delta y_i(t+\tau_2)$: prediction errors of frequency offset

$\Delta y_i'(t+\tau_2)$: prediction errors of frequency drift

The frequency offset of h-masers are modeled to be the liner functions calculated from the linear regression of frequency offsets comparison vs. UTCr from the time $t-\tau_1$ to

time t. If the frequency offset of h-masers truly keep linear during the average period τ_1 and the prediction span period τ_2, we can derive the predicted frequency offset $y(t+\tau_2)$ at the time $t+\tau_2$, from equation (1).

Fig. 6 shows the frequency offset prediction error of equation (1). The coefficients a_i and b_i of the frequency offset linear function are derived from τ_2= 35 days, and the prediction span is set to be 10 days, equal to the maximum windows period of UTCr. In the 440 days test from MJD 57760~58180, the standard deviation of prediction error of h-maser HM0311 is about 0.45 ns/day.

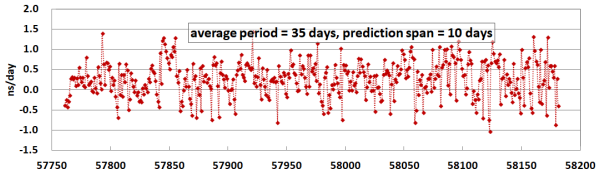

Fig. 6. The Frequency offsets prediction error Δy of HM0311, the average period τ_1 = 35 days, prediction span τ_2 = 10 days.

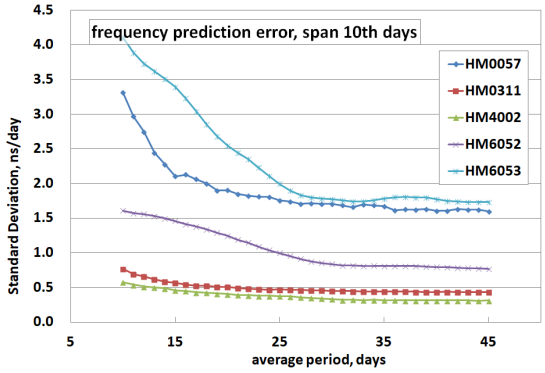

Fig. 7. The standard deviation of h-masers frequency prediction error Δy of each average period from 10 days to 45 days. The standard deviation of each h-maser converges after τ_2 > 30days.

Fig. 7 shows the standard deviations of Δy of all TL h-masers (τ_2 = 10 days, τ_1 = 10~45 days). We find: 1. the standard deviations of h-masers converge after the average period > 30 days; 2. each h-maser's characteristic is quite different, the h-masers HM0311 and HM4002 are much more predictable than the other h-masers. We expect the weighting result of h-masers ensemble would be contributed mostly by these two h-masers.

III. The Weighting Procedure of H-maser Ensemble

Since the frequency of UTCr is the only reference of h-maser prediction model, the weighting algorithm of the h-maser ensemble time scale, named ET(hm) here after, is designed to achieve to minimize the frequency offset prediction error vs. UTCr.

If the algorithm of UTCr, the time transfer results of UTC link, and the h-masers themselves are all perfect, the frequency of h-masers we predict from equation (1) would also be perfect, the residue frequency of [predicted frequency – measured frequency] for all h-masers should be the same, therefore we set the deviation of the average residue frequency to be the index of weight. The weight of each epoch t of each h-maser i is proportional to the inversely exponential of its residual prediction frequency deviation [2-6]:

$$w_i(t) = \frac{e^{-\beta \cdot \varepsilon_i(t)}}{\Sigma_1^n e^{-\beta \cdot \varepsilon_i(t)}} \qquad (2)$$

Where

$\varepsilon_i(t)$: frequency deviation relative to the average residual frequency of h-masers

β: weight adjustment coefficient, smaller β will let the process approaches equal weighting.

In section II, the 10 days span prediction test showed the frequency offset prediction errors would be convergent when the average period $\tau_1 \geq 30$ days. Thus we set τ_1 = 30 days to calculate the linear frequency prediction function of equation (1), and set the weight adjustment coefficient β = 10, to reduce influence of the h-masers which deviate the linear prediction functions.

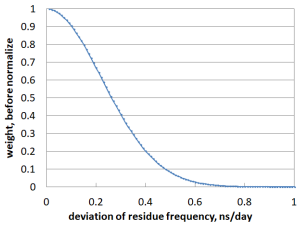

Fig. 8. The weight of inversely exponential weighting function (before normolized).

Fig. 8 is the graph of $w_i(t)$ in equation (2) before normalized. The equation (2) is considerate for gently increasing the weigh contribution when deviation > 0.4 ns/day, and neglect the un-predictable h-masers if their frequency deviations > 0.7 ns/day. For the predictability of our h-masers are so different (Fig. 7), the weight of ET(hm) would mainly contributed by only 2 h-masers (HM0311 and HM4002).

IV. Preliminary ET(hm) and Its Simulation Test

The weighting procedure of ET(hm) is based on the frequency domain calculation only, we note its phase errors would be accumulated by each frequency prediction error. A proportional control steering policy based on the phase difference of ET(hm) and UTCr/UTC are performed 5 times per month whenever BIPM publishes UTCr/UTC to reduce the phase errors of ET(hm). Since the standard deviation of [UTC(TL)-UTCr(TL)] is about 1.7 ns after MJD 57300, we set the control effort policy to be:

1. 0.03 ns/day per ns phase difference vs. UTC
2. 0.14 ns/day per ns phase difference vs. UTCr if UTCr(TL)-ET(hm) > ±1.7 ns

3. Do nothing if UTCr(TL)-ET(hm) < ±1.7 ns

4. Manually steer if phase difference vs. UTC > 5 ns

A simulation test was done for verifying the phase prediction ability of ET(hm). Because there exist phase jump points in UTCr, and the UTC is the current official time scale published from BIPM, we examine the phase difference between UTC(TL) and ET(hm) for 5 and 10 days prediction span. To simplify the simulation test, we neglect the proportional control steps and concentrate the phase prediction errors due to the weighting procedure. The estimated phase prediction error at time t:

$$\Delta x = [UTC(TL)_{t+\tau 2} - UTC(TL)_t] - [ET(hm)_{t+\tau 2} - ET(hm)_t] \qquad (3)$$

Where τ_2 = 5 or 10 days for UTCr windows period = 10 days.

Fig. 9 is the results of the simulation test. The prediction error of ET(hm) (neglect the proportional control steps, results of equation (3)) is from -4~2 ns for prediction span = 10 day, from -2~1 ns for prediction span = 5 days. We also note the UTCr(TL) and UTC(TL) has a larger discrepancy in MJD 58124, except this point, the prediction error of ET(hm) is under ±2 ns for prediction span = 10 days.

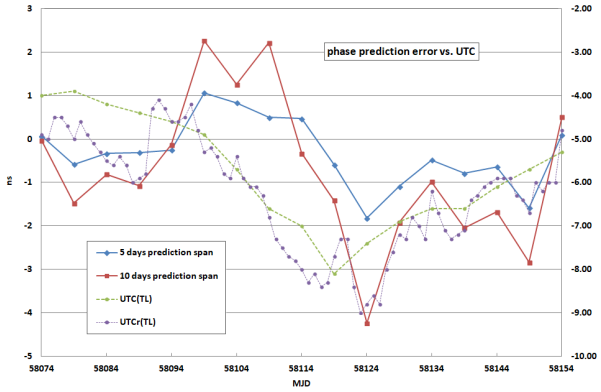

Fig. 9. The phase prediction error of the preliminary h-maser ensemble time scale with respect to UTC.

V. Conclusion And Discussion

The characteristics of atomic clocks in TL cesium clock and h-maser ensemble are investigated and the frequency of h-masers are modeled and predicted as a linear function with respect to UTCr. We weight each h-maser according to their prediction ability and then generate a preliminary h-maser ensemble time scale, ET(hm). In the simulation test, the phase errors of 10 days prediction span are from -4 ns to 2 ns.

Although the simulation test does not consider the phase error accumulation affected by each frequency prediction error, for there are 2 h-masers in ensemble which frequency prediction error is less than 0.5 ns, we estimate the frequency prediction error of ET(hm) is around 0.3~0.35 ns/day (prediction span = 10 days) and may cause roughly 1~2 ns phase error in 10 days prediction span. We set the proportional control steps to compensate the phase error accumulation, but it needs long term observation to evaluate the effects.

Except the instability of h-maser itself and uncertainty of UTCr link time transfer, parts of the prediction errors are came from the discrepancy between UTC and UTCr. If the UTCr is more correspondent with UTC, we believe the ET(hm) will be more predicable with respect to UTC and UTCr.

References

[1] ftp://ftp2.bipm.org/pub/tai/publication

[2] S. Lin and H. Peng H, "A paper clock model for cesium clock ensemble of TL". 35th Annual Precise Time and Time Interval Meeting, 2003.

[3] S. Lin, H. Peng,W. Tseng, H. Lin, and C. Liao, "The Future Model of TA(TL)", 36th Annual Precise Time and Time Interval Meeting, 2004

[4] S. Lin, H. Peng, W. Tseng, H. Lin, and C. Liao, "An Improvement of TA(TL): Using the Combination of a Hydrogen Maser And a Cesium-Clock Ensemble", Joint Meeting of IEEE International Frequency Control Symposium and European Frequency and Time Forum, 2007

[5] S. Lin, H. Peng, W. Tseng, H. Lin, and C. Liao, "An Improvement of the Controlling Algorithm for Taiwan's Time Scaling System", Joint IEEE International Frequency Control Symposium and Precise Time and Time Interval Systems and Applications Meeting, 2005.

[6] S. Lin "A Paper Clock Prediction Model for UTC(TL)", 2016 European Frequency and Time Forum

[7] G Panfilo, A Harmegnies and L Tisserand, "A new weighting procedure for UTC", 2014 Metrologia, Volume 51, Number 3

[8] T. Walter, "A Multi-Variance Analysis in the Time Domain", Proceedings of PTTI-92, 1-3 Dec 92

[9] S. T. Hutsell, "Relating the Hadamard variance to MCS Kalman filter clock estimation", Proc. 27th Annu. Precise Time and Time Interval, pp. 291-302, 1995.

[10] J.A. Barnes, "The Measurement of Linear Frequency Drift in Oscillators," Proc. 15th Annu. PTTI Meeting, pp. 551-582, Dec. 1983

[11] Petit G., Arias F., Harmegnies A., Panfilo G., Tisserand L., UTCr: a rapid realization of UTC, Metrologia, 2014, 51(1), 33-39

[12] P. Tavella and C. Thomas C. "Comparative study of time scale algorithms. Metrologia", Vol. 28, 57-63, 1991.

[13] D. W. Allan, "Time and Frequency (time domain) characterization, estimation, and prediction of precision clocks and oscillators". IEEE trans. Ultrasonics. Ferroelectrics and Frequency Control, UFFC-34, 647-654, 1987.

[14] J. Azoubib, M. Granveaud, and B. Guinot B, "Estimation of the scale unit duration of time scales", Metrologia, Vol. 13, 87-93, 1977.

[15] S. Lin, "A Phase Locked Mechanism for Time Scaling Frequency Control System" IEEE International Ultrasonics, Ferroelectrics, and Frequency Control Joint 50th Anniversary Conference, 2004.

[16] ITU Handbook selection and use of precise frequency and time system, Chapter 6, 1997.

[17] Symmetricon Co. Ltd. "5071A Primary Frequency Standard Operating and Programming Manual", Rev. H, August 14, 2009

Automatic calibration of the actively stabilized fiber-optic time transfer

P. Krehlik, J. Kołodziej and Ł. Śliwczyński
Faculty of Computer Science, Electronics and Telecommunications
AGH University of Science and Technology
Krakow, Poland

***Abstract*— In this work we present the automated device for calibration of the actively stabilized fiber-optic time transfer system. We show a practical verification of the calibrator by comparing the results of automated calibration with much more cumbersome previous method based on step-by-step measurements with bulky equipment. Basing of this experiments we assess an uncertainty of the calibrator as ±50 ps.**

Keywords—time and frequency distribution; fiber optics; ELSTAB

I. INTRODUCTION

In last years fiber-optic based installations for time transfer become not only experimental, but operational as well. The calibration of such links is necessary for tractability of the output time signal (usually 1 PPS) to the UTC(k) timescale, and needs to be repeated after a fiber break or modifications in the installation. In this situation some relatively simple means for time transfer calibration become important for maintaining the time transfer links by persons having no particular knowledge nor special equipment for step-by-step measurements and calculations. In this work we present a dedicated device which serves as an automatic calibrator for the ELSTAB system [1], however the idea would be used in any other actively stabilized time transfer system based on a bidirectional signal transmission in a single fiber.

II. THE IDEA OF AUTOMATED CALIBRATOR

The simplified diagram of the calibration setup with the proposed in-box calibrator and the realized algorithm are shown in Figs. 1 and 2, respectively. The calibrator performs the measurement of the chromatic dispersion of the optical path, of the $\tau_{SOURCE\rightarrow REF}$ and $\tau_{REF\rightarrow RET}$ time intervals, calculate the Sagnac correction term, and finally provides the offset between the UTC(k) timescale and the remote 1 PPS train, according to the ELSTAB calibration formula (see Fig. 1 and [1]):

$$\tau_{SOURCE\rightarrow REMOTE} = \tau_{SOURCE\rightarrow REF} + \frac{1}{2}\left[\tau_{REF\rightarrow RET} + \Delta\tau_{DISPERSION} + \Delta\tau_{SAGNAC} + \tau_C\right],$$

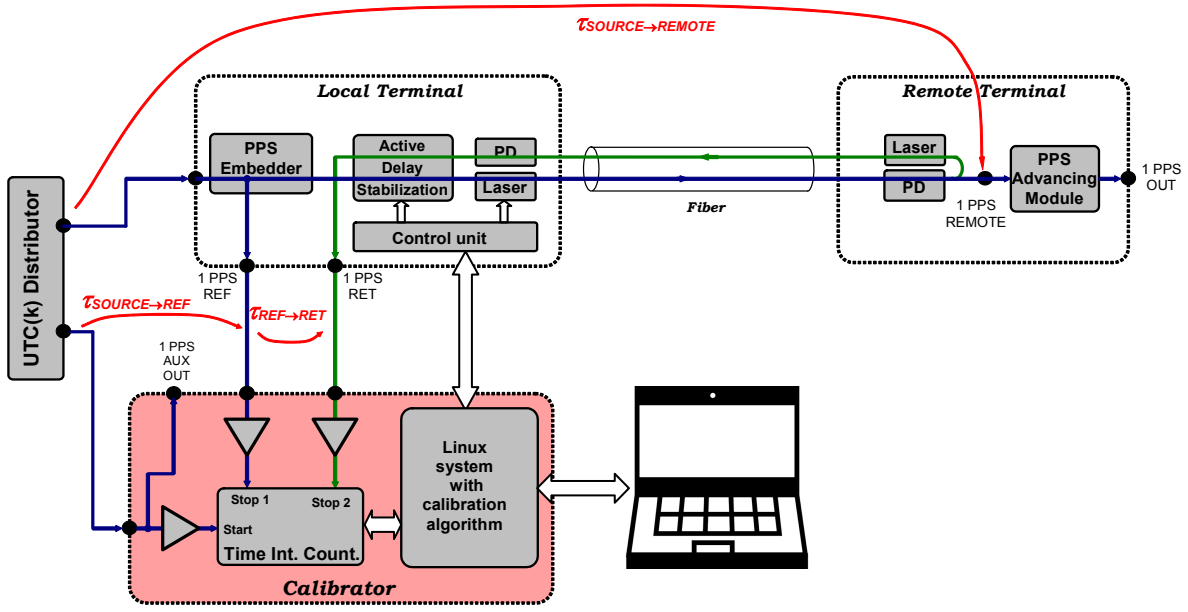

Fig. 1. The simplified diagram of the calibration setup.

This work was supported by Polish National Science Center (NCN) under project no. 2015/17/B/ST7/03628.

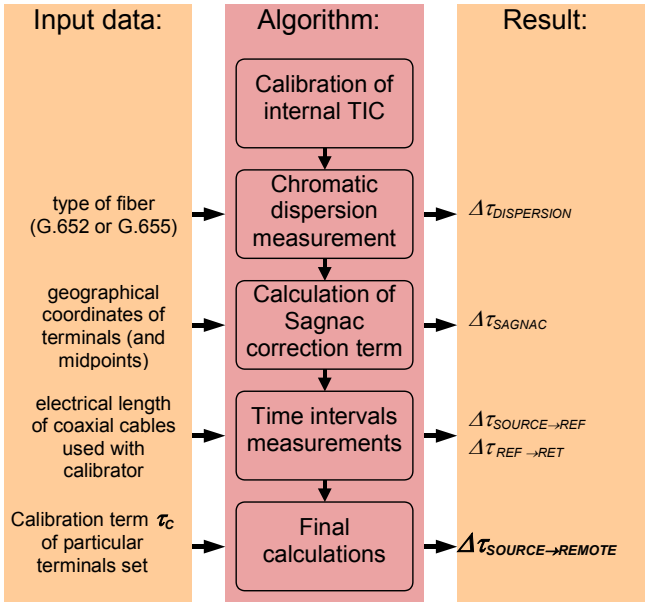

Fig. 2. Calibration algotithm.

where $\Delta\tau_{DISPERSION}$ and $\Delta\tau_{SAGNAC}$ are in-fiber propagation asymmetry in forward and backward directions, caused by a chromatic dispersion and Sagnac effect, respectively, and τ_C is a constant term assigned to particular pair of local and remote terminals, related to internal delays inside the terminals.

The measurement of chromatic dispersion is realized by changing the wavelength of the local laser and measuring the resulting change of the round-trip propagation delay of 1 PPS pulses $\tau_{REF\to RET}$ [2]. (During this measurement the active delay stabilization is temporarily deactivated.) In our solution the wavelength shift is realized by temperature control of the laser chip and its amount is ±0.15 nm. Basing on this procedure the asymmetry in forward and backward directions, caused by the chromatic dispersion can be determined as:

$$\Delta\tau_{DISPERSION} = \frac{\Delta\tau_{REF\to RET}}{\Delta\lambda_F}(\lambda_F - \lambda_B),$$

where $\Delta\tau_{REF\to RET}$ is the change of the round-trip propagation delay caused by the wavelength shift $\Delta\lambda_F$, and $(\lambda_F - \lambda_B)$ is the forward – backward wavelength difference during normal operation.

The Sagnac correction term is estimated from a simplified formula:

$$\Delta\tau_{SAGNAC} \approx \frac{2\omega R}{c^2}\sum_{i=1}^{N-1}\cos(\phi_i)\cos(\phi_{i+1})(\lambda_{i+1} - \lambda_i),$$

where ϕ_i and λ_i are geographical latitude and longitude of consecutive points along the optical path. Basically, locations of the local and remote terminals are sufficient for a first-order estimation, but adding some amount of midpoints (as for instance the locations of regeneration stations) is recommended for best accuracy [3].

The duration of the calibration is approximately five minutes. It is determined by averaging of multiple time intervals measurements, repeated for reducing the impact of the TIC noise, and by repeated detuning of the local laser, which takes ten seconds each time.

Tab. 1. Calibration performed with previous method and with the in-box calibrator

		τSOURCE→REF [ns]	τ REF →RET [ns]	ΔτDISPERSION [ns]	ΔτSAGNAC [ns]	τC [ns]	τSOURCE→REMOTE [ns]
Link #1	"manual":	1141.229	850 040.601	1.178	-0.341	61.050	426192.473
	calibrator:	1141.192	850 040.604	1.190			426192.444
	difference:	**Δ = -0.037**	**Δ = 0.003**	**Δ = 0.012**			**Δ = -0.029**
Link #2	"manual":	1088.522	1 390 040.568	1.891	-0.393	50.090	696134.600
	calibrator:	1088.532	1 390 040.583	1.897			696134.621
	difference:	**Δ = 0.010**	**Δ = 0.015**	**Δ = 0.006**			**Δ = 0.021**
Link #3	"manual":	1098.731	1 390 040.554	1.907	0.393	58.210	696149.305
	calibrator:	1098.773	1 390 040.561	1.904			696149.307
	difference:	**Δ = 0.042**	**Δ = 0.007**	**Δ = -0.003**			**Δ = 0.002**
Link #4	"manual":	1 104.418	850 040.538	1.172	0.341	58.250	426154.569
	calibrator:	1 104.426	850 040.539	1.198			426154.590
	difference:	**Δ = 0.008**	**Δ = 0.001**	**Δ = 0.026**			**Δ = 0.029**
Link #5	"manual":	1183.000	2 243 485.971	2.962	-0.734	57.383	1122955.791
	calibrator:	1182.920	2 243 485.979	2.959			1122955.714
	difference:	**Δ = -0.080**	**Δ = 0.008**	**Δ = -0.003**			**Δ = -0.077**

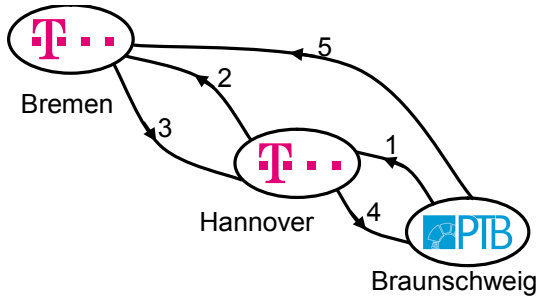

Fig. 3. Schematic localization of the links.

III. EXPERIMENTAL VERIFICATION

The calibrator was used in a campaign of calibration of the five ELSTAB links (see Fig. 3) connecting UTC laboratory at Physikalisch-Technische Bundesanstalt with Deutsche Telekom locations [4]. In parallel we performed this calibration using our earlier developed method, which is much more cumbersome and needs expensive equipment, but may be regarded as ultimately accurate. We observed a very good agreement between both methods for calibration of each of five links – see Table 1. The final results ($\tau_{SOURCE \rightarrow REMOTE}$) obtained from two methods usually differ less than 30 ps, with the only one exception in the case of Link#5. This is related to the fact that in this case the interval is measured between two pulses of substantially different shapes and amplitudes. No systematic bias between the methods was observed.

IV. CONCLUSION AND FURTHER PLANS

In this work we presented the automated, all-in-one-box calibrator for the fiber-optic time transfer system. The idea is related to our ELSTAB technology, but may be used in similar systems dedicated for stabilized time and frequency transfer. The entire calibration process is performed in the local side of the link, without any human actions except connecting the device and entering a few basic data. The process of calibration lasted for approximately five minutes.

We have evaluated the calibrator performance in a real installation consisting of five field-deployed, long distance ELSTAB links. We estimated the expanded uncertainty of the calibrator as ±50 ps.

In the next step we are going to automatically adjust a PPS Advancing Module in the remote terminal, sending the data from the calibrator via an Internet connection. The PPS Advancing Module allows to reduce the delay of the 1 PPS tags, introduced by the fiber route, thus the output PPS signal can be closed to UTC.

REFERENCES

[1] P. Krehlik at al., "ELSTAB - fiber optic time and frequency distribution technology - a general characterization and fundamental limits," IEEE Trans. Ultrason., Ferroelect., Freq. Control, vol. 63, no. 7, 2016, pp. 993-1004.

[2] P. Krehlik, L. Sliwczynski, „Fiber-optic time distribution with the autonomous calibration of dispersion-induced offset," Proc. EFTF 2016, York, UK, 2016.

[3] A. Czubla, P. Krehlik, L. Sliwczynski, J. Kołodziej, a. Binczewski, K. Turza, W. Bogacki, P. Rydlichowski, „ Some Approximated Methods of Calculation Sagnac Correction For Optical Fiber Time Transfer," Proc. EFTF 2017, Besançon, France, 2017.

[4] Ł. Śliwczyński, P. Krehlik, J. Kołodziej, H. Imlau, H. Ender,H. Schnatz, D. Piester, A. Bauch, "Fibre optic time transfer between PTB and Deutsche Telekom using multi-link redundant topology," Proc. EFTF 2017, Besançon, France, 2017.

On-line optimization of time and frequency fiber optic links exploiting bi-directional amplifiers

Ł. Śliwczyński, P. Krehlik, K. Salwik, J. Kołodziej
Faculty of Computer Science, Electronics and Telecommunications
AGH University of Science and Technology
Krakow, Poland

***Abstract*—In the paper we present the algorithms intended to launch the long distance, bi-directional fiber optic time and RF frequency transfer system and optimize its performance by minimizing the jitter. The pre-setting procedure is based on the assumption, that for the proper signal transfer and amplification, the optical power in any point of the link cannot decrease below the wisely chosen threshold level. When the power exceeds this level and the time and frequency signals transfer is performed, the optimization procedure is started and tries to minimize the jitter measured at both ends of the link.**

Keywords—fiber optic link; bi-directional optical amplifier; frequency transfer; time transfer;

I. INTRODUCTION

Long distance fiber optic systems for time and frequency distribution usually use a single fiber links, that operate bi-directionally and provide inherent symmetry for forward and backward signals [1]. Loses introduced by the fibers are compensated by the dedicated optical amplifiers (SPBA – Single-Path Bi-directional Amplifier). The gains of these amplifiers need to be reasonably chosen to provide the proper conditions for the signals transfer, but also to minimize the generation and propagation of undesirable signals (e.g. resulted from Rayleigh backscattering or amplified spontaneous emission).

The set of gains can be obtained from the simulation [2] and preset in the SPBAs before the installation of the link is done. However, it is difficult to prepare the accurate mathematical model, because of the lack of actual knowledge about the fiber optic link, like exact attenuations of fiber spans, attenuations and reflections of optical connectors, values of backscattering coefficients, spectral properties of exploited lasers, etc. The other approach, adopted in current work, is to use the real-time measurements of the link [3] that allow to start-up the system and perform the optimization procedures on-line.

The general scheme of the fiber optic time and frequency (T&F) transfer system with the control algorithms blocks marked in, is shown in Fig. 1. The signals supplied to the Local module (LM) from the external source are transferred to the Remote module (RM) through the bi-directional, long distance fiber optic link with a number of bi-directional optical amplifiers. The optical signal is exposed to the phenomena occurring in the link (Rayleigh backscattering, amplified spontaneous emission, residual reflections from connectors, phase noise of the lasers involved etc.) that generate the jitter. Both modules are equipped with the jitter measurement devices, that allow to estimate the signals quality (in particular to observe changes of the quality). The control and the management of all the devices is provided by dedicated Ethernet-based VPN network.

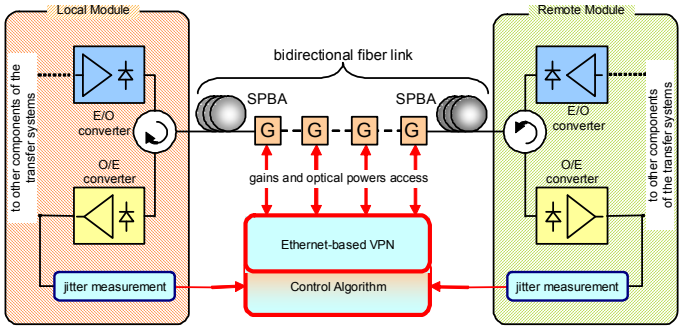

Fig. 1. A simplified block diagram of the T&F transfer system with the control algorithm blocks marked on.

II. GAINS PRESET ALGORITHM

Proper transmission of optical signals in a T&F transfer system requires that the SPBA or RM input powers exceed some wisely chosen threshold. While all these devices are able

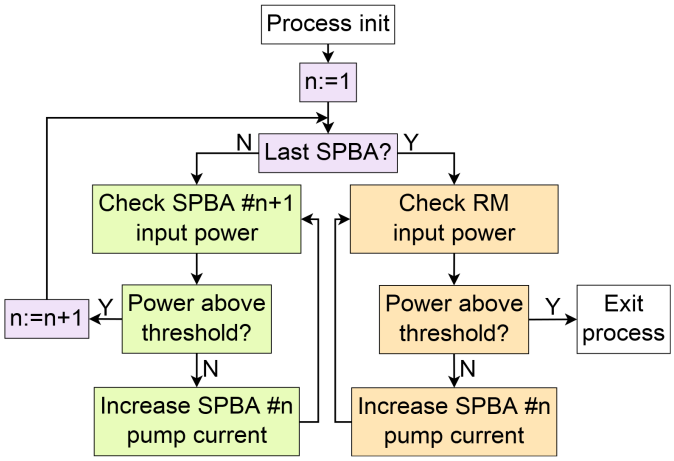

Fig. 2. SPBAs pre-setting algorithm.

This work was supported by Polish National Science Center under the decision DEC-2014/15/B/ST7/00471.

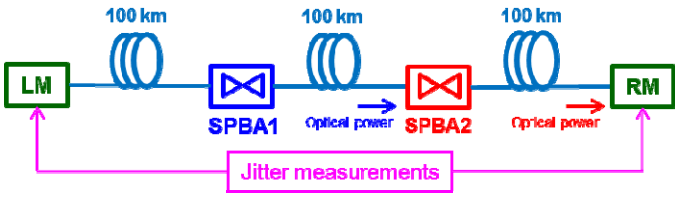

Fig. 3. A test T&F transfer system for the algorithms validation.

to perform the optical power measurements, the transfer of desirable signals from the LM to the RM can be established by setting the gains of the SPBAs one-by-one.

First, all the amplifiers are turned off to eliminate propagation of the noise. Before the pre-setting procedure is started, the optical power at the first SPBA input is measured. If it is insufficient, the algorithm cannot proceed, as it is not possible to control the transmitter laser (in the LM) to provide the appropriate power level. Otherwise, the pump current of each SPBA starting from the first in the link is increased until the required optical power at the input of the next device (SPBA or RM) is obtained (see Fig. 2 for the algorithm block diagram).

The algorithm was implemented and validated in a test T&F transfer system composed of Local and Remote modules with jitter measurements devices, 300 km of spooled fiber and two SPBAs, installed every 100 km (see Fig. 3). Increasing the pump current of individual amplifiers allowed to establish the required optical power, first, at the input of the second amplifier (SPBA2), next, at the input of the Remote module (RM). Fig. 4 shows the changes of the pumps current of both SPBAs and the corresponding optical power changes.

The relative pumps current is incremented by 1% in each iteration, starting from 10% (100% is the maximum current specified by pump manufacturer). For the lowest values the corresponding power measurements are below the noise floor of the circuitry used to measure the optical power. With the increase of the pump current the results are first above the noise floor and then above the assumed threshold level (see Fig. 4b). When the optical power is appropriate in every point of the fiber link, both the Local and Remote modules are able to acquire synchronism that allows T&F transfer. This condition stops the SPBAs pre-setting algorithm and allows starting the optimization procedure.

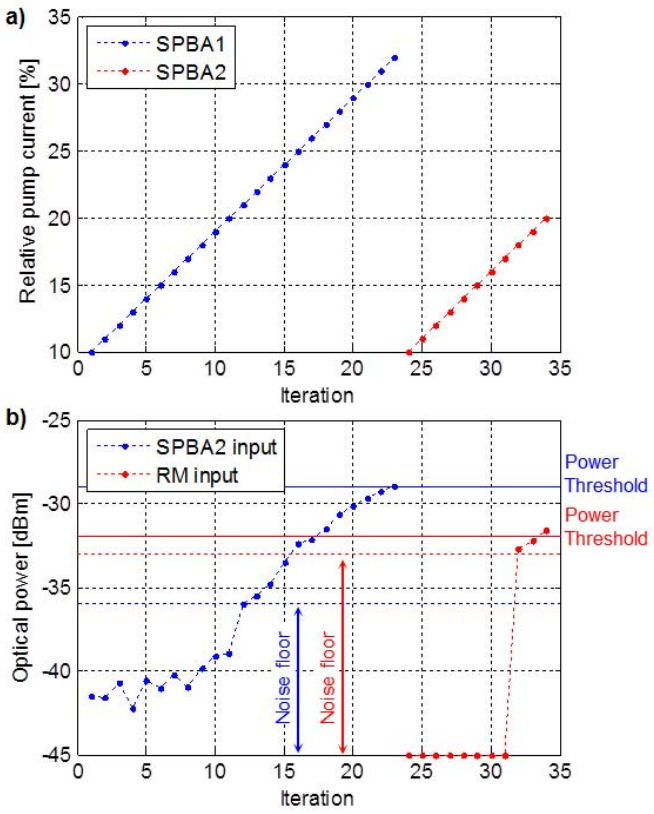

Fig. 4. SPBAs pre-setting algorithm results - the pump current modifications (a) and the corresponding optical power changes (b).

III. Link Optimization Procedure

The performance of the T&F system launched with a set of initial gains obtained either from simulation or pre-setting algorithm can be far from the optimal. It reveals as a low signal to noise ratio and significant jitter occurring in the transferred signals. Based on the jitter measurements performed in the Local and Remote modules, the proposed optimization algorithm allows to modify the gains to obtain optimal link performance (i.e. the lowest possible jitter).

The procedure analyzes how the gain modification of each SPBA affects the jitter. First, the gain of selected SPBA is increased. If the jitter is reduced, the change is hold on and another gain modification of the same type is done. Otherwise, it is reversed and the procedure tries to decrease the gain. The modifications are repeated as long as the jitter is reduced. When no change (gain increase or decrease) is possible, the SPBA is found as set optimally and the procedure switches to the next SPBA. The algorithm operation stops when no change is done for any amplifier (all the SPBAs are found as

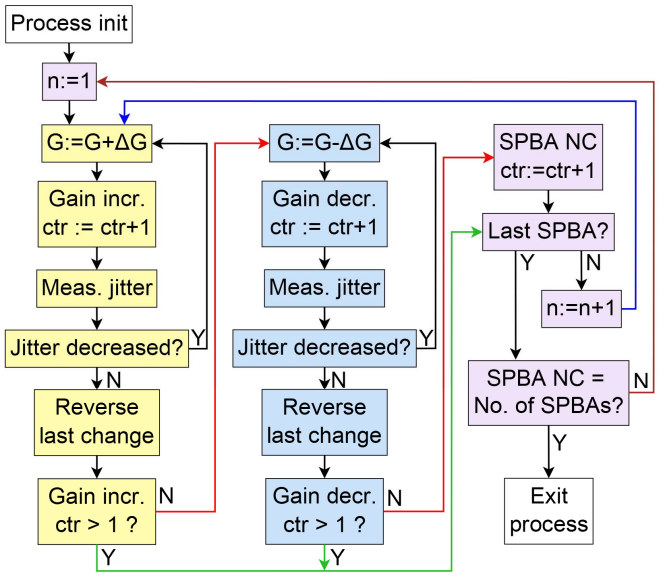

Fig. 5. The link optimization algorithm.

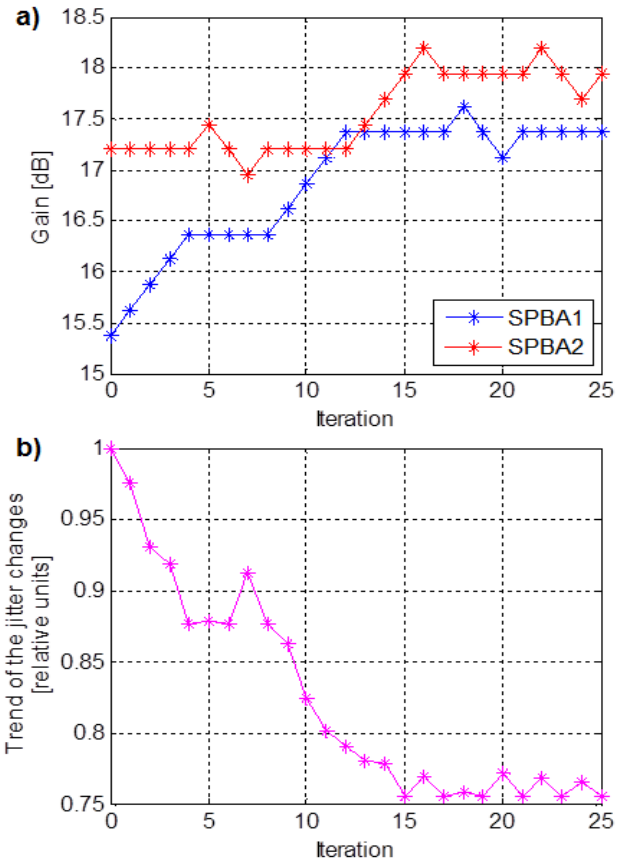

Fig. 6. SPBAs optimization results – the gain modifications (a) and the corresponding RMS jitter changes (b).

set optimally). The block diagram of the procedure in shown in Fig. 5.

The algorithm was tested in the same T&F system as has been used to test the pre-setting algorithm (the system was initially set using this procedure). As the jitter was measured in the RM and LM, the evaluation of the system performance was based on the root mean square value of both results.

The results of the optimization procedure are shown in Fig. 6. The increase of the gains allowed to decrease the jitter by about 25% comparing to the value obtained after the pre-setting procedure. The number of the gain modifications of the same type (gain increase or decrease) in a single series was limited to four to provide better control over the process. It resulted is some additional iterations - in the steps 5-8 the procedure tries to modify the SPBA2 gain, but the trial is rejected. For the iterations above 15, the system is set optimally and any gain modification can only increases the jitter.

IV. Summary

The developed pre-setting and optimization algorithms allow to launch the time and frequency transfer system and provide the best operating conditions. These procedures can be used while a new link is going to be installed, but the lack of its parameters makes creating the mathematical model difficult. On the other hand, the pre-setting algorithm measures the actual attenuations of the spans which are required in the mathematical link model. The usage of this data in the simulation to obtain better initial conditions (initial set of the amplifiers gains) for the optimization procedure will be a part of further research.

References

[1] Ł. Śliwczyński, P. Krehlik, Ł. Buczek, M. Lipiński, "Frequency transfer in electronically stabilized fiber optic link exploiting bidirectional optical amplifiers", IEEE Trans. Instr. and Meas., vol. 61, pp. 2573-2580, 2012.

[2] Ł. Śliwczyński, J. Kołodziej: „Bidirectional optical amplification in long-distance two-way fiber optic time and frequency transfer systems", IEEE Trans. Instr. and Meas., vol. 62, pp. 253-262, 2013.

[3] Ł. Śliwczyński, P. Krehlik, K. Salwik: "Real-time performance monitoring of fiber optic long-distance time and RF frequency transfer links", Proc. EFTF 2016, York, United Kingdom, DOI 10.1109/EFTF.2016.7477757.

An Anti-Jamming System for GNSS Timing Applications

Jorge Querol and Adriano Camps
CommSensLab, Signal Theory and Communications (TSC)
UPC-BarcelonaTech, IEEC/CTE and MITIC Solutions
Barcelona, Spain
jorge.querol@tsc.upc.edu, camps@tsc.upc.edu

Esteban Garbin Manfredini and Ricardo Píriz
GMV
Tres Cantos, Madrid, Spain
egarbin@gmv.com, rpiriz@gmv.com

***Abstract*—Radio-Frequency Interference (RFI) and jamming are increasing problems for timing applications based on Global Navigation Satellite Systems (GNSS). FENIX-lite is a real-time pre-correlation anti-jamming system designed to provide increased resilience against RFI/jamming in critical GNSS-enabled applications. This work aims to evaluate the combined performance of FENIX-lite and a timing setup composed by two GNSS disciplined oscillators named DOWR. The results show that FENIX provides an anti-jamming resilience of 10–30 dB, at the expense of introducing a small bias and an additional jitter of 2–4 ns.**

Keywords—GNSS; timing; jamming; RFI; anti-jamming

I. INTRODUCTION

Global Navigation Satellite Systems (GNSS) is a key technology for timing and synchronization in critical infrastructures such as telecommunication networks, power distribution grids and finance operations, among others. GNSS guarantee 24/7 worldwide availability of their signals, which allows synchronizing multiple receivers located far away.

Nevertheless, GNSS signals are quite vulnerable to GNSS jammers and other unintentional Radio-Frequency Interference (RFI) signals, due to their extreme low power. GNSS signals reach the Earth's surface with a signal power below -120 dBm. Neither the inherent protection of Direct Sequence Spread-Spectrum (DSSS) modulations nor the regulations that protect reserved frequency bands are enough to solve the problem. Moreover, RFI and jamming are particularly threatening for critical GNSS-enabled applications, such as timing. This fact triggers the development of reliable GNSS systems.

Recent publications have highlighted the ever-growing presence of interference sources in urban areas both from intentional and unintentional nature. On the one hand, the increasing market penetration of GNSS in critical infrastructures makes necessary the development of anti-jamming systems capable to protect them from jamming attacks. On the other hand, the overcrowding of frequency spectrum fosters the appearance of unintentional RFI events coming from GNSS near-band services. The number of these events is likely to increase with broadband technologies like 5G, which makes an intensive use of the spectrum.

This project has received funding from "AGORA: Técnicas Avanzadas en Teledetección Aplicada Usando Señales GNSS y Otras Señales de Oportunidad", grant ESP2015-70014-C2-1-R and support grant MDM-2016-0600 to "María de Maeztu Excellence Units" CommSensLab, from the Spanish Ministerio de Economía y Competitividad (MINECO / FEDER); ICREA Academia Award 2014, projects "FENIX - Front-End GNSS Interference eXcisor" LLAVOR (2014 LLAV 0002) and PRODUCTE (2016 PROD 00062) and the grant for the recruitment of early-stage research staff FI-DGR 2016 (2016FI-B00738) of the AGAUR - Generalitat de Catalunya.

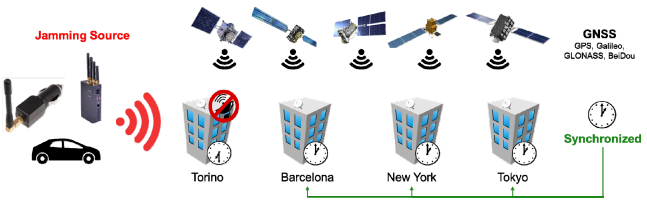

Fig. 1. Illustration of a jamming attack on a GNSS timing system.

II. REAL-TIME ANTI-JAMMING SYSYEM

The Front-End GNSS Interference eXcisor (FENIX) is a GNSS anti-jamming technology based on the patented combination of statistical interference detection, and a multiresolution time-frequency blanking algorithm for jamming mitigation in DSSS-based multi-constellation GNSS receivers [1]. The main goal of FENIX is to increase the C/N_0 in the presence of interference signals, thus improving the continuity of GNSS services. Moreover, the mitigation algorithm has been designed to be DSSS-based multi-constellation, frequency independent (i.e. it works at L1 and L2, L5…), and it is capable of mitigating almost all kinds of jamming signals. A general description of the major building blocks of FENIX was first presented in [2].

The FENIX-lite demonstrator has been implemented using a Software Defined Radio (SDR) model USRP B205mini, covering either GPS L1 C/A and Galileo E1 OS, or GPS L2C services. The SDR front-end is tuned to either L1 or L2 band, and the FENIX interference detection and mitigation algorithm is running in real-time in its FPGA. The FENIX algorithm first detects the interference signal using a statistical domain analysis based on normality tests. Then, samples containing most part of interference power signal are excised in the time-frequency space computed using the Multiresolution Fourier Transform (MFT). The use of the MFT allows mitigating almost all kinds of jamming signals, since it maximizes the projection of the interference signal in the transformed domain.

This work aims to evaluate the performance of FENIX-lite in a GNSS-based timing setup, in terms of jamming resilience and timing performance under different representative jamming scenarios.

III. GNSS TIMING SETUP

The GNSS timing setup proposed in this work is based on two GNSS disciplined oscillators named DOWR, which have been developed in conjunction by Seven Solutions and GMV. DOWR stands for Disciplined Oscillator White Rabbit. The DOWR combines a u-blox LEA-M8F receiver with precise output timing protocols such as Pulse Per Second (PPS), Network Time Protocol (NTP), Precision Time Protocol (PTP), and in particular White Rabbit (WR). WR allows time distribution over optical fiber along hundreds of km with ns-level accuracy.

DOWR is currently the only product in the market combining GNSS-based time generation and WR-based time distribution. The main limitation of DOWR comes from the usage of an inexpensive, single-frequency GNSS receiver. Single-frequency makes the timing solution susceptible to the ionospheric error, which can reach tenths of ns in the worst case. Single-frequency also makes the receiver more vulnerable to jamming and interference. Although the LEA-M8F has some jamming/interference detection capabilities, it is not clear from the documentation to what extent the receiver implements also mitigation measures.

Fig. 2 shows a diagram of the proposed GNSS timing setup. The two DOWR units are connected to a common antenna with an open-sky configuration located at the rooftop of the building. Both LEA-M8F receivers are configured in an identical way: use only Global Positioning System (GPS) and set "fixed" antenna position. The first DOWR is used unperturbed, as PPS reference (REF). The second DOWR acts as the Device-Under-Test (DUT), in order to evaluate the combined performance of FENIX-lite and the timing setup in terms of resilience against different common GNSS jamming and RFI scenarios.

Eventually, the setup is designed to measure the phase difference between PPS pulses generated by both DOWR devices, using a Time Interval Counter (TIC), and to record the GPS receiver messages while it is suffering RFI/jamming attacks. The REF DOWR is connected directly to the antenna signal, while the DUT DOWR is connected to the FENIX-lite, which receives the combined signal of the antenna and the RFI/jamming signal generator. Fig. 3 shows a picture of the final setup tested at UPC-BarcelonaTech premises.

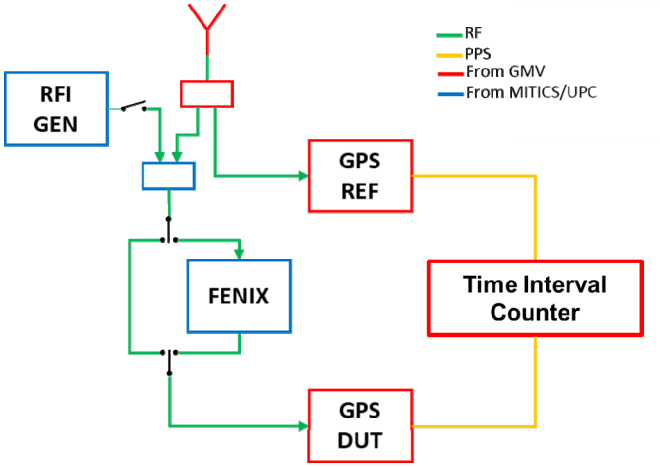

Fig. 2. Diagram of the GNSS timing setup.

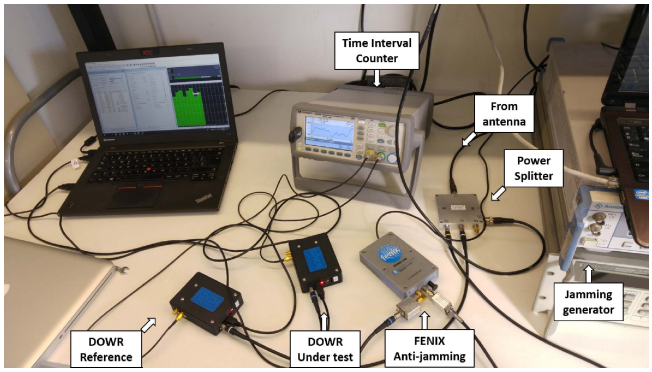

Fig. 3. Picture of the GNSS timing setup.

IV. RESULTS UNDER JAMMING CONDITIONS

A. Jamming scenarios

Even though, an RFI or jamming signal can be any undesired signal present at the bandwidth of the receiver, the authors have chosen three representative scenarios based on the literature and their own experience. These signals are a Continuous Wave (CW) and two different linear chirp signals.

CW is the most frequently observed RFI signal in the literature. It can be generated unintentionally from an intermodulation product, a lower harmonic, or a spurious signal from a near-band service. In this work, it has been considered centered at L1 (1575.42 MHz) since it represents the worst case for the receiver.

Moreover, two kinds of chirps jammers have been tested, both centered at L1. The first one (Chirp 1) has a bandwidth of 10 MHz and repetition frequency of 100 kHz, which is the most common type of commercially available Personal Privacy Devices (PPD). The second one (Chirp 2) has a narrower bandwidth of 2 MHz and repetition frequency of 200 Hz, which according to the authors' experience, is the worst type of interference for the LEA-M8F receiver.

In all three cases, jamming power has been swept from -90 to -20 dBm both with and without FENIX. Considering free space propagation, line-of-sight (LOS) between jammer and antenna, and a 2 W typical jammer, this sweep corresponds to a jamming range from 30 km to 10 m (see equivalence in Table I). These values have been validated in the laboratory for 10 and 30 m. Note that jamming antenna is typically a monopole with poor efficiency.

TABLE I. EQUIVALENCE BETWEEN JAMMING POWER AND RANGE.

Power [dBm]	-90	-80	-70	-60	-50	-40	-30	-20
Jamm. Range [m][a]	30000	10000	3000	1000	300	100	30	10

[a] Considering free space propagation, LOS, and 2 W typical PPD jammer with monopole antenna.

B. *Anti-jamming performance*

Under no RFI/jamming conditions, the maximum C/N_0 level is around 50–52 dB-Hz, which is large enough to perform a C/N_0 degradation analysis. Once the jamming signal is injected, the C/N_0 level (i.e. Signal-to-Noise Ratio) is degraded in concordance to the results presented in [3]. When C/N_0 level drops below 15–17 dB-Hz, the GPS receiver loses the tracking of the signal, and then no timing solution is provided. However, this happens at different jamming power level depending on whether FENIX is connected or not, and on which jamming scenario is evaluated.

In the case of a CW jamming signal, the GPS receiver works nominally with jamming power up to -60 dBm (1 km) without FENIX. Beyond that, no positioning/timing solution is provided. However, when FENIX is used, the GPS receiver can still work up to -30 dBm (30 m). Timing performance for -40 and -30 dBm CW jamming is discussed in next subsection.

Regarding chirp signal scenarios, in both cases, the GPS receiver works nominally up to -60 dBm (1 km) without FENIX. On the other hand, when FENIX is used, the GPS receiver can still work up to -50 dBm (300 m) for both chirp signals. However, timing performance is slightly different for each chirp signal scenario.

C. *Timing performance*

One of the observables available from the LEA-M8F receiver regarding timing performance is the uncertainty. Under no RFI/jamming conditions, the receiver reports values of 2–4 ns without FENIX, and of 4–6 ns when FENIX is connected between antenna and receiver. Similar values are reported under jamming conditions for all scenarios up to -60 dBm. Beyond that, the system cannot work without FENIX as it was mentioned in previous subsection. However, when FENIX is used, the GPS receiver is working and reporting uncertainty values of 10 ns for CW at -40 dBm (100 m), of 25 ns for CW at -30 dBm (30 m), of 7 ns for Chirp 1 at -50 dBm (300 m), and of 4 ns for Chirp 2 at -50 dBm (300 m).

As above mentioned, the phase difference between PPS signals coming from REF and DUT receivers is recorded using a TIC. This data allows analyzing in more detail the performance of the system under extreme jamming cases, when FENIX mitigation makes the difference.

Fig. 4 shows the time evolution of the phase difference during 10 minutes. The mean delay value measured when no RFI/jamming signal is present has been subtracted for all plots. The magnitude of this delay is 1650225 ns, which is the contribution of all delays of FENIX internal processing blocks. This delay is constant by construction, and thus it can be calibrated and compensated. Moreover, it can be appreciated the correspondence between each plot and the uncertainty values above mentioned. Even though the use of FENIX allows the receiver to work under jamming conditions with an acceptable increased uncertainty, the RFI/jamming signal also introduces some bias in the phase difference. This bias is about 45 ns in the worst case (CW -30 dBm), mainly due to changes on the group delay of the equivalent transfer function of FENIX. In the case of Chirp 1 at -50 dBm, the bias is about

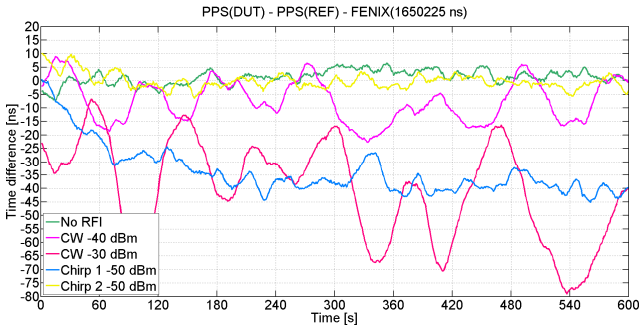

Fig. 5. Time plot of phase difference between PPS signals from DUT and REF devices. FENIX constant delay of 1650225 ns has been subtracted in all plots

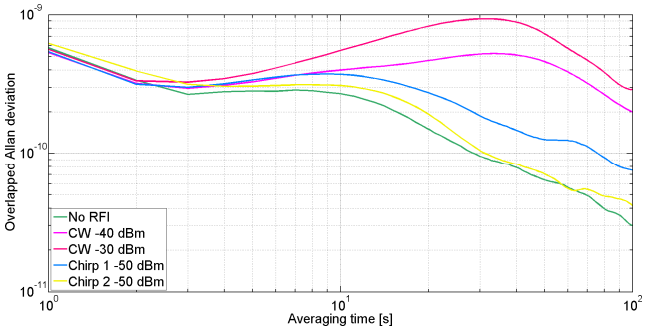

Fig. 4. Overlapped Allan deviation of phase difference between PPS signals from DUT and REF devices.

40 ns, but the uncertainty is much less than in previous case. These bias values are acceptable for current telecommunication network technologies which require 100 ns precision.

Eventually, Fig. 5 shows the overlapped Allan deviation for the cases of study. This plot shows the additional instability introduced by the RFI/jamming signal once mitigated by FENIX.

V. CONCLUSIONS

The results of this work show that FENIX-lite prototype provides real-time anti-jamming resilience for GNSS timing devices. In particular, up to 30 dB for CW RFI/jamming signals, and of 10–15 dB for representative chirp signals under evaluation. Thus, FENIX allows the proposed timing system to work in the presence of jamming signals.

Moreover, a trade-off between jamming resilience and time uncertainty has also been found. Under nominal conditions, when no RFI/jamming signal is present, a small additional jitter on the order of 2–4 ns is introduced in the PPS signal. In addition, a large but constant delay of about 1.65 ms is introduced by inner digital signal processing blocks of FENIX. However, it can be easily calibrated and compensated. Furthermore, a maximum bias of 45 ns has been measured under heavy jamming conditions, which is still acceptable for current timing systems requiring accuracy levels of 100 ns.

Despite this trade-off, FENIX has proven to be an effective standalone solution for GNSS-based timing systems suffering from the problem of RFI and jamming.

REFERENCES

[1] J. Querol, and A. Camps, “System and method for detecting and eliminating radio frequency interferences in real time,” U.S. Patent 9,596,610, issued March 14, 2017.

[2] J. Querol, E. M. Julian, R. Onrubia, A. Alonso-Arroyo, D. Pascual and A. Camps, "Preliminary results of FENIX: Front-End GNSS Interference eXcisor," 2016 IEEE International Geoscience and Remote Sensing Symposium (IGARSS), Beijing, 2016, pp. 5627-5630.

[3] J. Querol and A. Camps, “Real-time Pre-correlation Anti-jamming System for Civilian GNSS Receivers,” Proceedings of the 30th International Technical Meeting of The Satellite Division of the Institute of Navigation (ION GNSS+ 2017), Portland, Oregon, September 2017, pp. 1267-1288.

Evaluation of CGGTTS Time Transfer Software Using Multiple GNSS Constellations

Kenneth Jaldehag, Carsten Rieck and Per Jarlemark
Measurement Science and Technology
RISE Research Institutes of Sweden
Borås, Sweden
kenneth.jaldehag@ri.se

Abstract—A new software tool for GNSS time transfer implementing the Common GNSS Generic Time Transfer Standard (CGGTTS) has been developed by the time and frequency group at RISE Research Institutes of Sweden. The software handles signals from the satellite navigation systems GPS, GLONASS, Galileo and BeiDou including the most important ranging codes for time transfer applications. The aim of the development is to provide an alternative to existing software and to support time transfer with new GNSS. The paper presents an evaluation of CGGTTS data calculated with the new software tool in comparison with those calculated using two other, independently developed software tools. It is shown that the results obtained from the different software agree to the sub-nanosecond level. Specifically, the agreement seen between individual GPS, Galileo and BeiDou CGGTTS data is at the 100- to 200-picosecond level. Similarly, GLONASS CGGTTS data agree to the sub-nanosecond level. Further, the paper presents a comparison between time transfer links for both long baselines and short, common-clock baselines obtained from a common view analysis of CGGTTS data from the four mentioned GNSS, as well as a combination of them. It finally discusses other features available from the RISE software, such as non-smoothed CGGTTS data, adoption of satellite orbit and clock products from the IGS as well as the results of an evaluation using linear combinations with non-standard CGGTTS codes and signals.

Keywords—GNSS; Time Transfer; CGGTTS; Software; IGS

I. INTRODUCTION

Methods for accurate time and frequency transfer using Global Navigation Satellite Systems (GNSS) have been used for more than three decades. The method described in [1] relies on measurements of the time difference between a local clock and GPS-time simultaneously at two remote locations. Simultaneous measurements at two remote location to a specific satellite in common view, cancel or greatly reduces common error sources such as the inaccuracy of the satellite orbits and give accurate access to the time difference between the remote clocks. To strengthen the early development and to simplify the usability of the Common-View (CV) method, a standard for GPS data processing and exchange was developed [2], with a further development to include also GLONASS satellites [3]. The latest version of the Common GNSS Generic Time Transfer Standard (CGGTTS) [4] supports in addition observations with the Galileo and BeiDou satellite navigation systems.

The work presented in this paper is supported by the Swedish Governmental Agency for Innovation Systems (Dnr: 2014-05075).

As mentioned, the GNSS CGGTTS CV-method relies on the measured time difference between a local clock and GNSS system time. In the early years, one-channel, single-frequency C/A code receivers were used, and the remote stations followed an agreed-upon schedule that specified which satellite to be locked to and during which time slot. The measured pseudoranges to individual satellites together with parameters in the disseminated navigational message, gave access to GNSS system time (at that time only GPS) and was compared to the local clock using a time interval counter. For the receiver to get a full navigation message and to remove some of the inherent noise in the pseudorange, as well as other intentional unwanted effects such as Selective Availability (SA), the observational time slot was extended to 13 minutes. This, together with a 3-minute slot for the receivers to lock on the next scheduled satellite, gave a 16-minute data interval between each observation with up to 90 observations per day. This procedure is also followed today. The difference is the capability of the receivers. These are today multi-channel, multi-frequency, multi-system devices capable to lock to external time signals that replaces the internal oscillator with the result that all observations are related to the external clock or time scale. The procedure is to retrieve observation in raw data format from the receiver, transform the data to RINEX [5] format and in a following step, either directly within the receiver or using an external software tool, to the CGGTTS data format.

The described GNSS CGGTTS CV-method has been used many years for international time keeping. The International Bureau of Weights and Measures (BIPM) is since the nineteen-eighties using the method to compare national UTC realisations for the generation of the International Atomic Time TAI and the Coordinated Universal Time UTC. Also, National Metrology Institutes (NMIs) use the method for the distribution and dissemination of national time scales. National distribution will most likely grow during the following years due to applications within several public and commercial areas with increased requirements for time synchronisation. Just one example is the financial market where time synchronisation is presently regulated, see e.g. [6]. Also, the development of new time distribution and comparison methods, for instance via optical fibre networks, are often validated by appropriate GNSS-methods. To meet the growing need for time synchronisation within both commercial and non-commercial applications as well as the GNSS receiver development, a new

software tool for GNSS time and frequency transfer has been developed by RISE.

The presented software tool for GNSS time transfer implements the CGGTTS standard and handles signals from the satellite navigation systems GPS, GLONASS, Galileo and BeiDou including the most important ranging codes for time transfer applications. All features of the software are briefly described in Section II. Section III presents an evaluation of the software by a comparison with two other independent software tools. Further, Section IV presents some example results of time transfer including both short- and long baselines as well the use of IGS products and non-standard linear combinations. Finally, Section V presents two applications of combining the CGGTTS data of the four available GNSS. The paper ends with concluding remarks.

II. DESCRIPTION OF THE SOFTWARE

The aim of the new software tool is to provide an alternative to existing software and to support time transfer with new GNSS. The software supports the classical GNSS CGGTTS data processing and output format [4], and is thus compatible with existing, similar software tools. In addition to standard 13-minute smoothed data, the software also produces non-smoothed, single-epoch CGGTTS data. The software is called "**RISEGNSS**", is written in plain C-code, compiles preferably in a GNU/Linux environment, and currently offers a command-line user interface only.

The input to the software are pseudorange measurements and navigational broadcast data defined in the RINEX format [5] in either version 2 or 3. The software uses RINEX data with 30-second sampling rate to produce 13-minute tracks from a total of 26 pseudorange measurements. Alternatively, using 15-seconds sampling rate using a total of 52 pseudorange measurements. The RINEX files may be mixed or system dependent. Preferably, but not mandatory, is, in addition to provide RINEX files for the specific day to be processed, to provide a file also for the consecutive day. This will allow the last 13-minute track for the present day to be calculated. For single-frequency processing, there is a possibility to input a specific navigation data file with the needed ionospheric parameters used in the implemented model as well as a file including satellite code biases. All files needed for processing are specified using option flags in the command-line user interface. These includes also the user-selected names of the output files as well as the necessary parameter file.

The parameter file describes detailed settings for processing and is also used for creating the CGGTTS file header. To mention some of the most important settings:

- The X, Y, and Z-coordinates for the phase centre of the antenna. An option is to give the coordinates in a specific frame together with a date and velocity coordinates;
- Receiver internal delays, antenna cable delay and reference clock delay. The internal delays are separately defined for each specified observable;
- Observables to be selected as given in the RINEX file. Usually two observables are selected which are then processed as a linear combination. For single-frequency users, only one observable is given;
- The elevation cut-off angle (other than using the default of 0 degrees);
- The number of Leap seconds since GPS-time start epoch (used if not given in RINEX file);
- A satellite health indicator to unselect non-healthy satellites as indicated in the navigation files;
- The output sample rate of non-smoothed single-epoch CGGTTS data.

Finally, the RISEGNSS software tool is capable of handle the adoption of satellite orbits and clocks in SP3 format, in this case from the IGS [7]. It can also produce results using linear combinations, or single-frequency observations, of non-standard CGGTTS codes and signals.

III. EVALUATION OF THE SOFTWARE

The CGGTTS data obtained from the RISEGNSS software tool have been evaluated for the standard linear combinations that are recommended in [4] for GPS, GLONASS, Galileo and BeiDou. The evaluation was performed by a comparison with the CGGTTS data obtained using two other, independently developed software tools. The first software, commonly used by the international UTC-labs, is developed by the time and frequency group at the Royal Observatory of Belgium (ORB), see e.g. [8]. The present, available version of the ORB software (R2CGGTTS 7.1b) produces CGGTTS data for observations with GPS, GLONASS and Galileo. The second software is developed by the National Time Service Center (NTSC), P.R. of China, and CGGTTS data produced by NTSC have been used for the evaluation of observations with BeiDou. All three software comply with the CGGTTS-Version 2E standard [4].

The software evaluation study involves RINEX (V.3) data from two receivers: NTP3 (Septentrio PolaRx4TR)[1], maintained by NTSC and SP05 (Septentrio PolaRx5TR), maintained by RISE. Both receivers observe a variety of codes and signals from the satellites in all four mentioned GNSS. The receivers are referenced to the national time scales UTC(NTSC) and UTC(SP), respectively. CGGTTS data were calculated for 22 days (MJD 57903 to 57924) with an elevation cut-off angle of 10°. With reference to [5], the following code observables have been used for the calculation of ionosphere-free linear combinations: for GPS the C1W and C2W (L1 and L2 carrier), for GLONASS[2] C1C and C2C (G1 and G2 carrier), for Galileo C1C and C5Q (E1 and E5a carrier), and for BDS C2I and C7I (B1 and B2 carrier). It is shown that the results obtained from the different software agree to less than sub-nanosecond level while comparing the CGGTTS REFSYS values [4].

[1] Product names of the equipment are included for reference only. No endorsement or critique is implied.

[2] For GLONASS the recommended observables used for linear combination are C1P and C2P, but as NTP3 did not provide these for the dates studied the evaluation was performed using C1C and C2C.

Figures 1a-c, show, respectively, the difference between individual 13-minute (epoch-by-epoch and satellite-by-satellite) GPS, GLONASS, and Galileo data as calculated with the RISEGNSS and R2CGGTTS software. Figure 1d shows the difference for BeiDou as calculated with the RISEGNSS and NTSC software. The agreement for GPS (Figure 1a) and Galileo (Figure 1c) is at the 100- to 200-picosecond level. This insignificant difference may be explained by compiler and software-code related issues (Fortran is used for R2CGGTTS and plain C-code for RISEGNSS). The agreement for GLONASS (Figure 1b) is at the sub-nanosecond level. This lesser agreement may be explained by a possible different handling of the satellite orbit calculations but will be further investigated. The agreement for BeiDou data is also at the 100- to 200-picosecond level but with some obvious outliers. One important issue in the comparison is the use of the same broadcast ephemerides or Issue of Ephemerides IOE [4]. For GPS and Galileo, the numbering of data ephemerides is strict with little risk for misinterpretation. For GLONASS and BeiDou the ephemerides are instead indicated as an Age of Operation or Ephemerides. While comparing two different software it is necessary that these are interpreted in the same way and may be a reason for the lesser agreement for GLONASS and BeiDou.

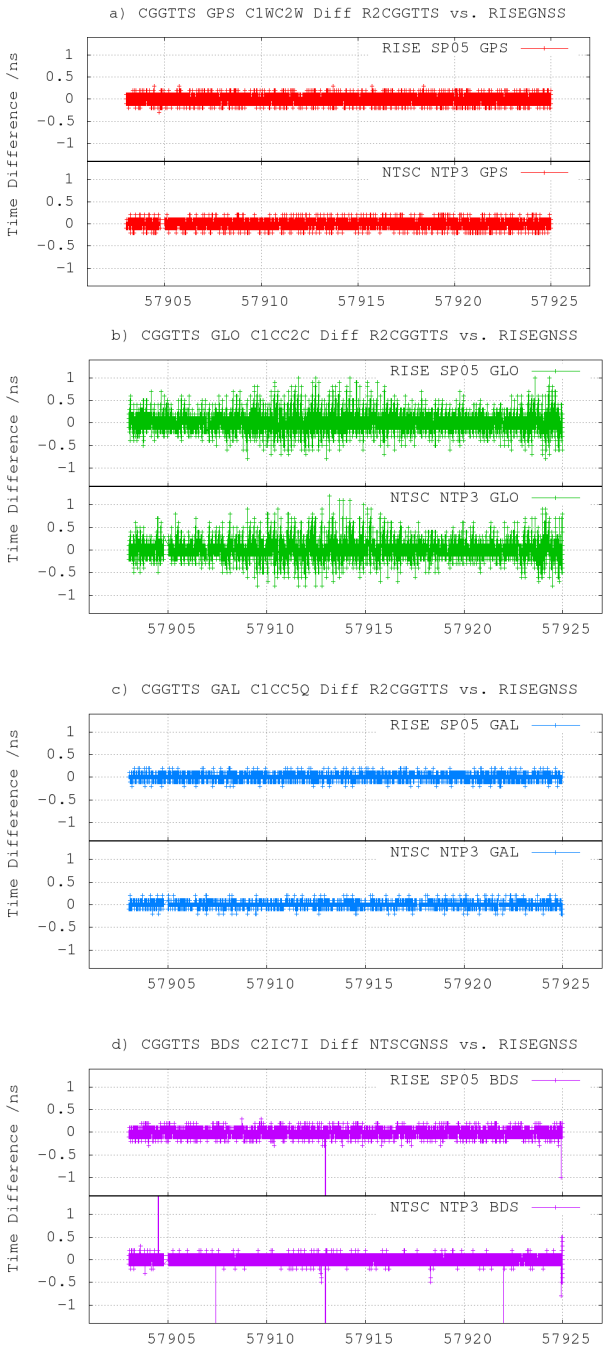

Fig. 1. Difference between CGGTTS REFSYS values [4] as calculated with the RISEGNSS and R2CGGTTS software for GPS (a), GLONASS (b), and Galileo (c) data, and those calculated with the RISEGNSS and NTSC software for BeiDou (d) data.

IV. TIME TRANSFER RESULTS

This section presents time transfer results obtained with the RISEGNSS software for GPS, GLONASS, Galileo and BeiDou. The results presented in the first sub-section (A) are based on the same data as used for the evaluation in Section III, for the long baseline RISE (Sweden) to NTSC (P.R. of China) with standard pseudorange codes for ionosphere-free linear combinations. The second sub-section (B) presents results for a short, common-clock baseline using data from two RISE receivers. This sub-section also includes results using linear combinations of non-standard codes and signals for GPS and Galileo. The third sub-section (C) demonstrates the adoption of IGS products, and, finally, the fourth sub-section (D) gives some examples using non-smoothed, single-epoch CGGTTS data. The aim of the analysis is mainly for demonstration and validation of the RISEGNSS software tool rather than studying the different time transfer results in detail.

A. Long baseline

The performance of the time transfer links for the long baseline (>6800 km) between RISE and NTSC, using receivers SP05 and NTP3 represented by the national time scales UTC(SP) and UTC(NTSC), respectively, is shown in Figure 2. The results are obtained from a CV-analysis of CGGTTS data produced with the RISEGNSS software for the four mentioned GNSS. The only receiver-calibrated system is GPS, and a link offset has been estimated and applied for the other GNSS. Table I presents the least-squares estimated link offsets relative to the GPS-link.

TABLE I. LEAST-SQUARES ESTIMATED LINK OFFSETS RELATIVE TO GPS-LINK FOR THE NTSC TO RISE BASELINE USING RECEIVERS NTP3 AND SP05

System	*Code combination*	*Offset*	*rms*
GLONASS	C1C & C2C	-142.2 ns	3.3 ns
Galileo	C1C & C5Q	-166.0 ns	1.3 ns
BeiDou	C2I & C7I	-155.4 ns	1.9 ns

Figure 3 shows the Allan deviation for the data in Figure 2, and for the long baseline between RISE and NTSC it is shown that GPS and Galileo have the lowest link noise followed by BeiDou and GLONASS. It should be noted that the GEO satellites of BeiDou are included in the solution. Although only one BeiDou GEO satellite (C05) is presently tracked at RISE, this satellite degrades the stability of BeiDou (see also [9]). For GLONASS, an effect on the noise due to receiver inter-channel frequency biases has been demonstrated [10] and is most likely seen also here. In addition, in this study the C/A code (C1C and C2C) is used for GLONASS as NTP3 did not provide the P-code for GLONASS. The number of common observations for this long baseline, shown in Figures 4, may affect the link noise (for all GNSS), for example due to the, naturally, lower satellite elevation for common observations. This is especially a limiting factor for Galileo and BeiDou (in Europe) but should improve as more operational satellites become available.

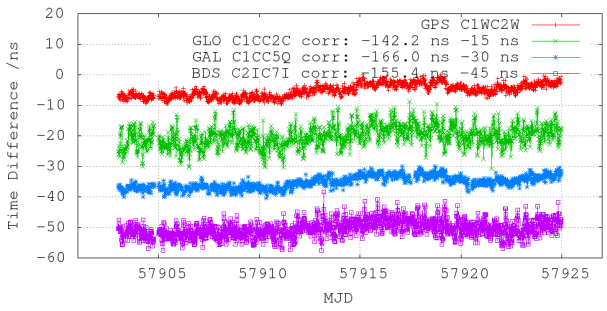

Fig. 2. Time scale difference [UTC(NTSC) – UTC(SP)] obtained from CV-analysis of CGGTTS data using the RISEGNSS software. A link offset has been estimated for GLONASS, Galileo and BeiDoU relative to the GPS-link. The different links are further separated for clarity.

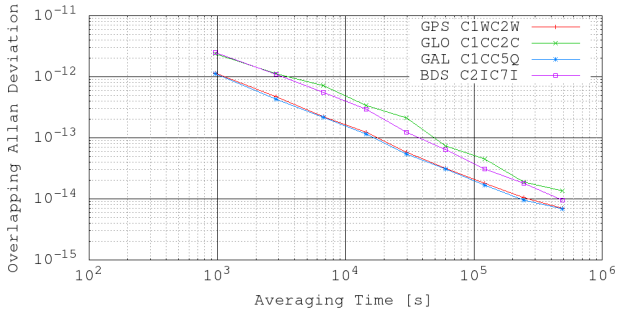

Fig. 3. Link noise represented by the overlapping Allan deviation for the time differences shown in Figure 2.

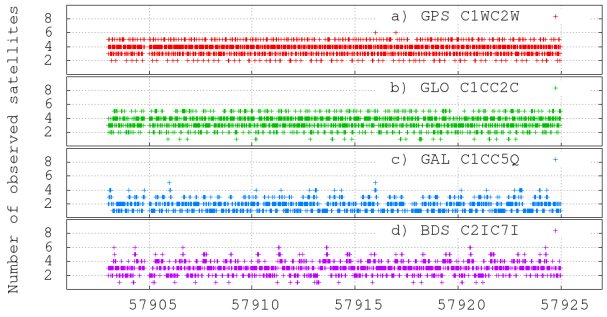

Fig. 4. Number of common 13-minute CV-data for the links presented in Figure 2. GPS (a), GLONASS (b), Galileo (c), and BeiDoU (d).

B. *Short baseline*

1) Standard linear combinations

To further study the link noise for the present GNSS, Figure 5 shows the time transfer results for a short, common-clock baseline. Data from two receivers (SP05 and RIT1) of the same type (Septentrio PolaRx5TR) with separate antennas some 50 metres apart were analysed in the same way as for the long baseline in sub-section IV-A. Figure 6 shows the Allan deviation for the data in Figure 5. It is seen that for this short baseline, GPS and Galileo has the lowest link noise while BeiDou is noisier than GLONASS. Table II presents the least-squares estimated link offsets relative to the GPS-link.

TABLE II. LEAST-SQUARES ESTIMATED LINK OFFSETS RELATIVE TO GPS-LINK FOR THE SHORT RISE BASELINE USING RECEIVERS RIT1 AND SP05

System	*Code combination*	*Offset*	*rms*
GLONASS	C1C & C2C	76.9 ns	1.0 ns
Galileo	C1C & C5Q	73.0 ns	0.6 ns
BeiDou	C2I & C7I	57.0 ns	1.5 ns

The link noise for GLONASS for this short baseline is more than three time less than for the long baseline (see Table I above). For Galileo, the difference is a factor of 2.1 and for BeiDou a factor of 1.3. The reason for the high factor of improved link noise for GLONASS on this short baseline relative to the long baseline may be related to the different receiver types used at NTSC and RISE. Remembering that the model of Septentrio receiver used at NTSC (PolaRx4) is different to that used at RISE (PolaRx5). It must be investigated further, but the inter-channel frequency biases may cancel out when using the same receiver model as for the short RISE baseline [10].

2) Non-standard linear combinations

For this short, common-clock baseline, a functional test has also been performed using non-standard linear combinations. The standard linear combination for GPS using codes on L1 and L2 (C1W and C2W) was replaced by L1 and L5 (C5Q). Similarly, for Galileo, E1 and E5a (C1C and C5Q) was replaced by E1 and E5b (C7Q) as well as E1 and E5-altboc (C8Q).

Figure 7 shows a comparison of the Allan deviation of the two linear combinations calculated for GPS. It is seen that for this test the standard linear combination using L1 and L2 gives the lowest noise. In general, the combination of L1 and L5 should have more potential due to the carrier frequency separation, but presently the number of available satellites transmitting L5 are too low. See also [11] that discusses the use of GPS C5 code. Figure 8 shows a comparison of the Allan deviation of the three linear combinations processed for

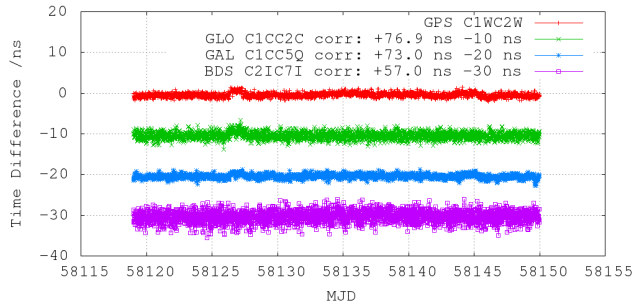

Fig. 5. Common-clock time difference obtained from a CV-analysis of CGGTTS data using the RISEGNSS software. A link offset has been estimated for GLONASS, Galileo and BeiDou relative to the GPS-link. The different links are separated for clarity.

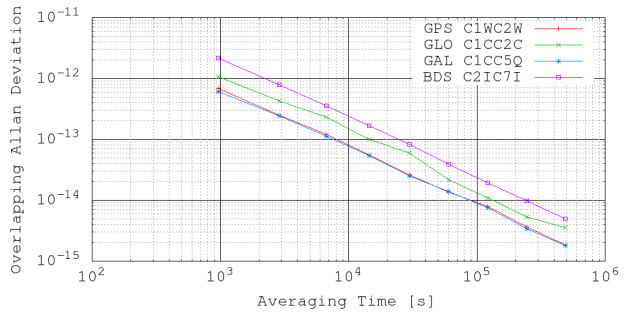

Fig. 6. Link noise represented by the overlapping Allan deviation for the time differences shown in Figure 5.

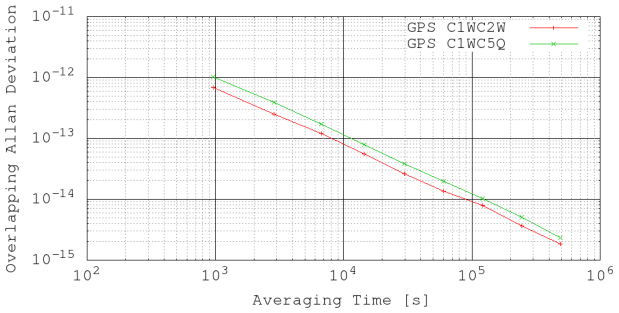

Fig. 7. Link noise represented by the overlapping Allan deviation for two different linear combinations of GPS codes..

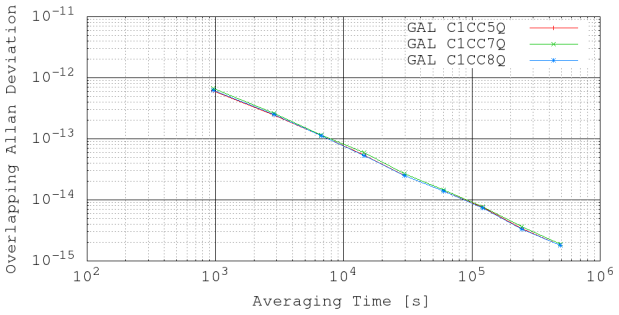

Fig. 8. Link noise represented by the overlapping Allan deviation for three different linear combinations of Galileo codes.

Galileo. It is demonstrated that for this test the standard linear combinations using E1 and E5a and E1 and E5-altboc give similar link noise. The combination of E1 and E5b gives marginally higher link noise which is also demonstrated in [12]. Although realistic results are obtained for non-standard linear combinations, it should be kept in mind that these are not fully verified in the present version of RISEGNSS and further studies are needed.

C. Implementation of IGS products

IGS satellite orbit and clock products have been used by the BIPM for improving international GPS-based time links for many years [13]. The so-called All-in-View (AV) method [14] corrects the CGGTTS data based on broadcast ephemerides and clocks using precise orbits and clocks estimated by the analysis centres of IGS [7]. The CGGTTS data are by the method inherently referenced to IGS-time instead of GNSS system time and global, common observations are induced by the accuracy of the satellite orbits and clocks. This allows the AV method to apply an averaging (often weighted by satellite elevation) of all available measurements for an observational epoch. The time transfer improvements are mostly notable for inter-continental baselines. Several IGS MGEX analysis centres are providing products for all four GNSS involved in this study.

The RISEGNSS software tool is developed for the use of IGS satellite orbits and clocks. To test the implementation, the time transfer links between NTSC and RISE as presented in sub-section IV-A, were corrected with accurate orbits and clocks from the IGS analysis centre GFZ in Potsdam [7]. Figures 9 to 12 show a comparison of the Allan deviation of the standard CV-results with those obtained with IGS MGEX products and analysed with the AV method. Some stability improvements are seen for GPS and Galileo even if these are marginal. For GLONASS there is no visible improvement and the cause of this must be analysed further. A possible explanation can be that the effect due to receiver inter-channel frequency biases still dominates the GLONASS link.

For the time period processed in this study, the GFZ products include the BeiDou GEO satellites and using them gives no improvement relative to using broadcast ephemerides. An analyse was also performed using products from the IGS MGEX analysis centre CODE, which did not provide products for the GEO satellites for the dates processed. Without the GEO satellite there is an improvement in the link noise. However, relative to the results using broadcast ephemerides no improvement is obtained as seen in Figure 12.

To achieve improvements, it is essential that the fixed antenna coordinates are accurate, that satellite antenna three-dimensional phase offsets are corrected for using the IGS ANTEX file, that the antenna position is corrected for using solid Earth tide models, and that the tropospheric delay is estimated or modelled more accurately than in the present CGGTTS standard. The latter two are not yet implemented in RISEGNSS.

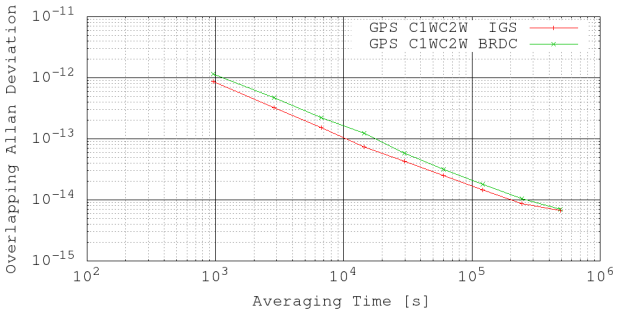

Fig. 9. GPS link noise represented by the overlapping Allan deviation for the time scale difference [UTC(NTSC – UTC(SP)] obtained from CV-analysis of CGGTTS data and from AV-analysis of the IGS-corrected CGGTTS data using the RISEGNSS software.

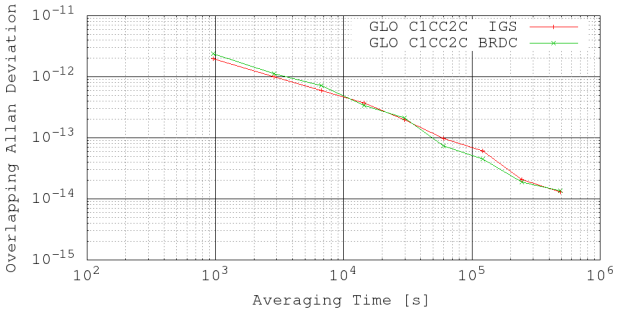

Fig. 10. Same as Figure 9 but for GLONASS.

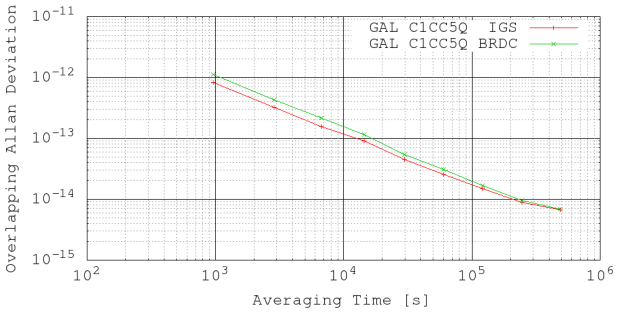

Fig. 11. Same as Figure 9 but for Galileo.

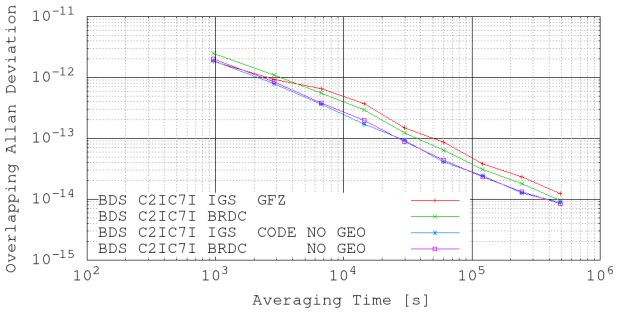

Fig. 12. Same as Figure 9 but for BeiDou.

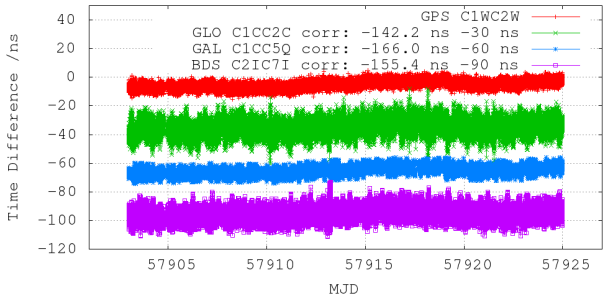

Fig. 13. Time scale difference [UTC(NTSC) – UTC(SP)] obtained from CV-analysis of non-smoothed single-epoch CGGTTS data with an interval rate of 30 seconds using the RISEGNSS software. A link offset has been estimated for GLONASS, Galileo and BeiDoU relative to the GPS-link. The different links are further separated for clarity.

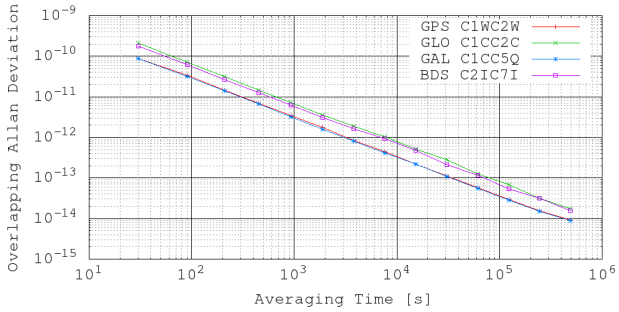

Fig. 14. Link noise represented by the overlapping Allan deviation for the time differences shpwn in Figure 13.

D. Non-smoothed single-epoch CGGTTS data

A feature of the RISEGNSS software tool is to output non-smoothed CGGTTS data. Rather than combining 26 (or 52) pseudorange measurements into 13-minute tracks as described in Section II, the non-smoothed data contain the analysis of single-epoch pseudorange data with an interval rate depending on the RINEX file content. Figure 13 shows the time scale difference [UTC(NTSC) – UTC(SP)] based on single-epoch CV-results with an interval rate of 30 seconds for GPS, GLONASS, Galileo and BeiDou. The corresponding results for standard 13-minute CV-data are shown in Figure 2.

The non-smoothed, single-epoch CGGTTS data is by nature much noisier, but the aim of the feature is to have the own choice of data smoothing. An alternative smoothing interval may be performed instead of the standard 13-minute span. Smoothing may also be performed on a link level. The advantage is the availability to create smoothed data at an interval that is evenly divisible by 24 hours which is an advantage for stability analysis. The Allan deviation of single-epoch CV-results for the links shown in Figure 13 are shown in Figure 14.

V. APPLICATIONS

Typically, CGGTTS data are distributed between peers or to a central data holding on a daily basis. Interested parties

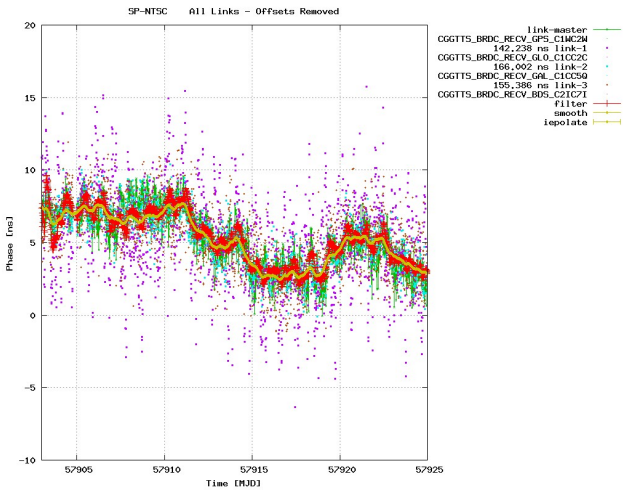

Fig. 15. Combination at link level for the time scale differences shown in Figure 2.

would then differentiate the data in order to create time transfer links as exemplified in Section IV. This is usually done in post processing and per constellation and code combination. In the following two applications are suggested that treats the CGGTTS data differently.

A. Link Combination

For reasons of redundancy and possible link performance improvements, a combination of individual links may be performed. Also, often only one GNSS constellation is used to establish a time link calibration. A separate or relative calibration is then needed in order to make proper use of the additional observed constellation. Link combination is one convenient solution to obtain calibration offsets [10]. Figure 15 shows an example for a combination at link level of the four GNSS links available between NTSC and RISE. The combination is based on a Kalman filter that estimates constant biases for the uncalibrated links (GLONASS, Galileo and BeiDou) using the calibrated GPS-link as reference. By modelling the typical behavior of the connected time scales, the filter maintains a correct estimate of the differences between them, even in case of loss of several and/or the calibrated sub-links. The estimated biases are very similar to those presented in Figure 2 and in Table 1.

B. Real-Time Processing

Many applications that today use the positioning solution of a GNSS receiver as a time source, may be served in a more traceable and possibly more robust way by using common view. This however relies on a (near) real-time processing of the GNSS observables. A modified version of the presented software can handle observations in a sequential, i.e. forward direction. Paired with an appropriated receiver dependent reading front-end, observations are processed in real-time and output is offered to socket communication relaying the CGGTTS data in unicast or multicast using IP networks. Together with before mentioned link combination, a typical user may relate its time scale using multiple constellations and using the full potential of its local clock in hold over situations.

VI. CONCLUSIONS

A new independent software tool for GNSS time transfer implementing the satellite navigation systems GPS, GLONASS, Galileo and BeiDou has been developed. The evaluation shows good agreement with established software for classical CGGTTS time transfer data using the CGGTTS V2E standard. Comparing the CGGTTS REFSYS values from the RISEGNSS and R2CGGTTS (version 7.1b) software an agreement at the 100- to 200-picosecond level is obtained for GPS and Galileo, while the agreement for GLONASS is at the sub-nanosecond level. The lesser agreement for GLONASS is believed to be explained by different handling of the satellite orbit calculations. This will however be further investigated. The agreement between the RISEGNSS and NTSC software for BeiDou data is also at the 100- to 200-picosecond level but with some obvious outliers. A further evaluation of BeiDou CGGTTS data is foreseen with the new version of the R2CGGTTS software [15]. Also, in a very recent paper [16] the progress of time transfer with BeiDou is further analysed by NTSC using their software.

The adoption of IGS precise satellite orbit and clock products is demonstrated using IGS MGEX products from the analysis centres GFZ and CODE. The improvement using IGS MGEX products for the long baseline between RISE (Sweden) and NTSC (P.R. of China) is shown to be relatively marginal for GPS and Galileo. No visible improvement is seen for GLONASS. The same yields for BeiDou if the GEO satellites are removed from the data. It is seen that by removing the GEO satellites the general time link performance with BeiDou is improved both using broadcast navigational data as well as using IGS MGEX products. The adoptions of IGS products will be further developed and investigated by the implementation of solid Earth tide models for the correction of antenna position and the use of IGS-estimated, rather than modelled, station tropospheric delays.

The use of non-standard codes and signals, non-smoothed CGGTTS data and the application of link combinations are all interesting aspects in time transfer analysis and development. The brief results presented in this paper will be further investigated.

The intension is to make the RISEGNSS software freely available for both scientific and commercial users under a “ShareAlike” license.

ACKNOWLEDGMENT

The authors would like to thank their colleagues at the time and frequency groups at ORB, for providing the UTC-community with the R2CGGTTS software, at NTSC, for discussions around BeiDou analysis as well as providing CGGTTS data for this paper, and the IGS community for accurate orbit and clock products.

REFERENCES

[1] D. W. Allan and M. Weiss, "Accurate time and frequency transfer during common-view of a GPS satellite," in Proc. of 34th Annual Frequency Control Symposium, Ft. Monmouth, MJ, USA, May 1980, pp. 334-346.

[2] D. W. Allan and C. Thomas, "Technical directives for standardization of GPS time receiver software," Metrologia, vol. 31, no. 1, pp. 69-79, Jan 1994.

[3] J. Azoubib and W. Lewandowski, "CGGTTS GPS/GLONASS data format version 02," prsented at the 7th CGGTTS Meeting, Reston, VA, USA, 1998.

[4] P. Defraigne and G. Petit, "CGGTTS-Version 2E: an extended standard for GNSS time transfer," Metrologia, vol. 52, no. 6, G1, Jan 2015.

[5] RINEX – The receiver independent exchange format. Version 3.03. International GNSS Service (IGS), RINEX Working Group and Radio Technical Commission for Maritime Services Special Committee 104 (RTCM-SC104), July 2015.

[6] Transaction reporting, order record keeping and clock synchronisation under MiFID II. European Securities and Market Authority (ESMA), Guidline ESMA/2016/1452, Oct 2016.

[7] The Multi-GNSS Experiment and Pilot Project (MGEX), International GNSS Service (IGS). http://mgex.igs.org/index.php.

[8] P. Defraigne and G. Petit, "Time transfer to TAI using geodetic receivers," Metrologia, vol. 40, no. 4, pp. 184-188, June 2003.

[9] W. Huang and P. Defraigne, "BeiDou time transfer with the standard CGGTTS," IEEE trans. on Ultrasonics, Ferroelectrics, and Frequency Control, vol. 63, no. 7, pp. 1005-1012, July 2016.

[10] A. Harmegnies, P. Defraigne, and G. Petit, "Combining GPS and GLONASS in all in view for time transfer," Metrologia, vol. 50, no. 3, pp. 277-287, May 2013.

[11] P. Defraigne, W. Aerts, G. Cerretto, E. Cantoni, and J.-M. Sleewaegen, "Calibration of Galileo signals for time metrology," IEEE trans. on Ultrasonics, Ferroelectrics, and Frequency Control, vol. 61, no. 12, pp. 1967-1975, Dec 2014.

[12] P. Defraigne et al., "Advances on the use of Galileo signals in time metrology: calibrated time transfer and estimation of UTC and GGTO using a combined commercial GPS-Galileo receiver, " in Proc. of 45th Annual Precise Time and Time Interval Systems and Applications Meeting, Bellevue, WA, USA, Dec 2013, pp. 256-262.

[13] G. Petit and E. F. Arias, "Use of IGS products in TAI applications," J. Geodesy, vol. 83, pp. 327-334, 2009.

[14] G. Petit and Z. Jiang, "GPS All in View time transfer for TAI computaion," Metrologia, vol. 45, no. 1, pp. 35-45, Feb 2008.

[15] P. Defraigne and K. Verhasselt, "Multi GNSS time transfer with CGGTTS-V2E,", in press, this proceedings.

[16] W. Guang et al. "Progress of BeiDou time transfer at NTSC," Metrologia, vol. 55, no. 2, pp. 175-187, Apr 2018.

Evaluation and development of optical time transfer (OTT) links between PTB and Deutsche Telekom

Ł. Śliwczyński, P. Krehlik, J. Kołodziej
Faculty of Computer Science, Electronics and Telecommunications
AGH University of Science and Technology
Krakow, Poland

H. Imlau, H. Ender
Deutsche Telekom Technik GmbH
Bremen, Germany

H. Schnatz, D. Piester, A. Bauch
Physikalisch-Technische Bundesanstalt (PTB)
Braunschweig, Germany

***Abstract*—Optical time transfer between PTB and Deutsche Telekom started in 2015. Since December 2016 it has been upgraded to a permanent installation connecting PTB and Deutsche Telekom facilities in Hannover and Bremen. In this paper we report on the evaluation of the performance of this installation and describe future perspectives.**

Keywords—time transfer; fiber optic; dark fiber; bi-directional link; ELSTAB

I. INTRODUCTION

Synchronization is a key element of all telecom networks. A special hierarchical structure is employed for this purpose, typically including a few layers with different stability and accuracy requirements (see Fig. 1 for a general concept). At the top of this structure, the so-called core level is implemented, which includes a number (10-20 in practice, depending on the size of the specific network) of Cs-based enhanced Primary Reference Time Clock (ePRTC) functions. Time and frequency signals from the core level are passed down the hierarchy to lower levels, which include a large number (more than 10000) of nodes that need to be synchronized. Besides the requirements concerning stability and accuracy of frequency and time signals according to the relevant ITU-T standards [1], the recent ITU-T recommendations [2] require that ePRTC functions should be traceable to a recognized standard, like UTC. To fulfil this requirement ePRTCs can either be compared against a local realization of UTC, UTC(k) in a National Metrological Institute (NMI) "k", using e.g. the GNSS Common View time transfer method or linked to the NMI via a direct optical time transfer link (OTT).

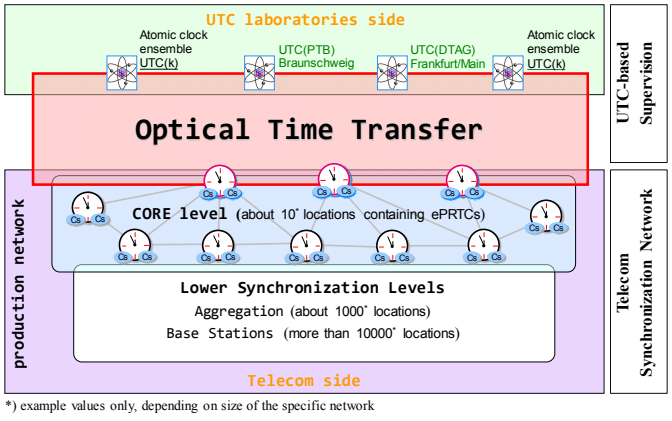

*) example values only, depending on size of the specific network

Fig. 1. General idea of OTT.

Using OTT to supervise a telecom synchronization network has been started in 2015 by establishing a first connection between PTB in Braunschweig and a test centre of Deutsche Telekom located in Bremen [3]. Since then, the OTT network has been modified and extended [4]. In the current development stage it connects PTB and Bremen via a time and frequency hub located in Hannover (see Fig. 2) from which an additional connection to Frankfurt/Main has been set up recently, where German's Telekom timescale UTC(DTAG) is maintained (this connection is expected to be operational in summer 2018). This connection will allow a direct comparison between UTC(PTB) and UTC(DTAG).

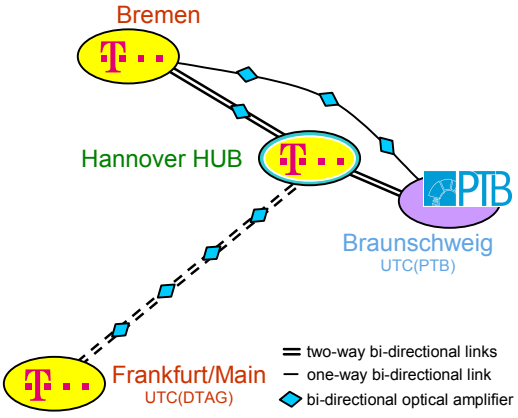

Fig. 2. Diagram showing locations involved in OTT installation.

This work was partially supported by the EMPIR initiative co-funded by the European Union's Horizon 2020 research and innovation programme and the Participating States via project 15SIB05. Support was also received from the Faculty of Computer Science, Electronics and Telecommunications, AGH University of Science and Technology, Krakow, Poland.

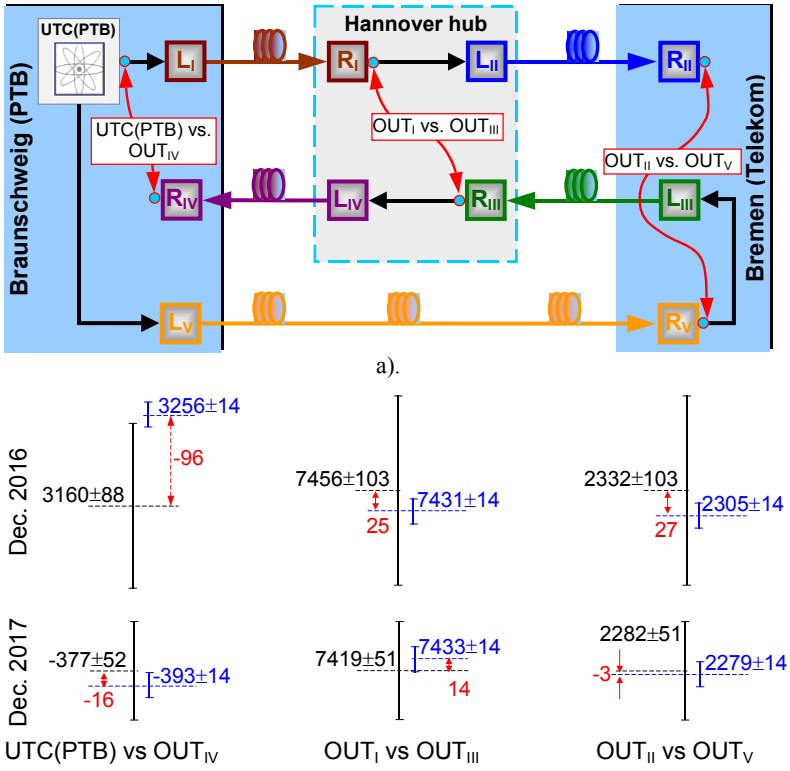

Fig. 3. a) Sketch of the links connecting PTB and Deutsche Telekom; b) results of the calibration validation (in black: predicted values based on calibration, in blue: measured values, in red: differences between predictions and measurements). All quantities are in ps.

II. Calibration and its Validation

The OTT links (see Fig. 3a) use a number of electronically stabilized fiber optic time and frequency dissemination systems (known as ELSTAB) developed by AGH University of Science and Technology. Each ELSTAB system, composed of a local (L) and a remote (R) module, comprises proprietary electronic circuitry for the compensation of the fiber propagation delays and their fluctuations. An ELSTAB system disseminates time (1 PPS) and frequency signals (10 MHz) in a bi-directional fiber link using a dark fiber or dark channel approach. To compensate the loss of optical power due to fibers attenuation, special bi-directional optical amplifiers are used.

Calibration of the entire OTT architecture requires calibration of each individual link. This procedure is performed for each link at the local module side and requires measurements of a few time intervals [5]. Having done this, the propagation delays between all points inside the OTT architecture are known. Thanks to the unique redundant structure of the implemented OTT links between Braunschweig and Bremen it was possible to validate the calibration. This was done on two occasions: in December 2016 and December 2017.

The results of direct cross-measurements in Braunschweig, Hannover and Bremen have been compared with the calibration predictions - see Fig. 3b. The difference that can be seen between the results obtained in 2016 and 2017 are due to the change in the length of the fiber connecting Hannover and Bremen (due to construction works) and a change in the distribution chain of 1 PPS and 10 MHz signals at PTB.

Both calibration campaigns showed good agreement between predicted values and direct measurements - in all cases the results stay within the uncertainty limits. The difference between the predicted value and direct measurement do not exceed 100 ps and 20 ps in 2016 and 2017 campaigns, respectively. The generally better results of 2017 campaign are related to a more systematic approach when performing the measurements required to get the calibration predictions. In December 2016, the measurements at PTB were based on a Stanford Research SR620 time interval counter (TIC), whereas all measurements of the time intervals in December 2017 were performed using a high-speed digital oscilloscope (model DSO81004B by Agilent). This resulted in lower uncertainty bounds in 2017. In addition, all the measurements were referenced to the signals derived from UTC(PTB) in 2017 instead of an oven controlled crystal oscillator (OCXO) used in December 2016.

III. Transfer Stability

The measurement of the stability of the time transfer has been performed by comparing UTC(PTB) with the signal transmitted back to PTB via Hannover and Bremen, using three cascaded links (named V, III and IV in the Fig. 3a). The resulting modified Allan deviation (ModADEV) calculated for a period of 150 days is shown in Fig. 4. Up to a few hundreds seconds the measurement is limited by the noise of the TIC

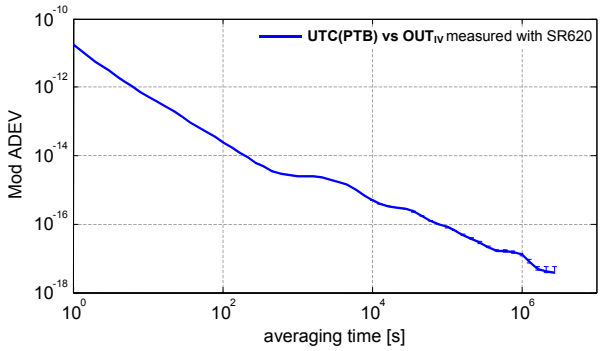

Fig. 4. Results of time transfer stability measurement.

(SR620). The bump around the averaging time of 2000 s is due to temperature fluctuations in Bremen laboratory. Even despite these limitations, the obtained results surpass the requirements for the telecom network supervision by at least two orders of magnitude.

IV. Conclusion

In this paper we presented the current status of OTT links intended for the supervision of Deutsche Telekom synchronization network. Good agreement between OTT calibration and direct measurements has been achieved. Differences between calibration data of the two campaigns resulted from changes in routing of the time/frequency signals at PTB and a change of the fiber length. For times longer than ~1000 s temperature fluctuations in Bremen affect the stability of signals delivered there and returned back to PTB. This can be improved by improving temperature stability in the locations where ELSTAB equipment is installed. The instability at short time intervals (<1000 s) is limited by the noise of the TICs. Despite these limitations signals delivered by OTT are adequate for ePRTC supervision as they surpass telecom requirements by 2-3 orders of magnitude. Establishing the connection between Frankfurt/Main and PTB in near future will enable a direct comparison of UTC(PTB) and UTC(DTAG) via fiber.

Acknowledgment

We acknowledge the support of Jürgen Becker, Thomas Polewka and Holger Seifert of PTB and of Marvin Barasi, Christiane Feldmann, Uwe Habighorst, Olaf Kappner and André Krüger of Deutsche Telekom during the planning, installation and supervision of operations.

References

[1] ITU-T Recommendation ITU-T G.8271.1/Y.1366.1: "Network limits for time synchronization," ITU, 2013.

[2] ITU-T Recommendation ITU-T G.8272/Y.1367: "Timing characteristics of primary reference time clocks," ITU, 2015.

[3] Ł. Śliwczyński, P. Krehlik, H. Imlau, H. Ender, H. Schnatz, D. Piester, A. Bauch, "Towards sub-nanosecond synchronization of a telecom network by fiber optic distribution of UTC(k)," Proc. European Frequency and Time Forum, 4-7 Apr. 2016, York, UK.

[4] Ł. Śliwczyński, P. Krehlik, J. Kołodziej, H. Imlau, H. Ender, H. Schnatz, D. Piester, A. Bauch, "Fiber optic time transfer between PTB and Deutsche Telekom using multi-link redundant topology," Proc. 2017 European Frequency and Time Forum & International Frequency Control Symposium, 10-13 Jul 2017, Besançon, France, pp. 681-682, 2017.

[5] Ł. Śliwczyński, P. Krehlik, J. Kołodziej, H. Imlau, H. Ender, H. Schnatz, D. Piester, A. Bauch, "Fiber optic time transfer for UTC-traceable synchronization for telecom networks," IEEE Communications Standards Magazine, DOI 10.1109/MCOMSTD.2017.1600766ST, vol. 1, no. 1, pp. 66-73, 2017.

Study on BeiDou All-in-View Time Transfer

Zhang Jihai[1, 2], Wu Wenjun[1, 2], Guang Wei[1, 2, 3], Yan Lulu[1, 2, 3], Li Wei[1, 2], Yuan Haibo[1, 2], Dong Shaowu[1, 2, 4]
zhangntsc@126.com; wuwj@ntsc.ac.cn; yuanhb@ntsc.ac.cn; sdong@ntsc.ac.cn
1: National Time Service Center, Chinese Academy of Sciences, Xi'an Shaanxi China 710600
2: Key Lab of Time-frequency Standard of the Chinese Academy of Sciences, Xi'an Shaanxi China 710600
3: University of Chinese Academy of Sciences, Beijing China 100039
4: School of Astronomy and Space Science, Chinese Academy of Sciences, Beijing China 100049

***Abstract*—With the development of Global Navigation Satellite System (GNSS) time transfer, the GPS All-in-View (AV) time transfer has being considered to replace common-view for computing the links of International Atomic Time (TAI). Now, GPS AV is one of the major technologies by BIPM to link all the time keeping labs in the world. To promote the application of Chinese BeiDou navigation system for the realization of TAI. In this paper, BeiDou All-in-view time transfer was studied between National Time Service Center, Chinese Academy of Sciences (NTSC) and Telecommunication Laboratories, Chunghwa Telecom. Co., Ltd (TL) through the IGS precise satellite orbit and clock products. It is proved that the STD of Common Clock Difference (CCD) through BeiDou All-in-view is less than 1ns, the STD of NTSC-TL AV link is better 1.5ns and the it's stability can reach to 1E-14 (1 day). This is almost the same level with GPS. It is show that BeiDou can be used for the nanosecond level time transfer. And this is also support that BeiDou will be involved as the official method in the calculation of TAI in future.**

Keywords—BDS; All-In-View time transfer; International time comparison

I. INTRODUCTION

High precise time transfer is playing an important role for many scientific research fields. With the development of GNSS, the GNSS time transfer is applied more and more widely. It mainly includes Common View (CV), Precise Point Positioning (PPP), and All-In-View (AV) time transfer. Since 1980's, GPS time transfer is one of the major technologies for generation of Coordinated Universal Time (UTC) and International Atomic Time (TAI) by Bureau International des Poids et Mesures (BIPM). AS the development of satellite orbit and clock products, the GPS All-in-view time transfer was presented for the first time in 2004. The BeiDou system (BDS) is currently developed by China, a process that can be divided into three phases. In the first phase (BDS-1), an experimental system composed of three satellites was built from 2000 to 2003 to carry out a technical verification. In the second phase (BDS-2), the Asia-Pacific regional system was built starting in 2012. It mainly provides the Positioning, Velocity and Timing (PVT) service for China and its surrounding areas. Even now, in other areas around the world a few of the BeiDou satellites can be observed. In the third phase (BDS-3), the BDS will be completed for global coverage up to 2020 [1]. Now, the BDS-3 phase has been started and eight BDS-3 satellites have been launched until April of 2018 successfully. In this paper, we study and evaluated the BeiDou All-in-view time transfer between the time keeping labs of NTSC and TL.

II. THEORY OF BEIDOU ALL-IN-VIEW

In order to measure the time difference between station A and station B by BDS all-in-view. Firstly, we need to measure the time difference between the local time (RefT) and IGST by receiving broadcasting signal of BeiDou satelltes, the precise satellite orbit and clock products from IGS analysis center. Then we can measure the time difference between station A and station B. The principle of all-in-view based on BeiDou is showed as Figure 1.

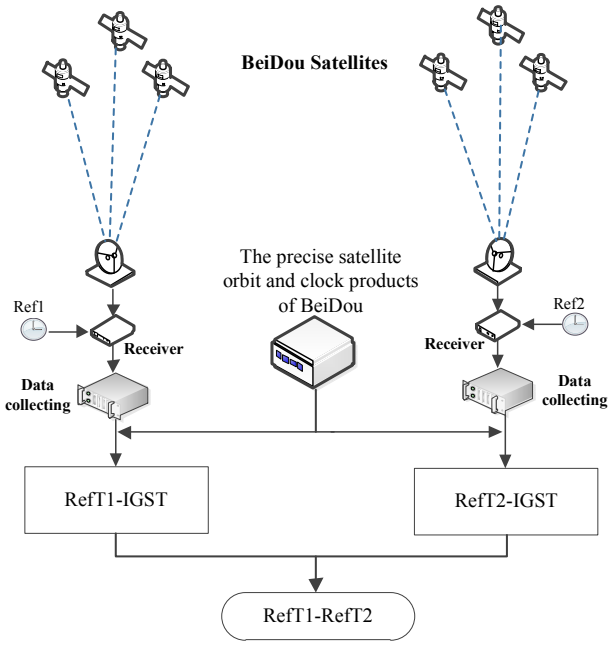

Fig. 1: The Principle of BeiDou All-In-View

As shown in figure 1, the data collecting platform consists of BDS receiver, a data collecting computer and a data processing computer, the input signal to BeiDou receiver includes a 1PPS and a 5/10MHz frequency signal which are

provided by local reference signal. The measurements data in which include BeiDou pseudo-range data are collected by data collecting center in real time. Then the correlation processing method is used to obtain the time difference between local RefT and IGST by each satellite. For example, the data of BeiDou satellite pseudo-range (P) is received by BeiDou receiver at the time t , the expression is as follows [2]:

$$P_i^k = p + c\left(\delta t_u - \delta t^s\right) + d_{ion} + d_{trop} + d_{Sagnac} + d_{mult} + \varepsilon_\rho \quad (1)$$

P is expressed in meters, and k , i are the superscript or subscripts respectively identifying the satellite ,the receiver and carrier frequency(k =B1, B2). The different terms of Eq. (1) are as follows:

p : Geometry distance traveled by the signal between the satellite at transmission time and the receiver at reception time. And the satellite orbit is used from the MGEX of IGS precise satellite orbit product.

δt_u : Receiver clock error. The time difference between the receiver clock and the IGST.

δt^s : Satellite clock error. The time difference between the satellite clock and the IGST, which is used from the MGEX of IGS precise satellite clock products.

d_{ion} : Ionosphere delay. This delay is caused by the traveling of the signal through the ionized atmosphere, which is independent of the carrier frequency.

d_{trop} : Tropospheric delay. This delay is caused by the traveling of the signal through the neutral atmosphere, which is independent of the carrier frequency.

d_{Sagnac} : Time delay caused by the rotation of the earth.

d_{mult} : Code multipath delay.

ε_ρ : Code measurement noise.

By modifying the above, the formulas (1) can be written as:

$$\delta t_u = \mathrm{Re}\, fT - IGST = \frac{p - P'}{c} \quad (2)$$

P' is corrected value of pseudo-range, c is the speed of light.

A. *The Satellite orbit and clock interpolation*

Since the local antenna coordinates are known, Therefore, we need to insert the precise satellite orbit from Multi-GNSS Experiment (MGEX) of IGS, which is supported by GFZ in Potsdam to calculate the geometry distance p . The Lagrange satellite orbit interpolation method is used as follow:

$$f(x) = \sum_{k=0}^{n} \prod_{i=0, i\neq k}^{n} \left(\frac{x - x_i}{x_k - x_i} \right) y_k \quad (3)$$

By the above equation, we can interpolate the any point x in the interpolating interval.

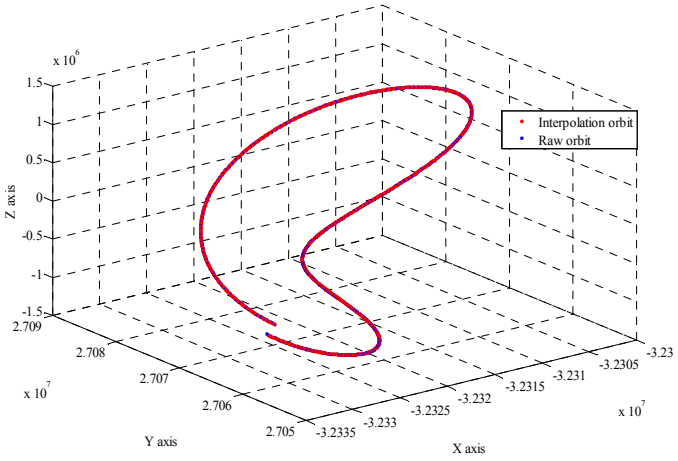

Fig. 2: Lagrange orbital interpolation

As shown in figure 2, we take the C01 of BeiDou satellites as an example (Date: 2018.3.9), the orbit interpolation interval is 60s and compare with the sample interval 300s precise orbit products, which is supported by MGEX of IGS BeiDou precise orbit products.

The linear interpolation method is used in satellite clock interpolation. The precise clock products are used from MGEX of IGS.

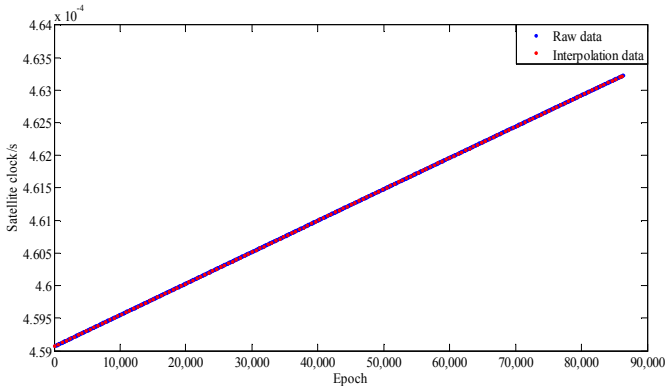

Fig. 3: Linear clock interpolation

As shown in figure 3, we also take the C01 of BeiDou satellites as an example (Date:2018.3.9), the clock interpolation interval is 600s and compare with the sample interval 30s precise clock products, which is supported by MGEX of IGS BeiDou precise clock products.

B. *The Ionosphere correction*

The dual frequency ionosphere combined pseudo range is used to correct the delay caused by ionosphere effect, the calculation method as follows [3]:

$$P = \frac{PR_{B2I} - k(f)\cdot PR_{B1I}}{1 - k(f)} - \frac{C\cdot(T_{GD2} - k(f)\cdot T_{GD1})}{1 - k(f)} \quad (4)$$

As shown above,

$k(f)=\frac{B_1^2}{B_2^2}=\left(\frac{1561.098}{1207.140}\right)^2$;

P : The pseudo range is modified by dual frequency ionosphere combined.

PR_{B1I} : The observation pseudo range of B1I.

PR_{B2I} : The observation pseudo range of B2I.

T_{GD1} : The time group delay of B1I.

T_{GD2} : The time group delay of B2I.

C : The speed of light, 2.99792458×10^8 m/s.

C. *The tropospheric correction*

The tropospheric delay correction is computed using the standard NATO hydrostatic model given for the satellites of all the systems [4]:

$$\Delta t_{tropo}=f(e)*\Delta R(h) \tag{5}$$

In the above formula,

$$f(e)=\frac{1}{\sin(e)+\frac{0.00143}{\tan(e)+0.0455}} \tag{6}$$

$\Delta R(h)$ is the total tropospheric delay at the zenith, and receiver located at an altitude h (in Km). $\Delta R(h)$ is to be computed as:

$$\Delta R(h)=\frac{1}{c}\left[2162+N_s(1-h)+0.5\Delta N(1-h^2)\right]10^{-3} \text{ for } h<1 \text{ km} \tag{7}$$

$$\Delta R(h)=\frac{1}{c}\left[732-8\frac{N_s+\Delta N}{Ns\log}\left(e^{-Ns\log}-e^{0.125(1-h)Ns\log}\right)\right]10^{-3} \text{ for } h>1 \text{ km} \tag{8}$$

Where,

N_s=324.8 is the refractivity index at the mean sea level.

ΔN=-7.32 $e^{0.005577N_s}$.

$Ns\log=\ln\left((N_s+\Delta N)/105\right)$.

D. The sagnac effect

The error by Sagnac effect can be corrected in the calculating process of satellite position.

$$\begin{bmatrix}x'\\y'\\z'\end{bmatrix}=\begin{bmatrix}\cos(\omega\tau) & \sin(\omega\tau) & 0\\ -\sin(\omega\tau) & \cos(\omega\tau) & 0\\ 0 & 0 & 1\end{bmatrix}\begin{bmatrix}x_s\\y_s\\z_s\end{bmatrix} \tag{9}$$

(x',y',z') stands for the corrected satellite position, ω is the earth auto-rotation speed, here ω=7.2921150×10^{-5}rad/s, τ is the transmission time of satellite semaphore. The calculation of τ need to use recursive calculation to correct satellite position with the initial value, which can be obtained using the pseudo range divided by the light speed C, then the new τ can be gotten by the new pseudo range to compute the new sent time of satellite semaphore.

III. TEST AND RESULTS ANALYSIS

Through the algorithms and principle, the BeiDou all-in-view time transfer is studied. The data are from BeiDou dual-frequency multichannel receiver of time keeping laboratory of NTSC and TL. The input reference signal of BeiDou receiver includes a 1PPS and a 5/10MHz from local reference signal. Base on the all-in-view principle, according the GNSS standard common view file, we developed the BeiDou all-in-view processing software. Table I shows the Receivers are used in the experiment.

TABLE I THE RECEIVERS USING IN THE EXPERIMENT

Laboratories	Receiver code	Receiver type	Antenna type
NTSC	NTP4	SEPT POLARX4TR	SEPCHOKE_MC
	NTP7	SEPT POLARX5TR	SEPCHOKE_MC
TL	TL04	SEPT POLARX4TR	ASH701945C_M

A. *The common clock difference*

In order to improvement performance of time transfer by BeiDou all-in-view link, the BeiDou receiver calibration according two receivers which are operated at NTSC. The CCD is shown between NTP7 and NTP4 in Fig 4, (MJD: 58159-58188).

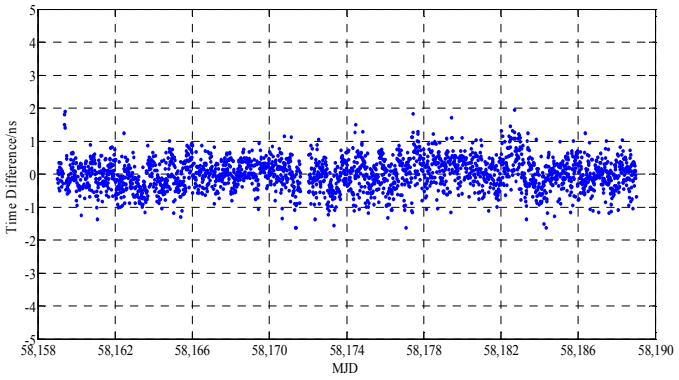

Fig. 4: The CCD of NTP7-NTP4

As shown in the figure above, the results of CCD are mainly within ±1ns by all-in-view, and the STD is 0.4725ns.

B. *The Result of BeiDou All-in-view*

The result of BeiDou all-in-view is shown in figure 5. (MJD: 58176-58190)

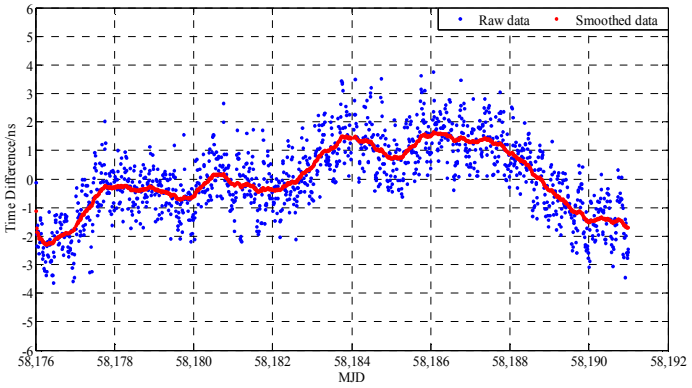

Fig. 5: The time difference bewteen UTC (NTSC) and UTC (TL)

As shown in figure 5, the time difference between UTC (NTSC) and UTC (TL) are calculated through the BeiDou all-in-view, we can see the result fluctuate within 6ns. And the STD is 1.0589ns. Figure 6 and Figure 7 had shown the Allan Deviation and Time Deviation of the UTC (NTSC) -UTC (TL).

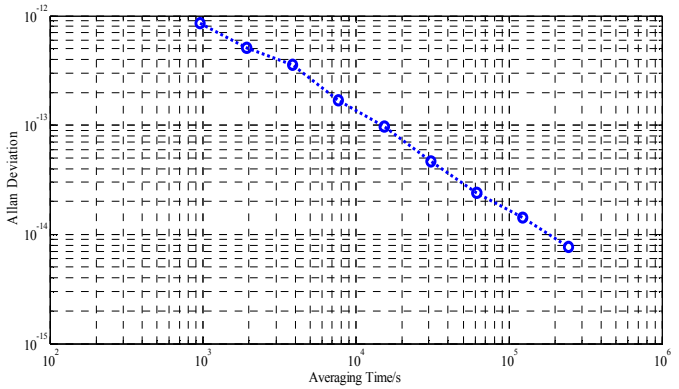

Fig. 6: The Allan deviation of UTC (NTSC)-UTC (TL)

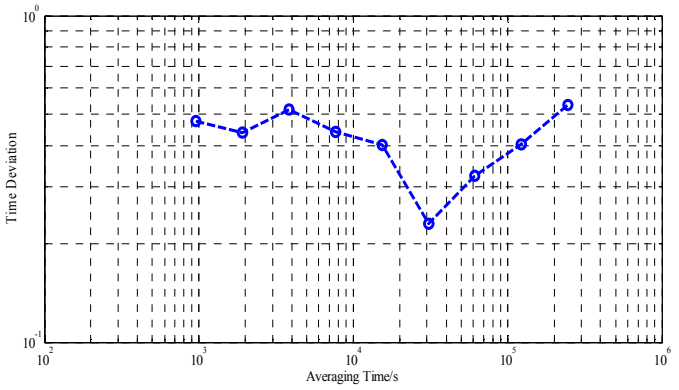

Fig. 7: The Time deviation of UTC (NTSC)- UTC (TL)

Table2 shows the Allan Deviation and Time Deviation of the UTC (NTSC) -UTC (TL) from the numerical.

TABLE II THT ADEV/TDEV DEVIATION OF UTC (NTSC)-UTC(TL)

Tau(s)	ADEV	TDEV
960	8.60E-13	4.77E-01
1920	5.10E-13	4.39E-01
3840	3.54E-13	5.16E-01
7680	1.68E-13	4.40E-01
15360	9.65E-14	4.02E-01
30720	4.67E-14	2.31E-01
61440	2.39E-14	3.24E-01
122880	1.44E-14	4.04E-01
245760	7.72E-15	5.34E-01

From the result, we can see that the figure6, figure7 and table III, the stability can arrive to 1E-14 (1 day); it is show that BeiDou all-in-view can be used for the nanosecond level of international time transfer or time comparison.

IV. SUMMARY

In this paper, firstly we review of the principle of GNSS All-In-View, and based on the BeiDou B1, B2 pseudo-code measured data among the NTSC and TL, the precise orbit and clock products from MGEX of IGS are used for BeiDou all-in-view time transfer between UTC (NTSC) and UTC (TL). The experimental results show that STDEV of CCD through BeiDou all-in-view is less than 1ns, the STDEV of time transfer between two time keeping Laboratories is better than 1.5ns, and the stability of result can arrive to E-14 (1 day). The above analysis shows that, BeiDou all-in-view time transfer is almost the same level with GPS all-in-view. It is also can promote the application of BeiDou in high precise time transfer and in calculation of UTC/TAI in future.

ACKNOWLEDGMENTS

The authors would like to thank Telecommunication Laboratories, Chunghwa Telecom. Co., Ltd for sharing their BeiDou Rinex data. And also thanks the National Natural Science Foundation of China (Grant No. 11703030) and CAS “Light of West China” program (Grant No. XAB2017A06).

REFERENCES

[1] The State Council Information Office of the People’s Republic of China. “China’s BeiDou Navigation Satellite System” white-book. The State Council Information Office of the People’s Republic of China, 2016.

[2] Jihai Zhang, Haibo Yuan, Wei Guang et al, “The Application of Phase Smoothed Pseudo-range in Beidou Satellite clock evaluation,” Frequency Control Symposium, 2016, pp. 1-4.

[3] Wei Guang, Shaowu Dong, Wenjun Wu et al, “Progress of BeiDou time transfer at NTSC,” Metrologia, 2018, 55 (2): pp.175-187.

[4] P Defraigne, G Petit, “CGGTTS-Version 2E : an extended standard for GNSS Time Transfer,” Metrologia, 2015, 52 (6): pp.1-22.

[5] Shinn Yan Lin, Zhiheng Jiang, “GPS All in View Time Comparison using Multi-receiver Ensemble,” Joint Conference of the European Frequency and Time Forum and IEEE International Frequency Control Symposium ((EFTF/IFC), 2017: pp.362-365.

[6] Oleg Bogdanov; Ali Cepe, “Precise orbit determination for GPS and GLONASS satellites on the basis of IGS data,” Proceedings of 5th

International Conference on Recent Advances in Space Technologies - RAST2011, 2011, pp.915-919.

[7] Fumin Lu, Jin Li, "Precise point positioning study to use different IGS precise ephemeris," 2011 IEEE International Conference on Computer Science and Automation Engineering, 2011, pp.592-595.

[8] G. Petit, E. F. Arias, "Use of IGS products in TAI applications," Journal of Geodesy, 2009, 83 (3-4): pp.327-334.

[9] M. A. Weiss, G. Petit, Z. Jiang, "A Comparison of GPS Common-View Time Transfer to All-in-View," IEEE International Frequency Control Symposium & Exposition, 2005, 36 (1): 5 pp.324-328.

[10] Chunhao Han, Yuanxi Yang, Zhiwu Cai, "BeiDou Navigation Satellite System and its time scales," Metrologia, 2011, 48 (4): pp.213-218.

[11] D.W. Allan and C. Thomas, "Technical Directives for Standardization of GPS Time Receiver Software", Metrologia, 1994, 31, pp. 69-79.

Study on the relation between laser noise and optical frequency transmission

Zhang Xi [1,3*], Yang Fei[1*], Feng Zitong [1,3], Gui YouZhen[2], Cai Haiwen[1*] and Qu ronghui[1]
[1]Key Laboratory of All Solid-State Laser and Applied Techniques, Shanghai Institute of Optics and Fine Mechanics, Chinese Academy of Science, Shanghai 201800, China;
[2]Key Laboratory for Quantum Optics, Shanghai Institute of Optics and Fine Mechanics, Chinese Academy of Science, Shanghai 201800, China;
[3]University of Chinese Academy of Sciences, Beijing 100049
Email: zhangxi@siom.ac.cn fyang@siom.ac.cn hwcai@siom.ac.cn

***Abstract*—By use of a linewidth measurement method based on the 120 degree difference interferometer, we study on the relation between laser noise and optical frequency transmission, such as the evolution of frequency noise and linewidth characteristics before and after transmission. Meanwhile, we chose some different typical commercial narrow-linewidth lasers: EMCORE, RIO, and NKT-X15 as optical carrier to demonstrate the effect of linewidth on transmission stability.**

Keywords—optical frequency transfer; linewidth; noise measurement

I. INTRODUCTION

The length of optical fiber transmission link is limited by the coherence length of the light sources[1], meanwhile the relationship between the laser linewidth and its coherence length in the optical fiber is expressed as:

$$L_c = \frac{c/n}{\Delta v}$$

Therefore it is very important to accurately measure the laser linewidth.

Linewidth can be divided into the intrinsic linewidth and technical linewidth. It is difficult for traditional methods of measuring laser linewidth, such as optical spectrum analyzer (OSA), to meet the demands of narrow linewidth lasers for its resolution is not enough. Therefore, scientists take advantages of the characteristics of low noise and high stability of interference demodulation to develop a series of measurement techniques. First, it is beat note method[2], which needs a high coherent source as a reference. The second is DSH technique based on the Mach-Zehnder interferometer with 2×2 coupler[3] or Michelson interferometer[4], which needs complicated control of quadrature point using active feedback methods and accurate calibration. Another is recirculating delayed self-heterodyne method[5], in which the length of the delay fiber decreases, while the optical power loss increases.

In this paper, we used our proposed linewidth measurement method based on the 120 degree phase difference interference technique[6] to extract the integral time linewidth and the intrinsic linewidth of the narrow-linewidth laser simultaneously in a single-shot measurement by processing the laser frequency noise power spectral density in algorithm. The phase noise characteristics of several typical commercial lasers were tested before and after the transmission. Active noise compensation (ANC) method[7] was also set up to test the transfer stability of the lasers.

II. EXPERIMENTS SETUP

The set up of laser linewidth measurement system is shown in Fig.1. The laser passed through the optical fiber link is injected into the circulator port1, whose port 2 is connected to one of the input port of the 3 × 3 coupler. The two beams reflected by Faraday mirrors and with different delay time interfere with each other. The interference fringes are collected by high-precision acquisition card after they enter the detector, and used to compute the phase/frequency noise of the laser under test by the algorithm in [6].

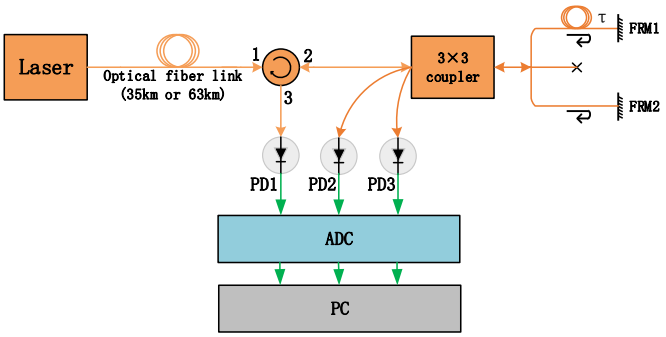

Fig.1. Linewidth measurement system (FRM, Faraday rotator mirror; PD, Photodiode; ADC, Analog to digital converter; PC, Personal computer)

We measured the frequency noise PSD of several typical commercial lasers before passing through the fiber link as shown in Fig.2 and take the NKT-X15 as an example obtaining the frequency noise PSD after the fiber link of 35km and 63km respectively as Fig.3.

We found that the frequency noise characteristics of the laser have changed after its transmitted through the optical fiber link. Plenty of spike noise was superimposed on the low frequency area (within 1kHz), which we considered as vibration noise components coupling in the optical fiber links

such as the vibrating of power supply noise, etc. The white noise level of the laser also increases with the increase of transmission distance. The intrinsic linewidth changes from 28.27 Hz (0 delay) to 78.54 Hz (35 km delay) and 113.1 Hz (63 km delay), proving that the coherence of laser deteriorated

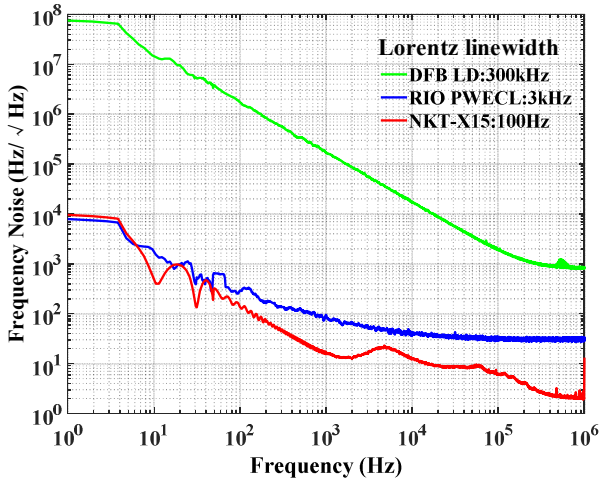

Fig.2. Frequency noise PSD of several typical commercial lasers before going through the fiber link. Green, EMCORE; Blue, RIO PWECL; Red, NKT X15.

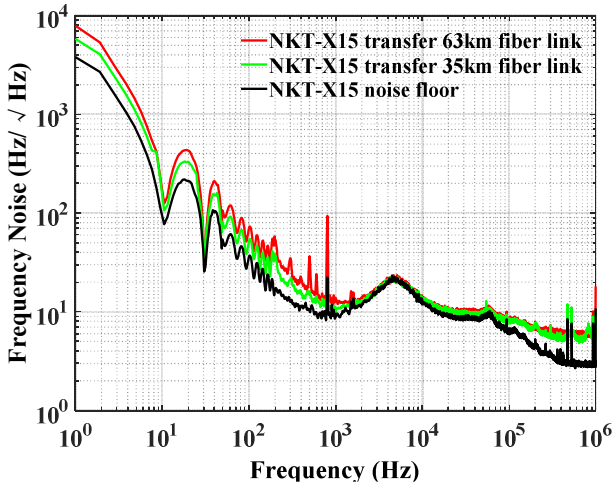

Fig.3. Frequency noise PSD of NKT-X15 after the fiber link. Red, 0km ;Green, 35km; Blue,65km.

during the process of transmission. In our opinion, the reason is the influence of spontaneous emission increases with the decrease of the power during the transmission result in the phase of the photon changing more randomly. So the coherence of light decreases after the transmission.

In order to further study the influence of lasers with different linewidth in the process of optical frequency transmission, we adopt the ANC technique[7] to test the stability of transmission under different conditions. The results are shown in fig4.

The transmission stability of NKT-X15 laser (intrinsic linewidth is 100Hz) and RIO laser (intrinsic linewidth is 3kHz) can reach 2.5×10^{-17}@1s and 5×10^{-19}@10000s after 30km optical fiber link. The transmission stability of EMCORE laser (intrinsic linewidth is 300kHz) will degrade to 1.3×10^{-15}@1s and 2.8×10^{-17}@10000s. The correspondence between the laser linewidth and the coherence length is shown in Tab.1. Because the length of transmission link is within the coherence length of NKT-X15 and RIO, There is no deterioration in the stability performance of the optical frequency transmission, but the transfer stability of EMCORE laser is badly deteriorated for the length of fiber link exceeds its coherence length.

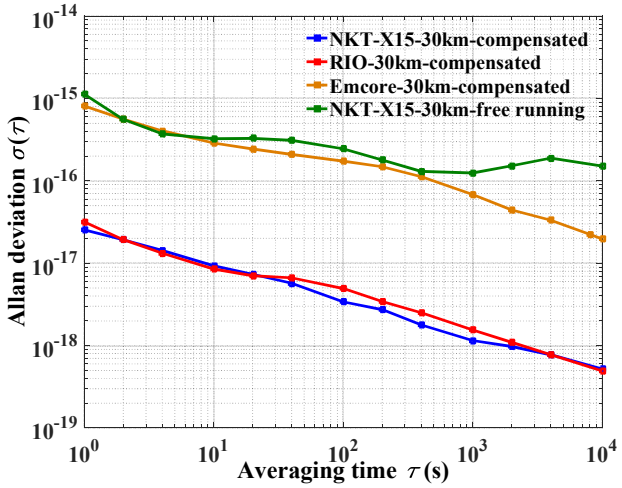

Fig.4. Frequency stability of 30km fiber link. Blue, NKT X15 after 30km with compensation;Green, NKT X15 after 30km without compensation; Red, RIO after 30km with compensation; Brown, EMCORE after 30km with compensation.

TABLE 1. The correspondence between the laser linewidth and the coherence length

(Laser) Linewidth	(NKT-X15) 100 Hz	(RIO) 3 kHz	(EMCORE) 300 kHz
Coherent length	2000 km	66 km	660 m

III. CONCLUSION

We used our proposed laser phase and frequency noise measurement system based on the 120 degree difference interferometer to study the variation trend of the frequency noise characteristics of commercial narrow linewidth lasers, including RIO, NKT-X15 and EMCORE. The results show that the frequency noise characteristics of the laser is degraded after the transmission. Meanwhile, the ANC experiment also reveals that the laser linewidth has little effect on the transmission stability if the link length is less than the coherence length of the laser. Next, we will study more complete relations by use of the Hz and sub-Hz linewidth laser and longer optical fiber.

REFERENCES

[1] Droste S, Ozimek F, Udem T, et al. Optical-frequency transfer over a single-span 1840 km fiber link[J]. Physical review letters, 2013, 111(11): 110801.

[2] H. Lee, M.G. Suh, T. Chen, J. Li, S. A. Diddams, and K. J. Vahala, "Spiral resonators for on-chip laser frequency stabilization," Nat. Commun. 4, 1-6 (2013)..

[3] T. Okoshi, K. Kikuchi, and A. Nakayama, "Novel method for high resolution measurement of laser output spectrum," Electron. Lett. 16(16), 630-631 (1980).

[4] S. Piazzolla, P. Spano, and M. Tamburrini, "Characterization of phase noise in semiconductor lasers," Appl. Phys. Lett. 41(8), 695-696 (1982).

[5] H. Tsuchida, "Laser frequency modulation noise measurement by recirculating delayed self-heterodyne method," Opt. Lett. 36(5), 681-683 (2011).

[6] Xu D, Yang F, Chen D, et al. Laser phase and frequency noise measurement by Michelson interferometer composed of a 3× 3 optical fiber coupler [J]. Optics express, 2015, 23(17): 22386-22393.

[7] Ma L S, Jungner P, Ye J, et al. Delivering the same optical frequency at two places: accurate cancellation of phase noise introduced by an optical fiber or other time-varying path[J]. Optics letters, 1994, 19(21): 1777-1779

Stabilized optical-frequency transfer using optical injection locking amplifier

Feng Zitong [1,3*], Yang Fei[1*], Zhang Xi[1,3], Chen Dijun[1], Cheng Nan[2], Gui YouZhen[2] and Cai Haiwen[1*]
[1]Key Laboratory of All Solid-State Laser and Applied Techniques, Shanghai Institute of Optics and Fine Mechanics, Chinese Academy of Science, Shanghai 201800, China;
[2]Key Laboratory for Quantum Optics, Shanghai Institute of Optics and Fine Mechanics, Chinese Academy of Science, Shanghai 201800, China;
[3]University of Chinese Academy of Sciences, Beijing 100049
Email: ztfeng@siom.ac.cn fyang@siom.ac.cn hwcai@siom.ac.cn

***Abstract*—A simple and novel optical injection locking amplifier (OILA) for optical frequency transfer applications is experimentally demonstrated. A commercial distributed feedback diode laser is injection locked to the resonance of optical frequency signal with the optical path length of hundreds of kilometers, providing more than 50dB gain and ensure that the input carrier frequency fractional stability can reach 10^{-20} at 1000s. The amplifier was tested for the transfer of commercial narrow linewidth laser carrier over bidirectional operated 200 km fiber link with only single gain step. The transferred frequency at the remote end can reach 4.7×10^{-20} at 20000s, which is suitable for the optical frequency distribution and remote comparison among optical atomic clocks.**

Keywords—optical frequency transfer; optical injection locking; regenerative amplifier

I. INTRODUCTION

With the progress in the development of optical atomic clocks, it is necessary to develop a way for its precise transfer. The traditional satellite-based frequency transfer is far from meeting the requirements for its stability is only 10^{-16} level in an entire day. Therefore, optical fiber-based high-precision optical frequency transmission technology has emerged and the distances of transmission up to 1840km has been demonstrated [1]. In order to transmit such a long distance, not only the noise introduced by the optical fiber link should be eliminated, but also the power loss caused by long-distance transmission should be compensated for significantly improving the signal-to-noise ratio of the detected signal.

Erbium-doped fiber amplifiers (EDFA) is the most commonly used method for optical fiber link amplification. However, the bidirectional nature of the frequency transfer system pose a limit on its gain and also deteriorate the stability of transmission due to the fact that point reflections and Rayleigh scattering existing in the fiber link will feedback into the EDFAs to trigger the stimulated effect [2]. Brillouin amplification has the advantage of a small gain bandwidth, so it can hardly be affected by Rayleigh scattering in an optical frequency transmission system, but in order to achieve a narrow gain bandwidth, it is necessary for the pump laser frequency to be locked at the signal laser frequency which increases the complexity of the system [3]. Joonyoung Kim et al. [4] has proposed an optical injection locking-based amplification scheme which provides high gain within a narrow bandwidth and can preserve the frequency stability to 10^{-18} at 1000s.

We propose a novel regenerative amplification scheme based on laser injection locking technology. This amplifier enables the amplification of a very small input signal (a few nano Watt) to more than 10mW in a single gain step with approximately 60MHz gain bandwidth. Moreover, it can preserve frequency stability as good as 10^{-20} at an averaging time of 1000s.

II. EXPERIMENTS SETUP

The amplifier scheme we implement is shown in Fig.1. It is a combination of optical injection locking and optical phase-locked loop technology. The input port inputs a weak optical carrier, which is divided into two parts, part A is used as a reference while the other part (B) is injected into a DFB laser ('Slave laser') through an optical circulator. When the frequency difference of the input signal and 'slave' laser is less than the bandwidth of the injection locking, the "slave" can establish a stable oscillation at the optical frequency of the input carrier, and its free running mode is suppressed. So the output of DFB laser at point C can be seen as the amplified signal. But there will have additional phase noise added in this process. In order to obtain an amplifier with high gain and low noise, the amplified signal is also divided into two parts at point D. One part is beat with the reference A in PD to detect

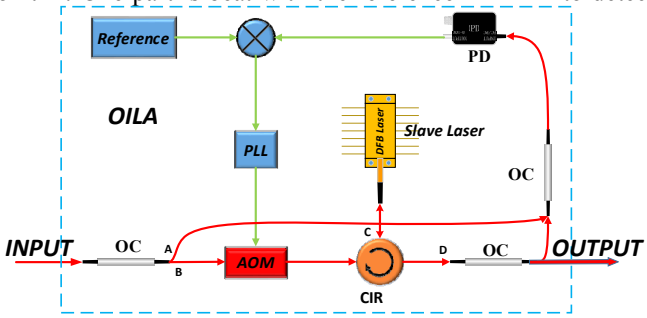

Fig.1. Optical injection locking amplifier (OILA). PD, photodiode; OC, optical coupler; CIR, circulator; AOM, acousto-optic modulator; PLL, Phase Locking Loop.

the phase noise of the optical injection locking process to feedback to an AOM so that the additional phase noise of output signal is canceled, while the other part is the accurate regeneration of the input signal.

There are two advantages when using AOM to execute the injection locking feedback process: First, The bandwidth of the feedback loop is greater than 200kHz by using the AOM to realize the optical phase-locked loop. It is a great progress because the bandwidth of the previous scheme is less than 1kHz [4]; Second, we use the single sideband coherent detection to detect the optical phase rather than the previous Intensity modulation direct detection (IMDD) scheme, so it can provide higher detection sensitivity and improve the amplification gain. Both of these make the amplifier with high gain and more stable.

We test the performance of this amplifier and compare it with a commercial EDFA. As shown in Fig.2, we can see when the injection ratio is -43 dB (the injection ratio means the ratio of output optical power to the injected optical power of "Slave" laser or EDFA), the stability of OILA can reach 5.6×10^{-20} at 1000s. The stability of OILA shows degradation with a decreasing injection ratio. So, the stability of OILA is 8.4×10^{-20} at 1000s when the injection ratio is -55 dB, but it still superiors to commercial EDFA which stability is 5.4×10^{-19} at 1000s at -43 dB injection ratio.

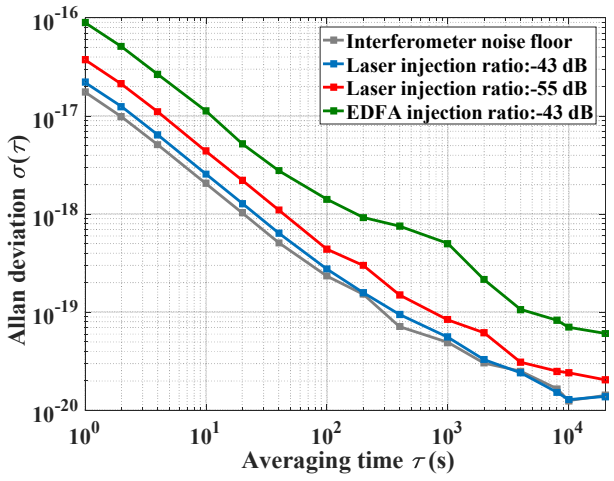

Fig.2. Frequency stability of optical injection locking amplifier (OILA) and commercial EDFA. Gray, interferometer noise floor; Blue, laser injection ratio:-43dB; Red, laser injection ratio:-55dB; Green: EDFA injection ratio: -43dB.

Further, we test the OILA in a system of optical frequency transmission [5]. Experimental system schematic shown in Fig.3. The laser is NKT-X15 commercial narrow linewidth laser. The 100 km fiber link is connected by a 65 km and a 35 km fiber spool. The optical power injected into the 'Slave' laser or EDFA is approximately -33 dBm. The OILA is placed at the far end of the link and the power of the signal can be amplified to 10dBm. Since the OILA includes an AOM for phase-locking, it can also function as a frequency shifter.

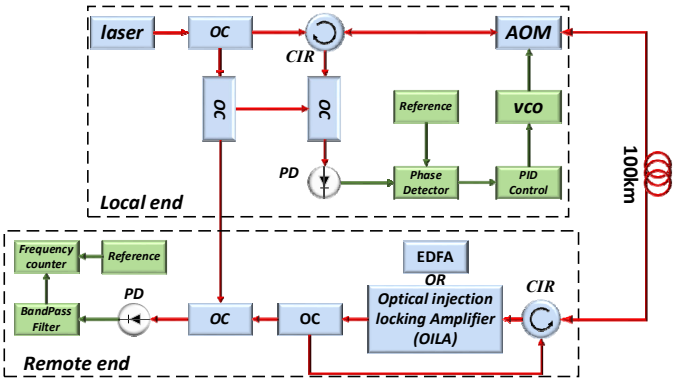

Fig.3. Schematic diagram of optical frequency transfer with100km fiber link by using optical injection locking amplifier (OILA). Laser, NKT-X15 narrow-linewidth fiber laser; PD, photodiode; VCO, voltage controlled oscillator; AOM, acousto-optic modulator; OC, optical coupler.

Therefore, the remote end does not need to place an additional AOM for frequency-shifting. Experimental results shown in Fig. 4, the stability of transfer by using OILA is 2.6×10^{-16} at 1s and improve to 4.7×10^{-20} at 20000s which is obviously better than the stability of using EDFA for transmission. So we can conclude that the OILA can be used for the most accurate optical frequency transfer.

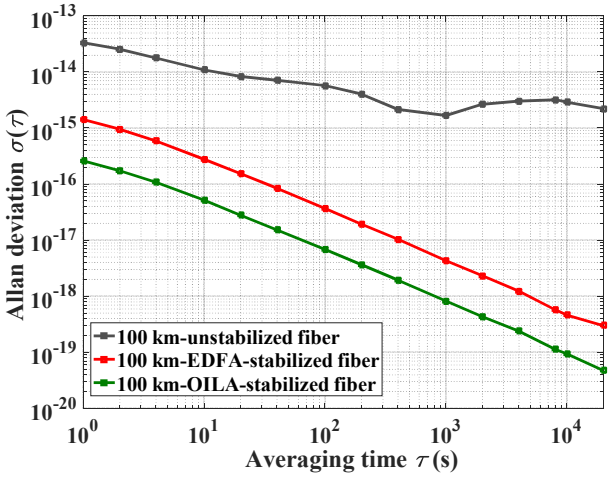

Fig.4. Frequency stability of light after 100km fiber link with optical injection locking amplifier (OILA) and EDFA. Green, 100km stabilized fiber with OILA; Red, 100km stabilized fiber with EDFA; Gray, 100km unstabilized fiber.

III. CONCLUSION

We propose an optical injection-locking amplifier (OILA) that can be used for optical frequency transmission which provides high amplification gain of greater than 50 dB and still maintains the stability of input carrier to 5.6×10^{-20} at 1000s. Further, experiments on the optical frequency transmission of the 100km optical fiber link in the laboratory have tested the OILA and obtained the transfer stability of 2.6×10^{-16} at 1s and 4.7×10^{-20} at 20000s. In the next step, we will transfer a cavity-

stable laser carrier on urban fiber link to extend the length of the transfer and further optimize the performance of OILA.

REFERENCES

[1] Droste S, Ozimek F, Udem T, et al. Optical-frequency transfer over a single-span 1840 km fiber link[J]. Physical review letters, 2013, 111(11): 110801.

[2] Grosche G, Terra O, Predehl K, et al. Optical frequency transfer via 146 km fiber link with 10− 19 relative accuracy[J]. Optics letters, 2009, 34(15): 2270-2272.

[3] Terra O, Grosche G, Schnatz H. Brillouin amplification in phase coherent transfer of optical frequencies over 480 km fiber[J]. Optics express, 2010, 18(15): 16102-16111.

[4] Kim J, Schnatz H, Wu D S, et al. Optical injection locking-based amplification in phase-coherent transfer of optical frequencies[J]. Optics letters, 2015, 40(18): 4198-4201.

[5] Ma L S, Jungner P, Ye J, et al. Delivering the same optical frequency at two places: accurate cancellation of phase noise introduced by an optical fiber or other time-varying path[J]. Optics letters, 1994, 19(21): 1777-1779.

Analysis of GNSS Time Scales

Petr Bogdanov, Andrei Druzhin, Tatiana Primakina, Arkadii Tiuliakov
Russian Institute of Radionavigation and Time
Saint-Petersburg, Russia
Bogdanov_pp@rirt.ru

***Abstract*— In all GNSS satellite time scales are referenced to GNSS Time and GNSS Time is synchronized to Reference Time which is steered to UTC. GNSS Time accuracy parameters influence the accuracy of positioning and timing as well as the accuracy of calculating and predicting GNSS-GNSS Time Offsets for GNSS interoperability. GNSS time scales generation and maintenance have been analyzed and the results of their accuracy estimation are provided on the basis of available information.**

Keywords—Global Navigation Satellite System; time scale; time offset; correction; accuracy

I. INTRODUCTION

GNSS time scales are either mathematical or physical time scales that are generated on the basis of either ground stations clocks or ground stations and satellite clocks. GNSS reference time scales are provided by Timing Laboratories and maintained within specified limits relative to UTC.

GNSS time scales are generated at GNSS Control Centers or Master Stations and, as a result, their parameters can't be directly estimated "from outside". Therefore, GNSS time scales can be analyzed only indirectly by using available information: broadcast corrections to convert from GNSS Time to Reference Time or the values of GNSS Time-Reference Time offsets calculated by measurement processing at the reference time generating facility.

In this paper GNSS time scales are analyzed and their accuracy parameters are estimated independently by means of both approaches on the basis of available information.

II. ANALYSIS OF GNSS TIME GENERATION

GNSS Time accuracy parameters are specified in GNSS Interface Control Documents, Interface Specifications and GNSS Time Scale Templates. Their generation and maintenance are described in papers introduced at international conferences and meetings.

A. GPS Time Generation and Maintenance

GPS Time is a composite time scale based on clock ensemble of monitor station frequency standards and satellite clocks [1]. GPS Time is computed as part of the overall clock and orbit estimation process. GPS operates 6 monitor stations distributed around the world in addition to using 6 monitoring stations operated by NGA. Each reference station receiver is referenced to a Cesium atomic clock. At two reference stations Hydrogen maser clocks are used.

GPS Time is established by the GPS Control Segment and is referenced to UTC(USNO) generated by the U.S. Naval Observatory. USNO monitors the offset of GPS Time from UTC(USNO) and reports these data to GPS Operations for use in timescale steering and UTC broadcast corrections.

GPS Time-UTC(USNO) offset shall be within 1 microsecond and accuracy of the corrections to convert from system to Reference Time (2 parameters of the linear model) is 40 ns (95% probability). Satellites are nominally updated at least once per day.

GPS Time is not corrected by ±1 s with UTC leap second corrections. As a result, since January 2017 GPS Time has been 18 seconds ahead of UTC.

B. GLONASS Time Generation and Maintenance

GLONASS Time is generated on the basis of GLONASS Central Synchronizers (CS) that are located at two sites of GLONASS Control Segment and include an ensemble of Hydrogen frequency standards with daily frequency instability below $2 \cdot 10^{-15}$ [2]. One of them is the Main CS, the other is Reserved CS. GLONASS Time is formed on the basis of the Main Central Synchronizer's time scale. The time scale of Reserved CS is referenced to the Main CS time scale by "all-in-view" method with using satellite signals.

GLONASS Reference Time is national time scale of Russia UTC(SU) that is generated by State Time/Frequency Reference (STFR).

GLONASS time is maintained within 1 millisecond of UTC(SU). The specified accuracy of the corrections to convert from system to Reference Time is 1 microsecond. The corrections are computed and uploaded once per day.

GLONASS Time is corrected by ±1 s simultaneously with UTC corrections and, as a result, there is no whole second time offset between GLONASS Time and UTC(SU). However, there is a three-hour constant offset between GLONASS Time and UTC due to GLONASS Ground Control Segment operational principles.

C. Galileo Time Generation and Maintenance

Galileo Time (GST) is based on Master Clock at the Precise Time Facility (PTF) [3]. The two redundant Galileo PTF are located in the Galileo Control Centers in Fucino (Italy) and Oberpfaffenhofen (Germany). Each PTF is equipped with Hydrogen masers (used as Master Clocks) and Cesium clocks. These clocks, and optionally the other ground station and satellite clocks, are ensembled and the PTF Master Clocks are

steered to this ensemble to produce the physical realization of the Galileo Time.

Galileo Reference Time is UTC prediction as provided by the Galileo Time Service Provider based on contributions from European UTC laboratories.

The offset between Galileo Time and UTC is monitored by the Galileo Time Service Provider which computes a GST-UTC offset and GST-UTC steering parameters.

The offset between Galileo Time and UTC (modulo 1 s) shall be less than 50 ns (95%). The specified accuracy of the corrections to convert from system to Reference Time (2 parameters) is 28 ns (95%). The Galileo Time-UTC offset parameters are nominally updated daily.

Galileo Time is not corrected by ±1 s with UTC leap second corrections and, as a result, since January 2017 Galileo Time has been 18 seconds ahead of UTC.

D. Beidou Time Generation and Maintenance

Beidou Time (BDT) is a composite time scale that is generated and maintained by the Master Control Station [4]. Beidou Time is calculated based on the Hydrogen clocks at Master Control Station and monitor stations. The master clock of BDT is high performance Hydrogen which is steered to BDT and provides time signals for the other subsystems of Beidou. The specified stability of BDT is about $2 \cdot 10^{-14}$ at 1 day interval and $1 \cdot 10^{-14}$ at 7 day interval.

Beidou Time is linked to UTC through UTC(NTSC) provided by China National Time Service Center. Maximum offset of BDT from Reference Time is 100 ns (modulo 1 s). The specified accuracy of the corrections to convert from system to Reference Time (2 parameters) is 5 ns (95%). The offset parameters which are broadcast by navigation message are updated once an hour.

From January 2006 Beidou Time is not corrected by ±1 s with UTC leap second corrections and, as a result, since January 2017 Beidou Time has been 4 seconds ahead of UTC.

E. QZSS Time Generation and Maintenance

QZSS Time is computed as part of the overall clock and orbit estimation process [5]. QZSS Time is generated based on Master Clock which is the receiver clock located at Koganei. The QZSS Master Control Station (MCS) is located in Tsukuba Space Center, Ibaragi, Japan, and QZSS operates 9 monitor stations regionally distributed around Asia-Oceania area. The Koganei and Hawaii monitor stations use Hydrogen maser clocks, and the other monitor station receivers are referenced to a Cesium clocks.

QZSS Time is steered to the reference time scale UTC(NICT) generated by National Institute of Information and Communications Technology. Actually the source of QZSS Time is the UTC(NICT) physical clock with some amount of the offset due to the line length. The transfer from the reference time scale to QZSS Time is realized by physical connection. NICT monitors the offset data between QZSS Time and UTC(NICT) and transfers these data to MCS. MCS calculates the UTC parameters based on the data from NICT and the time offset of the Koganei receiver clock from GPS Time.

QZSS Time is maintained within 1 microsecond of UTC(NICT). The accuracy of the corrections to convert from system to Reference Time (2 parameters) is not specified. Satellites are nominally updated at least once per day.

QZSS Time is not corrected by ±1 s with UTC leap second corrections and, as a result, since January 2017 QZSS Time has been 18 seconds ahead of UTC.

F. Summary

GNSS time scales are either mathematical or physical time scales generated at special GNSS Control Centers or Master Stations and, as a result, their parameters can't be directly estimated "from outside".

GPS Time, Galileo Time, Beidou Time and QZSS Time are continuous time scales and are ahead of UTC with an integer number of leap seconds. GLONASS Time is corrected by ±1 s simultaneously with UTC corrections and, as a result, there is no whole second time offset between GLONASS Time and UTC.

III. ESTIMATES OF GNSS TIME ACCURACY PARAMETERS

According to the analysis information provided above the following key performance parameters can be used to analyze GNSS Time:

- the offset from the Reference Time;

- the accuracy of GNSS Time–Reference Time corrections;

- stability of GNSS Time.

The values of these parameters specified by GNSS Providers are introduced in Table 1.

As it was mentioned above, GNSS time scales can be estimated "from outside" only indirectly by using either broadcast corrections to convert from GNSS Time to Reference Time or the values of GNSS Time-Reference Time offsets calculated by measurements at the reference time generating facility.

TABLE I. SPECIFIED GNSS PERFORMANCE PARAMETERS

Parameter	Navigation System				
	GPS	***GLN***	***Galileo***	***Beidou***	***QZSS***
GNSS Time-Reference Time offset (mod 1 s)	1 μs	1 ms	50 ns (95%)	100 ns	1 μs
The accuracy of GNSS Time-Reference Time corrections	40 ns (95%)	1 μs	28 ns (95%)	5 ns (95%)	n/a
Stability of GNSS Time	-	-	-	$2 \cdot 10^{-14}$ (1 day) $1 \cdot 10^{-14}$ (7 days)	-

In the first case the accuracy of the estimates depends on the accuracy of broadcast corrections to convert from GNSS Time to Reference Time. In the second case it depends on the error of the measured offsets of satellite clocks from the Reference Time and the accuracy of broadcast corrections to convert from satellite time to GNSS Time.

As the specified accuracy of broadcast corrections is limited the trustworthy results can be obtained only for the values of GNSS Time offsets of Reference Time.

IV. The Obtained Offsets of GNSS Time from Reference Time

GPS Time, GLONASS Time, Galileo Time, Beidou Time and QZSS Time offsets of their reference time scales have been obtained based on broadcast corrections for the period from January 2017 to January 2018. The results are presented in Fig. 1.

GNSS Time offsets of UTC based on broadcast corrections and the values of UTC-UTC(k) offsets provided by BIPM Time Department are presented in Fig. 2.

GPS Time-UTC(USNO) and GLONASS Time-UTC(SU) offsets based on broadcast corrections and measurement processing at USNO and STFR are presented in Fig. 3 and Fig. 4 respectively.

The analysis of the GNSS Time–Reference Time offsets shows the following:

- GPS Time-UTC(USNO) offset is maintained within ±10 ns;

- GLONASS Time-UTC(SU) offset is maintained within ±20 ns except for the period of 8-23 December 2017, and there is a systematic error component of broadcast GLONASS Time of about 20 ns;

- Galileo Time-UTC offset is maintained within ±10 ns;

- Beidou Time-UTC(NTSC) offset is maintained within ±20 ns;

- QZSS Time-UTC(NICT) offset is maintained within ±20 ns.

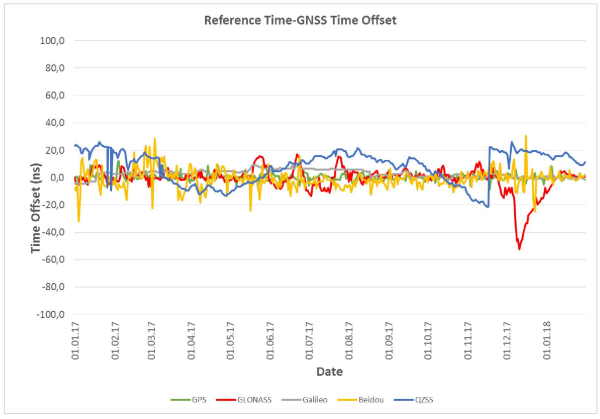

Fig. 1. GNSS Time-Reference Time offsets based on broadcast corrections

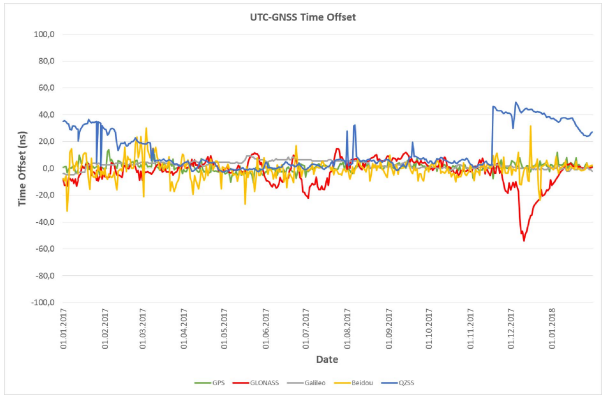

Fig. 2. GNSS Time-UTC offsets based on broadcast corrections and BIPM data

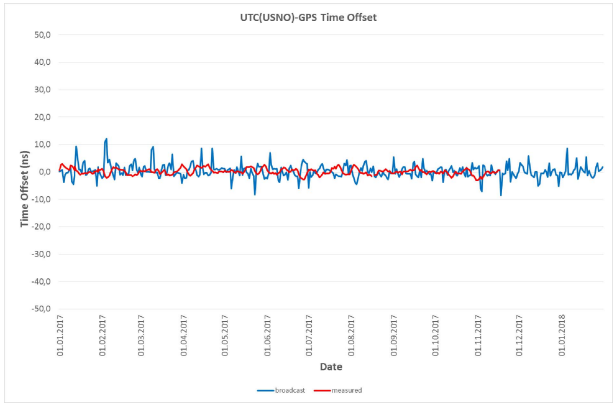

Fig. 3. GPS Time-UTC(USNO) offset based on broadcast corrections and measurement processing at USNO

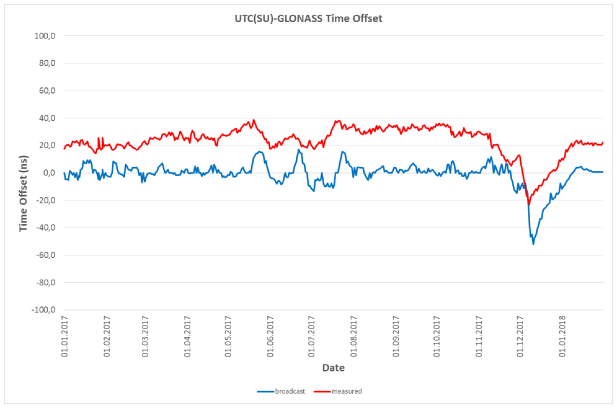

Fig. 4. GLONASS Time-UTC(SU) offset based on broadcast corrections and measurement processing at STFR

V. Conclusion

GNSS time scales are either mathematical or physical time scales generated at GNSS Control Centers or Master Stations. As a result, they can be analyzed “from outside” only indirectly by using either broadcast corrections to convert from GNSS Time to Reference Time or the values of GNSS Time–Reference Time offsets calculated by measurement processing at the reference time generating facility.

The analysis of the GNSS Time–Reference Time offsets shows the following:

- GPS Time-UTC(USNO) offset is within ±10 ns;

- GLONASS Time-UTC(SU) offset is maintained within ±20 ns except for the period of 8-23 December 2017, and there is a systematic error component of broadcast GLONASS Time of about 20 ns;

- Galileo Time-UTC offset is within ±10 ns;

- Beidou Time-UTC(NTSC) offset is within ±20 ns;

- QZSS Time-UTC(NICT) offset is maintained within ±20 ns.

REFERENCES

[1] "GNSS Timescale Description. GPS. Definition of System." www.unoosa/pdf/icg/2012/Timescale-GPS.pdf.

[2] GLONASS Interface Control Document. Issue 5.1, 2008.

[3] "GNSS Timescale Description. Galileo. Definition of System." www.unoosa/pdf/icg/2016/gst2016.pdf.

[4] "Beidou Timescale Description. Definition of time system." www.unoosa/pdf/icg/2016/ Beidou-Timescale2016.pdf.

[5] "GNSS Timescale Description. QZSS. Definition of System." www.unoosa/pdf/icg/2016/ QZSS-Timescale2016.pdf.

Optimal traceability to the SI second through TAI

Gérard Petit, and Gianna Panfilo
Bureau International des Poids et Mesures
92312 Sèvres, France
gpetit@bipm.org

***Abstract*— The frequency of a secondary frequency standard needs to be determined in the SI, by comparison to that of the Cs hyperfine transition. When no direct comparison to such a primary frequency standard is possible, the SI second can also be accessed through TAI. Based on the experience of several recent experiments, we propose an approach providing optimal access to the SI second through TAI and show that it can be used for any laboratory even those not participating to UTC. We estimate the presently achievable uncertainty and show how it could be improved under realistic considerations in the coming years.**

Keywords*— *Frequency standards, SI second, TAI, TT(BIPM), uncertainty

I. INTRODUCTION

The list of secondary representations of the second (SRS) is maintained by the Frequency Standards Working Group (WGFS), a joint body of the Consultative Committees for Length (CCL) and for Time and Frequency (CCTF). In order for a clock to be recognized as a secondary frequency standard (SFS), the frequency of its transition must be documented with an uncertainty budget of all systematic effects not much larger than that of the primary frequency standard (PFS), and it must be referenced to the frequency of the Cs transition. As of 2017, some 59 such measurements have been carried out in 16 different laboratories for 14 transitions, mostly in the optical domain, see an account of the work of WGFS [1]. The latest release of the list of SRS values and uncertainties has been approved by the CCTF in 2017.

In this paper we study how a clock transition frequency is compared to the Cs transition when no local PFS is available for comparison and how the corresponding uncertainty can be estimated. We envision the main techniques corresponding to typical situations described in the literature and estimate the typical uncertainty that can be achieved for each. We propose an optimal technique to perform this comparison and estimate the achievable uncertainty in applying it.

II. COMPARING A SFS TO THE SI SECOND

In subsection A we briefly mention the case of the direct comparison to a PFS. In the next subsections we assume that the SFS is compared to UTC(k) and we estimate how to access the SI second with the BIPM timescales in subsection B and with the proposed method using all PFSs reported for TAI in subsection C. In both cases, the user should compare its SFS to UTC(k), where k represents a laboratory participating to UTC, over an interval between two standard UTC dates, i.e. MJD ending with 4 or 9. In the whole paper, we note the relative rate of two timescales as y(scale1 – scale2).

A. Direct comparison to a primary standard

A common situation is for the laboratory developing a SFS to already have an operating PFS. In this case it is simplest to directly compare locally the SFS to the simultaneously operating PFS. The main advantage is that the uncertainty in the frequency comparison is minimal, however there are some drawbacks: on the practical side, it is necessary to succeed in having the two standards simultaneously operating; in addition the comparison is always to one and the same PFS (or a small number of PFS) with some risk of undetected systematics.

B. Comparison to TAI or TT(BIPM)

When a laboratory has no easy access to an operational PFS, it is always possible to access the SI second through the BIPM timescales. There are two options:

1) Each year (e.g. year 20yy), the BIPM computes a new realization of TT as the scale TT(BIPMyy) which is provided through its difference to TAI every 10 days at ftp://tai.bipm.org/TFG/TT(BIPM). Unlike TAI which is computed in real time each month and never corrected, each new version TT(BIPMyy) is a new computation and its scale unit aims at exactly realizing the SI second. The access to the SI second is then

$$y(\text{SI–UTC}(k)) = y(\text{TT(BIPM)-TAI}) + y(\text{UTC-UTC}(k)) \quad (1)$$

2) With each monthly Circular T, the duration of the scale interval of TAI, as realized over that month, is estimated with respect to that of TT (in practice the SI second on the geoid). The fractional deviation of the scale unit, noted d_{TAI}, is provided with a standard uncertainty valid for the given month. The access to the SI second is then

$$y(\text{SI - UTC}(k)) = d_{TAI} + y(\text{TAI - UTC}(k)) \quad (2)$$

In option 1, the user obtains a direct link to the SI second through TT(BIPM) but there is no specified uncertainty on the result. In option 2, the uncertainty in d_{TAI} is specified in the

Circular T but the user needs to account for the difference between the interval of SFS operation and the monthly interval for which d_{TAI} is valid. It means that the uncertainty originating from the two terms in (2) must be complemented by an uncertainty for extrapolating TAI between the interval of SFS operation and the month of Circular T.

Such access to the SI second has been used for many SFS evaluations, using mostly option B2. This is e.g. the case for the Sr lattice at NICT [2] and for the $^{171}Yb^{+}$ E3 optical clock transition at NPL [3]. We'll come back on these two cases in the next subsection.

C. An optimal comparison to the SI second

The access to the SI second using d_{TAI} envisioned in the previous section may be expanded to provide an optimal comparison to the SI second. Instead of using the published monthly values of d_{TAI} it is possible for the BIPM to compute d values for any specific interval ending at UTC standard dates. This computation is based on the same algorithm [4] and the same PFS and SFS data used for the standard monthly computations. Given the present (2017-2018) availability of about 4-5 fountain evaluations per month, and the reported uncertainties of these evaluations, the standard uncertainty of the d value varies with the length of the estimation interval, from about 7-8x10^{-16} for 5 days to about 2x10^{-16} for 30 days, see also Table I for more values.

There are several advantages to this method: Compared to method B2, the accuracy is improved because there is no need to account for the difference in TAI frequency over the interval of SFS operation with respect to the value over the whole month, which introduces extrapolation noise (also sometimes referred to as dead time noise). Compared to method A, the final uncertainty will improve with the number of repeated SFS evaluations because most components of the uncertainty of d are essentially statistical and can be reduced by averaging. We note that, in methods B and C, one limiting factor is the uncertainty in frequency transfer to UTC, presently estimated at ~9x10^{-16} for 5 days to ~1.9x10^{-16} for 30 days (see also Table I for more values). In this respect, method C allows each laboratory to optimize its modus operandi, finding the best compromise between the possible duration of the SFS operation, the ability of the local flywheel to expand the report interval, the frequency transfer performance over the report interval and the number of different intervals that are used to estimate the transition frequency.

The case of the Sr lattice at NICT is interesting in this respect. Initially three 5-day periods were used with method B2 to estimate a total uncertainty of the transition frequency of 11x10^{-16} (15.5x10^{-16} for each 5-day period) [2]. The same data using method C yielded a total uncertainty of 9.5x10^{-16} (12.7x10^{-16} for each 5-day period) [5]. Finally, three 10-day periods using method C yielded a total uncertainty of 4.3x10^{-16} (7.3x10^{-16} for each 10-day period) [6]. Similarly, at the NPL, the frequency of the $^{171}Yb^{+}$ E3 optical clock transition was initially determined using method B2 with an uncertainty of 3.98x10^{-16} [3]. When using method C, the uncertainty was reduced to 3.41x10^{-16} [7].

III. Optimal Access to the SI Second from any Laboratory

From (2) it seems that laboratories participating to UTC, named UTC(k), have a privileged access to the SI second through TAI. Indeed, if the SFS is operated in Lab, which is not a UTC(k), equation (2) would be complemented to read

$$y(\text{SI - Lab}) = d_{TAI} + y(\text{TAI - UTC}(k)) + y(\text{UTC}(k)\text{-Lab}) \quad (3)$$

so that an additional uncertainty would appear in the access to the SI second.

However, in the computation of UTC, any laboratory can be considered as a virtual "additional laboratory" that could be included in Circular T but would not change the existing values and uncertainties of [UTC-UTC(k)] computed following [8]. The conditions to achieve this are that the laboratory can be linked to UTC without bringing correlation to the existing time links that have been used in the true UTC computation, i.e. it brings no new clock that would have a weight in the ensemble timescale, and it uses a time transfer technique which is independent of other time links of UTC. This is illustrated in Figure (1).

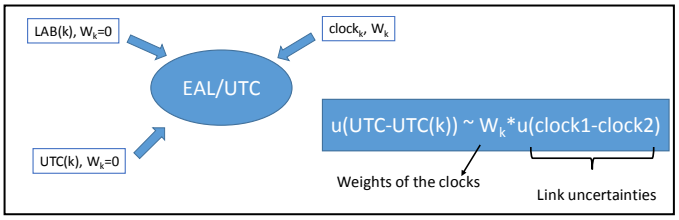

Fig. 1. Uuncertainty evaluation for laboratories participating to UTC. Adding any laboratory with no weight on the left side does not change the terms of the uncertainty evaluation.

Such conditions are realized by linking with a station-based GNSS technique such as GPS Precise point positioning (PPP). This provides y(IGRT – Lab) where IGRT is the time scale to which the satellite clocks provided by the International GNSS Service, used in the PPP solution, are referred to. In fact, the access to UTC is then

$$y(\text{UTC - Lab}) = y(\text{UTC - IGRT}) + y(\text{IGRT - Lab}) \quad (4).$$

Because y(UTC - IGRT) is not published by the BIPM at this moment, the access must be provided by a comparison to another UTC(k) also linked to UTC by GPS PPP and using for the PPP analysis the same parameters as are used in the BIPM analysis. This is equivalent to using

$$y(\text{UTC-IGRT}) = y(\text{UTC-UTC}(k)) + y(\text{UTC}(k)\text{-IGRT}) \quad (5)$$

where the relevant links (UTC(k)-IGRT) can be provided by the BIPM.

Therefore, the uncertainty in y(UTC-Lab) can be estimated in the same way as the uncertainty of y(UTC-UTC(k)) for any UTC(k) which has no weighted clock and is linked with the same GPS PPP technique. Such a link uncertainty is given in Table I, which also provides the total uncertainty that can be achieved in the access to the SI second for SFS located in such laboratories.

TABLE I. TYPICAL UNCERTAINTY VALUES FOR THE ACCESS TO THE SI SECOND FROM A LABORATORY FOR VARIOUS DURATIONS OF THE INTERVAL USED TO COMPUTE THE LINK TO TAI

Dur	y(Lab-SFS)	y(UTC-Lab)	y(SI-UTC)	Total
10 d	< 1 x $\mathbf{10}^{-16}$	~5.1 x $\mathbf{10}^{-16}$	~5 x $\mathbf{10}^{-16}$	~7.1 x $\mathbf{10}^{-16}$
20 d	< 1 x $\mathbf{10}^{-16}$	~2.7 x $\mathbf{10}^{-16}$	~3.5 x $\mathbf{10}^{-16}$	~4.5 x $\mathbf{10}^{-16}$
30 d	< 1 x $\mathbf{10}^{-16}$	~1.9 x $\mathbf{10}^{-16}$	~2 x $\mathbf{10}^{-16}$	~2.9 x $\mathbf{10}^{-16}$

IV. DISCUSSION AND FUTURE IMPROVEMENTS

As presented above, two factors limit the access to the SI second through TAI at the low 10^{-16} level. One is the uncertainty of frequency transfer, the other one is the number and uncertainty budget of the Cs fountains contributing to TAI on a given month. Here we consider how realistic improvements could push the limit brought by these two factors.

Frequency transfer techniques presently used in TAI, GPS PPP and Two way satellite time and frequency transfer (TWSTFT), have estimated uncertainties of order $2x10^{-16}$ at one-month averaging. This limits not only the quality of the link from an external laboratory to UTC (by GPS PPP through IGRT) but also the uncertainty associated to the frequency y(UTC-UTC(k)) for any participating laboratory k. Indeed, the uncertainty of time links is the dominant source in the uncertainties in [UTC-UTC(k)] published in Circular T, with the weights of the clocks participating in the calculation [8].

It is however reasonable to assume that progresses in the existing techniques can bring the frequency transfer uncertainty well below the 10^{-16} level: Fibre links are one obvious candidate even though spatial extension and operational problems are still limiting factors. For the satellite links, the PPP technique with Integer ambiguity resolution (IPPP) [9] is expected to reach $2x10^{-17}$ at 20-30 days [10], and advanced TWSTFT techniques could provide similar or possibly better performance. Such advanced techniques are Software defined radio TWSTFT [11] and TW carrier phase [12, 13].

The best reported uncertainty budgets for Cs fountains already claim values at or very close to $1x10^{-16}$ for the statistical part and/or the systematic part [14]. For the devices actually operating and regularly reporting data to TAI, the uncertainty values may be slightly larger though still in the low 10^{-16} level, so that the monthly contribution of 4-5 such fountains contributes to the uncertainty in y(SI-UTC) as specified in Table I. It is nevertheless conceivable that up to ten Cs fountains can be operated in any given month, with uncertainties at $1x10^{-16}$ for the statistical part and/or the systematic part. In such a case the uncertainty in y(SI-UTC) would be reduced to well below $1x10^{-16}$ for a 30-day interval.

If such progresses in frequency transfer and in the operation of PFS are realized, the uncertainty budget of the access to the SI second could be reduced to the levels shown in Table II.

TABLE II. FORESEEABLE UNCERTAINTY VALUES FOR THE ACCESS TO THE SI SECOND FROM A LABORATORY FOR VARIOUS DURATIONS OF THE INTERVAL USED TO COMPUTE THE LINK TO TAI

Dur	y(Lab-SFS)	y(UTC-Lab)	y(SI-UTC)	Total
10 d	< 1 x $\mathbf{10}^{-16}$	~1 x $\mathbf{10}^{-16}$	~3.3 x $\mathbf{10}^{-16}$	~3.4 x $\mathbf{10}^{-16}$
20 d	< 1 x $\mathbf{10}^{-16}$	~0.5 x $\mathbf{10}^{-16}$	~1.9 x $\mathbf{10}^{-16}$	~2.0 x $\mathbf{10}^{-16}$
30 d	< 1 x $\mathbf{10}^{-16}$	~0.3 x $\mathbf{10}^{-16}$	~0.5 x $\mathbf{10}^{-16}$	~0.6 x $\mathbf{10}^{-16}$

We conclude that it is possible to access the SI second with an uncertainty in the low 10^{-16} through TAI without direct access to a Cs fountain. This uncertainty can be provided to any laboratory whether it is taking part to the UTC ensemble or not. In this process some interaction with the BIPM Time department may be necessary to obtain the specific processing results needed. Taking advantage of these possibilities will provide a better uncertainty in the evaluation of secondary frequency standards and a more robust list of secondary representations of the second.

REFERENCES

[1] Riehle F., Gill P., Arias F., Robertsson L., The CIPM list of recommended frequency standard values: guidelines and procedures, Metrologia, 55, 188, 2018.

[2] Hachisu H., Ido T, Jpn. J. Appl. Phys, 54, 112401, 2015

[3] Baynham C.F.A., Godun R.M. et al., J. Modern Optics, 65, 585-591, 2018.

[4] Azoubib, M. Graveaud and B. Guinot, "Estimation of the scale unit duration of time scales", Metrologia 13 pp 87-93, 1977.

[5] Hachisu H., Petit G., Ido T., Absolute frequency measurement with uncertainty below $1x10^{-15}$ using International Atomic Time, Applied Physics B, 123: 34, 2017; DOI 10.1007/s00340-016-6603-9.

[6] Hachisu H., Petit G., Nakagawa F., Hanado Y., Ido T, SI-traceable measurement of an optical frequency at the low 10^{-16} level without a local primary standard, Opt. Express **25**, 8511-8523, 2017.

[7] Godun R.M. et al., Absolute frequency measurement of the $^{171}Yb^{+}$ E3 optical clock transition using international atomic time, Proceedings EFTF meeting, 2018.

[8] Lewandowski W., Matsakis D., Panfilo G., Tavella P.. The evaluation of uncertainties in [UTC-UTC(k)]. Metrologia 43, 2006, No 3, 278-286.

[9] Petit G., Kanj A., Loyer S., Delporte J., Mercier F., Perosanz F., "$1x10^{-16}$ frequency transfer by GPS PPP with integer ambiguity resolution", Metrologia 52, 301-309, 2015.

[10] Petit G., Leute J., Loyer S., Perosanz F., Sub 10^{-16} frequency transfer with IPPP: Recent results, Proc. 2017 Joint EFTF/IFCS, 784-787, 2017.

[11] Huang Y.J., Fujieda M., Takiguchi H., Tseng W.H., Tsao H.W., Stability improvement of an operational two-way satellite time and frequency transfer system, Metrologia, 53-2,881–890, 2016.

[12] Fujieda M., D Piester, T Gotoh, J Becker, M Aida, A Bauch, "Carrier-phase two-way satellite frequency transfer over a very long baseline", Metrologia 51, 253-262, 2014.

[13] Fujieda M. et al., Advanced satellite-based frequency transfer at the 10^{-16} level, IEEE Trans. UFFC, 2018; DOI: 10.1109/TUFFC.2018.2821159.

[14] BIPM report on time activities, yearly, Table 6, available at https://www.bipm.org/en/bipm/tai/annual-report.html.

Improvements on the UTC(IT) timescale at INRIM

Marco Sellone, Roberto Costa, Alberto Mura, Giancarlo Cerretto and Filippo Levi
Time and Frequency Laboratory
INRIM – Istituto Nazionale di Ricerca Metrologica
Torino, Italy
m.sellone@inrim.it

Marco Siccardi
SKK Electronics
Cuneo, Italy

***Abstract*—A new measurement system (in the following indicated as *switch*) had been introduced at INRIM Time Laboratory (TL), to grant to UTC(IT) time scale better characteristics in terms of robustness and reliability, especially when a change from primary and backup time scale realizations, is required. A complete description of the system implementing such a switching process is described in the present paper, together with the analysis of the results and the performed functional tests.**

Keywords— time; timescale generation; UTC(IT); robustness; reliability

I. INTRODUCTION

INRIM realization of UTC, namely UTC(IT), is currently generated by means of an Active Hydrogen Maser (AHM) conceived as a Master Clock (MC), supported by an Atomic Caesium Fountain, as well as by an ensemble of 10 other commercial clocks (Ceasium Beam Clocks and H-Masers). The MC signal drives a microstepper device - hereafter indicated as Auxiliary Output Generator (AOG) - used to correct its frequency offset/drift, keeping the so generated UTC(IT) time scale, aligned as much as possible to UTC. This UTC(IT) generation system, is then duplicated, in order to have a backup time scale ready to be used either in case of failures or maintenance activities. The primary and the backup time scales (here indicated as UTC(IT)_1 and UTC(IT)_2), are kept aligned at the highest level of accuracy, in order to prevent possible time jumps when the switch between the time scales is required. In particular, the commutation will be possible thorough a newly designed automatic *switch* that will be introduced in the UTC(IT) generation chain as soon as its characterization will be concluded. This new device, is an automatic *switch* between the 5 MHz signals generated by two independent AOGs, generating 1PPS, 10 MHz and 100 MHz output signals, available to the TL users. When the new *switch* will be permanently installed at TL, the two inputs will come directly from UTC(IT)_1 and UTC(IT)_2, allowing a simple and transparent commutation process (if the two scales are properly aligned), making UTC(IT) generation more robust and reliable.

II. THE SWITCH

The *switch* has been designed and built by SKK. It is provided by two independent 5 MHz inputs, compatible with the 5 MHz output signals of two AOGs employed to generate the two TL internal realization of UTC(IT). As outputs, the *switch* provides one 100 MHz, five 10 MHz and five 1PPS signals. It is also equipped with a RJ45 connector, allowing to remotely Monitor&Control the device, through a dedicated external workstation. The commutation between the two inputs can be controlled either manually, by means of a selector installed in the device front panel, or by the remote interface. The selector allows for three different configurations: CH1 and CH2, to force the *switch* output to the selected channel; and "AUTO", to allow the remote control. Moreover, in "AUTO" mode of operation, the device can perform an automatic switch in case the signal of one of the two input time scales is missing. Conversely, the manual switch from CH1 to CH2 - or vice versa - can be performed in case of one of the two input time scales has to be intervened for maintenance activities.

Beside the channel switching, by means of the remote interface it is possible to control other device's features. The *switch*, in fact, is equipped with an inner local oscillator working a 100 MHz and locked to the selected input, that provides the 100 MHz and 1PPS output signals (10 MHz is synthetized from the 100 MHz). The switch contains also an internal phase meter that can measure the phase difference of the two input signals, with respect to the internal oscillator. To avoid unexpected 1PPS output jumps due to the cycle ambiguity of the input signals and the internal oscillator, the phase offset between the two input signals has to be kept within ±100 ns (linked to the signals at 10 MHz), but with the internal phase meter[1], the alignment can be performed at a level of a few tens of picoseconds. Furthermore, the 1PPS output signal can be shifted in order to allow the alignment to an external reference, with a resolution of 10 ns. To improve the resolution, it's mandatory to operate directly on the input AOGs.

[1] With a proper procedure, it is possible to calibrate the inner phase meter, with the main aim to compensate the time offset between the two input channels, when they are fed with two aligned signals. It is enough to perform the calibration only once, due to the possibility to storage the correction parameter directly into the device's memory.

In the frame of the *switch* use at TL, *one* of the five 1PPS output signals will be considered as the reference plane of UTC(IT) time scale. Being it the "reference", it won't be used to feed any TFL users/services, but it will be kept free and only used for calibration measurements and/or direct measurements purposes. The other four 1PPS outputs are quite good UTC(IT) replicas, considering the negligible inter-channel bias (at few picosecond level).

A. Long Term Stability

Several functional and performance tests had been carried out on *the switch.*

Firstly, the long term stability has been investigated, considering the measurement setup indicated in the following Fig. 1:

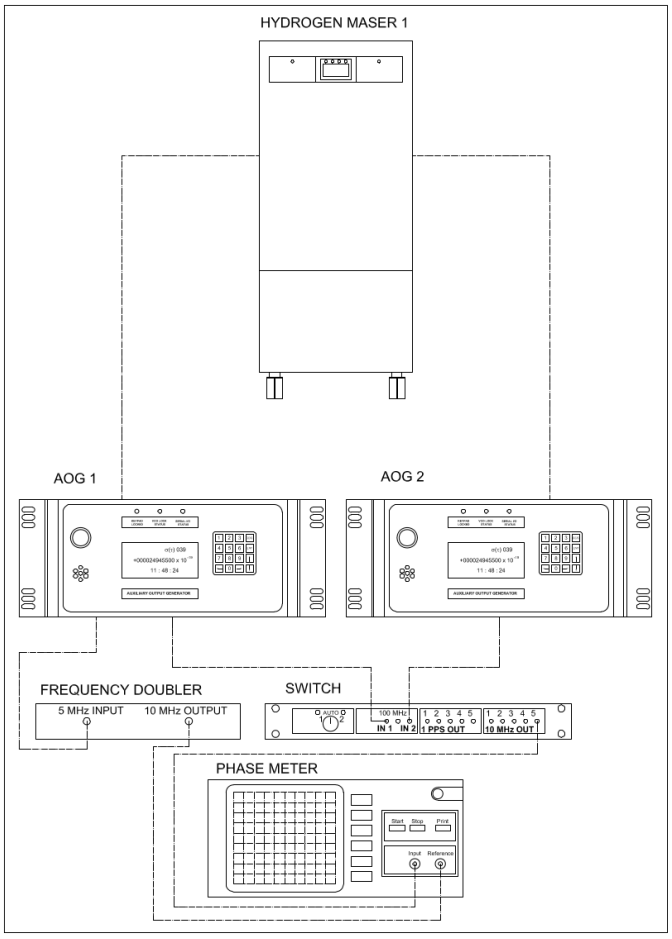

Fig. 1. Pictorial view of the measurement setup used for the characterization of the switch.

The 5 MHz signal generated by an AOG driven by an Active Hydrogen Maser (AHM), has been connected to the switch CH1 input. A second AOG (driven by the same AHM) was connected to CH2. Furthermore, one of the switch 10 MHz output signals, has been measured with respect to the CH1 AOG doubled frequency, by means of a Microsemi 5125A phase meter. The CH1 selected channel, has been kept unaltered for all the 22 hours of the measurement process.

With this configuration, the CH1 AOG can be considered in *common mode*, leading to get a good estimation of the *switch* system noise.

As it can be seen from the next Fig. 2 and Fig.3, the system noise (expressed in terms of phase measurements and Allan Deviation) is low, granting for the *switch* usage in the frame of the generation of an AHM atomic time scale, like UTC(IT). In particular the ADev shows a $1/\tau$ profile, with a Frequency Stability of 6E-14 at 1 s averaging time, this figure comparable with the one of the considered AHM. The (negligible) 3 ps transition depictable at the beginning of the phase measurement series reported in Fig. 2, is most likely related to the temperature effect on the whole measurement system.

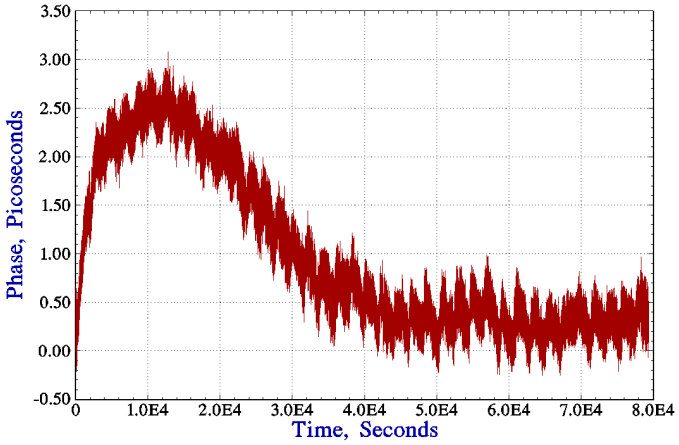

Fig. 2. Phase difference from the switch output and the reference AOG for the long term stability test.

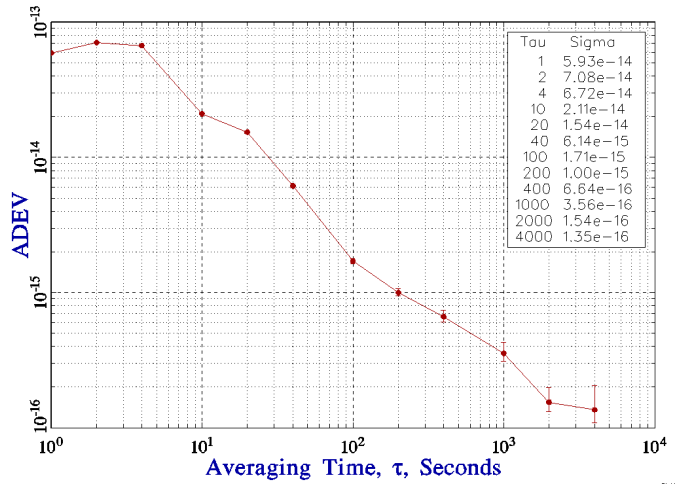

Fig. 3. Allan deviation of the long term stability test.

B. Switching Behaviour with perfectly aligned scales

A second important test has been carried out, to measure the commutation performances of the *switch*, in particular the presence of frequency lacks and the size of time jumps, during

the commutation between two perfectly aligned input signals. The two *switch* input signals, generated following the functional scheme of Fig. 1, have been aligned through the phase measurements performed by the *switch* internal phase meter, at a level of a few ps. Fig. 4, shows the impact of the switching process, when manually commuting from CH1 to CH2, and viceversa. As it can be noticed, the process introduces phase jumps at the level of 35 ps. The repeatable characteristics of this behavior, together with the magnitude of the phase jumps, leads to consider the *switch* commutation process fully compatible with the needs foreseen in the generation of UTC(IT).

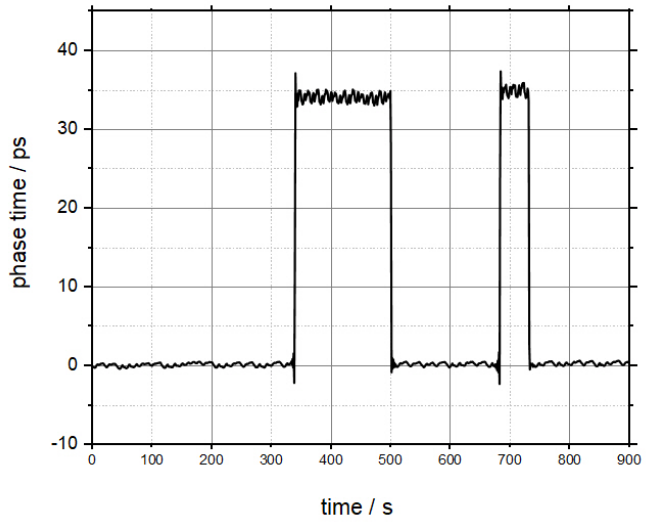

Fig. 4. Phase difference during the switching procedure

C. *Other operational tests*

Together with above mentioned performances test, other tests have been considered, in order to verify the *switch* behavior in an operative context. In particular, the commutation when one of the two input signals lacks (simulating a failure in one of the two input time scales generation chain), as well as when a drift among such signals occurs (simulating a problem in the frequency/drift correction on one - or both – input time scales generation chains).

These tests, led to fully characterize the behavior of the switch, in the perspective of its introduction in the hardware used to generate UTC(IT) time scale.

III. THE NEW SETUP FOR THE REALIZATION OF UTC(IT)

The introduction of the *switch* in the generation scheme of UTC(IT) time scale, indicated in the next Fig. 5, will provide several improvements, as already mentioned in the introduction.

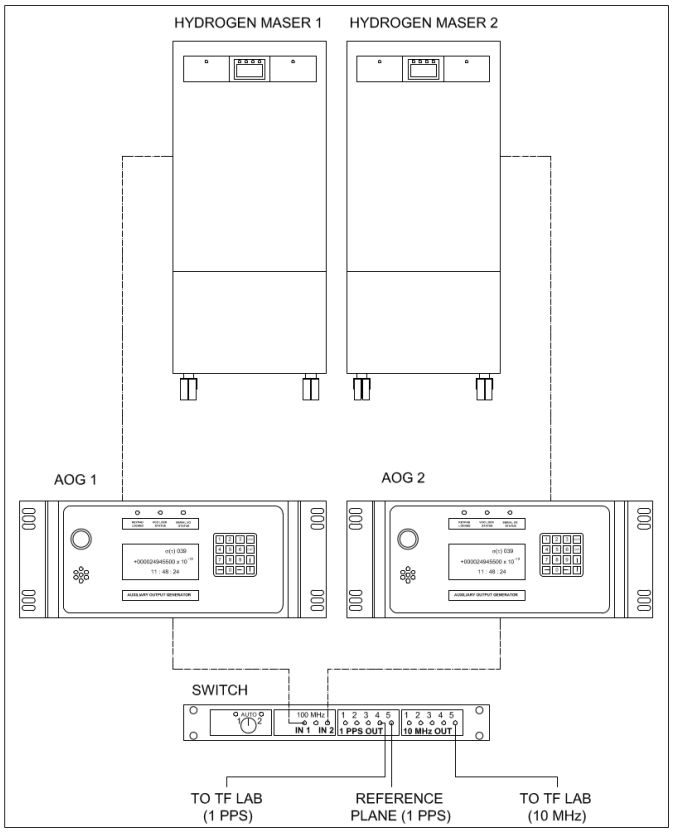

Fig. 5. Pictorial view of the new setup for the generation of UTC(IT) that uses the new switch.

First of all, the switch will allow a transparent commutation from UTC(IT)_1 to UTC(IT)_2. This is very important both in case of maintenance and in case of emergency. In fact, when a scheduled intervention is necessary on the primary scale, having the possibility of switching transparently to the backup one without affecting any of the users/services, is very important, to preserve the continuity of Time and Frequency signals. Moreover, also in case of sudden failure of one or more components of the primary scale, the automatic switch will allow to commute to the backup scale, even though the two connected time scales must be maintained aligned constantly to be ready for the switching procedure.

Another improvement introduced by the presence of the switch, is that the reference plane of the whole laboratory will be redefined in accordance with the new hardware structure. As already mentioned before, the new reference plane will be one of the 1 PPS outputs of the switch. This connector will always be kept free, so that it will always be available as reference to be used to calibrate and/or to perform direct measurements. Also, the cascade Time and Frequency distribution system will be updated, as well as the distribution cables, in order to have a more rationale and – hence – more robust system.

The implementation of this new setup is currently under development and will be completed most likely by the end of the year 2018.

IV. Conclusions

The *switch* to be introduced in the UTC(IT) generation chain, has been successfully tested and it has been demonstrated that its characteristics perfectly fit with the INRIM TL needs. The introduction of the *switch* into the operative TL scheme is still an ongoing process, but when the migration from the old to the new system will be concluded, the robustness of the UTC(IT) generation system will be considerably improved. The new device will guarantee the continuity of the Italian standard time generation, also in case of unexpected events, providing a better contribution of the Italian Time Laboratory to the realization of TAI and UTC time scales.

Acknowledgment

Authors wish to thank G. D. Rovera for the productive discussions and help.

References

[1] Cerretto, G., Costa, R., Fantino, G., Cantoni, E., Sesia, I., Signorile, G., Tavella, P., "INRIM Time and Frequency Laboratory: An Update on the Status and on the Ongoing Enhancement Activities," Proceedings of the 46th Annual Precise Time and Time Interval Systems and Applications Meeting, Boston, Massachusetts, December 2014, pp. 33-40.

Phase Synchronization for 5G Using Mass Market GNSS Receivers

Zdenek Chaloupka*, Lionel Ries, Andrea Samperi, Pierre Waller, Massimo Crisci
European Space Agency/European Space Research and Technology Centre
Keplerlaan 1, 2201 AZ Noordwijk
The Netherlands
*z.c.nl@ieee.org

***Abstract*— Industry and academia have been quite active in defining the next generation telecommunication technology (5G). Even though significant progress has been achieved in 3GPP standardization organization, requirements on frequency and time synchronization are not yet fully consolidated. However, looking at the requirements of already published standards for 4G, one could conclude that the telecommunication technology synchronization shifts from frequency synchronization (for LTE) to phase synchronization (for LTE-A) due to advantages that the latter offers for MIMO techniques. Indeed, coordinated multipoint technology introduced in the latest release of 3GPP recommendations requires the time alignment error to stay below 65ns at the base station transmitter port. It is more than evident that in order to enable a smooth roll out of 5G technology, industry and academia should look for an affordable technology capable to deliver accuracies in the above mentioned range. Our paper contributes toward that goal by evaluating relative time (phase) synchronization of mass market Global Navigation Satellite System (GNSS) receivers and hence giving an overview of what is possible to achieve with the current technology.**

Keywords—4G; 5G; frequency synchronziation; time synchronization; phase synchronization, GNSS

I. INTRODUCTION

Industry and academia have been quite active in defining the next generation telecommunication technology (5G) and its requirements for quite some time now. The unwavering effort (from industry) is fueled mainly by the expected revenues, but also by the need to have the first technology standard in place before 2020 to follow the schedule laid out by ITU in IMT-2020 [1]. Even though the standard definition is progressing quite quickly now, it is not clear yet what are the key requirements of the 5G technology with respect to time, phase or frequency synchronization accuracy and precision.

Looking at the requirements of already published standards for 4G, however, one could conclude that the telecommunication technology synchronization shifts from frequency synchronization (for LTE) to phase synchronization (for LTE-A) due to advantages that the latter offers for MIMO techniques. Indeed, the document [2] clearly states that a time alignment error for MIMO transmissions shall not exceed 65 ns at the base station transmitter port. It is more than evident that in order to enable a smooth roll out of 5G technology, industry and academia should look for an affordable technology capable to deliver such accuracy. Quite possibly, even more accurate one to allow for more future proof solutions.

Our paper contributes toward that goal by evaluating relative time (phase) synchronization of mass-market Global Navigation Satellite System (GNSS) receivers and hence giving an overview of what is possible to achieve with the current technologies. Even though the evaluation is performed in rather idealistic conditions, it will help to understand a lower bound of relative synchronization accuracy achievable by commercial-off-the-shelf (COTS) receivers.

II. USE CASE SCENARIO & TEST BED DESCRIPTION

A. Use Case Scenario

The evolution of telecom technology seems to be heading into the utilization of the higher frequency carriers (6-100 GHz, i.e., millimeter wave range – mmWave) [3], simply due to limits of spectrum allocation in the heavily crowded L band (and below) range. Such technological move places new challenges on the base station (BS) deployment density [4], since the reach of mmWave based RF signal will be quite short (due to high free space loss). This will mandate higher density of 5G mobile network BS, which in turn means that many of the BSs would be deployed in areas with partially obstructed sky. Based on the above we can derive few observations related to the 5G use case scenario:

- Due to number of BSs required (densification process), low cost mass-market technology for synchronization is required, one candidate solution considered in this paper is based on GNSS.
- Open sky conditions cannot be assumed in urban deployment (e.g. BSs can be co-located at lamp posts, or not too distant buildings). It is highly likely that receivers will experience urban canyon conditions with only partial sky visibility.
- Clusters of GNSS receivers (nearby lamp posts) will experience very similar conditions in terms of ionosphere delay, multipath and satellite visibility.

Above mentioned 5G use case scenario sets very specific requirements on the environment of use and hence clear limitations for our test bed. For example, it was not possible to mount receivers at lamp posts, since it would be very difficult

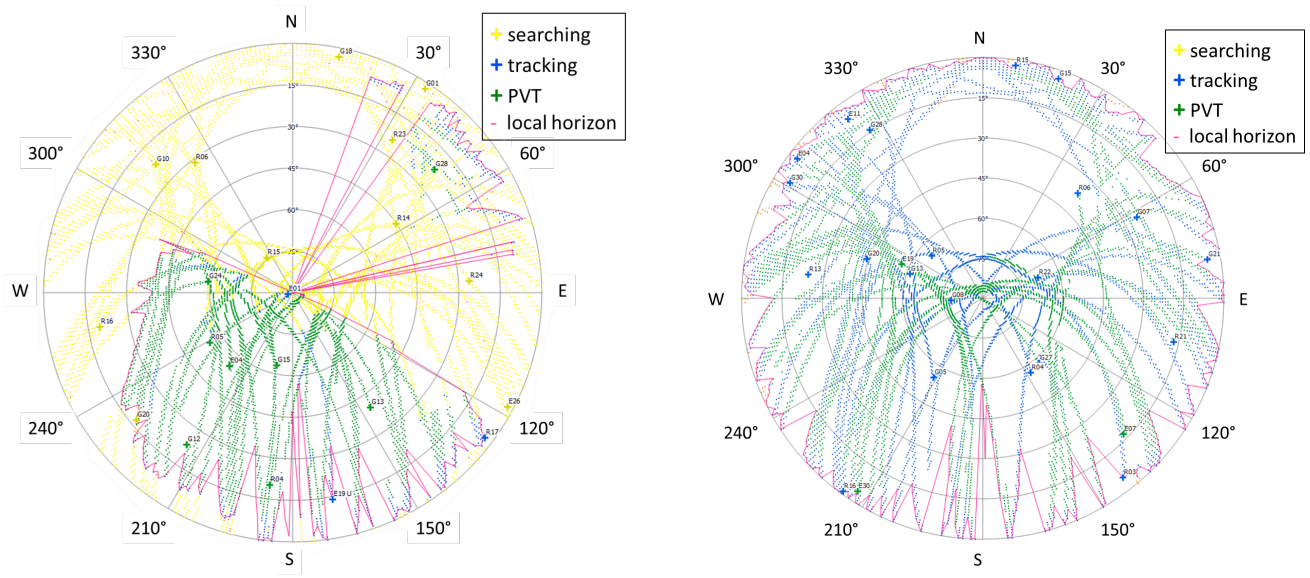

Fig. 1. Sky plot details as viewed by the receivers: left – urban canyon-like conditions, right – open sky conditions (an alternative setup).

to measure their relative phase synchronization. As an alternative we grouped the antennae of receivers at a location with partially obstructed sky (window frame in ESTEC building) and hence achieved urban canyon-like conditions while maintaining accessibility to the phase synchronization signal of the receivers under test. Note that the antennae were packed close to each other on an area of 50x20 cm, so the maximum timing bias introduced by the antenna displacement is capped at about 1.5 ns. Since we are interested in relative characteristics (see Section III.B), all biases are removed intrinsically anyway.

Figure 1. (above this text) clearly demonstrates the conditions experienced by the GNSS receivers during the measurement campaign. We believe that the partial obstruction of the sky due to the ESTEC building's structure is a good representative of urban canyon conditions. Note that the GNSS antennae placement is still far from realistic, as in real-life deployment the antennae would be separated by tens to hundreds of meters. Despite this limitation, we believe that the measurement campaign can draw a picture of the lower bound of the relative phase synchronization accuracy of mass-market receivers.

B. *Test Bed Setup*

Since the measurement campaign was focused on a relative phase synchronization accuracy evaluation by a side-by-side measurement, the main problem was how to carry out simultaneous measurements of one pulse-per-second (1PPS) synchronization signal output by the GNSS receivers. We decided to use Tektronix's MSO58 oscilloscope (referred to as a scope in the rest of the paper), since it is equipped with eight measurement ports. The test bed diagram is depicted in Fig. 2.

The scope measures simultaneously difference between 1PPS signal from RxT (port P8) and other scope's ports (P1-P7). These measurements are periodically retrieved using LAN cable through scope's socket server and stored in the laptop,

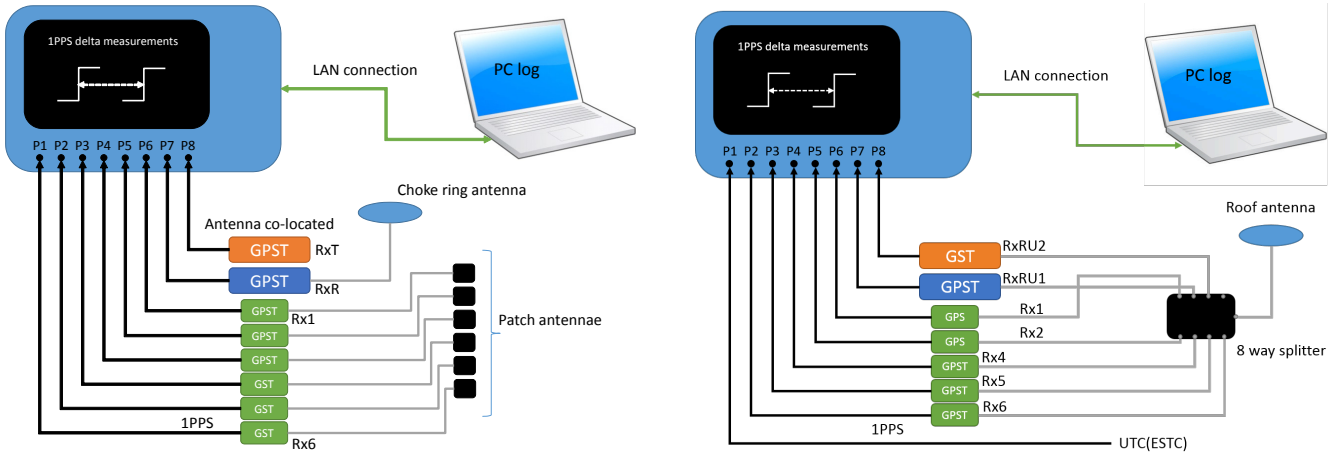

Fig. 2. Simplified diagram of the measurement test bed: left – urban canyon-like setup; right – open sky setup.

where the data are further processed offline.

Note that we have also set up an alternative test bed, which was installed after the main measurement campaign was finished. This alternative test bed was set to verify conclusions drawn from the main measurement campaign. The alternative test bed consists of two professional receivers and five mass-market receivers fed by GNSS signals from an antenna (with clear sky visibility) using a splitter. The alternative test bed uses ESTEC's realization of UTC (UTC(ESTC)) as a reference. The timing measurements of RxRU will give us a fundamental lower bound for accuracy and stability of timing realized by GNSS.

C. GNSS Receivers Under Test

Since the objective of our measurement campaign is to understand the limits of relative synchronization accuracy of mass-market GNSS receivers (single frequency, multi-constellation, Klobuchar model of ionosphere delay), we thought it would be best to compare multiple identical COTS GNSS units (designed specifically for timing) in a side-by-side comparison with two professional products (one timing and one high-end reference receiver) for diversity purposes. By multiple identical units we mean multiple identical models (same chipset & firmware) of a GNSS receiver from one vendor. COTS units (denoted further as Rx1-Rx6) were in the price range of hundred euros, whereas the professional products were in the range of a thousand and six thousands of euros (for RxT and RxR in the main test bed respectively). Professional receivers in the alternative test bed (RxRU1 and RxRU2) were in the range of fifteen thousands of euros. Note that RxT is used as a source of reference signal in the main measurement campaign, as its 1PPS timing signal has similar stability as the high-end RxR, and on top of that it showed a stable performance in the case of partially obstructed sky (which was not the case for RxR nor RxRU).

It should be stated that all receivers output 1PPS rounded to the nearest tick of the internal clock. This results in an offset between the output 1PPS and the estimated true time. All receivers offer a functionality that reports the offset to the estimated true position, but since in real applications BSs are synchronized to the 1PPS without this correction information, we also used 1PPS as is. Comparing the actual true estimates will be part of the future work.

III. Measurements & Results

Highly accurate relative phase synchronization is a major enabler of the next generation telecommunication technology as explained in the Section I. Therefore, a relative phase accuracy evaluation is the main focus of this paper.

A. Measurement Campaign

Since the inception of a satellite based navigation, the number global navigation systems has increased significantly. This means that multi-constellation receivers can simultaneously track multiple of satellites from different constellations. This new paradigm raises question about whether there is any significant difference of timing stability and accuracy between the systems from the receiver's point of view. This paper does not try to evaluate the quality of the system's time realization on the ground or its transfer to receivers, but rather how receivers realize selected constellation's system time. We decided to test receiver realization of two main system times: GPS system time (GPST) and Galileo system time (GST). The systematic testing of other systems was not possible due to a limited time for measurement campaign, but is part of the future work.

In order to facilitate the data collection we decided to set receivers Rx1-Rx3 to realize GPST and Rx4-Rx6 to realize GST. Reference receivers both realize GPST, because of the number of GPS satellites available. Since the measurement campaign was focused on timing, we have considered only a static mode of the GNSS receivers in which the position is fixed by averaging over time, or set manually (we used the latter) and only time information is estimated. Note that timing receivers working in the static mode should be able to retrieve GNSS time even through a single available satellite. The measurement campaign was separated into three distinct parts:

- SMS – static mode in single-constellation – GPS or Galileo system time is tracked.
- SMD – static mode in dual-constellation – fixed position mode with the main navigation system being GPS or Galileo and second system being GLONASS.
- SMM – static mode in multi-constellation – fixed position mode with tracking of all constellation available (GPS, Galileo, GLONASS).

The above cases form the core of our data set. Each of the cases was tested over a significant period of time (see Table I for details) to gain more confidence when producing the final timing statistics. This means that the experiment totaled about 48 days of data with sampling period of one second (1PPS signal).

B. Timing Measurement Characterisation

A standardized set of timing characteristics is used to describe the stability of the timing signals:

- MTIE – Maximum Time Interval Error;
- TDEV – Time Deviation;
- TIERMS – RMS of Time Interval Error.

The first two characteristics are widely used in telecom industry for synchronization signal quality description and the third one (TIERMS) is used to give readers a better understanding of an average time error performance, since this is not obvious from the first two. Note that there is a number of other standard timing characteristics, but we wanted to limit the results to fit the scope of the paper. Mathematical definitions of the above characteristics can be found in [5].

C. Availability of Timing Signals

First let us have a brief look at the availability of the sync signals themselves. The table below this text summarizes our observations for each constellation settings.

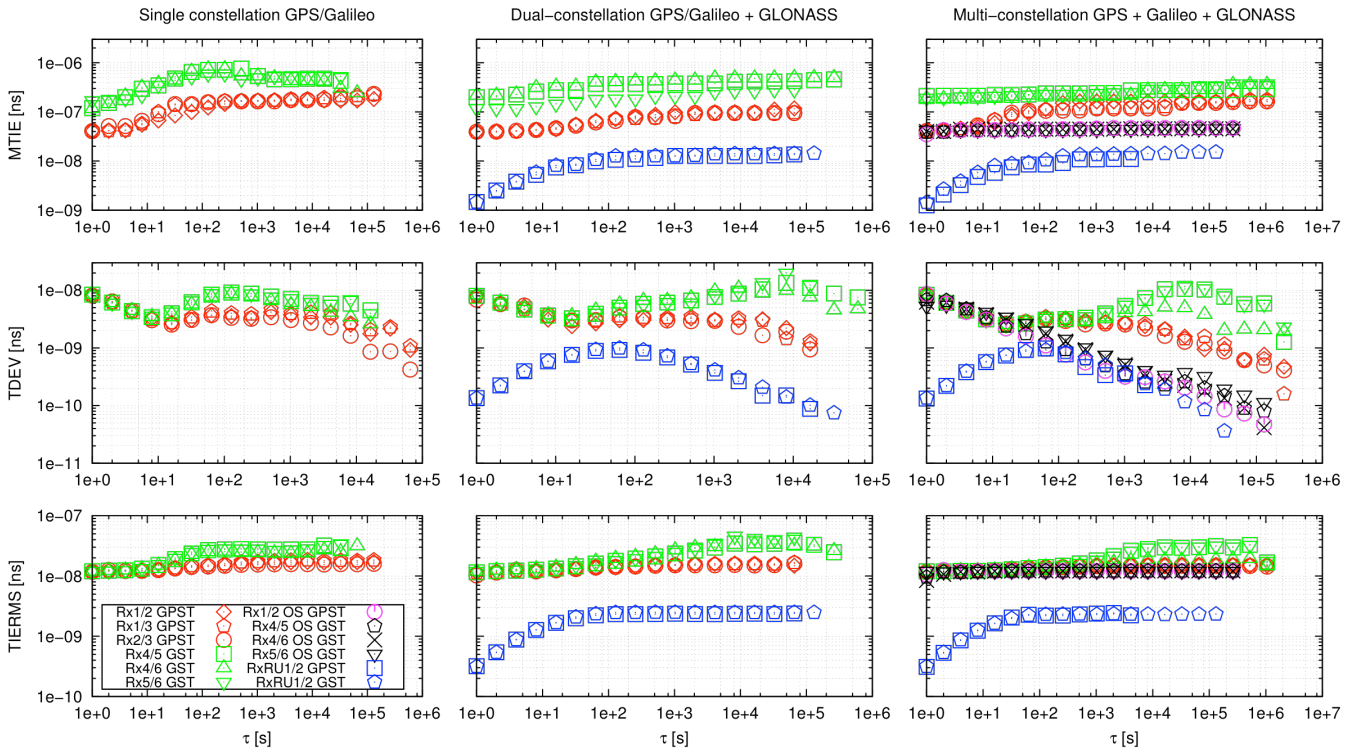

Fig. 3. Relative synchronization analysis for single, dual and multi-constellation GNSS receivers realizing GPST or GST. Blue points show relative sync performance of professional receivers. Performance achieved in open sky conditions is drawn by magenta and black points.

TABLE I. AVAILABILITY OF TIMING SIGNAL

Table Head	Availability in percent		
	SMS ***22 days***	***SMD*** ***13 days***	***SMM*** ***13 days***
Rx1 GPST	100	100	100
Rx2 GPST	100	100	100
Rx3 GPST	100	100	100
Rx4 GST	88	99	100
Rx5 GST	97	100	100
Rx6 GST	92	100	100

It is clear that in terms of availability the GPS single constellation guarantees full availability in our use case. On the other hand, Galileo system gains significant advantage when at least one other constellation is available, because the system has not yet reached full operational capability (14 satellites are operational and 4 under commissioning at the time of writing out of 24 planned for full operational capability).

D. Relative Synchronization of Timing Signals

The results discussed in this section are depicted in the Fig. 3. First, let us have a look at the MTIE characteristics from which we can draw conclusions about the maximum observable errors. The relative sync performance is the worst for a single constellation setting for both Galileo (reaching a little less than 1 µs) and GPS (less than 300 ns). There is a significant improvement when receivers are set to a dual constellation, at least for MTIE characteristics (less then 200 ns for GPST and 600 ns for GST). This indicates that the synchronization signals are exhibiting more consistency (smoothness) compared to the single constellation setting. Such outcome was expected as adding second constellation improves satellite availability. GPST based relative synchronization does not improve much when three constellations are used. Actually, it seems that the performance degrades a bit for multi-constellation (going from 100 ns to 200 ns maximum error), which is an interesting observation. Further measurement campaign is required to find out if the same effect happens for open sky conditions and different combination of dual constellation (e.g. GPS + Galileo). Receivers realizing GST gain quite an advantage from increased number of available satellites, specifically for the case when GPS is also tracked (multi-constellation case), in which the maximum relative sync error decreases to about 400 ns. We can observe that outliers are removed significantly resulting in more smoothed timing signals.

Looking at TDEV characteristics we can conclude that adding constellations results in a better performance for longer observation windows for both, GPST and GST relative sync performance. The same conclusions apply for TIERMS characteristics. TIERMS characteristic also suggests that GPST and GST relative phase synchronization error is below 20 ns and 40 ns, respectively, in an average sense.

From the comparison of relative sync accuracy of GST and GPST in the urban canyon-like conditions it seems that mass-market receivers realize GPST with a better consistency. Our

conclusion is that there are two possible causes for this. A very obvious one is that there is far more GPS satellites available. The second one, maybe less obvious would be that the mass-market receivers have less matured Galileo signal processing/tracking.

In order to find the true source of the worse performance of GST in the urban canyon-like scenario, we used our alternative setup (with open sky visibility) to rule out the effect of the lower satellite availability. The first important observation is that the two professional receivers (RxRU1 and RxRU2) have entirely comparable relative phase accuracy for GPST and GST in multi-constellation settings (see blue pointed curves in Fig. 3.). The second important observation is that mass-market receivers under open sky conditions (with multi-constellation option) also exhibit comparable performance for both GPST and GST. Notice that the maximum relative timing error for relative phase synchronization is bounded at 40 ns, which is quite an impressive result for low cost mass-market receivers.

One may object that since all of the receivers were connected to the same antenna (through a splitter), the relative phase synchronization results may be too optimistic compared to what was observed from the main measurement campaign, where each receiver was connected to a separate antenna. This is indeed true, so the final performance is way too optimistic to be relied upon in the real deployment.

Since the alternative measurement campaign used high quality reference – UTC(ESTC) – for the measurements, we computed statistics of the timing error relative to UTC(ESTC) – see Fig. 4. The results further confirm that the stability of the receivers' realization of GST and GPST is entirely comparable. It is interesting to notice that while professional receivers (not timing ones) have a superior performance in terms of maximum time error, mass-market timing receivers show better performance in terms of RMS time error and time deviation.

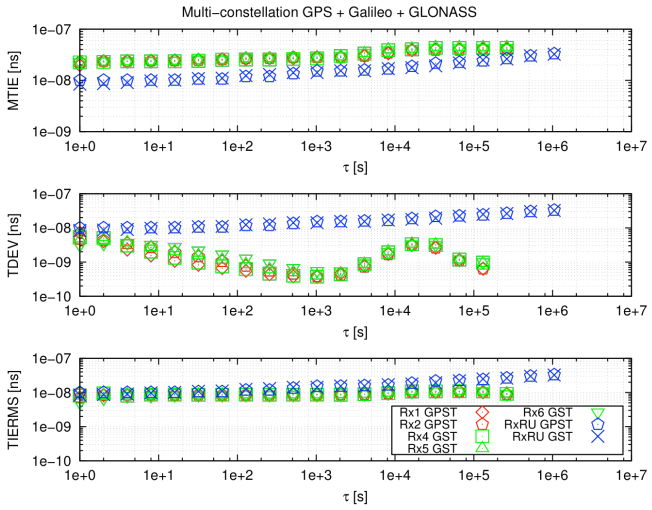

Fig. 4. Performance of receiver realized GST and GPST in multi-constellation and open sky environment.

IV. Summary and Conclusions

The next generation telecommunication technology will require much better phase synchronization accuracy than the current LTE standard. GNSS based time synchronization could be one possible candidate technology in many use case scenarios. In order to understand what is possible with the current mass-market timing GNSS receivers, we have tested multiple identical receivers (the same vendor, model, and firmware) with different settings (single, dual and multi-constellation) realizing GPS or Galileo system time. In order to understand the technology limits we have tested those receivers in urban canyon-like conditions. To have a complete picture, we also tested mass-market receivers in parallel with two professional products in rather idealistic conditions (single antenna and open sky conditions).

We have come to three main conclusions. The first conclusion is that relative phase synchronization of mass-market receivers realizing GPS time (GPST) is better than that of receivers realizing Galileo system time (GST) in urban canyon-like conditions. The sole cause of GST performance degradation is the limited availability of Galileo satellites. This degradation will disappear when Galileo reaches full operation capability.

The second conclusion is that in open sky conditions the mass-market receivers realization of GST has a comparable performance to that of GPST, which means that signal tracking and processing of Galileo signals has a good level of maturity at least for one mass-market GNSS timing receiver manufacturer.

The third conclusion is that given the recent requirements of advanced LTE technology (being relative phase synchronization of 65 ns), the current mass-market receiver technology is not too far from being able to provide such accurate relative phase synchronization – achieving 40 ns in rather idealistic conditions and about 200 ns in urban canyon-like conditions. It is also clear that far more work is required to achieve higher accuracy in degraded (urban canyon) conditions. Further investigation is needed to evaluate impacts of other effects (e.g. multi-path, antenna type), since those may play a significant role in driving the final accuracy of the (relative) phase synchronization.

References

[1] IMT Vision - Framework and Overall Objectives of the Future Development of IMT for 2020 and Beyond Recommendation ITU-R M. 2083-0, Sept. 2015.

[2] ETSI TS 136 104, LTE; Evolved Universal Terrestrial Radio Access (E-UTRA); Base Station (BS) radio transmission and reception, October 2016.

[3] Ali A. Zaidi, et al., "Evaluation of Waveforms for Mobile Radio Communications above 6 GHz", 2016 IEEE Globecom Workshops, ISSN 2166-0069.

[4] J. Liu, et al., "Network Densification in 5G: From the Short-Range Communications Perspective", IEEE Communications Magazine, vol. 55, December 2017.

[5] IEEE Std™ 1139-2008: IEEE Standard Definitions of Physical Quantities for Fundamental Frequency and Time Metrology—Random Instabilities.

Joint Time Scale Algorithm of UTC(NTSC) and UTC(SU)

Shanshan BAI *†‡, Shuhong ZHAO *†, Shaowu DONG *†, Lulu YAN *†,Lili QU *†

Email: xfydy5@163.com, zsh@ntsc.ac.cn, sdong@ntsc.ac.cn

* National Time Service Center, Chinese Academy of Sciences, Xi'an, China

† Key Laboratory of Time and Frequency Primary Standards, National Time Service Center, CAS, Xi'an, China

‡ University of Chinese Academy of Sciences, Beijing, China

***Abstract*—Russian-Chinese Cooperation Committee on Satellite Navigation was established by the two sides of China and Russia under the regular meeting mechanism, In order to effectively pro-mote the cooperation between China and Russia in the field of satellite navigation. The technical communication of existing and future compatibility, interoperability and time system interoperability, etc was established by the committee. UTC(NTSC) and UTC(SU) joint time scale is a unified reference for compatibility and interoperability of GLONASS and BeiDou navigation system. The unified reference is necessary for effectively promoting the cooperation between the two sides in the field of satellite navigation. In this paper, through atomic clock stability analysis, the linear prediction model was used for cesium clocks and the quadratic prediction model was used for hydrogen maser clocks. The weight of clock was determined by the 'predictability' of clock. UTC(NTSC) and UTC(SU) joint time scale and the time scale generated using only the NTSC laboratory atomic clocks was calculated from MJD 57754 to 58119. The results shows that the stability of the joint time scale is better than the stability of the time scale calculated using only the NTSC laboratory atomic clock.**

Keywords—Allan variance; Time scale; Frequency prediction; Weight

INTRODUCTION

In order to effectively promote the cooperation between China and Russia in the field of satellite navigation, Russian-Chinese Cooperation Committee on Satellite Navigation was established by the two sides under the regular meeting mechanism. The first meeting was successfully hosted in Beijing by the project committee on February 10, 2015. The Russian-Chinese satellite navigation compatibility and interoperability work group was established in the meeting. In order to make the technical communication flexible, four sub-working groups which were orbit constellation interoperability work group, existing and future compatibility and interoperability work group, time system interoperability work group and geodetic reference frame interoperability work group was established.

In order to promote the time system interoperability work. Russian-Chinese joint time keeping lab was established by the two sides of China and Russia. Chinese responsible institute is National Time Service Center, Chinese Academy of Sciences(NTSC), UTC(NTSC) was maintained by NTSC, UTC(NTSC) is the traceability reference of BeiDou time. Russian responsible institute is Institute of Metrology for Time and Space (RIRT), UTC(SU) was maintained by RIRT, UTC(SU) is the traceability reference of GLONASS time. UTC(NTSC) and UTC(SU) joint time scale was established in the frame of Russian-Chinese joint time keeping lab. The joint time scale with clocks in different place and multiple type was calculated which is a unified reference for compatibility and interoperability of GLONASS and BeiDou navigation system. The unified reference is necessary for further work. Now, the data sharing platform of time interoperability work based on FTP data server was established. The data sharing software interface was shown in Figure 1.

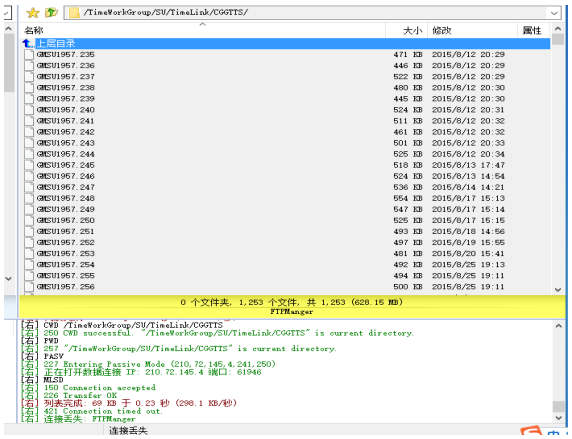

Fig. 1: The data sharing software interface

THEORY OF TIME SCALE ALGORITHM

Allan Variance Estimate

Allan variance is the first order difference based on frequency data and is the second order difference based on phase data. The iterative Allan variance is a special form of the common Allan variance. The iterative Allan based on frequency data is given by formula (1):

$$\sigma_y^2(\tau)=\frac{1}{2m^2(M-2m+1)}\sum_{j=1}^{M-2m+1}\left\{\sum_{i=j}^{j+m-1}\left[y_{i+m}-y_i\right]\right\}^2 \qquad (1)$$

Where,

m : The average factors.

M : The frequency sampling number.

y_i : The ith measured value.

τ : The sampling interval.

The iterative Allan based on phase data is given by formula (2):

$$\sigma_y^2(\tau)=\frac{1}{2\tau^2(N-2m)}\sum_{i=1}^{N-2m}\left[x_{i+2m}-2x_{i+m}+x_i\right]^2 \qquad (2)$$

Where N is sampling number, N=M+1.

Time Scale Algorithm

The TA time scale is calculated based on ALGOS algorithm using atomic clock comparison data by multiple atomic clocks. The TA is calculated by formula (3):

$$x_j(t)=EAL(t)-h_j(t)=\sum_{i=1}^{N}\omega_i(t)[h_i^{'}(t)-x_{i,j}(t)] \qquad (3)$$

As shown above,

N : The total number of the atomic clocks.

ω_i : The relative weight of clock Hi.

$h_i(t)$: The reading of clock Hi at the t moment.

$h_i'(t)$: The predicted phase correction of the atomic clock i (which make the phase and the frequency of time scale to be continuous).

$x_{i,j}(t)$: The direct measurement of the phase differences between clock i and clock j.

$$x_{i,j}(t)=h_j(t)-h_i(t) \qquad (4)$$

frequency prediction algorithm

In order to ensure continuity of phase and frequency, we need to predict the correct value $h_i'(t)$ of the clock $h_i(t)$ at the moment t_k .when we compute the time scale in two consecutive periods of time $I_{k-1}(t_{k-1},t_k)$ and $I_k(t_k,t_{k+1})$. $h_i'(t)$ is estimated by linear model using formula (5):

$$h_i'(t)=a_{i,I_k}(t_k)+B_{ip,I_k}(t)\cdot(t-t_k) \qquad (5)$$

Where,

$a_i(t_k)$: The phase difference between the clock Hi and the time scale (TA) at t_k moment.

$B_{ip,I_k}(t_k)$: The frequency of the clock Hi relative to the TA. Here, $B_{ip,I_k}(t_k)$ is a fixed constant.

$h_i'(t)$ is estimated by quadratic model using formula (6):

$$\hat{h}_i'(t)=\hat{a}_{i,I_k}(t_k)+\hat{B}_{ip,I_k}(t)\cdot(t-t_k)+\frac{1}{2}\hat{C}_{ip,I_{k-1}}(t)\cdot(t_k-t_{k-1})\cdot(t-t_k)+\frac{1}{2}\hat{C}_{ip,I_k}(t)\cdot(t-t_k)^2 \qquad (6)$$

Where,

$a_i(t_k)$: The phase difference between the clock Hi and the time scale (TA) at t_k moment.

$B_{ip,I_k}(t_k)$: The frequency estimated value of the clock Hi relative to the TA in time interval $[t_k,t]$.

$\hat{C}_{ip,I_k}$: The drift estimated value of the clock Hi relative to the TA in time interval $[t_k,t]$.

$\hat{C}_{ip,I_{k-1}}$: The drift estimated value of the clock Hi relative to the TA in time interval $[t_{k-1},t_k]$.

weight algorithm

The weight of the clock is according to the "predictability" of the atomic clock, the Allan variance or the standard variance is calculated of the predicted residual of each atomic clock, and the weight of each atomic clock is obtained by the following formula:

$$\omega_i(t)=\frac{1/\sigma_i^2}{\sum_{j=1}^{N}1/\sigma_j^2},\ j=1,2,...,N \qquad (7)$$

Where, σ_i^2 is the Allan variance or the standard variance of the predicted residual of atomic clock i.

The limiting of the maximum weight is given by formula (8):

$$when:\omega_i(t)\geq W_{\max},\begin{cases}\omega_i(t)=W_{\max}\\ W_{\max}=\dfrac{A}{N}\end{cases} \qquad (8)$$

As shown above,

N : The total number of the atomic clocks.

A : The experience value, usually, A=2.5.

The other weight which is less than maximum weight is given by formula (9):

$$when:\omega_i(t)\prec W_{\max},\omega_i(t)=\frac{\omega_i\times(1-k\times W_{\max})}{\sum_{j=1}^{m}\omega_j} \qquad (9)$$

As shown above,

k : The number of the maximum weight.

m : The number of not maximum weight.

Formula 7 and formula 8 are computed iteratively until each weight doesn't exceed the maximum weight.

THE STABILITY OF ATOMIC CLOCKS

We have studied cesium clocks and H-maser clocks behavior for the one-year period Jan. 2017-Jan. 2018, the standard time UTC are used as the reference to evaluate the NTSC clocks ensemble. We made this analysis on nine cesium clocks and two MHM-2010 hydrogen masers, compared the frequency stability of those atomic clocks. The frequency stability is calculated by formula (2).

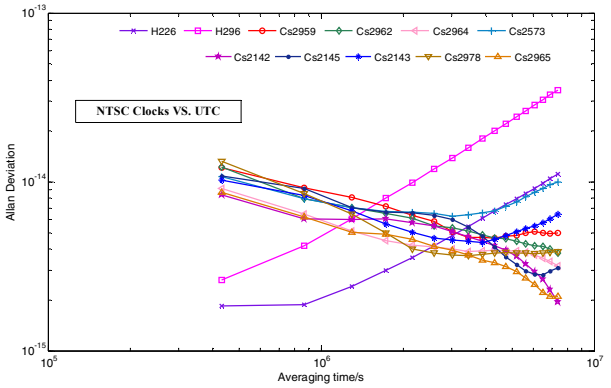

Fig. 2: Stability analysis of UTC-cesium clocks and UTC-H-maser clocks

In figure 2, the performance of each cesium clock looks like the same when averaging time less than 40 days. After 40 days, because of clock drift, random walk and other reasons, the performance of each cesium clock looks different. Therefore, the frequency prediction of cesium clock use linear prediction model when the forecast period is less than 40 days.

Whereas the stability of H-maser is more stable than cesium clocks when averaging time is less than 10 days, and random walk and clock drift dominate when averaging time is more than 10 days. Therefore, the frequency prediction of H-maser use quadratic prediction model when the forecast period is more than 10 days.

TIME SCALE CALCULATION

The data for time scale calculation are the phase difference between each atomic clock and reference at UTC0h per day. The time scale calculation period is one month. The interval of time scale calculation is from the 1st of this month to the 1st of next month. It ensures the phase continuity of time scale through data link for more than one month time scale calculation.

Firstly, the frequency of cesium atomic clock is predicted by formula (5). The frequency of hydrogen maser clock is predicted by formula (6).Get the prediction residual. Secondly, the weight of each atomic clock is calculated by the formula 7 and formula 8. Finally, the time scale is calculated by the formula (3). The time scale calculation procedure is in figure 3.

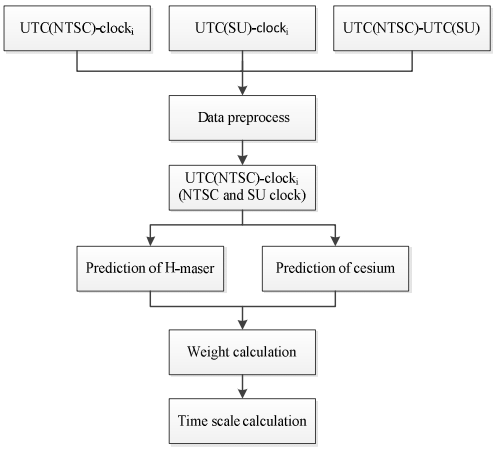

Fig. 3: The time scale calculation procedures

A. the predictabilty of H-maser clocks and cesium clocks

Prediction each clock relative to a reference standard to involve in time scale calculation, finally a stable and accurate atomic time scale is obtained. To predict clock rate and drift, the length of time period and predict method are the key questions.

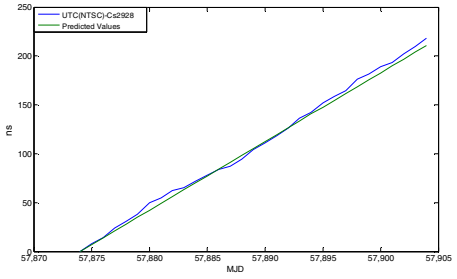

Fig. 4: UTC(NTSC)-Cs2928(blue line)and predicted values(green line)

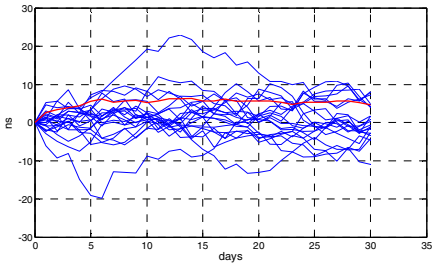

Fig. 5: The differences between UTC(NTSC)-cesium clocks and the predicted values are reported(blue lines), the 1 sigma uncertainty is reported(red lines)

We chose 20 cesium clocks and estimated the rates of those cesium clocks using linear prediction method. In Figure 4 the real value UTC(NTSC) – Cs2928 (blue line) and predicted values (green line) are shown, they align well. Figure 5 shows the differences between UTC(NTSC)-cesium clocks and the predicted values (blue lines), and the 1 sigma uncertainty(red lines), Residuals vary around zero, which shows that linear model is suitable for cesium clocks.

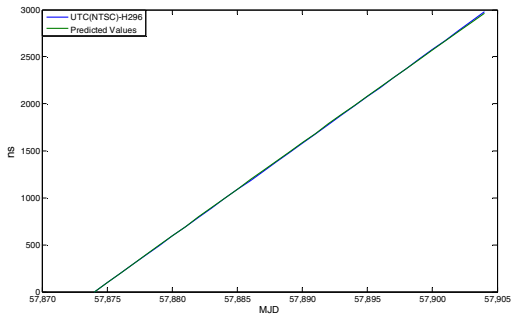

Fig. 6: UTC(NTSC)-H296(blue line)and predicted values(green line)

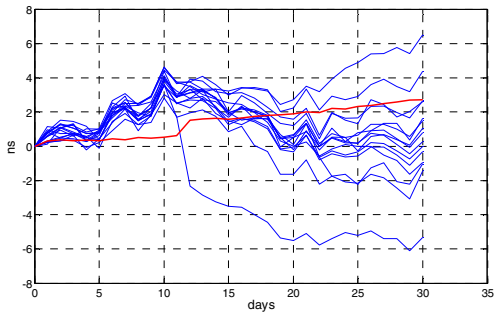

Fig. 7: The differences between UTC(NTSC)-H-maser clocks and the predicted values are reported with blue lines.With the red lines the 1 sigma uncertainty is reported

The same analysis on H-maser clocks, we chose 15 H-masers and estimated the rates of those clocks using quadratic prediction method. In Figure 6 the real value UTC(NTSC)-H296(blue line)and predicted values(green line) are shown, they align well. Figure 7 shows the differences between UTC(NTSC)-H-maser and the predicted values, it shows that quadratic model is suitable for H-maser clocks.

From what has been discussed above, the performance between cesium clocks and H-maser clocks are quite different, the noise of H-maser clock is smaller than cesium clock, but the H-maser drift can lead to poor prediction. Whereas the performance of cesium clocks is stable, the long-term stability looks well, but with poor short-term stability. Thereby according to different characteristic of H-maser and cesium clocks, we choose different prediction method to involve in time scale calculation, which can help to improve the stability of time scale.

B. UTC(NTSC) and UTC(SU) joint time scale

UTC(NTSC) and UTC(SU) joint time scale (TA_{join}) is calculated from MJD 57754to 58119 by 35 clocks where 20 cesium clocks and 3 H-maser clocks belongs to NTSC time keeping laboratory,12 H-maser clocks belongs to SU time keeping laboratory. Time scale (TA_{NTSC}) is calculated only by NTSC clocks. The phase difference between time scale and UTC(NTSC) is shown in Fig 8. The stability of time scale is shown in Fig 9.

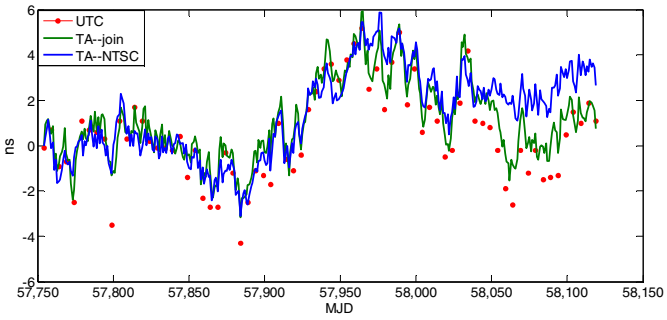

Fig. 8: The phase difference between time scale and UTC(NTSC)

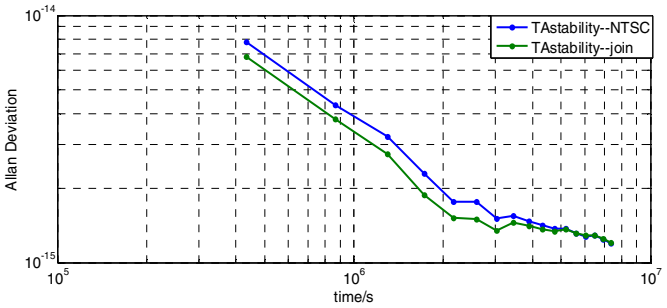

Fig. 9: The stability of time scale

As shown in the figure above, the stability of join time scale is better than the time scale calculated by only NTSC atomic clocks.

SUMMARY

In this paper, we first review the principle of time scale algorithm, second based on the phase difference between UTC and clocks which are in the National Time Service Center, CAS, analysis the stability of cesium clock and H-maser, third calculate the time scale. The stability analysis result shows that linear model is suitable for cesium clocks and quadratic model is suitable for H-maser clocks. The weight algorithm shows that the weight of H-maser clocks in the time scale are improved by weighted atomic clocks using the predictability. The time scale result shows that the stability of UTC(NTSC) and UTC(SU) joint time scale is better than the time scale calculated by single laboratory atomic clocks. The reliability of joint time scale is improved because more number of clocks are used in the time scale calculation. UTC(NTSC) and UTC(SU) joint time scale is a unified reference for compatibility and interoperability of GLONASS and BeiDou navigation system which is necessary for further work.

ACKNOWLEDGMENTS

The authors would like to thank the laboratory of Institute of Metrology for Time and Space (RIRT), for use of the phase difference data between UTC(SU) and clocks. And also thanks the National Natural Science Foundation of China (Grant No. 11773030) and CAS “Light of West China” program (Grant No. XAB2015B19).

REFERENCES

[1] Shaowu Dong, “Recent advances in time and frequency measurement at NTSC ”,Metrologia, vol(40), pp:249-251, 2003.

[2] Demetrios Matsakis etc. “Steering strategies for the master clock of the U.S. Naval Observatory (USNO)”, PTTI 2003.

[3] Arias E F, Jiang Z, Lewandowski W,et.al. “BIPM Annual Report on Time Activities for 2016”, France:BIPM Publication, 2017..

[4] Panfilo G., Harmegnies A., Tisserand L., “A new weighting procedure for UTC”, Metrologia, vol.51, 2014, pp. 285-292..

[5] Yuan Haibo,Wang Zhengming, “Automatic steering strategy for UTC(NTSC)”, Asia-Pacific workshop on Time and Frequency 2004,225-229..

[6] ZHAO Shu-hong,WANG Zheng-ming,YIN Dong-shan,A Study on the Steering Strategy for the Master Clock,Chinese Astronomy and Astrophysics ,vol(39), pp118–128, 2015.

[7] Panfilo G, Harmegnies A , Tisserand L, A new prediction algorithm for EAL, Proc. EFTF-IFCS, 2011: pp.362-365.

[8] Panfilo G ,Arias E F, Studies and possible improvements on EAL algorithm ,IEEE Trans. UFFC,2012, pp. 265-269.

[9] Federica Parisi, Gianna Panfilo, A new approach to UTC calculation by means of the Kalman filter, Metrologia,2016, pp.592-595.

[10] Demetrios Matsakis, Patrizia Tavella, “Special issue on time scale algorithms” Metrologia, vol(45), pp.327-334,2008,

Comparison of highly-stable optical frequency transfer in a single bidirectional and double unidirectional fibers

P. Włodarczyk, P. Krehlik, Ł. Śliwczyński
Faculty of Computer Science, Electronics and Telecommunications
AGH University of Science and Technology
Krakow, Poland

***Abstract*—The stability of the transmitted optical frequency in a single bidirectionally operated fiber was compared with stability in a link consisting of two separate unidirectional fibers. The measurements were performed in a standard closed-loop system canceling the fiber induced phase noise. It was found that phase fluctuations in the higher frequency band (acoustic noise) are well suppressed in both configurations (single bidirectional fiber and separate unidirectional fibers). The long-term drifts however are not fully compensated in a link consisting of two separate unidirectional fibers, but still about two orders of magnitude noise reduction was observed in comparison with not compensated transfer.**

Keywords—optical frequency transfer; fiber optics; dark fiber; bi-directional link;

I. INTRODUCTION

Due to the growing interest in the distribution of time and frequency signals, several fiber optic systems designed for this purpose have been built in the recent years. It is demonstrated that best results for this type of systems are obtained by using so called dark fiber operated bidirectionally to ensure the highest symmetry of phase fluctuation in transmission in both directions. However, in many practical situations the only possibility for fiber-optic frequency transfer is to use a channel in a DWDM (Dense Wavelength Division Multiplexing) telecom network, which as a rule uses two parallel fibers for both directions. Therefore it is advisable to compare the stability of the transmitted optical frequency in a single bidirectionally operated fiber with a link consisting of two separate unidirectional fibers, to examine behavior of optical

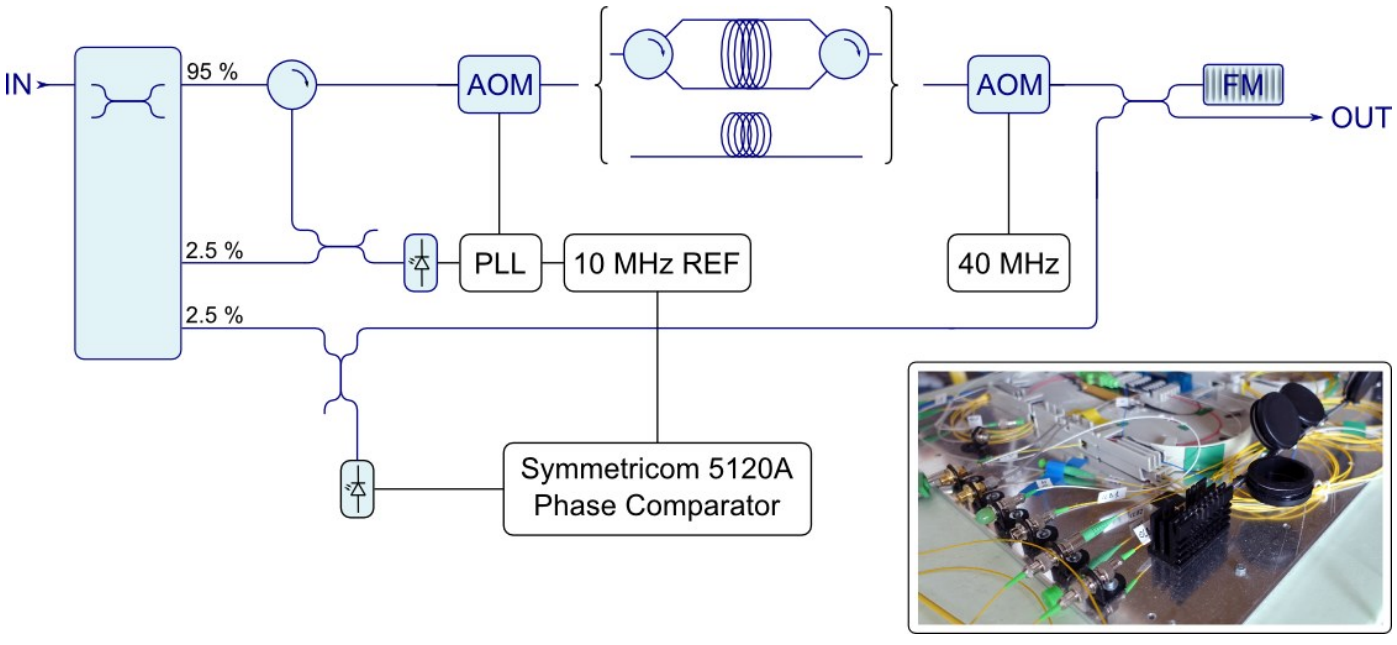

Fig. 1. Block diagram of the experimental setup and its photo (inset). Description in text.

This work was supported by the EMPIR initiative co-funded by the European Union's Horizon 2020 research and innovation programme and the Participating States via project 15SIB05.

cable itself. This kind of measurement should allow to determine the stability limit for such a link, excluding influence of DWDM equipment, which is always present in a real network (i.e. optical amplifiers, WDM splitters etc.). This kind of experiments were carried out previously [1, 2], but the results were not consistent. Thus, we have decided to undertake more research based on similar approach to enrich the experimental data for future analysis and discussions.

II. EXPERIMETAL SETUP

The measurements were performed in a standard closed-loop system canceling the fiber induced phase noise [3]. The block diagram of the experimental setup is shown in the Fig. 1.

Fig. 2. Map of fiber optic link used in the experiment. The link is 60 km long and runs through urban areas of Krakow

In the local station the input optical frequency signal is directed to the system of couplers, where it is splitted into three beams. The main beam (95% of input power) enters the circulator, goes through the first acousto-optic modulator (AOM) and is transmitted by optical fiber to the remote station. The other two beams (2.5% of input power each) are used by the link stabilization subsystem and as an additional output of the optical frequency. At the remote station, the beam passes through the second acousto-optic modulator and then is reflected by the Faraday's mirror. Then it returns through the acousto-optic modulator to the optical fiber link and to the local station. The coupler placed in the remote station is used to direct part of the light to the station's output ports. The returned beam, after reaching the local station, goes through the first acousto-optic modulator second time and is separated by the circulator. Subsequently it is directed to the phase stabilization subsystem, where it is combined with the reference optical frequency beam. The resulting beam is shone on the photodetector. Since both AOMs are driven by a signal with a frequency of approximately 40 MHz, the generated beat note has frequency of about 160 MHz (the beam passes twice through each of the modulators). The phase of the obtained signal conform to phase disturbances of the optical carrier transmitted in the fiber loop (roundtrip). It is stabilized by means of a phase locked loop (PLL) that controls the first of the modulators. A 10 MHz oven controlled quartz oscillator is used as a reference. Assuming that the optical link is reciprocal, the stabilization of the phase at the local station implies that the phase at the remote end of the link is also stabilized. The second AOM (in the remote station) is used to avoid the impact of backscattered light in the optical fiber. The light resulted from the backscattering, similarly to the returned, useful, optical frequency signal, goes to the stabilization subsystem, where it generates undesirable beat note. However backscattered light passes only through one of the AOMs twice, so the undesirable beat note has an 80 MHz frequency and can be removed using a simple electrical filter. Because in the presented experiment both stations are located in one laboratory, it is possible to compare the stability of the transmitted optical carrier directly with the reference signal. This is done by combining both beams in the coupler and then directing the light on the photodetector (bottom part of the drawing). The resulting beat note has a frequency of 80 MHz and its phase stability conforms to the stability of the optical frequency in the remote station. It is measured using Symmetricom 5120A phase comparator.

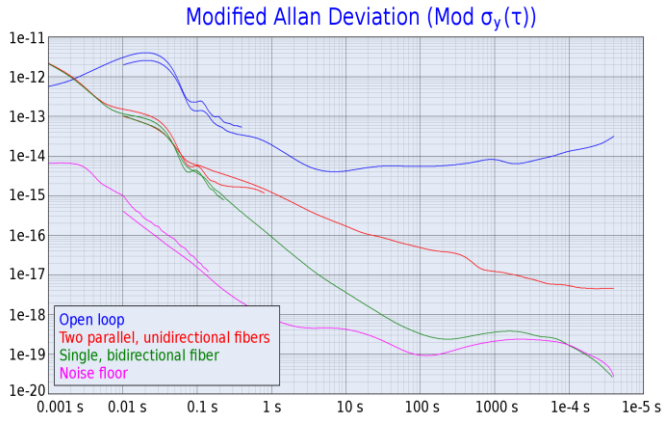

Fig. 3. Stability of optical frequency transfer through the investigated optical links.

Frequency transfer stability was evaluated both in a single-fiber configuration and in two parallel optical fibers. To obtain configuration with two parallel fibers optical circulators were used to split the signals into two adjacent fibers placed in the same cable. In both cases a real, 60 km long fiber optic link, running through urban areas of Krakow, was used (Fig. 2). The link starts in the vicinity of the city center and runs along Krakow's ring road to the nearby small town. The link is mainly underground, but it has few short sections running along telecommunication shafts inside buildings. As a part of real infrastructure it also runs through some telecom stations. As investigated link formed a loop, both ends of optical fiber were available in laboratory. It allowed to conveniently measure the stability of transferred optical frequency using phase comparator. The transmission stability was also measured in non-stabilized (open loop) link. In this case the experimental setup was modified in such a way that both acousto-optic modulators (marked as AOM's in Fig. 1) were driven from the 40 MHz oscillator.

III. RESULTS

The stability of the optical frequency transfer through the investigated link is shown in the Fig. 3. For each link configuration two measurements were taken. Firstly the data were recorded for a 60 hours long period of time with 100 samples per second sample rate. Phase difference recorded in

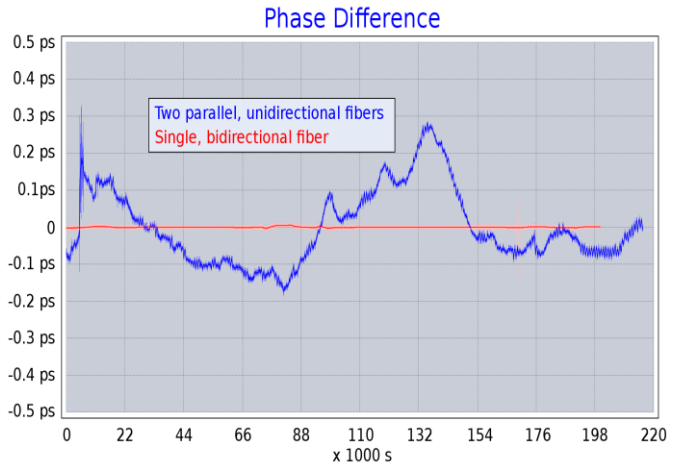

Fig. 4. Phase fluctuation of the optical frequency transferred through the investigated optical links.

this measurement is plotted in the Fig. 4. To complete the modified Allan deviation plot for short observation period the second, short measurement with 1000 samples per second sample rate was taken. Based on the recorded data, it was found that phase fluctuations in the higher frequency band (acoustic noise) are well suppressed in both configurations (single bidirectional fiber and separate unidirectional fibers). The long-term drifts however are not fully compensated in a link consisting of two separate unidirectional fibers. The possible explanation of obtained results is that the acoustic noise is generated mostly by ground vibrations along the ring road and is coupled almost equally to all adjacent fibers in the same cable, so it may be compensated. The long-term drift is caused mainly by the temperature drifts of the fibers. While temperature difference between two adjacent fibers in the underground cable should remain negligible there are some sections of the link located in telecom stations connected with patch cords. This patch cords may be spatially separated and therefore susceptible to temperature gradients, causing uncompensated thermal drift. Although the result in a link consisting of two separate unidirectional fibers was noticeably worse than in single fiber configuration, still about two orders of magnitude noise reduction was observed in comparison with a one way, not compensated transfer.

IV. CONCLUSION

In this paper we presented comparison of the stability of the transmitted optical frequency in a single bidirectionally operated fiber with a link consisting of two separate unidirectional fibers. As it was expected the observed stability of the optical frequency transferred through the link with configuration employing two separate fibers was lower than through the single fiber bidirectional link. However it still offers much better performance than open loop approach, and may be useful in many applications that do not require the highest possible accuracy. Therefore we plan to run similar experiment in real DWDM telecom network in the future to investigate degradation of the optical frequency transfer stability in comparison with dark fiber link.

REFERENCES

[1] P. A. Williams, W. C. Swann, N. R. Newbury, "High-stability transfer of an optical frequency over long fiber-optic links", J. Opt. Soc. Am. B, Vol. 25, Issue 8, pp. 1284-1293

[2] A. Bercy et al., "Two-way optical frequency comparisons at 5·10-21 relative stability over 100-km telecommunication network fibers", Phys. Rev. A 90, 061802(R)

[3] L.S. Ma, P. Jungner, J. Ye, J.L. Hall, Delivering the same optical frequency at two places: accurate cancellation of phase noise introduced by an optical fiber or other time-varying path, Opt Lett. 1994 Nov 1;19(21):1777-9.

Timing jitter characterization of dual-comb system via TWTFT method*

Honglei Yang*, Shengkang Zhang, Huan Zhao, Hongbo Wang, Xueyun Wang, Haifeng Wang, Hang Yi, Wenzhe Yang, Shuwei Wang
Science and Technology on Metrology and Calibration Laboratory
Beijing Institute of Radio Metrology and Measurement
Beijing China
*yhlpc@163.com

***Abstract*—We present a method of timing jitter characterization for dual-comb system. The concept of two-way time and frequency transfer (TWTFT) is adopted for cancelling path drift. The method is verified by a numerical simulation. Based on simulation, we investigated the effect on the precision from the number of fitting points, and quantizing noise as well. The simulation could enhance the understanding of timing jitter characterization of dual-comb system, and dual-comb time and frequency transfer. The proposed method could significantly reduce the environmental variation when confronting with remote combs and clocks.**

Keywords—Timing Jitter; Time and frequency transfer; Mode-locked laser

I. INTRODUCTION

In dual-comb system, timing jitter is of utmost crucial for promoting diverse scientific applications, such as high-precision absolute distance measurement [1,2], high-speed and high-resolution molecular spectroscopy [3], time and frequency distribution [2,4,5], to name a few. Characterization of timing jitter could give a general performance evaluation of dual-comb system [6].

Basic timing jitter of mode-locked lasers is revealed by the phase noise of microwave signals converted from the optical pulse trains by fast photodiodes. This detection method only achieves picosecond-level precision, due to the excess phase noise by amplitude-to-phase conversion in the photodetection and microwave amplification, and shot noise and thermal noise in the photodetectors [7]. The alternative balanced optical cross-correlation enables extremely high timing resolution up to several attoseconds over the Nyquist frequency with minimal influence of intensity noise [8]. The balanced optical cross-correlation method is usually implemented in laboratory or in projects via optical fiber links for precise synchronization of mode-locked lasers. Due to the identical repetition rate of mode-locked lasers is configured in these systems. Delicate delay control of the femtosecond pulses is needed, which is complex and additional process. Besides, dispersion managements of long fiber links are troublesome and prerequisite for precise timing jitter measurement and timing synchronization [9]. To some extent, this method is not suitable for timing jitter measurement of remote mode-locked lasers.

Here we present a method of timing jitter characterization for dual-comb system combining the concept of two-way time and frequency transfer, which allows characterization between remote mode-locked lasers or clocks.

II. EXPERIMENTAL SETUP

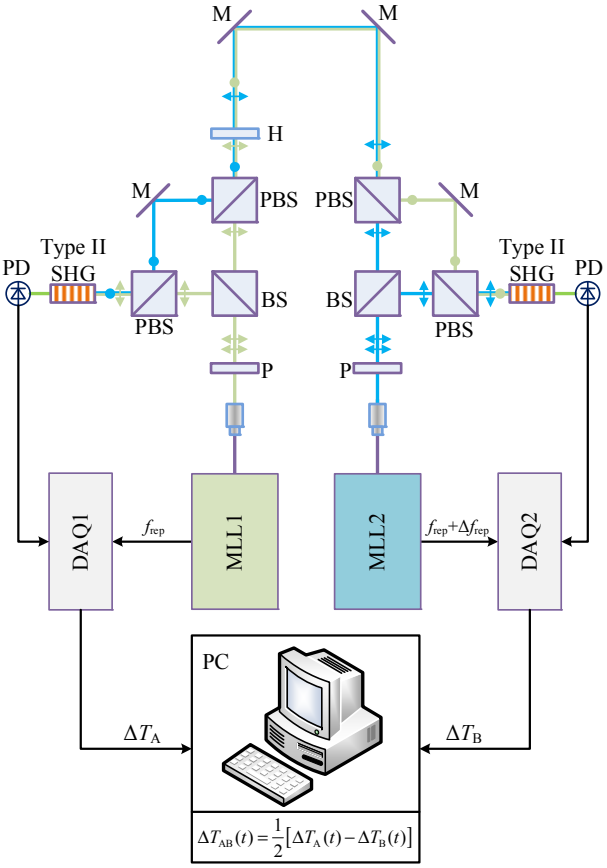

Fig. 1. Simplified schematic of TWTFT-based timing jitter characterization of dual-comb system. MLL, mode-locked laser; P, polarizer; BS, beam splitter; PBS, polarized beam splitter; H, half-wave plate; M, mirror; Type-II

SHG, Type-II second harmonic generation; PD, photodiode; DAQ, data acquisition board; The dots and double-side arrows denote beam polarizations.

The proposed timing jitter characterization system is illustrated in Fig. 1. The concept of TWTFT is adopted in order to cancel path drift. Two mode-locked lasers with slightly detuned repetition rates send pulse trains to the other along common free-space link. In each side periodic detuned pulses lead to linear optical sampling, which achieves femtosecond-level pulse-to-pulse scanning. This releases the requirement of femtosecond pulse superposition in balanced optical cross-correlation. Moreover, flexible free-space link avoids fiber dispersion, which is promising in ground-satellite time and frequency transfer and space timing network in the future. The down-converted periodic correlation signals of pulses, extracted by means of Type-II second-order harmonic generation, provide the timing jitter information, and are recorded by high-speed data acquisition boards referenced to individual mode-locked lasers.

For verification, we conducted a preliminary numerical simulation in one-way transfer configuration in the assumption of no path drift due to environmental variation. In practice, two-way reciprocal transfer configuration, which has been adopted in optical TWTFT, is set to cancel the path drift caused by refractive index change due to environmental variation.

III. RESULTS

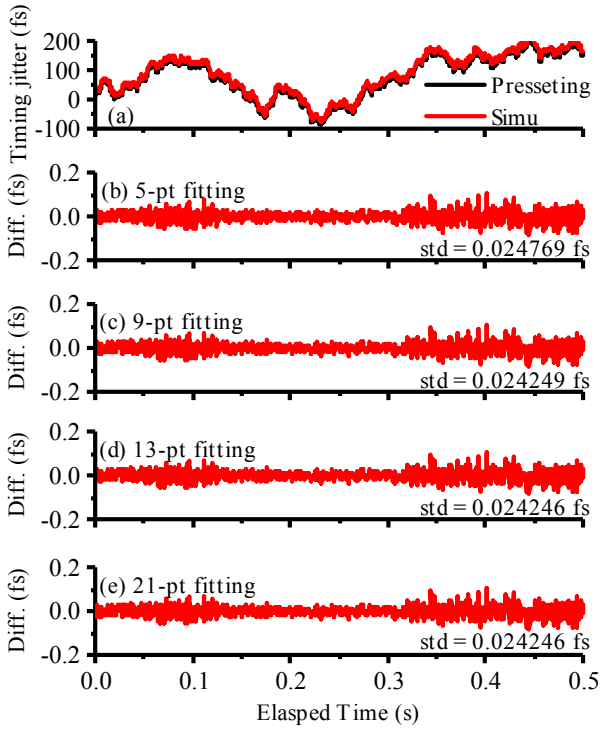

Fig. 2. (a) Comparison between presetting timing jitter and simulated results that are plotted with 10-fs offset for clear view; (b-e) The simulated results in the case of different number of fitting points without quantizing noise.

From Fig. 2(a), the simulation being in well agreement with presetting timing jitter verifies the proposed characterization method. Based on simulation, we investigated the effect on the precision from the number of fitting points. As depicted in Figs. 2(b-e), fitting with 9 data points is optimized assuming unlimited quantizing resolution. This, in some extent, shows the limit with no digitizing.

Figures. 3 exhibit the effect from quantizing noise. The number of fitting points was fixed to 9. The simulation indicates at-least 12-bit data acquisition board is needed. Although the simulation could achieve high precision, the practical measurement could only reach around 1-fs precision due to environmental variation and optical-electronic conversion noise [4,5]. The simulation could enhance the understanding of timing jitter characterization of dual-comb system, and dual-comb optical time and frequency transfer. The proposed method could significantly reduce the environmental variation when confronting with the timing jitter measurement between remote mode-locked lasers or clocks. Moreover, it also avoids calibration in balanced optical cross-correlation.

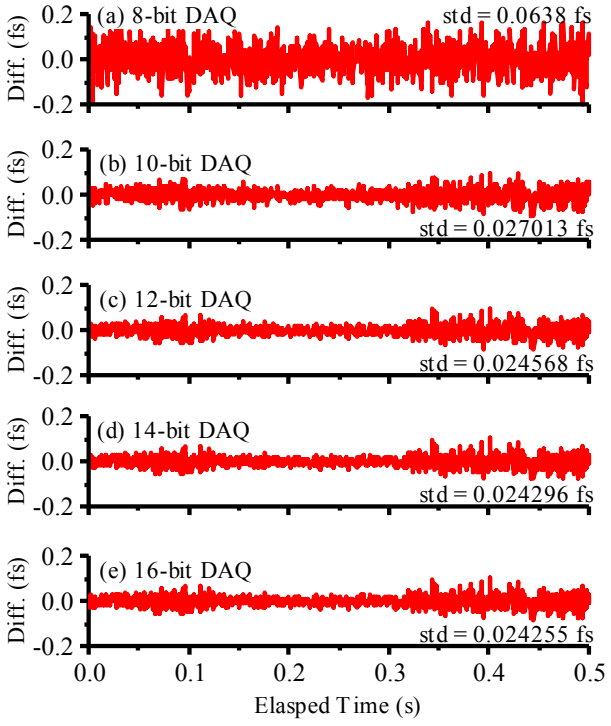

Fig. 3. The simulated results in the case of different digitizing resolutions via 9-point fitting.

IV. CONCLUSIONS

We present a method of timing jitter characterization for dual-comb system combining the concept of two-way time and frequency transfer for cancelling path drift in practice. The preliminary numerical simulation verifies the method and shows that 9-point fitting and 12-bit digitization are necessary. The method allows timing jitter characterization between remote mode-locked lasers or clocks and is promising in ground-satellite time and frequency transfer and space timing network in the future.

REFERENCES

[1] I. Coddington, W. Swann, L. Nenadovic, and N. Newbury, "Rapid and precise absolute distance measurements at long range," Nat. Photonics 3, 351-356 (2009).

[2] H. Zhang, H. Wei, X. Wu, H. Yang, and Y. Li, "Absolute distance measurement by dual-comb nonlinear asynchronous optical sampling," Opt. Express 22, 6597-6604 (2014).

[3] I. Coddington, W. Swan, and N. Newbury, "Coherent multiheterodyne spectroscopy using stabilized optical frequency combs," Phys. Rev. Lett. 100, 013902 (2008).

[4] F. Giorgetta, W. Swan, L. Sinclair, E. Baumann, I. Coddington, and N. Newbury. "Optical two-way time and frequency transfer over free space," Nature Photonics, 7(6): 434-438 (2013).

[5] J. Deschênes, L. Sinclair, F. Giorgetta, W. Swan, E. Baumann, H. Bergeron, M. Cermak, I. Coddington, and N. Newbury. "Synchronization of distant optical clocks at the femtosecond level," Physical Review X, 6, 021016 (2016).

[6] H. Yang, H. Wei, H. Zhang, K. Chen, Y. Li, V. Smolski, and K. Vodopyanov, "Performance estimation of dual-comb spectroscopy in different frequency-control schemes," Appl. Opt. 55, 6321-6330 (2016).

[7] J. Kim and F. X. Kärtner, "Attosecond-precision ultrafast photonics," Laser & Photon. Rev. 4(3): 432-456 (2010).

[8] J. Kim, J. Chen, J. Cox, and F. X. Kärtner, "Attosecond-resolution timing jitter characterization of free-running mode-locked lasers," Opt. Lett. 32(24): 3519-3521 (2007).

[9] J. Lee, Y. Kim, K. Lee, S. Lee and S. Kim, "Time-of-flight measurement with femtosecond light pulses," Nat. Photonics 4, 716-720 (2010).

GNSS antenna multipath effects

G.D. Rovera, M. Abgrall, P. Uhrich
LNE-SYRTE, Observatoire de Paris, Université PSL,
CNRS, Sorbonne Université
61 avenue de l'Observatoire 75014 Paris, France
daniele.rovera@obspm.fr

P. Defraigne, B. Bertrand
Observatoire Royal de Belgique
Avenue Circulaire, 3, B-1180 Brussels, Belgium

***Abstract*—This paper is presenting results from experiments aiming at quantifying the multipath effects on GNSS antennas in some moderate and extreme implementation cases. In Observatoire de Paris (OP), the multipath due to a metallic plate nearby the GNSS antenna might generate a relative calibration offset reaching about 3 ns on P-code delays. But proper Common-View (CV) software is able to get rid of such offsets, reaching P3 CV deviation mean values below 100 ps. At the Royal Observatory of Belgium (ORB), with three different receiver types, different antenna positions are showing that P-code offsets might reach about 350 ps in P1 and 750 ps in P2, hence a significant bias in relative calibration results. The results are showing that a more extensive work is required before trying to fix an upper limit for the multipath uncertainties in the guidelines uncertainty budget for GNSS relative calibration.**

Keywords—GNSS time transfer; multipath; uncertainty.

I. INTRODUCTION

For a better organization of the network of laboratories contributing to the Temps Atomique International (TAI), the Bureau International des Poids et Mesures (BIPM) released a document aiming at homogenizing Global Navigation Satellite System (GNSS) link calibrations called "BIPM guidelines for GNSS calibration" [1]. The Working Group on GNSS of the Consultative Committee on Time and Frequency (CCTF) formally approved these guidelines in 2017. Among other elements inside this document, BIPM is providing a comprehensive model of uncertainty budget for GNSS link calibration. One of the components is the uncertainty related to multipath of the satellite signals, which can be different in each of the sites visited by the traveling station. But, even if in the past there were some papers on impedance match effects in antenna cables for time transfer [2, 3], there are only scarce published works on such effects at antenna level, and the quantization of such uncertainties remains to be estimated more precisely.

In this paper, we propose in Section 2 a series of tests between two GNSS receiving chains in common-clock set-up, with one of the antennas placed either in a normal environment, or in an environment generating multipath signals at close range. This experiment is carried out in LNE-SYRTE at Observatoire de Paris (OP). On the other hand, a mobile antenna connected to three different receivers is placed in different environments at the Observatoire Royal de Belgique (ORB), and the multipath is in each case estimated from the pseudorange differences with respect to a fixed reference station. This experiment is documented in Section 3. The goal of this paper is an attempt to provide a quantitative analysis of the results, in preparation of some upper limit computation of multipath effects on GNSS antennas. This should eventually lead to a better estimate of the uncertainties to be used in the guidelines for a GNSS calibration link uncertainty budget.

II. SHORT RANGE EFFECT IN OP

A. Location and equipment

For this experiment, all data are issued from two GNSS receiving chains usually part of the OP traveling equipment devoted to relative calibration activities. Both ensembles of GNSS receiver, antenna cable and antenna were implemented on top of the A building in OP campus, which is 32 m high. This location is currently prepared for the implementation of equipment for the Atomic Clock Ensemble in Space (ACES) project [4]. It is providing an improved clear panoramic view compared to the site on top of the B building currently used for OP operational time transfer. Fig. 1 is showing the satellites in view from reference position at the start of the experiment. The reference clock signals up there are based on the current UTC(OP) signal, which is exhibiting the short term stability of an active H-maser and the long term stability of fountain frequency standards [5]. Both GNSS chains were implemented in a common-clock set-up.

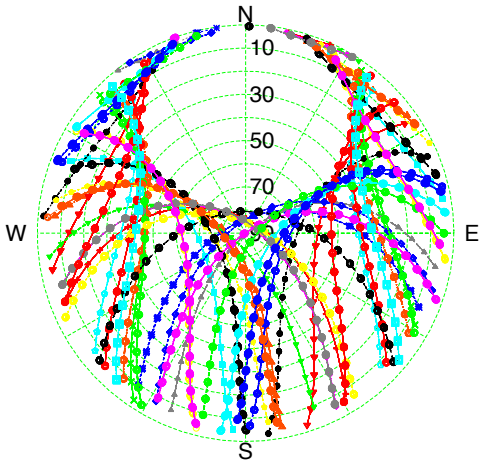

Fig. 1. Diagram of satellites in view from antenna reference position in OP.

The GNSS receivers were two Septentrio PolaRx4TR geodetic receivers called OPM3 and OPM7, OPM3 being the reference receiver. Antenna cables were of similar type of 25 m length. Both antennas were Choke-Ring Ashtech antennas. We used GPS geodetic RINEX files, transformed into CGGTTS

format by using the ORB software [6] for P3 Common-Views (CV) between both chains. Note that accurate calibration is not an issue here, because we only want to detect potential changes due to multipath between given relative antenna positions.

B. *Experimental CV results*

In order to build a reference set of CV between both receivers, OPM7 antenna was first implemented about 2 m away from OPM3 antenna in a similar panoramic view as in Fig. 1. OPM7 antenna was then moved down to Position 1 in the middle of the metallic platform, which is surrounded by the protection fence made of wooden plates fixed on a metallic structure. The third part of the experiment was called Position 2, where OPM7 antenna is still down on the metallic platform, but about 50 cm away from a metallic plate of about 60 x 150 cm. Fig. 2 is a picture of Position 2 implementation, where the metallic platform and the metallic plate can be seen. With respect to the reference position where about 923 satellite tracks are available per day in CGGTTS files, we obtained from more than 10 d of continuous data collection an average downsize of satellites in CGGTTS files of about 216 in Position 1 (≈ 23 %) and about 285 in Position 2 (≈ 31 %).

Fig. 2. Picture of Position 2 for OPM7 antenna, down on the metallic platform alongside a large metallic plate.

Fig. 3 is showing the resulting P3 CV between both receiving chains, after alignment of the Reference position CV mean value on 0. For this computation based on CGGTTS data, we used the CV software developed in LNE-SYRTE [7], and the P1 and P2 internal delays of OPM3 and OPM7 issued from former calibration results. The antenna coordinates were also computed especially for each position. As expected, Fig. 3 is showing first an augmentation of the filtered CV noise. A small offset is also observed in the CV mean value, as shown in Table I, which summarizes the numerical results. This Table also provides the impact on reference position CV results when applying an elevation cut-off of either 10 ° or 20 °. We see that the CV mean value is only noticeably changed for an elevation cut-off of 20 °, reaching an offset of about 107 ps, which is remaining small enough with respect to the current state of the art CV uncertainty. But the CV noise is clearly affected by the multipath signals as can be seen for both Positions 1 and 2. After averaging out the outliers in the CV computation, the number of daily CV in Position 2 is still larger than the number of daily CV for an elevation cut-off of 20 °, even if this large cut-off is less noisy than Position 2. This is confirming that the noise increase is mostly coming from multipath.

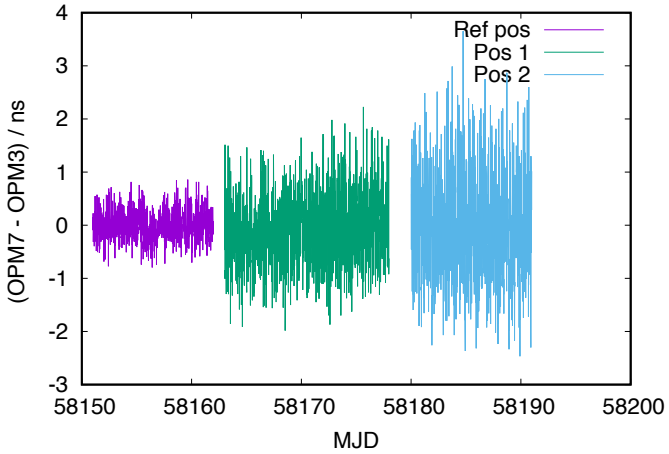

Fig. 3. Resulting P3 CV between OPM7 and OPM3 for Reference position (lilac), aligned on the 0 mean value, Position 1 (green) and Position 2 (light blue) for OPM7 antenna.

TABLE I. EFFECTS ON FILTERED CV RESULTS

OPM7 – OPM3 CV	Mean Value Offset (ns)	Standard Deviation (ns)	Average number of daily CV
Reference position	0	0.28	878
Position 1	- 0.068	0.67	631
Position 2	- 0.033	1.03	590
10° Elevation cut-off	0.035	0.26	720
20° Elevation cut-off	0.107	0.28	567

C. *Experimental P-code offset results*

We also computed P1-code and P2-code differences based on RINEX files, in order to quantify the multipath effects on relative calibrations, assuming OPM7 as traveling equipment. Fig. 4 is showing the P1-code and P2-code differences when OPM7 antenna is located in Position 2. We can clearly see the large impact of the severe multipath generated by the metallic plate near the antenna, as the same ensemble of data is repeated periodically every day about 10 ns away from the expected results.

In the case we would use the data collected from OPM7 in either Position 1 or Position 2 for a relative calibration of the reference receiver OPM3, we would get the offsets with respect to the expected delays given in Table II. Without a proper filtering, such multipath would bias the relative calibration results. As can be seen in the Table, in the extreme case of Position 2, the calibration results might be biased by about 3 ns on both P-codes, both Positions having an impact on P1 – P2 at about 0.4 ns and 0.5 ns, respectively.

Note however that these multipath offsets do not appear in the CGGTTS CV computed in the former Section (green and light blue plots in Fig. 3), because the multipath data were properly identified as outliers by the LNE-SYRTE CV software and averaged out accordingly, at the additional cost of about 11 % of the daily CV for both Positions 1 and 2.

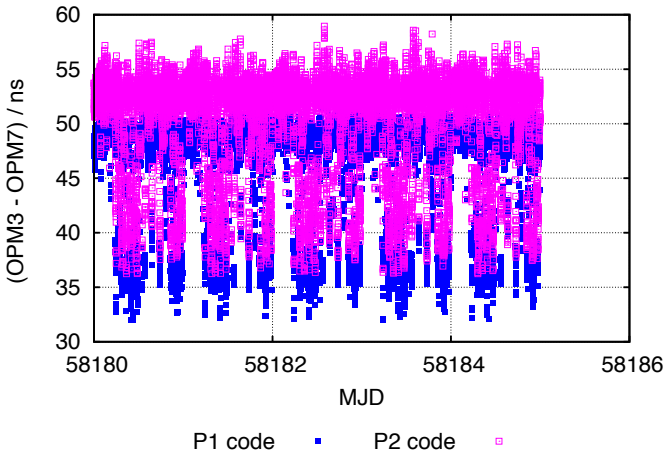

Fig. 4. Effect of multipath from the metallic plate at close range on the P1-code and P2-code relative calibration between OPM3 in reference position and OPM7 in Position 2.

TABLE II. POTENTIAL CALIBRATION OFFSETS DUE TO MULTIPATH.

OPM7 – OPM3	P1-Code (ns)	P2-Code (ns)	P1-P2 (ns)
Reference delays	49.908	53.402	- 3.494
Position 1 delays	49.077	52.983	- 3.906
Offset Position 1	*- 0.831*	*- 0.419*	*- 0.412*
Position 2 delays	46.457	50.467	- 4.010
Offset Position 2	*- 3.451*	*- 2.935*	*- 0.516*

III. MULTIPATH EFFECTS AT ORB

A. Description of the setup

The second part of the experiment takes place at ORB where two receiving chains are also used. The first one is the fixed reference station BRUX: its antenna is located on the top of a dome with an unobstructed view to the sky within 360° circumference and without any other antenna in the vicinity. In order to mitigate as much as possible the effect of reflections, radio frequency absorbing material was applied at the level of the support of the antenna. The receiver of the BRUX station is a Septentrio PolaRx4TR.

Besides the reference station, another GNSS receiving chain with a mobile antenna shares a common-clock set-up. This antenna is a Sepchoke B3E6. An active power splitter divides the signal coming from the antenna to three different receivers, as described in Fig. 5. Subsequently, this set up enables to compare how different types of receivers deal with multipath effects and to look for the receiver-dependence on the impact on GNSS pseudorange biases. These three receivers are: one Septentrio PolaRx4TR (called ZTB3, and so the same model as the BRUX receiver), one Septentrio PolaRx2 (ZTBR) and one Ashtech Z-XII3T (ZTB1).

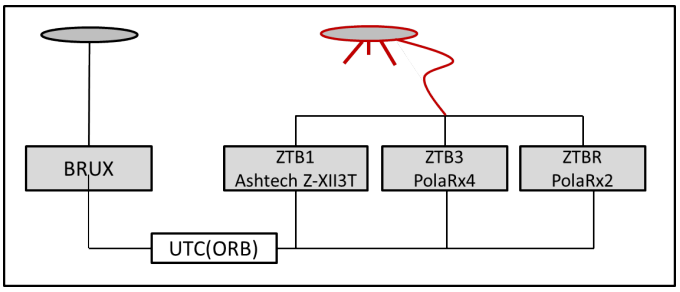

Fig. 5. Experiment setup at ORB. The red antenna has been installed in three different sites. The station BRUX is used as fixed reference.

In a similar way as what has been described in the previous Section, the mobile antenna was moved to three different positions. On the first site a metal plate laying under the antenna reduces the effect of reflections. Two other active GNSS antennas are in the close neighborhood of the travelling antenna, the three antennas being separated by a distance of only 0.5 m (considering the antenna phase centers as reference). This setup allows highlighting possible coupling effects between antennas. Moreover, as can be seen in Fig. 2 (1), the antennas are surrounded by a triangle-shaped zinc roof with a slope of 45° oriented towards the North.

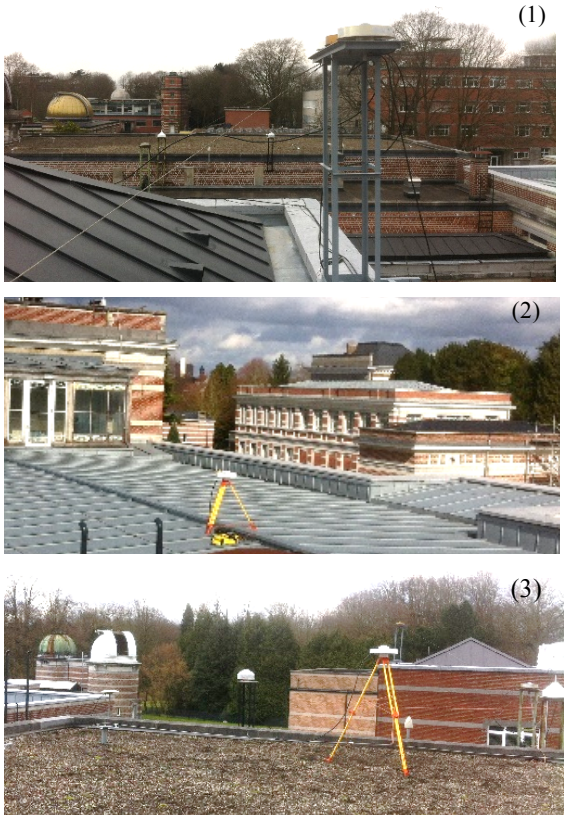

Fig. 6. Different sites of the mobile antenna at ORB.

In the second position, the antenna is located on a large quasi-horizontal zinc roof, see Fig. 2 (2). The antenna is fixed on a tripod at a height of 1m, without any plate just underneath the antenna anymore like in the first setup. The minimum distance between the closest edge of the roof and the tripod is at least 9m. The furthest edge is at a distance of 30 m. During

the test in this second position, the multipath mitigation option, initially enabled, was disabled the third day in the ZTB3 receiver.

Finally, for the sake of comparison, the antenna was implemented in quasi-ideal site. In this third position, the antenna is fixed on a tripod at the maximum height of 1.6 m above the roof and far enough from any other antenna (at least 3 m), see Fig. 2 (3).

B. Pseudorange P1 and P2 analysis

The differences between the pseudorange measurements of BRUX and each of the three stations connected to the mobile antenna are plotted in Fig. 7. In the series ZTB3-BRUX, the increase of noise during the second setup (red part) corresponds to the change in the receiver configuration of ZTB3 where the multipath mitigation option was deactivated. This option was then reactivated for the third setup (green part). The impact of the option multipath enabled/disabled on the pseudorange biases is less than 50 ps on P1 and P2. However it must be noted that we observed biases as large as 500 ps on C1 (not shown here) and on Galileo signals. The use of such option will therefore need some guideline, or at least a recommendation to not change it during the operational life time of the receiver.

In Fig. 7 we can observe that the last setup provides as expected the less noisy results. For all the setups the differences ZTB1-BRUX are the noisiest. This can be explained by the fact that these differences concern two receivers of a different manufacturer (Ashtech and Septentrio), while the two other sets of differences are between two Septentrio receivers.

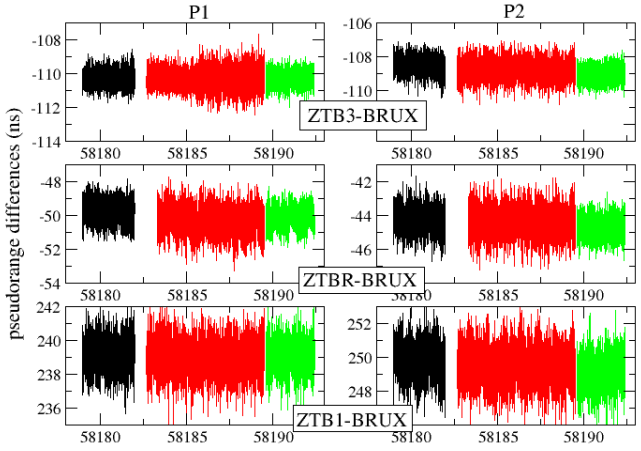

Fig. 7. Pseudorange differences between each receiver connected to the traveling antenna and the fixed reference BRUX.

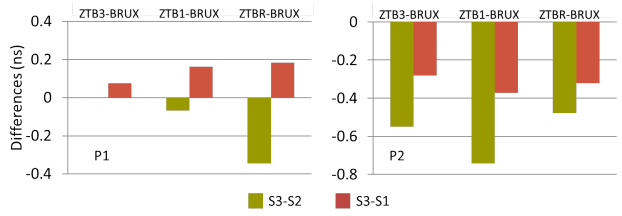

Fig. 8. Change of pseudorange differences from setup 1 to 3 (S3-S1), and from setup 2 to 3 (S3-S2).

Fig. 8 displays the mean values of the differences obtained between setups 1 and 3, and between setups 2 and 3. These differences are significantly larger for P2 than for P1. They reach the level of 350 ps on P1, and up to 750 ps on P2. The setup 2, i.e. when the antenna tripod is placed on a metallic roof, provides the largest differences with respect to our 'quasi-ideal' setup 3.

It can also be seen in Fig. 8 that the biases induced in the pseudorange measurements when moving the antenna in different positions are receiver-dependent. Indeed, if the trend is similar, the magnitude of the bias varies from one receiver to another by up to 300 ps. This can be explained by the sensitivity of the receiver correlator to multipath.

IV. Conclusion

This work aimed at quantifying the impact of multipath signals on GNSS pseudorange biases. Two sets of experiments were organized. The first experiment was carried out at OP, between two similar GNSS receiving chains located on top of a building, one of the antennas being placed either in a nominal environment, or in an environment generating multipath at close range. As expected, the increase of multipath is leading to a noise increase in the dual-frequency filtered P3 CV, and to an increase in satellite tracks averaged out daily by the efficient LNE-SYRTE CV processing. In addition, the P3 CV mean values are changed by small offsets below 100 ps. But the offset of close range multipath on P-code relative calibration data might reach about 3 ns in the extreme case of a metallic plate nearby the antenna. A second experiment was carried out at ORB, where a mobile antenna connected to three different receivers was placed in three different environments. The pseudoranges measured on P1 and P2 were in each case compared with respect to a fixed reference station. The differences between the three setups are visible on both P1 and P2, but significantly larger on P2, where it reached 750 ps in the worst case. Differences up to 300 ps between the three receivers connected to the same mobile antenna were also pointed out.

We do not pretend to have considered all types of GNSS antennas and receivers comprehensively. Moreover, these tests are remaining limited to the existing available equipment in both our laboratories. But we assume that the results obtained are consistently representative of a common situation in time metrology laboratories. Therefore, this study is clearly requiring additional work and analysis, in order to eventually allow for setting some upper limits in the multipath uncertainties in the GNSS relative calibration BIPM guidelines uncertainty budget.

Disclaimer

Product names and model numbers of the equipment are included for reference only. No endorsement or criticism is implied.

References

[1] Bureau International des Poids et Mesures, "BIPM guidelines for GNSS calibration", v3.2, 15/02/2016.

[2] F.G. Ascarrunz, S.R. Jefferts and T.E. Parker, “Earth station errors in two-way time and frequency transfer”, 1998 *IEEE Trans. Instrum. Meas.* **46** 205–8.

[3] M.A. Weiss, F.G. Ascarrunz, T.E. Parker, V. Zhang, and X. Gao, “Effects of Antenna Cables on GPS Timing Receivers”, Proc. 1999 Joint Mtg. IEEE Intl. Freq. Cont. Symp. and 13th EFTF, Besançon, 1999, 259 – 262.

[4] M. Abgrall, Ph. Laurent, G. D. Rovera « Reference signal distribution for the ACES microwave link ground terminal at SYRTE », Proc. of the 2017 Joint Conference of the IEEE Intl. Freq. Cont. Symp. and of the 30th EFTF, Besançon, France, July 10-13, 2017.

[5] G.D. Rovera, S. Bize, B. Chupin, J. Guéna, Ph. Laurent, P. Rosenbusch, P. Uhrich and M. Abgrall, “UTC(OP) based on LNE-SYRTE Primary Frequency Standards”, Metrologia **53** (2016) S81-S88.

[6] P. Defraigne and G. Petit, “Time transfer to TAI using geodetic receivers”, Metrologia **40** (2003) 184-8.

[7] G.D. Rovera, B. Chupin, M. Abgrall and P. Uhrich, “A simple computation technique for improving the short term stability and the robustness of GPS TAIP3 Common-Views”, Proc. of the 26th EFTF, Pragues, Czech Republic, 2013.

DWDM Stabilized Optics for White Rabbit

Paul Boven
JIVE (Joint Institute for VLBI ERIC)
Dwingeloo, The Netherlands
Email: boven@jive.eu

***Abstract*—We describe the design of time distribution for the SKA using WR with DWDM optics. Included are accuracy estimates accounting for temperature, dispersion, calibration, attenuation, wavelength uncertainty and the Sagnac effect, and experimental results on long distance links.**

I. Introduction

The Square Kilometre Array (SKA) is a future radio telescope with an unprecedented sensitivity due to its large collecting area. In its first phase (SKA1) it will consist of two radio telescopes, each made up of numerous receptors (parabolic dishes for the SKA1 Mid-frequency array in South Africa, and arrays of log-periodic antennas for SKA1 Low-frequency array in Australia) that will act as interferometers. Phasing up these receptors requires the distribution of accurate timing signals over fiber distances of up to 173 km, with the fiber and some of the equipment exposed to the semi-desert environment. Meeting the SKA scientific objectives requires a timing distribution accuracy of better than 2 ns.

White Rabbit (WR)[1] is an extension of the IEEE 1588v2 protocol that allows for sub-ns accuracy in timing distribution over fiber for distances of up to 10 km. Our design for the SKA makes use of Dense Wavelength Division Multiplexing (DWDM) optics and filters to extend the reach, accuracy and stability of the links.

II. A Simplified Link Model

In this section, a simplified model of the operation of a WR link is introduced. WR works by synchronizing the clock of the slave device to the received timestamps of the master. It measures the round-trip time from the WR master to the WR slave device and back, and retards the slave clock by the one-way delay approximated from the round-trip. This is depicted in figure 1. Here the d_{TX} and d_{RX} are the fixed delays inside the hardware up to the optical port, while δ_{MS} and δ_{SM} are the one-way fiber delays from master to slave and back.

The WR standard proscribes the use of 1000Base-BX10 SFPs, which are BiDi (bi-directional) SFPs that make use of internal wavelength division multiplexing to use only a single strand of fiber. Having the outward and return signals on the same fiber is important for timing distribution as it ensures that there are no delay asymmetries due to fiber length differences. These SFPs transmit at a wavelength of 1490 nm for the 'Down' SFP, and 1310 nm for the complementary 'Up' SFP.

The speed of propagation (group velocity) in fiber depends on the wavelength, and the slight difference in propagation

Fig. 1. A simplified link model for WR

speed for the two wavelengths in use is compensated for by the WR calibration value α, with $|\alpha| \ll 1$:

$$\alpha = \frac{\delta_{\mathrm{MS}}}{\delta_{\mathrm{SM}}} - 1 = \frac{v_g(\lambda_{\mathrm{S}})}{v_g(\lambda_{\mathrm{M}})} - 1$$

where δ_{MS} is the propagation delay in the fiber from WR master to slave, δ_{SM} the delay in the opposite direction, and the v_g the group velocities for the laser wavelengths in use. Calibration (as described in [2]) is required to determine the fixed delays and α.

WR measures the total round trip time, and after subtracting the fixed delays, the fiber round trip time δ remains. From this, the fiber delay from master to slave is calculated:

$$\delta = \delta_{\mathrm{MS}} + \delta_{\mathrm{SM}}$$
$$\delta_{\mathrm{MS}} = \frac{1+\alpha}{2+\alpha}\delta$$

Finally, adding back in the appropriate fixed delays results in the one-way delay from master to slave, which the system compensates for.

III. Sources of Error

This section describes the influences on the timing performance of WR links, beyond the corrections from the previous section that are already implemented in WR. Most of these only become significant when one exceeds the 10 km range of the WR specification.

BiDi SFPs are available commercially in various combinations of reach and wavelength. Due to the higher attenuation at 1310 nm it becomes more economical to use SFPs that use e.g. the wavelength pair of 1490 nm and 1550 nm for longer links. Our initial tests were carried out with 60 km reach 1310 nm/1490 nm and 80 km reach 1490 nm/1550 nm SFP pairs.

A. Chromatic Dispersion

The first derivative of the group velocity as function of wavelength is the chromatic dispersion. For G.652.D fiber it is described and specified in ITU T-REC-G.652 [5]. Small

978-1-5386-5620-4/18/$31.00 ©2018 IEEE

changes in laser wavelength result in changes in the one-way delay, due to the chromatic dispersion. And whereas at 1310 nm the dispersion on G.652.D fiber is near zero, at the longer wavelengths required to operate over the SKA distances the dispersion is significant.

The temperature of the laser in an SFP directly affects its output wavelength. Tests with a small climate chamber and optical spectrum analyzer showed that these effects are very linear, with a slope of about 0.1 nm/K. Some of the SKA equipment will only have forced air-cooling with ambient air, with expected temperature ranges between 0°C and 50°C. These large temperature changes would result in significant timing distribution errors due to the dispersion and the long fiber distances.

Assuming calibration at the midpoint of 25°C, then a worst-case temperature excursion of 25°C on an 80km link, with $D_{1550\,\mathrm{nm}} = 17\,\mathrm{ps/nm{\cdot}km}$ would result in an error of $\frac{1}{2} L D_\lambda \mathrm{TC}_{\mathrm{SFP}} \Delta T = 1.7\,\mathrm{ns}$, a significant fraction of the allowed error budget. The factor $\frac{1}{2}$ comes in as the change in round trip time causes WR to compensate by $(\alpha+1)/(\alpha+2) \approx \frac{1}{2}$. The sign of the error will depend on whether the wavelength change occurs in the outward or return link.

Another factor is the uncertainty of the SFP laser wavelength itself, irrespective of its temperature. The IEEE 802.3ah standard allows these to differ from the nominal value by up to 10 nm at 1490 nm, and by 50 nm at 1310 nm. Although we did not encounter offsets that large, on the basis of our measurements the wavelength uncertainty for BiDi SFPs in our model is 1 nm (1σ).

Given the linear dependence between laser temperature and wavelength, it is in theory possible to compensate for this effect, and the author has contributed code[8] to the WR project to digitally read out the SFP laser temperature. But due to the large wavelength uncertainty between SFPs this approach would require measuring the wavelength of every individual SFP and this was ultimately considered not suitable for the large number of WR links in the SKA.

B. Equipment Temperature Effects

The WR equipment itself is also affected by its environmental temperature. In our design for the SKA we use WR switches as grand masters to distribute the timing signals from the central atomic clock ensemble to the receptors. In the SKA1-Mid, where link distances exceed 80 km, WR switches are also employed in shelters located along three spiral arms to re-generate the signals and provide additional fan-out to connect further dishes. The end points of each link, in both SKA1-LOW and SKA1-MID, are WR Zen [9] devices.

Measurements were carried out in a climate chamber and spanned the range of 0°C to 50°C in 10°C steps. The temperature coefficient for the WR switch was found to be 8 ps/K, for the WR Zen we found 4 ps/K. For WR switches used as a signal repeater, no discernible effect of temperature on the delay could be measured. In the SKA, the WR switches will be colocated with the hydrogen masers in a room with temperatures stabilized to within 1°C. In contrast, the WR-Zen in the SKA1-Mid dish pedestals will need to operate over the full range of 0°C to 50°C.

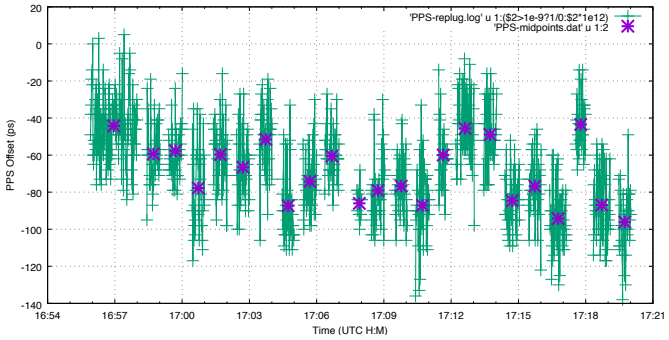

Fig. 2. Link Restarts

C. Link Restart

We found that every time a link WR link is restarted, e.g. by disconnecting and then reconnecting the fiber, or a power outage, there is a small jump in the PPS offset after the link gets re-established again. As depicted in figure 2, this variation is larger than the random variations on the link. The measurement was carried out by disconnecting the fiber for about 3 seconds every 2 minutes, and then measuring about 100 seconds of data to average out the 20 ps jitter of the time-interval counter in use. The depicted measurement series has a sample standard deviation of 17 ps, but in other runs larger and smaller variations were found, and 25 ps (1σ) is budgeted for this effect. The cause of the PPS jump on each link restart is likely the shift of the master and slave oscillators while unlocked, leading to a different bit-slice value, but this needs further research.

D. Variability of α

In 2015 we performed loop-back stability tests on already deployed fiber between the locations Klerefontein and Carnavron in South Africa. These locations are connected by 16.3 km of overhead G.652.D fiber in MASS (Metal Armored Self Supporting) configuration, suspended between regularly spaced high-voltage poles. This is the same configuration as intended for the SKA1. Using overhead fiber significantly reduces the installation costs, but one also foregoes the thermal shielding provided by burying the fiber.

As shown in figure 3, the outside temperature changes (middle panel) induce significant variations in the round trip time over the overhead fiber link (bottom panel). The top panel shows that the actual variation in the PPS difference between WR master and slave is significantly suppressed, but a diurnal component remains.

The thermo-optic delay coefficient of the fiber in question is measured to be $1.2 \cdot 10^{-5}/\mathrm{K}$, much larger than the thermal expansion for fused silica of $0.55 \cdot 10^{-6}/K$. WR assumes that the ratio of group velocities (expressed as α) of the outward and return signals remains constant. This is true for changes in length of the fiber. But for temperature changes, the change

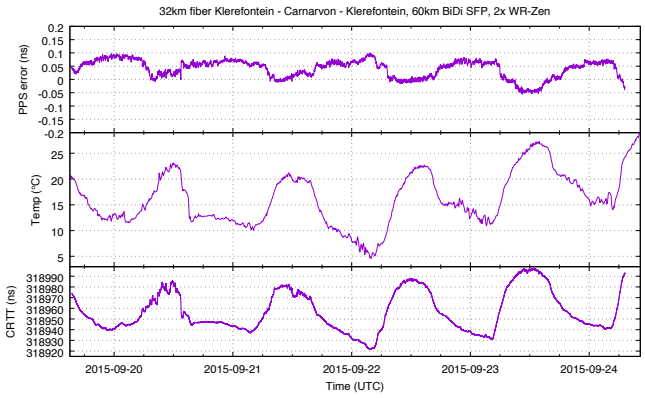

Fig. 3. Measurements on 32.6km of overhead fiber

TABLE I
MEASURED AND PREDICTED VALUES FOR α

λ(nm)	α (meas.)	α (calc.)	$d\alpha/dT$ (meas.)	$d\alpha/dT$ (calc.)
1310/1490	$2.7 \cdot 10^{-4}$	$3.1 \cdot 10^{-4}$	$-8 \cdot 10^{-8}$	$-7.5 \cdot 10^{-8}$
1490/1550	$1.8 \cdot 10^{-4}$	$2.1 \cdot 10^{-4}$	$-2 \cdot 10^{-8}$	$-2.1 \cdot 10^{-8}$
C21/C23	$5.6 \cdot 10^{-6}$	$6.5 \cdot 10^{-6}$	n.a.	$-5.5 \cdot 10^{-10}$

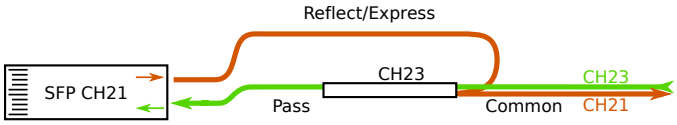

Fig. 4. Bi-Directional use of DWDM SFPs

in group velocity dominates over the temperature induced length variation, and is not precisely the same for each wavelength. The resulting dependency at 1310 nm/1490 nm was measured to be $-0.12\,\mathrm{ps/km\,K}$, and for 1490 nm/1550 nm only $-0.05\,\mathrm{ps/km\,K}$ on this particular fiber.

Temperature dependent Sellmeier coefficients [3] allow an approximation of the index of refraction and dispersion for fused silica. Then [4] can be used to calculate the waveguide contribution to the group delay for the single mode fiber in use. As the actual doping levels and profile are generally not available, some assumptions need to be made for this approximation:

$$\Delta = \frac{(n_1 - n_2)}{n_1} \approx 0.25\%, \quad n_{1,2} \approx n_{SiO_2}$$

The normalized frequency V can be expressed as

$$V = \frac{2\pi a}{\lambda_0}\mathrm{NA}$$

with the numerical aperture (NA) and the core radius a both available in the product data-sheet.

$$\frac{d(BV)}{dV} = A^2 - \frac{B^2}{V^2}, \quad A = 1.1428, B = 0.996$$

is an empirical formula to calculate the waveguide dispersion. The group index N_{eff} can now be calculated:

$$N_{\mathit{eff}}(\lambda_0) = n(\lambda_0) - \lambda_0 n'(\lambda_0) + n(\lambda_0)\Delta\frac{d(BV)}{dV}$$

The three terms in this equation represent the bulk refractive index of the material, the contribution due to the material dispersion, and that due to the waveguide dispersion.

Finally, the parameter α can be expressed as the ratio of the group indices of the two wavelengths in use on a WR link. Even with the assumptions and approximations above, the predicted values for α as shown in table I are reasonably close to our measurements. The temperature dependence of α is also calculated, and comparable to what we found in the field.

E. Delay Calibration

The calibration of the fixed delays that are part of the WR link can be done to high accuracy because no external equipment is required. The calibration itself consists of performing three round-trip measurements on short fibers, by reading out the value reported by the WR slave device. These measurements have a standard deviation of only 2 ps, and the resulting uncertainty can be reduced by averaging. The use of a fiber coupler adds a few ps as well. Our error model includes a conservative 10 ps per link.

F. Power Variations

SFPs themselves have a delay which is dependent on input power, as shown in [10]. There is a random spread in output power between SFPs, and SFP power will decrease due to aging. Assuming a worst case power difference of 3dB between a pair of SFPs on a link, and using the steepest part of the curve, a 30 ps uncertainty is assigned per link.

G. Sagnac Effect

Light co-rotating with the Earth's rotation arrives slightly later than one would calculate purely from the distance and group velocity in a fiber, and signals that counter-rotate (i.e. travel Westwards) will arrive slightly earlier, an effect known as the Sagnac[6] effect.

The SKA1-Mid will have baselines up to 150 km. At the latitude of the Karoo site (30.7 °S, and 1070 m elevation), an East-West link of 150 km will incur a Sagnac effect of 668 ps between its ends. As shown in [7], knowing the coordinates of the fiber stretches that make up the path to better than 200 m will keep the uncertainty in the contribution of the Sagnac effect to below 1 ps.

IV. WR WITH DWDM

The uncertainty of the wavelength inherent in BiDi SFPs, combined with the long distance links and dispersion, causes the allowed error budget to be exceeded. DWDM SFPs have a temperature controlled laser, and offer wavelength accuracy better than 0.1 nm. Unfortunately these are not available as bi-directional devices. Their receiving window does cover the whole C-band, which allows them to be used bi-directionally

TABLE II
ERROR BUDGET FOR WR LINKS (ALL VALUES IN PS)

	BiDi 1310/1490	BiDi 1490/1550		BiDi + TC		DWDM C21/C22	
	20 km	80 km	173 km	80 km	173 km	80 km	173 km
Delay Calibration	10	10	30	10	30	10	30
Link Restart	75	75	225	75	225	75	225
Received Power var.	30	30	90	30	90	30	90
Determination of α	75	75	225	75	225	75	225
Wavelength Uncertainty	141	1240	2683	1240	2682	160	346
Temp. dependence α	25	100	216	100	216	3	6
TC of WR Zen	94	94	94	94	94	94	94
TC of WR Switch	8	8	8	8	8	8	8
Uplink SFP Temp.	3	1400	1580	280	460	0	0
Downlink SFP Temp.	14	68	442	68	136	0	0
Total	**475**	3100	5550	**1915**	4600	**545**	**1174**

on a single fiber by adding a simple DWDM channel filter as shown in figure 4. The purpose of the filter is to ensure that the transmitter output, and any reflections, are kept out of the receiver. Commercially available filters have slightly worse performance at the neighboring channel, so in our design one channel is skipped as a guard. Due to availability we selected ITU channels C21 (1560.61 nm) and C23 (1558.98 nm) for the DWDM SFPs and filters.

The DWDM filter and its fiber leads could cause asymmetry on the link. The manufacturer of the filters specifies its fiber lengths to be equal within 0.05 mm which is less than 1 ps of difference. Any asymmetry due to the filter itself is canceled out by the opposing filter at the other end of the link, and no effect due to the use of the filters could be measured.

Having the wavelengths only 1.6 nm apart significantly reduces the value of α, which is 2.7E-4 for 1310 nm/1490 nm but only 6E-6 when using DWDM channels C21/C23. In our Sellmeier model the effect of fiber temperature on α is also significantly reduced.

V. ERROR BUDGET FOR WR LINKS

Using the model developed in the previous subsections, a complete error budget for a WR link can be drawn up. Summing the error contributions gives the (somewhat pessimistic) error model in table II. It lists the worst case error for a single 80 km link (the longest link distance in the SKA1-Low), and for the longest link (173 km) in SKA1-Mid which consists of three cascaded links with WR switches acting as repeaters in two locations. Randomly distributed effects are included as a 3σ contribution. All values in the table are in ps, and those sums that meet the 2 ns budget are indicated in bold.

VI. CONCLUSION

The presented design for timing distribution in the SKA using WR meets the requirement of 2 ns accuracy, even on the longest links and assuming the worst temperature excursions. The design uses DWDM optics to get sufficient stability for the laser output wavelength, as otherwise the combination of dispersion and length would cause timing distribution offsets exceeding the allowed uncertainty budget. For the shortest links, regular BiDi SFPs provide sufficient accuracy.

ACKNOWLEDGMENT

This work was carried out as part of the Signal and Data Transport (SADT) consortium effort, led by the University of Manchester, UK. We would particularly like to thank:

- NWO for funding this research through the NL-SKA project (184.033.109)
- ASTRON and SURFnet for providing access to dark fibers in the Netherlands
- ASTRON for access to climate chambers, EMI testing room and measurement equipment
- SKA-SA for their support and hospitality during the on-site tests
- The White Rabbit Open Hardware community
- C-Bass South for their weather station data
- SevenSolutions for providing us with the very first WR Zen-board prototypes and custom firmware modifications for these tests, and their ongoing support

REFERENCES

[1] T. Włostowski, *Precise time and frequency transfer in a White Rabbit network*, 2011, https://www.ohwr.org/documents/80
[2] G. Daniluk, *WR Calibration Procedure v1.1*, 2015, http://www.ohwr.org/documents/213
[3] G. Ghosh e.a., *Temperature Dependent Sellmeier Coefficients and Chromatic Dispersions for some Optical Fiber Glasses*, Journal of Lightwave Technology Vol. 12 No. 8, August 1994
[4] D. Gloge, *Weakly Guiding Fibers*, Applied Optics Vol. 10 No. 10 p. 2552
[5] ITU REC-G.652 *Characteristics of single-mode optical fibre and cable*, https://www.itu.int/rec/T-REC-G.652/en
[6] G. Sagnac, *L'éther lumineux démontré par l'effet du vent relatif d'éther dans un interféromètre en rotation uniforme*, Comptes Rendus 157: 708-710
[7] J. Geršl e.a., *Relativistic Corrections for Time and Frequency Transfer in Optical Fibres*, Metrologia Volume 52 Number 4
[8] https://www.ohwr.org/projects/wr-switch-sw/repository/revision/de57d4ae54d763c1c5f81190cab075b1c018d22d
[9] Miguel Jiménez-López e.a., *WR-Zen: Ultra-accurate synchronization SoC based on Zynq Technology*, proceedings of the EFTF 2016 (page 227)
[10] T. Pinkert e.a., *High-accuracy long-haul time & frequency transfer using White Rabbit*, Ninth White Rabbit Workshop (2016), https://www.ohwr.org/attachments/4265/3_160314-WR-workshop_amsterdam.pdf

Study on Time Scale Algorithm of Hydrogen Maser Based on Minimum Error Theory

Meng Jiang[*+], ShaoWu Dong[*&#], Mojuan Yin[*&], WenJun Wu[*&], Huijie Song[*&+], LiLi Qu[*&], WeiXiong Wang[*+]

Email: m13259460281@163.com

[*]National Time Service Center， Chinese Academy of Sciences, Xi'an, China

[&]Key Laboratory of Time and Frequency Primary Standards, National Time Service Center, CAS, Xi'an, China

[+]University of Chinese Academy of Science, Beijing, China

[#]School of Astronomy and Space Sciences, University of Chinese Academy of Science, Beijing 100049

***Abstract*—With the rapid development of science and technology, the demand for time and time signal is getting higher and higher by users in various fields. Most of the world's time laboratories use high performance cesium clocks and hydrogen masers for timekeeping in order to ensure the accuracy and stability of their atomic time scale. The hydrogen maser has excellent stability. However, the hydrogen maser has frequency drift, and the inaccurate deduction of the frequency drift of the maser will affect the accuracy of the atomic time calculation directly. Therefore, in this paper, a method based on the minimum error theory is used to estimate the frequency drift parameter of masers in a certain time interval. Three hydrogen masers operated in NTSC (National Time Service Center) are used to determine the frequency drift parameter. After removing hydrogen maser frequency drift, we use exponential filtering method to calculate the time scale based on hydrogen masers. At the same time, according to the frequency drift parameters of the hydrogen masers published in BIPM Circular T, the frequency drift is deducted and the time scale is calculated. The former is a dynamic estimation of the drift and the initial values is set to the values which come from Circular T. Then the comparative analysis is made at the end. The results show that the method based on minimum error theory can accurately estimate the drift of hydrogen maser, and the accuracy of this time scale is significantly higher than another atomic time scale, and the absolute value of maximum deviation with TA(NTSC) is 3.51ns.**

Keywords—*minimum error； hydrogen maser; time scale; frequency drift estimation*

I. INTRODUCTION

At present, the establishment of international time scale and local time scales mainly use cesium clocks and hydrogen masers, so it is of great significance for the establishment of accurate and stable time scale method. As everyone knows, the cesium standards are much nosier in the short term than the hydrogen masers and consequently have very little short-term (less than a few days) weight [1]. Hydrogen maser has excellent short term performance [2]. The number of hydrogen maser is increasing day by day in the national time laboratories all over the world. Even the Institute of Metrology for Time and Space(IMVP) NPO "VNIIFTRI" Mendeleevo, Moscow Region, Russian Federation (SU) which is at the forefront of the world in timekeeping uses hydrogen maser as the only clock to obtain its time scale. In 2014, BIPM changed the way of weighting of the atomic clock in the UTC production process to its predictability [3]-[4]. After that, by 2017, hydrogen masers involved in the UTC calculation accounted for 28% of the total, and the full weight of the atomic clocks was 12% of the total. And the full weights of the atomic clocks are almost hydrogen masers [5]. Thus it can be seen, the hydrogen maser is becoming more and more important in the generation of time standard. However, the hydrogen maser has frequency drift. Therefore, in order to make full use of its excellent short stability, it is important and urgent to study the frequency drift estimation and time scale algorithm of hydrogen masers.

A constant drift is not a problem with respect to predictability [6]. The time scale can be calculated by taking the frequency drift parameters into different atomic clock models. The difficulty lies in the prediction of the changing frequency drift of hydrogen maser. The accurate estimation of the frequency drift of hydrogen maser will directly affect the accuracy and stability of time scale, and the dynamic frequency drift will increase the difficulty of its estimation accurately.

This paper adopts a method based on the theory of minimum error to estimate hydrogen maser frequency drift parameter effectively. First, this method is used to estimate the two parameters which are the drift and the average time, and then replace the parameter into the exponential filtering time scale algorithm to calculate the time scale of the hydrogen maser ensemble. And the time scale which is the parameter of frequency drift was published by BIPM once a month is also computed. In the end, the performance of two time scales is compared. The main ideas of the method are shortly outlined. The second section introduces the theory of method for frequency drift estimation based on minimum error theory and the exponential filtering time scale algorithm. The third section is the selection of parameters and the implementation of the algorithm. The fourth section is the conclusion.

This work is supported by Nature Science Foundation of China under Grant No.11703030 and No.11473029.

II. MINIMUM ERROR THEORY AND EXPONENTIAL FILITERING ALGORITHM PRINCIPLES

The detailed process of the hydrogen maser time scale algorithm based on the minimum error theory is as follows: [7]-[11]:

We usually define the time difference process as x(t), it is the integral of the frequency process y(t):

$$x(t) = \int_{-\infty}^{t} y(u)du \tag{1}$$

We define the causal first increment operator as:

$$\Delta(t)\{x(t)\} = x(t) - x(t-\tau) \tag{2}$$

Among them, τ is the time interval. And the casual moving average operator as:

$$y(t,\tau) = \frac{1}{\tau}\int_{t-\tau}^{t} y(u)du \tag{3}$$

DGSF-1(Drift Generalized Structure Function prediction of order 1) is defined as:

$$\hat{x}(t+\tau_1) = x(t) + \tau_1 y(t,\tau_2) + \frac{1}{2}d_{\tau_1}^2(1+\frac{\tau_2}{\tau_1}) \tag{4}$$

τ_1 is prediction interval, $\tau_2$is average time, d is frequency drift.

The prediction error is defined as:

$$\begin{aligned}\varepsilon(t,\tau_1,\tau_2) &= x(t+\tau_1) - \hat{x}(t+\tau_1) \\ &= \Delta(\tau_1)\{x(t+\tau_1)\} - \frac{\tau_1}{\tau_2}\Delta(\tau_1)\{x(t)\}\end{aligned} \tag{5}$$

The definition of RMS prediction error is:

$$rms\{\varepsilon(t,\tau_1,\tau_1)\} = \sqrt{\int_0^{\infty} S_{xx}(f)\times\left|H(2\pi f)\right|^2 df} \tag{6}$$

The transfer function $4\left|H(2\pi f)\right|^2$ is defined as:

$$\begin{aligned}&4(\frac{\tau_1}{\tau_2})(1+\frac{\tau_1}{\tau_2})\sin^2(\pi f\tau_2) + 4(1+\frac{\tau_1}{\tau_2})\sin^2(\pi f\tau_1) \\ &-4(\frac{\tau_1}{\tau_2})\sin^2(\pi f(\tau_1+\tau_2))\end{aligned} \tag{7}$$

The calculation steps of the frequency drift parameter estimation based on the minimum error theory are as follows:

- The first step is to set the initial value: frequency drift parameter d, the average time τ_2.
- The second step is to minimize the RMS by adjusting the frequency drift parameter d, so the obtained parameter d is the optimal estimation.
- The third step is to minimize the RMS by adjusting the average interval parameter τ_2, this is the optimal estimation of τ_2. This yields the optimum averaging interval. There is very little interaction between the two parameters. Therefore only one or two iterations are necessary to find the optimum values.

This And then, the exponential filtering algorithm is used to calculate the time scale of the hydrogen maser ensemble and the rate and weight of the atomic clocks are estimated as follows:

Definitions:

- X_i(t), Y_i(t) is estimates of time and frequency offsets respectively of clock i at time t with respect to a reference times scale, respectively;
- $\hat{X}_i(t)$ is predicted time offset of clock i at time t;
- $\hat{Y}_i(t)$ is estimate of frequency of clock i at t over the interval t to $t+\tau$;
- X_{ij}(t) is measured time difference between clocks i and j at time t;
- $\varepsilon_i(\tau)$ is accumulated error in time estimate of clock i over the interval τ;
- $<\varepsilon^2_x(\tau)>$ is mean squared error in ensemble time over the interval τ at time t;
- τ is time interval between measurements;
- $N\tau$ is time constant of exponential filter to estimate the current mean squared error;
- n is number of clocks in the ensemble;
- τ_{mini} is value of τ at minimum $\sigma_y^2(\tau)$ on Allan Variance curve for clock i.

Time estimate is calculated by the formula (4).

Frequency estimate:

$$\hat{Y}_i(t+\tau) = \frac{X_i(t+\tau) - X_i(t)}{\tau} \tag{8}$$

$$Y_i(t+\tau) = \frac{1}{m_i+1}[\hat{Y}_i(t+\tau) + m_i Y_i(t)] \tag{9}$$

m_i is the time constant of exponential frequency-weighting.

$$m_i = \frac{1}{2}(-1+(\frac{1}{3}+\frac{4\tau_{\min i}^2}{3\tau^2})^{1/2}) \tag{10}$$

Weight estimates:

$$\varepsilon_i = \left|\hat{X}_i(t+\tau) - X_i(t+\tau)\right| + K_i \tag{11}$$

K_i is the deviation of error estimation.

$$\left\langle \varepsilon_i^2(\tau)\right\rangle_{t+\tau} = \frac{1}{N_\tau+1}[\varepsilon_i^2(\tau) + N_\tau\left\langle \varepsilon_i^2(\tau)\right\rangle_t] \tag{12}$$

The time constant for the filter is typically chosen to be N_τ =20 days. The initial value of $\left\langle \varepsilon_i^2(\tau) \right\rangle$ can be estimate as $\tau^2\sigma_y^2(\tau)$.

$$\left\langle \varepsilon_x^2(\tau) \right\rangle = \left(\sum_{i=1}^{n} \frac{1}{\left\langle \varepsilon_i^2(\tau) \right\rangle} \right)^{-1} \tag{13}$$

$$w_i = \frac{\left\langle \varepsilon_x^2(\tau) \right\rangle}{\left\langle \varepsilon_i^2(\tau) \right\rangle} \tag{14}$$

$$k_i = \frac{8\left\langle \varepsilon_x^2 \right\rangle}{\left\langle \varepsilon_i^2 \right\rangle^{1/2}} \tag{15}$$

III. PARAMETER ESTIMATION AND ALGORITHM IMPLEMENTATION

In this paper, the clock difference data of three hydrogen masers (H226, H227 and H336) which are owned by National Time Service Center (NTSC) are used to calculate the time scale. The clock rate and frequency drift of each hydrogen maser obtained by the method secondary fitting of clock difference data in several previous days. And they were selected as the initial value of the clock rate and frequency drift. The initial values of the rate of the clocks are 0.8466, 0.7247, 0.7714 ns/h. The initial value of frequency drift is -2e-5, -1e-5, 1e-4(ns/h)/h, respectively. Basic measurement interval τ_1 is 4h, the initial value of average time interval τ_2 is 20h.

A. Optimal estimation of frequency drift parameter d

The minimum error theory is used to estimate the frequency drift parameter of the hydrogen masers. First of all, keep the average time interval constant. And then, change the frequency drift parameter and slide step to calculate the RMS value corresponding to each frequency drift parameter. Finally, compare the values and find the minimum. Here, the corresponding parameter is the optimal estimation of *d* at this average time interval. As shown in Table 1, the initial value of frequency drift is -2e-5、-1e-5、1e-4(ns/h)/h, respectively. And the initial value of τ_2 is 20h. Moving interval is 5e-4 (ns/h)/h. From table I, it can be seen that RMS are the smallest when the step length is 1*5e-4 of all three hydrogen masers. Therefore, the optimal estimation of *d* of each maser is -2e-5+1*5e-4=4.8e-5、-1e-5+1*5e-4=4.9e-5、1e-4+1*5e-4=6e-4 (ns/h)/h. The unit of RMS is ns in the table I.

B. Optimal estimation of average time interval parameter τ_2

The average time interval parameters τ_2 are estimated optimally after *d* are determined. The approach is to ensure that *d* is a invariant, and adjusting τ_2 to minimize the RMS. Here is the optimal estimation of τ_2. The initial values of the above parameters of hydrogen masers are the same. Frequency drift *d* are equal to the optimal estimations above. The results of the calculation are shown in table II. From table 1, it can be seen that RMS are the smallest when τ_2 is 32h, 36h, 32h, respectively. Those are the optimal estimation of average time interval parameters. The unit of RMS is ns in the table II.

TABLE I. THE OPTIMAL ESTIMATION OF FREQUENCY DRIFT PARAMETER

Moving step length((ns/h)/h)	H226(RMS)	H227(RMS)	H336(RMS)
-4*5e-4	0.903	0.212	0.222
-3*5e-4	0.817	0.191	0.204
-2*5e-4	0.744	0.173	0.189
-1*5e-4	0.690	0.159	0.178
0*5e-4	0.658	0.150	0.172
1*5e-4	0.652	0.147	0.171
2*5e-4	0.672	0.150	0.175
3*5e-4	0.717	0.159	0.185
4*5e-4	0.782	0.173	0.199

TABLE II. THE OPTIMAL ESTIMATION OF AVERAGE TIME INTERVAL PARAMETER

τ2(h)	H226(RMS)	H227(RMS)	H336(RMS)
4	0.658207	0.148649	0.172352
8	0.656269	0.148307	0.171912
12	0.654631	0.148009	0.171540
16	0.653294	0.147754	0.171234
20	0.652260	0.147544	0.170996
24	0.651532	0.147377	0.170826
28	0.651110	0.147256	0.170724
32	0.650993	0.147178	0.170690
36	0.651184	0.147145	0.170725
40	0.651681	0.147156	0.170828
44	0.652485	0.147211	0.170999
48	0.653589	0.147312	0.171237
52	0.655001	0.147456	0.171544
56	0.656714	0.147645	0.171918

C. Algorithm implementation and analysis

Design block diagram of time scale algorithm for hydrogen maser ensemble based on minimum error theory is shown in Figure 1. At the same time, the time scale is also computed which the frequency drift parameters are published by BIPM. The results are shown in Figure 2. The absolute value of the maximum deviation between two results and TA(NTSC) are shown in table III. Because TAI is a time scale which is delay and its data are produced every five days one point. And the real time and dense data are needed here. So a local implementation of TAI time scale TA(NTSC) is selected for evaluation of results. In table III, time scale 1 means the result that used the minimum error theory to estimate the drift and then calculate the time scale. And time scale 2 is another result which adopts the drift in Circular T.

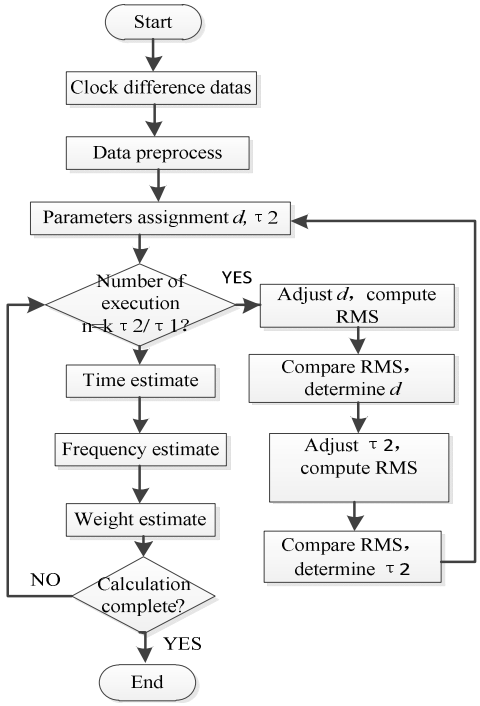

Fig 1: Block diagram of algorithm

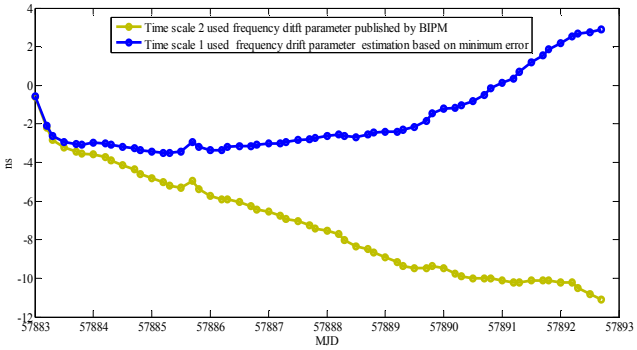

Fig 2: The difference between calculated time scale and TA(NTSC) which used two methods to estimate the frequency drift parameters

TABLE III. THE ABSOLUTE VALUE OF MAXIMIUM DEVIATION BETWEEN TA(NTSC) AND TIME SCALES CALCULATED BY TWO METHODS TO ESTIMATE THE FREQUENCY DRIFT PARANETERS

MJD	Time scale 1-TA(NTSC) (ns)	Time scale 2-TA(NTSC) (ns)
57883-57884	3.13	4.80
57885-57886	3.51	6.42
57887-57888	3.02	8.65
57889-57890	2.42	10.03
57891-57892	3.27	11.06

It is can be seen from Table 3 and Figure 2 that the parameters of frequency drift of hydrogen masers can be estimated accurately through the method which based on the minimum error theory. The accuracy of time scale which uses the minimum error theory is better than that of the time scale calculated which adopts the frequency drift in Circular T. The absolute value of maximum deviation of the time scale 1 minus TA(NTSC) is 3.51ns. And another one time scale 2 minus TA(NTSC) is 11.06 ns. That is to say, the method based on the minimum error theory can estimate the drift of hydrogen maser effectively.

IV. CONCLUSION

Due to its good performance, hydrogen masers have been paying more and more attention to timekeeping. This paper uses the language FORTRAN to develop a software system. The frequency drift parameters are studied by using the clock difference data. The minimum error theory is used to estimate the drift and the average time interval of each hydrogen maser, and the time scale is computed by exponential filtering method. The absolute value of maximum deviation of the time scale minus TA(NTSC) is 3.51ns in ten days. The results show that the method based on the minimum error theory can remove the frequency drift of hydrogen maser for the time scale effectively and the method will be introduced to some time sale algorithms to improve its performance in the future.

REFERENCES

[1] TE Parker and S Romisch, “A Clock Ensemble Using Only Active Hydrogen,” Precise Time and Time Interval Meeting (PTTI), 2017, pp.44-47

[2] SH Zhao, SW Dong, LL Qu and HB Yuan, “A New Steering Strategy For UTC(NTSC) Based on Hydrogen Maser,” IEEE Frequency Control Symposium (IFCS), 2016

[3] G Panfilo, A Harmegnies and L Tisserand, “A new weighting procedure for UTC,” Metrologia, 3rd ed., vol. 51, 2014, pp.285–292.

[4] HJ Song, SW Dong and ZM Wang, “An Analysis of NTSC’s Timekeeping Hydrogen Masers,” Chinese Astronomy and Astrophysics 40, 2016, pp.569-577.

[5] BIPM Annual Report on Time Activities.2016.

[6] L.G. Bernier, “Predictability of a Hydrogen maser time scale,” European Frequency and Time Forum(EFTF), 2005. pp. 438-441.

[7] L.G. Bernier, “Application of the GSF-1 Algorithm to the Near-optimal Timescale Prediction of Hydrogen Maser,” Precise Time and Time Interval Meeting (PTTI), 2003, pp.221-236.

[8] L.G. Bernier, G. Dudle and C. Schlunegger, “New Real Time UTC(CH) Generation Scheme at METAS: Recent Progress in Control and Calibration Methods,” IEEE International Frequency Control Symposium(IFCS) & European Frequency and Time Forum(EFTF), 2007.

[9] Levine J, “Invited Review Article: The statistical modeling of atomic clocks and the design of time scales,” Review of Scientific Instruments, 2rd ed., vol. 83, 2012.

[10] R J de Carvalho, “The establishment of a Brazilian atomic time scale,” Frequency Control Symposium and Exposition, 2005. Proceedings of the 2005 IEEE International. IEEE, 2005, pp.254-260.

[11] M Jiang, SW Dong and WJ Wu, “The Study of the Time Scale Algorithm of Hydrogen maser,” China Time and Frequency Symposium, 2017.

Comparison of Two Methods of Time-Interval Measurement Based on SAWF and SAWDDL

Haifeng WANG[1], Shengkang ZHANG[1], Xie Yong[2], Xueyun WANG[1], Hongbo WANG[1], Hang YI[1], Honglei YANG[1], Wenzhe YANG[1], Shuwei WANG[1]

1. Science and Technology on Metrology and Calibration Laboratory, Beijing Institute of Radio Metrology and Measurement Beijing, China

2. Tianjin 764 Communication Navigation Technology Co., Ltd., Tianjin, China

Email:haifengwang203@163.com

***Abstract*—In this paper, we demonstrate our work details on two methods of time-interval measurement based on SAWF (Surface Acoustic Wave Filter) and SAWDDL (Surface Acoustic Wave Dispersive Delay Line) and compare which one is easy and precise to be implemented. The two methods are based on the fact that transversal SAW components can be used as the time interpolator to reach precise time interval measurement which is much shorter than the sampling period. We have done an experiment using SAWF as the time interpolator in time-interval measurement with low frequency sampling clock which can be implemented easily on hardware platform and the result shows that the time interval measurement is about 2ps precision and stability.**

Keywords—time-interval measurement; interpolation; SAWF; SAWDDL

I. INTRODUCTION

With the higher performance of the Time-Interval Counter technology that people are looking for, researchers have done large numbers of work to achieve it, most of these are based on time interpolation. Traditional time interpolation methods are usually utilize interval-to-voltage increment conversion, different variants of the vernier principle, or pulse propagation through tapped delay lines[1]. At the present time, two methods of Time-Interval Measurement with 1ps precision and stability are realized based on Surface Acoustic Wave Filter (SAWF) and Surface Acoustic Wave Dispersive Delay Line (SAWDDL) which are used as the time interpolator.

In this paper, we demonstrate our work details on these two interpolation methods to compare which one is easy and precise to be implemented. The two methods are all based on the fact that a transversal SAW component excited by a short pulse can generate a finite signal with highly suppressed spectra outside a narrow frequency band. The shape of the output signal envelop from SAW filter is as SINC function, and the out-put signal from SAW delay line is a chirp signal which is commonly use in radar systems. If the two band limit signals are sampled at clock ticks, they can be approximately reconstructed from a finite number of samples according to the Shannon sampling theory[2] and then compared to determine the interval between the two pulses.

We all know that the peak shape of the self-correlation function (SCF) determine the precision of the time interval measured. The SCF of SAWDDL is shaper than the SCF of SAWF with the same bandwidth and duration time of response. So if we use the SAWDDL as the time interpolator, the result must be better than the SAWF in theory. But when we take it in practice, the result is cross to our expectation because of Gibbs Phenomena when using SINC interpolation to reconstruct the original signal on the steep boundary. Steeper boundary of samples envelope will increase the reconstruction error. Obviously, the response envelope of SAWF is gradually approaching to zero on the boundary, it can be easily and precisely to reconstruct from samples with small interpolation error.

We have done a experiment using SAWF as the time interpolator in time-interval measurement with low frequency sampling clock which can be implemented easily on hardware platform and the result shows that the time interval measurement is about 2ps precision and stability.

II. THEORY SIMULATION OF TWO METHODS

A. Time Domain of Two Responses

As can be seen from Fig.1, the shape of the output signal envelop from SAWF is as SINC function, and the output signal from SAWDDL is a chirp signal which is commonly use in radar systems.

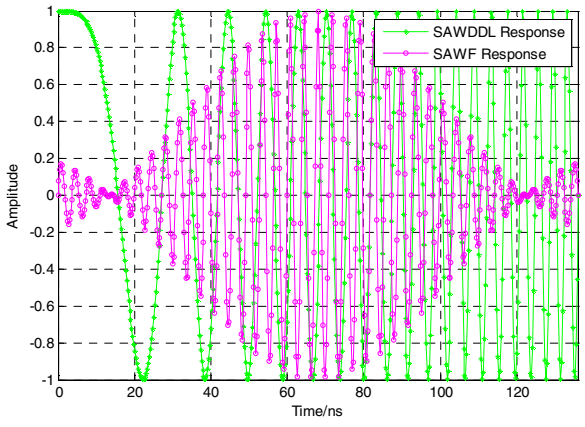

Fig.1 The Response of SAWF and SAWDDL

B. Self-Correlation Function of Two Components

We all know that the peak shape of the self-correlation function (SCF) determine the precision of the time interval measured, therefore the characteristic of self-correlation function of the component in use is the crucial point of this time-interval measurement system. The self-correlation function is described by the following:

$$R(\tau) = \int_{-\infty}^{\infty} S_{SAW}(t) S_{SAW}(t+\tau) e^{-j2\pi ft} dt \qquad (1)$$

The self-correlation function (SCF) of SAWF and SAWDDL are shown in Fig.2, where the central frequency and the bandwidth of the two kinds of component are 545MHz and 30MHz. The SCF of SAWDDL is shaper than the SCF of SAWF with the same bandwidth and duration time of response. So if we use the SAWDDL as the time interpolator, the result must be better than the SAWF in theory. But when we take it in practice, the result is cross to our expectation, and the reason will be discussed in details in chapter IV.

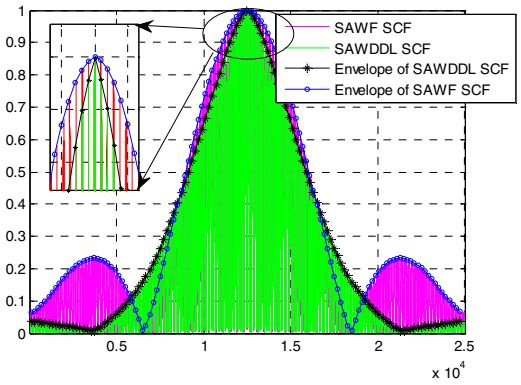

Fig.2 The Self-Correlation Function of SAWF and SAWDDL

C. Frequency Domain of Two Components

The choice of the component bandwidth is complicated. The influence of jitter and quantization errors decreases by reducing the bandwidth, and however is limited due to the increasing probability of false ambiguity solution[1]. To make the comparison easily, the bandwidth of two components is same. The power spectral density of SAWF and SAWDDL is shown in Fig.3, where frequency is from 530MHz to 560MHz.

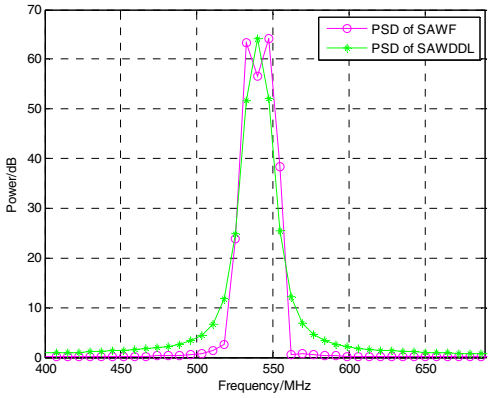

Fig.3 The PSD of SAWF and SAWDDL

III. THE RECONSTUCTION THEORY

The theory of Fourier signal analysis is extensive and has proven fruitful to a variety of applications. One such application is interpolation. The Shannon sampling theory establishes that a bandlimited continuous-time signal can be completely represented by a set of equidistantly spaced signal samples. In turn, the continuous signal could be recovered from this set of samples via sinc interpolation[2].

A. Classical SINC Reconstruction

The classical SINC reconstruction formula for discrete signals as presented in (2) is

$$x(t) = \sum_{n=-\infty}^{\infty} x(nT) \frac{\sin(\pi(t-nT)/T)}{\pi(t-nT)/T} \qquad (2)$$

It is the lowpass signal reconstruction.

B. Bandpass Signal Reconstruction

Bandpass signal is also a kind of band-limited signal. If it's sampled according to Shannon sampling theorem, a too high sampling rate would be required. Since the spectrum of bandpass signal confined to two bands symmetrically located about zero and vanishes outside, it can be sampled at a rate less than Niquist rate.

The Bandpass signal reconstruction formula for discrete signals as presented in (3) is

$$x(t) = 2WT \sum_{n=-\infty}^{\infty} x(nT) \frac{\sin(\pi W(t-nT))}{\pi W(t-nT)} \cos 2\pi f_0 (t-nT) \qquad (3)$$

Where W is the bandwidth of the component and f_0 is the central frequency of the component.

IV. THE RECONSTRUCTION SIMULATION

We demonstrate our work details on these two interpolation methods to compare which one is easy and precise to be implemented. To compare the performance of the algorithm, a simulation was done, as shown in Fig.4 and Fig.5.

Fig.4 shows the sampling, reconstruction process and the reconstruction error of SAWF, the Gibbs Phenomena when using SINC interpolation to reconstruct the original signal on the boundary. Obviously, the response envelope of SAWF is gradually approaching to zero on the boundary, it can be easily and precisely to reconstruct from samples with small interpolation error.

Fig.5 shows the sampling, reconstruction process and the reconstruction error of SAWDDL, the Gibbs Phenomena when using SINC interpolation to reconstruct the original signal on the sharp boundary. The response envelope of SAWDDL is sharper than SAWF on the boundary. It cannot be easily and precisely to reconstruct from samples and interpolation error is too big on the boundary. That is why although the SCF of SAWDDL is sharper than SAWF , the time-interval measurement result is bad in practice. So we should find other interpolation methods to deal with the sharp boundary

reconstruction problem, like wavelet transform theory, and this will be our future work.

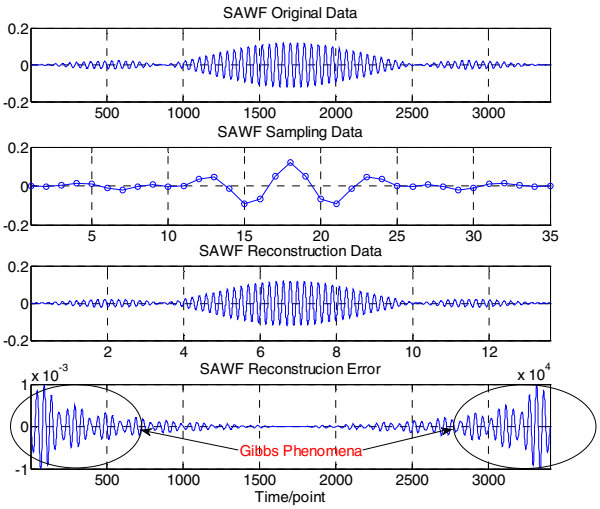

Fig.4 The Sampling and Reconstruction Error of SAWF

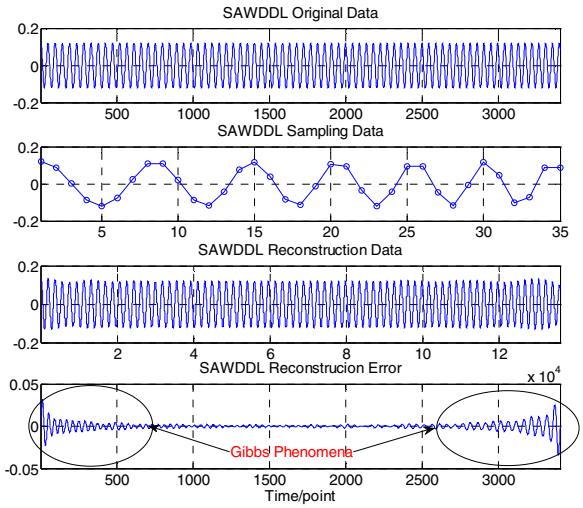

Fig.5 The Sampling and Reconstruction Error of SAWDDL

V. THE SAWF EXPERIMENT

To evaluate the performance of the SAWF in our system, an experiment was done, as shown in Fig.6. In the process of the experiment, we use two channels of an Arbitrary Waveform Generator (AWG) with the sampling rate 25GHz as our short pulse source, meanwhile the pulse repeat rate from the AWG is 2.5MHz, and we choose a SAWF which central frequency and the bandwidth are 545MHz and 30MHz, and then we use a Digital Oscilloscope with the sampling rate 250MHz to store the original data. Fig.7 shows two channels of SAWF response on Digital Oscilloscope. After that, we implement the algorithm on a PC and obtain the time interval of two short pulses. Finally, we shift the time interval of two channels of AWG and repeat the upper process. The measurement result shows in Fig.8 and TABLE I. The measurement data is consistent with time interval shift we set, and the deviation is about 2ps.

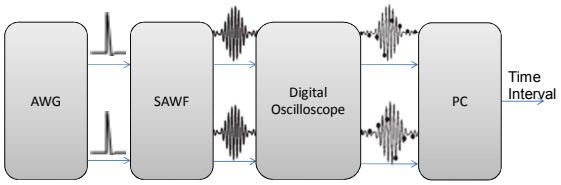

Fig.6 The Experiment Structure

Fig.7 Two Channels of SAWF Response

TABLE I. TIME SHIFT MEASUREMENT

Time Shift set (ps)	Measurement Data											
	1st	2nd	3rd	4th	5th	6th	7th	8th	9th	10th	mean	deviation
0	4	0	-2	3	2	1	2	3	1	2	1.6	1.713
40	-38	-40	-41	-39	-38	-37	-39	-36	-36	-40	-38.4	1.713
80	-79	-79	-80	-77	-79	-76	-78	-76	-78	-77	-77.9	1.37
120	-119	-120	-123	-119	-120	-117	-117	-116	-118	-119	-118.8	1.989
160	-159	-160	-162	-159	-159	-157	-157	-157	-157	-159	-158.6	1.647
200	-199	-200	-200	-198	-199	-196	-199	-196	-199	-200	-198.6	1.506
240	-240	-239	-242	-240	-239	-237	-237	-236	-237	-241	-238.8	1.989
280	-282	-282	-281	-280	-281	-277	-278	-277	-279	-281	-279.8	1.932
320	-321	-318	-321	-320	-320	-314	-319	-317	-319	-321	-319	2.211
360	-360	-360	-360	-360	-360	-356	-358	-357	-361	-361	-359.3	1.703
400	-398	-399	-401	-399	-401	-395	-399	-398	-399	-401	-399	1.826
440	-440	-441	-440	-439	-440	-437	-436	-436	-442	-440	-439.1	2.079
480	-479	-480	-480	-480	-482	-477	-476	-478	-479	-478	-478.9	1.729
520	-520	-520	-519	-519	-520	-517	-515	-516	-520	-519	-518.5	1.841

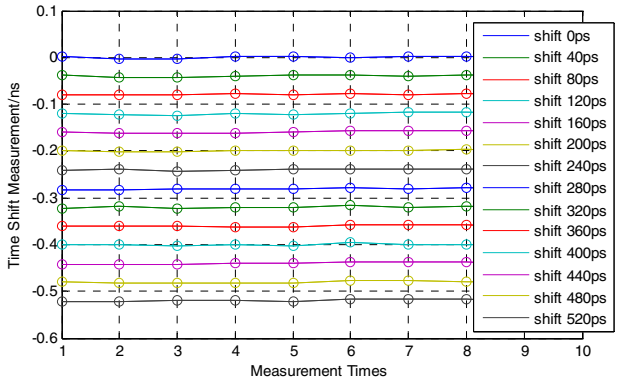

Fig.8 Time Shift Measurement

VI. CONCLUSION

We have demonstrated our work details on two interpolation methods to compare which one is easy and precise to be implemented. Although the SCF of SAWDDL is shaper than the SCF of SAWF with the same bandwidth and duration time of response, the reconstruction error in SAWDDL method is bigger than SAWF method because of Gibbs Phenomena on the sharp boundary, so the SAWDDL methods is not suitable in the time interval measurement with low sampling clock. An experiment using SAWDDL as the time interpolator with high sampling clock will be our future work.

REFERENCES

[1] P. Pánek, "Random errors in time interval measurement based on SAW filter excitation," IEEE Trans. Instrum. Meas., vol. 57, no. 6, pp. 1244–1250, Jun. 2008.

[2] F. Candocia and J. C. Principe, "Comments on "Sinc interpolation of discrete periodic sig-nals"," IEEE Trans. Signal Processing, vol. 46, pp. 2044–2047, July 1998.

Long term simulations for bi-static radar and test bench design

R. Granados*, A. Herique, S. Rochat E., Le-Coarer
Univ. Grenoble Alpes,
CNRS, IPAG,
F-38000 Grenoble, France
*ricardo.granados-alfaro@univ-grenoble-alpes.fr

***Abstract*—Instruments like CONSERT aboard Rosetta mission, is a technology capable to study the interior of small bodies (asteroids and comets) in the Solar System. Nowadays the knowledge of internal structure is based in remote sensing and theoretical modeling. This approaches cannot give enough details to completely unveil the evolution of the body. Bi-static radar instead offers this possibility. This type of radar demands high accuracy time synchronization between both electronics. One way to improve science is to understand the clock generation signals and how this will affect the measurement to propose compensation techniques. In this paper we present first the bi-static radar concept, we then expose the time analysis and propose a modification of the transponder structure to measure the clock drift between both clocks. We develop a Kalman filter to improve the estimation and compensate the time error. To verify our models and evaluate them, we present a test bench design to collect data from real clocks.**

Keywords—synchronization, bi-static radar, asteroid tomography, kalman filter, clock drift, OCXO)

I. INTRODUCTION

Small bodies like comets and asteroids are of interest to learn about the origin of the Solar System. This bodies are considered to have experienced minor changes through its evolution. And therefore is a way to understand their evolution through time. This information can also be useful for future space exploration or for planetary defense [1]. Actually there are several space missions studying or going to study small bodies, but only few instruments are destined to study the interior of their cores [2].

We are developing a new generation of bi-static radar for asteroids tomography [3]. This Low Frequency Radar (LFR) counts with the heritage of CONSERT, an instrument aboard Rosetta mission, which studied the comet 67P/Churyumov-Gerasimenko [4]. The bi-static radar is composed by two electronics, one placed in the asteroids surface (Lander) and the other orbits the body (Orbiter). They transmit a low frequency radio wave (60MHz) through the asteroids body. The main objective is to measure the propagation delay of the radio wave through the asteroid. From the propagation delay is possible to deduce the dielectric permittivity of the material in the interior which relates to mineralogy and porosity. The secondary objective is the measurement of the signal scattering which relates to internal structure homogeneity [5]. LFR is specified to resolve a 10% change of the mean porosity along a 150 meter path. This means that the time accuracy on the propagation delay measurement has to be better than the code symbol time of 50ns.

A planetary mission imposes design and operational constraints. Mass, size, power consumption, link budget among others are limited. This reduces the possible components for design and also limits the techniques used for operation. For this mission there was no suitable clock within power and mass limits for the stability required. The stability needed to have synchronization between Orbiter and Lander during the whole measurement was$\Delta f/f \approx 10^{-12}$. The in-time transponder structure used in CONSERT allows to reduce this requirement to $\Delta f/f = 10^{-7}$ and split it into four different time scales. This frequency stability is achievable with an Oven Controlled Crystal Oscillator (OCXO).

Since LFR is a bi-static radar and the main objective is to measure propagation delay, time synchronization and frequency drift impose limitations in the measurement accuracy. In a planetary mission we lack an external signal to lock our devices (i.e. GPS) [6], [7]. The low SNR at reception caused by the transmission of the radio wave through the asteroid does not allow the time stamp interchange [8]. To improve this low SNR a coherent accumulation is done at reception but due to clock drift it is not possible to have a continuous accumulation, therefore we have specific times of reception limiting the classic time stamp free synchronization methods [9]. All these constraints set the instrument to depend completely in the clock stability, the clock characterization, the time stamp free synchronization with scheduled times in reception and the on-board or post-processing compensation techniques.

II. RADAR TOMOGRAPHY

A. Transponder Concept

The transponder concept consists in two separate electronics, therefore two clocks and two calendars. The electronics perform a double way transmission, named Ping-Pong. They transmit a coded signal (Binary Phase Shift Key BPKS) through the asteroids body. At the reception a coherent accumulation of 1024 codes is performed to improve SNR. This accumulated signal is then pulse compressed to find a peak that represents the propagation delay [10]. See Figure 1.

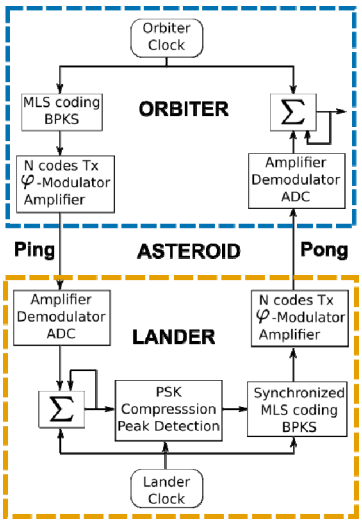

Fig. 1. In-time transponder concept block diagram.

Fig. 2. Synchronization diagram. Transmission from Orbiter to Lander is Synchronization signal (Ping), and transmission Lander to Orbiter is Science signal (Pong).

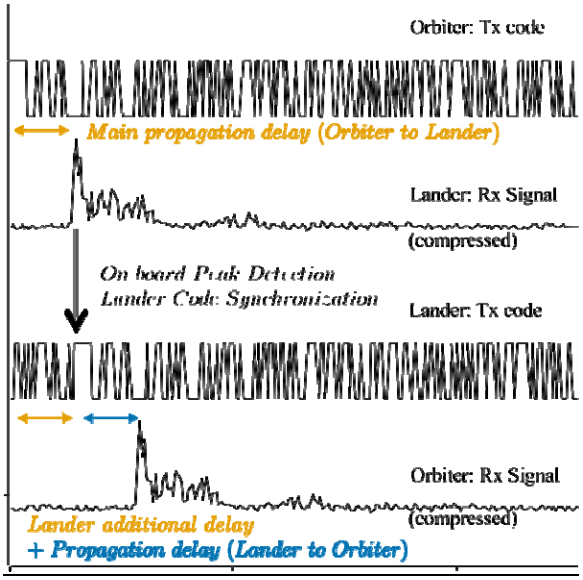

The Orbiter sends the first transmission to Lander, this is a synchronization signal (Ping). The Lander will send back the same signal but time shifted to the delay calculated by the pulse compression. This second transmission from Lander to Orbiter is the Science signal (Pong). See Figure 2. This double transmission Ping-Pong is referred in this work as a Sounding. Soundings are repeated for different geometries of the position of the Orbiter until it covers one orbit around the body to generate a Scan of the asteroid. There is need of several Scans of the asteroid to complete the tomography of the body.

Each electronic have its own clock and this clock runs all the components inside. The transmission and reception are driven by a FPGA running with this clock autonomously. This automats work in parallel with a microcontroller for certain functions in the digital processing of the signal on-board (i.e. peak detection).

III. TIME ANALYSIS

A. Time Scales

The transponder concept reduces the absolute frequency requirement by split it into four different time scales. Coherent Accumulation needs to preserve phase during reception duration. Ping to Pong (Sounding), must preserve calendar scheduling 20 times better than the symbol time. Sounding to Sounding phase should remain stable to allow coherent processing. In a Scan reception window must be inside transmission window to ensure communication. See Figure 3.

Each time scale has different time and frequency requirements. We recognize two different types of requirements, absolute type that demand that the frequency stability is less than a given maximum to allow science (No post-processing correction possible), and stability type, where knowledge of the stability frequency allows compensation. In Table 1 we show each time scale per column and the time reference per row. In gray are shown the absolute type requirements.

In the fact, this 4 different time scales are driven by a unique clock per electronic and are affected by its drift. We developed a simulator to understand the impact and the correlations of the clock drift for long term. This simulator generates the schedules of the reception and transmission windows of the automats. This is done for the whole measurement duration. For small timescale we consider that the coherent accumulation is performed correctly, and phase noise is negligible. Both propositions are reliable since the clocks are sufficiently stable in this periods of time (Clocks proposed, have an Allan variance of $\sim 5 \times 10^{-12}$ @ 1 s. and low phase noise). Temperature and aging will be the main processes driving clock drift in long term, therefore during one Sounding clock drift is considered constant.

TABLE I. FREQUENCY REQUIREMENT FOR DIFFERENT TIME SCALE.

	Accumulation	**Ping to Pong**	**Sounding to Sounding**	**Tx-Rx Window**
Carrier Phase	10^{-7}		10^{-12}	
Time Symbol		10^{-8}	10^{-11}	
Time Codes				10^{-7}

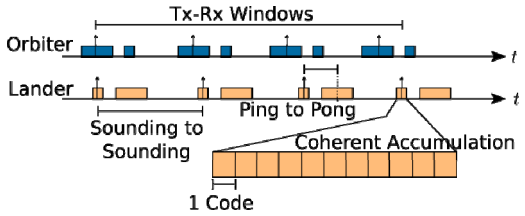

Fig. 3. The four time scales off interest. Each one has different frequency and time requirements.

B. Simulation

The simulations reproduce the schedules for the 2 electronics. One will be considered the reference and therefore perfect (Orbiter), and the other schedule will be affected by the clock drift (Lander). The simulator generates all the time event for the two calendars. The time events used are depicted in Figure 4. With this time events we are able to calculate the propagation delay in the Lander (τ_{LAN}) and in the Orbiter (τ_{ORB}).

In our model we included two errors present in the measurement. On board the Lander the received signal is sampled and processed at 120MHz. The peak received could be between two sampling points. This causes that the peak moves to the nearest sampling point introducing a time error ($\Delta\tau_{LAN}$). This error is introduce in the synchronization part of the transmission but it can be partially corrected by on-ground processing using the raw data available [11]. The SNR of the received signal also introduce an error in time. A simple model was used due that we consider that there is a peak detection for each transmission and therefore SNR is high enough to limit this error.

The propagation delays measured are:

$$\tau_{LAN} = t_{OT} - t_{lR} = \tau_0 - T_0 - \Delta Ping\frac{\Delta f}{f} + \Delta\tau_{LAN} + \Delta\tau_{SNR}$$

$$\tau_{ORB} = t_{lT} - t_{OR} + \tau_{LAN}$$

$$\tau_{ORB} = 2\tau_0 + \Delta Pong\frac{\Delta f}{f} + \Delta\tau_{LAN} + \Delta\tau_{SNR}$$

where T_0 is the time error at the beginning between clocks. Notice also the propagation delay calculated in the Lander is added to the propagation delay in the Orbiter. From time analysis, the error in propagation delay measurement is introduced by the time error between the reception and transmission, added with sampling and SNR errors.

This simulation shows the basic transponder behaviour of the synchronization and science signal. And it helped us to visualize the effects of the clock drift.

To improve science a modification of the transponder structure was conceived, this change allows to follow the clock drift between both clocks. This modification is called Pong-Pong, it consists in the double transmission back of the Lander to the Orbiter (Figure 4). The time between the transmissions

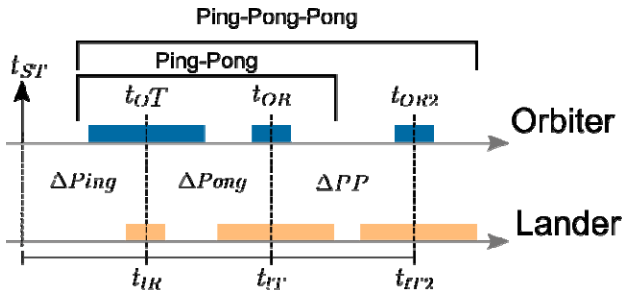

Fig. 4. Ping-Pong and Ping-Pong-Pong time diagrams, based in time events. Here is no depicted the initial time error between Orbiter and Lander.

should be sufficiently close to represent the same path travel of the wave. In this scenario all the other parameters causing error are fixed and the only error in the propagation delay measured is the clock drift component.

$$\frac{\Delta f}{f} = \frac{\tau_{ORB2} - \tau_{ORB1}}{\Delta PP}$$

From this modification we can propose different combinations to be able to measure clock drift in the Lander and compensate on board, by using Ping-Ping-Pong. This combinations are limited by the transmission power available and the processing capabilities. The clock drift measurement will be limited by the SNR and the accurate peak detection.

To improve the estimation of the clock drift we proposed a Kalman filter that uses the temperature coming from the housekeeping. Considering that frequency stability is linearly affected by temperature we can propose the state equations for a Kalman filter. This assumption is also considered for other OCXO [12] and the data received from manufacturer shows for one clock a linear relation. However this dependence on temperature will be characterized and analyzed to have the best model.

An advantage of the Kalman filter is that can be used on board as a real time clock drift compensation or on ground for post-processing. The updated state matrix is as follows

$$\begin{bmatrix} \frac{\Delta f}{f}_{k+1} \\ \frac{d}{dT}\frac{\Delta f}{f}_{k+1} \end{bmatrix} = \begin{bmatrix} 1 & \Delta T \\ 0 & 1 \end{bmatrix} \begin{bmatrix} \frac{\Delta f}{f}_{k} \\ \frac{d}{dT}\frac{\Delta f}{f}_{k} \end{bmatrix}$$

where ΔT represent a change in Temperature.

The simulator shows the behavior expected for the propagation delay measured in the Lander and Orbiter. Also the Kalman filter demonstrated that can improve the clock drift value coming from the Pong-Pong technique. But to validate and evaluate this techniques, it is mandatory to have real data coming from real clocks. For this we propose a test bench which let us gather the data needed.

IV. Test Bench

The test bench was designed under the needs of the simulator. It needs the phase and time error information between both clocks for all time events during the measurement time. Also we added some hardware constraints as: quick development and low cost.

A. Design

We considered 4 different ideas for the test bench. The first idea to be explored was the direct measurement with an ADC due that the implementation could be fast and low cost. After simulations we noticed that the accuracy achievable by this design was not enough for our purpose. Acquisition board was rejected due to the cost. The Time Interval Counter was postponed after reviewing the Dual Mixer Time Difference which includes one TIC to perform the measurement. One advantage of the latter was the fast implementation as we can

produce a version fully digital. And it is low cost as we already count with the FPGA board.

1) DMTD

The system used in this test bench was presented by Allan in 1975 [13]. The idea is to create two beat frequencies at slower rate than the original by multiplying both clocks with a common oscillator with a frequency lower but close to the one of the original clocks. This new beat frequencies kept the original phase difference but in a slower frequency which is possible to measure with a time interval counter. Figure 5. This technique was redesign into an all-digital version in a FPGA [9]. In our design the PLL is implemented in the same FPGA board.

One direct advantage in using digital signals is that there is no need of a filter after the mixing, in this case made by a couple of flip flops. The relationship between the original time difference and the time difference at the output of the DMTD is known as the zooming factor:

$$\Delta t = \Delta t_{DMTD} \frac{f_{beat}}{f_{CLK}}$$

For testing and evaluation of the board. We introduced several more counters to measure different values of the clocks. In Figure 5 are shown all the counters implemented in the FPGA board.

Counter 1 measure time difference between clocks considering Start signal Beat1 and Stop signal Beat2. Being the beat signals the output of mixing original clocks and PLL signal. Counter 2 measure time difference (equal as Counter 1) but interchange the Start and the Stop signals giving the complementary part of the phase in Counter 1. Counter 3 gives the period of Beat 1 this value should remain constant for all the measurement. Counter 4 is the period of Beat2 this value will change during time. Counter 5 counts the number of periods of the other beat frequency in its own period. This value should remain 1 all the time except when we have one cycle error in time. So this counter will help to follow the time error accumulation. We can do the same with the signals interchanged Counter 6. The counter 7 gives a count of the data transmitted, this counter will be used to know that there is no data missing in the transmission and storage (Figure 6).

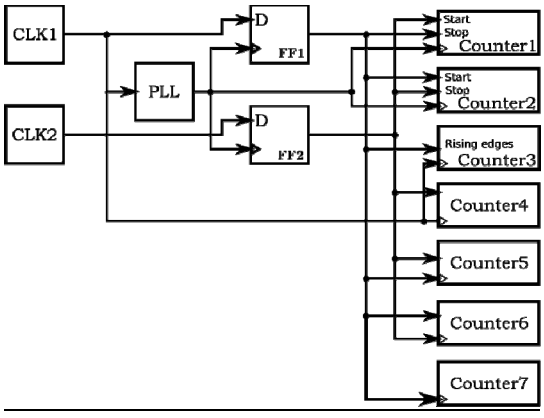

Fig. 5. Block diagram of the DMTD system implemented. All this counters will help to evaluate the board, and give more information to follow the clock drift.

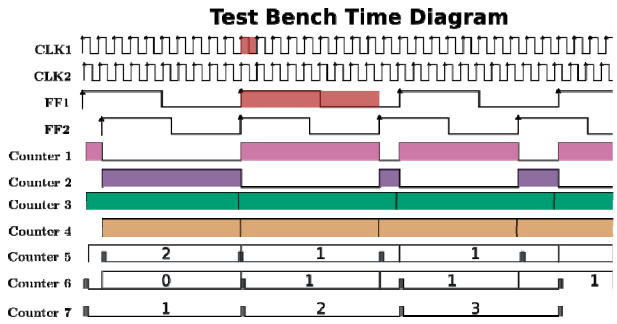

Fig. 6. Time diagram from the DMTD system, showing the outputs of each Counter. For the last 3 counters, the numbers show the value of the output of the counter.

Each oscillator has its own board and each board includes a temperature sensor. This separated boards will allow the temperature characterization of one clock by regard to the other. The data from this two temperature sensors are sent via I2C to the FPGA board, which will deliver the data to the PC via UART port.

B. *Requirements*

To have significant value, the test bench needs to measure phase difference between the two original clocks with an accuracy of 0.6°. Also it is needed to take a measurement of the phase in periods of time smaller or at least the same size that the time events of interest. The reception window considering a code of 255 symbols with a bandwidth of 20MHz and an accumulation of 1024 codes is of 13ms duration. For this we choose a beat frequency of 1000Hz. Therefore there are 13 measurements of phase during one Rx window which means the system able to follow phase change inside the accumulation time.

This parameter gives the transmission speed from board to PC. The data volume generated is 9 values of 16bit each millisecond. The board is able to handle an UART transmission fast enough to transfer all data to PC.

The storage of the data is done directly with the binary reception, and processed later.

C. *Hardware selection*

The clock trade off was based on space qualified oscillators that match our requirements in terms of frequency stability, mass, weight, power consumption in warm-up and in stable mode, size constraints and the cost. From the possible catalogue of space oscillators only two manufacturers were inside the trade off needs. The technology chose was Oven Controlled Crystal Oscillator versions to reduce frequency drift due to temperature. The two clocks chosen were RK408 from Rakon and the EWOS0830 from Syrlinks. Both clocks lets us cover almost directly the absolute type requirements, show very low power consumption, and are the two best prices.

The test board manufacture was performed in the electronic Lab at the IPAG. The FPGA board used is the SocKit evaluation board, of Altera with Cyclon V FPGA (Figure 7).

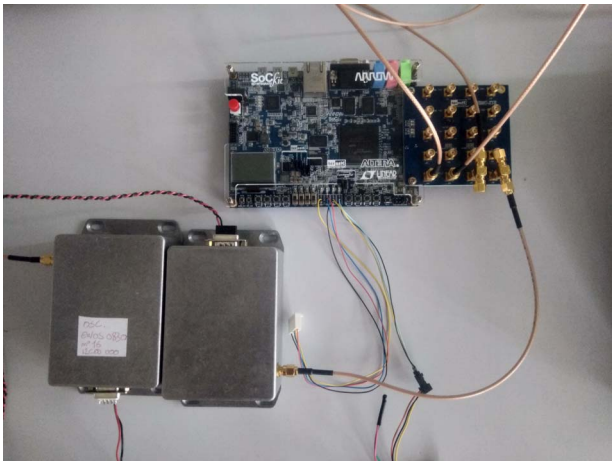

Fig. 7. System implemented. The two boxes contain each one an oscillator and a temperature sensor, to let us characterize the clocks against temperature changes between them. The system uses now the EWOS0830 Syrlinks clocks.

D. *Tests*

We have developed a test plan which include different tests to verify the test bench and characterize the clocks. The tests proposed are tests to validate the data coming from the TB, to validate and evaluate the board performance, to characterize the two pair of clocks available for different temperatures and to test the clock drift follow and phase compensation methods.

Ten hours acquisition test was performed to evaluate the board and communication. First we checked that there was no missing data coming from FPGA to computer and that it was stored correctly. For this we used the above mentioned Counter 7. This data is still under study. In result section we give the first insights coming from this test. Due to problems with signal splitter the evaluation using only one clock continues under progress. The other tests are queued until the test bench is completely evaluated.

V. PRELIMINARY RESULTS

The analysis of the 10 hours data test showed that there are some data lines missing and errors in the stored data. We are now studying this problems to find a correction for this errors. However we performed some analysis of the data to continue with the board validation using parts with no missing values.

Due to the PLL frequency generation possibilities in the FPGA, the original 1000Hz for the beat frequencies was changed to 1080Hz. The expected period was not seen in the data, but instead a stable 1108Hz period was observed with a 0.5Hz standard deviation coming from the Counter 2. This value was confirmed by measuring the beat frequency with two different instruments, PM6676 frequency counter 1108.03Hz and MDO3034 Oscilloscope from Tektronix 1108.64 Hz. This only means that the input oscillator is not exactly 10MHz measuring the oscillator with this two mentioned equipment's the frequency obtained was 9.99995 MHz which is consistent with the PLL frequency and beat frequency observed (Figure 8).

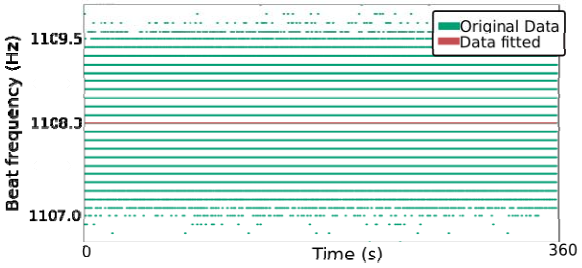

Fig. 8. Period measured from Counter 3, we observe 2 hrs. but this behavior is constant for the 10 hrs test. In red there is a fitted line to the data

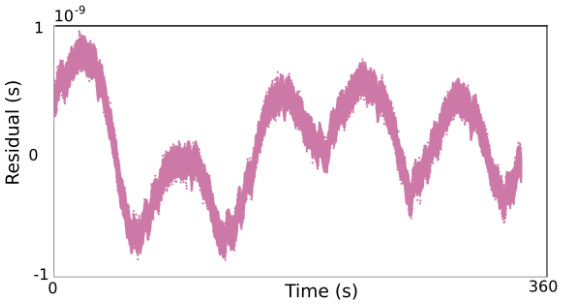

Fig. 9. Phase residual after removing trend of the phase measured by Counter 2. This noise is still under study to know the origin of it.

From the phase measurements we were able to test the Pong-Pong technique, obtaining a value near to the one expected of the frequency stability. But after removing the trend from the phase data. The residual showed a colored noise. This is still under study to know the origin of the noise (Figure 9).

VI. CONCLUSIONS AND DISCUSSION

We have described the complete time analysis to understand and correct the time errors caused by the clock drift in the LFR instrument. The results conclusions are still in progress but further measurements can improve the understanding of the possibilities in compensation of phase and time.

The system shows enough accuracy for our purpose, but further study of the data is needed to be conclusive of the tests. The short term objective for now is to perform the one clock test to evaluate noise of the board and confirm the accuracy of the test bench.

The next step after validation of the test bench, is to perform the temperature tests with the more realistic parameters. This will let to characterize the clocks by regard to each other. This test will be performed for the two pair of clocks from different manufacturers to compare their stabilities. And choose the optimal ones for our needs.

With this information we will be able to verify and quantify the compensation technique proposed. The Kalman filter will be evaluated to confirm the improvement of the clock drift measurement. Also the frequency calibration and time synchronization schemes can be defined completely. Noticing that this methods will function for a low SNR environment, with limited link budget and no external or direct link.

VII. AKNOWLEDGEMENTS

The Low Frequency Radar inherits from CONSERT/Rosetta founded by CNES and DLR.

The LFR development has been supported by the CNES's R&T program ("CONSERT Next Generation" study) and by the ESA's General Studies Program (AIM Phase A).

Granados is a Ph.D. student currently funded by CONACYT-México.

[1] P. Michel *et al.*, "Science case for the Asteroid Impact Mission (AIM): A component of the Asteroid Impact & Deflection Assessment (AIDA) mission," *Adv. Space Res.*, vol. 57, no. 12, pp. 2529–2547, Jun. 2016.

[2] A. Herique *et al.*, "Direct observations of asteroid interior and regolith structure: Science measurement requirements," *Adv. Space Res.*, Oct. 2017. *DOI: 10.1016/j.asr.2017.10.020*

[3] A. Herique *et al.*, "A radar package for asteroid subsurface investigations: Implications of implementing and integration into the MASCOT nanoscale landing platform from science requirements to baseline design," *Acta Astronaut. DOI 10.1016/j.actaastro.2018.03.058:*

[4] W. Kofman *et al.*, "The Comet Nucleus Sounding Experiment by Radiowave Transmission (CONSERT): A Short Description of the Instrument and of the Commissioning Stages," *Space Sci. Rev.*, vol. 128, no. 1–4, pp. 413–432, Feb. 2007.

[5] W. Kofman *et al.*, "Properties of the 67P/Churyumov-Gerasimenko interior revealed by CONSERT radar," *Science*, vol. 349, no. 6247, p. aab0639, Jul. 2015.

[6] M. Weib, "Synchronisation of bistatic radar systems," in *IGARSS 2004. 2004 IEEE International Geoscience and Remote Sensing Symposium*, 2004, vol. 3, pp. 1750–1753 vol.3.

[7] S. Sarno, M. D. Graziano, G. Fasano, and M. D'Errico, "Very-low altitude parasitic radar distributed on small satellites," *Adv. Space Res.*

[8] B. Sundararaman, U. Buy, and A. D. Kshemkalyani, "Clock synchronization for wireless sensor networks: a survey," *Ad Hoc Netw.*, vol. 3, no. 3, pp. 281–323, May 2005.

[9] D. R. Brown and A. G. Klein, "Precise timestamp-free network synchronization," in *2013 47th Annual Conference on Information Sciences and Systems (CISS)*, 2013, pp. 1–6.

[10] W. Kofman *et al.*, "Comet nucleus sounding experiment by radiowave transmission," *Adv. Space Res.*, vol. 21, no. 11, pp. 1589–1598, Jan. 1998.

[11] O. P. Pasquero, A. Hérique, and W. Kofman, "Oversampled Pulse Compression Based on Signal Modeling: Application to CONSERT/Rosetta Radar," *IEEE Trans. Geosci. Remote Sens.*, vol. 55, no. 4, pp. 2225–2238, Apr. 2017.

[12] C. W. T. Nicholls and G. C. Carleton, "Adaptive OCXO drift correction algorithm," in *Proceedings of the 2004 IEEE International Frequency Control Symposium and Exposition, 2004.*, 2004, pp. 509–517.

[13] D. W. Allan and H. Daams, "Picosecond Time Difference Measurement System," in *29th Annual Symposium on Frequency Control*, 1975, pp. 404–411.

[14] P. Moreira, P. Alvarez, J. Serrano, I. Darwezeh, and T. Wlostowski, "Digital dual mixer time difference for sub-nanosecond time synchronization in Ethernet," in *2010 IEEE International Frequency Control Symposium*, 2010, pp. 449–453.

Final characterization of InLambda delay standards for Supplementary Time Interval Comparison

Albin Czubla, Piotr Szterk, Roman Osmyk
Time and Frequency Laboratory
Central Office of Measures (GUM)
Warsaw, Poland
a.czubla@gum.gov.pl

Borut Pinter
Metrology Department
Slovenian Institute of Quality and Metrology (SIQ)
Ljubljana, Slovenia

Rado Lapuh
Metrology Institute of the Republic of Slovenia (MIRS)
Ljubljana, Slovenia

Uros Dragonja, Jurij Tratnik
InLambda Company
Ljubljana, Slovenia

***Abstract*—In this paper we present the final results of characterization of three time interval standards developed and produced by InLambda Company in cooperation with MIRS/SIQ within the EURAMET Project #1288, coordinated by MIRS/SIQ, as a part of preparation for a new Inter-Laboratory Comparison planned as a Supplementary Comparison in the KCDB. Our purpose was to assess the real accuracy of the generated time intervals, covering short- and long-term stability and possible influence of systematic factors/possible errors, in order to define required repeatability and reproducibility conditions giving reduction of systematic effects to a single picoseconds level. We finally obtained 10 ps accuracy and finished characterization.**

Keywords—delay standard, time interval comparison, picosecond accuracy; optical fiber

I. INTRODUCTION

The EURAMET Project #1288, started in 2013, was aimed to prepare travelling standards for a new Inter-Laboratory Comparison of Time Intervals planned as a Supplementary Comparison in the KCDB, as a response to negative experiences of EUROMET TF community with a cable delay measurement within the EUROMET Project #828 [1] which showed that a cable delay is not well-defined measured quantity and its value is significantly dependent on the shape of signals used for cable delay measurements and the selected trigger levels (maximum difference of about 1 % of the measured cable delay) – Fig. 1.

Within this project, there were developed and studied two types of standards: the electronic based Time Interval Generator (TIGen) developed by AGH and GUM, characterized before – poster presentation during EFTF 2016 [2], and the based on stabilized optical delay lines Time Interval standards developed and produced by InLambda Company in cooperation with MIRS/SIQ. Here, we present the final results of characterization of three InLambda standards: the assessment of the real accuracy of the generated time intervals, including short- and long-term stability and possible influence of systematic factors, as well as determination of the required repeatability and reproducibility conditions resulting in reduction of systematic effects to a single picoseconds (≤ 10 ps) level.

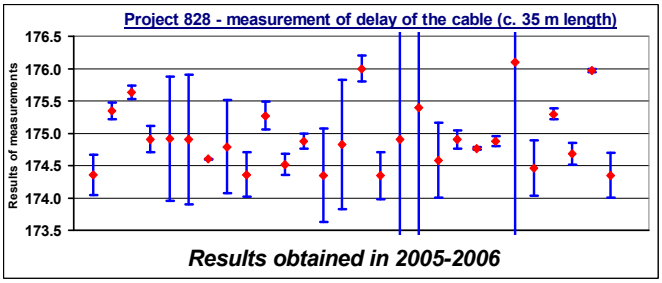

Fig. 1. Examplary results of cable delay measurements within #828 EUROMET project. There is visible a big discrepency (up to 1.751 ns) following different shapes of pulse signals used for delay measuremens.

II. INLAMBDA DELAY STANDARDS

The specially developed for TI comparison travelling InLambda standards (Fig. 2) are based on stabilised optical delay lines maintained by internal temperature stabilization of the fibers at approximately 35 °C (Fig. 3). Each of three InLambda standards realizes a single value of time interval defined between rising slopes of START and STOP output pulses: c. 20 ns, c.100 ns or c. 300 ns appropriately. The outputs are precisely matched, so the parameters of output signals are closely the same. Together with very sharp slopes (rise time < 500 ps), it allows to minimize the undesirable effects of start/stop trigger errors and trigger level timing errors. InLambda standards require the external pulses (passed into the input) that are the flywheel of the output signals. The external input pulses should fulfill the special requirements verified below in order to achieve the required repeatability and reproducibility conditions. All signal inputs/outputs are BNC-female connectors. In the fixed external conditions, the observed long-term instability (TDev) does not exceed 2 ps, including the instability of Time Interval Counter (TIC).

Fig. 2. The set of prepered and characterised three InLambda delay standards realized time intervals of about 20 ns, 100 ns and 300 ns.

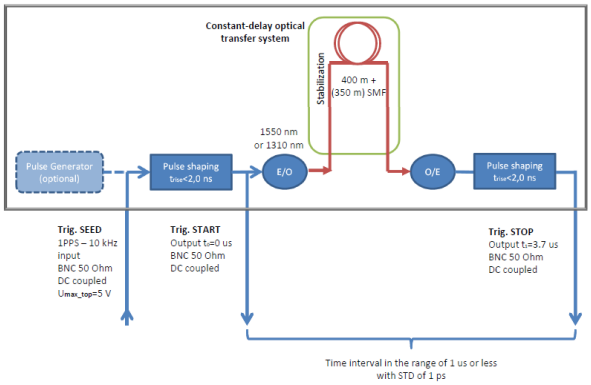

Fig. 3. The block scheme of operation of InLambda delay standards.

III. RESULTS OF CHARACTERIZATION

Characterization of InLambda standards were performed in the last two years. The preliminary tests were carried out at SIQ and. next, the further more detailed and more time consuming tests were made at GUM. The tests were made in different configurations: with different sources and parameters of the input signals, with different TIC settings (trigger level), with fixed or variable environmental conditions, short-term only or long-term continuous measurements in the fixed laboratory conditions. All GUM measurements were performed with T4100U counter, giving precision of a few picoseconds and with non-linearities not exceeding 12 ps (peak-to-peak). In order not to reveal the true values of the measured TI, all presented here results are raw measurement results without reduction of the auxiliary cable delays, differential channel delays or connector delays. If different cable configuration were applied to the same standards then the obtained values of the raw results can be different, too.

A. Rising time of the input signals

During tests with different sources and parameters of the input signals, required to produce output signals, there was observed a slight dependence of the delay value of the input pulse rise time (about 9 ps by 1 ns change of the rising time) – Fig. 4. That problem was fixed by the auxiliary usage of the output signal of the other InLambda standard (steered by external input signal) as the input signal of the currently measured standard which resulted in the disappearance of the effect, if the rising time of the original external input signal is

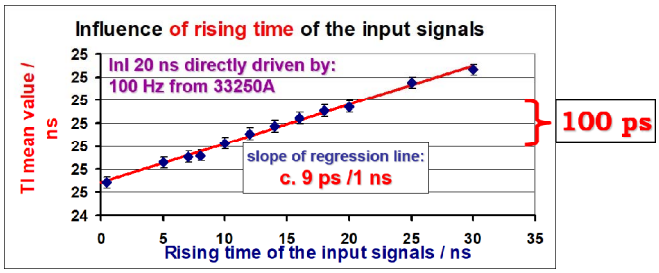

Fig. 4. Depenence of the realized time intervals of the rising time of the input signals, if InL 20 is steered directly by the external signal source.

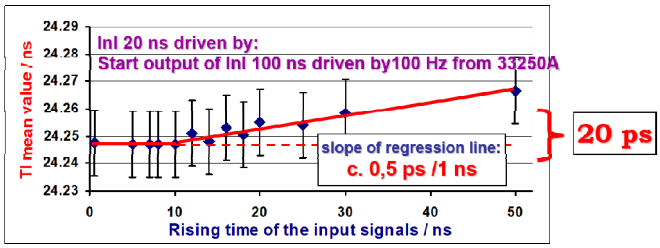

Fig. 5. Depenence of the realized time intervals of the rising time of the input signals, if InL 20 is steered by the START output of InL 100 steered by the external signal source. Up to rising time of 10 ns, there is no visible influence.

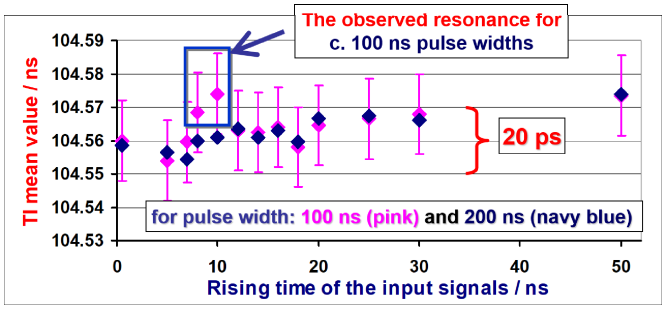

Fig. 6. The observed interference/ resonance for InL 100 standard if the pulse width of 100 ns was used. For the pulse width of 200 ns, the effect is not visible.

less than or equal 10 ns, and about 20-times less sensitivity than before, if the rising time of the original external input signal is more than 10 ns – Fig. 5.

It is recommended to use the START output signals of the auxiliary used the other InLambda standard, in order to avoid a bit more possible instabilities of the STOP output signals due to a more complex internal path inside the device to the STOP output than to the START output.

B. Pulse width of the input signals

For some combination of the pulse width and rising time of the input signals, there was observed a some interference or resonance of the output signals with the input signals manifesting by a small increasing the realized time interval – Fig. 6. The effect is observed for each standard when the input pulse widths are close to the realized time intervals (for Inλ 20 – at pulse widths approx. 20 ns, for Inλ 100 – at pulse widths

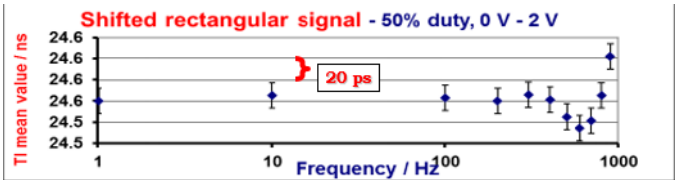

Fig. 7. The observed dependence of the realized time interval of the frequency of the input signal for rectangular signals with low level of 0 V and high level of 2 V.

(a)

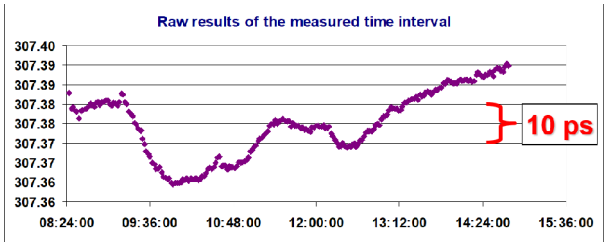

(b)

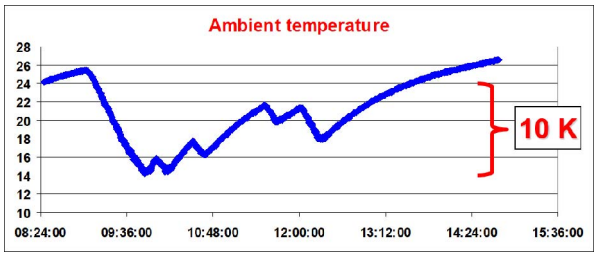

Fig. 8. The observed influence of ambient temperature for InL 100 standard (a) the changes of the realized time inteerval and (b) the corresponding changes of ambient temperature.

approx. 100 ns, and for Inλ 300 – at pulse widths approx. 300 ns). A difference does not exceed 10 ps, but for possible more precise measurements (e.g. with high-speed oscilloscopes) it can lead to ambiguity.

C. *Frequency of the input pulses*

The input pulses can be passed with different frequencies, however the fixed value of the realized time interval is only observed until the input signal frequency reaches a limit value dependent on the input pulse parameters. If a limit value of the input signal frequency is exceeded then the realized time interval is no longer fixed and starts to be variable with changing input frequency. Exemplary, for the shifted rectangular signals there is no observed change of the realized time interval up to about 200 Hz (Fig. 7), and for the fixed pulse width, the upper limit frequency is be changeable, e.g. about 5 kHz – for the pulse width of about 100 ns, or about 200 Hz – for the pulse width of about 15 µs.

D. *Influence of ambient temperature*

During measurements performed with InLambda standards exposed to a variable ambient temperature, there was observed a small influence of temperature changes on the realized time intervals (0,6 ps/ K, 1,4 ps/ K and 2,5 ps/ K accordingly) – Fig. 8, probably caused by imperfection of temperature fiber stabilization. This effect can not to be omitted at more precise measurements and requires, first, to fix the reference ambient temperature and, next, to monitor the ambient temperature during measurements in order to recalculate results relatively to the temperature offset and temperature coefficient of the standard if it is not negligible.

The InLambda standards have also signaling system of the improper temperature stabilization (signaling warm-up period and overheating) and the measurements should be performed only if the red led alarm light is not calling and the green led light that confirms proper temperature stabilization is on.

IV. Conclusions

The InLambda standards are ready for Time Interval Supplementary Comparison. The required measurement conditions have been defined and the possible sources of errors have been recognized. A stability and reproducibility of generated Time Intervals was verified and it can be assign 10 ps of expanded uncertainty to each travelling standard.

References

[1] A. Niessner, W. Mache, “Final report. Project No 828. EUROMET TF.TI-K1 Comparison of time interval (cable delay) measurement”, BEV, 2007

[2] A. Czubla, P. Szterk, P. Krehlik, Ł. Śliwczyński, M. Yogun, R. Hamid, K. AlDawood, F. Almuhlaki, A. Aljawan, I. Alboraih, B. Pinter, M. Marszalec, M. Lusawa, “Pilot Comparison of Time Interval Measurements with High Speed Oscilloscopes – initial results”, presented during EFTF 2016, unpublished.

Preprocessing for fast synchronization of high-stability oscillators disciplined by GNSS 1 PPS signal

Pawel Kubczak, Michal Kasznia, Mieczyslaw Jessa
Chair of Telecommunication Systems and Optoelectronics
Poznan University of Technology
Poznań, Poland
pawel.w.kubczak@doctorate.put.poznan.pl

***Abstract*—This paper presents a novel algorithm for preprocessing of pulses coming from GNSS and signals produced locally by a rubidium oscillator to reduce synchronization time without changing the main algorithm of the control loop. Moving average and Kalman filtration were used as the preprocessing methods. The experimental results for different rubidium oscillators are presented.**

Keywords— GNSS; PPS; synchronisation loop; Kalman filtering; preprocessing

I. INTRODUCTION

The rubidium oscillators are commonly used as time and frequency sources for many purposes. Their good properties, combined with disciplining by 1 Pulse Per Second (PPS) signal from generally available Global Navigation Satellite Systems (GNSS), give excellent globally available tool for synchronization of many sources. The precise time and frequency are used in many different areas, such as telecommunications, networking, monitoring, navigation, electricity, measurement, and control systems.

The paper contains the description of the proposed solutions and the experimental results for three rubidium oscillators with different parameters, coming from different manufactures. Fast synchronization is achieved by preprocessing of 1 PPS pulses coming from commonly available GNSS and includes the outliers rejection procedure, moving average with averaging time adequate to the phase characteristic of 1 PPS pulses, and Kalman filtering. Additionally, we reset of the phase of the feedback signal and use the prediction of the control word based on the knowledge obtained during power-on self-test of the device. The experimental servo-loop consists of a phase detector implemented in a Field Programmable Gate Array (FPGA) resources, microcontroller realizing control algorithm and providing communication with PC, and rubidium oscillator. The experiments were performed for compact size as well as for chip scale size rubidium oscillators. The influence of the proposed solutions on the synchronization time and the quality parameters MTIE and TDEV were also examined and discussed. A synchronization time of less than three minutes was obtained, after which the signal met the PRC standards. The proposed algorithm is considered a new, effective and simple hardware defined time and frequency source upgrade that addresses the challenges of modern synchronization.

II. SYSTEM DESCRIPTION

A. Synchronisation loop principles

The experimental synchronization loop considered in the paper consists of the source of the reference signal, phase detector, loop filter, and local oscillator (Fig. 1). As a reference the 1 PPS signal generated by Trimble Accutime GNSS receiver is used. The values of the phase error have the Gaussian distribution with the mean value of 0 ns and the standard deviation of 3 ns (Fig. 2) [1].

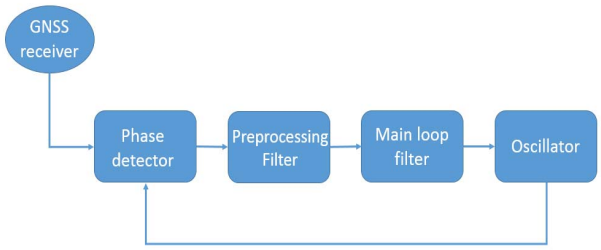

Fig. 1. Synchronization loop.

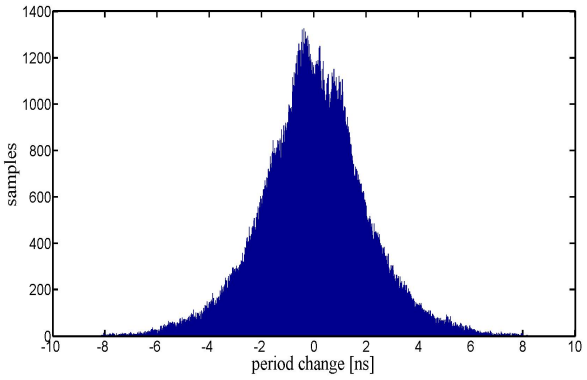

Fig. 2. Distribution of the phase error of 1 PPS pulses.

The presented work has been funded by the Polish Ministry of Science and Higher Education within the status activity task "80/83/DSPB/4722" in 2017.

The phase detector was implemented using FPGA structure (Fig. 3) as a time-to-digit converter. The counter enabled and disabled by rising edges of the input signals counts the pulses of an internal clock with high frequency. The phase difference measured using this technique is a number of pulses multiplied by their length (the period of the internal clock) and features the measuring error. As result, the output value of the phase detector combines the measuring error and the random properties of the phase of both signals – the 1 PPS signal form the GNSS receiver and the signal from the local oscillator.

The loop filter is implemented as a digital control algorithm with a single input and a single output. The input of the filter is a value representing phase difference between the reference signal and the local one. The output of the filter is a code word used to control the frequency of a local oscillator directly or through a DAC. The main control algorithm can exploit the knowledge about the system elements obtained previously. It also may contain additional filters and subalgorithms.

The final part of the system considered is an oscillator which frequency is usually tuned by changing control voltage (VCO). Depending on application different clocks may be applied. They can differ in many parameters as the output frequency, long and short-term properties, noise level, ageing characteristic. The frequency of the feedback signal generated by the local oscillator and passed to the phase detector can be divided to increase maximal measured phase difference and prevent from phase jumps.

B. Implementation of the control algorithm

In order to verify the solutions proposed the experimental setup communicating with PC was created (Fig. 3). The value of the phase difference calculated using FPGA structure (SPARTAN 6) is sent to the microcontroller via SPI. Then the microprocessor (XMEGA 256) sends data to the PC trough the USB virtual serial port. The main control algorithm implemented using Matlab reads data from the port, executes the iteration, and sends back the control word to the microcontroller that communicates via Two Wire Interface (TWI) with precise DAC to control the local oscillator.

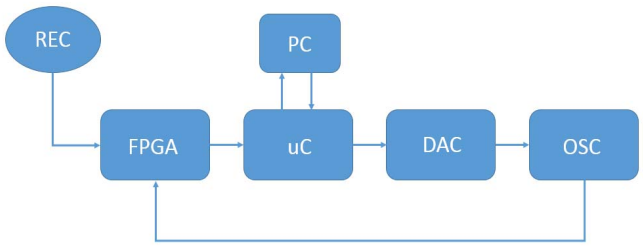

Fig. 3. Hardware experimental setup.

The experiments were performed for three rubidium oscillators: Temex LPFRS, Symmetricom CSAC SA.45s, and Quartzlock E10-MRX.

Because the digital part of the system was moved to the PC and it is executed using Matlab we can observe in the real time the values of phase difference from the phase detector, the output of preprocessing filter, and the control code word at the input of the oscillator. In artificial way the initial phase error can be set as well as some disturbances to the phase can be added. This structure can also be used to perform the identification experiments of the oscillators.

C. Proposed algorithm description

To achieve fast synchronism without changing the main control algorithm three methods based on the preprocessing of the phase difference are proposed: power on self-test with remembered control word, phase reset technique, and filtration method indicating the trend of signal. First method exploits the knowledge of synchronization state obtained earlier and the code word providing synchronism in the past. Second method reduces the initial phase error which is used then by the main control algorithm. Third solution is an idea based on filtration of data to provide the best trajectory. These solutions can be used together or separately. All methods proposed will be described in detail in the next section.

III. PREPROCESSING METHODS

A. Power on self-test

Power on self-test method utilizes the knowledge about the synchronization state obtained just before the system was shut down. When the circuit is turn on, the last remembered control code word is applied as an initial value of a new process of synchronization. This value is kept until oscillator provides information that is ready to work. Next, the performance of the clock is observed within 30 s. The average phase difference within this time interval is computed and used to apply correction to the initial frequency.

B. Phase reset

In the phase reset method the value of the initial phase error is reduced. As we can see in Fig. 2, the pulse of the 1 PPS signal indicates the beginning of a new second with accuracy of 9 ns (3 sigma). When one of the 1 PPS pulses is used to reset the output frequency synthesizer or frequency divider in the feedback loop, we can start with small phase error. In the worst case the phase error is equal to a sum of the 1 PPS phase error (in our case 9 ns) and the time of propagation of reset signal (in our case less than 20 ns). As result the initial phase error is less than 30 ns.

C. Kalman filtering and object identification

The Kalman filter applied in the PLL provides an optimal trajectory tracking in the presence of noise. When the filter provides accurate information about a phase, the state of synchronism can be reached faster. The prediction and correction of the phase is performed within a single iteration of the filter according to the formulas [2]:

$$\mathbf{x}_{pred} = \mathbf{A} \times \mathbf{x} + \mathbf{B} \times \mathbf{u} \tag{1}$$

$$\mathbf{P}_{pred} = \mathbf{A} \times \mathbf{P} \times \mathbf{A}^T + \mathbf{Q} \tag{2}$$

$$\mathbf{K} = \mathbf{P}_{pred} \times \mathbf{C}^T \times \left(\mathbf{C} \times \mathbf{P}_{pred} \times \mathbf{C}^T + \mathbf{R}\right)^{-1} \quad (3)$$

$$\mathbf{x} = \mathbf{x}_{pred} + \mathbf{K} \times \left(\mathbf{z} - \mathbf{C} \times \mathbf{x}_{pred}\right) \quad (4)$$

$$\mathbf{P} = \left(\mathbf{I} - \mathbf{K} \times \mathbf{C}\right) \times \mathbf{P}_{pred} \quad (5)$$

where: **x** is the state vector, **u** is the control, **A** is the state matrix, **B** is the input matrix, **P** is the process error covariance matrix, **Q** is the process noise covariance matrix, **K** is the Kalman gain matrix, **C** is the output matrix, **R** is the measurement noise covariance matrix, **z** is the actual measurement, **I** is the identity matrix, and the subindex *pred* indicates the matrix or vector with predicted values.

Because the oscillators used in telecommunication are very stable, we can strongly trust the clock prediction and set the Matrix **Q** with near zero coefficients. In order to get other coefficients of space state model the control object identification experiment was proposed. As a control stimulus a bipolar signal was used having the amplitude equal to one quarter of the control range. The control and output signals for the CSAC oscillator are presented in Figure 4. After the experiment the matrices **A** (state), **B** (input), and **C** (output) were found using the Mean Squared Error Method. Because first order system with 1x1 **A** matrix had a bad dynamic prediction, second order with 2x2 **A** matrix was used. The solution of the next orders matrix increases the complexity and does not provide better curve fitting to experimental data.

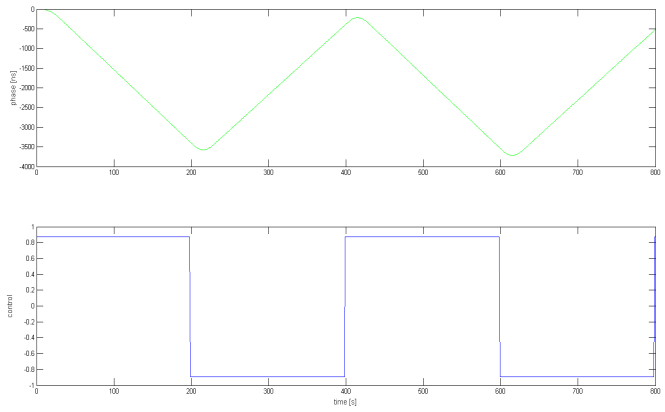

Fig. 4. Signals in the identification experiment of CSAC oscillator.

D. MAV filter

The implementation of the Kalman filter using a microcontroller requires applying the floating point operations that could exceed computational capabilities of device without floating point coprocessor. In this case simple moving average (MAV) filtration of the phase error can be used instead. Different lengths of the MAV filter were tested during the experiments.

IV. Experimental Results Analysis

A. Testing procedure

In order to verify the influence of the proposed preprocessing methods on the synchronization process a series of experiments was performed. An initial phase difference was set to 100 ns. Then the time of the phase error reduction was observed. As a synchronism such state was assumed, when the average phase (60 s averaging time) observed at the phase detector during 60 s was less then +/– 10 ns. As a main loop filter algorithm the proportional-integrating algorithm was applied. The experiments were rejected when some unexpected jumps occurred in the 1 PPS signal obtained from the GNSS receiver.

B. Time of phase reduction

In the Table I the influence of the MAV filter length on the synchronization time is presented. We can see that the increase of the number of averaged samples (until some value) reduces the time of synchronization. For value 30 for the CSAC and 25 for the LPFRS the overshoot was significant and signal get into the convergence region from the other side. Further increasing of the length of the MAV filter is not suggested because it introduces additional delay in the loop transfer function and may cause oscillations.

TABLE I. Time of synchronization using MAV filter

MAV Length	Time of phase reduction [s]		
	CSAC	***LPFRS***	***E10-MRX***
1	108	129	132
5	109	124	130
10	98	124	125
15	97	123	124
20	93	120	120
25	93	160	122
30	122	210	122
40	144	240	124

In the Table II the results obtained for different values of the Q parameter of the Kalman filter are presented. Similarly as in the previous case the time of synchronization decreases (until the value of 90 s) when the Q parameter is decreased (until the value of 0.001). Further decrease of the Q parameter causes increase of the synchronization time.

TABLE II. Time of synchrozation usig Kalman filter

Kalman Q value	Time of phase reduction [s]		
	CSAC	***LPFRS***	***E10-MRX***
1	108	132	136
0.1	107	128	136
0.01	106	127	132
0.005	95	123	132
0.001	90	120	128
0.0005	110	123	120
0.0001	135	126	122
0.00001	160	125	144
0.000001	210	133	165

The CSAC oscillator revealed as the most sensitive item: the changes of the parameters of the filters results in the significant changes of the synchronization time.

The LPRFS oscillator cooperates very well with the Kalman filter – even very low Q value does not increase the time of synchronization dramatically. This is probably caused by very good short term properties of this oscillator, and therefore the predictions of the Kalman filter are very accurate.

The loop containing the E10-MRX oscillator showed better performance for the MAV filter than the Kalman filter. It could be caused by weak short term properties of the oscillator that were reduced by the averaging.

The shortest time of the phase reduction process (90 s) was observed for the system containing the CSAC oscillator and the Kalman filter with the parameter Q=0.001. The shortest phase reduction time for the compact rubidium oscillators (120 s) was observed for the loop with LPFRS oscillator and 20 s MAV filter or Kalman filter having Q=0.001 and for the loop with E10 oscillator and 20 s MAV filter or Kalman filter having Q=0.0005.

The total time of pull-in process of the loop must be considered as a sum of 30 s self-test time of the oscillator, the time of the phase reduction process described above and the 60 s time of the confirmation of the synchronism state (observation of the 60 s MAV value of the phase error within assumed limit). Finally, the minimum total synchronization time obtained in the experiment was 3 minutes for the loop with the CSAC oscillator and the Kalman filter with the parameter Q=0.001. This time may be reduced using the initial phase reset.

C. Time plots examples

In this section the time plots illustrating the performance of the analyzed loop with the preprocessing methods applied for different oscillators are presented. The phase difference between the input 1 PPS signal and the output of the rubidium oscillator observed at the output of the phase detector is presented using green line. The red line shows the output preprocessing filter. The blue line represents the average value of the phase difference computed within the last 60 s used as an indicator of the synchronism state.

In Figures 5–7 typical performance of the loop with MAV filter having the length of 20 s for different oscillators is presented. Different shapes of the phase difference were caused by the performance of the GNSS 1 PPS signal.

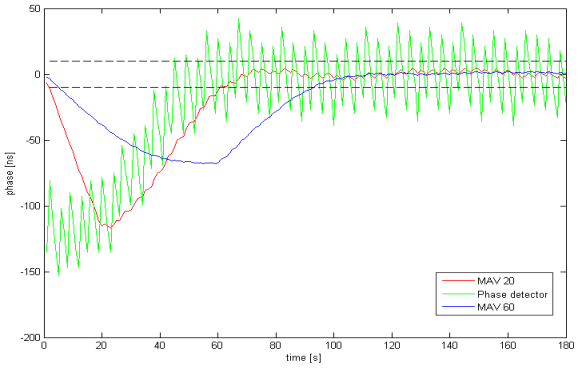

Fig. 5. Loop performance for CSAC oscillator and 20 s MAV filter.

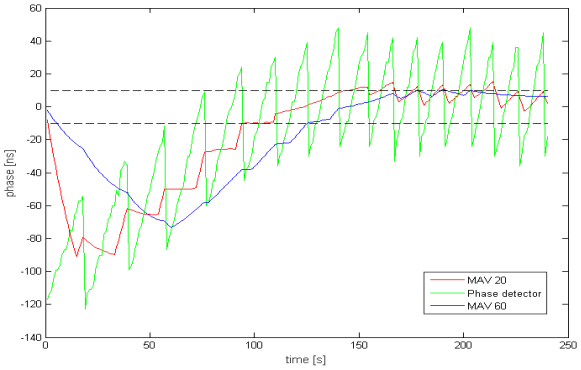

Fig. 6. Loop performance for LPFRS oscillator and 20 s MAV filetr.

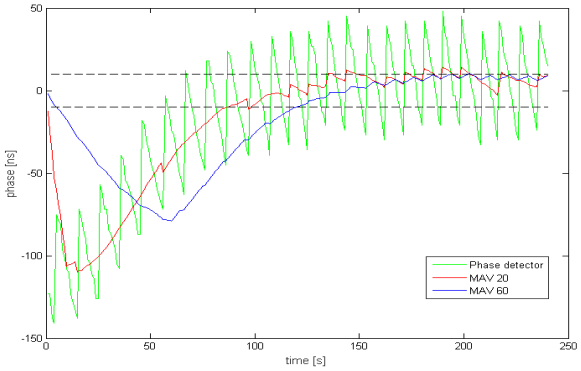

Fig. 7. Loop performance for E10-MRX oscillator and 20 s MAV filter.

In Figures 8–10 the loop performance for 40 s MAV filter is shown. Long MAV filter introduces a delay into the loop and the overshoot effect is visible

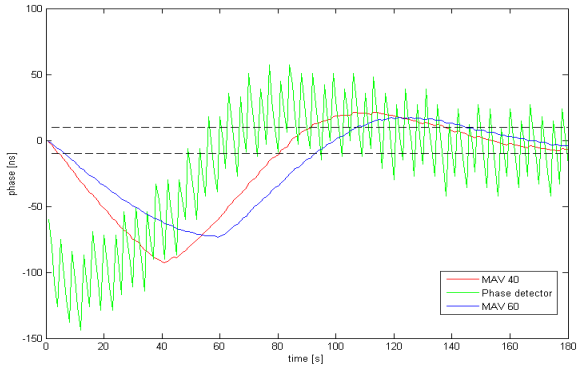

Fig. 8. Loop performance for CSAC oscillator and 40 s MAV filter.

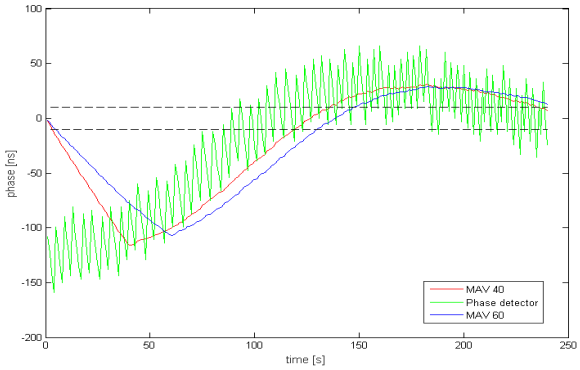

Fig. 9. Loop performance for LPFRS oscillator and 40 s MAV filetr.

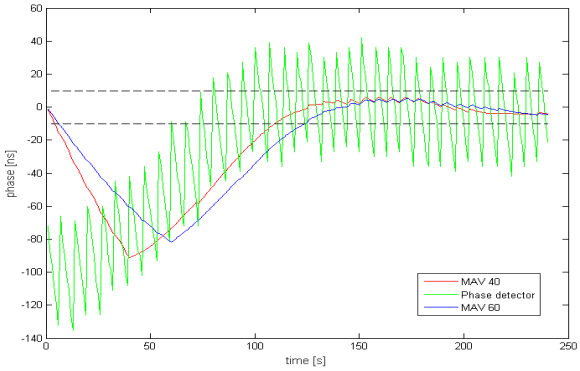

Fig. 10. Loop performance for E10-MRX oscillator and 40 s MAV filter.

Figures 11–13 illustrate the loop performance for the Kalman filter with Q=0.001. This filter removes the short-term fluctuations but the filter output follows the long-term performance of the 1 PPS signal.

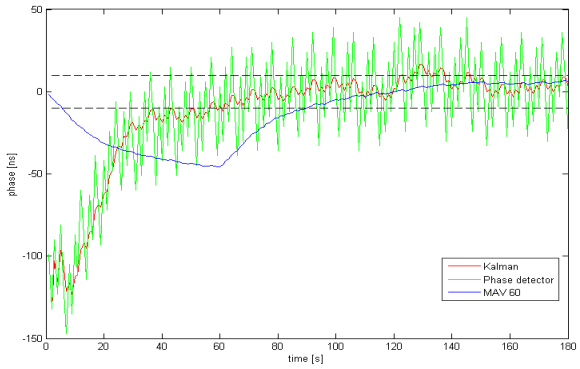

Fig. 11. Loop performance for CSAC oscillator and Kalman filter with Q=0.001.

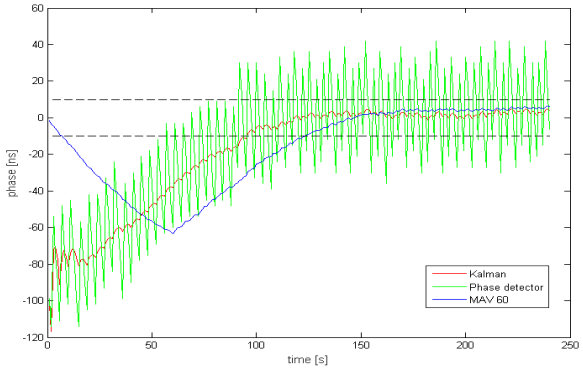

Fig. 12. Loop performance for LPFRS oscillator and Kalman filter with Q=0.001.

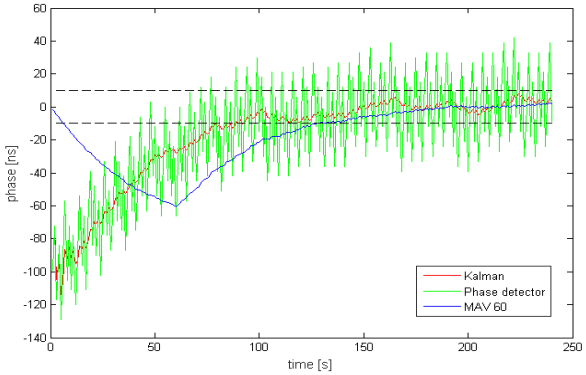

Fig. 13. Loop performance for E10-MRX oscillator and Kalman filter with Q=0.001.

Figures 14-16 present the loop performance for the Kalman filter with Q=0.000001. Filter provides very smooth output even in the presence of short-term effects.

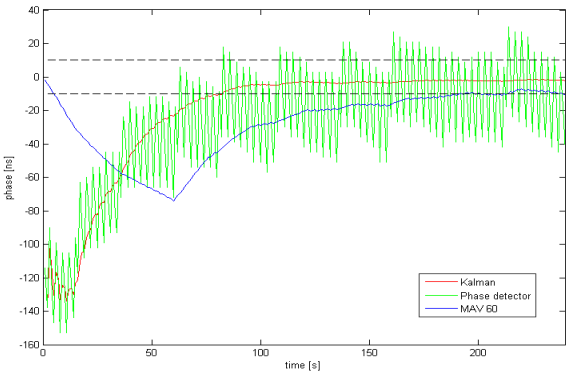

Fig. 14. Loop performance for CSAC oscillator and Kalman filter with Q=0.000001.

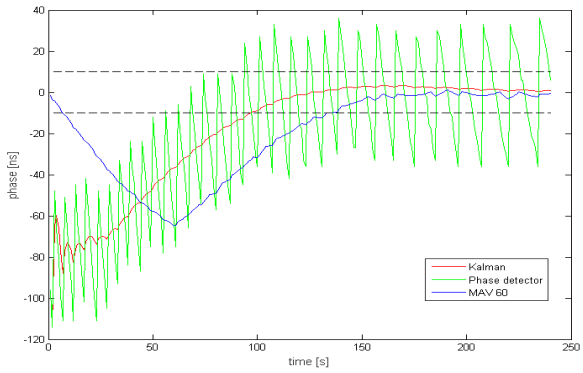

Fig. 15. Loop performance for LPFRS oscillator and Kalman filter with Q=0.000001.

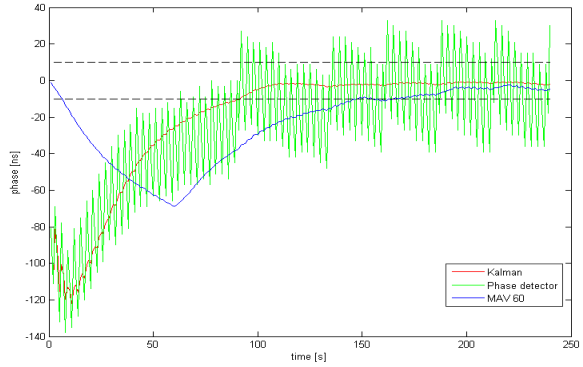

Fig. 16. Loop performance for E10-MRX oscillator and Kalman filter with Q=0.000001.

D. Long term performance of the loop

In order to analyze the performance of the system in the synchronism state two parameters commonly used for evaluation of the timing signals in telecommunications – Maximum Time Interval Error MTIE and Time Deviation TDEV [3,4] – were measured experimentally using multi-purposes SP4000c measuring system [5]. The results for the CSAC (blue line), LPFRS (red line) and E10-MRX (green line) oscillators are presented in Figures 17 and 18. The values of the parameters are compared with the limit values required for the Primary Reference Clock (PRC).

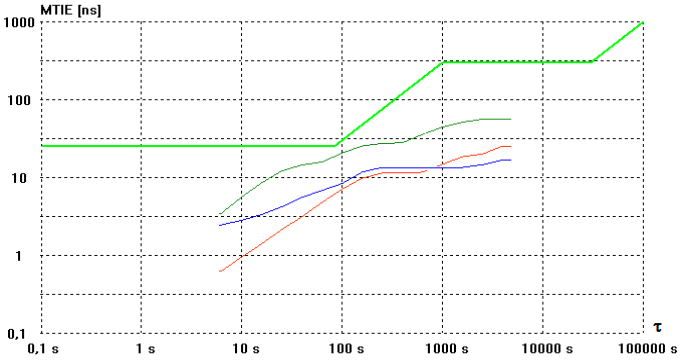

Fig. 17. MTIE of synchronized CSAC, LPFRS, and E10-MRX oscillators.

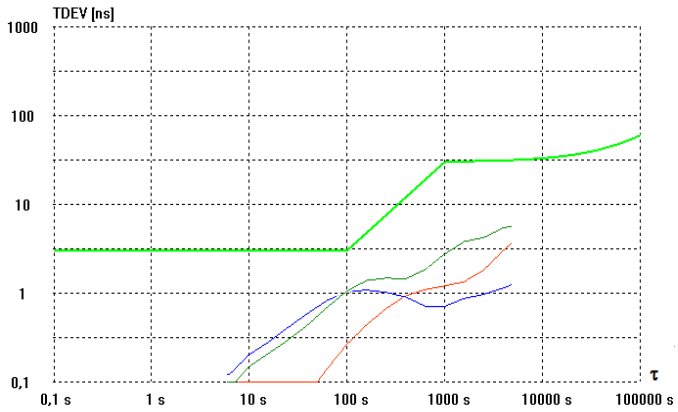

Fig. 18. TDEV of synchronized CSAC, LPFRS, and E10-MRX oscillators.

V. CONCLUSIONS

In this paper some preprocessing methods enabling fast synchronization of the rubidium oscillators were proposed. These methods allow obtaining the synchronism state within the total time less than 3 minutes. The output signals have good long term properties that met the requirements of the telecommunication PRC standards. The methods described are simple and can be introduced to existing solutions to improve the process of synchronization.

REFERENCES

[1] P. Kubczak, Ł. Matuszewski, "PPS Quality Estimation From Different Receivers," Measurement Automation Monitoring 2016 no. 11, pp. 383-386.

[2] R. E. Kalman, "A New Approach to Linear Filtering and Prediction Problems," Transactions of ASME, Series D, Journal of Basic Engineering, Vol. 82, No. 1, 1960, pp. 35-45.

[3] ITU-T Rec. G.810, "Considerations on timing and synchronization issues" (08/96)

[4] ITU-T Rec. G.811, "Timing characteristics of primary reference clocks" (09/97)

[5] A. Dobrogowski, M. Jessa, M. Kasznia, K. Lange and M. Jaworski, "Hardware and software realization of time error measurements with real-time assessment of ADEV, TDEV, and MTIE, " *EFTF-2010 24th European Frequency and Time Forum*, Noordwijk, 2010, pp. 1-8. doi: 10.1109/EFTF.2010.6533710

Relativistic Corrections for Intersatellite Frequency Transfer

Bethany Kroese*, Gabriele Giorgi, and Christoph Günther
Institute of Communication and Navigation
German Aerospace Center (DLR)
Oberpfaffenhofen, Germany
Email: bethany.kroese.2@us.af.mil and bethany.kroese@dlr.de
*Exchange Researcher working at DLR from the Air Force Research Laboratory, Albuquerque, NM USA

***Abstract*—Highly accurate time and frequency synchronization is crucial for navigation. Constant improvements in clock technology enable more precise systems. This in turn places stricter demands on coordination and dissemination of timescales. This paper is motivated by an interest in evaluating future concepts for GNSS (Global Navigation Satellite System) constellations. Within the field of space-based time and frequency transfer, intersatellite links are of high interest for GNSS clock synchronization. In addition to synchronizing clocks, these links can improve orbit determination through precise ranging. Transmissions resolve time and frequency information (i.e. clock offsets and drifts) by modeling satellite orbit effects and propagation delays. In order to fully capitalize on the stability of next-generation space clocks, relativistic corrections must be described to a high level of precision and satellite positions must be accurately known.**

***Keywords*—frequency transfer, clock synchronization, relativity corrections, intersatellite links**

I. Introduction

Today's atomic frequency standards based on microwave frequencies remain the standard for both laboratory and GNSS timing solutions. The global trend now looks to the optical regime and laser cooling for improved performance. A number of high-performance frequency standards based on optical transitions and cold atom technology exist in laboratories and designs have also been proposed for space [1]–[3]. These next-generation clocks present stabilities down to the level of 10^{-16}. The dissemination of the resulting timescales requires careful control of noise and modeling of physical effects. Relativity corrections have been implemented in GNSS since GPS's inception but reaching these new performance levels requires a more complete picture. Blanchet, for example, determined a relativity model for the ACES experiment, with fractional frequency below 5×10^{-17}, must include all terms up to $1/c^3$ [4]. In the present paper, we are interested in evaluating frequency transfer or clock syntonization for future GNSS concepts [5]. We evaluate a published relativity model for a set of intersatellite links to determine the required terms for two thresholds. 10^{-16} should support space-based synchronization of current optical oscillators and 10^{-18} should support future space clocks.

II. The Frequency Transfer Framework

Accurate comparison of clocks must be performed using the general theory of relativity. This gives us a reference frame to resolve proper quantities from measurements as observed quantities are location dependent. Relativity predicts that clocks in a different gravitational potential and/or moving relative to an observer will exhibit a frequency shift when recorded by said observer. The International Astronomical Union (IAU) established the Geocentric Celestial Reference System (GCRS) and Geocentric Coordinate Time (TCG) in order to relate events to a terrestrial timescale [6]. The relationship between proper (τ) and coordinate (t) time is defined by the spacetime metric. The first post-Newtonian approximation of the Minkowski metric is sufficient within the vicinity of the Earth (i.e. weak gravitational fields and low velocities) for the intended level of accuracy [7]. The rate of the clock on satellite S compared to TCG is given by [4]

$$\frac{d\tau_S}{dt} = 1 - \frac{1}{c^2}\Big[U_E(\mathbf{x}_S) + \frac{\mathbf{v}_S^2}{2} + V(\boldsymbol{\chi}_S) - V(\boldsymbol{\chi}_E) - x_S^i \partial_i V(\boldsymbol{\chi}_E)\Big]. \tag{1}$$

Here, U_E is the gravitational potential of the Earth evaluated at the position of the satellite, $\mathbf{x}_N$, and the velocity, $\mathbf{v}_N$, is used in the second-order Doppler effect. Both position and velocity are expressed in geocentric coordinates. V is the sum of gravitational potentials of all other bodies evaluated in barycentric coordinates at the location of the satellite ($\boldsymbol{\chi}_N$) and of the Earth ($\boldsymbol{\chi}_E$).

A. Simulation Definition

The aim of the present paper is to evaluate the contributions needed for relativity corrections in future GNSS systems. Thus, equation (1) for satellites in a Medium Earth Orbit (MEO) should be evaluated for the target frequency stability. In this present study, we select a nominal Galileo orbit with a semi-major axis of 29600 km and an eccentricity of 0.0003. Eight satellites are evenly spaced within a plane to match the existing constellation. We evaluate links between adjacent and next-neighbor satellites in the same orbital plane.

The satellites' orbits are simulated using the open source software, GMAT, available from NASA [8]. EGM2008 provides the coefficients to implement the geopotential, $U_E(\mathbf{x})$,

as a series expansion in spherical harmonics [9]. The impact of external bodies can be modeled as

$$V(\boldsymbol{\chi}_C) - V(\boldsymbol{\chi}_E) - x_C^i \partial_i V(\boldsymbol{\chi}_E) = \sum_{C \neq E} GM_C \Big[\frac{1}{r_{SC}} - \frac{1}{r_{EC}} + \frac{\boldsymbol{r}_{EC} \cdot \boldsymbol{r}_{SE}}{r_{EC}^3} \Big] \quad (2)$$

when referring to terrestrial satellites and use either barycentric or geocentric coordinates [7], [10]. Here, subscripts S, E, and C refer respectively to the satellite, the Earth, and the other celestial bodies. For example, $\boldsymbol{r}_{SE}$ is the vector between the satellite and the Earth and r_{SE} is its magnitude.

B. Comparison of Proper Frequencies

Equations (1) and (2) define the rate of a single clock when referenced to geocentric coordinate time. In intersatellite frequency transfer the quantity of interest is the comparison of the proper frequencies between two clocks, f_A/f_B, obtained via an optical link between the two platforms. The relativistic shift is

$$\begin{aligned} \frac{f_A}{f_B} &= \Big(\frac{f_A}{\nu_A}\Big)\Big(\frac{\nu_A}{\nu_B}\Big)\Big(\frac{\nu_B}{f_B}\Big) \\ &= \Big(\frac{f_A}{\nu_A}\Big)\Big(\frac{dt}{d\tau_A}\frac{d\tau_B}{dt}\frac{q_A}{q_B}\Big)\Big(\frac{\nu_B}{f_B}\Big) \end{aligned} \quad (3)$$

with

$$q_A = 1 - \frac{\mathbf{N}_{AB} \cdot \mathbf{v}_A}{c} - \frac{4GM_{\mathrm{E}}}{c^3} \frac{(r_A + r_B)\mathbf{N}_{AB} \cdot \mathbf{v}_A + \mathrm{R}_{AB} \frac{\mathbf{r}_A \cdot \mathbf{v}_A}{r_A}}{(r_A + r_B)^2 - \mathrm{R}_{AB}^2} \quad (4)$$

$$q_B = 1 - \frac{\mathbf{N}_{AB} \cdot \mathbf{v}_B}{c} - \frac{4GM_{\mathrm{E}}}{c^3} \frac{(r_A + r_B)\mathbf{N}_{AB} \cdot \mathbf{v}_B - \mathrm{R}_{AB} \frac{\mathbf{r}_B \cdot \mathbf{v}_B}{r_B}}{(r_A + r_B)^2 - \mathrm{R}_{AB}^2} \quad (5)$$

where ν_A is the proper frequency of the photon sent from A and ν_B the frequency of the same photon received at B. GM_{E} is the Earth's standard gravitational parameter, $\mathrm{R}_{AB} = |r_B(t_B) - r_A(t_A)|$ is the magnitude of the vector between the satellites with t_A being the time of transmission and t_B being the time of reception, and $\mathrm{N}_{AB} = \mathbf{R}_{AB}/\mathrm{R}_{AB}$ is the line of sight unit vector. For a full description and derivation the reader is referred to [4]. We see that the equations include proper and coordinate time as well as influence from first-order Doppler and $1/c^3$ terms. The first and last ratios on the right hand side of (3) are measured quantities between the clock and generated photon signals. For the purposes of this study they are set to 1 and ignored. The middle ratio is the modeled relativistic shift and therefore the subject of this analysis.

III. Determining the Relevant Terms

Equations (3)-(5) model the expected relativistic frequency shift between the proper frequencies of two clock signals. We are interested in using our knowledge of the satellites' configuration and expected clock performance to determine the necessary terms. The result is therefore only valid for the defined configuration. Here, the analysis reflects a single MEO orbital plane as described in Section II-A.

A. Rate of a Single Satellite's Clock to TCG

We start our analysis by evaluating (1) for each of the simulated satellites. Contributions due to the geopotential, second-order Doppler, and external bodies are computed for each of the eight satellites in the same orbital plane. Figure 1.a summarizes the impact of each by recording the range of $\Delta f/f$. The geopotential and second-order Doppler contributions appear as single points because their variation is several orders of magnitude smaller than their mean. Figures 1.b-f are a breakout of each contribution propagated over 10 days. The contributions exhibit a periodic behavior due to the impact of orbit eccentricity, asymmetry of the Earth's gravitational field, and orbital movement of the satellites. For example, in Figures 1.b-c the geopotential and second-order Doppler contributions repeat with the orbital period. Figures 1.d-f are impacted by the movement of the satellite as well as the orbit of the external body. This is clearly illustrated in the envelope of the lunar impact (gray) in Figure 1.d. These plots are an example of all the contributions for one satellite. Each additional satellite experiences a similar behavior but with a phase offset due to its orbital placement. The simulation epoch is chosen to coincide with Venus' closest approach in order to produce the largest possible impact from this body. Its impact falls below the defined threshold and can therefore be ignored. With this, we restrict our model to the four highest contributions for both thresholds: the geopotential, the second-order Doppler, and the impact of the Moon and the Sun.

B. Earth's Gravitational Potential

We focus our attention next on the geopotential which is a summation of harmonic terms. EGM2008 provides coefficients up to degree 2190 but this complete model can be truncated in most cases. For our purposes, we evaluate the impact of the summation's individual terms on (3). To do this, we consider only the geopotential and ignore all other terms. Figure 2 shows the impact of each degree n. Looking at links between adjacent and next-neighbor satellites, we can limit the geopotential model to degree 2 for the 10^{-16} threshold and degree 4 for the stricter 10^{-18} threshold. The latter result is important to note as current GNSS analysis typically discusses only uniform and quadrupole (J2) terms of the geopotential (i.e. terms up to degree 2).

C. Ratio of Proper Frequencies

Having analyzed the impact on individual satellites, we now consider the full model. It consists of the ratio of proper frequencies scaled by the three factors of (4) and (5). When fully expanded each satellite has 4 contributions (treating all geopotential terms as 1) with 3 scaling factors for a total of 15 terms in the numerator and denominator. We use an expansion of (3) to determine the necessary terms,

$$\frac{f_A}{f_B} = \frac{1-g}{1-h} \approx (1-g)\sum_{n=0}^{\infty} h^n. \quad (6)$$

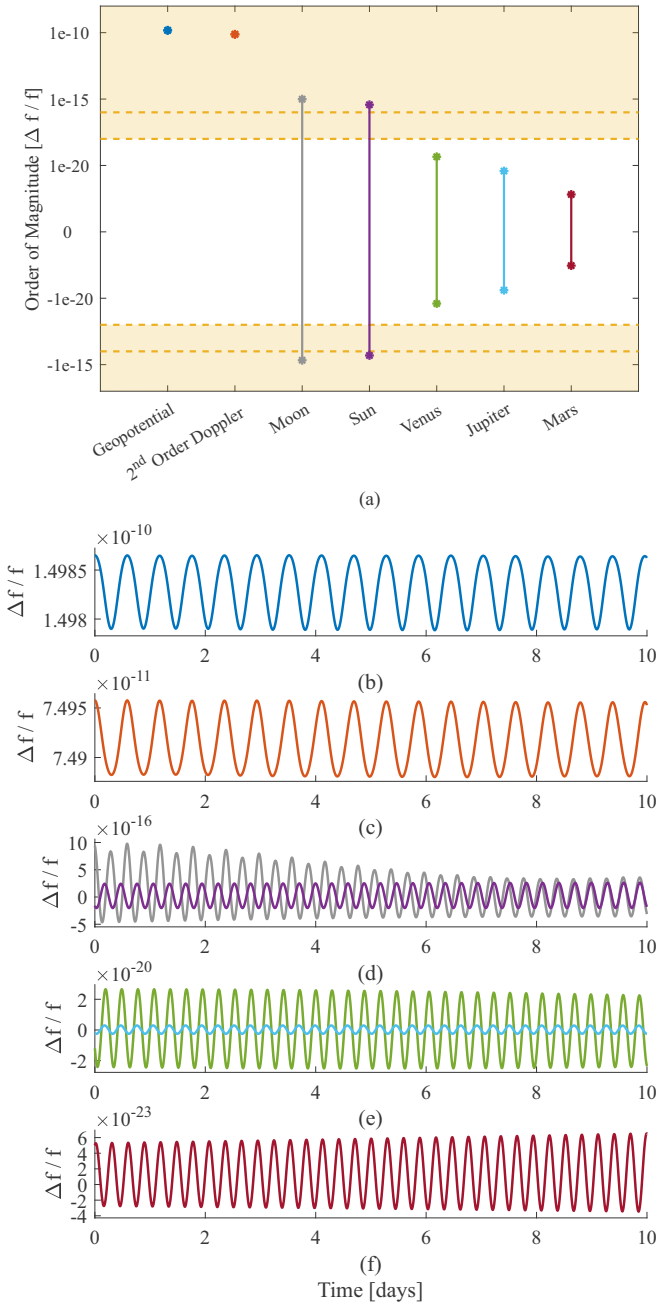

Fig. 1. Relativistic frequency shift for a single satellite observed on Earth. In (a), a single line shows the range (maximum and minimum) of the frequency shift for a single satellite in the described orbit. The dashed lines denote two thresholds. The geopotential and second-order Doppler contributions appear as single points because their variation is several orders of magnitude smaller than their mean. In the bottom view, (b-f), a breakout of each contribution shows its evolution over time. The envelope of the lunar impact (gray) illustrates the longer-term influence of external celestial bodies. The color scheme in (a) is preserved in the individual plots: (b) is the geopotential contribution, (c) is the second-order Doppler impact, (d) contains the Lunar (gray) and Solar (purple) impacts, (e) are the impacts of Venus (green) and Jupiter (light blue), and (f) is the impact from Mars.

Because we are interested in the frequency shift we can use (6) to write

$$\frac{\Delta f}{f} \approx (h-g) + h(h-g) + h^2(h-g). \tag{7}$$

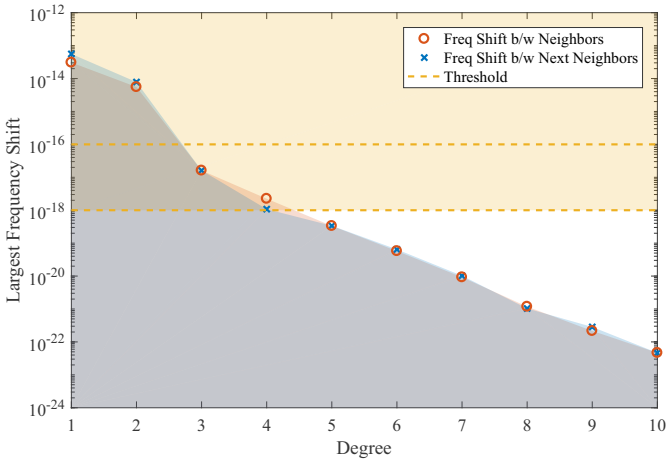

Fig. 2. Impact of the Earth's spherical harmonic gravitational terms (EGM2008). The maximum frequency shift is recorded for each subsequent degree. Expected frequency shifts are considered between neighboring satellites as well as their next neighbors.

Equation (7) gives us a convenient way to evaluate the impact of individual terms. In this expansion, $h-g$ is simply the difference of the corresponding terms from the two satellites. Figure 3 shows the breakout of each term evaluating the function $h-g$. Here, i denotes the contribution (i.e. i = {geopotential, second-order Doppler, Lunar, Solar}) and $j = \{1,2,3\}$ is the index of the first, second, and third terms listed in (4) and (5). For example, $\{1,2\}$ is the term where the geopotential contribution is scaled by the first-order Doppler effect. The leftmost points are the sum of all terms for reference. We can see that the contributions scaled by the higher order terms of q_A and q_B (i.e. $j > 1$) are below the thresholds and can be ignored. Using the same analysis we also evaluate the impact of additional terms in (7). The function $h(h-g)$ against our thresholds results in a two additional terms from the first-order Doppler effect.

D. The Truncated Model

Using the results of the last three sections we can now summarize the terms needed for intersatellite links between MEO satellites. The predicted relativistic frequency shift between two satellites is

$$\begin{aligned}\frac{f_A}{f_B} =& \frac{1-\frac{1}{c^2}\left[U_E(\mathbf{x}_B)+\frac{\mathbf{v}_B^2}{2}+V_{B,Moon}+V_{B,Sun}\right]}{1-\frac{1}{c^2}\left[U_E(\mathbf{x}_A)+\frac{\mathbf{v}_A^2}{2}+V_{A,Moon}+V_{A,Sun}\right]} \\ &+ (1+d_B)\cdot(d_B-d_A)+(m_B-m_A)\end{aligned} \tag{8}$$

where the geopotential contains the first 4 degrees,

$$V_{S,C} = GM_C\left[\frac{1}{r_{SC}} - \frac{1}{r_{EC}} + \frac{\boldsymbol{r}_{EC}\cdot\boldsymbol{r}_{SE}}{r_{EC}^3}\right]$$

is the effect of an external body C on satellite S, d_A and d_B are the first-order Doppler, and m_A and m_B are the respective third terms in (4) and (5).

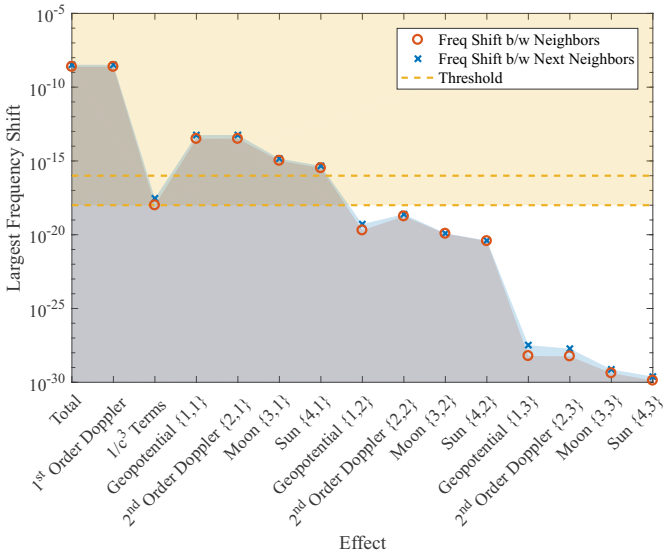

Fig. 3. Impact of individual terms on the relativistic frequency shift between satellites. The absolute value of the largest impact is recorded for each differential term. The leftmost pair of points is the summation of all terms. Each subsequent pair is the impact of the indicated contribution. The label {i,j} refers to the indices described in Section III-C.

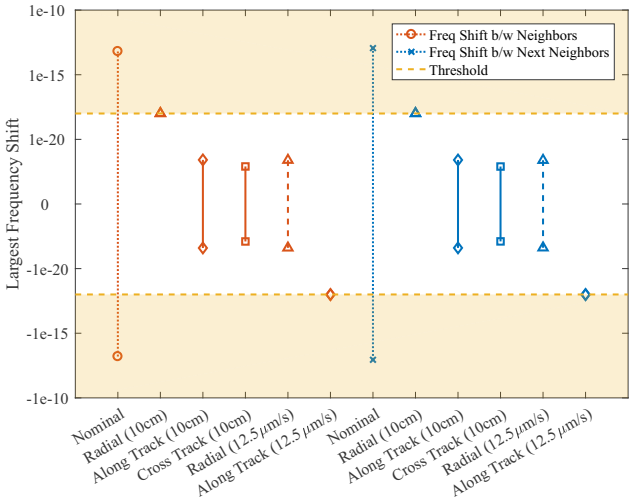

Fig. 4. Residual frequency shift error due to incorrect position and velocity. Error is added in the radial (triangle), along track (diamond), and cross track (square) directions of each satellite pair. The frequency shift using an erroneous position is subtracted from the nominal case. This impact for neighboring (red) and next-neighbor pairs (blue) is displayed. The first line in each group shows the range of the nominal frequency shift (without error) predicted by relativity. The next three solid lines are the residual frequency shifts due to 10 cm position error on each satellite. The remaining two lines are the result of 12.5 μm/s velocity error.

IV. Perturbing the Model

Having determined the terms necessary for the chosen orbit, we are interested in the sensitivity of this model to orbital errors (i.e. position and velocity). For this, we use (8) to generate the frequency shift, $\Delta f/f$, for each pair and compare the results with and without error,

$$\frac{\Delta f}{f}\Big|_{\text{w/o Error}} - \frac{\Delta f}{f}\Big|_{\text{w/ Error}} = 1 \times 10^{-18}.$$

Assuming that the error for each satellite in the pair is of equal magnitude and acts in opposite directions,

$$2(\Delta - \Delta_o) = 1 \times 10^{-18}$$

can be used to find the maximum allowable error. Δ and Δ_o are the sum of relativistic corrections for one satellite with (Δ) and without (Δ_o) error. Satellite error is usually described in relation to the nominal orbit (i.e. along track, cross track, and radial directions). Here, the error is imposed on the satellites' inertial position and then rotated to Earth-fixed coordinates when evaluating the geopotential.

A. Impact of First-order Doppler Terms

The dominant terms in the model, as shown in Figure 3, are due to first-order Doppler contributions. In addition to the obvious impact of velocity error, position accuracy affects the line-of-sight vector. Evaluating the maximum allowable error for this contribution results in stringent constraints on orbit determination. Position must be determined with 1 μm accuracy and velocity to 1.5×10^{-10} m/s. These strict requirements are limiting when considering the use of this one-way transfer model. Measurements to characterize and remove this first-order Doppler effect would be necessary.

B. Position Sensitivity

Assuming a measurement scheme to remove the first-order Doppler, we then ignore these terms in the model. With this, the largest contribution affected by a satellite's position is the geopotential. Looking only at the largest, uniform gravity contribution, we can determine the orbital error which causes a frequency shift equivalent to the defined threshold

$$\frac{2(U - U_o)}{c^2} = \frac{2GM_E}{c^2}\left(\frac{1}{r} - \frac{1}{r_o}\right) = 1 \times 10^{-18}$$

$$r - r_o = 10 \text{ cm}.$$

To illustrate this, a 10 cm error is added to the position of each satellite in each local direction. Applying this bias at each time step allows us to evaluate the frequency sensitivity to individual errors. Figure 4 shows the range of the residual frequency error for both neighboring (blue) and next-neighbor (red) pairs. The left-most line of each colored set is the range of the original frequency ratio for reference (i.e. $\Delta f/f$ without error). As expected, the error in the radial direction has the largest impact. This error produces a residual bias whereas the along track and cross track errors have a zero mean offset.

C. Velocity Sensitivity

Again excluding the first-order Doppler terms, the largest contribution affected by a satellite's known velocity is the second-order Doppler effect. Looking only at this contribution, we use the same procedure to determine the maximum allowable error

$$\frac{v^2 - v_o^2}{c^2} = 1 \times 10^{-18}.$$

To give us an estimate, we assume a circular orbit and

$$v = \sqrt{\frac{GM_E}{r_o} - c^2 \times 10^{-18}}$$

$$v - v_o = 1.25 \times 10^{-5} \text{ m/s}.$$

A 12.5 μm/s offset was added to each satellite. The results in Figure 4 are indicated as dashed lines. As expected, the maximum impact is observed in the along track direction. Velocity error in the cross track direction produces a negligible frequency shift which is even below the resolution of data type used in the simulation. As such, it falls well below the defined threshold and is not included in the figure. Though a tight constraint, intersatellite links will provide constant, high resolution ranging between satellites which improves monitoring of the along track direction. We can use this ranging to further constrain the orbit determination solution and reduce the overall uncertainty.

V. Conclusion

Next-generation atomic clocks offer a future of highly accurate time and frequency references. Methods to utilize these improved clocks must necessarily control or model all contributions down to the expected device performance. For satellite-based transfer this means describing the relativistic behavior of clocks and transmissions. In this paper, we focus on frequency transfer between terrestrial satellites. We evaluate an equation relating the proper time of two clocks for a given configuration and determine its position and velocity requirements. We find for a nominal Galileo orbit, we must consider up to 4 degrees of the geopotential model and include the contributions of the Moon and the Sun. In future, we can use this framework to evaluate proposed time and frequency protocols.

References

[1] T. Schuldt, K. Dringshoff, E. V. Kovalchuk, A. Keetman, J. Pahl, A. Peters, and C. Braxmaier, "Development of a compact optical absolute frequency reference for space with 10^{-15} instability," *Appl. Opt.*, vol. 56, pp. 1101–1106, 2017.

[2] K. W. Martin, G. Phelps, N. D. Lemke, M. S. Bigelow, B. Stuhl, M. Wojcik, M. Holt, I. Coddington, M. W. Bishop, and J. H. Burke, "Compact optical atomic clock based on a two-photon transition in rubidium," *Phys. Rev. Applied*, vol. 9, pp. 014 019–014 029, Jan 2018.

[3] P. Delva, A. Hees, and P. Wolf, "Clocks in space for tests of fundamental physics," *Space Sci Rev*, vol. 212, pp. 1385–1421, 2017.

[4] L. Blanchet, C. Salomon, P. Teyssandier, and P. W. Daly, "Relativistic theory of time and frequency transfer to order c-3," *Astron. Astrophys*, vol. 370, pp. 320–329, 2011.

[5] C. Günther, "Kepler - a concept for a future system for navigation, geodesy and metrology," *Journal of Navigation*, unpublished.

[6] G. Petit and B. Luzum, "IERS conventions (2010)," International Astronomical Union (IAU), IERS Technical Note No. 36, 2010.

[7] P. Wolf and G. Petit, "Relativitistic theory for clock synchronization," *Astron. Astrophys.*, vol. 304, pp. 653–661, 1995.

[8] (2017) General mission analysis tool (GMAT). [Online]. Available: http://gmatcentral.org/display/GW

[9] N. K. Pavlis, S. A. Holmes, S. C. Kenyon, and J. K. Factor, "The development and evaluation of the earth gravitational model 2008 (EGM2008)," *J. Geophys. Res.*, vol. 117, no. B4, Apr. 2012.

[10] S. Kopeikin, M. Efroimsky, and G. Kaplan, *Relativistic Celestial Mechanics of the Solar System*. Weinheim, Germany: Wiley-VCH Verlag GmbH & Co. KGaA, 2011.

A Recursive Clock Anomalies Detector with Double Exponential Smoothing

Valerio Formichella
Department of Physical Metrology
Istituto Nazionale di Ricerca Metrologica
Torino, Italy
v.formichella@inrim.it

Patrizia Tavella
Time Department
Bureau International des Poids et Mesures
Sèvres, France
patrizia.tavella@bipm.org

***Abstract*—Space qualified atomic clocks are fundamental in Global Navigation Satellite Systems, but they can suffer from different types of anomalies, like phase and frequency jumps, frequency drift changes and variance changes. Different solutions have been proposed for an automated on-board detection of clock anomalies, among which a frequency jump detector based on a recursive exponential filter, with soft requirements in terms of memory and computational power and hence particularly useful for on-board applications. Here, we propose a generalization of this recursive detector, based on double exponential smoothing: it properly takes into account the frequency drift and also detects drift and variance changes. Then, we test a first version of our detector on simulated and real data, and we discuss the results.**

Keywords—clock anomalies; anomalies detection; integrity; GNSS; double exponential smoothing

I. INTRODUCTION

Space qualified atomic clocks are one of the fundamental components of Global Navigation Satellite Systems (GNSS). It is well known that such clocks suffer from different types of anomalies [1], like phase and frequency jumps, frequency drift changes and variance changes. These anomalies can affect the quality of the navigation message and the eventual navigation performance, unless they are rapidly detected and corrected or at least notified to the users. Therefore, the automated on-board detection of clock anomalies is a topic of great interest, which could significantly improve the systems' integrity (see [2] for a definition of "integrity" within a GNSS).

Different solutions have been proposed, e.g. in [3], [4] and [5]. In particular, the frequency jump detector proposed in [6] is based on a recursive exponential filter, which makes it particularly useful for on-board applications thanks to softer requirements in terms of memory and computational power. Indeed, most of the detectors are based on the processing of a batch of past data, requiring a certain effort in terms of CPU and memory consumption which is not always possible on board of a spacecraft. Instead, a recursive detector needs much less input data (low memory consumption) and mathematical operations (low computational power required).

Here, we propose a generalization of the recursive detector presented in [6], based on double exponential smoothing [7-9]. As new features, it properly takes into account the frequency drift and also detects drift and variance changes. Then, we test a first version of our detector on simulated and real data, and we discuss the results. We also compare the performance of the recursive detector with those of a standard (i.e., non-recursive) detector and we show that, for similar detection performance, the number of data to be stored in memory and the number of computations to be performed is much higher for the standard detector, as expected.

The paper is structured as follows. Section II discusses the theory, in particular: Section IIA gives an introduction to the problem of the detection of clock anomalies, with standard or recursive detectors; Section IIB briefly summarize the theory of double exponential smoothing; Section IIC briefly presents the theory of our recursive detector. Section III presents the results of the test performed on real and simulated data, and the comparison between the performance of our detector and of a standard one. Finally, the conclusions are given in Section IV.

II. THEORY

A. Clock Anomalies Detection

The fundamental idea behind any clock anomalies detector is to compare the actual clock behavior with the expected one. As an example, let us consider the standard frequency jump detector described in [3]: the expected clock behavior is the extrapolated frequency at a certain epoch t, the extrapolation being the result of a fit performed on a batch of past frequency data according to the deterministic clock model; the actual behavior, instead, is the measured frequency at the same epoch t. Typically, in order to perform a god fit and properly smooth the measured data, a large number of measures must be stored in memory and then processed. Instead, a recursive detector is based on a recursive fitting/extrapolation and smoothing of the clock data. This lowers the number of values to be stored in memory to a few units, which are the results of the latest step of the recursive calculation, and also reduces the number of operations necessary to update these values and to detect the possible anomalies.

Another fundamental feature of a detector, useful when past data are used to predict the clock behavior, is to give a lower weight to older measures. Within a recursive detector, this can be accomplished by using an exponential smoothing, where the

weights of past measures decrease exponentially with time. The basic theory of double exponential smoothing is presented in the next section.

B. Double Exponential Smoothing

Let us consider a time series $\{y_i\}$ such that

$$y_i = a + bt_i + \xi_i \quad \text{with} \quad t_i = t_{i-1} + \tau_0 \tag{1}$$

where ξ_i is a Gaussian random variable, and we want to find an estimate of the coefficients a and b. Note that (1) can be used as a simplified model for the fractional frequency offset of a clock, where a is the initial frequency offset, b is the frequency drift and ξ_i is the white frequency noise.

The basic equation of the exponential smoothing is

$$\bar{y}_i = \alpha y_i + (1-\alpha)\bar{y}_{i-1} \tag{2}$$

where α is the smoothing constant. At the epoch t_i, a prediction of y_{i+k} can be obtained as

$$\hat{y}_{i+k} = \bar{y}_i + [(1-\alpha)/\alpha + k]b\tau_0 \tag{3}$$

where, however, the coefficient b (the slope) is still unknown. In order to estimate the slope, we can use a second filter (hence the name "double" exponential smoothing):

$$\hat{b}_i = \beta B_i + (1-\beta)\hat{b}_{i-1} \tag{4}$$

where β is the smoothing constant and B_i is defined as

$$B_i = (\bar{y}_i - \bar{y}_{i-1})/\tau_0 . \tag{5}$$

Therefore, at the epoch t_i, a prediction of y_{i+k} can be obtained as

$$\hat{y}_{i+k} = \bar{y}_i + [(1-\alpha)/\alpha + k]\hat{b}_i\tau_0 . \tag{6}$$

The smoothing constants α and β determine the memory of the filter, and hence how fast it reacts to the possible changes of the coefficients a and b. Note that, if y is the frequency of a clock, a frequency jump corresponds to a change of a, whereas a drift change corresponds to a change of b.

C. The Recursive Detector

The recursive frequency jump detector presented in [6] uses two filters written as in (2), one with a long memory (fixed by a smoothing constant α_L) and the other with a short memory (smoothing constant $\alpha_S > \alpha_L$). The former is used to compute the expected frequency, whereas the latter (which reacts faster to a frequency jump) is used to smooth the actual frequency. At each epoch t_i, the difference between the outputs of the two filters, Y_i, is computed. The detector decides that a jump occurred at the epoch t_i if $|Y_i| > \gamma$, where γ is the threshold.

First of all, we observe that this recursive detector works properly only in the case of null frequency drift. In order to generalize the detector to the case of non-null drift, we use the double exponential smoothing and we substitute (2) with (6) where we set $k = 0$. Moreover, since now we have a new estimate of the frequency drift at each epoch, we can also implement a drift change detector: when the initial transient is finished, the first available drift estimate is stored in memory and compared with the successive estimates; if the absolute difference between the two values is larger than a certain threshold, the detector decides that a drift change occurred; after each detection, the reference drift value is updated with a new estimate, computed after the drift change.

Finally, we further improve the recursive detector and make it able to detect also variance changes. First of all, we need a recursive equation for estimating the variance, with a finite memory: at each epoch, we estimate the variance as

$$\hat{V}_i = \eta V_i + (1-\eta)\hat{V}_{i-1} \tag{7}$$

where η is the smoothing constant and V_i is defined as

$$V_i = (y_i - \hat{y}_i)^2 \tag{8}$$

where $\hat{y}_i$ is the output of the long-memory filter used for the detection of frequency jumps. Analogously to the detection of drift changes, a first, reference variance estimate is stored in memory and compared with the successive estimates. If the absolute difference between the two values is larger than a certain threshold, the detector decides that a variance change occurred, and the reference variance value is updated with a new estimate computed after the variance change.

III. Test Results

A. Test on Simulated Data

As a first test, we simulate a frequency data series with white noise and affected by a frequency jump, a drift change and a variance change, so that we can test not only the ability to detect the different types of anomaly, but also the ability to react to the anomalies and reinitialize the reference values for the following detections. Fig. 1 (the detector output) shows that all of the anomalies are properly detected. The vertical lines indicate the detection epochs: the red one, the detection of a frequency jump; the green one, the detection of a drift change; the blue one, the detection of a variance change. Fig 2 shows a detail of each detection, with a dashed vertical line indicating the epoch at which the anomaly actually occurred.

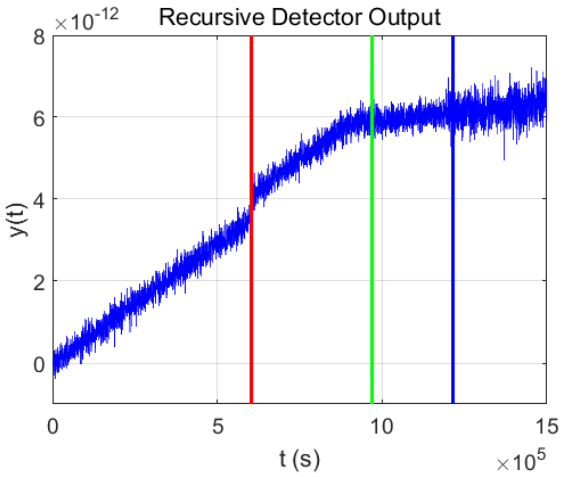

Fig. 1. The successful detection of a frequency jump (red vertical line), of a drift change (green line), and of a variance change (blue line), on simulated frequency data affected by a white noise.

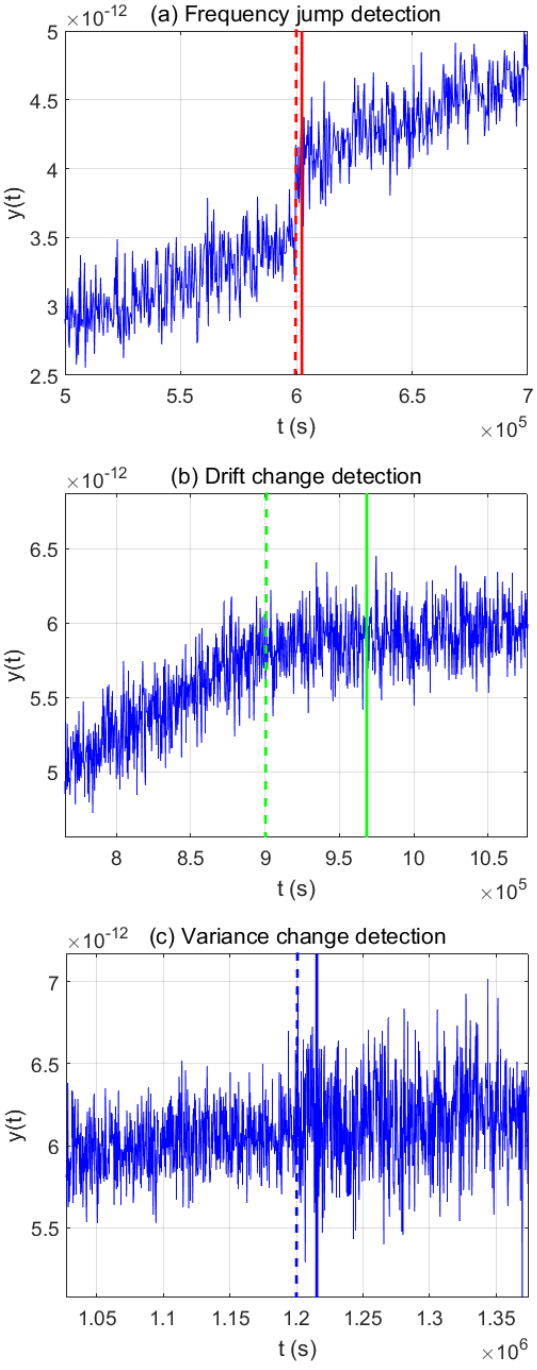

Fig. 2. Details of the anomalies detected in Fig. 1: the vertical dashed lines indicate the epochs at which the anomalies actually occurred, while the solid lines indicate the detection epochs.

Then, we simulate frequency data from a rubidium clock and from a passive hydrogen maser like those on board of the Galileo satellites, with noise and drift as per specifications and as can be observed from the ground. We assume that the two clocks can be measured on board the satellite, one with respect to the other, with a sampling time of 300 s. We inject a frequency jump with an amplitude of 8×10^{-13} (which is a realistic one, considering the observed anomalies) , and we run the detector with a threshold of 5×10^{-13}. Practically, we perform a Monte Carlo simulation to determine the following detection performance parameters:

- the false alarm probability, P_{fa};
- the missed detection probability, P_{md};
- the detection delay, T_d;
- the jump amplitude estimation error, E_A.

By properly tuning the smoothing constants, we easily reach the following detection performance (note that we are limited by the number of simulations when estimating P_{fa} and P_{md}):

- $P_{fa} < 1\times10^{-4}$;
- $P_{md} < 1\times10^{-4}$;
- $T_d < 3$ epochs;
- $E_A < 10\%$.

These values will be also used in the next section IIIC for the comparison between the performance of the recursive detector and those of a standard one.

B. Test on Real Data

We used public data from the Multi GNSS Experiment (MGEX, mgex.igs.org) to test the detector on real data from space clocks. As an example, Fig. 3 shows the detection of a frequency jump on the master clock on board the GPS satellite G11, and the detection of two drift changes on the master clock on board the GPS satellite G10.

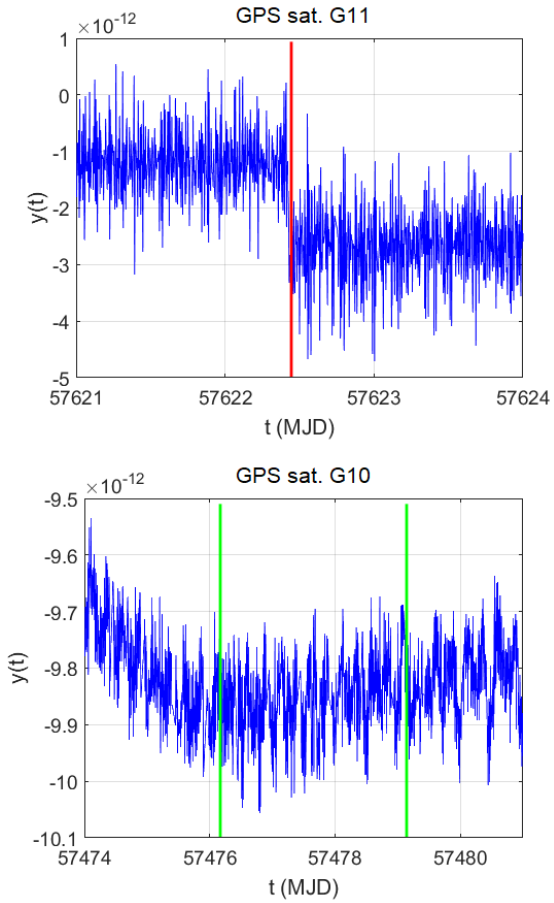

Fig. 3. Detection of a frequency jump (red line) on GPS satellite G11 and of two drift changes (green lines) on GPS satellite G10, using real data collected on ground by MGEX.

C. Performance Comparison

We compare our recursive detector with the standard one proposed in [3]. Practically, we consider the same scenario used for the Monte Carlo simulation of Section IIIA, and we determine how many past values must be stored in memory and then processed by the standard detector in order to reach the same level of detection performance of the recursive one.

With the standard detector, in order to get below the 1×10^{-4} level both with P_{fa} and P_{md} without increasing too much the detection delay, we need to handle about 100 frequency values, so that the following detection performance (theoretically computed) can be reached:

- $P_{fa} = 6\times10^{-6}$;
- $P_{md} = 3\times10^{-6}$;
- $T_d < 5$ epochs;
- $E_A < 10\%$.

It is then clear that the standard detector requires a much larger number of data to be stored in memory, i.e. about 100 instead of the 2 required by the recursive detector, which are $\bar{y}_{i-1}$ and $\hat{b}_{i-1}$ at the epoch t_i. The number of operations is also strongly reduced, from those necessary to linearly fit 100 frequency values in the standard detector, to the few additions and multiplications necessary to implement the double exponential smoothing and update the old estimates $\bar{y}_{i-1}$ and $\hat{b}_{i-1}$ to the new estimates $\bar{y}_i$ and $\hat{b}_i$.

Note that the performance comparison is not really related to the detection performance, rather to the requirements of the two detectors in terms of memory and computational power, assuming they can be tuned to reach the same level of detection performance (P_{fa}, P_{md}, T_d, E_A). Indeed, the main advantage of our recursive detector with respect to a standard one, is not a better detection performance, rather its softer requirements and ease of implementation, which make it a good candidate as an on-board detector for GNSS clock anomalies.

IV. Conclusions

We have successfully developed and tested a recursive clock anomalies detector based on double exponential smoothing. With respect to a similar work proposed in [6], our detector properly takes into account the frequency drift and detects not only frequency jumps, but also drift changes and variance changes. With respect to a standard, non-recursive detector, our recursive detector has mush softer requirements in terms of memory and computational power, nonetheless reaching the same level of detection performance. Therefore, this detector is well suited for implementation on board of GNSS satellites, for an autonomous on-board detection of clock anomalies.

The future developments of this work include a complete theoretical description of the detection performance parameters as a function of smoothing constants, detection thresholds and amplitude of the anomalies (analogous to the one already available for the standard detector described in [3]), and further tests on real GNSS clocks data.

References

[1] A. Cernigliaro, G. Fantino, I. Sesia, L. Galleani, and P. Tavella, "Nonstationarities in space clocks: investigations on experimental data," in Proc. 28th European Freq. and Time Forum, 2014, pp. 126-129.

[2] www.navipedia.net/index.php/Integrity.

[3] L. Galleani and P. Tavella, "Robust detection of fast and slow frequency jumps of atomic clocks," IEEE Trans. Ultrason., Ferroelect., Freq. Control 64, 2, 2017, pp. 475-485.

[4] Q. Wang and P. Rochat, "An anomaly clock detection algorithm for a robust clock ensemble," in Proc. 41st Precise Time and Time Interval Meeting, 2009, pp. 121-130.

[5] X. Huang, H. Gong, and G. Ou, "Detection of weak frequency jumps for GNSS on board clocks," IEEE Trans. Ultrason., Ferroelect., Freq. Control 61, 5, 2014, pp. 747-755.

[6] Q. Wang, F. Droz, and P. Rochat, "Robust clock ensemble for time and frequency reference system," in Proc. 2015 European Freq. and Time Forum joint with Int. Freq. Control Symposium, 2015, pp. 374-378.

[7] R. G. Brown, "Exponential smoothing for predicting demand," Arthur D. Little, Inc., 1956.

[8] C. C. Holt, "Forecasting seasonals and trends by exponentially weighted moving averages," report to the Office of Naval Research (ONR 52), 1957, reprinted in International Journal of Forecasting 20, 2004, pp. 5-10.

[9] NIST's "Engineering Statistics Handbook", available at the following link: www.itl.nist.gov/div898/handbook/pmc/section4/pmc433.htm.

High accuracy continuous time transfer with GPS IPPP and T2L2

Julia Leute, Gérard Petit
BIPM,
Sèvres, France
Email: julia.leute@bipm.org

Pierre Exertier, Etienne Samain
GeoAzur, Observatoire de la Côte d'Azur,
Valbonne, France

Daniele Rovera, Pierre Uhrich
LNE-SYRTE, Observatoire de Paris,
Université PSL, CNRS, Sorbonne Université,
Paris, France

***Abstract*—We present a comparison of time transfer results over European baselines obtained with two space-based techniques: Precise Point Positioning with integer ambiguity resolution (IPPP) using GPS satellites and Time Transfer by Laser Link (T2L2) using the low orbiting satellite Jason-2. The data was obtained in a 3-month experiment in Autumn 2013 for baselines between Paris, Herstmonceux and Grasse.**

We find that the difference between the 30-s IPPP link results and the closest 1-s T2L2 data points has a standard deviation below 100 ps for all three baselines.

These results provide the basis for a continuous time transfer technique with accuracy at the 100 ps level for baselines over which T2L2 can operate in CV. Occasional T2L2 measurements provide the absolute time difference with a high accuracy and a continuous IPPP link maintains the accuracy for weeks to months between calibrations.

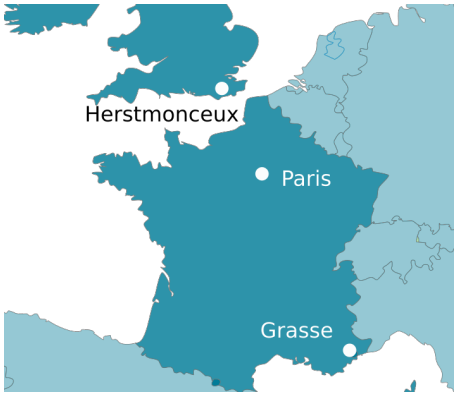

Fig. 1. European baselines studied in this work.

I. Introduction

Space-based time transfer techniques in the microwave regime, GPS time transfer and Two-Way Satellite Time and Frequency Transfer (TWSTFT), play an important role in remote time and frequency comparisons and atomic time scales [1]. The standard code-based time transfer techniques are limited by the precision and accuracy of the ranging code, which is about a factor 100 less precise than the carrier-phase. New techniques like IPPP [2] and Carrier-Phase TWSTFT [3] have been developed that make use of the carrier-phase to achieve an improved time transfer stability. For IPPP a stability of around 20 ps up to several weeks of averaging time has been reported [4]. The carrier-phase only methods provide no improvement of the time transfer accuracy, due to the ambiguity of the carrier-phase.

T2L2 [5] is a space-based time transfer technique with high time accuracy and stability, which uses laser telemetry technology and dedicated space instruments, which have been flying on the Jason-2 satellite since 2008. The time transfer accuracy for Common View (CV) time transfer between remote sites with T2L2 is below 140 ps [6], an order of magnitude improvement over GPS code-based methods. A drawback of this optical method is its dependence on weather conditions which does not allow for a continuous time transfer.

Space-based continuous time transfer with high accuracy can be achieved by combining a continuous and sufficiently stable microwave-based time transfer technique with an accurate optical time transfer method like T2L2 for occasional calibrations. This approach was already envisioned in [7] relying on a GPS CV carrier-phase technique based on single-difference ambiguity fixing. The advantage of IPPP over this GPS CV carrier-phase method is that ambiguities are fixed for each station independently in an All in View approach and IPPP can therefore be used on intercontinental baselines, where only few satellites are in common view.

In this paper the feasibility of combining IPPP time links with T2L2 links for calibrations is studied. Data from a measurement campaign on baselines between Paris, Herstmonceux and Grasse over a three month period in 2013 is analyzed to study the short and long-term agreement between both techniques.

II. Measurement campaign

GPS and T2L2 data was collected from beginning of August until end of October in 2013, accompanied by a parallel calibration campaign of the GPS and T2L2 stations. In previous work a sub-ns agreement between time transfer with a code-based GPS data analysis and T2L2 was reported, with standard deviations below 500 ps [8]. In this work the calibration of the stations will not be taken into account, because the carrier-phase GPS technique doesn't provide the absolute time offset. Therefore only the stability of the difference between both methods is of interest.

The station in Herstmonceux at the NERC Space Geodesy Facility (SGF) and the station in Grasse at the Observatoire

978-1-5386-5620-4/18/$31.00 ©2018 IEEE

de la Côte d'Azur (OCA) use existing laser ranging stations, whereas at Observatoire de Paris (OP) a mobile laser ranging station (FLTRS [9]) was temporarily installed.

The GPS station hardware at SGF (HERS station), OP (OPMT station) and OCA (OC03 station) used for this campaign is summarized in tab. I. All stations use geodetic GPS receivers and provide data in the RINEX format suitable for this analysis.

TABLE I
GPS STATION HARDWARE.

station	receiver	antenna
SGF (HERS)	Septentrio PolaRx3	Leica AR25 (rev. 3)
OP (OPMT)	Ashtech Z-XII3T	3S Navigation TSA-100
OCA (OC03)	Dicom GTR50	Novatel GPS-702-GG

The time and frequency reference at all three sites were active hydrogen maser standards, providing 10 MHz and pulse per second signals to both the GPS and T2L2 stations. A detailed description of the experimental setup can be found in [8].

III. GPS DATA ANALYSIS

Precise Point Positioning is a one-way method based on dual-frequency GPS code and carrier-phase observations [10]. While the standard PPP technique uses the code measurements to fix the carrier-phase ambiguities as floating numbers, the IPPP technique properly decouples the code and carrier-phase observations and preserves the integer nature of the ambiguities. IPPP therefore successfully removes the code noise from the clock solution, resulting in an improved long-term time transfer stability [2].

A. IPPP links

A direct fixing of the ambiguity in the ionosphere-free linear combination of phase measurements $L_{IF}(L1, L2)$ is not possible, due to the small ionosphere-free wavelength $\lambda_{IF} = 6.3\,\text{mm}$ compared to the noise level of L_{IF}. Therefore, the ambiguity fixing in IPPP is done in two steps: First the widelane ambiguity $N_w = N_2 - N_1$ is fixed and then one of the uncombined ambiguities e.g. N_1 can be determined (for details see [11], [12]).

1) The widelane ambiguity fixing is based on the Melbourne-Wübbena linear combination $L_{MW}(P_1, P_2, L_2 - L_1)$, which is a function of the code (P) and carrier-phase (L) observations at the two frequencies:

$$N_w \lambda_w = L_{MW} + \mu_i - \mu^j, \quad (1)$$

where λ_w is the widelane wavelength and μ_i and μ^j are the widelane biases for the receiver i and the satellite j. The daily widelane satellite biases need to be provided by the satellite clock products, while the widelane receiver biases and the integer widelane ambiguity are estimated together.

2) The ionosphere-free linear combination of phase measurements can be expressed as

$$L_{IF} = cT_c + W - \lambda_{NL} N_1 + \lambda_2 N_w + \Delta h, \quad (2)$$

where λ_{NL} is the narrow-lane wavelength, c is the velocity of light, T_c is the coordinate time of signal propagation in seconds including all delays, e.g. the tropospheric delay, W is the phase-windup effect in meter and Δh is the clock difference between satellite and receiver. Due to the prior fixing of N_w and the increased wavelength $\lambda_{NL} = 17\lambda_{IF} = 10.7\,\text{cm}$ compared to the ionosphere-free wavelength λ_{IF} a fixing of N_1 is possible for the typical noise level of L_{IF}.

The IPPP analysis was performed in daily batches using the GINS software [13] and the GRG satellite products that provide the required information about the widelane satellite biases and the satellite phase clock. After the ambiguities have been fixed, the time difference between the receiver and the reference time scale of the satellites is estimated together with the tropospheric zenith delays (24 per day with the GMF mapping function and without gradients) and the daily static station coordinates. The clock solutions of the individual stations are combined resulting in a continuous ground-ground clock comparison on a 30 s grid.

The IPPP links suffer from discontinuities when ambiguity resets occur, e.g. at the day-boundary or due to data gaps. Fortunately, this discontinuities are an integer multiple of λ_{NL} and can therefore be corrected without introducing additional noise. Since the reference clocks of the stations used in this work are highly stable hydrogen masers, a simple extrapolation approach is used (for details see [2]).

B. PPP links

For comparison a second GPS analysis based on the classic PPP model was performed using the GPSPPP software from Natural Resources Canada [14] and IGS satellite products [15].

The solutions have been generated in the standard configuration used for UTC links, except that the final IGS products are used to generate clock solutions on a 30 s grid. Three non-overlapping batches of 35 days each were processed using a Kalman filter and the resulting clock solutions were concatenated. The elevation cut-off was set to 10°, and the tropospheric zenith delay was modeled as $3\,\text{mm}/\sqrt{\text{hr}}$ random walk with the GMF mapping function and without estimating horizontal gradients. The station coordinates are estimated on each batch.

IV. T2L2 DATA ANALYSIS

T2L2 is a two-way method developed by the laboratory Géoazur of Observatoire de la Côte d'Azur (OCA) with the support of the French Space Agency CNES. It uses the timing of optical pulses emitted by ground laser stations and reflected by the satellite. A measurement triplet consists of the emission time t_E and the arrival time t_R of the reflected pulse measured by the ground station and the arrival time on-board the satellite t_B measured in the time scale of the on-board clock.

The arrival time at the satellite in the time scale of the ground station can be estimated from the emission and arrival time at the laser station. Comparing the estimated arrival time with the arrival time recorded on-board the satellite enables a ground-space time transfer. The time difference between the station clock and the satellite clock Δh is given as

$$\Delta h = t_E + \frac{t_R - t_E}{2} - t_B + C, \tag{3}$$

where C is a correction term including corrections due to speed aberrations, relativistic effects, atmospheric effects and instrumental calibrations.

A simultaneous ground-space time transfer of multiple ground stations allows to compare the stations time scales with high accuracy. But it is only possible for baselines up to 6000 km. The accuracy of the ground-ground time transfer in non-CV mode depends on the stability of the on-board clock, which in case of Jason-2 is a ultra stable quartz oscillator of the DORIS system [16]. In [17] the uncertainty for non-CV time transfer with T2L2 was estimated to be around 730 ps for a baseline between Europe and China.

The optical pulses are emitted at a 10 Hz rate with a loss of 40-60% within a pass. The successful ground-space measurements are averaged over a one second period if at least three measurements are present. For the ground-ground time transfer only CV measurements are taken into account for which the time difference between the ground-space measurements is not more than one second.

V. Results

The GPS and T2L2 links are compared by taking the difference between the GPS measurements and the closest T2L2 measurement, which must be within 15 s of the GPS data point. This approach maximizes the number of data points due to the 30 s grid of the GPS measurements and the sparse CV T2L2 measurements. The additional short-term noise due to the asynchronous measurements is negligible due to the highly stable reference clocks at all stations.

The resulting total number of individual differences between the GPS and T2L2 links and the number of CV passes for the three baselines are summarized in tab. II. With 43 passes the

TABLE II
Number of CV passes and total number of individual data points of the GPS / T2L2 comparison for three baselines during the campaign in 2013.

Link	# passes	# points
SGF / OCA	43	220
OP / OCA	11	58
OP / SGF	6	22

link between SGF and OCA has the largest number of passes, whereas the link between SGF and OP has only 6 passes. The difference in successful measurements are partly due to the weather dependence of the T2L2 technique and due to other technical issues that limited the measurements for some links.

The time differences between the stations based on the IPPP and T2L2 links and the comparison between the IPPP and T2L2 links are shown in fig. 2. The plot shows all individual data points of the comparison between the IPPP and T2L2 links based on the analysis described above, therefore several data points per pass are shown.

The short- and long-term agreement between the IPPP links and the T2L2 links is determined by calculating the standard deviation within a pass and the standard deviation over all data points respectively. There are on average 5 data points per pass and for the mean standard deviation per pass only passes with at least 3 data points are considered.

TABLE III
Comparison between GPS and T2L2 links for three European baselines. The mean standard deviation within a pass and the standard deviation over all data points are presented.

Link	**IPPP**		**PPP**	
	STD / pass [ps]	STD [ps]	STD / pass [ps]	STD [ps]
SGF / OCA	27	90	27	205
OP / OCA	17	53	17	144
OP / SGF	15	36	17	71

Tab. III summarizes the results of the comparison between the GPS links and the T2L2 links. For the IPPP links all standard deviations are below 100 ps, down to 36 ps for the link between OP and SGF, admittedly based on very low statistic. The standard deviation per pass (short-term noise) is similar for the comparisons based on the IPPP and the PPP analysis, whereas the standard deviation over all data points (long-term noise) is on average a factor of 2.3 smaller for the IPPP links compared to the PPP links. Additionally, a long-term trend versus the T2L2 links could be observed for some of the PPP links, e.g. a drift of 7 ± 0 ps per day for the link between SGF and OCA.

VI. Conclusions and Outlook

The agreement between two independent space-based time transfer techniques, IPPP based on GPS carrier-phase observations and T2L2 based on laser ranging with the Jason-2 satellite, was studied for a three month period in 2013 for the baselines between Herstmonceux, Paris and Grasse. We have demonstrated that the long-term agreement between IPPP links and T2L2 links is below 100 ps for baselines on which T2L2 can operate in CV. The IPPP time transfer stability maintains the accuracy of the T2L2 calibration for several weeks of measurements. The combination of IPPP and T2L2 therefore enables a continuous time transfer with an accuracy that is improved by one order of magnitude compared to the standard code-based techniques in the microwave regime.

For T2L2 with the Jason-2 satellite this accuracy is restricted to CV baselines, but a more stable on-board oscillator would enable high accuracy time transfer even in non-CV mode. The planned European Laser Timing (ELT) project [18] hosted on-board the International Space Station (ISS) inside

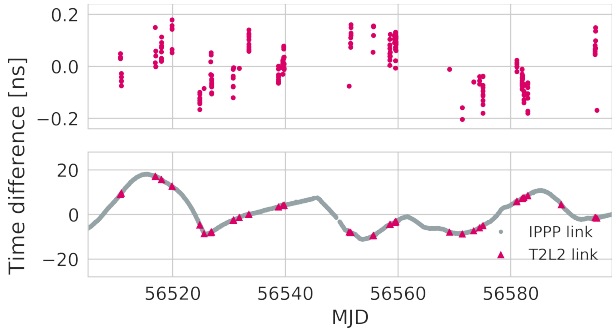

(a) SGF / OCA

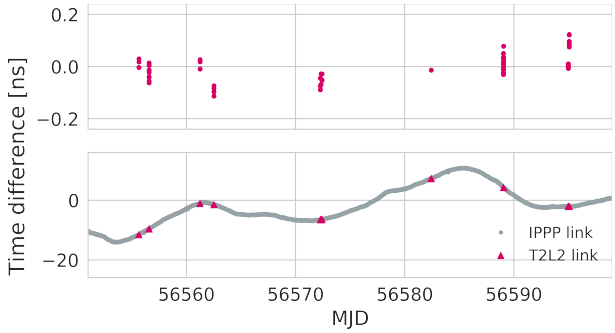

(b) OP / OCA

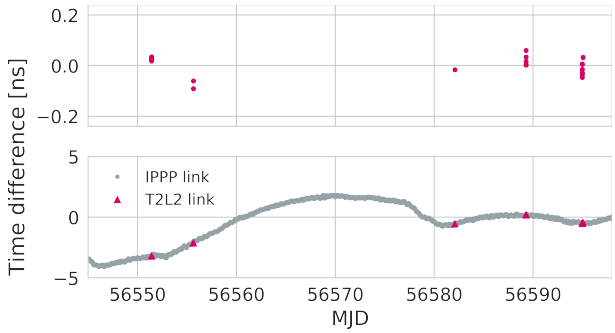

(c) OP / SGF

Fig. 2. Comparison between IPPP and T2L2 links on three baselines between OP, OCA and SGF. The top plot shows the difference between the IPPP and T2L2 link. The bottom plot shows the time difference between the stations based on the IPPP and T2L2 links after an identical quadratic fit has been removed. The IPPP links were calibrated using the mean difference between the IPPP and the corresponding T2L2 link.

the Atomic Clock Ensemble in Space (ACES) [19] will use an atomic reference timescale.

VII. Acknowledgment

The GINS software and the necessary GRG satellite products are provided by CNES-CLS and the NRCan GPSPPP software is provided by Natural Resources Canada. We thank them for their continuous support. For the PPP processing we used the IGS satellite products. Furthermore we thank the laboratories that provided data used in this study, notably SGF, OP and OCA.

This work was supported by the LABEX Cluster of Excellence FIRST-TF (ANR-10-LABX-48-01), within the Program "Investissements d'Avenir" operated by the French National Research Agency (ANR).

References

[1] E.F. Arias, G. Panfilo and G. Petit, "Timescales at the BIPM", *Metrologia* 48, 145-153, 2011.

[2] G. Petit et al., "1×10^{-16} frequency transfer by GPS PPP with integer ambiguity resolution", *Metrologia* 52, 301-309, 2015.

[3] F. Nakagawa et al., "Carrier-phase TWSTFT experiments using the ETS-VIII satellite", *Metrologia* 50, 200-207, 2013.

[4] G. Petit, J. Leute, S. Loyer, F. Perosanz, "Sub 10^{-16} frequency transfer with IPPP: Recent results", *Proc. EFTF Conf. 2017*, 784-787, 2017.

[5] P. Fridelance, E. Samain and C. Veillet, "T2L2 - Time transfer by Laser link: A New Optical Time Transfer Generation", *Experimental Astronomy* 7, 191-207, 1997.

[6] E. Samain et al., "Time transfer by laser link: a complete analysis of the uncertainty budget", *Metrologia* 52, 423-432, 2015.

[7] P. Guillemot et al., "Combination of T2L2 and GPS-CP Data: Towards an improvement of Time Transfer accuracy", *Proceedings of the IFCS/EFTF 2013*, 372-375, 2013.

[8] P. Exertier et al., "Sub-ns time transfer consistency: a direct comparison between GPS CV and T2L2", *Metrologia* 53, 1395-1401, 2016.

[9] J. Nicolas et al., "French transportable laser ranging station: scientific objectives, technical features, and performance", *Appl. Opt.* 39, 402-410, 2000.

[10] J. F. Zumberge et al., "Precise point positioning for the efficient and robust analysis of GPS data from large networks", *J Geophys Res Solid Earth* 102, 5005-5017, 1997.

[11] S. Loyer et al., "Zero-difference GPS ambiguity resolution at CNES-CLS IGS Analysis Center", *J. Geod* 86, 991-1003, 2012.

[12] J. Delporte, F. Mercier, D. Laurichesse, O. Galy, "GPS Carrier Phase Time Transfer Using Single Difference Integer Ambiguity Resolution", *IJNO*, 273785, 2008.

[13] J.-C. Marty, "Algorithmic Documentation of the Gins Software", grgs.obs-mip.fr/content/download/1460/9226/file/GINS_Algo_2013.pdf, 2013.

[14] J. Kouba and P. Héroux, "Precise Point Positioning Using IGS Orbit and Clock Products.", *GPS Solutions* 5(2), 12-28, 2001.

[15] J. M. Dow, R. E. Neilan and G. Gendt, "The international GPS service (IGS): celebrating the 10th anniversary and looking to the next decade", *Adv. Space Res.* 36, 320-326, 2005.

[16] A. Auriol and C. Tourain, "DORIS system: the new age", *Adv. Space Res.* 46, 1484-1496, 2010.

[17] E. Samain et al., "Time Transfer by Laser Link (T2L2) in non common view between Europe and China", *IEEE Trans. Ultrason. Ferroelectr. Freq. Control* PP(99), 1-1, 2018.

[18] K. U. Schreiber et al., "Ground-based demonstration of the European Laser Timing (ELT) experiment", *IEEE Trans. Ultrason. Ferroelectr. Freq. Control* 57(3), 728-737, 2010.

[19] L. Cacciapuoti and Ch. Salomon, "Space clocks and fundamental tests: The ACES experiment", *Eur. Phys. J. Spec. Top.* 172(1), 57-68, 2009.

Analysis and Compensation of Polarization in an Optical Frequency Transfer through a Fiber Communication Network

Per Olof Hedekvist, Ludwig Weddig and Sven-Christian Ebenhag
Dept of Measurement Science and Technologies
RISE Research Institutes of Sweden
Borås, Sweden
per.olof.hedekvist@ri.se

***Abstract*—In the fiber optic link, connecting RISE research facilities in Borås with the Photonics Lab at Chalmers University of Technology in Gothenburg, the signal is substantially distorted by polarization variations. It has been verified that the variations are induced by the electrical power grid, however unknown at which segment of the link that it occurs. While this distortion is effectively handled by standard equipment for the data transmission, it deteriorates the detection of a transmitted ultra-stable frequency, using heterodyne mixing. Thus, the magnitude and severity of this distortion is quantified, and some compensation techniques are evaluated.**

Keywords—fiber; frequency transfer; heterodyne detection; coherent; polarization;

I. INTRODUCTION

The time and frequency laboratory at RISE in Borås, Sweden, which are realizing the UTC(SP) timescale, is connected to the fiber optics research laboratory at Chalmers University of Technology through an active DWDM communication network. It is the Swedish University Computer Network (SUNET) and is a modern network, where the connected sites have access to 100 Gbit/s on a single wavelength through multi-level amplitude and phase modulation in combination with utilization of both polarizations. The link between the two laboratories is implemented mainly as a designated wavelength in the DWDM network, with a few km of dark fiber on each side, with a total distance of approximately 60 km single way. As it all operates in an active data communication network with amplifiers, the transfer must be implemented in duplex fiber, meaning that the light runs in separate parallel fibers to the university lab and back.

Present analysis is performed on the output of the returned signal at RISE, where the light has been transmitted approximately 120 km. It has previously been observed that the polarization of the light varies with the 50 Hz frequency harmonics of the power grid [1, 2], and that the variation during one 20 ms period is substantial. With an optical interrogation of heterodyne beating with a local laser oscillator, this polarization variation will deteriorate the detection of the frequency difference.

This work is supported the Swedish Innovation Agency, Vinnova, under contract "Riksmätplatsuppdraget", and by EMPIR-15SIB05-OFTEN, which has received funding from the EMPIR programme co-financed by the Participating States and from the European Union's Horizon 2020 research and innovation programme.

This extended analysis evaluates the polarization variation using two different polarization analyzers, with different sampling frequencies. The fastest analyzer is utilized as the detection unit for a digital polarization tracker, where the output polarization is steered to be at a linear state. The purpose of the polarization tracking and the parameters it will be evaluated against, are the applicability of compensating the polarization variations in optical frequency tracking through deployed and active DWDM networks.

II. POLARIZATION

The polarization of the light transmitted through a fiber can be described by its Degree-Of-Polarization (DOP) and its State-Of-Polarization (SOP). The DOP, which described how much of the optical power of the light is polarized, does not change during transmission in a passive fiber, but degrades from the noise of amplifiers and improves from passing a polarizing components. The SOP, which describes the actual polarization at a specific location, will change from any perturbation along the fiber, such as mechanical movement, temperature change or vicinity of magnetic fields through the Faraday effect.

The SOP is often described by the Stokes parameters (1-4) or the Jones vector. To visualize SOP, the Poincaré-sphere is commonly used, where the polarized light is described by its coordinates on a 3D-sphere

$$S_0 = I. \tag{1}$$

$$S_1 = I_p \cos 2\psi cos2\chi. \tag{2}$$

$$S_2 = I_p \sin 2\psi cos2\chi. \tag{3}$$

$$S_3 = I_p \sin 2\chi. \tag{4}$$

When the polarization is stable after transmission, the SOP is described by a small dot of the sphere, and through mechanical adjustments of the fiber, it can be tuned to any specific SOP at the output. A polarimeter will divide the optical signal in further

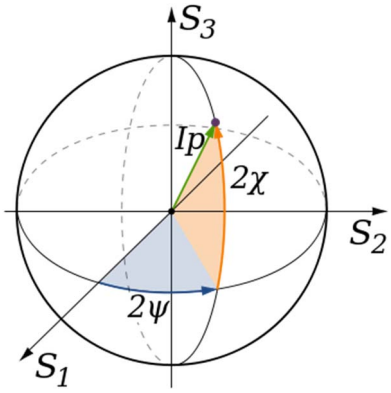

Fig. 1. Illustration of the Poincaré sphere, with the parameters from the Jones vectors inserted [3]

detail and calculate the Stokes parameters of the light, which forms a 1x4 matrix describing SOP and DOP. The SOP is often best visualized on the Poincaré sphere [4], where the poles are right- and left-handed circular polarizations and the equator is linearly polarized at a different angle with reference to the alignment of the input fiber. The radius of the sphere may also be used to visualize the DOP, however in Fig. 1, have the radius been normalized.

The detrimental effects of polarization variation in frequency transfer links can be described by the theory for heterodyne mixing of optical signals on a photodetector. The two incoming light signals, signal (s) and Local Oscillator (LO) can be described by two electromagnetic waves E with amplitude A, frequency ω, and phase φ (5-6).

The output current will be proportional to the intensity of the incoming light, which is the square of the addition of the two electromagnetic waves E_s and E_{LO} (7). It should be noted that in the addition, the two waves are described by a vector in the polarization space, and thus there is a parameter cosθ(t) corresponding to the misalignment of polarization between the two waves.

$$E_s(t) = A_s \cos[\omega_s t + \varphi_s(t)]. \quad (5)$$

$$E_{LO}(t) = A_{LO} \cos[\omega_{LO} t + \varphi_{LO}(t)]. \quad (6)$$

$$I_{coh}(t) = (E_s(t) + E_{LO}(t))^2$$

$$\frac{1}{2} A_s^2 + \frac{1}{2} A_{LO}^2 + A_s A_{LO} \cos[(\omega_s - \omega_{LO})t + \varphi(t)] \cos\theta(t). \quad (7)$$

If the two waves are orthogonal in polarization, the output signal at IF-frequency is thereby zero, and when the polarization changes substantially with the frequency of the electrical power grid, this happens on a millisecond scale.

III. Experimental Setup

Laboratory equipment

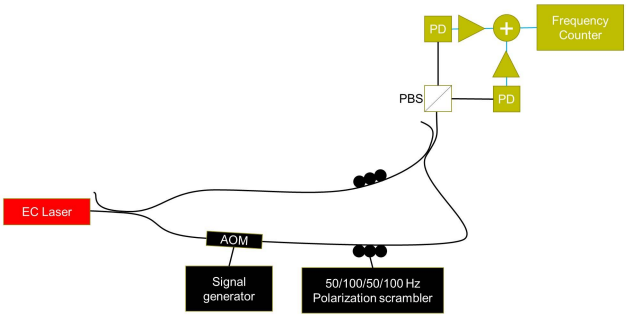

Fig. 2. Experimental setup

In the experiment, the transmission fiber is replaced by a polarization scrambler, to isolate the effects of polarization variations at 50 Hz. The scrambler has four different modules, where each module can change the polarization with 2.5π, and to simulate the effect of the power grid, modules number 1 and 3 are driven by a 50 Hz signal while modules 2 and 4 are driven by a 100 Hz signal, all at full swing. The transmitter is an External Cavity laser (ECL) emitting light at 1542.14 nm, which is the wavelength channel assigned by SUNET and therefore the reference wavelength for all experiments at RISE. At the receiving end, the signal is received through heterodyne mixing with the transmitted signal and the frequency is analyzed.

The setup is illustrated in Fig. 2. The light source is an External Cavity Laser, each power splitter/combiner has a 50/50 ratio. The Acousto-Optic Modulator (AOM) is driven by an 80 MHz signal from a signal generator, and the 4 modules of the polarization scrambler is controlled by a 50 Hz, 100 Hz, 50 Hz and 100 Hz signal, respectively. The polarization of the upper fiber is adjusted with respect to the splitting in the Polarization Beam Splitter (PBS).

At the detection, heterodyne mixing occurs at both Photodetectors (PD), thereafter the IF signals from both PDs are amplified and combined in a passive resistive microwave combiner. The sum of the signals is analyzed using an oscilloscope and a frequency counter. The polarization division technique for detection of coherent signals was first proposed in 1987 for data communication applications [6]

IV. Measurements and Results

A. Polarization Measurements

To illustrate the magnitude of the polarization variation in a deployed active fiber optic network, the output polarization is measured using a commercial polarimeter. Since the variation induced by the electrical power grid, at 50 Hz and its additional

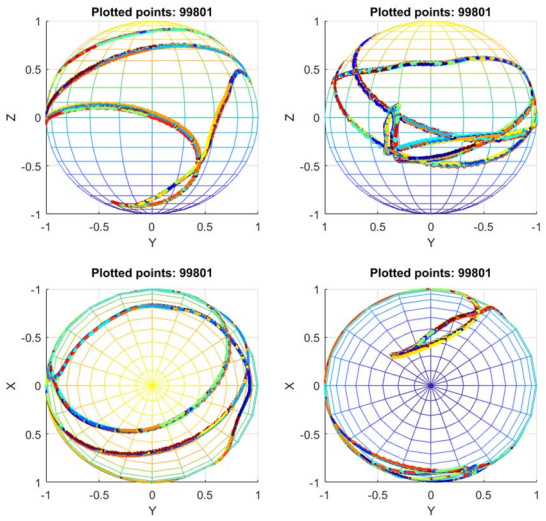

Fig. 3. Poincaré sphere showing the polarization variation at the output of a fiber transmission during 100 ms perimental setup and it corresponds to 5 periods of the polarization scrambling. The color coding presents 100 markers per color and there are 64 colors before it starts over

harmonics, a fast polarimeter is necessary to resolve the details in the signal. Fig. 3, shows how the polarization varies through multiple revolutions around the sphere within each 20 ms period.

B. Polarization division detection

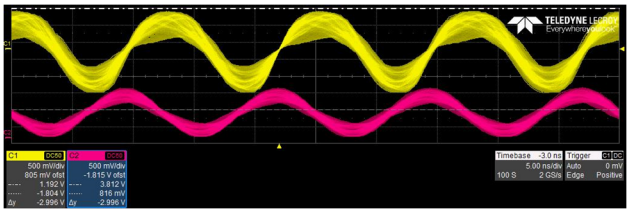

Fig. 4. Oscilloscope traces of received signals

Using the technique of dividing the signal into two orthogonal polarizations and extract the IF signal through the addition of the two complementary signals from heterodyne mixing in the two PDs, the frequency is analyzed in a frequency counter. Since the focus of the analysis is the short-term stability, the measurement time is 100 ms, corresponding to 5 periods of the polarization scrambling. The signal of the combined signal is compared with a signal from heterodyne detection in a single PD without any polarization compensation in use. Fig. 4, shows the oscilloscope traces for combined signal (upper yellow) and single signal (lower pink).

In the measurements using the frequency counter, one sample from each detector is recorded every 10 s and plotted in Fig. 5. The deviation from average is mainly limited by the linewidth of the ECL and the low isolation of a passive microwave power combiner, and thus the improvement of polarization division is negligible.

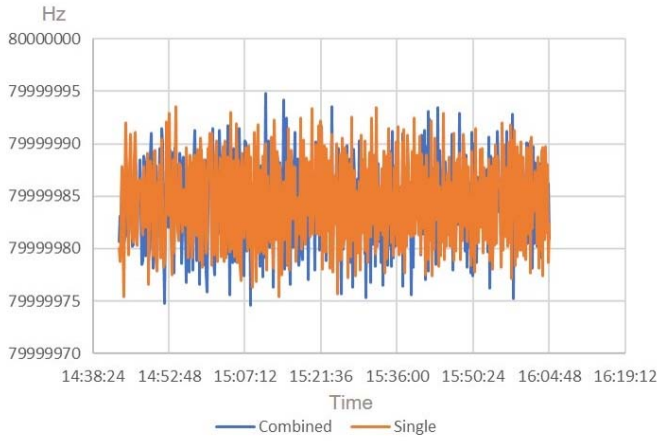

Fig. 5. Measured frequency from combined detector pair (blue) and single detector (orange)

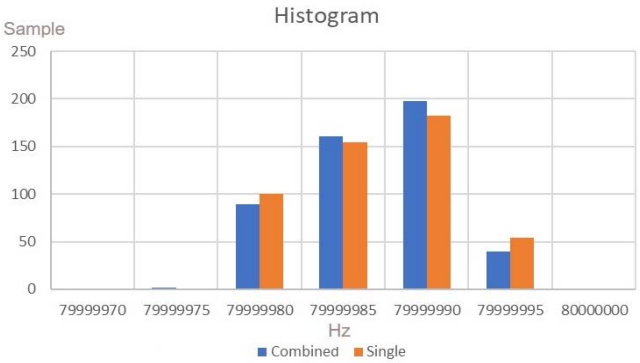

Fig. 6. Histograms of sampled data

When a histogram is calculated from the data samples, as shown in Fig. 6, there are small discrepancies between the two signals, and the standard deviation of the two techniques are slightly lower for the data from the combined signal (4.34 Hz) than for the single detector signal (4.44 Hz), however mainly an indication that further analysis is required.

V. CONCLUSIONS

The experiments and evaluation show that when the detection is polarization dependent, the variation of polarization must be addressed in the solution. The influence of 50 Hz from the power grid will induce a substantial variation that is very difficult to stabilize. By using the parallel polarization splitting detection technique, there are possibilities to overcome this deterioration, however the microwave electronics must be improved further.

REFERENCES

[1] S.C. Ebenhag, M. Zelan, P.O. Hedekvist, M. Karlsson and B. Josefsson, "Coherent Optical Two-Way Fre-quency Transfer in a Commercial DWDM Network", The Institute of Navigation 47th Precise Time and Time Interval (PTTI) Systems and Applications Meeting, pp. 116–120, 2016.

[2] S-C. Ebenhag, P. O. Hedekvist and L. Weddig, “Measurement and analysis of polarization variations in an optical coherent fiber communication network utilized for time and frequency distribution”, The Institute of Navigation 49th Precise Time and Time Interval (PTTI) Systems and Applications Meeting, pp. 233 - 236, 2018.

[3] https://en.wikipedia.org/wiki/Polarization_(waves)#Poincaré_sphere.

[4] D. Derickson, Fiber Optic Test and Measurement, ISBN 0-13-534330-5, Prentice Hall PTR, 1998.

[5] S.C. Ebenhag, P.O. Hedekvist, P. Jarlemark, R. Emardson, K. Jaldehag, C. Rieck and P. Löthberg, "Measurements and Error Sources in Time Transfer Using Asynchronous Fiber Network", IEEE Trans. Instr. Meas., vol. 59, pp1918 - 1924, 2010.

[6] B. Glance, “Polarization Independent Coherent Optical Receiver”, IEEE J. Lightwave Technol., vol. 5, pp. 274 – 276, 1987.

First Experiments on Application of Rb Fountain Frequency Standards for TA(SU) Time Scale Maintenance

Blinov I., Boiko A., Kosheliaevskii N., Kupalova O. and Sokolova O.

Department of Metrology for Time and Space
VNIIFTRI
Mendeleevo, 141570, Russia
Email: nkoshelyaevsky@vniiftri.ru

Abstract— **Abstract - At previous PTTI meeting, PTTI'17, we mentioned that VNIIFTRI has got four Rb fountain frequency standards, which run as frequency standards, not clocks. These instruments are not intended for secondary presentation of the time unit the second SI. These are indeed very stable frequency reference without frequency drift inherent, for example, to H-masers. During last year output frequency of these standards has been calibrated against operational CsF02 primary fountain frequency standard and now one may use these instruments as time and frequency unit keepers. This report will present preliminary results of the first experiments on application of Rb fountain frequency standards for maintenance the national atomic time scale TA(SU). According internal regulation TA(SU) is independent atomic time scale with the unit of time the second SU, reproduced by operational primary Cs fountain frequency standards. This time scale by-turn is maintained by ensemble of continuously operating high stable hydrogen masers. On other hand, each H-maser demonstrates more or less predictable frequency drift the value of which may be quite comparable to daily H-maser frequency stability. That is why one has times to times re-evaluate H-maser output frequency parameters. The more often one will re-evaluate H-maser output frequency parameters the more stable and accurate (in sense unit of time the second SU) time scale will be produced. The key problem is interruptible Cs standard mode of operation. Typically, Cs standard produces two or three sessions per month, but sometimes happens gaps for some months. In such cases availability of more or less continuously operating stable and none drifting frequency reference such as Rb fountain frequency standards may be a solution of the problem. The paper presents comparisons of some scenarios of TA(SU) maintenance: a. purely based on H-maser ensemble and primary Cs fountain frequency standards data and b. based on H-maser ensemble and Rb fountain frequency standards data**.

Keywords— Time Algorithm, Atomic Time Scale

INTRODUCTION

Each self-respect time laboratory maintains atomic time scale. Atomic time scale ensures particular laboratory k maintenance of independent time scale and protects against any problems regarding possible gaps in local realization of UTC(k).

For many years VNIIFTRI atomic time scale TA(SU) was based on free ensemble of continuously operating H-masers [1, 2]. During that period TA(SU) was free running time scale due to inevitable frequency drift inherent to H-maser itself. On other hand this was autonomous and more or less predictable time scale which frequency stability $\sigma_y(\tau)$ was about 1×10^{-15} for $10 \leq \tau \leq 30$ days. Situation changed drastically in 2012 when VNIIFTRI time laboratory started utilize primary CsF02 fountain frequency standard with accuracy $\leq 5\times10^{-16}$ [3] for regular H-maser output frequency calibration. About two or three years later CsF02 uncertainty level was twice improved up to $\leq 2.5\times10^{-16}$ [4]. Basing on application CsF02 the new time algorithm [5] was introduced started 00h00m MJD 56289 (28 DEC 2012). About two years later [6] time algorithm was somewhat updated.

The core idea of the new algorithm is rigid connection of TA(SU) time unit – the second SU – to that reproduced by primary CsF02 fountain frequency standard. Because of CsF02 standard is not continuously operating instrument, more over during its operational session some parameters of standard have to be essentially changed, one get the total frequency difference between used clock and unperturbed Cs transition after ending of the operational session. The operational session may continue from a few days up to a week or even more. During that period total frequency change of reference clock under measurement may exceed $1\text{-}2\times10^{-15}$. This value considerably exceeds CsF02 standard accuracy. On other hand due to some hardware problems CsF02 standard may be out of operation sometimes for two or even three months. Such CsF02 performances produce a severe problem for continuously operating H-maser frequency prediction. Usually we predict clock frequency for one month ahead basing on 10 to 11 month readings.

In 2016 our laboratory got four ^{87}Rb fountain frequency standards. These were neither instruments intended for secondary presentation of the SI second, nor clocks. One may treat these instruments as a keeper of frequency value. The most positive feature of these Rb standards is continuous operation and in contrast to primary Cs standards these one operates under permanent parameters. So one may expect that they will reproduce

unknown but extremely stable frequency. After half a year preliminary tests we gained measuring data and then tried to test new time algorithm.

I. M-WAVE FOUNTAIN FREQUENCY STANDARDS, THEIR LINKING AND H-MASER ENSEMBLE

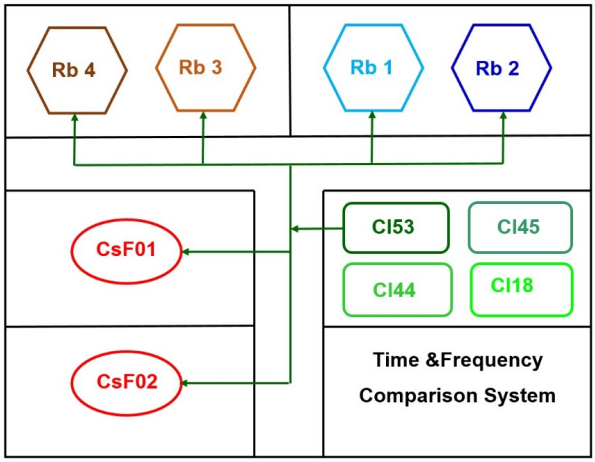

Fig.1 μ-wave standard layout

In our disposal there were two Cs fountain frequency standards: CsF01 and CsF02, and four ^{87}Rb fountain frequency standards: Rb1 to Rb4, Fig.1. Each Cs fountain located in separate housing, Rb standards were placed in pairs in accordance to their design. Rb1 and Rb2 design considerably differed from other pair Rb3 and Rb4 [7]. All these instruments were fed by 5 MHz signal of H-maser no.403853 (Cl 53). This H-maser was chosen from the whole ensemble of 16 masers because of its high short term frequency stability ($\sigma_y(\tau) \sim 6\text{-}7\times10^{-14}$ τ =1 s) and high spectral purity of 5 MHz signal. Each quadriga of H-masers occupied separated temperature/humidity controlled housing.

All μ-wave fountain frequency standards do not had output frequency signals but their internal control system produced output readings of frequency difference between applied H-maser's signal and the fountain standard.

Output frequencies of all H-masers were compared across each other by phase comparators at 1 s basis. The accuracy of the H-maser frequency difference measurement at 1 day basis exceeded 1×10^{-16}.

II. RB M-WAVE FOUNTAINS AND H-MASERS FREQUENCY COMPARISON DATA

Fig.2 presents all available source frequency difference data Rbi – Cl 53 for the period of about 9 month. Looking at this dependences one may conclude that Cl 53 manifests nonlinear frequency drift at least at the depicted time interval MJD 57895 – MJD 58158.

To estimate long term stability of the Rb standards and its conformance as time unit reference we chose somewhat indirect way: we decided to compare frequency drift of two clocks

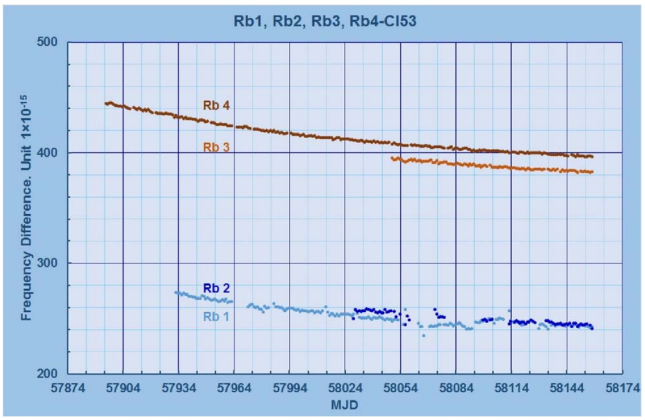

Fig.2 Rb$_i$-Cl 53 source frequency difference

(namely Cl 14 and Cl 52) which manifest linear frequency drift relative to all available Rb standards as well as relative to CsF02 and TAI, Fig. 3-4.

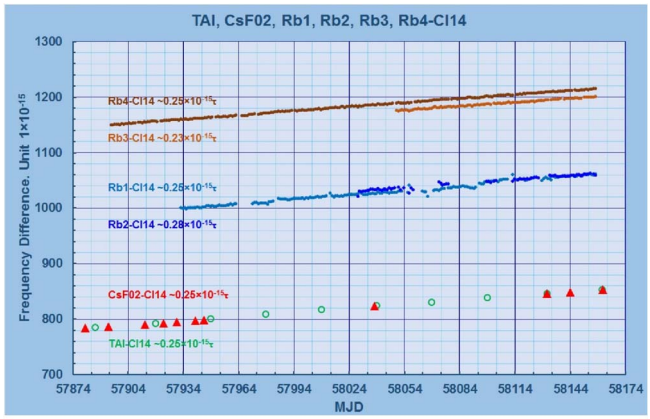

Fig.3 Rb$_i$-Cl 14 frequency difference data

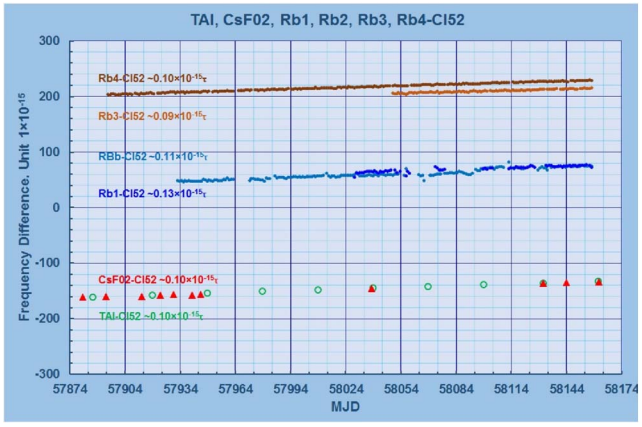

Fig.4 Rb$_i$-Cl 52 frequency difference data

In both cases absolute frequency drift estimation of Cl14 relative Rb1-Rb4 coincide within $\pm1\times10^{-17}$ per day (mean value $(2.52\pm0.16)\times10^{-16}$/day) as well as relative to CsF02 and TAI (2.50×10^{-16}/day).

Quite the same situation of drift estimation of Cl52 relative Rb1-Rb4 (mean value $(1.05\pm0.13)\times10^{-16}$/day) as well as relative to CsF02 and TAI (1.00×10^{-16}/day).

III. Current Time and Frequency Algorithm for TA(SU)

The algorithm defines how basing on independent clock ensemble with essentially different frequencies and time scales one generates the National Atomic Time Scale TA(SU) which in turn maintain time unit SI(SU) matched to that reproduced independently by primary CsF01(SU) and CsF02(SU) in accordance to its definition in SI [6].

Striking features of the algorithm:

- the time unit reproduced by VNIIFTRI Cs fountain standards is keeping by ensemble of continuously operating H masers;
- the time unit in TA(SU) correspond to the second SI(SU), reproduced by VNIIFTRI CsF01(SU) and CsF02(SU) fountain standards;
- the time scale TA(SU) is completely autonomous and independent. This is based purely on the VNIIFTRI domestic hardware and software means;
- the clock rate prediction interval for maintenance TA(SU) is equal to 1 month. The forecast is based on CsF01/02(SU)–Cl 4038ij reading collected within a few months (typically 10-11). The clock's frequency forecast model depends on particular clock performances and may be first or second order;
- to avoid inevitable frequency steps in case of changes or absence CsF01/02(SU)–Cl 4038ij data, or at the month end rollover there are some precautions in algorithm;
- the whole clock ensemble is involved in TA(SU) forecast to full extend by means of weighting procedure;
- particular clock contribution to TA(SU) depends on clock's statistical weight;
- clock's statistical weight is composition of a few components:
  - the proximity of successive clock's frequency prediction relative to primary fountain standards (the main contribution);
  - clock's frequency prediction uncertainty relative to primary standards;

IV. Ideas to the Free Atomic Time Algorithm Based on the Rb Fountains

Since we have convinced of long term frequency stability of the Rb standards one may advance ideas to the Free Atomic Time (FAT) algorithm. Keeping in mind that referring to the Rb standards one may get Rb-Clock data at daily basis we tried to predict frequency difference Rb-Cl one day ahead basing on the three previous months readings Rb-Cl. The prediction model was sliding process based on linear in frequency least square equation.

As a first step we do not involved in the model all available H-maser – quite the contrary we tested only two clocks: one Cl 403814 (Cl 14) resides chamber no.203 and other Cl 403852 (Cl 52) resides chamber no.205. These both clocks are the same as were used in Rb fountain stability tests. The results presented at following pictures, Fig.5-8, are referred to the Rb4 because of only this Rb fountain has the most long operational life.

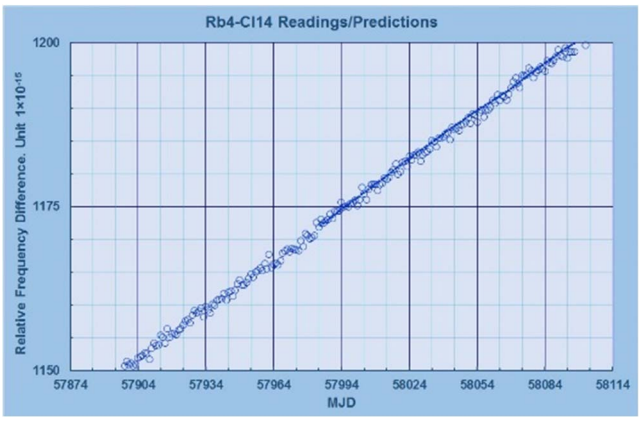

Fig.5 Rb4-Cl14 source frequency difference and prediction data

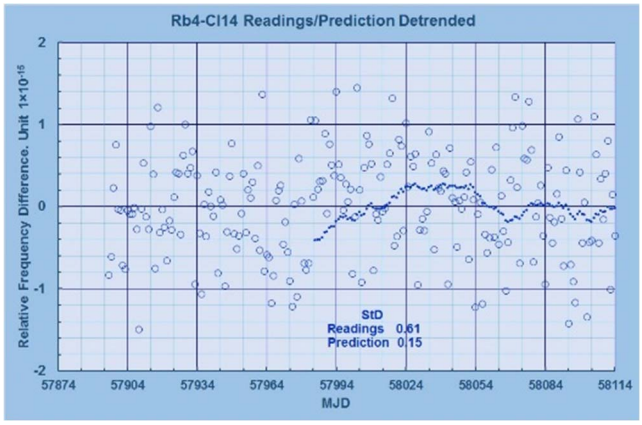

Fig.6 Rb4-Cl14 detrended frequency difference and prediction data

The standard deviation of the detrended daily frequency differences Rb-Cl for both clocks (Cl 14 and Cl52) looks quite similar, somewhat about 6×10^{-16}. On the other hand, standard deviation of the detrended prediction daily frequency differences for clocks Cl14 and Cl52 differs more than 1½ times. We consider that standard deviation of the detrended daily Rb-Cl frequency differences is mainly defined by Rb itself frequency noises. On the other hand standard deviation of the detrended prediction daily clocks frequency differences essentially dependent on individual clock stability itself. The measurement data from H-maser intercomparison system demonstrate Cl 52 daily frequency stability about twice better than that for Cl14.

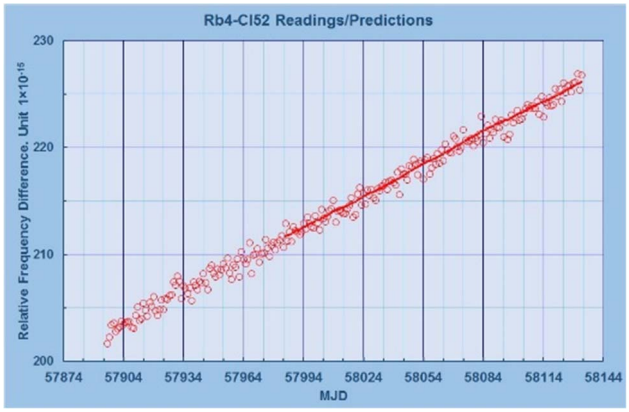

Fig.7 Rb4-Cl14 source frequency difference and prediction data

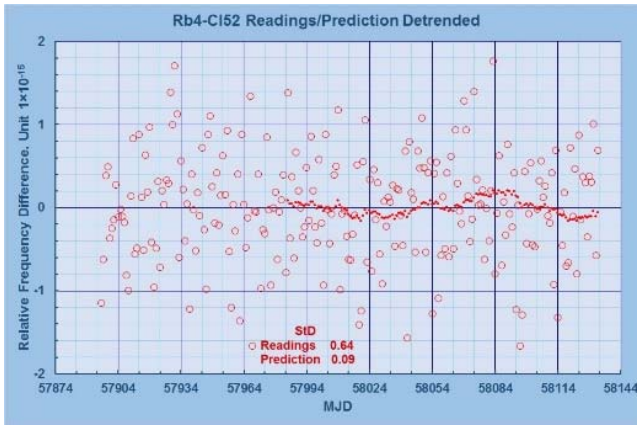

Fig.8 Rb4-Cl52 detrended frequency difference and prediction data

The FAT algorithm is based on following equations:

$$FAT - Cl_j = \sum_{i=1}^{N} w_i[(Cl_i - \tilde{Cl}_i) - Cl_j]$$

$$w_i = (1/\varepsilon_i^2)/\sum_{k=1}^{N} 1/\varepsilon_k^2$$

where w_i and ε_i statistical weight and prediction uncertainty of clock i correspondingly;

Cl_i, Cl_j are Rb4 – Cl_i, Cl_j frequency difference;

$\tilde{Cl}_i$ is Rb4 – Cl_i frequency difference prediction.

Since summation is executed by i index statistical properties of FAT may be presented by $\sum_{i=1}^{N} w_i(Cl_i - \tilde{Cl}_i)$

Gave at Fig.9 frequency stability dependences presented FAT realizations based on clock ensembles in chambers no.102 and no.205 correspondingly. These estimations are purely based on internal data – Rb4-Cl53 clock differences and clock intercomparisons.

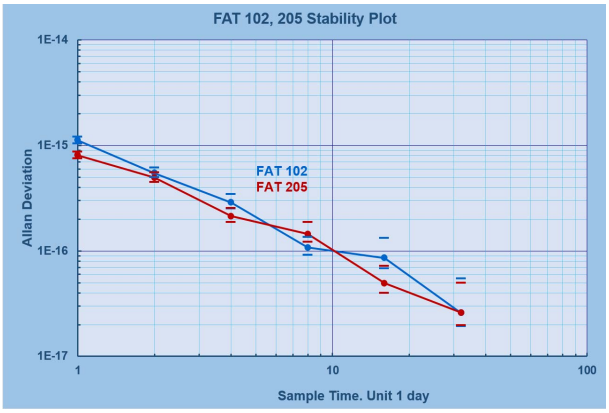

Fig.9 FAT 102 and FAT 205 frequency stability estimation

V.TAI-FAT BASED ON THE LIMITED H-MASER ENSEMBLES FREQUENCY STABILITY ESTIMATIONS

As far as we have link to TAI there were no problems to get analogous stability estimations relative to TAI, Fig.10. These one are somewhat moderate – on one hand stability corresponds sample time 5 days is considerably limited by time link to TAI, for one month and more by TAI stability itself. In the sequel we will touch this issue more detailed.

Nevertheless we have got positive output – both FAT sources demonstrate visible improvement compare to that of TA(SU) based on the same clock ensemble and irregular CsF02 comparisons. More over FAT 205, based on the ensemble of more stable and predictable clocks demonstrates obvious superiority over FAT 102.

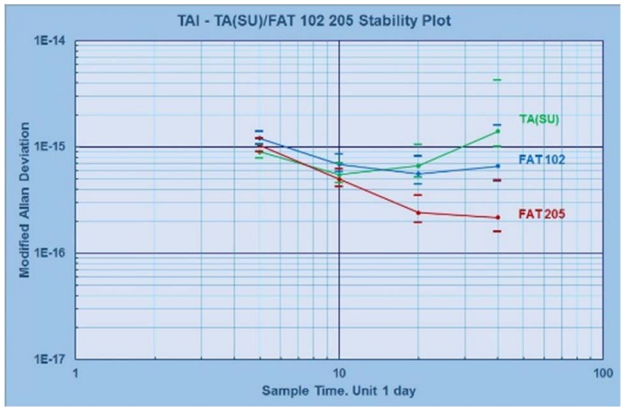

Fig.10 TAI-TA(SU), FAT 102 and FAT 205 frequency stability estimation

VI. TAI-FAT BASED ON THE WHOLE H-MASER ENSEMBLE FREQUENCY STABILITY ESTIMATIONS

Fig.11 demonstrates once more frequency stability dependences for FAT 102 and FAT 205. Apart from these one may see stability plot FAT TOTAL based on the whole ensemble of available clocks in our disposal. The most striking feature is that FAT TOTAL obtained using operational software usually used for every day TA(SU) maintenance with minor changes.

These changes concerned only clock prediction model based on Rb standard and one day prediction algorithm presented above.

FAT TOTAL stability results looks a little bit better than that for FAT 205. Such a result is reasonable enough because of clock ensemble is much more than that for FAT 102 and FAT 205. On other hand one may expect more considerable gain, but one has took into consideration that clocks in the ensemble is not uniform. If one compares more uniform set of clocks for example in chamber no.102 and the whole ensemble gain factor will be ~3 times. Even for this case actual gain factor ~3 exceeds expected value ~2 (square root of total clock number/clock number in chamber no.102). The source of discrepancy may be in more significant statistical contribution clocks located in chamber 205.

The other important issue is long term stability limitations. Strictly speaking, TAI is not the "sacred cow" - its stability is also limited. The short term TAI stability limitations may be extracted from EAL frequency stability published in Circular T [8] – top green line "EAL stability". The other estimation linked to TT-TAI time scale difference is published at the beginning of next to the reporting year. The corresponding stability estimation at Fig.11 for the period of 2016-2017 is labeled as "TT-TAI stability".

Since "EAL stability" limit is based on the EAL level corresponding to year 2015 and maybe since that time EAL algorithm has been improved resulting in improvement the EAL itself, let us appeal to more modern and fundamental source – TT-TAI difference published annually. TT-TAI reflects possible changes in TAI during previous reporting years. That is TT is the definitive version of the TAI, which in turn plays a role of "real time" atomic time scale.

If we follow this idea flattering FAT 205 and FAT TOTAL dependences on Fig.11 for sample times more than 20 days have obvious explanation – this is consequence of the TAI stability limits.

Fig.11 TAI-all FATs frequency stability estimation
TAI frequency stability limitations

CONCLUSION

The main goal of this work was to improve long term frequency stability of FAT compare to existing TA(SU). In this presentation we demonstrated first results of application continuously operating Rb fountain standard as a reference to maintain time scale FAT based on the ensemble of hydrogen clocks.

The core of this idea is fast prediction procedure-one day ahead basing on three months estimation period. It turns to be very beneficial compare to TA(SU) operational algorithm used one month ahead prediction based on 10-11 months estimation period.

FAT frequency stability estimations based on internal measurements demonstrate level $\leq 1\times10^{-16}$ for sample time more than 10 days. If we will produce mental experiment on FAT synchronization to TA(SU) at the beginning of test interval MJD 57895-58149 one get RMS difference TAI-FAT$_i$ within 1-4 ns compare to that TAI-TA(SU) 13 ns following operational algorithm, Fig.12.

Fig.12 TAI-TA(SU) & all FATs
time scale difference

Examined experiment produced very beneficial and far going results, which have to be implemented into operational algorithm. To use these to the full extend some urgent problems have to be solved:

- first MTBF (mean time before failure) of all Rb fountain standards have to be considerably improved;
- mean restoration time has to be considerably reduced, let us say about weeks;
- all available Rb fountain standards have to be regularly calibrated relative to primary Cs standards;
- TA(SU) operational software has to be updated and include module which will realize ensemble time unit keeper basing on all available Rb fountain standards.

REFERENCES

[1] И.Ю. Блинов, С.И. Донченко, Н.Б. Кошеляевский, А.Н.Щипунов, ГЭВЧ – десять лет развития, Альманах современной метрологии, № 11, 2017, стр. 43-80, ISSN 2313-8068.

[2] N.Koshelyaevsky, H.Neustroeva, O.Sokolova, The National Atomic Time Scale Algorithm Updating, Proceeding of the 8th International

Symposium “Metrology of Time and Space”, 14-16 September 2016, Azimut Hotel, Saint Petersburg, Russia.

[3] Yu.S.Domnin, V.N.Barishev, A.I.Boyko, G.A.Yolkin, A.V.Novosyolov, L.N.Kopilov, D.S.Kupalov, Cesium fountain VNIIFTRI CsF02, Proceeding of the 6th International Symposium “Metrology of Time and Space”, 17-19 September 2012, Morozovka Holiday Hotel, Mendeleevo, Moscow Region, Russia.

[4] Ю.С.Домнин, В.Н.Барышев, А.И.Бойко, Г.А.Елкин, А.В.Новоселов, Л.Н.Копылов, Д.С.Купалов, «Цезиевый репер частоты фонтанного типа МЦР-Ф2», Измерительная техника, 2012, №10, стр. 26-30.

[5] N.Koshelyaevskiy, O.Sokolova and M.Maslennikova, The new time algorithm for national time scales of Russian Federation, Proceeding of the 6th International Symposium “Metrology of Time and Space”, 17-19 September 2012, Morozovka Holiday Hotel, Mendeleevo, Moscow Region, Russia.

[6] N.Koshelyaevsky, H.Neustroeva, O.Sokolova, The National Atomic Time Scale Algorithm Updating, Proceeding of the 8th International Symposium “Metrology of Time and Space”, 14-16 September 2016, Azimut Hotel, Saint Petersburg, Russia.

[7] I.Blinov, Yu.Domnin, S.Donchenko, A.Goncharov, N.Kosheliaevskii, A.Naumov, S.Slyusarev, Russian State Time and Frequency Standard Laboratory Activities and Updates, Proceedings of the 48th Annual Precise Time and Time Interval Systems and Applications Meeting, (PTTI 2017), January 30-February 02, 2017, Hyatt Regency Monterey, Monterey, California, USA.

[8] Circular T 336, Bureau International des Poids et Mesures, Organisation Intergouvernementale de la Convention du Metre, Pavillon de Breteuil F-92312 Sevres CEDEX, 2016 January 06.

[9] ftp://ftp2.bipm.org/pub/tai/ttbipm/TTBIPM.17.

Passive Utilization of the TWSTFT Technique

Carsten Rieck, Per Jarlemark and Kenneth Jaldehag,
Measurement Science and Technology
RISE Research Institutes of Sweden
Borås, Sweden
carsten.rieck@ri.se

Abstract— As an active technique TWSTFT is limited in the number of concurrent users on the same communication channel. Using the transmissions of the reference network, passive users can observe the signals in a common view sense and by knowing the orbit of the relaying satellite, corrections describing the dynamic path delay can be used to estimate the clock difference between passive stations. Reliable orbit determination can be achieved using all the active measurements performed by the regular active users. For the EU/US network using Telesat Telstar 11N, the orbit estimation uncertainty is in the order of 1m for the area spanned by the contributing stations. The corresponding time uncertainty for a passive user is about 1 ns, slightly larger than achievable by active links. A passive use of TWSTFT may provide increased timing resiliency for a number of applications. The design of a passive ground station based on a SDR receiver is suggested.

Keywords—TWSTFT; time transfer; orbit determination; passive approach; real-time; resiliency

I. INTRODUCTION

Two Way Satellite Time and Frequency Transfer (TWSTFT, also denoted TW in the following) is a well-established time transfer method for both continental and inter-continental baselines [1]. Despite the current performance problems [2,3], TWSTFT is the most accurate of the long distance methods used today and can be considered the backbone of international time keeping as it links more than half of all the clock weight in TAI [4].

TWSTFT is an inherently active technique with transmission at both ends of a link. As a pseudo random noise code division multiplex technique its performance is limited by the available bandwidth and the number of concurrent signals on a single communication channel. With the current single Rx-channel use and the schedule driven measurement scheme, it is difficult to add more stations without further degrading the measurement quality. This is particularly true for the crowded EU/EU transponder of Telstar 11N, where, as of 2018, up to 14 active stations participate in a bi-hourly schedule.

One possible way to introduce more users could be achieved by a passive exploitation of the transmitted signals in a common view sense. In a straight-forward situation, a passive user observes, possibly multiple, codes sent by the active users of a TWSTFT-network. Common view observations of the same signals by a pair of observers can be used to compare their local clocks. This requires precise orbit information in order to correct the common measurements with the differential path delay. Depending on the position of the geostationary slot, the used satellite's apparent steady 3D position varies in the order of 10 km per component over a day [5]. Because the orbit is usually poorly known, it is essential to establish an infrastructure that provides the passive users with satellite ephemerides or appropriate correction.

As the advantages of a two-way method, with mostly reciprocal path delays, do not apply for common view, the suggested one-way technique also needs to account for additional delays by measuring or modelling errors due to various atmospheric delays and Earth tides. Calibration of the passive user equipment is of course mandatory for any timing application requiring traceability.

II. DESCRIPTION OF THE METHOD

The principle method was presented in [6], which has been refined in some details. The original scheme was twofold: (*a*) estimation of precise satellite positions using ranging measurements only, and (b) their temporal interpolation with help of pairs of single way measurements. Such pairs constitute the majority of all regular TWSTFT measurements as they are the basis for the two-way differences. For orbit determination the sums of pairs are used, where a single sum is equal to the sum of two equivalent ranging measurements[1]. With such a summation (or differentiation) the apparent fiducial *midpoint*, i.e. where the satellite relays the signal, is lost and thus such measurements carry less information than single ranges. However, in order to be able to measure ranges, a station needs to receive its own signal. If the Rx and Tx beams are different for certain stations, such it is for the US stations in the current EU/US network on T11N[2], then these are not able to contribute to the precise satellite positions. The two-step processing is intuitional, but in such circumstances it fails to represent the satellite position with sufficient accuracy outside of the contributing area of stations. Therefore it is essential to directly include even non-ranging capable stations to the orbit determination. A method for the single-step assimilation of all available measurements is briefly described below.

The work presented in this paper is supported by the Swedish Governmental Agency for Innovating Systems, diarienr: 2016-02729.

[1] On synchronized and calibrated systems

[2] EU uses ones transponder for both up- and downlink within Europe, whereas US stations use two transponders to communicate with European stations and are not able to see their own signals

A. Orbit Determination

The measurement vector $\bar{m}$ constists of:

1. ranging measurements r_i for any station *i,* and
2. pairs of single way measurements s_j for any pair of mutually observing stations *a* and *b* as $s_j = (r_a + r_b)$,

corrected for various station position dependent delays.

For each run of the orbit determination at time *t*, a window of epochs $n_t = [t_{-4\mathrm{h}} .. t]$ are collected, defining an observation vector $\bar{m}_t = [r_i , s_j]_{n_t}$ for any available *i* and *j*. The orbit is described by a GPS ICD [7] compatible Kepler model $\bar{k}_t$, which is estimated using iterative nonlinear least squares as

$$\bar{m}_t = \boldsymbol{A}_t \Delta \bar{k}_t ,$$

starting with $\bar{k}_{t_0}$ derived from a set of ranging measurements r_i available during the epochs of n_t. $\boldsymbol{A}_t$ is a design matrix consisting of the partial derivatives that link the measurements $\bar{m}$ to the elements of the Kepler model $\bar{k}$. Estimation epochs *t* are typically chosen such that they coincide with the epoch times of ITU measurements of the active network[3] [8]. This allows to conveniently post-process published measurements and may also establish a good convention for the real-time application of the method.

The orbit of the satellite is regularly perturbed, such as by solar pressure on the vessel's body or by gravitational instability. The most severe perturbations however, are caused by orbit station keeping maneuvers intended to keep the satellite in its assigned orbital slot. In order to handle these regular events, the orbit determination evaluates the dynamics of the LSQ residuals. In case of T11N, the orbit is typically corrected twice a sidereal day by shortly pushing the satellite towards Earth. This results into lateral and latitude displacements of several hundred meters, whereas the longitude is minimally affected. The pushing-scheme seems to *switch* occasionally by dropping one of the thrusts of a daily pair. Figure 1 gives an example of the estimated displacement for a number of orbit corrections.

If residuals to the analysis suggest that the last epoch of the nominal four hour data window is disturbed by an orbital maneuver, the algorithm discards the window contents, declares the current orbit description invalid and reinitializes the data collection. In a real-time scenario a passive user will, during the following hours, be restricted to epochs with enough ranging measurements that would allow determining precise single point satellite positions. In order to provide a new usable real-time Kepler description, a sufficient part of the orbit's arc has to be integrated, >1/8 orbit, or 3h, can suffice. In post-processing the window can be populated in a backward fashion in order to provide a valid orbit close to the epoch of the maneuver.

[3] EU/US use slots *n* of 180s with the first 60 s preparation time and the following 120 s measurements, with its midpoint defining the epoch.

B. Orbit Distribution and Use

The derived orbit model $\bar{k}_t$ can be distributed as is, or a real-time service can be established that, on demand, calculates and streams time series of Rx range differences for pairs of passive receivers for fixed geo locations. Apart from the geometry, the stream can also include station specific corrections for Sagnac, atmospheric delays and Earth tides.

In the simplest case, a passive station would use the same signaling scheme as the active network provides. A passive station notes the time of arrival of the decoded signals from satellite according to its own clock and applies calibrations and range corrections to the satellite by means of precise ephemerides distributed by the network of active stations. All stations observing the same signals can easily determine their clock offsets in common view. If the signals from the network carry time information, a passive station may directly determine a clock offset to the reference station(s). This may be convenient in some cases, but has the disadvantage that remaining common errors, e.g. in the distributed orbit, cannot be *canceled* and may result in increased timing errors.

III. CHALLENGES

Single way methods, such as common view, are subject to a number of challenges that need to be addressed. Both the passive use and, in particular, the orbit determination is sensitive to the following, but not necessarily excluding other possible issues:

A. Synchronized and calibrated reference network

The estimation of the Kepler orbit $\bar{k}_t$ assumes synchronized measurements, preferably as corrections to the observations. Based on the active TW measurements, the reference network should easily be able to provide relative differences among each other and should also relate those to the orbit defining timescale. This also assumes that the network is sufficiently well calibrated.

B. Continous tracking of all system changes

Orbit determination is sensitive to changes in the station delays. If changes happen distinctively and sequentially throughout the network, then the algorithm that senses orbital station keeping may also be used to detect and to track individual changes in the stations. The network should have established means for documentation of all changes.

C. Reference station positions and local Rx+Tx delays

Due to the quasi-stationary co-rotating satellite it is difficult to distinguish between geometry, i.e. the position of the antenna phase centers, and the individual station Rx+Tx delays. Prior to an operative orbit determination the reference network needs a geometrical pre-calibration. This usually requires sufficient knowledge of a suitable subset of the stations. Station positions, describing the phase centers, can likely be determined on the 0.1 m level for most of the stations. Rx+Tx delays, however, are usually not known and are in general cumbersome to determine. Some stations are equipped with

satellite simulators that are able to estimate some of the delays. If enough stations, theoretically at least three[4], are known, the remaining unknown Tx+Rx delays can be estimated using the active measurements in a network tuning stage. A helpful constraint is the fact that the satellite moves, in a mean sense, symmetrically about the horizontal plane.

D. Delays of the neutral atmosphere

Hydrostatic delays and, with some restrictions, delays due to atmospheric water vapor can be modelled using ground based meteorology [9]. Wet delay, especially on low elevations, is one of the major error sources. As a single observation system in a quasi-stationary geometry it is impossible to estimate the delays from the TW observations themselves. Co-located GNSS can help to support the determination of atmospheric delays. For a passive station this may not really be an option, but may be used in a resilient setup with both GNSS and passive TW.

E. Delays of the ionosphere

Due to the high transmission frequencies involved, the ionosphere has a minor influence on the overall error budget. For long baselines it is however beneficial to apply corrections. IGS TEC [10] maps are one possible solution; or, similar to the suggestion for tropospheric delay estimation, co-located GNSS can be used to separately determine TEC as part of the computations done for the orbit determination. Figure 2 depicts a few days of ionospheric behavior for the EU/US network on T11N.

F. Solid Earth tides

On long baselines the differential tides can be significant and should thus be accounted for. A simple model can suffice. Other tidal errors are not of current concern.

G. Real-time

If the user application requires a (near) real-time service, orbit determination needs to assimilate the measurements $\bar{m}$ from the reference network in real-time. As obvious this may seem, real networks are not homogeneous and place various hinders for a real-time use. A typical reference network is usually distributed among as many administrations as there are stations and the distribution of measurements is often restricted because IP networks are protected by individual policies. The EU/US network has currently four stations[5] that allow a UDP data stream to reach a central IP receiver with redistribution capabilities. As a future alternative, the capabilities of the in-band distribution[6] of measurements should be considered. The coding of the station timing can carry an information overlay that could be used to distribute reduced measurements, e.g. in an ITU compatible sampling. In the same way, the estimated Kepler orbit could be distributed. Ultimately, the complete state of the reference network could be distributed in such a way, enabling a passive user to autonomously determine the orbit of the satellite and make estimates of its clock relative any other active station.

H. Transponder delays, multi-transponder configurations

Frequency dependent delays in the satellite transponder are currently modeled as constants. In multi-transponder configurations the delays in the measurements must be separated. Dynamics in the delays are difficult to model.

I. Orbit perturbations

The robust detection and mitigation of satellite orbit maneuvers are most important and can, if erroneous in a real-time scenario, cause substantial timing errors and/or downtime for a passive station. Also, the lifetime of a published orbit is limited. Continuous active measurements are expected to always reflect the true orbit with sufficient accuracy[7]. A default window length of 1/6 orbit, i.e. 4h, is chosen to dynamically describe the orbit with rapid updates. If the orbit defining measurements are temporary sparse, it may however be important to include orbit perturbation models to aid the orbit determination.

IV. Opportunities

Potentially, the passive use of TWSTFT offers many possibilities of which some are listed here:

- *The number of users*
  is unlimited. While active TW is limited in the number of concurrent users per communication channel, a passive use does not have such limitations. It will reach out to a new group of users, both commercial and scientific, that will benefit from current and future developments of TWSTFT. NMIs will be able to offer an independent method for robust and resilient distribution of their national time scales.
- *Directive antennas*
  minimize the effect of intentional and unintentional disturbances[8] compared to techniques with omni-directional antenna systems such as GNSS. Different frequency bands and generally higher power levels increase the resiliency with or without GNSS or other wired methods.
- *No Tx*
  means a simpler Earth station. It does not require a transmit license and eliminates risks of unintentional interference on the transponder. Applications that require radio silence must exclude actively transmitting methods.
- *Precise orbits*
  allow the determination of precise dynamic Sagnac corrections for active TW.
- *Optimization of the noise budget*
  in active TW may be necessary to increase the overall measurement quality. Orbit determination may also

[4] Spanning well enough geometry to define the area of the entire reference network, needs synchronized measurements

[5] NIST, ROA, PTB, RISE

[6] Currently provides a reduced measurements from the opposite side of a TW link; originally intended for real-time applications

[7] GPS ICD orbit descriptions seem to fit geostationary orbits well

[8] Denial of service due to jamming, spoofing, etc.

benefit from reduced noise. The reduced number of active measurements between stations can be compensated by passive measurements. It can also be used to increase the number of measurements without increasing the noise level on the transponder and thus improve the current poor bandwidth utilization in the scheduled peer-to-peer measurement configuration.

- *Cost effective*
  passive ground stations are preferably designed using SDR technology. A large user community will attract industrial manufactures to invest in ground station design.
- *Passive measurements on different and larger bands*
  may increase the quality of a passive time transfer. Even though the orbit determination is bound to the signals and the bandwidth of the leased transponder(s), a passive user may exploit the provided orbit description in different ways. Communication satellites relay digital signals of high power on large bandwidths that may be used with a correlation technique in-between a set of passive users.

In order to offer passive TW as a production rated service with realistic SLA terms, the partners operating the reference stations need to work in tight cooperation. The current NMI reference network will be a good test network to prove the concept for its own purpose and selected test users, and may allow establishing the foundation for a future service.

V. RESULTS

Results published in [6] are still valid and visualize some of the technical issues with current TWSTFT, such as diurnal signatures, most likely caused by a combination of station hardware, code interference and satellite motion. In extend, results of passive time transfer with help of single stage orbit determination using inter-transponder measurements are presented here. The EU/US network is using two extra transponders of T11N to allow intercontinental measurements. Inclusion of UNSO and NIST in the orbit determination dramatically improves the observational geometry and increases the east-west accuracy of the orbit. Figure 3 and Figure 4 respectively show traces of differences of single way measurements to orbits estimated without and with input from the US stations to the orbit. As expected, a European only orbit, due to the distorted geometry, does not fit the US stations well, whereas a contribution from each of NIST and USNO creates very small residuals for both and only slightly increases the deviation in the set of the European measurements. This shows that the active measurements and their calibrations fit the used GPS based Kepler orbit description well. The larger European residual is mostly due to the larger diurnal signatures on the crowded EU/EU transponder.

The regular TW schedule does not provide any common view measurements and consequently does not natively support passive links. For testing, NIST arranged to measure the UNSO schedule on its second Rx-channel. Similarly, RISE implemented a dynamic schedule on its second Rx-channel. The real-time SATRE[9] data stream provided by PTB, ROA, NIST and RISE is parsed and the best suited common view observation is chosen to be measured on the second Rx channel, common observations with PTB are prioritized.

Figure 5 and 6 show sample results for a passive time transfer between USNO and NIST, Figure 7 and 8 between RISE/SP and PTB. The upper of these plots show the Kalman-filtered time difference of the respective active link, and serves here as the *true* link phase for comparisons. For USNO-NIST, the difference is achieved by differencing individual links with PTB[10]. Plotted as a residual, two versions of the unfiltered passive link data are shown: biased and bias removed. From the lower plots it can be seen that the measurements of the individual signal originators are biased with respect to each other. Reasons for such biases are still unknown, but are probably caused by differences in the Earth-station pair, e.g. code dependent differences in the individual receiver hardware. Considering that all signals shall represent a single common clock, individual calibration of each received code is necessary. By removing the apparent biases, a small noise level reduction is achieved.

VI. PASSIVE GROUND STATION DESIGN

A passive configuration only needs to implement a receive path, therefore the ground station is rather simple. Figure 9 depicts the high level view for a design based on software defined radio receivers (SDR) [11]. In this proposal most time- and RF-power critical parts are placed close to the antenna, allowing a very compact installation. Very likely, the outdoor placement makes the equipment susceptible to environmental changes and therefore its sensitivity needs to be characterized in order to be able to dynamically correct for the variable delays during operation. The local time base uses White Rabbit (WR) as an indoor to outdoor distribution. WR allows transparently replicating the local time scale with high enough accuracy and stability at the sampling frontend and thus a ground station calibration can be done by the different equipment manufacturers. This also allows to place the receiving frontend away from the time keeping facility, which in turn assists finding a free line of sight to the, possibly low elevation, satellite. In order to further add to system resiliency, the antenna shall be installed far from other antennas of the same installation, such as GNSS. The indoor part contains a White Rabbit grand master (GM) and a processing unit that does the signal decoding, communication, storage and distribution of the measurements. A typical application will also implement local time base steering.

For use with a pre-calibrated ground station, good knowledge of the position of the antenna phase center is necessary. The installation shall support a rotation invariant position estimate, e.g. using an integrated GNSS receiver.

---

[9] **SA**tellite **T**ime and **R**anging **E**quipment;
disclaimer: Commercial products are identified for the sake of technical clarity. No endorsement by the authors or their institutes is implied.

[10] Transponder configuration does not allow direct measurements between NIST and USNO.

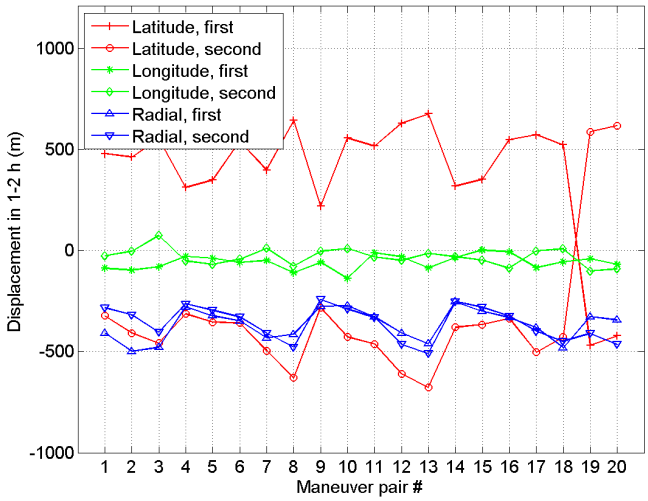

Fig. 1 Example of the 3D satellite displacements during orbit maneuvers, are shown. T11N orbital station keeping normally occurs twice a sidereal day as counter-acting pairs in order to maintain the assigned geo-slot. The pushes are believed to be roughly directed towards the Earth's center resulting into radial and latitude displacements of the satellite. Even though the maneuvers are very brief, orbit determination requires considerable time to recover.

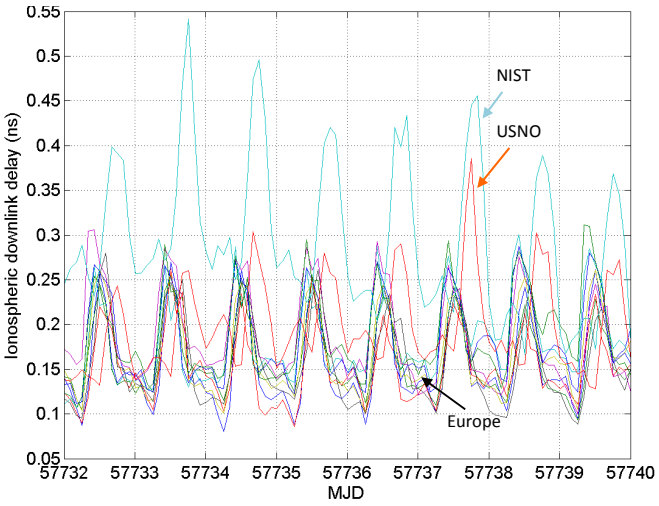

Fig. 2 Estimated slant delays induced by the Ionosphere for the Ku band downlink delays at about 11 GHz for the EU/US network using Telstar 11N are exemplified. The traces are derived using near or co-located GNSS stations. If uncompensated, the worst case differential delay is in the order of half a nanosecond, thus being a significant error source of long East-West baselines.

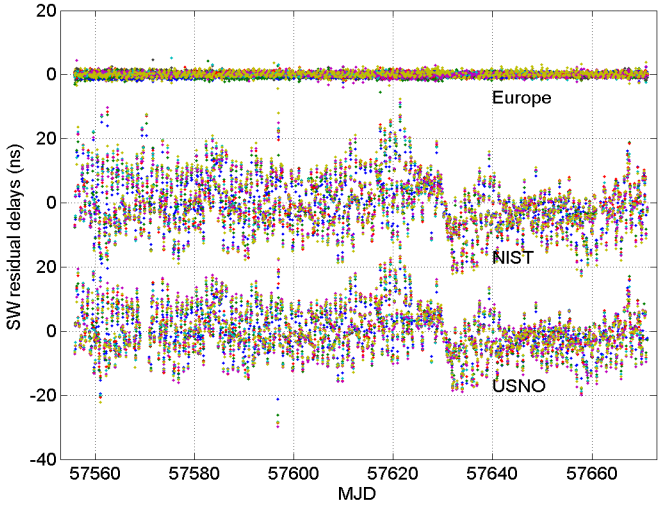

Fig. 3 Orbit determination during about 120 days with orbit maneuvers removed. The plots show residuals of single way measurements in the orbit determination when NIST and USNO are not contributing to the orbit. Colors distinguish pairs of observations. RMS for the European residual is about 3 ns. Diurnals are strong on the European transponder and are visible in the residuals.

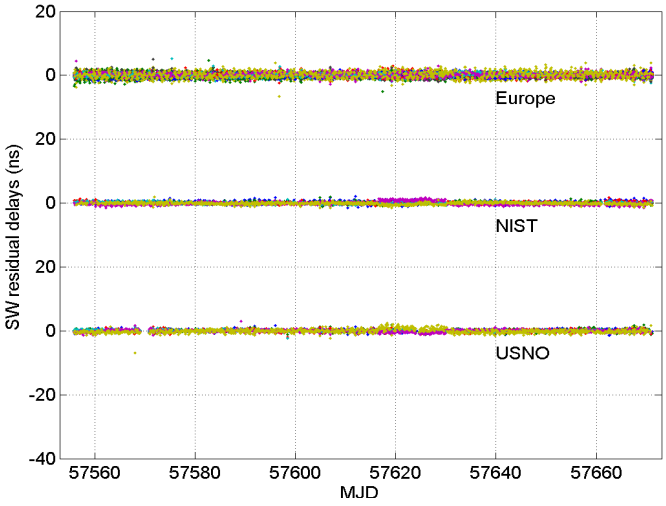

Fig. 4 Residuals of the orbit determination using all data, spanning the same range of epochs as in Figure 3 are shown. The inclusion of NIST and USNO does slightly increase the deviation of the European residuals, but greatly improves the usability of the orbit over the US. Diurnals/noise on the transatlantic transponders is minimal due to few concurrent signals (4/2 to/from the US, compared to up to 14 for the EU/EU transponder) and results in RMS values of about 1.5 ns.

VII. Outlook and Future Work

Hitherto, all data, retrieved from BIPM-ITU publications or collected from the real-time data streams, were post-processed, but treated as captured in real-time. It is planned to use the current set of RT stations of the EU/US network and their respective in-band high-rate return data to test a continuous real-time estimation and evaluation of the satellite orbit, and will subsequently test a passive use within the network. Work on network calibration routines, the use of multichannel SDR measurements [11] for improved orbit determination, and the design and prototyping of a passive ground station are also planned. Furthermore, cause of code dependent biases and their statistics over time will be investigated.

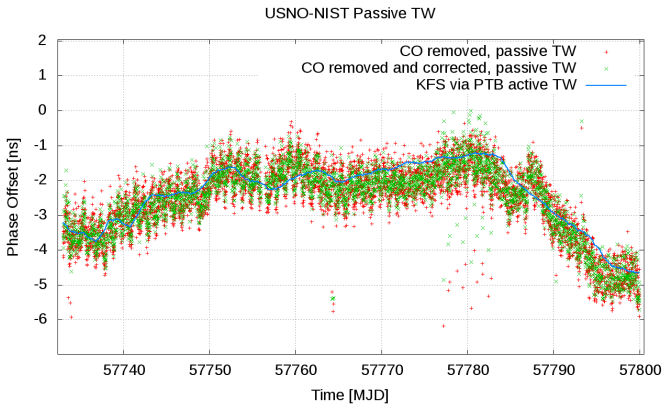

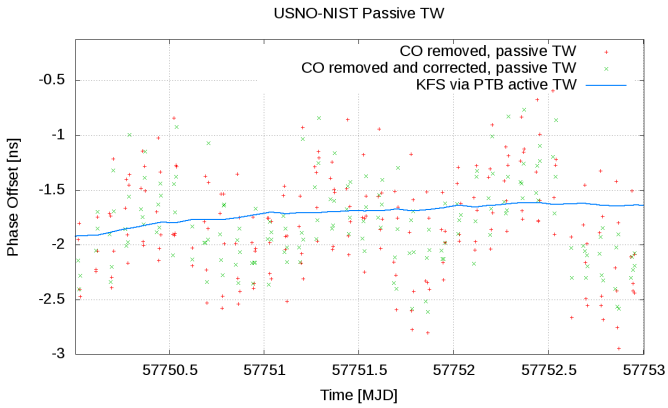

Fig. 5 Results of 68 days of passive TW time transfer on the not directly observable USNO-NIST baseline. The blue trace is the Kalman-filtered difference between USNO-PTB and NIST-PTB of the regular transatlantic active TWSTFT as published at the BIPM. Red dots show the results of the common view difference corrected for atmospheric/tide related delays and the satellite ranges derived from the estimated Kepler orbit. Green dots correct for the code induced bias visible in Figure 6 below. The arbitrary common offset to the active solution is removed. The lower plot shows representative details of the upper plot.

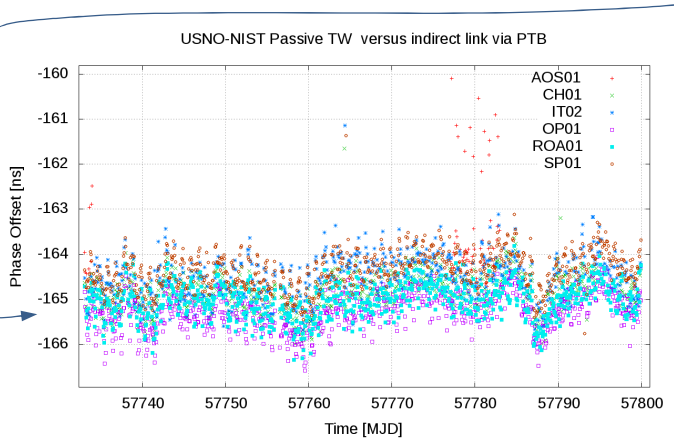

Fig. 6 Difference between active and passive TW corresponding to the time series of Figure 5 are shown. The different colors represent the signal originating stations used in the common view difference. The largest bias, between OP01 and IT02, is in the order of 1 ns.

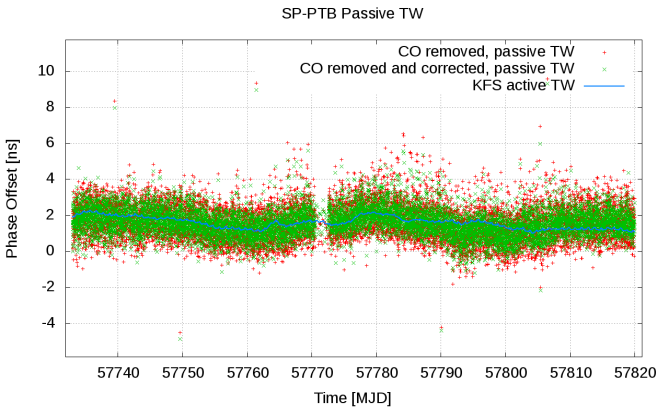

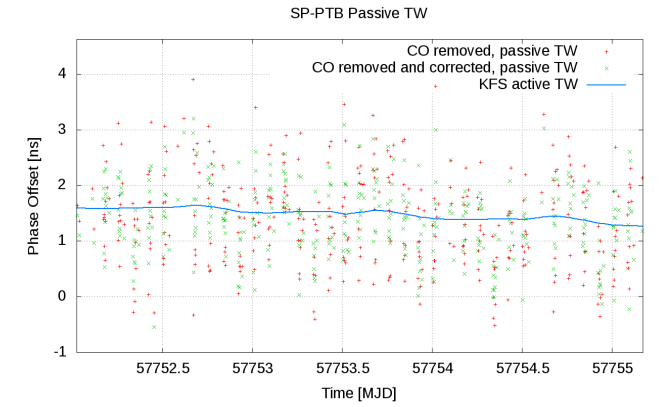

Fig. 7 Similar to Figure 5, results of a passive time transfer between RISE/SP and PTB are show. In this case the difference is directly observable using active TW on the European transponder of T11N. In blue the trace of the Kalman filtered active link is show. In red and green the orignial and bias reduced passive estimate of the RISE/SP-PTB difference. Both are aligned to the filtered reference by removing an arbitrary constant offset, which represents a relative link calibration. Epochs during orbit maneuvors are detected and exluded from the time transfer. The lower plot shows representative details of the upper plot.

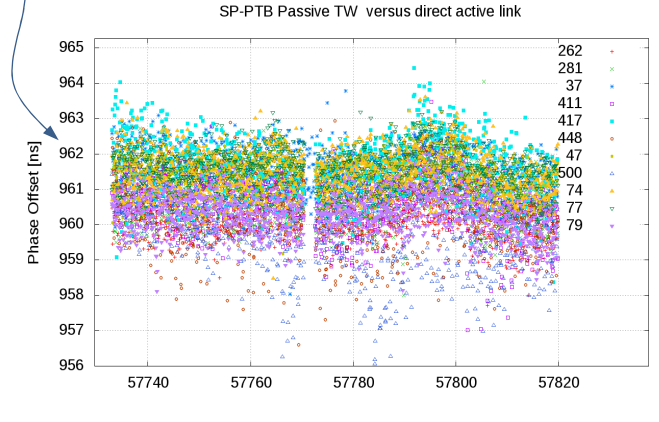

Fig. 8 Difference between active and passive TW corresponding to the time series of Figure 7. The different signal originating modems are color coded and show significant biases, which spread about 5 ns. Their source is of unknow origin, but must be caused by differences in the two ground stations involved.

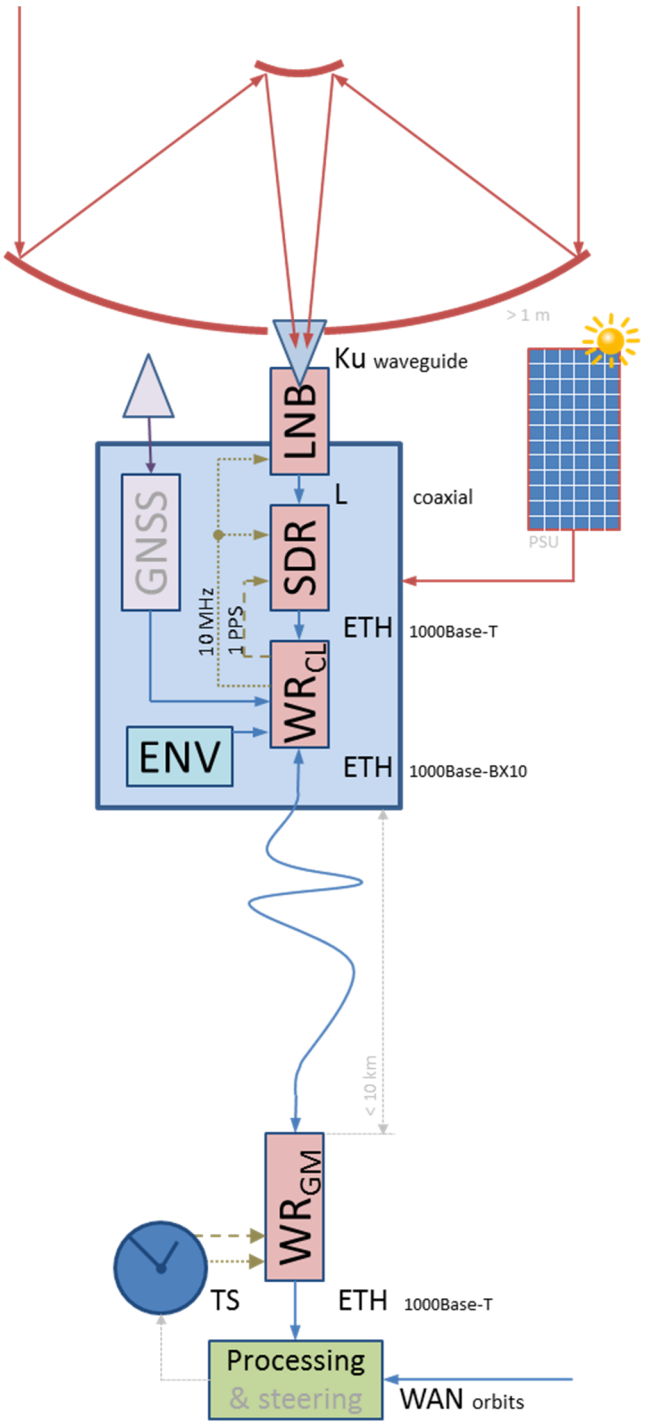

Fig. 9 Overview of a possible passive ground station. A Rx only SDR based implementation allows a compact and flexible design, which consists of an outdoor and indoor installation connected by White Rabbit for communication and transparent distribution of the local time scale. The outdoor unit is preferably solar powered and the optical solution also insures electrical isolation and freedom in where to place the antenna. The indoor unit processes the SDR raw data and combines its results with corrections from the network and common view measurements of other stations. A typical application would also implement a steering loop for its local time scale.

VIII. Conclusions

The paper summarizes the concept, challenges and advantages of a passive use of TWSTFT. As a prerequisite a real-time capable method for orbit determination using regular TW measurements has been developed. Extended Kepler descriptions of the satellite orbit can be used to estimate ranges from the satellite to a passive user at arbitrary station positions and arbitrary epochs. Residual ranges of the position estimates are below 1 m allowing potential time transfer with a few nanoseconds statistical uncertainty (ua). For the PTB-RISE baseline, using the full potential of the European network for orbit determination, we observe typical standard deviations of about 700 ps in bias-removed differences to the filtered active TW link. The paper also suggests a design of a passive ground station based on software defined receivers.
One immediate use of passive TW is to optimize the quality of the metrological time transfer by reducing the number of concurrent transmission, replacing and supplementing some of the active measurements with passive equivalents.

Acknowledgment

Time metrology is a truly international collaboration, so is TWSTFT. We hereby acknowledge the work and contribution of the individuals researching in our area, especially past and present members of the CCTF WG TWSTFT. Special thanks to Victor Zhang of NIST, Dirk Piester of PTB, and Hector Esteban of ROA for their continued support of real-time TWSTFT. Further, we recognise the support of RISE NMI, the IGS for the products applicable to TWSTFT, and the open source community for many of the tools we use.

References

[1] D. Piester et al., ”Time transfer with nanosecond accuracy for the realization of International Atomic Time”, Metrologia 45 (2008) 185–198 doi:10.1088/0026-1394/45/2/008

[2] V.S. Zhang, , T.E. Parker, S. Zhang “A Study on Reducing the Diurnal in the Europe-to-Europe TWSTFT Links.” 2016, 30th European Frequency and Time Forum, 4-7 April, York, United Kingdom.

[3] D. Matsakis, “Characterizing the Diurnal Signature in Two Way Satellite Time Transfer (TWSTT) Data with a Kalman Filter”, PTTI2016

[4] https://www.bipm.org/en/bipm-services/timescales/time-ftp/Circular-T.html#nohref

[5] CELESTRAK derived T11N motion https://www.satellite-calculations.com/Satellite/satellitemotion.php?26/171/0/34111

[6] C.Rieck, P.Jarlemark, K.Jaldehag, “Utilizing TWSTFT in a Passive Configuration”, PTTI2017 Monterey, CA, USA, 2017

[7] GPS Navstar, “GLOBAL POSITIONING SYSTEM STANDARD POSITIONING SERVICE SIGNAL SPECIFICATION”, 2nd edition 1995 https://www.gps.gov/technical/ps/1995-SPS-signal-specification.pdf

[8] ITU-R TF.1153-4, “The operational use of two-way satellite time and frequency transfer employing pseudorandom noise codes”, 2015

[9] A. Martellucci and R. Prieto Cerdeira, "Review of tropospheric, ionospheric and multipath data and models for Global Navigation Satellite Systems", 3rd European Conference on Antennas and Propagation (EuCAP) in 2009, Berlin (Germany).

[10] https://cddis.nasa.gov/Data_and_Derived_Products/GNSS/atmospheric_products.html

[11] V.S. Zhang et al. “A Study on Using the SDR Receiver for the Europe-Europe and Transatlantic TWSTFT Links”, PTTI2017 Monterey, CA, USA, 2017

Multi-GNSS Time Transfer with CGGTTS-V2E

Pascale Defraigne, Katrijn Verhasselt
Royal Observatory of Belgium
Avenue Circulaire, 3
Brussels, Belgium
Contact: p.defraigne@oma.be

***Abstract*—A software tool was developed at the Royal Observatory of Belgium for building the CGGTTS products from the RINEX observation and navigation files provided by the GNSS receivers. This software has been completely re-built in order to increase the robustness, the computation speed, and to include GPS, GLONASS, BeiDou and Galileo. The first part of the paper describes this new software tool. Then some time transfer experiments are realized for a short and a long baseline, comparing the results obtained from single-constellation with the multi-constellation solutions. We show that even with an incomplete constellation, Galileo already provides time transfer results with nearly the same quality as GPS for the short baseline, and 1.5 times better for the long baseline time link. Combining GPS and Galileo satellites furthermore improves the time transfer link with respect to the GPS-only or Galileo-only solutions, reducing the noise by a factor of about 1.4. Adding moreover BeiDou satellites in the combination gives a solution similar to the solution obtained from GPS+Galileo.**

Keywords—GNSS; time transfer;combination

I. INTRODUCTION

The GPS time transfer [1] has been used since the eighties to compare the UTC(k) realizations of timing laboratories in order to generate the International Atomic Time (TAI). The standard code-only analysis and associated format for clock solutions and time transfer is the CGGTTS, for Common GNSS Generic Time Transfer Standard. Its last version, CGGTTS-V2E [2], includes all the constellations presently available, i.e. GPS, GLONASS, BeiDou, Galileo, and QZSS.

While the original GPS time transfer was based on single-frequency results, it was upgraded to the use of dual-frequency receivers measuring the GPS P codes, enabling to remove the ionosphere delays at the first order, and leading to a factor 2 improvement in the precision of the intercontinental time links [3]. Notice that for short baselines, the increase of noise in the ionosphere-free combination with respect to the single-frequency time transfer solution can be larger than the residual ionospheric errors associated with the Klobuchar model or with the IONEX maps; a similar ionospheric delay is indeed suffered by the GNSS signals when they arrive in stations close to each other. However, the timing community prefers using the ionosphere-free combination so that the CGGTTS files can be used easily whatever the distance of the second clock entering into the comparison.

The CGGTTS files can either be produced directly by the receiver or reconstructed from raw measurements and navigation data provided by the receiver in the RINEX (Receiver INdependent EXchange) format, the standard used by the International GNSS Service (IGS), see e.g. http://igscb.jpl.nasa.gov/components/formats.html). To that aim, a software tool named R2CGGTTS and developed at the Royal Observatory of Belgium is made available on the BIPM server (ftp://tai.bipm.org/temp). In its original version [4], only GPS observations were taken into account. An updated version, described in [5], was proposed to include GLONASS observations as well. The inclusion of Galileo [6] and BeiDou [7] required the upgrade to RINEX 3.

The software has now been completely re-built in a version V8, in order to increase the robustness, the computation speed, and to provide clock solutions for all the signals from GPS, GLONASS, BeiDou, and Galileo, supported by the CGGTTS-V2E.

The first part of the paper describes this new software tool. In the second part, some time transfer experiments are realized for short and long baselines, comparing the results obtained from single-constellation with the multi-constellation solutions.

II. R2CGGTTS V8

The main added value of R2CGGTTS V8 is the multi-constellation solution, i.e. supporting GPS, GLONASS, Galileo and BeiDou. In addition, the software structure was completely rebuilt, increasing its processing speed. Additional new features of R2CGGTTS V8 are described here:

- Accepts and detects automatically RINEX 2.xx and RINEX 3.xx formats.
- Provides results for the constellations/signals found in the observation files and for which there are navigation messages.
- Accepts per-constellation or mixed navigation files.
- Does not require any manual information like the MJD in the previous version.
- Provides CGGTTS files for the single-frequency and double frequency combinations in agreement with the CGGTTS-V2E standard.
- Provides in addition 30-second files in a CGGTTS-like format for all the single-frequency codes and ionosphere-free combination (file name CTTS, see Fig. 1.). These files can serve e.g. for calibration purposes.

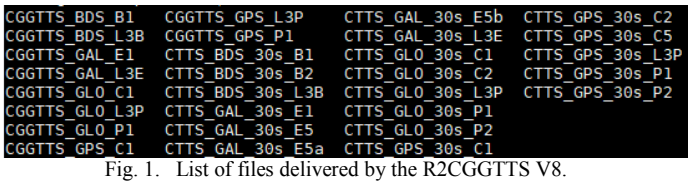

Fig. 1. List of files delivered by the R2CGGTTS V8.

Some slight changes between the Galileo results obtained by previous version of the R2CGGTTS (V7) can exist due to the updated choice of the ephemeris data set among the RINEX navigation file. The new procedure has been based on the Galileo Open Services/Service Definition Document [8]. It is however very important that in a common-view software a test is made on the Index of Ephemeris (column IOE), and to use common view data of a satellite track only if the clock solutions in both stations are based on the same IOE; this statement is valid for each of the 4 constellations.

III. TIME TRANSFER WITH DIFFERENT CONSTELLATIONS

This section presents the current performances of time transfer based on the CGGTTS-V2E standard with the different constellations and with their combination. A one month period is chosen for the tests (February 2018). Two different time links are investigated here: ORB-PTB (450 km) and ORB-MGUE (12400 km). MGUE is located in Argentina, it is an IGS station equipped with a stable H-maser but is not a realization of UTC. A linear drift computed over the whole period is removed from the MGUE solutions but this does not affect the conclusions of our study.

Only GPS, Galileo and BeiDou are investigated here. GLONASS time transfer requires a dedicated treatment in order to solve for the inter-satellite biases due to the different hardware delays associated with the different carrier frequencies used by the each of the satellites. A deep analysis of GLONASS time transfer and its combination with GPS is proposed in [5]. To date (March 2018), the GPS constellation is considered as complete, with 31 satellites in Medium Earth Orbits (MEO), while Galileo and BeiDou are partially developed, with 16 usable satellites for Galileo in MEO, and 15 usable satellites for BeiDou, of which 6 are in Geostationary orbits (GEO), 6 are in Inclined Geosynchronous orbits (IGSO), and 3 are in MEO.

Only MEO and IGSO satellites are used here for the BeiDou constellation. It was shown indeed in [7] that the noise of the GEO satellite is significantly larger than the noise of the signals generated by MEO and IGSO satellites. In addition, all the BeiDou CGGTTS results have been corrected for the elevation-dependent biases using the empirically determined values provided in [9]. MGUE is located in South America, no IGSO satellite is therefore visible from there which reduces considerably the number of BeiDou observations.

The GNSS calibration in the TAI network currently only concerns the GPS signals [11]. Galileo calibration has been proposed in [12] based on GPS signals and ionosphere measurements from dual-frequency signals. This calibration is for each station separately, no relative calibration campaign has been organized to date as for GPS. BeiDou calibration is only starting in some preliminary experiments. The stations at ORB and PTB have been calibrated for GPS as Group2 and Group1 stations in the TAI network. The method described in [12] was then applied to determine the hardware delays of Galileo signals for both BRUX and PT09. We have presently no calibration for BeiDou signals. We therefore removed an empirical bias to the time links based on BeiDou in order to make the comparison easier.

A. *Separate solution per constellation*

Fig. 2 (resp. Fig. 3) presents the time transfer solutions obtained and Allan deviations for ORB-PTB (resp. ORB-MGUE) using either the broadcast satellite clocks and orbits, or the combined products provided in the frame of the Multi-GNSS-Experiment (MGEX) [13] by the analysis center COD from the IGS. In each case the CV and AV solutions are computed using a cleaning of outliers similar as proposed in [14] as well as an elevation-dependent weighting. Furthermore, as there are gaps in the BeiDou solutions the Allan deviations has been computed using the appropriate method described in [10].

Due to the large uncertainties in the GPS broadcast satellite orbits and clocks, it was shown in [15] that the AV solution should be used only with precise satellite orbits and clocks. Considering the possible better accuracy of the broadcast satellite products of the new constellations, we also consider here the AV solutions even with broadcast satellite clocks and orbits, for each constellation separately.

From the time links presented in Fig. 2 and Fig. 3 from the different constellations separately, we can confirm the results of [7], i.e. a larger noise for BeiDou time transfer than for GPS and Galileo, whatever the satellite products used, broadcast or MGEX. We also observe that even with an incomplete constellation, Galileo already provides time transfer results with the same quality as GPS, or even better in the long baseline time link.

The solutions for ORB-PTB obtained in CV, AV, with broadcast or MGEX products are all very similar, for all the constellations. In this short baseline, as the satellites in view of both stations are nearly the same all the time, the errors on satellite orbits or clocks are the same and cancel out in the differences.

For the long baseline ORB-MGUE, the AV is better than the CV solutions, both with the MGEX and broadcast products. The main reason is that the number of satellites in common view is very small, as seen in Table I. This Table presents the number of satellite tracks from the CGGTTS file available for each constellation in a typical daily solution of BRUX and MGUE (these are therefore the satellites used in the AV solutions), as well as the number of satellites in the CV solutions ORB-PTB and ORB-MGUE. The values are based on February 16, 2018. As mentioned previously, the location of MGUE does not allow to see BeiDou satellites others than MEOs which explains the low number of BDS observations for this station.

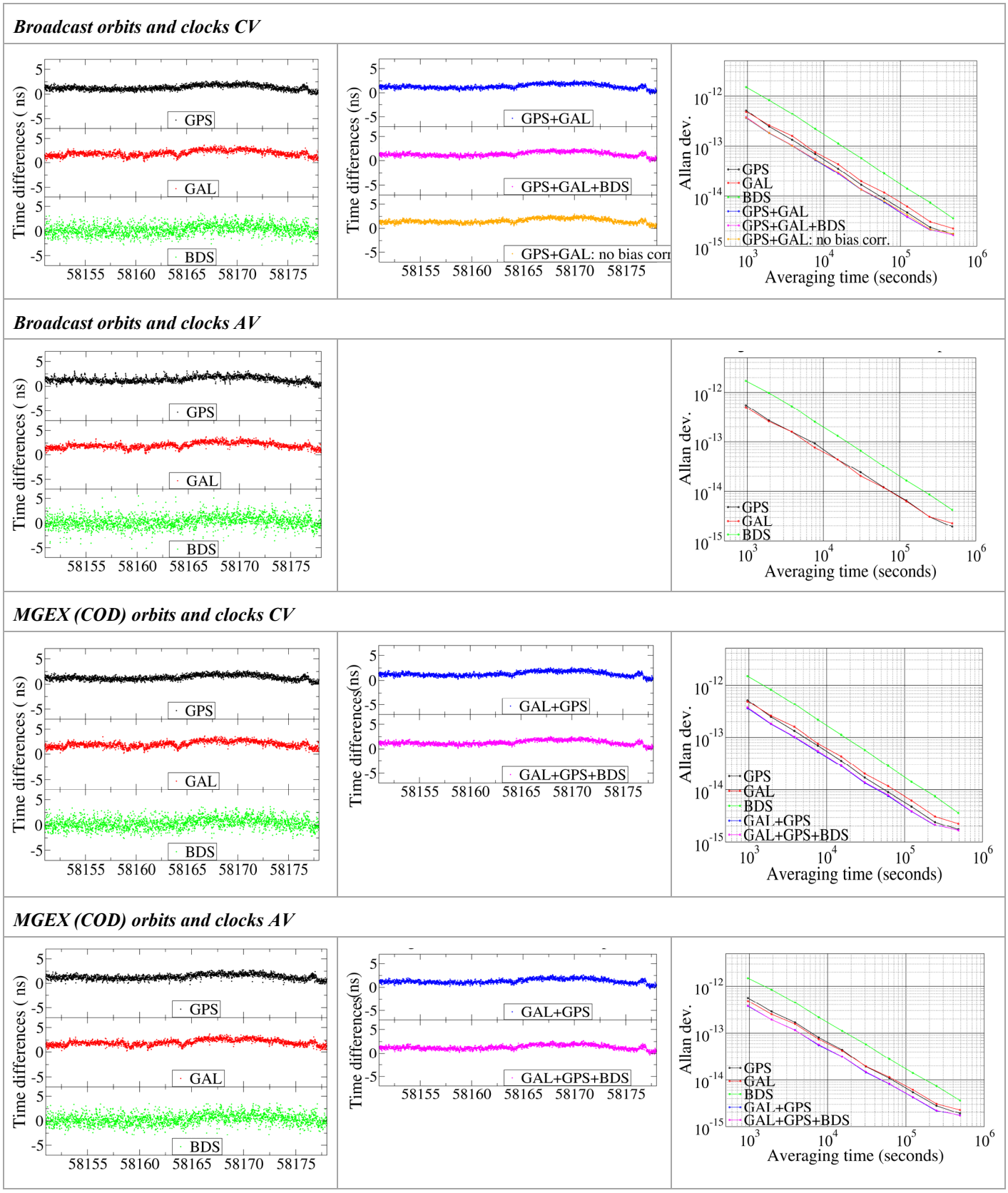

Fig. 2. UTC(PTB)-UTC(ORB) using the receivers BRUX and PT09 and different CGGTTS results.

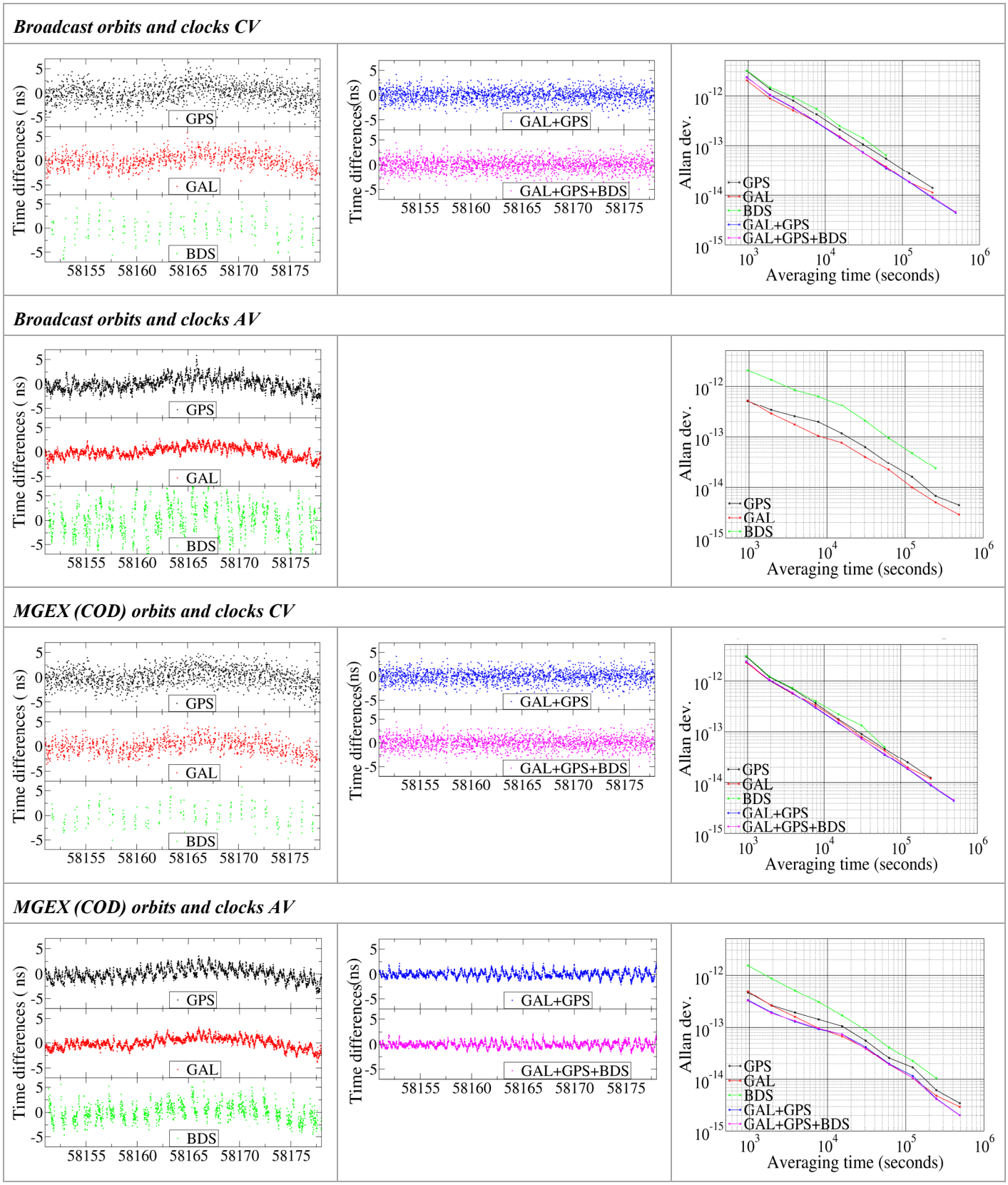

Fig. 3. Hmaser(MGUE)-UTC(ORB) using the receivers BRUX and MGUE and different CGGTTS results.

For this long baseline ORB-MGUE, we can also observe that the AV solution obtained with Galileo is better than the solution obtained with GPS Satellites, even with the incomplete Galileo constellation. We get, for an averaging time of 1 day, an improvement of about a factor 1.5 when using Galileo rather than GPS, both when using broadcast products and when using MGEX products.

B. Combining satellite from different constellations

We propose here to combine the different constellations at the level of the observations. The solution at each epoch is therefore obtained from the weighted average of all the satellites in view for All in View (AV) solutions or all the satellites in common view for the Common View (CV) solutions. Due to the possible differences in the reference time scale of the different constellations, a specific procedure has to be adopted, and this one differs depending on the approach, CV or AV.

Common View

The CV of all the constellations can be combined directly as no reference time scale is present in these quantities. The signals from the different constellations must however all be calibrated.

As explained before, only the stations BRUX and PT09 have been calibrated, and only for GPS and Galileo signals. For this reason, the only single CV combination that can be tested here is a combination of GPS+Galileo for the link ORB-PTB.

However if the signals of the different constellations are not calibrated, or even if they are calibrated separately, there can be a disagreement between these calibrations which can introduce noise in the combined solution. For this reason, an alternative is to use the GPS calibration and to determine inter-system biases. This approach consists in using only the calibration of GPS signals. The bias between the Galileo/BeiDou and GPS solutions is first determined, then applied on the CGGTTS results and the CV combined solution is finally computed with these adjusted results. This is therefore a three-step procedure. For the CV combination it reads:

1. Determine the biases KGal and KBDS
   $$Kx=\langle(UTC(k)-UTC(j))_x\rangle - \langle(UTC(k)-UTC(j))_{GPS_calibrated}\rangle$$
   Where x is for Gal or BDS and < > means averaging.
2. Correct the Galileo and BeiDou CGGTTS files:
   CGGTTS'(Gal) = CGGTTS(Gal) – KGAL
   CGGTTS'(BDS) = CGGTTS(BDS) – KBDS
3. Compute the CV solutions combining satellite track solutions from CGGTTS(GPS), CGGTTS'(Gal) and CGGTTS'(BDS).

All in View

When combining multi-GNSS in an AV, the reference time scale of all the satellites must be the same. Combination of satellites from different constellations in AV can therefore not be applied with CGGTTS results based on broadcast products. The reference in this case in indeed GPS Time (GPST) for GPS satellites, Galileo System Time (GST) for Galileo satellites and BeiDou Time (BDT) for BeiDou satellites. In the present study, we use the MGEX products described in the previous section, and in which the satellite clocks from all constellations are referred to a same reference. However it is only the same reference frequency; there is a bias between the reference as computed from the different constellations. This is illustrated in Fig. 4 presenting the CGGTTS results UTC(ORB)–ref(MGEX) obtained with GPS, Galileo, and BeiDou satellites. We clearly observe the biases just mentioned. These biases are inherent to the MGEX clock products as some station inter-system biases have to be fixed to get rid of the degree of freedom in the computation. As a consequence, in order to combine in an AV solution the satellites from different constellations it is first necessary to determine the inter-system bias. This one accounts for both the inter-system bias in the MGEX clock products and the inter-system bias of the local station (or disagreement between the station calibration for the different systems). The same 3-steps procedure as explained before for the CV combination can be applied, only the first step is different: KGal and KBDS are here computed as

$$Kx=\langle(UTC(k)-ref)_x - (UTC(k)-ref)_{GPS,calibrated}\rangle$$

where $\langle(UTC(k)-ref)_x$ corresponds to the CGGTTS solution (column REFSYS) obtained for satellites from the constellation x with the MGEX products.

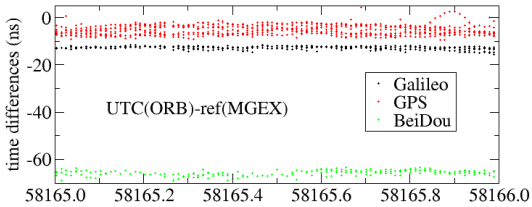

Fig. 4. UTC(ORB)-ref(MGEX) obtained as CGGTTS results using the combined MGEX satellite orbits and clock products.

Analysis of the result

In addition to the time links based on separate constellations, Fig. 2 (resp. Fig. 3) also presents the time transfer solutions and Allan deviations obtained for ORB-PTB (resp. ORB-MGUE) using the combinations GPS+Galileo and GPS+Galileo+GPS. Both solutions based on the broadcast and the MGEX satellite clocks and orbits are presented. In each case, we provide the CV and AV solutions using the same cleaning procedure and elevation-dependent weighting as for the separate solutions.

The results presented in Fig. 2 and Fig. 3 show that in all cases, combining GPS and Galileo satellites improves the time transfer link with respect to the GPS-only or Galileo-only solutions, reducing the noise by about a factor 1.4. Adding moreover BeiDou satellites in the combination does not improve and does not degrade the solution. The gain obtained by the increased number of satellites is counter-

balanced by the larger noise of the BeiDou data. In order to look at the exact contribution of the Galileo and BDS satellites in the combination, Table I also presents the number of satellites in the combined solutions. Note that the number for Galileo+GPS+BeiDou is not always the sum of the three separate numbers due to the cleaning procedure.

Galileo is already providing more than 50% of additional tracks than GPS. The total number of satellites in a combined AV time transfer is double with respect to GPS alone. This is in agreement with the improvement of the noise by a factor of about 1.4 as seen in the Allan deviation plots. However for the long baseline, we can see that even when combining the three constellations, the number of satellites in Common View is still insufficient to get a solution of the same quality as the AV solution.

TABLE I. NUMBER OF SATELLITE TRACKS ON FEB. 16, 2018

	AV		CV	
	BRUX	**MGUE**	**ORB-PTB**	**ORB-MGUE**
GPS	769	761	715	77
Galileo	431	435	405	40
BeiDou	211	89	205	9
Galileo+GPS+BeiDou	1408	1284	1320	125

Two types of combination GPS+Galileo are proposed in Fig. 2 for the link PTB-ORB. One is based on a direct averaging of the calibrated Galileo and GPS CGGTTS results (orange curve), and the other one is first determining a bias between the Galileo and the GPS results before making the combination (blue curve). The difference between both is here not significant because the receivers BRUX and PT09 have both been calibrated for Galileo in the same way, i.e. from their GPS calibration using the ionospheric measurements and the satellite groups delays from GPS and Galileo.

IV. CONCLUSION

This paper presented the new version of the R2CGGTTS V8, to be distributed to the time laboratories for their participation to the realization of the Universal Time Coordinated (UTC) using GNSS time transfer from GPS, Galileo, BeiDou and GLONASS. We then presented the time transfer results for one short baseline (400 km) and one long baseline (12000 km), based on either separate constellations, or on the combination of CGGTTS results from GPS, Galileo and BeiDou. The results show a larger noise for BeiDou time transfer than for GPS and Galileo, whatever the satellite products used, broadcast or reprocessed (MGEX). We also observe that even with an incomplete constellation, Galileo already provides time transfer results with the same quality as GPS for the short baseline and the short term. For longer term, the solution is affected by periods where no satellite at high elevation is available. For long baseline, Galileo provides time transfer results 1.5 times better than GPS.

For the combination we proposed an approach which allows to compensate for the biases between the signals of the different constellations due to the different hardware delays. With this technique, we showed that combining GPS and Galileo satellites improves the time transfer link with respect to the GPS-only or Galileo-only solutions, reducing the noise by a factor of about 1.4. Adding moreover BeiDou satellites in the combination does not improve and does not degrade the solution.

ACKNOWLEDGMENT

Part of this work was realized in the frame of a grant provided by the Laboratoire National et d'Essais (LNE), Paris, France. The COD analysis center of the IGS is acknowledged for providing multi-GNSS satellite clocks and orbits. We also thank the PTB for the availability of their data.

REFERENCES

[1] Allan, D.W., Weiss, M., "Accurate time and frequency transfer during common-view of a GPS satellite", Proc. 1980 IEEE Freq. Contr. Symp., Philadelphia, PA, pp. 334-356, 1980.

[2] P. Defraigne and G. Petit, CGGTTS-Version 2E: an extended standard for GNSS Time Transfer, Metrologia 52 (6), G1, 2015.

[3] P. Defraigne P and G. Petit, "Time transfer to TAI using geodetic receivers," Metrologia, vol. 40, no. 4, pp. 184-188, Jun. 2003.

[4] P. Defraigne, G. Petit and, C Bruyninx, "Use of geodetic receivers for TAI," presented at the 33rd annual Precise Time and Time Interval, Long Beach, CA, 2001

[5] A. Harmegnies, P. Defraigne, G. Petit, "Combining GPS and GLONASS in All in View for time transfer", Metrologia, vol. 50, no. 3, pp. 277–287, May, 2013

[6] P. Defraigne, W. Aerts, G. Cerretto, G. Signorile, E. Cantoni, I. Sesia, P. Tavella, J.M. Sleewaegen, A. Cernigliaro, A. Samperi, "Advances on the use of Galileo signals in time metrology: calibrated time transfer and estimation of UTC and GGTO using a combined commercial GPS-Galileo receiver", in Proc. of the Precise Time and Time Interval Systems and Applications, Bellevue, WA, 3-5 December, 2013.

[7] W. Huang and P. Defraigne, CGGTTS Results with BeiDou Using the R2CGGTTS, IEEE transactions on ultrasonics, ferroelectrics, and frequency control, vol. 63 (7), pp. 1005-1012, 2016. DOI: 10.1109/TUFFC.2016.2517818

[8] https://www.gsc-europa.eu/system/files/galileo_documents/Galileo-OS-SDD.pdf

[9] L. Wanninger, S. Beer. "BeiDou satellite-induced code pseudorange variations: diagnosis and therapy," GPS Solut., 19(4), pp. 639-648, Nov. 2014.

[10] I. Sesia, P. Tavella, (2008, Dec.). Estimating the Allan variance in the presence of long periods of missing data and outliers. Metrologia 45, pp. s134-s142

[11] Bureau International des Poids et Mesures, "BIPM guidelines for GNSS calibration", v3.2, 15/02/2016

[12] P. Defraigne, W. Aerts, G. Cerretto E. Cantoni and J.-M. Sleewaegen, Calibration of Galileo signals for time metrology, *IEEE UFFC*, 12/2014 61(12):1967-75

[13] G.D. Rovera, B. Chupin, M. Abgrall and P. Uhrich, "A simple computation technique for improving the short term stability and the robustness of GPS TAIP3 Common-Views", Proc. of the 26th EFTF, Pragues, Czech Republic, 2013.

[14] O. Montenbruck, P. Steigenberger, R. Khachikyan, G. Weber, R.B. Langley, L. Mervart, U. Hugentobler, "IGS-MGEX: Preparing the Ground for Multi-Constellation GNSS Science," InsideGNSS 9(1):pp. 42-49, Feb. 2014

[15] M. Weiss, G. Petit and Z. Jiang, "A Comparison of GPS Common-View Time Transfer to All-in-View," Proc. Joint. IEEE IFCS and PTTI Mtg., Vancouver, BC, Canada, 2005.

Galileo and GNSS Time Offsets

Giovanna Signorile[1], Ilaria Sesia[1], Tung Thanh Thai[1], Pascale Defraigne[2], Patrizia Tavella [1,3]
[1]Istituto Nazionale di Ricerca Metrologica, INRIM, Turin, Italy
[2]Royal Observatory of Belgium, ORB, Brussels, Belgium
[3]Bureau International des Poids et Mesures, BIPM, Sevres, France - since November 2017
Email: {g.signorile,i.sesia,t.thai}@inrim.it, p.defraigne@oma.be, patrizia.tavella@bipm.org

***Abstract*—Galileo disseminates the GPS to Galileo Time Offset (GGTO) through the navigation message. This broadcast offset allows the user of a combined GSP/Galileo receiver to achieve a unique navigation solution by using measurements from both GPS and Galileo satellites. Nowadays, many positioning systems are available, the topic of interoperability is therefore crucial. The time offsets between the different systems should therefore be made available to the multi-GNSS users. An alternative would be that each constellation broadcasts only the time offset between its time scale and a reference common to all GNSS. In this paper we propose two alternative for, for this reference: either it can be based on the combination of the different GNSS time scales , or it can be directly UTC, as predicted and broadcast by the different systems. This paper presents a first assessment of the performances that can be achieved with each of these two approaches.**

Keywords—GNSS, GGTO, Galileo, GPS, timescale, interoperability

I. INTRODUCTION

The US Global Positioning System (GPS) and European Galileo are two examples of Global Navigation Satellite Systems (GNSS). Galileo is currently disseminating the GPS to Galileo Time Offset (GGTO) through its navigation message, enabling users equipped with a combined GPS/Galileo receiver to achieve Position, Velocity and Time (PVT) solution using measurements from both systems together, improving in this way the final positioning accuracy [1]. However, as other GNSSs are available, the time offsets between all the different systems should be available to users in the multi-GNSS scenario, e.g. GPS to GLONASS, GPS to BDS (BeiDou Navigation Satellite System) etc. Alternatively, the users have to estimate these time offsets between different systems by themselves adding unknowns to their PVT equation set.

Broadcasting the time offsets with respect to all other systems would impose a high level of complexity and would require significant changes to the GNSS providers. On the other hand, the user cannot estimate the time offsets XYTO unless they have enough usable satellites in view to solve the enlarged equation set. This can be a limitation in urban environment, precisely where the benefit of a multi-constellation is noticeable.

Thinking to such, constraints it was recently proposed at the 2017 annual meeting of the International Committee on Global Navigation Satellite Systems (ICG) [2] that each GNSS system can broadcast only the time offset between its own time scale (GNSST) and a reference common to all GNSS. This paper proposes two candidates for this common reference and presents a first assessment of the performances that can be achieved with each of these two approaches.

II. TWO POSSIBLE APPROACHES INVESTIGATED

Following such discussions and recommendation [3] we investigated two possible methods of achieving this point. For the first one the common reference is chosen as a combination of the different GNSS time scales. For the second one, the common reference is the already broadcast information on the offset of GNSST with respect to the international timing reference UTC [4][5][6][7].

In the first case, each GNSS would broadcast the difference between its GNSST and the average of different systems ($GNSST_{mean}$), namely $GNSST-GNSST_{mean}$, determined by making use of calibrated multi-GNSS receivers owned by the system providers. In the second case instead, the user could use directly the GNSST−UTC predictions currently broadcast by each system and already available in the different GNSS navigation messages.

We analyzed 4 months of data from November 2017 to February 2018 to understand the viability of these two possible approaches. For the first case (based on $GNSST_{mean}$), CGGTTS v2E [8][9] files from a multi-GNSS receiver connected to UTC(ORB) were used. Such files contain the difference between the local clock (UTC(ORB) in our case) and the GNSS time scales for GPS, Galileo, GLONASS and BDS. For the second case, we used the GNSST-UTC predictions from the RINEX navigation files collected from INRIM multi-GNSS receiver (for GPS and Galileo) and from an IGS station in Hongkong, HKWS (for BDS and GLONASS). Results obtained are presented and discussed in the following sections.

III. DIFFERENTIAL CALIBRATION OF BRUX RECEIVER FOR GLONASS AND BDS

Since we are interested in timing, all the analysis should be carried out with calibrated measurements. The ORB station used is BRUX, equipped with a timing multi-GNSS receiver capable of measuring pseudoranges from satellites of GPS, Galileo, GLONASS and BDS. It was calibrated for GPS following BIPM guidelines [10] under calibration ID 1018-2017, and for Galileo signals using the procedure described in [11]. For the goal of the current study, an estimation of the calibration of BRUX for GLONASS and BeiDou signals has

been carried out. Our calibration procedures and results are presented here below as preparatory step.

1) Calibration for GLONASS signals

From the ftp server of BIPM [12], we can retrieve UTC−UTC(ORB) and UTC−GLONASST. The difference of these quantities yields $[UTC(ORB)-GLONASST]_{BIPM}$. At the same time, CGGTTS files from BRUX contain the information $[UTC(ORB)-GLONASST]_{SIS}$ for each GLONASS satellite, but uncalibrated. Taking into account the fact that GLONASS uses FDMA (Frequency Division Multi Access) inducing inter-frequency biases, calibration values are obtained per satellite by comparing the quantity UTC(ORB)−GLONASST from BIPM data and from BRUX data for the same period. The calibration results so-obtained are then applied to the CGGTTS files for GLONASS. The calibrated CGGTTS results are presented in Fig. 1 together with the values determined from BIPM Circular T.

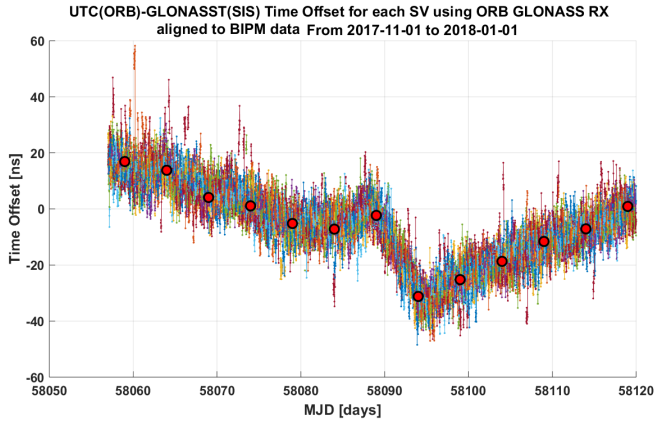

Fig. 1. Calibrated UTC(ORB)−GLONASST. *(In red circles the quantity as obtained using BIPM data; in multi-colored dots the quantity as obtained by BRUX receiver for each GLONASS satellite after calibration.)*

2) Calibration for BDS signal

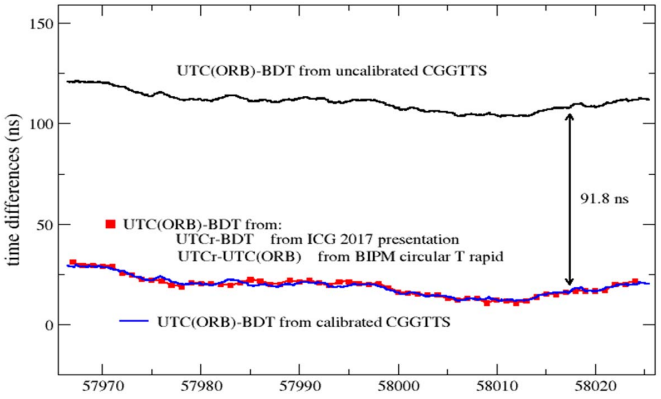

Fig. 2. Calibrated UTC(ORB)−BDT.

A similar approach is used to calibrate BDS signal for BRUX. While it is possible to obtain the difference between GLONASST and UTC as published by BIPM, such quantity for BDT (BDS Time) is not yet published by BIPM. We turned instead to data presented in [13] which reported $[UTCr-BDT]_{ICG_2017}$. Combining with BIPM data $[UTCr-UTC(ORB)]_{BIPM}$ of the same period we obtain UTC(ORB)−BDT as reference to calibrate BRUX for BeiDou signals (Fig. 2).

IV. CASE 1: XYTO VIA $GNSST_{mean}$

In this approach we consider that each system can broadcast a prediction of the time offset between its time scale GNSST and the average of the four GNSS time scales, namely $GNSST_{mean}$.

At the system level, each provider can determine the time offset using a calibrated multi-GNSS receiver connected to a clock K:

$$(K- GNSST_{mean})=<K- GNSST_i>$$

$$GNSST_X-GNSST_{mean}=(K- GNSST_{mean})- (K- GNSST_X)$$

where <> means averaging. This quantity $GNSST_X-GNSST_{mean}$ must then be predicted and broadcast to the users.

At user level, when the user wants to combine observations from systems X and Y, the XYTO can be obtained by taking the difference of the quantity broadcast by systems X and Y:

$$(GNSST_X - GNSST_{mean}) - (GNSST_Y - GNSST_{mean}) =$$

$$GNSST_X - GNSST_Y = XYTO \qquad (1)$$

In order to simulate what the user could experience in this situation, we use measurements $UTC(ORB)-GNSST_i$ contained in the calibrated files CGGTTS v2E from the station BRUX, where $GNSST_i$ is the reference time scale of each different GNSS.

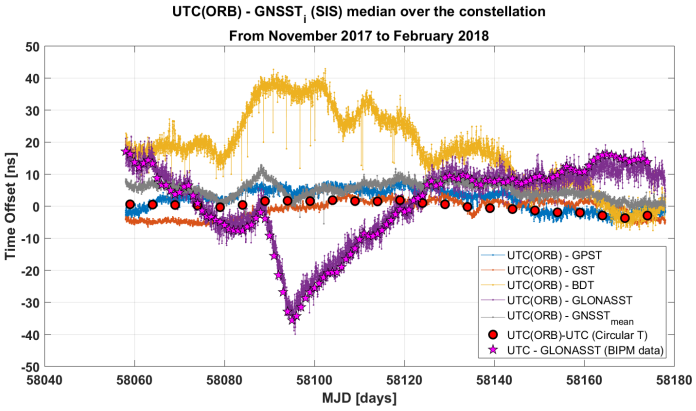

Fig. 3. Time offset between UTC(ORB) and each time scale of each GNSS and the mean time scale, along with reference BIPM data.

These quantities are shown in Fig. 3, using for each epoch and for each constellation the median of the satellite results. By making the average per epoch of the four solutions $UTC(ORB)-GNSST_i$ (with i for GPS, Galileo, BDS and GLONASS), we obtain $UTC(ORB)-GNSST_{mean}$ in grey. It is visible from the plot that during this period some GNSS time scales present some instability, which is then embedded in the mean. The contribution of UTC(ORB) can be ruled out, as its

stable and accurate behavior can be seen from UTC(ORB)–UTC as reported in BIPM's Circular T (red circles). A further confirmation is the behavior of GLONASS time scale with respect to UTC as published by BIPM (purple stars) that closely follows the evolution of UTC(ORB)–GLONASST as obtained through multi GNSS receiver.

By using UTC(ORB) as a pivot it is possible to calculate the difference between each GNSS time scale and the mean time scale as mentioned in (1) as follow:

$$GNSST_{mean} - GNSST_i = (UTC(ORB) - GNSST_i) - (UTC(ORB) - GNSST_{mean}) \quad (2)$$

However, this information once determined, cannot be communicated in real-time to the users, as it is the case for any timing information broadcast by GNSS nowadays. Only a prediction can be broadcast. We then propose a simple prediction scheme that can be applied to $GNSST_{mean} - GNSST_i$: the value to be applied at any given time is the mean of measurements of the day before. With this rule, it is possible to determine the quality of the XYTO determined by the user.

In this paper, we only investigate the GPS to Galileo Time Offset and concentrate the analysis on the second half of the period analyzed above (January and February 2018), noting that the various GNSS time scales are more stable with respect to November and December 2017. We compare in Fig. 4 what the user could obtain by using only the pseudorange measurements (SIS, in blue), with what was broadcast by Galileo (BRDC, in red) and with what the user can obtain via the $GNSST_{mean}$ prediction (in black) assuming both GPS and Galileo transmit a prediction of their own time scale with respect to the GNSSmean. A good agreement can be observed between GGTO (SIS) and GGTO via prediction of $GNSST_{mean}$. The rms of the difference between the two is at the nanosecond level. It has to be noted that such results correspond to an optimistic case because in this analysis the same receiver is used at system level (to compute GNSSmean) and at user level (to combining the different XYTO). Moreover, we are assuming that both systems are using the same algorithm to compute and predict $GNSST_{mean}$.

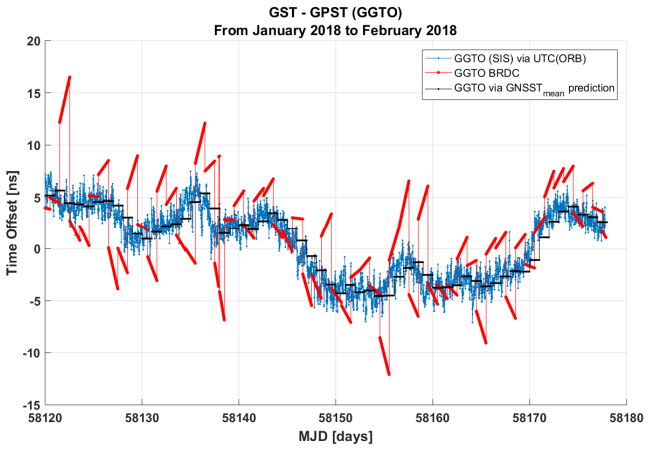

Fig. 4. GGTO using receiver measurements, broadcast values by Galileo and via prediction of $GNSST_{mean}$.

V. Case 2: XYTO via GNSST–UTC predictions

With the previous case, each GNSS would still have to apply some modification to its own system implementation to accommodate such $GNSST_{mean}$ value to be broadcast. An alternative is proposed here, which would not impose any change to the system providers. It consists in using UTC as reference common to all the systems. Indeed each system broadcast a prediction of the offset between its time scale and UTC. If these predictions are accurate enough, the user can use them as a common reference to determine the offsets between the different GNSS time scales. Let us look at this solution in more details.

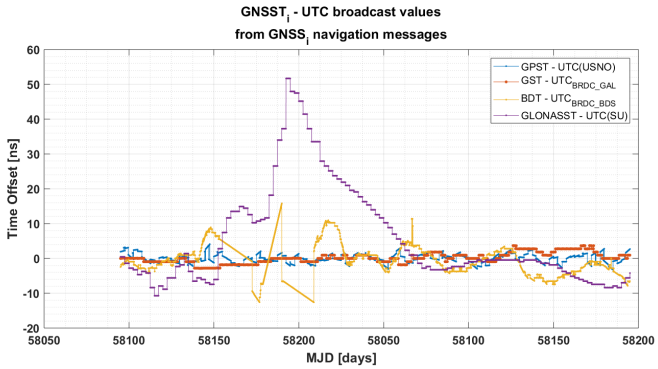

Fig. 5. GNSST–UTC predictions as broadcast in each GNSS' navigation message.

We report in Fig. 5 the broadcast GNSST-UTC for the entire 4-month period and for the four constellations. Each system has their own implementation to determine this prediction. The first difference is the actual UTC referenced by each system, i.e. GPS broadcasts GPST–UTC(USNO), GLONASS broadcasts GLONASST–UTC(SU), for Galileo it is GST–UTC_{BRDC_GAL} and for Beidou BDT–UTC_{BRDC_BDS}. Then each system also uses different prediction algorithms to calculate the broadcast values. Therefore, the GNSST–UTC predicted value is not strictly equivalent between each system. Nevertheless, if the predictions are good enough, the GNSST–UTC broadcast can be considered equivalent to a certain extent.

Like in (IV), we focus on the second half of the period for estimating XYTO via prediction of GNSST–UTC:

$$[GNSST_X - UTC]_{BRDC} - [GNSST_Y - \mathrm{UTC}]_{BRDC} = XYTO \quad (3)$$

For the GPS to Galileo Time Offset (GGTO), that means:

$$[GST - UTC]_{BRDC} - [GPST - \mathrm{UTC}]_{BRDC} = GGTO \quad (4)$$

Fig. 6 shows in green the quantity GGTO obtained using this method, in addition to the information reported in Fig. 4.

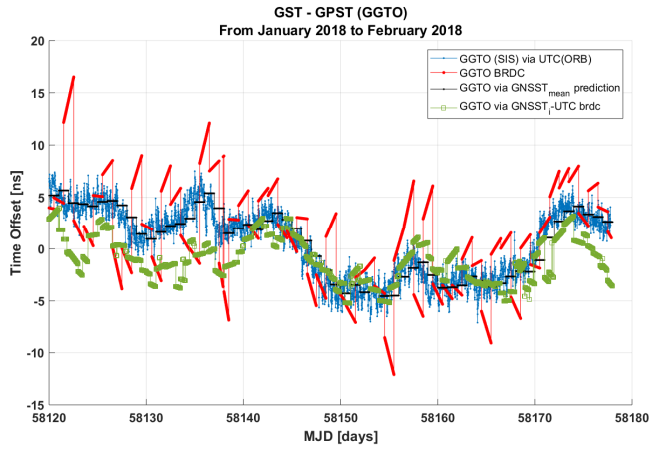

Fig. 6. GST – GNSST via GNSST – UTC predictions

VI. Comparison of the Two Cases

From Fig. 6 it can be observed that for the period considered, the GGTO values in the first case are in agreement at nanosecond level with the GGTO observed at user level, while in the second case, the differences are a bit larger but with a maximum of 5 ns. This is due to the differences in the GNSST–UTC predictions by Galileo and GPS. Of course, the better the GNSST–UTC predictions, the better the performances of this second approach.

Whether case 1 or case 2 is applied, users would benefit from the multi-GNSS scenario where they can solve the PVT equations with contribution of many satellites of different constellations.

In case 1, each GNSS would have to estimate $GNSST_{mean}$ and transmit information in its navigation message, which means some changes would need to be made in the navigation message structure to accommodate such value. Furthermore, similar to case 2, each system could choose different methods of estimating this quantity and thus cause a small discrepancy between them. Many other factors could also contribute to the uncertainty at user level, e.g. different instruments at each system or different physical locations of receivers creating different view of the constellations.

However, using $GNSST_{mean}$ would have the advantage that only one difference has to be broadcast by each GNSS, instead of all the different XYTO (as currently foreseen by some of the systems, e.g BDS [6]).

On the other hand, if using directly the GNSST–UTC prediction as broadcast currently, users would not have to refer to an additional time scale to navigate (i.e. different than the GNSST and the international reference), and systems would not have to make many changes to provide service interoperability. The performance of this solution is however directly linked to the quality of the UTC predictions broadcast by the different systems.

Concerning the uncertainty of these methods, it is in common that either GNSST–$GNSST_{mean}$ or GNSST–UTC would have to be estimated posteriori then predicted, so the prediction error gives some contribution. In the case of estimating the mean time scale, it contains instability of each GNSS time scale that might affect the ability of predicting $GNSST_{mean}$. The latter case in current situation would actually have larger uncertainty because the UTC contribution in GNSST–UTC predictions is not yet "equivalent", and results between case 1 (IV) and case 2 (V) suggest that each system would have to improve its own time scale and its prediction to UTC to minimize the effect on users.

VII. Conclusion

Interoperability between different GNSS is partially achieved by the availability of time offsets between each system. While it is straight-forward that each XYTO can be estimated and transmitted by each system, an alternative solution can be to provide users only one information i.e. the time offset between each system time scale with respect to a common reference.

In this paper we investigated two possibilities to achieve this. In the first one the common reference is the average of all GNSST obtained by using a multi-GNSS receiver, preferably at each system level. The second case is to refer to UTC by using GNSST–UTC as currently predicted by each system.

Results in the considered period show that for the pair GPS/Galileo, GGTO values in the first case are in agreement at nanosecond level with the GGTO observed at user level. In the latter case, errors are included in the results due to different GNSST–UTC predictions, but the difference between the two cases remains also at some nanoseconds.

While the preliminary results are promising, each method has its own pros and cons. Further investigation must be done to further understand the impact on users of different algorithms amongst GNSS providers and of the use of different receivers to achieve a common solution, especially that some GNSSs are not yet fully operational, and might improve over time.

References

[1] R. Píriz, A. Mozo, G. Tobías, V. Fernandez, P. Tavella, I. Sesia, G. Cerretto, J. Hahn, "GNSS Interoperability: Offset between reference Time Scales and Timing Biases", Metrologia, Volume 45, Number 6, December 2008, pp. 87-102.

[2] Meeting documents, ICG-12 , Kyoto, Japan, Dec. 2-7, 2017 http://www.unoosa.org/oosa/en/ourwork/icg/meetings/ICG-2017.html

[3] "Recommendation for Committee Decision #21-B," Working Group D, ICG-12 , Kyoto, Japan, Dec. 2-7, 2017.

[4] "European GNSS (Galileo) Open Service Signal-In-Space Interface Control Document", Issue 1 Revision 3, Dec. 2016 https://www.gsc-europa.eu/system/files/galileo_documents/Galileo-OS-SIS-ICD.pdf

[5] "Interface Specification IS-GPS-200", Revision H, Sep. 2013 https://www.gps.gov/technical/icwg/IS-GPS-200H.pdf

[6] "Global Navigation Satellite System GLONASS Interface Control Document", Version 4.0, 1998

https://www.unavco.org/help/glossary/docs/ICD_GLONASS_4.0_(1998)_en.pdf

[7] "BeiDou Navigation Satellite System Signal In Space Interface Control Document, Open Service Signal B3I", Version 1.0, Feb. 2018 http://beidou.gov.cn/xt/gfxz/201802/P020180209623601401189.pdf

[8] P. Defraigne, G. Petit, "CGGTTS-Version 2E : an extended standard for GNSS Time Transfer," Metrologia, vol. 52 G1, 2015.

[9] P. Defraigne, K. Verhasselt, "Multi-GNSS Time Transfer with CGGTTS-V2E", 32nd European Frequency and Time Forum Proceedings, Turin, Italy, 2018

[10] BIPM FPT server, ftp://ftp2.bipm.org/pub/tai/publication

[11] P. Defraigne, W. Aerts, G. Cerretto E. Cantoni and J.-M. Sleewaegen, Calibration of Galileo signals for time metrology, IEEE transactions on ultrasonics, ferroelectrics, and frequency control, 12/2014 61(12):1967-75

[12] Bureau International des Poids et Mesures, "BIPM guidelines for GNSS calibration", v3.2, 15/02/2016

[13] Z. Cai, C. Han, B. Yang, "Update on BeiDou time system and its performance evaluation," China National Administration of GNSS and Application, Beijing Satellite Navigation Centre, ICG-12, Kyoto, Japan, Dec. 2-7, 2017.

Time-Frequency Analysis of Atomic Clock Anomalies

Lorenzo Galleani
Politecnico di Torino, Torino, Italy
Email: galleani@polito.it

***Abstract*—Atomic clocks are key elements in several applications, such as global navigation satellite systems. Monitoring their behavior is therefore fundamental. Since during an anomaly the frequency spectrum of the signal made by the clock frequency measurements changes with time, we transform this signal into the time-frequency domain by computing the spectrogram. In the time-frequency domain, the spectrogram localizes and separates the anomalies, and it can be hence used to reveal the nonstationary structure of the clock signal, such as, for instance, the presence of time-varying sinusuoidal terms.**

I. Introduction

Monitoring atomic clocks is a fundamental task, because atomic clocks are essential elements in many applications, such as global navigation satellite systems (GNSSs). The positioning service provided by GPS and Galileo, for example, depend on the atomic clocks onboard the system satellites and in the ground stations. Monitoring is first achieved by analyzing the signals corresponding to the clock time and frequency deviations in the time domain. Here we consider the discrete-time signal made by the frequency measurements

$$y[n] = \frac{1}{\tau_0} \int_{(n-1)\tau_0}^{n\tau_0} y(t')dt' \tag{1}$$

where τ_0 is the sampling time, $n = t/\tau_0$ is the discrete time, and $y(t)$ is the normalized frequency deviation [1], defined as,

$$y(t) = \frac{\nu(t) - \nu_0}{\nu_0} \tag{2}$$

The quantity $\nu(t)$ is the clock oscillation frequency, whereas ν_0 is the nominal oscillation frequency.

In addition to time domain analysis, a powerful approach consists in transforming the signal $y[n]$ in another domain, where its properties are easier to understand. The Allan variance, for instance, is an effective transformation, because it defines the clock stability [2]-[5]. Also frequency analysis, in the Fourier sense, is a powerful transformation, because frequency is a fundamental attribute of physical systems and signals. Since during a clock anomaly the properties of $y[n]$ changes with time, including its frequency spectrum, as we show in Sect. II, we transform $y[n]$ to the time-frequency domain by using time-frequency analysis, a body of techniques for the representation of signals with a time-varying frequency content [6], [7].

Contrary to frequency analysis, where the signal in time is transformed to the frequency domain by using the Fourier transform, a signal can be transformed to the time-frequency domain in infinite ways [6]. We consider the spectrogram, a time-frequency representation defined as

$$P(n, f) = \left| \sum_{n'=-\infty}^{+\infty} h[n' - n]y[n']e^{-i2\pi f n'} \right|^2 \tag{3}$$

where $h[n]$ is an analysis window, such as, for example, a Hamming, Hahn, or rectangular window. Basically, the spectrogram is the squared magnitude of the short-time Fourier transform [6], obtained by taking the Fourier transform of the windowed signal $h[n' - n]y[n']$.

In the next section we obtain and discuss the spectrogram for some of the most common anomalies of atomic clocks. The results show that the spectrogram localizes and separates the clock anomalies, and it can therefore be used as a tool to monitor the behavior of atomic clocks.

II. The Time-Frequency Spectrum of Atomic Clock Anomalies

We consider a white frequency noise (WFN) as the dominant noise, which means that we are observing the clock over an interval where other noise components, such as a random walk frequency noise, are negligible. We first obtain the spectrogram for a series of common atomic clock anomalies. Then, we consider a case where the anomalies are mixed. This general case can be understood only by first understanding the time-frequency representation of the individual anomalies separately. We choose $h[n]$ to be a Hamming window. For the individual anomalies, the window length is $N = 100$, whereas for the general case we take $N = 200$ to increase the frequency resolution of the sinusoidal terms.

A. Sinusoidal Terms

Sinusoidal terms are common anomalies, due, for example, to periodic variations of temperature, to residuals of the orbit estimation algorithm, or to relativistic effects. In Fig. 1 we show a WFN with two sinusoidal terms. The signal $y[n]$ does not reveal their presence, but we can immediately see them from the corresponding spectrogram in Fig. 2, which highlights that the sinusoidal terms have constant frequency and amplitude. From the spectrogram we can readily obtain the frequency of the sinusoids, a result which is not immediate when we use the Allan deviation. We also note that the background noise in Fig. 2 corresponds to the WFN, whose time-frequency representation is in fact made by random noise components.

978-1-5386-5620-4/18/$31.00 ©2018 IEEE

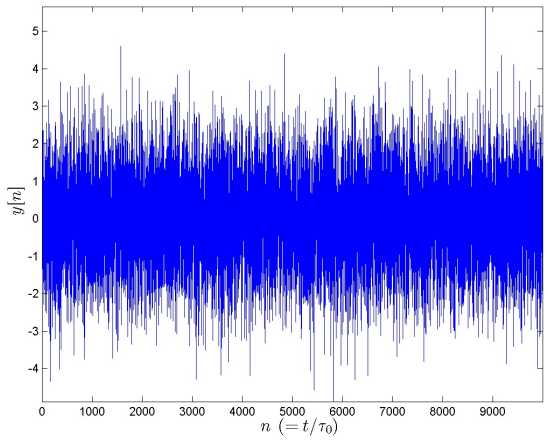

Fig. 1. Frequency measurements $y[n]$ of a WFN component plus two sinusoidal terms.

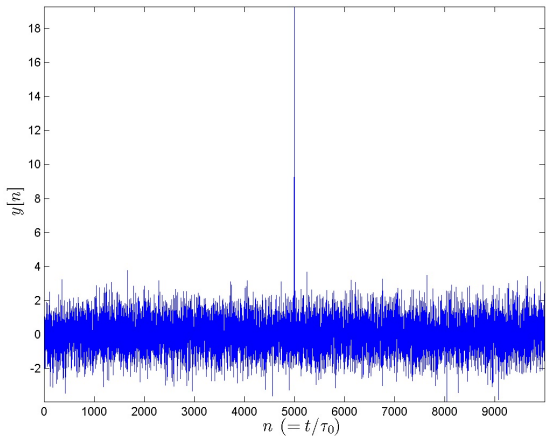

Fig. 3. Frequency measurements $y[n]$ of a WFN component with a phase jump (outlier in frequency).

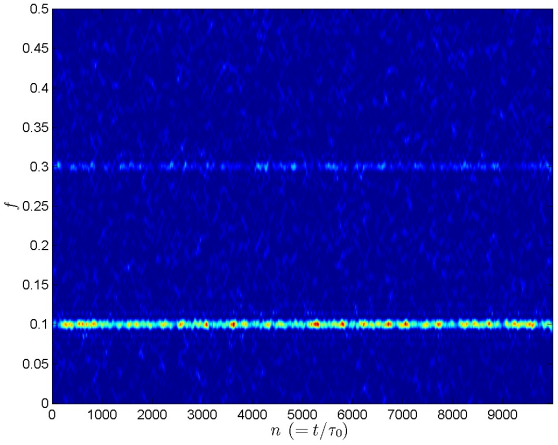

Fig. 2. Spectrogram of a WFN component with two sinusoidal terms.

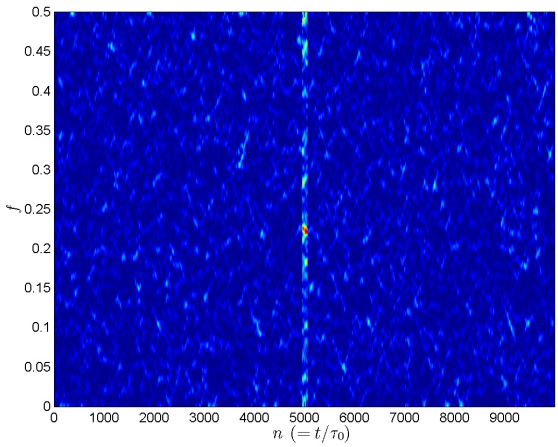

Fig. 4. Spectrogram of a WFN component with a phase jump (outlier in frequency).

B. Phase Jump (Outlier)

As Fig. 3 shows, a phase jump, namely, a step variation in the clock time deviation, corresponds to an impulse, or outlier, in the signal $y[n]$, because frequency is the derivative of phase [1]. Outliers are common in frequency measurements, and therefore it is interesting to understand their time-frequency signature. In Fig. 4 we show the spectrogram. Aside from the noise floor due to the WFN, we see a component located in the middle of the signal, exactly at the time instant of the outlier. This localized concentration of energy is due to the fact that the Fourier transform of an impulse is a flat spectrum, but this flat spectrum, in the time-frequency domain, is localized when the impulse occurs.

C. Frequency Jump

Figure 5 shows a frequency jump. The corresponding spectrogram in Fig. 6 shows that the frequency jump is localized in the zero frequency component. This result can be explained by considering that, after the frequency jump, the mean value of the WFN changes to a non-zero constant, and the Fourier transform of a constant is a delta function concentrated about the zero frequency, also referred to as the DC component.

D. Change of Variance

Figure 7 shows a WFN whose variance increases at half the signal duration. The corresponding spectrogram in Fig. 8 clearly reveals this nonstationarity by showing random noise components with a larger size in the second part of the signal.

E. General Case

Figure 9 shows a signal $y[n]$ made by a WFN which exhibits a frequency jump, and, at the same time, a change of frequency drift. Two outliers are also visible. The spectrogram in Fig. 10, shown with a logarithmic scaling, immediately reveals two sinusoidal components. The first component has a constant frequency, but a time-varying amplitude. The component, in

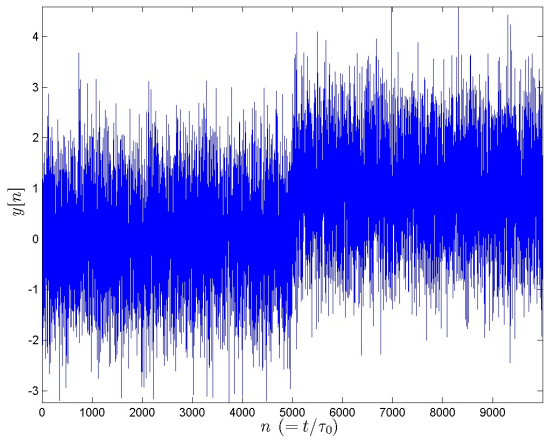

Fig. 5. Frequency measurements $y[n]$ of a WFN component with a frequency jump.

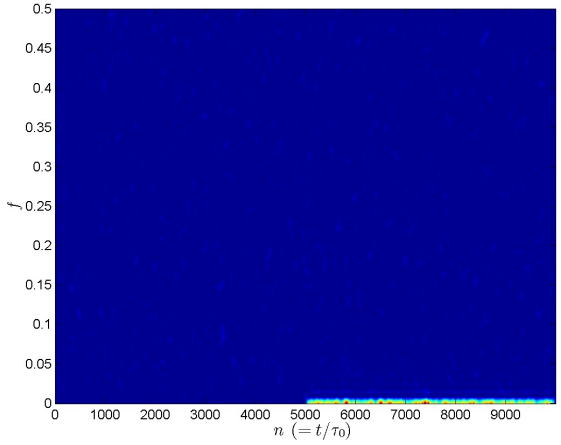

Fig. 6. Spectrogram of a WFN component with a frequency jump.

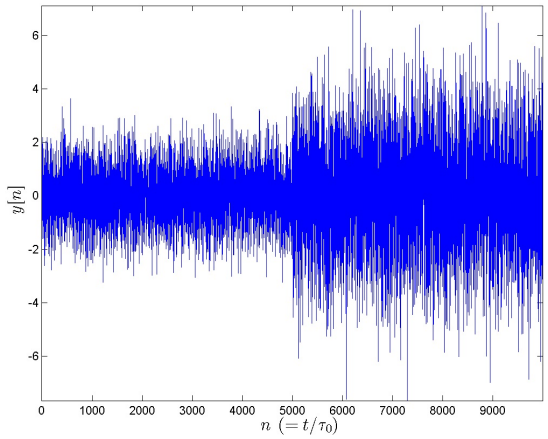

Fig. 7. Frequency measurements $y[n]$ of a WFN component with an increase in variance.

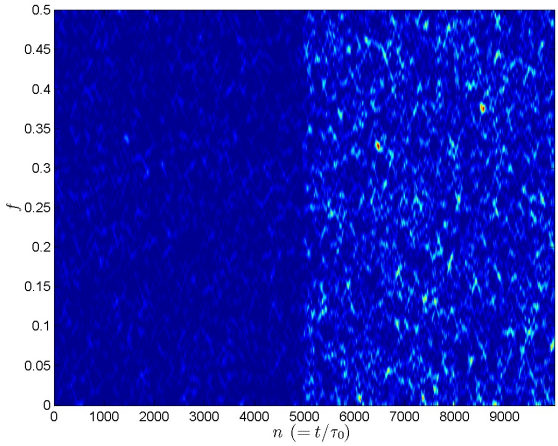

Fig. 8. Spectrogram of a WFN component with an increase in variance.

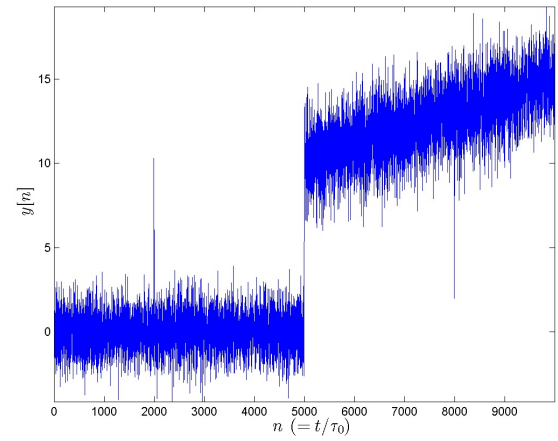

Fig. 9. Frequency measurements $y[n]$ of a WFN component with a frequency jump, a change of drift, and two outliers.

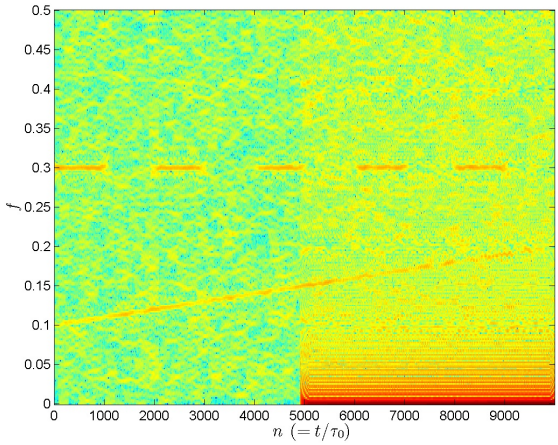

Fig. 10. Spectrogram of a WFN component with a frequency jump and a change of drift. Two nonstationary sinusoidal components and an increase in the noise variance are also visible.

fact, goes on and off several times. The second component is a linear chirp, namely, a sinusoid whose frequency increases linearly with time. The frequency jump is clearly localized in the DC component of the second half of the spectrogram. Its size slightly increases due to the increasing frequency drift. We also notice something not evident from the signal $y[n]$, namely, an increase in the variance of the WFN happening simultaneously with the frequency jump. As a result of this increase in variance, only the outlier located in the first part of the signal is recognizable.

III. Conclusions

We have obtained the time-frequency representation for a series of common anomalies of atomic clocks by computing the spectrogram of the corresponding frequency measurements. The results show that the considered anomalies are clearly recognizable in the time-frequency domain, and therefore the spectrogram can be used as an effective monitoring tool for atomic clocks, together with nonstationary analysis tools such as the dynamic Allan variance (DAVAR), which describes the variation with time of the clock stability [8]-[13]. Among the many applications, these nonstationary tools can be used to monitor the integrity of GNSSs [14]. Furthermore, anomaly detectors designed for the time domain, such as [15], can be extended to the time-frequency domain.

References

[1] P. Kartaschoff, *Frequency and time*, Academic Press, 1978.

[2] D. W. Allan, "Statistics of atomic frequency standards," *Proc. IEEE*, vol. 54, no. 2, pp. 221-230, 1966.

[3] D. W. Allan, "Time and Frequency (Time-Domain) Characterization, Estimation, and Prediction of Precision Clocks and Oscillators," *IEEE Trans. Ultra. Ferro. Freq. Contr.*, vol. 34, no. 6, pp. 647-654, 1987.

[4] IEEE Standard Definitions of Physical Quantities for Fundamental Frequency and Time Metrology, IEEE Std. 1139-1999.

[5] ITU-R Recommendation TF 538-3, "Measures for random instabilities in frequency and time (phase)," *International Telecommunication Union – Radiocommunication ITU-R*, vol. 2000, TF Series, Geneva, 2001.

[6] L. Cohen, *Time-Frequency Analysis*, Prentice-Hall, 1995.

[7] B. Boashash (Ed.), *Time-Frequency Signal Analysis and Processing: A Comprehensive Reference*, Academic Press, 2015.

[8] L. Galleani and P. Tavella, "The Dynamic Allan Variance," *IEEE Trans. Ultra. Ferro. Freq. Contr.*, vol. 56, no. 3, pp. 450-464, 2009.

[9] L. Galleani, "The Dynamic Allan Variance II: A Fast Computational Algorithm," *IEEE Trans. Ultra. Ferro. Freq. Contr.*, vol. 57, no. 1, pp. 182-188, 2010.

[10] L. Galleani, "The Dynamic Allan Variance III: Confidence and Detection Surfaces," *IEEE Trans. Ultra. Ferro. Freq. Contr.*, vol. 58, no. 8, pp. 1550-1558, 2011.

[11] L. Galleani and P. Tavella, "The Dynamic Allan Variance IV: Characterization of Atomic Clock Anomalies," *IEEE Trans. Ultra. Ferro. Freq. Contr.*, vol. 62, no. 5, pp. 791-801, May 2015.

[12] L. Galleani and P. Tavella, "The Dynamic Allan Variance V: Recent Advances in Dynamic Stability Analysis," *IEEE Trans. Ultra. Ferro. Freq. Contr.*, vol. 63, no. 4, pp. 624-635, April 2016.

[13] I. Sesia, L. Galleani, and P. Tavella, "Application of the Dynamic Allan Variance for the Characterization of Space Clock Behavior," *IEEE Trans. Aero. Elec. Sys.*, vol. 47, no. 2, pp. 884-895, Apr. 2011.

[14] I. Rodríguez-Pérez, C. García-Serrano, C. Catalán Catalán, A. M. García, P. Tavella, L. Galleani, and F. Amarillo, "Inter-satellite links for satellite autonomous integrity monitoring," *Advances in Space Research*, vol. 47, no. 2, pp. 197-212, January 2011.

[15] L. Galleani and P. Tavella, "Robust Detection of Fast and Slow Frequency Jumps of Atomic Clocks," *IEEE Trans. Ultra. Ferro. Freq. Contr.*, vol. 64, no. 2, pp. 475-485, February 2017.

The H2020 European Project CLONETS: clock services over optical-fibre networks in Europe

Davide Calonico, Cecilia Clivati, Filippo Levi
Istituto Nazionale di Ricerca Metrologica,
Turin, Italy
d.calonico@inrim.it

Przemysław Krehlik, Łukasz Śliwczyński
AGH University of Science and Technology
Cracow, Poland

Jiri Dostal, Jan Radil, Vladimir Smotlacha,
Radek Velc, Josef Vojtěch
CESNET
Prague, Czech Republic

Mauro Campanella
Consortium GARR
Rome, Italy

Ondřej Číp, Simon Rerucha
Institute of Scientific Instruments of the ASCR, v.v.i. (ISI)
Brno, Czech Republic

Ronald Holzwarth, Maurice Lessing, Sarah Saint-Jalm
Menlo Systems GmbH
Martinsried, Germany

Fabiola Camargo, Bruno Desruelle, Jean Lautier-Gaud
Muquans
Talence, France

Elizabeth Laier English, Jochen Kronjäger, Peter Whibberley
National Physical Laboratory
Teddington, United Kingdom

Fratišek John, Milan Šnajder, Jiří Štefl
OPTOKON a.s. Jihlava, Czech Republic

Paweł Nogaś, Robert Urbaniak
Piktime Systems sp. z o.o. Poznan, Poland

Artur Binczewski, Wojbor Bogacki, Krzysztof Turza
Poznan Supercomputing and Networking Center
Poznan, Poland

Gesine Grosche, Harald Schnatz
Physikalisch-Technische Bundesanstalt
Braunschweig, Germany

Emilie Camisard, Nicolas Quintin
GIP-Renater
Paris, France

Javier Diaz, Trinidad García, Eduardo Ros
Seven Solutions S.L. Granada, Spain

Alessandro Galardini
Conzorzio ToP-IX
Turin, Italy

Alwyn Seeds, Zhen Yang
University College
London, United Kingdom

Anne Amy-Klein
LPL, Université Paris 13, CNRS
Villetaneuse, France

Eva Bookjans, Paul-Eric Pottie, and Philip Tuckey
LNE-SYRTE, Observatoire de Paris, PSL Research University, CNRS, Sorbonne Université
Paris, France

***Abstract*— The H2020 project CLONETS (www.clonets.eu) is a coordination and support action started in January 2017, and it aims at accelerating the take-up of the fibre link technology by indus-try, research and society. One of the main target is to prepare the deployment of a permanent pan-European fibre network, providing high performance clock services to European re-search, and supporting wider services to industry and society. We report an update of the project.**

978-1-5386-5620-4/18/$31.00 ©2018 IEEE

Keywords— fiber link, T/F dissemination

I. INTRODUCTION

Time and frequency transfer based on optical fibre links techniques have demonstrated excel-lent performances. They are a key technology for very demanding application in metrology and science, e.g. optical clock comparisons, and also for applications in industry and society. They are complementary and/or alternative to radio- and satellite-based transfer.

The –H2020 project CLONETS (www.clonets.eu) brings together National Metrology Institutes (NMIs), academic research groups, National Research and Education Network providers (NRENs), an internet exchange and small and medium-sized high-technology companies.

The main objectives include collecting information on needs, studying industrial and societal applications, defining strategies to support future work, training, focusing on contractual aspects.

Here, we present the advances on the different objectives. In particular, we describe (i) the first outcomes from a survey of needs and applications for time and frequency transfer over optical fibre, aimed at research infrastructures (ii) the presentation of a university master program (post-graduate level) and the short training courses. The survey activity will allow a better decision process about the future infrastructure. The training activity is intended to gain new competences useful for optical T/F metrology over fibre and to offer to scientists, metrologists, industry, society and research the opportunity of focusing on needs and possibilities presently available.

II. HIGH PRECISION T/F NEEDS OF RESEARCH INFRASTRUCTURESE

The availability of high performance time & frequency (T/F) signals is at the very heart of research activities in fundamental physics, such as high-resolution spectroscopy, special and general relativity, the search for temporal variations of fundamental constants and quantum optics. Additionally, it will have a strong impact on a wide range of applied sciences, such as geodesy (chronometric levelling), Very Long Baseline Interferometry (VLBI) and laser ranging. The industrial applications of high performance T/F signals are not limited to telecommunication (i.e. the supervision of the next generation of mobile networks), but will also include applications such as high-speed trading, synchronisation in smart grids and the augmentation of existing techniques of the Global Navigation Satellite Systems (GNSS) such as Global Positioning System (GPS), or Galileo. In the future, high performance T/F signals derived from ultra-stable lasers or optical clocks will play a similarly important role in the development of novel applications and fundamental research as low noise RF-oscillators and primary Cs clocks have done over the last decades.

Today's best optical clocks can reach an estimated systematic fractional frequency uncertainty at the level of a few 10-18 ([1-3]). Satellite-based frequency comparison techniques offer world-wide coverage, but lack the performance required for optical clock comparisons (e.g. [4]). A transportable clock has become available recently ([5, 6]), but with an accuracy of 7×10^{-17} it is still far from the full performance of its stationary counterparts. The unprecedented accuracy of modern optical clocks has spurred the development frequency comparison techniques with an equivalent performance. An optical frequency transfer over fibre is currently the only technique capable of comparing high-performance clocks across long distances without degrading the stability and accuracy of the comparison ([7, 8]). In the European Union (EU) funded projects NEAT-FT and OFTEN of the European Metrology and Research Programme (EMRP) and its successor European Metrology Programme for Innovation and Research (EMPIR), technologies for disseminating and comparing ultra-stable optical and radio-frequencies over fibre links have been demonstrated. The efforts of these projects have culminated in the first international comparison of primary Cs fountains and optical clocks, which was not limited by the link between the clocks ([9, 10]).

Although an optical fibre frequency transfer is capable of reaching a stability and an accuracy in the 10^{-19} to 10^{-20} range [11, 12], the fibre-based frequency transfer capabilities in Europe have not yet advanced towards the development of a sustainable, universal tool for T/F metrology for Europe. Creating a T/F infrastructure benefitting European society, the main issues hampering this development need to be addressed. Firstly, there is neither a reliable data base describing the T/F transfer techniques currently being used or evaluated by Research Infrastructures (RIs) nor is there a clear understanding of the current and future needs of such RIs for precise and accurate T/F transfers. Secondly, the capability and the benefits of fibre based T/F services are largely unknown to the user community and thirdly, the capacity for the integration of an T/F transfer in existing networks provided e.g. by National Research and Education Network (NRENs) is up to now unexplored.

This deliverable focuses on the needs of RIs for a high precision T/F transfer, whereby high precision refers to performances superior to those provided by standard Precision Time Protocol (PTP), e.g currently served by H-masers, Rb clocks or GNSS. The report is based on data collected through a survey of RIs, which previously had been identified as relevant..

A. Relevant Research Infrastructures

Relevant RIs in the context of this deliverable are institutes and organizations, which have timing needs in excess of standard PTP, H-masers or GNSS based services. They include National Metrology Institutes (NMIs), university based research groups in the field of quantum optics, research organizations (e.g. academies of science, the Max-Planck Society and the Fraunhofer Gesellschaft) and certain pertinent consortia interested in sharing T/F transfer technology (e.g. the ACES consortium, the Geodetic Observatory Wettzell and the International Association of Geodesy).

Additionally, big infrastructures according to European Strategy Forum on Research Infrastructures (ESFRI) were considered as relevant, in particular, RIs from PHYSICAL SCIENCES & ENGINEERING [13], such as the European Extremely Large Telescope [14], the European X-Ray Free-Electron Laser [15], the Facility for Antiproton and Ion Research [16], the European Organization for Nuclear Research [17], the

Square Kilometre Array [18], the European VLBI Network [19], the Joint Institute for VLBI ERIC [20], and the European Space Agency [21] were contacted.

In total, 52 RIs deemed as representative of the institutes and organizations having high precision timing needs were identified and contacted for the survey by means of an electronic questionnaire. Among these 52 RIs are 17 NMIs with the remaining 35 RIs being classified as non-NMIs. Previously established contacts to the relevant RIs were exploited to ensure an adequate response to the survey. Overall, 37 RIs (11 NMIs and 26 non-NMIs) responded to the survey, which is sufficient to obtain a general overview of the T/Fneeds of RIs. Fig.1-4 show some relevant information on the RI interviewed for the survey.

The RIs that participated in the survey are located throughout Europe with responses coming from a wide range of different countries (Figure 1). There is a relatively large participation in France and the Czech Republic. The NRENs in these countries are very active in the field Time & Frequency distribution potentially leading to a greater awareness of the topic.

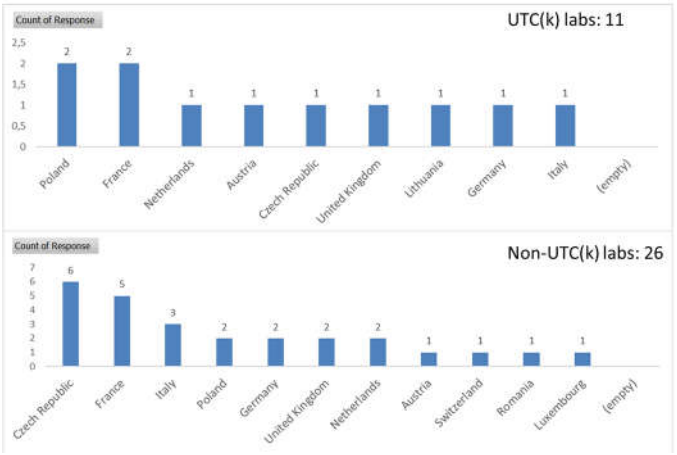

Fig. 1. Responses received by UTC(k) labs (top) and non-UTC(k) labs (bottom) according to county.

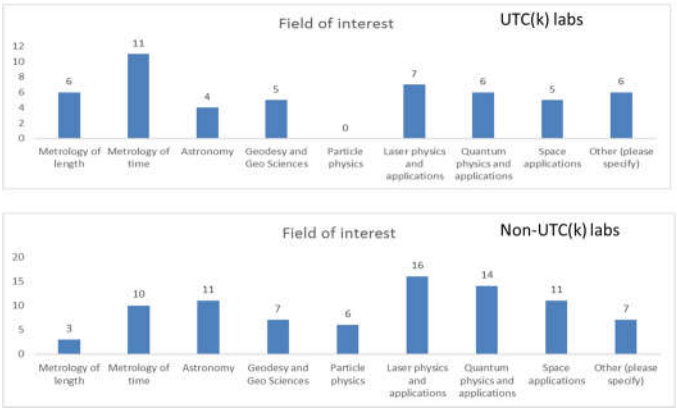

Fig. 2. Field of interest for UTC(k) and Non-UTC(k) labs.

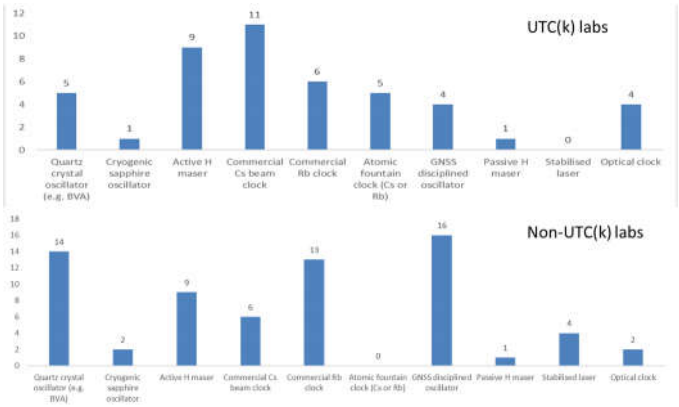

Fig. 3. Frequency standards and clocks operated at the surveyed UTC-labs (above) and non- UTC-labs (below).

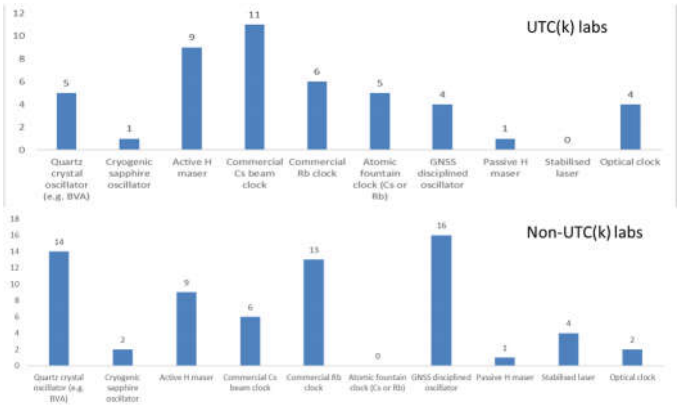

Fig. 4. *S*ource of external T/Freference signals for UTC-labs (above) and non-UTC-labs (below).

B. Results from the Survey

The results of the survey are described in the Fig. 4 to 9. In general, the survey has revealed that applications requiring highest-performance frequency accuracy and instability prevail upon those requiring precise timing. As of today, receiving time is still based on satellite techniques. However, the most demanding timing applications already require an instability that can only be met by dissemination through optical fibres. Among the respondents there seems to be a clear view and ranking of the importance of traceability to the SI, the availability of T/Fsignals at a remote location, the resilience of such signals and issues related to security. The availability of a fibre based T/Fservice is considered as of highest importance for UTC labs as well as for non-UTC labs. While traceability is considered important (especially by UTC(k) labs), it is not regarded as particularly problematic by non-UTC labs. Considering that availability is rated highest, it is clear that resilience attracted significantly more consideration than security. Overall, the results of the survey support the CLONETS consortium's current understanding of the relevance of high precision T/F reference signals for RIs. The communities that believe to benefit most from a fibre based T/F service are –as expected– radio-astronomy, geodesy, accelerator- and spectroscopy-laboratories, calibration laboratories and potentially space agencies. There is a growing awareness of the potential of a

fibre-based T/F service and at the same time an increasing need for better performance than currently available via satellite based technology. The survey intended to identify the current and future needs of such research infrastructures for precise and accurate T/F transfer. We received an adequate number of responses to consider the outcome of the survey as a representative spectrum of the high precision T/F needs of European RIs. Together with the outcome of a survey performed in WP3 addressing the needs of European industry we will be able to shape a future time and frequency service that covers the needs of science, industry and society.

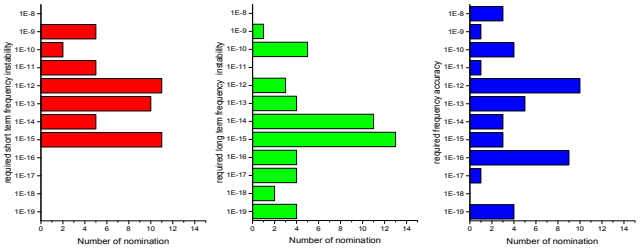

Fig. 5. Frequency instability required by RI

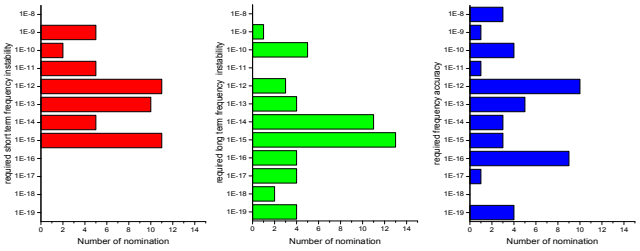

Fig. 6. Timing instability required by RI

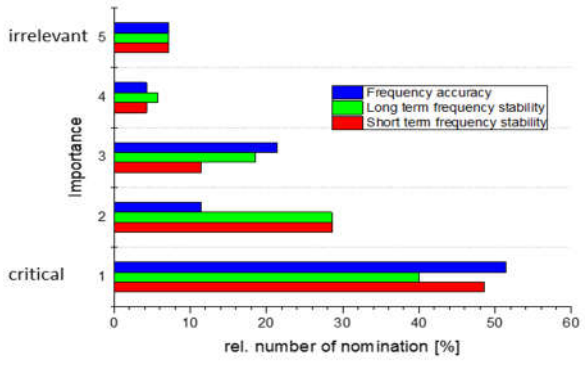

Fig. 7. Rating of the importance of frequency accuracy and instability

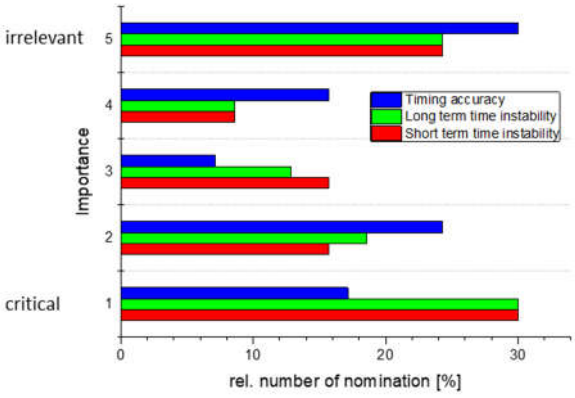

Fig. 8. Rating of the importance of timing accuracy and instability

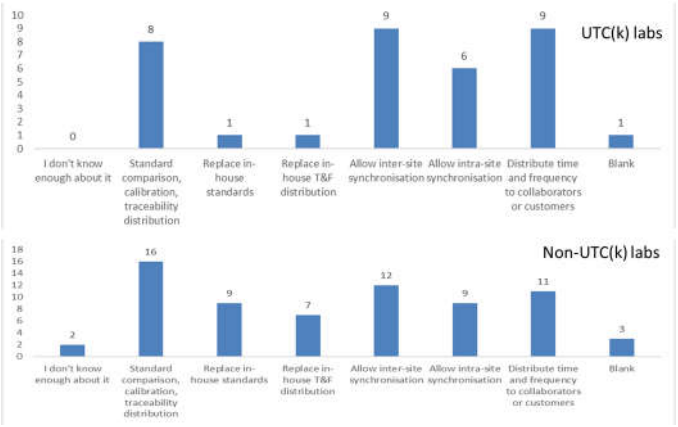

Fig. 9. Respones to the question: How could high performance T/Fdelivered over optical fibre open new possibilities that your organisation would be interested in?

III. A SECOND LEVEL MASTER PROGRAMME

A. Motivations

CLONETS organizes a second level master with the Politecnico of Turin, "Photonics for Data Networks and Metrology". Data traffic will experience a dramatic growth over the next years driven by 5G access, high-definition video, virtual and augmented-reality contents, and the considerable growth in cloud services due to Big Data Exchange. Photonic data networks will be required to be more and more pervasive and elastic, to supporting the paradigm of Internet of Thing and to enabling Industry 4.0. Besides data transport, photonic networks will also distribute time and frequency (T/F) standards for research and industry, enabling orders of magnitude performance improvements with respect to satellite systems, over continental geographical areas. The list of institutions supporting the initiative testifies the need for a vertical multidisciplinary knowledge, from the transmission layer up to the IP layer, and training such new professional figures is indeed the mission of the 2nd level Specializing Master's Programme.

The Programme will offer theoretical and practical lecturing, hand-on experiences and a final internship in European industrial and/or research environments.

The purpose of the Programme is to give multidisciplinary knowledge and competence on photonics transmission and networking as well as on fundamentals of metrology and of time reference distribution on telecommunications infrastructure based on optical fiber transmission. The Programme is aimed at students with different backgrounds: graduated in the ICT field and graduated from schools of Physics and Metrology, and will train hybrid professional figures who will be able to design and manage state-of-the-art photonic networks to support the ever-increasing IP traffic demands well as to distribute time references from and among metrology centers.

The 2nd level Specializing Master is a full time Programme of one academic year duration for a total of 69 European Credits Transfer System; it will start in September 2018 and will end in November 2019.

Lectures will be held in English at Politecnico di Torino premises – starting in September 2018 and ending in June 2019.

Lectures include classroom activities with academic and corporate teaching staff.

The internship period will start in July/August 2019 and will end in October/November 2019.

The teaching Programme is organized as follows:

i) courses: 32 weeks of full-time classroom activities (September 2018 – June 2019)

ii) internship: of on the job training at companies and/or research institutes in the photonic technologies field (July/August 2019 – October/November 2019).

TABLE I. **ERRORE. L'ORIGINE RIFERIMENTO NON È STATA TROVATA.**COURSES AT THE CLONETS MASTER.

n.	Subject	Ects	Hours
1	Digital Communication	6	60
2	Optical Transmission	5	50
3	Photonic Devices	4	40
4	Time and frequency metrology	5	50
5	Ultrabroadband access networks	5	50
6	Long-haul optical transport	4	40
7	Photonic Networks	6	60
8	Quantum Communications	4	40
9	Photonics applications in metrology	4	40
10	Time and frequency laboratory	6	60
11	Security for ICT	4	40
12	Communications laboratory	6	60
13	Internship	>10	>250

ACKNOWLEDGMENT

The Consortium thanks Prof. Vittorio Curri of the Politecnico of Torino for the organizion of the Master.

REFERENCES

[1] N. Huntemann, C. Sanner, B. Lipphardt, Chr. Tamm, and E. Peik. 'Single-Ion Atomic Clock with 3×10−18 Systematic Uncertainty'. Physical Review Letters 116, no. 6 (8 February 2016): 063001. https://doi.org/10.1103/PhysRevLett.116.063001.

[2] T. L. Nicholson, S.L. Campbell, R.B. Hutson, G.E. Marti, B.J. Bloom, R.L. McNally, W. Zhang, et al. 'Systematic Evaluation of an Atomic Clock at 2 × 10−18 Total Uncertainty'. Nature Communications 6 (21 April 2015): 6896. https://doi.org/10.1038/ncomms7896.

[3] I. Ushijima, M. Takamoto, M. Das, T. Ohkubo, and H. Katori. 'Cryogenic Optical Lattice Clocks'. Nature Photonics 9 (9 February 2015): 185. https://doi.org/10.1038/nphoton.2015.5.

[4] S. Droste, C. Grebing, J. Leute, S. M. F. Raupach, A. Matveev, T. W. Hänsch, A. Bauch, R. Holzwarth, and G. Grosche. 'Characterization of a 450 Km Baseline GPS Carrier-Phase Link Using an Optical Fiber Link'. New Journal of Physics 17, no. 8 (2015): 083044. https://doi.org/10.1088/1367-2630/17/8/083044.

[5] S. B. Koller, , J. Grotti, St. Vogt, A. Al-Masoudi, S. Dörscher, S. Häfner, U. Sterr, and Ch. Lisdat. 'Transportable Optical Lattice Clock with 7x10-17 Uncertainty'. Physical Review Letters 118, no. 7 (13 February 2017): 073601. https://doi.org/10.1103/PhysRevLett.118.073601.

[6] J. Grotti, et al. 'Geodesy and Metrology with a Transportable Optical Clock'. Nature Physics, 12 February 2018. https://doi.org/10.1038/s41567-017-0042-3.

[7] R. Sebastian, A. Koczwara, and G. Grosche. 'Brillouin Amplification Supports 1x10-20 Uncertainty in Optical Frequency Transfer over 1400 Km of Underground Fiber'. Physical Review A 92, no. 2 (24 August 2015): 021801.

[8] C., Nicola, N. Quintin, F. Stefani, F. Wiotte, E. Camisard, C. Chardonnet, G. Santarelli, A. Amy-Klein, P. E. Pottie, and O. Lopez. 'Cascaded Optical Fiber Link Using the Internet Network for Remote Clocks Comparison'. Optics Express 23, no. 26 (28 December 2015): 33927–37. https://doi.org/10.1364/OE.23.033927.

[9] C. Lisdat, G. Grosche, N. Quintin, C. Shi, S.M.F. Raupach, C. Grebing, D. Nicolodi, et al. 'A Clock Network for Geodesy and Fundamental Science'. Nature Communications 7 (9 August 2016): 12443.

[10] .J Guéna, S Weyers, M Abgrall, C Grebing, V Gerginov, P Rosenbusch, S Bize, et al. 'First International Comparison of Fountain Primary Frequency Standards via a Long Distance Optical Fiber Link'. Metrologia 54, no. 3 (2017): 348. https://doi.org/10.1088/1681-7575/aa65fe.

[11] S. M. F. Raupach, A. Koczwara and G. Grosche Brillouin amplification supports 10-20 accuracy in optical frequency transfer over 1400~km of underground fibre, Phys. Rev.~A 92, 021801(R) (2015)

[12] A. Bercy, O. Lopez, P.-E. Pottie and A. Amy-Klein Ultrastable optical frequency dissemination on a multi-access fibre network Appl. Phys.~B 122, 189 (2016)

[13] https://ec.europa.eu/research/infrastructures/pdf/ri_landscape_2017.pdf#view=fit&pagemode=none

[14] http://www.eso.org/public/about-eso/faq/faq-elt/

[15] https://www.xfel.eu/

[16] http://www.fair-center.de/index.php?id=1&L=1

[17] https://home.cern/

[18] https://www.skatelescope.org/

[19] http://www.evlbi.org/

[20] https://www.jive.nl/

[21] https://www.esa.int/ESA

Two-way Optical Phase Comparison at 10^{-21} Level

Zang Qi, Deng Xue, Liu Jie, Jiao Dongdong, Gao Jing, Zhang Xiang, Wang Dan, Xu Guanjun, Dong Ruifang, Liu Tao†, Zhang Shougang
National Time Service Center, Chinese Academy of Sciences
Xi'an, China
†Corresponding author: taoliu@ntsc.ac.cn

***Abstract*—This works demonstrates an improved local two-way optical phase comparison method without the requirement of synchronization. Based on this scheme, we implement a real-time frequency comparison over a bi-directional 50-km fiber spool. The achieved relative frequency stability is 1.2E-16 at 1 s integration time and reaches 1.3E-21 at 40,000 s.**

Keywords—two-way comparison; optical phase transfer; local measurement; fiber net work; fiber optics

I. INTRODUCTION

High-precision frequency comparison between remote atomic clocks over fiber links has become increasingly important in many research fields including metrology [1], fundamental physics [2-3], time keeping, and relativistic geodesy [4-5]. Current optical clocks have achieved the 10^{-18} level of uncertainty and instability [6-7]. To realize such a frequency comparison, a two-way optical phase comparison technique has been previously reported [8-11]. In their method, the frequency difference was measured by beating between the local laser and the remote one at each end of the fiber link. Assuming that the propagation noise is equal for the two directions, one can efficiently reject the extra noise by synchronizing and post processing the data. However, under an insufficient synchronization, the short-term laser noise could degrade the precision.

In this letter, we demonstrate an improved optical phase comparison method without the requirement of synchronization. In this method, the remote signal at one end of the fiber link is sent back. At the other end of the fiber link, the beatings between the local laser and the remote laser as well as the laser after the round-trip propagation are simultaneously measured by a single photodetector and a multi-channel phase recorder. Since the single-trip propagation noise can be directly subtracted, no post processing is needed and therefore a real-time frequency comparison can be achieved. Furthermore, as the beating measurements are based on the same setup, the effect of common-mode noise suppression can be more efficient compared with previous method.

II. THE EXPERIMENT

A. Local measurement of two-way optical phase comparison

We demonstrate the proposed local two-way phase comparison using 50-km spooled fiber to investigate its overall instability. The scheme of system is illustrated in Fig. 1.

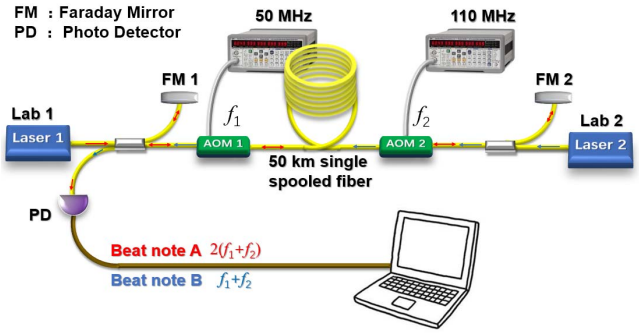

Fig.1. The scheme of two-way bidirectional phase comparison.

In lab 1, part of the light is reflected into the photo detector (PD) by Faraday mirror (FM) 1 while the remaining light is injected into the acousto-optical modulator (AOM1) with driving frequency f_1 of 50 MHz. The AOM is used to shift the optical frequency and discriminate the return signal from the stray reflections caused by the connectors and splices. This light is reflected by FM 2 and returned to lab 1. The beat note (A) between laser 1 and itself after a round-trip is then detected by the PD at frequency $2(f_1+f_2)$.

At the same time, the light from laser 2 in lab 2 is injected into the fiber link after AOM 2 at frequency f_2 (about 110 MHz). The beat note (B) at the frequency of (f_1+f_2) between laser 1 and laser 2 is detected by the PD. By carefully choosing the AOM driving frequency, the beat-note signals A and B can be filtered and separately easily. Beat-note signals A and B are simultaneously compared by a dead-time free-phase noise analyzer or a frequency counter.

B. Phase noise analysis

The phase noises of two beat-note signals ϕ_A and ϕ_B can be written as follows:

$$\phi_A = 2\left(\phi_{AOM1} + \phi_{AOM2}\right) + \phi_{12}\left(t - \tau\right) + \phi_{21} \quad (1)$$

$$\phi_B = \left(\phi_2 - \phi_1\right) + \phi_{AOM1} + \phi_{AOM2} + \phi_{21} \quad (2)$$

where τ is the single-trip delay time, referred to as $\tau = \frac{L}{C_n}$, C_n is the speed of light in the fiber, and L is the length of fiber link. In addition, ϕ_1 and ϕ_2 are the phase noise of lasers 1 and 2, respectively, ϕ_{AOM1} and ϕ_{AOM2} are the phase noises of AOM 1 and AOM 2, respectively, and ϕ_{12} and ϕ_{21} are the phase noises added by the bidirectional fiber. Combining Eqs. (1) and (2) in post-processing, we have

$$\phi_B - \frac{1}{2}\phi_A = \left(\phi_2 - \phi_1\right) + \frac{1}{2}\phi_{21} - \frac{1}{2}\phi_{12}\left(t - \tau\right) \quad (3)$$

Equation (3) shows that if the phase noises of AOM 1 and AOM 2 are neglected, the result of phase comparison consists of the laser's phase difference $(\phi_2 - \phi_1)$ and fiber's phase noises. Here, lasers 1 and 2 originate from the same laser source, so we can assume $\left(\phi_2 - \phi_1\right) = 0$. If $\left(\phi_2 - \phi_1\right)$ vanishes in Eq. (3), the result of phase comparison is only sensitive to the fiber's phase noise [10]. We express the two-way comparison phase noise as

$$\phi_{two}\left(z,t\right) = \phi_B - \frac{1}{2}\phi_A \approx \frac{1}{2}\left[\phi_{21} - \phi_{12}\left(t - \tau\right)\right] \quad (4)$$

We transform Eq. (4) into the frequency domain using a Fourier transform.

$$\tilde{\phi}_{two}\left(\omega\right) = \int_0^L e^{-j\omega\tau}\left[j\ sin\omega\left(\tau - \frac{z}{c_n}\right)\right]\delta\tilde{\phi}\left(z,\omega\right)dz \quad (5)$$

The two-way phase noise power spectral density (PSD) of this signal is

$$S_{fiber,two}\left(\omega\right) = \frac{S_{fiber}\left(\omega\right)}{L}\int_0^L \frac{1}{2}\left(1 - cos2\omega\left(\tau - \frac{z}{c_n}\right)\right)dz$$
$$= \frac{S_{fiber}\left(\omega\right)}{2}\left[1 - sinc\left(2\omega\tau\right)\right] = \frac{S_{fiber}\left(\omega\right)}{3}\omega^2\tau^2 \quad (6)$$

Because $sinc\left(0\right) \approx 1$, the suppression of bidirectional phase noise is better at low frequencies, and is half of the one-way phase noise at higher frequencies. It has been assumed that the noise PSD does not depend on z [12], hence, Eq. (6) holds in the spectral region where $4\pi f\tau \ll 1$. As we can see, Eq. (6) is same as that obtained for an optical link with active noise compensation [13], which means the two-way optical phase comparison link is more robust and does not need a complicated active fiber noise control loop.

C. Results and discussion

Thanks to the single bidirectional fiber and the synchronous phase measurement, the beat note A has a double fiber phase noise because the light travels twice in the fiber link. Hence, it can be divided by two and compared with the beat note B. In such data post-processing, the phase noise can easily cancelled. The phase noise power spectral density (PSD) of our system is shown in Fig. 2. Because of the limitations of the measuring instruments, the phase noise PSDs of a one-way fiber noise of round-trip signal and single-trip signal (blue line and red line, respectively) are not measured at the same time, so their curves are not completely coincident. When measuring our system performance, these two phase noise PSDs overlap between 0.1 Hz and 100 Hz, which means the common phase noise of two beat note signals can be easily rejected using the two-way setup. Hence, the phase noise PSD of the two-way phase comparison (red line) is smooth between Fourier frequencies 0.1 Hz and 100 Hz. This value is almost five magnitudes below one-way fiber noise at 1 Hz.

This experimental structure is not affected by the transfer function of the interferometer, so the measured bandwidth of phase noise is large and could help measure broadband phase noise. However, we also know the conclusion from Eq. (7) is based on slow and small changes in light. As for actual light, in practice, there is always some rapidly changing noise. Because we cannot eliminate it completely using our system, our comparison accuracy is degraded. Hence, a measurement bandwidth still exists for our two-way system.

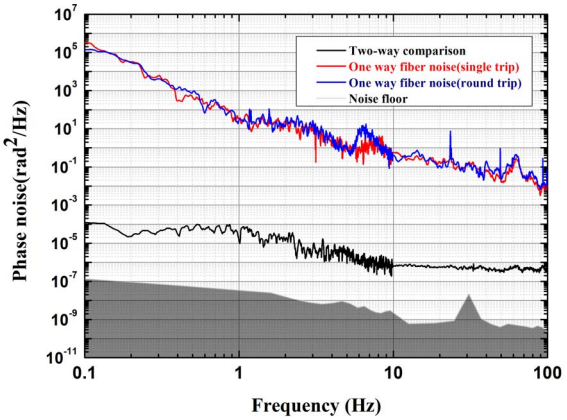

Fig.2. Phase noise spectral density (PSD) of the round-trip signal (blue line), signal-trip signal (red line), system noise floor (light gray area), and two-way phase comparison (black line).

The relative frequency instability of the two-way optical phase comparison over the 50-km spool fiber link is shown in Fig. 3, expressed as an Allan deviation (ADEV) for one-way fiber noise (black dots) and two-way phase comparison (red squares). The two-way bidirectional comparison stability is as low as 1.2×10^{-16} at 1 s on average and reaches 1.3×10^{-21} at 40,000 s. This level of performance is already far beyond most advanced Global Positioning System and two-way carrier phase capabilities.

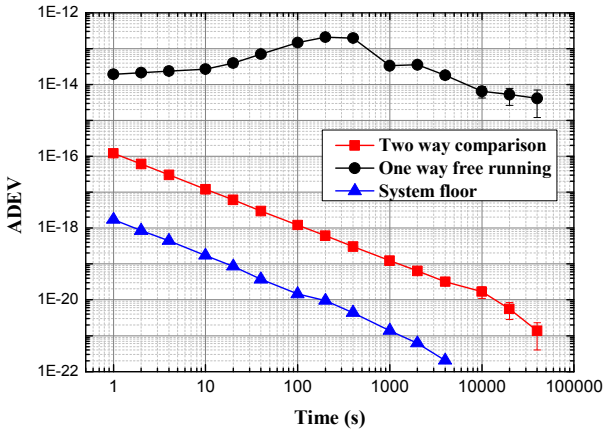

Fig.3. Allan deviation (ADEV) of one-way fiber noise (black dots) and of two-way phase comparison (red squares), blue triangles is system floor.

III. SUMMARY

In conclusion, we proposed a local two-way optical phase comparison method for a 50-km optical fiber that does not require synchronous remote measurement of the optical phase. The method cancels phase noise efficiently because of the bidirectional propagation in a single fiber, and the method is also insensitive to the phase noise of the fiber link. The relative frequency instability is 1.2×10^{-16} at 1 s and 1.3×10^{-21} at 40,000 s. The two-way optical phase comparison link is robust without the use of a complicated active fiber noise control loop. This scheme also has the advantage of enabling the comparison to be completed at a single site without the remote transfer of data via communication. This bidirectional setup is expected to be a more reliable approach than conventional methods for high-precision frequency comparison between remote optical clocks and other advanced atomic clocks.

ACKNOWLEDGMENT

The authors thank Cao Qun for the previous work. The authors acknowledge National Key Research and Development Program of China (2016YFF0200200); Young Scientists Fund of the National Natural Science Foundation of China (11403031); West Light Foundation of the Chinese Academy of Sciences (XAB2016B47); Strategic Priority Research Program of the Chinese Academy of Sciences(XDB21030800).

REFERENCES

[1] M. Fujieda, M. Kumagai, S. Nagano, A. Yamaguchi, H. Hachisu and T. Ido, "All-optical link for direct comparison of distant optical clocks," Opt. Express **19**, 16498 (2011)

[2] C.W. Chou, D.B. Hume, T. Rosenband and D. J. Wineland, "Optical clocks and relativity," Science 329, 1630 (2010).

[3] S. Schiller, G. Tino, P. Gill, C. Salomon, U. Sterr, and E. Peik, et al, "Einstein gravity explorer–a medium-experimental astronomy class fundamental physics mission," Exp. Astron. 23, 573-610 (2009).

[4] A. Bjerhammar, "On a relativistic geodesy," B. Géod. 59(3), 207-220 (1985).

[5] P. Delva, and J. Lodewyck, "Atomic clocks: New prospects in metrology and geodesy," Acta Futura **7** (2013).

[6] C. W. Chou, D. B. Hume, J. C. J. Koelemeij, D. J. Wineland, and T. Rosenband, "Frequency comparison of two high-accuracy Al+ optical clocks," Phys. Rev. Lett. **104**, 070802 (2010)

[7] N. Huntemann, M. Okhapkin, B. Lipphardt, S. Weyers, C. Tamm, and E. Peik, "High-accuracy optical clock based on the octupole transition in Yb+ 171," Phys. Rev. Lett. **108**, 090801(2012).

[8] C. E. Calosso, E. K. Bertacco, D. Calonico, F. Levi, S. Micalizio, A. Mura, C. Clivati, and G. A. Costanzo, "Tracking DDS for Coherent Optical Links," in Proceedings of the Joint UFFC, EFTF and PFM Symposium 858 (2013).

[9] C. E. Calosso, E. Bertacco, D. Calonico, C. Clivati, G. A. Costanzo, M. Frittelli, et al. "Frequency transfer via a two-way optical phase comparison on a multiplexed fiber network." Opt. Lett. **39**, 1177-1180 (2014).

[10] A. Bercy, F. Stefani, O. Lopez, C. Chardonnet, P. Pottie, and A. Amy-Klein, "Two-way optical frequency comparisons at 5×10^{-21} relative stability over 100-km telecommunication network fibers." Phys. Rev. A. **90**, 6 (2014).

[11] Won-Kyu-Lee, Fabio Stefani, Anthony Bercy, Olivier Lopez, Anne Amy-Klein, and Paul-Eric Pottie, "Hybird fiber links for accurate optical frequency comparisons" Applied Physics B. **123** (5) (2017).

[12] P. A. Williams, W. C. Swann, and N. R. Newbury, "High-stability transfer of an optical frequency over long fiber-optic links," JOSA B 25, 1284 (2008).

[13] N. R. Newbury, P. A. Williams, and W. C. Swann, "Coherent transfer of an optical carrier over 251 km," Opt. Lett. **32**, 3056 (2007).

Phase-Coherent Transfer of Optical Frequency Between ISI CAS and CESNET

Martin Cizek, Lenka Pravdova, Vaclav Hucl, Simon Rerucha, Jan Hrabina, Michal Jelinek, Bretislav Mikel, Josef Lazar, Ondrej Cip
Department of Coherence Optics
Institute of Scientific Instruments of the CAS
Brno, Czech Republic

Vladimir Smotlacha, Ondrej Havlis, Josef Vojtech
CESNET, z. s. p. o.
Prague, Czech Republic

***Abstract*— The contribution reports on the current state of the fibre link for phase-coherent transfer of optical frequency between ISI CAS (Brno, CZ) and CESNET (Prague, CZ). The 306 km long link is operated on an internet communication fibre in a dedicated 1540-1546 nm DWDM window. The narrow linewidth laser Kohereas ADJUSTIK working at 1540.5 nm locked to the nearest tooth of the stabilized optical frequency comb referenced by the H-Maser serves as the laser standard at the transmitting side.**

Keywords—optical fibre link; stable optical frequency transfer; GNSS; DWDM

I. INTRODUCTION

Optical fibre links in Europe are often used for comparison measurements of experimental optical clocks to verify their ultimate relative stability [1-4]. We present a 306 km long optical fibre link established in the Czech Republic between ISI CAS Brno and CESNET Prague, Fig. 1.

In the first step, the purpose of this link is to connect ISI CAS in Brno, which has a significant background of developing optical frequency standards for laser metrology of length [5], [6], with prospective academic and industrial partners in the Prague area.

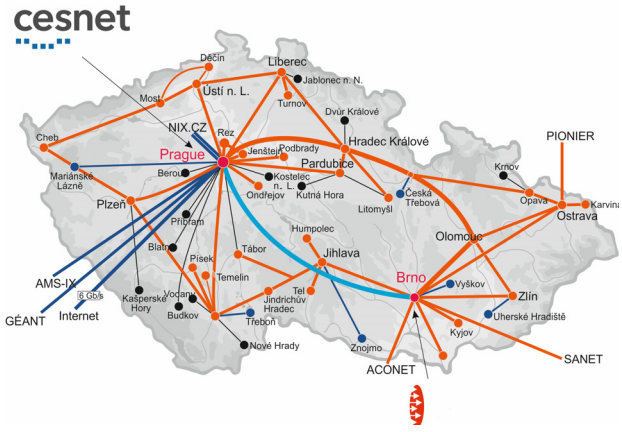

Fig. 1. CESNET fibre optic infrastructure at national level. The light blue line represents the fibre-optic link between ISI CAS in Brno and CESNET in Prague.

The link uses an internet communication fibre where a window 1540 to 1546 nm in DWDM grid is dedicated for the coherent transfer and bidirectional 1 PPS signal transmission [7]. The optical frequency standard working at 1540.5 nm is used for the coherent transfer. The total length of the fibre is 306 km and it is equipped with 5 bidirectional EDFA amplifiers as can be seen in detail in Fig. 2.

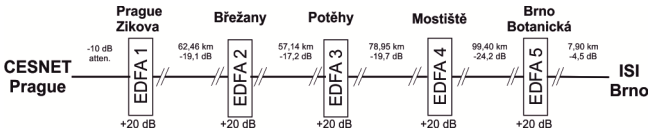

Fig. 2. CESNET fibre optic infrastructure at national level. The detailed block schematic of the two-way fibre-optic link between CESNET and ISI CAS.

II. METHODOLOGY

The setup of the local end of the link located at ISI CAS in Brno is shown in Fig. 3. An internet communication fibre with window 1540 to 1546 nm in DWDM grid is dedicated for the phase coherent transfer and bidirectional 1 PPS signal transmission. Highly coherent laser Koheras Adjustik working at 1540.5 nm with a linewidth < 100 Hz is used as the optical frequency standard for the coherent transfer. The optical frequency of this laser is locked using a slow (bandwidth < 20 Hz) phase-locked loop to the nearest tooth of an optical frequency comb referenced to an H-maser. The Doppler frequency shifts in the coherent transfer induced by the fibre link are suppressed using a closed-loop control system based on PLL. The bandwidth of the control loop is limited by the roundtrip delay of the optical fibre link and it is 300 Hz approx. for 306 km link length [6], [8].

To detect the optical frequency shifts a 90% portion of the light is sent back from the far end setup shown in Fig. 4. At the local end (Fig. 3) the returned portion of the light is mixed with the light being transmitted and the beat note signal is detected by a photodetector PD. In order to distinguish the unwanted reflections throughout the optical fibre link from the useful component returning from the far end several optical frequency translations are used.

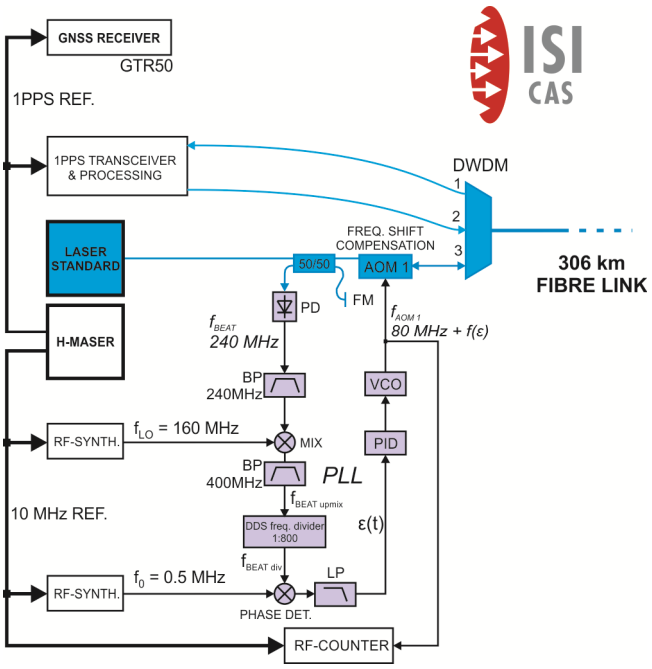

Fig. 3. Block schematics of the local-end setup operated by ISI CAS in Brno. RF amplifiers omitted for clarity.

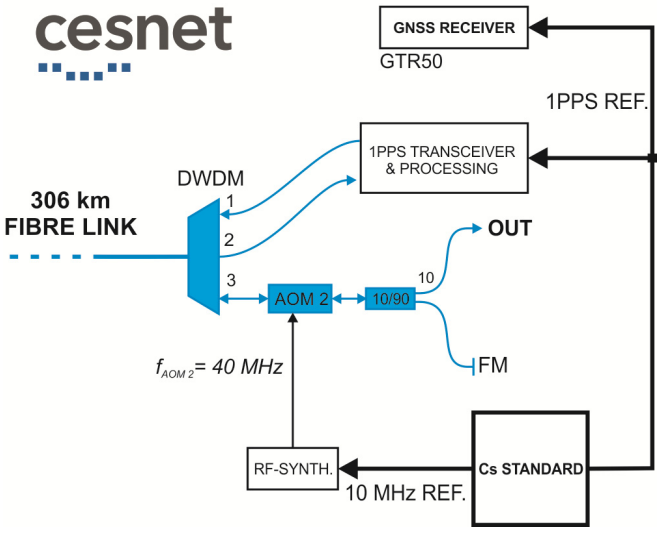

Fig. 4. Block schematics of the far-end setup operated by CESNET in Prague. RF amplifiers omitted for clarity.

The first frequency translation takes place as the coherent light passes AOM1 working at the nominal frequency of f_{AOM1} = 80 MHz. At the far end a portion of the light is returned back by Faraday mirror (FM) and passes AOM2 driven by f_{AOM2} = 40 MHz two times. At the local end the returned light passes AOM1 once more and is again shifted by 80 MHz. As a result the RF output signal of PD1 contains a spectrum of beat notes at various frequencies. Only the beat-note centered around 240 MHz is the product of mixing the transmitted coherent light with the returned portion that has passed all acousto-optic modulators and the optical fibre link two times. Its instantaneous frequency is equal to $2f_{AOM1} + 2f_{AOM2} + 2v_\varepsilon(t)$ where $v_\varepsilon(t)$ is the optical frequency shift induced by the optical link in a single pass.

The useful spectral component is selected by a 240MHz band-pass filter and amplified. To meet the 300Hz limitation in the bandwidth of the phase-locked loop mentioned earlier the locking is not done directly at 240 MHz. The input beat-note frequency is translated by mixing with a 160 MHz local oscillator to 400 MHz. After necessary band-pass filtering and amplification this intermediate-frequency signal is divided using a DDS (AD9959) by a factor of 800. The bandwidth of the resulting frequency-divided beat note centered around 0.5 MHz is then narrower than the bandwidth limit of the control loop. Finally the frequency-divided beat note is phase locked to a 0.5MHz reference signal and thus Doppler optical frequency shifts $v_\varepsilon(t)$ induced by the optical fibre link are suppressed while voltage-controlled oscillator driving AOM1 serves as the optical frequency actuator.

All RF equipment and electronics at the ISI CAS is referenced from an active Hydrogen maser standard while at the CESNET Prague uses cesium standard for the same purpose. To avoid possible errors caused by drifts of these RF standards they are compared with GPS using GNSS receivers on a regular basis, [8].

III. Experimental Results

At the local end the setup is still placed on an optical breadboard. However the far-end setup has been transformed into a modular 19" rackmount unit containing both the fibre-optic parts (AOM, splitter, FM) and electronics (reference oscillator, DDS, RF amplifier, Ethernet communication module).

Fig. 5. A photo of the far-end rackmount unit.

A zero dead-time RF counter continuously measures the output frequency of the VCO at the local end. In the closed loop regime the absolute deviations of f_{AOM1} from the nominal 80 MHz are equal to $-v_\varepsilon(t)$. By integrating these absolute deviations equal to the closed-loop action we can compute the changes in the transport delay in a non-compensated optical fibre link, [8]. Fig. 6 shows a result of such a measurement obtained during an 8-day period in November 2017.

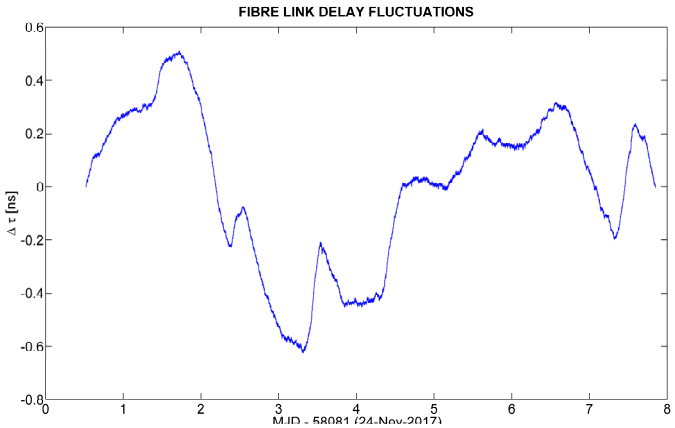

Fig. 6. Transport delay absolute deviations observed during an 8-day measurement in November 2017. The fluctuations were computed by integrating the frequency corrections applied to AOM1 at the local end.

The measured absolute deviations of the transport delay are below 1 ns.

Fig. 7 shows the relative frequency stability at 1540.5 nm of an uncompensated fibre-optic link computed from the AOM1 frequency detuning. The measured relative stability of the transfer over the fibre link in uncompensated state is better than 10^{-13} for 1s integration time and 10^{-14} for 10^3s integration time.

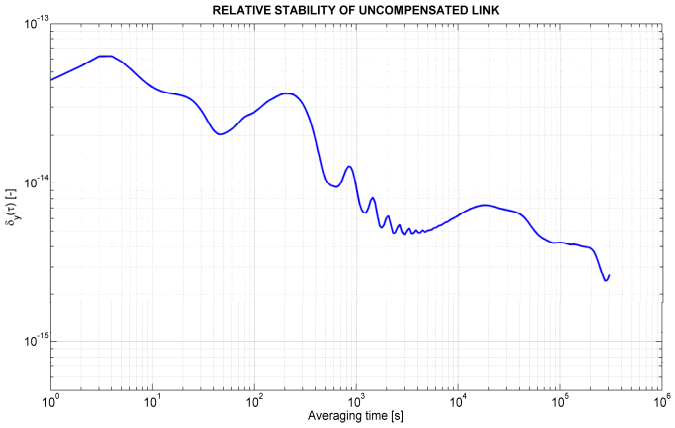

Fig. 7. Relative frequency stability of uncompensated fibre-optic link computed from the frequency corrections applied to AOM1 at the local end.

IV. Conclusion

We have established a 306 km long bidirectional optical fibre link for simultaneous phase-coherent transfer of stable optical frequency and 1 PPS time signals from atomic clocks between lab of ISI CAS in Brno (CZ) and CESNET site in Prague (CZ). The optical frequency standard based on a narrow-linewidth laser locked to optical frequency comb is operaded at the local end at ISI in Brno. The far-end setup has been implemented as a standalone rack-mount unit and is operated at CESNET site in Prague. Measurements of the uncompensated link show relative frequency stability of 10^{-14} for 10^3s integration time.

Acknowledgment

The authors acknowledge the support from Technology Agency of CR (project TH01011254) for establishing long-haul fibre link. The issues with optical frequency shift compensation have been supported by Grant Agency of CR (project GB14-36681G).

References

[1] Terra, O. at al., "Brillouin amplification in phase coherent transfer of optical frequencies over 480 km fibre," Optics Express 18, pp. 16102-16111 (2010).

[2] C. E. Calosso, E. Bertacco, D. Calonico, C. Clivati, G. A. Costanzo, M. Frittelli, F. Levi, A. Mura, and A. Godone, "Frequency transfer via a two-way optical phase comparison on a multiplexed fiber network," Opt. Lett. 39, 1177-1180 (2014)

[3] G. Grosche, M. Eggert, D. A. Humphreys, C. Campbell, J. C. Petersen, J. Henningsen, and B. Skipper, "Transmission of wavelength references via a commercial transparent optical network over 534 km," in Conference on Lasers and Electro-Optics/International Quantum Electronics Conference and Photonic Applications Systems Technologies, Technical Digest (CD) (Optical Society of America, 2004), paper CTuH4.

[4] G. SANTARELLI, "Ultra-stable Long Distance Optical Frequency/Time Distribution Using the Internet Network," in Frontiers in Optics 2013, I. Kang, D. Reitze, N. Alic, and D. Hagan, eds., OSA Technical Digest (online) (Optical Society of America, 2013), paper FTh3B.1.

[5] Hrabina, J., Sarbort, M., Acef, O., Du Burck, F., Chiodo, N., Hola, M., Cip, O. and Lazar, J., "Spectral properties of molecular iodine in absorption cells filled to specified saturation pressure," Appl Optics 53, p. 7435-7441, (2014).

[6] Šmíd, R.; Čížek, M.; Mikel, B.; Číp, O. Frequency Noise Suppression of a Single Mode Laser with an Unbalanced Fiber Interferometer for Subnanometer Interferometry. Sensors 2015, 15, 1342-1353.

[7] Smotlacha V., Kuna A., "Two-Way Optical Time and Frequency Transfer between IPE and BEV," EUROPEAN FREQUENCY AND TIME FORUM 2012 Proceedings, pp 375-378 (2012).

[8] Cizek, M., Pravdova, L., Hucl, V., Rerucha, S., Hrabina, J., Mikel, B., Lazar, J., Cip, O., Smotlacha, V., and Vojtech, J.: "Transfer of Stable Optical Frequency for Sensory Networks via 306 km Optical Fiber Link", 2016 European Frequency and Time Forum (EFTF), 2016

Kalman filter simulation and characterization of BDS satellite clock

Bin Wang[*], Junping Chen[*†] and Binghao Wang[‡]
Email: {binw, junping}@shao.ac.cn wangbinghao7@126.com
[*]Shanghai Astronomical Observatory, CAS, Shanghai, China
[†]School of Astronomy and Space Science, UCAS, Beijing, China
[‡]Zhengzhou Institute of Surveying and Mapping, Zhengzhou, China

***Abstract*—In this paper, a Kalman filter algorithm for simulation and characterization of BDS (beidou satellite system) satellite clock in orbit is presented. The algorithm is designed to produce near optimal estimation of characteristic parameters for BDS satellite clock. Besides normal clock noises, white frequency modulation, random walk frequency modulation and random run frequency modulation, the flicker phase modulation and flicker frequency modulation are also considered as the linear combination of several Gauss Markov processes. Additional states are used to model the periodic variations of BDS satellite clock, and the first type model of clock periodic states is used in the paper. It is shown that simulation results fit the real oscillator behavior well.**

Keywords—BDS; clock simulation; clock characteristic parmeter estimation; kalman filter; flicker noise

I. INTRODUCTION

An accurate and correct characterization of satellite clock is of great importance for clock prediction, and the prerequisite and basis for the production of time scale in GNSS (global navigation satellite system). Significant effort has been reported on the analysis of the clock stability and systematic variations of GNSS satellite clocks. Periodic variations are found in BDS (beidou satellite system) satellite clocks [1]. Through spectral analysis, the presence of 1 and 2 cpr (cycle per revolution) periodicities is evident. BDS satellite clock fundamental harmonic period is different from that of satellite orbit. It is inferred that clock periodic variations are related to solar illumination. Besides harmonics, in time intervals smaller than 1e3s, flicker phase modulation (FLPM) can be found, and in time intervals larger than 2e5s, flicker frequency modulation (FLFM) is remarkable for BDS satellite clock [2].

Kalman filter is extensively used in real-time applications of clocks and oscillators. Two-state model was suggested by Fran to describe the behavior of cesium clock [3]. The inclusion of a linear clock drift term brought about three state clock models, particularly necessary to model the drift of masers and rubidium clocks [4]. Kalman filter algorithms usually model the clock noise as a linear combination of white frequency modulation (WHFM), random walk frequency modulation (RWFM) and random run frequency modulation (RRFM). However, flicker noise and periodic variations are common in the GNSS satellite clock. Flicker noise processes can be modelled approximately as a linear combination of Gauss Markov processes [5]. There are three different models of clock periodic states can be used in Kalman filter [6]. The first model that adds the periodic states to only the phase state without any stochastic correlation between the stochastics driving the harmonics and the stochastics driving the base model, is simple and fast. It is preferred in the use of simulation and characterization of GNSS satellite clock.

In this paper, to simulate and characterize the BDS satellite clock in orbit, the satellite clock model that account for the periodic signals and flicker noise processes (FLPM and FLFM) is presented. After that Kalman filter algorithm to characterize BDS satellite clocks from real measurements is proposed.

II. BDS SATELLITE CLOCK MODEL

A. Clock base model

Basic clock model $x_{base}(t)$, is typically represented as:

$$x_{base}(t) = x_0 + y_0(t-t_0) + \frac{1}{2}z_0(t-t_0)^2 \tag{1}$$

where x_0, y_0 and z_0 is the initial values of clock-offset, frequency offset and linear frequency drift, respectively at epoch t_0, and t-t_0 can be denoted by τ. In general, the basic clock model is a purely deterministic of clock behavior.

B. Harmonic signals

The harmonic signals, denoted by $x_{har}(t)$, can be expressed as

$$x_{har}(t) = \sum_{i=1}^{n_{har}} \left[c_i \cos(2\pi f_i t) + s_i \sin(2\pi f_i t) \right] \tag{2}$$

where n_{har} is the number of harmonics, c_i and s_i is harmonic coefficients, f_i is the frequency of i-th harmonic, and $f_i = if_0$, f_0 is the basic frequency. In this paper, it is assumed that the basic frequency is known.

This work is support by the NSFC (No.11673050), the 863 (No. 2014AA123102) projects and also the open project program of the key lab of space navigation and positioning technology (No. KFKT-201705), Shanghai.

C. Gauss-Markov noise

Non-stationary flicker noise (over a finite time period) can be approximated as a linear combination of several independent Gauss-Markov processes [5]:

$$x_{Flicker}(t) = \sum_{i=1}^{n_{flicker}} x_{GM_i}(t) \tag{3}$$

For BDS satellite clock, four independent Gauss-Markov processes are used to approximate the FLPM and FLFM respectively in time intervals smaller than 1e3s and larger than 2e5s.

BDS satellite clock model is composed of above three components, and can be expressed as

$$x(t) = x_{base}(t) + x_{har}(t) + x_{flpm}(t) + x_{flfm}(t) \tag{4}$$

III. KALMAN FILTER IMPLEMENTATION

In order to implement BDS satellite clock model with the Kalman filter algorithm, several elements should be defined. In this section, state vector, state-transition matrix, process noise covariance matrix, measurement matrix is introduced. Besides, process noise parameters estimation and Kalman filter initialization are also discussed.

A. State vector

At epoch k, state vector of BDS satellite clock Kalman filter can be defined as

$$\mathbf{X}_k = \begin{bmatrix} \mathbf{x}_{base} & \mathbf{x}_{har} & \mathbf{x}_{flpm} & \mathbf{x}_{flfm} \end{bmatrix}^T \tag{5}$$

where $\mathbf{x}_{base} = [x_k, y_k, z_k]$ is used to describe the basic clock model, $\mathbf{x}_{har} = [c_{1,k}, s_{1,k}, \ldots, c_{n1,k}, s_{n1,k}]$ is used to describe n1 harmonics, $\mathbf{x}_{flpm} = [GM_{1,k}, GM_{2,k}, \ldots, GM_{n2,k}]$ is n2 Gauss-Markov components used to approximate the FLPM in the time interval smaller than 1e3s, and $\mathbf{x}_{flfm} = [GM_{n2+1,k}, GM_{n2+2,k}, \ldots, GM_{n2+n3,k}]$ is n3 Gauss-Markov components used to approximate the FLFM in the time interval larger than 2e5s.

B. State transition matrix

State-transition matrix of BDS satellite clock model Kalman filter can be expressed as

$$\mathbf{\Phi}_k = \begin{bmatrix} 1 & \tau & \tau^2/2 & & & & \mathbf{\Phi}_{GMf1} \\ & 1 & \tau & & & & \mathbf{0}_{1,n3} \\ & & 1 & & & & \mathbf{0}_{1,n3} \\ & & & \mathbf{I}_{2n1} & & & \\ & & & & \mathbf{\Phi}_{GMp} & & \\ & & & & & & \mathbf{\Phi}_{GMf2} \end{bmatrix} \tag{6}$$

where $\mathbf{I}_{2n1}$ is a $2n1 \times 2n1$ identity matrix used for the harmonics, $\mathbf{\Phi}_{GMp}$ is a $n2 \times n2$ matrix used for the approximation of FLPM, $\mathbf{\Phi}_{GMf1}$ is a $1 \times n3$ vector used to describe the influences of FLFM on clock offset, $\mathbf{\Phi}_{GMf2}$ is a $n3 \times n3$ matrix used for the approximation of FLFM, the expression of $\mathbf{\Phi}_{GMp}$, $\mathbf{\Phi}_{GMf1}$ and $\mathbf{\Phi}_{GMf2}$ can be found in [5].

C. Process noise covariance matrix

Process noise covariance matrix is given as

$$\mathbf{Q}_k = \begin{bmatrix} Q_{11} & Q_{base,12} & Q_{base,13} & & & Q_{GMf1} \\ Q_{base,21} & Q_{base,22} & Q_{base,23} & & & \mathbf{0}_{1,n3} \\ Q_{base,31} & Q_{base,32} & Q_{base,33} & & & \mathbf{0}_{1,n3} \\ & & & q_{har}\mathbf{I}_{2n1} & & \\ & & & & Q_{GMp} & \\ Q_{GMf1}^T & \mathbf{0}_{n3,1} & \mathbf{0}_{n3,1} & & & Q_{GMf2} \end{bmatrix} \tag{7}$$

where Q_{base} is the process noise covariance matrix of the basic clock model:

$$Q_{base} = \begin{bmatrix} \sigma_1^2\tau + \frac{1}{3}\sigma_2^2\tau^3 + \frac{1}{20}\sigma_3^2\tau^5 & \frac{1}{2}\sigma_2^2\tau^2 + \frac{1}{8}\sigma_3^2\tau^4 & \frac{1}{6}\sigma_3^2\tau^3 \\ \frac{1}{2}\sigma_2^2\tau^2 + \frac{1}{8}\sigma_3^2\tau^4 & \sigma_2^2\tau + \frac{1}{3}\sigma_3^2\tau^3 & \frac{1}{2}\sigma_3^2\tau^2 \\ \frac{1}{6}\sigma_3^2\tau^3 & \frac{1}{2}\sigma_3^2\tau^2 & \sigma_3^2\tau \end{bmatrix} \tag{8}$$

where $\sigma_i^2 (i = 1,2,3)$ is the noise spectral density of WHFM, RWFM and RRFM respectively, $Q_{base,ij}$ is the (i, j)th element of Q_{base} matrix. It is noted that

$$Q_{11} = Q_{base,11} + \tau^3 \sum_{i=1}^{n_3} \sigma_{GMf_i}^2 a_{11}\left(R_{f_i}\tau\right) \tag{9}$$

where $\sigma_{GMf_i}^2$ is two-sided spectral density of the ith Gauss-Markov processes associated with the FLFM, a_{11} is defined in [5]. q_{har} is the variance of process noise associated with harmonics. Q_{GMp} is used for the approximation of FLPM, Q_{GMf1} and Q_{GMf2} are used for FLFM.

D. Measurement matrix

BDS satellite clock Kalman filter is designed to use IGS (international GNSS service) MGEX (multi-GNSS experiment) satellite clock data. The measurement matrix, describes the relationship between state-vector and the measurements, can be defined as

$$\mathbf{H}_k = \begin{bmatrix} 1 & 0 & 0 & H_{har} & \mathbf{1}_{1,n2} & \mathbf{0}_{1,n3} \end{bmatrix} \tag{10}$$

where H_{har} is $1 \times 2n1$ vector, used to relate the harmonics with clock offset:

$$H_{har} = \left[\cos(\omega_1 t) \quad \sin(\omega_1 t) \quad \cdots \quad \cos(\omega_{n1} t) \quad \sin(\omega_{n1} t) \right] \quad (11)$$

where $\omega_i = 2\pi f_i$ is the angular velocity of i-th harmonic.

E. Process noise parameters estimation

In order to obtain optimal estimation results, it is necessary to carefully configure Kalman filter parameters for each BDS satellite clock. Determination of process noise parameter associated with each of state vector is of vital importance. These parameters are usually estimated using a sufficient set of past data and some judging criteria should be defined [7]:

1) prediciton error deviation matches with RMS prediciton errors obtained from the Kalman filter predicitons;

2) time domain variances estimated from simulation data match with that estimated from real measurements;

3) kalman filter residuals obey white noise processes.

Simulating data using Kalman filter can be found in [8]. Simulation vector $\mathbf{X}$ evolve between epoch k-1 and k:

$$\mathbf{X}_k = \mathbf{\Phi}(\tau)\mathbf{X}_{k-1} + \mathbf{L}_Q(\tau)\mathbf{e}(\tau) \quad (12)$$

where $\boldsymbol{L}_Q$ is lower triangle matrix, can be obtained from the cholesky decomposition of $\mathbf{Q}$:

$$\mathbf{Q} = \mathbf{L}_Q(\tau)\mathbf{L}_Q^T(\tau) \quad (13)$$

$\mathbf{e}_Q$ is Gauss white noise, and process noise covariance matrix $\mathbf{P}_k$ evolves as:

$$\mathbf{P}_k = \mathbf{\Phi}(\tau)\mathbf{P}_{k-1}\mathbf{\Phi}^T(\tau) + \mathbf{Q}(\tau) \quad (14)$$

F. Kalman filter initialisation

State vector and their error covariance matrix should be set to realistic estimates. The non-diagonal elements of error covariance matrix can be set to zero. Three measurements can be used to initialize the state vector of basic clock model [9]. In addition, initialization process can be completed using the empirical value.

IV. Results and Disccusion

Noise spectral densities of BDS satellite clock are estimated using the Kalman filter simulation algorithm. BDS constellation are comprised by GEO (geostationary earth orbit), IGSO (inclined geosynchronous satellite orbit) and MEO (middle earth orbit) satellites. Clock on each satellite orbit type are simulated and the results are discussed.

A. Data source

Two types of satellite clock data can be obtained for BDS, ODTS (orbit determination and time synchronization) and TWTT (two-way time transfer) satellite clock data [2]. However, ODTS satellite clock data is easy to get, and IGS MGEX provides public services of satellite clock and satellite orbit. In this paper, BDS satellite clock data provided by WHU (wuhan university) analysis center are used. The analysis period is the entire week of GPS week 1945. Sampling interval of BDS satellite clock data is 5min.

B. Kalman filter simulaiton results and discussion

In order to evaluate the BDS satellite clock simulation result, we should choose reasonable judging criteria. Hereinafter, difference between time domain variances respectively estimated from simulation data and real measurements is selected to evaluate the simulation or parameter estimation results. In view of the facts that overlapping allan deviation of BDS satellite clock at one day interval is about 1e-14. Therefore, it is defined that if the difference is smaller than 1e-14, then the simulation is valid.

Comparison of overlapping allan deviation estimated from Kalman filter simulation data and real measurements for GEO satellite is shown in Fig. 1. Frequency stability analysis result of simulation data is plotted with yellow line, while that of the measurements is plotted with green line, and the difference between them is plotted using blue-dot line.

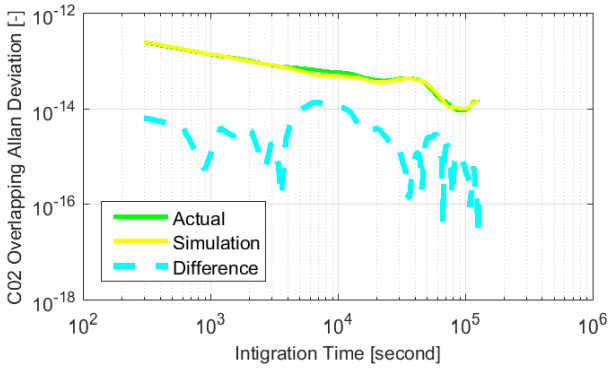

Fig. 1. Comparison of frequency stability between simulation data and real measurements of C02 (GEO) satellite clock.

From Fig. 1, it can be seen that for most of time period, Kalman filter simulation results can approximate the stochastic characterization of real measurements, except for the time interval of 4e3s-1e4s. In time interval of 4e4s-8e4s, periodic variations of GEO satellite clock are notable.

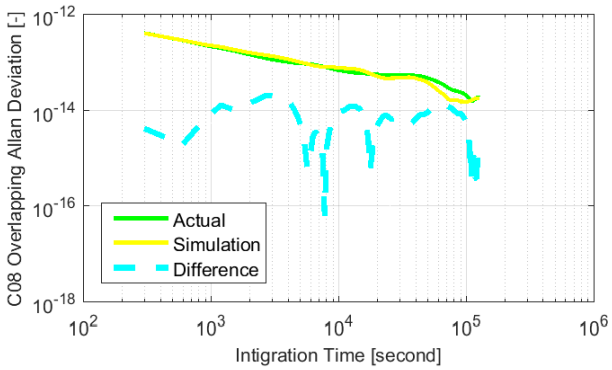

Fig. 2. Comparison of frequency stability between simulation data and real data of C08 (IGSO) satellite clock.

Simulation result of IGSO (C08) satellite clock is shown in Fig. 2. Long influences duration of IGSO satellite clock periodic variations can be found. In the time interval of 4e4s-8e4s, simulation result of IGSO satellite clock is worse than that of GEO satellite clock. But in the time interval of 1e3s-4e3s, simulation result of IGSO satellite clock is not good.

Simulation result of MEO (C12) satellite clock is shown in Fig. 3. It is found that Kalman filter simulation performance of MEO satellite is better than that of GEO/IGSO satellite clock.

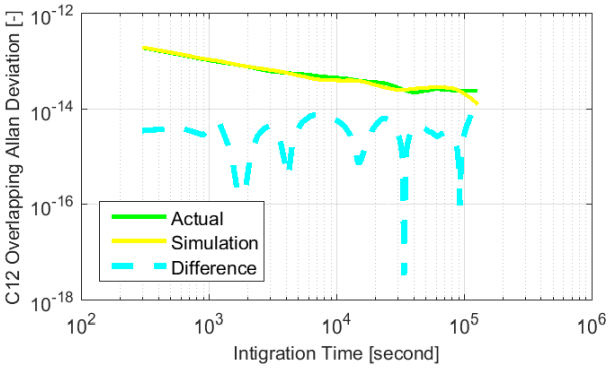

Fig. 3. Comparison of frequency stability between simulation data and real data of C12 (MEO) satellite clock.

Model parameters used in the BDS satellite clock Kalman filter are shown in Table I. It can be seen that for BDS satellite clock, spectral densities of WHFM is about 1e-23, while 1e-35 and 1e-47 for RWFM and RRFM respectively.

TABLE I. MOLDEL PARAMETERS USED IN THE BDS SATELLITE CLOCK KALMAN FILTER

PRN	Spectral Densities		
	WHFM (sec^2/sec)	***RWFM*** (sec^2/sec^3)	***RRFM*** (sec^2/sec^5)
C02	2e-23	9e-35	1e-47
C08	5e-23	1e-35	1e-47
C12	1e-23	1e-35	1e-47

V. CONCLUSIONS AND FUTURE WORK

Kalman filter algorithm for simulation and characterization of BDS satellite clock in orbit is presented. The algorithm is designed to produce near optimal estimation of characteristic parameters for BDS satellite clock. Several types of noise are considered in the algorithm, including WHPM, WHFM, RWFM, FLFM and also RRFM. Flicker noise is approximated by the linear combination of several Gauss-Markov processes. Besides, clock periodic variations are also considered and the simple model is used. Periodic states are only added to the phase state without any stochastic correlation between the stochastics driving the harmonics and the stochastics driving the base model.

For most of time period, Kalman filter simulation results can approximate the stochastic characterization of real measurements, except for the time interval of 4e3s-1e4s and time interval of 4e4s-8e4s. In the time interval of 4e4s-8e4s, the periodic variations of GEO are more remarkable than that of IGSO/MEO satellite clock. Simulation results show that for BDS satellite clock, spectral densities of WHFM is about 1e-23, while 1e-35 and 1e-47 for RWFM and RRFM respectively.

In this paper, only one week data is used to estimate the model parameters of BDS satellite clock Kalman filter, and the data may be not enough. In the future, more historical data would be used. And the processes of initialization and configuration of Kalman filter parameters may be automated with the help of machine learning.

ACKNOWLEDGMENT

We would like to thank Wang Wei for valuable discussions, and also the IGS MGEX campaign for providing multi-GNSS data and products.

REFERENCES

[1] Bin Wang, Yidong Lou, Jingnan Liu, Qile Zhao and Xing Su, "Analysis of BDS satellite clocks in orbit," GPS Solutions. vol. 20, pp. 783-794, 2016.

[2] Bin Wang and Junping Chen, "Analysis of BDS satellite clock in orbit with ODTS and TWTT satelltie clock data," Preoceedings of China Satellite Navigation Conference (CSNC) 2018, in press.

[3] Fran B. Varnum, "Kalman filtering with a two-state clock model." Proceedings of the 15th Annual PTTI Meeting 1983. Washington, D.C., USA.

[4] P.V. Tryon and R.H. Jones, "Estimation of parameters in models for cesium beam atomic clocks," Journal of Research of the National Bureau of Standards. vol. 88, pp. 3–16, 1983.

[5] J.A. Davis, C.A. Greenhall, and P.W. Stacey, "A Kalman filter clock algorithm for use in the presence of flicker frequency modulation noise," Metrologia, vol. 42, pp. 1-10, 2005.

[6] M.J. Coleman, and Ken Senior, "A comparison of GPS clock models for the next generation GPS system timescale," Proceedings of the 43rd Annual Precise Time and Time Interval Systems and Applications Meeting. Long Beach, CA, 2011.

[7] Bhattarai S., "Satellite clock time offset prediction in global navigation satellite systems," Department of Civil, Environmental and Geomatic Engineering, University College London, 2014.

[8] Davis, John, "Use of Kalman filters in time and frequency analysis," Proceedings of the 25th European Frequency and Time Forum, 2011.

[9] Stein S R, Filler R L, "Kalman filter analysis for real time applications of clocks and oscillators," Proceedings of the 42nd Frequency Control Symposium, Baltimore, MD, USA, 1988.

Real Like Transmission Lines for Sagnac Correction Study

Martin Šlapák
Department of Photonic Networks
CESNET, a.l.e.
Prague; Czech Republic
Email: slapak@cesnet.cz

Josef Vojtěch
Department of Photonic Networks
CESNET, a.l.e.
Prague; Czech Republic
Email: vojtech@cesnet.cz

***Abstract*—The highly accurate time and frequency transfers need stable underlying line and knowledge of its parameters. The relativistic effects must be considered – especially at one-way transfers the Sagnac correction must be evaluated. In our previous work we proposed automated method for estimation of Sagnac correction for links with unknown or uncertain paths. This paper proposes a new idea of using artificial paths for comparison of Sagnac correction estimation approaches.**

I. Introduction

In our previous work [1] we proposed automated method for estimation of Sagnac correction for links with unknown or uncertain paths. The method was validated on four artificial lines and two real lines [2]. There are similar works [3], [4], [5] aiming to the estimation of Sagnac correction and its bounds based on limited knowledge of the lines. The mentioned works differ practically in the estimation of the lower and upper bounds.

The comparison of these approaches is a logical step. The major problem is the fact that no fiber line operator is willing to share even an approximate path of the line due to security reasons. The comparison can be made only on artificial paths with parameters of existing lines and real-like tracing. The real like tracing is an approach when the artificial path is projected and drawn into the map according to the practice of projecting a real optical infrastructure.

The concept of real like transmission lines brings us the ability to assemble the validation dataset of optical paths with properties similar to the existing optical lines. Such dataset can be used for comparison and validation of distinct approaches which cannot be compared directly on paths on which they are developed.

II. Benchmark real like optical paths

The intercity optical path is situated at its ends in the city infrastructure and the middle part goes through the suburban and countryside areas. When the fibre owner projects a new path they utilize at first the existing infrastructure. Only in necessary cases – often for the "last mile" the new trenches are excavated. From our experience with path projection we can state that the following infrastructure objects are used at the maximal possible extent: linear infrastructure objects like cable collectors in the city and along the railways or highways, along the gas or oil pipelines common cable collectors in the dense urban areas, metro's tunnels (when possible), bridges and sometimes the power lines.

There are also specific requirements for the benchmark paths. The paths should cover distinct use cases and given edge constraints. For the Sagnac correction there are interesting cases when paths go parallel to the meridians or equator on distinct latitudes. From the algorithmic point of view the mentioned edge constraints could be the case when path passes over the 180th meridian, contains loops or when the the path is situated on the south hemisphere of the Earth. Also the short range (endpoints are in the same city) or the longhaul paths with considerable amount of points should be incorporated into the benchmark dataset.

With respect to the criteria given above we proposed following six paths: Berlin–Poznan, Berlin–Ústí nad Labem, Bethel–Pakhachi, Düsseldorf (see Fig. 1), Karlskoga–Gustavberg, Sydney–Adelaide (see Fig. 2). For the basic parameters of paths see the table Tab. I. All these paths are publicly available as GPX files[1].

TABLE I
The overview of parameters of proposed benchmarking paths and the values of Sagnac correction computed by our algorithm.

Endpoints	Length [km]	Points	Sagnac correction [ps]
Berlin–Poznan	260	51	756.561 ± 0.415
Berlin–Ústí nad Labem	265	89	145.421 ± 0.317
Bethel–Pakhachi	1943	31	-4063.525 ± 63.392
Düsseldorf	30	46	-11.910 ± 0.010
Karlskoga–Gustavberg	260	99	582.180 ± 0.243
Sydney–Adelaide	1397	137	-5006.103 ± 10.037

III. Evaluation

At first we evaluated the proposed benchmarking paths with our algorithm [1]. The results of computed Sagnac correction are presented in the table Tab. I. The average uncertainty is 0.12 % (without Bethel–Pakhachi path) or 0.36 % with that longhaul path with small amount of points.

[1]https://photonics.cesnet.cz/en/sagnac-benchmark

978-1-5386-5620-4/18/$31.00 ©2018 IEEE

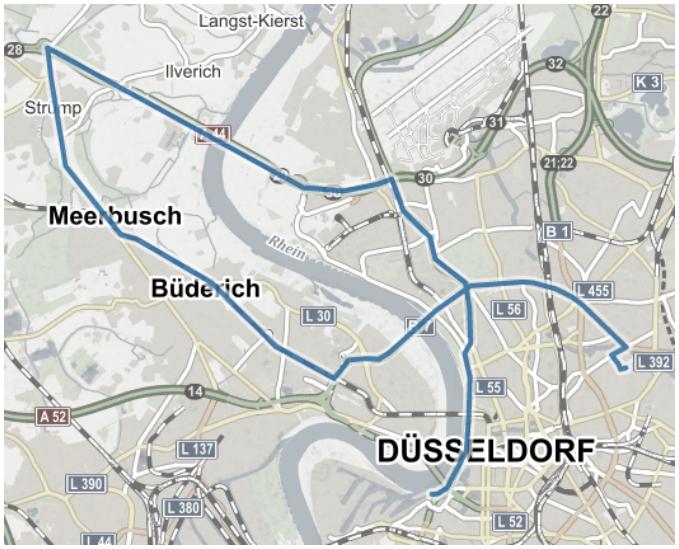

Fig. 1. The benchmark path with a loop in Düsseldorf.

Fig. 2. The benchmark path from Sydney to Adelaide.

The second step was the effort to compare the results of our algorithm with results proposed by [3], [4], [5] even when we have no access to the paths on which the authors evaluated their algorithms. In the work [4] aiming on longhaul lines, there authors used four paths where each of them consists only from two endpoints. Other two papers provided us a low resolution map – see Fig. 3 and Fig. 4. These maps served us as a reference for the paths. We aligned these maps to coordinate system and mapped all visible points to the WGS84 coordinate system. This process is a source of undefined uncertainty which cannot be avoided without a knowledge of the original paths.

The result of the comparison of all proposed algorithms are sumarized in the table Tab. II. The ”N/A” label in some cells means that the value was not available. In the 3rd column there are lengths estimated from the above mentioned maps (paths A* and B*). In case of paths C* there are values provided by online maps mapy.cz. Next column holds the values proclaimed by authors of compared works for relevant path. A certain inconsistency comes from the estimation based on available low resolution maps. The artificial mistakes could

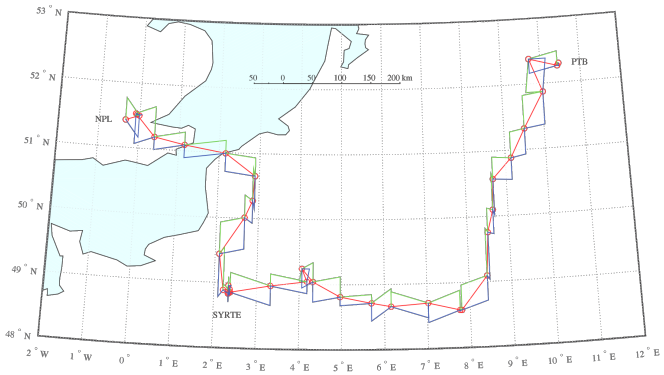

Fig. 3. Map 1. Paths PTB–SYTRE and NPL–SYTRE. (The source of graphics: [3]).

also be present in the maps for security reasons.

The estimations for paths A* are based on Map 1 (see Fig. 3) published in the paper of Geršl [3]. Even with maximal precision during estimation with calibrated map the path lengths differ suspiciously (139 % in the case of PTB-SYTRE and 156 % in the case NPL-SYTRE). The fibre must be significantly tangled.

The estimations for paths B* are based on Map 2 (see Fig. 4) published in the paper of Czubla [5]. The proclaimed length is on average on 126 % of the known path (direct connection of known points). It looks more realistic than the previous case.

The values of Sagnac correction presented in [3] are computed for the two-way transfer, therefore we derived the half value for the one-way transfer.

The authors of [5] proposed three methods. The first one – Method I – takes as input the direct connection between two endpoints. The Method II takes as input the the direct connection between two endpoints and also the known length of the fibre. This approach brings us more realistic estimation of uncertainty because we can compute the lower and upper bound of the correction. The last Method III takes as input the detailed path with lots of nodes. Authors of [5] take these values as a reference. The results of Method III lack the estimation of uncertainty.

The authors of [4] proclaim enumerated length of air-distance from the start to the endpoint. In the case of the path Prague-Rome the value 1189 km seems to be a mistake.

In all considered cases the paths estimated from maps are used as approximate paths with fixed known points. The path lengths proclaimed in papers were used as a ”real” fibre length for our algorithm [1]. This fiber length may differ from real-world length which is probably not known at least for paths published in [5] because of a very low number of points.

The average uncertainty achieved by our algorithm [1] on paths estimated from publicly accessible sources is 8,75 %. In the case of uncertainty achieved by authors of [3], [5] who know their paths, the averaged uncertainty is 3.5 %.

TABLE II

THE RESULTS OVERVIEW OF SAGNAC CORRECTIONS ON DISTINCT PATHS USED AS DEMONSTRATION FOR APPROACHES PROPOSED BY AUTHORS OF [3] (PATHS A1 AND A2), [5] (PATHS B3–B5) AND [4] (PATHS C6–C9). ALL PROPOSED PATHS WERE EVALUATED ALSO WITH OUR ALGORITHM [1].

				Original authors		Our approach		
Path #	Start-End point	Length on map [km]	Length proclaimed [km]	Correction [ps]	Uncertainty [ps]	Correction [ps]	Uncertainty [ps]	Comment
A1	PTB–SYTRE	1003	1401	3976	27			2-way transfer
				1988	27	-1952	10.4	path estimation 22 pts.
A2	NPL–SYTRE	520	813	1214	6			2-way transfer
				607	6	558	4.8	path estimation 14 pts.
B3	Poznan–Warsaw	290	360	885	3.5			method I
				884	19			method II
				885	N/A	879	5.1	method III; 2458 pts.; path estimation 7 pts.
B4	Poznan–Gdansk	394	530	350	16			method I
				350	35			method II
				369	N/A	371	4.5	method III; 7488 pts.; path estimation 14 pts.
B5	Poznan–Wroclaw	283	345	31	1			method I
				31	2			method II
				48	N/A	12.8	2.6	method III; 7292 pts.; path estimation 11 pts.
C6	Prague–London	1033	1024	-3290	N/A	-3322	45.4	
C7	Prague–Rome	922	1189	-635	N/A	-571	99.0	
C8	Prague–Moscow	1664	1667	4736	N/A	4700	574.8	
C9	Prague–Stockholm	1052	1054	686	N/A	681	165.7	

Fig. 4. Map 2. Paths from Poznan to Warsaw, Gdansk and Wroclaw. (The source of graphics: [5]).

IV. CONCLUSION

The results show that in the case when we have the knowledge of the optical fibre path we are capable to achieve at least two times lower uncertainty. Our algorithm [1] achieved average uncertainty 0.36 % on detailed known paths and 8.75 % on paths estimated from publicly available sources. The authors of [3], [5] achieved uncertainty 3.58 % on detailed known paths. Therefore it can be stated that the proposed benchmarking path dataset provides the essential basis for more precise comparison of different approaches to calculation of Sagnac correction when the sharing of detailed knowledge of fibre path is not possible.

ACKNOWLEDGMENT

This work was supported partially by the Ministry of Education, Youth and Sport of the Czech Republic as part of the E-infrastructure CESNET project LM2015042 and by the project ”E infrastructure CESNET – modernization”, reg. nr. CZ.02.1.01/0.0/0.0/16_013/0001797.

REFERENCES

[1] M. Šlapák, J. Vojtěch, and R. Velc, “Automated numerical calculation of sagnac correction for photonic paths,” *Optics Communications*, vol. 389, pp. 230–233, 2017.

[2] J. Vojtěch, M. Šlapák, P. Škoda, V. Smotlacha, R. Velc, P. Münster, J. Kundrát, O. Havliš, L. Altmannová, and M. Altmann, “Precise time transfer on the ipe-vugkt line-a detailed analysis,” in *Telecommunications and Signal Processing (TSP), 2016 39th International Conference on*. IEEE, 2016, pp. 757–760.

[3] J. Geršl, P. Delva, and P. Wolf, “Relativistic corrections for time and frequency transfer in optical fibres,” *Metrologia*, vol. 52, no. 4, p. 552, 2015.

[4] Y. Longqiang, L. Lin, W. R. J. Jisong, W. Chuanxin, Z. Yong, and Z. Baofu, “Analysis of the sagnac effect on the accuracy of the long haul optical fiber time transfer system,” in *European Frequency and Time Forum International Frequency Control Symposium (EFTF/IFC), 2013 Joint*, July 2013, pp. 303–305.

[5] A. Czubla, P. Krehlik, L. Śliwczyński, J. Kolodziej, A. Binczewski, K. Turza, W. Bogacki, and P. Rydlichowski, “Some approximated methods of calculation sagnac correction for optical fiber time transfer,” in *Frequency and Time Forum and IEEE International Frequency Control Symposium (EFTF/IFC), 2017 Joint Conference of the European*. IEEE, 2017, pp. 399–401.

Bidirectional optical amplifier delivering high gain

Ondrej Havlis[1], Josef Vojtech[1], Radek Velc[1], Martin Slapak[1], Miloslav Hula[1], Jan Radil[1] Smotlacha Vladimir[2], Kolbe Martin[2],
Email: {havlis,vojtech,slapak,radek,hula,radil,vs,kolbemar}@cesnet.cz
[1]Department of Optical Networks, CESNET, Prague, Czech Republic
[2]Department of Technology for network applications, CESNET, Prague, Czech Republic

***Abstract*—For long distance transmission of highly accurate time or stable frequency it is important to keep the reciprocal propagation path. It allows us to improve transmission stability (slow effect will cancel in first order) and also to establish active compensation of propagation fluctuations. Unfortunately, single fiber transmission introduces necessity of bidirectional symmetrical amplifiers in order not to lose advantage of a reciprocal path. In case of time transfer, quasi-bidirectional amplification might be acceptable. It means that amplifiers contain short nonreciprocal path, e.g. wavelength routers or even active fibers. But the ultra-stable frequency transfer requires truly single path optical amplifiers that are considered further. This paper proposes the new idea of using bidirectional EDFA amplifier with optical channel monitor for to detect and suppress unwanted laser of amplifier.**

Keywords—CLA BiDi NoLase; T&F; bidirectional amplification; EDFA; OCM

I. INTRODUCTION

The motivation for design and development of the bidirectional amplifier CLA BiDi NoLase were applications of precise time and stable frequency (T&F) transfer in an optical fibre where unwanted oscillations can occur within the transfer of T&F. This very device was developed exactly to suppress these undesirable oscillations. One of the main tasks for metrology is comparison of precise T&F, or distribution from stabilized normal respectively, e.g. from atomic clock. In recent decade, more and more often there are common optical fibres used for T&F transfers. The speed of optical signal transmission is given by refractive index which depends not only on wavelength but e.g. also on changing temperature. Other significant influences are polarization and mechanical influence of the optical fibre environment: vibrations, bends, tension and other influences. E.g., regarding a buried fibre with the length of 100 km, there are typical diurnal fluctuations of 1ns, and about 100 ns within a year caused exclusively by temperature changes. For required hi-performance T&F transfers, we have to use a method based on concurrent propagation of the signal in both directions to enable measurements and compensations of the changing propagation delays or frequencies.

Within T&F transfers on optical fibres the basic assumption is utilized, i.e. the time of transmission there and back is the same, or it differs with exactly known value, e.g. because of the various lengths of the fibres or various wavelength. This difference must be determined by calibration, yet another difference can occur by various circumstances, e.g. by service anywhere on the path, or just by the changed environment which influences each transmission fibre individually. Because of the reasons mentioned above, it is very suitable to use single fibre solution. Such a solution eliminates also the troubles with differences caused by temperature influence (length of the fibre, refractive index). This preferred solution is verified and based on experience with the real lines where the results show triple reduction of white phase noise.

For such optical bidirectional amplifier suitable for T&F transfers within the telecommunication data network, there are relatively demanding requirements:

- ability to operate in that part of telecommunication spectrum where the attenuation of the standardized single-mode optical fibres (SMF) is at the lowest level,
- should be able to reach gains common for telecommunication transmissions (20+ dB),
- must have noise figure as lowest as possible,
- should be broadband enough to be able to amplify more transmissions without influencing each other.

II. BIDIRECTIONAL AMPLIFICATION

In the fibre optics field, most amplifiers being used are those with fibres doped by ions of rare earths, for telecommunication bands specifically Erbium is used (Erbium Doped Fibre Amplifier - EDFA), then amplifiers using stimulated Raman scattering and semiconductor optical amplifiers. Semiconductor amplifiers can be designed and used for more or less any spectral transmission window of SMF, yet they do not completely fulfil the requirements for not influencing of amplified channels and low attenuation value. Raman amplifiers also allow to be used for any spectral transmission window, they have low noise figure, they provide no influencing of the transmitted signals but because of relatively low efficiency, they require very high powers directly in the transmission fibre (27 dBm). Theoretically, also amplifiers based on Brillouin dispersion can be used; unfortunately their operational band is very narrow, approx. 10 MHz. Natural request on high and broadband gain together

with multi-channel operation unfortunately exclude SOAs (as they have limited possibility of multichannel operation [1]), Raman amplifiers (as they provide only moderate gains in common telecommunication fibers due to low gain coefficient [2]) and also Brillouin amplifiers (as their gain bandwidth is very limited [3]).

The EDFAs can deliver high small signal gains (e.g. over 30 dB) but are very sensitive to unwanted oscillations. It is very difficult to avoid these oscillations as they are caused by feedback provided from two sources: Rayleigh backscattering and reflection from fiber splices, connectors and passive components.

III. EDFA AMPLIFIERS

Amplifiers with the fibre doped with Erbium are able to provide high gains (up to 30 dB) in an operational area approx. from 1530 to 1610nm without mutual influencing amplified channels with low noise figure. Fig. 1 shows operation principle of such amplifier. Ions Er^{3+} are excited by optical pumping to metastable layer E3 which they leave within spontaneous non-radiation transition for layer E2. From this layer they go over by stimulated emission with present photons with suitable wavelength within radiation transition to basic energetic layer E1.

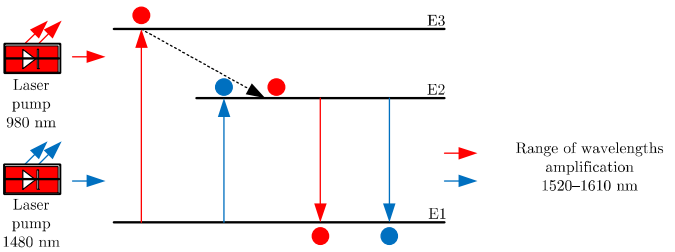

Fig. 1. Operation principle of the optical amplifier with Erbium doped fibre [4]

Fig. 2 describes block schema of EDFA amplifier components of both, the basic and the enhanced type. The basic arrangement consists of the main elements as a laser pump with 980 nm or 1480 nm wavelength which can be installed at frontward, backward or both directions, then there is a multiplexor and a special optical fibre doped with Erbium Er^{3+}. Inside the multiplexor there are the weak transmitted signal and the laser pump signal being merged. This merged signal enters the Erbium Er^{3+} doped optical fibre where the stimulated emission generates new photons with similar wavelength and therefore the signal is amplified. Except these basic elements, there are other parts improving its functionality, these are shown in Fig. 2 in enhanced disposition. The couple of optical isolators connected to each side of the fibre prevent the back radiation propagation of the signal to cause any damage on the laser. Isolator on the input of the amplifier prevents the radiation emitted during spontaneous emission from disrupting the previous phase of amplification. The isolator on the output prevents from transmission of laser beams and any damage in case the output beam is reflected back to the amplifier.

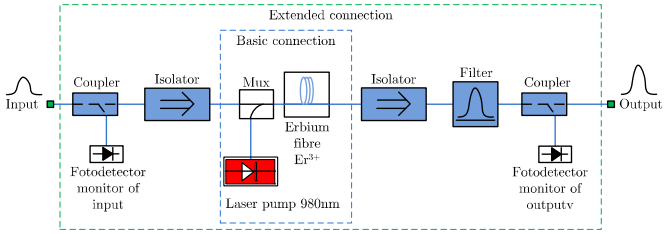

Fig. 2. Scheme of unidirectional optical amplifier with Erbium doped fibre

Behind the output insulator of the amplifier, there is an optical filter connected in most cases, for suitable corrections of the amplified signal. The filter ensures flattening the gain curve in the C band which has the maximum value at 1530 nm as can be seen in Fig 3. They are also couplers there which separate a very small part of optical signal to connected photodetectors which monitor power levels of the optical signal at the input and output of the EDFA amplifier.

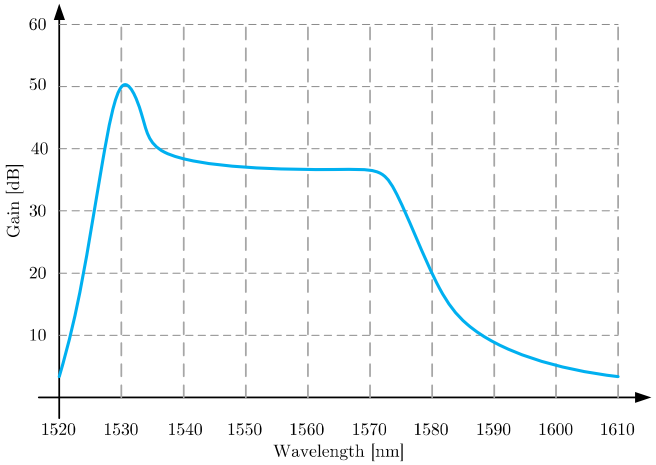

Fig. 3. Principle of unidirectional optical amplifier with Erbium doped fibre [4]

For the amplifier, see Fig. 2, to work bidirectionally, in fact only isolators must be removed. In such connection the amplification would not be symmetrical and the signals being propagated to one direction would be amplified with different gain than the signals to the other direction. This trouble can be solved by symmetrisation of the connection where the energy of the pumping laser would be fed to the Erbium fibre from both sides, as shown in Fig. 4 where you can also see "star" directional branches being added to enable monitoring of input and output levels for both directions.

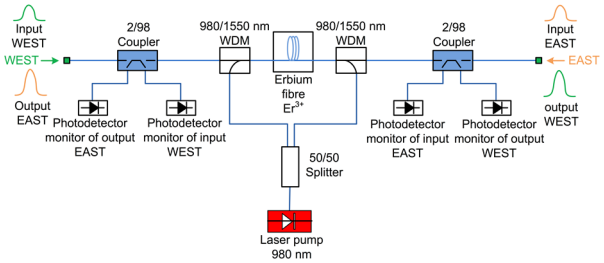

Fig. 4. Scheme of bidirectional optical amplifier with Erbium doped fibre

Above, we described the device amplifying signals being propagated in both directions inside one physical media. Within the signal propagation in an optical fibre, backscattering occurs [5] and also other reflections caused by non-homogeneities like splices, and especially the connectors. These phenomena are not a problem at all in case of common unidirectional transmission, yet within bidirectional transmission, these are being amplified as well. This causes decreasing of the optical signal to noise ratio (OSNR), in case of a high gain such backscattering together with reflections might cause feedbacks and the whole optical amplifier comes to vibrations, typically in the area of maximal gain, see Fig. 5 and the very undesirable phenomena occur, i.e. oscillation or spontaneous lasering. This fact limits the maximal usable gain, as mentioned in literature [6], practically the maximal reachable gain is approx. 22 dB.

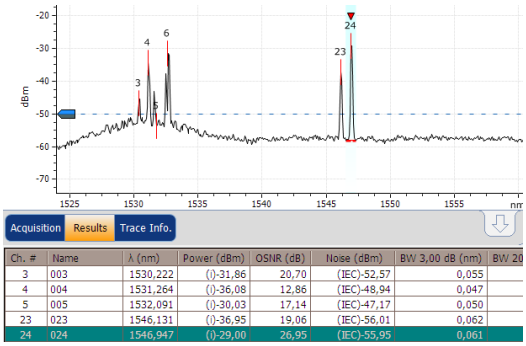

Fig. 5. Sample measurement in the transmission line where the bidirectional amplifier vibrates spontaneously (left part of spectrum)

Vibrating is uncontrollable in both, spectral and amplitude way. Especially, it causes exhaustion of carriers (Er^{3+} ions on higher energetic layer) which influences in a negative way the amplification of signals spectrally located out of the area of these oscillations.

In practise, the reflections inside real optical lines can be changed after any servicing but also after any manipulation with the fibres. If we want to reach maximal available gain without spontaneous vibrating/lasering, it is necessary to have the possibility of check-up whether the vibrating occurs or not. Therefore, we place in the device a module of optical channel monitor (OCM) which is connected by branches to outputs of the active fibre, see Fig. 6. It allows efficient monitoring of the signal spectrum output of active fibres.

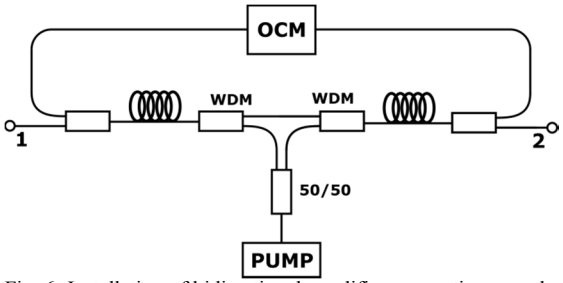

Fig. 6. Installation of bidirectional amplifier connection complemented with a monitoring module

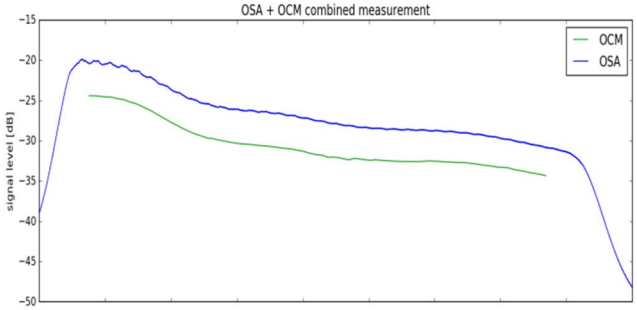

Fig. 7. Amplified spontaneous emission of the amplifier (I_{pump} = 150 mA) measured by the filter and verified by spectral analyser

We then designed the installation for manageable creation of back reflections in the way we could further examine and verify the system of detection of undesirable oscillations. This installation is shown on Fig. 8. The signal entering the bidirectional amplifier from both sides is attenuated with 18 dB by a fibre 100 km long. This fibre also generates back scattering. Additional reflections are made by mirrors through attenuators connected also to input of the amplifier. One of the attenuators is variable so the level of reflection is manageable.

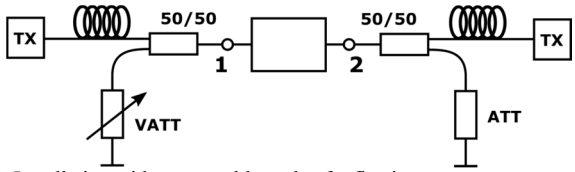

Fig. 8. Installation with manageable scale of reflections

IV. Measurements and Results

The wavelength and intensity of undesirable lasering significantly changes over time. Graphs in Fig. 9 and Fig. 10 show the record of 50 measurements by module OCM (with a period of approx. 1 second). At the wavelengths of 1546.12 nm and 1546.92 nm, there is the useful signal transmitted, at the low wavelengths, see Fig. 9 (in the Fig. on the left side) there is recorded lasering (vibrating/oscillations), see Fig. 10. The first graph shows the current of the pumping diod 100 mA and the lasering has not occured yet. In the other graph with the current 105 mA, there is the lasering clearly apparent.

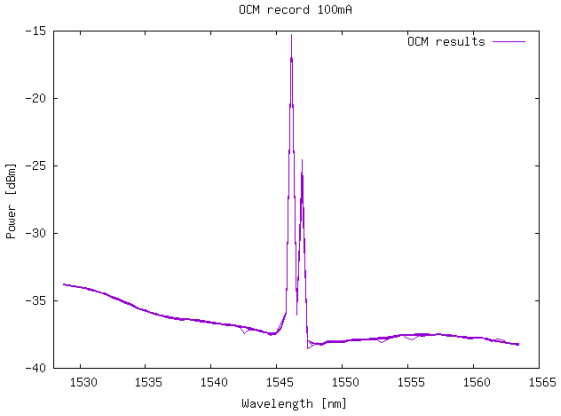

Fig. 9. Time stability of the output spectrum in the situation without the undesirable oscillation being present

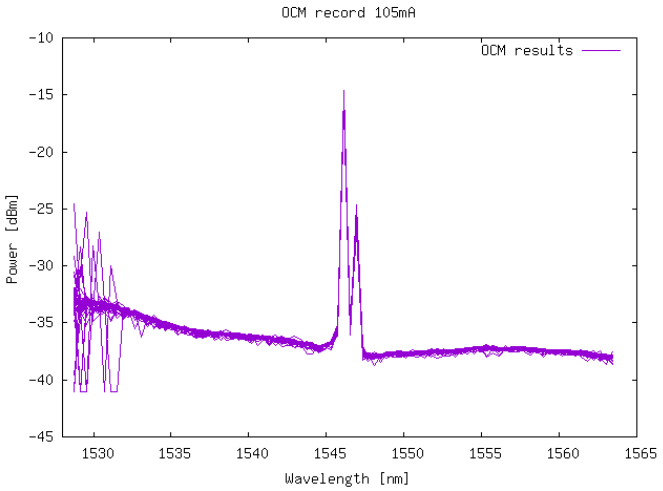

Fig. 10. Time stability of the output spectrum in the situation with the undesirable oscillation being present

The basic idea of the detection of unwanted lasering is based on the fact such lasering has higher dispersion of both, amplitude and position of the wavelength where it occurs compared to common noise. When averaging sufficient amount of samples, see Fig. 11), the noise practically disappears, yet lasering phenomena is apparent even with higher scale of average value of the signal in the area of lasering. After deducting the average from the specific measurement the detected peaks keep being caused by lasering.

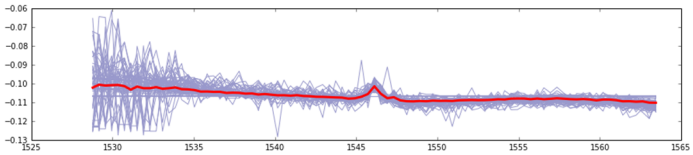

Fig. 11. Normalized partial processes of 72 measurements by OCM (blue) with supressed local maximum in the area of 1446 nm and the resulting average value (red)

The measured process by OCM detects positive local maxima at first, and these are substituted with the average from the annular environment to a distance of 5 and a width of 3. Such a procedure flattens the signal process and suppresses maximum values at the wavelength where the laser radiation is legitimate. The amplitude in the area of undesirable lasering is not influenced that much by application of above mentioned filter compared to the influence on the chosen and selected wavelength of the used laser we work with. In case of utilizing the detection of undesirable lasering measured on laser operating exclusively on the given wavelength, it is possible to filter this local maximum of the signal level in a more efficiently.

Then the data is normalized to the range of 0-1. There is the average value of calibration measurements deducted from the measurement currently being processed. The differences are squared, see Fig. 12 down. If the resulting signal exceeds the threshold value 0.00025, the lasering is detected. In the other case it can be said that based on data from OCM the undesirable lasering cannot be detected. The threshold value 0.00025 was determined experimentally.

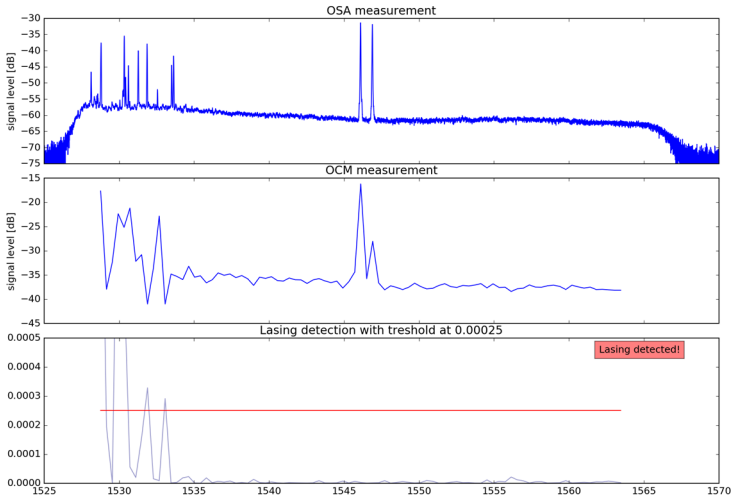

Fig. 12. For comparison, there are measurements by OSA (top), by OCM (middle) and currently processed signal (bottom blue) with marked threshold value 0.00025 which is limitation for detection of unwanted lasering

Fig. 13. Functional sample of bidirectional optical amplifier which enables both direction signal propagation in one media and detection of undesirable lasering CLA BiDi NoLase built in standardized rack 1U chassis

V. Conclusion

CLA BiDi NoLase equipped with detector of unwanted oscillations allows us to achieve higher gain compared with legacy approach which keeps safe low gain. We will continue to develop this device and would like to deploy it in our CESNET2 network, which currently allows the transfer of ultra-stable quantities with a total length over 1200 km.

Acknowledgment

This work was supported partially by the Ministry of Education, Youth and Sport of the Czech Republic as part of the CESNET E-infrastructure project LM2015042 and by the project "E infrastructure CESNET - modernization", reg. nr. CZ.02.1.01/0.0/0.0/16_013/0001797.

References

[1] Vojtech, J., Radil, J., and Smotlacha, V., "Semiconductor Optical Amplifier with Holding Beam Injection for Single Path Accurate Time Transmission," Proc. CLEO, JTh2A.78 (2015).

[2] Clivati, C., "Distributed Raman Amplification for long-haul optical frequency dissemination," Proc. IFCS-EFTF-SPC, 184 (2013).

[3] Droste, S. et al., "Optical Frequency Transfer over a Single-span 1840 km Fiber Link," Proc. IFCS-EFTF-SPC, 183 (2013).

[4] BECKER, P. C., N. A. OLSSON a J. R. SIMPSON. Erbium-doped ber am- pli ers: fundamentals and technology. San Diego: Academic Press, c1999. ISBN 978-0120845903.

[5] Masataka Nakazawa, "Rayleigh backscattering theory for single-mode optical fibers," J. Opt. Soc. Am. 73, 1175-1180 (1983).

[6] Vojtech, J., Smotlacha, V., and Radil, J., "All optical two-way time transfer in strongly heterogeneous networks," Proc. SPIE 9202, 92020S (2014).

Remote atomic clock contribution to UTC(TP)

Vladimir Smotlacha
CESNET, z.s.p.o.
Prague, Czech Republic

Alexander Kuna
Institute of Photonics and Electronics, Czech Academy of Sciences
Prague, Czech Republic

***Abstract*—This document describes usage of optical network for linking of remote atomic clock to the Institute of Photonics and Electronics where is maintained the UTC(TP) time scale.**

Keywords—time transfer, optical network, atomic clock

I. INTRODUCTION

The Laboratory of the National Time and Frequency Standard (LNTFS) in the Institute of Photonics and Electronics (UFE) generates the Czech national timescale denoted as UTC(TP) as a local physical approximation of the Universal Coordinated Time – UTC. The Laboratory is a designated institute of the Czech Metrology Institutes, who is responsible for maintaining almost all of the national standards in the Czech Republic.

II. THE TIMESCALE UTC(TP)

The Laboratory operates a pair of high performance Cesium clocks (5071A). One of the clock serves as a master generating the national timescale UTC(TP), the other one is spare used as a backup in case of failure or maintenance such as cesium tube replacement in the master clock. Both of these clocks are reported to the BIPM for contribution to the calculation of the UTC and UTCr within the key comparison CCTF-K001.UTC and Rapid UTC project of the BIPM [1].

Among the atomic clocks in the LNTFS, there are several other atomic standards operated by independent institutes and organizations. This list includes:

- CETIN (former Telefónica O_2 or Czech Telecom)

This institute operates two high performance Cesium clocks type 5071A. These clocks are linked to the LNTFS using dedicated optical fibers of the length about 10 km. The time differences UTC(TP) – AT(c) are continuously measured and reported to the BIPM on monthly basis since 1995 and on daily basis since 2016.

- Geodetic Observatory (VUGTK)

The institute, which is located about 50 km south-east from Prague, operates one Cesium clock type 5071A and one passive hydrogen maser. The Cesium clock is reported to the BIPM on daily and monthly basis since 2016. Details about optical path to UFE are described in next session.

- CESNET

CESNET is an institute which operates own optical network in order to provide Internet connectivity and other services to the Czech universities and research organizations. CESNET operates Cs clock 5071A located in its Prague headquarter. The clock is linked to the UTC(TP) since 2015?

- Faculty of Electrical Engineering (FEL)

The Department of Measurement at the Faculty of Electrical Engineering of the Czech Technical University in Prague also operates their own Cs clock 5071A. The clock is linked to the UTC(TP) and reported to the BIPM on daily and monthly basis since 2017.

- Institute of Scientific Instruments (ISI)

The Institute of Scientific Instruments is part of the Czech Academy of Sciences. Its research activities include coherent optics and the institute operates active H-maser. The institute is located in Brno, about 200 km south-east from Prague. The clock is currently experimentally linked to the Cs clock in CESNET.

III. TF-INFRASTRUCTURE

CESNET, the Czech NREN (National Research and Education Network) started development of Time and Frequency (TF) infrastructure in 2011 [2]. The total length of utilized links is more than 1600 km and majority of the infrastructure fibers are in routine operation, as shown at Figure 1. The model of joint TF and data channels has been chosen because of high fiber rental costs. The infrastructure is based on wavelength division multiplexing (WDM) and allows parallel transfer of radio frequency (RF) modulated time and stable optical frequency [3]. The two way time transfer is based on our own Time Transfer Adapters (TTAs), which have been designed using Field Programmable Gate Array (FPGA), for more details see [4]. TTAs are able of operation in very heterogeneous environments, including: multimode fibers, single mode dedicated fibers, telecom lambdas, and passive channels within other WDM systems. Also the transmission is performed over both single fiber bidirectional channel and also over traditional fiber pair setups. More details can be found here [5]. Recent progress in TF-infrastructure is operation of stabilized transfer of optical frequency between ISI and CESNET (306 km of fiber). Transmitting laser is locked to highly stable acetylene cavity. It is an important step towards future optical clock. More details are published in [6].

The TF-infrastructure is utilized for linking of all clocks mentioned in previous chapter, the only one exception are clocks operated by CETIN, as this telecommunication operator provides its own dedicate fiber.

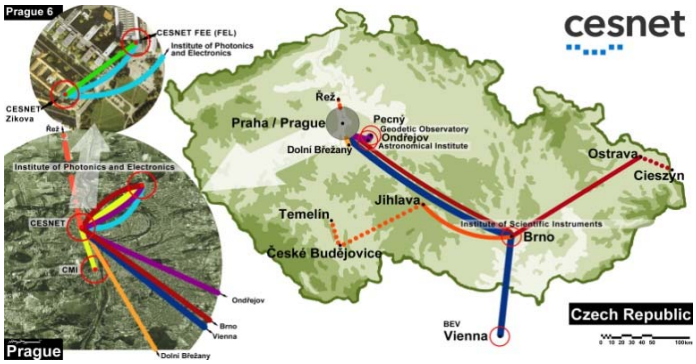

Fig. 1. Map of TF-infrastructure

A. Optical path VUGTK – UFE

The path between UFE and VUGTK (Geodetic Observatory in Pecny) consists of two parts: one is 200 GHz reserved bandwidth in fiber shared with standard data service (N x 10 Gb/s) between CESNET and VUGTK, and 200 GHz reserved bandwidth within DWDM multiplex running over CWDM (Coarse Wavelength-division Multiplexing) network channel in the Prague metropolitan network between UFE and CESNET. The first part is 78 km long with attenuation of 22 dB, the second part is only 17 km long with attenuation of 21 dB. Between both parts is installed a single path bidirectional optical amplifier. The schematic is depicted in Fig. 3. The link setup reserves four unamplified wavelengths in 50 GHz ITU grid for time transfer.

B. Optical paths CESNET – UFE and FEL – UFE

The link between CESNET and UFE utilizing CWDM system in Prague metropolitan network, which is part of link VUGTK – UFE, is also used for time transfer CESNET – UFE and FEL – UFE. In reality, they all share the same fiber running at different wavelengths. As these paths are only 17 (resp. 18) km long, no optical amplification is required.

C. Optical link CESNET – UPT

The time transfer link between CESNET and UPT (Institute of Scientific Instruments) in Brno uses reserved bandwidth in CESNET experimental link Prague – Brno. While data channels utilize a pair of unidirectional fibers, the time transfer is implemented as bidirectional single fiber. Structure of the link is showed in Fig. 4. The link length is 306 km and has attenuation of 85 dB including two extensive 26 and 28 dB spans. The link from UPT currently ends in CESNET. We plan to extend it to UFE in near future, until now the time transfer to UFE is done indirectly, using Cesium clock in CESNET.

D. Time transfer method

The main application of the TF infrastructure is time transfer. We use the two-way method based on our own Time Transfer Adapters (TTAs) [2] with symmetrical setup. Each adapter transmits time signal to the opposite site, where the received time scale is compared with local time scale. An important issue here is to ensure that the propagation time is the same for both directions $\delta = \delta AB = \delta BA$. Alternatively the difference Δ needs to be known – either calculated or measured in phase of calibration. TTAs can be operated either using a pair of unidirectional fibers or single bidirectional fiber.

Although we operate also time transfer between UFE and BEV (Vienna) which utilizes pair of fibers, all time transfers described in this paper use single bidirectional fiber. In such case, different wavelengths in both directions have to be used and the propagation delay is not equal due to the refractive index, which value is wavelength dependent for fiber. Difference in propagation time of two signals with wavelength difference $\Delta\lambda$ is done by the rule:

$$\Delta T = d \cdot L \cdot \Delta\lambda \qquad (1)$$

where L is length of the fiber. A standard single mode fiber has refractive index coefficient around of d = 17.5 ps/nm/km.

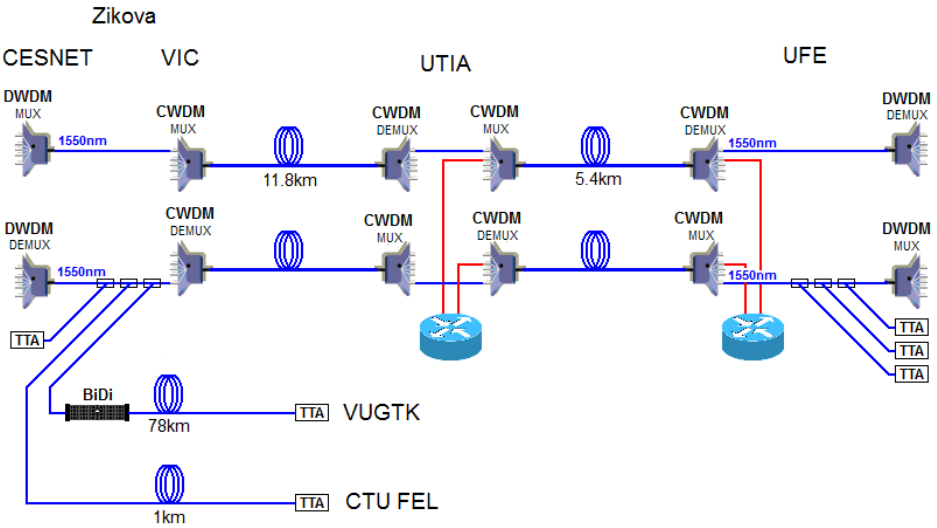

Fig. 2. Optical path VUGTK - FEL - CESNET - UFE

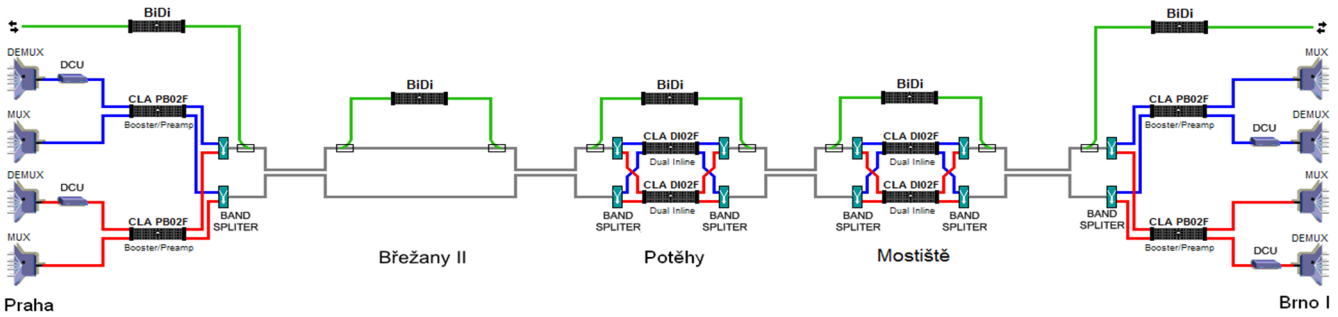

Fig. 3. Optical path UPT - CESNET

III. RESULTS

Time laboratory in UFE, continuously reproduces remote clocks time scale – it calculates difference between local clock and remote clock 1 PPS signals. Using these results, data in CGGTTS format are also calculated. Graphs at Figs. 4., 5, and 6. represent comparison between UTC(TP) and clock in CESNET, VUGTK and FEL. We can see lost signal in Fig. 4., while steps in Fig. 5. and 6. are an intentional time scale steps in VUGTK and FEL.

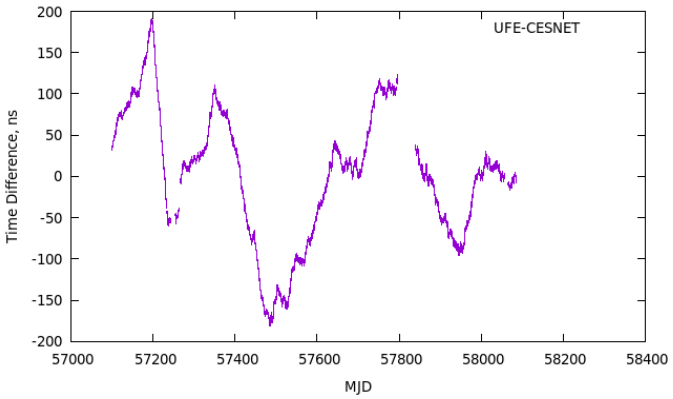

Fig. 4. Comparison of UFE and CESNET time scale

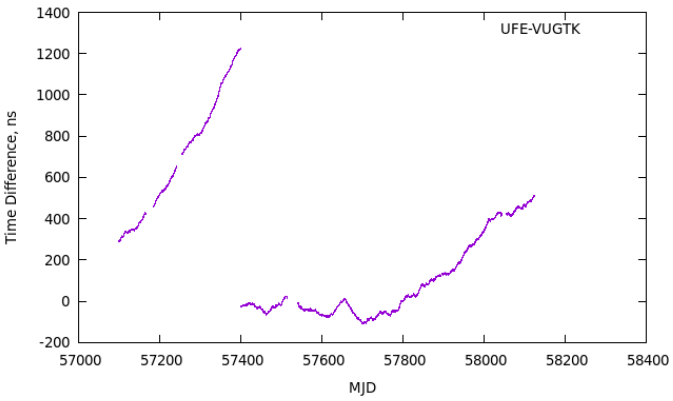

Fig. 5. Comparison of UFE and VUGTK time scale

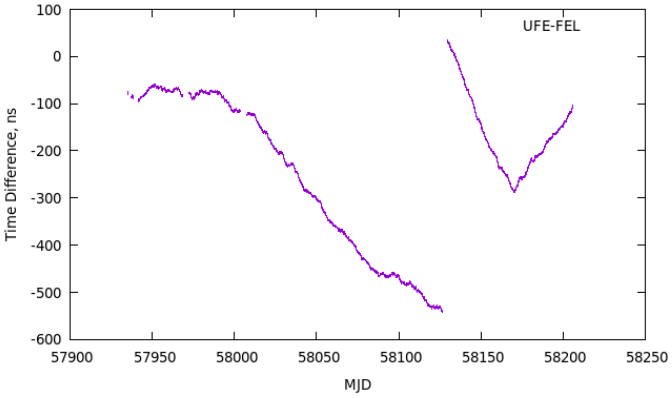

Fig. 6. Comparison of UFE and FEL time scale

We have evaluated our time transfer method based on TTAs using180 km long field deployed fiber loop. The performance in term of TDEV is shown in Fig. 7. We see that TDEV is below 10 ps for averaging interval 16 s and longer.

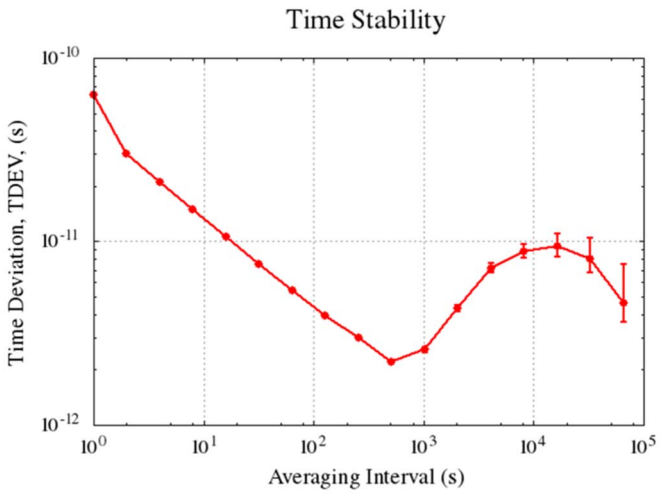

Fig. 7. Stability of time transfer method

We calculated TDEV between UFE and three of linked clocks: CESNET, VUGTK and UPT as shown in Figs. 8., 9., and 10.

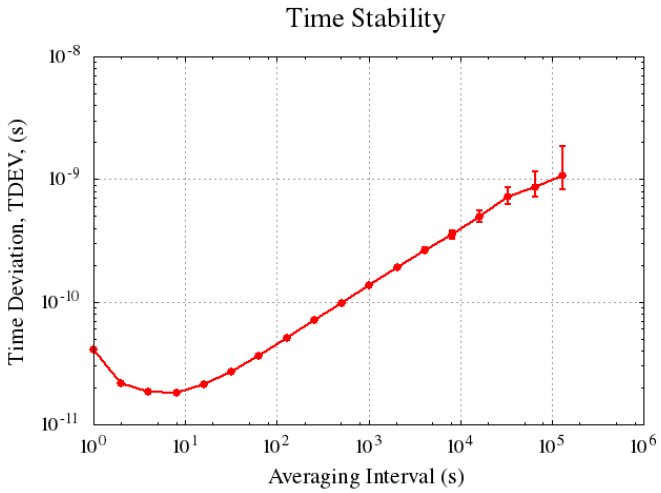

Fig. 8. TDEV of clock in CESNET

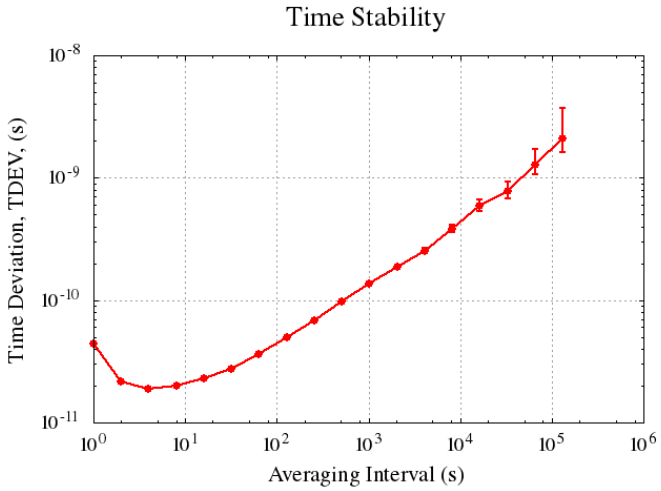

Fig. 9. TDEV of clock in VUGTK

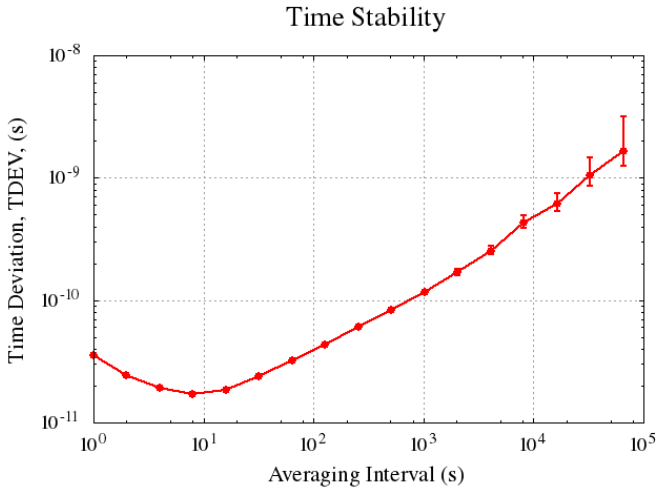

Fig. 10. TDEV of clock in UPT

IV. CONCLUSIONS

We linked 3 additional cesium clocks to UTC(TP), all of them are reported to BIPM. In experimental phase is indirect linking of another H-maser. For this purpose we utilize TF-infrastructure that has been built on top of Czech academic network CESNET. According to performed measurement, we can conclude that time transfer method adds uncertainty not exceeding 10 ps when clocks are reporting using CGGTTS format – i.e. the cesium clock time scale is not degraded using our time transfer method.

ACKNOWLEDGMENT

This work was supported partially by the Ministry of Education, Youth and Sport of the Czech Republic as part of the E-infrastructure CESNET project LM2015042

REFERENCES

[1] G Petit, F Arias, A Harmegnies, G Panfilo and L Tisserand, “UTCr: a rapid realization of UTC”, Metrologia, Vol. 51, No. 1.

[2] V. Smotlacha, J.Vojtech, A. Kuna, "Optical infrastructure for time and frequency transfer", Proc. EFTF, 2013

[3] M. Cizek, et al, "Transfer of stable optical frequency for sensory networks via 306 km optical fiber link, Proc. EFTF, 2016.

[4] V. Smotlacha, J.Vojtech, A. Kuna, “Two-way optical time and frequency transfer between IPE and BEV”, Proc. EFTF, pp. 375–378, 2012.

[5] J. Vojtech, V. Smotlacha, P. Skoda, “Simultaneous transmission of accurate time in parallel with stable optical frequency in real fibre network over 612 km,” Proc. OPTOELECTRONICS GLOBAL CONFERENCE (OGC), pp. 39-41, (2015).

[6] M. Cizek, at al., "Phase-coherent transfer of optical frequency between ISI CAS and CESNET", EFTF, 2018.

Absolute frequency measurement of the ytterbium ion E3 optical clock transition using international atomic time

Rachel M. Godun[1], Charles F. A. Baynham[1,2], Jonathan M. Jones[1,3], Steven A. King[1], Peter B. R. Nisbet-Jones[1], Fred Baynes[1], Antoine Rolland[1], Patrick E. G. Baird[2], Kai Bongs[3], Patrick Gill[1], Gérard Petit[4], Helen S. Margolis[1]

[1]National Physical Laboratory, Teddington, UK
[2]Clarendon Laboratory, University of Oxford, Oxford, UK
[3]School of Physics and Astronomy, University of Birmingham, Birmingham, UK
[4]Time Department, International Bureau of Weights and Measures (BIPM), Sèvres, France

***Abstract*—We report a revised absolute frequency measurement of the $^{171}Yb^{+}$ electric octupole optical clock transition of 642 121 496 772 645.17(22) Hz, with a fractional uncertainty of 3.4×10^{-16}. This newer value, with lower uncertainty, is achieved through additional analysis of previously reported experimental data that links the optical frequency to the SI second through international atomic time (TAI). The new step in the data analysis involves a special computation of the fractional frequency offset between the scale interval of TAI and the SI second, over a time interval more closely matched to the experimental data acquisition period.**

Keywords—frequency metrology; optical frequency standards; international atomic time

I. INTRODUCTION

It is anticipated that there will be a future redefinition of the SI second in terms of an optical frequency standard. When this occurs, it is essential that the new definition is consistent with the existing definition to within the uncertainty with which the primary frequency standards realize that definition. It is therefore necessary, ahead of the redefinition, to make high accuracy absolute frequency measurements of the candidate optical reference transitions. In this paper, we present an absolute frequency value for the electric octupole (*E3:* $^{2}S_{1/2} \rightarrow {}^{2}F_{7/2}$) optical clock transition in $^{171}Yb^{+}$, with the lowest reported uncertainty to date.

The most direct approach to measuring absolute frequencies of optical standards is by comparison to local caesium primary standards, which provide a realization of the SI second. The best reported absolute frequency measurement of the $^{171}Yb^{+}$ *E3* optical transition against local caesium standards has been carried out at the Physikalisch-Technische Bundesanstalt (PTB) and has an uncertainty of 3.9×10^{-16} [1].

Alternatively, however, the SI second can be accessed via a frequency link to International Atomic Time (TAI) [2-7]. Most measurements carried out in this way suffer a degradation due to additional uncertainty introduced by non-continuous operation of the optical frequency standard during the measurement period. To date, only one other group has reached an uncertainty below 1×10^{-15} [6, 7] for a TAI-based absolute frequency measurement. This relied on special computations of the fractional frequency offset *d* between the scale interval of TAI and the SI second, calculated for shorter periods than the one-month mean value that is routinely reported by the International Bureau of Weights and Measures (BIPM). We have previously reported that we have been able to measure a TAI-based absolute frequency of the $^{171}Yb^{+}$ *E3* transition with an uncertainty of 4.0×10^{-16} *without* needing to use a special computation of *d* [8]. This was achievable because of the high up-time attained with our optical standard, which was operational for 76% of a 25-day period in June 2015. In this paper, we now re-analyze that same experimental data, but this time *with* a special computation of the fractional frequency offset *d* between the scale interval of TAI and the SI second to reduce the uncertainty of the absolute frequency still further.

II. EXPERIMENTAL OVERVIEW

As described in [8], the National Physical Laboratory's $^{171}Yb^{+}$ *E3* optical frequency standard was operated over a 25-day period in June 2015. Traceability to the SI second was provided by a frequency link to TAI, which was achieved via the frequency chain depicted in Fig. 1. In the first step of this chain (shown by the blue arrow and data in Fig. 1), a femtosecond frequency comb was used to measure the Yb^{+} optical frequency relative to the 10 MHz output of the hydrogen maser that maintains UTC(NPL). In the second step (shown in yellow), the local timescale UTC(NPL) was compared continuously to TAI via satellite-based time and frequency transfer. The resulting frequency offset between UTC(NPL) and TAI was derived from the BIPM monthly bulletin Circular T. In the final step (shown in green), a

This work was financially supported by the UK Department for Business, Energy and Industrial Strategy as part of the National Measurement System Programme; the European Metrology Research Programme (EMRP) project SIB55-ITOC; and the European Metrology Programme for Innovation and Research (EMPIR) project 15SIB03-OC18. This project has received funding from the EMPIR programme co-financed by the Participating States and from the European Union's Horizon 2020 research and innovation programme. The EMRP is jointly funded by theEMRPparticipating countrieswithin EURAMET and the European Union.

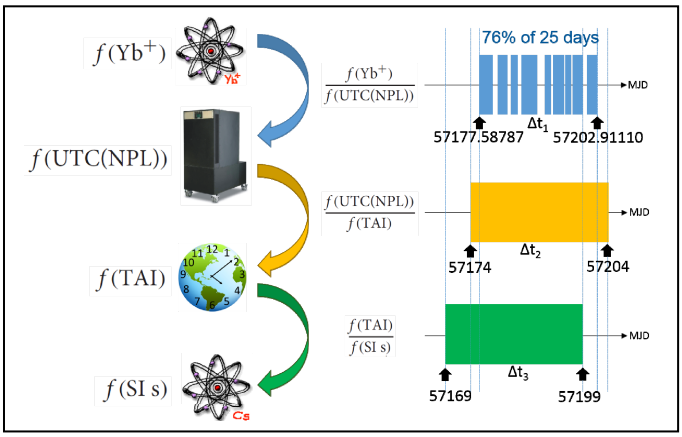

Fig 1. Shown on the left is the chain of frequency ratios used to evaluate the absolute frequency of the Yb^+ *E3* optical clock transition. Shown on the right are the corresponding measurement time intervals with the start and end times indicated as modified Julian days (MJD).

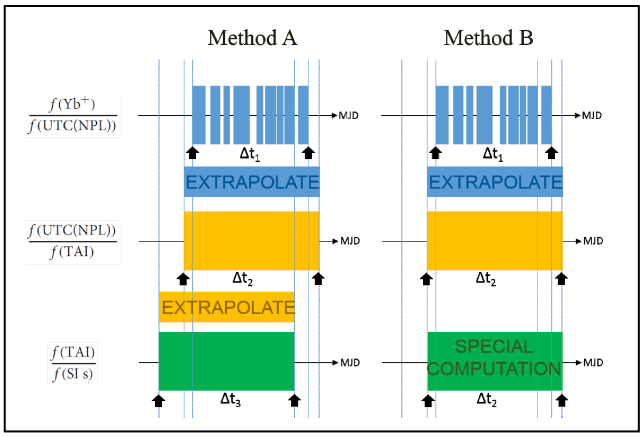

Fig 2. Schematic representation of the two different analysis methods, A and B, used to evaluate the absolute frequency. Note that they differ by method B having a special computation of the ratio f(TAI) / f(SI s), which removes the need for one of the extrapolation periods.

correction was made to account for the offset between the scale interval of TAI during the period of the measurement and the SI second. This series of frequency ratios thus allows the $^{171}Yb^+$ *E3* optical frequency to be related to the SI second, yielding an absolute frequency in units of hertz.

III. Data Analysis

The evaluation of the absolute frequency is not quite as straightforward as multiplying together the three frequency ratios depicted in Fig. 1. Due to dead-time in the operation of the optical frequency standard, and imperfect overlap between the 25-day measurement interval and the 5-day reporting intervals in Circular T, it can be seen that the three intervals for which frequency ratios are known (Δt_1, Δt_2, Δt_3) are all different. It is only appropriate to multiply ratios together when they cover exactly the same measurement periods. Some further extrapolation steps are therefore required in the analysis. Further details are given in [8], but the extrapolation amounts to assessing the offset and uncertainty associated with attributing the value of the frequency ratio measured during interval Δt_i to be representative of the value that would have been measured over a different interval Δt_j. This is determined using simulated data that take account of the contributing noise processes.

A schematic of the analysis steps is presented in Fig. 2, showing the extrapolation stages that must be inserted to allow each frequency ratio to match the measurement interval of the frequency ratio below. Method A, shown on the left of Fig. 2, refers to the analysis steps carried out in [8], with the corresponding ratios and uncertainties for each stage of the process shown in Table 1. The absolute frequency of the $^{171}Yb^+$ *E3* optical transition resulting from analysis method A is 642 121 496 772 645.14(26) Hz, corresponding to a fractional frequency uncertainty of 4.0×10^{-16}.

The analysis method A makes use of a published value of the fractional frequency offset d between the scale interval of TAI and the SI second [9]. This published value corresponds to the interval Δt_3 (MJD 57169 - 57199), shown in green in Fig. 1, and hence it is necessary to carry out an extrapolation from the interval Δt_2 to Δt_3 as shown in Fig. 2, Method A. But it can be seen from Table 1 that the Δt_2 to Δt_3 extrapolation is in fact the largest uncertainty contribution to the absolute frequency measurement. It would therefore be better if the fractional frequency offset d could be known over the interval Δt_2 instead, thus avoiding this extrapolation step altogether.

The analysis method B does just this: a special computation of the frequency offset between the scale interval of TAI and the SI second [6] is carried out to cover the interval Δt_2 (MJD

TABLE I.

Values (r) and uncertainties (u) of the frequency ratios determined for the five steps shown in Fig. 2 for each of the analysis methods A and B. For the optical ratios involving f(Yb^+), we (arbitrarily) choose a value of r_0 based on the 2013 CIPM recommended frequency value of the $^{171}Yb^+$ optical clock transition.

Ratio and interval		**Method A**		**Method B**	
	r_0	$[(r/r_0) - 1]$ / 10^{-18}	$u[(r/r_0) - 1]$ / 10^{-18}	$[(r/r_0) - 1]$ / 10^{-18}	$u[(r/r_0) - 1]$ / 10^{-18}
f(Yb^+) / f(UTC(NPL)); Δt_1	642 121 496 772 645.6	8197	148	8197	148
Extrapolation $\Delta t_1 \rightarrow \Delta t_2$	1	-312	122	-312	122
f(UTC(NPL)) / f(TAI); Δt_2	1	-7793	164	-7793	164
Extrapolation $\Delta t_2 \rightarrow \Delta t_3$	1	0	250	---	---
f(TAI) / f(SI s); Δt_3	1	-810	180	-760	230
Total: f(Yb^+) / f(SI s)	642 121 496 772 645.6	-718	398	-668	341

57174 - 57204). The algorithm [10] that is used for the monthly computation of the offset *d* based on all available measurements of primary and secondary frequency standards can in fact be applied to any interval between two standard TAI dates, i.e. MJD ending in 4 or 9. The resulting offset and uncertainty for *f* (TAI) / *f* (SI s) are given in Table 1 under method B. The uncertainty associated with this ratio is slightly higher for the interval Δt_2 than it is for Δt_3, even though they have the same duration. This is because the uncertainty of *d* from the algorithm in [10] is optimal if the reported intervals of operation of the standards and the interval of estimation of *d* are the same. As the individual measurements of primary standards usually match the monthly intervals of Circular T, they are more in line with the interval Δt_3 than with the interval Δt_2. However, the overall uncertainty of the absolute measurement is reduced with method B because the extrapolation step for Δt_2 to Δt_3 is no longer required. Using the data in Table 1, we find the absolute frequency of the $^{171}Yb^+$ *E3* optical transition with analysis method B is 642 121 496 772 645.17(22) Hz, corresponding to a fractional frequency uncertainty of 3.4×10^{-16}.

IV. Conclusion

Further analysis has been presented of previously reported experimental data to measure the absolute frequency of the ytterbium ion *E3* optical clock transition. Traceability of the optical frequency to the SI second was made through a frequency link to TAI. The new analysis has reduced the uncertainty of the measurement by using a special computation of the fractional frequency offset *d* between TAI and the SI second over an interval more closely matched to the experimental measurement period. This has reduced the uncertainty of the absolute frequency from 4.0×10^{-16} to 3.4×10^{-16}, making it the most accurate measurement to date of this optical transition.

References

[1] N. Huntemann, B. Lipphardt, Chr. Tamm, V. Gerginov, S. Weyers, E. Peik, "Improved limit on a temporal variation of m_p/m_e from comparisons of Yb^+ and Cs atomic clocks," Phys. Rev. Lett., vol. 113, 210802, 2014.

[2] C.Y. Park, D.-H. Yu, W.-K. Lee, S.E. Park, E.B. Kim, S.K. Lee, J.W. Cho, T.H. Yoon, J. Mun, S.J. Park, T.Y. Kwon, S.-B. Lee, "Absolute frequency measurement of $^1S_0$ (F = 1/2) - $^3P_0$ (F = 1/2) transition of ^{171}Yb atoms in a one-dimensional optical lattice at KRISS," Metrologia, vol. 50, pp. 119–128, 2013.

[3] D. Akamatsu, H. Inaba, K. Hosaka, M. Yasuda, A. Onae, T. Suzuyama, M. Amemiya, F.-L. Hong, "Spectroscopy and frequency measurement of the ^{87}Sr clock transition by laser linewidth transfer using an optical frequency comb," Appl. Phys. Express, vol. 7, 012401, 2014.

[4] Y. Huang, H. Guan, P. Liu, W. Bian, L. Ma, K. Liang, T. Li, K. Gao, "Frequency comparison of two $^{40}Ca^+$ optical clocks with an uncertainty at the 10^{-17} level," Phys. Rev. Lett., vol. 116, 013001, 2016.

[5] P. Dubé, J. E. Bernard, M. Gertsvolf, "Absolute frequency measurement of the $^{88}Sr^+$ clock transition using a link to the SI second," Metrologia, vol. 54, pp. 290–298, 2017.

[6] H. Hachisu, G. Petit, T. Ido, "Absolute frequency measurement with uncertainty below 1×10^{-15} using international atomic time," Appl. Phys. B, vol. 123, 34, 2017.

[7] H. Hachisu, G. Petit, F. Nakagawa, Y. Hanado, T. Ido, "SI-traceable measurement of an optical frequency at the low 10^{-16} level without a local primary standard," Opt. Express, vol. 25, pp. 8511–8523, 2017.

[8] C.F.A. Baynham, R.M. Godun, J.M. Jones, S.A. King, P.B.R. Nisbet-Jones, F. Baynes, A. Rolland, P.E.G. Baird, K. Bongs, P. Gill and H.S. Margolis, "Absolute frequency measurement of the $^2S_{1/2} \rightarrow {}^2F_{7/2}$ optical clock transition in $^{171}Yb^+$ with an uncertainty of 4×10^{-16} using a frequency link to international atomic time," Journal of Modern Optics, vol. 65, pp. 585-591, 2018.

[9] https://www.bipm.org/utils/en/pdf/time_ann_rep/Time_annual_report_2015/23_Table7_TAR15.pdf

[10] J. Azoubib, M. Granveaud, B. Guinot, "Estimation of the scale unit duration of time scales," Metrologia, vol. 13, pp.87-94, 1977.

Advances in the uncertainty evaluation of a $^{88}Sr^{+}$ single ion optical clock

Pierre Dubé and Bin Jian
National Research Council Canada
Ottawa, Ontario, Canada, K1A 0R6
Email: pierre.dube@nrc-cnrc.gc.ca

Amar C. Vutha
Department of Physics
University of Toronto
Toronto, Ontario, Canada, M5S 1A7

***Abstract*—We report on recent progress in the evaluation and reduction of the systematic shifts of the strontium ion clock, addressing effects such as the collisional frequency shift, the servo tracking errors, and the blackbody radiation (BBR) shift. The total uncertainty is currently dominated by the BBR field evaluation. All the other known contributions are at least one order of magnitude smaller. Experiments are underway to improve the BBR field evaluation using thermal imaging of a dummy ion trap.**

***Keywords*—single ion clock; optical atomic clock; collisional frequency shift; servo tracking error; blackbody radiation shift; uncertainty evaluation**

I. Introduction

The $5s^2S_{1/2}-4d^2D_{5/2}$ electric quadrupole transition of the $^{88}Sr^{+}$ ion is suitable to realize high-accuracy single-ion optical clocks, with the potential for evaluated uncertainties approaching the 10^{-18} level with current knowledge and technology. The $^{88}Sr^{+}$ ion system has the advantage that it can be operated using commercially available low power laser sources, that it uses a simple cooling and interrogation sequence, and that it allows for a robust control of several sources of frequency shifts. These qualities make the $^{88}Sr^{+}$ ion an excellent candidate for the realization of high-accuracy single-ion clocks, fundamental physics investigations, transportable optical clocks, and for space applications.

Several important systematic shifts of the 445 THz *S–D* clock transition are very well controlled by using methods based on its physical properties. For example, the electric quadrupole shift in the $^{88}Sr^{+}$ ion can cause fractional frequency shifts of 10^{-14} on the most sensitive Zeeman components when no attenuation measures are in place. Fortunately, the electric quadrupole interaction Hamiltonian of the *S–D* transition is traceless. This property is used to reduce the electric quadrupole shift to a vanishingly small value by averaging over the magnetic sublevel energies of the $^2D_{5/2}$ state [1], [2].

Another very beneficial property of the *S–D* transition for clock accuracy is that its static scalar polarizability, $\Delta\alpha_0$, is negative. As a consequence, the micromotion-induced quadratic Stark shift and second-order Doppler shift have opposite signs. This property has provided a means to measure $\Delta\alpha_0$ to high-accuracy in an ion system, which, after accounting for the small and well-known dynamic correction η [3], gives the blackbody radiation (BBR) shift coefficient [4]. In addition, by tuning the trap drive frequency to the optimum value determined by $\Delta\alpha_0$, the two shifts can be made to compensate each other, resulting in a suppression of the excess micromotion shifts by a factor exceeding two orders of magnitude, and a reduction of the thermal motion shifts by a factor of 3 [4].

As the largest contributors to the uncertainty of $^{88}Sr^{+}$ have become well-controlled, other shifts have become dominant and are requiring further investigation to attain the 10^{-18} level. Three of these, the collisional frequency shift, the servo tracking errors, and the BBR shift, are discussed in more detail in the following sections. First, a brief overview of the $^{88}Sr^{+}$ ion is given.

II. Strontium ion optical clock

Figure 1 shows the energy level diagram and laser wavelengths relevant for the operation the $^{88}Sr^{+}$ clock. The ion is cooled on the strongly allowed $5s^2S_{1/2}-5p^2P_{1/2}$ transition at 422 nm, with observed ion kinetic temperatures of typically 2 mK. A repump laser at 1092 nm prevents decay of the $^2P_{1/2}$ state to the metastable $^2D_{3/2}$ state. The 422 nm light is also used for state detection using the electron-shelving method, and for state preparation [5]. A clearout laser at 1033 nm is used to return the ion to the ground state as part of the state preparation sequence. The clock transition linecenter is determined by independently locking the probe laser to six resonances that connect to all the magnetic sublevels of the $^2D_{5/2}$ state. The linecenter frequency is determined from the average of those frequencies. More details about the experimental setup and operation of the optical clock are given in [1], [2], [4], [6].

III. Collisional Frequency Shift

Collisions with background gas atoms and molecules can modify momentarily the clock transition frequency of a trapped ion. A worst-case estimate, based on the assumption that each collision results in a $\pi/2$ differential phase shift between the ground and excited states can be used to estimate the average collisional frequency shift (CFS) [7]. Using this model, the 16 nPa pressure in the NRC ion trap vacuum system yields a frequency shift magnitude and uncertainty of 2×10^{-18} for the the *S–D* transition of $^{88}Sr^{+}$ [2]. Considering

978-1-5386-5620-4/18/$31.00 ©2018 Crown

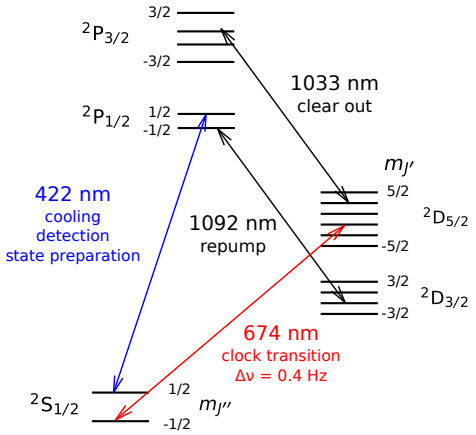

Fig. 1. Partial energy level diagram of $^{88}Sr^+$.

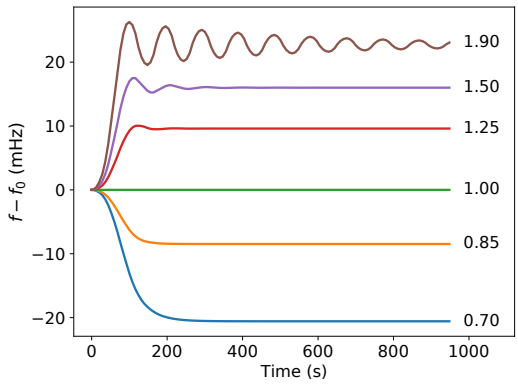

Fig. 2. Simulations of the servo response to a −1 mHz/s laser drift rate. The curves are labeled by the normalized servo gain $g = G/G_{\text{opt}}$, where G_{opt} is the gain that gives an exact frequency correction at each step. In this simulation, the laser frequency servo cycles through six resonances with a dwell time of 8 s at each resonance, for a total cycle time of 48 s. These parameters are commonly used to operate our optical clock.

the expected reduction of the BBR shift uncertainty, either by evaluation of the current system or with a new ion trap, the CFS evaluation could become a limitation to the ultimate accuracy of the $^{88}Sr^+$ ion clock.

Given that the above evaluation is a worst-case estimate, it is expected that the actual frequency shifts should be smaller. To address this problem, a non-perturbative general formalism has been developed recently to estimate with better accuracy the CFS of a two-level ion clock with background gas [8]. The formalism was applied to the special case of elastic collisions of Sr^+ with He gas, using *ab initio* $SrHe^+$ molecular potential energy curves. The calculated systematic fractional frequency shift is $-6(19) \times 10^{-21}$/nPa [8]. The frequency shifts with other types of collision partners, in particular H_2 molecules, have not yet been investigated. A rough estimate of the total CFS was obtained by scaling the helium pressure shifts by the Langevin collision rates of H_2 and N_2 with Sr^+ [2]. The fractional CFS for the NRC $^{88}Sr^+$ ion clock estimated by this method is $-2(6) \times 10^{-19}$.

IV. Servo Tracking Errors

As mentioned earlier, the unperturbed *S–D* frequency of the $^{88}Sr^+$ ion is obtained by averaging the linecenters of six Zeeman components. This averaging provides a very high level of cancellation of the linear Zeeman shift, the electric quadrupole shift (EQS), and the tensor Stark shifts [1], [2]. A consequence of this interrogation sequence is a six-fold increase in the servo tracking errors compared to the case of a system operated on a magnetic and EQS insensitive clock transition.

Our 674 nm clock laser is locked to a reference cavity made of ultra-low expansion (ULE) glass material. The cavity is housed in a vacuum chamber that is set at a temperature where the thermal expansion coefficient vanishes [9]. The long-term isothermal drift rate is on average 10 mHz/s, with observed deviations of a few mHz/s [2]. Although this drift rate is relatively small, it can sometimes lead to important tracking errors. For example, an average tracking error of 0.12 Hz or 2×10^{-16} was observed during a measurement campaign performed a few years ago [2]. In this case, the cycle time through the resonances was 200 s, the gain was set empirically, the laser power was not adjusted for π-pulse excitation, and the cavity drift rate was compensated with a constant value.

The cycle time through the resonances has since been reduced by a factor of four with the implementation of state-preparation and the adjustment of the laser power to obtain π-pulse excitation on each Zeeman component [5]. The servo algorithm was modified to include tracking of the cavity drift rate [10], [11]. This reduces the momentary deviations of the drift rate compensation from the real cavity drift rate to less than 1 mHz/s [11]. These deviations tend to average to zero over long measurement times, with a corresponding reduction in the average tracking error.

The choice of servo gain can have a strong impact on reducing further the tracking errors. There is a servo gain setting that provides an exact correction in a single step [2], [5], [10], [12], [13], but it seems to be used infrequently in practice because of concerns for the frequency stability. A simulation of the servo response to a 1 mHz/s uncompensated drift rate is shown in Fig. 2 for various gain settings. For the optimum normalized gain $g = G/G_{\text{opt}} = 1$ there is no tracking error. The impulse response in that case is a delta function. For $g > 1$, damped oscillations are observed and the laser leads the resonance linecenter. For $g < 1$ the laser frequency lags, and the response time increases with a decrease in g. The servo loop is unstable for $g > 2$. Frequency errors of 20 mHz are obtained for a cavity drift rate compensation error of only 1 mHz/s for the parameters specified in Fig. 2.

We usually operate our optical clock at the optimum gain setting, determined from the calculated Rabi lineshape for a given pulse duration. The laser noise is not included in the model and may cause a slight deviation from the optimum gain. Using typical experimental lock data to the *S–D* linecenter and a gain 5% smaller than the optimum value to account for laser noise linewidth broadening, we find a tracking error

TABLE I
SIMPLIFIED UNCERTAINTY BUDGET OF THE NRC $^{88}Sr^{+}$ ION OPTICAL CLOCK. SHIFTS AND UNCERTAINTIES ARE GIVEN IN UNITS OF 10^{-18} FRACTIONAL FREQUENCY

Source	Shift	Uncertainty
BBR field evaluation, $\langle E^2 \rangle_T$	557	11
Second-order Doppler (thermal)	−3	1
BBR coefficient, $\Delta\alpha_0$	0	0.83
Collisional shift†	−0.2	0.6
AOM chirps	0	0.3
Servo tracking errors	0	0.1
1092 nm ac Stark shift	−0.2	0.1
Excess micromotion	0	0.1
Thermal micromotion	−0.1	0.03
Electric quadrupole shift	0	0.03
Total	554	11

† preliminary estimate

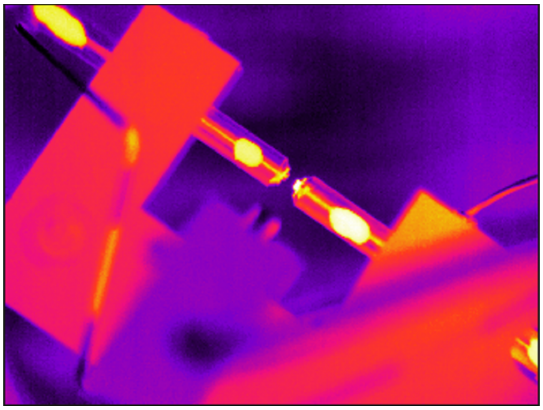

Fig. 3. Thermal image of the dummy ion trap driven with an rf voltage of 424 Vpp at a frequency of 14.408 MHz. The bright patches on the electrodes are areas painted with high emissivity paint for more accurate temperature determinations. This preliminary data indicates that the temperatures of the shield electrodes increase by ≈ 10 to 13°C in the present conditions.

estimated at $\approx 1 \times 10^{-19}$ after 12 h of measurement time. The choice of $g = 1$ provides the fastest servo response to sudden frequency changes and it helps improve the cancellation level of the linear Zeeman shift, the EQS, and the tensor Stark shifts. The cancellation levels could be improved further by reducing the cycle time through the resonances.

V. BLACKBODY RADIATION SHIFT

Table I summarizes the main contributions to the uncertainty budget of the $^{88}Sr^{+}$ ion clock developed at NRC. The total uncertainty is estimated to be 1.1×10^{-17}, dominated by the evaluation of the BBR field. In the past we have relied on contact measurements of the trap components temperatures for this evaluation [2]. The resulting uncertainties were large and the temperatures likely overestimated because of rf heating of the thermistor [14]. A dummy ion trap built to be as identical as possible to the optical frequency standard at NRC was recently assembled for a better determination of the temperatures and evaluation of the BBR field. Figure 3 shows a thermal image of the dummy trap driven with the same voltage and frequency as the frequency standard.

VI. CONCLUSION

The BBR shift is the dominant source of uncertainty in the $^{88}Sr^{+}$ ion, limiting its accuracy to 1.1×10^{-17}. A dummy trap was recently constructed for the evaluation of the BBR field using a thermal imaging camera to make non-invasive temperature measurements of the trap components. These measurements should allow a reduction of the uncertainty to the mid-10^{-18} level. We have also reported improvements to the evaluation of the collisional frequency shift and the servo tracking errors. Except for the BBR shift, all the sources of uncertainty are now evaluated at the 10^{-18} level or lower. A new trap designed to minimize the BBR shift would allow the $^{88}Sr^{+}$ ion clock to reach the low 10^{-18} level [14], [15].

REFERENCES

[1] P. Dubé, A. A. Madej, J. E. Bernard, L. Marmet, J.-S. Boulanger, and S. Cundy, "Electric quadrupole shift cancellation in single-ion optical frequency standards," *Phys. Rev. Lett.*, vol. 95, p. 033001, 2005.

[2] P. Dubé, A. A. Madej, Z. Zhou, and J. E. Bernard, "Evaluation of systematic shifts of the $^{88}Sr^{+}$ single-ion optical frequency standard at the 10^{-17} level," *Phys. Rev.* A, vol. 87, p. 023806, 2013.

[3] D. Jiang, B. Arora, M. S. Safronova, and C. W. Clark, "Blackbody-radiation shift in a $^{88}Sr^{+}$ ion optical frequency standard," *J. Phys. B: At. Mol. Opt. Phys.*, vol. 42, no. 15, p. 154020, 2009.

[4] P. Dubé, A. A. Madej, M. Tibbo, and J. E. Bernard, "High-accuracy measurement of the differential scalar polarizability of a $^{88}Sr^{+}$ clock using the time-dilation effect," *Phys. Rev. Lett.*, vol. 112, p. 173002, 2014.

[5] P. Dubé, A. A. Madej, A. Shiner, and B. Jian, "$^{88}Sr^{+}$ single-ion optical clock with a stability approaching the quantum projection noise limit," *Phys. Rev. A*, vol. 92, p. 042119, 2015.

[6] A. A. Madej, P. Dubé, Z. Zhou, J. E. Bernard, and M. Gertsvolf, "$^{88}Sr^{+}$ 445-THz single-ion reference at the 10^{-17} level via control and cancellation of systematic uncertainties and its measurement against the SI second," *Phys. Rev. Lett.*, vol. 109, p. 203002, 2012.

[7] T. Rosenband *et al.*, "Frequency ratio of Al^{+} and Hg^{+} single-ion optical clocks; metrology at the 17^{th} decimal place," *Science*, vol. 319, no. 5871, pp. 1808–1812, 2008.

[8] A. C. Vutha, T. Kirchner, and P. Dubé, "Collisional frequency shift of a trapped-ion optical clock," *Phys. Rev. A*, vol. 96, p. 022704, Aug 2017.

[9] P. Dubé, A. A. Madej, J. E. Bernard, L. Marmet, and A. D. Shiner, "A narrow linewidth and frequency-stable probe laser source for the $^{88}Sr^{+}$ single ion optical frequency standard," *Appl. Phys. B*, vol. 95, no. 1, pp. 43–54, 2009.

[10] E. Peik, T. Schneider, and Chr. Tamm, "Laser frequency stabilization to a single ion," *J. Phys. B: At. Mol. Opt. Phys.*, vol. 39, pp. 145–158, 2006.

[11] P. Dubé, J. E. Bernard, and M. Gertsvolf, "Absolute frequency measurement of the $^{88}Sr^{+}$ clock transition using a GPS link to the SI second," *Metrologia*, 2017, in print.

[12] J. E. Bernard, L. Marmet, and A. A. Madej, "A laser frequency lock referenced to a single trapped ion," *Opt. Commun.*, vol. 150, pp. 170–174, 1998.

[13] E. Riis and A. G. Sinclair, "Optimum measurement strategies for trapped ion optical frequency standards," *J. Phys. B: At. Mol. Opt. Phys.*, vol. 37, no. 24, pp. 4719–4732, 2004.

[14] M. Doležal *et al.*, "Analysis of thermal radiation in ion traps for optical frequency standards," *Metrologia*, vol. 52, no. 6, p. 842, Nov. 2015.

[15] P. B. R. Nisbet-Jones, S. A. King, J. M. Jones, R. M. Godun, C. F. A. Baynham, K. Bongs, M. Doležal, P. Balling, and P. Gill, "A single-ion trap with minimized ion–environment interactions," *Appl. Phys. B*, vol. 122:57, no. 3, pp. 1–8, Mar. 2016.

Effect of pulse duration fluctuation on the photodetection of a train of pulses from an optical frequency comb

Xiaopeng Xie[1], Romain Bouchand[1†], Michele Giunta[2,3], Wolfgang Hänsel[2], Matthias Lezius[2], Ronald Holzwarth[2,3], Giorgio Santarelli[4] and Yann Le Coq[1⋆]
[1]LNE-SYRTE, Observatoire de Paris, Université PSL, CNRS, Sorbonne Université, 61 avenue de I'Observatoire, 75014 Paris, France
[2]Menlo Systems GmbH, Am Klopferspitz 19a, D-82152 Martinsried, Germany
[3]Max-Planck-Institut für Quantenoptik, 85748 Garching, Germany
[4]LP2N, IOGS-CNRS-Université de Bordeaux 1, rue F. Mitterand, 33400 Talence, France
[†]Present address: École Polytechnique Fédérale de Lausanne (EPFL), CH-1015 Lausanne, Switzerland
[⋆]e-mail: yann.lecoq@obspm.fr

***Abstract*—Microwave signals with unprecedented ultra-low phase noise can be generated by photo-detecting stabilized optical pulse trains from femtosecond laser. However, excess noise introduced by photodetection limits the phase noise performance of generated microwave signals. Here, we demonstrate a new limitation that arises from the pulse duration fluctuation of ultra-short optical pulses. Such fluctuations, although minute compared to the pulse duration itself, convert to phase fluctuations in the microwave electrical waveforms generated by photodetection in a fast InGaAS pin photodiode, due to nonlinear processes. We quantitatively characterize the pulse duration to phase conversion coefficient under various experimental configurations (bias voltage, optical power, etc). Furthermore, by combining this quantitative characterization with experimental microwave phase noise measurement under conditions where this new effect is the dominant source of noise, we have characterized quantitatively, to our knowledge for the first time, the pulse duration noise that is present at the output of an Erbium doped fiber based femtosecond laser and its optical amplification chain.**

***Keywords*—Opto-electronic microwave sources, optical frequency combs, photodiode, ultra-low phase noise.**

I. Introduction

Microwave signals with ultra-low phase noise are of great interested in the fields of radar, telecommunication, deep-space navigation, very long baseline interferometry and precision metrology [1]. Particularly, microwave signals with ultra-low phase noise both close and far from carrier Fourier frequencies can be generated by photo-detecting the train of optical pulses from phase-stabilized femtosecond lasers [2], [3]. However, various known excess noise sources inherent to photo-detection ($1/f$ noise, shot noise, thermal noise and amplitude noise to phase noise conversion (AM-PM) [4], [5], [6]) can drastically impair the timing noise performance of the generated electrical waveforms. Here, we demonstrate a new limitation: during photo-detection, the fluctuations in the duration of the optical pulses partially convert into phase fluctuations of the output electrical signal, due to nonlinearities. We introduce a conversion coefficient and quantitatively characterize it for an InGaAs fast photo-detector under various bias voltage and optical energy per pulse. Once the optical pulse duration noise conversion of a photo-detector is characterized, we show that the information can be conversely used to probe the duration fluctuation of optical pulses by measuring the electrical phase noise. We set up a photo-detection scheme in a condition where the new noise effect is the leading cause of excess phase noise and probe the duration fluctuation of optical pulses emitted by a low noise fiber-based optical frequency comb. The relative duration fluctuation $\triangle\tau/\tau$ we measured is below the 8×10^{-5} level, integrated between 1 kHz and 1 MHz, or below 20 as for our ≈150 fs compressed optical pulses, *i.e.* six orders of magnitude below the response of the photo-detector in use.

II. Experiment and results

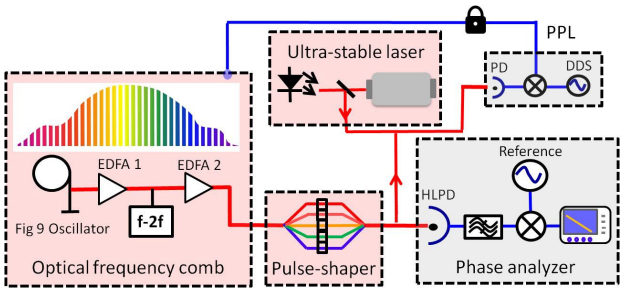

Fig. 1. Experimental set-up for exploring the effect of nonlinearities in the photo-detection of ultra-short optical pulse trains. An Erbium-doped fiber-based frequency comb system is used as the optical pulse source. A pulse-shaper is connected at the output of the comb system to modify the duration of the optical pulses by setting different group delay dispersion. The optical frequency comb system is phase locked to an ultra-stable laser reference. A high linear photo-diode is used to convert the stabilized optical pulses to electrical waveforms. The 12 GHz harmonic is isolated and its phase deviation is analyzed when different group delay dispersion are applied with the pulse-shaper. EDFA, Erbium-doped fiber amplifier; HLPD, High-linear photo-diode; PD, Photo-diode; DDS, Direct digital synthesizer; PLL, Phase lock loop.

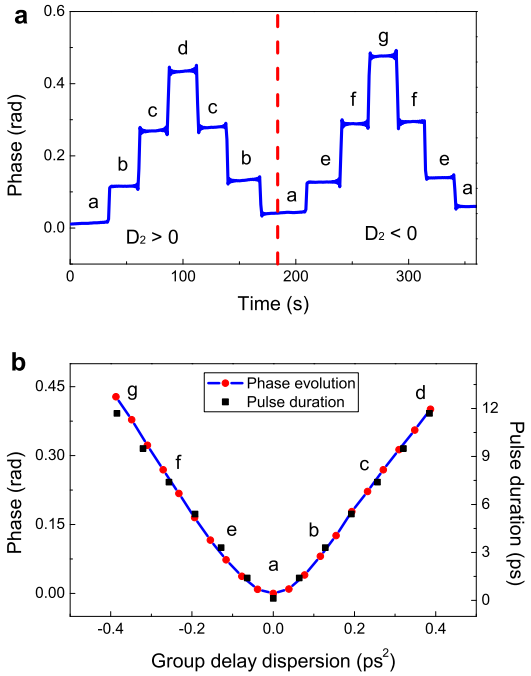

Fig. 2. Phase evolution of the 12 GHz signal when the optical pulse duration at photo-detection is modified. **a**, Measured phase evolution of the 12 GHz signal when switching different optical pulse durations by group delay dispersion. Each step corresponds to a situation in plot a referenced by a small caps letter. In between each step, the group delay dispersion is modified by the same amount $0.13\,\mathrm{ps}^2$. **b**, Normalized phase evolution of the 12 GHz signal with more measurement points.

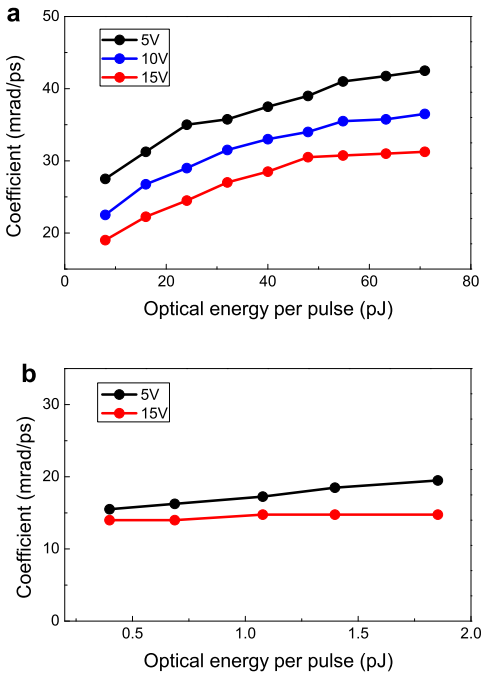

Fig. 3. Nonlinear coefficient of photo-detection of ultra-short optical pulse trains. The coefficient goes up when increasing the optical pulse energy shinning upon the photo-diode. Increasing the bias voltage of the photo-diode at constant optical energy per pulse sets its operation closer to the linear regime, hence, the decrease of the coefficient for increased bias voltage.

Figure 1 presents our experimental scheme to demonstrate the novel effect of nonlinearities in the photo-detection of ultra-short pulse trains. We photo-detect femtosecond optical pulses emitted from a low noise fiber-based frequency comb system. A programmable optical pulse-shaper is connected at the output of femtosecond laser source. Setting different group delay dispersion D_2 through the pulse-shaper, we can realize various optical pulses durations and chirps without modifying the mode-locked state of the laser. A low noise and highly-linear photodiode (DiscoverySemiconductor HLPD) with 12 GHz bandwidth is used to convert stabilized optical pulses into electrical waveforms. One of the harmonics of the repetition rate (12 GHz in our case) is isolated and analyzed. To access the phase of the 12 GHz harmonics, we set up another similar photonic microwave system as a phase reference [2]. The beat note signal, around 4.5 MHz, is sent to a phasemeter and noise analyzer to obtain the phase evolution of electrical waveform under test. Both optical frequency comb systems are phase locked to a common ultra-stable continuous-wave like we reported previously [2].

We first set a suitable D_2 value with the pulse-shaper in order to obtain the optical pulses with the shortest pulse duration on the photo-diode (HLPD in Fig. 1). This is referenced as point "a" in Fig. 2 and we take it as the zero effective D_2 reference. A pulse duration below 150 fs is obtained. From this point, setting different D_2 modifies the actual pulse duration impinging on the photo-diode, which is also observed to change in a repeatable manner the phase of the 12 GHz microwave signal that is generated by isolating the corresponding harmonics of the repetition rate after photo-detection. Furthermore, the point "a" of minimal pulse duration is observed to be an extremum of the microwave phase *vs* D_2 measurement.

Figure 2 shows the time evolution of the microwave phase when the group delay dispersion applied by the pulse-shaper is changed step by step. For both the positive dispersion regime and the negative regime, the phase is increasing when the pulse duration is. Furthermore, the phase is changing slower close to point "a", as expected from the pulse duration evolution close to its minimum.

A coefficient of conversion from pulse duration fluctuation to the induced microwave phase fluctuation can be extracted from data similar as those presented in Fig.2. We have characterized this coefficient for various experimental parameters, in particular varying the bias voltage of the photo-diode, and the optical energy per pulse. Fig.3 displays these measurements. Two important trends appear from these measurements: 1) the higher the optical energy per pulse (and therefore electron-hole pair creation at photo-detection), the higher the coefficient, and 2) the higher the bias voltage the lower the coefficient. These two trends are in good agreement with the expectation for a physical phenomenon caused by non-linearities akin to space

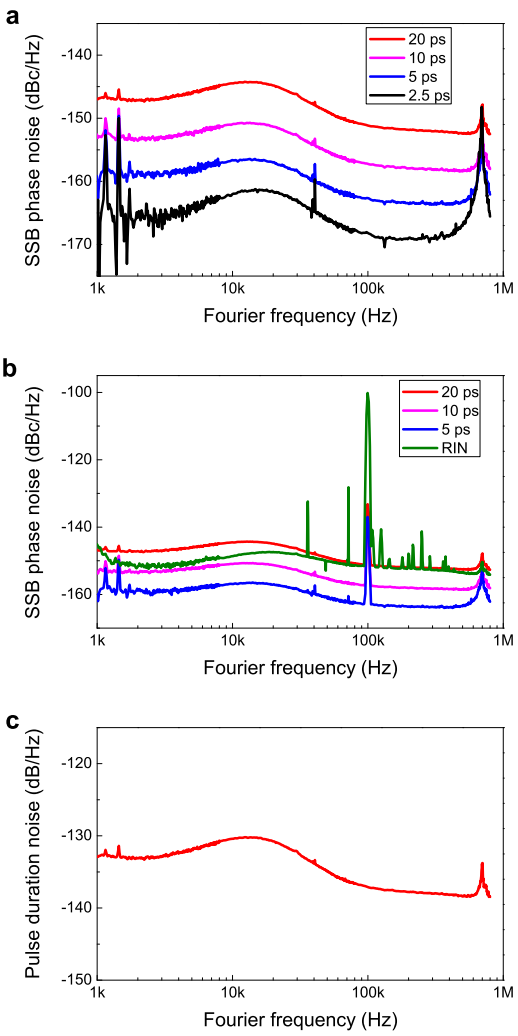

Fig. 4. Single sideband (SSB) phase noise power spectral density (PSD). **a**, Measured phase noise PSDs of the 12 GHz signal with different detected optical pulse durations. **b**, Modulated relative intensity noise (RIN) of the 12 GHz and phase noise PSD. A pure amplitude modulation is acted at 100 kHz offset frequency. **c**, Normalized relative optical pulse duration noise PSD.

charge screening effect of the mobility of the carriers in the photo-diode.

Since the phase of the electrical signal generated from a train of pulse *via* photo-detection is sensitive to the optical pulse duration, fluctuations of the later convert into excess phase noise when using this technique to generate ultra-low phase noise microwave signals. This is one of the reason why, in our previous work [2], it turned out essential to re-compress pulses before photo-detection, where this effect is strongly suppressed. Conversely, measuring the phase noise of the generated microwave signal in a configuration where this pulse-duration noise is the dominating contribution, one can have access to the power spectral density (PSD) of pulse duration noise, provided the conversion coefficient is known.

Figure 4 shows the phase noise PSD of isolated 12 GHz signal with different (relatively large) optical pulse durations, characterized with an advanced digital heterodyne cross correlation system we have used and reported in [2]. The phase noise PSD is linearly rising up with the optical pulse duration. This behavior is characteristic of excess phase noise introduced by pulse-duration noise conversion. For large pulse durations, it is the dominating noise source in the 1 kHz to 1 MHz Fourier frequency offsets for our system. In this configuration, both the pulse duration and its fluctuation are "amplified" by the external group delay dispersion before photo-detection. Contrary to the experiments described in the previous section, as we are here targeting low-phase noise microwave generation, and high signal to noise ratio of the 12 GHz harmonics is highly beneficial. We therefore use here a four stages Mach-Zehnder inter-leaver (MZI), which multiply the effective repetition rate from 250 MHz to 4 GHz before photo-detection so as to improve signal-to-noise-ratio [7]. The all-fibered MZI we use effectively interleaves successive pulses to increase the repetition rate, but as a result, each successive pulses travel along a tiny different length of fiber than the next. As a consequence, successive pulses have slightly different pulse durations at the photo-detection point. We have measured the *effective* pulse-duration fluctuation to microwave phase fluctuation conversion in this configuration in Fig.3 **b**.

As the curve shape of phase noise PSD is quite similar to that of the relative intensity noise (RIN) of the laser, one may believe that the well-known AM-PM conversion process is involved here. However, the linear increase of the excess noise with increasing pulse duration is not typical of this effect. In order to further exclude the contribution of AM-PM conversion, we apply a pure amplitude modulation to the optical pulses and monitor closely the AM-PM conversion coefficient [6]. Our digital heterodyne cross-correlation based noise measurement system can characterize both the amplitude and phase noise of the microwave signal simultaneously. As is presented in Fig.4 **b**, the green curve is the RIN of isolated 12 GHz signal. Comparing the modulation peak at 100 kHz frequency offset on the amplitude noise and phase noise PSDs, we can infer the AM-PM contributions are below 35 dB for all these measurement. It means the phase noise contribution from AM-PM conversion is below -180 dBc/Hz level, which is far below the pulse duration related noise we measure here. Using the calibration of the pulse-duration noise to phase noise conversion shown in Fig.3 **b**, we can deduce from these measurements the PSD of pulse duration noise of our optical frequency comb system (Fig.4 **c**). Integrated from 1 kHz to 1 MHz Fourier frequency, this corresponds to $\triangle\tau/\tau \approx 8 \times 10^{-5}$, which means a maximally compressed 150 fs optical pulse has ≤ 20 as pulse width fluctuations in our system. To the best of our knowledge, this is the first time experimentally showing the optical pulse width noise PSD.

III. CONCLUSION

In summary, we have demonstrated the pulse duration fluctuations of ultra-short optical pulses can convert into timing fluctuation of electrical waveforms generated by photo-

detection. This nonlinear effect conversely provides a unique way to characterize the pulse duration fluctuation of femtosecond laser systems. This demonstrated conclusion will benefit the ultra-low phase noise microwave generation with optical frequency comb [2], [3].

ACKNOWLEDGMENT

This work was funded by the DARPA PULSE Program (PμreComb project, under contract No. W31P4Q-14-C-0050); the Eurostar Eureka program (STAMIDOF project) ; and the LABEX Cluster of Excellence FIRST-TF (ANR-10-LABX-48-01), within the Program Investissements dAvenir operated by the French National Research Agency (ANR).

REFERENCES

[1] G. Santarelli, P. Laurent, P. Lemonde, A. Clairon, A. G. Mann, S. Chang, A. N. Luiten, and C. Salomon, "Quantum projection noise in an atomic fountain: A high stability cesium frequency standard", *Phys. Rev. Lett.*, vol. 82, no. 23, pp. 4619-4622, 1999.

[2] X. Xie, R. Bouchand, D. Nicolodi, M. Giunta, W. Hänsel, M. Lezius, A. Joshi, S. Datta, C. Alexandre, M. Lours, P.-A. Tremblin, G. Santarelli, R. Holzwarth, and Y. Le Coq, "Photonic microwave signals with zeptosecond-level absolute timing noise," *Nat. Photon.*, vol.11, pp.44-47, 2017.

[3] T. M. Fortier, M. S. Kirchner, F. Quinlan, J. Taylor, J. C. Bergquist, T. Rosenband, N. Lemke, A. Ludlow, Y. Jiang, C. W. Oates, and S. A. Diddams, "Generation of ultrastable microwaves via optical frequency division," *Nat. Photon.*, vol.5, pp.425-429, 2011.

[4] W. Zhang, T. Li, M. Lours, S. Seidelin, G. Santarelli, and Y. Le Coq, "Amplitude to phase conversion of InGaAs pin photo-diodes for femtosecond lasers microwave signal generation," *Appl. Phys. B*, vol.106, pp.301-308, 2012.

[5] J. Taylor, S. Datta, A. Hati, C. Nelson, F. Quinlan, A. Joshi, and S. Diddams, "Characterization of power-to-phase conversion in high-speed P-IN photodiodes," *IEEE Photon. J.*, vol. 3, no. 1, pp. 140C151, Feb. 2011.

[6] R. Bouchand, D. Nicolodi, X. Xie, C. Alexandre, and Y. Le Coq, "Accurate control of optoelectronic amplitude to phase noise conversion in photodetection of ultra-fast optical pulses," *Opt. Express*, vol. 25, pp. 12268-12281, 2017.

[7] A. Haboucha, W. Zhang, T. Li, M. Lours, A. N. Luiten, Y. L. Coq, and G. Santarelli, "Optical-fiber pulse rate multiplier for ultralow phase-noise signal generation", *Opt. Lett.*, vol.36, pp.3654-3656, 2011.

Dark matter searches within the intercontinental optical atomic clock network

P. Wcisło*, P. Ablewski*, K. Beloy†, S. Bilicki*‡, M. Bober*, R. Brown†, R. Fasano†, R. Ciuryło*, H. Hachisu§, T. Ido§, J. Lodewyck‡, A. Ludlow†, W. McGrew†, P. Morzyński*§, D. Nicolodi†, M. Schioppo†¶, M. Sekido§, R. Le Targat‡, P. Wolf‡, X. Zhang†, B. Zjawin*, and M. Zawada*

*Institute of Physics, Faculty of Physics, Astronomy and Informatics, Nicolaus Copernicus University, Grudziadzka 5, 87-100 Torun, Poland

Email: zawada@fizyka.umk.pl

†National Institute of Standards and Technology, 325 Broadway, Boulder, CO 80305, USA

‡SYRTE, Observatoire de Paris, Universit PSL, CNRS, Sorbonne Universit, LNE, 61 avenue de lObservatoire 75014 Paris, France

§National Institute of Information and Communications Technology 4-2-1 Nukuikitamachi, Koganei, 184-8795 Tokyo, Japan

¶National Physical Laboratory (NPL), Teddington, TW11 0LW, United Kingdom

***Abstract*—We report preliminary results of dark mater searches within the worldwide network made of our laboratories. We demonstrate that data routinely collected by our currently operating optical atomic clocks without any further developments of the experimental set-ups may be used to run a global program aimed on searches of dark matter.**

I. Introduction

A standard optical atomic clock consists of two state-of-the-art components: an ultra-stable high-Q optical cavity which transfers stability of the length into stability of the frequency, and an atomic sample which transfers accuracy of the energy of the ultra-precise atomic clock transition into accuracy of the frequency [1]. These two components have different susceptibilities to the external perturbations such as electric and magnetic fields, and to the possible changes of fundamental physical constants.

In our network we use this property to derive new constraints for oscillating massive scalar fields [2] and topological defects in the scalar fields [3] couplings to standard matter exceeding previously reported limits [4]–[8] by several orders of magnitude. These constraints were obtained by tracking the imprint of these effects in the frequency difference between cavities and atoms of several clocks distributed worldwide and running simultaneously. In this network of clocks, the technical noises (thermal noise, drift of cavities) is uncorrelated, while the effects we probe would yield correlations in remote measurements. As a consequence the optical clocks within our network do not have to be linked via phase-noise-compensated optical fibre links but only via a standard internet connection.

II. Methods and Results

The coupling of the scalar or pseudoscalar field ϕ to the SM fermion and electromagnetic fields may be represented by linear or quadratic interactions [3], [9]–[11]

$$\mathcal{L}_{int}^{lin} = \frac{\phi}{\Lambda_\gamma}\frac{\mathcal{F}_{\mu\nu}\mathcal{F}^{\mu\nu}}{4\mu_0} - \frac{\phi}{\Lambda_e}m_e c^2\overline{\psi_e}\psi_e - \frac{\phi}{\Lambda_p}m_p c^2\overline{\psi_p}\psi_p, \quad (1)$$

$$\mathcal{L}_{int}^{quad} = \frac{\phi^2}{(\Lambda'_\gamma)^2}\frac{\mathcal{F}_{\mu\nu}\mathcal{F}^{\mu\nu}}{4\mu_0} - \frac{\phi^2}{(\Lambda'_e)^2}m_e c^2\overline{\psi_e}\psi_e - \frac{\phi^2}{(\Lambda'_p)^2}m_p c^2\overline{\psi_p}\psi_p, \quad (2)$$

where μ_0 is the magnetic permeability, $m_{e,p}$ and $\psi_{e,p}$ are electron and proton masses, and fields, respectively, $\mathcal{F}$ is the electromagnetic field tensor, and Λ_γ (Λ'_γ) and Λ_f (Λ'_f) are the energy scales of the respective linear (quadratic) couplings. The interactions with the scalar field ϕ modify the QED Lagrangian and yield the effective fine-structure constant α

$$\alpha \to \frac{\alpha}{1-\phi/\Lambda_\gamma} \simeq \alpha\left(1+\frac{\phi}{\Lambda_\gamma}\right) \Rightarrow \frac{\delta\alpha}{\alpha} = \frac{\phi}{\Lambda_\gamma}, \quad (3)$$

$$\alpha \to \frac{\alpha}{1-\phi^2/(\Lambda'_\gamma)^2} \simeq \alpha\left(1+\frac{\phi^2}{(\Lambda'_\gamma)^2}\right) \Rightarrow \frac{\delta\alpha}{\alpha} = \frac{\phi^2}{(\Lambda'_\gamma)^2}, \quad (4)$$

and the effective masses $m_{e,p}$ [9], [12]

$$\frac{\delta m_{e,p}}{m_{e,p}} = \frac{\phi}{\Lambda_{e,p}}, \quad (5)$$

$$\frac{\delta m_{e,p}}{m_{e,p}} = \frac{\phi^2}{(\Lambda'_{e,p})^2}. \quad (6)$$

A response of an electronic transition to the variation of α with respect to the optical cavity can be derived from the electronic Schrödinger equation in the Born-Oppenheimer approximation, in SI units, in dimensionless form, for n electrons and m nuclei:

978-1-5386-5620-4/18/$31.00 ©2018 IEEE

$$\left(-\frac{1}{2}\sum_{i=1}^{n}\nabla_{x_i}^2 - \sum_{i,j=1}^{n,m}\frac{Z_j}{x_{ji}} + \frac{1}{2}\sum_{\substack{i,k=1\\ i\neq k}}^{n,n}\frac{1}{x_{ik}} \right)\psi = \epsilon\psi, \tag{7}$$

where $\epsilon = E/E_h$ and $x_i = R_i^e/a_0$, $x_{ji} = \left|\vec{R}_j^n - \vec{R}_i^e\right|/a_0$, and $x_{ik} = \left|\vec{R}_i^e - \vec{R}_k^e\right|/a_0$, with $E_h = \alpha^2 m_e c^2$ and $a_0 = \hbar/(m_e \alpha c)$, m_e is the electron mass, Z_j is the number of protons in the j-th nucleus. The coordinates of the j-th nucleus and the i-th electron are $\vec{R}_j^n$ and $\vec{R}_i^e$, respectively.

The values of the dimensionless energies ϵ and their dependence on the dimensionless positions of the nuclei $\vec{X}_j = \vec{R}_j^n/a_0$ do not depend on any fundamental constant. Therefore, within this approximation, the energy of the system scales as $\propto \alpha^2$ and its linear dimensions scale as $\propto \alpha^{-1}$ [13], [14] for any physical system. This approximation works well for light elements (including those relevant to our network, i.e., Sr, Si, O and Ti) when relativistic effects can be neglected [15], [16]. When relativistic effects are also considered, the dependence of the frequency of an electronic transition on the fine-structure constant α can be expressed, in SI units, as

$$\omega_0^{at} \propto \alpha^{2+k_\alpha^{at}}, \tag{8}$$

where k_α^{at} is a sensitivity factor [15], [16]. The lengths of optical cavity spacers made either of single-crystal silicon [17] or completely amorphous Ultra-Low Expansion glass follow the $L \propto \alpha^{-1}$ scaling. The frequency of the N_{cav}-th longitudinal cavity mode can be written as

$$\omega_0^{cav} = N_{cav}c/(2L) \propto \alpha. \tag{9}$$

Equations (8) and (9) provide the deviation of the frequency of the clock transition with respect to the cavity, $d\omega_0 = d(\omega_0^{at} - \omega_0^{cav})$ because of the variation of α

$$\frac{d\omega_0}{\omega_0} = k_\alpha \frac{d\alpha}{\alpha}, \tag{10}$$

where $k_\alpha = 1 + k_\alpha^{at} - 1 = 1 + k_\alpha^{at}$.

The possible variations of the α are therefore encoded in the frequency correction applied to the frequency shifter and the detection sensitivity is limited by the standard deviation of this signal (Fig. 1). To distinguish positive detection from false events a geographically dispersed network is necessary. Moreover, each sensor added to the network improves the sensitivity and the parameter space accessible for the network. In our approach, the readouts, i.e. differences between cavity and atomic frequencies, of the distant clocks do not need to be correlated in real time. Just as in the standard radio-astronomical technique, very-long-baseline interferometry, they can be locally recorded (with time stamps that are accurate to the level of 1 ms) and cross-correlated later. A concept of archiving data from various types of precise measurements was also proposed in [18]. Any number of scenarios of the fine structure constant variation can be tested during post-processing of the data.

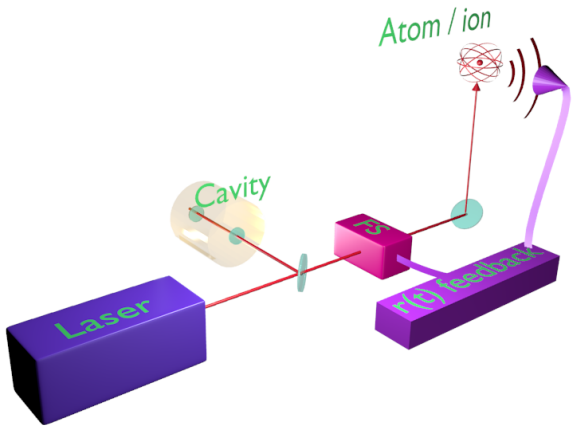

Fig. 1. Single optical atomic clock as a detector of the fine-structure constant variations. The frequency of the probe laser tightly locked to the ultra-stable cavity is compared to the frequency of atomic clock transition every few hundreds of milliseconds and a correction (feedback) is added to the laser frequency by a frequency shifter (FS). The variations of the fine-structure constantare encoded in the feedback (readout) $r(t)$.

Our measurements were performed by four optical lattice atomic clocks placed in NIST, Boulder, CO, USA [19], [20], in SYRTE, Paris, France [21], [22], in KL FAMO, Torun, Poland [23], [24] and in NICT, Tokyo, Japan [25], [26]. They cover the time period from 9 January 2015 to 17 December 2015. The measurements were collected for 11, 24, 42 and 54 days in NIST, SYRTE, KL FAMO and NICT laboratories respectively. Together the laboratories were assembling signal for 114 days (Fig. 2).

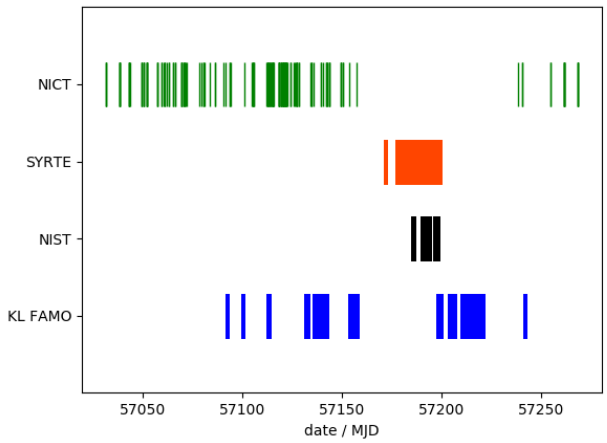

Fig. 2. Observation sessions spanning Jan. 2015 to Dec. 2015.

The campaign was aimed for detecting topological defect and massive scalar fields candidates. No signal consistent with a dark-matter coupling is identified, leading to significant improvements in constraints on the dark matter - standard

model couplings. In case of topological defects, the transient effect can be detected by cross-correlating the pairs of readouts recorded in the network of our worldwide dispersed clocks. To allow comparison between different clocks based on different atomic species and different transitions we used signals normalised to the sensitivity coefficient (equal to one in the non-relativistic case [10], [13]) and to the frequency of the particular clock transition. For the particular case of the topological defect size comparable to the size of the Earth (10,000 km) we determined a new constraint on the transient perturbation in the fine-structure constant $\delta\alpha/\alpha < 7.2\times10^{-17}$.

We also applied a procedure used in [5], [7] and described in [27] to search for harmonic-oscillation signatures of massive scalar fields. For each frequency of the oscillation ω, i.e. for each mass m_ϕ, we fitted the $R(t) = B + A(\omega)cos(\omega t + \delta)$ function to the normalised signals. We weight readouts from each clock with their standard deviations. For the masses higher than $m_\phi > 10^{-15.4}$ eV*c^2 the coherence time of the field is shorter than duration of our observations and we split readouts into periods equal to half of the given coherence time and assumed independent phases in each of the periods.

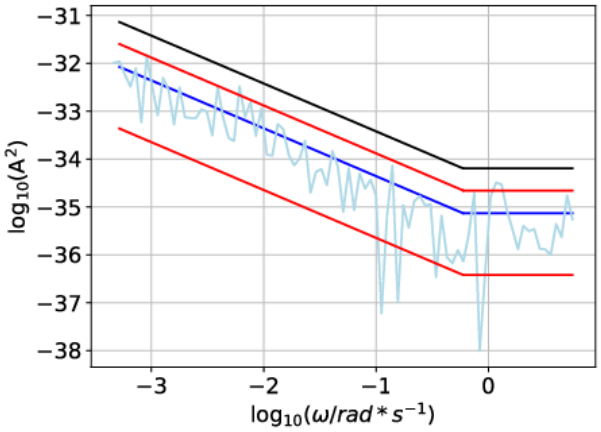

Fig. 3. Periodogram of the square of the fitted amplitude $A(\omega)$ (blue). Lower and upper red curves depict the confidence levels at 5% and 95%, respectively. The dark blue curve corresponds to the mean value based on the assumed noise models (pink and white noise for $\omega < 0.032$ Hz and $\omega > 0.032$ Hz, respectively). Black curve is the detection threshold.

III. Conclusion

We reported the first, preliminary results from the operation of the Earth-scale network of optical atomic clocks. Different susceptibilities to the fine-structure constant of the atoms and the cavity allowed the intercontinental comparison of different clocks without fibre optical links. Our measurements are aimed for searching for oscillations and transient variations in the fine-structure constant, possible signatures of the presence of the dark matter in a form of massive scalar fields or topological defects. We report two orders of magnitude improvement on transient variations of fine-structure constant.

Acknowledgment

Support has been received from the project EMPIR 15SIB03 OC18. This project has received funding from the EMPIR programme co-financed by the Participating States and from the European Unions Horizon 2020 research and innovation programme. The ”A next-generation worldwide quantum sensor network with optical atomic clocks” project is carried out within the TEAM IV programme of the Foundation for Polish Science co-financed by the European Union under the European Regional Development Fund. PW contribution is supported by the National Science Centre, Poland, Project no. 2015/19/D/ST2/02195.

References

[1] A. D. Ludlow, M. M. Boyd, J. Ye, E. Peik, and P. O. Schmidt, Optical atomic clocks, *Rev. Mod. Phys.* **87**, 637 (2015)
[2] A. Arvanitaki, J. Huang, and K. Van Tilburg, Searching for dilaton dark matter with atomic clocks, *Phys. Rev. D*, **91**, 015015 (2015)
[3] A. Derevianko, M. Pospelov, Hunting for topological dark matter with atomic clocks, *Nat. Phys*, **10**, 933 (2014)
[4] P. Wcisło, et al, Experimental constraint on dark matter detection with optical atomic clocks, *Nat. Astron.*, **1**, 0009 (2016)
[5] K. Van Tilburg, et al, Search for Ultralight Scalar Dark Matter with Atomic Spectroscopy, *Phys. Rev. Lett.*, **115**, 011802 (2015)
[6] B. M. Roberts, et al, Search for domain wall dark matter with atomic clocks on board global positioning system satellites, *Nat. Commun.*, **8**, 1195 (2017)
[7] A. Hees, et al, Searching for an Oscillating Massive Scalar Field as a Dark Matter Candidate Using Atomic Hyperfine Frequency Comparisons, *Phys. Rev. Lett.*, **117**, 061301 (2016)
[8] T. Kalaydzhyan, N. Yu, Extracting dark matter signatures from atomic clock stability measurements, *Phys. Rev. D*, **96** 075007 (2017)
[9] T. Damour and J. F. Donoghue, Equivalence Principle Violations and Couplings of a Light Dilaton, *Phys. Rev. D*, **82**, 1 (2010)
[10] Y. V. Stadnik and V. V. Flambaum, Improved limits on interactions of low-mass spin-0 dark matter from atomic clock spectroscopy, *Phys. Rev. A*, **94**, 1 (2016)
[11] Y. V. Stadnik and V. V. Flambaum, Searching for Topological Defect Dark Matter via Nongravitational Signatures, *Phys. Rev. Lett.* **113**, 151301 (2014)
[12] T. Damour and J. F. Donoghue, Phenomenology of the Equivalence Principle with Light Scalars, *Classical and Quantum Gravity* **27**, 202001 (2010)
[13] Y. V. Stadnik and V. V. Flambaum, Searching for Dark Matter and Variation of Fundamental Constants with Laser and Maser Interferometry, *Phys. Rev. Lett.* **114**, 161301 (2015)
[14] Y. V. Stadnik and V. V. Flambaum, Enhanced effects of variation of the fundamental constants in laser interferometers and application to dark-matter detection, *Phys. Rev. A* **93**, 063630 (2016)
[15] E. J. Angstmann, V. A. Dzuba, and V. V. Flambaum, Relativistic effects in two valence-electron atoms and ions and the search for variation of the fine-structure constant*Phys. Rev. A* **70**, 014102 (2004)
[16] V. V. Flambaum and V. A. Dzuba, Search for variation of the fundamental constants in atomic, molecular, and nuclear spectra, *Can. J. Phys.* **87**, 25 (2009)
[17] T. Kessler, et al, A sub-40-mHz-linewidth laser based on a silicon single-crystal optical cavity *Nat. Photonics* **6**, 687 (2012)
[18] D. Budker, A. Derevianko, A data archive for storing precision measurements, *Physics Today* **68**, 10 (2015)
[19] M. Schioppo, et al, Ultrastable optical clock with two cold-atom ensembles, *Nat Photonics* **11**, 48 (2016)
[20] N. Hinkley, et al, An atomic clock with 10(-18) instability, *Science* **341**, 1215 (2013)
[21] R. Le Targat, et al, Experimental realization of an optical second with strontium lattice clocks, *Nat Commun.*, **4**, 2109 (2013)
[22] J. Lodewyck, et al, Optical to microwave clock frequency ratios with a nearly continuous strontium optical lattice clock, *Metrologia* **53**, 1123 (2016)

[23] P. Morzyński, et al, Absolute measurement of the 1S0 - 3P0 clock transition in neutral 88Sr over the 330 km-long stabilized fibre optic link, *Sci Rep. 5*, 17495 (2015)
[24] M. Bober, et al, Strontium optical lattice clocks for practical realization of the metre and secondary representation of the second, *Meas. Sci. Technol.* **26**, 075201 (2015)
[25] H. Hachisu, T. Ido, Intermittent optical frequency measurements to reduce the dead time uncertainty of frequency link, *Jpn J Appl Phys.* **54**, 112401 (2015)
[26] A. Yamaguchi, et al, Direct Comparison of Distant Optical Lattice Clocks at the 10^{-16} Uncertainty, *Appl Phys Express.* **4**, 082203 (2011)
[27] J.D. Scargle, Studies in astronomical time series analysis. II - Statistical aspects of spectral analysis of unevenly spaced data, *ApJ.* **263**, 835 (1982)

Photoassociation measurements to evaluate collisional shifts in strontium and prospects for clock spectroscopy with ytterbium molecules

M. Bober, M. Borkowski, P. Morzynski, S. Bilicki, P. Ablewski, R. Ciuryło, and M. Zawada
Institute of Physics, Faculty of Physics, Astronomy and Informatics, Nicolaus Copernicus University
Grudziadzka 5, 87-100 Torun, Poland
e-mail: bober@fizyka.umk.pl

***Abstract*— We report on a photoassociation approach to determine the scattering lengths for $^1S_0$-$^3P_0$ and $^3P_0$-$^3P_0$ cold collisions. Positions of molecular states, connected with asymptotes of $^1S_0$+$^3S_1$ and $^3P_0$+$^3S_1$ states could be determined using a tunable 679 nm laser and atoms trapped in an optical lattice. This approach allows an indirect calculation (without direct probing of $^1S_0$-$^3P_0$ molecular state) of the effect of cold collisions on an optical atomic clock operation. We also propose to realize a molecular clock with bosonic ytterbium molecules.**

Keywords—photoassociation; cold molecules; strontium; ytterbium; optical clock

I. INTRODUCTION

Although high numbers of atoms in an optical atomic clock may lead to improved signal-to-noise ratios, the effects of cold collisions may limit the accuracy. It is especially important for optical clocks with atoms trapped in one dimensional optical lattices and with bosonic isotopes [1, 2]. Information about cold-collisional shifts may be obtained from molecular potentials [3,4]. While the ground state $^1S_0$+$^1S_0$ scattering length for ^{88}Sr is well known [5], we have little knowledge about scattering properties in $^1S_0$+$^3P_0$ or $^3P_0$+$^3P_0$ states.

II. PHOTOASSOCIATION MEASUREMENT

Direct photoassociative approach to measure $^1S_0$+$^3P_0$ and $^3P_0$+$^3P_0$ potentials may be challenging since nothing is known about bound states positions. Additionally, Franck-Condon factors may be unfavorable as it is in case of ytterbium [6] which will make direct measurement even more challenging. Here we report an indirect photoassociation approach which may allow to determine the scattering lengths for $^1S_0$+$^3P_0$ and $^3P_0$+$^3P_0$ cold collisions using 679 nm laser.

By using a mixture of atoms in $^1S_0$ and $^3P_0$ states we can determine bound state positions in molecular states connected to the $^1S_0$+$^3S_1$ asymptote using the 679 nm $^3P_0$-$^3S_1$ transition (Fig. 1). Additionally, at the same time we can look for bound states connected to $^3P_0$+$^3S_1$ potentials. Information about those vibrational levels could yield asymptotic molecular potentials. The $^1S_0$+$^3P_0$ and $^3P_0$+$^3P_0$ scattering properties can be worked out from photoassociation line intensities which depend on the respective free-bound Franck-Condon factors, which in turn depend on the scattering lengths. With this we will be able to calculate the effect of cold collisions on an optical atomic clock accuracy.

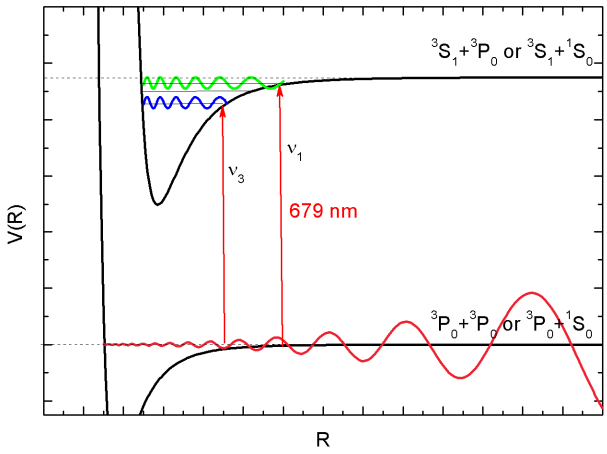

Fig. 1. Indirect photoassociative approach to the determination of $^1S_0$+$^3P_0$ and $^3P_0$+$^3P_0$ scattering properties. The strength of a photoassociation line is partially determined by the magnitude of the scattering wavefunction at the Condon point. The scattering length can be worked out from the position of a wave function node [18], which manifests itself as a drop of line intensity.

The expected photoassociation resonance will have width >10 MHz and thus a scan over a few GHz range does not take much time. Near the atomic transition the resonances may overlap. Even in this case an asymmetry around the atomic resonance should be visible. For molecular potentials determination scans at farther detunings may be necessary.

III. SETUP

Using one of our cold strontium setups [7] we perform first photoassociation spectroscopy measurements. We cool strontium atoms to a temperature of a few microkelvins and transfer them to an optical lattice operating at 813 nm. We control the temperature of the sample and lattice trap depth by sideband spectroscopy on the 698 nm clock transition. To monitor the density of our cold atomic sample we use

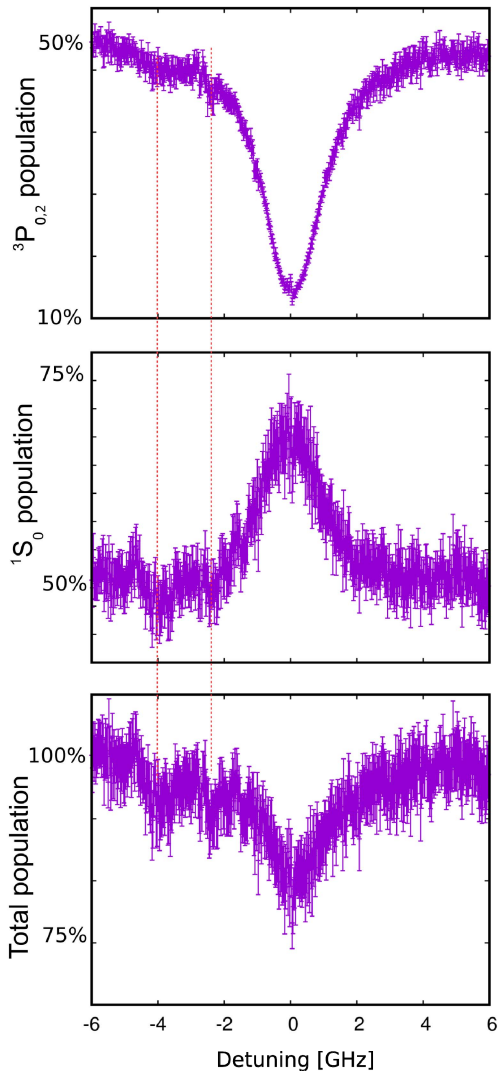

Fig. 2. Scan around atomic line with 679 nm laser with atom losses for detunings around -2 and -4 GHz from atomic resonance.

photoassociation measurements near intercombination $^1S_0$+$^3P_1$ transition. Using a 50-100 ms laser pulse, detuned around 24.5 MHz below the atomic resonance we observe around 50% atomic loses.

In the first approach we use for 679 nm photoassociation spectroscopy one of our repumping laser, which is used during cooling and in detection stage. The laser mode-hop-free scanning range is around 12-14 GHz. Using this laser we were not able to detune farther than 12 GHz from atomic resonance since in the same cycle it has to be tuned back to resonance. We stabilized and tune the laser using a wavemeter and with precise calibration we obtained around 10 MHz absolute accuracy. The laser beam waist is around 600 μm, available power is up to 3 mW.

Our detection scheme allows us to separately count atoms in ground $^1S_0$ state and atoms in ^3P_J states. By using two repumpers operating at 679 and 707 nm we can transfer atoms from long lived states $^3P_0$ and $^3P_2$ back to the ground state via $^3P_1$ state. We first count atoms in the ground state and then we repump the atoms from the triplet states. We can not distinguish atoms accumulated in $^3P_0$ from those in $^3P_2$ state. We should be able to find molecular bound states by observing atomic losses from the lattice. By making the spectroscopy with just atoms in $^3P_0$ state we will be able to distinguish molecular lines from $^1S_0$+$^3P_0$ and $^3P_0$+$^3P_0$ potentials.

IV. Preliminary Results and Prospects

On Fig. 2 we present our preliminary results. We can observe atomic losses both from $^1S_0$ and $^3P_{0,2}$ states. So far we were not able to confirm if those losses are connected with cold molecules creation. We were forced to use extremely low laser powers, on the order of a few microwatts, as the atomic resonance is broadened by several GHz at higher laser powers. Since with our states mixture and 679 nm laser we can reach $^3P_0$+$^3S_1$ molecular states we may have a problem with predissociation, which could significantly broaden the photoassociation lines and turn the spectrum into a continuum. We may not be able to clearly see the molecular lines due to the extremely low laser power we were using. In the next step we plan to use a separate laser, which will allow us to reach deeper bound states. We would be able to use higher laser powers and thus we should be able to clearly see losses. We also plan to investigate potential problem with predissociation by repeat measurements with most atoms in ground state and thus reduce probability for reaching $^3P_0$+$^3S_1$ states.

V. Prospects for Ultracold Molecular Clock Spectroscopy

Precise spectroscopy of cold diatomic molecules has been proposed as a means to detect hypothetical temporal variations of the proton to electron mass ratio [8]. Spectroscopy of ultracold molecules has seen significant progress in recent years and sub-kHz accuracies have been reported [9,10,11]. We propose to perform molecular spectroscopy with further improved precision using magnetically induced clock transitions analogous to those in optical atomic clocks.

Optical atomic clocks utilize the doubly forbidden $^1S_0$-$^3P_0$ transitions in spin singlet atoms, like strontium or ytterbium. In fermionic species the clock transition is slightly allowed (natural linewidth on the order of mHz) by the hyperfine interaction. In spinless bosonic species this transition is truly forbidden. The way around is to use a weak external magnetic field **B** which induces a Zeeman coupling between (m=0) $^3P_0$ and nearby (m=0) $^3P_1$ atomic states. This way one can "transfer" a small amount of the transition dipole moment from the $^1S_0$-$^3P_1$ intercombination line to the clock $^1S_0$-$^3P_0$ transition. Application of a laser of intensity I leads to atomic Rabi flipping at a frequency $\Omega_{at}(I,B)=\alpha\sqrt{I}B$ proportional to the magnetic field and the square root of I. For example, for Yb, $\alpha = 186 Hz/(T\sqrt{mW/cm^2})$ [12]. This mechanism can be extended to the case of a weakly bound molecule or a pair of atoms tightly confined to a 3D optical lattice site [6]. Here, a Laporte-rule-allowed clock transition between molecular states correlating with the gerade $^1S_0$+$^1S_0$ and ungerade $^1S_0$+$^3P_0$ asymptotes would be made possible by magnetic coupling between $^1S_0$+$^3P_0$ and $^1S_0$+$^3P_1$ asymptotic states. The use of an atomic basis is justified for weakly bound molecules, because

most of their radial wavefunction extends to distances where the atomic interaction potential is merely a correction to the atomic fine splitting. Within this regime it can be shown that a molecular Rabi oscillation frequency would be equal to $\Omega_{mol}(I,B) = \sqrt{2}\sqrt{f_{FC}}\Omega_{at}(I,B)$, where $f_{FC} = \int \Psi_g(R)\Psi_e(R)dR$ is a Franck-Condon factor describing the overlap of radial wavefunctions in ground and excited states. The wavefunctions can be either molecular bound state wavefunctions or wavefunctions describing the relative motion of two unbound atoms in a lattice site. In the latter case a lattice site may be approximated by a harmonic trap [13]. The square root of 2 factor stems from the superradiant nature of gerade-ungerade transitions in molecules, but also confirmed in the free-free transitions in pairs of ytterbium atoms tightly confined in 3D optical lattice sites [14].

The possibility of observing magnetically induced clock transitions in molecules relies on the Rabi flipping frequencies which, assuming an already working optical atomic clock setup, depend on the molecular Franck-Condon factors. Here we will focus on the $^{174}Yb_2$ molecule, where we can predict the positions of excited state vibrational states thanks to the recent determination of ground-ground state and ground-excited state scattering lengths. The ground state $a_{gg} = +105.0332(95)\ a_0$ [11], while the difference $a_{ge} - a_{gg} = -10.19(0.13)\ a_0$ has been measured by clock spectroscopy of a ^{174}Yb Mott insulator. Thus, immediately, the value of $a_{ge} = +94.84(0.14)\ a_0$. The positions of rotationless near-threshold $^1S_0+^3P_0\ 0_u^-$ vibrational levels depend for the most part on long range C_6 and C_8 van der Waals coefficients, which for Yb have been recently calculated to high accuracy using ab initio methods [15] and a total wavefunction phase, which can be tuned to match the experimental scattering length. The positions of the top three $^1S_0+^3P_0\ 0_u^-$ vibrational levels, calculated with a model potential, are -13.755(43) MHz, -322.5(4.2) MHz and -1439(23) MHz with respect to the dissociation limit. Remarkably, the positions of these state are very similar to the positions of ground state vibrational levels: -10.62513(53) MHz, -325.66378(98) MHz, and -1527.88543(34) MHz [11], which can be explained by similar s-wave scattering lengths and C_6 coefficients. This results in significant overlap between radial wavefunctions in ground and excited states. For example, the (-1, -1) molecular line at -3.130(43) MHz relative to atomic clock line has a Franck-Condon factor of 0.95. This results in molecular Rabi frequencies that exceed the atomic Rabi frequency at same laser intensities and magnetic fields. Note that the line position is determined to within several tens of kHz, which should significantly improve the chances of finding the resonance in a future experiment. Other strong molecular clock lines include the (-2, -2) +3.2(4.2) MHz (f_{FC}= 0.68) and the (-3, -3) +89(23) MHz (f_{FC} = 0.40) lines.

The last hurdle to overcome on the path towards clock molecular spectroscopy in ytterbium is the production of ultracold Yb_2 molecules. One could argue that this problem could be circumvented altogether by performing direct clock line photoassociation. Unfortunately, free-bound Franck-Condon factors tend to be notoriously small even in tight lattices. For Yb, free-bound FCFs for a 20 kHz 3D lattice calculated using the harmonic trap approximation [13] are on the order of 10^{-6} for all three predicted excited target states. Reaching a Rabi frequency of 1 Hz would require a moderate 150 W/cm^2 laser intensity at a magnetic field of 10 mT. In principle, this is perfectly achievable in an experiment, but leaves little room for higher Rabi oscillation rates that may could be helpful in the initial search for resonances. While to the best of our knowledge the production ultracold Yb_2 molecules have not been so far reported, numerical simulations of quantum three-level dynamics show [6] that they can be produced efficiently by STIRAP using known $^1S_0+^3P_1\ 0_u^+$ intermediary states, much like it is now routinely done with the similar Sr atoms [9].

The mechanism for clock spectroscopy reported here is universal and should be applicable to other spin singlet systems, most notably strontium. Ultracold ground state strontium molecules are already readily available [5, 9, 10]. Little is known, however, about the near-threshold physics - whether bound state positions or cold scattering properties near the $^1S_0+^3P_0$ asymptote of Sr_2 apart from a qualitative determination of the *magnitude* of the s-wave scattering length $|a_{ge}| = 100(50)\ a_0$ [17]. This value does not let us make any reasonable predictions of the positions of vibrational states. On the other hand, a successful blind search for $^1S_0+^3P_0$ resonances in ultracold Sr_2 molecules (with ab initio long range coefficients even one would suffice to fix the wavefunction phase) would make it possible to precisely determine a_{ge}, and improve our grasp of density shifts of bosonic strontium optical clocks.

ACKNOWLEDGMENT

Support has been received from the project EMPIR 15SIB03 OC18. This project has received funding from the EMPIR programme co-financed by the Participating States and from the European Union's Horizon 2020 research and innovation programme and from Polish National Science Centre, Grant nos. 2014/13/N/ST2/02591 and 2017/25/B/ST4/01486. Financial support from the Faculty of Physics, Astronomy and Informatics, NCU, task number 190 is acknowledged.

REFERENCES

[1] S. Origlia et al., arXiv:1803.03157v1, 2018.

[2] C. Radzewicz et al., "Accuracy budget of the ^{88}Sr optical atomic clocks at KL FAMO ", Phys. Scr. **91,** pp. 084003, 2016.

[3] M. Borkowski et al., "Mass scaling and nonadiabatic effects in photoassociation spectroscopy", Phys Rev. A, **90**, pp. 032713, 2014.

[4] W. Skomorowski et al., "Rovibrational dynamics of the strontium molecule in the A $^1\Sigma_u$, c $^3\Pi_u$ and a $^3\Sigma_u$, manifold from state-of-the-art ab initio calculations", J. Chem. Phys., **136**, pp. 194306, 2012.

[5] Y. N. Martinez de Escobar, "Two-photon photoassociative spectroscopy of ultracold ^{88}Sr", Phys. Rev. A, **78**, pp. 062708, 2008

[6] M. Borkowski. "Optical lattice clocks with weakly bound molecules", Phys. Rev. Lett., **120**, pp. 083202, 2018.

[7] Bober et al., "Strontium optical lattice clocks for practical realization of the metre and secondary representation of the second", Meas. Sci. Technol. **26**(7), pp. 075201, 2015.

[8] T. Zelevinsky et al., "Precision Test of Mass-Ratio Variation with Lattice-Confined Ultracold Molecules", Phys. Rev. Lett., **100**, pp. 043201, 2018.

[9] S. Stellmer, et al., "Creation of Ultracold Sr_2 Molecules in the Electronic Ground State", Phys. Rev. Lett., **109**, pp. 115302, 2012.

[10] B. H. McGuyer, et al., “High-precision spectroscopy of ultracold molecules in an optical lattice”, New J. Phys., **17**, pp.055004, 2015.

[11] M. Borkowski, et al., “Beyond-Born-Oppenheimer effects in sub-kHz-precision photoassociation spectroscopy of ytterbium atoms”, Phys. Rev. A, **96**, pp. 063405, 2017.

[12] A. Taichenachev, et al., “Magnetic field-induced spectroscopy of forbidden optical transitions with application to lattice-based optical atomic clocks”, Phys. Rev. Lett., **96**, pp. 083001, 2006.

[13] T. Busch, et al., “Two Cold Atoms in a Harmonic Trap”, Found. Phys., **28**, pp. 549, 1998.

[14] L. Franchi, L. F. Livi, G. Cappellini, G. Binella, M. Inguscio, J. Catani, and L. Fallani “State dependent interactions in ultracold ^{174}Yb probed by optical clock spectroscopy”, New Journal of Physics, **19**(10) pp. 103037, 2017.

[15] S.G.Porsev, et. al., “Long-range interaction coefficients for ytterbium dimers”, Phys. Rev. A, **89**, pp.012711, 2014.

[16] A. Goban, et al., “Emergence of multi-body interactions in few-atom sites of a fermionic lattice clock”, arXiv: 1803.11282, 2018

[17] A. Traverso, et al., “Inelastic and elastic collision rates for triplet states of ultracold strontium”, Phys. Rev. A, **79**, pp. 060702(R), 2009.

[18] S. Tojo et al., “Photoassociation Spectroscopy of Ultracold Ytterbium Atoms by Using the Intercombination Transition”, Phys. Rev. Lett., **96**, pp. 153201, 2006

Two-Photon Spectroscopy of Hydrogen Molecular Ions for Precision Measurements of Fundamental Constants

Florin Lucian Constantin
Laboratoire PhLAM
CNRS UMR 8523, University Lille 1
Villeneuve d'Ascq, France

***Abstract*—This contribution discusses a double resonance two-photon spectroscopy scheme on trapped HD^+ that provides detection of a two-photon rotational transition and a two-photon rovibrational transition by dissociation. The two-photon lineshapes are calculated using a rate equation model for HD^+ ions populations. The resolution is at better than the 10^{-12} level. The total lightshift for selected hyperfine components of the two-photon rotational transition is evaluated using the two-photon operator formalism. The lightshift of the rotational transition may be cancelled by adjusting the intensity of the laser that probes the rovibrational transition in the double resonance spectroscopy scheme. The experimental accuracy with two-photon transitions of trapped HD^+ ions is at the 10^{-12} level, which corresponds also to the accuracy of theoretical calculations. The comparison of experimental data and theoretical calculations for HD^+ and H_2^+ may provide an independent and accurate determination of the Rydberg constant, the proton-to-electron mass ratio and the deuteron-to-proton mass ratio, respectively. It provides an alternative way for the measurement of the proton and deuteron radii. Depending on possible issues of the proton radius puzzle in atomic spectroscopy, two-photon spectroscopy of hydrogen molecular ions may lead to an improvement of the determination of the proton-to-electron mass ratio and deuteron-to-proton mass ratio beyond the 10^{-11} level.**

Keywords—two-photon spectroscopy; two-photon lightshift; trapped ions; proton-to-electron mass ratio; deuteron-to-proton mass ratio; proton and deuteron radii

I. INTRODUCTION

The hydrogen molecular ions (HMI), as the simplest molecules, provide a test ground for molecular quantum mechanics. Uncertainties of ab-initio calculations of energy levels were reduced by taking into account quantum electrodynamics (QED) higher order corrections, leading to an uncertainty of the fundamental vibrational frequencies at 7.6×10^{-12} [1-6]. As a general rule, higher resolution allows better accuracy on the experimental frequencies. An increase of the resolution in Doppler-limited spectroscopy was provided with approaches based on HMI maintained in radiofrequency traps and sympathetically cooled by laser-cooled Be^+ ions. State-selective detection of HMI transitions may be provided by resonance-enhanced multiphoton dissociation (REMPD). Measurements of dipole-allowed E1 rovibrational overtone transitions of HD^+ were performed with an accuracy of 1.1×10^{-9} [7]. The agreement between experimental results and theoretical calculations with an accuracy of 1.1×10^{-9} [7] provided a way to test the quantum electrodynamics, to determine the proton-to-electron mass ratio and to constrain the effect of fifth forces [8] in molecular spectroscopy. The Doppler-free spectroscopy of HMI may provide an increase of the accuracy. Two-photon spectroscopy of transitions of trapped HD^+ ions was suggested [9,10]. Terahertz spectroscopy of cold trapped HD^+ ions in the Lamb-Dicke regime provides an alternative route to Doppler-free spectroscopy [11].

Double resonance two-photon spectroscopy may provide accurate measurements of pairs of transitions with different sensitivities to fundamental constants [10]. This contribution presents a spectroscopy scheme with trapped HD^+ ions that addresses the E1-E1 rotational transition (v,L)=(0,1)→(0,3) in the vibrational ground state and the E1-E1 rovibrational transition (v,L)=(0,3)→(9,3). The two-photon transition rates and the lightshifts are calculated using the two-photon operator formalism [12]. Blackbody radiation (BBR) at room temperature drives transitions between rotational energy levels in the vibrational ground state of the HD^+ ions. The two-photon lineshapes are calculated using a set of coupled rate equations of the populations in the energy levels addressed by these transitions. The Zeeman shifts and the lightshifts are calculated. Finally, this contribution proposes a determination of fundamental constants using the comparison of theoretical calculations with experimental frequencies of rotational and rovibrational transitions of HD^+ and H_2^+.

II. TWO-PHOTON TENSOR FORMALISM CALCULATIONS

A. Hyperfine structure of the energy levels

The particles that compose HD^+ ion posses spin and the molecular energy levels have hyperfine structure components due to various spin-spin and spin-orbit interactions. Spin couplings are those from [13] :

$$\vec{F} = \vec{S}_e + \vec{I}_p ; \vec{S} = \vec{F} + \vec{I}_d ; \vec{J} = \vec{L} + \vec{S} \qquad (1)$$

using the spin operators for the electron $\vec{S}_e$, the proton $\vec{I}_p$, the deuteron $\vec{I}_d$, the rotational angular momentum operator $\vec{L}$, and the total angular momentum operator $\vec{J}$. The basis vectors |vLFSJ> are expressed in terms of the vibrational quantum number v and the eigenvalues of $\vec{L}^2$, $\vec{F}^2$, $\vec{S}^2$, and $\vec{J}^2$ operators. For each rovibrational level, the spin couplings are described with an effective hyperfine Hamiltonian that is expressed in a simplified form [14]. The Fermi contact and the magnetic dipolar hyperfine parameters for the proton and the spin-rotation parameter are taken from [13]. The values of the parameters for the deuteron are estimated with the gyromagnetic factors of the proton and of the deuteron from CODATA 2014 recommended values of fundamental physical constants [15]. The dependences on v and L of values of the hyperfine parameters from lower [13] and higher vibrational states [16] are adjusted here to estimated the hyperfine parameters for the (v,L)=(9,3) level. The effective hyperfine Hamiltonian is diagonalized for each rovibrational level to calculate the hyperfine energies $\Delta E^{v,L,n}$ and the mixing coefficients $\beta_{F,S,J}^{v,L,n}$. The eigenvectors |vLn> of the mixed basis are labelled with an integer n and expressed as a linear combination of the pure basis eigenvectors :

$$\left|v,L,n\right\rangle = \sum_{F,S,J} \beta_{F,S,J}^{v,L,n} \left|v,L,F,S,J\right\rangle \tag{2}$$

The |v,L,n> level is labelled with the |vLFSJ> quantum numbers associated to the mixing coefficient with the highest contribution in the eigenvector. In presence of a magnetic field, the hyperfine levels are split into sublevels $|vLnJ_z\rangle$ labelled by the quantum number J_z of the projection of the total angular momentum on the field axis. The Zeeman Hamiltonian was diagonalized and the energies of the sublevels were approximated with a quadratic dependence on the magnetic field [17]. The values of the parameters were calculated for the lowest (v,L) levels and are extrapolated here to estimate the Zeeman splittings in the (v,L)=(9,3) level.

The interaction with an electric field $\vec{E}(t) = \vec{\varepsilon} E_0(t)$ with the polarisation state $\vec{\varepsilon}$ and the temporal dependence $E_0(t)$ is described in the electric dipole approximation. The coupling is derived with the spherical tensor formalism by rotating the molecule-fixed dipole operator $\vec{\mu}$ into the space-fixed system using the rotation matrix $D^{(1)}_{-p,0}(\omega)^*$ about the set of Euler angles ω [18]. The matrix elements in absence of a magnetic field are expressed by projection on the pure basis vectors |a> = |v,L,F,S,J,J_z> and |a′> = |v′,L′,F′,S′,J′,J'_z> :

$$\begin{aligned}
&\left\langle a\left|-T^1_p\left(\vec{E}\right)D^{(1)}_{-p,0}(\omega)^* T^1_0(\vec{\mu})\right|a'\right\rangle = \left(-E_0(t)\mu_{vL,v'L'}\right)\\
&\times(-1)^{J-J_z}\begin{pmatrix} J & 1 & J' \\ -J_z & -p & J'_z\end{pmatrix}\delta_{S,S'}\\
&\times(-1)^{J'+S+1}\sqrt{(2J'+1)(2J+1)(2L'+1)(2L+1)}\\
&\times\begin{Bmatrix} L' & J' & S \\ J & L & 1\end{Bmatrix}\begin{pmatrix} L & 1 & L' \\ 0 & 0 & 0\end{pmatrix}
\end{aligned} \tag{3}$$

The transition dipole moments $\mu_{vL,v'L'}$ are the matrix elements of HD^+ ion electric dipole function of the internuclear distance. The calculations in this contribution use $\mu_{vL,v'L'}$ from [19] numerically evaluated up to v=8 and L=6 with high-accuracy nonrelativistic variational wavefunctions of HD^+ and the relation $\mu_{vL,v'L'} = (-1)^{L'-L}\mu^*_{v'L',vL}$. Extrapolations of the dependences on v and L, respectively, provide additional values of $\mu_{vL,v'L'}$ up to v=16 and L=4. The calculations are limited to terms that obey to the selection rule L' = L±1.

2.2 Two-photon transition rates

Two-photon excitation of trapped HD^+ ions is performed using the interaction with two counterpropagating waves. The electric field amplitudes are $E_{01,02}$ and the polarisation states are $\vec{\varepsilon}_{1,2}$. When the typical relaxation rate Γ and the Doppler shift are negligible compared to the one-photon transition detuning to the intermediate energy level, the interaction with the electric field is described by a two-photon transition operator [12] :

$$\alpha + \beta = \chi. \tag{1}$$

$$Q^S_{\vec{\varepsilon}_1\vec{\varepsilon}_2} = \frac{Q_{\vec{\varepsilon}_1\vec{\varepsilon}_2} + Q_{\vec{\varepsilon}_2\vec{\varepsilon}_1}}{2}; Q_{\vec{\varepsilon}_1\vec{\varepsilon}_2} = \left(\vec{D}\vec{\varepsilon}_1\right)\frac{1}{\hbar\omega - H_0}\left(\vec{D}\vec{\varepsilon}_2\right) \tag{4}$$

Two-photon transition probability per unit time is derived using the second-order time-dependent perturbation theory :

$$\Gamma^{(2)}_{ge} = \frac{P_1 P_2}{(S\hbar\varepsilon_0 c)^2}\left|\left\langle g\left|Q^S_{\vec{\varepsilon}_1\vec{\varepsilon}_2}\right|e\right\rangle\right|^2 \frac{\Gamma_e}{4\delta\omega^2 + \Gamma_e^2/4} \tag{5}$$

where the powers of the waves are $P_{1,2} = 2\varepsilon_0 S c E^2_{01,02}$ (amplitudes of the electric fields are $2E_{01,02}$), the beam area is S, the lifetime of the excited state is Γ_e, and the detuning of the two-photon transition is $\delta\omega=\omega-\omega_{ge}/2$. Here, the excitation polarisations are chosen between the standard polarisations π, σ^+, σ^-. The two-photon transition operator Q^S_{p1p2} can be expressed in function of the standard components of the dipole operator in the space-fixed coordinate system $D_{pi} = T^1_{pi}(\vec{\mu})$ with $p_i=\{-1,0,1\}$. The two-photon operator is expressed in function of the scalar and the quadrupolar spherical tensors:

$$Q^{S}_{p_1p_2} = \sum_{p=-2}^{2} \langle 11 p_1 p_2 | 2p \rangle Q^{(2)}_{p} + \langle 11 p_1 p_2 | 00 \rangle Q^{(0)}_{0} \qquad (6)$$

Consider first a two-photon transition between pure hyperfine levels $|g,J,J_z\rangle=|v,L,F,S,J,J_z\rangle$ and $|e,J',J'_z\rangle=|v',L',F',S',J',J'_z\rangle$ that is driven by electric fields with standard polarisations p_1 and p_2. If the ground state is not polarized, and in absence of a magnetic field, the two-photon transition probability at the two-photon resonance is calculated with the average contribution of the magnetic sublevels :

$$\overline{\Gamma}^{(2)}_{ge} = \frac{4P_1P_2}{\Gamma_e (S\hbar\varepsilon_0 c)^2} \frac{1}{2J+1} \times \sum_{k=0,2} \frac{\left|\langle g, J \| Q^{(k)} \| e, J' \rangle\right|^2}{2k+1} \left(\sum_{p} \left| \langle 11 p_1 p_2 | kp \rangle \right|^2 \right) \qquad (7)$$

The transition probability may be expressed in terms of the reduced matrix elements of the two-photon operator:

$$\langle g, J \| Q^{(k)} \| e, J' \rangle = (-1)^{J'+L+k+S} \delta_{S,S'} \sqrt{(2J+1)(2J'+1)} \times \begin{Bmatrix} L' & J' & S \\ J & L & k \end{Bmatrix} \langle v, L \| Q^{(k)} \| v', L' \rangle \qquad (8)$$

The reduced matrix elements of the two-photon operator are expanded using the expression of the tensor product of dipole operators with the reduced matrix elements of the dipole operator with intermediate energy levels $|r\rangle = |v'',L'',F'',S'',J''\rangle$ and the detunings of the one-photon transitions from the ground level :

$$\frac{\langle v, L \| Q^{(k)} \| v', L' \rangle}{\sqrt{2k+1}} = (-1)^{k+2L+L'} \sqrt{(2L+1)(2L'+1)} \times \sum_{r(v'',L'')} \left[\begin{Bmatrix} 1 & 1 & k \\ L' & L & L'' \end{Bmatrix} \frac{\mu_{vL,v''L''} \mu_{v''L'',v'L'}}{\hbar(\omega - \omega_{gr})} \times (-1)^{L''} (2L''+1) \begin{pmatrix} L & 1 & L'' \\ 0 & 0 & 0 \end{pmatrix} \begin{pmatrix} L'' & 1 & L' \\ 0 & 0 & 0 \end{pmatrix} \right] \qquad (9)$$

Table I shows the reduced matrix elements of the two-photon operator for the transitions involved in the double resonance spectroscopy scheme.

TABLE I. REDUCED MATRIX ELEMENTS OF THE TWO-PHOTON OPERATOR FOR THE TRANSITIONS (V,L)→(V',L') IN ATOMIC UNITS.

V	L	v'	L'	frequency (THz)	$Q^{(2)}_{v,L;v',L'}$ (a.u.)	$Q^{(0)}_{v,L;v',L'}$ (a.u.)
0	1	0	3	3.268	-3228.723	0
0	3	9	3	207.634	0.0187276	0.0174899

The matrix elements of the two-photon operator between the mixed hyperfine eigenvectors can be derived from Eq. (8) by expressing the mixed hyperfine eigenvectors in function of linear combination of the pure hyperfine eigenvectors and the mixing coefficients $\beta^{v,L,n}_{F,S,J}$ and $\beta^{v',L',n'}_{F',S',J'}$, respectively.

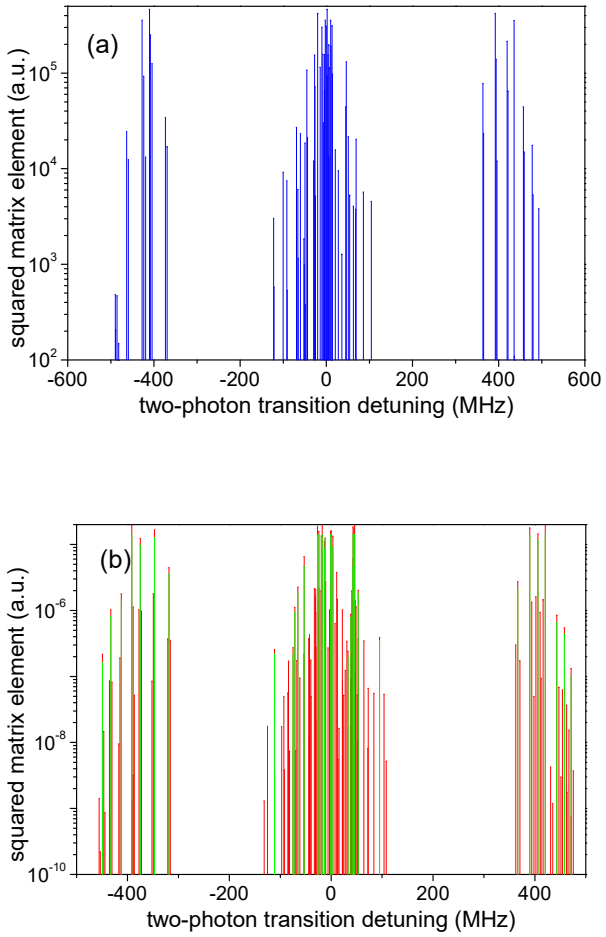

Fig. 1. Average of the squared two-photon reduced matrix elements, in atomic units, for the hyperfine components of the transition (a): (v,L)=(0,1)→(0,3) and (b): (v,L)=(0,3)→(9,3), respectively. Excitation with π–polarized counterpropagating waves. The green lines correspond to the contribution arising from the two-photon operator of rank 0 to the average squared two-photon reduced matrix elements. The spectra are centred on the hyperfine-free frequencies given in Table I.

The selection rules for the two-photon transitions between pure hyperfine levels are $|L-L'|=0,\ \pm2,\ |J-J'|\leq 2$ and $J_z-J'_z=-(p_1+p_2)$. There is also a strict selection rule on the total coupled spins $S'-S=0$ as the two-photon operator acts on the spatial part of the eigenvectors. These selection rules may be overridden for two-photon transitions between mixed hyperfine levels, where the hyperfine couplings lead to weakly allowed transitions.

The matrix elements of the two-photon operator for the rotational and the rovibrational transition between mixed hyperfine structure energy levels are calculated using Eq. (7)–

(9), the reduced matrix elements of the two-photon operators from Table I, and the mixing coefficients from the diagonalisation of the Hamiltonian. The mean squared matrix elements of the two-photon operator for standard ππ polarisations are shown in Figure 1 (a,b).

2.3 Zeeman shift and AC-Stark shift

The Zeeman components of hyperfine transitions may be addressed individually in Doppler-free spectroscopy of trapped HD^+. For metrological applications, it is interesting to probe transitions with minimal Zeeman shifts, that were suggested in [17,20] :

- Transitions ππ between $J_z=0 \rightarrow J'_z=0$ states with quadratic Zeeman shift.

- Pairs of transitions $\sigma^+\sigma^+$ and $\sigma^-\sigma^-$ between stretched states. They are pure eigenvectors with maximum total angular momentum and projection on the quantization axis $|v,L,F=1,S=2,J=L+2,J_z=\pm(L+2)\rangle$. The Zeeman shifts of these transitions depend linearly with the magnetic field, have the same magnitude but opposite values.

Selected transitions with small Zeeman shifts are shown in Table II. The hyperfine component of the rotational transition $(v,L,F,S,J,J_z)=(0,1,0,1,1,0) \rightarrow (0,3,0,1,3,0)$ has a quadratic Zeeman shift estimated at 71.2 mHz for a value of the magnetic field of B = 0.02 G, leading to an accuracy of 2.2×10^{-14} (here the systematic shift defines the value of the uncertainty). The hyperfine components of the rovibrational transition have accuracies in the range 10^{-14} to 10^{-15}. For the hyperfine component of the rovibrational transition $(v,L,F,S,J,J_z)=(0,3,0,1,2,0) \rightarrow (9,3,0,1,4,0)$, the Zeeman shift for B = 0.02 G is 2 Hz (accuracy 5×10^{-15}).

TABLE II. ZEEMAN SHIFT COEFFICIENTS FOR SELECTED HYPERFINE COMPONENTS OF THE TWO-PHOTON ROTATIONAL AND ROVIBRATIONAL TRANSITIONS. (A) TRANSITIONS BETWEEN $J_z=0$ STATES. (B) TRANSITIONS BETWEEN STRETCHED STATES

(a)		
v,L,F,S,J;J$_z$	**v',L',F',S',J';J'$_z$**	**$\Delta\eta_{B2}$ (Hz/G^2)**
0,1,0,1,0;0	0,3,0,1,2;0	-841.5
0,1,0,1,1;0	0,3,0,1,3;0	178
0,1,0,1,2;0	0,3,0,1,4;0	641.5
0,1,1,0,1;0	0,3,1,0,3;0	1356
0,1,1,1,2;0	0,3,1,1,4;0	-1426.5
0,1,1,2,1;0	0,3,1,2,3;0	2019
0,3,0,1,2;0	9,3,0,1,4;0	-2702
0,3,1,1,2;0	9,3,1,1,4;0	14279
0,3,1,2,1;0	9,3,1,2,3;0	15363.5
0,3,1,2,2;0	9,3,1,2,4;0	-4112.5
0,3,1,2,3;0	9,3,1,2,5;0	12931.5
(b)		
v,L,F,S,J;J$_z$	**v',L',F',S',J';J'$_z$**	**$\Delta\eta_B$ (Hz/G)**
0,1,1,2,3;3	0,3,1,2,5;5	-2270.5
0,3,1,2,5;5	9,3,1,2,5;5	115.7

A cancellation procedure for the Zeeman shift was proposed in [17,21]. The systematic effect is reduced for the mean frequency of a pair of transitions that have linear Zeeman shift coefficients with comparable absolute values but opposite signs, like a pair of transitions between stretched states. Let's suppose that the linecenter for each transition is determined at 1% of the linewidth and the precision may be improved by a factor of 10 by taking the linear regression of the Zeeman frequency shift dependence with the magnetic field. Two-photon rotational lines with Hz-level linewidth may be measured with $\sqrt{2}$ mHz uncertainty. Two-photon rovibrational lines with 20 Hz linewidth may be measured with $20\times\sqrt{2}$ mHz uncertainty. The accuracies are 4×10^{-16} and 10^{-16}, respectively.

The lightshift for the energy level $|n,J,J_z\rangle=|v,L,F,S,J,J_z\rangle$ for the interaction with counterpropagating beams with total intensity I (power in the standing-wave 2SI) is expressed as :

$$\delta E_n = -\frac{\alpha_n(\omega)}{2}\frac{I}{c} \tag{10}$$

The dynamic polarisability for a pure hyperfine level is calculated here with the two-photon operator :

$$\begin{aligned}
&\alpha_n(\omega) = -\left[\begin{array}{l}\langle n,J,J_z|Q^S_{\varepsilon\varepsilon^*}(E_n+\hbar\omega)|n,J,J_z\rangle \\ +\langle n,J,J_z|Q^S_{\varepsilon\varepsilon^*}(E_n-\hbar\omega)|n,J,J_z\rangle\end{array}\right] \\
&\langle n,J,J_z|Q^S_{\varepsilon\varepsilon^*}(E_n\pm\hbar\omega)|n,J,J_z\rangle = \\
&\sum_{r,J'',J''_z}\frac{\langle n,J,J_z|D_{-p}|r,J'',J''_z\rangle\langle r,J'',J''_z|D_p|n,J,J_z\rangle}{E_n\pm\hbar\omega-E_r}
\end{aligned} \tag{11}$$

by taking into account the off-resonant couplings to the rovibrational energy levels in the 1sσ electronic ground state of HD^+. The contributions to the dynamic polarisability arise from the scalar and quadrupolar tensors, that are expressed as :

$$\begin{aligned}
&\langle v,L,F,S,J,J_z|Q^{(k)}_0(E_{vL}\pm\hbar\omega)|v,L,F,S,J,J_z\rangle = (-1)^{2J-J_z+L+k+S} \\
&\times\begin{pmatrix} J & k & J \\ -J_z & 0 & J_z\end{pmatrix}(2J+1)\begin{Bmatrix} L & J & S \\ J & L & k\end{Bmatrix}\langle v,L\|Q^{(k)}(E_{vL}\pm\hbar\omega)\|v,L\rangle
\end{aligned} \tag{12}$$

The reduced matrix element of the two-photon operator is expressed further in function of the reduced matrix elements of the dipole operator :

$$\begin{aligned}
&\frac{\langle v,L\|Q^{(k)}(E_{vL}\pm\hbar\omega)\|v,L\rangle}{\sqrt{2k+1}} = (-1)^{k+3L}(2L+1) \\
&\times\sum_{v'',L''}\left[\begin{Bmatrix} 1 & 1 & k \\ L & L & L''\end{Bmatrix}\frac{(-1)^{L''}(2L''+1)\mu^2_{vL,v''L''}}{(E_{vL}\pm\hbar\omega)-E_{v''L''}}\right. \\
&\left.\times\begin{pmatrix} L & 1 & L'' \\ 0 & 0 & 0\end{pmatrix}\begin{pmatrix} L'' & 1 & L \\ 0 & 0 & 0\end{pmatrix}\right]
\end{aligned} \tag{13}$$

The dynamic polarisabilities are calculated for selected hyperfine levels addressed by the two-photon rotational transition at the frequencies of the two-photon transitions, the dissociation laser, and the cooling laser, respectively, for off-resonant couplings up to vibrational level v=16. That allows to

derive the lightshift parameters for selected hyperfine components the two-photon rotational transition that are displayed in Table III.

TABLE III. LIGHTSHIFT COEFFICIENTS FOR HYPERFINE COMPONENTS OF THE ROTATIONAL TRANSITION INDUCED BY RADIATION WITH STANDARD POLARISATIONS P_1, P_2 TUNED AT THE HYPERFINE-FREE FREQUENCY OF THE TWO-PHOTON TRANSITION $(v_1,L_1)\rightarrow(v_2,L_2)$, THE DISSOCIATION LASER FREQUENCY, AND THE COOLING LASER FREQUENCY, RESPECTIVELY

v,L,F,S, $J;J_z$	v',L',F',S', $J';J'_z$	v_1	L_1	v_2	L_2	p_1	p_2	$\Delta\eta_{LS}$ (Hzmm^2/W)
0,1,0,1,0;0	0,3,0,1,2;0	0	1	0	3	0	0	-17.853
0,1,0,1,1;0	0,3,0,1,3;0	0	1	0	3	0	0	11.212
0,1,0,1,2;0	0,3,0,1,4;0	0	1	0	3	0	0	7.153
0,1,1,0,1;0	0,3,1,0,3;0	0	1	0	3	0	0	-21.917
0,1,1,1,2;0	0,3,1,1,4;0	0	1	0	3	0	0	7.153
0,1,1,2,1;0	0,3,1,2,3;0	0	1	0	3	0	0	401.717
0,1,1,2,3;3	0,3,1,2,5;5	0	1	0	3	1	-1	-183.909
0,1,0,1,0;0	0,3,0,1,2;0	0	3	9	3	0	0	-0.167
0,1,0,1,1;0	0,3,0,1,3;0	0	3	9	3	0	0	-0.17
0,1,0,1,2;0	0,3,0,1,4;0	0	3	9	3	0	0	-0.161
0,1,1,0,1;0	0,3,1,0,3;0	0	3	9	3	0	0	-0.158
0,1,1,1,2;0	0,3,1,1,4;0	0	3	9	3	0	0	-0.161
0,1,1,2,1;0	0,3,1,2,3;0	0	3	9	3	0	0	-0.148
0,1,1,2,3;3	0,3,1,2,5;5	0	3	9	3	1	-1	0.135
0,1,0,1,0;0	0,3,0,1,2;0	532/313 nm				0	0	-0.0226
0,1,0,1,1;0	0,3,0,1,3;0	532/313 nm				0	0	-0.0229
0,1,0,1,2;0	0,3,0,1,4;0	532/313 nm				0	0	-0.0219
0,1,1,0,1;0	0,3,1,0,3;0	532/313 nm				0	0	-0.0215
0,1,1,2,1;0	0,3,1,2,3;0	532/313 nm				0	0	-0.0219
0,1,1,2,3;3	0,3,1,2,5;5	532/313 nm				0	0	-0.0201

The values of the lightshifts are estimated for a THz-wave intensity of 1 mW/mm^2, an infrared laser intensity of 189 W/mm^2, an intensity of 56 mW/mm^2 for the dissociation laser at 532 nm, and an intensity of 0.8 mW/mm^2 for the cooling laser at 313 nm. The hyperfine component $(v,L,F,S,J,J_z)=(0,1,0,1,2,0)\rightarrow(0,3,0,1,4,0)$ has a lightshift induced by the THz-wave of 7.2 mHz, that is 2×10^{-15} accuracy. Another contribution to the lightshift arises from the REMPD detection with the two-photon rovibrational transition at resonance. The lightshifts induced on hyperfine components of the rotational transition are by -30 Hz, that corresponds to an accuracy at 10^{-12} level. The selected hyperfine levels have the same dynamic polarisabilities arising from couplings with the dissociation laser or with the cooling laser. The dissociation laser induces a lightshift by -6 mHz on the selected transitions, that is an accuracy of 2×10^{-16}. The lightshifts induced by couplings with the cooling laser are smaller by two orders of magnitude.

The main contribution of the lightshift of the two-photon rotational transition arises from the REMPD detection with the two-photon rovibrational transition. Following the suggestion formulated in [9], this contribution proposes a way for cancellation of the lightshift by using suitable intensities for the THz-wave and for the infrared laser. This is possible for hyperfine transitions that have lightshift coefficients of opposite signs. Figure 2 displays the dependence of the total lighshift of the hyperfine component $(v,L,F,S,J,J_z)=(0,1,1,1,2,0)\rightarrow(0,3,1,1,4,0)$ with the intensity of the infrared laser. The cancellation of the total lightshift may be reached with an infrared laser intensity of 40.5 mW/mm^2. Unfortunately, the value of the two-photon rovibrational transition rate that is derived leads unfeasible the detection of the rotational transition.

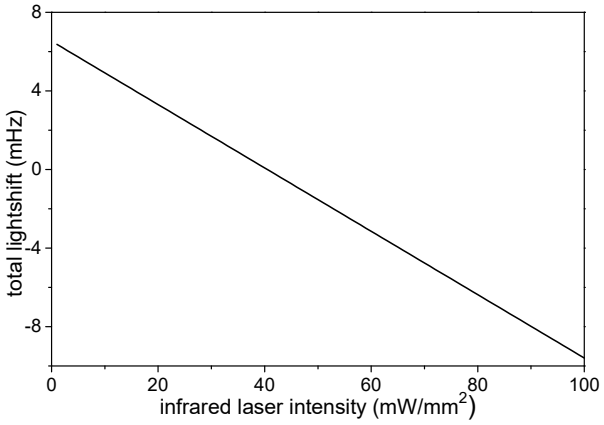

Fig. 2. Dependence of the total lightshift of the hyperfine component $(v,L,F,S,J,J_z)=(0,1,1,1,2,0)\rightarrow(0,3,1,1,4,0)$ on the infrared laser intensity. The THz-wave frequency is at the hyperfine-free two-photon rotational resonance and the intensity is 1 mW/mm^2. The infrared laser is tuned at the hyperfine-free two-photon rovibrational resonance. The dissociation laser at 532 nm has an intensity of 56 mW/mm^2. The cooling laser at 313 nm has an intensity of 0.8 mW/mm^2.

III. DOUBLE RESONANCE TWO-PHOTON SPECTROSCOPY

The spectroscopy scheme with trapped HD^+ ions addresses conjointly the two-photon rotational transition in the vibrational ground state $(v,L)=(0,1)\rightarrow(0,3)$, the two-photon rovibrational transition $(v,L)=(0,3)\rightarrow(9,3)$, followed by the photodissociation of the $(v,L)=(9,3)$ level. Doppler-free spectroscopy may be performed with counterpropagating waves tuned around the two-photon rotational transition, and the two-photon rovibrational transition, respectively. Interaction with blackbody radiation recycles continuously population in the ground vibrational level. A change of the population in the rovibrational levels is induced and may be detected on the dissociation signal. The intrinsic linewidths of the lasers and of the THz-wave are assumed negligible. The hyperfine structure is not taken into account in this section.

The transition rate for the two-photon rovibrational transition is assumed at $\Gamma_{2ph,v} = 10\ s^{-1}$ that corresponds to a laser intensity estimated at 189 W/mm^2. The two-photon rotational transition rate is estimated at $\Gamma_{2ph,r}=2\times10^3\ s^{-1}$ for a THz-wave intensity of 1 mW/mm^2 that can be provided by the THz quantum cascade laser technology. The 532 nm laser drives dissociation at a rate assumed here at $\Gamma_{diss}=200\ s^{-1}$ reached with an intensity of 56 mW/mm^2.

The trapped HD^+ ions are initially in the (v=0, L=0,…,5) levels with a population distribution given by thermal equilibrium with blackbody radiation at 300 K. These levels are coupled with BBR-driven E1 rotational transitions. The transition rates depend on the Einstein coefficients for the spontaneous emission, the stimulated absorption, and the

stimulated emission, respectively. The radiative decay widths of the rovibrational levels are given by [22].

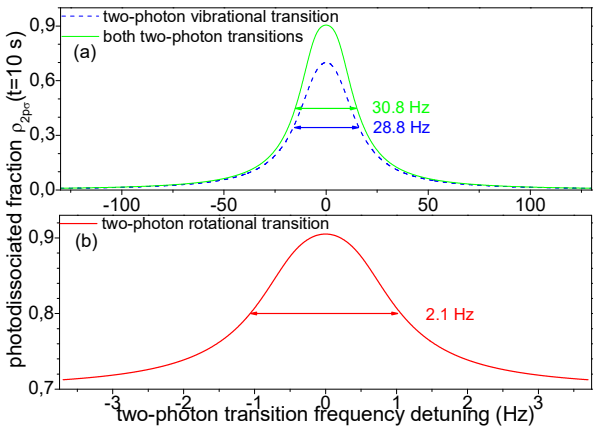

Fig. 3. (a) Spectra of the two-photon rovibrational transition calculated with (green line) and without (blue line) the THz-wave tuned at the two-photon rotational resonance. (b) Spectrum of the two-photon rotational transition (red line) at the two-photon rovibrational resonance. FWHM linewidths are shown on the plots. Parameters used for calculations $\Gamma_{2ph,r}$=2000 s^{-1}, $\Gamma_{2ph,v}$=10 s^{-1}, Γ_{diss}=200 s^{-1}, REMPD time 10 s.

Upon application of the THz-waves, the infrared and the dissociation lasers, the time dependences of the populations in different rovibrational levels $\rho_{v,L}(t)$ and in the dissociated state $\rho_{2p\sigma}(t)$ can be calculated with a set of rate equations depending on the two-photon transition rates at resonance $\Gamma_{2ph,r,v}$ and the two-photon transition detunings. The rate equations are numerically integrated. The dependence of the photodissociated fraction in function of the two-photon rovibrational detuning with or without coupling on the two-photon rotational resonance is displayed in Figure 3(a). The lineshapes are well adjusted by Lorentzians with a full width at half maximum (FWHM) linewidths of 28.8 Hz and 30.8 Hz, respectively. The dependence of the photodissociated fraction on the two-photon rotational detuning at the two-photon rovibrational resonance is shown in Figure 3(b). The lineshape is well adjusted by a Lorentzian with 2.1 Hz full width at half maximum (FWHM) linewidth. The rotational spectrum is superposed on a flat baseline determined by the contribution of rovibrational excitation at resonance. The resolution is at the 10^{-13} level, that improves by two orders of magnitude the resolution predicted for two-photon rovibrational spectroscopy of trapped HD^+ in the Lamb-Dicke regime [9].

The contrast of the two-photon rotational line is defined as $C=(\rho_{2p\sigma,res}-\rho_{2p\sigma,0})/\rho_{2p\sigma,0}$, where $\rho_{2p\sigma,res}$ is the photodissociated fraction at two-photon rotational and rovibrational resonances and $\rho_{2p\sigma,0}$ is the baseline due to the rovibrational excitation. The dependence of the contrast on the two-photon rotational transition rate, shown on Figure 4, left-axis, displays a linear increase followed by a flat dependence. On the contrary, the dependence of the FWHM linewidth, shown on Figure 4, right-axis, has a flat dependence followed by a linear increase. The lineshape for a two-photon rotational transition rate of $\Gamma_{2ph,r}=2\times10^{-3}$ s^{-1}, shown in Figure 5 (a), has a FWMH linewidth of 18.6 mHz (resolution at 6×10^{-16}), determined by the finite radiative lifetime of the (v,L)=(0,3) level. This transition rate is associated to a THz-wave intensity of 1 $\mu W/mm^2$, that may be achievable with the optical frequency down-conversion (photomixing) technology. This approach has the advantage to transpose directly the stability of the optical frequency references to the THz domain. The drawback of using such low intensity level is a contrast for the rotational line at the 10^{-3} level. The use of trapped HD^+ ions initially prepared in the (v,L)=(0,0) level [23,24] in the double resonance spectroscopy scheme leads to a significant increase of the contrast at the 10^{-1} level, as it is shown in Figure 5 (b).

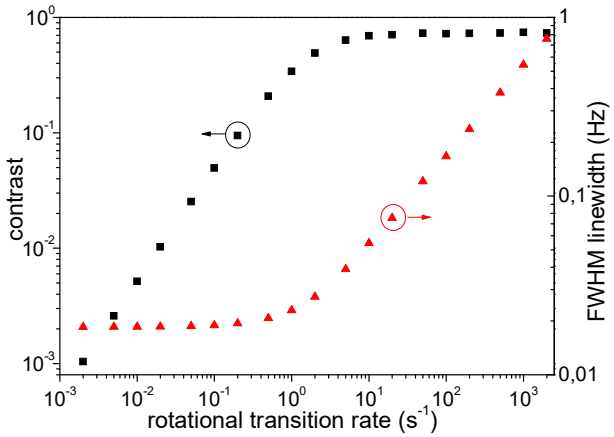

Fig. 4. (a) Dependence of the contrast of the two-photon rotational line on the two-photon rotational transition rate. (b) Dependence of the FWHM linewidth of the two-photon rotational line on the two-photon rotational transition rate. Parameters used for calculations $\Gamma_{2ph,v}$=10 s^{-1}, Γ_{diss}=200 s^{-1}, REMPD time 1 s.

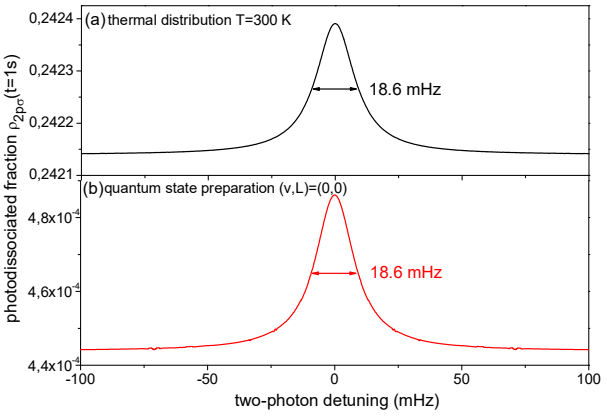

Fig. 5. Spectra of the two-photon rotational transition at the two-photon rovibrational resonance calculated for a THz-wave intensity of 1 $\mu W/mm^2$. (a) Rotational line detected with HD^+ ions initially at thermal equilibrium with BBR at 300 K (b) Rotational line detected with HD^+ ions prepared initially in the (v,L)=(0,0) level. FWHM linewidths are shown on the plots. Parameters used for calculations $\Gamma_{2ph,r}=2\times10^{-3}$ s^{-1}, $\Gamma_{2ph,v}$=10 s^{-1}, Γ_{diss}=200 s^{-1}, REMPD time 1 s.

IV. DETERMINATION OF FUNDAMENTAL CONSTANTS

A determination of fundamental constants may be provided by comparing the theoretical frequencies of two-photon hydrogen molecular ions rotational and rovibrational transitions with the experimental frequencies, following the approach of CODATA least-squares adjustment [15].

The energy levels of HD^+ ions can be expressed in the framework of the quantum electrodynamics as a series expansion :

$$E = R_\infty \left[\begin{array}{l} E_{nr}(\mu_{pe}, \mu_{dp}) + \alpha^2 F_{QED}(\alpha, \mu_{pe}, \mu_{dp}) \\ + \left(A_p^{fs} (r_p/a_0)^2 + A_d^{fs} (r_d/a_0)^2 \right) \end{array} \right] \quad (14)$$

in function of the Rydberg constant R_∞, the proton-to-electron mass ratio $\mu_{pe} = M_p/m_e$, the deuteron-to-proton mass ratio $\mu_{dp} = M_d/M_p$, the fine-structure constant α, the proton radius r_p, the deuteron radius r_d, and the Bohr radius $a_0 = \alpha/4\pi R_\infty$. The first term corresponds to the nonrelativistic energy, the next term to a series expansion of corrections that depend on α (QED corrections), $Z_{p,d}\alpha$ (relativistic corrections), and $m_e/M_{p,d}$ (recoil corrections). The last terms, depending on the Bohr radius, are associated to the finite-size of the proton and the deuteron.

The sensitivity coefficient of a transition frequency f to a constant c is :

$$K_c = \frac{c_0}{f_0} \left(\frac{df}{dc} \right)_{c_0} \quad (15)$$

HD^+ ion transition frequency f_0 is calculated with the set of the recommended values of fundamental constants $\{c_0\}$ given by CODATA. The sensitivity coefficients for selected two-photon hydrogen molecular ions transitions are calculated using the dependences of different terms in Eq. (14) and presented in Table IV. The sensitivity coefficients to proton-to-electron and deuteron-to-proton mass ratios are derived using non-relativistic calculations of $\partial E/\partial \ln(\mu_{pe,dp})$ from [25]. The recoil corrections have negligible contributions to these sensitivity coefficients. Sensitivity to α is not addressed in this contribution and the sensitivity coefficients to R_∞ are taken as 1. The sensitivity coefficients to proton and deuteron radii are derived using finite-size correction parameters from [2].

TABLE IV. SENSITIVITY COEFFICIENTS TO CONSTANTS FOR TWO-PHOTON TRANSITIONS OF HD^+ (LINES N° 1-4) AND H_2^+ (LINES N° 5-8). VALUES FOR H_2^+ ARE FROM [26].

N°	V	L	v'	L'	$K_{\mu pe}$	$K_{\mu dp}$	$10^9 \times K_{rp}$	$10^9 \times K_{rd}$
1	0	0	0	2	-0.9848	-0.3284	-1.0581	-6.3355
2	0	1	0	3	-0.9808	-0.3271	-1.0547	-6.3151
3	0	1	2	1	-0.4601	-0.1534	-0.6192	-3.7012
4	0	3	9	3	-0.3522	-0.1175	-0.5880	-3.5000
5	0	2	1	2	-0.4657	0	-1.2400	0
6	3	2	4	2	-0.3652	0	-1.1730	0
7	5	2	6	2	-0.2801	0	-1.1330	0
8	6	2	7	2	-0.2279	0	-1.1140	0

The uncertainty of the determination of fundamental constants through the least-squares adjustment depends on the accuracy of the experimental frequencies and the accuracy of the theoretical calculations. The accuracy of hydrogen molecular spectra can be estimated by considering the signal-to-noise ratio obtained in actual experimental setups and the expected linewidth for two-photon spectroscopy. The rovibrational lines may be measured with an accuracy of 10^{-12} [9]. The accuracy of the rotational lines is assumed at 5×10^{-13}. The theoretical calculations may reach an accuracy estimated at 3×10^{-12} [26].

The uncertainties of the determination of fundamental constants are calculated with the error propagation law for different combinations of two-photon transitions of hydrogen molecular ions. The values of R_∞, μ_{pe}, μ_{dp}, r_p, r_d may be derived from an adjustment of eight transitions shown in Table IV. The results are displayed in Table V on the first line. This adjustment may provide a determination of μ_{pe} with an accuracy improved by an order of magnitude comparing to the CODATA 2014 value [15], while the accuracy of μ_{dp} is improved by a factor of 20. The accuracies for the determination of R_∞, r_p, r_d are comparable with the appropriate values given by CODATA 2014 [15]. Note that this determination of fundamental constants is independent on previous results. As the uncertainties of the determination of proton and deuteron radii are smaller than the known discrepancies [27], this approach may add clues to the proton radius puzzle. Atomic spectroscopy may provide very accurate values for R_∞, r_p, and r_d. If the proton radius puzzle is solved, hydrogen molecular ions spectroscopy may allow accurate determination of μ_{pe} and μ_{dp}. The adjustment of three transitions, shown on the second line of Table V, yields values of μ_{pe} and μ_{dp} with accuracies improved by factors of 26 and 12, respectively, to the relevant values provided by CODATA 2014 [15]. Note that the use of the two-photon rotational line in the adjustment for the determination of μ_{pe} and μ_{dp} improves the accuracy by a factor of ~1.5 comparing to previous results [26].

$$\alpha + \beta = \chi. \quad (1)$$

$$\alpha + \beta = \chi. \quad (1)$$

TABLE V. DETERMINATION OF FUNDAMENTAL CONSTANTS WITH ADJUSTMENTS OF TWO-PHOTON TRANSITIONS OF HYDROGEN MOLECULAR IONS FROM TABLE IV.

Lines for adjustment	$\Delta x(R_\infty)$ $\times 10^{11}$	$\Delta x(\mu_{pe})$ $\times 10^{11}$	$\Delta x(\mu_{dp})$ $\times 10^{11}$	$\Delta x(r_p)$ $\times 10^{3}$	$\Delta x(r_d)$ $\times 10^{3}$
1,2,3,4,5,6,7,8	0.84	0.78	0.55	8.2	3.3
1,4,5		0.37	0.80		

V. CONCLUSION

Double resonance two-photon spectroscopy of trapped hydrogen molecular ions is exploited for a determination of fundamental constants. This contribution discusses the detection by photodissociation of a two-photon rotational transition and a two-photon rovibrational transition on trapped HD^+. The two-photon lineshapes are calculated using a rate equation model for HD^+ ions populations. The resolution is at better than the 10^{-12} level. The spectroscopy scheme involves a THz-wave, an infrared laser, a visible dissociation laser and an UV cooling laser that shift the frequencies of the two-photon

transitions due to the AC-Stark effect. The total lightshift for selected hyperfine components of the rotational transition is evaluated using the two-photon operator formalism. This contribution proposes a method for cancellation of the lightshift of the rotational transition based on an adjustment of the intensity of the laser that probes the rovibrational transition in the double resonance spectroscopy scheme. The Zeeman shifts for selected hyperfine components of the two-photon rotational transition are in the range from the 10^{-13} to 10^{-14} level.

The experimental accuracy with two-photon transitions of hydrogen molecular ions is estimated with signal-to-noise and linewidth considerations at the 10^{-12} level, which corresponds also to the level of accuracy of theoretical calculations. The comparison of experimental data and theoretical calculations may provide an independent and accurate determination of the Rydberg constant, the proton-to-electron mass ratio and the deuteron-to-proton mass ratio, respectively. It provides an alternative way for the measurement of the proton and deuteron radii. Depending on possible issues of the proton radius puzzle in atomic spectroscopy, two-photon spectroscopy of hydrogen molecular ions may lead to an improvement of the determination of the proton-to-electron mass ratio and deuteron-to-proton mass ratio beyond the 10^{-11} level.

ACKNOWLEDGMENT

The author acknowledges support for this work from the University Lille 1 and the CNRS.

REFERENCES

[1] V.I. Korobov, "Bethe logarithm for the hydrogen molecular ion HD^+," Phys. Rev. A, vol. 70, pp. 012505, July 2004.

[2] V.I. Korobov, "Leading-order relativistic and radiative corrections to the rovibrational spectrum of H_2^+ and HD^+," Phys. Rev. A, vol. 74, pp. 052506, November 2006.

[3] V.I. Korobov, "Relativistic corrections of $m\alpha^6$ order to the rovibrational spectrum of H_2^+ and HD^+ molecular ions," Phys. Rev. A, vol. 77, pp. 022509, February 2008.

[4] V.I. Korobov, L. Hilico, and J.-P. Karr, "Theoretical transition frequencies beyond 0.1 p.p.b. accuracy in H_2^+, HD^+, and antiprotonic helium," Phys. Rev. A, vol. 89, pp. 032511, March 2014.

[5] V.I. Korobov, L. Hilico, and J.-P. Karr, "$m\alpha^7$-Order corrections in the hydrogen molecular ions and antiprotonic helium," Phys. Rev. Lett., vol. 112, pp. 103003, March 2014.

[6] V.I. Korobov, L. Hilico, and J.-P Karr, "Fundamental transitions and ionization energies of the hydrogen molecular ions with few ppt uncertainty," Phys. Rev. Lett., vol. 118, pp. 233001, June 2017.

[7] J. Biesheuvel, J.-P. Karr, L. Hilico, K.S.E. Eikema, W. Ubachs, and J.C.J. Koelemeij, "Probing QED and fundamental constants through laser spectroscopy of vibrational transitions in HD^+," Nat. Commun., vol. 7, pp. 10385, January 2016.

[8] E.J. Salumbides, J.C.J. Koelemeij, J. Komasa, K. Pachucki, K.S.E. Eikema, and W. Ubachs, "Bounds on fifth forces from precision measurements on molecules," Phys. Rev. D, vol. 87, pp. 112008, June 2013.

[9] V.Q. Tran, J.-P. Karr, A. Douillet, J.C.J. Koelemeij, and L. Hilico, "Two-photon spectroscopy of trapped HD^+ ions in the Lamb-Dicke regime," Phys. Rev. A, vol. 88, pp. 033421, September 2013.

[10] F.L. Constantin, "THz/infrared double resonance two-photon spectroscopy of HD^+ for determination of fundamental constants," Atoms, vol. 5, pp. 38, October 2017.

[11] S. Alighanbari, M. Hansen, V.I. Korobov, and S. Schiller, "Rotational spectroscopy of cold and trapped molecular ions in the Lamb-Dicke regime," Nat. Phys., vol. 18, pp. 74-79, March 2018.

[12] B. Cagnac, G. Grynberg, and F. Biraben, "Spectroscopie d'absorption multiphotonique sans effet Doppler," J. Phys. France, vol. 34, pp. 845–858, Octobre 1973.

[13] D. Bakalov, V.I. Korobov, and S. Schiller, "High-precision calculation of the hyperfine structure of the HD^+ ion," Phys. Rev. Lett., vol. 97, pp. 243001, December 2006.

[14] A. Carrington, I.R. McNab, and C.A. Montgomerie, "Spectroscopy of the hydrogen molecular ion," J. Phys. B, vol. 22, pp. 3551–3586, November 1989.

[15] P.J. Mohr, B. Taylor, and D.B. Newell, "CODATA recommended values of the fundamental physical constants: 2014," Rev. Mod. Phys., vol. 88, pp. 035009, September 2016.

[16] A. Carrington, I. R. McNab and C. A. Montgomerie-Leach, "Vibration-rotation spectroscopy of the HD^+ ion near the dissociation limit. Part IV. Nuclear hyperfine interactions," Mol. Phys., vol. 91, pp. 735-762, August 1991.

[17] D. Bakalov, V.I. Korobov, and S. Schiller, "Magnetic field effects in the transitions of the HD^+ molecular ion and precision spectroscopy," J. Phys. B, vol. 44, pp. 025003, January 2011.

[18] J. Brown and A. Carrington, Rotational Spectroscopy of Diatomic Molecules, 1st ed, Cambridge: Cambridge University Press, 2003.

[19] D. Bakalov and S. Schiller, "Static Stark effect in the molecular ion HD^+," Hyperfine Interact., vol. 210, pp. 25–31, May 2012.

[20] D. Bakalov and S. Schiller, "The electric quadrupole moment of molecular hydrogen ions and their potential for a molecular ion clock," Appl. Phys. B, vol. 114, pp. 213–230, January 2014.

[21] S. Schiller, D. Bakalov, and V.I. Korobov, "Simplest molecules as candidates for precise optical clocks," Phys. Rev. Lett., vol. 113, pp. 023004, July 2014.

[22] Z. Amitay, D. Zajfman, and P. Forck, "Rotational and vibrational lifetime of isotopically asymmetrized homonuclear diatomic molecular ions," Phys. Rev. A, vol. 50, pp. 2304–2308, September 1994.

[23] P.F. Staanum, K. Hojbjerre, P.S. Skyt, A.K. Hansen, and M. Drewsen, "Rotational laser cooling of vibrationally and translationally cold molecular ions," Nat. Phys., vol. 6, pp. 271–274, March 2010.

[24] T. Schneider, B. Roth, H. Duncker, I. Ernsting, and S. Schiller, "All-optical preparation of molecular ions in the rovibrational ground state," Nat. Phys., vol. 6, pp. 275–278, March 2010.

[25] S. Schiller and V. Korobov, "Tests of time independence of the electron and nuclear masses with ultracold molecules," Phys. Rev. A, vol. 71, pp. 032505, March 2005.

[26] J.-P. Karr, L. Hilico, J.C.J. Koelemeij, and V.I. Korobov, "Hydrogen molecular ions for improved determination of fundamental constants," Phys. Rev. A, vol. 94, pp. 050501, November 2016.

[27] R. Pohl, F. Nez, T. Udem, A. Antognini, A. Beyer, H. Fleurbaey, A. Grinin, T.W. Hänsch, L. Julien, F. Kottmann, et al., "Deuteron charge radius and Rydberg constant from spectroscopy data in atomic deuterium," Metrologia, vol. 54, pp. L1–L10, March 2017.

Thermal noise further reduced ultrastable laser with frequency instability of 5×10^{-16}

Lulu Yan[1, 2], Zhaoyang Tai[1, 2], Yanyan Zhang[1, 2], Pan Zhang[1], Wenyu Zhao[1], Xiaofei Zhang[1, 2], Wenge Guo[1], Shougang Zhang[1], Haifeng Jiang[1, 2]

[1]Key Laboratory of Time and Frequency Primary Standards, National Time Service Center (NTSC), Chinese Academy of Sciences, Xi'an China

[2] School of Astronomy and Space Science, University of Chinese Academy of Sciences, Beijing, China

haifeng.jiang@ntsc.ac.cn

Abstract—**We report on the progress of the thermal noise further reduced method via enlarging the equivalent beam size without increasing the cavity length in cavity-stabilized lasers at 1555 nm, which are built as the frequency source for a photonic microwave generation system. In addition, we perform an experiment to evaluate the effect of thermal noise reduced method via estimating the frequency instability of a synthesized new ultrastable laser. The relative frequency instability reaches 5×10^{-16} at 1 s averaging time via reducing the thermal noise of the cavity.**

Keywords—Fabry-Perot; Thermal noise; Optical resonator; Laser stabilization; Frequency standard;

I. INTRODUCTION

Ultrastable lasers play key roles in accurate modern measurement systems, such as optical clock [1], ultra-low phase noise microwave generation [2], quantum many-body physics [3], gravitational wave detection [4], and dark matter searching [5]. Their frequency instability is mainly attributed to mirror surface fluctuation introduced by thermal noise. Usually, we improve the performance by using longer cavity; however, longer cavity is sensitive to mechanical noise, and faces more difficulties in space application.

We have reported our previous ultrastable lasers, which are referenced to 10-cm ULE Fabry-Pérot (F-P) cavities. Frequency instability of ultrastable laser is 7×10^{-16} [6] limited by the thermal noise. In this paper, we report on a new approach to reduce the thermal noise limitation by enlarging the equivalent beam size without increasing the cavity length. Preliminary results show that the advanced ultra-stable laser exhibit a frequency instability of near 5×10^{-16} @ 1s.

II. EXPERIMENTAL SETUP

The thermal noise of a F-P cavity, is introduced by the Brownian notion of the mirrors, including substrates and coatings, fundamentally limits the length instability of the cavity, and the corresponding double-sideband power spectrum of the mirror displacement is given by [7]

$$G_{\text{mirror}}(f)=\frac{4k_{\text{B}}T}{\omega}\frac{1-\sigma^2}{\sqrt{\pi}Ew_0}(\phi_{\text{sub}}+\frac{2}{\sqrt{\pi}}\frac{1-2\sigma}{1-\sigma}\frac{d}{w_0}\phi_{\text{coat}}) \quad (1)$$

where kB is the Boltzmann constant, T is the temperature and $\omega=2\pi f$ is the angular frequency. These terms constitute the transfer function from stress to displacement, $\cdot\phi_{\text{sub}}$ is the mechanical loss of the mirror substrate, w_0 is the beam radius, d is the coating thickness, and ϕ_{coat} is the mechanical loss of the coating. Consequently, these are three ways to reduce the thermal noise of a cavity: decrease the temperature of the cavity, decrease the loss of the mirrors, or increase the laser beam size in the cavity. After solving a few problems in enlarging the beam size, we increase the beam radius w_0 by a factor about 2 via a new method of increasing the equivalent beam size.

In this experiment, we perform an experiment to explore the averaging effect of a large equivalent beam size for reducing the thermal noise limit of F-P cavity. Fig. 1 shows the experimental setup, it consists of two ultrastable lasers, laser frequency synthesizer and measurement part.

Ultrastable laser 1 (U_1) and ultrastable laser 2 (U_2) are two identical but independent systems, based on two commercial 1555-nm continuous wavelength lasers, which are frequency stabilized to two independent 10-cm F-P cavities made of entire ULE via using Pound–Drever–Hall (PDH) technique [8], exhibit a frequency instability of 7×10^{-16} and a linewidth of ~100 mHz, mainly limited by the thermal noise effect of the ULE cavity [6].

The blue dash box shows the laser frequency synthesizer, which is constituted of several pairs of mirrors, and an AOM for synthesizing a new laser ($U_{1\&2}$) with frequency of $\nu_{1\&2}$ relative with U_1 & U_2 laser. Firstly, the beat note between two ultrastable lasers ($\nu_1-\nu_2$=1.70 GHz, with 2 dBm average power) is detected by a InGaAs photodiode (ET3000A, Electro-Optics Technology, Inc., USA). Then we obtain a divided frequency $(\nu_1-\nu_2)/2$ at 0.85 GHz with ~ -2 dBm power by a 2-times frequency divider (based on a MC10EP139, Onsemi, Inc.). Next, we down-convert this signal by mixing with a reference frequency ν_{SG1} (0.74 GHz) provided by a signal generator (SG382, Stanford) to 110 MHz, which is the resonant frequency of the tank circuits of the AOM. At the same time, the other part of laser from U_2 passes though the AOM via Bragg diffraction [9]. By picking up the positive first-order diffraction light, we can obtain the synthesized new laser with a frequency of

$$\nu_{1\&2} = \nu_2 + \nu_{AOM} = (\nu_1 + \nu_2)/2 - \nu_{SG} \quad (2)$$

In our experiment, we checked that the beat note frequency $\nu_1-\nu_2$ is negative, so we use the positive first-order diffraction light to get $U_{1\&2}$; however, this is not always the case. Actually, if the beat note frequency $(\nu_1-\nu_2)$ is positive, we can obtain the target frequency item of $(\nu_1+\nu_2)/2$ from the negative first-order diffraction light. Note that we use the beat note of $\nu_1-\nu_2$ at 1.70 GHz instead of a low frequency (e.g., 200 MHz) to avoid effects by stray noises due to laser frequency stabilization and fiber noise cancellations.

To measure the additional noise introduced by the optical frequency synthesizing process, we produce another beat note between U_1 and $U_{1\&2}$, and obtain the beat note signal by a photodiode detector (ET3000A) at $(\nu_1-\nu_2)/2+0.74$ GHz, as shown in the green box of Fig. 1. We down-convert two optical beat notes to the operational range of a multichannel frequency counter (FXQE80, K+K Messtechnik) by mixing them with reference frequencies given by two signal generators. A signal at ~1.37 MHz is obtained by mixing the beat note between original lasers of $(\nu_1-\nu_2)$ and SG2 (1.593 GHz). And the other beat note from new synthesized laser and ultrastable laser U_1 is down-concerting to ~1.49 MHz via mixing with SG3 (1.702 GHz). Since the optical beat notes are significantly noisier than the RF signals, we expect that the instability of these two beat notes has a relation of factor 2. For one laser, the relation rate is √2. The discrimination of such a ratio between two beat notes is the noise effect due to the frequency synthesizing. Note that we have synchronized SG2, SG3, and the frequency counter to a common 10 MHz reference frequency.

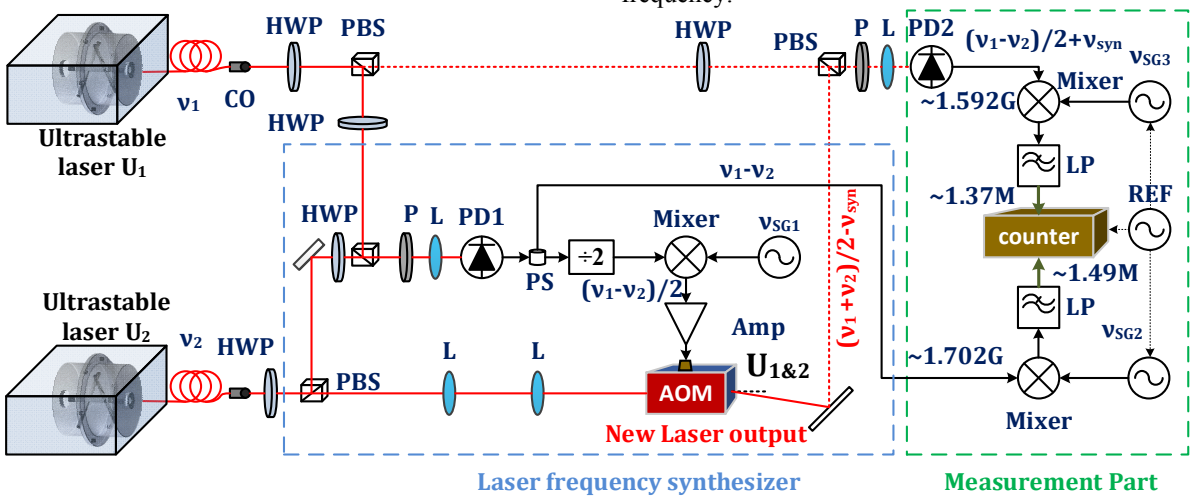

Fig. 1. Experimental setup of an ultrastable laser with two cavities. CO: collimator; HWP: half wavelength plate; U, ultrastable laser; PBS, polarization beam splitter; PD, photodiode; ÷2, frequency divider; SG, signal generator; LP, low-pass filter; PS, RF signal power splitter; L, lens; REF, reference; red line, optical signal; black line, electronic signal.

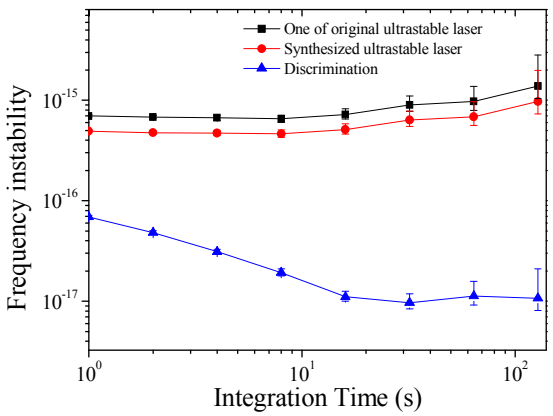

Fig. 2 The black squares: fractional frequency instability of ultrastable laser without using this improved method (characterized by the modified Allan deviation). The red circles: fractional frequency instability of the new ultra-stable laser using this beam size enlarging method. The blue triangles: the discrimination introduced by the optical frequency synthesizing process.

The frequency instabilities of the ultra-stable lasers are shown in Fig. 2. The black squares demonstrate the frequency instability of primary ultrastable laser with an frequency instability of 7×10^{-16} from 1 s to 10 s. The red circles show the frequency instability of the new ultra-laser in which the beam size enlarging method is used, the new result reaches 5×10^{-16} from 1 s to 10 s, about √2 better than the primary one, as expected. And the factor of frequency instability improvement fits well of increase factor of the beam size. The blue triangles demonstrate the discrimination from ratio √2 is 7×10^{-17} @ 1 s and rolls down to 1×10^{-17}@ 16 s. It is clear that the additional noise indicated by the discrimination is negligible. An article about the details had been submitted to a publication [10].

III. CONCLUSION

We demonstrate a new method to obtain a lower frequency instability of ultrastable laser by reducing the thermal noise of the F-P cavity via increasing the equivalent beam size in the cavity. The frequency instability reaches about 5×10^{-16} from 1 s to 10 s. The preliminary result shows that the improvement factor of instability is square root of 2 over the full measurement range. We could guess from this experiment that

a new laser which is synthesizing by n numbers cavities will performance square root of n times reduction in frequency instability. With this technique, we believe that relative instability can be achieved with 10-cm length cavity under room temperature. The further work is undergoing.

ACKNOWLEDGMENT

This work is supported by National Natural Science Foundation of China under Grant No 91536217, and the West Light Foundation of the Chinese Academy of Sciences under Grant No 2013ZD02.

REFERENCES

[1] Y. Y. Jiang, A. D. Ludlow, N. D. Lemke. R. W. Fox, J. A. Sherman, L. S. Ma and C. W. Oates, "Making optical atomic clocks more stable with 10^{-16} level laser stabilization," Nat. Photon. , vol.5, pp. 158, 2011.

[2] T. M. Fortier, M. S. Kirchner, F. Quinlan, J. Taylor, J. C. Bergquist, T. Rosenband, N. Lemke, A. Ludlow, Y. Jiang, C. W. Oates and S. A. Diddams, "Generation of ultrastable microwaves via optical frequency division," Nat. Photon., vol. 5, pp. 425, 2011.

[3] Abbott B. P. et al., "Prospects for observing and localizing gravitational-wave transients with advanced LIGO and advanced Virgo," Phys. Rev. Lett., vol. 116, pp. 061102, 2016.

[4] M. J. Martin, M. Bishof, M. D. Swallows, X. Zhang, C. Benko, J. von Stecher, A. V. Gorshkov, A.M. Rey, and J. Ye, "A quantum many-body spin system in an optical lattice clock," Science, vol. 341, pp. 632, 2013.

[5] A. Derevianko and M. Pospelov, "Hunting for topological dark matter with atomic clocks," Nat. Phys., vol. 10, pp. 933, 2014.

[6] Z. Y. Tai, L. L. Yan, Y. Y. Zhang, X. F. Zhang, W. G. Guo, S. G. Zhang and H. F. Jiang, "Transportable 1555-nm ultra-stable laser with sub-0.185-Hz linewidth," Chin. Phys. Lett., vol. 34, pp. 090602, 2017.

[7] K. Numata, A. Kemery and J. Camp, "Thermal-Noise limit in the frequency stabilization of lasers with rigid cavities," Phys. Rev. Lett., vol. 93, pp. 250602, 2004.

[8] R. W. P. Drever, J. L. Hall, F. V. Kowalski, J. Hough, G. M. Ford, A. J. Munley, and H. Ward, "Laser phase and frequency stabilization using an optical resonator," Applied Physics B vol. 31, 97-105, 1983.

[9] E. I. Gordon, "A review of acoustooptical deflection and modulation devices," Appl. Opt., vol. 5, pp. 1629-1639, 1966.

[10] Z. Y. Tai, L. L.Yan, Y. Y. Zhang, P. Zhang, X. F. Zhang, W. G. Guo, S. G. Zhang, and H. F. Jiang, "Multi-cavity ultrastable laser towards 10^{-18}," unpublished.

Progress on development of optical frequency combs at NTSC

Yanyan Zhang[1,2], Lulu Yan[1,2], Pan Zhang[1], Songtao Fan[1,2], Bingjie Rao[1], Xiaofei Zhang[1,2], Wenge Guo[1], Shougang Zhang[1,2]and Haifeng Jiang[1,2,*]

[1]Key Laboratory of Time and Frequency Primary Standards, National Time Service Center, Chinese Academy of Sciences, Xi'an, China

[2]School of Astronomy and Space Science, University of Chinese Academy of Sciences, Beijing, China

Email: *haifeng.jiang@ntsc.ac.cn*

***Abstract*—In this paper, we demonstrate two techniques to improve performance of Er:fiber frequency combs at NTSC. the first technique is to obtain a robustness and low noise laser, we combine the nonlinear polarization rotation (NPR) and the nonlinear amplifying loop mirror (NALM) mechanisms to a single system. the laser has a large mode-locking range and can self-starting. It works normally after being unpowered six months, and the noise level is similar to the pure NPR. The second technique is proposed a broad bandwidth and large range frequency control method by tuning the polarization state. A special-designed electro-optic modulator (EOM) is used to rotate the polarization state in the NPR system. Compared with the traditional EOM, the sensitivity of f_r to the electric field intensity applied to the EOM is about 100 times larger.**

Keywords—optical comb*; *robustness and low noise laser*; *frequency control*; *polarization state*; *electro-optic modulator

I. INTRODUCTION

National Time Service Center (NTSC) is a scientific research institution engaging in the fundamental research and technology in the fields of time-frequency and satellite navigation, including quantum frequency standard, measurement and control of time-frequency, time scale and time-keeping, transfer and comparison of time-frequency, time service and monitoring, time service terminal and time-user system, etc. NTSC started developing Er:fiber-based optical frequency combs in 2013[1-3].

Optical frequency comb is a frequency-controlled femtosecond laser, which has been widely used in many applications[4, 5]. Robust mode-locked laser and capability of its frequency control are critical in some cases. As the core component, the low noise and robustness laser is the guarantee to obtain the high performance optical frequency comb. there are a few different mode-locked mechanisms to get a femtosecond laser[6]. NPR mechanism is the most widely employed type for its low noise but it is sensitive to environmental disturbance. furthermore, it is difficult to start mode locking for the high threshold. The mode-locking laser with semiconductor saturable absorber mirror (SESAM) is robustness with high noise. The laser with NALM shows medium both in robust and noise level. Hybrid lasers that combine NPR and SESAM mechanisms have been reported[7, 8]. Here, we design a hybrid laser based on NPR and NALM mechanisms.

High-performance optical frequency combs require control repetition rate frequency (f_r) and carrier envelope offset frequency (f_{ceo}) precisely. The traditional way of stabilizing f_r is tuning the cavity length by a Piezotransducor (PZT), while f_{ceo} is typically controlled by tuning the pump power of the laser[9, 10]. To have a high bandwidth control of f_r, one usually use a EOM to tuning the optical length of the cavity[11]. Using the EOM, the bandwidth can reach to 1 MHz. But the sensitivity of f_r to the electric field intensity is small. In this paper, We propose a method that rotates of a NPR mode-locked laser the polarization state to steer laser`s frequencies. By taking advantage of birefringence of the whole laser cavity, this approach can tune frequencies in a broadband width and over a large dynamic range. Compared with other high bandwidth frequency control techniques, the control range of this approach is about 100 times larger.

II. EXPERIMENTAL SETUP AND MEASUREMENT RESULTS

Figure 1 shows the laser setup. Two loops are connected by a fiber splitter: the left part is the classical NPR configuration and the right part is the NALM. The NALM is used to initiate the mode locking state and yield the wide pulses, and then evoke the NPR mechanism. Polarization controller (PC) in the NALM loop is use to control the phase shift relationship of two counter propagating laser by changing the birefringence effect of the fiber in the cavity loop. Wave plates are used to optimize the NPE evolution in the cavity, and the isolator makes the laser transmission unidirectional. Both the EOM and the PZT are used to control the f_{rep} of the optical frequency combs based on this laser. The laser is pumped by two 976-nm diode lasers with a maximum power of ~1 W.

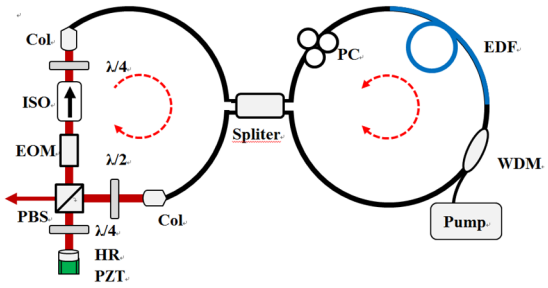

Fig. 1 Laser setup. Col, collimator; /2, half wave plate; /4, quarter wave plate; ISO, isolator; EOM, electro-optic modulator; PBS, polarization beam splitter; WDM, wavelength division multiplexing; PC, polarization controller; Thick solid lines and curves represent optical fibers; red solid lines represent free-space paths.

Figure 2 shows the optical spectrums at different mode locking states. The laser keeps single soliton state when the pump power change between 860 mW to 330 mW, which is verified by its autocorrelation. The spectrum width is from 40 nm to 80 nm, as shown in fig. 2(a). Fig. 2(b) shows the optical spectrums when we tuning the half wave plate in the NPR loop. The mode-locking state can be maintained when the wave plate is rotated more than 24°. Just changing the fringes width on the optical spectrums. The typical NPR system is usually sensitive to the rotation of the wave plates.

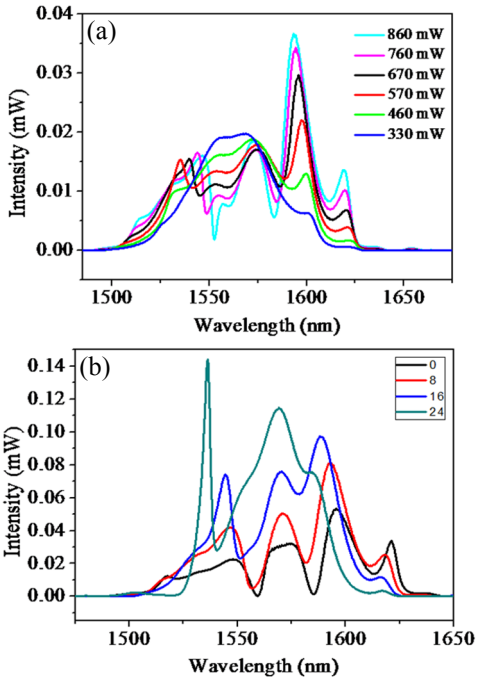

Fig. 2 Optical spectrums at different mode-locking states. (a) Different pump power; (b) Set the half wave plate at different polarization state.

For NPR mode-locked fiber laser, the laser cavity has birefringence. when rotating the polarization state of the laser, the power ratio change between fast and slow axis, leads to a group-velocity shift. On the other hand, the phase velocity, dominated by gain and nonlinear effects, be relatively stable in the case of deep saturation condition. So we can tune the polarization state of the laser to control the optical comb frequencies. Figure 3 shows experimental setup. A self-designed EOM is inserted in the NPR system. The EOM is designed based on the reflective index ellipsoid theory and the Jones matrix. When we input a laser which has a horizontal polarization state, the EOM tunes ellipticity only. we measure the polarization rotation's sensitivities of the f_{rep} f_{ceo} and the comb teeth @ 1555 nm with the electric field intensity on the EOM with the frequency counters. The results show in the fig. 4. The sensitivities of the f_{rep} f_{ceo} and the comb teeth @ 1555 nm are 4 $\times 10^{-4}$ MHz/(V/m), -3.3 $\times 10^{-4}$ MHz/(V/m) and 0.7 $\times 10^{-4}$ MHz/(V/m), respectively. Compared with the tranditional EOM technique (~6.25$\times 10^{-6}$ MHz/(V/m)), the sensitivity of our EOM of f_{rep} is about 100 times larger.

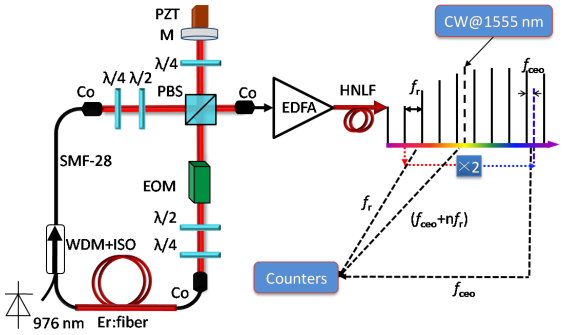

Fig. 3 Experimental setup of the Er:fiber femtosecond laser. Co, collimator; WDM, wavelength division multiplexer; ISO, isolator; M, mirror; HNLF, highly nonlinear fiber; EDFA, erbium-doped fiber amplifier.

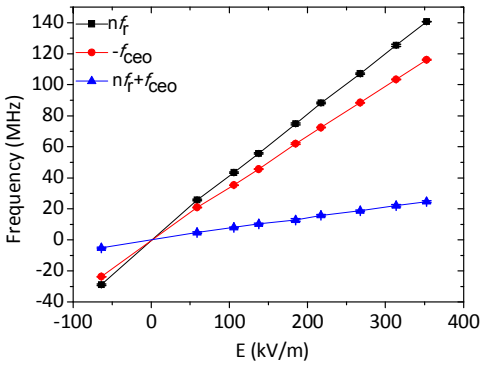

Fig. 4 Sensitivity of the comb teeth @1555 nm,f_{ceo}, and nf_r

III. CONCLUSION

A hybrid femtosecond laser has been designed. the laser combines the advantage of both low noise feature of NPR system and robustness of NALM system with very power efficiency. In order to enlarge the range of high bandwidth frequency control of f_{rep}, we proposed and realized a high bandwidth and large dynamic range frequency control method.

REFERENCES

[1] Y. Zhang, X. Zhang, L. Yan, P. Zhang, B. Rao, W. Han, W. Guo, S. Zhang, and H. Jiang, "Robust optical-frequency-comb based on the hybrid mode-locked Er:fiber femtosecond laser,"Optics Express, Vol. 25, pp. 21719-21725, 2017.

[2] Y. Zhang, S. Fan, L. Yan, L. Zhang, X. Zhang, W. Guo, S. Zhang, and H. Jiang, “Steering optical comb frequencies by rotating the polarization state,” Optics Letters, Vol. 42, pp. 5145-5148, 2017.

[3] Y. Lu, Y. Zhang, L. Zhang, T. Fan, X. Zhang, W. Guo, S. Zhang, and H. Jiang, “Attosecond-resolution Er:fiber-based optical frequency comb,” Chinese Physics Letters, Vol. 32, pp. 1042071-4, 2015.

[4] J. Kim, Y. Song, “Ultralow-noise mode-locked fiber lasers and frequency combs:principles, status, and applications,” Advances in Optics and Photonics, vol. 8, pp. 465-540, 2016.

[5] M. Lexius, T. Wilken, C. Deutsch, M. Giunta, O. Mandel, et. al., “Space-borne frequency comb metrology,”Optica, Vol. 3, pp. 1381-1388, 2016.

[6] S. Droste, G. Ycas, B. Washburn, I. Coddington, and N. Newbury, "Optical frequency comb generation based on erbium fiber lasers", Nanophotonics, 2016.

[7] S. Kim, Y. Kim, J. Park, S. Han, S. Park, Y. Kim, and S. Kim, "Hybrid mode-locked Er-doped fiber femtosecond oscillator with 156 mW output power", Optics Express, Vol. 20, pp. 15053-15059, 2012.

[8] X. Wu, L. Yang, H. Zhang, H. Yang, H. Wei, and Y. Li, "Hybrid mode-locked Er-fiber oscillator with a wide repetition rate stabilization range", Applied Optics, Vol. 54, pp. 1681-1687, 2015.

[9] B. Washburn, S. Diddams, N. Newbury, J. Nicholson, and M. Yan, "Phase-locked, erbium-fiber-laser-based frequency comb in the near infrared", Optics Letters, Vol. 29, pp. 250-252, 2004.

[10] T. Schibli, I. Hartl, D. Yost, M. Martin, A. Marcinkevicius, M. Fermann, J. Ye, "Optical frequency comb with submillihertz linewidth and more than 10 W average power", Nature Photonics, Vol. 2, pp. 355-359, 2008.

[11] D. Hudson, K. Holman, R. Jones, S. Cundiff, J. Ye, "Mode-locked fiber laser frequency-controlled with an intracavity electro-optic modulator", Optics Letters, Vol. 30, pp. 2948-2950, 2005.

Towards Compact Transportable Optical Clock Based on $^{171}Yb^{+}$

Ilya Zalivako*, Ksenia Khabarova, Ilya Semerikov, Alexander Borisenko, Nikolay Kolachevsky
P.N. Lebedev Physcal Institute
Moscow, Russia
*Email:zalivako.ilya@yandex.ru

Ivan Sherstov
Skolkovo Institute of Science and Technology
Moscow, Russia

Sergei Bagaev, Alexey Lugovoy, Alexey Taichenachev, Sergei Chepurov
Institute of Laser Physics SB RAS
Novosibirsk, Russia

***Abstract*—We report on a new project aimed for development of a transportable compact optical clock based on single $^{171}Yb^{+}$ ion trapped in a ion Paul trap. The goal is to reach relative frequency instability level of 5E-16 at 24 hours averaging time.**

Keywords—optical clock, transportable clock, modular design, Yb ion

I. INTRODUCTION

State-of-the-art optical clock have reached ultimate instability of several units in the 18th digit [1,2]. Such unprecedented performance allows to shed the light on fundamental problems like variation of fundamental constants, and opens new possibilities for different applications like navigation, gravimetry etc. Being one of the most sensitive tools, the wide use of optical clock is still limited. Most of optical clock are located in laboratories and cannot be transported. Development of a compact and robust transportable optical clock is one of the actual challenges.

Today Sr optical lattice clock is leading in accuracy and stability and is one of the most common optical clocks in the world. Thus, it is understandable that Sr lattice clock became first transportable optical clock [3]. The clock were designed and developed in frames of the "Space Optical Clock" (SOC) program of European Space Agency (ESA) at PTB and appears to be a car trailer of several m^3 in volume. It demonstrates 7.4E-17 systematic uncertainty and possesses instability in low 17th decimal digit place. Other prototypes of Sr and Yr based optical clock are under development in other groups of SOC consortium [4].

Another approach to the problem is to utilize single ions trapped into a Paul trap. In this case one has to deal with a low signals from single particles which leads to longer averaging time, but at the same time ions have important advantages. Paul ion traps allow to storage ions for extremely long times up to months. Also, choosing a suitable ion one can take another step in compactification and robustness of the system.

To our knowledge there are two perspective ion clocks based on $^{171}Yb^{+}$ and $^{40}Ca^{+}$ ions, respectively, which are today under consideration for mobile systems (and in the long run for space applications). The Ca^{+} based ion clock has demonstrated fractional uncertainty of 7.8E-17 with a target uncertainty of 1E-17. Being assembled in 0.54 m^3 volume (excluding electronics) this clock appears to be the most compact optical clock prototype [5]. The project "Optical single-ion clock for users" (opticlock) started in Germany by consortium uniting scientific institutes and industrial companied is aimed for development of Yb^{+} single-ion optical clock suitable for wide commercial applications including GALILEO and GPS navigation systems.

In this work we report on a new project "Ytterbium based ion standard" (YBIS) started last year by consortium of leading Russian scientific groups (LPI, Skoltech, ILP, Avesta project) for needs of Russian space agency (Russian Spaces Systems). We chose a modular design in order to guarantee fault tolerance of the whole system and to meet geometry requirements.

II. Yb^{+} ENERGY LEVEL SCHEME AND DESIGN OF THE CLOCK

The energy level structure of an Yb^{+} ion is quite fortunate since all the transitions wavelengths are addressable by laser diodes (fig.1). The ionization of neutral Yb requires two photons: the first one at 398 nm excites an atom to $^1P_1$ state and the second transfers an electron to continuum. For the second part a Doppler cooling laser at

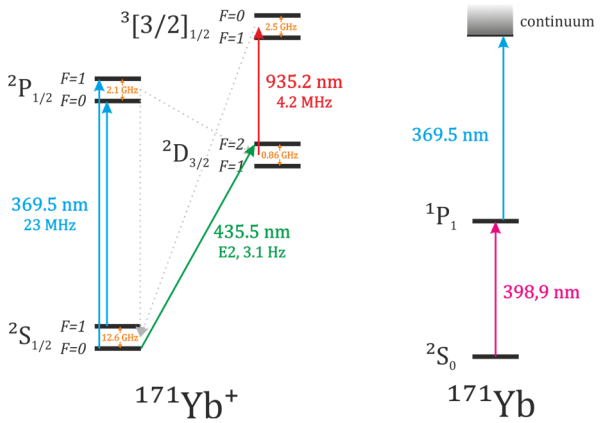

Fig.1 Partial energy level structure for 171Yb+ ion (left) and 171Yb neutral atom (right).

369.5 nm can be used. Doppler cooling is performed via $^2S_{1/2}$ -> $^2P_{1/2}$ transition with a natural linewidth of 23 MHz. With 0.5% probability the $^2P_{1/2}$ state decays to a long living $^2D_{3/2}$ state and an additional repumping laser at 935 nm is required in order to return an ion to the ground state. However in this process both hyperfine sublevels of the ground state are populated and the second 369.5 nm laser is required. To probe the clock $^1S_{1/2}(F=0)$ -> $^3D_{3/2}(F=2)$ transition with natural linewidth of 3.1 Hz one needs ultrastable clock laser at 435.5 nm. Thus we end with five laser systems needed for the experiment. All of them should be frequency stabilized although only clock laser requires tight stabilization by means of external high finesse cavity. Other lasers can be stabilized to a high quality wave meter, for example Angstrom WS-U. All the lasers can be located on the same board and united into one module with one rack of control electronics.

Another necessary module is a compact frequency comb for measuring of clock laser frequency and converting of the optical frequency to the radio frequency. To make it independent we plan to stabilize frequency comb by means of another high finesse cavity working at the wavelength of 1542 nm.

The vacuum chamber together with an optical system for detection of ion fluorescence forms a separate module. The laser irradiation will be delivered to the chamber via fibers, collimators will be fixed directly to the viewports.

The whole setup including electronics should fit 1 m^3 volume and its weight is limited by 300 kg. To meet the requirements we have chosen carbon fiber breadboards since they show excellent rigidity and mass properties. The 3D model of the setup is shown at Fig.2.

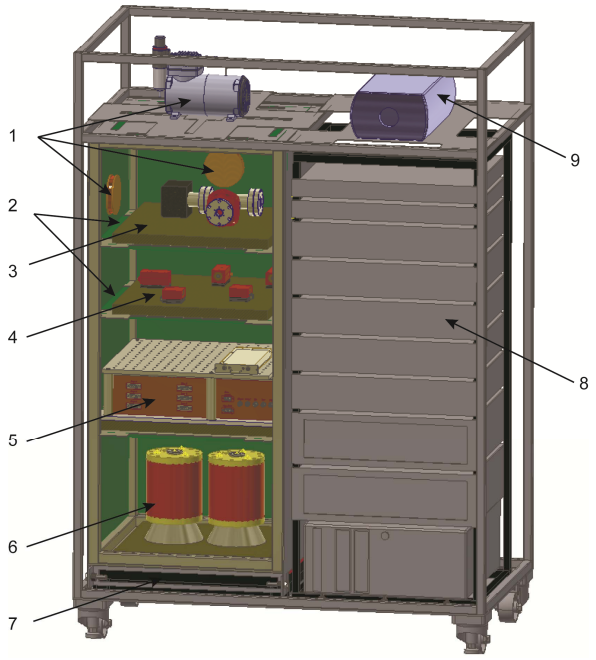

Fig.2 The setup model. 1 – temperature control system, 2 – carbon breadboards, 3 – ion trap module, 4 – laser module, 5 – frequency comb module, 6 – ULE cavities, 7 – vibration isolation, 8 – rack of electronics, 9 – wave meter.

III. LASER MODULE

The laser module appears to be the most challenging and sensitive from the list. Laser diodes are sensitive to temperature fluctuations and vibrations and tend to mode-hop and multimode regime. To decrease this undesirable behavior one has to choose a proper design of the laser system together with high quality vibrational isolation and temperature stabilization. We plan to use a compact design laser system in Littrow scheme at 369.5 nm and at 871 nm, DFB laser diode at 935 nm and interference filter based laser system at 399 nm. All the laser systems except DFB laser diode will be homemade including electronics which is necessary to collect them in a united module. To achieve 435.5 nm light for clock transition probing the 871 nm light will be frequency doubled be means of fiber coupled waveguide PPLN second harmonic generator (SHG) with high conversion efficiency.

As it was mentioned above all the lasers should be frequency stabilized. For this purpose we plan to use Angstrom High-Finesse WSU-2 wave meter. Together with auxiliary electronics it allows to measure and control the wavelengths of up to eight lasers with stability of 1-2 MHz. However the wave meter itself is quite sensitive to temperature fluctuations and vibrations. It should be calibrated every 30 second by an external reference. We plan to use 871 nm laser stabilized to a high-finesse ULE cavity as a reference for WSU-2. Another important requirement to the laser systems is the stability of their frequency on the time frames of the switching period of the wave meter. In order to control four lasers be means of WSU-2 the drift of their frequency should be low. Otherwise it will influence the experiment sequence during the clock cycle.

The clock 871 nm laser will be stabilized to a high-finesse ULE cavity. We developed a number of such systems and successfully integrated them in other projects [6]. The detail description of the cavity can be found in [7]. In the current case we only plan to use a room for improvement and reduce the volume of the vacuum chamber. All other parameters of the system will be the same: 77.5 mm long ULE cavity will be located inside a vacuum chamber at 10^{-8} Torr pressure, surrounded by internal thermal shielding.

IV. ION TRAP MODULE

The ion trap module includes a vacuum chamber with ion trap and ion getter pump and an optical system for fluorescence detection. In this section we describe some solutions we have chosen for the vacuum chamber and the ion trap in order to make the module more compact and robust.

A. Vacuum chamber

Ion trap module is based on a spherical cube low magnetic sensitive stainless steel vacuum chamber with five CF40 and four CF16 mounting ports (Fig.3). The upper CF40 flange is used for connection of a CF40 tee to the ion-NEG vacuum pump and a pinch off tube, which should be used for the first time pumping via turbo pump. Bottom CF40 reserved for 15 pins type C vacuum electrical feedthrough. Two atomic guns, two DC trap electrodes, two compensating electrodes are connected through it. Left CF40 has coaxial electrical feedthrough (up to 5000 V). The ion trap is also mounted on the flange. To make alignment of atomic guns, compensation electrodes and the trap easier all parts are assembled on the RF flange and then the flange is installed to the vacuum chamber and the DC plug is connected. Two other CF40 flanges and all the CF16 flanges are viewports. All CF16 viewports are equipped with optical fiber ports to make optical alignment more mechanically stable. Right CF40 viewport is used to collect the light from the ion. One could use condenser with EMCCD camera or PMT tube with a single lens for this purpose. We plan to use camera for the first alignment and then switch to PMT to reduce weight and size. The front CF40 viewport is intended for clock laser beam precise position adjustment and can be used as another light-collecting window to make easier the micromotion compensation. To prevent scattering of the clock laser light at the chamber walls there will be a light trap at the opposite wall.

B. Ion trap

The ion trap should form pure trapping field, compensate all electrical stray fields and provide Yb atoms in the trap center.

We use the trap of NPL design described elsewhere [8]. A 3D Paul trap has 0,620 mm spacing between the electrodes, trap holder is made of 8 mm thick OFHC copper and connected to a high voltage RF source (Fig.4). DC electrodes are made of molybdenum since it has good thermal conductivity and can be nicely machined [8]. These electrodes are isolated from the RF electrode by means of zerodur glass spacers. They also have small plates at the bottom to shield trapping region from a parasitic RF field that originates from the trap mount. Two atomic guns are made of tantalum 0.8 mm tubes filled with ytterbium and situated in the middle plane of the trap, perpendicular to each other and to the trap axis. The tubes can be also used as compensating electrodes. Using two atomic guns makes the whole system more reliable. As it was mentioned above, the trap is mounted on the CF40 flange, and all DC connections are connected to C type UHV comparable plug.

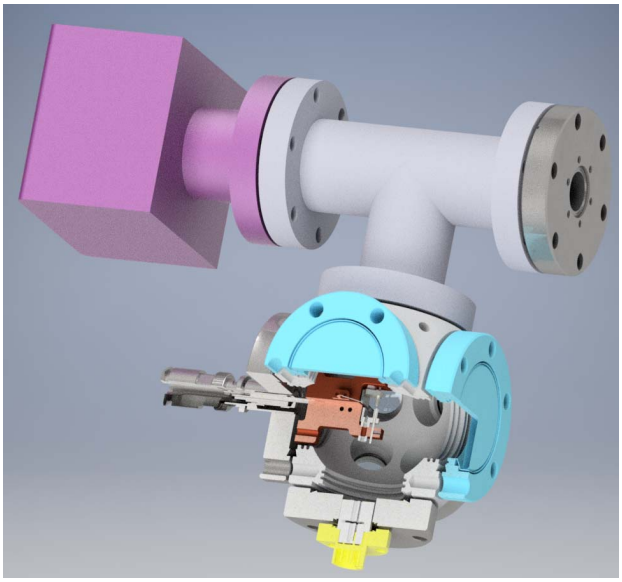

Fig 3. 3D model of ion trap vacuum system with one quarter cross section (screws, pinchoff tube and fiber ports are not shown.)

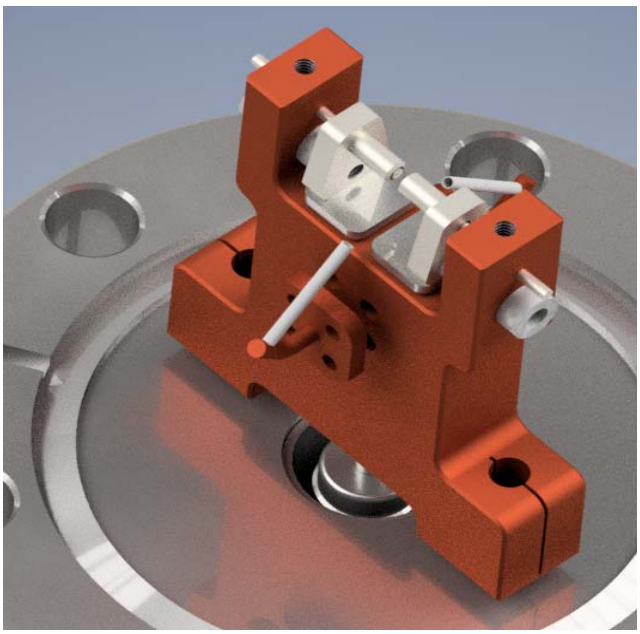

Fig 4. Ion trap module. (The screws and electrical connectors are not shown.)

V. FREQUENCY COMB MODULE

The frequency comb module will be developed by Avesta Project company and planned to be a separate unit. In order to make it independent we will include an extra high-finesse ULE cavity for 1542 nm laser frequency stabilization. It will allow choosing the reference for the comb between clock laser and 1542 nm laser. In future, on can use crystalline silicon cavity for 1542 nm laser stabilization and profit from the advantages like better stability and reduced linear drift. Together with reference cavity, the frequency comb module can be tested and used separately which is perspective for space applications.

VI. CONCLUSION AND OUTLOOK

We presented a new project aimed for a compact and transportable Yb^+ ion based optical clock for mobile applications. The main goal of the project is 5E-16 relative instability of the clock at 24 hours averaging time. The weight and volume of the clock is limited to 300 kg and 1 m^3 correspondingly. At the moment we work on modular design of the clock and look for new decisions for lasers, vacuum part, connections and electronics in order to meet this requirements. We plan to test all the modules separately to find the best solutions for every part. Meanwhile we work on a laboratory prototype of the clock utilizing our usual labor equipment.

ACKNOWLEDGMENT

The work is supported by Russian Ministry of Education (Project ID number: RFMEFI61017X0010).

REFERENCES

[1] N. Huntemann, C. Sanner, B. Lipphardt, C. Tamm, and E. Peik, “Single-Ion Atomic Clock with 3×10-18 Systematic Uncertainty,” Phys. Rev. Lett., vol. 116, no. 6, 2016, pp. 1–5.

[2] I. Ushijima, M. Takamoto, M. Das, T. Ohkubo, and H. Katori, “Cryogenic optical lattice clocks,” Nat. Photonics, vol. 9, no. 3, 2015, pp. 185–189.

[3] J. Grotti, S. Koller, S. Vogt, S. Häfner, U. Sterr, C. Lisdat, H. Denker, C. Voigt, L. Timmen, A. Rolland, F. N. Baynes, H. S. Margolis, M. Zampaolo, P. Thoumany, M. Pizzocaro, B. Rauf, F. Bregolin, A. Tampellini, P. Barbieri, M. Zucco, G. A. Costanzo, C. Clivati, F. Levi, and D. Calonico, “Geodesy and metrology with a transportable optical clock,” Nat. Phys., 2018, pp. 1–5.

[4] S. Schiller, P. Lemonde, G. M. Tino, U. Sterr, C. Lisdat, A. Görlitz, N. Poli, A. Nevsky, and C. Salomon, “The space optical clocks project,” Int. Conf. Sp. Opt. — ICSO 2010, vol. 10565, no. October 2010, 2017, p. 47.

[5] J. Cao, P. Zhang, J. Shang, K. Cui, J. Yuan, S. Chao, S. Wang, H. Shu, and X. Huang, “A transportable 40Ca+ single-ion clock with 7.7x10-17 systematic uncertainty,” arXiv Prepr. arXiv1607.03731, 2016, pp. 1–10.

[6] J. Alnis, A. Matveev, N. Kolachevsky, T. Udem, and T. W. Hänsch, “Subhertz linewidth diode lasers by stabilization to vibrationally and thermally compensated ultralow-expansion glass Fabry-Pérot cavities,” Phys. Rev. A - At. Mol. Opt. Phys., vol. 77, no. 5, 2008, pp. 1–9.

[7] A. A. Golovizin, E. S. Kalganova, D. D. Sukachev, G. A. Vishnyakova, I. A. Semerikov, V. V Soshenko, D. O. Tregubov, A. V Akimov, N. N. Kolachevsky, K. Y. Khabarova, and V. N. Sorokin, “Detection of the clock transition (1.14 μm) in ultra-cold thulium atoms,” Quantum Electron., vol. 45, no. 5, 2015, pp. 482–485.

[8] P. B. R. Nisbet-Jones, S. A. King, J. M. Jones, R. M. Godun, C. F. A. Baynham, K. Bongs, M. Doležal, P. Balling, and P. Gill, “A single-ion trap with minimized ion–environment interactions,” Appl. Phys. B Lasers Opt., vol. 122, no. 3, 2016, pp. 1–8.

Two-Loop Frequency Stabilization Using Concomitant Parameter

V. I. Yudin[1,2], A. V. Taichenachev[1,2], M. Yu. Basalaev[1,2], T. Zanon-Willette[3], J. W. Pollock[4], M. Shuker[4], E. A. Donley[4], and J. Kitching[4]

[1]Novosibirsk State University, Novosibirsk, Russia
[2]Institute of Laser Physics SB RAS, Novosibirsk, Russia
[3]LERMA, Observatoire de Paris, PSL Research University, Paris, France
[4]National Institute of Standards and Technology, Boulder, Colorado, USA
Email: viyudin@mail.ru

***Abstract*— When performing precision measurements, the quantity being measured is often perturbed by the measurement process itself. This includes precision frequency measurements for atomic clock applications carried out with Ramsey spectroscopy. With the aim of eliminating probe-induced perturbations, a method of generalized auto-balanced Ramsey spectroscopy (GABRS) is proposed. Here, the usual local oscillator frequency control loop is supplemented with a second control loop derived from secondary Ramsey sequences interspersed with the primary sequences and with a different Ramsey period. This second loop feeds back to a secondary clock variable and ultimately compensates for the perturbation of the clock frequency caused by the measurements in the first loop. We show that such a two-loop scheme can lead to perfect compensation of measurement-induced light shifts and does not suffer from the effects of relaxation, time-dependent pulse fluctuations and phase-jump modulation errors that are typical of other hyper-Ramsey schemes.**

Keywords—atomic clocks, light shift, Ramsey spectroscopy

I. INTRODUCTION

Atomic clocks are based on high-precision spectroscopy of isolated quantum systems and are currently the most precise scientific instruments. Fractional frequency instabilities and accuracies at the level of 10^{-18} have already been achieved, with the goal of 10^{-19} on the horizon [1]. Frequency measurements at such a level could enable new tests of quantum electrodynamics and cosmological models, searches for drifts of fundamental constants, and new types of chronometric geodesy [2].

For some of the promising clock systems, a key limitation is the frequency shift of the clock transition due to the excitation pulses themselves (probe-field-induced shift). In particular, for ultranarrow transitions (e.g., electric octupole [3] and two-photon transitions [4, 5]), the off-resonant ac-Stark shift can be so large in some cases that high-accuracy clock performance is not possible. In the case of magnetically induced spectroscopy [6, 7], these shifts (quadratic Zeeman and ac-Stark shifts) could ultimately limit the achievable performance. A similar limitation exists for clocks based on direct frequency comb spectroscopy [8, 9] due to off-resonant ac-Stark shifts induced by large numbers of off-resonant laser modes. In addition to optical standards, probe-field-induced shifts can create significant instability for atomic clocks in the microwave range based on coherent population trapping (CPT) [10-12].

In this paper, we present a method of generalized auto-balanced Ramsey spectroscopy (GABRS) for the suppression of the probe-field-induced shifts in atomic clocks. Our method uses a two-loop approach to feedback on and stabilizes the clock frequency ω as well as a second (concomitant) parameter ξ, which is an adjustable property of the first and/or second Ramsey pulses τ_1 and τ_2. To determine the error signals, it is necessary to use Ramsey sequences with two different dark times T_1 and T_2. The operation of GABRS consists of the correlated stabilization of both variable parameters ω and ξ. In addition to the suppression of probe-field-induced shifts, the GABRS technique is protected against various processes of decoherence and also technical issues including time-dependent pulse area fluctuations (even more powerful than the common weak pulse area variation from previous schemes) and phase-jump modulation errors needed to generate the error signal.

II. GENERAL THEORY OF GABRS

We will consider a two-level atom with unperturbed frequency ω_0 of the clock transition $|g\rangle \leftrightarrow |e\rangle$ (see Fig. 1), which interacts with a Ramsey sequence of two absolutely arbitrary pulses (with durations τ_1 and τ_2) of the resonant probe field with frequency ω:

$$E(t) = \mathrm{Re}\left\{\mathcal{E}(t)e^{-i\varphi(t)}e^{-i\omega t}\right\}, \qquad (1)$$

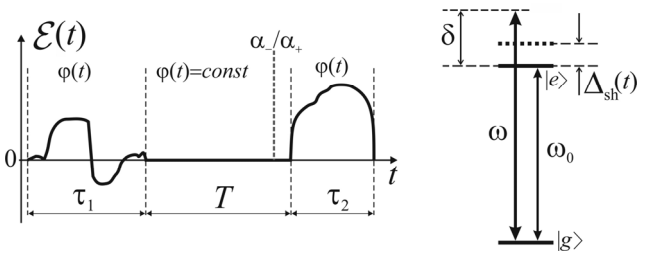

Fig. 1. Left part: schematic illustration of a sequence of two arbitrary Ramsey pulses (with the real amplitude $\mathcal{E}(t)$ and durations $\tau_{1,2}$) which are separated by the dark time T. Right part: scheme of the clock transition $|g\rangle \leftrightarrow |e\rangle$ (with unperturbed frequency ω_0) interacting with the probe field at the frequency ω.

which are separated by a free evolution interval (dark time) T, during which the atom-field interaction is absent (see Fig. 1). We emphasize that the Ramsey pulses with arbitrary durations τ_1 and τ_2 can have an arbitrary shape and amplitude (i.e., during τ_1 and τ_2 an amplitude $\mathcal{E}(t)$ can be arbitrary real function), and an arbitrary phase function $\varphi(t)$ (e.g., the Ramsey pulses can be composite pulses). We assume only one restriction: aside from a phase modulation applied to generate the error signal (discussed below), the phase function $\varphi(t)$ should be constant during the dark time T (as is usually the case for Ramsey spectroscopy of clock transitions).

We will use the formalism of density matrix $\hat{\rho}$, which has the following form

$$\hat{\rho}(t) = \sum_{j,k=g,e} |j\rangle \rho_{jk} \langle k|, \tag{2}$$

in the basis of states $|g\rangle$ and $|e\rangle$. In the resonance approximation, the density matrix components $\rho_{jk}(t)$ satisfy the following differential equations:

$$\begin{aligned}
&\left[\partial/\partial t + \Gamma - i\tilde{\delta}(t)\right]\rho_{eg} = i\Omega(t)\left(\rho_{gg} - \rho_{ee}\right)/2, \\
&\rho_{ge} = \rho_{eg}^*, \\
&\left[\partial/\partial t + \gamma_e\right]\rho_{ee} - \gamma_{g\to e}\rho_{gg} = i\left[\Omega(t)\rho_{ge} - \rho_{eg}\Omega^*(t)\right]/2, \\
&\left[\partial/\partial t + \gamma_g\right]\rho_{gg} - \gamma_{e\to g}\rho_{ee} = -i\left[\Omega(t)\rho_{ge} - \rho_{eg}\Omega^*(t)\right]/2.
\end{aligned} \tag{3}$$

Here the time dependencies $\Omega(t)$ and $\tilde{\delta}(t)$ are determined by the following: $\Omega(t) = \langle d \rangle \mathcal{E}(t) e^{-i\varphi(t)}$ and $\tilde{\delta}(t) = \delta - \Delta_{sh}(t)$ during the action of Ramsey pulses τ_1 and τ_2, but $\Omega(t) = 0$ and $\tilde{\delta}(t) = \delta$ during the dark time T; $\langle d \rangle$ is a matrix element of the atomic dipole moment; $\delta = \omega - \omega_0$ is the detuning of the probe field from the unperturbed atomic frequency ω_0; $\Delta_{sh}(t)$ is an actual probe-field-induced shift (see Fig. 1) of the clock transition during the Ramsey pulses (e.g., it can be ac-Stark shift). Also (3) contains five relaxation constants: γ_e is a decay rate (e.g., spontaneous) of the exited state $|e\rangle$; $\gamma_{e\to g}$ is a rate of the transmission (e.g., spontaneous) to the ground state $|g\rangle$; γ_g is a decay rate of the ground state $|g\rangle$ (e.g., due to black-body radiation and/or collisions); $\gamma_{g\to e}$ is a rate of the transmission from the ground state $|g\rangle$ to the exited state $|e\rangle$. Note that $\gamma_{e\to g} = \gamma_e$ and $\gamma_{g\to e} = \gamma_g$ in the case of closed two-level system, while $\gamma_{e\to g} < \gamma_e$ and/or $\gamma_{g\to e} < \gamma_g$ in the case of open system. The constant $\Gamma = \left(\gamma_e + \gamma_g\right)/2 + \tilde{\Gamma}$ describes the total rate of decoherence: spontaneous as well as all other processes, which are included in the parameter $\tilde{\Gamma}$ (e.g., an influence of the nonzero spectral width and phase noise of the probe field).

Equation (3) can be rewritten in the vector form:

$$\partial_t \vec{\rho}(t) = \hat{L}(t)\vec{\rho}(t), \tag{4}$$

where $\hat{L}(t)$ is 4×4 matrix, which is determined by the coefficients of Eq. (3), and $\vec{\rho}(t)$ is a vector formed by the matrix components $\rho_{jk}(t)$:

$$\vec{\rho}(t) = \left(\rho_{ee}(t), \rho_{eg}(t), \rho_{ge}(t), \rho_{gg}(t)\right)^T. \tag{5}$$

In this case, a spectroscopic Ramsey signal can be presented in the following general form, which describes Ramsey fringes (as a function of δ):

$$A_{\text{Rams}}(\delta) = \left(\vec{\rho}_{\text{obs}}, \hat{W}_{\tau_2}\hat{G}_T W_{\tau_1}\vec{\rho}_{\text{in}}\right), \tag{6}$$

where the scalar product is determined in the ordinary way: $(\vec{x}, \vec{y}) = \sum_m x_m^* y_m$. Operators W_{τ_1} and $\hat{W}_{\tau_2}$ describe an evolution of an atom during the first (τ_1) and second (τ_2) Ramsey pulses, respectively, and the operator $\hat{G}_T$ describes free evolution during the dark time T. Vectors $\vec{\rho}_{\text{in}}$ and $\vec{\rho}_{\text{obs}}$ are initial and observed states, respectively. For example, if an atom before the Ramsey sequence was in the ground state $|g\rangle$, and after the Ramsey sequence we detect the atom in the exited state $|e\rangle$, then vectors $\vec{\rho}_{\text{in}}$ and $\vec{\rho}_{\text{obs}}$ are determined, in accordance with definition (5), as the following:

$$\begin{aligned}
\vec{\rho}_{\text{in}} &= (0,0,0,1)^T, \\
\vec{\rho}_{\text{obs}} &= (1,0,0,0)^T.
\end{aligned} \tag{7}$$

However, for stabilization of the frequency ω we need to form an error signal (differential signal). In our approach, we use phase jumps α_+ and α_- of the probe field before the second pulse τ_2 (see Fig. 1), as it was proposed in [13]. These jumps

are described by the operators $\hat{\Phi}_+$ and $\hat{\Phi}_-$, respectively. As a result, the error signal can be presented as a difference:

$$S_T^{(\mathrm{err})} = \left(\vec{\rho}_{\mathrm{obs}}, \hat{W}_{\tau_2}\hat{\Phi}_+\hat{G}_T W_{\tau_1}\vec{\rho}_{\mathrm{in}}\right) - \left(\vec{\rho}_{\mathrm{obs}}, \hat{W}_{\tau_2}\hat{\Phi}_-\hat{G}_T W_{\tau_1}\vec{\rho}_{\mathrm{in}}\right) = \left(\vec{\rho}_{\mathrm{obs}}, \hat{W}_{\tau_2}\hat{D}_\Phi\hat{G}_T W_{\tau_1}\vec{\rho}_{\mathrm{in}}\right), \quad (8)$$

with $\hat{D}_\Phi = \hat{\Phi}_+ - \hat{\Phi}_-$. To maximize the error signal, $\alpha_\pm = \pm\pi/2$ is typically used. However, in real experiments, we can have $|\alpha_+| \neq |\alpha_-|$ due to various technical reasons (e.g., electronics) which will lead to a shift of the stabilized frequency ω in the case of standard Ramsey spectroscopy. Therefore, here we will consider the general case of arbitrary α_+ and α_- to demonstrate the robustness of generalized auto-balanced Ramsey spectroscopy, where the condition $|\alpha_+| \neq |\alpha_-|$ will not lead to a frequency shift in atomic clocks.

Let us consider now the structure of the following operators: $\hat{G}_T$, $\hat{\Phi}_+$, $\hat{\Phi}_-$, and $\hat{D}_\Phi$. The operator of the free evolution $\hat{G}_T$ has the following general matrix form:

$$\hat{G}_T = \begin{pmatrix} G_{11}(T) & 0 & 0 & G_{14}(T) \\ 0 & e^{-(\Gamma - i\delta)T} & 0 & 0 \\ 0 & 0 & e^{-(\Gamma + i\delta)T} & 0 \\ G_{41}(T) & 0 & 0 & G_{44}(T) \end{pmatrix}, \quad (9)$$

which corresponds to Eq. (3) if $\Omega(t) = 0$ and $\tilde{\delta}(t) = \delta$. The matrix elements $G_{11}(T)$, $G_{14}(T)$, $G_{41}(T)$ and $G_{44}(T)$ depend on four relaxation constants: γ_e, $\gamma_{e\to g}$, γ_g, $\gamma_{g\to e}$. Operators for the phase jumps $\hat{\Phi}_+$ and $\hat{\Phi}_-$ have forms:

$$\hat{\Phi}_\pm = \begin{pmatrix} 1 & 0 & 0 & 0 \\ 0 & e^{i\alpha_\pm} & 0 & 0 \\ 0 & 0 & e^{-i\alpha_\pm} & 0 \\ 0 & 0 & 0 & 1 \end{pmatrix}, \quad (10)$$

which lead to the following expression for $\hat{D}_\Phi$:

$$\hat{D}_\Phi = \begin{pmatrix} 0 & 0 & 0 & 0 \\ 0 & \left(e^{i\alpha_+} - e^{i\alpha_-}\right) & 0 & 0 \\ 0 & 0 & \left(e^{-i\alpha_+} - e^{-i\alpha_-}\right) & 0 \\ 0 & 0 & 0 & 0 \end{pmatrix}. \quad (11)$$

As a result, taking into account (9), we obtain a formula for the matrix product $\hat{D}_\Phi\hat{G}_T$:

$$\hat{D}_\Phi\hat{G}_T = e^{-\Gamma T}\hat{\Upsilon}_{\delta T}, \quad (12)$$

where the matrix $\hat{\Upsilon}_{\delta T}$ is defined as

$$\hat{\Upsilon}_{\delta T} = \begin{pmatrix} 0 & 0 & 0 & 0 \\ 0 & e^{i\delta T}\left(e^{i\alpha_+} - e^{i\alpha_-}\right) & 0 & 0 \\ 0 & 0 & e^{i\delta T}\left(e^{-i\alpha_+} - e^{-i\alpha_-}\right) & 0 \\ 0 & 0 & 0 & 0 \end{pmatrix}. \quad (13)$$

Note that

$$\hat{\Upsilon}_{\delta T=0} = \hat{D}_\Phi. \quad (14)$$

Thus, the error signal (8) can be rewritten in the following form:

$$S_T^{(\mathrm{err})} = e^{-\Gamma T}\left(\vec{\rho}_{\mathrm{obs}}, \hat{W}_{\tau_2}\hat{\Upsilon}_{\delta T}W_{\tau_1}\vec{\rho}_{\mathrm{in}}\right). \quad (15)$$

Note that this result will be the same if we apply phase jumps $\alpha_\pm$ at any arbitrary point during the dark interval T. It is interesting to note that the expression of the error signal in the presence of relaxation is formally different from the error signal in the absence of relaxation only due to the scalar multiplier $e^{-\Gamma T}$, which affects the amplitude, first of all, but not the overall shape of the error signal. This is one of the main specific properties of the phase jump technique for Ramsey spectroscopy that makes it robust against relaxation.

The main idea of GABRS is the following. First of all, apart from δ (i.e., frequency ω) for the frequency stabilization procedure we will use some additional (concomitant) variable parameter ξ, which is related to the first and/or second Ramsey pulses τ_1 and τ_2. For example, the parameter ξ can be equal to the phase ϕ^e of the second pulse as it was proposed in [14]. However, there are many other variants of the concomitant parameter ξ (e.g., frequency step, pulse duration and etc.) Thus, the error signal in (8) should be considered as a function of two variable parameters $S_T^{(\mathrm{err})}(\delta,\xi)$. Secondly, we will use the Ramsey interrogation of the clock transition for two different, fixed intervals of free evolution T_1 and T_2, i.e., we will use two error signals $S_{T_1}^{(\mathrm{err})}(\delta,\xi)$ and $S_{T_2}^{(\mathrm{err})}(\delta,\xi)$.

For GABRS, the procedure for the frequency stabilization is organized as a series of the following cycles. For interrogation with dark time T_1, the parameter ξ is fixed, and we stabilize the variable detuning δ (i.e., frequency ω) at the zero point of the error signal: $S_{T_1}^{(\mathrm{err})}(\delta,\xi_{fixed}) = 0$. After this procedure, we switch to interrogation with dark time T_2, where we fix the previously obtained detuning δ and stabilize the variable parameter ξ at the zero point of the second error signal: $S_{T_2}^{(\mathrm{err})}(\delta_{fixed},\xi) = 0$. If we continue these cycles, then the final result (formally for $t \to \infty$) consists of the stabilization of

both parameters, $\delta = \bar{\delta}_{\text{clock}}$ and $\xi = \bar{\xi}$, which correspond to the solution of a system of two equations:

$$S_{T_1}^{(\text{err})}(\delta, \xi) = 0, \quad S_{T_2}^{(\text{err})}(\delta, \xi) = 0, \tag{16}$$

in relation to the two unknowns δ and ξ. The value $\bar{\delta}_{\text{clock}}$ describes the frequency shift in an atomic clock.

Taking into account relationship (15), the system (16) can be written in the following form:

$$\left(\vec{\rho}_{\text{obs}}, \hat{W}_{\tau_2} \hat{\Upsilon}_{\delta T_1} W_{\tau_1} \vec{\rho}_{\text{in}}\right) = 0, \quad \left(\vec{\rho}_{\text{obs}}, \hat{W}_{\tau_2} \hat{\Upsilon}_{\delta T_2} W_{\tau_1} \vec{\rho}_{\text{in}}\right) = 0 . \tag{17}$$

Let us show that (17) always contains the solution $\delta = 0$. Indeed, if we apply $\delta = 0$ for operators $\hat{\Upsilon}_{\delta T_1}$ and $\hat{\Upsilon}_{\delta T_2}$, then due to (14) we obtain that the system of two equations (17) is reduced to the following single equation:

$$\left(\vec{\rho}_{\text{obs}}, \hat{W}_{\tau_2} \hat{D}_{\Phi} W_{\tau_1} \vec{\rho}_{\text{in}}\right)\Big|_{\delta=0} = 0 . \tag{18}$$

in relation to only one unknown ξ, which always has a solution under appropriate choice of the parameter ξ.

Thus, we have analytically shown that the GABRS method always leads to zero field-induced shift of the stabilized frequency ω in an atomic clock, $\bar{\delta}_{\text{clock}} = 0$. This fundamental result does not depend on relaxation constants $\{\gamma_e, \gamma_{e\to g}, \gamma_g, \gamma_{g\to e}, \Gamma\}$, the values of phase jumps α_+ and α_- used for error signals, or the parameters (such as: amplitude, shape, duration, phase structure $\varphi(t)$, shift Δ_{sh}, etc.) of the two Ramsey pulses τ_1 and τ_2. Such a robustness is unprecedented for Ramsey spectroscopy. Summarizing, practically all non-idealities of the interrogation procedure (including: field-induced shifts of atomic levels, AOM-induced phase variations, and so on) and all relaxation processes (including decoherence) only influence the stabilized concomitant parameter $\bar{\xi}$, while the stabilized frequency ω remains unshifted, with $\bar{\delta}_{\text{clock}} = 0$. Note that this result is rigorously valid in the absence of atomic "phase memory", because in our theory we assume that the initial state $\vec{\rho}_{\text{in}}$ [see (7)] does not depend on field parameters and is the same for all interrogation cycles (with T_1 and T_2).

Note that the solution of (17)-(18) does not formally depend on the values T_1 and T_2 at all. However, from an experimental viewpoint it is better to use the condition $T_2 \ll T_1$. Indeed, because during the interrogation procedure with dark time T_1 we stabilize the frequency ω using the error signal $S_{T_1}^{(\text{err})}(\delta, \xi_{fixed}) = 0$, we always have $\delta < 1/T_1$ even during the first cycles of the clock stabilization. On the other hand, nonzero detuning $\delta \neq 0$ will influence the second interrogation procedure with dark time T_2 (to stabilize the concomitant parameter ξ) in conformity with the value δT_2, which is contained in the error signal $S_{T_2}^{(\text{err})}(\delta, \xi)$. Therefore, if $T_2 \ll T_1$, then we obtain an estimation: $|\delta T_2| < T_2/T_1 \ll 1$, i.e., the results of the stabilization of the concomitant parameter ξ (using $S_{T_2}^{(\text{err})}(\delta_{fixed}, \xi) = 0$) will weakly depend on the results of the frequency stabilization during interrogation procedure with dark time T_1. An additional advantage of the condition $T_2 \ll T_1$ is connected with the short-term stability of an atomic clock. Indeed, because the second feedback loop (stabilization of ξ) increases the total period of each cycle, then it is better to use shortest possible T_2. Formally we can even use $T_2 = 0$ (with the phase jumps $\alpha_\pm$ in the virtual point between pulses τ_1 and τ_2). However, due to technical transient regimes (i.e., in acousto-optic modulators) under switching off/on of Ramsey pulses in real experiments, we believe that it is necessary to keep some nonzero dark time, $T_2 \neq 0$, which significantly exceeds any various transient times.

ACKNOWLEDGMENT

This work was supported by the Russian Scientific Foundation (No. 16-12-10147). A. V. Taichenachev was supported by Russian Foundation for Basic Research (No. 18-02-00822). M. Yu. Basalaev was supported by the Ministry of Education and Science of the Russian Federation (No. 3.1326.2017/4.6), and Russian Foundation for Basic Research (No. 17-02-00570 and 16-32-60050 mol_a_dk).

REFERENCES

[1] M. Schioppo, R.C. Brown, W.F. McGrew et al., Nature Photonics, vol. 11, 48 (2017).

[2] A.D. Ludlow, M.M. Boyd, J. Ye, E. Peik, and P.O. Schmidt, Rev. Mod. Phys., vol. 87, 637 (2015).

[3] K. Hosaka, S.A. Webster, A. Stannard, B.R. Walton, H.S. Margolis, and P. Gill, Phys. Rev. A, vol. 79, 033403 (2009).

[4] M. Fischer, N. Kolachevsky, M. Zimmermann et al., Phys. Rev. Lett., vol. 92, 230802 (2004).

[5] T. Badr, M.D. Plimmer, P. Juncar, M.E. Himbert, Y. Louyer, and D.J.E. Knight, Phys. Rev. A, vol. 74, 062509 (2006).

[6] A.V. Taichenachev, V.I. Yudin, C.W. Oates, C.W. Hoyt, Z.W. Barber, and L. Hollberg, Phys. Rev. Lett., vol. 96, 083001 (2006).

[7] Z.W. Barber, C.W. Hoyt, C.W. Oates, L. Hollberg, A.V. Taichenachev, and V.I. Yudin, Phys. Rev. Lett., vol. 96, 083002 (2006).

[8] T.M. Fortier, Y.Le Coq, J.E. Stalnaker et al., Phys. Rev. Lett., vol. 97, 163905 (2006).

[9] M.C. Stowe, M.J. Thorpe, A.Pe'er et al., Adv. At. Mol. Opt. Phys., vol. 55, 1 (2008).

[10] G.S. Pati, Z. Warren, N. Yu and M. S. Shahriar, J. Opt. Soc. Am. B, vol. 32, 388 (2015).

[11] M.A. Hafiz, G. Coget, P. Yun, S. Guerandel, E. de Clercq, and R. Boudot, J. Appl. Phys., vol. 121, 104903 (2017).

[12] X. Liu, E. Ivanov, V.I. Yudin, J. Kitching, and E.A. Donley, Phys. Rev. Appl., vol. 8, 054001 (2017).

[13] A. Morinaga, F. Riehle, J. Ishikawa, and J. Helmcke, Appl. Phys. B, vol. 48, 165 (1989).

[14] Ch. Sanner, N. Huntemann, R. Lange, Ch. Tamm, and E. Peik, Phys. Rev. Lett., vol. 120, 053602 (2018).

Reducing blackbody radiation shift uncertainty in optical lattice clocks

Piotr Ablewski, Marcin Bober and Michał Zawada
Institute of Physics
Faculty of Physics, Astronomy and Informatics
Nicolaus Copernicus University
Grudziadzka 5, 87-100 Toruń, Poland
Email: piotra@fizyka.umk.pl

***Abstract*—We present an approach to reducing blackbody radiation shift uncertainty in optical lattice clocks based on precise temperature measurements and thermal simulations of heat transfer in vacuum chambers. Two approaches are discussed in this article - the first one is based only on the numerical simulation and the second one contains also analytical solutions of heat transfer problem. The preliminary results of this approach have been discussed.**

I. Introduction

Blackbody radiation shift (BBRs) uncertainty gives one of the most significant contribution to the uncertainty budget of modern optical atomic clocks operating with sub 10^{-18} uncertainties [1]–[4]. It comes from two independent factors - uncertainty of atoms' response to blackbody radiation [5]–[7] and from uncertainty of the temperature of environment visible for atoms [2], [8], [9]. The first factor has been reduced to the level below 10^{-18} over past few years [6], [7], [10], but the second one is still substantial. The main ideas to deal with the uncertainty of temperature are to operate with an optical atomic clock setup at cryogenic temperatures temperatures [1], shield atoms from environment by additional chambers [11] and coat the internal parts of vacuum chambers with high emissivity coatings [9], or combining these two approaches. These solutions are hard or even impossible to be implemented in already operating clocks without substantial modification of their vacuum systems.

Another way of reducing BBRs uncertainty due to the temperature uncertainty is a direct measurement of the temperatures visible by atoms. The temperature can be measured *in situ*, in a place where atoms in an optical lattice are stored [2]. It is also possible to measure temperatures of surfaces visible by atoms with an IR camera [8] or by calibrated PTR thermistors and use acquired data to simulate the heat transfer between optical atomic clock setup parts and atoms.

In this paper we propose the method for heat transfer description in optical atomic clock's vacuum parts, based on preliminary numerical and analytical calculations performed on a 3D model of a vacuum chamber of one of the strontium optical lattice clock build in National Laboratory FAMO in Toruń [14].

II. The brief theory of BBRs

The shift of atomic energy levels caused by a radiation of a hot environment has been calculated based on an atomic structure [6], [7] and there is still lack of experimental data on this topic. The experimental BBRs estimation bases on measurements of DC Stark shift of the clock transition in hot and cold environments [5], [11].

Frequency shift due to the blackbody radiation for energy level indexed with i [11] is given by

$$\Delta\nu_i^{BBR}(T) = \Delta\nu_i^{STAT}(T) + \Delta\nu_i^{DYN}(T), \tag{1}$$

where $\Delta\nu_i^{STAT}$ is the static frequency shift and $\Delta\nu_i^{DYN}$ is the dynamic correction. Both corrections depend on temperature visible by atoms. They can be written in this form since the BBR frequencies in room temperatures are much lower than the frequencies of atomic transitions. The BBRs is a sum of a static part caused by average electric field and a dynamic correction caused by dipole transitions from level i to all other possible levels.

The static correction in units of frequency is given by

$$\Delta\nu_i^{STAT}(T) = -\frac{\alpha_i}{2h} c_1 T^4, \tag{2}$$

where α_i is the static polarizability, $c_1 = 8.545 \cdot 10^{-5} \frac{V^2}{m^2 K^4}$ is constant and T is a temperature visible by atoms.

Dynamic correction is given by

$$\Delta\nu_i^{DYN} = -\frac{1}{4\pi^2}\left(\frac{k_B T}{\hbar}\right)^3 \sum_k \frac{2J_k+1}{2J_i+1}\frac{A_{ki}}{\omega_{ik}^3} G\left(\frac{\hbar\omega_{ik}}{k_B T}\right), \tag{3}$$

where k_B is Boltzmann's constant, ω_{ik} are transition frequencies, A_{ki} are Einstein coefficients and function G() is weighting the transitions frequencies. The G() function is defined as

$$G(y) = \int_0^\infty \frac{x^3}{e^x - 1}\left(\frac{1}{y-x} + \frac{1}{y+x} - \frac{2}{y}\right) dx. \tag{4}$$

These values could be calculated analytically or with a help of symbolic algebra solvers and packages for numerical integration.

978-1-5386-5620-4/18/$31.00 ©2018 IEEE

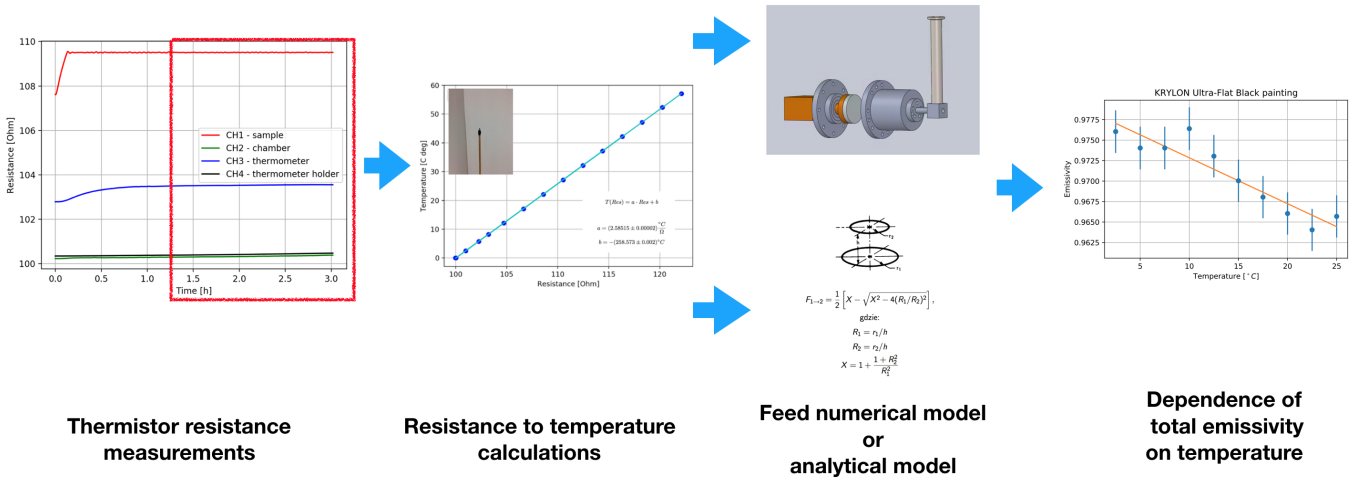

Fig. 1. Schematics of emissivity coefficients measurement procedure and setup

III. Emissivity coefficients measurements

An overview of the literature on high precision emissivity coefficients' measurements revealed the shortage of data which could be used for estimation of BBRs with the heat transfer simulation. Due to that, we have designed and build new setup for the measurements of emissivity coefficients of vacuum compatible materials in room temperatures with sub-percent uncertainty [12], [13].

The setup has been designed with the emphasis on a possibility of an analytical description of a heat transfer between surfaces. In this setup the geometry factor describing the amount of a heat transfered from the surface being measured to the surface of the thermometer is close to unity - like in the case of two infinite, parallel surfaces. All internal parts of the setup have been covered with the vacuum compatible painting with a high emissivity coefficient to minimize reflections inside the chamber. The platinum thin layer thermistors were calibrated with the uncertainty lower than 10 mK to the higher class temperature standard in range from 0°C to 30°C.

The schematics of the measurement can be seen in the Fig. 1. The measurement started with the temperature stabilization of a sample. Temperatures of the parts, both inside and outside measurement chamber, were measured independently to ensure the stationary state, where the heat transfer between surfaces is only a function of the temperature and the emissivity coefficient. The recorded data were used in the numerical heat transfer simulation of the 3D model of the setup to estimate the radiative heat transfer between the sample and the main thermometer.

We have also calculated the radiative heat transfer analytically. It was possible due to the purposely chosen shapes of the surfaces inside vacuum chamber. This approach allows analytical estimations of the uncertainties of heat transfer due to the uncertainties of temperature measurements and the geometry of the measurement setup.

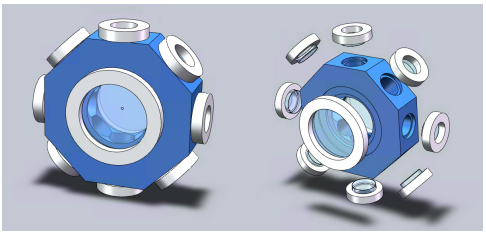

Fig. 2. 3D model of the vacuum chamber of one of the National Laboratory FAMO in Toruń strontium optical lattice clocks

These two complementary approaches enabled us to calculate the emissivity coefficients of samples made of vacuum compatible materials such like stainless steel, cooper, aluminum and titanium with different surface finishing. These materials are being used in constructions of optical atomic clocks' vacuum chambers.

IV. Radiative and convective heat transfer in optical lattice clocks' chambers

With the knowledge of emissivity coefficients of materials from which real optical clocks' chambers are made, we are able to simulate the heat transfer in the optical atomic clock setup [14]. For the simulation an knowledge of the temperatures of optical atomic clock setup parts is needed. They can be measured in the specific points outside the vacuum and the numerical simulation of conductive heat transfer can be applied. The simulation results yield the temperatures of the interior surfaces of clock's vacuum chamber. These temperatures and emissivity coefficients of the surfaces visible by atoms are the parameters for the radiative heat transfer numerical simulation with the finite element method (FEM) algorithm. This approach has been used for an estimation of BBRs in system of two strontium lattice optical clocks in National Laboratory FAMO in Toruń [15], [16].

This method has at least two serious disadvantages. The first one is caused by the FEM algorithm - a 3D model needs to be divided into finite number of vertices. This procedure is called meshing and it causes additional numerical errors due to the simplifications of curved surfaces to the set of vertices connected with edges to triangular shaped faces. The error scales with the size of the grid on which mesh is being calculated. The second disadvantage is the duration of the FEM simulation which increase with the number of vertices, since the heat transfer from one single triangle on the surface to every triangle of the model needs to be calculated. With this method an estimation of BBRs for one second of measurement at sensible level of uncertainty takes several dozen minutes. This approach can not be applied in the precise real time BBRs estimation during the measurements and is applicable only at post processing of the clock's readouts.

Our new approach combines numerical simulation with analytical calculations where it is applicable. The real time full analytical solution of a conductive heat transfer within the whole optical atomic clock vacuum setup is impossible to achieve. Therefore, the full setup still has to be calculated numerically with a FEM solver. Nevertheless, the radiative heat transfer can be partially solved analytically. The radiative heat transfer between two surfaces of any shapes indexed with 1 and 2 is defined as

$$Q_{net} = A_1 F_{1\to 2} \sigma \epsilon (T_1^4 - T_2^4), \tag{5}$$

where A_1 is the area of the surface indexed with 1, σ is the Stefan-Boltzmann constant and ϵ is the emissivity of the surface 1, which is equal to unity for black bodies, and lower than unity for gray bodies. The view factor denoted as $F_{1\to 2}$ is a proportional coefficient describing amount of radiation emitted from the surface indexed with 1 which reaches the surface 2. The expression for view factor between two arbitrary surfaces is given by

$$F_{1\to 2} = \frac{1}{A_1} \int_{A_1} \int_{A_2} \frac{\cos(\theta_1)\cos(\theta_2)}{\pi s^2} dA_1 dA_2, \tag{6}$$

where θ_i is the angle between normal to the surface indexed with i and the section between two surfaces, and s is the length of this section.

View factors for simple geometries can be calculated analytically. For complicated geometries which can be described with sets of analytical functions, Eq. 6 can be solved numerically, using typical methods for integration of continuous functions.

We have performed preliminary simulations with this method for one of our optical atomic clocks vacuum chamber. The 3D model has been simplified to a chamber with glass viewports without antireflective coatings. The material of the whole chamber has been set to stainless steel finished mechanically. Atoms were modeled as a 2 mm diameter sphere. The 3D model shown in the Fig. 2 was meshed with 2 mm grid size and 0.1 mm tolerance resulted in about 100,000 of triangles shown in the Fig. 3. Full FEM numerical simulation of the whole setup with this grid size and tolerance takes hours for a typical PC and analytical description of whole optical atomic clock setup is complicated that is why only a main part of the setup has been used for proof-of-principle calculations. The full set of triangles has been used to simulate the convective heat transfer in the chamber. The dense mesh helps to ensure the convergence of the simulation and gives the overview of temperature gradients inside the chamber.

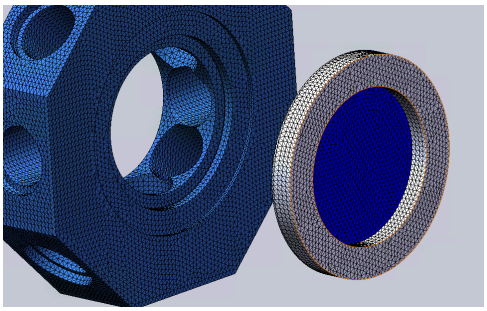

Fig. 3. 3D model of vacuum chamber with dense meshing

The 3D model of the setup has been also prepared to support analytical calculations of the radiative heat transfer. Thanks to the simplification of the mesh shown in the Fig. 4, model of the chamber can be described fully analytically and the view factors between the internal surfaces and the sphere that models the atomic cloud can be calculated analytically or with a symbolic solver.

Previous results of simulations were limited by the knowledge of the temperature visible for atoms. It was the main reason for working on cryogenicaly cooled optical atomic clocks chambers and shielding atoms from hot environment with cold fingers or increasing the emissivity to the value close to unity with special coatings. With the method discussed in this paper, we are able to estimate the blackbody radiation shift with the uncertainty at the level of 10^{-18} for room temperatures range. The uncertainty of temperature needed for 10^{-18} uncertainty of BBRs for discussed model is 10 mK. This level of precision can be achieved with calibrated typical platinum thermistors or thermocouples. With highest class thermometers, uncertainty of single milikelvins can be achieved. For our model, calculated BBRs uncertainty due to the temperature is at the level of $5 \cdot 10^{-19}$ for 1 mK temperature uncertainty in a room temperature. The total BBRs uncertainty is limited at the level of 10^{-18} by the uncertainty of measured strontium atoms polarizability [5].

V. Conclusions

We reported our approach to BBRs estimation in current constructions of optical atomic clocks based on precise measurements of emissivity coefficients of materials used in construction of optical atomic clocks setups. The emissivity coefficients combined with precise temperature measurements can lead to the estimation of BBRs in room temperatures at level lower than 10^{-18}.

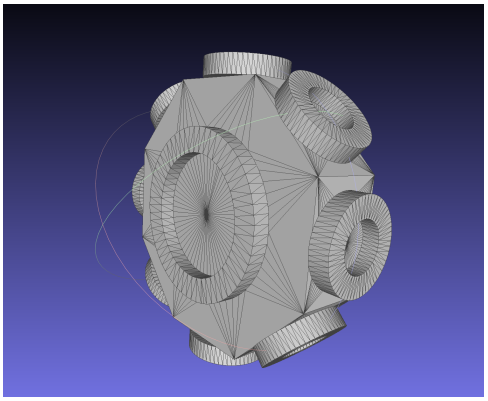

Fig. 4. Simplified 3D model of vacuum chamber for analytical calculations

ACKNOWLEDGMENTS

Support has been received from the project EMPIR 15SIB03 OC18. This project has received funding from the EMPIR programme co-financed by the Participating States and from the European Union's Horizon 2020 research and innovation programme. The "A next-generation worldwide quantum sensor network with optical atomic clocks" project is carried out within the TEAM IV programme of the Foundation for Polish Science co-financed by the European Union under the European Regional Development Fund. Financial support from the Faculty of Physics, Astronomy and Informatics, NCU, task number 190 is acknowledged.

REFERENCES

[1] I. Ushijima et al., *Cryogenic optical lattice clocks*, Nat. Photon. **9**, 185, 2015.
[2] T. L. Nicholson et al., *Systematic evaluation of an atomic clock at* 2×10^{-18} *total uncertainty*, Nat. Commun. **6**, 6896, 2015.
[3] N. Huntemann et al., *Single-Ion Atomic Clock with* 3×10^{-18} *Systematic Uncertainty*, Phys. Rev. Lett. **116** (6), 5, 2016.
[4] N. Nemitz et al., *Frequency ratio of Yb and Sr clocks with 5 10-17 uncertainty at 150 seconds averaging time*, Nature Photon. **10**, 258, 2016.
[5] Th. Middelmann et al., *High Accuracy Correction of Blackbody Radiation Shift in an Optical Lattice Clock*, Phys. Rev. Lett. **109**, 263004, 2012.
[6] M. S. Safronova et al., *Precision Calculation of Blackbody Radiation Shifts for Optical Frequency Metrology*, Phys. Rev. Lett. **107**, 143006, 2011.
[7] M. S. Safronova et al., *Blackbody radiation shift in the Sr optical atomic clock*, Phys. Rev. A **98**, 012509, 2013.
[8] M Doleal et al., *Analysis of thermal radiation in ion traps for optical frequency standards*, Metrologia **52** (6), 842, 2015.
[9] K. Beloy et al., *An atomic clock with* 1×10^{-18} *room-temperature blackbody Stark uncertainty*, Phys. Rev. Lett. **113**, 260801, 2014.
[10] V. V. Flambaum et al., *Energy shift due to anisotropic black body radiation*, Phys. Rev. A **93** (2), 022508, 2016.
[11] Th. Middelmann et al., *Tackling the blackbody shift in a strontium optical lattice clock*, IEEE Trans. Instrum. Meas. **60** (7), 2550, 2011.
[12] P. Ablewski et al., *Towards black body radiation shift uncertainty in optical lattice clocks at* 10^{18} *level at room temperatures*, EFTF/IFCS 2017 Proceedings, 437, 2017.
[13] P. Ablewski et al., *Emissivities of vacuum compatible materials: towards minimising blackbody radiation shift uncertainty in optical atomic clocks at room temperatures*, in preparation, 2018.
[14] M. Bober et al., *Strontium optical lattice clocks for practical realization of the metre and secondary representation of the second*, Meas. Sci. Technol. **26**, 0075201, 2015.
[15] P. Morzyński et al., *Absolute measurement of the* $^1S_0$-$^3P_0$ *clock transition in neutral* ^{88}*Sr over the 330 km-long stabilized fibre optic link*, Sci. Rep. **5**, 17495, 2015.
[16] Cz. Radzewicz et al., *Accuracy budget of the 88Sr optical atomic clocks at KL FAMO*, Phys. Scr. **91**, 084003, 2016.

Analysis of optical atomic clocks readouts aimed on searches for dark-matter signatures

B. Zjawin[1], P. Ablewski[1], K. Beloy[2], S. Bilicki[1,3], M. Bober[1], R. Brown[2], R. Ciuryło[1], R. Fasano[2], H. Hachisu[4], T. Ido[4], J. Lodewyck[2], A. Ludlow[2], W. McGrew[2], P. Morzyński[1,4],D. Nicolodi[2], M. Schioppo[2,5], M. Sekido[4], R. Le Targat[3], P. Wcisło[1], P. Wolf[3], X. Zhang[2] and M. Zawada[1]
[1]Institute of Physics, Faculty of Physics, Astronomy and Informatics, Nicolaus Copernicus University, Torun, Poland
[2]National Institute of Standards and Technology, Boulder, USA
[3]SYRTE, Observatoire de Paris, PSL Research University, CNRS, Sorbonne Universités, Paris, France
[4]National Institute of Information and Communications Technology, Tokyo, Japan
[5]National Physical Laboratory (NPL), Teddington, United Kingdom

***Abstract*—We describe optical atomic clocks readouts' analysis and provide a recipe for analysing data from transcontinental network made of already existing optical atomic clocks to search for dark-matter signatures. We show how to correlate the data and we discuss methods of computing cross-correlation of more than two readouts. Furthermore, we show how to analyse the data from a network of many clocks to exceed previously reported limits on oscillating massive scalar fields couplings to standard matter.**

I. Introduction

Observations at astronomical scales [1], [2] provide a strong evidence for the existence of dark matter (DM). This non - luminous matter is responsible for the structures that we see in the Universe, however we do not know what it consists of and how it was formed. We can observe the impact DM have on stars and galaxies through its gravitational interactions, but examining its composition requires fine models that also explain DM micro-structure. In recent years much attention has been paid to DM in form of topological defects [3], [4] and oscillating scalar massive fields [5], [6]. DM scalar fields ϕ couplings to the standard model (SM) fields are often represented by linear or quadratic interactions [7], [8] that induce variations of the fundamental constants, in particular the fine-structure constant, α. Such variations can be written as

$$\frac{\delta\alpha}{\alpha} = \frac{\phi}{\Lambda_\gamma}, \tag{1}$$

for the linear coupling, and

$$\frac{\delta\alpha}{\alpha} = \frac{\phi^2}{(\Lambda_{\gamma,2})^2}, \tag{2}$$

for the quadratic coupling. They depend on the energy scales, Λ_γ , $\Lambda_{\gamma,2}$, and can be detected by a single optical atomic clock, which precision makes it promising candidate for beyond-the-SM research.

II. Single atomic clock sensitivity to dark matter

It has been recently shown that a single optical atomic clock is sensitive to α variations [9]. Two main components of an optical atomic clock, an ultra-stable optical cavity and an atomic sample, have different susceptibilities to α. Atomic transition scales as α^2 and the length of a cavity follows $\propto \alpha^{-1}$ scaling. This feature makes all already existing clocks sensitive to dark-matter fields that yield α variations. Both transient variations and harmonic oscillations of α can be searched for in readouts, $r(t)$, that contain the correction between the frequency of the laser locked to the cavity and the frequency of clock transition. We consider a frequency of an electronic transition with respect to the cavity, $\omega_0 = \omega_0^X - \omega_{cav}$. Its deviation,

$$\frac{d\omega_0}{\omega_0} = K_\alpha \frac{d\alpha}{\alpha}, \tag{3}$$

introduces the sensitivity coefficient K_α which denotes the susceptibility of a given clock to α. In the non-relativistic approximation, K_α is equal to one.

III. Intercontinental network of optical atomic clocks

Single optical atomic clock sensitivity to DM makes a global network of currently operating optical atomic clocks possible, since they are already collecting data needed for DM searches. This approach can be applied to many clocks, both distant and closely spaced, without the use of phase-noise compensated optical fibre links, because considered effects would result in correlations in remotely recorded signals.

Analysis presented in this paper was used on signals recorded by four optical atomic clocks placed in NIST, Boulder, CO, USA [10], in SYRTE, Paris, France [11], in KL FAMO, Torun, Poland [12], and in NICT, Tokyo, Japan [13]. The network consists of three Sr optical atomic clocks and one Yb optical atomic clock which are placed on three continents.

Analysed redouts were recorded between 9 January 2015 and 17 December 2015. Signals were collected for 11 days in NIST, for 24 days in SYRTE, for 42 days in KL FAMO and for 54 days in NICT. Data resolution varies in different laboratories. The shortest clock cycle lasts 0.5 s in NIST, and the longest one reaches 7 s in NICT.

IV. Topological defects

Topological defects (TD) in scalar fields have been recently proposed as a form of DM [4],[9]. Their coupling to the standard model fields (DM-SM coupling) would lead to transient variations of α. Two overlapping pairs of records are

978-1-5386-5620-4/18/$31.00 ©2018 IEEE

used in topological defect analysis, 3274 s long signals from NIST and SYRTE, and 13471 s long signals from SYRTE and KL FAMO. In presented analysis the measurements need to overlap and have similar resolutions.

A. Pairs of clocks

For more than one pair of clocks, the analysis is based on the Very-Long-Baseline Interferometry techniques. We assume a plane wave model of TD and we compute time difference, τ_i, of clock and TD encounter at the geocenter and at the laboratory,

$$\tau_i = \frac{\vec{v}\vec{r}_i}{v^2}, \tag{4}$$

using the station position vector, $\vec{r}_i$, and the defect velocity vector in the geocentric frame of reference, $\vec{v}$. This model is presented in Fig. 1. It presents two laboratories at positions $\vec{r}_i$ and $\vec{r}_j$ that face TD that moves with $\vec{v}$. 'O' is the geocenter. The cross-correlation of readouts corrected by appropriate

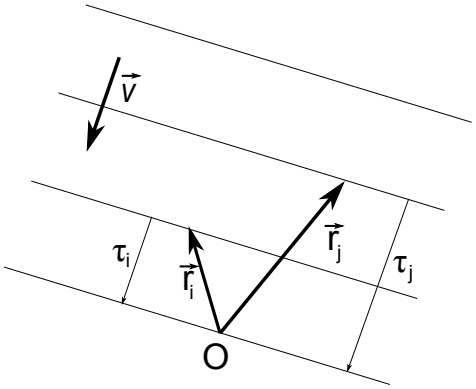

Fig. 1. Plane wave model of TD. Stations positions $\vec{r}_i$ and $\vec{r}_j$ and TD velocity $\vec{v}$ nominate time delays τ_i and τ_j.

time delays can be computed for every pair of clocks. Under assumed TD's velocity, the cross-correlation as a function of TD's direction can be obtained. We assume defect velocity, $v = 300$ km/s, and we compute the cross-correlation of simulated signals corrected by time delays for every possible direction of a defect. We approximate the readouts with white noise and we imitate perturbation of α by 30 s long square pulse. We assume the stations to be already existing laboratories with optical atomic clocks, and we express their vector positions in the International Terrestrial Reference Frame (ITRF). Positions used in the analysis are acquired form ITRF database that provide ITRF coordinates in requested frame and epoch. The averaged cross-correlation of simulated readouts is presented in Fig. 2 as a function of TD's direction expressed in spherical coordinates, where $\vec{v} = v_{TD}[cos\phi sin\theta, sin\phi sin\theta, cos\theta]$. The cross-correlation reaches higher values when $\vec{v}$ matches the imitated value. Presented analysis allows to designate the direction of TD if its adequate velocity is assumed.

B. Data filtering

We apply a high-pass Gaussian filter to all readouts. It eliminates the drifts caused by the cavity instabilities. Its

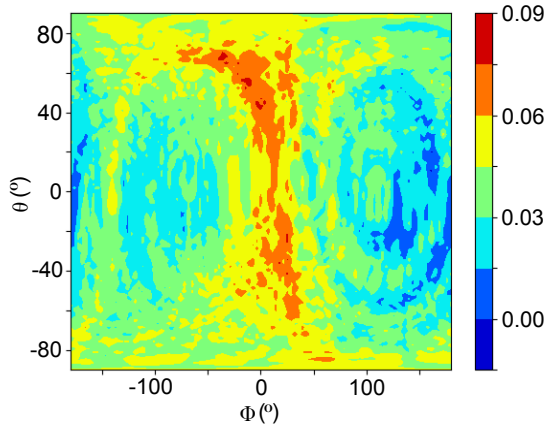

Fig. 2. Expected distribution of averaged cross-correlation values of signals from eight clocks placed on different continents. When a velocity of a defect is assumed, its direction can be estimated (here shown in spherical coordinates).

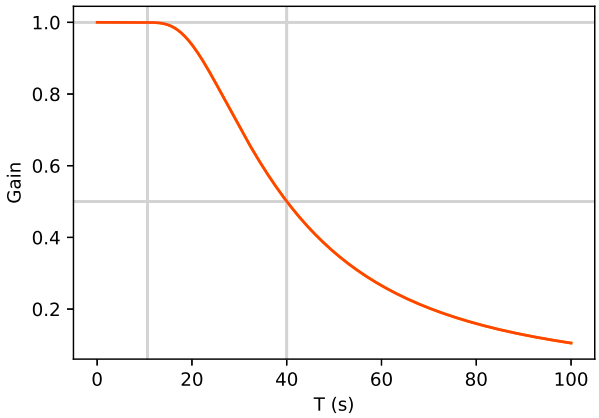

Fig. 3. Transmission characteristics of a high-pass Gaussian filter. Grey horizontal and vertical lines correspond to 100% and 50% transmission, and to $T = 40$ s and $T = 40\pi/\sqrt{ln2}$ s respectively.

transmission characteristics can be written as:

$$S(T) = 1 - e^{-(\pi \frac{T_0}{T})^2}, \tag{5}$$

where T_0 value implies the frequency where 50% of the signal is transmitted. The filter weights both past and future points with a Gaussian profile. The longest events that we consider last 30 s, hence we use $T_0 = 40\pi/\sqrt{ln2}$ s which corresponds to frequency cutoff at 0.025 Hz. The transmission characteristics with applied T_0 are presented in Fig. 3, where gray horizontal lines correspond to 100% and 50% transmission, and gray vertical lines correspond to $T = 40$ s and $T = 40\pi/\sqrt{ln2}$ s. This filter can be used only for continuous series of readouts. We use the same filter with the same frequency cutoff for all assumed sizes of topological defect.

C. Data analysis

We expect a transient variation of α. The simplest stable topological defect in a form of a domain wall is assumed

to have the transverse profile $\phi(x) \sim tanh(x)$ [3]. We approximate it with a square pulse of the size corresponding to the event duration. We test such approximation by repeating the whole analysis for two different profiles, square and $\sim tanh(x)$, and the results do not differ by more than a few percent. We also assume that observed deviation will be the same in all laboratories.

We extract the common part of the signal by cross-correlating the readouts,

$$(r_i * r_j)(\tau) = \frac{1}{t_2 - t_1} \int_{t_1}^{t_2} r_i(t) r_j(t+\tau) dt, \tag{6}$$

and we fit expected cross-correlation shape to obtained data. For a square profile, it is a triangular shape. This process is presented in Fig 4. It shows a fitted expected shape (a triangle with base twice longer than event duration and maximum at $\tau = 0$) for event of 30 s length. An inset presents a fragment of fitted function with the triangular shape.

D. Interpretation of the analysed readouts

The amplitude of a cross-correlation peak, A_0, reflects the common component of readouts r_i and r_j. It can be used to put a constraint on the transient variation of α with the formula introduced in ref. [9]

$$\frac{\delta\alpha}{\alpha} < \sqrt{A_0/\eta}. \tag{7}$$

Here, η is the ratio of duration of an event to the length of cross-correlated readouts. We adjust η to analysed defect size by cross-correlating portions of the readouts that are equal in length to event duration. For example, the duration of an event caused by a topological defect of size $d = 10^4$ km (comparable to the size of the Earth) that moves with velocity $v = 300$ km/h (velocity of the Earth in the galactic halo) would last $t_{dur} = 30$ s. In such case, we divide the measurements to pieces and we only cross-correlate 30 s portions of the readouts. For the analysis of one pair of clocks, before the cross-correlation, we also add time delays to the signals that correspond to different directions of a topological defect. We repeat the analysis for all defect sizes that are approachable by our network. We also analyse the readouts with d as a fixed parameter, and we compute the cross-correlation for different time between consecutive encounters with topological defects, $\mathcal{T}$. A_0 also gives a constrain on energy scale of DM-SM coupling

$$\Lambda_{\gamma,2} > d^{1/2} \sqrt{\sqrt{\frac{\eta}{A_0}} \rho_{DM} \hbar c \mathcal{T} v \sqrt{K_i K_j \omega_i \omega_j}}, \tag{8}$$

where ρ_{DM} is the mean DM energy density, v is the speed of a defect, and K_i and ω_i are sensitivity to α and clock transition frequency for a given clock, respectively.

V. Oscillating scalar massive fields

Ultralight fields are another DM candidate [5],[6]. They oscillate with the Compton frequency related to their mass, $\omega = (mc^2)/\hbar$, what can lead to oscillations of fundamental constants. Readouts from all four laboratories are used in oscillating scalar massive fields analysis.

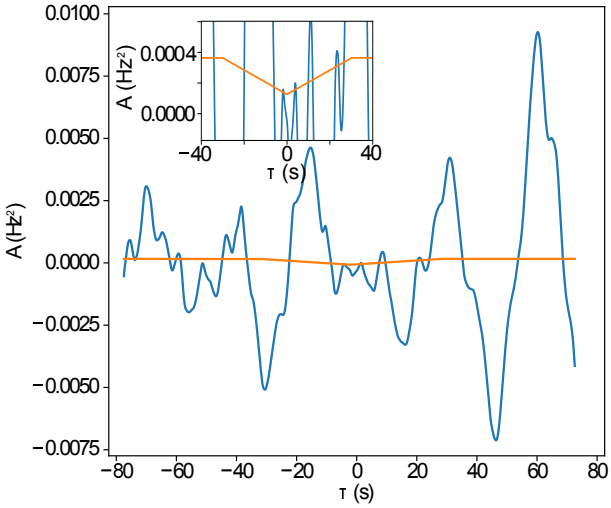

Fig. 4. Cross-correlation of two readouts and fit of expected cross-correlation function of a square perturbation.

A. Data filtering

We filter the data by extracting second degree polynomials from continuous sections of the readouts. Frequency cutoff of applied filter is not straight-forward and it depends on the filtered signal. To determine the cutoff, we add harmonic signals to the readouts in two ways: before and after filtering. We control the amplitude and the frequency of the simulated signals. Subsequently, we fit expected oscillations to both cases and we observe the filter response at different frequencies. Periodogram of the square of the fitted amplitude for both signals is presented in Fig. 5, where the red curve presents the amplitude fitted to filtered signal with fake harmonic signatures and the blue curve presents the amplitude fitted to the signal that was filtered after adding the fake signal. The vertical lines correspond to the frequencies of fake harmonic signal and the horizontal line correspond to its amplitude. Fig. 5 shows that applied filter did not affect high frequencies, however it filtered the low ones. We take 0.000043 Hz as a cutoff frequency in the analysis.

B. Harmonic signatures

We normalize the signals by dividing them by given clock sensitivity coefficient and frequency of a clock transition. We perform the linear least-squares fit with function $R(t) = O + A(\omega)cos(\omega t + \theta)$ for each ω. The duration of recorded measurements is longer than the coherence time of the field for masses higher than $m_\Phi > 10^{-15.4} eV * c^2$. We split readouts into shorter sections in this range. The length of a section corresponds to half of the coherence time. We fit expected function with independent phases and common amplitude in such ranges. Additionally, every readout is

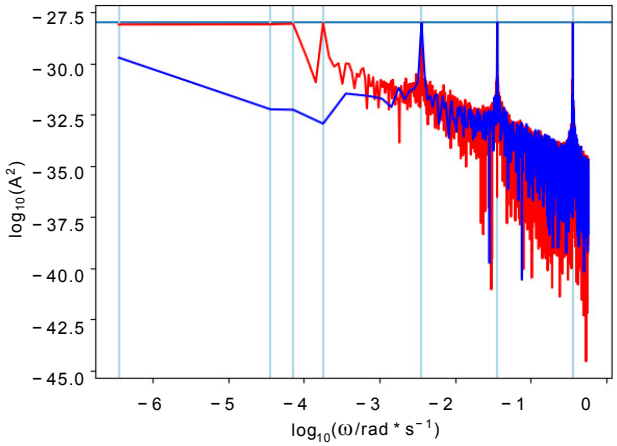

Fig. 5. Periodogram of the square of the fitted amplitude that visualize the frequency cutoff. The red curve shows the results for filtered signal with fake harmonic signatures, the blue one shows the results for signal that was filtered after adding the fake signal. The vertical and horizontal lines respond to the frequencies and the amplitude of fake harmonic signal.

weighted with its inverse variance.

C. Confidence level

The simplest possible model that describes the fitted amplitude is white noise. The probability that fitted amplitude exceeds the noise level is easy to express in such case. For a given confidence level (CL) X, the corresponding level of A^2 can be expressed as

$$A_X^2 = -\langle A^2 \rangle ln(1 - X). \tag{9}$$

It indicates that X is the probability that $A^2 < A_X^2$. For example, 50% CL (X=0.5) denotes that half of the frequency channels should exceed the level given in Eq. (9). Analogous to ref. [11], [6], we also determine a detection threshold. It can be expressed as

$$A_{DT}^2 = -\langle A^2 \rangle ln(0.05/N), \tag{10}$$

where N is the number of frequency channels. Any amplitude that exceeds limit given by Eq. (10) should be interpreted as a detection, and the probability that the noise will be interpreted as one is less than 5%. The amplitude fitted in presented analysis cannot be modeled with a white noise. Amplitude depend on a fitted frequency, $A = A(\omega)$, and we observe a pink noise, $A \propto 1/\omega$. Eq. (9) is valid in this case for 5% and 95% CLs, however the detection threshold needs to be scaled with numerically determined factor

$$A_{DT}^2(\omega) = -1.16\langle A^2 \rangle(\omega) ln(0.05/N). \tag{11}$$

We assume a pink noise for 0.000043 Hz$< \omega < 0.032$ Hz and a white noise for 0.032 Hz $< \omega$.

D. Interpretation of the analysed readouts

The strength of the linear coupling can be characterized by dimensionless coefficient, d_e. Its dependence on the fitted amplitude, $A(\omega)$, can be expressed as

$$d_e = \omega A(\omega)(\frac{8\pi G}{c^2}\rho_{DM})^{-\frac{1}{2}}, \tag{12}$$

where G is the gravitational constant.

VI. Conclusion

The approach presented in this paper makes an intercontinental network of already existing optical atomic clocks possible without making any improvements to already collected readouts. Provided analysis allows to put new limits on both transient and harmonic variations of α. Optical atomic clocks, by dint of their remarkable precision, can begin a new era of beyond-the-SM measurements and examine DM theories that introduce both topological defects and oscillating scalar massive fields.

Acknowledgment

Support has been received from the project EMPIR 15SIB03 OC18. This project has received funding from the EMPIR programme co-financed by the Participating States and from the European Unions Horizon 2020 research and innovation programme. The "A next-generation worldwide quantum sensor network with optical atomic clocks" project is carried out within the TEAM IV programme of the Foundation for Polish Science co-financed by the European Union under the European Regional Development Fund.

References

[1] V. C. Rubin, W. K. Ford Jr, and N. Thonnard, "Rotational properties of 21 sc galaxies with a large range of luminosities and radii, from ngc 4605/r= 4kpc/to ugc 2885/r= 122 kpc," *The Astrophysical Journal*, vol. 238, p. 471, 1980.

[2] G. Hinshaw, J. Weiland, R. Hill, N. Odegard, D. Larson, C. Bennett, J. Dunkley, B. Gold, M. Greason, N. Jarosik *et al.*, "Five-year wilkinson microwave anisotropy probe* observations: data processing, sky maps, and basic results," *The Astrophysical Journal Supplement Series*, vol. 180, no. 2, p. 225, 2009.

[3] A. Vilenkin, "Cosmic strings and domain walls," *Phys. Rep.*, vol. 121, no. 5, pp. 263 – 315, 1985. [Online]. Available: http://www.sciencedirect.com/science/article/pii/037015738590033X

[4] A. Derevianko and M. Pospelov, "Hunting for topological dark matter with atomic clocks," *Nature Physics*, vol. 10, no. 12, p. 933, 2014.

[5] K. Van Tilburg, N. Leefer, L. Bougas, and D. Budker, "Search for ultralight scalar dark matter with atomic spectroscopy," *Phys. Rev. Lett.*, vol. 115, p. 011802, Jun 2015. [Online]. Available: http://link.aps.org/doi/10.1103/PhysRevLett.115.011802

[6] A. Hees, J. Guéna, M. Abgrall, S. Bize, and P. Wolf, "Searching for an oscillating massive scalar field as a dark matter candidate using atomic hyperfine frequency comparisons," *Phys. Rev. Lett.*, vol. 117, p. 061301, Aug 2016. [Online]. Available: http://link.aps.org/doi/10.1103/PhysRevLett.117.061301

[7] T. Damour and J. F. Donoghue, "Equivalence principle violations and couplings of a light dilaton," *Physical Review D*, vol. 82, no. 8, p. 084033, 2010.

[8] Y. Stadnik and V. Flambaum, "Improved limits on interactions of low-mass spin-0 dark matter from atomic clock spectroscopy," *Physical Review A*, vol. 94, no. 2, p. 022111, 2016.

[9] P. Wcisło, P. Morzyński, M. Bober, A. Cygan, D. Lisak, R. Ciuryło, and M. Zawada, "Experimental constraint on dark matter detection with optical atomic clocks," *Nature Astronomy*, vol. 1, p. 0009, 2016.

[10] M. Schioppo, R. C. Brown, W. F. McGrew, N. Hinkley, R. J. Fasano, K. Beloy, T. Yoon, G. Milani, D. Nicolodi, J. Sherman *et al.*, "Ultrastable optical clock with two cold-atom ensembles," *Nature Photonics*, vol. 11, no. 1, p. 48, 2017.

[11] R. Le Targat, L. Lorini, Y. Le Coq, M. Zawada, J. Guéna, M. Abgrall, M. Gurov, P. Rosenbusch, D. G. Rovera, B. Nagórny, R. Gartman, P. G. Westergaard, M. E. Tobar, M. Lours, G. Santarelli, A. Clairon, S. Bize, P. Laurent, P. Lemonde, and J. Lodewyck, "Experimental realization of an optical second with strontium lattice clocks," *Nat. Commun.*, vol. 4, p. 2109, 2013. [Online]. Available: http://link.aps.org/doi/10.1038/ncomms3109

[12] P. Morzyński, M. Bober, D. Bartoszek-Bober, J. Nawrocki, P. Krehlik, Ł. Śliwczyński, M. Lipiński, P. Masłowski, A. Cygan, P. Dunst *et al.*, "Absolute measurement of the 1 s 0- 3 p 0 clock transition in neutral 88 sr over the 330 km-long stabilized fibre optic link," *Scientific Reports*, vol. 5, p. 17495, 2015.

[13] H. Hachisu and T. Ido, "Intermittent optical frequency measurements to reduce the dead time uncertainty of frequency link," *Japanese Journal of Applied Physics*, vol. 54, no. 11, p. 112401, 2015.

Telecom laser standard for time and frequency transfer

Jan Hrabina, Lenka Pravdova, Martin Cizek, Ondrej Cip
Institute of Scientific Instruments, Czech Academy of Sciences
Brno, Czech Republic
hrabina@isibrno.cz

***Abstract* — We present the development and the achieved parameters of the telecom C-band optical frequency laser standard mainly intended for the precise time and frequency dissemination through the optical fiber networks. The compact and robust system based on the ultra-narrow linewidth fiber laser achieves fractional frequency stabilities from 1e-12/1s down to 1e-13/1024s levels (measured through the 306 km long optical fiber link) and can serve as a stable frequency source for applications of the precise time and frequency dissipation, wavelength calibrations in optical telecommunication, remote calibrations or laser interferometry measurement systems.**

Keywords — laser standard; laser spectroscopy; spectral linewidth; frequency stability; optical links

I. INTRODUCTION

The technology development of the accurate time and high-stable optical frequencies dissemination over optical fiber links allows not only to realize precise measurements between scientific institutes and metrological laboratories (for example comparisons of optical clocks and laser standards performance, fundamental constants investigation, accurate time synchronizations), but it also opens new possibilities and applications for using novel specialized sensors in industry (precise laser interferometry, remote calibration of Fiber Bragg Grating strain sensor networks, wavelength calibration of optical communication devices and so on).

One of the key element for those optical links characterization and specified usage is represented by a suitable laser source, which match the requirements of the spectral purity (low linewidth needed for coherence transfer of long distances) and frequency stability (characterization of the link parameters, calibrations). This work is oriented to the development and tests of a frequency stabilized laser standard locked to the acetylene molecular transition operated in the telecom C-band.

II. EXPERIMENTAL SETUP OF THE LASER STANDARD

The stabilized system utilizes the optical fiber erbium doped single-frequency laser with the ultra-narrow linewidth at 100 Hz level (X15 Adjustik laser of the NKT Photonics). The laser frequency is stabilized by the saturated absorption spectroscopy method to the hyperfine transition of the isotopically pure acetylene gas $^{13}C_2H_2$. The absorption media is enclosed in a fused silica made absorption cell (pressure~3 Pa, length of the cell 0.5 m, the arrangement uses double-pass configuration). The hyperfine profile is detected by relatively simple-to-use and well-known 3th derivative technique with synchronous detection. The acetylene media offers a number of strong and spectrally narrow absorption lines in the telecommunication C band. As the laser system is intended to the DWDM (dense wavelength division multiplexing) dark channel optical link usage, we decided to use of P13 acetylene absorption line for locking of the laser (the wavelength of the line P13 of the 1540.567 nm has the smallest frequency difference to the selected C-band channel center, so the crosstalks with the neighboring channels are minimized). The experimental setup is depicted at Fig. 1.

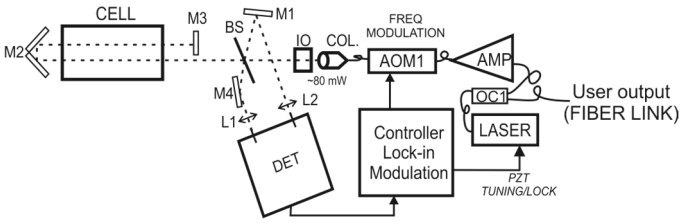

Fig. 1. Block scheme of the laser frequency stabilization. M1-M4 – High-reflective mirrors, BS – beamsampler, AOM1 – fibered acousto-optical modulator, AMP – Er:doped fiber amplifier, OC1 – optical coupler, POL – fiber polarization controller, COL – laserbeam output collimator, IO – optical isolator, L1-L2 – collimation lenses, DET – balanced photodetector for hyperfine transition detection.

The radiation from the laser source (PM fibered output with the ~20 mW of laser power) is divided into a part for the user and the part necessary for the laser frequency locking. To optimize the saturation intensity levels, the measuring beam is amplified by the polarization maintaining Er:doped fiber amplifier (output of 100 mW) and it further passes through the acousto-optical modulator providing the frequency modulation (~1.2 MHz modulation depth at 1.1 kHz modulation speed) required for the synchronous detection of the transition. The laser light is led through the output collimator (laser beam diameter of 2 mm) and optical isolator into the absorption cell

in double-pass configuration (active path of the light of 1 m) and the probe signal is captured by the balanced photodetector suppressing slow intensity drifts and residual amplitude modulation in laser beams. Whole system is enclosed in thermal changes protection shielding and thanks to its simple opto-mechanical setup, the laser standard is very robust and can be independently operated without any adjustment for at least several months.

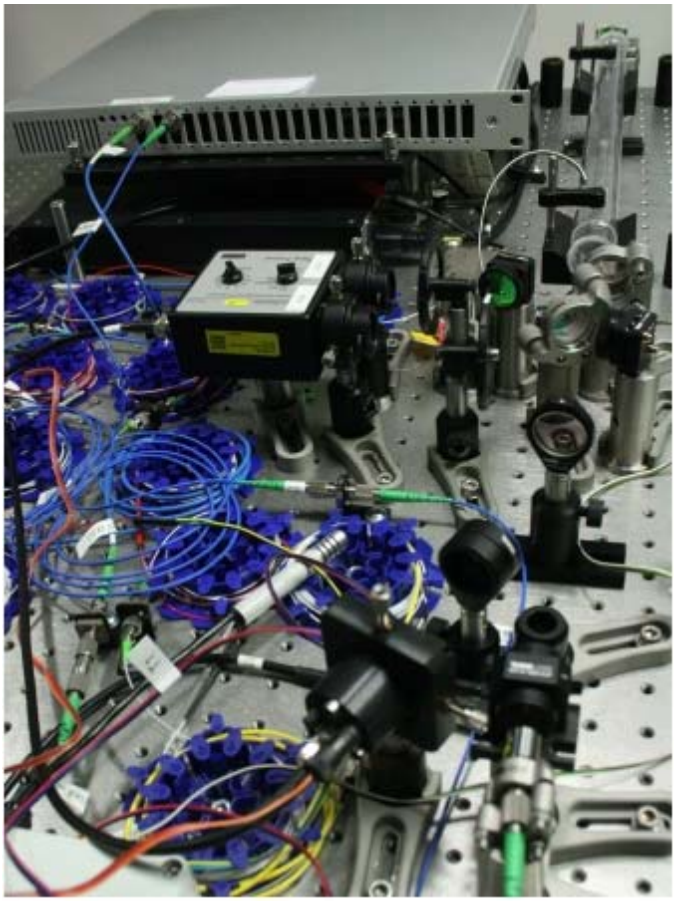

Fig. 2. The experimental setup of $^{13}C_2H_2$-stabilized laser standard.

III. Performance of the Laser Standard

The main purpose of the developed laser standard is to serve as a laser source for the precise optical frequency dissemination through the 306 km long optical fiber link operated between ISI CAS Brno and CESNET Prague. This fiber link uses an internet communication fiber where a DWDM window of 1540-1546 nm is dedicated for the optical frequency coherent transfer and 1 PPS signal dissemination. The characterization of the laser (measurement of the resulting fractional frequency stability of the system) was carried out by the radiofrequency counting of the beat-note signal between the measured laser (operated at CESNET, Prague) and the reference laser (operated at ISI CAS, Brno) through actively compensated fiber link. The reference laser is stabilized through the H-maser referenced optical frequency comb synthesizer. The schematics of the optical fiber link stabilization and fractional frequency stability measurement of the developed laser is at Fig.3.

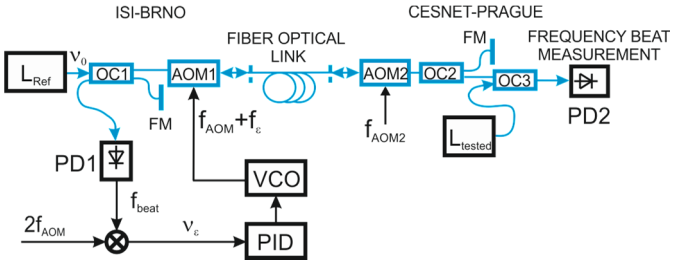

Fig. 3. Experimental setup for fiber link optical path stabilization and laser stability measurement: L_{Ref} – reference laser, OC1-OC3 – fiber couplers, FM – Faraday mirrors, PD1 – fast photodetector for original and AOMs-shifted frequencies beat-note detection, PID – fast PID regulator, VCO – voltage-controlled oscillator, ν_0 – original frequency of the laser, ν_ε – frequency error caused by the link noise, PD2 – frequency beat measurement, L_{tested} – measured laser.

The preliminary fractional frequency stability (Allan variances) measured over the fiber link starts at 1e-12/1 s (short-term) level and goes down to the minimum of the 1e-13/1024 s level, recorded at Fig.4. Thanks to these results, the laser system passes the requirements of the "Recommendation for the practical realization of the meter standard" ($^{13}C_2H_2$ standard) and its robust construction (laser permanently locked for several months without any re-adjustment) promises of passing the requirements for intended application. Furthermore, the improvement represented by the prelocking of the laser to an ultra-stable optical Fabry-Perot cavity (short-term stability) and better environmental influences protection (long-term stability), is in actual progress.

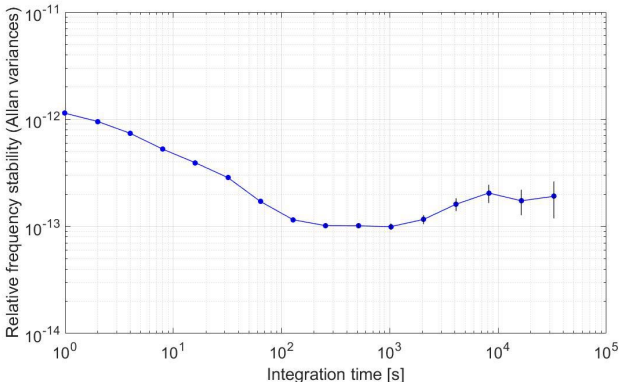

Fig. 4. Fractional frequency stability of the developed system (Allan variances) measured through the actively compensated optical fiber link.

IV. CONCLUSION

We developed the frequency stabilized laser standard intended for precise optical frequencies dissemination through the telecommunication fiber links. The system uses saturated spectroscopy method and the frequency locking of the laser to the selected acetylene hyperfine transition. The laser source exhibits fractional frequency stability from 1e-12/1s (short-term) down to the 1e-13/1024 s (long-term) levels. The improvement of these results is in progress (prelocking to the ultra-stable cavity and referenced frequency comb). Thanks to its robustness and easy-to-use operation, the system allows its utilization not only in a laboratory environment, but also in every-day practise and industrial applications (dissipation of precise time and frequency, free-space optical links research, optical telecommunications, distributed wavelength calibrations, laser interferometry, and so on).

ACKNOWLEDGMENT

The research was supported by the Grant Agency of the Czech Republic, project GA15-18430S and the Technology Agency of the Czech Republic, project TG03010046. The infrastructure for the research was funded by Ministry of Education, Youth and Sports CR, projects LO1212, CZ.1.05/2.1.00/01.0017, and by Academy of Sciences CR, project RVO:68081731.

REFERENCES

[1] T. J. Quinn, “Practical realization of the definition of the metre, including recommended radiations of other optical frequency standards (2001),” Metrologia, 40(2), 2003, p.103-33.

[2] J. Vojtech et al., “Joint accurate time and stable frequency distribution infrastructure sharing fiber footprint with research network”, Opt. Eng., vol. 56(2), 027101, 2017.

[3] M. Cizek et al., “Transfer of Stable Optical Frequency for Sensors Networks via 306 km Optical Fiber Link”, EFTF2016 Conference, York, UK, 2016.

[4] J. Hald et al. “Fiber laser optical frequency standard at 1.54 mu m”, Optics Express 19(3), 2011, p. 2052-2063.

Kinetics of Atoms Cooled on Clock Transitions: Behavior of Energy and Momentum

R.Ya Il'enkov, A.V. Taichenachev, V.I. Yudin, O.N.Prudnikov
Institute of Laser Physics, 630090, Novosibirsk, Russia
Novosibirsk State University, 630090, Novosibirsk, Russia

***Abstract*—We study laser cooling of atoms with narrow-line optical transition, i.e. in regimes when quantum nature of laser-light interactions results significant effect on atom kinetics. We demonstrate the minimum of laser cooing temperature is reached for the light field detuning close to -3 recoil frequency, i.e. is much differ from standard Doppler cooling theory is used for semiclassical description of laser cooling. We define a set of dimensionless parameters that describe the steady state solution of cold atom distribution in laser light and cooling time. The results can be used for analysis an optimal conditions of laser cooling of atoms with narrow lines Ca, Sr and Mg are of interest for optical time standards.**

Pacs 32.80.Pj, 42.50.Vk, 37.10.Jk,37.10.De

I. Introduction

Nowadays deep laser cooled of neutral atoms are routinely used for broad range of modern quantum physics researches including metrology, atom optics, and quantum degeneracy studies. There are well-known techniques for laser cooling below the Doppler limit, like sub-Doppler polarization gradient cooling [1]–[4], velocity selective coherent population trapping [5]–[7] or Raman cooling [8], [9] are restricted to atoms with degenerated over angular momentum energy levels or hyperfine structure. However, for atoms with single ground state like ^{24}Mg, ^{40}Ca, ^{88}Sr, ^{174}Yb are of interest for developing optical time standard these techniques can not be applied.

For atoms with nondegenerate ground state over the angular momentum, the basic theory based on semiclassical approach predicts the limit of laser cooling temperature with the minimum is proportional to natural linewidth γ of exited state $k_B T_D \approx \hbar\gamma/2$, is so called the Doppler limit [10], [11]. One of the way of reaching deeper cooling temperature for these atoms is to use a narrow optical transition (clock transition) with smaller natural linewidth γ. For these atoms we may expect the lower temperature, however the basic semiclassical theory becomes no more valid due to violation of the main requirement that is called semiclassical limit $\omega_R \ll \gamma$ (with $\omega_R = \hbar k^2/2M$ is recoil frequency describes the energy obtained by atom at rest due to spontaneous emission or absorption of the light field photon with momentum $\hbar k$). There are several experimental realization of laser cooling of atoms ^{174}Yb (on optical transition $^1S_0 \rightarrow^3 P_1$, $\lambda = 556$ nm with $\omega_R/\gamma = 0.02$), ^{88}Sr (transition $^1S_0 \rightarrow^3 P_1$, $\lambda = 689$ nm with $\omega_R/\gamma = 0.635$). For cooling ^{88}Sr atoms the authors choose frequency modulated spectrum of the stabilized laser is a comb and laser field detuning much large the optimal $\delta = -\gamma/2$ is predicted by semiclassical theory [12]. The direct cooling with the use of narrow lines of ^{40}Ca (for $\lambda = 657$ nm with $\omega_R/\gamma = 32.3$) and ^{24}Mg (for $\lambda = 457$ nm with $\omega_R/\gamma = 1100$) looks not possible due to significantly large recoil energy to transition linewidth. The table I gives an estimate of the Doppler temperature from quasiclassical approach $T_D = \hbar\gamma/2$ for laser cooling at a narrow clock transition $^1S_0 \rightarrow^3 P_1$ and value of semiclassicity parameter ω_R/γ of these transitions.

TABLE I
Semiclassical estimation of temperature of laser cooling on narrow lines.

Atom	T_D	λ	ω_R/γ
^{174}Yb	4.5 μK	556 nm	0.02
^{88}Sr	0.17 μK	689 nm	0.635
^{40}Ca	10 nK	657 nm	32.3
^{24}Mg	0.75 nK	457 nm	1100

Let us notes the deep laser cooling of Ca atoms on with narrow-line optical transition were realized with "quenching cooling" techniques [13]–[15]. This techniques imply the use of additional light field that allow to increase effective optical transition linewidth $\gamma_{eff} \gg \gamma$ to return back to semiclassical conditions $\omega_R/\gamma_{eff} \ll 1$ for standard regime of laser cooling. However, to our knowledge, it still do not show significant progress for ^{24}Mg atoms.

In our analysis we try to build a quantum theory of laser cooling for the case far beyond the semiclasical limit, i.e. for the case of $\omega_R/\gamma \geq 1$. This allows us to clarify the laser cooling mechanisms with narrow-line optical transitions and estimate the light field parameters for minimum cooling temperature and cooling time. Considering this task we also try to answer the principal question on possibility of direct laser cooling of atoms with applying the field resonant to narrow-line optical transition, or it just a matter of appropriate laser field parameters.

II. Laser cooling far beyond semiclasical limit

Let us consider the classical scheme of laser cooling of atoms in a field formed by two counterpropagating light waves Fig.1. The light field is close to resonance of atom optical transition with natural linewidth γ. The atoms behavior in laser light field with account of quantum recoil effects in the

processes of absorption and emission light field photons can be described entirely by density matrix master equation

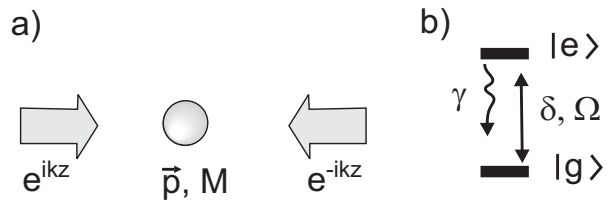

Fig. 1. *Classical scheme of laser cooling in a filed of counterpropagating light waves (a). Scheme of interaction of resonant laser light with atom energy levels (b).*

$$\frac{d}{dt}\hat{\rho} = -\frac{i}{\hbar}\left[\hat{H}, \hat{\rho}\right] + \hat{\Gamma}\left\{\hat{\rho}\right\}, \tag{1}$$

with $\hat{H}$ is Hamiltonian and $\hat{\Gamma}\left\{\hat{\rho}\right\}$ describes relaxation of atom density matrix $\hat{\rho}$ due to spontaneous emission of the photons (see for example [20]). The density matrix contains whole information on internal and external states and correlations of them in the possesses of atom-light interaction.

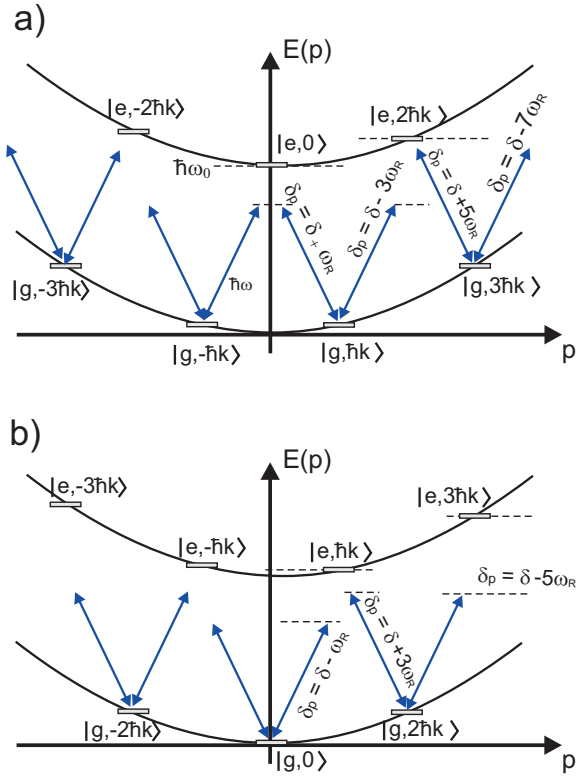

Fig. 2. *Schemes of atom light interaction for atoms with narrow lines in momentum representation.*

The Hamiltonian of atoms in resonant light field in rotating wave approximation (RWA) has a form:

$$\hat{H} = \frac{\hat{p}^2}{2M} - \hbar\delta\hat{P}_e|e\rangle\langle e| + \hat{V}_{ed} \tag{2}$$

The first term describe the atom kinetics energy, operator $\hat{P}_e = |e\rangle\langle e|$ is projection operator on excited state $|e\rangle$, $\hat{V}_{ed} = \hbar\Omega/2|e\rangle\langle g| + h.c.$ describes atom-light coupling of the ground (g) and excited (e) states in electro dipole approximation, Ω is Rabi frequency. In a standing light field created by counterpropagating light waves for laser cooling of atoms the Rabi has a spatial modulation $\Omega(z) = 4\Omega_0\cos^2(kz)$ with Ω_0 is Rabi frequency per one wave.

Let us first describe the parameters of the master equation (1) that describe a laser cooling of atoms:

- The first one is optical transition linewidth γ that describes the spontaneous decay rate and thus the evolution rate of internal states.
- The second one is detuning $\delta = \omega - \omega_0$ of the laser light frequency ω form the atom optical transition frequency ω_0
- The third one is the Rabi frequency Ω that can be expressed through the laser light field intensity $\Omega_0/\gamma = \sqrt{I_0/2I_S}$ with I_S is saturation intensity [16] and I_0 is intensity per one laser wave.
- The last one is recoil energy $\hbar\omega_R$ that describes atom inertia to light field photons mechanical action.

From this list one can separate three independent dimensionless parameters:

$$\delta/\gamma,\ \Omega/\gamma,\ \omega_R/\gamma \tag{3}$$

describing the steady state of atoms in the light field. Additionally, the last parameter in semiclassical description is considered to be negligible low

$$\omega_R/\gamma \ll 1 \tag{4}$$

that is valid for major atoms with "bright" optical transitions available for laser cooling (see for example [16]). Thus in the frame of two-level model the laser cooling is equivalent for all these atoms and steady state distribution can be described by only two parameters:

$$\delta/\gamma,\ \ \Omega/\gamma. \tag{5}$$

Additionally, the laser cooling rate is determined by the slowest processes modification of atom momentum distribution function due to momentum exchange with light photons interaction. The cooling time is also equivalent for all atoms in the limit (4) can be estimated as

$$\tau_{cool} \simeq \omega_R^{-1}.$$

Let us note that for the regime of sub-Doppler cooling we are not considered here, the internal sublevels structure of atoms, the type of optical transition $F_g \to F_e$ (F_g, F_e are the angular momentum of the ground and excited states) and polarization configuration of light field (for example $\sigma_+ - \sigma_-$, $lin \perp lin$ [1], [2], or more general parametrization $\varepsilon - \theta - \overline{\varepsilon}$ [3], [4], [17], [18]) are also should be added to the list of main parameters for master equation (5).

For the regimes of laser cooling far beyond the semiclassical limit (4) the recoil effects becomes much essential. For example the simple scheme of atom-light interaction (Fig.1(b))

is significantly modified. The internal states of atom can be written in momentum representation as a set of families with different momentum p linked with a difference $\Delta p = 2\hbar k$ in the ground and excited states

$$|\psi(t)\rangle = \sum_n \alpha_n(t)|g, p_0 + 2n\hbar k\rangle + \beta_n(t)|e, p_0 + (2n+1)\hbar k\rangle \,. \tag{6}$$

The coupling schemes for families with different p_0 are shown on Fig.2. In the considered quantum regime

$$\omega_R \geq \gamma \tag{7}$$

the processes of induced absorption and emission of light field photons are out of the resonance contour γ and refer different detuning

$$\delta_p = \delta - \omega_R \left(1 \mp 2p/\hbar k\right) \,, \tag{8}$$

depending on the atom momentum in the ground state p. Here the sign "-" is related to induced emission of the photon to copropagating wave or absorption from counterpropagating, and "+" sign for reverse processes. In the considering laser cooling in quantum regime (7) the small parameter is changed to ω_R/γ and the steady state solution of master equation should be described by the set of two parameters from original list (3):

$$\delta/\omega_R, \; \Omega/\omega_R \,, \tag{9}$$

i.e. we have to observe the equivalence of laser cooling of different atoms with use of the narrow-line transitions with dimensionless set of light field parameters (9). To prove this equivalence we perform numerical simulation of master equation (1) for different atoms (Sr, Mg, Ca) with narrow-line optical transitions for set of different parameters.

The steady-state momentum distribution is obtained by direct numerical solution of master equation (1) developed by us in [19], [20]. The suggested method allows to get a direct solution for density matrix containing whole information on internal and external states without any restrictions and limitations.

The Fig.3 shows the results of steady state momentum distribution different atoms (Sr, Mg, Ca) for parameters (9) in ω_R units. We see absolute equivalence for steady-state distribution of laser cooled atoms ^{24}Mg ($\omega_R/\gamma \simeq 1100$), ^{40}Ca ($\omega_R/\gamma \simeq 32.3$), and ^{88}Sr ($\omega_R/\gamma \simeq 0.635$) on narrow-line $^1S_0 \rightarrow ^3P_1$ optical transitions.

First of all, let us emphasize sharp peaks in momentum distribution placed at $p = \pm hk$. These peaks represent effects of velosity-selective coherent population trapping [5]–[7] for Λ scheme of families (6) with $p_0 = 0$ (Fig.2(a)) appeared for two-level atom (atom with nondegenerate ground state).

Additionally, we observe a strong modulation of momentum distribution for small detunings Fig.4. This behavior is a result of momentum selective resonance interaction of atoms with one of counterpropagating wave determined by δ_p.

For low field intensity we may expect the minimum temperature of laser cooling with low population of exited state. In this case the atom distribution in momentum space can be

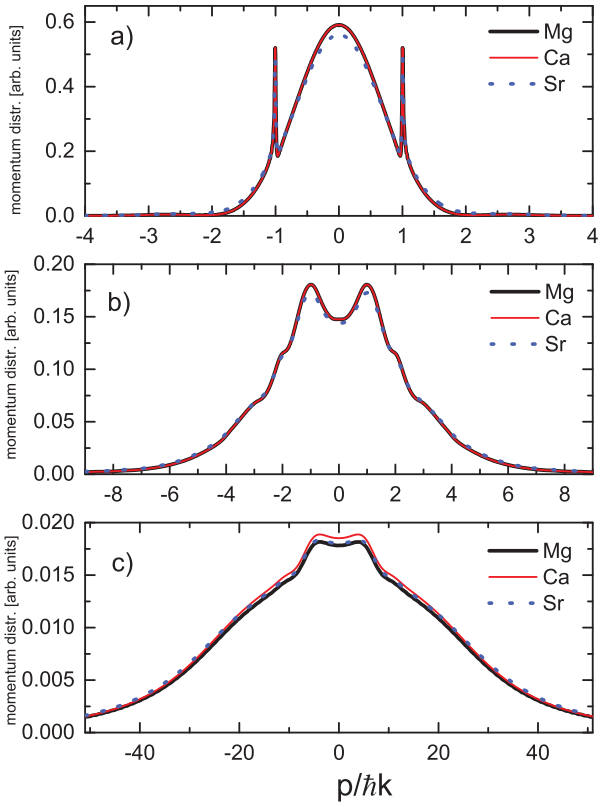

Fig. 3. *Momentum distribution os laser cooled steady-state of atoms for different set of equivalent parameters (9). The light field detuning* $\delta = -3\omega_R$ *and Rabi per one wave* $\Omega_0 = 0.64\,\omega_R$ *(a),* $\Omega_0 = 6.4\,\omega_R$ *(b), and* $\Omega_0 = 64\,\omega_R$ *(c).*

represented as a set of families (6) with nonzero amplitudes $\alpha_n(p_0)$ around $p_0 = 0$. This results to main peak in momentum distribution with $p = 0$ and side peaks with $p = \pm 2\hbar k$ (Fig. 4). To get the minimum temperature it is required to suppress the amplitudes of side peaks with $p = \pm 2\hbar k$. Depopulation of $|g, p = 2\hbar k\rangle$ state is reached for $\delta_p = 0$ and according to (8) results to suppression of side peaks at

$$\delta^* \simeq -3\,\omega_R \,. \tag{10}$$

Another is of important question is the cooling time. We may estimate the cooling time by the method suggested in [21]. The cooling time and the kinetics energy of atoms as function of light field intensity is shown on Figure 5. The cooling time depends on the width of the initial momentum distribution. We consider the second stage of laser cooling to subrecoil temperatures of atoms that were initially cooled with a use of resonant optical transitions $^1S_0 \rightarrow ^1P_1$ with wide linewidth to Doppler limit is about mK temperature. So, in our simulation of cooling time we choose the initial distribution of the atoms corresponds to $\Delta p \approx 20\hbar k$ (about $1mK$ temperature for magnesium atoms). For larger initial temperature, the time increases proportionally.

The cooling time is determined by the slowest processes of atom density matrix evolution. In semiclassical limit (4) it

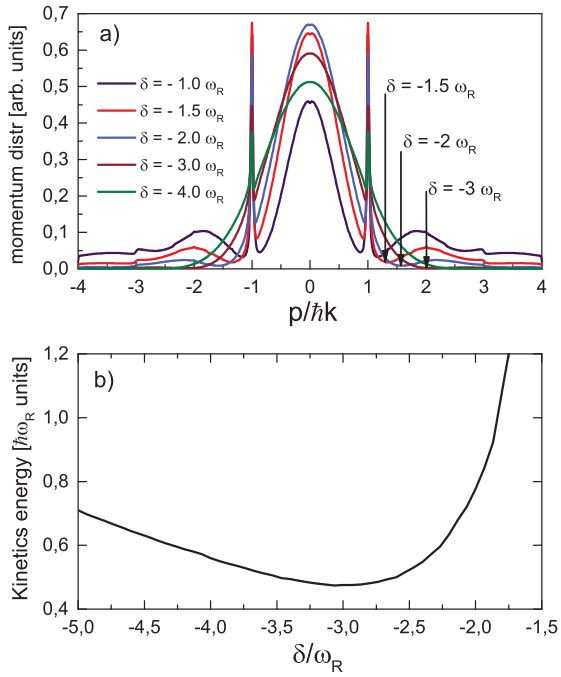

Fig. 4. *Momentum distribution os laser cooled steady-state of atoms for different detunings and small Rabi* $\Omega_0 = 0.64\,\omega_R$.

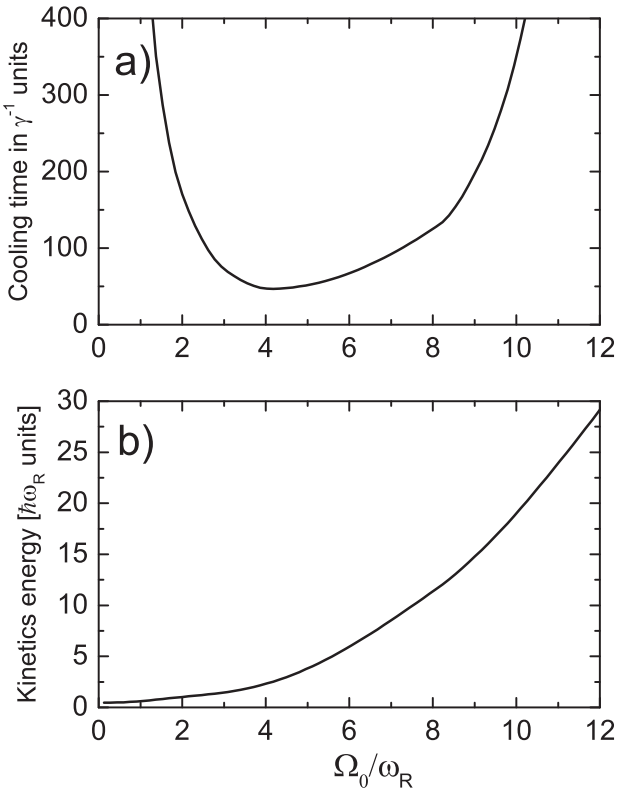

Fig. 5. *Cooling time (b) and kinetics energy of atoms (a) and as function of Rabi in* ω_R *units.*

is scaled by ω_R^{-1} units. We find that in considered quantum regime of laser cooling (7) the cooling time is also can be expressed in equivalent form for different atoms and scaled in γ^{-1} units.

III. Conclusion

Let us underline main results in conclusion. In attempts to get a deep laser cooling of atoms with nondedenerate ground states like ^{24}Mg, ^{40}Ca, ^{88}Sr the researchers tried to use the narrow-lines optical transitions. However due to limitation of semiclassical description of standard Doppler theory of laser cooling the optimal light field parameters might be significantly differ from well-known theory. It is required detailed study of laser cooling of atoms in essentially quantum regimes.

We show the equivalence of laser cooling of different atoms with $\omega_R \geq \gamma$ for the set of dimentionless parameters (9). We demonstrate the minimum of kinetic energy is reached for detuning close to $\delta \simeq -3\omega_R$.

The cooling time for laser cooling with use of narrow-lines optical transitions scales as $\tau_{cool} \sim \gamma^{-1}$ compare to semiclassical limit ($\tau_{cool} \sim \omega_R^{-1}$). The cooling time essentially depends on field intensity and has a minimum in the region of $\Omega_0 \simeq 3..8\omega_R$ that results to $\tau_{cool} \approx 40\,\gamma^{-1}$. For this intensity the kinetics energy of atoms large the minimal values and reaches $E_k \simeq 5\hbar\omega_R$. Thus for parameters $\Omega_0 = 5\omega_R$ and $\delta = -3\omega_R$, i.e. for conditions of fast laser cooling we may estimate the cooling time and the temperatures. The results are presented in table II;

TABLE II
Laser cooling at Rabi frequency corresponding to minimum cooling time

Atom	Temperature	Time
^{88}Sr	$T \simeq 2.5\mu K$	$\tau_{cool} \simeq 1ms$
^{40}Ca	$T \simeq 6\mu K$	$\tau_{cool} \simeq 20ms$
^{24}Mg	$T \simeq 16\mu K$	$\tau_{cool} \simeq 250ms$

The large cooling times looks the main obstacle for realization of cooling with use of narrow-line optical transitions.

The work was supported by Russian Science Foundation (project N 17-72-10139). V.I.Yudin acknowledges the support of the Ministry of Education and Science (3.1326.2017).

References

[1] J. Dalibard and C. Cohen-Tannoudji, J. Opt. Soc. Am. B **6,** 2023-2045 (1989).
[2] Y. Castin and J. Dalibard Europhys. Lett., **14,** 761-766 (1991)
[3] O.N. Prudnikov, A.V. Taichenachev, A.M. Tumaikin, V.I. Yudin "New friction force due to spontaneous light pressure" JETP Letters **v.70,** p.443 (1999)
[4] O.N. Prudnikov, A. V. Taichenachev, A. M. Tumaikin and V. I. Yudin, "Kinetics of atoms in the field produced by elliptically polarized waves", JETP **v.98,** p. 438, (2004)

[5] A. Aspect, E. Arimondo, R. Kaiser, N. Vansteenkiste, and C. Cohen-Tannoudji, “Laser cooling below the one-photon recoil energy by velosity-selective coherent population trapping” Phys. Rev. Lett. **61,** 826 (1988)
[6] A. Aspect, E. Arimondo, R. Kaiser, N. Vansteenkiste, and C. Cohen-Tannoudji, “Laser cooling below the one-photon recoil energy by velocity-selective coherent population trapping: theoretical analysis” J. Opt. Soc. Am. B **6,** 2112 (1989)
[7] O.N. Prudnikov, E. Arimondo, “Sub-doppler laser cooling on combined optical transitions”, JOSA B **v.20,** pp. 909-14 (2003)
[8] M. Kasevich and S. Chu, Laser cooling below a photon recoil with three-level atoms, Phys. Rev. Lett. **69,** 1741 (1992).
[9] J. Reichel, F. Bardou, M. Ben Dahan, E. Peik, S. Rand, C. Salomon, and C. Cohen-Tannoudji, Raman cooling of cesium below 3 nK: new approach inspired by Levy flight statistics, Phys. Rev. Lett. **75,** 4575 (1995).
[10] A. P. Kazantsev, G. I. Surdutovich, and V. P. Yakovlev, *Mechanical Action of Light on Atoms* (World Scientific, Singapore, 1990).
[11] H. J. Metcalf and P. van der Straten *Laser cooling and trapping* Springer 1999
[12] S. A. Strelkina, K. Yu. Khabarova, A. A. Galysheva, O. I. Berdasova, A. Yu. Gribova, N. N. Kolachevsky, S. N. Slyusareva Secondary Laser Cooling of Strontium-88 Atoms JEPT**121,** 1926 (2015)
[13] E.A. Curtis, C.W. Oates, and L.Holberg Phys. Rev. A **64,** 031403 (2001)
[14] T. Binnewies, G. Wilpers, U. Sterr, J. Helmcke, T.E. Mehlstäbler, E.M. Rasel, and W. Ertmer Phys. Rev. Lett. **87,** 123002 (2001)
[15] T.E. Mehlstäbler, J. Keupp, A.Douillet, N. Rehbein, E.M. Rasel J.Opt.B: Quantum Semiclass. Opt. **5,** S183 (2003)
[16] C.S. Adams, E.Riis “Laser cooling and trapping of neutral atoms” Prog. Quant. Electr. **21,** 1-77 (1997)
[17] O.N. Prudnikov, A. V. Taichenachev, A. M. Tumaikin, and V. I. Yudin “Magneto-optical force in a resonant field of elliptically polarized light waves”, Phys. Rev. A **77,** 033420 (2008)
[18] A.V. Bezverbnyi, O.N. Prudnikov, A.V. Taichenachev, A.M. Tumaikin, V.I. Yudin “The light pressure force and the friction and diffusion coefficients for atoms in a resonant nonuniformly polarized laser field”, JETP **96,** 383-401, (2003)
[19] O.N. Prudnikov, A.V. Taichenachev, A.V. Tumaikin, V.I. Yudin, Dissipative Light Mask Generated by a Nonuniformly Polarized Field for Atomic Lithography , JETP **v. 104,** 839, (2007)
[20] O.N. Prudnikov, R.Ya. Ilenkov, A. V. Taichenachev, A. M. Tumaikin, and V. I. Yudin, JETP v.112, pp.939-945 (2011)
[21] R. Ya. Ilenkov, O. N. Prudnikov, A. V. Taichenachev, V. I. Yudin Quantum theory of laser cooling: Statistical description of the process dynamics JETP **123,** 111 (2016)

The Features of Collective Level Shift and Line Broadening in a Fabry-Perot Microcavity and Near the Conducting Surface

Alexei S. Kuraptsev, Igor M. Sokolov
Peter the Great St. Petersburg Polytechnic University
St. Petersburg, Russia, 195251
Email: aleksej-kurapcev@yandex.ru

***Abstract*—On the basis of consequent microscopic quantum approach we calculate collective level shifts and line broadening in the polyatomic ensemble located in the Fabry-Perot cavity or near the conducting surface. We show that the cavity or the surface can essentially modify dipole-dipole interaction and consequently spectral properties of studied impurity ensembles. This modification is explained by the peculiarities of the structure of modes of electromagnetic field in these cases.**

I. Introduction

Analysis of the influence of the interatomic interaction on the radiative properties of atoms or atomic ensembles is one of the key problems for a wide range of tasks of modern spectroscopy. Dipole-dipole interatomic interaction that arises from the exchange of virtual photons plays an important role in the case of dense atomic ensembles, where the average interatomic separation is comparable with the wavelength of quasi resonant radiation. Cooperative effects stimulate density-dependent shifts of atomic transition [1]-[4] as well as distortion of its spectral line shape [5]. These effects influence both on the properties of atoms [6]-[10] and on the properties of scattered radiation [11]-[19].

Dipole-dipole interatomic interaction may play a noticeable role even for dilute atomic system especially in the case of high precision spectroscopy. For example this interaction can limit the accuracy of an optical lattice clock based on cold atoms [20]. The influence of dipole-dipole interaction on level shift and broadening has recently been observed experimentally [21], [22].

Besides the cold atomic gases there are other systems which may be used in quantum metrology and where dipole-dipole interaction may be important. One of such systems is ensemble of impurity centers (atoms) embedded in a transparent dielectric matrix.

To increase the efficiency of utilization of such ensemble optical cavities or waveguides are often used. Since the seminal work of Purcell [23] a large number of theoretical and experimental works were devoted to study peculiarities of light interaction with atoms localized inside a cavity or waveguide. Now it is well understood that a cavity modifies the structure of modes of electromagnetic field. This leads to modification in radiative properties of atoms, in particular, to the enhancement or inhibition of the spontaneous decay rate [24]-[26].

Modification of the structure of the field modes takes place not only inside the cavity but also near any surface. Such modification attracts a lot of attention recently because of possible applications of atomic ensembles located near nanostructures such as photonic crystal [27]-[29] and nanofibers [30]-[34] for quantum metrology, scalable quantum networks and quantum information science.

Modification of the spatial structures of field modes near the surface or inside the cavity causes alterations not only in single atom properties but also in collective polyatomic effects. This alteration is connected with the changes in the nature of photon exchange between different atoms. In its turn it leads to modification of dipole-dipole interatomic interaction [35], [36]. As distinct from spontaneous decay the modification of the dipole-dipole interaction has been studied by now in less detail.

The main goal of the present work is theoretical analysis of the influence of dipole-dipole interaction on spectral properties of atomic systems in the case when they are located in Fabry-Perot cavity or near the conducting surface.

II. Basic Assumptions and Approach

The dynamics of atomic system located inside a Fabry-Perot cavity or near a conductive surface can be described on the basis of the general quantum microscopic approach developed and laid out in detail in our previous papers [37], [38]. In this section we make just a brief overview of the theoretical developments and explain how the general theory can be applied in the case of a single conductive plate.

As it was mentioned above, resonant dipole-dipole interatomic interaction can be explained as result of photon exchange between different atoms. Such view on this interaction allows one to suggest consequent quantum microscopic approach for simultaneous description of atomic interaction with external light and interaction between atoms.

This approach is based on the solution of nonstationary Schrödinger equation for joint system consisting of all atoms and electromagnetic field. We take into account all modes of the field including modes which are initially in the vacuum state. During the evolution these modes can be populated as a result of atomic decay, i.e. as a result of interaction of the excited atom with the field in the vacuum state. The light-atom

978-1-5386-5620-4/18/$31.00 ©2018 IEEE

interaction is described in dipole approximation. The atoms are assumed to be motionless and external radiation or/and initial excitation of atomic system is weak.

The feature of electric field in the cavity is taken into account by a proper choice of field operator. We write this operator in a standard way by quantization of the classical field which is a solution of Maxwell equations with boundary conditions corresponding to considered geometry of the cavity [37], [38]. We assume that the mirrors of a cavity are perfectly conducting and their sizes are much larger than resonant transition wavelength, the distance between the mirrors d and interatomic separation. It allows us to consider the sizes of the mirrors equal to infinity in the final equations.

We seek the solution of the Schrödinger equation as an expansion in a set of eigenfunctions of noninteracting atoms and field. For the coefficients (amplitudes) of this expansion we have infinite system of linear differential equations. The key simplification of the approach employed is in the restriction of the total number of states taken into account. In our problems we do not consider nonlinear optical phenomena. In such a case we can account for only the states with no more than one photon in the field.

In spite of the restriction of the total number of quantum states, the set of equations remains infinite because of infinite number of one photon states. We can, however, express the amplitudes of quantum states with one photon via the amplitudes of atomic excitation. It allows us to obtain finite set of equation for Fourier component of amplitudes $b_e(\omega)$ of states with one excited atom

$$\sum_{e'}\big[(\omega-\omega_a)\delta_{ee'}-\Sigma_{ee'}(\omega)\big]b_{e'}(\omega)=i\delta_{eo}. \qquad (1)$$

This set of equations was obtained under the assumption that one of the atoms denoted by the subscript o is excited at the initial time and all the other are in the ground state. Electromagnetic field is in the vacuum state at $t=0$; $\delta_{i,j}$ is the Kronecker delta.

The size of the system (1) depends on the number of the atoms and on the structure of their energy levels. In this paper we consider that the ground state is characterized by the total angular momentum $J=0$ and the excited state is $J=1$. The transition frequency of the atoms is ω_a. Note that in this case there are three excited sublevels for each atom $e=|J;m\rangle$, which differ by the value of angular momentum projection on the quantization axis z: $m=-1,0,1$. The quantization axis is directed perpendicular to the mirrors of the Fabry-Perot cavity or to considered conducting surface.

The matrix $\Sigma_{ee'}(\omega)$ describes both spontaneous decay of each atom and photon exchange between different atoms. It plays a key role in the microscopic theory. The explicit expression for this matrix in the case of the Fabry-Perot cavity was derived in [37], [38]. It significantly differs from the similar matrix corresponding to the free space [5]. For example the imaginary part of the diagonal elements of this matrix which determines the natural linewidth of the atomic sublevels in the cavity can be calculated as follows

$$\Sigma_{ee'}(\omega_a)\Big|_{e=e'}=-\frac{i\pi}{d}d^z_{e;g}d^z_{g;e}\frac{\omega_a^2}{c^2}-\frac{i\pi}{d}\sum_{n=1}^{[[\frac{\omega_a d}{\pi c}]]}\left\{2\left(\frac{\omega_a^2}{c^2}-k_n^2\right)\cos^2(k_nz)d^z_{e;g}d^z_{g;e}+\left(d^x_{e;g}d^x_{g;e}+d^y_{e;g}d^y_{g;e}\right)\left(\frac{\omega_a^2}{c^2}+k_n^2\right)\sin^2(k_nz)\right\}. \qquad (2)$$

Here $k_n=\pi n/d$, $n=0,1,2,\ldots$, $d^l_{i,j}$ is the matrix element of l projection of the dipole moment operator of the atom; z is the distance from the atom to the cavity's mirror. Double brackets in (2) means the integer part of the number.

The natural linewidth γ can be obtained from (2) using the relation $\Sigma_{ee'}(\omega_a)\Big|_{e=e'}=-i\Gamma/2$, see [38] for detail.

The difference between decay rate of the atom in the cavity Γ and in free space γ is connected with above mentioned modification of the structure of modes of electromagnetic field by the cavity.

Note that real part of the diagonal element of the matrix $\Sigma_{ee'}(\omega)$ which describe the Lamb shift of the levels canot be calculated in the frame of dipole approximation used here. We can, however, consider that this shift is included into ω_a.

To calculate the dynamics of atomic ensemble located near a single mirror we use the cavity formalism in the limit $d\to\infty$ and consider the atoms near one of the mirrors. In this case the influence of the second mirror on the dynamics of atomic system is negligible.

On the basis of the general approach in the next section we calculate the spontaneous decay dynamics of an excited atoms as well as the shape of the transition spectrum. Obtained results are compared with the case of the atomic ensemble in free space.

The corresponding case can be considered on the basis of (1) with the matrix $\Sigma_{ee'}(\omega)$ determined by the following expression [5]

$$\Sigma_{ee'}(\omega)=-i\gamma/2\delta_{ee'}+(1-\delta_{ee'})\times\sum_{\mu,\nu}\frac{\mathbf{d}^\mu_{eg}\mathbf{d}^\nu_{g'e'}}{\hbar r^3}\exp\left(i\frac{\omega_a r}{c}\right)\times\left[\delta_{\mu\nu}\left(1-i\frac{\omega_a r}{c}-\left(\frac{\omega_a r}{c}\right)^2\right)-\frac{\mathbf{r}_\mu\mathbf{r}_\nu}{r^2}\left(3-3i\frac{\omega_a r}{c}-\left(\frac{\omega_a r}{c}\right)^2\right)\right]. \qquad (3)$$

Here $\mathbf{r}_\mu$ is projection of the vector $\mathbf{r}$ on axis of chosen coordinate system and $r=|\mathbf{r}|$ is separation between the atoms excited to the states e and e' .

In the next section we will show that the cavity or conducting surface can essentially modify dipole-dipole interaction and consequently spectral properties of studied atomic ensembles.

III. Results and Discussion

As we mentioned above the main goal of the present work is to consider the peculiarities of collective polyatomic effects

in the cavity or near the conducting surface. We will analyse these effects on the basis of calculation of the spectrum of transition of one atom which is initially excited in the ensemble of identical unexcited atoms. The influence of collective effects will be estimated by spectral shift, broadening and distortion of the shape of the transition line.

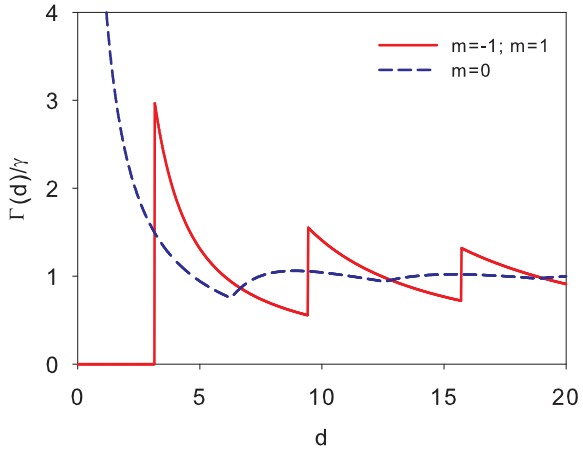

Fig. 1. Dependence of decay constatnt of different atomic excited states Γ on the size of the cavity. The calculation is performed for the atom located in the middle of the cavity $z = d/2$.

We will compare the results of three calculations. The first one is the calculation of single atom transition spectrum without ensemble, but in resonator or near surface. The second case corresponds to atomic excitation in the cloud when mirrors are absent. And at last we will calculate atomic transition spectrum when it is determined simultaneously by interaction with other atoms in the cloud and with the one or two conducting mirrors.

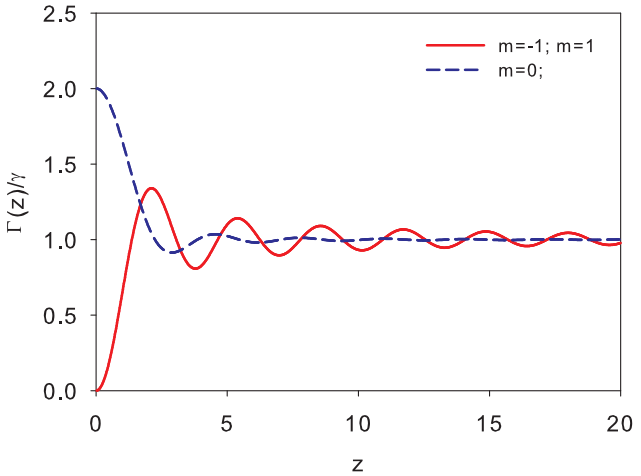

Fig. 2. Dependence of decay constatnt of different atomic excit states Γ on the distance from the conducting surface.

As regards the single atom transition in Fabry-Perot cavity or near conducting surface, it can be completely described by relations (1) and (2). In this case the system (1) consists of only three independent equations and the shape of the transition is determined by spectral dependence $b_o(\omega)$ of amplitude initially excited sublevel o. The imaginary part of $b_o(\omega)$ which defines the absorption coefficient is Lorentz profile centered at resonant atomic frequency. The real part of $b_o(\omega)$ has the shape of corresponding dispersion curve. The width of both contours can be calculated on the basis of (2).

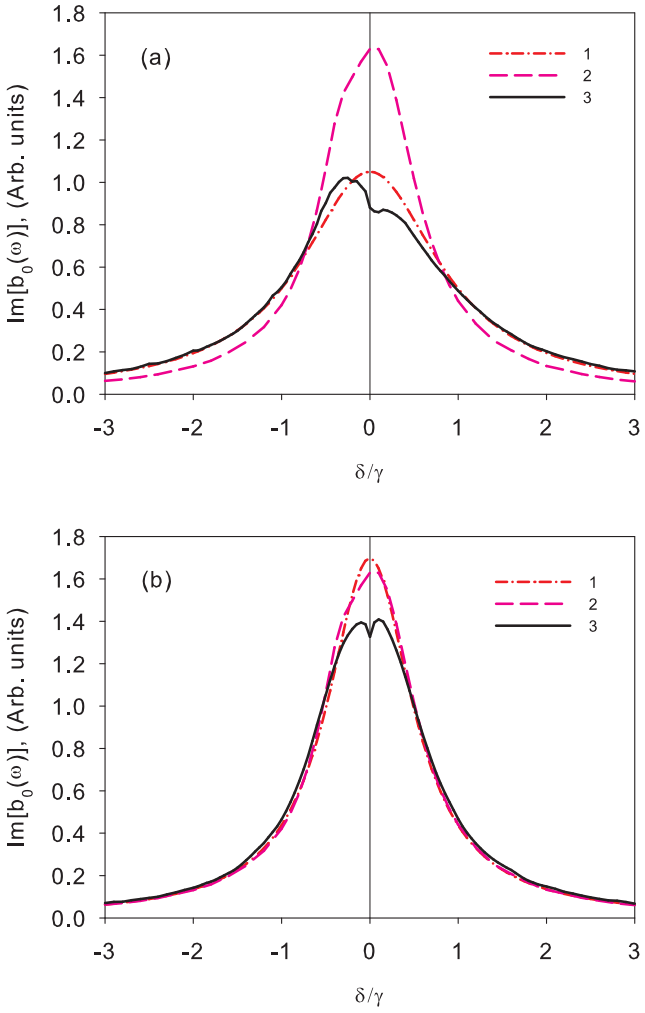

Fig. 3. Transition spectrun of the atom. (a) $m = \pm 1$; (b) $m = 0$. 1 – single atom in the cavity, $z = d/2$; 2 – spherical atomic ensemble in free space, excited atom is located in the center; 3 – atomic ensemble in the cavity, $z = d/2$. The calculation is performed for $d = 4$ and for atomic density n equals to 0.01.

Equation (2) allows us to calculate the width of the spectrum Γ for any size of the cavity d and for arbitrary position z of the atom inside it. As example we show in the Fig. 1 the dependence of the Γ on the distance between two mirrors. The calculation is performed for the atom located exactly in the middle of the cavity $z = d/2$. Two curves correspond to different initial states of the atom. In the Fig. 1 and further in this paper we use wavelength of resonant light divided by two pee $(\lambda/2\pi)$ as a unit of length.

The case of the atom near one conducting surface is depicted by the Fig. 2. Here we show the dependence of Γ on distance

z from the atom to the surface.

The case of atomic ensemble in the free space can be analysed using (1) and (3). In this case interatomic interaction causes the formation of polyatomic collective states. Among these states there are sub and super-radiant ones. The decay dynamics cannot be described by one-exponential law [5] and the shape of the atomic transition becomes complicated.

And at last, the description of atomic ensemble located in the cavity or near the conducting surface is even more complex. It can be done on he basis of (1) with utilization of matrix $\Sigma_{ee'}(\omega)$ from [37], [38].

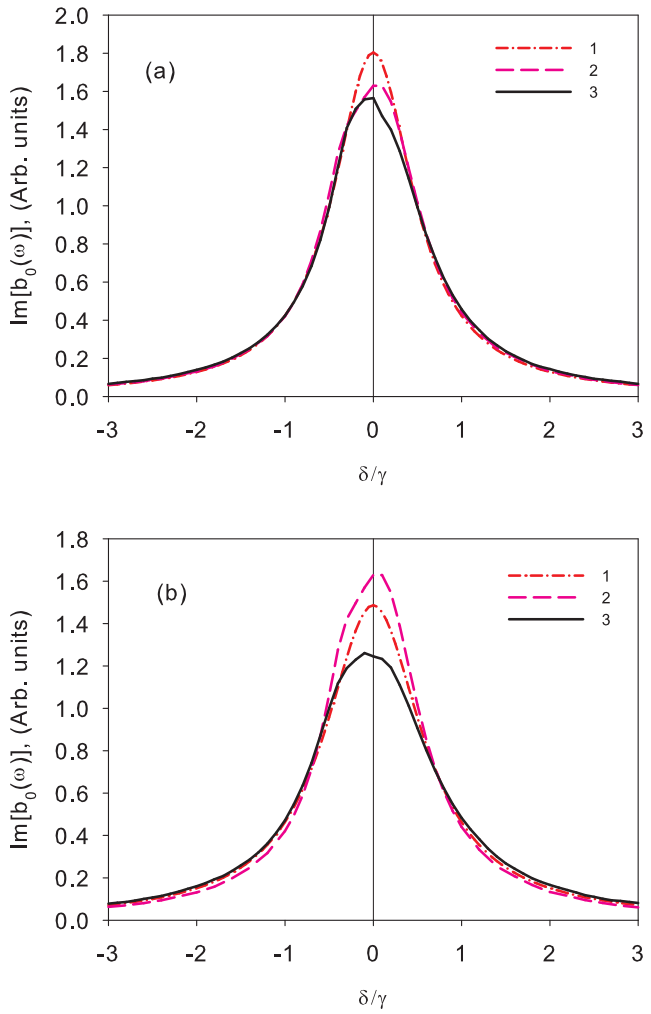

Fig. 4. The shape of atomic transition in the case of one mirror. (a) $m = \pm 1$; (b) $m = 0$. 1 – single atom near the surface; 2 – spherical atomic ensemble if free space, excited atom is located in the center; 3 – atomic ensemble near the surface. The calculation is performed for $z = 1.5$ and $n = 0.01$.

The influence of Fabry-Perot cavity on the collective effects is illustrated by the Fig. 3. Here we show the shape of different atomic transitions for three considered cases. Dash-doted lines describe influence of the cavity on monoatomic effects. The calculation is made for $d = 4$.

Dashed lines correspond to the case of polyatomic system in free space. The atomic density n is not very big $n = 0.01$. For such density the collective effects in free space is relatively weak [5]. We can see that these effects cause some distortion of the line shape. It becomes asymmetrical. But asymmetry of the curve is small as well as its shift. Note that these curves were obtained for big enough atomic cloud so that further increasing of its size does not change the shape of the curves.

The manifestation of polyatomic phenomena changes qualitatively when atomic system is in the cavity. The solid black lines in the Fig. 3 which describes this case differ essentially from the other curves in this figure. For both transitions $J = 0$, $m = 0 \leftrightarrow J = 1$, $m = \pm 1$ and $J = 0$, $m = 0 \leftrightarrow J = 1$, $m = 0$ this line is noticeably dissimilar to Lorentz profile. It has two local peaks. For $J = 0$, $m = 0 \leftrightarrow J = 1$, $m = 0$ the amplitudes of these two peaks are approximately the same and the profile is practically symmetric, but for the other transitions $J = 0$, $m = 0 \leftrightarrow J = 1$, $m = \pm 1$ we have substantially asymmetric curve with evident shift of spectral maximum of absorption. As it was mentioned above, this modification of collective effects is caused by differences in the structure of electromagnetic field modes in the cavity and in the free space and consequently by modification of resonant dipole-dipole interaction between atoms.

Field mode modification in the case of the only one conducting surface is weaker and transformation of spectral line is less pronounced. It can be seen from the Fig. 4. This figure corresponds to particular case, when the distance between the excited atom and the surface is $z = 1.5$ and the density of atomic ensemble is $n = 0.01$. For smaller z the influence of the surface becomes stronger as it is clear from the Fig. 2. However even in considered case the location of atomic cloud near the surface causes quite noticeable spectral shift of the atomic transitions.

IV. Conclusion

We have developed a consistent quantum approach to describe cooperative polyatomic effects in dense atomic ensembles located in a Fabry-Perot cavity or near conducting surface. This approach is based on the solution of the non-steady-state Schrodinger equation for the wave function of the joint system consisting of all atoms and a weak electromagnetic field including the vacuum reservoir. In the frame of this approach we take into account the peculiarities of the field modes of a cavity or near the surface and Zeeman structure of atomic levels.

On the basis of the general theory we calculate the spontaneous decay dynamics of an excited atom as well as the shape of the transition spectrum. Obtained results are compared with the case of the system in free space. We show that the cavity or conducting surface can essentially modify dipole-dipole interaction and consequently spectral properties of studied atomic ensembles. This modification is explained by the peculiarities of the structure of modes of electromagnetic field in these cases.

Acknowledgment

This work is supported by the Russian Science Foundation under grant 17-12-01085. The results were obtained with the use of the computational resources of the supercomputer center at the Peter the Great St. Petersburg Polytechnic University.

REFERENCES

[1] R. Friedberg, S. R. Hartmann, and J. T. Manassah, "Frequency shifts in emission and absorption by resonant systems ot two-level atoms," Physics Reports, vol. 7, pp. 101-179, 1973.

[2] T. Ido, T. H. Loftus, M. M. Boyd, A. D. Ludlow, K. W. Holman, and J. Ye, "Precision Spectroscopy and Density-Dependent Frequency Shifts in Ultracold Sr," Phys. Rev. Lett., vol. 94, pp. 153001, 1-5, 2005.

[3] J. Javanainen, J. Ruostekoski, Y. Li, and S.-M. Yoo, "Shifts of a Resonance Line in a Dense Atomic Sample," Phys. Rev. Lett., vol. 112, pp. 113603, 1-5, 2014.

[4] S. D. Jenkins, J. Ruostekoski, J. Javanainen, R. Bourgain, S. Jennewein, Y. R. P. Sortais, and A. Browaeys, "Optical Resonance Shifts in the Fluorescence of Thermal and Cold Atomic Gases," Phys. Rev Lett., vol. 116, pp. 183601, 1-5, 2016.

[5] A. S. Kuraptsev and I. M. Sokolov, "Spontaneous decay of an atom excited in a dense and disordered atomic ensemble: Quantum microscopic approach," Phys. Rev. A, vol. 90, pp. 012511, 1-7, 2014.

[6] Ya. A. Fofanov, A. S. Kuraptsev, I. M. Sokolov, and M. D. Havey, "Dispersion of the dielectric permittivity of dense and cold atomic gases," Phys. Rev. A, vol. 84, pp. 053811, 1-9, 2011.

[7] Ya. A. Fofanov, A. S. Kuraptsev, I. M. Sokolov, and M. D. Havey, "Spatial distribution of optically induced atomic excitation in a dense and cold atomic ensemble," Phys. Rev. A, vol. 87, pp. 063839, 1-7, 2013.

[8] M. G. Gladush, "A many-particle quantum-kinetic formalism for describing properties of light emitters in frozen dielectrics," EPJ Web of Conferences, vol. 132, pp. 03007, 1-2, 2017.

[9] A. V. Golovanova, M. Yu. Gubin, M. G. Gladush, A. V. Prokhorov, "Cooperative effects in a quartz medium with quantum dots," Bulletin of the Russian Academy of Sciences: Physics, vol. 80, pp. 808-813, 2016.

[10] I. M. Sokolov, D. V. Kupriyanov, R. G. Olave, and M. D. Havey, "Light trapping in high-density ultracold atomic gases for quantum memory applications," J. Mod. Opt., vol. 57, pp. 1833-1841, 2010.

[11] I. M. Sokolov, D. V. Kupriyanov, and M. D. Havey "Microscopic Theory of Scattering of Weak Electromagnetic Radiation by a Dense Ensemble of Ultracold Atoms," Journal of Experimental and Theoretical Physics, vol. 112, pp. 246-260, 2011.

[12] S. Balik, A. L. Win, M. D. Havey, I. M. Sokolov, and D. V. Kupriyanov, "Near-resonance light scattering from a high-density ultracold atomic ^{87}Rb gas," Phys. Rev. A, vol. 87, pp. 053817, 1-12, 2013.

[13] I. M. Sokolov, A. S. Kuraptsev, D. V. Kupriyanov, M. D. Havey, and S. Balik, "A scaling law for light scattering from dense and cold atomic ensembles," J. Mod. Opt., vol. 60, pp. 50-56, 2013.

[14] J. Pellegrino, R. Bourgain, S. Jennewein, Y. R. P. Sortais, A. Browaeys, S. D. Jenkins, and J. Ruostekoski, "Observation of Suppression of Light Scattering Induced by Dipole-Dipole Interactions in a Cold-Atom Ensemble," Phys. Rev. Lett., vol. 113, pp. 133602, 1-5, 2014.

[15] S. Roof, K. Kemp, M. Havey, I. M. Sokolov, and D. V. Kupriyanov, "Microscopic lensing by a dense, cold atomic sample," Optics Letters, vol. 40, pp. 1137-1140, 2015.

[16] A. S. Kuraptsev and I. M. Sokolov, "Reflection of resonant light from a plane surface of an ensemble of motionless point scatters: Quantum microscopic approach," Phys. Rev. A, vol. 91, pp. 053822, 1-6, 2015.

[17] S. D. Jenkins, J. Ruostekoski, J. Javanainen, S. Jennewein, R. Bourgain, J. Pellegrino, Y. R. P. Sortais, and A. Browaeys, "Collective resonance fluorescence in small and dense atom clouds: Comparison between theory and experiment," Phys. Rev. A, vol. 94, pp. 023842, 1-13, 2016.

[18] S. E. Skipetrov, I. M. Sokolov, and M. D. Havey, "Control of light trapping in a large atomic system by a static magnetic field," Phys. Rev. A, vol. 94, pp. 013825, 1-7, 2016.

[19] N. A. Lozing and M. G. Gladush, "Cooperative effects and slow dynamics of fluorescence intensity from quantum emitters in a dielectric," EPJ Web of Conferences, vol. 132, pp. 03029, 1-2, 2017.

[20] D. E. Chang, J. Ye, M. D. Lukin, "Controlling dipole-dipole frequency shifts in a lattice-based optical atomic clock," Phys. Rev. A vol. 69, pp. 023810, 1-10, 2004.

[21] S. J. Roof, K. J. Kemp, M. D. Havey, and I. M. Sokolov, "Observation of single-photon superradiance and the cooperative Lamb shift in an extended sample of cold atoms," Phys. Rev. Lett., vol. 117, pp. 073003, 1-5, 2016.

[22] S. L. Bromley, B. Zhu, M. Bishof, X. Zhang, T. Bothwell, J. Schachenmayer, T. L. Nicholson, R. Kaiser, S. F. Yelin, M. D. Lukin, A.M. Rey, J. Ye, "Collective atomic scattering and motional effects in a dense coherent medium," Nature Communications, vol. 7, pp. 11039, 1-7, 2016.

[23] E. M. Purcell, "Spontaneous emission probabilities at radio frequencies," Phys. Rev. vol. 69, pp. 681-681, 1946.

[24] G. S. Agarwal, "Quantum electrodynamics in the presence of dielectrics and conductors. IV. General theory for spontaneous emission in finite geometries," Phys. Rev. A, vol. 12, pp. 1475-1497, 1975.

[25] D. Kleppner, "Inhibited Spontaneous Emission," Phys. Rev. Lett., vol. 47, pp. 233-236, 1981.

[26] A. O. Barut and J. P. Dowling, "Quantum electrodynamics based on self-energy: Spontaneous emission in cavities," Phys. Rev. A, vol. 36, pp. 649-654, 1987.

[27] J. S. Douglas, H. Habibian, C.-L. Hung, A. V. Gorshkov, H. J. Kimble, and D. E. Chang, "Quantum many-body models with cold atoms coupled to photonic crystals," Nat. Photonics, vol. 9, pp. 326-331, 2015.

[28] A. Gonzalez-Tudela, C.-L. Hung, D. E. Chang, J. I. Cirac, and H. J. Kimble, "Subwavelength vacuum lattices and atom-atom interactions in two-dimensional photonic crystals," Nat. Photonics, vol. 9, pp. 320-325, 2015.

[29] A. Goban, C.-L. Hung, J. D. Hood, S.-P. Yu, J. A. Muniz, O. Painter, and H. J. Kimble, "Superradiance for atoms trapped along a photonic crystal waveguide," Phys. Rev. Lett., vol. 115, pp. 063601, 1-5, 2015.

[30] F. Le Kien, S. Dutta Gupta, K. P. Nayak, and K. Hakuta, "Nanofiber-mediated radiative transfer between two distant atoms," Phys. Rev. A, vol. 72, pp. 063815, 1-11, 2005.

[31] N. V. Corzo, B. Gouraud, A. Chandra, A. Goban, A. S. Sheremet, D. V. Kupriyanov, and J. Laurat, "Large Bragg Reflection from One-Dimensional Chains of Trapped Atoms Near a Nanoscale Waveguide," Phys. Rev. Lett., vol. 117, pp. 133603, 1-5, 2016.

[32] Guo-an Yan, Hua Lu, Hao-xue Qiao, Ai-xi Chen, and Wan-qing Wu, "Coupled-resonator waveguide perfect transport single-photon by interatomic dipole-dipole interaction," Optics Communications, vol. 416, pp. 50-53, 2018.

[33] P. Solano, F. K. Fatemi, L. A. Orozco, and S. L. Rolston, "Dynamics of trapped atoms around an optical nanofiber probed through polarimetry," Optics Letters, vol. 42, pp. 2283-2286, 2017.

[34] M.-T. Cheng, J. Xu, and G. S. Agarwal, "Waveguide transport mediated by strong coupling with atoms," Phys. Rev. A., vol. 95, 053807, 1-8, 2017.

[35] G. S. Agarwal and S. D. Gupta, "Microcavity-induced modification of the dipole-dipole interaction," Phys. Rev. A, vol. 57, pp. 667-670, 1998.

[36] R. Rohlsberger, K. Schlage, B. Sahoo, S. Couet, and R. Ruffer, "Collective Lamb Shift in Single-Photon Superradiance," Science, vol. 328, 1248-1251, 2010.

[37] A. S. Kuraptsev and I. M. Sokolov, "Microscopic Theory of Dipole-Dipole Interaction in Ensembles of Impurity Atoms in a Fabry-Perot Cavity," Journal of Experimental and Theoretical Physics, vol. 123, pp. 237-248, 2016.

[38] A. S. Kuraptsev and I. M. Sokolov, "Light trapping in an ensemble of point-like impurity centers in Fabry-Perot cavity," Phys. Rev. A., vol. 94, pp. 022511, 1-10, 2016.

Development of the Strontium Optical Lattice Clock at National Time Service Center

Mojuan Yin[1], Qinfang Xu[1], Yebing Wang[1,2], Jie Ren[1], Yang Guo[1,2], Hong Chang[1*]
[1]CAS Key Laboratory of Time and Frequency Primary Standards, National Time Service Center, Chinese Academy of Sciences, Xi'an 710600, China
[2]School of Astronomy and Space Science, University of Chinese Academy of Sciences, Beijing 100049, China
*Email: changhong@ntsc.ac.cn

***Abstract*—A closed-loop operation optical lattice clock of ^{87}Sr has been realized built in National Time Service Center of China. The linewidth of spin-polarized clock transition spectrum is 3.9 Hz with a interrogating time of 300 ms. The instability is measured to be about $5\times10^{-15}/\tau^{1/2}$ from the fit function of the in-loop error signal data, which affected mainly by the white noise. The fractional frequency difference averages down to 6×10^{-17} at an average time of 3000 s.**

Keywords—optical clock; optical lattice; strontium atoms; instability;

I. INTRODUCTION

In past decades, atomic optical lattice clock based on neutral atoms and single ions have made remarkable development on instability and uncertainty achieving 10^{-18} level.[1,2] The application of optical lattice clock covers lots of field, such as the fundamental constant precision measurement, gravitational wave detection, and clock-based geodesy[3-5]. Recently, a measurement precision of 5×10^{-19} in 1 hour of averaging time based on ^{87}Sr three-dimensional optical lattice clock was reported.[6] Since the ^{87}Sr optical lattice clock became one of the most promising candidates for redefinition of the second of the SI.

Based on the observation of the $5s^2\ ^1S_0$-$5s5p\ ^3P_0$ transition spectrum of bosonic ^{88}Sr[7], we began to develop optical lattice clock with employing the fermionic ^{87}Sr atoms. Finally, the closed-loop operation of ^{87}Sr optical lattice clock was realized with Allan diviation of the clock transition frequency of $5\times10^{-15}/\tau^{1/2}$.

II. EXPERIMENTAL SETUP AND RESULTS

The experiment begins with slowing the ^{87}Sr atoms from a thermal atom source, a Zeeman slower constructed of ten coils and a slowing light are combined to reduce the velocity of the atoms from 500 m/s to 50 m/s, approximately. Then these atoms are loaded into a two-stage magneto-optical traps (MOT) subsequently, called as the blue MOT and the red MOT, respectively. This two-stage MOT is constructed with cooling and trapping laser at 461 nm & 689 nm of three dimensions, axis X, Y, Z, as depicted in Fig. 1. Except there are repumping lasers at 679 nm, 707 nm, and another stirring laser at 689 nm for improving the number of the trapped atoms in the MOT. And a photomultiplier tube (PMT) and an electron multiplying charge-coupled device (EMCCD) are employed for capturing the fluorescence of the atoms.

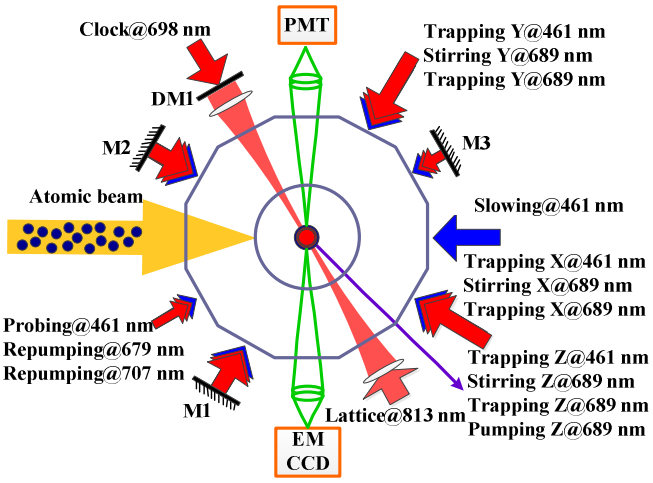

Fig. 1. Experimental setup of ^{87}Sr optical lattice clock

After the red MOT preparation, there are about 3.5×10^6 atoms trapped, and the average logitudinal temperature of the red MOT is 3.9 μK, which measured by the method of time-of-flight. Among these atoms, approximate 10^4 atoms are confined into a one-dimensional (1D) optical lattice formed by counter propagating optical beams with the magic wavelength of 813.4 nm. The incident optical beam with the linear polarization is focused on the center of the MOT, where the waist diameter of the incident beam is around 120 μm. Furthermore, the retro-reflected beam without polarization rotation is adjusted to overlap the original incident beam and focused on the point with the same parameters. The incident laser beam power is around 300 mW. According to the power and the beam waist of the lattice laser, a trap lattice depth is about 56 E_r can be calculated where E_r is the lattice photon recoil energy. As the Fig. 2 shown, the 1/e lifetime of the 1D optical lattice is measured by 1.6 s. It could afford the enough long interrogation time and the detection signal-noise rate for our experiment.

For the forbidden state $5s^2\ ^1S_0$ (F=9/2)→$5s5p\ ^3P_0$ (F=9/2) of the fermionic ^{87}Sr atoms, which has the nuclear spin I=9/2, it means that there are $2I$+1=10 nuclear spin states. These nuclear spin states are almost degenerate under tiny or ignorable background magnetic fields. Under nonzero field, due to Zeeman broadening of the overlapped transitions, these nuclear spin states are no longer degenerate. To prepare the ideal two-level atomic samples of the forbidden state $^1S_0$→$^3P_0$ at 698 nm, three-dimensional bias coils are applied to zero the magnetic field at the atomic samples. It is achieved by scanning the magnetic field step by step in all dimensions and searching the narrowest spectrum of the transition at 698 nm.

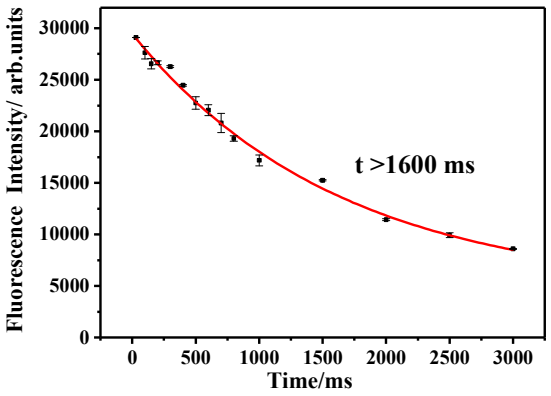

Fig. 2. The life time of the trapped atomes in 1D optical lattice

We used the normalized shelving detection method[8] to interrogate the clock transition of $5s^2\ ^1S_0$ (F=9/2)→$5s5p\ ^3P_0$ (F=9/2) (698 nm) in the 1D optical lattice. It is benefit for increasing the signal noise ratio and decreasing the effect of the fluctuation of atomic number in each clock cycle. The atoms in all m_F states will be prepared on the $5s^2\ ^1S_0(m_F$=+9/2) or $5s^2\ ^1S_0(m_F$=-9/2) states using the polarized pump laser at 689 nm. The clock is interrogated using 698 nm clock laser and probed with 461 nm laser. The frequency of clock laser is stabilized by locking it to a ultra-low-expansion (ULE) cavity with the help of Pound-Drever-Hall technique. The fineness of the cavity is near 400000 and the length is 10 cm. The linewidth of the 698 nm laser is narrowed below 2 Hz. A fiber phase noise cancellation system is employed to suppress the linewidth broadening caused by the delivery fiber. The system bases on a heterodyne Michelson interferometer, while the round trip fiber phase is locked to the phase of a local reference arm. The frequency of the clock laser sweeps across the resonance frequency of the transition by an acousto-optic modulator (AOM).

In order to increase signal noise ratio and transition rate, we pump the atoms into the either stretched states of m_F=±9/2 in the ground state using a weak 689 nm laser resonant with the $5s^2\ ^1S_0$(F=9/2)-$5s5p\ ^3P_0$(F=9/2) transition. The pumping laser propagates along the vertical direction and perpendicular with the direction of lattice and clock laser. With a σ^+ or σ^- polarized 689nm laser, the atoms in all m_F states will be prepared on the $5s^2\ ^1S_0(m_F$=+9/2) or $5s^2\ ^1S_0(m_F$=-9/2) states. Finally more than 90% atoms are pumped into either of the two stretched states and the excitation fraction is about 7 times bigger than that with no pumping laser. Using the spin-polarized spectra of m_F=+9/2—m_F=+9/2 and m_F=-9/2—m_F=-9/2 Zeeman transitions, the first-order Zeeman shift and vector Stark shift can be cancel[9]. Thought the differences of the excitation fractions at half maximum points of each spin-polarized spectrum in Fig. 3, the error signal can be calculated and the frequency of clock laser can be locked to the clock transition of ^{87}Sr atom using an AOM. The probe period is 1 second and the feedback cycle of clock is 4 second. The optical lattice clock can run continuously more than 5 hours.

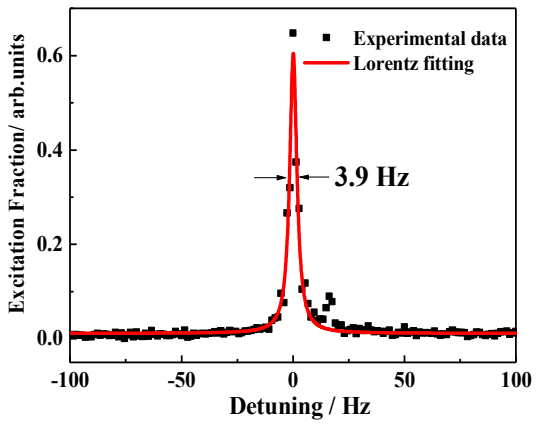

Fig. 3. The spin-polarized spectrum of the clock transition

Using the error signal from the clock laser locking to the clock transition, we can evaluate the in-loop instability of ^{87}Sr optical lattice clock though calculated the Allan deviation[9].

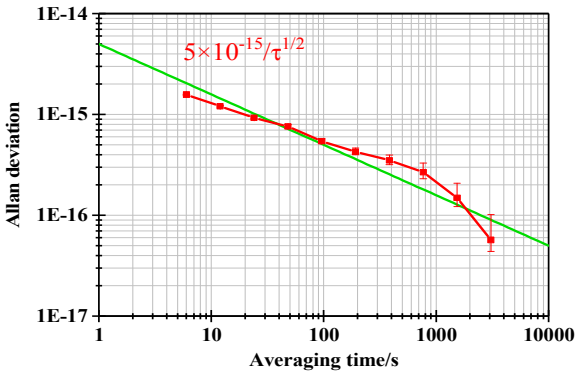

Fig. 4. An in-loop fractional frequency instability of 87Sr optical lattice clock

An in-loop fractional frequency instability is 6×10^{-17} at an averaging time of 3000 s, representing the best level for our interleaved measurement and shown in Fig. 4. From the fitting function of the green line in Fig. 4, an instability of $5\times10^{-15}/\tau^{1/2}$ is measured and affected mainly by white noise.

III. CONCLUSION AND PERSPECTIVES

In this paper our experiment is based on a ^{87}Sr 1D optical lattice clock at National Time Service Center. A closed-loop operation of a ^{87}Sr optical lattice clock is demonstrated. A two-stage MOT combined with a slowing laser at 461 nm and a Zeeman slower are employed to efficiently cooling and trapping the atoms. After the second-stage cooling process, the number of atoms in the red MOT is around 3.5×10^6 and the logitudinal temperature of the red MOT is 3.9 μK. Then we apply a 813 nm diode laser to form a 1D optical lattice for loading the atoms from the red MOT, and a 1/e lifetime of 1.6 s of the lattice is obtained. The clock transition spectrum was detected by the normalized shelving detection method with a narrow linewidth clock laser system at 698 nm (Hz level). Finally, a spin-polarized spectrum of transitions $^1S_0(m_F=+9/2)$-$^3P_0(m_F=+9/2)$ with a linewidth of 3.9 Hz is measured with the interrogating time of 300 ms. And an in-loop fractional frequency Allan deviation is achieved to $5\times10^{-15}/\tau^{1/2}$ at an average time of 3000 s. Furthermore, we will improve the instability and measure the accuracy of ^{87}Sr optical lattice clock.

ACKNOWLEDGMENT

This work was supported by National Natural Science Foundation of China (Grant No.11474282, No.61775220), the Strategic Priority Research Program of the Chinese Academy of Sciences (Grant No.XDB21030100), and the key research project of frontier science of the Chinese Academy of Sciences (Grant No. QYZDB-SSW-JSC004)

REFERENCES

[1] T. L. Nicholson, S. L. Campbell, R. B. Hutson, G. E. Marti, B. J. Bloom, R. L. Mcnally, W. Zhang, M. D. Barrett, M. S. Safronova, G. F. Strouse, W. L. Tew and J. Ye, "Systematic evaluation of an atomic clock at 2×10^{-18} total uncertainty", Nat. Commun., vol. 6, p. 6896, 2015.

[2] N. Hinkley, J. A. Sherman, N. B. Phillips, M. Schioppo, N. D. Lemke, K. Beloy, M. Pizzocaro, C. W. Oates and A. D. Ludlow, "An atomic clock with 10^{-18} instability", Science, vol 341, p. 1215, 2013.

[3] S. Kolkowitz, I. Pikovski, N. Langellier, M. D. Lukin, R. L. Walsworth and J. Ye, "Gravitational wave detection with optical lattice clocks", Phys. Rev. D, vol. 94, p. 124043, 2016

[4] A. Derevianko and M. Pospelov, "Hunting for topological dark matter with atomic clocks", Nat. Phys., vol. 10, p. 933, 2014.

[5] A. D. Ludlow, M. M. Boyd, J. Ye, E. Peik and P. O. Schmidt, "Optical Atomic Clocks", Rev. Mod. Phys. vol. 87, p. 637, 2015.

[6] S. L. Campbell, R. B. Hutson, G. E. Marti, A. Goban, N. Darkwah Oppong, R. L. McNally, L. Sonderhouse, J. M. Robinson, W. Zhang, B. J. Bloom, J. Ye, "A Fermi-degenerate three-dimensional optical lattice clock", Science, vol 358, p. 90-94, 2017.

[7] Q. F. Xu, H. Liu, B. Q. Lu, Y. B. Wang, M. J. Yin, D. H. Kong, J. Ren, X. Tian and H. Chang, "Observation of $^1S_0$-$^3P_0$ transition of bosonic strontium in the Lamb-Dicke regime", Chin. Opt. Lett. vol. 13, p. 100201, 2015.

[8] J. C. Bergquist, Randall G. Hulet, Wayne M. Itano, and D. J. Wineland, "Observation of Quantum Jumps in a Single Atom", Phys. Rev. Lett. vol. 57, p.1699, 1986.

[9] Y. G. Lin, Q. Wang, Y. Li, F. Meng, B. K. Lin, E. J. Zang, Z. Sun, F. Fang, T. C. Li and Z. J. Fang, "First Evaluation and Frequency Measurement of the Strontium Optical Lattice Clock at NIM", Chin. Phys. Lett. vol. 32, p. 090601, 2015.

[10] H. Liu, X. Zhang, K. L. Jiang, J.Q. Wang, Q. Zhu, Z. X. Xiong, L. X. He and B. L. Lyu, " Realization of Closed-Loop Operation of Optical Lattice Clock Based on ^{171}Yb", Chin. Phys. Lett. vol. 34, p. 020601, 2017.

Towards an $^{27}Al^{+}$ based optical clock

Khabarova Ksenia[1,2], Zalivako Ilia[1,2], Semerikov Ilya[1,2], Borisenko Alexander[1,2], Kolachevsky Nikolay[1,2]

[1]P.N. Lebedev Physical Institute of Russian Academy of Sciences, Moscow, Russia
[2]Russian Quantum Center, Skolkovo, Russia
Email: kseniakhabarova@gmail.com

***Abstract*—We present current status of a project aimed for development of an optical clock based on $^{27}Al^{+}$ ion and auxiliary $^{25}Mg^{+}$ ion started at LPI. Results on Mg^{+} ions trapping and cooling are presented as well as a clock laser design.**

Keywords—optical clock, trapped ions, laser cooling,

I. INTRODUCTION

For last several decades progress in a field of frequency standards led to a rapid development in other areas of technology and science. Compact and stable microwave atomic clocks [1], for instance, enabled development of global navigation satellite systems (GNSS), such as GPS and GLONASS. Today advances in GNSS accuracy are also mostly connected with improved performance of clocks used in space and control segments. Frequency standards also play an important role in telecommunications [2], distributed data storage and processing [3] as well as in radioastronomy [4]. Unprecedented level of relative uncertainty and instability achieved by state-of-the-art optical clocks (reaching 2.1×10^{-18} and $2.2\times10^{-16}\tau^{-1/2}$ correspondingly [5]–[8]) also opened new prospects in such fields as relativistic geodesy [9] and tests of fundamental theories [10]–[13].

Today the field of frequency standards continues its active development in a wide variety of ways. The uncertainty of existing optical clocks is being reduced by diminishing the value and more accurate estimation of systematic shifts. Thus a big effort is made on precise measurement of atom's polarizabilities and control over particle's environment temperature to suppress Stark and BBR shift uncertainties [5], [8] which often appear to have the largest contribution. In case of single-ion optical clocks a development of new ion traps providing low heating rates is also of a great importance because of high contribution of time dilation shift uncertainty [14]. At the same time new atomic species are tried as frequency references such as singly ionized Lutetium [15] and Indium [16] atoms. Small value of a quadrupole moment allows improvement of clock stability by trapping more than one spectroscopy ion in the same trap without significant accuracy reduction.

In this paper we present a current status of an $^{27}Al+$ ion based optical clock which is being under development by our group. A $^{1}S_0 \rightarrow {}^{3}P_0$ clock transition in Al^{+} has a wavelength of 267 nm, accessible with a forth harmonic of commercially available fiber or diode laser, and a natural linewidth of 8 mHz [17]. This ion has an advantage of a small BBR shift [18] of its clock transition frequency and extremely small quadrupole moments of its clock states [19]. The latter is particularly important for the development of multi-ion clocks since an influence of electric field gradients created by neighboring particles and trap itself on the transition frequency becomes negligible (relative frequency shift is less than 10^{-19} [19]). On the other hand the difficulty of reaching any of its transitions suitable for cooling (the one with the biggest wavelength is at 167 nm) makes its cooling, state preparation and readout challenging. Relatively small atomic mass of Al also makes it more sensitive to time dilation shifts due to thermal motion and excess micromotion in comparison to heavier clock ion candidates.

Several ways how to overcome obstacles described above were suggested and experimentally demonstrated. All of them involve trapping an additional auxiliary ion of another species allowing efficient direct laser cooling such as $^{25}Mg^{+}$, $^{9}Be^{+}$ or $^{40}Ca^{+}$ in the same trap. In this case dumping of Al^{+} ion motion can be achieved via sympathetic cooling [20]. Quantum state readout can be performed with quantum logic spectroscopy [7] or coherent motion excitation methods [21]. The latter method also can be adopted for simultaneous readout of several aluminum ions' states which can be used in multi-ion aluminum clock with improved stability. The suppression of time dilation shifts by cleverly designed and precisely manufactured traps exhibiting low heating rates along with 3D ground-state cooling of ions prior to clock transition excitation were also demonstrated [14] with time dilation shift uncertainty reduced down to 2×10^{-18}. In our experiment we plan to sympathetically cool an aluminum ion with a $^{25}Mg^{+}$ and perform the spectroscopy using quantum logic spectroscopy method.

Here we describe an experimental setup developed for this project and results of its characterization. Experimental results of Doppler cooling of $^{24}Mg^{+}$ ions with our setup are presented. Results and future plans are also discussed.

II. EXPERIMENTAL SETUP

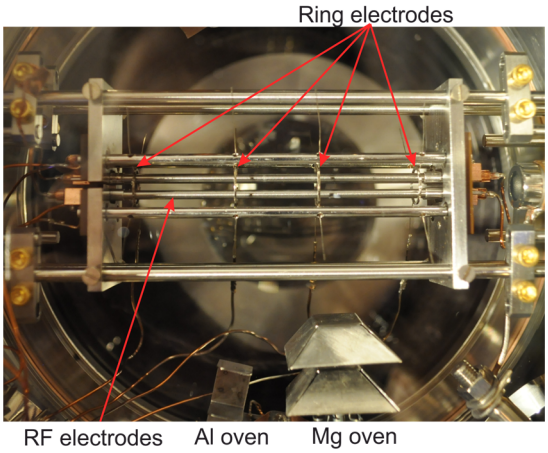

Fig. 1. The image of a linear Paul trap for storing Al^+ and Mg^+ ions. Ring electrodes provide axial confinement and divide trap into three segments. Radiofrequency (RF) electrodes provide radial confinement. Al and Mg ovens create atomic beams for the trap loading. RF electrodes are surrounded by four compensation electrodes for micromotion minimization.

A. *Ion trap*

For $^{27}Al^+$ and $^{25}Mg^+$ ions localization a linear Paul trap has been developed (Fig. 1), which details can be found elsewhere [22]. Radial confinement is provided by means of four cylindrical tungsten electrodes. The distance between their surfaces and trap axis is r_0=1.475 mm. Trap frequency ω is equal to $2\pi \times 18$ MHz. Axial confinement is created by four ring electrodes placed outside of the radiofrequency electrodes along trap axis. They divide the trap into three segments. One of the outer segments is used for magnesium ions loading while the spectroscopy is carried out inside of the central segment where trapped ions are shuttled afterwards. Separation of loading and spectroscopy trap zones helps to avoid appearance of strong stray fields due to loading process in the central segment.

Setup is equipped with two atomic ovens providing magnesium and aluminum atomic beams coming through a trapping region. At the moment magnesium ionization can be performed with electron impact or using a UV LED. The detailed description of the latter ionization method will be soon published elsewhere. A laser system for photoionization of the magnesium is under development now and will be similar to a laser system for Doppler cooling which is described below. For one-color photoionization of the aluminum an external cavity diode laser providing radiation at 396 nm was built.

Trap is enclosed in a vacuum chamber. According to the control unit of an ion getter pump used for chamber evacuating pressure on the level of 10^{-10} was achieved after baking. Trap geometry and chamber viewports allow good optical access to the ions along the trap axis and from side directions.

B. *Laser system for Doppler cooling of Mg^+*

Laser cooling of magnesium ions is performed on a strong cyclic $^2S_{1/2} \rightarrow {}^2P_{3/2}$ transition with a wavelength of 280 nm and natural linewidth of $\Gamma = 2\pi \times 41$ MHz. In case of $^{25}Mg^+$ isotope a repumping laser beam detuned from cooling one by 1.8 GHz is also required. It can be obtained from the cooling beam by pair of acousto-optic modulators (AOM) in double-pass configuration.

The laser system for Doppler cooling is based on a commercial diode laser Toptica TA Pro providing 830 mW of power at 1120 nm. Laser frequency is stabilized with an Angstrom/High-Finesse WS-U wave meter. This light is converted to the UV with two home-built second harmonic generators based on LBO and BBO nonlinear crystals in bow-tie cavities, correspondingly [23]. UV power of 10 mW (3 mW after beam shape correction) is obtained at 280 nm. Fast frequency tuning and switching of the cooling beam is achieved with an AOM.

Part of the beam is directed along the trap axis while another one pointing the ions from the side and has a projection on all three trap axes. During the ions loading an axial beam is used since it covers larger volume of a trap and makes cooling and trapping process more efficient. Further cooling and spectroscopy are performed using the second beam since it cools all motional degrees of freedom more efficiently.

For the ions fluorescence detection a high-aperture objective with 5-fold magnification has been designed and manufactured at LPI. Fluorescence is detected with both EMCCD camera and a photomultiplier tube (PMT).

C. *Laser system for clock transition excitation*

The clock laser system is based on a Koheras Adjustik fiber laser source at 1068 nm amplified up to 2 W of power with a Koheras Boostik fiber amplifier. Its emission will be converted to the UV with the pair of second harmonic generators analogous to the ones used for Doppler cooling laser.

For short-term frequency stabilization of the clock laser a ULE cavity similar to one described in [24] was built. The cavity has a length of 77.5 mm and is placed inside a vacuum chamber with a pressure of 10^{-8} Torr. Several thermal shields surround the cavity inside the chamber to prevent temperature fluctuations and gradients. The cavity temperature is stabilized at the cavity zero-point.

The stability of the clock laser has not been measured yet, but the similar systems built at our laboratory and used for thulium atoms spectroscopy experiments demonstrats the linewidth narrowing to the level of several Hz or less [25].

III. DOPPLER LASER COOLING OF $^{24}MG^+$ IONS

As a preliminary step before cooling of $^{25}Mg^+$ and $^{27}Al^+$ ions cooling of $^{24}Mg^+$ was performed. This isotope lacks of hyperfine structure that makes cooling process easier since it does not require repumper laser, however it cannot be used for ground state cooling and quantum logic spectroscopy.

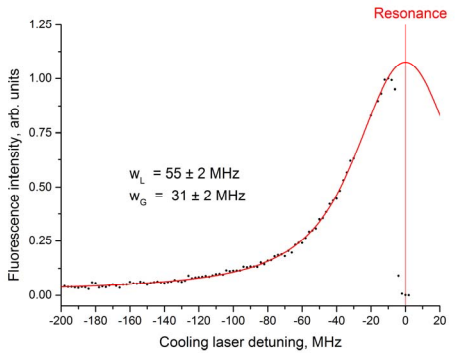

Fig. 2. $^{24}Mg^+$ ion fluorescence signal during cooling laser frequency scan through a resonance. Sharp drop in fluorescence close to the resonance caused by ion decrystallization due to laser heating. Data are fitted with a Voigt profile. Gaussian and Lorentzian widths of the profile are also shown.

The experiment starts from magnesium ions loading in side segment of a trap with a UV LED ionization method. Loading time was calibrated to trap on average one ion. After that a preliminary cooling with an axial laser beam is carried out. Laser is detuned by 2Γ to the red side of a spectrum from the cooling transition. Intensity of the beam is close to a saturation intensity of the transition. After precooling ion is shuttled to the central segment where it is cooled further with a diagonal beam. During this experiment an axial confinement is kept weak to prevent realization of Lamb-Dicke regime. Thus ions temperature can be estimated from Doppler broadening of the line.

Prior to ions temperature measurement an ion micromotion was minimized by compensating of stray electric fields with compensation electrodes. Detection of stray fields was accomplished by observing shift of ion crystal while trap depth was decreased.

To estimate ion temperature a frequency of the cooling laser was scanned through the cooling transition from the red detuning to the blue one and a fluorescence signal of an ion was recorded with the EMCCD camera. Obtained dependency of the fluorescence signal from the laser frequency is shown on a Fig. 2. A drop in the fluorescence level close to the zero detuning is determined by decrystallization of the ion due to laser heating. A fit of these data with a Voigt profile is also shown. A Lorentz width of the obtained line is in agreement with a power broadened natural linewidth and Gaussian width corresponds to the ion temperature of 40 mK. The ion temperature got from the fit is higher than a Doppler limit (that is 1 mK), but here it should be taken into account that this method gives only upper constraint on the temperature as the limit can be achieved only at optimal cooling parameters while during the scan most of the time they are not hold. Thus we can deduce that we achieved temperatures below 40 mK.

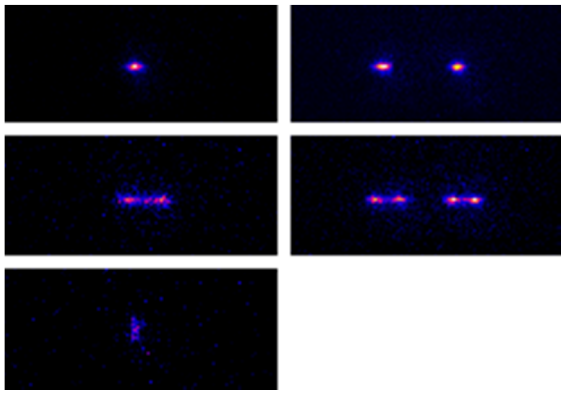

Fig. 3. Images of crystallized $^{24}Mg^+$ ions in our trap. Pictures on the top correspond to a single and pair of ions, correspondingly. Lower pictures show the change of the visible ions shape when cooling laser is modulated on the one of axial (in the middle) and radial (on the bottom) crystal modes frequencies.

IV. The Trap Characterization

Laser cooling of ions in a trap also allowed characterization of the trap itself. Dependency of the trapped ions secular frequencies on applied voltages was measured. Calibrated trap parameters allow distinguishing ions of other species trapped along with magnesium for sympathetic cooling by measuring secular frequencies of the formed two-ion crystal since these frequencies also depend on the "dark" ion mass.

Secular frequencies were determined by modulating the cooling laser frequency with an AOM and monitoring shape of the trapped ion with an EMCCD camera. When modulation frequency coincides with one of the ion secular frequencies the motion along its axis is amplified which can be seen from the ions image shape (Fig. 3). Secular frequencies for a single $^{24}Mg^+$ ion at the trap parameters used for the Doppler cooling experiment were measured to be $\omega_{\{x,y,z\}}=2\pi \times \{840, 840, 51\}$ kHz. Here z corresponds to the trap axis and x, y – to radial degrees of freedom.

V. Discussions and Future Plans

Experiments on magnesium ions trapping and Doppler cooling showed that our setup enables to crystallize and laser cool magnesium ions close to the Doppler limit. Although low trap secular frequencies due to large distance between electrodes make the process of ground state cooling and Al^+ ion spectroscopy more challenging. Therefore a new design of a trap is under development at the moment. It is planned to use gold-coated blade radiofrequency electrodes with smaller spacing between them for radial confinement and endcap electrodes for axial confinement.

Laser systems for photoionization and Raman ground-state cooling are also under development now. They will be similar to the one for the Doppler cooling unless the seed lasers and tapered amplifiers will be home-built (except the diodes and TA chips themselves).

VI. Conclusion

A current status of the project aimed for development of the optical frequency standard based on $^{27}Al^+$ ions being in progress at LPI is presented. The experimental setup for $^{27}Al^+$ and $^{25}Mg^+$ trapping and Doppler laser cooling is described.

Results on laser cooling of $^{24}Mg^{+}$ ions are demonstrated. It is shown that ion temperatures below 40 mK are achieved in our setup. The trapped ions secular spectrum is also measured. Future plans include modification of the ion trap used as well as finishing laser systems for photoionization and Raman resolved sideband cooling are presented.

ACKNOWLEDGMENT

The work was supported by the Russian Science Foundation (Grant No. 16-12-00096).

REFERENCES

[1] W. Lewandowski and E. F. Arias, "GNSS times and UTC," *Metrologia*, vol. 48, no. 4, pp. 219–224, 2011.

[2] S. L. Gilbert, W. C. Swann, and T. Dennis, "Wavelength standards for optical communications," in *Proceedings of SPIE*, 2001, vol. 4269, pp. 184–191.

[3] J. C. Corbett *et al.*, "Spanner: Google's Globally Distributed Database," *ACM Trans. Comput. Syst.*, vol. 31, no. 3, p. 8:1-8:22, 2013.

[4] Z. Arzoumanian *et al.*, "The NANOGrav Nine-year Data Set: Observations, Arrival Time Measurements, and Analysis of 37 Millisecond Pulsars," *Astrophys. J.*, vol. 813, no. 1, p. 65, 2015.

[5] T. L. Nicholson *et al.*, "Systematic evaluation of an atomic clock at 2 x 10^-18 total uncertainty," *Nat. Commun.*, vol. 6, p. 6896, 2015.

[6] N. Huntemann, C. Sanner, B. Lipphardt, C. Tamm, and E. Peik, "Single-Ion Atomic Clock with 3x10^-18 Systematic Uncertainty," *Phys. Rev. Lett.*, vol. 116, no. 6, p. 63001, 2016.

[7] C. W. Chou, D. B. Hume, J. C. J. Koelemeij, D. J. Wineland, and T. Rosenband, "Frequency comparison of two high-accuracy Al+ optical clocks," *Phys. Rev. Lett.*, vol. 104, no. 7, pp. 8–11, 2010.

[8] I. Ushijima, M. Takamoto, M. Das, T. Ohkubo, and H. Katori, "Cryogenic optical lattice clocks," *Nat. Photonics*, vol. 9, no. 3, pp. 185–189, 2015.

[9] J. Müller, M. Soffel, and S. A. Klioner, "Geodesy and relativity," *J. Geod.*, vol. 82, no. 3, pp. 133–145, 2008.

[10] N. Nemitz *et al.*, "Frequency ratio of Yb and Sr clocks with 5 × 10^−17 uncertainty at 150 seconds averaging time," *Nat. Photonics*, vol. 10, no. 4, pp. 258–261, 2016.

[11] T. Rosenband *et al.*, "Frequency Ratio of Al+ and Hg+ Single-Ion Optical Clocks; Metrology at the 17th Decimal Place," *Science*, vol. 319, no. 5871, pp. 1808–1812, 2008.

[12] S. Schiller *et al.*, "Einstein gravity explorer-a medium-class fundamental physics mission," *Exp. Astron.*, vol. 23, no. 2, pp. 573–610, 2009.

[13] P. Wolf *et al.*, "Quantum physics exploring gravity in the outer solar system: The SAGAS project," *Exp. Astron.*, vol. 23, no. 2, pp. 651–687, 2009.

[14] J. S. Chen, S. M. Brewer, C. W. Chou, D. J. Wineland, D. R. Leibrandt, and D. B. Hume, "Sympathetic Ground State Cooling and Time-Dilation Shifts in an Al 27 + Optical Clock," *Phys. Rev. Lett.*, vol. 118, no. 5, pp. 1–5, 2017.

[15] K. J. Arnold, R. Kaewuam, A. Roy, E. Paez, S. Wang, and M. D. Barrett, "Observation of the 1S0 to 3D1 clock transition in 175Lu+," *Phys. Rev. A*, vol. 94, no. 5, p. 52512, 2016.

[16] J. Keller *et al.*, "Controlling systematic frequency uncertainties at the 10^-19 level in linear Coulomb crystals," pp. 1–13, 2018.

[17] T. Rosenband *et al.*, "Observation of the S01→P03 clock transition in Al+27," *Phys. Rev. Lett.*, vol. 98, no. 22, pp. 1–4, 2007.

[18] T. Rosenband *et al.*, "Blackbody radiation shift of the 27Al+ 1S0-3P0 transition," in *Proceedings of the 20th European Frequency and Time Forum*, 2006, pp. 289–292.

[19] K. Beloy, D. R. Leibrandt, and W. M. Itano, "Hyperfine-mediated electric quadrupole shifts in Al+ and In+ ion clocks," *Phys. Rev. A*, vol. 95, no. 4, pp. 1–6, 2017.

[20] J. B. Wübbena, S. Amairi, O. Mandel, and P. O. Schmidt, "Sympathetic cooling of mixed-species two-ion crystals for precision spectroscopy," *Phys. Rev. A - At. Mol. Opt. Phys.*, vol. 85, no. 4, pp. 1–14, 2012.

[21] D. B. Hume, C. W. Chou, D. R. Leibrandt, M. J. Thorpe, D. J. Wineland, and T. Rosenband, "Trapped-ion state detection through coherent motion," *Phys. Rev. Lett.*, vol. 107, no. 24, pp. 1–5, 2011.

[22] I. A. Semerikov *et al.*, "Multiparticle losses in a linear quadrupole Paul trap," *Quantum Electron.*, vol. 46, no. 10, p. 935, 2016.

[23] T. V Shpakovsky *et al.*, "A Compact Second-Harmonic Generator for Tasks of Precision Spectroscopy Within the Range of 240-600 nm," *J. Russ. Laser Res.*, vol. 37, no. 5, pp. 440–447, 2016.

[24] J. Alnis, A. Matveev, N. Kolachevsky, T. Udem, and T. W. Hänsch, "Subhertz linewidth diode lasers by stabilization to vibrationally and thermally compensated ultralow-expansion glass Fabry-Perot cavities," *Phys. Rev. A - At. Mol. Opt. Phys.*, vol. 77, no. 5, pp. 1–9, 2008.

[25] A. A. Golovizin *et al.*, "Detection of the clock transition (1.14 mu m) in ultra-cold thulium atoms," *Quantum Electron.*, vol. 45, no. 5, pp. 482–485, 2015.

Characterization of the gravity gradiometer based on the Sr optical clock transition

Liang Hu, Leonardo Salvi, Enlong Wang, Guglielmo M. Tino, and Nicola Poli*
Dipartimento di Fisica e Astronomia and LENS - Università di Firenze, INFN - Sezione di Firenze,
Via Sansone 1, 50019 Sesto Fiorentino, Italy
*Email: poli@lens.unifi.it

***Abstract*—We present a gravity gradiometer with the strontium optical clock transition by integrating a double lattice launch technique to develop two atomic samples vertically and a new method to add an artificial phase shift between two samples. We experimentally characterize the launch performance and the robustness of adding the artificial phase shift. The tunable differential phase shift is particularly important for characterizing the performance of a gravity gradiometer when the separation of the two clouds is limited by the geometrical constraints. Moreover, numerical simulation results indicate that the systematic error of the differential phase measurement can be largely reduced when the ellipse phase approaches $\pm\pi/2$ rad by simply tuning the relative phase between two RF signals.**

I. Introduction

New quantum sensors based on atom interferometry have attracted widespread research interest in fundamental physics experiments and in several other applications over the last decades [1]. In particular, atom interferometers (AIs) based on multi-photon Raman/Bragg transitions, have been employed in precision measurements of the Newtonian gravitational constant [2], Earth gravity acceleration [3], [4], gravity gradients [5], [6] and gravity curvature [7], [8], as well as test of the weak equivalence principle [9]–[13] and the Lorentz invariance [14]. AIs have also been under consideration for their possible application to gravitational waves detection [15]. By taking an advantage of time-delay interferometry techniques, optical clock transition-based AIs have the capability to surpass the main limitation of standard two-photon atom interferometry for the gravitational wave detection by keeping a simple one-arm antenna geometry [16]–[18], Recently, in our group, we have experimentally demonstrated in the small scale both gravimeter and gradiometer configurations [19].

In this paper, we will characterize in detail the gravity gradiometer with the strontium optical clock transition where a lattice double launch technique, which was first used in Ref. [20], is adopted to build two atomic samples with different velocities in the vertical direction. Thanks to the different velocities, two different frequency components of the same clock laser can interact with two samples independently, and their relative phase shift can be tuned arbitrarily and precisely. Experimental results show that the measured phase shift and the applied phase shift are well matched, and numerical simulation results illustrate that the method is, in particular, important for reducing the inaccuracy of the differential pha measurement induced by the ellipse fitting when the separation of the two accelerometers is limited by the geometrical constraints.

II. Experimental apparatus and procedure

The experimental apparatus is shown in Fig. 1. The detailed description of the apparatus used to produce ultra-cold samples of strontium can be found to elsewhere [3], [21]. Here the most abundant bosonic isotope ^{88}Sr was selected as an accelerometer test mass and its clock transition induced by a static magnetic field [22]. In our case, the linewidth of the $^1S_0$-$^3P_0$ transition is approximately 35 μHz at the maximum magnetic field $B \simeq 300$ Gauss and the maximum beam intensity of $I \simeq 20$ W/cm^2. To drive this ultranarrow optical clock transition, a 1 Hz-linewidth clock laser system delivering up to 350 mW at $\lambda = 698$ nm was employed. The laser system consists of a master laser stabilized to a high finesse cavity made by a ultra-low expansion material (ULE) [23] and power amplified by an amplifier setup (AS) including a slave laser and a tapered amplifier. Here an acousto-optical modulator (AOM1) is used to bridge frequency difference between the ULE cavity and the resonance frequency of the $^1S_0$-$^3P_0$ transition. The light is transferred to the atoms by a 10-m polarization maintaining (PM) fiber. Eventually, we have a clock light with a power of 80 mW for the atoms.

A cloud of $\sim 5\times10^6$ ultra-cold ^{88}Sr atoms at a temperature of $\sim$1 μK, with horizontal (vertical) dimension of 300 μm (70 μm) at full width half maximum (FWHM), is produced by a two-stage magneto-optical trap (MOT). Afterwards, about 20% of the atoms are adiabatically loaded into a vertical 1D optical lattice at 532 nm. With a power on each beam $\sim$ 1 W and a beam waist of $\sim$ 350 μm, the trap depth in this condition is 9 $E_{r,g}$, where $E_{r,g} = \hbar^2 k_g^2/2m$ is the recoil energy of the green lattice (k_g is the lattice wave vector and m is the mass of ^{88}Sr atoms). The atoms are maintained in the trap for a time of about 65 ms, during which we invert the current direction in one of the MOT coils and then turn on the homogeneous magnetic field B. The lattice launch technique for ^{88}Sr atoms using 532 nm green lattice has been demonstrated in [21]. Here we extend the technique to perform a double-launch. The atoms in the lattice are accelerated upwards in 8 ms by frequency ramping down the top lattice beam at a rate of 100 kHz/ms, resulting in an acceleration of 2.7 g. After a delay of $\Delta\tau$ = 1 ms, the same launch procedure is repeated for the residual free-falling atoms with a duration of 6 ms.

978-1-5386-5620-4/18/$31.00 ©2018 IEEE

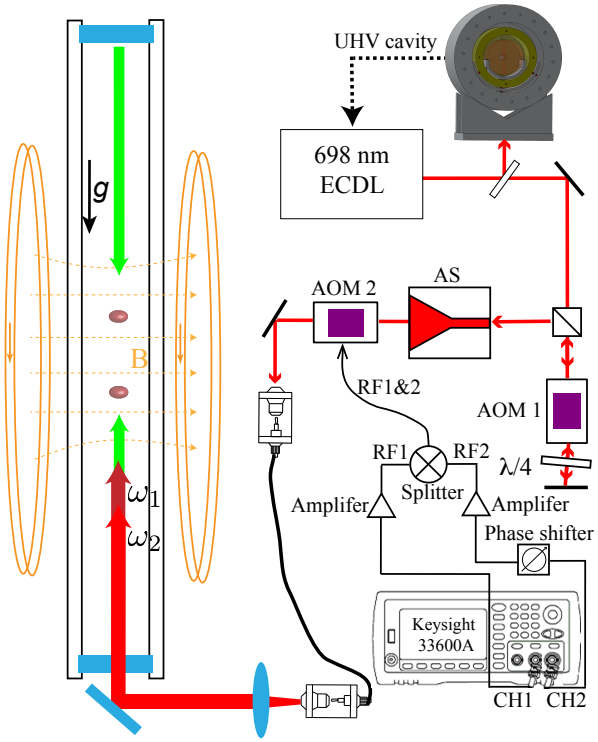

Fig. 1. Experimental apparatus. Laser radiation at 698 nm is frequency stabilized in two-steps via Pound-Drever-Hall (PDH) locking to optical cavities with finesses of 10 000 and 400 000, respectively. Electronic feedback from pre-stabilization cavity and high finesse cavity (ULE) are respectively sent to laser actuators (piezoelectric transducer and current) and to an external acousto-optical modulator (AOM). The stabilized light is then amplified by an amplifier setup (AS) consisting of a slave diode and a tapered amplifier (TA). A 10 m polarization maintaining (PM) fiber delivers the stabilized high power laser light to the atomic vacuum chamber. Pre-cooled ^{88}Sr atoms trapped in a vertical optical lattice operating at 532 nm (green lattice) are launched upwards two times. Then the first 'π' clock laser pulse is applied to velocity select the atoms along vertically followed by a 'blow away ' beam for blowing away the not selected atoms. Afterwards, a sequence of interferometer pulses is applied. Once the interferometer process is finished, a 'push beam' is applied to decelerate the atoms in the ground state for spatially separating them from atoms in the excited state. After repumping the excited atoms back into the ground state, two states are detected by observing atomic fluorescence collected onto a photomultiplier tube produced by a resonant sheet of blue light at 461 nm.

Eventually, we produce two clouds with a similar number of atoms ($\sim 2.5 \times 10^5$). The separation of the clouds can be tuned by adjusting the delay time $\Delta\tau$. Here, the double lattice launch technique can have a well-defined baseline because the single-source gradiometer presented here is insensitive to the atom source position [20], [24], [25]. A similar idea by using large momentum transfer (LMT) atom optics has been used to create a single-source gradiometer [8].

After the double launch, two clouds are velocity selected vertically by a first π-pulse on the clock transition, which puts the selected atoms into the excited clock state. Then, not selected atoms in the ground state are blown away using light resonant with the dipole-allowed ^{1}S$_0$-^{1}P$_1$ transition at 461 nm from the top side of the fountain. Eventually, about 4% of the atoms are selected, thus producing each sample including $\sim 10^4$ atoms with a narrow vertical momentum width of $\sim 0.04\ \hbar k$ (k is the wave vector of the clock laser) for each accelerometer. Afterwards, a $\pi/2-\pi-\pi/2$ Mach-Zehnder like interferometer pulse sequence on the optical clock transition is applied to both atomic samples. At the end of the gradiometer sequence, a vertical push beam on the ^{1}S$_0$-^{3}P$_1$ transition at 689 nm from the bottom side is used to decelerate atoms in the ground state for spatially separating from atoms in the excited state. After repumping the excited atoms back to the ground state, the relative population in the two arms of each interferometer is detected by collecting the fluorescence signal produced by a resonant sheet of blue light at 461 nm onto a photomultiplier tube, as shown in Fig. 1.

The phase difference between the two accelerometers can be used to determine the local gravity gradient. In our case the sensitivity is mainly limited by the small separation distance, and is not high enough to measure the gravity gradient [19]. Therefore, in order to characterize the performance of the common-noise rejection of gradiometer, we induced an artificial phase shift $\delta\phi$ between the two interferometers as shown in Fig. 1. The AOM2 before the fiber diffracts two different RF frequencies: RF1 and RF2 produced by a two-channel direct digital synthesizer (DDS) generator (Keysight 33600 A) and their relative phase shift of $\delta\phi$ can be precisely tuned by a internal phase shifter in the channel 2. In this way, the clock light including two different frequency components will interact with two clouds independently and their relative phase shift can be well controlled by tuning the internal phase shift function. Thus, the single clock light includes two frequency components (ω_1 and ω_2 shown Fig. 1) with an equal beam intensity of 10 W/cm^2 at the beam waist of 0.45 mm. As the light with two frequency components shares the same path to the atoms, most of the phase noise is common-mode. To be noticed, before sending the two RF signals to the AOM2, the signals need to be amplified by RF amplifiers. This can be realized by combining the two different frequencies by a RF splitter and then injecting into a single RF amplifier. In this way, the signals will experience a nonlinear effect inside the amplifier, creating sidebands carrying a few percent of the total output power at a separation in frequency spacing corresponding to the seed frequency difference in the output spectrum. In coherently manipulating an atomic ensemble, the presence of sidebands has to be avoided to mitigate resulting systematic biases through the beam splitting process via additional light shifts and/or parasitic transitions. Therefore, to avoid the nonlinear effect in the single RF amplifier, here we first amplify each RF signal by two independent RF amplifiers. Then two amplified signals are combined with a high power RF splitter and its output injects into the AOM2. By adopting this method, we can have pure RF spectrum before injecting into the AOM2. Although in this configuration, the two frequency components will feel slight different phase noise due to different amplifier paths, the phase noise between two channels can be negligible at a level below the sensitivity of the apparatus.

III. Numerical simulation

After plotting the signal of the upper AI versus the lower one, the experimental points distribute along an ellipse. Here the differential phase shift between the two simultaneous AIs includes the phase shifts induced by the gravity gradient, different initial velocities and artificial phase shift as calculated by Eq. 2 in Ref. [19]. The most popular and robust fitting method is the method based on fitting ellipses to the data to extract the differential phase [26]. Bayesian techniques [27] can also be applied to the ellipse phase estimation to reduce the required number of points and also reduce the noise and systematic offset associated with simple ellipse fitting, but this method needs to know all noise types. This requirement sometimes is difficult to be satisfied, because as usual we are not clear which types of noise will have in experimental results. The differential phase shift between two simultaneous interferometers can be extracted by a least-squares algorithm which fits the parametric equations

$$\begin{cases} x = A_x \sin(\phi_c) + C_x, \\ y = A_y \sin(\phi_c + \phi_d) + C_y, \end{cases} \tag{1}$$

where A_x and A_y are the normalized fringe contrast, C_x and C_y are the offsets, ϕ_c is the common phase shared between two AIs and ϕ_d is the differential phase that we are interested in.

As the ellipse fitting method is used to extract the differential phase shift of a gradiometer, it is crucial to understand any systematics caused by the ellipse fitting algorithm at a level below certain value, otherwise the ellipse fitting would contribute significantly to the uncertainty of the measurement. Here we use a simple model to analyze the uncertainty introduced by the ellipse fitting. The two normalized interferometer outputs have an offset noise $\epsilon_{x,y}$ with a Gaussian distribution. The Gaussian distribution has a variance of $\sigma^2_{x,y}$

$$\begin{cases} x = A_x \cos(\phi_c) + C_x + \epsilon_x, \\ y = A_y \cos(\phi_c + \phi_d) + C_y + \epsilon_y. \end{cases} \tag{2}$$

Figure 2 shows numerical simulation results of the ellipse fitting uncertainty $\Delta\phi$, which is obtained by calculating the difference between the applied phase and the ellipse fitted phase, as a function of the applied phase for different Gaussian amplitude variances of $\sigma_{x,y} = 1/2\sqrt{N}$ (blue square), $\sigma_{x,y} = 1/\sqrt{N}$ (red circle) and $\sigma_{x,y} = 2/\sqrt{N}$ (green triangle), respectively, at $N = 10,000$ atoms and a interferometer contrast of 30%. The inset shows an example of the ellipse with a relative phase shift $\pi/2$ rad and a variance of $\sigma_{x,y} = 1/\sqrt{N}$ for the same atom number and contrast. In the case of $\sigma_{x,y} = 2/\sqrt{N}$, a fitting uncertainty as large as 70 mrad was observed. In all cases, we can see that the fitted phase is more accurate around $\pm\pi/2$ rad and less accurate near 0, $\pm\pi$ rad where the ellipse becomes a line. Therefore it is best to operate the gradiometer at a net phase of $\pm\pi/2$ rad for optimizing the fitting performance. As shown in Fig. 2, when the relative phase shifts are away from the optimum

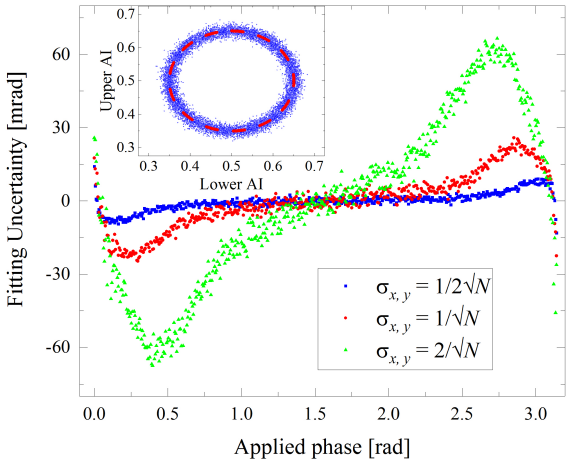

Fig. 2. Numerical simulation results of the ellipse fitting uncertainty $\Delta\phi$ obtained by calculating the difference between the applied phase and the ellipse fitted phase as a function of the applied phase in the presence of Gaussian noise with a variance of $\sigma_{x,y} = 1/2\sqrt{N}$ (blue square), $\sigma_{x,y} = 1/\sqrt{N}$ (red circle) and $\sigma_{x,y} = 2/\sqrt{N}$ (green triangle), respectively, at $N = 10,000$ atoms and a contrast of $\sim$ 30%. To be noticed, the ellipse fitting cannot determine the sign of the phase. Inset shows an example of a simulated ellipse with a differential phase $\pi/2$ rad and $\sigma_{x,y} = 1/\sqrt{N}$. The dashed red line indicates the least squares ellipse fitting.

points $\pm\pi/2$ rad the fitting uncertainty can also be optimized by reducing $\sigma_{x,y}$. A direct way is to increase the number of atoms participating in the interferometer and being detected. In the present configuration, only a small number of atoms are contributing to the signal. Although a relatively large number of atoms is trapped ($\sim 2\times10^6$) in an optical lattice, only 10^4 atoms contribute to the interference fringes. There are several reasons that lead to this inefficiency. The optical lattice launch is not efficient, a considerable number of atoms are lost in the atomic fountain itself, and the interference fringe contrast coupled with the velocity selection stage limits the signal size even more. Improving the signal level is expected to improve the overall sensitivity in a direct way. These inefficiencies all have straightforward solutions conceptually, but the solutions are not easy to implement for our experimental setup. Another powerful complementary approach is to take advantage of squeezing atomic quantum states to push towards Heisenberg-limited quantum measurements that scale as $1/N$ atoms. This technique has been widely demonstrated and applied for cavity-assisted atomic clocks and interferometers [28]–[30]. As we can observer in Fig. 2, the ellipse fitting uncertainty can be reduced by a factor of at least 2 by reducing the noise of 3 dB from $\sigma_{x,y} = 1/2\sqrt{N}$ to $\sigma_{x,y} = 1/\sqrt{N}$.

IV. Experimental results

For our 1D lattice at 532 nm, it is far detuned from the $^1S_0$-$^1P_1$ transition ($\delta \sim 2.7\times10^6\gamma$ and γ is the linewidth of the $^1S_0$-$^1P_1$ transition). The scattering rate induced by the spontaneous emission is negligible. Since the waist is comparable to the atomic radial dimension after releasing from the MOT cloud, this lattice also guarantees a transversal confinement during the lattice sequence [32], [33]. Therefore

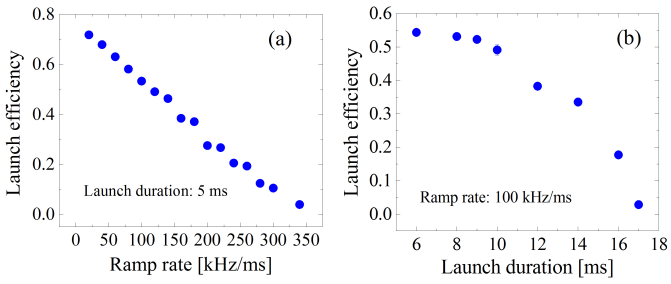

Fig. 3. Lattice launch efficiencies as a function of the frequency ramp rate (a) and lattice pulse duration (b). In order to keep a trade-off between the launched atoms and the loss of the atoms due to the Landau-Zener tunneling [31], we found that a reasonable chirping rate for the launch is close to 100 kHz/ms. Although a lower final lattice frequency results in more atoms being launched, for gaining sufficient height for the interferometer sequence, the final lattice frequency used was 800 kHz for the first launch and 600 kHz for the second launch. This launch sequence resulted in approximately $\sim 2.5 \times 10^5$ atoms in each launched cloud.

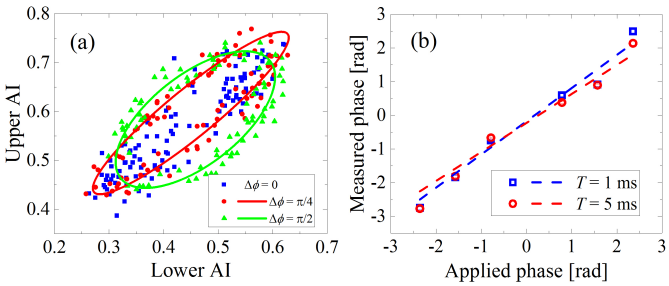

Fig. 4. (a) the measured relative populations for the upper and lower AIs with different applied phase shifts of 0 rad, $\pi/8$ rad and $\pi/4$ rad respectively at the interferometers time of $T = 5$ ms. By increasing the applied relative phase shifts, the ellipse opens progressively, demonstrating the appearance of a fixed relative phase between the upper and lower accelerometers. (b) Relative phase shifts obtained by the least-square ellipse fitting as a function of the different applied phase shifts $\delta\phi$ at two different interferometer times: T = 1 ms (blue square) and T = 5 ms (red circle).

here the main loss is due to the Landau-Zener (LZ) tunneling [31]. Lattice launch efficiencies as a function of the frequency chirp rate at a duration of 5 ms and lattice pulse duration (final lattice frequency) at a ramp rate of 100 kHz/ms are shown in Fig. 3. To have a tradeoff between the launched atoms and the loss of the atoms due to the Landau-Zener tunneling, we found that the acceptable chirping rate for the launch is close to 100 kHz/ms, and the launch duration $<$ 10 ms has a flat region where the loss almost keeps a constant as shown in Fig. 3 (b), thus we are choosing to work at a duration of 8 ms for the first launch and 6 ms for the second launch, respectively.

To demonstrate the artificial phase shift in the gradiometer configuration, we tune the artificial phase shit and measure the angle of the ellipse by the ellipse fitting. As shown in Fig. 4 (a), while no ellipse can be observed in absence of the artificial phase shift $\delta\phi$, by increasing the artificial phase shift the ellipse opens progressively. To further verify the robustness of this technique, we modulate the artificial phase shift and record a series of angles of the ellipse for two different interferometer times: $T = 1$ ms (red square points) and $T = 5$ ms (blue circle points). As shown in Fig.4 (b), we find a good agreement of the measured phase shifts and the applied artificial phase shifts with a slope of 0.98(8) for $T = 1$ ms (blue dashed line) and 0.86(9) for $T = 5$ ms (red dashed line). The slight offset from the ideal condition with a slope of 1 and the difference between two cases: $T = 1$ ms and $T = 5$ ms is mainly due to the fitting performance because of high detection noise from the photon collection efficiency at the output of the gradiometer [19].

V. Conclusions

In conclusion, taking advantage of the double lattice launch technique to have two atomic samples and high frequency selectivity of the clock transition allows us to add a well-controlled artificial relative phase shift by simply tuning the relative phase between two RF signals that injects into a single AOM on the clock laser path. The tunable artificial phase shift is important for characterizing the sensitivity of the gradiometer without the need of additional external fields and reducing the uncertainty from the ellipse fitting. Although in the present setup the sensitivity is not high due to technical factors, this ability to switch from a gravimeter to a gravity gradiometer with only a slight change to the experimental procedure is attractive in the context of precision inertial sensing. In the future, the implementation of this scheme in very-long-baseline gradiometers can be designed to fill the gap between space-borne laser interferometer detectors like LISA [34] and ground-based instruments like LIGO and Virgo[35], [36].

Acknowledgment

We acknowledge financial support from INFN and the Italian Ministry of Education, University and Research (MIUR) under the Progetto Premiale 'Interferometro Atomico' and PRIN 2015. This project has received funding from the Initial Training Network (ITN) supported by the European Commission's 7th Framework Programme under Grant Agreement No. 607493. L. Hu acknowledges support by Kayser Italia. E. Wang acknowledges the financial support from the program of China Scholarship Council (No.201703170201).

References

[1] *Atom Interferometry*. Proceedings of the International School of Physics "Enrico Fermi," Course CLXXXVIII, edit by G. M. Tino and M. A. Kasevich. Società Italiana di Fisica and IOS Press, Amsterdam, 2014.

[2] G. Rosi, F. Sorrentino, L. Cacciapuoti, M. Prevedelli, and G. M. Tino, "Precision measurement of the Newtonian gravitational constant using cold atoms," *Nature (London)*, vol. 510, no. 7506, pp. 518–521, 2014.

[3] T. Mazzoni, X. Zhang, R. Del Aguila, L. Salvi, N. Poli, and G. M. Tino, "Large-momentum-transfer Bragg interferometer with strontium atoms," *Phys. Rev. A*, vol. 92, no. 5, p. 053619, 2015.

[4] A. Peters, K. Y. Chung, and S. Chu, "Measurement of gravitational acceleration by dropping atoms," *Nature (London)*, vol. 400, no. 6747, pp. 849–852, 1999.

[5] F. Sorrentino, Q. Bodart, L. Cacciapuoti, Y.-H. Lien, M. Prevedelli, G. Rosi, L. Salvi, and G. M. Tino, "Sensitivity limits of a Raman atom interferometer as a gravity gradiometer," *Phys. Rev. A*, vol. 89, no. 2, p. 023607, 2014.

[6] G. D'Amico, F. Borselli, L. Cacciapuoti, M. Prevedelli, G. Rosi, F. Sorrentino, and G. M. Tino, "Bragg interferometer for gravity gradient measurements," *Phys. Rev. A*, vol. 93, no. 6, p. 063628, 2016.

[7] G. Rosi, L. Cacciapuoti, F. Sorrentino, M. Menchetti, M. Prevedelli, and G. M. Tino, "Measurement of the gravity-field curvature by atom interferometry," *Phys. Rev. Lett.*, vol. 114, no. 1, p. 013001, 2015.

[8] P. Asenbaum, C. Overstreet, T. Kovachy, D. D. Brown, J. M. Hogan, and M. A. Kasevich, "Phase shift in an atom interferometer due to spacetime curvature across its wave function," *Phys. Rev. Lett.*, vol. 118, no. 18, p. 183602, 2017.

[9] S. Fray, C. A. Diez, T. W. Hänsch, and M. Weitz, "Atomic interferometer with amplitude gratings of light and its applications to atom based tests of the equivalence principle," *Phys. Rev. Lett.*, vol. 93, no. 24, p. 240404, 2004.

[10] M. G. Tarallo, T. Mazzoni, N. Poli, D. V. Sutyrin, X. Zhang, and G. M. Tino, "Test of Einstein Equivalence Principle for 0-spin and half-integer-spin atoms: Search for spin-gravity coupling effects," *Phys. Rev. Lett.*, vol. 113, no. 2, p. 023005, 2014.

[11] B. Barrett, L. Antoni-Micollier, L. Chichet, B. Battelier, T. Lévèque, A. Landragin, and P. Bouyer, "Dual matter-wave inertial sensors in weightlessness," *Nat. Commun.*, vol. 7, p. 13786, 2016.

[12] X.-C. Duan, X.-B. Deng, M.-K. Zhou, K. Zhang, W.-J. Xu, F. Xiong, Y.-Y. Xu, C.-G. Shao, J. Luo, and Z.-K. Hu, "Test of the universality of free fall with atoms in different spin orientations," *Phys. Rev. Lett.*, vol. 117, no. 2, p. 023001, 2016.

[13] G. Rosi, G. D'Amico, L. Cacciapuoti, F. Sorrentino, M. Prevedelli, M. Zych, Č. Brukner, and G. M. Tino, "Quantum test of the equivalence principle for atoms in coherent superposition of internal energy states," *Nat. Commun.*, vol. 8, p. 15529, 2017.

[14] H. Müller, S.-w. Chiow, S. Herrmann, S. Chu, and K.-Y. Chung, "Atom-interferometry tests of the isotropy of post-newtonian gravity," *Phys. Rev. Lett.*, vol. 100, no. 3, p. 031101, 2008.

[15] S. Dimopoulos, P. W. Graham, J. M. Hogan, M. A. Kasevich, and S. Rajendran, "Atomic gravitational wave interferometric sensor," *Phys. Rev. D*, vol. 78, no. 12, p. 122002, 2008.

[16] N. Yu and M. Tinto, "Gravitational wave detection with single-laser atom interferometers," *Gen. Rel. Gravit.*, vol. 43, no. 7, pp. 1943–1952, 2011.

[17] P. W. Graham, J. M. Hogan, M. A. Kasevich, and S. Rajendran, "New method for gravitational wave detection with atomic sensors," *Phys. Rev. Lett.*, vol. 110, no. 17, p. 171102, 2013.

[18] S. Kolkowitz, I. Pikovski, N. Langellier, M. D. Lukin, R. L. Walsworth, and J. Ye, "Gravitational wave detection with optical lattice atomic clocks," *Phys. Rev. D*, vol. 94, no. 12, p. 124043, 2016.

[19] L. Hu, N. Poli, L. Salvi, and G. M. Tino, "Atom interferometry with the Sr optical clock transition," *Phys. Rev. Lett.*, vol. 119, no. 26, p. 263601, 2017.

[20] R. P. Del Aguila, T. Mazzoni, L. Hu, L. Salvi, G. M. Tino, and N. Poli, "Bragg gravity-gradiometer using the $^1S_0$-$^3P_1$ intercombination transition of ^{88}Sr," *New J. Phys.*, vol. 20, no. 4, p. 043002, 2018.

[21] X. Zhang, R. P. del Aguila, T. Mazzoni, N. Poli, and G. M. Tino, "Trapped-atom interferometer with ultracold Sr atoms," *Phys. Rev. A*, vol. 94, no. 4, p. 043608, 2016.

[22] A. Taichenachev, V. Yudin, C. Oates, C. Hoyt, Z. Barber, and L. Hollberg, "Magnetic field-induced spectroscopy of forbidden optical transitions with application to lattice-based optical atomic clocks," *Phys. Rev. Lett.*, vol. 96, no. 8, p. 083001, 2006.

[23] M. G. Tarallo, N. Poli, M. Schioppo, D. V. Sutyrin, and G. M. Tino, "A high-stability semiconductor laser system for a ^{88}Sr-based optical lattice clock," *Appl. Phys. B*, vol. 103, no. 1, pp. 17–25, 2011.

[24] G. Tackmann, P. Berg, S. Abend, C. Schubert, W. Ertmer, and E. M. Rasel, "Large-area sagnac atom interferometer with robust phase read out," *C. R. Phys.*, vol. 15, no. 10, pp. 884–897, 2014.

[25] O. Carraz, C. Siemes, L. Massotti, R. Haagmans, and P. Silvestrin, "A spaceborne gravity gradiometer concept based on cold atom interferometers for measuring earth's gravity field," *Microgravity Sci. Technol.*, vol. 26, no. 3, pp. 139–145, 2014.

[26] G. Foster, J. Fixler, J. McGuirk, and M. Kasevich, "Method of phase extraction between coupled atom interferometers using ellipse-specific fitting," *Opt. Lett.*, vol. 27, no. 11, pp. 951–953, 2002.

[27] J. K. Stockton, X. Wu, and M. A. Kasevich, "Bayesian estimation of differential interferometer phase," *Phys. Rev. A*, vol. 76, no. 3, p. 033613, 2007.

[28] O. Hosten, N. J. Engelsen, R. Krishnakumar, and M. A. Kasevich, "Measurement noise 100 times lower than the quantum-projection limit using entangled atoms," *Nature (London)*, vol. 529, no. 7587, p. 505, 2016.

[29] O. Hosten, R. Krishnakumar, N. Engelsen, and M. Kasevich, "Quantum phase magnification," *Science*, vol. 352, no. 6293, pp. 1552–1555, 2016.

[30] L. Salvi, N. Poli, V. Vuletić, and G. M. Tino, "Squeezing on momentum states for atom interferometry," *Phys. Rev. Lett.*, vol. 120, no. 3, p. 033601, 2018.

[31] E. Peik, M. B. Dahan, I. Bouchoule, Y. Castin, and C. Salomon, "Bloch oscillations of atoms, adiabatic rapid passage, and monokinetic atomic beams," *Phys. Rev. A*, vol. 55, no. 4, p. 2989, 1997.

[32] B. T. Wolschrijn, R. Cornelussen, R. Spreeuw, and H. V. L. Van Den Heuvell, "Guiding of cold atoms by a red-detuned laser beam of moderate power," *New J. Phys.*, vol. 4, no. 1, p. 69, 2002.

[33] L. Pruvost, D. Marescaux, O. Houde, and H. T. Duong, "Guiding and cooling of cold atoms in a dipole guide," *Opt. Comm.*, vol. 166, no. 1, pp. 199–209, 1999.

[34] K. Danzmann *et al.*, "LISA—an ESA cornerstone mission for the detection and observation of gravitational waves," *Adv. Space Res.*, vol. 32, no. 7, pp. 1233–1242, 2003.

[35] B. P. Abbott, R. Abbott, R. Adhikari, P. Ajith, B. Allen, G. Allen, R. S. Amin, S. B. Anderson, W. G. Anderson, M. A. Arain *et al.*, "LIGO: the laser interferometer gravitational-wave observatory," *Rep. Prog. Phys.*, vol. 72, no. 7, p. 076901, 2009.

[36] C. Bradaschia, R. Del Fabbro, A. Di Virgilio, A. Giazotto, H. Kautzky, V. Montelatici, D. Passuello, A. Brillet, O. Cregut, P. Hello *et al.*, "The VIRGO project: a wide band antenna for gravitational wave detection," *Nucl. Instrum. Methods Phys. Res. A.*, vol. 289, no. 3, pp. 518–525, 1990.

Two-stage stabilization setup of the laser working on 729 nm for spectroscopy with cold $^{40}Ca^{+}$ ion.

Tuan Minh Pham[1], Martin Cizek[1], Adam Lesundak[1], Vaclav Hucl[1], Josef Lazar[1], Ondrej Cip[1]
[1]Department of Coherent Optics, Institute of Scientific Instruments of the CAS,
Brno, Czech Republic
Email: tuan@isibrno.cz

***Abstract* — The paper deals with the stabilization of an Extended Cavity Diode Laser (ECDL) working at 729 nm for precision spectroscopy with trapped and cooled $^{40}Ca^{+}$ ion. For an interrogating and readout ion oscillation the laser with ultra-narrow linewidth is required. Main cornerstones are explained to achieve a laser with Hz or sub-Hz spectral linewidth. An optical setup for this laser and also the necessary electro-optic and electronic components are demonstrated. The paper presents the experimental design that comprises of the two-stage linewidth narrowing process and a facility for the frequency and noise analysis. The presented experimental results show the effect of the linewidth narrowing where the linewidth of the ECDL was narrowed down to a kHz level.**

Keywords — stabilization; spectroscopy; calcium ion; hight-finesse cavity; spectral linewidth; phase-locked loop; optical frequency comb.

I. INTRODUCTION

The experiments with trapped ions, such as precision spectroscopy techniques or experiments with quantum mechanical interaction and quantum computing experiments demand a narrow-linewidth excitation laser [1]. This requirement comes from the physical properties of the forbidden transitions of ultra-cold ions trapped into an electrical trap. To be able to coherently transfer a population into the dipole forbidden transition one need a laser working with Hz or sub-Hz linewidth. The spectral linewidth of the external cavity laser diode (ECDL) chosen for this purpose is 300 kHz approx. for the integration time of 1 s [2]. Because this relatively broader linewidth doesn't fulfil the requirement for the efficient pumping of the long lived forbidden transition, an implementation of a linewidth narrowing technique is necessary.

We present a two stage setup for a clock laser linewidth narrowing. In the first stage an optical frequency of the ECDL is phase locked to a selected component of an optical frequency comb which has a ten times narrower linewidth than the ECDL. The following stage is the frequency noise suppression with the high-finesse optical resonator which serves as a frequency discriminator allowing the further linewidth suppression. To verify the functionality of the narrowing process we used the laser for the spectroscopy of a narrow forbidden transition of a trapped and Doppler cooled calcium ion.

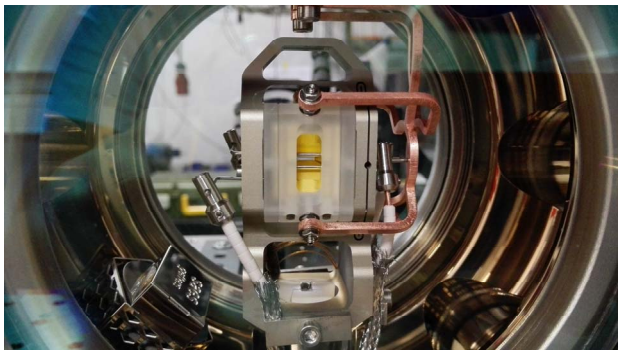

Fig. 1. A view of the the ion trap.

II. METHODOLOGY AND EXPERIMENTAL SETUP

Our group works with calcium ions, mainly with the isotope $^{40}Ca^{+}$. The energy level structure of this ion is shown in Figure 2. The dipole forbidden transition consists of the $S_{1/2}$ and $D_{5/2}$ level which is coupled by the clock laser. Other levels are used for the Doppler cooling and the detection using 397 nm and 866 nm lasers.

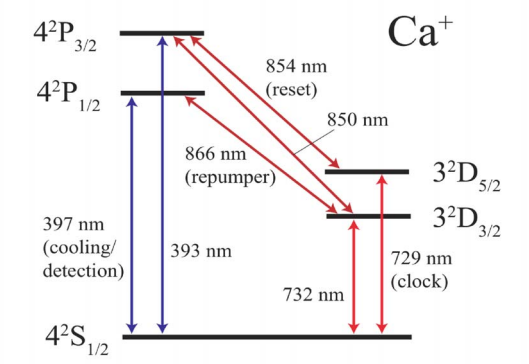

Fig. 2. A level strucure of $^{40}Ca^{+}$ ion. The qubit consists of the $S_{1/2}$ and $D_{5/2}$ levels which are coupled by a 729 nm laser.

The laser linewidth narrowing process is a combination of two methods. The complex scheme is shown in Figure 3. The first step is a phase-locked loop (PLL) of the ECDL laser optical frequency to a selected component (one tooth) of an optical frequency comb which has a ten times narrower linewidth than the ECDL. In this case, the result

of an implementation of this technique is that the profile of 729 nm laser will copy the spectral profile of the selected tooth of the optical frequency comb. The big advantage of this method is that the ECDL laser optical frequency is stabilized on the absolute scale thanks to the referencing of the optical frequency comb disciplined by an active Hydrogen maser. The ECDL laser optical frequency locked to the optical frequency comb is monitored by the wavelength meter for the absolute value of the laser wavelength and by the unbalanced Mach-Zehnder interferometer with a long fibre spool for the frequency spectrum analysis.

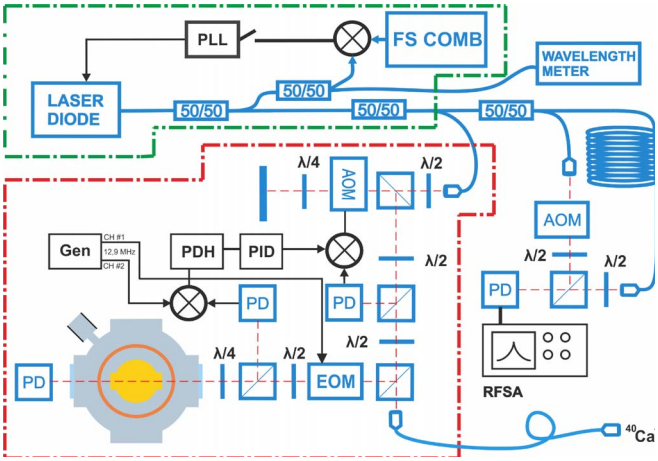

Fig. 3. The setup for the ECDL laser linewidth narrowing and the frequency noise properties analysis. The green section includes the ECDL laser (LASER DIODE) and a phase locked loop (PLL) to the selected spectral component of the optical frequency comb – FS COMB. The red section represents the second stage of the linewidth narrowing using the spectroscopy with a high-finesse optical resonator, λ/2 and λ/4 are waveplates, AOMs are accousto optical modulators, EOM is electrooptical modulator, 50/50 are splitters, PD are photodetectors

The heart of the second stabilization stage is a high-finesse optical resonator. Pound-Drever-Hall (PDH) detection technique is used for getting an error signal which indicates if the laser frequency is on the optical cavity resonance [4]. In this scheme, the laser beam is phase modulated with an electro-optic-modulator (EOM) and mode matched into the cavity. The beam reflected from the cavity is monitored by a fast photodetector. The signal is mixed down in a mixer with a local oscillator, which is in a phase with the EOM modulation to produce an error signal. The error signal is then used for the laser frequency control. It is provided by PID controller and voltage control oscillator driving the AOM modulator. When the second stage stabilization is switched on, the optical frequency of the output beam of the AOM modulator is locked to the optical cavity TEM_{00} resonance. The output beam is used for testing the narrowed laser on the cold ion setup.

The frequency stability of the clock laser is degraded by changes of the optical cavity length due to acoustic vibrations, temperature changes or air flow coming from the laboratory where the cavity is placed. For the elimination of these environmental disturbations we designed a wooden protecting box with many isolation elements. The optical setup of the cavity setup is built on the active anti-vibration platform, which lies on the 250 kg granite block surrounded by fine sand. The whole setup is then wrapped by layers of lead, high density glass wool, and wood. The optical cavity itself is situated inside the vacuum chamber with a Peltier element for controlling the temperature inside the chamber.

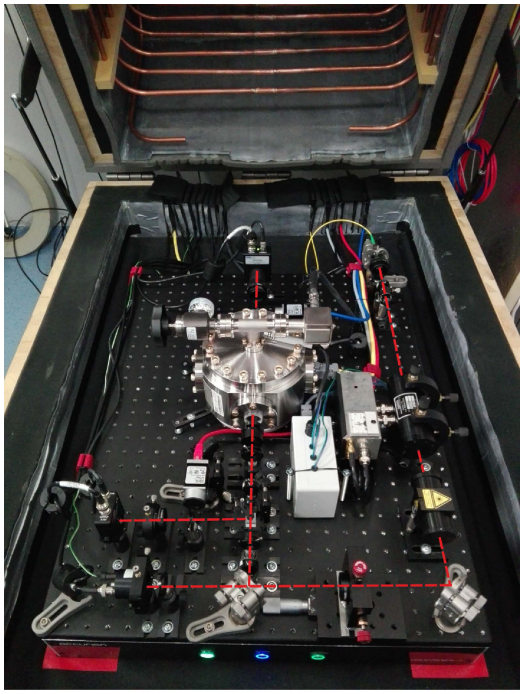

Fig. 4. The view of high-finesse cavity with collimating optics instaled inside an anti-vibration protected box.

III. Results

Usually the high-finesse cavities used for clock lasers have the finesse above hundreds of thousands. To determine the finesse of our cavity we used a ring down measurement technique [3]. This measurement indicates how fast the cavity loses its stored light after shutting the laser beam down. From that, the exact finesse and linewidth can be calculated. In our case the ring down identified the finesse of 345.000 and the linewidth of the fundamental cavity mode is 9 kHz approx.

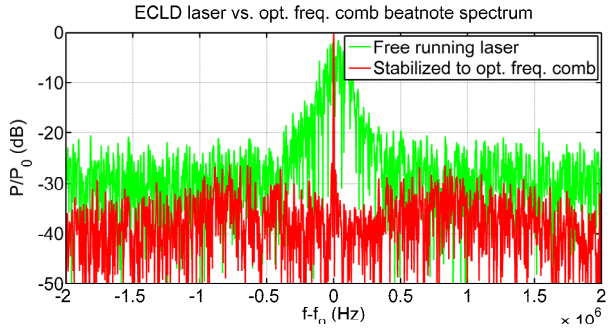

Fig. 5. The beat-note spectrum od the ECDL laser before (green) and after (red) stabilized to the optical frequency comb.

The spectral properties of the laser locked by the first stage are shown in Figure 5. The beat-note spectrum of the free running laser and of the stabilized ECDL laser is compared. There is clearly seen that a signal to noise ratio (SNR) of the stabilized ECDL laser is 10 dB above a SNR of the free running laser.

To measure the properties of the laser achieved by the second stage, we used the electron shelving based spectroscopy on the transition $S_{1/2}$ - $D_{5/2}$ of the single cooled ion [5]. After the Doppler cooling the ion is prepared at $S_{1/2}$ level. A short laser pulse at 729 nm is applied to the ion, then quantum jump consisting of the 397 nm and 866 nm excitation is used to test whether the excitation into forbidden transition was successful. This process is repeated hundred times before laser frequency of the 729 nm is detuned to a new value. The captured spectrum is shown in Figure 6. Where one can see the carrier transition and its axial sidebands while scanning over the frequencies

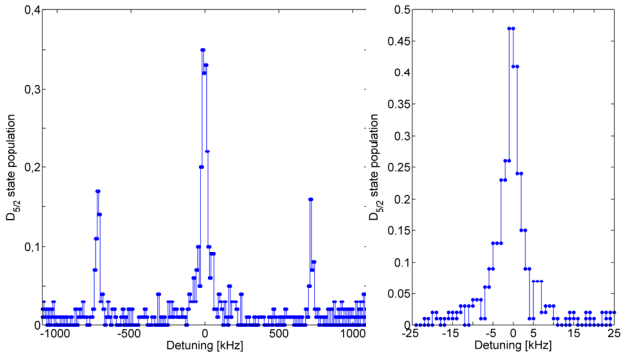

Fig. 6. The captured spectrum od the $S_{1/2}$ - $D_{5/2}$ transition of $^{40}Ca^{+}$ ion measured with ECDL laser narowed by means of high-finesse cavity. The carrier transition with its axial sidebands (left). A high resolution scan of $S_{1/2}$ - $D_{5/2}$ carrier transition (right).

IV. CONCLUSIONS

We designed and assembled the two-stage experimental setup for the ECDL laser linewidth narrowing, that incorporate the phase-lock onto an optical frequency comb and afterwards suppression of the frequency noise of the laser with the high-finesse optical cavity. We experimentally verified the linewidth suppression by the spectroscopy on quadrupole transition of the trapped and cooled calcium ion. The result indicates that using this method we achieved the expected suppression of the laser frequency noise and thus, the carrier transition and its axial sidebands have been observed. For many experiments of quantum optics and mechanics this result seems to be sufficient.

ACKNOWLEDGMENT

The authors wish to express thanks for support to the Czech Sciences Foundation, project GB14- 36681G.The support also came from RVO:68081731 and from Ministry of Education, Youth and Sports of the Czech Republic, project no. LO1212. Some of the experimental parts have been funded by Technology Agencey of the Czech Republic, project no. TH01011254. This work was partially supported by European Commission and Ministry of the Education, Youth and Sports of the Czech Republic, project no. CZ.1.05/2.1.00/01.0017.

REFERENCES

[1] W. Demtroder, Laser Spectroscopy, Basic concepts and Instrumentation, Third Edition, Springer (2003)

[2] High power Amplified lasers. (2016). 11th ed. [ebook] Munich: Toptica, p.5.Available at:http://www.toptica.com/fileadmin/Editors English/11 brochures_datasheets/toptica_BR_High_Power.pdf [Accessed 21 Oct. 2016].

[3] Kirchmair, G.: Frequency stabilization of a Titanium-Sapphire laser for preci-sion spectroscopy on Calcium ions, Dissertation. 2006

[4] Drever, P. W. R., Hall, L. J., Kowalski, V. F.: Laser Phase and Frequency Stabilization using an optical Resonator. Appl. Phys. 1983, B 31, 97.

[5] Crick, D. R., Donnellan, S., Segal, D. M., Thompson, R. C.: Magnetically induced electron shelving in a trapped Ca+ion. Physical Review, A, 81(5).

Study on the effect of ULE rings on the vibration sensitivity of horizontal ultra-stable optical cavities

G. Xu[1,2], L. Zhang[1,3], L. Chen[1,3], D. Jiao[1,3], J. Liu[1] , C. Jiang[1,3], X. Zhang[1,3], Q. Zang[1], X. Wang[1], R. Dong[1,3], and Tao Liu[1, *]

[1] National Time Service Center, Chinese Academy of Science, Xi'an , China
[2] School of Mechanical Engineering, Northwestern Polytechnical University, Xi'an , China
[3] Graduate University of Chinese Academy of Science, Beijing, China
E-mail: xuguanjun@ntsc.ac.cn, *taoliu@ntsc.ac.cn

***Abstract*—The mass vibration sensitivities are calculated by using FEA under a variety of variables including cavity's length and supporting position. The calculation results show that the effect of ULE rings on the vibration sensitivity is greater with increasing the cavity's length in the case of other variables unchanged. For longer cavities, as the distance between supporting position and ULE rings increases, the length variation induced by ULE rings is obvious, eventually leading to change the position of zero vibration sensitivity. In conclusion, the analysis results about the effect of ULE rings on the vibration sensitivity in this paper are helpful to optimization design of vibration sensitivity of horizontal ultra-stable optical reference cavities, specifically longer and thinner optical reference cavities.**

Keywords—optical clocks; ultra-stable optical cavities; thermal noise; ULE rings.

I. INTRODUCTION

The state-of-the-art narrow linewidth laser plays an important role in many domains, such as optical atomic clocks, high-precision laser spectroscopy, gravitational wave detection and tests of fundamental physics. The ultra-stable optical reference cavity is a core component for the state-of - the-art narrow linewidth laser. The stability of the ultra-narrow linewidth laser mainly depends on the stability of optical length of ultra-stable optical reference cavity. One of fundamental factors leading to the change of optical reference cavity length is the Brownian thermal noise from their constituents including mirror substrates, mirror coatings and space, in which the biggest contributions are mirror coatings and substrates.

At present, for 698nm ultra-narrow linewidth lasers, to reduce the noise, the most effective way is to increase the space length and use the fused silica (FS) as the mirror substrate with ultra-low expansion glass (ULE) rings, which is used to decrease the effect of the differential thermal expansion between the fused silica substrate and the ULE glass spacer.

However, the use of long cylindrical and heavier cavities makes it much more difficult to reach the required suppression of optical length changes through forces induced by seismic vibrations and through thermal expansion caused by temperature fluctuations.

Under the condition of vibration sensitivity with 10^{-11}/g to realize the 10^{-17} stability at 1 second, this raises a higher demand for the design of vibration sensitivity of the optical reference cavity, and any changes in the cavity's components are likely to lead to design failure.

In this paper, we focus on the effect of ULE rings on the vibration sensitivity of horizontal ultra-stable optical reference cavities.

II. FEA AND MECHANICAL MODEL OF THE VIBRATION SENSITIVITY OF ULTRA-STABLE OPTICAL REFERENCE CAVITIES

The finite element analysis (FEA) is used to calculate the vibration sensitivity of horizontal ultra-stable optical reference cavities. The horizontal ultra-stable optical cavities with ULE rings and no ULE rings are shown in Fig.1. As presented in Fig.1 (a), the spacer is ULE, and two mirrors are FS with lower thermal noise. The shape of the cross section of the horizontal ultra-stable optical reference cavity is a mushroom shape.

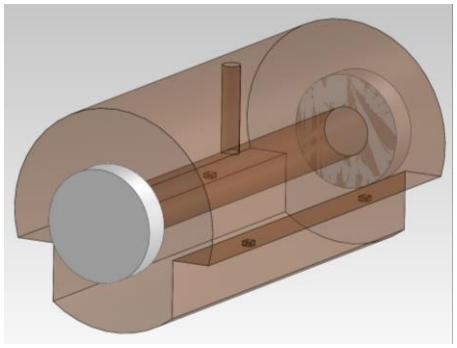

(a) no ULE rings

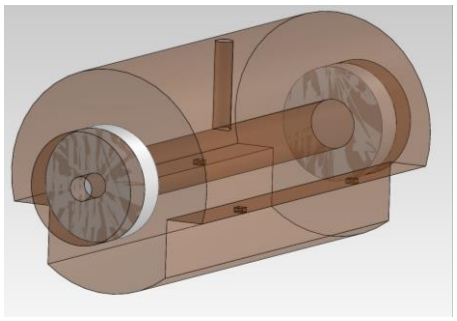

(b) ULE rings

Fig. 1. The horizontal ultra-stable optical cavities with ULE rings and no ULE rings.

The four support pads are symmetrically located on the two shoulders of the horizontal ultra-stable optical reference cavity in Fig.1. To decrease the effect of the differential thermal expansion between the fused silica substrate and the ULE glass spacer, ULE rings are optically contacted with two FS mirrors. Based on the Ref. [9], the dimension of two ULE rings is calculated by FEA .

The one-dimensional mechanical model of the vibration sensitivity of horizontal ultra-stable optical reference cavities is shown in Fig.2.

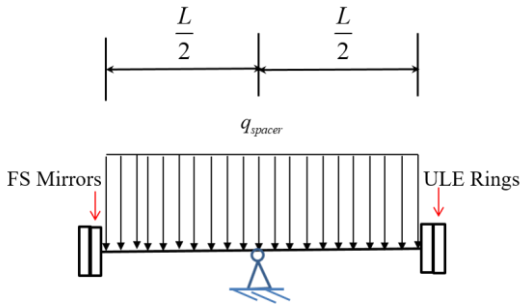

Fig. 2. The one-dimensional mechanical model of the vibration sensitivity of horizontal ultra-stable optical reference cavities.

As shown in Fig.3, the horizontal ultra-stable optical reference cavity is meshed approximately 200000 elements. In order to simplify calculation of the vibration sensitivity of the horizontal ultra-stable optical reference cavity, the type of elements used in the paper is tetrahedron.

The six freedoms of the four support pads are all constrained for FEA calculation. The spacer and two mirrors with two ULE rings are as linear elastic bodies for FEA calculations in this paper.

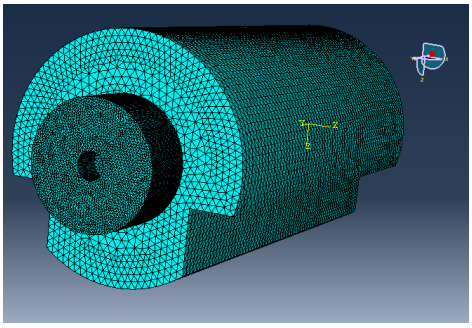

Fig. 3. The FEA meshes of horizontal ultra-stable optical reference cavity.

The materials of horizontal ultra-stable optical reference cavities for calculating vibration sensitivities are shown in Table 1, including density, Poisson ratio and Young modulus of ULE and FS.

Table 1. The materials for FEA of ultra-stable optical reference cavities.

Material	Density(kg/m^3)	Poisson ratio	Young modulus (GPa)
ULE	2210	0.17	67.6
FS	2200	0.16	73

III. ANALYSIS OF CALCULATION RESULTS

The mass vibration sensitivities are calculated by using FEA under a variety of variables including cavity's length, supporting position.

The deformation and contour plot of the horizontal ultra-stable optical reference cavity is shown in Fig.4. The total deformation of the horizontal ultra-stable optical reference cavity is presented in Fig.4 (a). The deformation of the horizontal ultra-stable optical reference cavity along the optical axis is show in Fig.4 (b).

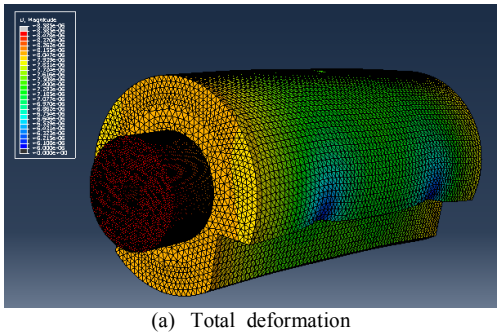

(a) Total deformation

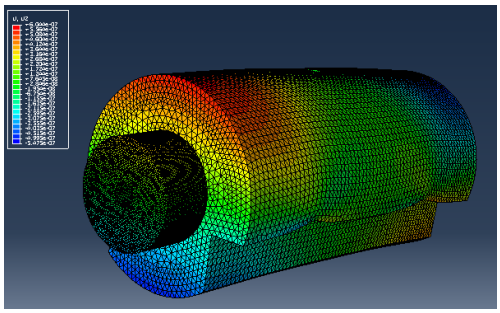

(b) Deformation along optical axis

Fig. 4. The deformation and contour plot of the horizontal ultra-stable optical reference cavity.

The simulation results for the vertical vibration sensitivity of the horizontal ultra-stable optical reference cavities with three lengths as a function of the support points distance from mirror is shown in Fig.5. The FEA calculation results show that the effect of ULE rings on the vibration sensitivity is greater with increasing the ultra-stable optical reference cavity's length in the case of other variables unchanged. For longer horizontal ultra-stable optical reference cavities, as the distance between supporting position and ULE rings increases, the length variation induced by ULE rings is obvious, eventually leading to change the position of zero vibration sensitivity.

In all FEA simulations, the contact plane for supporting cavities is square, and the contact areas 4 mm^2 is used to calculate for conveniently comparing with each other in the three lengths cavities. The diameter of all three spacers is 50 mm. The length of cavity is 100mm. The length of cavity is 200mm. The length of cavity is 300mm.

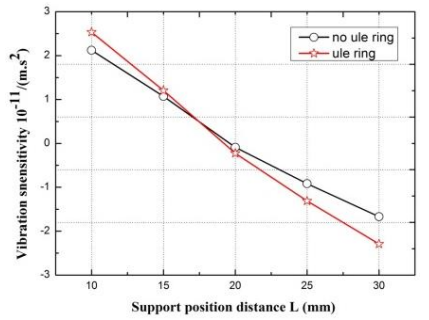

(a) 100mm

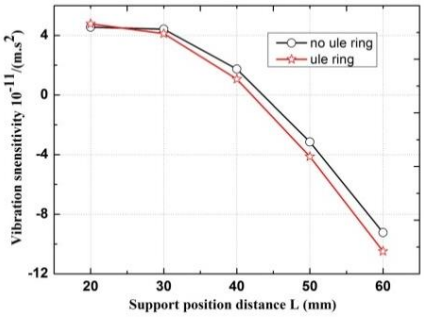

(b) 200mm

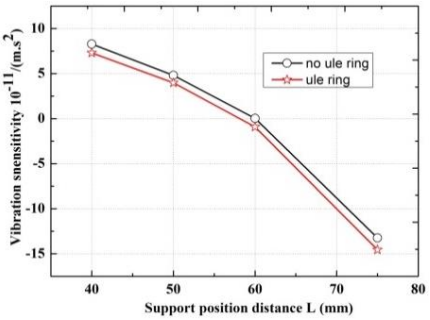

(c) 300mm

Fig. 5. The simulation results for the vertical vibration sensitivity of the three lengths cavities as a function of the support points distance from mirror.

IV. CONCLUSION

The mass vibration sensitivities are calculated by using FEA under a variety of variables including cavity's length and supporting position. The calculation results show that the effect of ULE rings on the vibration sensitivity is greater with increasing the cavity's length in the case of other variables unchanged. For longer cavities, as the distance between supporting position and ULE rings increases, the length variation induced by ULE rings is obvious, eventually leading to change the position of zero vibration sensitivity. In conclusion, the analysis results about the effect of ULE rings on the vibration sensitivity in this paper are helpful to optimization design of vibration sensitivity of horizontal ultra-stable optical reference cavities, specifically longer and thinner optical reference cavities.

ACKNOWLEDGMENT

We would like to acknowledge contributions to this paper from National Natural Science Foundation of China (11403031 and 11603031).

REFERENCES

[1] B.Willke, K. Danzmann, M. Frede, P. King, D. Kracht, P. Kwee, O. Puncken, R. L. Savage, B. Schulz, F. Seifert, C. Veltkamp, S. Wagner, P. Weßels, and L. Winkelmann, "Stabilized lasers for advanced gravitational wave detectors," Class. Quantum Grav. 25, p. 114040, 2008.

[2] J. Millo, D. V. Magalhaes, C. Mandache, Y. L. Coq, E. M. L. English, P. G. Westergaard, J. Lodewyck, S. Bize, P. Lemonde, and G. Santarelli, "Ultrastable lasers based on vibration insensitive cavities," Phys. Rev. A 79, p. 053829, 2009.

[3] Y. Levin, "Internal thermal noise in the LIGO test masses: A direct approach," Phys. Rev. D 57, pp. 659-663, 1998.

[4] T. Kessler, T. Legero, U. Sterr, "Thermal noise in optical cavities revisited," J. Opt. Soc. Am. B 29(1), p. 178, 2012.

[5] K. Numata, A. Kemery, J. Camp, Thermal-noise limit in the frequency stabilization of lasers with rigid cavities, Phys. Rev. Lett., 2004(93):250602

[6] A. D. Ludlow, X. Huang, M. Notcutt, T. Zanon-Willette, S. M. Foreman, M. M. Boyd, S. Blatt, and J. Ye, Compact, thermal-noise-limited optical cavity for diode laser stabilization at 1×10^{-15}, Opt. Lett., 2007(6):641-643

[7] S. A. Webster , M. Oxborrow, S. Pugla, J. Millo, and P. Gill., Thermal-noise-limited optical cavity, Phys. Rev. A., 2008(75):1-6

[8] J. Alnis, A. Matveev, N. Kolachevsky, Th. Udem, and T. W. Hänsch, Subhertz linewidth diode lasers by stabilization to vibrationally and thermally compensated ultralow-expansion glass Fabry-Pérot cavities, Phys. Rev. A.,2008(77):1-9

[9] T. Legero, Thomas Kessler, and Uwe Sterr, Tuning the thermal expansion properties of optical reference cavities with fused silica mirrors, J. Opt. Soc. Am. B., 2010(5):914-919

[10] L. S. Chen, John L. Hall, Jun Ye, Tao Yang, Erjun Zang, and Tianchu Li., Vibration-induced elastic deformation of Fabry-Perot cavities, Phys. Rev. A., 2006 (74):1-13

[11] T. Nazarova, F. Riehle, U. Sterr, Vibration-insensitive reference cavity for an ultra-narrow-linewidth laser, Appl. Phys. B., 2006 (83): 531-536

The compact setup for laser cooling and high-resolution spectroscopy with cold $^{40}Ca^{+}$ ions

Ondřej Číp, Adam Lešundák,Tuan M. Pham,
Václav Hucl, Martin Čížek, Jan Hrabina,
Šimon Řeřucha, Josef Lazar
Institute of Scientific Instruments of the CAS, Brno
Czech Republic
ocip@isibrno.cz

Petr Obšil, Radim Filip, Lukáš Slodička
Department of Optics
Palacky University of Olomouc
Olomouc, Czech Republic

***Abstract*—We report on the working scheme of the experimental infrastructure for $^{40}Ca^{+}$ ion trapping and laser cooling. The important effort is to put on the excitation lasers control and their referencing to an optical frequency comb disciplined by an active H-maser. The principle of other instruments control necessary for the trapping and laser cooling setup is presented as well. The work also reports the records of the spectroscopic measurements of the ion multi-level electronic structure i.e. the occurrence of the dark resonances in the fluorescence signal on the dipole transition and the forbidden transition spectrum of the trapped single $^{40}Ca^{+}$ ion.**

Keywords— laser cooling, cold ions, atomic optical clocks

I. INTRODUCTION

Trends in ultimate optical frequency standards led to joined laboratory of the Institute of Scientific Instruments Brno and the Palacky University Olomouc (both Czech Republic) where a research of quantum mechanical interactions of trapped ions with coherent laser lights is realized. The compact research infrastructure uses $^{40}Ca^{+}$ single ion and ion Coulomb crystals for experiments of quantum mechanics and spectroscopy in joined laboratory in Brno. For the metrology of optical frequencies where stable wavelength and narrow linewidth of interrogation lasers is required for getting ultimate stability (the clock laser mainly), an external optical reference is necessary for frequency stabilization of these lasers.

II. TRANSITION LEVELS OF CALCIUM ION

The singly charged Ca^{+} ion has an electronic configuration which is similar to Argon with an additional valence electron [1]. Transitions $S \leftrightarrow P$ and $P \leftrightarrow D$, appropriate wavelengths and transition lifetimes are listed in table [2, 3]:

transition	$S_{1/2} \leftrightarrow P_{1/2}$	$S_{1/2} \leftrightarrow P_{3/2}$	$P_{1/2} \leftrightarrow D_{3/2}$	$P_{3/2} \leftrightarrow D_{3/2}$	$P_{3/2} \leftrightarrow D_{5/2}$
lifetime	7.7 ns	7.4 ns	94.3 ns	901 ns	101 ns
λ/nm	396.847	393.366	866.214	849.802	854.209

The transition level scheme of an isotope 40 of the Ca^{+} ion is graphically shown in "Fig. 1". The Doppler cooling is based on the excitation the transition $S_{1/2} \leftrightarrow P_{1/2}$.

If the metastable level $D_{3/2}$ is reached then the repumping $P_{1/2} \leftrightarrow D_{3/2}$ is provided.

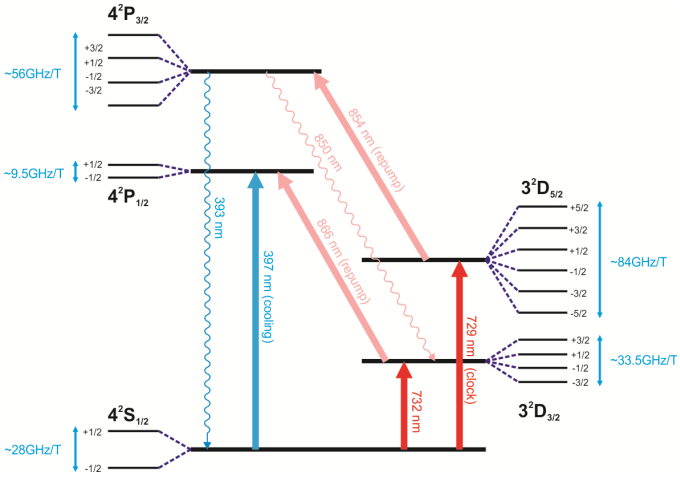

Fig. 1. Transition level scheme of $^{40}Ca^{+}$ ion.

$S_{1/2}$ level is connected to the $D_{3/2}$ and $D_{5/2}$ levels by electric-quadrupole transitions. The lifetime of the D levels is roughly 1 s as is presented in the table:

transition	$S_{1/2} \leftrightarrow D_{3/2}$	$S_{1/2} \leftrightarrow D_{5/2}$
lifetime	1.080 s	1.045 s
λ/nm	732.389	729.147

All of the relevant transitions are accessible by semiconductor lasers. We use the electric-quadrupole transition $S_{1/2} \leftrightarrow D_{5/2}$ for experiments with the optical clocks and quantum processing.

III. FREQUENCY CONTROL OF EXCITATION LASERS

Semiconductor lasers in the extended cavity configuration deal very broad mode-hop free tuning range (tens of GHz) and relatively good linewidth (about hundreds of kHz). On the other hand, the accuracy and stability of the optical frequencies for the excitation required transitions is needed.

"Fig. 2" presents optical frequency control of 397 nm, 866 nm, 729 nm and 854 nm excitation lasers by the optical frequency comb disciplined by the active H-maser. The set of

the phase locked loops (PLL) based on the beat note measurement (between the controlled laser and the comb) is used.

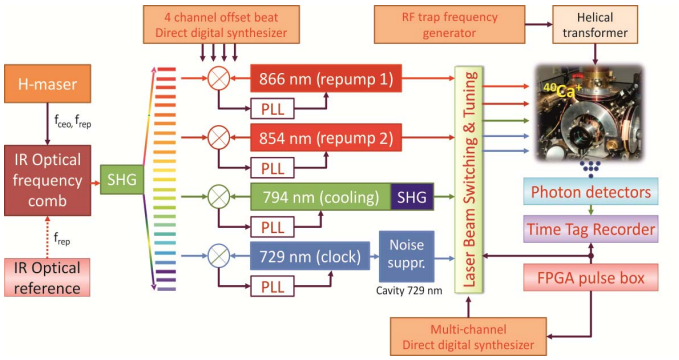

Fig. 2. Schematic diagram of the frequency control of the $^{40}Ca^+$ transition excitation lasers where the optical frequency comb is used as an optical reference. The beat-notes of particular lasers are used as the control values for the appropriate phase locked loops (PLL) and servo-loop controllers locking laser frequencies to the comb.

Laser wavelengths are monitored continuously by the wavelength meter for coarse control of their frequencies. If they agree, they are locked on a selected tooth of the optical frequency comb. If PLL is out, then the wavelength is controlled by the wavelength meter.

The design of the laser frequency control and the control of all parts of the setup respects requirements on the sufficient versatility when different experiments are planned. Therefore the instrumentation of our compact setup is scalable and based on unified communication over the data network, see "Fig. 3."

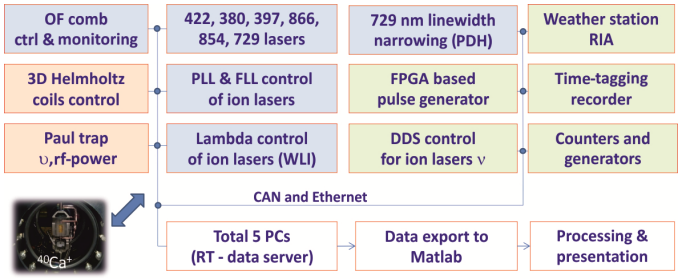

Fig. 3. Control system of the infrastructure with $^{40}Ca^+$ cold ions. The individual instruments are sorted by their function and interconnected by communication network bus CAN and Ethernet together.

We use the Controller Area Network communication bus for the time critical synchronization of variety of instruments. The Ethernet network is used for a fast transfer of large portion of data. This versatile communication scheme provides easy way to re-configure for variety of experiments. The control of the parameters and visualization is done with LabVIEW environment.

IV. Experimental Setup and Results

The compact setup was built from 2015. It uses the Innsbruck style linear trap with blade quadrupole electrodes and two hollow axial electrodes for collecting the fluorescence from ions along *z*-axis. The first trapped and laser cooled ion has been observed in August 2015. Examples of snapshots of cold ions in the trap are shown in "Fig. 4".

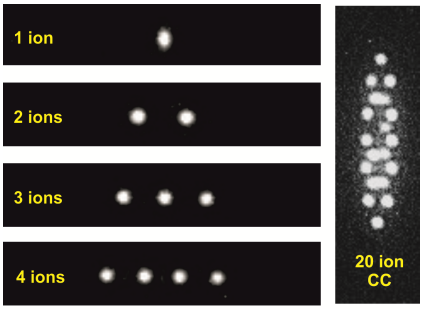

Fig. 4. Snapshots of ions: single ion and linear Coulomb crystals (left), 3D Coulomb crystal (right).

Experiments with "dark state" measured by λ-scheme $S_{1/2}\leftrightarrow P_{1/2}\leftrightarrow D_{3/2}$ excitation followed in 2016, see "Fig. 5".

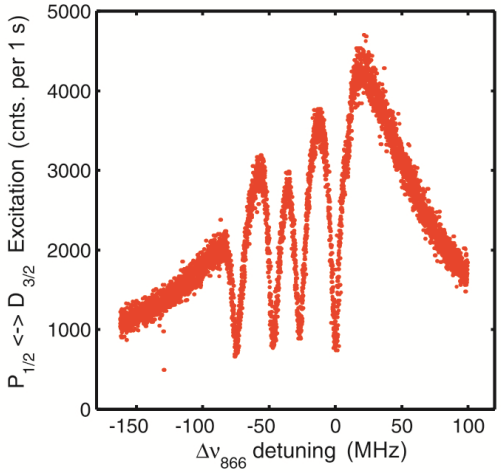

Fig. 5. Coherent population trapping in superpositions of $S_{1/2} \leftrightarrow D_{3/2}$ levels.

The programmable pulse generator based on the field programmable gate arrays has been used for spectroscopy on the $S_{1/2}\leftrightarrow D_{5/2}$ transition in February 2018, see "Fig. 6".

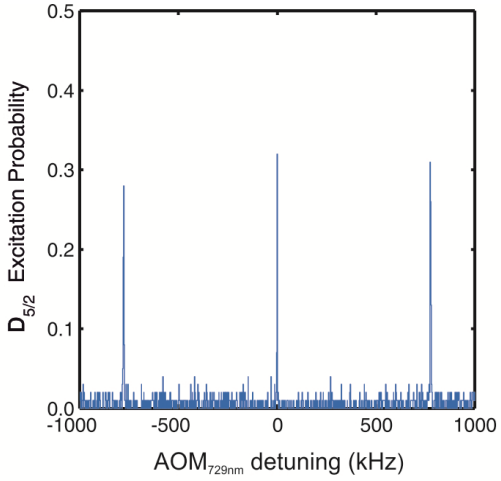

Fig. 6. Spectrum of $S_{1/2}\leftrightarrow D_{5/2}$ transition. It includes two motional axial-mode sidebands at frequencies ± 800 kHz. The carrier of transition is in the middle.

The ground state cooling of an axial motion of a single trapped $^{40}Ca^{+}$ ion has been demonstrated in March 2018, see "Fig 7."

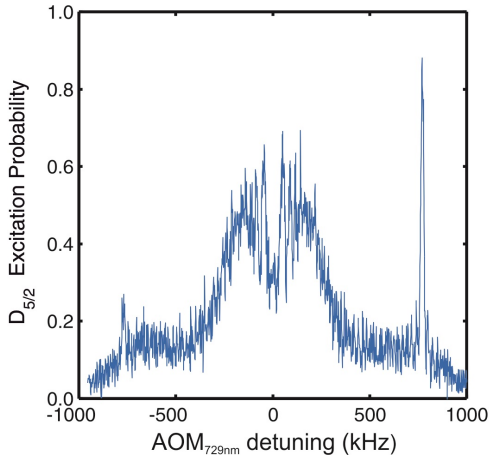

Fig. 7. An example of the spectrum of the $S_{1/2} \leftrightarrow D_{5/2}$ transition for ground state cooling of the ion axial motion. The red sideband (on the -800 kHz) is disappeared as the result of the sideband cooling process.

V. CONCLUSION

The presented setup of trapping and laser cooling of Calcium ion has been put into operation. The Doppler cooling, side-band cooling and control of the thermal state of the single ion are routinely used. A chain or 3D structure Coulomb crystal can be formed and used for quantum information processing, quantum mechanics or high-resolution spectroscopy for optical atomic clocks operation thanks to the linear configuration of the radiofrequency trap.

ACKNOWLEDGMENT

The authors wish to express thanks for support to the Czech Sciences Foundation, project GB14-36681G and to the Technology Agency of the Czech Republic, project TH01011254. The support also came from RVO:68081731 and from Ministry of Education, Youth and Sports of the Czech Republic, project no. LO1212. This work was partially supported by European Commission and Ministry of Education, Youth and Sports of the Czech Republic, project no. CZ.1.05/2.1.00/01.0017.

REFERENCES

[1] A. D. Ludlow, M. M. Boyd, J. Ye, E. Peik, and P. O. Schmidt, "Optical atomic clocks," Rev. Mod. Phys., vol. 87, pp. 637–701, 2015.

[2] C. Roos, "Controlling the quantum state of trapped ions," PhD thesis, Leopold-Franzens-Universitat Innsbruck, 2000.

[3] M. Block, P. Seibert, O. Rehm, and G. Werth, "$3D_{5/2}$ lifetime in laser cooled Ca^{+}: Influence of cooling laser power," Eur. Phys. J. D 7(3), 461, 1999.

Active Isolator Development of Ultra-stable Narrow Linewidth Laser of Atomic Clock

Min Xiong, Qing Li,Lei Liu
School of Astronautics
Northwestern Polytechnical University
Xi'an, China
leiliu@nwpu.edu.cn

Guanjun Xu, Qicheng Shi,Tao Liu
National Time Service Center Chinese Academy of Sciences
Xi'an, China
xuguanjun@ntsc.ac.cn

***Abstract*—In order to meet the g-level vibration isolation requirement of the narrow linewidth laser, which is one key component in high-precision time-frequency scientific experiments, a high-performance active vibration isolation system needs to be designed. This paper synthetically adopts the magnetic suspension based active vibration isolation technology, and propose a new active vibration isolation method. The active vibration isolation as well as the position and attitude control are realized by eight voice coil actuators between the ultra-quiet platform and the base. In this paper, the design of the vibration isolation platform, dynamics model, dual-loop coupling control scheme and simulation results are provided sequentially. The simulation results show that after the active vibration isolation control, the 4mg micro-vibration level in the space station is attenuated to 5g, and the vibration isolation capability is 58dB, which meets the requirements of narrow linewidth laser isolation.**

***Index Terms*—Active vibration isolation; Voice coil actuator; ultra-quiet; narrow linewidth laser.**

I. Introduction

China will launch a space station system in 2020 and carry out high-precision time-frequency scientific experiments in space applications. The narrow linewidth laser, the key component of this experiment, is extremely sensitive to micro-vibration of the space station and requires g micro-vibration level. From the result of micro-vibration environment testing in the International Space Station(ISS), due to a variety of disturbances, the micro-vibration level can reach mg. To achieve an ultra-quiet micro-vibration environment, a high-performance active vibration isolation system needs to be developed for the narrow linewidth laser. Compared with the required acceleration level of ISS [1], the requirements of the narrow linewidth laser are more stringent at low frequencies. Due to the limitation of the passive vibration isolation [2], space stations less rarely adopt passive vibration isolation.

Since 1990s, to meet the ultra-quiet environment of the scientific experimental platform requirements, various large-scale active vibration isolation systems, such as STABLE, g-LIMIT, MIM, and ARIS, have been successfully developed by the aerospace major countries including the United States and Canada. STABLE, was flown into space in1995, isolates by non-contact electromagnetic Lorentz force actuators and dual loop control system with acceleration and displacement feedback. STABLE can effectively attenuate vibrations in the high-frequency regime, which can attenuate up to 50dB, but the attenuation effect of low-frequency vibration is lower than 20dB [3]. g-LIMIT is an enhanced STABLE system that attenuates vibrations from 20,000g to 3.5g, achieving 60 dB vibration attenuation [4]. MIM was developed by the Canadian Space Agency(CSA) and uses magnetic suspension active vibration isolation technology. MIM can isolate vibrations above 0.01Hz [5]. What's more, an improved version, MIM2, can reduce vibrations from 2500g to 50g and achieve 40dB vibration attenuation. ARIS is a complete cabinet-based active vibration isolation device. It is mainly used to isolate vibrations below 1000Hz, and is most sensitive to the range of 20-200 Hz [6].

With the launch of Chinese space station in 2020, more and more scientific experiments need to be carried out in the Chinese space station. Aiming at the narrow linewidth laser, this paper develops the zero-stiffness active vibration isolation technology by using eight voice coil actuators, which covers the 0.5-100Hz regime vibration isolation. The simulation results show that the vibration isolation attenuation is better than 60dB, the output of the vibration isolation system can reach 5g level, which can suppress low-frequency vibrations caused by flexible cables.

II. Isolator Design Specifications

In order to effectively attenuate vibrations of the space station, this paper comprehensively uses the magnetic levitation technology and the active vibration isolation technology. Eight voice coil actuators mechanically connect the ultra-quiet platform to the base. What's more, they can generate the force to isolate vibration and control the relative position and attitude, and the designed active isolation range is 0.01 50Hz. In order to realize 60dB vibration attenuation of the low-frequency disturbances, the active vibration takes the robust H controller. A proportional-integral-derivative (PID) controller is implemented for position control to achieve 0.01 Hz low-bandwidth stability control, which can ensure that the distance between the ultra-quiet platform and the mounting base is in safety range (1cm) and the ultra-quiet platform has the same attitude and orbital motion as the space station. The overall design of the isolator is shown in Fig.1.

978-1-5386-5620-4/18/$31.00 ©2018 IEEE

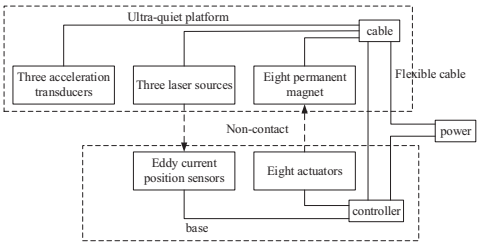

Fig. 1. Overall design plan of vibration isolator

A. Design of the isolator platform

The configuration of the ultra-quiet platform is cuboid, and the base is an outer frame. The ultra-quiet platform is entirely located inside the base frame. The layout of the eight voice coil actuators is shown in Fig.2 and Fig.3. Two voice coil actuators are arranged on the left and right sides of the ultra-quiet platform respectively, and four voice coil actuators are arranged on the lower surface. What's more, the actuators are all connected to the outer frame mounting base. The acting direction of the actuators is along the three coordinate axes of the ultra-quiet platform body coordinate, as a result, each voice coil actuator's leg is parallel or orthogonal with the others. This way of installation decouples the voice coil legs. Thus, the control algorithm design has virtue of briefness and efficiency. Four actuators on each side generate control torque about the z-axis and four actuators on the bottom side generate control torque about the x-axis and y-axis. When the actuator is changed, only the length of the leg is controlled, and the rotation angle is not controlled.

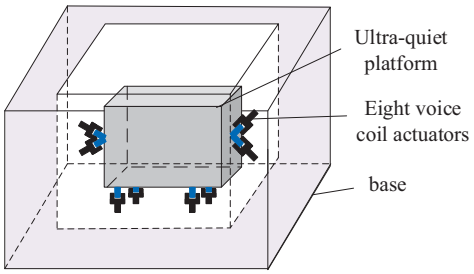

Fig. 2. Actuator layout side view

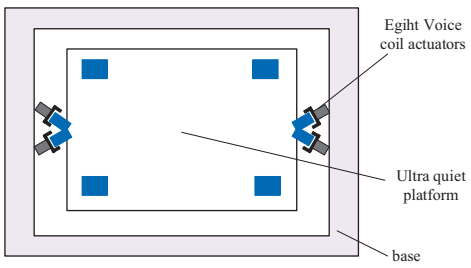

Fig. 3. Actuator layout top view

B. Measurement scheme design

The acceleration of the ultra-quiet platform is measured by three high-precision three-axial acceleration transducers. The relative position and attitude between the ultra-quiet platform and the mounting base is accurately measured by six eddy current position transducers. Six eddy current transducers are arranged on six different vertices of the ultra-quiet platform. Three high-precision three-axial acceleration transducers are respectively arranged on the three vertices on the left side of the ultra-quiet platform, and the three axes of each acceleration sensor are all along the body axis direction of the ultra-quiet platform, as shown in Fig.4. Such a layout is conducive to achieving high-precision measurement of attitude and position of the ultra-quiet platform relative to a mounting base, and measurement of acceleration and angular acceleration of an ultra-quiet platform.

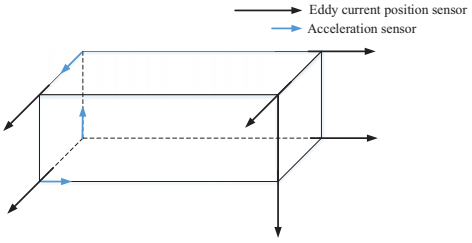

Fig. 4. Sensor measurement direction

1) Calculation of acceleration and angular acceleration: Accelerations is calculated according to the base point method:

$$a_p = a_o + \alpha + \omega \times (\omega \times r) \tag{1}$$

where a_P is the absolute acceleration of the point P, ω is the platform angular acceleration, ω is the angular velocity of the platform, and r is the displacement of point P relative to the platform centroid. Because of the low angular velocity of the ultra-quiet platform, $\omega\times(\omega\times r)$ can be ignored as a second-order small quantity. Therefore, the above formula is simplified as:

$$a_p = a_o + \alpha \times r \tag{2}$$

For the three acceleration transducers, three vector equations, like formula (1), can be obtained. After the scalarization, 9 equations are obtained, including 3 unknown center of mass linear accelerations and 3 angular accelerations. And the 9 equations can be solved by least square method.

2) Calculation of position and attitude: At the nominal position, the position of the ultra-quiet platform relative to the mounting base is known.Six measurement results provide six constraint equations for the positional relationship between the platform and the mounting base. Therefore, according to the geometric relationship, the coordinates of the ultra-quiet platform relative to the base can be determined, that is, three line positions and three angular positions.

C. Action plan design

The non-contact actuator between the ultra-quiet platform and the mounting base uses a voice coil actuator. The installation position is shown in Fig.3. It has the advantages of simple structure and flexible control. The basic structure of the voice coil actuator is shown in Fig.5, which is mainly composed of a base end, a loading end, a permanent magnet and coils. When the coils are electrified, the permanent magnet moves axially under the magnetic field generated by the electrified coils, thereby driving the loading end to move. The axial displacement can be changed by controlling the direction and strength of the coil current.

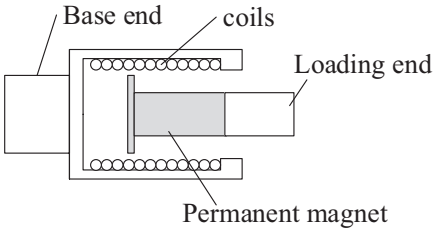

Fig. 5. Voice coil actuator diagram

The voice coil actuator mainly includes the structure, driving force, response time, driving force resolution, driving displacement and a magnetic field gradient of the permanent magnet. In addition, the voltage amplifier and the signal modulator also need to be configured.

III. Dynamic Modeling of Vibration Isolation Platform

The actual model of the voice coil actuator is simplified. The mathematical model of the voice coil actuator is established using the voltage balance equation of the actuator and the force balance equation of the moving iron end [6].

1) Voltage balance equation of the actuator: In the voice coil actuator, when the coils are powered by DC, the current i in the coils will generate a magnetic field force, which acts on the moving iron end to move the leg relative to the coil. At the same time, a back electromotive force e is generated. The size can be expressed as

$$e = Blv \tag{3}$$

where *v* is the movement speed of the leg relative to the coil, and *Bl* is the constant, depending on the size and material of the actuator.

Assume that the armature terminal voltage of the voice coil actuator is u_a, the armature circuit resistance is *R*, and the inductance is *L*, then the voltage equation is obtained as

$$u_a = e + iR + L\frac{di}{dt} \tag{4}$$

2) Force balance equation of legs: When the coils are electrified, its electromagnetic force acts on the legs and drives it to move. Assuming F_e is the electromagnetic force, it can be expressed as

$$F_e = Bli \tag{5}$$

According to the principle of the voice coil motor, the electromagnetic force overcomes the inertia force of the mover, and the dynamic equation is

$$F_e = m\frac{dv}{dt} \tag{6}$$

where *Bl* is the line speed of the leg. According to the formula above, the model block diagram for setting up the voice coil actuator is as follows:

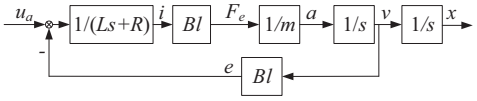

Fig. 6. Voice coil actuator model

IV. Control Plan Design

The double-loop decoupling control scheme is adopted. After the space station goes into orbit, it is unlocked first, and then the position loop control is started so that the ultra-quiet platform reaches the equilibrium state, and then the acceleration loop is activated for active vibration isolation, of which the control frequency band is 0.01 to 50 Hz. The double-loop works at the same time, which can not only perform high-performance active vibration isolation on the ultra-quiet platform, but also control the displacement precisely, maintaining the nominal position to avoid possible collisions. The structure of the control system is shown in Fig. 7.

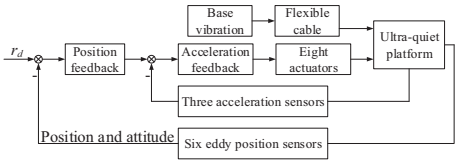

Fig. 7. Double loop control system structure diagram

Acceleration feedback has a significant effect on the suppression resonance peaks. The active control, by position feedback, improves the static stiffness of the base and avoid the collision between the ultra-quiet platform and the space station during vibration isolation.

A. Acceleration loop control

Acceleration loop control adopts robust H_∞ control to realize the super-static environment, and selects the performance weight function w_p and control function w_2.

$$w_p = \frac{0.6667s + 6283}{s + 0.6283} \tag{7}$$

Solve the H_∞ mixed sensitivity problem and get the reduced order H_∞ controller K of the acceleration loop as:

$$K = \frac{1.503 \cdot 10^5}{7.593s + 4.771} \tag{8}$$

B. Position loop PID control

The position loop adopts PID controller, and the solution obtained is

$$K = 1 + 10s + \frac{1}{10s} \tag{9}$$

V. Simulation Result

According to the model and control scheme of the voice coil actuators and platform, the simulation is carried out. It is assumed that the acceleration disturbance of the base is white Gaussian noise. If the ultra-quiet platform does not have any vibration isolation system, the ultra-quiet platform and the base are connected by an umbilical cable. Under the base disturbance of the base, the platform drifts a total of 8cm in 100s, as shown in Fig. 8.

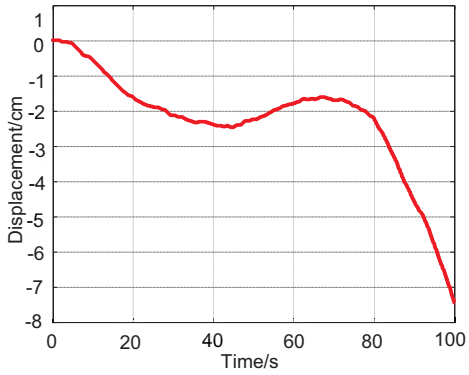

Fig. 8. Displacement of the ultra-quiet platform suspension without active vibration isolation

After double-loop active control, the displacement response of the ultra-quiet platform under disturbance is shown in Fig. 9.

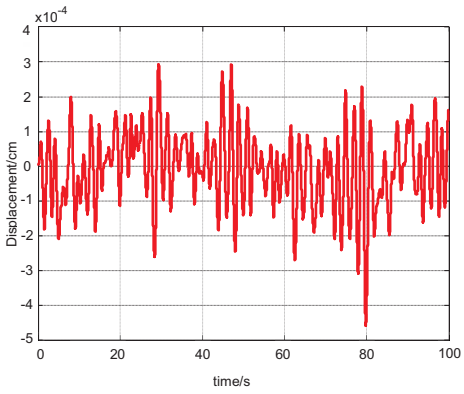

Fig. 9. Active vibration displacement of ultra-quiet platform

It can be seen from the above simulation results that the displacement response is limited to the magnitude of 10m, which indicates that the position loop controller has a good vibration isolation effect, and the position and attitude of the ultra-quiet platform position loop can be maintained.

Assume that the disturbance of the space station is 4mg and carry out the simulation. First, the suspension of the ultra-quiet platform without active vibration isolation is simulated. The result is shown in Fig. 10. The micro-vibration level of the space station is at mg. After the suspension passive vibration isolation, the acceleration of the ultra-quiet platform is reduced by an order of magnitude. It can be seen that the passive vibration isolation does have the vibration isolation effect, but it still cannot meet the requirements of the g level, so it is necessary to design an active vibration isolation system.

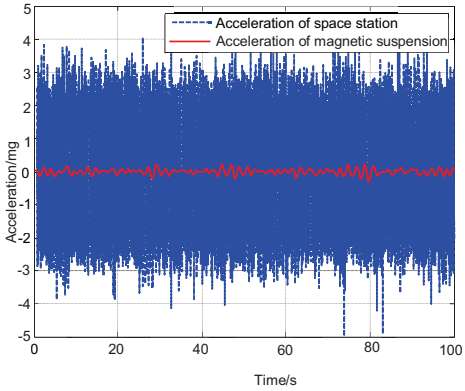

Fig. 10. The suspension passive isolation result

After the active vibration isolation, the comparison of the acceleration of the active and passive vibration isolation of the ultra-quiet platform is shown in Fig.11.

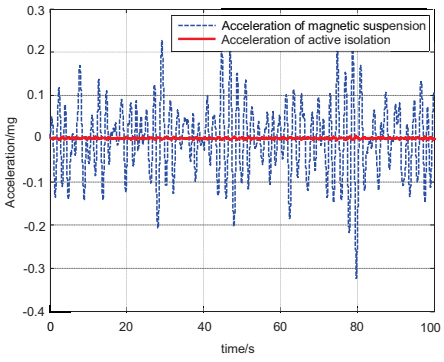

Fig. 11. Comparison of the results of active vibration isolation and suspension passive vibration isolation

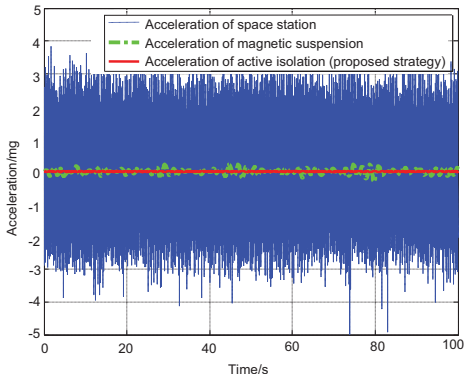

Fig. 12. Results of two isolation methods

As can be seen from Fig. 10-12, the initial acceleration of the space station is 4mg, after the active vibration isolation control, the residual micro-vibration of the ultra-quiet platform is 5g, and the vibration isolation capability reaches 58dB. Under the action of active vibration isolation, the acceleration amplitude of the ultra-quiet platform is reduced from mg to g level, and the results of vibration isolation performance are shown in Table 1. Compared with the acceleration responses of the passive vibration isolation, the performance of the ultra-quiet platform is greatly improved under the active vibration isolation. The simulation results show that the active isolator can effectively suppress the disturbance.

TABLE I
COMPARISON OF THE RESULTS BEFORE AND AFTER VIBRATION ISOLATION

	Acceleration peak (mg)	Vibration isolation performance (dB)
Space Station Disturbance	4	
Suspension passive vibration isolation	0.3	22.5
Proposed active vibration isolation	0.005	58.0

VI. CONCLUSION

In order to realize the ultra-quiet micro-vibration environment, it is necessary to develop a high-performance active vibration isolation subsystem for the narrow-linewidth laser, one key component in high-precision time-frequency scientific experiments. This component needs to meet the g micro-vibration level. In this paper, the design of the vibration isolation platform is introduced in detail. Dynamic modeling and decoupling control design is introduced in sequence. Then, a simulation experiment is conducted. The results show that the designed vibration isolation platform can effectively suppress the disturbance after active control, and the vibration isolation capability can reach 58dB. Compared with the vibration isolation devices of other countries, it can meet the vibration isolation requirements of the narrow linewidth laser. In the next step, the vibration isolation platform will be constructed to verify the designed performance of the isolator.

ACKNOWLEDGMENT

This work is supported by the National Natural Science Foundation of China (11603031,51675430 and 11403031).

REFERENCES

[1] Whorton, Mark. "Robust Control for Microgravity Vibration Isolation System." Journal of Spacecraft Rockets 1(2002):256-261 vol.1.

[2] Grodsinsky, Carlos M., and M. S. Whorton. "Survey of Active Vibration Isolation Systems for Microgravity Applications." Journal of Spacecraft Rockets 105.s 1-2(2000):146-152.

[3] Edberg Donald, Boucher Robert, Nurre Gerald, Whorton Mark. "Performance assessment of the STABLE Microgravity Vibration Isolation Flight Demonstration." 38th Structures, Structural Dynamics, and Materials Conference. 1997.

[4] Jackson, M., Y. Kim, and M. Whorton. "Design and Analysis of the g-LIMIT Baseline Vibration Isolation Control System." AIAA Guidance, Navigation, and Control Conference and Exhibit 2002.

[5] AIAA. "The Canadian Space Agency Microgravity Sciences Program Overview." Aiaa Journal (2000).

[6] DelBasso Steve, Laible Michael, O'Keefe Edmund, A.Scheer Steven. "International space station microgravity analytical model correlation and update." (2003).

[7] Chen Qiming, Li Liyi, Wang Mingyi, Pei Le. "The precise modeling and active disturbance rejection control of voice coil motor in high precision motion control system." Applied Mathematical Modelling 39.19(2015):5936-5948.

EFTF 2018 Author Index

A

Abgrall, Michel 208
Ablewski, Piotr 322, 326, 352, 356
Affolderbach, Christoph 75
Amy-Klein, Anne 285
Antcev, Ivan 101, 105
Arnold, Aidan S. 61
Arpesi, Pier Giorgio 72
Atutov, Sergei 83

B

Bagaev, Sergei 344
Bagayev, Sergei 83
Bai, Shanshan 197
Baird, Patrick E. G. 312
Ballandras, Sylvain 24
Barantsev, Konstantin 87
Basalaev, Maxim Yu. 348
Bauch, Andreas 167
Baynes, Fred 312
Baynham, Charles F. A. 312
Belfi, Jacopo 72
Belloni, Marco 72
Beloy, Kyle 322, 356
Bermbach, Rainer 138
Bertrand, Bruno 208
Beverini, Nicolo 119
Bilicki, Sławomir 322, 326, 356
Blinov, Igor 257
Bober, Marcin 322, 326, 352, 356
Bogacki, Wojbor 285
Bogdanov, Petr 181
Bogoslovsky, Sergey 101, 105
Boiko, Alexander 257
Bonfanti, Andrea Giovanni 122
Bongs, Kai 312
Bookjans, Eva 285
Borisenko, Alexander 344, 377
Borkowski, Mateusz 326
Bouchand, Romain 318
Boven, Paul 213
Boy, Jean-Jacques 37
Brazhnikov, Denis 83
Brown, Roger 322, 356

C

Cai, Haiwen 175, 178
Calonico, Davide 285
Calosso, Claudio Eligio 41, 72, 80
Campanella, Mauro 285
Camps, Adriano 155
Capdevila, Santiago 75
Carelli, Giorgio 119
Cash, Peter 65
Cerretto, Giancarlo 188
Chaloupka, Zdenek 192
Chang, Hong 374
Chapellier, Paul 20
Chen, Dijun 178
Chen, Junping 296
Chen, L. 389
Chen, Xing 50
Cheng, Nan 178
Chepurov, Sergei 344
Ciampini, D. 119
Cibiel, Gilles 37
Číp, Ondřej 285, 293, 361, 386, 392
Ciuryło, Roman 322, 326, 356
Čížek, Martin 293, 361, 386, 392
Clement, Marta 13, 17, 126
Constantin, Florin Lucian 330
Costa, Roberto 188
Crisci, Massimo 192
Czubla, Albin 231

D

De Clercq, Emeric 98
Debogovic, Tomislav 75
Defraigne, Pascale 208, 270, 276
Deng, Xue 290
deRijk, Emile 75
Derkach, Mikhail 105
Desruelle, Bruno 285
Di Virgilio, Angela 119
Domnin, Yury 53
Dong, Ruifang 290, 389
Dong, Shaowu 170, 197, 217
Donley, Elizabeth A. 348

Dragonja, Uros 231
Droz, Fabien 91
Druzhin, Andrei 181
Dubé, Pierre 315
Dubois, Benoit 41
Dulmet, Bernard 20

E

Ebenhag, Sven-Christian 253
Elvin, Rachel 61
Ender, Horst 167
Esnault, François-Xavier 37
Exertier, Pierre 249

F

Fan, Songtao 341
Fasano, Robert 322, 356
Felmetsger, Valeriy 13
Feng, Zitong 175, 178
Filip, Radim 392
Fluhr, Christophe 41
Formichella, Valerio 245
Fuso, F. 119

G

Galardini, Alessandro 285
Galleani, Lorenzo 281
Ganesan, Adarsh 6
Gao, Jing 290
Garbin Manfredini, Esteban 155
García, Trinidad 285
Garrido Alzar, Carlos L. 56
Giacomelli, Umberto 119
Gill, Patrick 312
Gioia, Marina 72
Giordano, Vincent 41
Giorgi, Gabriele 240
Giunta, Michele 318
Gobet, Jean 91
Godone, Aldo 80
Godun, Rachel M. 312
Goldovsky, Nadya 130
Gozzelino, Michele 72, 80
Granados Alfaro, Ricardo 225
Griffin, Paul F. 61
Guang, Wei 170
Guérandel, Stephane 98
Gui, Youzhen 175, 178
Günther, Christoph 240
Guo, Wenge 338, 341
Guo, Yang 374

H

Hachisu, Hidekazu 322, 356
Haesler, Jacques 91
Hagimoto, Ken 94
Hänsel, Wolfgang 318
Havlis, Ondrej 293, 303
Hedekvist, Per Olof 253
Herique, Alain 225
Hirano, Iku 94
Hoerni, Diane 75
Holzwarth, Ronald 285, 318
Hoth, Gregory W. 61
Hrabina, Jan 293, 361, 392
Hu, Liang 381
Huang, Meng-Zi 56
Hucl, Václav 293, 386, 392
Hula, Miloslav 303
Hwang, Gilgueng 10

I

Iborra, Enrique 13, 17, 126
Ido, Tetsuya 322, 356
Ignatovich, Stepan 83
Ikegami, Takeshi 94
Il'enkov, Roman Ya 364
Imbaud, Joel 37
Imlau, Helmut 167
Iskandar, Zyad 32
Ivanov, Anton 75

J

Jaldehag, Kenneth 159, 263
Jarlemark, Per 159, 263
Jelinek, Michal 293
Jessa, Mieczysław 234
Jian, Bin 315
Jiang, C. 389
Jiang, Haifeng 338, 341

Jiang, Meng 217
Jiao, Dongdong 290, 389
Jones, Jonathan M. 312
Juillard, Jérôme 109, 114

K

Karlen, Sylvain 91
Kasznia, Michał 234
Khabarova, Ksenia 344, 377
King, Steven A. 312
Kitching, John 348
Kolachevsky, Nikolay 344, 377
Kolbe, Martin 303
Kołodziej, Jacek 149, 152, 167
Kosheliaevskii, Nikolai 257
Krehlik, Przemysław 149, 152, 167, 202
Kroese, Bethany 240
Kronjäger, Jochen 285
Krzewick, Will 65
Kubczak, Paweł 234
Kuna, Alexander 308
Kupalova, Olga 53, 257
Kuraptsev, Alexey 369
Kvashnin, Gennady 1
Kvashnin, Nikolai 83

L

Lacaita, Andrea Leonardo 122
Laier English, Elizabeth 285
Langer, Martin 138
Langfelder, Giacomo 122
Lapuh, Rado 231
Laroche, Thierry 24
Laudat, Théo 56
Lautier Gaud, Jean 285
Lavenus, Pierre 10, 20
Lazar, Josef 293, 386, 392
Le Coq, Yann 318
Le Targat, Rodolphe 322, 356
Le Traon, Olivier 10, 20
Le-Coarer, Etienne 225
Lecomte, Steve 91
Lessing, Maurice 285
Lesundak, Adam 386
Lešundák, Adam 392
Leute, Julia 249
Levi, Filippo 72, 80, 188, 285
Lezius, Matthias 318
Li, Qing 395
Li, Wei 170
Lin, Shinn Yan 145
Litvinov, Andrey 87
Liu, Jie 290, 389
Liu, Lei 395
Liu, Tao 290, 389, 395
Lodewyck, Jérôme 322, 356
Ludlow, Andrew 322, 356
Lugovoy, Alexey 344

M

Maccioni, Enrico 119
Machado, Paul 65
Makarov, Anton 83
Margolis, Helen S. 312
Maris Ferreira, Pietro 109, 114
Marra, Cristiano Rocco 122
Marzoli, Nicholas 72
Mazzoni, Tommaso 56
McGilligan, James P. 61
McGrew, William 322, 356
Micalizio, Salvatore 72, 80
Mikel, Bretislav 293
Mileti, Gaetano 75
Minotti, Paolo 122
Mirea, Teona 13, 17, 126
Moreno, William 75
Moron Guerra, Jose 32
Morzyński, Piotr 322, 326, 356
Mostafa, Ali 109, 114
Mura, Alberto 188
Mussi, Giorgio 122

N

Nicolodi, Daniele 322, 356
Nisbet-Jones, Peter B. R. 312
Novoselov, Andrey 1

O

Obšil, Petr 392
Olivares, Jimena 17, 126

Osmyk, Roman 231
Overstolz, Thomas 91
Overstreet, K. Richard 65

P

Panfilo, Gianna 185
Pellaton, Matthieu 75
Petit, Gérard 185, 249, 312
Pham, Tuan Minh 386, 392
Piester, Dirk 167
Pinter, Borut 231
Píriz, Ricardo 155
Pokharel, Alok 37
Poli, Nicola 381
Pollock, James Wesley 348
Popov, Evgeniy 87
Pottie, Paul-Eric 285
Pravdova, Lenka 293, 361
Primakina, Tatiana 181
Prudnikov, Oleg 364

Q

Qu, Lili 197, 217
Qu, Ronghui 175
Querol, Jorge 155
Quintin, Nicolas 285

R

Radil, Jan 303
Rao, Bingjie 341
Reichel, Jakob 56
Ren, Jie 374
Rerucha, Simon 293
Řeřucha, Šimon 392
Rieck, Carsten 159, 263
Ries, Lionel 192
Riis, Erling 61
Rochat, Sylvain 225
Rolland, Antoine 312
Romani, Romano 72
Rovera, Giovanni Daniele 208, 249
Rubiola, Enrico 41
Ruggieri, Alessia Maria 122

S

Saadani, Amina 10
Sagnard, Marianne 24
Salvi, Leonardo 381
Salwik, Karol 152
Samain, Etienne 249
Samperi, Andrea 192
Santarelli, Giorgio 318
Sapia, Adalberto 72
Sapozhnikov, Gennadiy 101, 105
Schioppo, Marco 322, 356
Schnatz, Harald 167, 285
Seeds, Alwyn 285
Sekido, Mamoru 322, 356
Sellone, Marco 188
Semerikov, Ilya 344, 377
Seshia, Ashwin 6
Sesia, Ilaria 276
Sharar, Omer 130
Sherstov, Ivan 344
Shi, Qicheng 395
Shipilov, Anton 1
Shuker, Moshe 348
Shvetsov, Alexander 101
Sibold, Dieter 138
Siccardi, Marco 188
Signorile, Giovanna 276
Siligaris, Alexandre 32
Silveira, Mike 65
Skrivervik, Anja 75
Skvortsov, Mikhail 83
Šlapák, Martin 300, 303
Śliwczyński, Łukasz 149, 152, 167, 202, 285
Slodička, Lukáš 392
Smotlacha, Vladimir 285, 293, 303, 308
Sokolov, Igor M. 369
Sokolova, O. 257
Song, Huijie 217
Sorokin, Boris 1
Stanczyk, Matt 65
Stefani, Fabio 119
Štefl, Jiří 285
Sthal, Fabrice 10, 37
Szterk, Piotr 231

T

Tai, Zhaoyang ... 338
Taichenachev, Alexey V. 83, 344, 348, 364
Takamizawa, Akifumi ... 94
Tavella, Patrizia ... 245, 276
Taylor, Dwayne ... 65
Teichel, Kristof ... 138
Thai, Thanh Tùng ... 276
Tino, Guglielmo ... 381
Tiuliakov, Arkadii ... 181
Tratnik, Jurij ... 231
Tricot, Francois ... 98
Tuckey, Tuckey ... 285
Tuozzi, Alberto ... 72

U

Uhrich, Pierre ... 208, 249
Underhill, Michael ... 45
Urbaniak, Robert ... 285

V

Vaillant, Etienne ... 37
Vasiliev, Vadim ... 83
Velc, Radek ... 303
Verhasselt, Katrijn ... 270
Vernotte, François ... 41
Vishnyakov, Vladislav ... 83
Vojtěch, Josef ... 285, 293, 300, 303
Voloshin, Gavriil ... 87
Vutha, Amar ... 315

W

Waller, Pierre ... 192
Wang, Bin ... 296
Wang, Binghao ... 296
Wang, Dan ... 290
Wang, Enlong ... 381
Wang, Haifeng ... 135, 205, 221
Wang, Hongbo ... 135, 205, 221
Wang, Nuan-Rang ... 50
Wang, Shuwei ... 135, 205, 221
Wang, Weixiong ... 217
Wang, X. ... 389
Wang, Xueyun ... 135, 205, 221
Wang, Yebing ... 374
Wcisło, Piotr ... 322, 356
Weddig, Ludwig ... 253
Włodarczyk, Przemysław ... 202
Wolf, Peter ... 322, 356
Wright, Michael W. ... 61
Wu, Wenjun ... 170, 217

X

Xie, Xiaopeng ... 318
Xiong, Min ... 395
Xu, Guanjun ... 290, 389, 395
Xu, Qinfang ... 374

Y

Yan, Lulu ... 170, 197, 338, 341
Yanagimachi, Shinya ... 94
Yang, Fei ... 175, 178
Yang, Honglei ... 205, 221
Yang, Renfu ... 50
Yang, Wenzhe ... 135, 205, 221
Yang, Zhiqiang ... 135
Yi, Hang ... 205, 221
Yin, Mojuan ... 217, 374
Yong, Xie ... 221
Yuan, Haibo ... 170
Yudin, Valeriy I. ... 83, 348, 364

Z

Zalivako, Ilia ... 344, 377
Zang, Qi ... 290, 389
Zanon-Willette, Thomas ... 348
Zawada, Michał ... 322, 326, 352, 356
Zhang, Jihai ... 170
Zhang, L. ... 389
Zhang, Pan ... 338, 341
Zhang, Shengkang ... 135, 205, 221
Zhang, Shougang ... 290, 338, 341
Zhang, X. ... 389
Zhang, Xi ... 175, 178
Zhang, Xiang ... 290
Zhang, Xianli ... 65
Zhang, Xiaofei ... 338, 341
Zhang, Xiaogang ... 322, 356
Zhang, Yanyan ... 338, 341

Zhao, Huan 50, 205
Zhao, Shuhong 197
Zhao, Wenyu 338
Zhgoon, Sergei 101, 105
Zjawin, Beata 322, 356

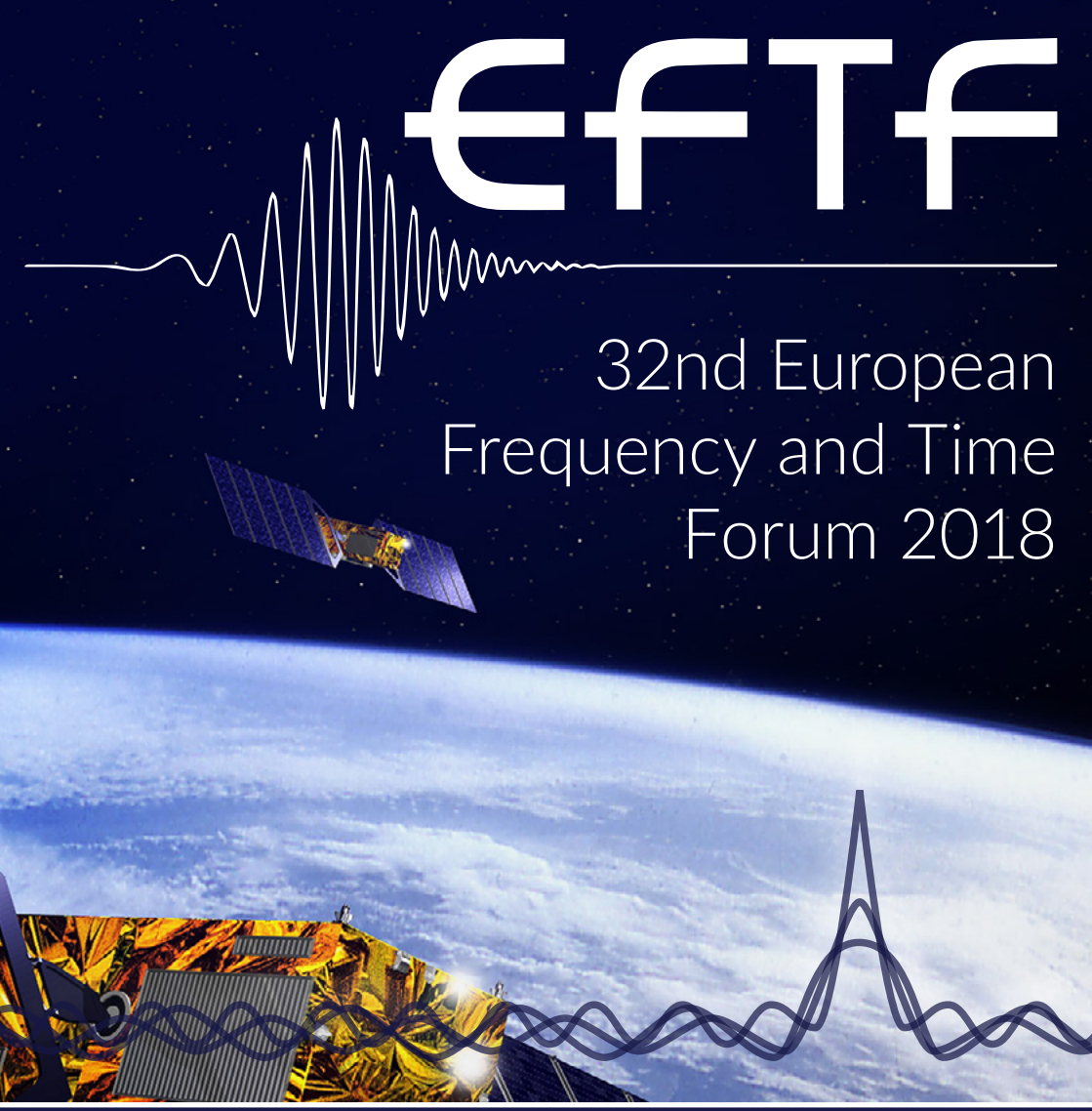

32nd European Frequency and Time Forum 2018

PROGRAMME

10-12 APRIL 2018 | TORINO, ITALY

NATIONAL MUSEUM OF AUTOMOBILES | *Congress Center "Carlo Biscaretti di Ruffia"*

organized by:

INRiM Istituto Nazionale di Ricerca Metrologica

Consiglio Nazionale delle Ricerche

in cooperation with

LEONARDO

Politecnico di Torino

top IX torino piemonte internet exchange

Organising Secretariat

AXEA

2018 European Frequency and Time Forum

April 10-12, 2018 National Museum of Automobiles, Turin - Italy

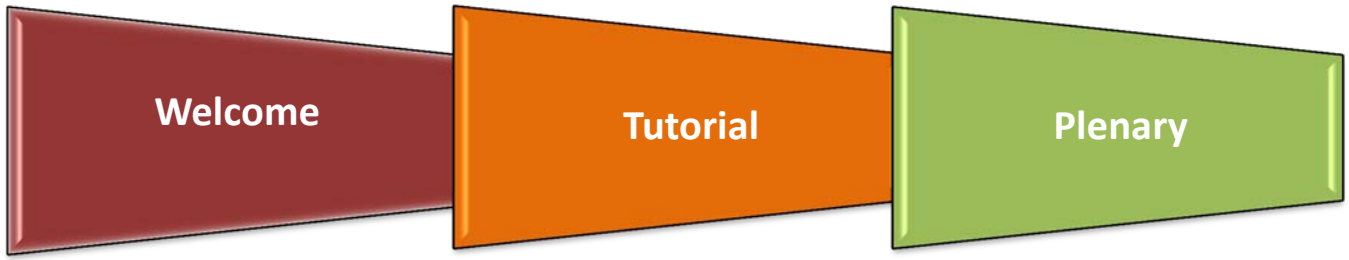

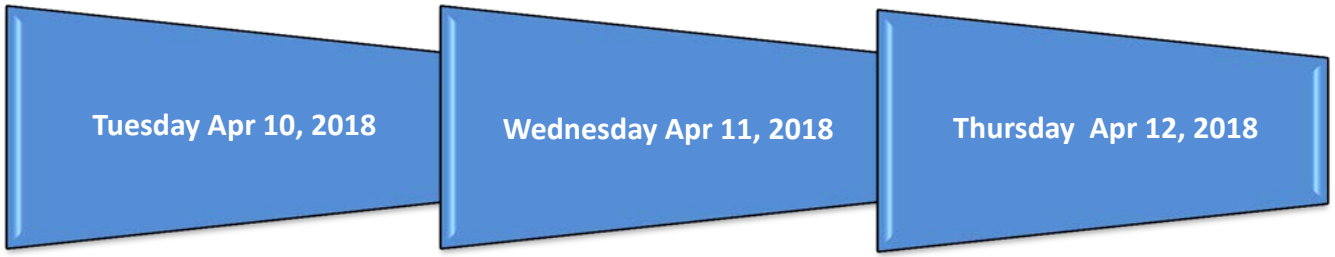

Table of Contents

Welcome to EFTF – 2018 in Torino 3
General Conference Schedule 6
Useful Information 8
Presenter Information 11
Plenary Sessions 13
EFTF 2018 AWARDS 14
Sponsors Of The Student Travel Support Programme 16
Topic List 17
Student Contest Finalist 17
Local Organising Committee 20
EFTF 2018 Executive Committee 20
EFTF 2018 Scientific Committee 21
Social Programme 24
    Welcome Cocktail 24
    Social Dinner 25
Monday April 9th, 2018 - Tutorial Schedule 26
Detailed Conference Programme 27
Tuesday April 10th, 2018 - Program Schedule 27
  Lecture Session 28
    Optical Lattice Clocks I Session 28
    Optical Links I Session 28
    Low Noise Signal Generation Session 29
    Combs & Spectroscopy Session 29
    Optical links II Session 30
    Compact Cold Atom Clocks Session 30
  Poster Session 32
    Student Paper Competition Session 32
    Microwave Frequency Standards I Session 35
    Optical Frequency Standards & Applications I Session 36
    Timekeeping, Time & Frequency Transfer, GNSS Applications I Session 38
Wednesday April 11th, 2018 - Program Schedule 40
  Lecture Session 41
    Optical Lattice Clocks II Session 41

GNSS timing Session 41
Down Conversion & Noise Measurement Session 42
Combs I Session 43
Nonlinear Effects in Devices & Oscillators Session 43
Cold Atoms Clocks & Interferometers Session 44
Exploring New Transitions Session 44
Optical Links III Session 45
MEMS & NEMS Devices Session 45
Thursday April 12th, 2018 - Program Schedule 47
Lecture Session 48
Microfabricated Cells & Applications Session 48
White Rabbit & NTP Session 48
Ion Optical Clocks Session 49
Advanced GNSS Session 49
Wave Propagation Session 50
Combs II Session 50
CPT & Double Resonance Clocks Session 51
Timescales & Clocks Session 51
Poster Session 53
Materials for Resonators & Waveguides Session 53
Microwave Frequency Standards II Session 53
Optical Frequency Standards & Applications II Session 54
Timekeeping, Time & Frequency Transfer, GNSS Applications II Session 56
Oscillators, Synthesizers, Noise, & Circuit Techniques Session 58
Sensors & Transducers Session 58
Exhibitors 60
Conference Venues Map 68
EXHIBITION CENTRE MAP, The National Automobile Museum 69
CASA UGI MAP 70
2019 Joint IFCS-EFTF Conference 71

Welcome to EFTF – 2018 in Torino

Welcome to Torino for the 32nd European Frequency and Time Forum!

The Istituto Nazionale di Ricerca Metrologica (INRIM) is organizing the conference in Torino for the second time, after the previous successful experience in 2000.

The **Local Organizing Committee** of EFTF-2018 includes representatives from research institutions and industries: INRIM, Politecnico di Torino, National Research Council (CNR), Leonardo – Finmeccanica, Consorzio TOP-IX and Axea who have joined their efforts to prepare this event.

We acknowledge the support coming from our sponsors, Leonardo, Top-IX, the National Research Council (CNR), the Italian Physical Society (SIF), Muquans, ADVA and Rhode&Schwarz.

We welcome the many companies that decided to take on Exhibitor Stands, which are always a very useful and interesting part of the forum bringing together over 300 people for scientific, social and friendly meetings during these days.

We are grateful to the members of the **Executive Committee** and particularly to Gaetano Mileti who organized the tutorials, to Pierre Waller in charge of the EFTF awards, to Bernard Dulmet and Fabrice Sthal who took care of the student travel support programme and to François Vernotte in charge of the student poster competition.

We thank all the members of the **Scientific Committee** and in particular the six group vice chairs: Alexandre Reinhardt, Jean-Pierre Aubry, Salvatore Micalizio, Ashwin Seshia, Pierre Waller, Helen Margolis for their hard work in preparing the conference schedule.

The Scientific Committee of EFTF-2018 has prepared a high quality programme resulting from over 240 submitted abstracts. The schedule includes three parallel sessions of lectures and two poster sessions on Tuesday and Thursday afternoon. The student contest posters will be displayed along the whole conference in a dedicated area.

We are pleased to announce the plenary lectures of EFTF-2018**.** On Tuesday morning **Viviana Fafone**, Professor of Physics at "Tor Vergata" University of Rome, will give a lecture entitled: **The Physics of (and with) Virgo and LIGO**. On Wednesday morning **Pierre Martinetti**, Researcher at the Mathematics department of the University of Genova, will give a lecture entitled: **On the thermodynamical origin of time.**

Our growing community is meeting once again to share knowledge, exchange experiences, and create friendship.

We wish you an exciting and inspiring forum.

Filippo Levi

Chair of the

EFTF 2018 LOC

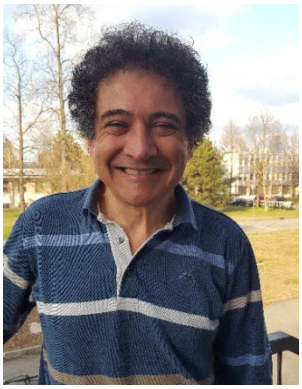

Jerome Delporte

Chair of the

EFTF 2018 SC

Ekkehard Peik

Chair of the

EFTF 2018 EC

UNDER THE AUSPICES OF

REGIONE PIEMONTE

CITTA' DI TORINO

SPONSOR

LEONARDO

Consiglio Nazionale delle Ricerche

LAVAZZA
TORINO, ITALIA, 1895

μQUANS

OSCILLOQUARTZ
An ADVA Optical Networking Company

ROHDE&SCHWARZ

PROVANDO E RIPROVANDO
Società Italiana di Fisica

top ix
torino piemonte internet exchange

General Conference Schedule

Monday Apr 9th

8:00 – 8:30	Registration Tutorial – INRIM
8:30 – 18:00	**Tutorials – INRIM**
14:00 – 15:00	Registration Exhibitors - National Museum of Automobiles
18:30 – 19:30	Registration Conference – Castello del Valentino
19:00 – 21:00	**Welcome Cocktail - Castello del Valentino**

Tuesday Apr 10th

8:00 – 9:00	Registration Conference – National Museum of Automobiles
9:00 – 10:50	**Plenary Session I**
	Welcome and Awards
	Lecture: **Viviana Fafone,** 'The Physics of (and with) Virgo and LIGO'
10:50 – 11:10	Coffee Break / Exhibits
11:10 – 12:50	**Lecture Sessions A1**
	A1L-A: Optical Lattice Clocks I
	A1L-B: Optical Links I
	A1L-C: Low Noise Signal Generation
12:50 – 14:00	**Lunch**
14:00 – 16:00	**Poster Session I**
	Student Poster Competition
16:00 – 16:20	Coffee Break / Exhibits
16:20 – 18:00	**Lecture Sessions A2**
	A2L-A: Combs & Spectroscopy
	A2L-B: Optical Links II
	A2L-C: Compact Cold Atoms Clocks

Wednesday Apr 11th

9:00 – 10:20	**Plenary Session II**
	Student Poster Competition Awards
	EFTF-IFCS 2019 announcement
	Lecture: **Pierre Martinetti,** 'On the thermodynamical origin of time'
10:20 – 10:50	Coffee Break / Exhibits
10:50 – 12:30	**Lecture Sessions B1**
	B1L-A: Optical Lattice Clocks II
	B1L-B: GNSS Timing
	B1L-C: Down Conversion & Noise Measurement
12:30 – 14:00	**Lunch**
14:00 – 16:00	**Lecture Sessions B2**
	B2L-A: Combs I
	B2L-B: Non-linear Effects in Devices & Oscillators
	B2L-C: Cold Atoms Clocks & Interferometry
16:00 – 16:20	Coffee Break / Exhibits
16:20 – 18:00	**Lecture Sessions B3**
	B3L-A: Exploring New Transitions
	B3L-B: Optical Links III
	B3L-C: MEMS & NEMS Devices

20:00 – 23.00	**Social Dinner – Villa Sassi**

Thursday Apr 12th

9:00 – 10:20	**Lecture Sessions C1**
	C1L-A: Microfabrication Cells & Applications
	C1L-B: White Rabbit & NTP
10:20 – 10:50	Coffee Break / Exhibits
10:50 – 12:30	**Lecture Sessions C2**
	C2L-A: Ion Optical Clocks
	C2L-B: Advanced GNSS
	C2L-C: Waves Propagation
12:30 – 14:00	**Lunch**
14:00 – 16:00	**Poster Session II**
16:00 – 16:20	Coffee Break /Exhibits
16:20 – 18:00	**Lecture Sessions C3**
	C3L-A: Combs II
	C3L-B: CPT & Double Resonance Clocks
	C3L-C: Timescales & Clocks

Friday Apr 13th

9:00 – 12:00	**Laboratory Tour at INRIM**

Useful Information

Tutorial

Tutorial on Monday 9th April will be held at the Italian National Institute of Metrological Research (INRIM)

INRIM - Istituto Nazionale di Ricerca Metrologica
Building M
Str. delle Cacce, n° 91
10135 Torino TO

The Tutorial's schedule can be downloaded from the Conference website.
INRIM can be reached by Tram n°4 or Bus n°63 or Bus n°34.
One way coach transport will be supplied at 18:00 from INRIM to Castello del Valentino, for the Welcome Cocktail.

Conference Venue

The National Automobile Museum
Congress Centre "Carlo Biscaretti di Ruffia"
Corso Unità d'Italia, 40, Torino

Casa UGI
Corso Unità d'Italia, 70, Torino

*Please Note **Casa UGI** is located just across the square from the Museum of Automobiles and will be used for parallel sessions.*

Please ensure to wear your badge to access sessions, events, refreshments and launches.

The National Museum of Automobiles offers a discounted ticket advantage to Conference attendees. Do not forget to show your Congress badge to the Ticket Office.

Bus Stop

The National Museum of Automobiles can be reached using public transportation:
- Buses/trams nr: 1 - 18 - 42 - 34 - 35
- Metro (Lingotto stop)
- Bus City Sightseeing line B (bus stop 4)

Welcome reception

The welcome reception will be at the Valentino Castle from 7:00 pm to 9:00 pm on Monday. **Please note that the floor is uneven at the Valentino Castle and therefore high heels are discouraged.** One way coach transport will be supplied to people attending tutorials at 6 pm from INRIM to the Valentino Castle.
Please find further details on page 24

Conference dinner

The conference dinner will be at Villa Sassi at 8:00 pm on Wednesday.
Coach transport will be supplied from the National Automobile Museum and from Porta Nuova Station at 7:00/7:15 pm. As well, at the end of the dinner a coach transport back will be provided.
Be aware that the location is far from the city centre and quite difficult to reach using public transportations. Taxi is strongly recommended (RADIO TAXI 011.5730).
Please find further details on page 25.

Emergency numbers

Fo all emergency services - **medical, fire and police** - dial number **112**. The operator connects the caller with the required emergency service. This Pan-European **emergency number 112** can be called from any telephone (landline, pay phone or mobile cellular phone). Calls are free.

Registration and information desk

Tutorial registration: on Monday morning the registration desk will be located in the INRIM, Building M reception area from 8:00 am to 8:30 am.

Exhibitors registration: on Monday afternoon the conference Staff will be at the National Automobile Museum for the venue set up. Exhibitors registration will be open from 2:00 pm to 3:00 pm.

Conference registration: Registration will be available at the Welcome Cocktail on Monday evening. On Tuesday, registration will be in the National Museum of Automobiles reception area from 8:00 am.

Internet service

National Museum of Automobiles:
ROOM 150 password: kzxe-ib6r-w7h0
AUDITORIUM password: kzx1-ib62-w7h3
COMMON AREAS wi-fi: MAUTO (free wi-fi, no password needed)

Casa UGI:

CASA UGI password: 5C7a9S0u$

Food

On Monday the 9th, lunches for Tutorial's attendants will be held in the INRIM. Further instructions will be given on-site.

Tuesday - Thursday lunches and coffee breaks will be held in the National Museum of Automobiles Foyer.

For evening meals, guests are free to make their own arrangements.

Smoking

All areas inside the National Museum of Automobiles are strictly **No Smoking**.

Tipping and Taxes in Italy

Goods and services in Italy are subject to 22% VAT tax (VAT = IVA in Italian). This tax is usually included in the price and, if not, it should be clearly stated. Prices in restaurants include service. It is discretionary to leave tip for good service.

Presenter Information

Sessions chairs

Please ensure that you meet your presenters before the start of the session and that you know who is presenting each paper. Ensure that the presentations have been loaded onto the computer at the Slide Center located in the Control Room at the 2nd floor. If a speaker is absent, please do not change the session schedule, which may cause people to miss a presentation they had intended to listen to.

Sessions held at Casa UGI have there an autonomous Slide Center.

Oral presentations

- Length of presentation slot: 20 minutes, including ~5 minutes for questions. Invited talks have 40 minutes, including questions.
- LCD projectors and computers (MS PowerPoint and Adobe Acrobat Reader) will be available. Overhead projectors, 35 mm slides projectors and VHS videotape players are NOT available.
- Please bring a memory stick containing your presentation. All presentations must be pre-loaded in the slide center area. Please do this the previous day if possible.
- **Important note -** two slide centers will be set up (1 at MAUTO and 1 at CASA UGI) : Presenters who will have a speech at MAUTO have to pre-load their presentation in the slide center set up at MAUTO. Presenters who will have a speech at Casa UGI have to pre-load their presentation in the slide center set up at CASA UGI**.**
- **Important note:** at CASA UGI, there will be only a VGA connection, HDMI connection is not available.
- If you have special requests, please let us know well in advance. An AV technician will be available should any assistance be needed.

To avoid software compatibility problems (MS PowerPoint), speakers are advised to save their PowerPoint presentation in 'pack-n-go' format AND bring a backup PDF version of their presentation. 'Pack-n-go' format is used when burning a presentation to a CD for use on another computer that may or may not have your current version of PowerPoint installed. It installs a viewer capability. The file should be saved as 'Package for CD' under the 'File' tab in PowerPoint 2003; under the 'File > Publish' tab in PowerPoint 2007; under 'File > Save & Send > Package Presentation for CD' in PowerPoint 2010; and under 'File > Export > Package Presentation for CD' in PowerPoint 2013.

Poster presentations

- Poster size: up to A0, portrait orientation
- Fixings will be provided
- Conference Organizers do not have the responsibility of loss or damage of posters
- You are required to be beside your poster during the hours listed in the programme
- The location of your poster will be noted on each board in accordance with the corresponding number listed in the Programme Book given out at registration
- There will be a dedicated area for the student poster competition

Poster schedule information:

POSTER SESSION 1

- Posters have to be displayed on April 10th starting from 09:00am
- Posters have to be removed within April 11th at lunch time

POSTER SESSION 2

- Posters have to be displayed on April 11th starting from lunch time
- Posters have to be removed within April 12th at 06:00pm (end of the Conference)

STUDENT PAPER COMPETITION

- Posters have to be displayed on April 10th starting from 09:00am until the end of the conference

Plenary Sessions

The EFTF 2018 Scientific Committee is pleased to announce the following plenary sessions:

PLENARY SESSION I: Tuesday 10th April, 09:00 - 10:50, Room Auditorium

Viviana Fafone

Professor of Physics at "Tor Vergata" University of Rome

'The Physics of (and with) Virgo and LIGO'

Recent gravitational-wave observations by LIGO and Virgo not only confirm the century-old prediction of Einstein, but also herald the beginning of a new era of astronomy. This talk will summarize the current status of gravitational-wave detectors, the observations carried out, what we learned from them, and prospects for the near future.

PLENARY SESSION II: Wednesday 11th April, 09:00 - 10:20, Room Auditorium

Pierre Martinetti

Researcher at the Mathematic department of the University of Genova

'On the thermodynamical origin of time'

Even though the "flight of time" may be the most universally shared experience, physics is not able to explain in a coherent manner what time is. For Newton, time is an absolute parameter; for Einstein, it is a geometrical quantity that depends on the observer. In quantum mechanics, it is an abstract parameter in the space of observables. We shall see how thermodynamics combined with advanced mathematics share a new light on the nature of time, which, hopefully might be meaningful in a still to come theory of quantum gravity.

EFTF 2018 AWARDS

The European Frequency and Time Award 2018:

Dr. Ekkehard Peik

"for seminal contributions to single-ion optical frequency standards and high-precision spectroscopy thereby establishing most stringent limits on possible variations of fundamental constants”

The Marcel Ecabert Award 2018:

Dr. Elisa Felicitas Arias

"for her initiative and leadership in the development and realization of international atomic time"

The EFTF Young Scientist Award 2018:

Dr. Cecilia Clivati

"for outstanding contributions in the developments of optical fiber link technology and related scientific applications"

Dr. Maxim Goryachev

"for the development of cryogenic Bulk Acoustic Wave technology, and application to precision oscillators, fundamental physics tests and quantum measurements"

Dr. Tobias Herr

"for seminal contributions to ultra-fast physics and soliton pulse generation in nonlinear optical microresonators"

Sponsors Of The Student Travel Support Programme

The EFTF 2018 Organising committee gratefully acknowledges the support of the following companies and institutions.

csem	CSEM Centre Suisse d'Electronique et de Microtechnique
FIRST TF	First-TF
fsrm CROSSROADS OF MICROTECHNOLOGY	FSRM Fondation Suisse pour la recherche en microtechnique
HELMHOLTZ FONDS e.V.	Helmholtz Fonds e.V.
MEINBERG	Meinberg Funkuhren
sfmc μ	Société Française des Microtechniques et de Chronométrie (SFMC)
spectratime iPrecision Timing Solutions®	Spectratime
T4Science iPRECISION MASER SOLUTIONS™	T4Science
unine UNIVERSITÉ DE NEUCHÂTEL	Université de Neuchâtel

Topic List

Track	Topic Name
1	Materials, Resonators, & Resonator Circuits
2	Oscillators, Synthesizers, Noise, & Circuit Techniques
3	Microwave Frequency Standards
4	Sensors & Transducers
5	Timekeeping, Time and Frequency Transfer, GNSS Applications
6	Optical Frequency Standards and Applications

Student Contest Finalist

The following papers were selected as finalists by the EFTF 2018 Scientific Committee for the Student Poster Competition.

Location: Poster Area
Date & Time: Tuesday April 10, 2018 (14:00 - 16:00)

Paper Id	Track	Title/Author
7219	3	**The ACES-PHARAO Test of the Gravitational Redshift: Refined Performance Estimates** *Christine Guerlin, Etienne Savalle, Frédéric Meynadier, Pacôme Delva, Christophe Le P oncin-Lafitte, Philippe Laurent, Peter Wolf.*
7052	5	**Study on the Relation Between Laser Noise and Optical Frequency Transmission** *Xi Zhang, Fei Yang, Zitong Feng, Youzhen Gui, Haiwen Cai, Ronghui Qu.*
7053	5	**Stabilized Optical-Frequency Transfer Using Optical Injection Locking Amplifier** *Zitong Feng, Fei Yang, Xi Zhang, Dijun Chen, Nan Cheng, Youzhen Gui, Haiwen Cai.*
7112	5	**Long Term Simulations for Bi-Static Radar and Test Bench Design** *Ricardo Granados Alfaro, Alain Herique, Sylvain Rochat, Etienne L e-Coarer.*
7118	5	**Preprocessing for Fast Synchronization of High-Stability Oscillators Disciplined by GNSS 1PPS Signal** *Paweł Kubczak, Michał Kasznia, Mieczysław Jessa.*
7167	1	**Inkjet Printing of Thin Electrodes for Quartz Resonators** *Amina Saadani, Pierre Lavenus, Gilgueng Hwang, Fabric e Sthal, Olivier Le Traon.*
7229	1	**Consideration and Implementation of Inherent Losses in SAW Devices Design** *Marianne Sagnard, Thierry Laroche, Sylvain Ballandras.*
7093	2	**Electronic Instrumentation for Experiments with Ultracold Atoms and Ions**

Paper Id	Track	Title/Author
		Marco Pomponio, Carlo Sias, Claudio Eligio Calosso.
7109	2	**Study of the Phase Noise of Langatate Crystal Resonators** *Alok Pokharel, Etienne Vaillant, Joel Imbaud, Jean-Jacque s Boy, François-Xavier Esnault, Gilles Cibiel, Fabrice Sthal.*
7131	6	**Analysis of Optical Atomic Clocks Readouts Aimed on Searches for Dark-Matter Signatures** *Beata Zjawin, Piotr Ablewski, Kyle Beloy, Sławomir Bilicki, Marcin Bober, Roger Brown, Rom an Ciuryło, Robert Fasano, Hidekazu Hachisu, Tetsuya Ido, Jérôme Lodewyck, Andrew Ludlow, William McGrew, Piotr Morzyński, Daniele Nicolodi, Marco Schioppo, Mamoru Sekido, Rodolphe Le Targat, Piotr Wcisło, Peter Wolf, Xiaogang Zhang, Michał Zawada.*
7136	6	**Operational Transfer of Spectral Purity at LNE-SYRTE** *Héctor Álvarez-Martínez, Yann Le Coq, Rodolphe Le Targat.*
7028	4	**STUDENT CONTEST: Enhanced Performance Surface Acoustic Resonance (SAR) Lab-on-a-Chip Sensor** *Kiryl Kustanovich.*
7040	6	**STUDENT CONTEST: A High-Performance Optical Lattice Clock Based on Bosonic Atoms** *Stefano Origlia.*
7047	3	**STUDENT CONTEST: Portable Microwave Clock Using Laser-Cooled Trapped 171Yb+ Ions** *Sean Mulholland.*
7087	6	**STUDENT CONTEST: Frequency Comb Stabilization of a 4 W, 50-fs Thin-Disk Laser Oscillator** *Norbert Modsching.*
7088	3	**STUDENT CONTEST: Utilising Grating Chip Technology for Raman-Ramsey CPT** *Rachel Elvin.*
7096	5	**STUDENT CONTEST: Clock Anomaly Detection Using L1 Norm Optimization** *Masato Hirano.*
7107	6	**STUDENT CONTEST: Hysteresis in Phononic Frequency Combs** *Adarsh Ganesan.*
7110	6	**STUDENT CONTEST: Progress on Development of Optical Frequency Combs at NTSC** *Yanyan Zhang.*
7132	6	**STUDENT CONTEST: Self-Controlled Offset-Free Er:Fiber Frequency Combs** *Andreas Liehl.*
7139	3	**STUDENT CONTEST: Microwave Field Amplitude Stabilization Using Ramsey Spectroscopy Signal** *Michele Gozzelino.*

Paper Id	Track	Title/Author
7145	2	**STUDENT CONTEST: Optical-to-RF Frequency Division for Ultra-Low Noise Microwave Generation Using a Transfer Oscillator Method** *Pierre Brochard.*
7147	4	**STUDENT CONTEST: A-Si:H Thin-Film MEMS Resonators: Towards Mass Sensing Applications** *Rui Pinto.*
7150	6	**STUDENT CONTEST: Relativistic Geodesy with a Transportable Optical Clock** *Jacopo Grotti.*
7152	6	**STUDENT CONTEST: Cryogenic Yb Lattice Clock Below 10^-17 Uncertainty** *Filippo Bregolin.*
7155	4	**STUDENT CONTEST: Optimization of Low-Power Oscillator Topology for Frequency Modulated MEMS Inertial Sensors** *Cristiano Rocco Marra.*
7165	1	**STUDENT CONTEST: Elastic Strain Engineering for Exceptional Mechanical Coherence** *Amirhossein Ghadimi.*

Local Organising Committee

Filippo Levi (Chair) - INRIM Istituto Nazionale di Ricerca Metrologica, Italy
Davide Calonico - INRIM Istituto Nazionale di Ricerca Metrologica, Italy
Ilaria Sesia - INRIM Istituto Nazionale di Ricerca Metrologica, Italy
Salvatore Micalizio - INRIM Istituto Nazionale di Ricerca Metrologica, Italy
Claudio Calosso - INRIM Istituto Nazionale di Ricerca Metrologica, Italy
Giovanni Costanzo – Politecnico di Torino, Italy
Lorenzo Galleani – Politecnico di Torino, Italy
Gianluca Galzerano – Consiglio Nazionale delle Ricerche, Istituto di Fotonica e Nanotecnologia, Italy
Jacopo Catani – Consiglio Nazionale delle Ricerche, Istituto Nazionale di Ottica, Italy
Elisabetta Melli - INRIM Istituto Nazionale di Ricerca Metrologica, Italy
Silvia Cavallero - INRIM Istituto Nazionale di Ricerca Metrologica, Italy
Marina Gioia – Leonardo, Italy
Luca Cicchelli – Consorzio TOP-IX, Itlay
Giovanna Possio – Axea, Italy

EFTF 2018 Executive Committee

Elected Members

- ✓ Ekkehard Peik - Physikalisch-Technische Bundesanstalt, Germany (Chair)
- ✓ Gaetano Mileti - Laboratoire Temps-Fréquence, Switzerland (Tutorials Chair)
- ✓ Pascale Defraigne – Royal Observatory of Belgium
- ✓ Bernard Dulmet - ENSMM - LCEP, France, SFMC President
- ✓ Jeremy Everard - University of York, United Kingdom
- ✓ Per-Olof Hedekvist – RISE, Sweden
- ✓ Ronald Holzwarth – Menlo Systems, Germany
- ✓ Helen Margolis - NPL - National Physical Laboratory, United Kingdom
- ✓ Pascal Rochat - Spectratime SA, Switzerland
- ✓ Wolfgang Schäfer - TimeTech, Germany, Exhibition Chair
- ✓ Patrizia Tavella - INRIM Istituto Nazionale di Ricerca Metrologica, Italy, Vice Chair
- ✓ Philip Tuckey – SYRTE Observatoire de Paris, France
- ✓ Francois Vernotte - Observatoire de Besançon, France, Academic Chair
- ✓ Pierre Waller - European Space Agency, The Netherlands, Awards Chair

Ex officio members

- ✓ Fabrice Sthal - SFMC, France
- ✓ Elizabeth Donley - NIST, United States, IEEE-IFCS Standing Committee Chair
- ✓ Jérôme Delporte - CNES, France, Scientific Committee Chair
- ✓ Filippo Levi - INRIM, Italy, 2018 Chair of the local organising committee
- ✓ Debra Coler - OEWaves, United States, 2019 General Co-chair

EFTF 2018 Scientific Committee

Chair: Jérôme Delporte - CNES

Group 1: Materials, Resonators, & Resonator Circuits

Alexandre Reinhardt (Vice chair) - CEA-LETI, France

Thomas Baron - FEMTO-ST, France
Emmanuel Defay - Luxembourg Institute of Science and Technology, Luxembourg
Marc Faucher - IEMN, France
Songbin Gong - University of Illinois at Urbana-Champaign, USA
Ken Hashimoto - Chiba University, Japan
Olivier Le Traon - ONERA, France
Matteo Rinaldi - Northeastern University, USA
Ashwin Seshia - University of Cambridge, UK
Ventsislav Yantchev - Uppsala University, Sweden

Group 2 : Oscillators, Synthesizers, Noise, and Circuit Techniques

Jean-Pierre Aubry (vice-chair) - AubryConseil, Switzerland

Claudio Calosso - INRIM, Italy
Gilles Cibiel - CNES, France
Jeremy Everard - York University, UK
Serge Galliou - ENSMM, France
David Howe - NIST, USA
Olivier Lopis - LAAS, France
Enrico Rubiola - Femto-ST, France
Fabrice Sthal - Femto-ST, France
Michael Tobar - University Western Australia, Australia
Mike Underhill - Underhill Research, UK

Group 3 : Microwave Frequency Standards

Salvatore Micalizio (vice-chair) - INRIM, Italy

Marco Belloni - ESA, Italy
Rodolphe Boudot - Femto-ST, France
Kurt Gibble - Penn State University, USA
John Kitching - NIST, USA
Svenja Knappe - University of Colorado, USA
Motohiro Kumagai - NICT, Japan
Arnaud Landragin - SYRTE, France
Gaetano Mileti - Universite de Neuchatel, Switzerland
Krzysztof Szymaniec - NPL, UK
Qinghua Wang - Spectratime, Switzerland
Stefan Weyers - PTB, Germany

Group 4 : Sensors and Transducers
Ashwin Seshia (vice-chair) - University of Cambridge, UK
Sylvain Ballandras - Frecnsys, France
Alfred Binder - CTR AG, Austria
Virginia Chu - INSEC MN, Portugal
Holger Fritze - TU Clausthal, Germany
Jérôme Juillard
Michael Kraft - University of Liège
Ralf Lucklum - University of Magdeburg, Germany
Paul Muralt - EPFL, Switserland
Laura Popa - Analog, USA
Leonhard Reindl - Uni Freibourg, Germany
Ventsislav Yantchev - Uppsala Observatory, Sweden

Group 5 : Timekeeping, T&F Transfer, Telecom and GNSS applications
Pierre Waller (vice-chair) - ESA-ESTEC, The Netherlands
Anne Amy-Klein - LPL (CNRS, UP13), France
Andreas Bauch - PTB, Germany
Laurent-Guy Bernier - METAS, Switzerland
Pascale Defraigne - ORB, Belgium
Miho Fujieda - NICT, Japan
Gesine Grosche - PTB, Germany
Per Olof Hedekvist - SP, Sweden
Judah Levine - NIST, US
Huang-Tien Lin - NTFSL - TL, Taiwan
Xiao Chun Lu - NTSC, China
Nathan Newbury - NIST, US
Vitaly Pal'chikov - VNIIFTR, Russia
Ed Powers - USNO, US
Wolfgang Schäffer – Timetech, Germany
Amitava Sen Gupta - NPLI, India
Pierre Uhrich - LNE-SYRTE OP, France
Hongbo Wang - BIRM, China
Peter Whibberley - NPL, UK
Michael Wouters - NMI, Australia
Aimin Zhang - NIM, China
Victor Zhang - NIST, US

Group 6 : Optical Frequency Standards and Applications
Helen Margolis (vice-chair) - NPL, UK
Luigi Cacciapuoti - ESA, The Netherlands
Davide Calonico - INRIM, Italy
Roman Ciuryło - Nicolaus Copernicus University, Poland
Pierre Dubé - NRC, Canada
Tara Fortier, NIST, USA

Patrick Gill - NPL, UK
Rachel Godun, NPL, UK
Tetsuya Ido - NICT, Japan
Steve Lecomte - CSEM, Switzerland
Yann Le Coq - LNE-SYRTE, France
Christian Lisdat - PTB, Germany
Jérôme Lodewyck - LNE-SYRTE, France
Andrew Ludlow - NIST, USA
Andre Luiten - University of Adelaide, Australia
Long-Sheng Ma - East China Normal University, China
Mikko Merimaa - MIKES Metrology, VTT Technical Research Centre of Finland Ltd, Finland
Jacques Morel - METAS, Switzerland
Ekkehard Peik - PTB, Germany
Thomas Südmeyer - LTF-UNINE, Switzerland
Alexey Taichenachev - Institute of Laser Physics, Russia
Masami Yasuda - AIST/NMIJ, Japan

Social Programme

Welcome Cocktail

Join us for a welcome drink and a selection of light food.
Please note that the floor is uneven at the Valentino Castle and therefore high heels are discouraged.
One way coach transport will be provided at 6 pm from INRIM to the Valentino Castle.

Monday 9th April
19:00 – 21:00

Valentino Castle
Sala delle Colonne
Viale Mattioli, 39 - Torino

Social Dinner

We take pleasure in inviting you to the EFTF 2018 Social Dinner.

Courtesy bus service will be supplied from the National Automobile Museum and from Porta Nuova Station and return. Departure at 7:00/7:15 pm.

Be aware that the location is far from the city centre and quite difficult to reach using public transportations. Taxi is strongly recommended (RADIO TAXI 011.5730).

Wednesday 11th April

20:00

Villa Sassi

Strada al Traforo di Pino, 47 – Torino

Monday April 9th, 2018 - Tutorial Schedule

Monday April 9th, 2018		
Tutorial		
	INRIM, "M" Building	
08:45-10:15	Giacomo Langfelder *Politecnico di Milano (Italy)* **MEMS inertial sensorss**	Eric Burt Jet *Propulsion Laboratory (USA)* **Microwave atomic clocks**
10:15-10:30	*Coffee Break*	
10:30-12:00	Patrizia Tavella *Bureau International des Poids et Mesures (BIPM)* **Precise Time Scales and Time Metrology**	Ekkehard Peik *Physikalisch-Technische Bundesanstalt (Germany)* **Optical clocks**
12:00-13:00	*Lunch*	
13:00-14:30	Pascale Defraigne *Observatoire Royal de Belgique (Belgium)* **Timing with Global Navigation Satellite Systems**	Yann Le Coq *Observatoire de Paris – SYRTE (France)* **Femtosecond combs**
14:30-16:00	John Kitching *National Institute of Standards and Technology (USA)* **Atomic sensors and applications**	David Leibrandt *National Institute of Standards and Technology (USA)* **Lasers for optical frequency standards**
16:00-16:15	*Coffee Break*	
16:15-17:45	Anne Amy-Klein *LPL, Université Paris 13 – CNRS (France)* **Optical fiber link for ultrastable time and frequency dissemination**	Craig Nelson *National Institute of Standards and Technology (USA)* **Phase noise metrology**

Detailed Conference Programme

Tuesday April 10th, 2018 - Program Schedule

Tuesday April 10th, 2018				
	Opening Session and Plenary Session I			
9:00-10:20	Viviana Fafone - Professor of Physics at "Tor Vergata" university of Rome **The Physics of (and with) Virgo and LIGO** Location: Room AUDITORIUM			
10:20-11:00	*Coffee Break*			
	Lecture Session			
	AUDITORIUM	**SALA 150**	**CASA UGI**	
11:00-12:40	A1L-A Optical Lattice Clock I *Chr: Ekkehard Peik* Track: Optical Frequency Standards and Applications	A1L-B Optical Links I *Chr: Peter Whibberley* Track: Timekeeping, Time and Frequency Transfer, GNSS Applications	A1L-C Low Noise Signal Generation *Chr: Claudio Calosso* Track: Oscillators, Synthesizers, Noise, & Circuit Techniques	
12:40-14:00	*Lunch*			
	Poster Session			
14:00-16:00	A2P-D Student Paper Competition *Chr: Francois Vernotte*	A2P-E Microwave Frequency Standards I *Chr: Fabien Droz*	A2P-F Optical Frequency Standards & Applications I *Chr: Marco Pizzocaro*	A2P-G Timekeeping, Time & Frequency Transfer, GNSS Applications I *Chr: Pierre Waller*
	Coffee Break			
	Lecture Session			
	AUDITORIUM	**SALA 150**	**CASA UGI**	
16:20-18:00	A3L-A Combs & Spectroscopy *Chr: Giorgio Santarelli* Track: Optical Frequency Standards and Applications	A3L-B Optical links II *Chr: Per Olof Hedekvist* Track: Timekeeping, Time and Frequency Transfer, GNSS Applications	A3L-C Compact Cold Atom Clocks *Chr: Liz Donley* Track: Microwave Frequency Standards	

Lecture Session

Optical Lattice Clocks I Session

Session Type: Lecture
Session Code: A1L-A
Location: Auditorium
Date & Time: Tuesday April 10, 2018 (11:00 - 12:40)
Chair: Ekkehard Peik

11:00 Ytterbium Optical Lattice Clocks at Nist: Stability, Accuracy, and Agreement at Low 10^–18
Kyle Beloy, William McGrew, Xiaogang Zhang, Robert Fasano, Daniele Nicolodi, Stefan Schäffer, Roger Brown, Richard Fox, Nathan Hinkley, Tai Hyun Yoon, Andrew Ludlow.

11:20 First Frequency Comparison of a Bosonic Magnesium Lattice Clock Based on the 1S0 – 3P0 Transition
Dominika Fim, Steffen Rühmann, Klaus Zipfel, Nandan Jha, Steffen Sauer, Waldemar Friesen-Piepenbrink, Wolfgang Ertmer, Ernst M. Rasel, Thomas Waterholter, Alexander Kuhl, Sebastian Koke, Gesine Grosche, Ali Al-Masoudi, Sören Dörscher, Christian Lisdat.

11:40 Generalized Auto-Balanced Ramsey Spectroscopy of Clock Transitions
Valeriy I. Yudin, Alexey V. Taichenachev, Maxim Yu. Basalaev, Thomas Zanon-Willette, James Wesley Pollock, Moshe Shuker, Elizabeth A. Donley, John Kitching.

12:00 A High-Performance Optical Lattice Clock Based on Bosonic Atoms
Stefano Origlia, Mysore Srinivas Pramod, Stephan Schiller, Yeshpal Singh, Kai Bongs, Sebastian Häfner, Sofia Herbers, Sören Dörscher, Ali Al-Masoudi, Roman Schwarz, Uwe Sterr, Christian Lisdat.

12:20 Cryogenic Yb Lattice Clock Below 10^-17 Uncertainty
Nils Nemitz, Filippo Bregolin, Ryotatsu Yanagimoto, Ray Mizushima, Hidetoshi Katori.

Optical Links I Session

Session Type: Lecture
Session Code: A1L-B
Location: Sala 150
Date & Time: Tuesday April 10, 2018 (11:00 - 12:40)
Chair: Peter Whibberley

11:00 Operation of the Fibre Links PTB–UoS and NPL–LPL in the First Trinational Fibre Link Clock-Comparison Campaign
Sebastian Koke, Jochen Kronjäger, Etienne Cantin, Olivier Lopez, Alexander Kuhl, Thomas Waterholter, Erik Benkler, Anne Amy-Klein, Paul-Eric Pottie, Gesine Grosche.

11:20 Operation of the World's First Industrial Autonomous Long-Haul Optical Fiber Link at a 10^-20 Level of Frequency Stability
Bruno Desruelle, Fabiola Guillou-Camargo, Mathieu Corradini, Vincent Ménore, Etienne Cantin, Anne Amy-Klein, Paul-Eric Pottie, Olivier Lopez, Emilie Camisard, Giorgio Santarelli, Christian Chardonnet.

11:40 Two-Way Optical Frequency Transfer on in-Field Long-Haul Fiber Link
Anna Tampellini, Cecilia Clivati, Filippo Levi, Alberto Mura, Davide Calonico.

12:00 REFIMEVE+ : Towards a Wide Optical Fiber Network for Optical Frequency Standard Dissemination
Etienne Cantin, Olivier Lopez, Nicolas Quintin, Emilie Camisard, Christian Chardonnet, Giorgio Santarelli, Anne Amy-Klein, Paul-Eric Pottie. *** INVITED ***

Low Noise Signal Generation Session

Session Type: Lecture
Session Code: A1L-C
Location: Casa UGI
Date & Time: Tuesday April 10, 2018 (11:00 - 12:40)
Chair: Claudio Calosso

11:00 Above 100-GHz Low Phase Noise Frequency Generation in Silicon Integrated Technologies
Alexandre Siligaris *** INVITED ***

11:40 Noise Characterization of Red Pitaya Internal PLL
Andrea Carolina Cardenas-Olaya, Claudio Eligio Calosso, Jean Michel Friedt, Salvatore Micalizio, Enrico Rubiola.

12:00 RF/MW Signal Generations Aiming SDR & IoT Applications
Ulrich L. Rohde, Ajay Poddar, Alexandru Marius Silaghi.

12:20 Möbius Metamaterial Strips: Opportunities for Next Generation Frequency Sources and Design Challenges
Ulrich L. Rohde, Ajay Poddar, Enrico Rubiola, Alexandru Marius Silaghi.

Combs & Spectroscopy Session

Session Type: Lecture
Session Code: A3L-A
Location: Auditorium
Date & Time: Tuesday April 10, 2018 (16:20 - 18:00)
Chair: Giorgio Santarelli

16:20 Mid-Infrared Optical Frequency Comb via Coherent Supercontinuum Processes in Nano-Photonic Waveguides
Hairun Guo, Wenle Weng, Martin Pfeiffer, Tobias Kippenberg.

16:40 Ro-Vibrational Fine Structure of CF3H by Frequency-Comb-Assisted Saturated Spectroscopy at 8.6 µm
Edoardo Vicentini, Alessio Gambetta, Nicola Coluccelli, Eugenio Fasci, Antonio Castrillo, Livio Gianfrani, Valentina Di Sarno, Pasquale Maddaloni, Adina Ceausu-Velcescu, Paolo De Natale, Yuchen Wang, Toney T. Fernandez, Paolo Laporta, and Gianluca Galzerano.

17:00 A Compact Optical Iodine Frequency Reference for a Sounding Rocket Mission

Franz B. Gutsch, Klaus Döringshoff, Vladimir Schkolnik, Evgeny V. Kovalchuk, Markus Oswald, Christian Kürbis, Thilo Schuldt, Benjamin Pröbster, Matthias Lezius, Ronald Holzwarth, Andreas Wicht, Claus Braxmaier, Markus Krutzik, Achim Peters.

17:20 Dual-Comb Spectroscopy

Nathalie Picqué. ***INVITED ***

Optical links II Session

Session Type: Lecture
Session Code: A3L-B
Location: Sala 150
Date & Time: Tuesday April 10, 2018 (16:20 - 18:00)
Chair: Per Olof Hedekvist

16:20 Local Two-Way Time and Frequency Distribution for Optical Time Transfer

Ulrich Schreiber, Jan Kodet, Christoph Bürkel, Gerhard Kronschnabl, Torben Schüler, Urs Hugentobler.

16:40 Operation of an Atomic Fountain Frequency Standard with a Remote Maser Reference

Krzysztof Szymaniec, Richard Hendricks, Krzysztof Turza, Bartlomiej Nagórny, Piotr Dunst, Jerzy Nawrocki, Przemysław Krehlik, Łukasz Śliwczyński.

17:00 Two-Branch Fiber Links for International Clock Networks

Dan Xu, Etienne Cantin, Florian Frank, Nicolas Quintin, Frédéric Meynadier, Philip Tuckey, Anne Amy-Klein, Olivier Lopez, and Paul-Eric Pottie.

17:20 Analysis and Compensation of Polarization in an Optical Frequency Transfer Through a Fiber Communication Network

Per Olof Hedekvist, Ludwig Weddig, Sven-Christian Ebenhag

17:40 OFDR – a Diagnostic Tool for Long-Distance Metrological Fiber Links

Jochen Kronjäger, Giuseppe Marra, Jannik Dierks, Etienne Cantin, Nicolas Quintin, Anne Amy-Klein, Olivier Lopez, and Paul-Eric Pottie.

Compact Cold Atom Clocks Session

Session Type: Lecture
Session Code: A3L-C
Location: Casa UGI
Date & Time: Tuesday April 10, 2018 (16:20 - 18:00)
Chair: Liz Donley

16 :20 Cold-Atom-Based Commercial Microwave Clock at the 10^-15 Level

Ramon Szmuk, Bruno Pelle, David Holleville, Bruno Desruelle. **** INVITED ****

17 :00 Utilising Grating Chip Technology for Raman-Ramsey CPT

Rachel Elvin, James P. McGilligan, Gregory W. Hoth, Michael W. Wright, Aidan S. Arnold, Paul F. Griffin, Erling Riis.

17:20 Towards a Quantum-Enhanced Atomic Clock on a Chip

Tommaso Mazzoni, Meng-Zi Huang, Théo Laudat, Carlos L. Garrido Alzar, Jakob Reichel.

17 :40 Portable Microwave Clock Using Laser-Cooled Trapped 171Yb+ Ions

Sean Mulholland, Geoffrey Barwood, Sean Donnellan, David Gentle, Guilong Huang, Hugh Klein, Pravin Patel, Greg Walsh, P.E.G Baird, P. Gill.

Poster Session

Student Paper Competition Session

Session Type: Poster
Session Code: A2P-D
Location: Poster Area
Date & Time: Tuesday April 10, 2018 (14:00 - 16:00)
Chair: Francois Vernotte

#7219 The ACES-PHARAO Test of the Gravitational Redshift: Refined Performance Estimates
Christine Guerlin, Etienne Savalle, Frédéric Meynadier, Pacôme Delva, Christophe Le P oncin-Lafitte, Philippe Laurent, Peter Wolf.

#7052 Study on the Relation Between Laser Noise and Optical Frequency Transmission
Xi Zhang, Fei Yang, Zitong Feng, Youzhen Gui, Haiwen Cai, Ronghui Qu.

#7053 Stabilized Optical-Frequency Transfer Using Optical Injection Locking Amplifier
Zitong Feng, Fei Yang, Xi Zhang, Dijun Chen, Nan Cheng, Youzhen Gui, Haiwen Cai.

#7112 Long Term Simulations for Bi-Static Radar and Test Bench Design
Ricardo Granados Alfaro, Alain Herique, Sylvain Rochat, Etienne L e-Coarer.

#7118 Preprocessing for Fast Synchronization of High-Stability Oscillators Disciplined by GNSS 1PPS Signal
Paweł Kubczak, Michał Kasznia, Mieczysław Jessa.

#7167 Inkjet Printing of Thin Electrodes for Quartz Resonators
Amina Saadani, Pierre Lavenus, Gilgueng Hwang, Fabric e Sthal, Olivier Le Traon.

#7229 Consideration and Implementation of Inherent Losses in SAW Devices Design
Marianne Sagnard, Thierry Laroche, Sylvain Ballandras.

#7093 Electronic Instrumentation for Experiments with Ultracold Atoms and Ions
Marco Pomponio, Carlo Sias, Claudio Eligio Calosso.

#7109 Study of the Phase Noise of Langatate Crystal Resonators
Alok Pokharel, Etienne Vaillant, Joel Imbaud, Jean-Jacque s Boy, François-Xavier Esnault, Gilles Cibiel, Fabrice Sthal.

#7131 Analysis of Optical Atomic Clocks Readouts Aimed on Searches for Dark-Matter Signatures
Beata Zjawin, Piotr Ablewski, Kyle Beloy, Sławomir Bilicki, Marcin Bober, Roger Brown, Rom an Ciuryło, Robert Fasano, Hidekazu Hachisu, Tetsuya Ido, Jérôme Lodewyck, Andrew Ludlow, William McGrew, Piotr Morzyński, Daniele Nicolodi, Marco Schioppo, Mamoru Sekido, Rodolphe Le Targat, Piotr Wcisło, Peter Wolf, Xiaogang Zhang, Michał Zawada.

#7136 Operational Transfer of Spectral Purity at LNE-SYRTE
Héctor Álvarez-Martínez, Yann Le Coq, Rodolphe Le Targat.

#7028 STUDENT CONTEST: Enhanced Performance Surface Acoustic Resonance (SAR) Lab-on-a-Chip Sensor

Kiryl Kustanovich1, Ventsislav Yantchev, Aldo Jesorka.

#7040 STUDENT CONTEST: A High-Performance Optical Lattice Clock Based on Bosonic Atoms

Stefano Origlia, Mysore Srinivas Pramod, Stephan Schiller, Yeshpal Singh, Kai Bongs, Sebastian Häfner, Sofia Herbers, Sören Dörscher, Ali Al-Masoudi, Roman Schwarz,Uwe Sterr, and Christian Lisdat.

#7047 STUDENT CONTEST: Portable Microwave Clock Using Laser-Cooled Trapped 171Yb+ Ions

Sean Mulholland, G.P. Barwood, S. Donnellan, D. Gentle, G. Huang, H.A. Klein, P. Patel, G. Walsh, P.E.G Baird, P. Gill.

#7087 STUDENT CONTEST: Frequency Comb Stabilization of a 4 W, 50-fs Thin-Disk Laser Oscillator

Norbert Modsching, Clément Paradis, Pierre Brochard, Nayara Jornod, Kutan Gürel, Christian Kränkel, Stéphane Schilt, Valentin J. Wittwer, and Thomas Südmeyer.

#7088 STUDENT CONTEST: Utilising Grating Chip Technology for Raman-Ramsey CPT

Rachel Elvin, James P. McGilligan, Gregory W. Hoth, Michael W. Wright, Aidan S. Arnold1, Paul F. Griffin, and Erling Riis.

#7096 STUDENT CONTEST: Clock Anomaly Detection Using L1 Norm Optimization

Masato Hirano, Kazumune Hashimoto, Fumimaru Nakagawa, Tetsuya Ido, Yuko Hanado, Shuichi Adachi.

#7107 STUDENT CONTEST: Hysteresis in Phononic Frequency Combs

Adarsh Ganesan, and Ashwin Seshia.

#7110 STUDENT CONTEST: Progress on Development of Optical Frequency Combs at NTSC

Yanyan Zhang, Lulu Yan, Pan Zhang, Songtao Fan, Bingjie Rao, Xiaofei Zhang, Wenge Guo, Shougang Zhang, and Haifeng Jiang.

#7132 STUDENT CONTEST: Self-Controlled Offset-Free Er:Fiber Frequency Combs

Andreas Liehl, D. Fehrenbacher, P. Sulzer, A. Leitenstorfer, and D. V. Seletskiy.

#7139 STUDENT CONTEST: Microwave Field Amplitude Stabilization Using Ramsey Spectroscopy Signal

Michele Gozzelino, Salvatore Micalizio, Filippo Levi, Aldo Godone, Claudio E. Calosso.

#7145 STUDENT CONTEST: Optical-to-RF Frequency Division for Ultra-Low Noise Microwave Generation Using a Transfer Oscillator Method

Pierre Brochard, Stéphane Schilt, Thomas Südmeyer.

#7147 STUDENT CONTEST: A-Si:H Thin-Film MEMS Resonators: Towards Mass Sensing Applications

Rui Pinto, Pedro Brito, Virginia Chu, João Pedro Conde.

#7150 STUDENT CONTEST: Relativistic Geodesy with a Transportable Optical Clock

Jacopo Grotti, S. B. Koller, S. Herbers, S. Vogt, A. Al-Masoudi, S. Dörscher, R. Schwarz, S. Häfner, U. Sterr, E. Benkler, S. Koke, A. Kuhl, T. Waterholter, G. Grosche, R. Le Targat, J. Lodewyck, H. Á. Martinez, M. Abgrall, E. Cantin, D. Xu, O. Lopez, A. Amy-Klein, P.-E. Pottie, H. Denker and C. Lisdat.

#7152 STUDENT CONTEST: Cryogenic Yb Lattice Clock Below 10^-17 Uncertainty

Filippo Bregolin, N. Nemitz, R. Yanagimoto, R. Mizushima and H. Katori.

#7155 STUDENT CONTEST: Optimization of Low-Power Oscillator Topology for Frequency Modulated MEMS Inertial Sensors

Cristiano Rocco Marra, Alessia M. Ruggieri, Paolo Minotti, Giorgio Mussi, Andrea G. Bonfanti, Andrea L. Lacaita, and Giacomo Langfelder.

#7165 STUDENT CONTEST: Elastic Strain Engineering for Exceptional Mechanical Coherence

Amirhossein Ghadimi, Sergey A. Fedorov, Nils J. Engelsen, Mohammad J. Bereyhi, Ryan Schilling, Dalziel J. Wilson, Tobias J. Kippenberg.

Microwave Frequency Standards I Session

Session Type: Poster
Session Code: A2P-E
Location: Poster Area
Date & Time: Tuesday April 10, 2018 (14:00 - 16:00)
Chair: Fabien Droz

#7002 Electromagnetically-Induced Absorption Resonances for Applications in Quantum Sensing and Optical Switches
Denis Brazhnikov, Stepan Ignatovich, Vladislav Vishnyakov, Mikhail Skvortsov.

#7004 Miniature Cs Vapor Cells and Atomic Clocks in FEMTO-ST
Rémy Vicarini, Vincent Maurice, Moustafa Abdel Hafiz, Ra vinder Chutani, Sylwester Bargiel, Serge Galliou,Nicolas Passilly, Christophe Gorecki, Rodolphe Boudot.

#7011 Uncertainty Contributions of the Microwave Synthesis for PTB's Fountain Clocks
Michael Kazda, Johannes Rahm, Burghard Lipphardt, Stefan Weyers.

#7012 High Contrast Ramsey-CPT Spectrum with Differential Detection in Rb Vapor Cell
Yuan Tian, Yi Zhang, Jiehua Chen, Sihong Gu.

#7039 A Campact Magnetron Cavity for Pop Rb Clock
Qiang Hao, Wenxiang Xue, Kemu Wang, Peter Yun, Wenge Guo, Shougang Zhang.

#7065 A Model for Detection of Topological Dark Matter Using GNSS Networks
Bruno Bertrand, Pascale Defraigne.

#7078 An Alignment Technique for Optimal Atomic Trajectory of an Atomic Fountain Clock
Sangmin Lee, Hyun-Gue Hong, Myoung-Sun Heo, Taeg Yong Kwon, Sang-Bum Lee, Sang Eon Park.

#7092 Accuracy Evaluation of the NRC-FCs2 Atomic Fountain Clock at the National Research Council of Canada
Bin Jian, Scott Beattie, A. John Alcock, Marina Gertsvolf, Richard Hendricks, Filip Ozimek, Krzysztof Szym aniec, Kurt Gibble.

#7104 Simple Analytical Expressions and Experimental Verifications for the Dark Resonance Amplitude in a VacuumVapour Cell
Denis Brazh nikov, Stepan Ignatovich, Vladislav Vishnyakov, Mikhail Skvortsov, Christophe Gorecki, Rodolphe Boudot.

#7175 Watt Level Narrow Linewidth Transportable Laser Source at 852 nm for Laser Cooling of Cesium Atoms
Laura Antoni-Micollier, Baptiste Battelier, Daniel Comparat, Bruno Desruelle, Matthieu Viteau, Giorgio Santarelli.

#7009 Design of Mercury Lamp for Trapped Ion Frequency Standard
Nuan-Rang Wang, Xing Chen, Huan Zhao, Renfu Yang.

#7033 Fountain Equation and Frequency Calculation
Yury Domnin.

Optical Frequency Standards & Applications I Session

Session Type: Poster
Session Code: A2P-F
Location: Poster Area
Date & Time: Tuesday April 10, 2018 (14:00 - 16:00)
Chair: Marco Pizzocaro

#7025 Improving the Yb Optical Lattice Clock at INRIM
Marco Pizzocaro, Pierre Thoumany, Filippo Bregolin, Gianmaria Milani, Benjamin Rauf, María Del Carmen Vélez López, Filippo Levi, Davide Calonico.

#7034 The Strontium Optical Lattice Clock at INRIM
Marco Giacinto Tarallo, Matteo Barbiero, Giacomo Lamporesi, Gabriele Ferrari, Davide Calonico, Filippo Levi.

#7076 Towards a Cryogenic Silicon Resonator with Low Thermal Noise Crystalline Mirrors
Thomas Legero, Dan G. Matei, Robin Weyrich, Sebastian Häfner, Fritz Riehle, Linds ay Sonderhouse, John M. Robinson, Eric Oelker, Wei Zhang, Jun Ye, Paula Heu, David Follman, Christoph Deutsch, Garrett Cole, Uwe Sterr.

#7077 Development of an Ytterbium Optical Lattice Clock at NMIJ
Takumi Kobayashi, Daisuke Akamatsu, Yusuke Hisai, Takeh iko Tanabe, Hajime Inaba, Tomonari Suzuyama, Feng-Lei Hong, Kazumoto Hosaka, and Masami Yasuda.

#7079 Lattice Induced Decoherence in an Optical Lattice Clock
Roman Schwarz, Sören Dörscher, Ali Al-Masoudi, Marcin Bober, Richard Hobson, Stephan Falke, Uwe Sterr, Christian Lisdat.

#7091 Photoassociation Measurements to Evaluate Collisional Shifts in Strontium
Marcin Bober, Piotr Morzyński, Sławomir Bilicki, Mateusz Borkowski, Piotr Ablewski, Roman Ciuryło, Michał Zawada.

#7157 High-Precision Mid-IR Molecular Spectroscopy with Traceability to Primary Standards
Dang Bao An Tran, Rosa Santagata, Olivier Lopez, Sean Tokunaga, Michel Abgrall, Ya nn Le Coq, Rodolphe Le Targat, Won-Kyu Lee, Dan Xu, Paul-Eric Pottie, Benoit Darquié, Anne Amy-Klein.

#7162 The Features of Collective Level Shift and Line Broadening in a Fabry-Perot Microcavity and Near the Conducting Surface
Alexey Kuraptsev, Igor M. Sokolov.

#7187 Progress Report of an 27Al+ Ion Optical Clock
Ke Deng, Zetian Xu, Huang Che, Wenhao Yuan , Hongli Liu, Jie Zhang, Zehuang Lu.

#7188 Reduction of Thermal Noise Limit for Ultra-Stable Lasers with a Higher-Order Hermit-Gaussian Mode

Yanxia Ye, Xiaoyi Zeng, Xiaohui Shi, Zhiyuan Wang, Jie Zhang, Zehuang Lu.

#7191 Ultra-Stable Cryogenic Optical Resonator Composed of Sapphire and Silicon

Yunlong Sun, Xiaohui Shi, Yanxia Ye, Chunjie Yan, Jie Zhang, Zehuang Lu.

#7198 Towards an 27Al+ Based Optical Clock

Ksenia Khabarova, Ilia Zalivako, Ilia Se merikov, Alexander Borisenko, Nikolay Kolachevsky.

#7215 Optical Iodine Frequency References for Space

Markus Oswald, Thilo Schuldt, Klaus Döringsho ff, Vladimir Schkolnik, Tobias D. Schmidt, Johann Furthner, Markus Krutzik, Ulrich Johann, Achim Peters, Claus Braxmaier.

#7224 Two-Stage Stabilization Setup of the Laser Working on 729 nm for Spectroscopy with Cold 40Ca+ Ion

Tuan Minh Pham, Martin Cizek, Adam Lesundak, Vaclav Hucl, Lukas Slodicka, Petr Obsil, Radim Filip, J osef Lazar, Ondřej Cip.

#7231 Study on the Effect of Ule Rings on the Vibration Sensitivity of Ultra-Stable Optical Reference Cavities

Guanjun Xu, L. Zhang, L. Chen, Jie Liu, Dongdong Jiao, C. Jiang, X. Zhang, Ruifang Dong, Tao Liu.

#7233 The Compact Setup for Laser Cooling and High-Resolution Spectroscopy with Cold 40Ca+ Ions

Ondřej Cip, Adam Lesundak, Tuan Minh Pham, Vaclav Hucl, Martin Cizek, Jan Hrabina, Simon R erucha, Petr Obsil, Radim Filip, Lukas Slodicka, Josef Lazar.

#7240 Active Isolator Development of Ultra-Stable Narrow Linewidth Laser of Atomic Clock

Qing Li, Min Xiong, Lei Liu, Guanjun Xu.

#7032 Influence of Heating of Ion in a Trap on the Efficiency of Generalized Ramsey Schemes of Suppression of Probe-Induced Frequency Shift

Alexey V. Taichenachev, Sergey Kuznetsov, Valeriy I. Yudin, Nils Huntemann, Christian Sanner, Christian Tamm, Ekkehard Peik.

#7041 Technical Developments for Portable Optical Clocks

Nathan Gemmell, Callan Jobson, Matthias Keller.

#7064 Towards a Single-Ion Compact Optical Clock: Experimental Apparatus and Current Status

Marion Delehaye, Lucas Groult, Maël Souidi, Pierre-Yves Bourgeois, Jacques Millo, Emman uel Bigler, Yann Kersalé, Clément Lacroûte.

#7094 Two-Photon Spectroscopy of Hydrogen Molecular Ions for Precision Measurements of Fundamental Constants

Florin Lucian Constantin.

#7108 Thermal Noise Further Reduced Ultrastable Laser with Frequency Instability of 5×10^-16

Lulu Yan, Zhaoyang Tai, Yanyan Zhang, Pan Zhang, Wenyu Zhao, Xiaofei Zhang, Wenge G uo, Shougang Zhang, Haifeng Jiang.

#7111 Towards Compact Transportable Optical Clock Based on 171Yb+

Ilia Zalivako, Ksenia Khabarova, Ilia Semerikov, Alexander Boris enko, Ivan Sherstov, Sergei Bagayev, Alexey Lugovoy, Alexey Taichenachev, Sergei Chepurov, Nikolay Kolachevsky.

#7130 Reducing Blackbody Radiation Shift Uncertainty in Optical Lattice Clocks

Piotr Ablewski, Marcin Bober, Michał Zawada.

Timekeeping, Time & Frequency Transfer, GNSS Applications I Session

Session Type: Poster
Session Code: A2P-G
Location: Poster Area
Date & Time: Tuesday April 10, 2018 (14:00 - 16:00)
Chair: Pierre Waller

#7042 Experiments on 475 km of Spooled Fibre Link Comprising Two Different Amplification Techniques

Fei Meng, Alexander Kuhl, Thomas Waterholter, Gesine Grosche.

#7046 Preliminary Algorithms for Simulating and Analysing Microwave Link Data from the Atomic Clock Ensemble in Space (ACES) Mission

Setnam Shemar, Kath ryn Burrows, Hannah Collingwood.

#7049 Evaluation and Development of Optical Time Transfer (OTT) Links Between PTB and Deutsche Telekom

Łukasz Śliwczyński, Przemysław Krehlik, Jacek Kołodziej, Helmut Imlau, Horst Ender, Harald Schnatz, D irk Piester, Andreas Bauch.

#7057 GNSS Time Scales Analysis

Petr Bogdanov, Andrei Druz hin, Arkadii Tiuliakov, Tatiana Primakina.

#7062 GNSS Antenna Group Delay Characterization at the ESTEC Compact Test Range

Esteban Garbin, Piotr Krystek, Ricardo Piriz, Pierre Waller, Damiano Trenta, Luis Rolo, Pascale Defraigne, Bruno Bertrand.

#7068 Improvements on the UTC(IT) Timescale at INRIM

Marco Sellone, Roberto Costa, Alberto Mura, Giancarlo Cerretto, Marco Siccardi, Filippo Levi.

#7074 Comparison of Highly-Stable Optical Frequency Transfer in a Single Bidirectional and Double Unidirectional Fibers

Przem ysław Włodarczyk, Przemysław Krehlik, Łukasz Śliwczyński.

#7080 GNSS Antenna Multipath Effects

Giovanni Daniele Rovera, Michel Abgrall, Pierre Uhrich, Pascale Defraigne, Bruno Bertrand.

#7102 Study on Time Scale Algorithm of Hydrogen Maser Based on Minimum Error Theory

Meng Jiang, Shaowu Dong, Mojuan Yin, Wenjun Wu, Huijie Song, Lili Qu, Weixiong Wang.

#7103 Comparision of Two Methods of Time-Interval Measurement Based on SAWF and SAWDDL

Haifeng Wang, Xueyun Wang, Hongbo Wang, Hang Yi, Honglei Yang, Wenzhe Yang, Shuwe i Wang, Yong Xie, Shengkang Zhang.

#7127 Fiber-Based Traceability Chain for Molecular Spectrosopy at 5.8 µm

Cecilia Clivati, Simone Borri, Davide Calonico, Pablo Cancio Pastor, D avide D'Ambrosio, Paolo De Natale, Giacomo Insero, Massimo Inguscio, Filippo LevI, Gabriele Santambrogio.

#7133 First Experiments on Application of Rb Fountain Frequency Standards for TA(SU) Time Scale Maintenance

Igor Blinov, Alexander Boiko, Nikolai Kosheliaevskii, Ol'Ga Kupalova.

#7137 Passive Utilization of the TWSTFT Technique

Carsten Rieck, Per Jarlemark, Kenneth Jalde hag.

#7154 Real-Time Detection of Frequency Jumps in GNSS Satellite Clocks Using Stand-Alone Receiver

Wei Huang, Patrizia Tavella, Pascale Defraigne.

#7178 Air Pressure Dependence and Compensation of a Passive Hydrogen Maser

Harald Hauglin, Tim Dunker.

#7212 Evaluation of Optical Frequency Transfer via 500 km Fiber Links

Deng Xue, Qi Zang, Jie Liu, Dongdong Jiao, Xiang Zhang, Dan W ang, Ruifang Dong, Tao Liu.

#7230 Bidirectional Optical Amplifier Delivering High Gain

Josef Vojtech, Ondrej Havlis, Martin Slapak, Milosla v Hula, Vladimir Smotlacha, Martin Kolbe, Jan Radil.

#7232 Remote Atomic Clock Contribution to UTC(TP)

Vladimir Smotlacha, Alexander Kuna.

#7234 Stabilized Time Transfer Between CESNET and UFE

Vladimir Smotlacha, Josef Vojtěch.

#7008 Measuring the Mitigation of a Jamming Attack on a GPS Server at the National Physical Laboratory of Israel

Nadya Goldovsky, Omer Sharar.

#7026 Automatic Calibration of the Actively Stabilized Fiber-Optic Time Transfer

Przemysław Krehlik, Jacek Kołodziej, Łukasz Śliwczyński.

#7035 An Anti-Jamming System for GNSS Timing Applications

Jorge Querol, Ricardo Píriz, Esteban Garbin, Adriano Camps.

#7036 Evaluation of CGGTTS Time Transfer Using Multiple Software and GNSS Constellations

Kenneth Jaldehag, Per Jarlemark, Carsten Rieck.

Wednesday April 11th, 2018 - Program Schedule

Wednesday April 11th, 2018			
Plenary Session II			
9:00-10:20	Pierre Martinetti - *Researcher at the Mathematic department of the University of Genova* **On the thermodynamical origin of time** Location: Room AUDITORIUM		
10:20-10:50	*Coffee Break*		
	Lecture Session		
	AUDITORIUM	**SALA 150**	**CASA UGI**
11:00-12:30	B1L-A Optical Lattice Clocks II *Chr: Andrew Ludlow* Track: Optical Frequency Standards and Applications	B1L-B GNSS timing *Chr: Pierre Uhrich* Track: Timekeeping, Time and Frequency Transfer, GNSS Applications	B1L-C Down Conversion & Noise Measurement *Chr: Jean-Pierre Aubry* Track: Oscillators, Synthesizers, Noise, & Circuit Techniques
12:40-14:00	*Lunch*		
	Lecture Session		
	AUDITORIUM	**SALA 150**	**CASA UGI**
14:00-16:00	B2L-A Combs I *Chr: Yann Le Coq* Track:Optical Frequency Standards and Applications	B2L-B Nonlinear Effects in Devices & Oscillators *Chr: Thierry Laroche, Alexandre Reinhardt* Track:Materials, Resonators, & Resonator Circuits	B2L-C Cold Atoms Clocks & Interferometers *Chr: Arnaud Landragin* Track:Microwave Frequency Standards
16:00-16:20	*Coffee Break*		
	Lecture Session		
	AUDITORIUM	**SALA 150**	**CASA UGI**
16:20-18:00	B3L-A Exploring New Transitions *Chr: Davide Calonico* Track:Optical Frequency Standards and Applications	B3L-B Optical Links III *Chr: Gesine Grosche* Track:Timekeeping, Time and Frequency Transfer, GNSS Applications	B3L-C MEMS & NEMS Devices *Chr: Ashwin Seshia, Thomas Baron* Track:Sensors & Transducers

Social Dinner 08.00pm at Villa Sassi 20.00.

Lecture Session

Optical Lattice Clocks II Session

Session Type: *Lecture*
Session Code: B1L-A
Location: Auditorium
Date & Time: Wednesday April 11, 2018 (10:50 - 12:30)
Chair: Andrew Ludlow

10:50 Relativistic Geodesy with a Transportable Optical Clock

Jacopo Grotti, Silvio Bernd Koller, Sofia Herbers, Stefan Vogt, Ali Al-Masoudi, Sören Dörscher, Roman Schwarz, Sebastian Häfner, Uwe Sterr, Erik Benkler, Sebastian Koke, Alexander Kuhl, Thomas Waterholter, Gesine Grosche, Rodolphe Le Targat, Jérôme Lodewyck, Héctor Álvarez Martinez, Michel Abgrall, Etienne Cantin, Dan Xu, Olivier Lopez, Anne Amy-Klein, Paul-Eric Pottie, Heiner Denker, Christian Lisdat.

11:10 Dark Matter Searches Within the Intercontinental Optical Atomic Clock Network

Piotr Wcisło, Piotr Ablewski, Kyle Beloy, Sławomir Bilicki, Marcin Bober, Roger Brown, Robert Fasano, Roman Ciuryło, Hidekazu Hachisu, Tetsuya Ido, Jérôme Lodewyck, Andrew Ludlow, William McGrew, Piotr Morzyński, Daniele Nicolodi, Marco Schioppo, Mamoru Sekido, Rodolphe Le Targat, Peter Wolf, Xiaogang Zhang, Beata Zjawin, Michał Zawada.

11:30 VFC Chip with Comb for Narrow-Line Laser Cooling

John McFerran.

11:50 Exploiting Coherent Fiber Links with a Hg Optical Lattice Clock

Luigi De Sarlo, M. Favier, V. Cambier, J. Calvert, C. Guo, Jérôme Lodewyck, Héctor Álvarez-Martínez, Yann Le Coq, Rodolphe Le Targat, Etienne Cantin, Dan Xu, Olivier Lopez, Anne Amy-Klein, Giorgio Santarelli, Christian Chardonnet, Paul-Eric Pottie, Nils Huntemann, Christian Sanner, Richard Lange, Burghard Lipphardt, Christian Tamm, Ekkehard Peik, Roman Schwarz, Ali Al-Masoudi, Sören Dörscher, Christian Lisdat, Erik Benkler, Sebastian Koke, Alexander Kuhl, Thomas Waterholter, Gesine Grosche, Sébastien Bize.

12:10 Pushing Forward the Stability and Accuracy of Sr Optical Lattice Clocks

Grégoire Vallet, Eva Bookjans, Slawomir Bilicki, Rodolphe Le Targat, Jérôme Lodewyck.

GNSS timing Session

Session Type: Lecture
Session Code: B1L-B
BLocation: BSala 150
Date & Time: Wednesday April 11, 2018 (10:50 - 12:30)
Chair: Pierre Uhrich

10:50 The Galileo Time Service Provider: Design and Operational Key Elements

Ilaria Sesia, Giovanna Signorile, Thanh Tung Thai, Elena Cantoni, Concetta De Stefano, Patrizia Tavella, Marc Gandara, Pierre Louis Puech, Vincent Hamoniaux, Vickie Jacquard, Sebastien Capou, Tony Deboschere, Victor Lafon, Giovanna Chiara Rodi, Franco Fiasca, Alice Cernigliaro, Rocco Affinito, Federico Aricò, Giacomo Pantalone, Andrea Perucca, Marco Raimondi.

11:10 Phase Synchronization for 5G Using Mass Market GNSS Receivers

Zdenek Chaloupka, Lionel Ries, Andrea Samperi, Pierre Waller, Massimo Crisci

11:30 Galileo and GNSS Time Offsets

Giovanna Signorile, Ilaria Sesia, Pascale Defraigne, Patrizia Tavella

11:50 The operation and performance of Galielo on-board clocks

Pierre Waller, Marco Belloni. *** INVITED ***

Down Conversion & Noise Measurement Session

Session Type: Lecture
Session Code: B1L-C
Location: Casa UGI
Date & Time: Wednesday April 11, 2018 (10:50 - 12:30)
Chair: Jean-Pierre Aubry

10:50 Nonlinear Optoelectronic Down-Conversion and Phase Locking of mm-Wave and THz Signals – Invited

Mehdi Alouini, Antoine Rolland, Marc Brunel, Marc Vallet, Gael Kervella, Fréderic Van Dijk, Guillaume Ducournau, Jean-François Lampin, Goulc'Hen Loas, Ludovic Frein, Cyril Hamel.
*** INVITED ***

11:30 Optical-to-RF Frequency Division for Ultra-Low Noise Microwave Generation Using a Transfer Oscillator Method

Pierre Brochard, Stéphane Schilt, Thomas Südmeyer.

11:50 Direct Measurement of Cryogenic Sapphire Oscillators with Tracking DDSs and Two-Sample Covariance

Claudio Eligio Calosso, Francçois Vernotte, Vincent Giordano, Christophe Fluhr, Benoit Dubois, Enrico Rubiola.

12:10 Measuring Small Propagation Frequency Shifts and Fluctuations by Phase to Avoid Cross-Correlation Errors

Michael Underhill.

Combs I Session

Session Type: Lecture
Session Code: B2L-A
Location: Auditorium
Date & Time: Wednesday April 11, 2018 (14:00 - 16:00)
Chair: Yann Le Coq

14:00 Self-Controlled Offset-Free Er:Fiber Frequency Combs
Andreas Liehl, David Fehrenbacher, Philipp Sulzer, Alfred Leitenstorfer, Denis Seletskiy.

14:20 High Coherence Visible Comb from an Er Fiber Laser
Antoine Rolland, Peng Li, Marco Cassinerio, Jie Jiang, Martin Fermann.

14:40 Novel Methods for CEO Stabilization in Fiber Laser Frequency Combs
Kutan Gürel, Sargis Hakobyan, Valentin Johannes Wittwer, Nayara Jornod, Stéphane Schilt, Thomas Südmeyer.

15:00 Frequency Stability Transfer with a Fully Stabilized and a Transfer-Oscillator Optical Frequency Comb
Erik Benkler, Michele Giunta, Sofia Herbers, Thomas Legero, Dan Matei, Wolfgang Hänsel, Ronald Holzwarth, Uwe Sterr.

15:20 Progress on Development of Optical Frequency Combs at NTSC
Yanyan Zhang, Lulu Yan, Pan Zhang, Songtao Fan, Bingjie Rao, Xiaofei Zhang, Wenge Guo, Shougang Zhang, Haifeng Jiang.

15:40 Frequency Comb Stabilization of a 4 W, 50-fs Thin-Disk Laser Oscillator
Norbert Modsching, Clément Paradis, Pierre Brochard, Nayara Jornod, Kutan Gürel, Christian Kränkel, Stéphane Schilt, Valentin J. Wittwer, and Thomas Südmeyer.

Nonlinear Effects in Devices & Oscillators Session

Session Type: Lecture
Session Code: B2L-B
Location: Sala 150
Date & Time: Wednesday April 11, 2018 (14:00 - 16:00)
Chair: Thierry Laroche, Alexandre Reinhardt

14:00 Nonlinear Dynamics in MEMS Resonators
Steven Shaw. *** INVITED ***

14:40 Nonlinear Enhancement of Locking Range of Mutually Injection Locked Oscillators for Resonant Sensing Applications
Jérôme Juillard, Ali Mostafa, Pietro Maris Ferreira.

15:00 Hysteresis in Phononic Frequency Combs
Adarsh Ganesan, Ashwin Seshia.

15:20 Elastic Strain Engineering for Exceptional Mechanical Coherence
Amirhossein H. Ghadimi, Sergey A. Fedorov, Nils J. Engelsen, Mohammad J. Bereyhi, Ryan Schilling, Dalziel J. Wilson, Tobias J. Kippenberg.

Cold Atoms Clocks & Interferometers Session

Session Type: Lecture
Session Code: B2L-C
Location: Casa UGI
Date & Time: Wednesday April 11, 2018 (14:00 - 16:00)
Chair: Arnaud Landragin

14:00 Recent Progress of Development of Cesium Fountain Primary Frequency Standard NMIJ-F2
Akifumi Takamizawa, Shinya Yanagimachi, Ken Hagimoto, Iku Hirano, Takeshi Ikegami.

14:20 Stability Analysis and Continuous Operation of Rb Fountains for Timescale Generation
Luca Lorini, Konstantin Pavlenko, Sébastien Bize, Bruno Desruelle, Guillaume Stern, I. Doronin, Yuri Pavlenko, Igor Blinov.

14:40 LNE-SYRTE (Ultra) Cold Atom Gravimeter
Romain Karcher, Almazbek Imanaliev, Sébastien Merlet, Franck Pereira Dos Santos.

15:00 High Precision Test of Gravity with the MIGA Large Scale Atom Interferometer
Benjamin Canuel.

15:20 Atom Interferometry from Earth to Space
Waldemar Herr. *** INVITED** ***

Exploring New Transitions Session

Session Type: Lecture
Session Code: B3L-A
Location: Auditorium
Date & Time: Wednesday April 11, 2018 (16:20 - 18:00)
Chair: Davide Calonico

16:20 Spectroscopy of Trapped Antihydrogen in the ALPHA Experiment
Stefan Eriksson. *** INVITED ***

17:00 Quantum Logic Spectroscopy on an Optical Magnetic Dipole Transition in a Highly Charged Ion
Steven A. King, Tobias Leopold, Peter Micke, José Crespo López-Urrutia, Piet O. Schmidt

17:20 Towards Laser Excitation of the Th-229 Nuclear Clock Isomer
David-Marcel Meier, Johannes Thielking, Przemyslaw Glowacki, Maxim Okhapkin, Ekkehard Peik.

17:40 Atom Interferometry on Narrow Intercombination Transi-Tions of Alkali-Earth Atoms
Nicola Poli, Leonardo Salvi, Liang Hu, Guglielmo Tino.

Optical Links III Session

Session Type: Lecture
Session Code:B3L-B
Location: Sala 150
Date & Time: Wednesday April 11, 2018 (16:20 - 18:00)
Chair: Gesine Grosche

16:20 Milliradian Phase Comparison Between Optical Oscillators Across Turbulent Air
Laura Sinclair, Hugo Bergeron, William Swann, Esther Baumann, Jean-Daniel Deschênes, Nathan Newbury.

16:40 Effects of Atmospheric Turbulence on Optical Two-Way Time-Frequency Transfer Across Partially Reciprocal Free-Space Links
Martha Bodine, William Swann, Isaac Khader, Laura Sinclair, Esther Baumann, Jean-Daniel Deschenes, Nathan Newbury.

17:00 Two-Way Optical Phase Comparison at 10^-21 Level
Qi Zang, Qun Cao, Xue Deng, Jie Liu, Dongdong Jiao, Jing Gao, Xiang Zhang, Dan Wang, Guanjun Xu, Ruifang Dong, Tao Liu, Shougang Zhang.

17:20 Optical Frequency Transfer Across the Sea: Two Case Studies
Cecilia Clivati, Filippo Levi, Giuseppe Marra, Alberto Mura, Anna Tampellini, André Xuereb, Davide Calonico. *** INVITED ***

MEMS & NEMS Devices Session

Session Type: Lecture
Session Code: B3L-C
Location: Casa UGI
Date & Time: Wednesday April 11, 2018 (16:20 - 18:00)
Chair: Ashwin Seshia, Thomas Baron

16:20 Nanomechanical Resonators: Frequency Stability and Mass Spectrometry Applications
Sébastien Hentz, Marc Sansa, Shawn Fostner, Sergio Dominguez Medina, Martial De-foort, Marc Gély, Thomas Alava, Guillaume Jourdan, Christophe Masselon. *** INVITED ***

17:00 A-Si:H Thin-Film MEMS Resonators: Towards Mass Sensing Applications
Rui Pinto, Pedro Brito, Virginia Chu, João Conde.

17:20 Optimization of Low-Power Oscillator Topology for Frequency Modulated MEMS Inertial Sensors
Cristiano Rocco Marra, Alessia Maria Ruggieri, Paolo Minotti, Giorgio Mussi, Andrea Giovanni Bonfanti, Andrea L. Lacaita, and Giacomo Langfelder.

17:40 Design Optimization for Surface Acoustic Wave Devices Considering Simultaneously Apodization and Transverse Modes Effects in Mixed Matrix Approach

Thierry Laroche, Sylvain Ballandras, Marianne Sagnard, William Daniau.

Thursday April 12th, 2018 - Program Schedule

Thursday April 12th, 2018			
	Lecture Session		
	AUDITORIUM	**SALA 150**	
9:00 - 10:20	C1L-A Microfabricated Cells & Applications *Chr: Gaetano Mileti* Track: Microwave Frequency Standards	C1L-B White Rabbit & NTP *Chr: Carsten Rieck* Track:Timekeeping, Time and Frequency Transfer, GNSS Applications	
10:20 - 10:50	Coffee Break		
	Lecture Session		
	AUDITORIUM	**SALA 150**	**CASA UGI**
10:50 - 12:30	C2L-A Ion Optical Clocks *Chr: Jérôme Lodewyck* Track: Optical Frequency Standards and Applications	C2L-B Advanced GNSS *Chr: Pascale Defraigne* Track:Timekeeping, Time and Frequency Transfer, GNSS Applications	C2L-C Wave Propagation *Chr: Ventsislav Yantchev* Track:Materials, Resonators, & Resonator Circuits
12:30 - 14:00	Lunch		
	Poster Session		
14:00 - 16:00	C3P-D Materials for Resonators & Waveguides *Chr: Enrique Iborra*	C3P-E Microwave Frequency Standards II *Chr: Stephane Guerandel*	C3P-F Optical Frequency Standards & Applications II *Chr: Christian Lisdat*
	C3P-G Timekeeping, Time & Frequency Transfer, GNSS Applications II *Chr: Cecilia Clivati*	C3P-H Oscillators, Synthesizers, Noise, & Circuit Techniques *Chr: Jean-Pierre Aubry*	C3P-J Sensors & Transducers *Chr: Ventsislav Yantchev*
16:00-16:20	Coffee Break		
	Lecture Session		
	AUDITORIUM	**SALA 150**	**CASA UGI**
16:20 - 18:00	C4L-A Combs II *Chr: Thomas Südmeyer* Track: Optical Frequency Standards and Applications	C4L-B CPT & Double Resonance Clocks *Chr: Salvatore Micalizio* Track: Microwave Frequency Standards	C4L-C Timescales & Clocks *Chr: Pierre Waller* Track: Timekeeping, Time and Frequency Transfer, GNSS Applications

Lecture Session

Microfabricated Cells & Applications Session

Session Type: Lecture
Session Code: C1L-A
Location: Auditorium
Date & Time: Thursday April 12, 2018 (09:00 - 10:20)
Chair: Gaetano Mileti

09:00 Microsemi Chip Scale Atomic Clock (CSAC) Technical Status, Applications and Future Plans
Peter Cash, Will Krzewick, Paul Machado, Richard Overstreet, Mike Silveira, Dwayne Taylor, Xianli Zhang. *** INVITED ***

09:40 Gold Micro-Discs As Alkali Preferential Condensation Spots for Cell Clock Long-Term Frequency Improvement
Sylvain Karlen, Thomas Overstolz, Jean Gobet, Jacques Haesler, Fabien Droz, Steve Lecomte.

10:00 Low-Power Optical Frequency Standard Based on a Cavity-Enhanced Two-Photon Transition in a Rb Microfabricated Vapor Cell
Vincent Maurice, Zach Newman, Matt Hummon, Liron Stern, Leo Hollberg, John Kitching.

White Rabbit & NTP Session

Session Type: Lecture
Session Code: C1L-B
Location: Sala 150
Date & Time: Thursday April 12, 2018 (09:00 - 10:20)
Chair: Carsten Rieck

09:00 Observed Time Synchronization Performance Using the Network Time Security Protocol
Martin Langer, Kristof Teichel, Dieter Sibold, Rainer Bermbach.

09:20 Evaluation of White Rabbit for Time Service Distribution
Peter Whibberley, Elizabeth Laier English, Conway Langham, David Hicks, Simon Ashford.

09:40 DWDM Stabilized Optics for White Rabbit
Paul Boven.

10:00 Improved Systematic and Random Errors for Long-Distance Time-Transfer Using PTP White Rabbit
Anders Wallin, Mattia Rizzi, Guifré Molera Calvés, Thomas Fordell, Jyri Näränen.

Ion Optical Clocks Session

Session Type: Lecture
Session Code: C2L-A
Location: Auditorium
Date & Time: Thursday April 12, 2018 (10:50 - 12:30)
Chair: Jérôme Lodewyck

10:50 Comparisons of Single-Ion Yb+ and Cs Fountain Clocks for Searches for New Physics
Nils Huntemann, Christian Sanner, Richard Lange, Burghard Lipphardt, Johannes Rahm, Stefan Weyers, Christian Tamm, Ekkehard Peik.

11:10 Advances in the Uncertainty Evaluation of a 88Sr+ Single Ion Optical Clock
Pierre Dubé, Bin Jian, Amar Vutha.

11:30 Absolute Frequency Measurement of the 171Yb+ E3 Optical Clock Transition Using International Atomic Time
Rachel M. Godun, Charles F. A. Baynham, Jonathan M. Jones, Steven A. King, Peter B. R. Nisbet-Jones, Fred Baynes, Antoine Rolland, Patrick E. G. Baird, Kai Bongs, Patrick Gill, Gérard Petit, Helen Margolis.

11:50 Portable Atomic Clock Based on a Single Ca+
Callan Jobson, Nathan Gemmell, Matthias Keller.

12:10 Systematic Uncertainty Evaluation of an 27Al+ Quantum-Logic Clock
Samuel Brewer, Jwo-Sy Chen, David Hume, Aaron Hankin, Ethan Clements, Chin-Wen Chou, David Wineland, David Leibrandt.

Advanced GNSS Session

Session Type: Lecture
Session Code: C2L-B
Location: Sala 150
Date & Time: Thursday April 12, 2018 (10:50 - 12:30)
Chair: Pascale Defraigne

10:50 High Accuracy Continuous Time Transfer with GPS IPPP and T2L2
Julia Leute, Gérard Petit, Pierre Exertier, Etienne Samain, Giovanni Daniele Rovera, Pierre Uhrich.

11:10 Enhanced Techniques for Absolute Calibration of GNSS Receiver Chains
Esteban Garbin, Piotr Krystek, Ricardo Piriz, Pierre Waller, Pascale Defraigne, Bruno Bertrand.

11:30 Investigation and Study on Combination of Multiple GNSS Techniques Using a New GNSS Time Transfer Receiver Developed at Nim
Kun Liang, Aimin Zhang, Zhiqiang Yang, Ye Wang.

11:50 Galileo Gravitational Redshift Test with Eccentric sATellites: the GREAT Experiment
Pacôme Delva, N. Puchades. *** INVITED ***

Wave Propagation Session

Session Type: Lecture
Session Code: C2L-C
Location: Casa UGI
Date & Time: Thursday April 12, 2018 (10:50 - 12:30)
Chair: Ventsislav Yantchev

10:50 Breaking Lorentz Reciprocity with Spatio-Temporal Modulation
Andrea Alù, Dimitrios L. Sounas, Ahmed Kord. *** INVITED ***

11:30 Enhanced Performance Surface Acoustic Resonance (SAR) Lab-on-a-Chip Sensor
Kiryl Kustanovich, Ventsislav Yantchev, Aldo Jesorka.

11:50 A High Q Length-Extension Mode Quartz Resonator for MEMS Oscillator and Time-Frequency Applications
Paul Chapellier, Pierre Lavenus, Bernard Dulmet, Olivier Le Traon.

12:10 Influence of the Acoustic Energy Distribution on the in-Liquid Sensitivity of Thin Film Electroacoustic Resonators
Teona Mirea, Jimena Olivares, Marta Clement, Enrique Iborra.

Combs II Session

Session Type: Lecture
Session Code:C4L-A
Location: Auditorium
Date & Time: Thursday April 12, 2018 (16:20 - 18:00)
Chair: Thomas Südmeyer

16:20 Effect of Pulse Duration Fluctuation on the Photodetection of a Train of Pulses from an Optical Frequency Comb
Xiaopeng Xie, Romain Bouchand, Michele Giunta, Wolfgang Hänsel, Matthias Lezius, Ronald Holzwarth, Giorgio Santarelli, Yann Le Coq.

16:40 Cross-Spectrum Approach to Absolute Timing Jitter Measurement of Mode-Locked Lasers
Alexis Casanova, Benoit Trophème, Antoine Courjaud, Giorgio Santarelli.

17:00 Transportable Ultra-Low Noise Photonic Microwave Synthesizer
Michele Giunta, Xiaopeng Xie, Wolfgang Hänsel, Maurice Lessing, Matthias Lezius, Marc Fischer, Romain Bouchand, Daniele Nicolodi, Pierre-Alaine Tremblin, Abhay Joshi, Shubo Datta, Giorgio Santarelli, Yann Le Coq, Ronald Holzwarth.

17:20 Injection Locking of Dissipative Kerr Solitons

Wenle Weng, Erwan Lucas, Hairun Guo, Grigory Lihachev, Valery E. Lobanov, Michael L. Gorodetsky, Tobias J. Kippenberg.

17:40 Spatially-Multiplexed Solitons in Optical Microresonators

Erwan Lucas, Grigory Lihachev, Michael L. Gorodetsky, Tobias J. Kippenberg.

CPT & Double Resonance Clocks Session

Session Type: Lecture
Session Code: C4L-B
Location: Sala 150
Date & Time: Thursday April 12, 2018 (16:20 - 18:00)
Chair: Salvatore Micalizio

16:20 Demonstration of Vapor Temperature Stabilization Using an Atomic Isoclinic-Point Thermometer

Travis Driskell, James Camparo.

16:40 Microwave Field Amplitude Stabilization Using Ramsey Spectroscopy Signal

Michele Gozzelino, Salvatore Micalizio, Filippo Levi, Aldo Godone, Claudio Eligio Calosso.

17:00 Understanding Light Shifts in CPT Clocks

James Wesley Pollock, Valeriy I. Yudin, Moshe Shuker, Maxim Yu. Basalaev, Alexey V. Taichenachev, Xiaochi Liu, John Kitching, and Elizabeth A. Donley.

17:20 Ramsey-Mode Rb Cell Clock Demonstration with a 3D-Printed Microwave Cavity

William Moreno, Christoph Affolderbach, Anton Ivanov, Tomislav Debogovic, Matthieu Pellaton, Anja Skrivervik, Emile de Rijk, and Gaetano Mileti.

17:40 A CPT-Based Cs Cell Atomic Clock Using Auto-Balanced Ramsey Spectroscopy

Moustafa Abdel Hafiz, Gregoire Coget, Michael Petersen, Emeric De Clercq, Stephane Guérandel, Thomas Zanon-Willette, Claudio Eligio Calosso, Rodolphe Boudot.

Timescales & Clocks Session

Session Type: Lecture
Session Code: C4L-C
Location: Casa UGI
Date & Time: Thursday April 12, 2018 (16:20 - 18:00)
Chair: Pierre Waller

16:20 Optimal Traceability to the SI Second Through TAI

Gérard Petit, Gianna Panfilo.

16:40 The Study of Using Hydrogen Maser Ensemble to Steer UTC(TL)

Shinn Yan Lin.

17:00 Modified Primary Time and Frequency Standard of VNIIFTRI

Sergei Donchenko, Andrei Schipunov, Igor Blinov, Nikolay Koshelyaevsky, Igor Noretz, Yury Smirnov, Vitaly Palchikov.

17:20 Clock Anomaly Detection Using L1 Norm Optimization

Masato Hirano, Kazumune Hashimoto, Fumimaru Nakagawa, Tetsuya Ido, Yuko Hanado, Shuichi Adachi.

17:40 Practical Approach to the Use of Linear Quadratic Gaussian Control for Time Scale Signals

Konstantin Mishagin, Vladimir Lysenko, Svetlana Podogova, Sergey Medvedev.

Poster Session

Materials for Resonators & Waveguides Session

Session Type: Poster
Session Code: C3P-D
Location: Poster Area
Date & Time: Thursday April 12, 2018 (14:00 - 16:00)
Chair: Enrique Iborra

#7054 Microwave Acoustic Properties of Diamond Based HBAR at Low Temperatures
Boris Sorokin, Gennady Kvashnin, Andrey Novoselov, Anton Shipilov.

#7182 Poling Conditions for PZT Thin Film-Based Resonators
Alexandre Reinhardt, Guillaume Tochou, Selimen Bena hmed, Amy N'Hari, Marie Bousquet, Henri Sibuet.

#7183 Reactive Sputtering of AlScN Thin Films with Variable Sc Content on 200 mm Wafers
Marta Clement, Valeriy Felmetsger, Enrique Iborra.

#7220 Photonic Damascene Process with Reflow Step for Ultra-Smooth Si3N4 Waveguides
Martin Pfeiffer, Junqiu Liu, Tiago Morais, Bahareh Ghadiani, Tobias Kippenberg.

#7227 Oscillator with Electrostrictive Resonator
Thomas Baron, William Daniau, Gilles Martin, Valérie Soumann, Roland Salut, Sylvain Ballandras.

Microwave Frequency Standards II Session

Session Type: Poster
Session Code: C3P-E
Location: Poster Area
Date & Time: Thursday April 12, 2018 (14:00 - 16:00)
Chair: Stephane Guerandel

#7050 FBAR-Based 3.4 GHz Oscillator Without Frequency Multiplications Aiming for an Integrated Atomic Clock Chip
Motoaki Hara, Yuichiro Yano, Masatoshi Kajita, Shinsuke Hara, Akifumi Kasamatsu, Masaya Toda, Hiroyuki Ito, Takahito Ono, Tetsuya Ido.

#7105 Electromagnetically Induced Tansparency Ramsey Sequence Interference CANCELLED
Zhengfeng Hu, Chengpu Liu, Yuzhu Wang.

#7113 Design Status of the Rb Pop Space Clock for GNSS Applications

Pier Giorgio Arpesi, Jacopo Belfi, Marina Gioia, Nicholas Marzoli, Romano Romani, Adalberto Sapia, Michele Gozzelino, Claudio Eligio Calosso, Filippo Levi and Salvatore Micalizio.

#7125 The Important Phase Phenomena in Quantum Frequency Standard

Wei Zhou, Qianqian Guo, Shen Zhang, Wei Shang, Shihao Zhao

#7148 CPT Atomic Clock Based on an Antirelaxation-Coated Cell and Quadrature-Signal Method of the Light Shift Cancellation

Stepan Igna tovich, Vladislav Vishnyakov, Anton Makarov, Mikhail Skvortsov, Nikolai Kvashnin, Vadim Vasiliev, Vadim Vasiliev, Sergei Atutov, Denis Brazhnikov, Valeriy I. Yudin, Alexey V. Taichenachev, Sergei Bagayev.

#7163 Influence of an Optical Dense Medium at the Ramsey Method of CPT Resonance Detection

Konstantin Barantsev, Igor M. Sokolov, Gavriil Voloshin, Andrey Litvinov, Evgeniy Popov.

#7168 Interleaved Cold Atom Gyroscope

Denis Savoie, Matteo Altorio, Bess Fang, Leonid Sidorenkov, Remi Geiger, Arnaud Landragin.

#7209 ACES Mission Status

Luigi Cacciapuoti, Rudolf Much, Claudio Moratto, Johannes Kehrer, Marc Peter Hess, Achim Helm, Thomas Niedermaier, François-Xavier Esnault, Didier Massonnet, Wolfgang Schaefer, Jacques Pittet, Didier Goujon, Pascal Rochat, Philippe Laurent, Peter Wolf, Frederic Meynadier, Ivan Prochazka, Anja Schlicht, Ulrich Schreiber, Christophe Salomon.

#7238 Mid-Term Contributions to the Frequency Noise of the Pulsed CPT Clock at SYRTE

Francois Tricot, Emeric De Clercq, Stephane Guérandel.

#7019 Mesoscopic Physics in Vapor-Phase Atomic Systems: Collision-Shift Gradients and the 0-0 Hyperfine Transition

Andrew Hudson, James Camparo.

Optical Frequency Standards & Applications II Session

Session Type: Poster
Session Code: C3P-F
Location: Poster Area
Date & Time: Thursday April 12, 2018 (14:00 - 16:00)
Chair: Christian Lisdat

#7038 Transfer Technique Based, Continuously Operating Frequency Comb for Frequency Metrology in the Optical and Microwave Domain

Burghard Lipphardt , Erik Benkler, Stefan Weyers, Johannes Rahm, Nils Huntemann, Christian Sanner, Richard Lange, Christian Tamm, Ekkehard Peik.

#7055 1.14 Um Clock Transition in Tm

Artem Golovizin, Elena Kalganov a, Dmitry Tregubov, Ksenia Khabarova, Vadim Sorokin, Nikolay Kolachevsky.

#7058 Characterization of a Reference Cavity for a Transportable Strontium Optical Clock

Sofia Herbers, Sebastian Häfner, Erik Benkler, Uwe Sterr, Christian Lisdat.

#7083 Development of Cryogenic Silicon Cavity Stabilized Laser

Baptiste Marechal, Santerelli Falzon Tetsing, Jacques Millo , Cyrus Rocher, Clément Lacroûte, Enrico Rubiola, Yann Kersalé.

#7089 Preliminary Progress in the Development of an Operational Calcium Thermal Beam Clock at the U. S. Naval Observatory

Jennifer Taylor, Bryan Hemingway, Tom Swanson, Steve Peil.

#7099 Measurement of the Infrared Magic Wavelengths for the 40Ca+ Ion Clock Transition

Yao Huang, Huaqing Zhang, Baolin Zhang, Mengyan Zeng, Hua Guan, Kelin Gao.

#7106 Status Report on Two (171)^Yb Optical Lattice Clocks at KRISS

Huidong Kim, Myoung-Sun Heo, Won-Kyu Lee, Dai-Hyuk Yu, Sa ng Eon Park, Chang Yong Park.

#7134 Beyond the First Frequency Measurement of the Magnesium Lattice Clock at the IQ Hannover

Waldemar Friesen-Piepenbrink, Steffen Rühmann, Dominika Fim, Klaus Zipfel, Nandan Jha, Steffen Sauer, Sebastian Häfner, Thomas Legero, Wolfgang Ertmer, Uwe Sterr, and Ernst Rasel.

#7141 Telecomm Laser Standard for Time and Frequency Transfer

Jan Hrabina, Lenka Pravdova, Martin Cizek, Ondřej Cip.

#7144 Micro-Integrated Ultra-Narrow Linewidth Diode Laser Module with Resonant Optical Feedback from a Monolithic Cavity

Max Sc hiemangk, Bassem Arar, Ahmad Bawamia, Heike Christopher, Mandy Krüger, Christian Kürbis, Wojciech Lewoczko- Adamczyk, Christoph Pyrlik, Robert Smol, Andreas Wicht, Achim Peters, Günther Tränkle.

#7146 Development and Research of the System for Long Time Continues Frequency Measurements Based on Sr87 Clock Transition

Oleg Berdasov, A rtem Gribov, Sergei Strelkin, Denis Sutyrin, Gleb Belotelov, Evgeniya Stelmashenko, Sergei Slusarev.

#7153 Kinetics of Atoms Cooled on Clock Transitions: the Behavior of Energy and Momentum

Roman Ilenkov, Oleg Prudnikov, Alexey V. Taichenachev, Valeriy I. Yudin.

#7171 Development of the Strontium Optical Lattice Clock at National Time Service Center

Mojuan Yin, Qinfang Xu, Yebing Wang, Jie Ren, Yang Guo, Hong Chang.

#7189 An Atomic Clock with a Measurement Stability at 10^-18 Level

Qiang Wang, Yige Lin, Ye Li, Zhen Sun, Baike Lin, Tao Yang, Tia nchu Li, Zhanjun Fang.

#7193 Investigation of Methane Based Microwave Reference Oscillator for Cs/Rb Fountains

Alexander Shelkovnikov, Alexander Boiko, Alexey Kireev, Dmitry Tyurikov, Anton Ta usenev, Alexander Konyashchenko, Mikhail Gubin.

#7199 Tool Kit for a Portable Optical Clock

Sruthi Viswam, Jonathan Bass, Marc o Menchetti, Qasim Obaid, Jonathan M. Jones, David Morris, Peter Molony, Matthew Aldous, Markus Gellesch, Kai Bongs and Yeshpal Singh.

#7200 CO2-Filled Hollow-Core Fiber Reference Gas Cells for Laser Frequency Stabilization at 2 µm

Renaud Matthey, Benoît Debord, Kenny Hey-Tow, Fan Yang, Stéphane Schilt, Fetah Benabid, Luc Thévenaz, Thomas Südmeyer.

#7210 Low Thermal Noise Fabry-Perot Cavities for Ultrastable Lasers

Nikita Zhadnov, Konstantin Kydeyarov, Ilia Semerikov, Ksenia Khabarova, Nikolay Kolachevsky.

Timekeeping, Time & Frequency Transfer, GNSS Applications II Session

Session Type: Poster
Session Code: C3P-G
Location: Poster Area
Date & Time: Thursday April 12, 2018 (14:00 - 16:00)
Chair: Cecilia Clivati

#7029 On-Line Optimization of Time and Frequency Fiber Optic Links Exploiting Bi-Directional Amplifiers

Łukasz Śliwczyński, Przemysław Krehlik, Karol Salwik, Jacek Kołodziej.

#7043 1880 km Looped Optical Fibre Link Combining Two Amplification Techniques

Thomas Waterholter, Gulnara Vishnyakova, Alexander Kuhl, Ronald Holzwart h, Gesine Grosche.

#7071 The Research of UTC(NTSC) and UTC(SU) Joint Time Scale Algorithm

Shanshan Bai, Shaowu Dong, Shuhong Zhao, Lulu Yan, Lili Qu.

#7075 Timing Jitter Characterization of Dual-Comb System via TWTFT Method

Honglei Yang, Shengkang Zhang, Huan Zhao, Hongbo Wang, Xueyun W ang, Haifeng Wang, Hang Yi, Wenzhe Yang, Shuwei Wang.

#7095 Improvements of Fibre Brillouin Amplifier Modules for Optical Frequency Dissemination

Alexander Kuhl, Thomas Waterholter, Sebastian Koke, Gesine Grosche.

#7115 Final Characterization of InLambda Delay Standards for Supplementary Time Interval Comparison

Albin Czubla, Piotr Szterk, Roman Osmyk, Borut Pinter, Rado Lapuh, Uros Dragonja, Jurij Tratnik.

#7123 Analysis of Intersatellite Frequency Transfer

Bethany Kroese, Gabriele Giorgi, Christoph Günther.

#7124 A Recursive Clock Anomalies Detector with Double Exponential Smoothing

Valerio Formichella, Patrizia Tavella.

#7143 A Simple High-Performance Remote-Maser Concept

Thomas Fordell, Anders Wallin.

#7172 Multi-GNSS Time Transfer with CGGTTS-V2E

Pascale Defraigne, Katrijn Verhasselt.

#7181 Time-Frequency Analysis of Atomic Clock Anomalies

Lorenzo Galleani.

#7203 The H2020 European Project CLONETS: Clock Services Over Optical-Fibre Networks in Europe

Davide Calonico, Cecilia Clivati, Filippo Levi, Przemysław Krehlik, Łukasz Śliwczyński, Jiri Dostal, Jan Radil, Vladimir Smotlacha, Radek Velc, Josef Vojtěch, Mauro Campanella, Ondřej Číp, Simon Rerucha, Ronald Holzwarth, Maurice Lessing, Sarah Saint-Jalm, Fabiola Camargo, Bruno Desruelle, Jean Lautier-Gaud, Elizabeth Laier English, Jochen Kronjäger, Peter Whibberley, Fratišek John, Milan Šnajder, Jiří Štefl, Paweł Nogaś, Robert Urbaniak, Artur Binczewski, Wojbor Bogacki, Krzysztof Turza, Gesine Grosche, Harald Schnatz, Emilie Camisard, Nicolas Quintin, Javier Diaz, Trinidad García, Eduardo Ros, Alessandro Galardini, Alwyn Seeds, Zhen Yang, Anne Amy-Klein , Eva Bookjans, Paul-Eric Pottie, and Philip Tuckey.

#7208 High-Precision Long-Haul Time Transfer Between Multi Stations Over Field Fiber Link

Faxi Chen, Kan Zhao, Xu Zhou, Tao Liu, Shougang Zhang.

#7214 Phase-Coherent Transfer of Optical Frequency Between ISI CAS and CESNET

Martin Cizek, Lenka Pravdova, Vaclav Hucl, Simon Rerucha, Jan Hrabina, Mic hal Jelinek, Bretislav Mikel, Vladimir Smotlacha, Ondrej Havlis, Josef Vojtech, Josef Lazar, Ondrej Cip.

#7216 Kalman Filter Simulation and Characterization of BDS Satellite Clock

Bin Wang, Junping Chen, Binghao Wang.

#7223 Real Like Transmission Lines for Sagnac Correction Study

Martin Šlapák, Josef Vojtěch.

#7051 Study on BeiDou All-in-View Time Transfer

Jihai Zhang, Wei Guang, Wenjun Wu, Lulu Yan, Wei Li, Haibo Yuan, Shaowu Dong.

#7015 Carrier-Phase Two-Way Satellite Frequency Transfer Between BIRMM and NIM

Shuwei Wang, Xueyun Wang, Haifeng Wang, Zhiqiang Yang, Wenzhe Yang, Hongbo Wang, Shengkang Zhang.

#7179 The INRIM Timing Performance Monitoring Facility

Ilaria Sesia, Giovanna Signorile, Franco Fiasca, Valerio Formichella, Patrizia Tavella.

Oscillators, Synthesizers, Noise, & Circuit Techniques Session

Session Type: Poster
Session Code: C3P-H
Location: Poster Area
Date & Time: Thursday April 12, 2018 (14:00 - 16:00)
Chair: Jean-Pierre Aubry

#7186 A Low Phase Noise Microwave Frequency Synthesizer Based on Parameters Optimized NLTL for Cs Fountain Clocks

Wenbin g Li, Yuanbo Du, Hui Li, Zehuang Lu.

Sensors & Transducers Session

Session Type: Poster
Session Code: C3P-J
Location: Poster Area
Date & Time: Thursday April 12, 2018 (14:00 - 16:00)
Chair: Ventsislav Yantchev

#7005 SAW Temperature Sensor with Mirror Topology

Ivan Antcev, Sergey Bogoslovsky, Gennadiy Sa pozhnikov, Sergei Zhgoon, Alexander Shvetsov

#7006 Choice of SAW Humidity Sensor Coatings

Ivan Antcev, Sergey Bogoslovsky, Mikhai l Derkach, Gennadiy Sapozhnikov, Sergei Zhgoon

#7017 Analysis of Resonant Sensors Based on Mutually Injection Locked Oscillators Beyond the Critical Duffing Amplitude

Jérôme Ju illard, Ali Mostafa, Pietro Maris Ferreira

#7056 Effect of Dipping in Liquids on the Resonance Characteristics of a Backward-Wave-Type Trapped-Energy Resonator

Ken Yamad a, Koji Ito

#7119 Geometric Scale Factor Stabilization of a Large Frame Ring Laser Gyroscope

Fabio Stefani, Nicolo Beverini, Giorgio Carelli, Angela Di Virgilio, Umberto Gia comelli, Enrico Maccioni

#7190 1 Finding the Upper Mass Limit Until Which Gravimetric Sensors Preserve Their Original TCF and Sensitivity

Teona Mirea, Marta Clement, Jimena Olivares, Enrique Iborra

Exhibitors

Carmel Instruments, LLC is a leading manufacturer of precision time and frequency measurement instruments for research and automated test applications. Carmel's products are in use worldwide by major research laboratories such as NIST, Jet Propulsion Lab and the US Naval Observatory, by semiconductor manufacturers for production testing of millions of devices on a 24 hour basis, and others.

www.carmelinst.com ***Exhibition Table 8***

Cycle GmbH was founded with the mission of building innovative ultrafast technology for science and industry applications.
We are producing world-leading timing equipment that synchronizes RF and optical equipment to each other with sub-femtosecond resolution. Key developments for these technologies started more than a decade ago at MIT and have been improved at Deutsches Elektronen-Synchrotron (DESY). Sub-femtosecond synchronization across several kilometers has been demonstrated [1] and is currently being commercialized. Cycle GmbH, a DESY spinoff company founded by Prof. Franz X. Kaertner and other scientists, holds the exclusive license to commercialize the key synchronization technologies from his research at MIT.

www.cyclelasers.com ***Exhibition Table 23***

Cristal Innov , a team of crystal growth experts with the support of LIP and EZUS Lyon, for project management high tech building and industrial equipments

Services and products

- ✓ High tech facilities and crystal growth equipments for R&D&Innovation projects
- ✓ Co-development process in crystal micro-machining
- ✓ High grade piezoelectric crystals and components for high performance devices
- ✓ 4. European project (H2020) and FabLab (TechnoFab) management.

www.cristalinnov.com ***Exhibition Table 11***

IMRA America, Inc. is dedicated to creative research and innovation leading to the development of essential technologies for industrial use. Our history as the oldest and most experienced femtosecond fiber laser company reflects the successful implementation of breakthrough technologies. IMRA continues to expand its capabilities, from fundamental research to commercial laser products and full-featured laser processing solutions. With strong product development and engineering competencies, IMRA continues to lead the industry with high volume manufacturing capability and rigorous quality control.

www.imra.com ***Exhibition Table 9***

Lange Electronic GmbH, founded in 1977, develops, manufactures and distributes high precision time & frequency systems worldwide.
Besides this we represent the Positioning Technology branch of Spirent Communications Plc. in the field of GNSS simulation, Masterclock (precision timing and network synchronization solutions) and Oktal-SE, a leading mathematical company doing 3D simulation via ray-tracing and several other methods in the areas of RF and radar simulation.
Our products are used in aerospace and on board of ships, in scientific experiments, in time laboratories and testing facilities e.g. the Aviation Gate in Braunschweig as well as in banks and insurance companies. The products on display are found in research and science as well as in development and testing of GNSS receivers/systems.

PikTime Systems: area of expertise

- ✓ Designing and manufacturing scientific equipment for long-distance precise atomic clocks comparison (time transfer systems),
- ✓ Development of time based products and services (navigation, security, data and document exchange, time stamping),
- ✓ Advisory on precise time and time scales,
- ✓ Time & frequency software and algorithms,
- ✓ Designing and execution of complete time laboratories on a turn-key basis.

www.lange-electronic.de

Exhibition Table 20

www.piktime.com

Laser Quantum is a world-class manufacturer of revolutionary solid-state and ultrafast laser systems. Our products lead the industry in performance specifications, reliability, compactness and operational lifetime. They have been used in ground-breaking research, and continue to push boundaries of science. You will find Laser Quantum lasers in laboratories worldwide and used in diverse applications including attosecond physics, forensics and genomics due to the wide range of wavelengths and powers we offer. Our wealth of experience, together with our passionate team, mean we are committed to providing you with a service and laser system that exceeds your expectations.
We have recently launched our first complete 1GHz frequency comb, an exceptional supercontinuum typ.1uW per mode with easy access to VIS and NIR ranges, and will be showcasing its capabilities at the European Time and Frequency Forum. For more information please visit our website.

www.laserquantum.com ***Exhibition Table 4***

Excitement is not measurable. Light is. Menlo Systems, a leading developer and global supplier of instrumentation for high-precision metrology, was founded in 2001 as a spin-off of Max Planck Institute for QuantumOptics, with the foremost aim to commercialize optical measurement technologies and make it available to newly emerging application fields. Menlo Systems maintains a strong bond to co-founder Theodor W.Hansch, who pioneered precision laser techniques.
Known for the Nobel Prize-winning optical frequency comb technology, the Munich-based company offers complete solutions based on ultrafast lasers and synchronization electronics. Applications for our products and solutions span from research laboratories to truly industrial tasks. The patented technology is recognized by global laser manufacturers to whom we deliver OEM solutions for integration into cutting-edge products.

www.menlosystems.com ***Exhibition Table 18***

Microsemi, the world leader in precise time solutions, sets the world's standard for time by offering solutions to generate, distribute and apply precise time for communications, aerospace/defence, IT infrastructure and metrology industries. Customers use Microsemi's advanced timing algorithms, atomic clocks and frequency reference technologies to build more reliable and highly efficient networks.

www.microsemi.com ***Exhibition Table 7***

M Squared is a leading developer of photonic and quantum technologies, harnessing the power of light to drive society changing innovation.
The tools it designs and manufactures are used in collaboration with Nobel Prize-winning scientists, the world's top universities and innovative manufacturers.
From idea, to lab, to real life – the company plays a part in every step of the journey towards bringing new solutions to market. Its light-based applications are used in a number of fields, including quantum technology, biophotonics and chemical sensing. When it comes to industry, they are utilised in advanced manufacturing, oil and gas research, space technology and the medical sector – where partnerships have led to breakthroughs in areas as diverse as dementia research, cancer diagnosis, whisky maturation and realising novel quantum sensors and quantum information systems.
Founded in Scotland, M Squared has offices across the UK, Europe and the USA, serving its international customer base. Its contribution to science and innovation has been recognised with the Queen's Award for Enterprise in Innovation as well as International Trade and the Institute of Physics Innovation Award. It has also featured in the Deloitte Technology Fast 50 and The Sunday Times Tech Track and Export Track 100.

www.m2lasers.com ***Exhibition Table 3***

Muquans proposes a complete portfolio of high performance solutions dedicated to metrological applications:

- ✓ An absolute quantum gravimeter capable of measuring gravity with a relative accuracy of 10^-9, dedicated to various applications in geophysics.
- ✓ An atomic clock, which provides time reference signal offering relative stability and accuracy close to 10^-15 and dedicated to time metrology applications.
- ✓ Laser and optical solutions dedicated to atom cooling, trapping and quantum manipulation.
- ✓ Optical repeaters dedicated to high performance transfer of optical frequencies along fiber links.

Muquans is a spin-off from two academic laboratories (LP2N and SYRTE) specialized in high precision measurements based on quantum manipulation of cold atoms. The technology developed by Muquans therefore benefits from all the experience and know how resulting from more than 15 years of academic research.

www.muquans.com ***Exhibition Table 21***

NEL Frequency Controls is a technology leader in the development and manufacture of leading edge frequency control products. Customers choose NEL to supply the optimal solution for applications requiring crystal oscillators with challenging performance specifications such as ultra low phase noise, ultra low power, and ultra high frequency capability. NEL's research and product development efforts support next generation customer applications that push performance boundaries in system speed, bandwidth, resolution, accuracy, and power consumption. Our customers benefit from our broad, low cost product offering, which reflects globally competitive frequency control solutions. Customer technologists can rely on NEL for total technical support in selecting the best frequency control solution for their application.

www.nelfc.com ***Exhibition Table 10***

As European distributor network, Optoprim serves research and industrial photonics markets. Anywhere photons are we offer solutions from source to the end control and data acquisition. With our customers we define the most suitable equipments, standard or customized, we install and service them, providing technical support. Optoprim's aim is to develop long term relationships with his principals and his customers. Established since 1994, Optoprim has grown up year after year and plays todays a major role in the photonic industry.

www.optoprim.com ***Exhibition Table 6***

Syrlinks designs and manufactures high-end products and solutions for the following markets :

- ✓ Space : radiocommunication systems and positioning equipment for low earth orbit satellites (TTC transceivers, high data rate transmitters, GNSS receivers)
- ✓ Defense : electronic warfare equipment and embedded positioning systems easy to deploy for operational units on the battlefield
- ✓ Safety : miniature distress beacons for companies who want to integrate a Save And Rescue functionality into their existing products

Syrlinks has all the skills required in the following technical areas(Electronics, Radio Frequency, Signal Processing, Software, Mechanical, ...) and also has the necessary resources in its manufacturing facility toproduce small series of high-value equipment.

www.syrlinks.com ***Exhibition Table 19***

For over seventy years, SAES Group has been the leading supplier of UHV and XHV solutions based on the Non-Evaporative Getter (NEG) technology for a variety of industrial and research applications. These solutions include compact NEG pumps with a large pumping speed for active atmospheric gases and, in particular, hydrogen, without generating vibrations or magnetic fields. In 2011, SAES Group introduced the PATENTED NEXTorr® pump, a revolutionary product that combines the NEG and sputtering ion pump technologies on one single flange. These pumps are widely used in a variety of UHV and XHV systems, particularly in the Atom Trap segment and in atomic clocks

www.saesgroup.com ***Exhibition Table 2***

Leader in aeronautical and military programs, the SPHEREA group develops innovative know-how and expertise. SPHEREA specialised in the design and realisation of modular testing solutions for the entire life cycle of complex and critical electronic, microwave, optronic and mechatronic systems.
Our main missions are to provide lasting, innovative solutions and to accompany our Clients throughout their projects in order to guarantee their satisfaction.
Noise XT is one of the most experienced company in the world regarding Phase Noise. Being about frequency synthesizers or Phase Noise analyzers, our expertise can certainly help you achieve performance goals or solve issues.
Since 1992, our continuous innovation on low phase noise design made us highest performance provider on the market. Our customers are tipically in the Defense, Space, Telecommunication or Time and Frequency community.

www.spherea.com/en
www.noisext.com

Exhibition Table 22

Founded in 2006 in Neuchatel, Switzerland, T4Science is a leading designer and manufacturer of a full range of advanced, cost-effective and high-performance maser clock solutions. Its products are used in a wide variety of scientific applications and in time and frequency industry.

Products

The iMaser™ is a high-performance, compact Active Hydrogen MASER. It features advanced phase noise and short term stability for high-precision Frequency & timing applications like VLBI, Deep space tracking, National Timing/Frequency Station, Navigation…

Passive Hydrogen Maser offers long term reference with excellent stability and price.

Services

We offer a complete set of first-class services over the product lifecycle for total customer satisfaction. These services include: Supply & Installation, Training, Remote & On-Site Maintenance and On-Site Support.

Founded in 1995 in Neuchatel, Switzerland, Spectratime designs, manufactures and markets a full range of high-performance, low-cost crystal, rubidium and maser sources, smart integrated GPS or GNSS reference clocks, and clock testing systems. Its products are used in a wide variety of applications, including telecommunications, defense, navigation, instrument, broadcasting, and space. The company is a recognized leader in the industries it serves and distributes its products globally through Spectratime's sales offices in Europe, Asia, and United States.

www.t4science.com

Exhibition Table 12,13

www.spectratime.com

TimeTech GmbH was set up in 1990 as a spin off from the University of Stuttgart's Institute for Navigation. The team here specializes in intercontinental time transfer and very precise satellite positioning services.

TimeTech is a reliable provider of high-tech space systems and ground stations equipment and instruments for precise frequency and time transfer. TimeTech is mainly export-oriented with customers in Europe, North America, Asia and Australia. TimeTech's business areas are subdivided into project Business and Products. Since November 2012, TimeTech has embarked upon providing systematic and regular two-way link calibration service to our customers primarily the national metrological laboratories.

Project business encompasses scientific studies as well as hardware projects, related to Galileo, Aces, Rosetta, Venus Express and other space projects and ground stations. The Product Business takes care of development, production, testing and installing equipment and complex systems for orbit determination and positioning as well as high precision synchronization and transmission of time and frequency.

www.timetech.de

Exhibition Table 16,17

TOPTICA develops and manufactures high-end laser systems for scientific and industrial applications. The portfolio includes diode lasers, ultrafast fiber lasers, terahertz systems and frequency combs. TOPTICA's products provide an ultra-broad laser wavelength coverage: 190 nm to 0.1 THz (corresponding to 3 mm). They enable a big variety of demanding applications in quantum optics, spectroscopy, biophotonics, microscopy, test & measurement, as well as materials inspection.
OEM customers, scientists, and over a dozen Nobel laureates all acknowledge the world-class exceptional specifications of TOPTICA's lasers, as well as their reliability and longevity. Founded in 1998 near Munich (Germany), TOPTICA became one of the leading laser photonics companies by aiming for, and consistently delivering high-end specifications. TOPTICA's diode lasers are appreciated for excellent coherence, wide tuning range and ideal beam profiles.
With "A Passion for Precision" TOPTICA's 230 employees take pride in developing customized systems. In close collaboration with several universities and institutes, latest scientific discoveries are frequently incorporated into commercial products. With a global distribution network, TOPTICA provides exceptional service worldwide.

www.toptica.com ***Exhibition Table 14,15***

Zurich Instruments is a test and measurement company based in Zurich, Switzerland, developing and selling measurement instruments and delivering customer support in key markets around the world, either directly or with carefully selected partners. We are a growing, independent and founder-led company.

Zurich Instruments makes cutting-edge instrumentation for scientists and technologists in advanced labs who are passionate about phenomena that are often notoriously difficult to measure. Our core offering includes lock-in amplifiers, phase-locked loops, arbitrary waveform generator, impedance analyzers, digitizers and boxcar averagers.

We believe that system integration is good. We believe that system integration leads to significant time savings, reduced lab setup complexity, efficient workflows and reliable, accurate measurements.

www.zhinst.com ***Exhibition Table 5***

Conference Venues Map

The National Automobile Museum
Congress Centre “Carlo Biscaretti di Ruffia”
Corso Unità d’Italia, 40, 10126 Torino

Casa UGI
Corso Unità d’Italia, 70, Torino
Casa UGI is located just across the square from the Museum of Automobiles and will be used for some parallel sessions.

EXHIBITION CENTRE MAP, The National Automobile Museum

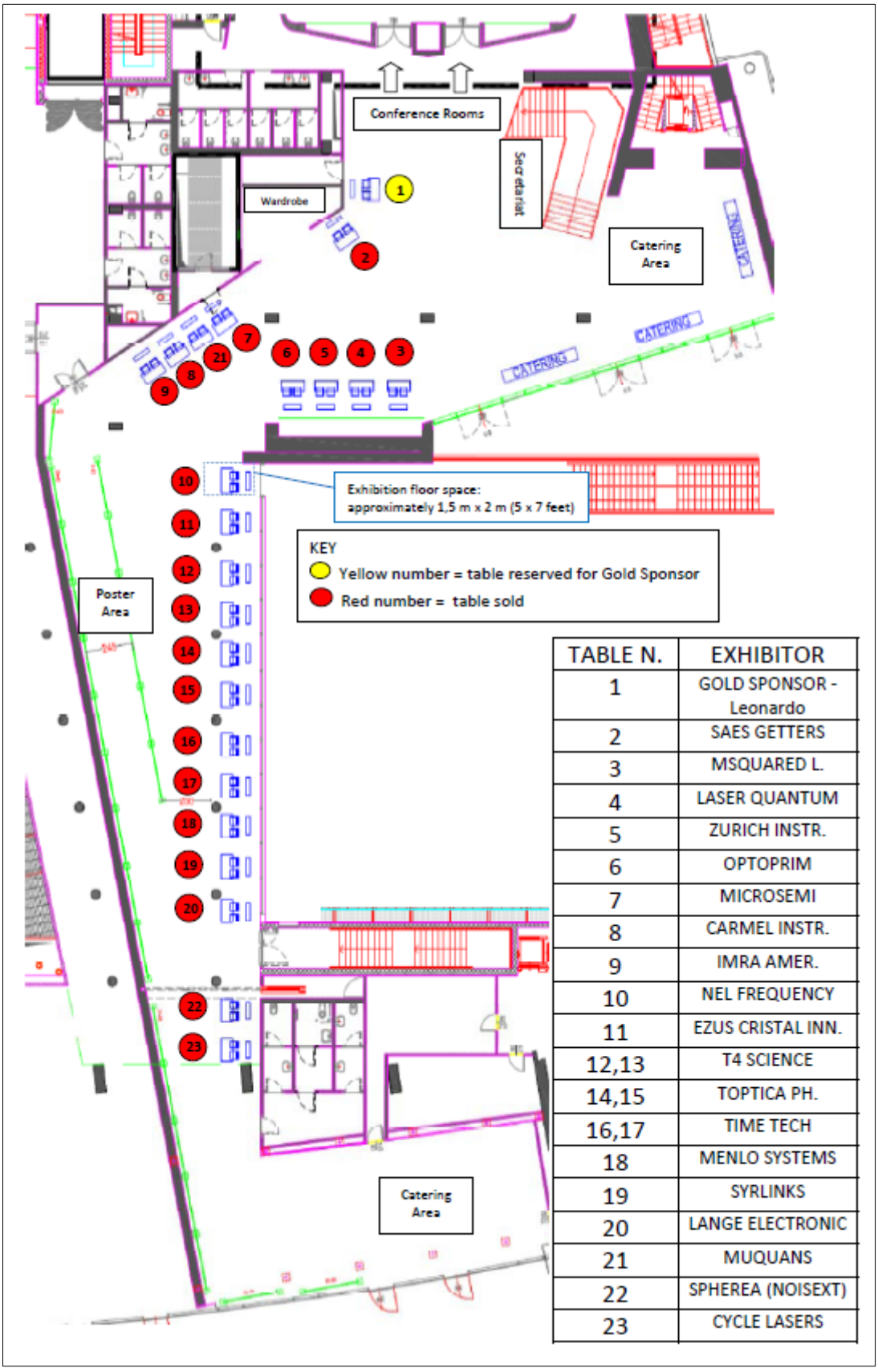

TABLE N.	EXHIBITOR
1	GOLD SPONSOR - Leonardo
2	SAES GETTERS
3	MSQUARED L.
4	LASER QUANTUM
5	ZURICH INSTR.
6	OPTOPRIM
7	MICROSEMI
8	CARMEL INSTR.
9	IMRA AMER.
10	NEL FREQUENCY
11	EZUS CRISTAL INN.
12,13	T4 SCIENCE
14,15	TOPTICA PH.
16,17	TIME TECH
18	MENLO SYSTEMS
19	SYRLINKS
20	LANGE ELECTRONIC
21	MUQUANS
22	SPHEREA (NOISEXT)
23	CYCLE LASERS

CASA UGI MAP

Casa UGI
Corso Unità d'Italia,
70, Torino

Casa UGI is located just across the square from the Museum of Automobiles and will be used for some parallel sessions.

Presenters who will have a speech at Casa UGI have to pre-load their presentation in the slide center set up at CASA UGI.

Please note that at CASA UGI, there will be only a VGA connection, HDMI connection could not be provided.

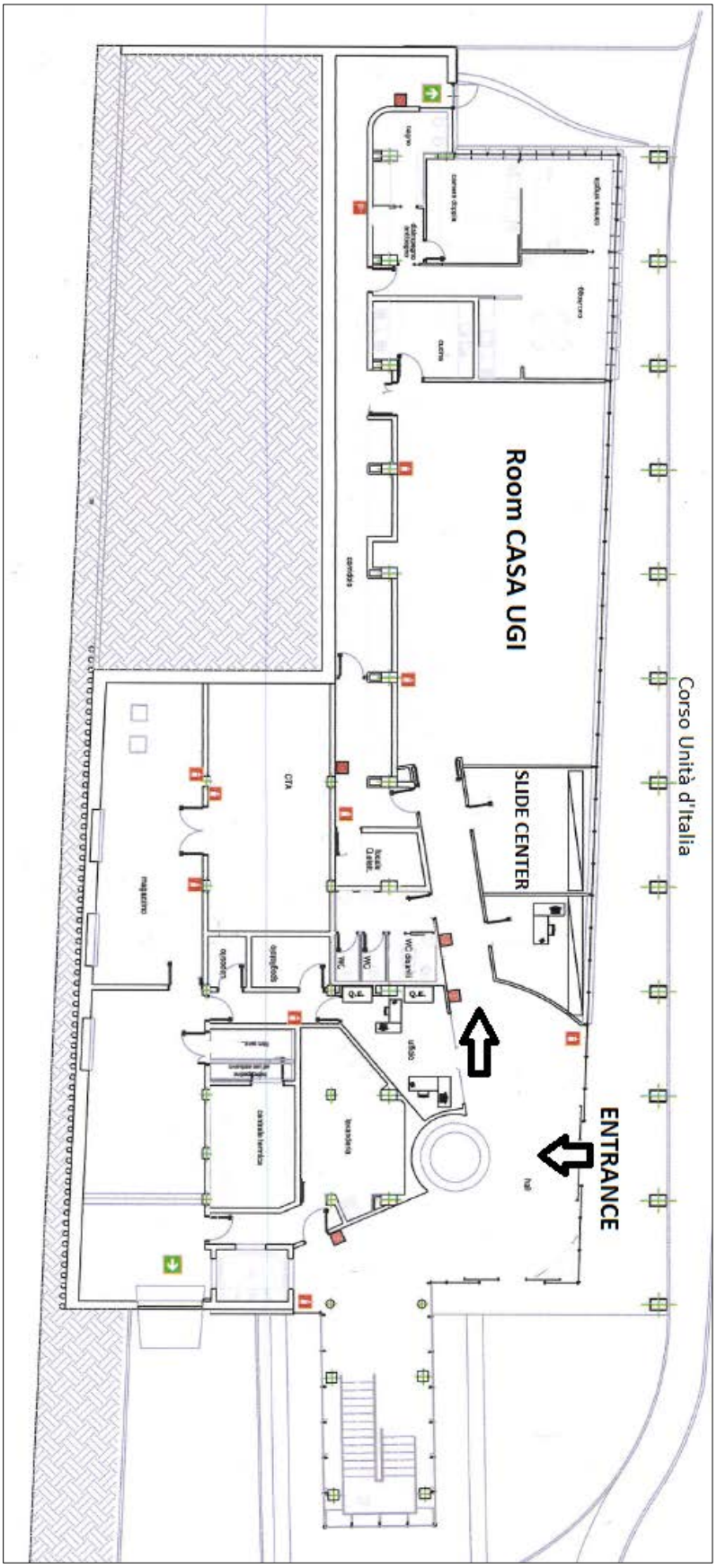

2019 Joint IFCS-EFTF Conference

April 14 – 18, 2019

Caribe Royale Resort, Orlando, Florida

- Co-General Chairs: Debra Coler, Gaetano Mileti
- Co-JTPC Chairs: Robert Lutwak, Davide Calonico
- Co-Awards Chairs: James Camparo, Pierre Waller
- Co-Academic Chairs: Rob Candler, François Vernotte
- Finance Chair: Dan Stevens
- Tutorials Chair: John Kitching
- Exhibits Chairs: Craig Nelson, Wolfgang Schäfer

Plenary Speaker

Plenary Session I
Tuesday 10th April, 09:00 - 10:20

Viviana Fafone
Professor of Physics at "Tor Vergata" university of Rome

‘The Physics of (and with) Virgo and LIGO’

abstract
Recent gravitational-wave observations by LIGO and Virgo not only confirm the century-old prediction of Einstein, but also herald the beginning of a new era of astronomy. This talk will summarize the current status of gravitational-wave detectors, the observations carried out, what we learned from them, and prospects for the near future.

bio
Viviana Fafone is professor of physics at "Tor Vergata" university in Rome. Her research activity is mainly devoted to experiments for gravitational wave detection, with interests also for the physics of cosmic background radiation.
She is participating in the Virgo experiment, the largest European laser interferometer, located in Cascina (Pisa). Back in September 2015 he was in the team that detected the first gravitational.
In 1993 she received the prize for young physicists of the Italian Physic Society; in 2002, the prize of the General Relativity Italian Society; in 2016, for the first observation of gravitational waves, she also won the Special Breakthrough Prize in Fundamental Physics and the Gruber Cosmology Prize.
She gave lectures all around the world and she is the author of more than 200 papers on international journals.

Plenary Speaker

Plenary Session II
Wednesday 11th April, 09:00 - 10:20

Pierre Martinetti
Researcher at the Mathematic department of the University of Genova

‘On the thermodynamical origin of time’

abstract

Even though the ”flight of time” may be the most universally shared experience, physics is not able to explain in a coherent manner what time is.
For Newton, time is an absolute parameter; for Einstein, it is a geometrical quantity that depends on the observer. In quantum mechanics, it is an abstract parameter in the space of observables. We shall see how thermodynamics combined with advanced mathematics share a new light on the nature of time, which, hopefully might be meaningful in a still to come theory of quantum gravity.

bio

Pierre Martinetti obtained his PhD in 2001 in the Centre de Physique Théorique at Marseille University, where he worked, among others, with Carlo Rovelli.
He is now a researcher at the Mathematic department of the University of Genova. His research is mainly focused on the understanding of the geometry of space and time, in particular using technics of non-commutative geometry. He is also interested in the so-called thermal time hypothesis of Alain Connes and Carlo Rovelli that he applied to various examples in algebraic quantum field theory.

Electromagnetically-Induced Absorption Resonances for Applications in Quantum Sensing and Optical Switches

D.V. Brazhnikov[1,2], S.M. Ignatovich[1], V.I. Vishnyakov[1], M.N. Skvortsov[1]

[1]Institute of Laser Physics SB RAS, Novosibirsk, Russia
[2]Novosibirsk State University, Novosibirsk, Russia

Email: brazhnikov@laser.nsc.ru

Electromagnetically induced absorption was discovered in 1997 [1]. It manifests itself as a steep decrease in transparency of a vapour cell when the two-photon (Raman) frequency detuning equals to zero. In contrast to the electromagnetically-induced-transparency effect (EIT) resulted from the coherent population trapping phenomenon (CPT) [2], the EIA resonances have not attracted much attention for real applications. The main reason consists in the problem of obtaining a high-contrast and, at the same time, sufficiently narrow nonlinear resonances of EIA.

Recently, we have tested experimentally a new scheme for observing the EIA resonances with high contrast and narrow width using 2.5-cm size rubidium vapour cell (all details are presented in [3]). The scheme seemed to us very interesting for further study, because it can be relevant for many applications in optics and photonics. Here we focus on a small vapour cell (a glass-blown bulb of about 0.7-cm diameter) filled with Cs atoms and neon buffer gas. The probe-wave transmission vs. magnitude of applied longitudinal magnetic field is studied. We consider two key regimes of light-atom interaction. The first regime provides a high level of EIA contrast with respect to a very wide "Doppler" pedestal. Let us call it as a “relative contrast”. Our experiments revealed the relative contrast of more than 100%. The second regime results to high contrast values (> 100%) with respect to a background level of transmitted probe-wave power (we call it as a “technical contrast”). In both regimes the resonances show FWHM as low as several kHz.

The high-contrast magneto-optical resonances observed can be used for designing various compact and efficient optical devices, which are controlled by weak magnetic fields (~ mG). For example, the first regime considered can be interesting for optical communications and all-optical quantum information processing. The second regime is attractive from the quantum magnetometry view of point (for example, for Hanle magnetometers [4]). It should be noted that the achieved levels of contrast together with relatively small FWHM make the EIA resonances absolutely competitive with respect to the EIT ones.

The work was supported by the Russian Science Foundation (project no. 17-72-20089).

References

[1] A.M. Akulshin et al., “Electromagnetically induced absorption and transparency due to resonant two-field excitation of quasidegenerate levels in Rb vapor”, Phys. Rev. A, vol. 57, pp. 2996–3002, 1998.

[2] E. Arimondo, “Coherent population trapping in laser spectroscopy”, in Progress in Optics, vol. XXXV, pp. 257-354, 1996.

[3] D.V. Brazhnikov et al., “High-quality electromagnetically-induced absorption resonances in a buffer-gas-filled vapour cell”, Laser Phys. Lett., to be published.

[4] E. Alipieva et al., “Potential of the single-frequency CPT resonances for magnetic field measurement”, IEEE Trans. Instrum. Meas., vol. 54, pp. 738–741 (2005).

A CPT-based Cs cell atomic clock using auto-balanced Ramsey spectroscopy

Moustafa Abdel Hafiz[1], Grégoire Coget[1], Michael Petersen[1], Emeric de Clercq[2], Stéphane Guérandel[2], Thomas Zanon-Willette[3], Claudio Eligio Calosso[4]
Rodolphe Boudot[1]

[1] FEMTO-ST, CNRS/UBFC/ENSMM, 26 rue de l'épitaphe 25000 Besançon, France
[2]LNE-SYRTE, Observatoire de Paris, 61 avenue de l'observatoire 75014 Paris, France
[3]LERMA, Observatoire de Paris, Paris, France
[4]INRIM, Strada delle Cacce 91, 10135 Torino, Italy

Email: rodolphe.boudot@femto-st.fr

We report the in-progress development of a high-performance compact coherent population trapping (CPT) Cs cell microwave atomic clock. This clock combines the optimized push-pull optical pumping technique [1,2] and a pulsed interrogation method, yielding the detection of high-contrast and narrow Ramsey-CPT fringes. In EFTF2017, the clock fractional frequency stability was reported to be $2.3 \times 10^{-13}\ \tau^{-1/2}$ up to 100 s averaging time, limited on short term by laser AM noise and after 100 s by light-induced frequency shift effects [3].
Over the last months, advanced electronics dedicated to stabilize the laser power in the pulsed regime have been developed. Moreover, the thermal isolation of the clock optical setup has been greatly reinforced. Thanks to these efforts, the clock short-term fractional frequency stability has been improved to the level of $1.4 \times 10^{-13}\ \tau^{-1/2}$ up to 100 s, but still limited on longer time scales by light shift effects.
To tackle this issue, we investigate the application of the auto-balanced Ramsey (ABR) interrogation protocol, recently proposed in [4], to our 3-level system CPT-based atomic clock. The latter interrogation protocol is found to reduce the sensitivity of the clock transition frequency to laser power variations, compared to the usual Ramsey-CPT case.
Combining this method and improvements previously described, the Allan deviation of the clock has been preliminary improved at the level of 6×10^{-15} at 2000 s averaging time, representing an improvement by a factor 33 compared to our best previously reported results [3]. These performances tend to demonstrate that the achievement of low drift CPT-based atomic frequency references using hot vapor cells is possible.
Several tests are under progress to improve further the clock frequency stability performances. This includes the recent implementation on this CPT clock of an ultra-low phase noise microwave frequency synthesizer [5], combined with a high-performance FPGA-based electronics system, for piloting the clock experiment [6]. This also includes the further investigation and characterization of the ABR-CPT protocol. Latest results will be shown at the conference.

References

[1] Y.-Y. Jau et al., Phys. Rev. Lett., 93, p. 160802-1-4 (2004).
[2] X. Liu et al., Phys. Rev. A. **87**, 013416 (2013).
[3] M. Abdel Hafiz et al., Journ. Appl. Phys. 121, 104903 (2017).
[4] C. Sanner et al., arXiv preprint arXiv :1707.02630 (2017).
[5] B. Francois et al., Rev. Sci. Instr. 86, 094707 (2015).
[6] C. Calosso et al., Generalized electronics for compact atomic clocks, Proceedings IFCS-EFTF2017, Besançon (2017).

Miniature Cs vapor cells and atomic clocks in FEMTO-ST

Rémy Vicarini, Vincent Maurice, Moustafa Abdel Hafiz, Ravinder Chutani, Sylwester Bargiel, Serge Galliou, Nicolas Passilly, Christophe Gorecki, Rodolphe Boudot

[1] FEMTO-ST, CNRS/UBFC/ENSMM, 26 rue de l'épitaphe 25000 Besançon

Email: christophe.gorecki@femto-st.fr, nicolas.passilly@femto-st.fr, rodolphe.boudot@femto-st.fr

The present paper aims to give an overview on MEMS Cs cell technology and CPT-based clocks activities performed in FEMTO-ST over the last ten years.
Our MEMS Cs vapor cell technology, using post-sealing laser activation of a Cs pill dispenser, will be briefly presented [1-2]. Different buffer gas or buffer gas mixtures, using generally Ne buffer gas, have been proposed to cancel the temperature dependence of the Cs clock frequency around a desired inversion temperature [3]. More recently, the use of a cesium dispensing paste has been proposed and studied in detail [4]. The latter avoids the delicate manipulation of numerous individual pills during the cell wafer development and is expected to be more suitable with the mass production of such MEMS cells. The cell technology developed in FEMTO-ST has been fully transferred to a MEMS foundry and manufacturer industrial partner, whose facilities allows the production of about 500 microcells on 6-inch wafers. Some first statistics on this production will be given.
Two automated dedicated setups, developed in FEMTO-ST for tests of MEMS Cs cells, will be presented. The first one is used to perform Cs activation and linear spectroscopy of multiple buffer-gas filled MEMS cells at the wafer-level. The second setup is a specific CPT clock setup dedicated to measure the contribution onto the clock long-term fractional frequency stability of the buffer gas permeation process through the cell windows [5-6]. Such tests, under progress with various MEMS Cs cells using borofloat glass or alumina-silicate glass (ASG), including industrial cells, will be reported.
Laboratory-prototype microcell-based Cs cell atomic clocks will be presented. These clocks use VCSELs tuned on the Cs D_1 line [7]. The typical clock fractional frequency stability is measured to be $2.5 \times 10^{-11}\ \tau^{-1/2}$ up to 500 s averaging time and better than 2×10^{-11} at 10^5 s (without drift removal). A detailed short-term and mid-term stability budget, at 1 s and 1 day averaging time respectively, will be reported. The implementation of advanced electronics stabilization loops has been tested to improve the clock long-term stability.

References

[1] : A. Douahi et al., Elec. Lett. 43, 5, 34-35 (2007).
[2] : M. Hasegawa et al., Sensors Actuators Phys. A 167, 2, 594-601 (2011).
[3]: O. Kozlova et al., Phys. Rev. A 83, 062714 (2011) ; D. Miletic et al., Elec. Lett. 46, 15 (2010); E. Kroemer et al., Opt. Express 23, 14, 18373 (2015).
[4]: V. Maurice et al., Appl. Phys. Lett. 110, 164103 (2017).
[5]: S. Abdullah et al., Appl. Phys. Lett. 106, 163505 (2016).
[6]: A. T. Dellis et al., Opt. Lett. 41, 12, 2775-2778 (2016).
[7] : E. Kroemer et al., Appl. Opt. 55, 31, 8839 (2016).

SAW Temperature Sensor with Mirror Topology

Ivan Antcev[1], Sergey Bogoslovsky[1], Gennadiy Sapozhnikov[1], Sergei Zhgoon[2], Alexander Shvetsov[2]

[1]JSC "Radar-mms", St Petersburg, Russian Federation
[2]National Research University "MPEI", Moscow, Russian Federation

Email: zhgoon@ieee.org

Passive wireless surface acoustic wave (SAW) sensors find applications in monitoring equipment for various purposes. One of the main directions for improving SAW sensors is to increase the range of operation. In the conditions of practical application, the echo signals reflected from nearby buildings and other obstacles have a significant effect on the receiving channel of the reader. This justifies the need to provide an initial signal delay of at least 2-3 μs. It is traditional to use the time delay to measure the temperature. Besides achieving greater interrogation distances, the aim of this work is to increase the amount of information that can be obtained from the sensor.

We describe a SAW temperature sensor based on the principles of mirror topology that were successfully used in SAW force sensors [1]. The design of sensors with a mirror topology assumes that there is a significant difference in variation of SAW propagation velocity with temperature in two different substrates (Fig. 1, top). The gratings realize the required type of the sensor impulse response (an example of the impulse responses of individual substrates is shown in Fig. 1, bottom). Since in the time domain the minimum values of the impulse response of one substrate correspond to the maximum values of the impulse response of the other substrate, then with different SAW velocity variation on different substrates, the response signal (convolution of the interrogating signal and of the combined impulse response) will be different at different temperatures. Thus, a change in SAW velocity will not only lead to a change in the delay time, but also to a change in the envelope and internal structure of the response signal. The search for optimum piezoelectric materials showed that it is preferable to use two different cuts of lithium niobate (Y-Z-cut and 128°Y-X-cut). The achieved measurement distance with a 1.8 μs long interrogation pulse and 10 mW average power exceeded 30 m at 433 MHz. Measurement accuracy in the range of -50 to 50 °C was better than ±5°C.

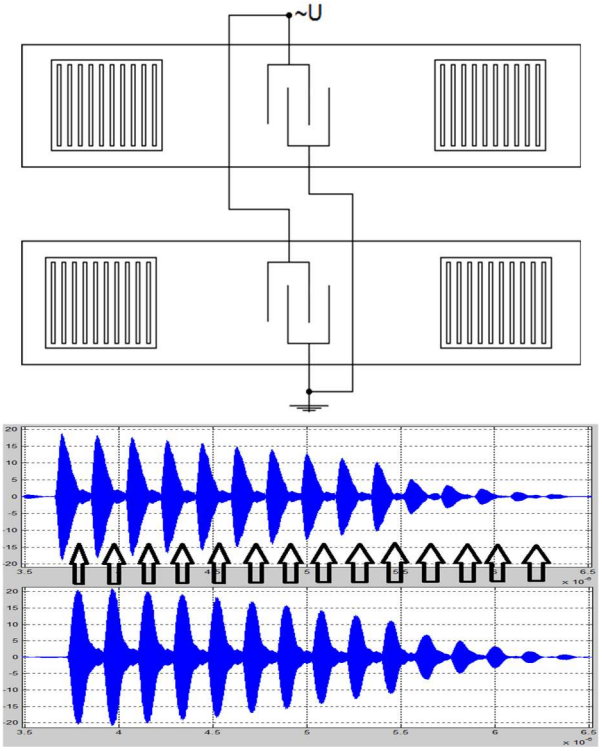

Fig. 1: Temperature sensor design (top) and impulse response of individual substrates (bottom).

References

[1] I. Antcev, S. Bogoslovsky, G. Sapozhnikov, S. Zhgoon. "SAW force sensor based on reflective delay line quasi-mirror topology", IEEE Int. Ultrasonics Symp. Proc., pp. 53-56, 2015

Choice of SAW Humidity Sensor Coatings

Ivan Antcev[1], Sergey Bogoslovsky[1], Mikhail Derkach[1], Sergei Zhgoon[2], Gennadiy Sapozhnikov[1]

[1]JSC "Radar-mms", St Petersburg, Russian Federation
[2]Department, National Research University "MPEI", Moscow, Russian Federation

Email: zhgoon@ieee.org

Among chemical gas sensors humidity sensors are the simplest and the most demanded. Very thin sensitive layers deposited on the surface of SAW resonators were investigated (ST-Quartz was used as substrate). The thickness of the layers did not exceed several percent of the wavelength at the operating frequency of the device. The humidity sensitivity and hysteresis of several organic and inorganic sensitive coatings were studied at different temperatures, the reproducibility and stability of the results were analyzed. The following materials were applied by centrifugation and subjected to heat treatment: Nafion polymer (Nafion); polybenzoxazole polymer; silicate films of the general composition nP_2O_5 * SiO_2; single-layer and multilayered carbon nanotubes (CNTs); polymethyl methacrylate (PMMA); PMMA with CNT; polymer Nafion with CNT. Based on the results of this study, the polymer Nafion was selected.

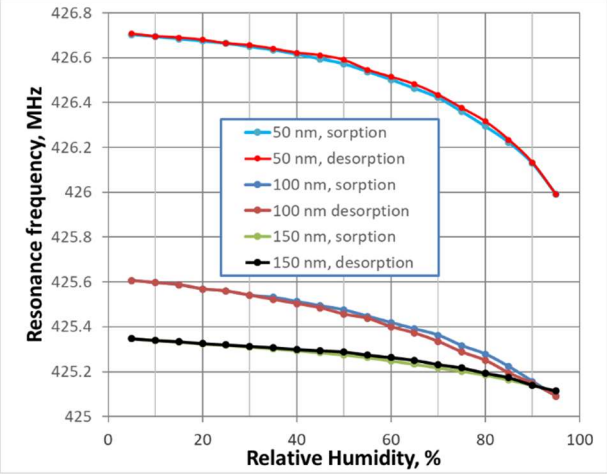

Fig. 1: Frequency dependence on relative humidity for different thicknesses of Nafion film.

Comparing resonators with three different thicknesses of the deposited Nafion polymer film (50, 100 and 150 nm) has shown that the larger is the thickness, the higher is the initial frequency offset from the initial frequency of the resonator at 434 MHz (Fig. 1). This required topology modifications to compensate for the frequency change due to film deposition. The plot of the resonance frequency variation with relative humidity - demonstrates that the resonance frequency sensitivity to humidity increases with decreasing coating thickness. It was also found that the hysteresis and the sensitivity of the relative humidity measurement varied with temperature - with the increase in air temperature the hysteresis decreased from ± 2 % RH at 0 ° C to ± 1% RH at 60 ° C, and the sensitivity to relative humidity increased from 4.5-5.0 kHz /% RH at 0 ° C to 6.5-7.0 kHz /% RH at 60 ° C for 434 MHz resonators. This behavior is consistent with the existence of two mechanisms of the SAW velocity sensitivity to the sorption of molecules.

Measurements with Nafion films thinner than 150 nm revealed that the resonator impedance reduction induced by humidity moderate increase started to decrease back to initial value with further humidity increase towards the values approaching 100%. This experimental feature has proven to be very useful for wireless sensor interrogation setup operation, as it allowed to maintain the impedance matching conditions in the electrical circuit of the antenna connection to the sensor and thus to reduce the readout and interrogation distance sensibility on the potential impedance mismatch induced by humidity changes. A conclusion was made that for Nafion polymer, the recommended layer thickness should not exceed 100 nm for operation at 434 MHz.

Cold-atom-based commercial microwave clock at the 10^{-15} level

Ramon Szmuk[1], Bruno Pelle[1], David Holleville[2], Bruno Desruelle[1]

[1]Muquans, Institut d'Optique d'Aquitaine, rue François Mitterrand, F-33400 Talence
[2]LNE-SYRTE, 61 avenue de l'Observatoire, F-75014 Paris

Email: ramon.szmuk@muquans.com

Microwave clocks have reached their best short-term [1] and long-term stabilities [2], as well as their best accuracy [1], with cold atoms based fountain clocks. So far, these results have required laboratory-size experiments, but current efforts are underway to develop more compact and fully autonomous setups for space [3] or civil applications.
Our objective is to propose the first commercially available atomic clock that can reach the 10^{-15} level. With a second generation prototype, we have already demonstrated a short-term fractional frequency uncertainty of $3 \times 10^{-13}\, 1/\sqrt{\tau}$, and a final Flicker noise floor at 3×10^{-15}. A detailed technical analysis is ongoing to improve the performances of our prototypes and several improvements are in progress to demonstrate a long-term stability at 1×10^{-15} or better. We target an accuracy in the 5×10^{-15} range and an accuracy budget is under preparation.

In this talk, we will present the latest results of this prototype (see Fig. 1). The apparatus is based on a copper cavity, which is first used as an integrating sphere for isotropic cooling where 10^7 atoms are cooled to sub-Doppler temperatures. We then interrogate the free-falling atoms with microwave pulses injected into the resonant cavity in a Ramsey type sequence with T_R = 40 ms. We then detect the atoms in one of the hyperfine states in an absorption column. By employing atom recapture, we increase the cycle time to repetition rates of the order of 10 Hz. We emphasize the fact that this atomic clock is a turnkey product designed for continuous long term operation.

Fig. 1: Fully integrated MuClock prototype.

References:

[1] J. Guéna, M. Abgrall, D. Rovera, P. Laurent, B. Chupin, M. Lours, G. Santarelli, P. Rosenbusch, M.E. Tobar, R. Li, K. Gibble, A. Clairon, and S. Bize, "Progress in atomic fountains at LNE-SYRTE," in *IEEE Transactions on Ultrasonics, Ferroelectrics, and Frequency Control*, vol. 59, no. 3, pp. 391-409 (2012).
[2] S. Peil, J. L. Hanssen, T. B. Swanson, J. Taylor, and C. R. Ekstrom, "Evaluation of long term performance of continuously running atomic fountains," in *Metrologia*, vol. 51, no. 3, pp. 263-269 (2014).
[3] P. Laurent, D. Massonnet, L. Cacciapuoti, C. Salomon, "The ACES/PHARAO space mission", in *Comptes Rendus Physique*, Vol. 16, no. 5, pp. 540-552 (2015).

MEASURING THE MITIGATION OF A JAMMING ATTACK ON A GPS SERVER AT THE NATIONAL PHYSICAL LABORATORY OF ISRAEL

Dr. Nadya Goldovsky[1], Omer Sharar[2]

[1]The National Physical Laboratory of Israel (INPL), Jerusalem, Israel
[2]GPSdome Ltd., Caesarea Industrial Park, Caesarea, Israel

E-mail: Nadya.Goldovsky@Economy.gov.il
E-mail: Omer@focus-telecom.com

In recent years, the threat of GNSS vulnerabilities has become real. Such events as signal anomalies, regional disruptions, loss of position and time in the presence of certain types of jammers had already occurred a multitude of times and affected critical applications all over the world. The solution of this problem for time-keeping, navigation, time and frequency synchronization which mitigated such threats is actual, and in the last several years many efforts are made for protection against jamming and spoofing.

Based in Israel, GPSdome, the GPS cyber company, develops and manufactures a GPS anti-jamming / anti-spoofing module protecting GPS-based systems against jamming and spoofing of the GPS signal. GPSdome implements a null-steering algorithm which significantly reduces the effect of a high-powered jamming/spoofing attack.

The calibration is performed against the Israeli National Time and Frequency Standard, using new time and frequency equipment, including new high performance Cs-clocks, GNSS dual-frequency multi-channel Time Transfer System and high performance Allan Deviation and phase noise measurement system. The calibration procedure was developed by INPL in collaboration with GPSdome, and is presented in this paper. The calibration procedure consists of several stages: 1) calibration of GPSdome time reference (the high performance Cs-clock 5071A) versus Israeli National Time UTC (INPL) at the INPL; 2) calibration of time difference between the GPS controlled device (without and with GPSdome Rev 1.0 anti-jamming module) and the time reference in the absence of jamming; 3) calibration of time difference between the GPS controlled device (without and with GPSdome anti-jamming module) and the time reference in the presence of jamming.

Two GPSdome modules (Rev 1.0) were calibrated with two GPS-locked servers (Microsemi's SyncServer S650): one with an internal (basic) quartz oscillator OCXO and one with an internal Rb oscillator. The testing of protection quality of GPSdome modules were performed during two days for each module. For each GPSdome module the internal time delay was evaluated.

The measurements were performed simultaneously for two servers S650: one with GPSdome protection and one without protection. First the measurements were carried out without jamming, and then with jamming.

The calibration results evidently show, that both servers with GPSdome protection save traceability to high performance time reference with standard deviation only 10-13 ns in the presence of jamming. Without the GPSdome protection, both servers (with internal quartz and Rb oscillator) have large drift. For quartz oscillator the drift is 1183.9 ns per hour. For rubidium oscillator the drift is about 201.2 ns per hour.

Our measurements have showed the effect of a jamming attack on a timing system and how such an attack could be mitigated using the GPSdome.

Design of Mercury Lamp for Trapped Ion Frequency Standard

Nuan-rang Wang，Xing Chen，Huan Zhao，Ren-fu Yang

(1. Science and Technology on Metrology and Calibration Laboratory, Beijing 100854, China;

2. Beijing Institute of Radio Metrology & Measurement, Beijing 100854, China)

Email:lorious@163.com

The mercury ion trapped microwave frequency standard has the potential applications for the future satellite, deep space explorations, time keeping and broadcasting for its great advantages in the total volume, stability and lifetime. The high frequency spectrum of mercury ion trapped microwave frequency standard is pumped by the mercury lamp which has small volume and long lifetime, as the base of superiority of mercury ion trapped microwave frequency standard. However, the mercury RF discharge lamp used for optical pumping and state detection may limit the ultimate stability performance of the clock. So we have carried out many experiments to enhance the light stability and the ratio of useful light at 194.02 nm and unwanted background light at 253.7 nm (194.02/253.7). Finally, the stability of light power is about 3% in 3 days, the 194.02/253.7 ratio is about 1/35, and with filter bulb the ratio is about 1/3. The experiment system of mercury ion trapped microwave frequency standard will be introduced and the mercury lamp device is presented with the radiation regime.

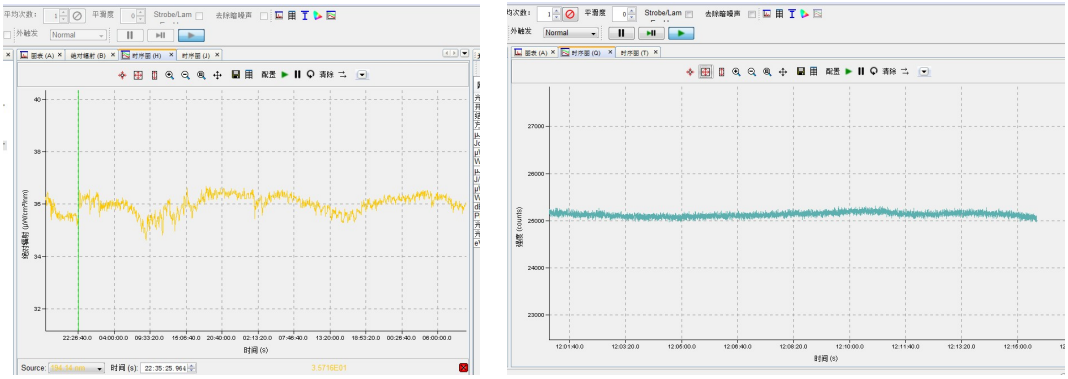

(a) (b)

Fig.1 the picture of testing curve at 194.2nm of mercury lamp. It was been tested for 3 days in Fig.1 (a) and 15 minutes in Fig.1 (b).

References

[1] Douglas D J, Frank A J, Mao D. Linear ion traps in mass spectrometry[J]. Mass Spectrometry Reviews, 2005, 24:1-29.

[2] Olver F, Lozier D, Boisvert R. NIST handbook of mathematical functions[M]. Cambridge: Cambridge University Press, 2010.

Local Two-Way Time and Frequency Distribution for Optical Time Transfer

K. Ulrich Schreiber[1], Jan Kodet[1], Christoph Bürkel[2], Gerhard Kronschnabl[2] Torben Schüler[2] and Urs Hugentobler[1]

[1]Forschungseinrichtung Satellitengeodaesie, Technical University of Munich, Munich, Germany

[2]Geodetic Observatory Wettzell, Bundesamt fuer Kartographie und Geodaesie, Bad Kötzting, Germany

Email: ulrich.schreiber@bv.tum.de

Optical time transfer requires the complete control over all the involved system delays in an optical time of flight measurement system, such as it is used in satellite laser ranging (SLR). This means that the local clock is linked to the time of flight measurement process without further delay. More generally, if the phase of the clock frequency can be made coherent over an area large enough to cover an entire geodetic observatory, the otherwise inaccessible (and unfortunately variable) system delays, of the order of several picoseconds, can be reliably recovered in situ from local time comparisons in a closure measurement approach.

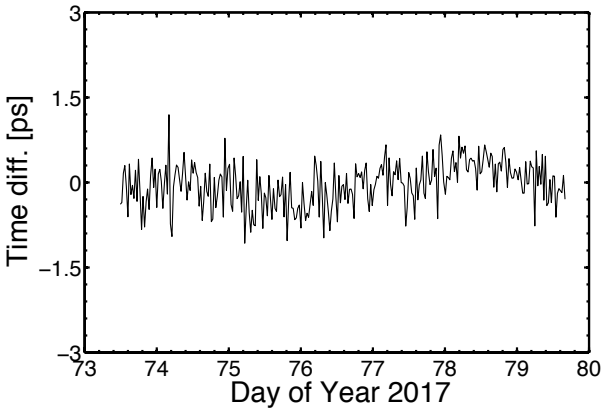

Fig. 1: Time comparison of two local fiber coupled two-way time transfer terminals, based on a common mode-locked fs-pulse laser distribution system, several hundred meters apart. Due to the active control the pulse per second clock pips remain coherent to within 1 ps over approximately one week.

We have designed and built such a coherent time and frequency distribution system for the Geodetic Observatory Wettzell. It is based on a mode-locked fs- pulse laser [1], fed into a network of actively delay controlled two-way optical pulse transmission links. This utilizes the ultra low noise properties of optical frequency combs, both in the optical and electronic regime. Currently the system is capable of maintaining a system stability of $\Delta\tau \approx 1$ ps for the electronic representation of the two-way optically distributed time in the long-term over several hundred meters of distance as indicated by fig. 1. The system had been set up to support the laser time transfer experiment for the Atomic Clock Ensemble in Space (ACES). Due to the high coherence of the distributed clock pips this time and frequency distribution system can be used to measure and remove systematic measurement errors at the same time. Therefore it can provide consistency in the complex instrumentation of SLR and VLBI systems in situ, which was not possible before. This talk outlines the concept and discusses the obtained results.

References

[1] J. Kim, F. Ludwig, M. Felber, and F. X. Kärtner, “Long-term stable microwave signal extraction from mode-locked lasers”, Optics Express, vol. 15 (1), p. 8951 – 8959, 2007

Uncertainty contributions of the microwave synthesis for PTB's fountain clocks

M. Kazda, J. Rahm, B. Lipphardt, S. Weyers

Physikalisch-Technische Bundesanstalt (PTB),
Bundesallee 100, 38116 Braunschweig, Germany
E-mail: Michael.Kazda@ptb.de

Using atomic fountain clocks, the SI-second can be realized with overall uncertainties of a few parts in 10^{16}. Fountain clocks are used for the steering of local atomic time scales and contribute to the steering of the international atomic time scale TAI. The generation of microwave signals is a key aspect for the operation of fountain clocks, as these signals can significantly contribute as well to the clocks statistical as to the systematic uncertainty. When designing a microwave synthesizer, other aspects such as operational reliability, operating life and the ease of maintenance also have to be taken into account.

In recent years the PTB fountain clocks CSF1 and CSF2 have been equipped with a purposefully developed microwave synthesizer, which features a modular design ensuring high reliability and availability. The synthesizer integrates an optically stabilized microwave oscillator [1] and enables utilization of the rapid adiabatic passage technique for the state selection process [2]. The synthesizer setup has been fully characterized for its contribution to the systematic and statistical uncertainty of the fountains. This includes investigations of the effects of phase noise, its long-term stability, and first and second order frequency shifts caused by sidebands. Details of these investigations will be presented. Even at the achieved fountain frequency instability level of $2.5\text{x}10^{-14}$ $(\text{t/s})^{-1/2}$, the contribution of the microwave synthesizer is insignificant [1]. Its contribution to the systematic uncertainty of the fountains is at the $4\text{x}10^{-18}$ level only.

Furthermore, we have realized two different methods for suppressing possible frequency shifts caused by microwave interrogation field leakage during the free atomic state evolution. The synthesizer designated for CSF1 has been equipped with an interferometric switch [3] to attenuate the field amplitude. For the CSF2 synthesizer, a frequency detuning scheme has been implemented [4]. Both setups have been thoroughly characterized for their contributions to the systematic uncertainty of the fountains, also taking into account phase transients and the phase sensitivity of the employed Ramsey scheme. In either case the systematic uncertainty contribution associated with microwave leakage could be confirmed not to exceed the low 10^{-17} level.

References

[1] B. Lipphardt, V. Gerginov and S. Weyers, „ Optical Stabilization of a Microwave Oscillator for Fountain Clock Interrogation", IEEE Trans. Ultrason. Ferroelectr. Freq. Control 64 (2017).

[2] M. Kazda, V. Gerginov, N. Nemitz and S. Weyers, „Investigation of Rapid Adiabatic Passage for Controlling Collisional Frequency Shifts in a Caesium Fountain Clock", IEEE Trans. Instrum. Meas. 62 (2013).

[3] G. Santarelli, G. Governatori, D. Chambon, M. Lours, P. Rosenbusch, J. Guéna, F. Chapelet, S. Bize, M.E. Tobar, P. Laurent, T. Potier and A. Clairon, "Switching atomic fountain clock microwave interrogation signal and high-resolution phase measurements", IEEE Trans. Ultrason., Ferroelect., Freq. Contr. 56 (2009).

[4] M. Kazda and V. Gerginov, "Suppression of Microwave Leakage Shifts in Fountain Clocks by Frequency Detuning", IEEE Trans. Instrum. Meas. 65 (2016)

High Contrast Ramsey-CPT Spectrum with Differential Detection in Rb Vapor Cell

Yuan Tian, Yi Zhang, Jiehua Chen, Sihong Gu

Key Laboratory of Atomic Frequency Standards, Wuhan Institute of Physics and Mathematics, Chinese Academy of Sciences, Wuhan 430071, China

Email: shgu@wipm.ac.cn

We have recently explored a scheme that uses elliptically polarized light interacts with atoms and a differential detection technique to effectively suppress laser noise [1]. This scheme is competitive for implementation in a practical compact CPT atomic clock. Inspired by the research, we now propose a method using the differential detection technology to obtain the high contrast Ramsey-CPT spectrum in a Rb vapor cell, and discuss its potential for a packaged CPT-based atomic clock.

Fig. 1(a) shows a schematic of the apparatus. Fig. 1(b) presents the Ramsey-CPT spectrum and continuous CPT signal from Ref. 1 separately. Though the amplitude of the central Ramsey-CPT fringe is twice as small as that of the continuous CPT signal, the linewidth of the central Ramsey-CPT fringe is only 10% of the continuous CPT signal. Compared with the conventional CPT atomic clock, the scheme of the Ref. 1 has significantly better short-term frequency stability and a similar power volume, power consumption, and cost. The results indicates that the scheme proposed in this publication has further potential to improve the short-term frequency stability than that of the Ref. 1.

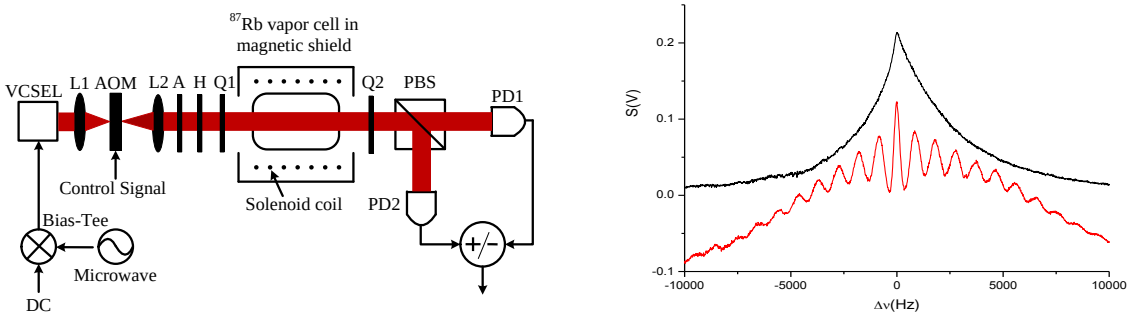

(a) (b)

Fig. 1: (a) Schematic of the experimental apparatus. L1, L2: lens; AOM: acousto-optic modulator; A: attenuator; H: half-wavelength plate; Q1, Q2: quarter-wavelength plate; PBS: polarizing beam splitter; PD1, PD2: photodetector. (b) Ramsey-CPT spectrum (red line) and CPT signal (black line) recorded. Experimental conditions: laser intensity of 1.7mW/cm^2, magnetic field of 10 μT.

Reference

[1] H. Lin, Y. Tian, B. Tan and S. Gu, "Differential detection scheme for compact CPT atomic clocks", Europhys. Lett., vol. 119, p. 23001, 2017.

Nonlinear enhancement of locking range of mutually injection locked oscillators for resonant sensing applications

Jérôme Juillard[1], Ali Mostafa[1], Pietro Maris Ferreira[1]

Sensor architectures based on coupled resonators are receiving increased interest from the resonant sensing community [1-3]. This is first motivated by the fact that such architectures can provide differential measurements of the physical quantity of interest, without being hampered by spurious couplings between the resonant elements, even when these are in close proximity. Furthermore, certain output metrics of such sensors have an increased sensitivity to the measurand, compared to conventional resonant sensors with frequency-modulated outputs, although this gain in sensitivity does not necessarily entail a gain in sensor resolution, as recently shown [4].

In the present paper, we investigate the properties of a differential architecture based on mutually injection-locked oscillators (MILO, Fig. 1) beyond the theoretical framework of [4], by driving the resonators higher than the critical Duffing amplitude. Our experimental results are obtained on high-Q silicon resonators with electrostatic drive and detection, with a purely softening nonlinearity [5], coupled with discrete electronics. This architecture is highly sensitive to stiffness mismatch between the resonators, which can be induced for testing purposes by tuning their bias voltages.

Our results (Fig. 2) show that a trade-off can be made between sensitivity and measurement (locking) range, and that the relation between these two quantities is no longer as trivial as in the linear regime [3]. Experimental results obtained with our MILO architecture and the amplitude ratio output metric are also reported for the first time (Fig. 2).

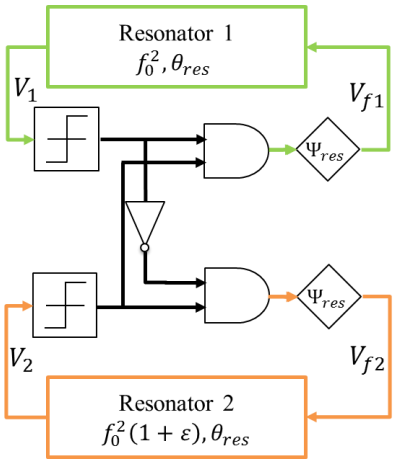

Fig. 1 – System-level view of MILO, consisting of two resonators and their readouts, a digital mixer stage and phase delay elements ψ_{res}. For optimal operation at f_0, one should have $\psi_{res}+\theta_{res}= \pi/4$, where θ_{res} is the phase delay at f_0 between V_{fi} and V_i.

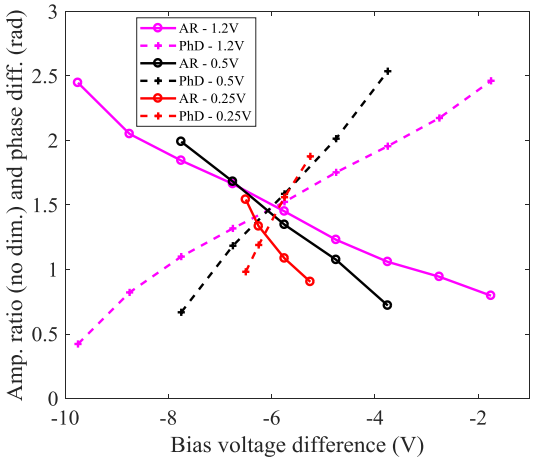

Fig. 2 – Experimental results obtained with the phase difference (crosses) and amplitude ratio (circle) output metrics, while varying the bias voltage of one of the two resonators.

[1] C. Zhao et al., "A review on coupled MEMS resonators for sensing applications utilizing mode localization," Sensors and Actuators A: Physical, vol. 249, pp. 93-111, 2016.
[2] P. Thiruvenkatanathan, J. Yan and A. A. Seshia, "Differential amplification of structural perturbations in weakly coupled MEMS resonators," IEEE Transactions on Ultrasonics, Ferroelectrics 9and Frequency Control, vol. 57, pp. 690-697, 2010.
[3] J. Juillard, P. Prache and N. Barniol, "Analysis of mutually injection-locked oscillators for differential resonant sensing," IEEE Transactions on Circuits and Systems I: Regular Papers, vol. 63, pp. 1055-1066, 2016.
[4] J. Juillard, P. Prache, P.M. Ferreira, N. Barniol, "Ultimate limits of differential resonant MEMS sensors based on two coupled resonators", IEEE Transactions on Ultrasonics, Ferroelectrics and Frequency Control, 2018 (submitted).
[5] A. Brenes, J. Juillard, L. Bourgois, F. Vinci dos Santos, "Influence of the Driving Waveform on the Open-Loop Frequency Response of MEMS Resonators With Nonlinear Actuation Schemes", Journal of Microelectromechanical Systems, vol. 25, pp. 812-820, 2016.

[1] GEEPS, UMR8507, CNRS, CentraleSupélec, UPSud, UPMC
3, rue Joliot-Curie – 91192 Gif-sur-Yvette – France

Carrier-Phase Two-Way Satellite Frequency Transfer between BIRMM and NIM

Shuwei Wang[1], Xueyun Wang[1], Haifeng Wang[1], Zhiqiang Yang[2],
Wenzhe Yang[1], Hongbo Wang[1], Shengkang Zhang[1]
[1]Science and Technology and Metrology and Calibration Laboratory,
Beijing Institute of Radio Metrology and Measurement, Beijing, China
[2]National Institute of Metrology, Beijing, China
Email:wsw_203@163.com

With the development of highly accurate atomic clock, there is an increasing requirement for time and frequency transfer with corresponding accuracy level to compare the clock in different places. Two-way satellite time and frequency transfer (TWSTFT) is a commonly used method of comparing time and frequency over a long distance and can achieve the performance on the level 1ns in accuracy and about 3E-15/d in precision. So there is a need to improve the accuracy and precision in TWSTFT links. According to the principle of carrier phase measurement, it can theoretically increase the time transfer precision of TWSTFT system by 1~2 orders of magnitude using the carrier phase observations comparing to the pseudorandom code measurement. M. Fujieda [1] et al have done a series of TWSTFT carrier phase experiments which showed a dramatic performance increase to the order of 2E-13/s in precision.

Recently, we have carried out a two-way satellite frequency transfer carrier phase experiment using the SATRE modem between BIRMM and NIM. We use UTC(BIRMM) as the reference of the TWSTFT station at BIRMM, and use UTC(NIM) as the reference of the station at NIM. Both stations have a two channels SATRE modem, one channel is used to receive the signal transmitted by satellite from the remote station, the other channel is used to receive the signal from its own. We use the receiving frequency measurements of the modem to obtain the carrier phase observations. During the experiment, the signal to noise ratio was set to about 55dBHz. Both station transmitted a signal with a frequency 14456MHz, which was defined with respect to the system frequency 5MHz. At the satellite, the frequency of the received signal mixed with the satellite's local oscillator frequency 1750MHz. We chose an hour of sampling data and exchanged the data of two ground stations. Then the data was processed and the offset between the frequencies of two clock was obtained after processing.

The result showed that we reached the instability for frequency comparisons at short averaging times in the order of 10^{-12} at 1s.There is a bump in the frequency stability curve at the integral time of 10s. This may come from the PLL noise in the frequency up/down converter.

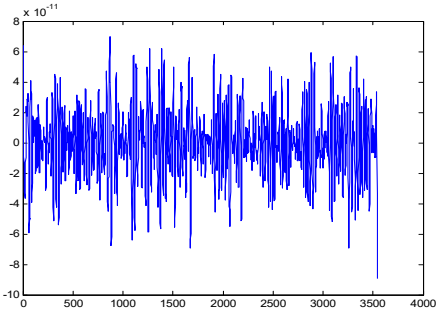

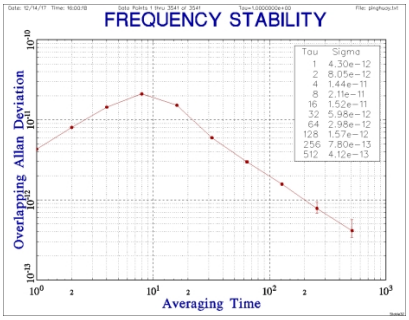

(a) Relative frequency difference (b) Frequency stability of the link

Fig.1: Frequency differences between BIRMM andNIM measured by TWCP

Reference

[1] M. Fujieda et al., “Carrier-phase two-way satellite frequency transfer over a very long baseline”, Metrologia, vol. 51, p. 253-262, 2014.

[2] M. Fujieda et al., “Carrier-Phase-Based Two-Way Satellite Time and Frequency Transfer”, IEEE Trans. Ultrason. Ferroelectr. Freq. Control, vol. 59, no. 12, 2625-2630, 2012.

Observed Time Synchronization Performance Using the Network Time Security Protocol

Martin Langer[1], Kristof Teichel[2], Dieter Sibold[2], Rainer Bermbach[1]

[1]Ostfalia University of Applied Sciences, Wolfenbüttel, Germany
[2]Physikalisch-Technische Bundesanstalt (PTB), Braunschweig, Germany

Email: kristof.teichel@ptb.de

Internet-based clock synchronization is essential for correctness of many computer applications, and thus needs to be reliable and secure. The Network Time Protocol (NTP) [1] is the most widely used protocol for internet based synchronization around the world. However, its communication is mostly unsecured, or at best with flawed security mechanisms, which enables potential attackers. The Network Time Security (NTS) specification is intended to solve the known security issues of NTP without sacrificing significantly the precision compared to standard NTP. To substantiate the practical impacts of NTS, a proof-of-concept implementation of NTS-secured NTP reflecting an intermediate design state of the specification was created at the Ostfalia University in cooperation with PTB, based on the Internet Engineering Task Force (IETF) draft NTS4NTP-06 [2].
In this paper, the achievable precision of standard unsecured NTP ("*ntpd*") versus unsecured and versus NTS-secured Ostfalia NTP ("*ntpo*" and "*ntso*", respectively) is compared for the first time. The results of our measurements offer insight into the essential properties of the proof-of-concept implementation, which provide a lower bound for the performance expected of implementations adhering to a final NTS specification. They allow early conclusions about NTS regarding efficiency and precision: it is both possible and practical to secure NTP traffic with NTS. The provided security does come at a cost of round-trip delay and of CPU load for client and server being increased asymmetrically (see Tab. 1), both of which combined can decrease precision. However, this cost is negligible at least in standard internet environments, where tens or hundreds of milliseconds are normal delay times. Furthermore, we identify potential for improvement, namely optimizations of the implementation code which will cause *ntso* performance to be closer to that of *ntpo*, which in turn can be optimized to be closer to the performance of *ntpd*.

Impl.	Role	CPU time / day [s]	RT delay (mean) [ms]
ntpd	Client	7,18	0,519
ntpd	Server	6,57	
ntpo	Client	25,46	0,877
ntpo	Server	11,28	
ntso	Client	41,33	2,06
ntso	Server	22,85	

Tab. 1: Overview of the implementation performance measurement results

References

[1] D. Mills; et al., "Network Time Protocol Version 4: Protocol and Algorithms Specification", RFC 5905: Internet Engineering Task Force (IETF), June 2010, DOI: 10.17487/RFC5905.

[2] D. Sibold; K. Teichel; et al., "Using the Network Time Security Specification to Secure the Network Time Protocol (NTS4NTP)" Internet-Draft: draft-ietf-ntp-using-nts-for-ntp-06, Sep 2016

Analysis of resonant sensors based on mutually injection locked oscillators beyond the critical Duffing amplitude.

Jérôme Juillard[1], Ali Mostafa[1], Pietro Maris Ferreira[1]

Sensor architectures based on coupled resonators are receiving increased interest from the resonant sensing community [1-3]. This is first motivated by the fact that such architectures can provide differential measurements of the physical quantity of interest, without being hampered by spurious couplings between the resonant elements, even when these are in close proximity. Furthermore, certain output metrics of such sensors have an increased sensitivity to the measurand, compared to conventional resonant sensors with frequency-modulated outputs, although this gain in sensitivity does not necessarily entail a gain in sensor resolution, as recently shown [4].

In the present paper, we investigate the properties of a differential architecture based on mutually injection-locked oscillators (MILO, Fig. 1) beyond the theoretical framework of [4]. A new analysis framework is developed for taking into account the limits imposed by thermomechanical phenomena on the different output metrics of this architecture, when the resonators can be modelled as Duffing resonators (with cubic restoring forces). Our results (Fig. 2) show that, for certain choices of the design parameters (hardening / softening nonlinearity, feedback phase, etc.), the ultimate resolution of amplitude-based output metrics improves monotonically with the driving force, whereas time- or frequency-based output metrics are limited by the conversion of amplitude noise to phase / frequency noise through the A-f effect. These theoretical results are supported by transient simulations.

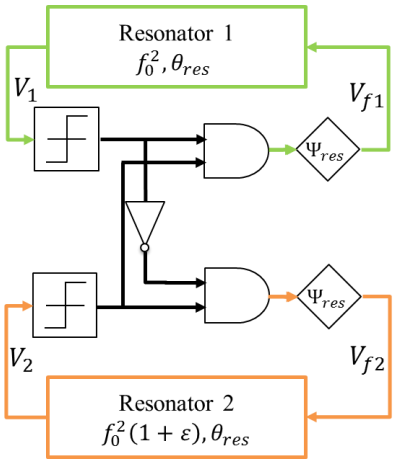

Fig. 1 – System-level view of MILO, consisting of two resonators and their readouts, a digital mixer stage and phase delay elements ψ_{res}. For optimal operation at f_0, one should have $\psi_{res}+\theta_{res}= \pi/4$, where θ_{res} is the phase delay at f_0 between V_{fi} and V_i. The phase difference and the amplitude ratio of V_1 and V_2 are highly sensitive to the relative stiffness mismatch ε.

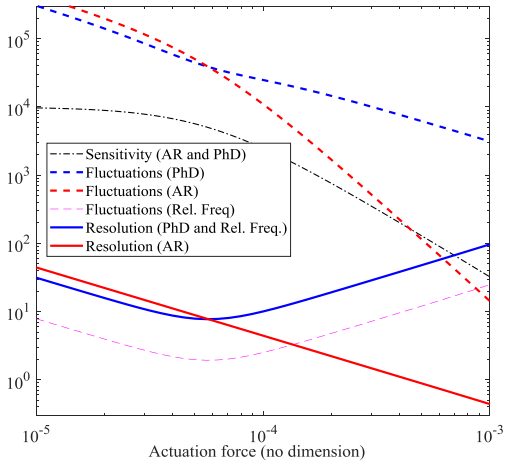

Fig. 2 – Analysis results for the MILO of Fig. 1, showing how sensitivity and fluctuations of different output metrics are affected by increasing driving force. The ultimate resolution of amplitude ratio measurements improves beyond the critical Duffing amplitude, while that of phase difference or oscillation frequency measurements becomes worse.

[1] C. Zhao et al., "A review on coupled MEMS resonators for sensing applications utilizing mode localization," Sensors and Actuators A: Physical, vol. 249, pp. 93-111, 2016.
[2] P. Thiruvenkatanathan, J. Yan and A. A. Seshia, "Differential amplification of structural perturbations in weakly coupled MEMS resonators," IEEE Transactions on Ultrasonics, Ferroelectrics 9and Frequency Control, vol. 57, pp. 690-697, 2010.
[3] J. Juillard, P. Prache and N. Barniol, "Analysis of mutually injection-locked oscillators for differential resonant sensing," IEEE Transactions on Circuits and Systems I: Regular Papers, vol. 63, pp. 1055-1066, 2016.
[4] J. Juillard, P. Prache, P.M. Ferreira, N. Barniol, "Ultimate limits of differential resonant MEMS sensors based on two coupled resonators", IEEE Transactions on Ultrasonics, Ferroelectrics and Frequency Control, 2018 (submitted).

[1] GEEPS, UMR8507, CNRS, CentraleSupélec, UPSud, UPMC
3, rue Joliot-Curie – 91192 Gif-sur-Yvette – France

Demonstration of Vapor Temperature Stabilization Using an Atomic Isoclinic-Point Thermometer

Travis Driskell and James Camparo

Photonics Technology Laboratory, The Aerospace Corp., El Segundo, CA/USA

Email: james.c.camparo@aero.org

In the Rb clock, the atomic signal is generated by atoms contained within a glass cell. To achieve good long-term frequency stability, the average temperature of the vapor must be stable as well as temperature gradients across the signal volume. Routinely, temperature control is achieved by placing a thermocouple or thermistor at the cold point on the resonance cell's exterior (*i.e.*, near the liquid Rb pool). Employing a feedback loop, temperature fluctuations at that one location are minimized by varying the cell's heating elements. Unfortunately, there are at least two problems with this approach: 1) the vapor's temperature is not measured directly, only the temperature at a point on the glass cell's exterior, and 2) changes in (possible) temperature gradients may not be compensated. Here, we discuss a solution to these problems.

Alkali (optical) absorption resonances have temperature dependences that arise from the spectral overlap of Doppler-broadened resonances. However, in the absorption spectra of nuclear-spin 3/2 alkalis (*e.g.*, ^{87}Rb) there is a spectral feature midway between the $F_g = 2 \rightarrow F_e = 1,2$ D_1 resonances whose resonant frequency is insensitive to temperature variations; it is an isoclinic point. For our work, we lock the frequency of a laser to the isoclinic-point in a reference cell. We then detect the transmission of a frequency-shifted 2nd beam from the laser through the clock's resonance cell. (The 2nd beam is frequency-shifted to a temperature-*dependent* spectral feature in the clock cell). With the laser locked to the isoclinic point in the reference cell, changes in the 2nd beam's transmission can only come from clock-cell temperature variations.

Figure 1 shows the ADEV of various temperatures open loop (left) and closed loop (right); T_{cell} and T_{air} are defined in the figure caption, while T_{AOM} is the vapor temperature as assessed by the transmission of the frequency-shifted 2nd beam. Open loop, the long-term fluctuations in T_{air}, T_{AOM}, and T_{cell} are all essentially the same, as one would expect, and indicate that T_{AOM} is a good measure of vapor temperature and that fluctuations in T_{AOM} derive from vapor temperature fluctuations. With the loop closed, there is clear improvement in the clock cell's temperature stability, likely *better* than T_{cell} since this is affected by the air around it.

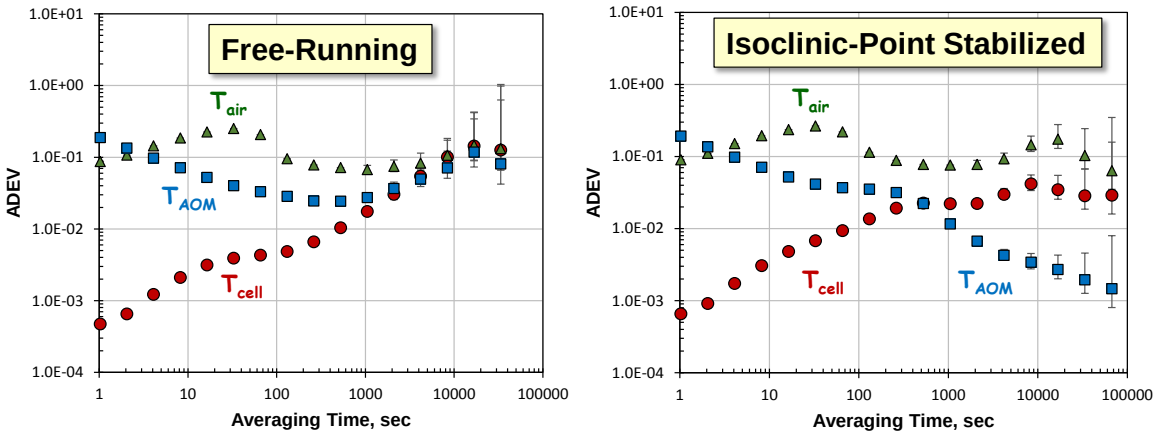

Figure 1: Allan deviations (units of Kelvin) for various temperatures. T_{air} corresponds to the temperature of the air two centimeters away from the clock cell. T_{cell} corresponds to the temperature of the clock cell as measured by a thermistor on the *outside* of the cell. T_{AOM} is the temperature of the vapor inferred from the acousto-optic modulator (AOM) frequency-shifted 2nd laser beam's transmission through the clock cell.

Mesoscopic Physics in Vapor-Phase Atomic Systems: Collision-Shift Gradients and the 0-0 Hyperfine Transition

Andrew Hudson and James Camparo

Photonics Technology Department
Physical Sciences Laboratories
The Aerospace Corporation, El Segundo, CA/USA

Email: james.c.camparo@aero.org

At the microscopic level, perturbations affecting the 0-0 hyperfine transition are fairly well understood (*e.g.*, the ac-Stark shift, spin-exchange, etc.). However, evidence has been mounting for another scale of physics, which is not so well understood: the *mesoscopic* scale. Since vapor-phase atoms are typically confined by buffer-gas collisions on time intervals long compared to the Rabi period, atoms in the vapor's signal volume experience *local* perturbations, which combine nonlinearly to produce the overall atomic signal. One important manifestation of mesoscopic physics arises from temperature gradients. These result in buffer-gas density gradients, which yield spatially-varying collision broadenings and shifts. In the present work, we examine temperature-gradients and the ^{87}Rb 0-0 hyperfine transition lineshape.

A VCSEL diode laser is split into two beams, one passes into a reference cell containing isotopically enriched ^{87}Rb & 10 torr N_2, and locks the laser to the Rb D_2 transition. The other beam is expanded and apertured (making a "top-hat" beam), and passes into our "clock" cell (^{87}Rb & 10 torr N_2), which sits in an oven allowing temperature gradients along the cell length. The oven sits in a mu-metal tube to limit environmental magnetic fields to the axial direction.

Some results are presented in Fig. 1: Fig 1a shows the linewidth (HWHM, $\Delta\nu_{1/2}$) of the 0-0 transition after extrapolating to zero microwave power, while Fig. 2b shows a skewness parameter for the lineshape. (We define skewness as $(\nu_{fit}-\nu_{deriv})/2\Delta\nu_{1/2}$, where ν_{fit} is the resonant frequency obtained from a Lorentzian fit, and ν_{deriv} corresponds to the zero-crossing of the lineshape's first derivative.) Clearly, temperature gradients result in increased 0-0 transition linewidths, and an asymmetry in the lineshape. These and other effects of temperature gradients on the 0-0 hyperfine transition lineshape will be discussed in the presentation.

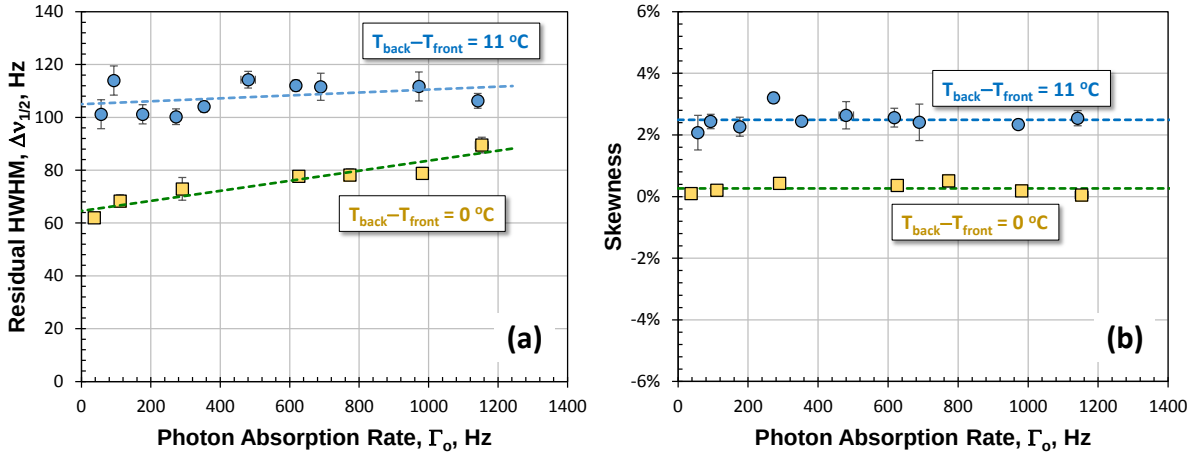

Figure 1: (a) HWHM of the observed 0-0 transition lineshape for temperature-gradient and no-gradient conditions; in both cases the measured NσL of the vapor was 1.92. (b) Skewness of the observed lineshape as defined in the text for temperature-gradient and no-gradient conditions.

OFDR – a diagnostic tool for long-distance metrological fiber links

Jochen Kronjäger[1], Giuseppe Marra[1], Jannik Dierks[1], Etienne Cantin[2,3], Nicolas Quintin[2], Anne Amy-Klein[2], Olivier Lopez[2], Paul-Eric Pottie[3]

[1] National Physical Laboratory, Teddington, UK
[2] Laboratoire de Physique des Lasers, Université Paris 13, CNRS, Villetaneuse, France
[3] Laboratoire National de Métrologie et d'Essais–Système de Références Temps-Espace, Observatoire de Paris, CNRS, UPMC, Paris, France
Email: jochen.kronjaeger@npl.co.uk

Optical frequency transfer over telecommunication fiber has become the method of choice for comparison of optical clocks and dissemination of ultra-stable reference signals [1,2]. With this technique, an ultra-stable laser in the telecom C-band (1530-1565 nm) is transmitted through an optical fiber link; fluctuations of the transmission delay are sensed using double-passed light and corrected for under the assumption of reciprocity. On long distance links (> approx. 100 km), fiber loss has to be compensated, for example using Erbium-doped fiber amplifiers. For best stability and accuracy, a single optical fiber is operated bi-directionally, including any optical amplifiers.

Unplanned outages during operation of a fiber link can and will generally happen, for any number of reasons. Fibers can be damaged during building work, or re-connected erroneously by fiber operators. Amplifiers can malfunction or experience power supply failures. On top of this, even small reflections e.g. from connectors can badly impair the effective operation of a bi-directional fiber link.

Optical frequency domain reflectometry (OFDR) [3] is a well-known technique to diagnose and characterize fibers. Like optical time domain reflectometry (OTDR) it detects backscattered or reflected light, but it uses a frequency-swept cw carrier to map distance to frequency. As a result, it does not suffer from the same sensitivity-vs-resolution trade-off as OTDR.

Here we show how a typical setup for optical frequency transfer is conveniently modified to perform OFDR, and how this is then used to remotely diagnose bi-directional EDFAs and locate reflective faults. The fiber used is the 760 km long London-Paris link between NPL (UK) and LPL (France) [4], part of a network connecting the National Metrology Institutes of the UK, France and Germany.

References

[1] C. Lisdat et al., "A clock network for geodesy and fundamental science", Nature Communications, vol. 7, 12443, 2016.

[2] C. Clivati et al., "Measuring absolute frequencies beyond the GPS limit via long-haul optical frequency dissemination", Optics Express, vol. 24, p. 11865-11875, 2016.

[3] W. Eickhoff and R. Ulrich, "Optical frequency domain reflectometry in single-mode fiber", Appl. Phys. Lett., vol. 39, p. 693-695, 1981.

[4] P. Delva et al., "Test of Special Relativity Using a Fiber Network of Optical Clocks", Phys. Rev. Lett., vol. 118, 221102, 2017.

Absolute frequency measurement of the $^{171}Yb^+$ E3 optical clock transition using international atomic time

Rachel M. Godun[1], Charles F. A. Baynham[1,2], Jonathan M. Jones[1,3], Steven A. King[1], Peter B. R. Nisbet-Jones[1], Fred Baynes[1], Antoine Rolland[1], Patrick E. G. Baird[2], Kai Bongs[3], Patrick Gill[1], Gérard Petit[4], Helen Margolis[1]

[1]National Physical Laboratory, Teddington, UK
[2]Clarendon Laboratory, University of Oxford, Oxford, UK
[3]School of Physics and Astronomy, University of Birmingham, Birmingham, UK
[4]Time Department, International Bureau of Weights and Measures (BIPM), Sèvres, France

Email: rachel.godun@npl.co.uk

We present a measurement of the absolute frequency of the $^2S_{1/2} \rightarrow {}^2F_{7/2}$ electric octupole clock transition at 467 nm in $^{171}Yb^+$, with the lowest reported uncertainty to date.

Traceability to the SI second was provided by a frequency link to international atomic time (TAI), which was achieved via the frequency chain depicted in Fig. 1. In the first step of this chain, a femtosecond frequency comb was used to measure the Yb^+ optical frequency relative to the 10 MHz output of the hydrogen maser that maintains UTC(NPL). In the second step, the local timescale UTC(NPL) was compared continuously to TAI via satellite-based time and frequency transfer, and the resulting frequency offset between UTC(NPL) and TAI was derived from the BIPM monthly bulletin Circular T. In the final step, a correction was made to account for the offset between the scale interval of TAI during the period of the measurement and the SI second.

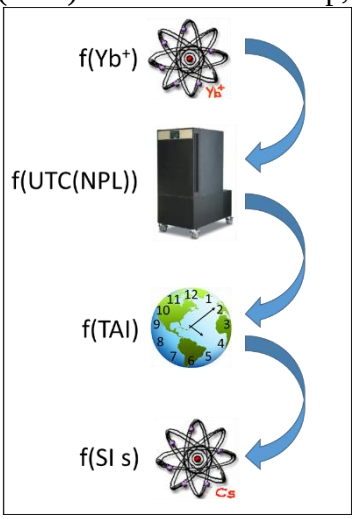

Fig. 1: Schematic of the frequency measurement chain linking the optical clock transition in $^{171}Yb^+$ to the microwave transition in Cs that is used to define the SI second.

The optical frequency was measured for 76% of a 25-day period. Dead times in the measurement inflate the uncertainty, yet the low dead-time of the optical standard allowed the total fractional uncertainty of the absolute frequency to be just 4×10^{-16} [1]. This initial analysis corrected for the fractional offset, *d*, between the scale interval of TAI and the SI second using data from the annual calculation of the time scale TT(BIPM) published for 10-day intervals. Further analysis was then carried out using a direct computation of *d* over a time interval directly relevant to our experiment [2]. This reduced the amount of data extrapolation over measurement dead-times, resulting in a final absolute frequency of 642 121 496 772 645.17(22) Hz, with a reduced fractional uncertainty of 3.4×10^{-16}.

References

[1] C.F.A. Baynham *et al.*, "Absolute frequency measurement of the $^2S_{1/2} \rightarrow {}^2F_{7/2}$ optical clock transition in $^{171}Yb^+$ with an uncertainty of 4×10^{-16} using a frequency link to international atomic time", J. Mod. Opt., vol. 65, p. 221–227, 2018.

[2] H. Hachisu *et al.*, "Absolute frequency measurement with uncertainty below 1 x 10^{-15} using International Atomic Time", Appl. Phys. B, vol. 123, 34, 2017.

Above 100-GHz Low Phase Noise Frequency Generation in Silicon Integrated Technologies

Alexandre Siligaris

CEA, LETI, Grenoble F-38054, France and the University of Grenoble Alpes, France

Email: alexandre.siligaris@cea.fr

Sub-THZ frequency bands (>100-GHz) are gaining interest among the scientific community for RF system development. Indeed, in many fields such as radio-communications, radars, or imaging, sub-THz bands offer ultra large bandwidth, high spatial precision and high resolution images, respectively. Such systems need high performance local oscillators (LO) in terms of frequency stability and phase noise (PhN) [1].

Figure 1 illustrates the PhN of recent frequency synthesizers at 1 MHz offset, as a function of the LO frequency in the synthesizer. We observe that increasing the LO frequency in the synthesizer leads to higher PhN than the ideal $20 \cdot log(N)$. N is a multiplication factor when using a lower frequency LO synthesizer. Thus, high frequency LO with outstanding PhN can be obtained using a low frequency synthesizer combined to a high order multiplication factor.

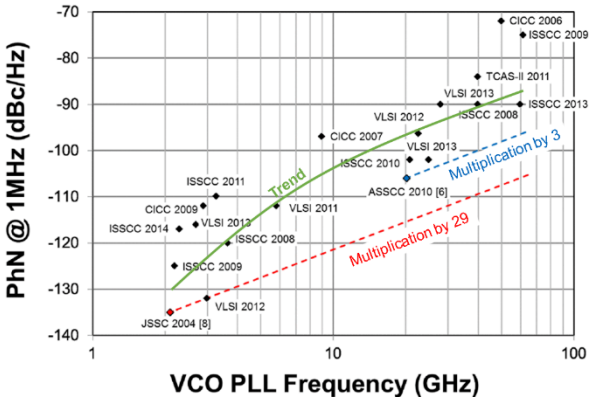

Fig. 1: Synthesizers with LO operating in the 2 – 60 GHz range. Trend is the green line.

This paper deals with two main challenges for high performance, above 100-GHz frequency synthesizers, in standard CMOS and BiCMOS Silicon technologies. Firstly, the paper describes high order programmable multiplication techniques that have been developed and implemented in CMOS technologies. This is realized by using high frequency switched and synchronized oscillators, as described in [2].

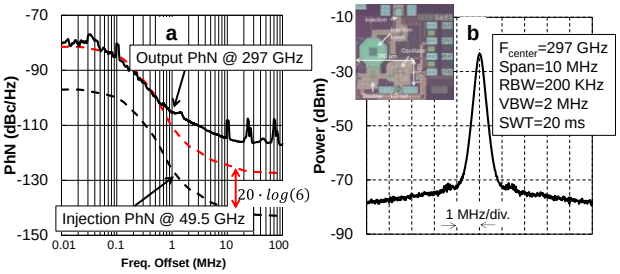

Fig. 2: Measured output phase noise at 297 GHz under locking conditions on an injection signal at 49.5 GHz. b. Output spectrum locked at 297 GHz.

Secondly, design techniques for oscillators that operate above the technology cut-off frequency f_{max} (maximum oscillation frequency defined by Masson's gain) are addressed. For example, multi-push techniques are commonly used and lead to above-300 GHz oscillators even using technologies that have lower than 200-GHz f_{max}. Figure 2 illustrates an example of a BiCMOS 297-GHz oscillator with less than -105 dBc/Hz phase at 1 MHz offset [3].

References

[1] K. Katayama, et al., "A 300GHz 40nm CMOS Transmitter with 32-QAM 17.5Gb/s/ch Capability over 6 Channels," *ISSCC*, pp. 342–343, 2016.

[2] C. Jany, et al., "A Programmable Frequency Multiplier-by-29 Architecture for Millimeter Wave Applications," *IEEE JSSC*, vol. 50, pp. 1669-1679, July 2015.

[1] A. Siligaris et al., "A 270-to-300 GHz Sub-Harmonic Injection Locked Oscillator for Frequency Synthesis in Sub-mmW Systems," *IEEE MWCL*, vol. 25, pp. 259-261, April 2015.

Quantum logic spectroscopy on an optical magnetic dipole transition in a highly charged ion

Steven A. King[1], Tobias Leopold[1], Peter Micke[1,2],
José R. Crespo López-Urrutia[2], Piet O. Schmidt[1,3]

[1]QUEST Institute, Physikalisch-Technische Bundesanstalt, Braunschweig, Germany
[2] Max-Planck-Institut für Kernphysik, Heidelberg, Germany
[3]Institut für Quantenoptik, Leibniz Universität Hannover, Hannover, Germany

Email: steven.king@quantummetrology.de

Highly charged ions (HCIs) are sensitive tools for tests of quantum electrodynamics and searches for physics beyond the Standard Model as observed by time-variation of fundamental constants. Since their electric dipole-allowed (E1) transitions are shifted from the optical to the X-ray range, they have an extremely small polarisability for infrared and optical radiation making them exciting candidates for the next generation of optical atomic clocks. In addition, their E1-forbidden optical-frequency transitions between fine and hyperfine structure levels, or between different configurations near a level crossing, are among the most sensitive of all atomic systems for detecting any present-day changes in the fine-structure constant and the proton-to-electron mass ratio. Until recently however, precision laser spectroscopy on HCI was limited by GHz-level Doppler broadening due to the megakelvin ion temperatures prevalent in electron beam ion traps (EBITs) [1,2]. In order to fully exploit E1-forbidden optical transitions in HCI with natural linewidths substantially below the hertz level for frequency metrology at the highest levels of precision and accuracy, significant cooling is therefore required.

We present our progress towards quantum logic spectroscopy [3] on an optical magnetic-dipole (M1) transition in a cold HCI, in this case the $^2P_{1/2} \rightarrow {}^2P_{3/2}$ fine structure transition at 441 nm in the ground state configuration $1s^2 2s^2 2p$ of the boron-like Ar^{13+} ion (Ar XIV). The HCIs are bred in a novel room-temperature EBIT based on permanent magnets, and then released into an electrodynamic deceleration beamline that compresses and pre-cools the HCI bunch for injection into a precision-engineered cryogenic linear Paul trap operating at T<5 K. Once confined in the Paul trap, a single Ar^{13+} ion is sympathetically cooled by Be^+ ions [4]. Following evaporation of excess Be^+ ions, a two-ion Coulomb crystal (Be^+/Ar^{13+}) remains. Thereafter, the crystal is cooled via stimulated Raman transitions driven on the Be^+ ion to the ground state of two of its motional modes, corresponding to a temperature of 100 μK. The E1-forbidden "clock" transition in the Ar^{13+} ion is then interrogated using a stable laser with a wavelength of 441 nm, followed by quantum logic operations on the Be^+/Ar^{13+} crystal that allows determination of the internal state of the Ar^{13+} ion. This work opens up a new field of study in which the cutting-edge tools of optical frequency metrology will be applied to an enormous variety of species of atomic ions that hitherto were beyond their reach.

References

[1] V. Mäckel *et al*., "Laser spectroscopy on forbidden transitions in trapped highly charged Ar^{13+} ions", PRL **107** 143002 (2011)
[2] K. Schnorr *et al*., "Coronium in the laboratory: Measuring the Fe XIV green coronal line by laser spectroscopy", Astrophys. J. **776**, 121 (2013)
[3] P. O. Schmidt *et al*., "Spectroscopy using quantum logic", Science **309** 749 (2005)
[4] L. Schmöger *et al.*, "Coulomb crystallization of highly charged ions", Science **347** 1233 (2015)

The Study of Using Hydrogen Maser Ensemble to Steer UTC(TL)

Shinn Yan Lin[1]

[1]National Standard Time and Frequency Laboratory, Telecommunication Laboratories, Chunghwa Telecom Co. Ltd., Taiwan

Email: sylin@cht.com.tw

This paper study the using of limited numbers of hydrogen masers combining cesium clock ensemble to enhance the mid-term performance of the national standard time and frequency of Taiwan, UTC(TL). Currently the UTC(TL) is generated from a micro phase stepper which referenced by a hydrogen maser and steered according to both UTC (announced by BIPM Circular T every month) and the paper clock timescale weighted of cesium clock ensemble of TL, TATL1[1]. Since the windows period of the BIPM Circular T monthly report could be as long as 45 days, TLT1 is used to be the mid-term prediction reference before the next coming announcement of BIPM Circular T. For TL's 12-cesium-clock ensemble, the phase error of the modified paper clock time scale is less than 10 ns in 45 days.

Since 2014, follow the new weighting algorithm introduced into UTC calculation, we smoothly changed the composition of clock ensemble from major cesium clocks into hydrogen masers[2]. Due to the TATL1 would be getting less stable for the less number cesium clocks in ensemble, we began to study and test a new hybrid reference paper clock model generated by both limited numbers of hydrogen masers and cesium clock ensemble. In the new model, we removed the frequency offset pattern of hydrogen masers according to the least squares linear regression to the frequency data with respect to cesium clock ensemble. The white FM noise would be minimized to get more predictable hydrogen masers. The evaluating period of least squares linear regression and the steering period of the new TATL1 algorithm will be tested to fit the characters of hydrogen masers and cesium clock ensemble for getting the most stable paper clock during the window period between BIPM Circular T announcement. Since the Hadamard deviation floor of TL's hydrogen masers are around 5×10^{-16} at 5 days average time, we expect the 10 days prediction error of new TATL1 model will be less than 5 ns.

References

[1] S. Lin "A Paper Clock Prediction Model for UTC(TL)", 2016 European Frequency and Time Forum

[2] G Panfilo, A Harmegnies and L Tisserand, "A new weighting procedure for UTC", 2014 Metrologia, Volume 51, Number 3

[3] S. Lin and H. Peng "An Improvement of TA(TL): Using the Combination of a Hydrogen Maser And a Cesium-Clock Ensemble", JOINT MEETING of the European Frequency and Time Forum EFTF and the IEEE International Frequency Control Symposium IEEE-FCS, 2007

Improving the Yb optical lattice clock at INRIM

Marco Pizzocaro[1] , Pierre Thoumany[1] , Filippo Bregolin[1,2] , Gianmaria Milani[1,2] , Benjamin Rauf[1], María del Carmen Vélez López[3,1], Filippo Levi[1], Davide Calonico[1]

[1]Istituto Nazionale di Ricerca Metrologica (INRIM),
Strada delle Cacce 91, 10135 Torino, Italy
[2]Politecnico di Torino, Corso duca degli Abruzzi 24, 10129 Torino, Italy
[3]Real Instituto y Observatorio de la Armada (ROA),
Calle Cecilio Pujazón, 11100 San Fernándo, Spain
Email: m.pizzocaro@inrim.it

We designed and operated an optical lattice clock based on cold ytterbium atoms. Its absolute frequency was measured against the cryogenic caesium fountain ITCsF2 with a relative standard uncertainty of 5.9e-16. The result was 518 295 836 590 863.59(31) Hz [1]. The systematic uncertainty of the Yb optical lattice frequency standard was 1.6e-16, below that of ITCsF2. Moreover we measured a Yb/Sr ratio of 1.207 507 039 343 338 41(34) together with a transportable optical clock developed at PTB [2].

At the conference we will discuss the improvements made on the Yb clock aiming at reducing its uncertainty at the 1e-17 level. We have improved the setup of the clock laser that is locked to a 10 cm ultrastable cavity, reducing the seismic noise on the cavity. With the new setup we can achieve spectroscopy with a linewidth of 7 Hz and a 5-fold improvement in the clock stability respect to our previous work. A re-evaluation of the uncertainty budget of the clock is ongoing exploiting the better stability. Moreover we are working on a vertical enhancement cavity to achieve a lattice trap depth up to 1000 Er to better investigate non-linear light shifts. Finally we are building a new vacuum chamber that will feature a copper shield with high thermal uniformity at room temperature similar to the one presented by Beloy et al. [3]. We aim to reduce the uncertainty coming from the blackbody radiation shift at the 1e-18 level while at the same time assuring a very clean vacuum environment to prevent shift from background gas collisions.

This work has been funded by the European Metrology Program for Innovation and Research (EMPIR) project 15SIB03 OC18 and the ASI project DTF. This project has received funding from the EMPIR programme co-financed by the Participating States and from the European Union's Horizon 2020 research and innovation programme.

References

[1] Pizzocaro et al., "Absolute frequency measurement of the 1S0-3P0 transition of 171Yb", Metrologia 54, p. 102, 2017

[2] Grotti et al., "Geodesy and metrology with a transportable optical clock", to be published on Nature Physics

[3] Beloy et al., "Atomic Clock with 1e-18 Room-Temperature Blackbody Stark Uncertainty", Phys. Rev. Lett. 113, 260801, 2014

Automatic calibration of the actively stabilized fiber-optic time transfer

P. Krehlik, J. Kołodziej, Ł. Śliwczyński

Faculty of Computer Science, Electronics and Telecommunications
AGH University of Science and Technology Kraków, Poland

Email: krehlik@agh.edu.pl

In last years fiber-optic based installations for time transfer become not only experimental, but operational as well. The calibration of such links is necessary for tractability of the output time signal (usually 1PPS) to the UTC(k) timescale, and needs to be repeated after a fiber break or modifications in the installation. In this situation some relatively simple means for time transfer calibration become important for maintaining the time transfer links by persons having no particular knowledge nor special equipment for step-by-step measurements and calculations. In this work we present a dedicate device which serves as an automatic calibrator for the ELSTAB system [1], however the idea would be used in any other actively stabilized time transfer system.

The simplified diagram of the calibration setup is shown in Fig. 1. The calibrator performs the measurement of the chromatic dispersion of the optical path, of the $\tau_{UTC(k)\rightarrow REF}$ and $\tau_{REF\rightarrow RET}$ time intervals, calculate the Sagniac correction term, and finally provides the offset between the UTC(k) timescale and the remote 1 PPS train. According to the calibration result, the PPS Advancing Module in the remote terminal may be set to obtain the output 1 PPS closed to UTC and precisely calibrated.

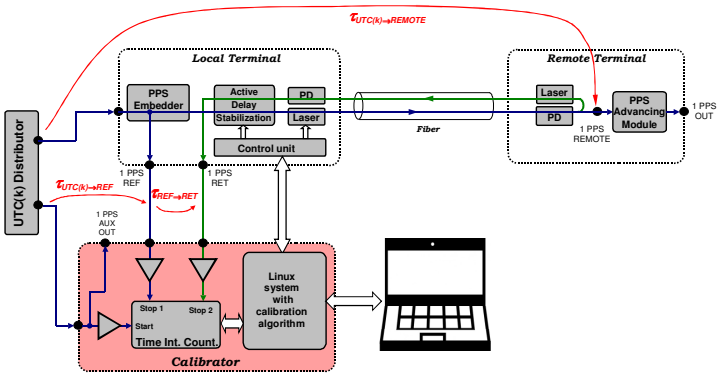

Fig. 1: The simplified diagram of the calibration setup.

The calibrator was used in a campaign of calibration of the five ELSTAB links connecting UTC laboratory at Physikalisch-Technische Bundesanstalt with Deutsche Telekom locations [2]. In parallel we performed this calibration using our earlier developed method, which is much more cumbersome and needs expensive equipment, but may be regarded as ultimately accurate. We observed a very good agreement between both methods for calibration of each of five links. The results obtained from two methods differ less than 40 ps, with no evident systematic bias. In the work we analyze the reasons for this small differences, and try to assess the uncertainty of the automatic calibrator.

Acknowledgement: Work supported by Polish National Science Center NCN (2015/17/B/ST7/03628 project).

References

[1] P. Krehlik, L. Sliwczynski, L. Buczek, J. Kolodziej and M. Lipinski, “ELSTAB - Fiber-Optic Time and Frequency Distribution Technology: A General Characterization and Fundamental Limits”, IEEE Trans. UFFC, vol. 63, p. 993-1004, 2016.

[2] Ł. Śliwczyński, P. Krehlik, J. Kołodziej, H. Imlau, H. Ender,H. Schnatz, D. Piester, A. Bauch, “Fibre optic time transfer between PTB and Deutsche Telekom using multi-link redundant topology,” Proc. EFTF 2017, Besançon, France, pp. 681-682, 2017.

Advances in the uncertainty evaluation of a $^{88}Sr^{+}$ single ion optical clock

Pierre Dubé[1], Bin Jian[1], Amar C. Vutha[2]

[1]National Research Council Canada, Ottawa, Ontario, Canada
[2]Department of Physics, University of Toronto, Toronto, Ontario, Canada

E-mail: Pierre.Dube@nrc-cnrc.gc.ca

The $5s^2S_{1/2}-4d^2D_{5/2}$ electric quadrupole transition of the $^{88}Sr^{+}$ ion is suitable to realize high-accuracy single-ion optical clocks, with the potential for evaluated uncertainties approaching the 10^{-18} level with current knowledge and technology. The $^{88}Sr^{+}$ ion system has the advantage that it can be operated using commercially available low power laser sources, that it uses a simple cooling and interrogation sequence, and that it allows for a robust control of several sources of frequency shifts. These qualities make the $^{88}Sr^{+}$ ion a good candidate for the realization of high-accuracy single-ion clocks, transportable optical clocks and for space applications.

Several important systematic shifts of the *S*–*D* transition are very well controlled by using methods based on physical properties. For example, the electric quadrupole interaction Hamiltonian is traceless. This property is used to reduce the electric quadrupole shift of the clock transition to a vanishingly small value by averaging over the magnetic sublevel energies of the $^2D_{5/2}$ state [1, 2]. Another very beneficial property of the *S*–*D* transition for clock accuracy is that its static scalar polarizability, $\Delta\alpha_0$, is negative. As a consequence, the quadratic Stark and second-order Doppler shifts caused by micromotion have opposite signs. This property has provided a means to measure $\Delta\alpha_0$ to high-accuracy, with a direct benefit to the evaluation of the blackbody radiation (BBR) shift [3]. In addition, by tuning the trap drive frequency to the optimum value determined by $\Delta\alpha_0$, the two shifts can be made to compensate each other, resulting in a suppression of the excess micromotion shifts by a factor exceeding two orders of magnitude, and a reduction of the thermal motion shifts by a factor of 3 [3].

The current uncertainty evaluation of the $^{88}Sr^{+}$ ion clock developed at NRC is 1.1×10^{-17}. We report on recent progress in the evaluation and reduction of systematic shifts, addressing effects such as the evaluation of the BBR field, the collisional frequency shift [4], and the servo tracking errors. We will discuss the impact of this work on the accuracy of the single ion clock.

References

[1] P. Dubé, A. A. Madej, J. E. Bernard, L. Marmet, J.-S. Boulanger, and S. Cundy, "Electric quadrupole shift cancellation in single-ion optical frequency standards," *Phys. Rev. Lett.*, vol. 95, p. 033001, 2005.

[2] P. Dubé, A. A. Madej, Z. Zhou, and J. E. Bernard, "Evaluation of systematic shifts of the $^{88}Sr^{+}$ single-ion optical frequency standard at the 10^{-17} level," *Phys. Rev.* A, vol. 87, p. 023806, 2013.

[3] P. Dubé, A. A. Madej, M. Tibbo, and J. E. Bernard, "High-accuracy measurement of the differential scalar polarizability of a $^{88}Sr^{+}$ clock using the time-dilation effect," *Phys. Rev. Lett.*, vol. 112, p. 173002, 2014.

[4] A. C. Vutha, T. Kirchner, and P. Dubé, "Collisional frequency shift of a trapped-ion optical clock," *Phys. Rev. A*, vol. 96, p. 022704, Aug 2017.

Enhanced Performance Surface Acoustic Resonance (SAR) Lab-on-a-Chip Sensor

Kiryl Kustanovich[1], Ventsislav Yantchev[1], Aldo Jesorka[1]

[1]Department of Chemistry and Chemical Engineering, Chalmers University of Technology, Göteborg 412 96, Sweden

Email: kiryl@chalmers.se

A novel in-liquid sensing concept based on the surface acoustic resonance (SAR) has been recently demonstrated in a Lab-on-a-Chip resonant device with one electrical port [1]. SAR sensors employ SAW *reflective gratings* as *sensing elements*. PDMS microfluidic delivery system is designed to supply the liquid over the SAW reflectors, while the IDT is isolated from the sensing environment by the air-gap cavity. The SAR sensing platform has low impedance at resonance, high sensitivity and retained Q when immersed in liquid, the ability to work under highly viscous load with small performance degradation, and significantly smaller dimensions than conventional (delay-line) high-frequency SAW in-liquid sensors. SAR approach is applicable to SAW phononics and the new hetero-acoustic layer substrates with zero TCF.

In this work, we demonstrate key-enabling enhancements over the state of the art SAR sensor design. The novel "acoustic trap" design is introduced for the first time, where the spatially varying reflectivity of the SAW reflectors enables strong SAW localization inside the sensing domain at resonance. As a result, more than **100%** improvement in mass-sensitivity at resonance is achieved. At antiresonance, the SAW that is strongly localized under the IDT exhibits a **4.2** times smaller mass-sensitivity as compared to resonance, thus enabling efficient subtraction of temperature variations within the device. Finally, we demonstrate an inherent integration of the SAR sensing with a low frequency (<1MHz) electric impedance spectroscopy (EIS). EIS employs the SAW reflectors formed as capacitors connected to a second port (i.e. the reflector strips are electrically connected in interdigitated split electrode geometry). Selected data is present on Fig. 1 and in Table 1. The EIS integration is sketched in Fig. 2

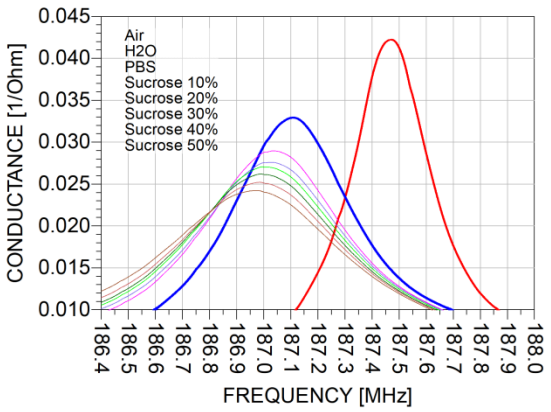

Fig. 1 SAR sensing performance. The input impedance changes by 7 Ohms from PBS to 50% sucrose solution.

Table I. Brief summary of measured sensitivities:

Designs:	Original	**Improved**
Air to Water	-915ppm	**-2000ppm**
Water to PBS	-160ppm	**-360ppm**
PBS to 20% Sucr.	-160ppm	**-220ppm**

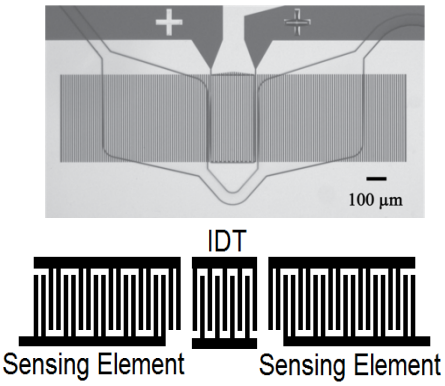

Fig. 2 SAR Sensor and EIS integration

References

[1] K. Kustanovich et. al, "A high-performance lab-on-a-chip liquid sensor employing surface acoustic wave resonance", J. Micromech. Microeng., vol. 27 (11), p. 114002, 2017.

On-line optimization of time and frequency fiber optic links exploiting bi-directional amplifiers

Ł. Śliwczyński, P. Krehlik, K. Salwik, J. Kołodziej

[1]Faculty of Computer Science, Electronics and Telecommunications,
AGH University of science and Technology, Krakow, Poland

Email: sliwczyn@agh.edu.pl

Long-distance fiber optic links for time and frequency transfer need to employ special, single-path bi-directional optical amplifiers (SPBA) for compensation for the attenuation of the fiber. Amplifiers bi-directionality is a very desirable feature from a point of view of the transfer, however, it simultaneously allows the propagation of scattered signals (like e.g. Rayleigh backscattering), resulting in a degradation of signal to noise ratio [1]. This requires great level of care when setting SPBA gains in order to achieve expected link performance.

The optimization of a bi-directional fiber link is a cumbersome process because it requires accessing the distributed system that may span hundreds of kilometers and include a number of SPBAs. Simulating a model of the link [2] may serve as an off-line tool to find the optimum gains that should then be preset in the SPBAs before the installation of the link is done. This approach, however, is loaded with problems with the lack of accurate knowledge about the fiber link, like exact attenuations of fiber spans, attenuations and reflections of optical connectors, values of backscattering coefficients, spectral properties of exploited lasers, etc.

In the paper we consider a novel approach where the optimization of the link is performed on-line (see Fig. 1). Basing on the measurement of the jitter of time/frequency signals at the ends of the link [3], a special algorithm adapts in a real time the gains of the amplifiers to minimize the jitter at both ends. Two variants of the algorithm are investigated, one requiring initial gains from simulation (a hot start), and the other one requiring no prior presetting of SPBAs gains (a cold-start).

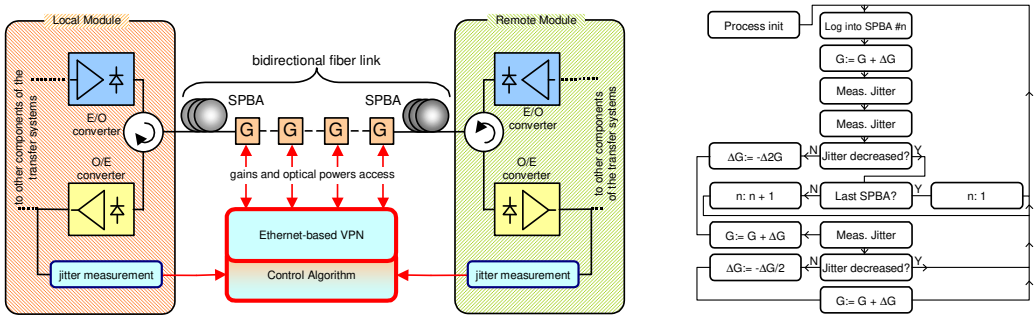

Fig. 1. Idea of the on-line link optimization and simplified block diagram of the control algorithm.

This work was supported by Polish National Science Center under the decision DEC-2014/15/B/ST7/00471.

References

[1] Ł. Śliwczyński, P. Krehlik, Ł. Buczek, M. Lipiński, "Frequency transfer in electronically stabilized fiber optic link exploiting bidirectional optical amplifiers", IEEE Trans. Instr. and Meas., vol. 61, pp. 2573-2580, 2012.

[2] Ł. Śliwczyński, J. Kołodziej: „Bidirectional optical amplification in long-distance two-way fiber optic time and frequency transfer systems", IEEE Trans. Instr. and Meas., vol. 62, pp. 253-262, 2013.

[3] Ł. Śliwczyński, P. Krehlik, K. Salwik: "Real-time performance monitoring of fiber optic long-distance time and RF frequency transfer links", Proc. EFTF 2016, York, United Kingdom, DOI 10.1109/EFTF.2016.7477757.

Understanding Light Shifts in CPT Clocks

J. W. Pollock[1], V. I. Yudin[2,3,4], M. Shuker[1], M. Yu. Basalaev, A. V. Taichenachev[2, 3], X, Liu[1], J. Kitching[1], and E. A. Donley[1]

[1]NIST Time and Frequency Division, Boulder, CO, USA, [2]Novosibirsk State University, Novosibirsk, 630090, Russia, [3]Institute of Laser Physics SB RAS, Novosibirsk, 630090, Russia, [4]Novosibirsk State Technical University, Novosibirsk, 630073, Russia

Email: vyudin@mail.ru, elizabeth.donley@nist.gov

The light shift for coherent population trapping (CPT) clocks probed with Ramsey spectroscopy can be divided into two parts – a resonant transient shift arising from incomplete dark-state formation, and an off-resonant contribution from the well-known ac Stark effect. By varying the pulse parameters, NIST's cold-atom CPT clock allows these two shifts to be distinguished and studied. An overview of our understanding of the shifts and their contributions will be presented.

The resonant transient shift was first studied in an atomic-beam clock based on sodium atoms [1]. For small optical detuning and low intensities, the shift is proportional to detuning and decays exponentially with increasing intensity and length of the first Ramsey pulse. The original theory applies very well to the cold-atom CPT clock [2, 3].

It was already known that off-resonance shifts from detuned hyperfine levels can be smaller when probing with Ramsey spectroscopy as opposed to continuously [4, 5]. The clean spectra in NIST's cold-atom CPT Ramsey clock have allowed the shift to be carefully investigated theoretically and experimentally [6]. Estimates of the shift made with a simple theory agree quantitatively with experiments. The shifts have several interesting properties:

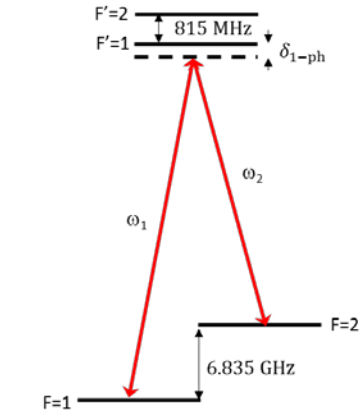

Fig. 1: Energy-level diagram for D1 CPT excitation through the F'=1 excited state in ^{87}Rb. δ_{1-ph} is the optical detuning and the off-resonance excited state is detuned by 815 MHz.

- They depend only weakly on laser intensity and are quite stable with respect to the fluctuations of light power.
- They are much larger for Λ systems resonant with the F'=1 state than the F'=2 state.
- Like for continuous excitation, they depend on the ratio of the Rabi frequencies of the of the two CPT frequency components, which can limit stability if this quantity varies.
- They are significantly worse for D2 interrogation than D1 interrogation, since there are more excited-state hyperfine levels than for D1 and they are all closer together.

References

[1] P. R. Hemmer, M. S. Shahriar, V. D. Natoli, and S. Ezekiel, *J. Opt. Soc. Am. B*, vol. 6, pp. 1519-1528, 1989.
[2] E. Blanshan, S. M. Rochester, E. A. Donley, and J. Kitching, *Physical Review A*, vol. 91, p. 041401, (2015).
[3] X. Liu, E. Ivanov, V. I. Yudin, J. Kitching, and E. A. Donley, *Physical Review Applied*, 8, p. 054001, 2017.
[4] N. Castagna, R. Boudot, S. Guérandel, E. de Clercq, N. Dimarcq, and A. Clairon, *IEEE Trans. UFFC*, 56, 246, 2009.
[5] M. A. Hafiz, G. Coget, P. Yun, S. Guérandel, E. d. Clercq, and R. Boudot, *Journal of Applied Physics*, 121, p. 104903, 2017.
[6] J. W. Pollock, V. I. Yudin, M. Shuker, M. Yu. Basalaev, A. V. Taichenachev, X. Liu, J. Kitching, and E. A. Donley, to be published (2018).

VFC chip with comb for narrow-line laser cooling

McFerran John

School of Physics, University of Western Australia, 6009 Crawley, Australia

Email: john.mcferran@uwa.edu.au

Laser stabilization for narrow-line laser cooling is often accomplished using high finesse optical cavities [1,2]. We demonstrate that an alternative approach is to use frequency-to-voltage conversion [3] of a heterodyne beat signal formed between a cw laser and an element of a frequency comb. The general set-up is sketched in Fig. 1. The beat frequency is converted into a DC voltage where it is differenced with a voltage reference and then becomes the input to a loop filter before feeding back to the cw laser. When the comb is stabilized to a suitable reference (e.g. H-maser) the stability of the cw laser is limited by the VFC integrated circuit (IC), but this we show to be sufficient for applications such as narrow-line laser cooling. As an example we consider the intercombination line in neutral ytterbium and produce an atom cloud temperature of 22(3)μK (averaged over 90 measurements).

The intercombination line wavelength is 555.8nm. A master laser at the sub-harmonic wavelength of 1111.6nm requires frequency stabilization for reliable magneto-optical trapping of Yb. An RF beat signal is produced with an avalanche photo-detector where light at 1111.6nm from both comb and cw laser fall. This signal is bandpass filtered and amplified before entering a prescaler with a division of 64. The prescaler output goes to a comparator before being received by the VFC chip. The IC produces a linear response between frequency and voltage.

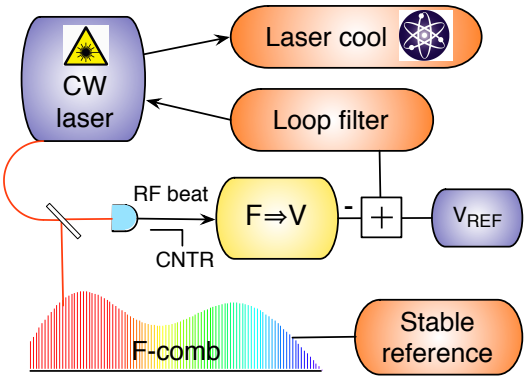

Fig. 1: Laser frequency stabilisation using frequency-to-voltage conversion with an integrated circuit and a frequency comb.

The fractional frequency instability (FFI) noise floor set by the VFC chip and level of frequency division is 2×10^{-13} at 1s falling to 1×10^{-13} at 10s before steadily rising — as measured with an artificial beat signal. Measurements of the instability of the locked 1111.6nm beat signal almost match this noise floor. For integration times below 1s this represents an improvement by two orders of magnitude in comparison to instabilities produced with an atomic beam lock on the same transition [4]. The two methods produce similar atomic temperatures. We conclude that factors other than the remaining laser instability limit the temperature. Significant advantages of this technique are the robustness of the servo and its capture range (≳55MHz). The scheme can be applied to any laser wavelength accessible by the frequency comb.

References

[1] H. Katori *et al.* "Magneto-optical trapping and cooling of strontium atoms down to the photon recoil temperature," Phys. Rev. Lett. 82, 1116 (1999).

[2] E. Curtis, C. Oates, and L. Hollberg, "Quenched narrow-line laser cooling of ^{40}Ca to near the photon recoil limit," Phys. Rev. A 64, 031403–1 (2001).

[3] T. Stace, A. Luiten, and R. Kovacich, "Laser offset-frequency locking using a frequency-to-voltage converter," Meas. Sci. Technol. 9, 1635 (1998).

[4] L. A. Salter, *et al*. "Inverted crossover resonance...," J. Phys. B, 50, 165003 (2017).

Influence of heating of ion in a trap on the efficiency of generalized Ramsey schemes of suppression of probe-induced frequency shift

Alexey Taichenachev[1], Sergey Kuznetsov[1], Valeriy Yudin[1], Nils Huntemann[2], Christian Sanner[2], Christian Tamm[2], Ekkehard Peik[2]

[1]Institute of Laser Physics SB RAS, Novosibirsk, Russia
[2]Physikalisch-Technische Bundesanstalt, Braunschweig, Germany

Email: taich.alex@gmail.com

In modern optical frequency standards based on ultracold atoms or ions strongly forbidden clock transitions (such as E3 transition in $^{171}Yb^{+}$ ion) are excited by a strong probe field. This leads to significant probe-field induced off-resonant AC Stark shift of the transition frequency. Several modifications of the Ramsey method have been proposed to suppress this shift [1]. Theoretical treatment of these methods is usually based on unitary evolution of pure quantum states under the action of a sequence of exciting pulses. Such approaches assume negligible relaxation and dephasing. These ideal conditions are not always realized in experiments. For example, one of possible imperfections is connected with a finite heating rate of ion in Paul trap. In this paper we analyze the influence of ion heating on the efficiency of several generalized Ramsey schemes of suppression of probe-induced shifts in ion-based optical clocks.

We consider a two-level system interacting with a sequence of light pulses, taking into account the vibrational degrees of freedom of the ion in a trap. The quantum kinetic equation for the ion density matrix can be written in the form

$$\frac{\partial}{\partial t}\rho = -\frac{i}{\hbar}[H_0,\rho] - \frac{i}{\hbar}[V,\rho] + \left[\frac{\partial}{\partial t}\rho\right]_{heating}, \qquad (1)$$

where the Hamiltonian of the ion in a trap ($H_0 = -\hbar\delta|e><e| + \hbar\omega_v\left(a^{\dagger}a + \frac{1}{2}\right)$) and the interaction Hamiltonian ($V = \hbar\Omega_0|e><g|e^{ikx} + h.c$) are taken in the rotating wave approximation. The last term in eq.(1) describes the density matrix evolution due to heating of the ion: $\left[\frac{\partial}{\partial t}\rho\right]_{heating} = K(\bar{N}+1)\left[a\rho a^{\dagger} - \frac{1}{2}\{a^{\dagger}a,\rho\}\right] + K\bar{N}\left[a^{\dagger}\rho a - \frac{1}{2}\{aa^{\dagger},\rho\}\right]$, where K is a phenomenological constant, and an average equilibrium number of vibrational quanta $\bar{N} = \left(e^{\hbar\omega_v/k_BT} - 1\right)^{-1} \approx \frac{k_BT}{\hbar\omega_v} \gg 1$. For vibrational frequency 1 MHz and room temperature $\bar{N} \approx 10^7$. The experimentally measured heating rate $\nu = K\bar{N}$ usually lies in the range $1 - 10^3$ 1/s. Using numerical solution of eq.(1) we show that the finite heating rate limits the efficiency of all proposed generalized Ramsey schemes, mainly due to the reduction of effective Rabi frequency.

This work was supported by the Russian Scientific Foundation (Project No. 16-12-00052).

References

[1] V.I. Yudin et al., Phys. Rev. A 82 011804 (2010); R. Hobson R., et al., Phys. Rev. A 93, 010501 (2016); T. Zanon-Willette et al., Phys. Rev. A 93, 042506 (2016).

Fountain equation and frequency calculation

Yu. S. Domnin

FGUP "VNIIFTRI", Mendeleevo, Moscow Region

Email: ydomnin@vniiftri.ru

An application of time and frequency standards concerns practically any human activity. The most striking effect from the time and frequency measurement accuracy is in the directions of communication, navigation, geodesy and dynamics etc.

For new level of accuracy it is necessary to implement new approach in the measurements and data processing. Par example spin exchange shift in fountains standards leads to changing of modes of measurements. One should have to measure the frequency with different density of atoms in cloud and so on [1,2]. In the work [3] the model of atomic fountain noises is proposed. The noises are separated by their dependence from number of atoms in cloud. According to this model it is necessary to carry out the frequency measurements at five different fluxes of atoms.

Investigation had shown, that one need one more term in fountain equation because spin exchange term depends on microwave power. A term D=2CS was introduced into the fountain formulae.

According to this model, an algorithm of data processing was developed and two years results of H-maser frequency measurements presented. H-maser frequency meaning is published in BIPM circular T. There are also the data about frequencies of national fountains and **pfs** – mean frequency all of these fountains. SUFO2 determines the same H-maser frequency and using these data one can find positions of **pfs** and SUFO2 regarding TAI

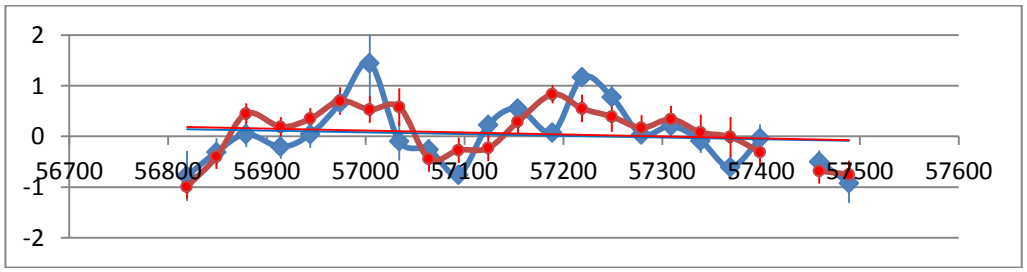

Fig. 1: Frequency difference between TAI and pfs (circle) and TAI and SUFO2 (rhombus). X is MJD, Y – one division is 1E-15. Duration company is two years.

When we find equations solutions from atomic fountain formulae we introduce corrections for the shifts produced by photodetector noise, quantum projection noise, temperature noise, synthesizer noise and spin exchange noise.

An application of the algorithm developed enable as to increase the accuracy to the level below 1×10^{-16}. The calculations produced for five densities. Application of six densities may give us an accuracy a few units in power 10^{-17}. The algorithm is applicable to any quantum frequency standard.

References:

1 S. Weyers, U. Hübner, R. Schröder, Chr. Tamm, A. Bauch, Metrologia 38 (4), pp. 343–352 (2001)

2 S.R. Jefferts, J. Shirley, T. E. Parker, T.P. Heavner, D.M. Meekhof, C. Nelson, F. Levi, G. Costanzo, A. DeMarchi, R. Drullinger, L. Hollberg, W.D. Lee and F.L. Walls, "Accuracy Evaluation of NIST-F1," Metrologia, vol. 39, pp 321-336, 2002.

3 Yu.S.Domnin "Atomic Fountain Equation" Measurement Techniques, 58(10), 1135-1138 **DOI** 10.1007/s11018-015-0854-4

The Strontium Optical Lattice Clock at INRIM

M. G. Tarallo[1], M. Barbiero[2], G. Lamporesi[3], G. Ferrari[3], D. Calonico[1], F. Levi[1]

[1]Istituto Nazionale di Ricerca Metrologica, Strada delle Cacce 91, Torino 10135, Italy
[2]Politecnico di Torino, Corso Duca degli Abruzzi 24, 10129 Torino, Italy
[3]CNR–INO Trento, Via Sommarive 13, 38123 Trento, Italy

Email: m.tarallo@inrim.it

We present the advancement of the strontium optical clock at the Italian National Metrology Institute (INRIM). The atomic source employs a novel design based on two-dimensional magneto optical trapping (MOT) [1]. We report on the cold Sr atomic source and its loading into a MOT trap on a test vacuum cell. Prospects for a second-generation quantum optical clock is also outlined.

The technical description of the atomic source and its expected advantages were previously discussed [2]. A schematic drawing of the vacuum apparatus is shown in Fig.1. In short, a hot flux of Sr atoms is ejected from the oven at a temperature of T_{ov} = 650 K through a 2-cm long bundle of nickel capillaries. This is directed to a 2D-MOT, which is formed by two parallel couples of permanent magnets with opposite direction forming a quadrupole magnetic field. Two counter-propagating laser beams at the strong $^1S_0$-$^1P_1$ transition with opposite circular polarization (saturation parameter $s \sim 3$, $\delta \sim -1.5\Gamma$) cross the atomic beam direction with ±45° to form the magneto-optical trap. We got a first evidence of two-dimensional optical trapping by experimentally observing an increased fluorescence at the very center of the trap, with very narrow transverse dimensions and elongated toward the direction orthogonal to the 2D-MOT plane. Further steps will be the addition of the Zeeman slower beam counter-propagating against the oven beam and the push beam to transfer the atoms in the UHV region.

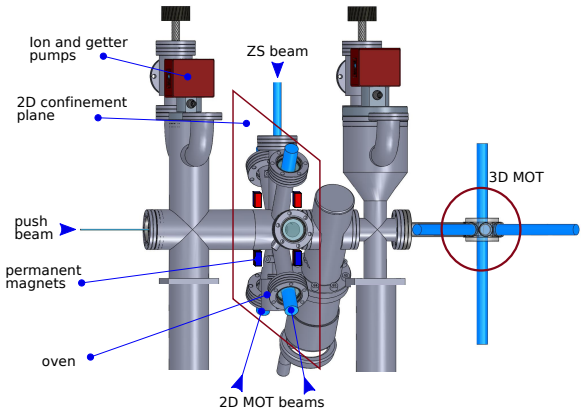

Fig. 1: A 3D drawing (in scale) of experimental apparatus. The 3D MOT chamber here depicted is meant only for visualization.

An ultra-stable three-color cavity is under construction to stabilize the frequencies of the 922 nm seed laser used to generate the blue laser at 461 nm, the 689 nm laser used for second-stage cooling and nondestructive measurements [3], and the lattice laser at 813 nm.

References

[1] G. Lamporesi, S. Donadello, S. Serafini, and G. Ferrari, “Compact high-flux source of cold sodium atoms”, Rev. Sci. Instrum., vol. 84, pp. 063102, 2013.

[2] M.G. Tarallo et. al. “A strontium optical lattice clock apparatus for precise frequency metrology and beyond,” 2017 Joint Conference of the European Frequency and Time Forum and IEEE International Frequency Control Symposium (EFTF/IFCS), Besancon, 2017, pp. 748-750

[3] M. A. Norcia, J. K. Thompson, “Strong coupling on a forbidden transition in strontium and nondestructive atom counting”, Phys. Rev. A, vol. 93, pp. 023804, 2016.

An Anti-Jamming System for GNSS Timing Applications

Jorge Querol[1,2], Ricardo Píriz[3], Esteban Garbin[3], Adriano Camps[1,2]

[1]MITIC Solutions, Spain
[2]CommSensLab, Universitat Politecnica de Catalunya and IEEC/CTE-UPC, Barcelona, Spain
[3]GMV, Spain

Email: jorge.querol@tsc.upc.edu

Global Navigation Satellite Systems (GNSS) is a key technology for timing and synchronization in critical infrastructures such as telecommunication, power distribution networks and finance, among others. However, due to their extreme low power, GNSS signals are quite vulnerable to GNSS jammers and other unintentional Radio-Frequency Interference (RFI) signals. This is particularly threatening for critical GNSS-enabled applications, and it triggers the development of reliable GNSS systems.

FENIX is a real-time GNSS anti-jamming system that provides up to 30 dB of extra resilience to any GNSS receiver against commercial jammers. This performance can be achieved thanks to its patented algorithm [1] based on a combination of time, frequency and statistical mitigation techniques. Its transparent real-time architecture described in [2] allows to connect it to any GNSS receiver and to work with all spread-spectrum services. In particular, FENIX-lite is a narrow-band implementation which works with GPS L1CA/L2C and Galileo E1OS.

Two GPS Disciplined Oscillators (GPSDOs) based on a u-blox LEA-M8F receiver are used during the anti-jamming tests. The first GPSDO is used unperturbed, as PPS reference. The second GPSDO allows verifying the combined performance of FENIX-lite and the synchronization system in terms of resilience against different common GNSS jamming and RFI scenarios.

The setup, shown in Fig. 1, measures the time delay difference of PPS signals from the two GPSDOs using a Time Interval Counter (TIC). The reference GPSDO is connected directly to the antenna signal, while the GPSDO under test is connected to FENIX-lite output. At its input, the signal combination of antenna and jamming generator is connected.

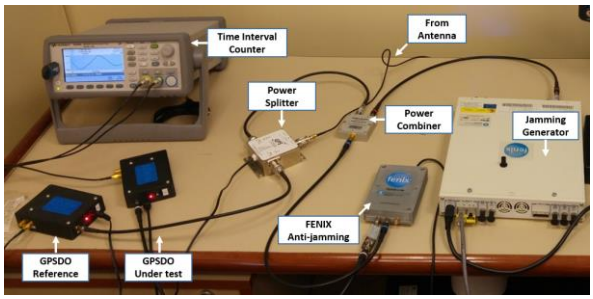

Fig. 1: GPS timing testing setup with FENX-lite.

Preliminary results show that FENIX-lite shows an extra resilience from 15 to 30 dB against PPS degradation for continuous wave and common chirp jamming signals, in concordance with the results presented in [3]. A large, but constant delay in the PPS signal of 1.65 ms is introduced, which can be easily calibrated. The added PPS jitter is on the order of only 1-2 ns. Further description of the evaluated jamming scenarios, PPS stability under jamming conditions, and FENIX-lite performance will be detailed at the conference.

[1] J. Querol, and A. Camps, "System and method for detecting and eliminating radio frequency interferences in real time," U.S. Patent Application 15 222 036, issued July 28, 2016.

[2] J. Querol, E. M. Julian, R. Onrubia, A. Alonso-Arroyo, D. Pascual and A. Camps, "Preliminary results of FENIX: Front-End GNSS Interference eXcisor," 2016 IEEE International Geoscience and Remote Sensing Symposium (IGARSS), Beijing, 2016, pp. 5627-5630.

[3] J. Querol and A. Camps, "Real-time Pre-correlation Anti-jamming System for Civilian GNSS Receivers," Proceedings of the 30th International Technical Meeting of The Satellite Division of the Institute of Navigation (ION GNSS+ 2017), Portland, Oregon, September 2017, pp. 1267-1288.

Evaluation of CGGTTS time transfer using multiple software and GNSS constellations

Kenneth Jaldehag[1], Per Jarlemark[1], Carsten Rieck[1]

[1]Measurement Science and Technology, RISE Research Institutes of Sweden, Borås, Sweden

Email: kenneth.jaldehag@ri.se

A new software tool for GNSS time transfer implementing the Common GNSS Generic Time Transfer Standard (CGGTTS) has recently been developed by the time and frequency group at RISE Research Institutes of Sweden. The software handles signals from the four satellite navigation systems GPS, GLONASS, Galileo and BeiDou including the most important ranging codes for time transfer applications. The aim of the development is to provide an alternative to existing software and to support time transfer with new GNSS.

The paper presents an evaluation of CGGTTS data obtained using the new software tool in comparison with those obtained using two other, independently developed software tools. The first software, commonly used by the international UTC-labs, is developed by the time and frequency group at the Royal Observatory of Belgium (ROB), see *e.g.* [1]. The present, available version of the ROB software (R2CGGTTS 7.1b) produces CGGTTS data for observations with GPS, GLONASS and Galileo. The second software is developed by the National Time Service Center (NTSC), Xi'an, China, and CGGTTS data produced by NTSC have been used for the evaluation of observations with BeiDou. All three software comply with the CGGTTS-Version 2E standard [2] and produce CGGTTS data files from raw observation and navigation data provided by the receiver in the RINEX format.

The software evaluation study involves RINEX (V.3) data from two receivers: NTP3, maintained by NTSC, China, and SP05, maintained by RISE, Sweden, capable of observing a variety of codes and signals from the satellites in all four mentioned GNSS, and referenced to the national time scales UTC(NTSC) and UTC(SP), respectively. CGGTTS data were calculated for 22 days (MJD 57903 to 57924). It is shown that the results obtained from the different software agree to less than sub-nanosecond level while comparing the so called REFSYS values [2]. Specifically, the agreement seen between individual GPS and Galileo CGGTTS data obtained with the RISE and ROB software is at the 100-picosecond level. Similarly, GLONASS and BeiDou CGGTTS data agree to the sub-nanosecond level, a lesser agreement which will be discussed in the paper.

Further, the paper presents a comparison between time transfer links for the long baseline between UTC(SP) and UTC(NTSC) obtained from a common view analysis using data from the four mentioned GNSS, as well as shorter and common-clock baselines for other receivers located in Sweden. It finally discusses other features available from the RISE software such as non-smoothed CGGTTS data, adaption of satellite orbit and clock products from IGS as well as the results of an evaluation using linear combinations with non-standard codes and signals. The paper concludes that a new independent software tool for GNSS time transfer using four different navigation systems is available. Once fully evaluated, the intension is to make the RISE software freely available for scientific users.

References

[1]: A. Harmegnies, P. Defraigne, and G. Petit, Metrologia **50** (2013) 277-287
[2]: P. Defraigne and G. Petit, Metrologia **52** (2015) G1

Operation of an atomic fountain frequency standard with a remote maser reference

K. Szymaniec[1], R. Hendricks[1], K. Turza[2], B. Nagórny[3], P. Dunst[3], J. Nawrocki[3], P. Krehlik[4], Ł. Śliwczyński[4],

[1]National Physical Laboratory, Teddington, UK
[2] Poznań Supercomputing and Networking Center, Poznań, Poland
[3]AOS Astrogeodynamical Observatory, Borowiec, Poland
[4]AGH University of Science and Technology, Kraków, Poland

Email: krzysztof.szymaniec@npl.co.uk

Maintaining a robust and largely autonomous timescale is a task not only for national measurement institutes, but also for timing labs at large scientific facilities, military and security agencies or telecom and financial service providers. The most stable local timescales consist of a flywheel clock (usually a hydrogen maser) that is frequently steered using corrections provided by an atomic fountain frequency standard whose local oscillator is weakly locked to that clock. A need may arise to install the fountain in a suitably equipped room that is not co-located with the flywheel. In such case a frequency transfer link between the two devices would have to assure that both long- and short-term stability of the fountain is not compromised.

We report the operation of Cs fountains referenced to remote masers using stabilised optical fibre links. We carried out laboratory tests at NPL using a 50 km section of spooled fibre and field tests in Poland with a 35 km dark fibre link between the AOS lab in Borowiec and the PSNC site in Poznan. In both cases the optical fibre links were stabilised in terms of their delay time using ELSTAB systems [1]. These systems measure the round-trip delay in the fibre and compensate for variations by adding an electronically generated variable delay. Since they were designed primarily for long-term stability, their ability to transfer a reference signal without degrading fountain signal-to-noise ratio required verification. At NPL, the tests were performed with two fountain systems using two different techniques to filter the phase noise of the reference signal to minimise the aliasing effect that increases the short-term frequency noise (Dick effect). One fountain, AOS-CsF2 (later moved to PSNC), used a quartz-based local oscillator and had a short-term stability of $1.5 \times 10^{-13}\ \tau^{-1/2}$. A second system, NPL-CsF3, used an optical-based microwave source which resulted in a stability of $5 \times 10^{-14}\ \tau^{-1/2}$. This latter system allowed for a more stringent test for noise contributed by the optical fibre link and ELSTAB units. As the fountains were co-located with the reference maser it was possible to directly compare their performance when operated with either a short (30 m) coaxial cable or a long fibre link. During the field tests the performances of two fountains of identical construction and referenced to the same maser were compared: AOS-CsF1, co-located with the maser, and AOS-CsF2 operated remotely at PSNC.

In all tested configurations the use of the stabilised optical fibre link did not affect the fountains' short-term stability, as long as the lock of the local oscillator to the maser was optimised. With the use of additional amplifiers it is possible to stabilise much longer links by ELSTAB, so the distance between the fountain and the reference clock could be significantly increased.

References

[1] P. Krehlik, Ł. Śliwczyński, Ł. Buczek, J. Kołodziej and M. Lipiński, "ELSTAB—Fiber-Optic Time and Frequency Distribution Technology: A General Characterization and Fundamental Limits", IEEE Trans. UFFC, vol. 63, p. 993-1004, 2016.

Transfer technique based, continuously operating frequency comb for frequency metrology in the optical and microwave domain

B. Lipphardt, E. Benkler, S. Weyers, J. Rahm, N. Huntemann, Chr. Sanner, R. Lange, Chr. Tamm, E. Peik

Physikalisch-Technische Bundesanstalt, Bundesallee 100, 38116 Braunschweig, Germany
E-mail: Burghard.Lipphardt@ptb.de

Femtosecond frequency comb generators are key components in time and frequency metrology. Our commercial fiber based comb in PTB is optimized to measure the two reference transitions of $^{171}Yb^{+}$ single-ion optical clocks. Over the last years, several measurements of the frequency of the $^{2}S_{1/2}$ - $^{2}D_{3/2}$ electric quadrupole (E2) and the $^{2}S_{1/2}$ - $^{2}F_{7/2}$ electric octupole (E3) transition have been performed with our primary Cs fountain clocks CSF1 and CSF2, limited by their systematic uncertainties at the low 10^{-16} level [1,2].

Even for the direct comparisons of optical clocks with systematic uncertainties as low as 3×10^{-18}, our data from the comparison of two combs indicate that the frequency comb does not contribute significantly to the achievable total uncertainties. We furthermore utilize the frequency comb to reduce the short-term instability of the $^{171}Yb^{+}$ E3 clock by more than a factor of two by stabilizing the clock's reference laser to a silicon single-crystal optical cavity at 1.5 µm [3] instead of a room temperature ULE cavity.

In addition, the frequency comb transfers the frequency stability of another ultra-stable laser at 1.5 µm to a microwave oscillator. Using a low-bandwidth digital control loop, the oscillator's frequency is steered by a hydrogen maser. The signal of the optically stabilized microwave oscillator serves as the local oscillator for the fountain clocks, enabling quantum projection noise limited frequency instabilities at the low 10^{-14} (1s) level [4].

All applications require a robust and continuous operation. The use of the transfer technique [5] mitigates the requirements on the frequency comb's locking technique. This enables almost maintenance free continuous operation over weeks. As a result, in 2017 the optically stabilized microwave oscillator was used during 10 months for a number of calibrations of the scale interval of International Atomic Time TAI by the fountain clocks, in measurement campaigns with typical durations of 30 days.

References

[1] Chr. Tamm, N. Huntemann, B. Lipphardt, V. Gerginov, N. Nemitz, M. Kazda, S. Weyers and E. Peik, Phys. Rev. A **89**, 023820 (2014).
[2] N. Huntemann, B. Lipphardt, Chr. Tamm, V. Gerginov, S. Weyers, and E. Peik, PRL **113,** 210802 (2014).
[3] D. G. Matei, T. Legero, S. Häfner, C. Grebing, R. Weyrich, W. Zhang, L. Sonderhouse, J. M. Robinson, J. Ye, F. Riehle, and U. Sterr, PRL **118**, 263202 (2017).
[4] B. Lipphardt, V. Gerginov and S. Weyers, IEEE Trans. Ultrason. Ferroelectr. Freq. Control **64**, 761 (2017).
[5] H. R. Telle, B. Lipphardt, and J. Stenger, Appl. Phys. B **74**, 1 (2002).

CANCELLED

A Campact Magnetron Cavity for POP Rb Clock

Qiang Hao[1], Wenxiang Xue[1,2], Kemu Wang[1,2], Peter Yun[1], Wenge Guo[1,3], Shougang Zhang[1*]

[1] Key Lab. of Time and Freq. Primary Standards, National Time Service Center, Xi'an, China
[2] University of Chinese Academy of Sciences, Beijing, China
[3] Xi'an Shiyou University, Xi'an, China

Email: haoq@ntsc.ac.cn ;*szhang@ntsc.ac.cn

Recently years, the Loop Gap Resonator (LGR) microwave cavity has been widely used in the vapor cell frequency standards, such as the lamp pumped Rb frequency standard[1] and passive hydrogen maser[2], and has promoted the performance of the frequency standards to a great extent. Pulsed Optical Pumping(POP) Rb frequency standard is a promising alternative for the next generation Global Navigation Satellite Systems(GNSS), while its long-term frequency stability is undesirable currently for the high temperature sensitivity.In this paper, we present a compact magnetron microwave cavity for POP Rb frequency standard to shrink the size of physics package and improve its temperature sensitivity. Unlike the existing magnetron cavity used in POP Rb frequency standard[3], the new one has a smaller size and can be manufactured as one whole body. The resonance frequency of the cavity was tuned to 6.384GHz, the ^{87}Rb ground state hyperfine frequency. The field orientation factor was optimized to be 0.9, indicating the atoms in the cavity can be efficiently simulated for the clock transition. The performance of the cavity was verified in a POP Rb clock and a contrast of Ramsey fringe of 32% was obtained. The short noise limit was evaluated as $1.4\times10^{-14}\tau^{-1/2}$, close to the result of previously lager cavity[3]. Since smaller volume could reduce the heat exchange with the environment, the new cavity makes it possible to reduce the temperature sensitivity without losing the signal to noise ratio.

Fig. 2 Main component of the magnetron cavity

References

[1] G. Mei, D. Zhong, S. An, et al. Main features of space rubidium atomic frequency standard for BeiDou satellites[C], 2016 European Frequency and Time Forum (EFTF). IEEE, 2016: 1-4.

[2] Q.Wang , P. Mosset , F. Droz, P. Rochat, "Lifetime of Space Passive Hydrogen Maser", in Proceedings of Joint International Frequency Control Symposium (IFCS) and European Frequency and Time Forum (EFTF)(2013), pp. 973 - 976 .

[3] S. Kang, M. Gharavipour, C. Affolderbach, et al. Demonstration of a high-performance pulsed optically pumped Rb clock based on a compact magnetron-type microwave cavity[J]. Journal of Applied Physics, 2015, 117(10): 104510.

A high-performance optical lattice clock based on bosonic atoms

Stefano Origlia[1], Mysore Srinivas Pramod[1], Stephan Schiller[1], Yeshpal Singh[2], Kai Bongs[2], Sebastian Häfner[3], Sofia Herbers[3], Sören Dörscher[3], Ali Al-Masoudi[3], Roman Schwarz[3], Uwe Sterr[3], and Christian Lisdat[3]

[1]Institut für Experimentalphysik, Heinrich-Heine-Universität, Düsseldorf, Germany
[2] University of Birmingham, Birmingham, United Kingdom
[3] Physikalisch-Technische Bundesanstalt, Braunschweig, Germany

Email: stefano.origlia@hhu.de

Bosonic optical lattice clocks present some disadvantages compared with the fermionic ones, which have prevented their development for metrological applications. These are the presence of s-wave collisions (suppressed for spin-polarized fermions), and a completely forbidden clock transition, requiring one or more external fields for inducing a transition moment. Nevertheless, bosonic clocks can be interesting for applications where simplicity and reliability are required, as for transportable clocks or if extreme lifetimes of the clock transition will be required in the future.

Here, we exploit the recent development in ultra-stable reference cavities in order to overcome the bosonic clock disadvantages and realize an ultrastable and low-uncertainty ^{88}Sr clock. State mixing is induced by applying a magnetic field to induce a transition moment [1]. The clock laser is stabilized to a cryogenic Si cavity [2], allowing for interrogation times up to 4 s, corresponding to 200 mHz Fourier-limited linewidth. This permits the use of low clock laser intensity and small magnetic field, with consequent reduction of clock laser AC Stark shift and 2nd-order Zeeman shift to the sub-Hz level. In addition, with longer interrogation time, the QPN-limited clock instability is strongly reduced, allowing working with lower atom number, thus reducing the collision shift.

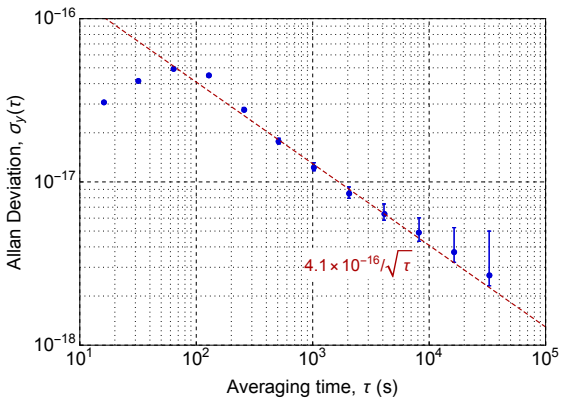

Fig. 1: Allan deviation of the beat note between the bosonic and the fermionic Sr clocks.

The clock is a rack-type clock with fully modular laser system [3]. The clock laser power and the current in the coils used for generating the mixing magnetic field are actively stabilized. This allows reaching an instability of 3×10^{-18} at 2×10^4 s averaging time, as shown by a comparison with the PTB ^{87}Sr clock [4] (Fig. 1). The bosonic clock uncertainty was characterized to be 2.0×10^{-17}. This is a factor 30 improvement compared with previous works on bosonic clocks. The ^{88}Sr–^{87}Sr isotope shift was measured with an uncertainty of 12 mHz and is within 2σ of the recently reported one [5].

References

[1] A. V. Taichenachev et al., Phys. Rev. Lett. 96, 083001 (2006).

[2] D. G. Matei, et al., Phys. Rev. Lett. 118, 263202 (2017).

[3] K. Bongs, et al., C.R. Phys. 16, 553 (2015).

[4] S. Falke et al., New J. Phys. 16, 073023 (2014).

[5] T. Takano, et al., Appl. Phys. Exp. 10, 072801 (2017).

Technical developments for portable optical clocks

Nathan R. Gemmell, Callan Jobson, Matthias Keller

School of Mathematical and Physical Sciences, University of Sussex, Falmer, UK
Email: N.Gemmell@sussex.ac.uk

Optical clocks represent the pinnacle of precise timekeeping [1]. However, their impact and penetration into the market remains hindered by their size and cost. Here we present several technological developments which have allowed us to progress towards a complete, turn-key, portable optical clock system, able to fit within a 19" rack module.

We have developed a miniaturized trapping system complete with integrated fibre optical laser delivery (cooling, two-stage photo-ionisation, re-pumping, and quenching) as well as fluorescence collection. This compact design has allowed us to achieve a complete vacuum system volume of less than one litre.

The use of calcium as the ion source allows for all laser wavelengths required to be accessible with commercial diodes. All narrow linewidth diode lasers are coupled into low loss optical fibres. Fibre-based splitters, SHGs, and switches have been employed to ensure minimal free space beam propagation; eliminating the need for optical benches, reducing risk of misalignment, and increasing system ruggedness.

Microcontroller based control electronics ensure that the system can have fully automated control of lasers, measurements, and trap parameters, thus requiring no external PC required to run. This generation of a turn-key, portable system will eventually allow use by laymen.

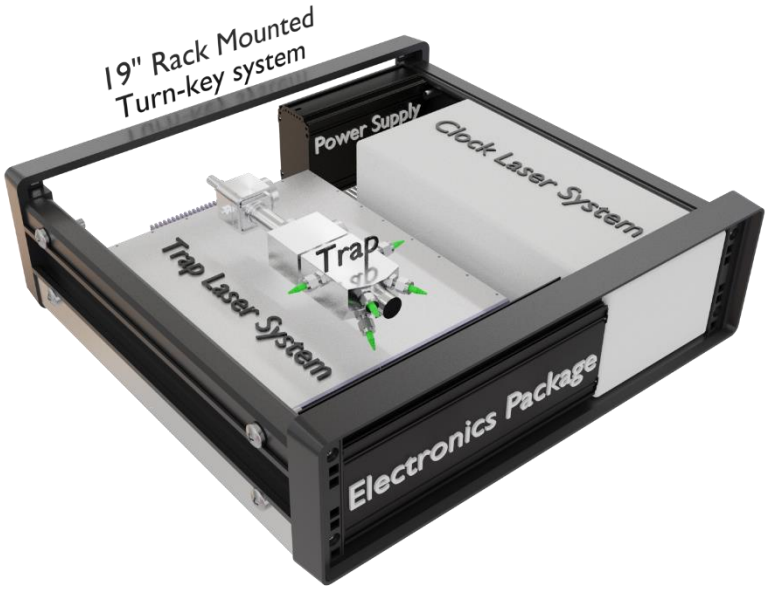

.

Fig 1. Schematic of the miniaturised ion trap based optical clock system.

References

[1] N. Huntemann, C. Sanner, B. Lipphardt, Chr. Tamm, and E. Peik, "Single-Ion Atomic Clock with 3×10^{-18} Systematic Uncertainty", Phys. Rev. Lett. Vol. 116, 063001, 2016

Experiments on 475 km of Spooled Fibre Link Comprising Two Different Amplification Techniques

Fei Meng[1,2,3], Alexander Kuhl[1], Thomas Waterholter[1], Gesine Grosche[1]

[1]Physikalisch-Technische Bundesanstalt, Braunschweig, Germany
[2]National Institute of Metrology, Beijing, China
[3]School of Electronics Engineering and Computer Science, Peking University, Beijing, China

Email: fei.meng.ext@ptb.de, mfei@nim.ac.cn

High stability optical frequency dissemination via phase-stabilized long-distance telecommunication fibre links is the precondition of many applications, e.g., the remote comparison of optical clocks, the verification of fundamental physics, and the determination of geodetic height levels differences with high resolution. In order to compensate the attenuation of the optical signal during transit in the long distance single mode fibre link, it is a key technique to effectively amplify the weak signal to ensure stable transmission. In the case of frequency dissemination using the interferometrical link stabilization technique from [1], bidirectional amplifiers are mandatory due to the two-way nature of link stabilization employed.

To simulate parts of the national fibre link from Physikalisch-Technische Bundesanstalt (PTB) to Max-Planck-Institut für Quantenoptik (MPQ), we set up a 475 km link of spooled fibre comprising one fibre Brillouin fibre amplifier (FBA) [2] and four bidirectional Erbium-doped fibre amplifiers (BiEDFA). The amplifiers can provide a combined gain of more than 110 dB. To avoid spontaneous lasing effects due to Rayleigh backscattering or reflections from the link, the gain of the BiEDFA has to be carefully optimized [3]. We found a regime for stable operation for gain lower than 20 dB each.

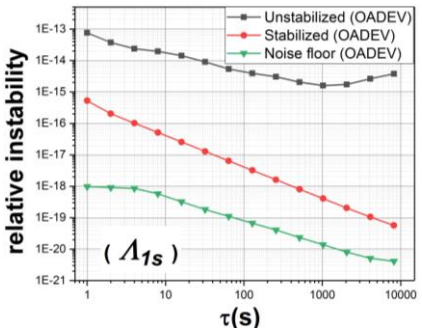

Fig.1 Frequency transfer instability, overlapped ADEV, Λ–weighted data, 1s gate time

Fig. 1 shows the relative frequency instability of the signal at the remote end of the link with and without stabilization, as well as the noise floor of the interferometer. In the stabilized case, the optical frequency transfer instability declines with 6×10^{-16} s/τ (Λ_{1s}- OADEV[1]), and reaches 10^{-19} for averaging times of more than 3 hours.

Fig. 2 shows the phase noise power spectral density (PSD) of the remote signal for the unsterilized and the stabilized case; the letter coincides with the calculated theoretical limit [2] for frequencies below the control bandwidth. We find about 42 dB noise suppression at 1Hz Fourier frequency.

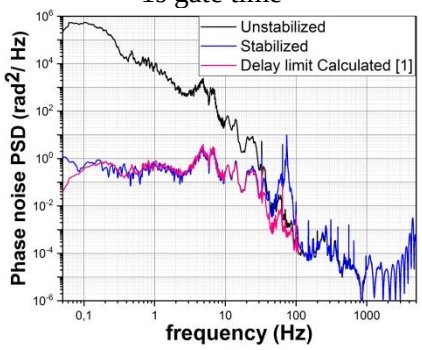

Fig.2 Phase noise power spectral density at the remote end of the link

References

[1] P.A. Williams, W. C. Swann, and N. R. Newbury, "High-stability transfer of an optical frequency over long fiber-optic links", J. Opt. Soc. Am. B/ Vol. 25, No. 8, 2008
[2] S.M.F. Raupach, A. Koczwara, and G. Grosche, "Brillouin amplification supports 1×10^{-20} uncertainty in optical frequency transfer over 1400 km of underground fiber", Phys. Rev. A 92, 021801(R), 2015
[3] Predehl K., Grosche G., Raupach S. et al., "A 920-Kilometer Optical Fiber Link for Frequency Metrology at the 19th Decimal Place" Science 336, 441, 2012

1880 km Looped Optical Fibre Link Combining Two Amplification Techniques

Thomas Waterholter[1], Gulnara Vishnyakova[2,3], Alexander Kuhl[1], Ronald Holzwarth[2,4], Gesine Grosche[1]

[1] Physikalisch-Technische Bundesanstalt, Bundesallee 100, 38116 Braunschweig, Germany

[2] Max-Planck-Institut für Quantenoptik, Hans-Kopfermann-Str. 1, 85748 Garching, Germany

[3] P.N. Lebedev Physical Institute of the Russian Academy of Sciences, Leninskiy Prosp. 53, 119991 Moscow, Russia

[4] Menlo Systems GmbH, Am Klopferspitz 19a, 82152 Marinsried, Germany

Email: thomas.waterholter@ptb.de

We study optical frequency transfer over a 1880 km loop of underground dark fiber connecting the Physikalisch-Technische Bundesanstalt (PTB) in Braunschweig and the Max-Planck-Institut für Quantenoptik (MPQ) in Garching near Munich via the Karlsruhe Institute of Technology (KIT). To this end, we adapt the optical fibre link from Braunschweig to Strasbourg (STB) [1] to the MPQ, by installing a branching node at KIT, that allows the connection to the link between MPQ and KIT, that has already been set up by the MPQ group.

The newly formed fibre link is composed of two parts, and currently combines two techniques for intermediate amplification of the metrology signal: the PTB-KIT segment with a one-way distance of 600 km is equipped with three fiber Brillouin amplifiers (FBA) [1] and the MPQ-KIT segment with a one-way distance of 340 km is equipped with three bidirectional Erbium-doped fiber amplifiers (biEDFA [2]). BiEDFAs are suitable for time transfer as well, but gains must be set carefully, since Rayleigh backscattering and reflections have been observed to lead to cycle slips [2,3,4]. The link is currently looped at MPQ for characterization purposes.

We aim at a link uncertainty $< 1\times10^{-18}$ (at $\sim 40\,000$ s): such performance would enable tests of the transportable Sr optical clock [5] developed at PTB and chronometric levelling experiments [6] with negligible link uncertainty contributions for the clock frequency comparisons (with PTB stationary frequency standards).

To date, we have established the connection of the two link segments in Karlsruhe and performed first tests with the phase stabilized link.

We thank the DFG Sonderforschungsbereich (SFB) 1128 (geo-Q), the European Metrology Programme for Innovation and Research (EMPIR) in project 15SIB05 (OFTEN) for financial support, as well as the DFN and Gasline for optical fibers and Stefan Droste for support in the early stage of the experiment.

Fig. 1: Current experimental set-up of the optical fiber link PTB-KIT-MPQ

References:

[1] Raupach S., Koczwara A., and Grosche G., Physical Review A 92.2, p. 021801, 2015
[2] Predehl K., Grosche G., Raupach S. et al., Science 336.6080, pp. 441–444, 2012
[3] Chiodo N., Quintin N., Stefani F. et al., Opt. Express 23.26, pp. 33927–33937, 2015
[4] S. Droste, F. Ozimek, T. Udem, et al., Phys. Rev. Lett. 111, 110801, 2013
[5] Koller S., Grotti J., Al-Masoudi A. et al., Physical Review Letters 118.7, p. 073601, 2017
[6] Vermeer M., Reports of the Finnish Geodetic Institute. Geodeettinen Laitos, Geodetiska Institutet, 1983

Evaluation of White Rabbit for Time Service Distribution

Peter Whibberley, Elizabeth Laier English, Conway Langham, David Hicks, Simon Ashford

Time and Frequency Group, National Physical Laboratory, Teddington, UK

Email: peter.whibberley@npl.co.uk

Time dissemination through packet-based optical fibre networks is becoming increasingly important for synchronisation in finance, telecommunications and other sectors of the economy, providing an alternative or complement to the use of GPS. The main method in use to provide accuracy better than milliseconds is the well-established Precision Time Protocol (PTP), which is currently under version 2, formalised as IEEE 1588-2008. More recently, an enhanced form of PTP known as White Rabbit (WR) has been developed, combining improved hardware timestamping with synchronous Ethernet to deliver sub-nanosecond instability and, potentially, accuracy [1].

NPL operates a service, known as NPL*Time*®, that disseminates time to multiple users over fibre links using PTPv2 [2]. The NPL*Time*® distribution model is based on two hubs, located in datacentres in London and Reading that are both connected to NPL by around 80 km of leased fibres. A caesium clock installed in each hub provides holdover and maintains continuous service provision within the specifications in the event of the fibre link back to NPL being interrupted. Distribution of time onwards from the hubs to the customers is over PTP-compatible fibre links provided by distributors working in partnership with NPL. The service endpoints, which are PTP slave devices that feed time into the customer networks, are calibrated and monitored by NPL to ensure that they remain traceable to UTC(NPL) with an offset no greater than ±1 μs.

To improve the performance and resilience of the NPL*Time*® service, we have set up a WR link to each hub using commercially-available switches (from Seven Solutions). The WR links operate on a different wavelength to the existing PTP links, with passive optical multiplexers at each end of the fibres to combine and separate the signals. The fibres are normally operated as a unidirectional pair, but the absence of amplifiers between NPL and the hubs allows bidirectional operation on the individual fibres in each pair to determine the round-trip time difference, and therefore the required offset correction when in normal use as a pair. We will report the performance of the WR links, and compare them with the corresponding PTP-based services.

We are also carrying out trials of WR for linking two NPL clock laboratories over 200 m (or 400 m round-trip) of highly-stable internal fibre to establish the optimum frequency and time transfer performance that can be achieved, in comparison with both phase-stable coaxial cable and a stabilised fibre link based on a commercial system (the PikTime ELSTAB equipment). The results of this work will also be presented.

References

[1] E. Dierikx et al., “White Rabbit Precision Time Protocol on long distance fiber links”, IEEE Trans. UFFC, vol. 63 (7), p. 945-952, 2016.

[2] E. Laier English, P. Whibberley, C. Langham, D. Hicks and L. Lobo, “Update on the NPL*Time*® service and future developments with White Rabbit”, Proc. Precise Time and Time Interval Systems and Applications (PTTI) Meeting, January 2017.

High coherence visible comb from an Er fiber laser

Antoine Rolland[1], Peng Li[2], Marco Cassinerio[2], Jie Jiang[2] and Martin Fermann[2]

[1]IMRA America, Boulder Research Labs,1551 S Sunset st, Longmont CO 80501, USA
[2]IMRA America, 1044 Woodridge avenue, Ann Arbor, USA

Email: arolland@imra.com

For the future redefinition of the second, it is generally desirable to engage frequency ratio measurements between different clock transitions to ensure overall reliability and precision. As optical clocks are starting to reach an instability of 5×10^{-17} in 1 sec, present comb architectures as required for precision clock comparison are reaching their limits. On the one hand, solid-state lasers do not provide the level of required reliability, on the other hand Er fiber based multi-branch and single branch comb architectures do not provide sufficient frequency stability beyond the 10^{-17} level.

Here we demonstrate a new comb architecture that promises to deliver beyond the 10^{-18} level in a signal branch system based on highly coherent broadband visible comb generation from frequency doubling of an Er comb. The 250 MHz Er comb is amplified with an Er fiber similariton amplifier [1] optimized for power, pulse width and amplifier efficiency. After frequency doubling we demonstrate a frequency comb spanning 500 nm to 1200 nm, as shown in figure 1(a). Using an *f*-2*f* interferometer based on the visible comb, we detect the f_{ceo} with a signal-to-noise ratio (SNR) of 40 dB in 100 kHz resolution bandwidth in the visible domain.

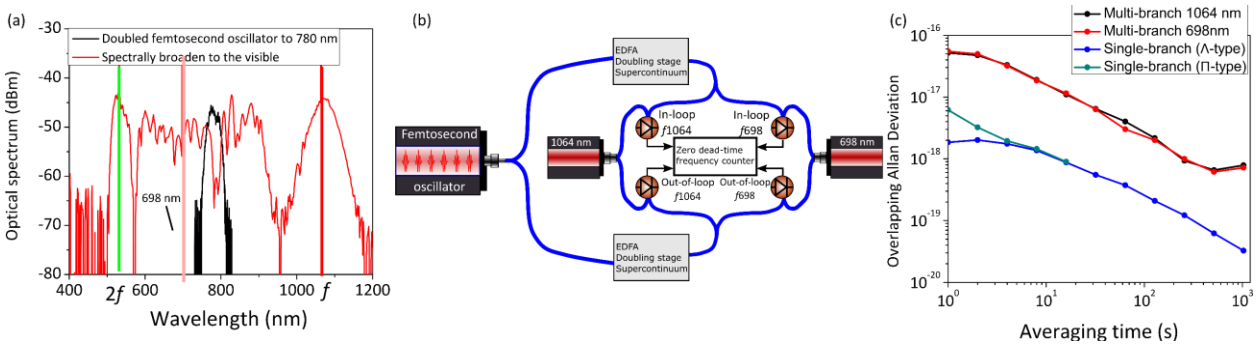

Figure 1: (a) Optical spectrum of the doubled 1.5 µm frequency comb and the visible frequency comb. (b) Experimental setup to characterize the residual noise of the visible arm frequency comb. See text for details. (c) Out-of-loop fractional frequency instability of the 698 nm and 1064 nm beatnote with the visible comb and the frequency ratio.

As an additional check of coherence we further detect two beatnotes at 698 nm (wavelength corresponding to the strontium lattice clock transition) and at 1064 nm. We have measured a SNR higher than 40 dB for both wavelengths. In order to measure the residual instability of the visible comb, we set up a dual branch system (Fig. 1b) using two broadband visible continua seeded with one common comb oscillator. The first branch is then configured for stabilization of the comb with the 1064 nm reference laser and stabilization of the 698 nm laser with the comb simultaneously, where the 698 nm laser is phase locked to the 1064 nm laser through the comb. The second branch is used for out-of-loop measurements. We obtain a residual instability at $< 6\times10^{-17}$ at 1 s integration time reaching 2×10^{-18} for both wavelengths (accuracy of the best optical clock) at 100 s. In the context of comparing two optical clocks we show data of a visible single branch frequency comb. As the comb branch noise is correlated to both wavelengths, the residual noise of a frequency ratio (comb agreement) is reduced to 1.8×10^{-18} at 1s and reaches 4×10^{-20} at 1000 s (See figure 1 (c)). This work opens the way to ultra-low noise spectral purity transfer from the IR to the visible.

References:

[1] M. E. Fermann, V.I. Kruglov, B.C. Thomsen, J.M. Dudley and JD Harvey, "Self-similar propagation and amplification of parabolic pulses in optical fibers", Phys. Rev. Lett., **84**, 6010 (2000)

[2] N. Hinkley, J. A. Sherman, N. B. Phillips, M. Schioppo, N. D. Lemke, K. Beloy, M. Pizzocaro, C. W. Oates, and A. D. Ludlow, "An atomic clock with 10^{-18} instability", Science, vol. 341, pp. 1215–1218 (2013).

[3] D. Nicolodi, B. Argence, W. Zhang, R. Le Targat, G. Santarelli, and Y. Le Coq, "Spectral purity transfer between optical wavelengths at the 10^{-18} level", Nat. Photon., vol. 8, pp. 219–223 (2014)

Preliminary Algorithms for Simulating and Analysing Microwave Link Data from the Atomic Clock Ensemble in Space (ACES) Mission

S. Shemar, K. Burrows, H. Collingwood

Quantum Science Department, National Physical Laboratory, Teddington, TW11 0LW, UK

Email: setnam.shemar@npl.co.uk

ESA's ACES mission comprises a payload to be installed on the International Space Station for demonstrating the PHARAO and SHM space clocks, as well as a high performance Micro-Wave Link (MWL). The latter will compare the space clocks with advanced clocks on the ground, such as caesium fountains and optical clocks, enabling tests of fundamental physics. Comparisons will also be possible between ground clocks at different laboratories to 1 part in 10^{17}. Here we present the outputs of a one-year study to develop early-stage algorithms for simulating and analysing data from the MWL.

The study has focused on space-to-ground transfer of microwave timing signals by use of a PRN-code sequence. Preliminary ACES data simulations have been investigated, including the motion of the ISS and ground terminals, the propagation times of signals, ionosphere de-lays, relativistic effects and the signal processing outputs. Although the signal carrier-phase would enable lower uncertainties, the emphasis in the work has been on the code-phase.

Preliminary analysis algorithms have been developed for one-way code transfer between the clocks in the ACES payload and a clock in a laboratory connected to an ACES MWL ground terminal. These have mainly been tested using simulated data for the Ku-/S-band downlink signals, with limited results obtained using simulated data for the Ku-band uplink signal. We find that use of the code observables enables the time-of-arrival of a particular chip in the code to be estimated to a precision of approximately 20 ps relative to the local clock.

There are presently limitations in the algorithms including: a perfectly circular orbit is assumed for the ISS, tropospheric delays are not simulated and the signal carrier-phase and data from multiple ISS passes are not considered.

Although further developments of the software would be required before use in processing real ACES data, including the two-way time and frequency transfer, the software provides a frame-work of algorithms which could in future be extended.

We acknowledge funding from the UK Space Agency and the UK Department of Business, Energy & Industrial Strategy, and helpful discussions with and information provided by Time-Tech GmbH and LNE-SYRTE.

References

[1] F. Meynadier, P. Delva, C. le Poncin-Lafitte, C. Guerlin, P. Wolf, "Atomic Clock Ensem-ble in Space (ACES) data analysis", arXiv:1709.06491v1 [astro-ph.IM], 2017.

Portable microwave clock using laser-cooled trapped $^{171}Yb^{+}$ ions

S. Mulholland[1,2], G.P. Barwood[1], S. Donnellan[1], D. Gentle[1], G. Huang[1], H.A. Klein[1], P. Patel[1], G. Walsh[1], P.E.G Baird[2], P. Gill[1,2]

[1]National Physical Laboratory, Teddington, UK
[2]Clarendon Laboratory, University of Oxford, Oxford, UK
Email: sean.mulholland@npl.co.uk

A portable microwave clock incorporating laser cooling of $^{171}Yb^{+}$ promises to bring significantly improved performance over existing thermal commercial devices. We report on progress in the development of a compact microwave frequency standard designed to fit in a 19-inch rack enclosure that comprises laser, electronics and physics package subsystems. Recent results in which a local oscillator was disciplined by laser-cooled trapped $^{171}Yb^{+}$ ions will be presented.

Clouds of ions created by photo-ionisation of a weak ytterbium atomic flux emitted from a miniature oven are confined and laser-cooled within a linear RF trap at ultra-high-vacuum. Photo-ionisation requires 399 nm laser light which is generated by frequency doubling. Up to 900 µW of 369 nm from a diode laser is used to cool the ions, with additional infra-red diode-laser light at 935 nm needed to maintain a closed cooling cycle. A 760 nm diode-laser is used to clear out a long lived F-state and improve the trapped ions' lifetime. The output of a microwave local oscillator (LO) derived from a very stable quartz reference, is locked to the narrow 12.6 GHz $^{171}Yb^{+}$ ground-state hyperfine clock transition. A stabilised 10 MHz output is derived from the error signal. Preliminary measurements have demonstrated a frequency instability of $1x10^{-13}$ at 10,000 s (fig 1). Potential applications include telecommunications and financial reference systems as well as navigation system integrity.

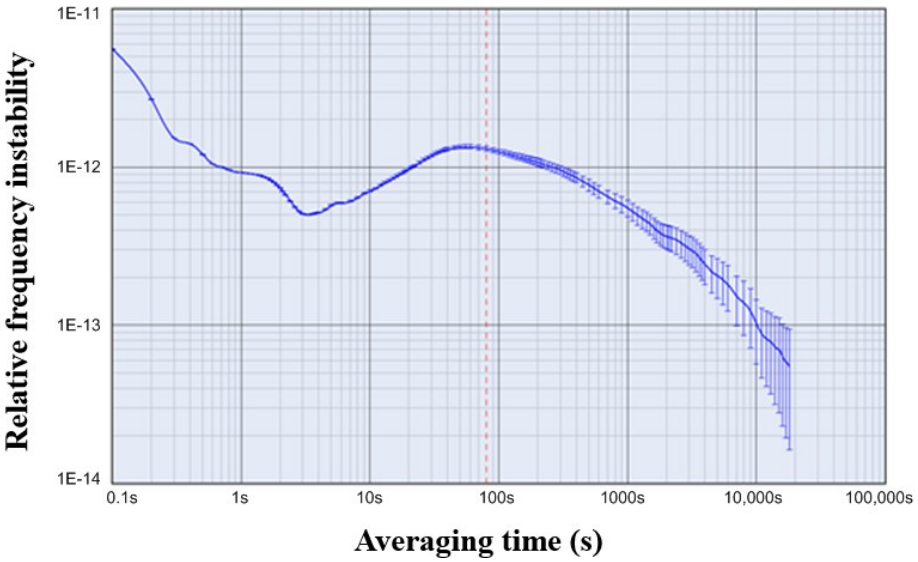

Fig 1: Allan deviation of the laser-cooled trapped $^{171}Yb^{+}$ ion microwave clock output versus a hydrogen maser derived 10 MHz reference. Feedback is applied at 30 s.

We acknowledge U.K. Defence Science and Technology Laboratory (Dstl) financial support.

Möbius Metamaterial Strips: Opportunities for Next Generation Frequency Sources and Design Challenges

Ulrich L. Rohde[1,2], Ajay K. Poddar[1,2], Enrico Rubiola[3], Alexandru M. Silaghi[1]

[1]University of Oradea, Faculty of EE and IT, Oradea, Romania
[2]Synergy Microwave Corp., Paterson, NJ, USA
[3]FEMTO-ST Institute, Besancon, France

Email: akpoddar@synergymwave.com

This paper reports the MMS resonator structure based Ka-band signal sources for the applications in 5G communication systems and associated design challenges. Homogeneous electrical resonator use 'regular' materials having positive index 'n' ($n = \sqrt{\epsilon\mu}$; $\varepsilon > 0$, $\mu > 0$), where ε and μ are the electric permittivity and magnetic permeability. Their noise contribution are usually modelled using current and voltage sources, whose average values are obtained from the fluctuation dissipation theorem based on normalized impedance.

Conversely, non-homogeneous metamaterial structure enable the implementation of either positive or negative ε and μ, opening the way to new and exciting design options. Of course, ε and μ are now local properties which hold in a given frequency range, and the refraction index has to be re-defined as $n = \pm\sqrt{\epsilon\mu}$ or $n = j\sqrt{\epsilon\mu}$, depending upon the combination of signs [1]. In a resonator, implemented with $\varepsilon < 0$ and $\mu < 0$, hence $n = -\sqrt{\epsilon\mu}$, the noise source degenerate into magneto-inductive noise, leading to the propagation in the form of forward and backward noise waves. Any material supporting single propagating mode at a given frequency has a well-defined index n and normalized impedance z, whether the material is homogeneous and continuous or not. By contrast, it is not easy to assign a normalized impedance z to a non-homogeneous materiel. The negative-index resonator shows distinct values of the impedance z for the waves propagating in forward or backward direction. This happens because the ratio of electric/magnetic field varies periodically throughout the structure. Figure (1) shows the Möbius Metamaterial Strips resonator structure based Ka-band signal sources operating at 26-39 GHz, exhibits typical phase noise -90dBc/Hz @ 10 kHz offset from the carrier. The oscillator circuit is built on substrate (8-mill thick), uses BFP740 SiGeHBT transistor for providing negative resistance to compensate the losses of the resonator tank. The total DC power consumption is 400 mW. We observed that Mobius phase shifter shown in Figure (1) increases the tuning ranges (26-39 GHz), and also yield a noise reduction 3-6 dB over the operating band. A possible explanation could be that injection locking and mode-locking evanescent-mode EM coupling, detailed analysis will be shown in the final version of the paper.

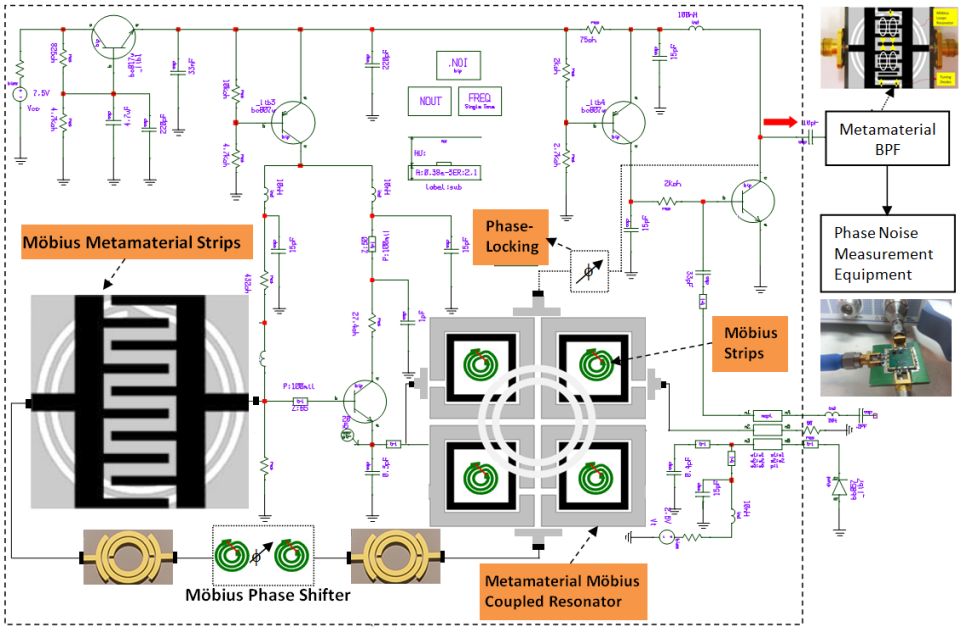

Fig. 1: MMS inspired Ka band (30-38 GHz) tunable frequency source

References

[1] A. K. Poddar and U. L. Rohde, "Metamaterial Mobius strips (MMS): Application in resonators for oscillators and synthesizers," in Proc. Int'l Freq. Control Symp., May 19–22, 2014, pp. 1–9.

Evaluation and development of optical time transfer (OTT) links between PTB and Deutsche Telekom

Ł. Śliwczyński[1], P. Krehlik[1], J. Kołodziej[1], H. Imlau[2], H. Ender[2], H. Schnatz[3], D. Piester[3], A. Bauch[3]

[1]Faculty of Computer Science, Electronics and Telecommunications, AGH University of Science and Technology, Krakow, Poland
[2]Deutsche Telekom Technik GmbH, Bremen, Germany
[3]Physikalisch-Technische Bundesanstalt (PTB), Braunschweig, Germany

Email: sliwczyn@agh.edu.pl

Experiments with transfer of 10 MHz and 1 PPS signals via optical fibers between Deutsche Telekom and PTB using AGH-developed ELSTAB technology started in 2015 with a first proof of concept (PoC) phase 1 link connecting PTB in Braunschweig with a Deutsche Telekom test center in Bremen [1]. At the end of 2016, a time and frequency hub has been established in Deutsche Telekom premises in Hannover and connected with PTB and Bremen using a redundant multi-link permanent architecture (phase 2) [2]. Since then all these links are in continuous operation, creating a unique opportunity to monitor the stability and reliability of time transfer calibration. In 2017 efforts have been undertaken to establish two more fiber links with the purpose to connect the premises of Deutsche Telekom in Frankfurt/Main hosting its realization of Coordinated Universal Time UTC(DTAG) with UTC(PTB).

In this paper we present the results of one-year stability measurements of 1 PPS and 10 MHz signals and of a calibration campaign performed in December 2017. These results are compared with the data from the initial calibration campaign [2] performed during the installation of the PoC phase 2 link. All five links show good calibration repeatability after one year of operation as shown in Tab. 1 for a) chromatic dispersion, b) total round trip delay, c) connection to the local time reference.

Table 1. Fragment of a table with calibration details of two of five links connecting PTB and Deutsche Telekom site in Bremen.

Link	Parameter Quantities in ps		December 2016	December 2017	Difference	Comments
5.2 Hannover-Bremen	a)	$\Delta\tau_{F-B}$	1 900	1 891	-9	
	b)	$\tau_{REF-RET}$	1 389 040 567	1 390 040 568	+1 000 001	offset caused by fiber change due to a bridge construction in Bremen
	c)	$\tau_{source-REF}$	1 088 541	1 088 522	-19	
5.4 Hannover-PTB	a)	$\Delta\tau_{F-B}$	1 179	1 172	-4	
	b)	$\tau_{REF-RET}$	850 040 534	850 040 538	+4	
	c)	$\tau_{source-REF}$	1 104 427	1 104 418	-9	

This work was partially supported by the EMPIR initiative co-funded by the European Union's Horizon 2020 research and innovation programme and the Participating States via project 15SIB05 and also by the Faculty of Computer Science, Electronics and Telecommunications, AGH University of Science and Technology.

References

[1] Ł. Śliwczyński et al.: "Fiber-Optic Time Transfer for UTC-Traceable Synchronization for Telecom Networks," IEEE Comm. Standards Mag., vol. 1, no. 1, pp. 66-73, 2017.

[2] Ł. Śliwczyński et al.: "Fibre optic time transfer between PTB and Deutsche Telekom using multi-link redundant topology," Proc. EFTF 2017, Besançon, France, pp. 681-682, 2017.

FBAR-based 3.4 GHz Oscillator without Frequency Multiplications Aiming for an Integrated Atomic Clock Chip

M. Hara[1], Y. Yano[1], M. Kajita[1], S. Hara[1], A. Kasamatsu[1],
M. Toda,[3] H. Ito[2], T. Ono[3] and T. Ido[1]
[1]National Institute of Information and Communications Technology, Tokyo, Japan
[2]Tokyo Institute of Technology, Yokohama, Japan
[3]Tohoku University, Sendai, Japan

Email: hara.motoaki@nict.go.jp

We propose a simple system of a chip-scale atomic clock without complicated PLL based frequency multiplications. The system exploits a 3.5-GHz-band thin film bulk acoustic resonator (FBAR) as a heart of the voltage controlled oscillator (VCO), generating the half of the ^{87}Rb clock frequency directly ($f_{clk}/2 \approx 3.4$ GHz) without an off-chip quartz oscillator and a PLL circuitry.

This technique provides cost and size merits as well as a low power operation by the simplification of the micro wave generator [1]. The FBAR is a thin film device fabricated on the substrate, and is widely accepted as passive filters or duplexers [2-4]. The advantages of the FBAR are found not only in a high-Q resonance and an excellent power durability but also in a CMOS-compatibility. So, it could be integrated on any silicon devices [5], such as amplifiers, photonic devices, or even a MEMS-based gas cell.

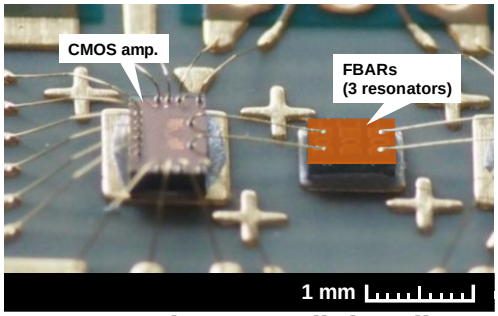

Fig. 1: A voltage controlled oscillator on the board: A negative amplifier of the oscillator was implemented in a 65-nm CMOS technology. Chip size was 1 mm×0.67 mm. The chip size of the FBAR was about 0.6 mm×0.8 mm. Three FBARs were fabricated on a chip for demonstrations. They were mounted on the PCB and connected with a gold wire.

We originally developed the FBAR-VCO as shown in Fig.1. Besides that, a bulk-micromachined Rb gas cell was also developed. These two key devices were incorporated into a desktop-size test bench of the CPT atomic clock [6]. As a result, the FBAR-VCO was directly stabilized to a CPT resonance of ^{87}Rb without the frequency multiplication using a PLL circuitry. A sustainable clock operation was achieved successfully with a frequency instability of 2.1×10^{-11} at 1 s. To the best of the authors knowledge, it is a top-level performance of the short-term frequency stability among the CPT based atomic clocks using the micromachined gas cell.

References

[1] R. Lutwak et. al., “The MAC - a miniature atomic clock”, in Proc IFCS 2005, p. 752-757, 2005.
[2] R. Ruby et. al., “PCS 1900 MHz duplexer using thin film bulk acoustic resonators (FBARs)”, Electron. Lett., vol. 35(10), p. 794-795, 1999.
[3] R. Aigner, “Advancement of MEMS into RF-filter applications”, in Proc. IEDM 2002, p. 897-900, 2002.
[4] T. Nishihara et. al., “High performance and miniature thin film bulk acoustic wave filters for 5 GHz”, in Proc. IUS 2002, p. 969-972, 2002.
[5] M. A. Dubois et. al., “Monolithic above-IC resonator technology for integrated architectures in mobile and wireless communication”, IEEE JSSC, vol. 41(1), p. 7-16, 2006.
[6] Y. Yano et. al., “Coherent population trapping atomic clock by phase modulation for wide locking range”, Appl. Phys. Lett., vol. 111(20), 2011107, 2017.

Study on BeiDou All-in-View Time Transfer

Zhang Jihai[1, 2], Guang Wei[1, 2, 3], Wu Wenjun[1, 2], Li Wei[1, 2], Yuan Haibo[1, 2], Dong Shaowu[1, 2, 4]

[1] National Time Service Center, CAS, Xi'an, China
[2] Key Lab of Time-frequency Standard, CAS, Xi'an, China
[3] University of Chinese Academy of Sciences, Beijing, China
[4] School of Astronomy and Space Science, CAS, Beijing, China

Email: zhangntsc@126.com, yuanhb@ntsc.ac.cn, sdong@ntsc.ac.cn

GNSS time transfer is one of the major technologies for generation of Coordinated Universal Time (UTC) and International Atomic Time (TAI). The GPS Common View (CV) was presented in 1980, and has been used as the main time transfer technology by BIPM. With the developing of satellite orbits and clock products, the GPS All-in-view time transfer was presented for the first time in 2004. Now, with the development and promotion of Chinese BeiDou Navigation Satellite System (BDS), the BDS has already provide with regional navigation, position, velocity and time (PVT) service capabilities. Meanwhile, many of the application and related research are executed actively based on BDS. By 2020, the BDS will be build a global system for user with real-time and high-precision PVT.

In this paper, the BDS AV time transfer technology is studied, and the data of BeiDou receivers which is operated in the Time Keeping Laboratory of National Time Service Center (NTSC) and Telecommunication Laboratories (TL) is used for BeiDou AV time transfer study. The test is from MJD 58088 to 58094, and sampling interval is 300s. The Fig.1 shows the UTC(NTSC)-UTC(TL) by BeiDou AV, and the Fig.2 shows the Allan Deviation UTC(NTSC)-UTC(TL) by BeiDou AV, the RMS of UTC(NTSC)-UTC(TL) is 1.2303 ns, and it is shows that the BeiDou AV can be used in nanosecond level time transfer

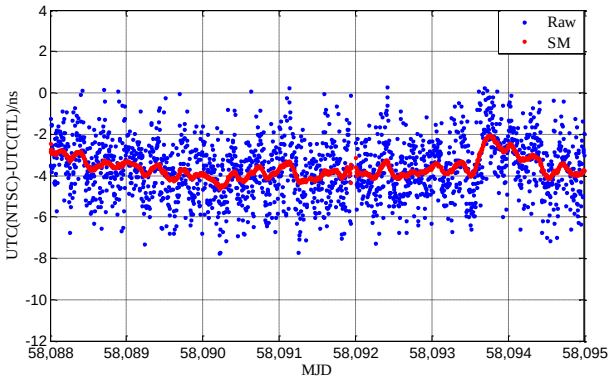

Fig.1 The UTC(NTSC)-UTC(TL) by BeiDou AV

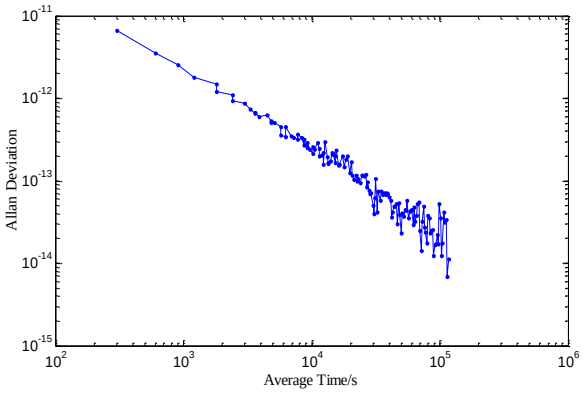

Fig.2 The Allan Deviation by BeiDou AV

References

[1] M. A. Weiss, G. Petit, Z. Jiang, "A Comparison of GPS Common- View Time Transfer to All-in-View", IEEE, p. 324-328, 2005.

[2] Shinn Yan Lin, Zhiheng Jiang, "GPS All in View Time Comparison using Multi-receiver Ensemble", IEEE, p. 362-365, 2017.

[3] Petit G, Jiang Z, "GPS All in View time transfer for TAI computation", Metrologia 45(1),p. 35-45, 2008.

[4] Yuan HaiBo, Guang Wei, Yang Fan, "Time Service Through BD GEO Satellite", EFTF&IFCS, p. 496-500, 2013.

[5] Guang Wei, Yuan Haibo, Dong Shaowu, Zhao Shuhong, Zhang Jihai, Wei Yajing, "The evaluation of BeiDou time transfer performance", IFCS, p. 1-4, 2016

Study on the relation between laser noise and optical frequency transmission

Zhang Xi [1,3*], Yang Fei[1*], Feng Zitong [1,3], Gui YouZhen[2], Cai Haiwen[1*] and Qu ronghui[1]
[1]Key Laboratory of All Solid-State Laser and Applied Techniques, Shanghai Institute of Optics and Fine Mechanics, Chinese Academy of Science, Shanghai 201800, China;
[2]Key Laboratory for Quantum Optics, Shanghai Institute of Optics and Fine Mechanics, Chinese Academy of Science, Shanghai 201800, China;
[3]University of Chinese Academy of Sciences, Beijing 100049
Email: zhangxi@siom.ac.cn fyang@siom.ac.cn hwcai@siom.ac.cn

***Abstract*—By use of a linewidth measurement method based on the 120 degree difference interferometer, we study on the relation between laser noise and optical frequency transmission, such as the evolution of frequency noise and linewidth characteristics before and after transmission. Meanwhile, we chose some different typical commercial narrow-linewidth lasers: EMCORE, RIO, and NKT-X15 as optical carrier to demonstrate the effect of linewidth on transmission stability.**

Keywords—optical frequency transfer; linewidth; noise measurement

I. INTRODUCTION

The length of optical fiber transmission link is limited by the coherence length of the light sources[1], meanwhile the relationship between the laser linewidth and its coherence length in the optical fiber is expressed as:

$$L_c = \frac{c/n}{\Delta v}$$

Therefore it is very important to accurately measure the laser linewidth.

Linewidth can be divided into the intrinsic linewidth and technical linewidth. It is difficult for traditional methods of measuring laser linewidth, such as optical spectrum analyzer (OSA), to meet the demands of narrow linewidth lasers for its resolution is not enough. Therefore, scientists take advantages of the characteristics of low noise and high stability of interference demodulation to develop a series of measurement techniques. First, it is beat note method[2], which needs a high coherent source as a reference. The second is DSH technique based on the Mach-Zehnder interferometer with 2×2 coupler[3] or Michelson interferometer[4], which needs complicated control of quadrature point using active feedback methods and accurate calibration. Another is recirculating delayed self-heterodyne method[5], in which the length of the delay fiber decreases, while the optical power loss increases.

In this paper, we used our proposed linewidth measurement method based on the 120 degree phase difference interference technique[6] to extract the integral time linewidth and the intrinsic linewidth of the narrow-linewidth laser simultaneously in a single-shot measurement by processing the laser frequency noise power spectral density in algorithm. The phase noise characteristics of several typical commercial lasers were tested before and after the transmission. Active noise compensation (ANC) method[7] was also set up to test the transfer stability of the lasers.

II. EXPERIMENTS SETUP

The set up of laser linewidth measurement system is shown in Fig.1. The laser passed through the optical fiber link is injected into the circulator port1, whose port 2 is connected to one of the input port of the 3 × 3 coupler. The two beams reflected by Faraday mirrors and with different delay time interfere with each other. The interference fringes are collected by high-precision acquisition card after they enter the detector, and used to compute the phase/frequency noise of the laser under test by the algorithm in [6].

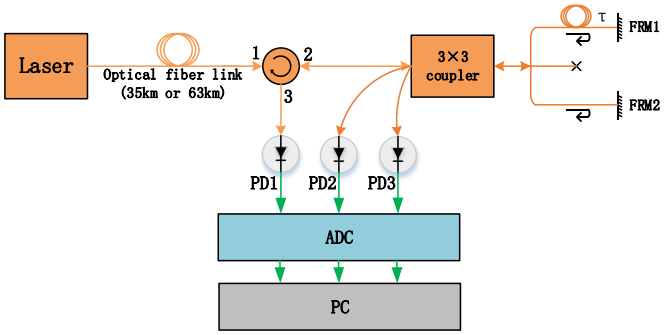

Fig.1. Linewidth measurement system (FRM, Faraday rotator mirror; PD, Photodiode; ADC, Analog to digital converter; PC, Personal computer)

We measured the frequency noise PSD of several typical commercial lasers before passing through the fiber link as shown in Fig.2 and take the NKT-X15 as an example obtaining the frequency noise PSD after the fiber link of 35km and 63km respectively as Fig.3.

We found that the frequency noise characteristics of the laser have changed after its transmitted through the optical fiber link. Plenty of spike noise was superimposed on the low frequency area (within 1kHz), which we considered as vibration noise components coupling in the optical fiber links

such as the vibrating of power supply noise, etc. The white noise level of the laser also increases with the increase of transmission distance. The intrinsic linewidth changes from 28.27 Hz (0 delay) to 78.54 Hz (35 km delay) and 113.1 Hz (63 km delay), proving that the coherence of laser deteriorated

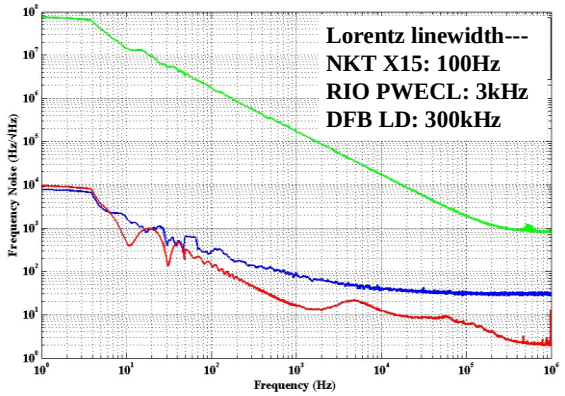

Fig.2. Frequency noise PSD of several typical commercial lasers before going through the fiber link. Green, EMCORE; Blue, RIO PWECL; Red, NKT X15.

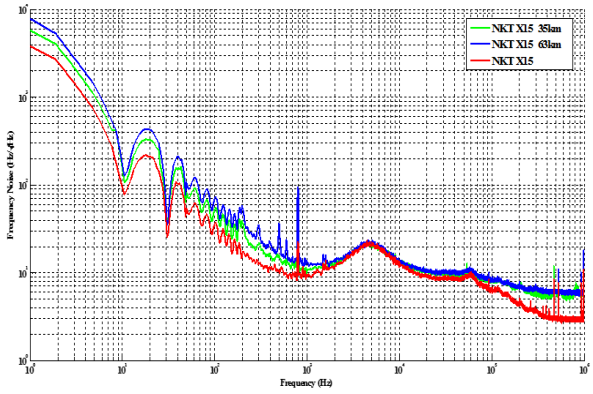

Fig.3. Frequency noise PSD of NKT-X15 after the fiber link. Red, 0km ;Green, 35km; Blue,65km.

during the process of transmission. In our opinion, the reason is the influence of spontaneous emission increases with the decrease of the power during the transmission result in the phase of the photon changing more randomly. So the coherence of light decreases after the transmission.

In order to further study the influence of lasers with different linewidth in the process of optical frequency transmission, we adopt the ANC technique[7] to test the stability of transmission under different conditions. The results are shown in fig4.

The transmission stability of NKT-X15 laser (intrinsic linewidth is 100Hz) and RIO laser (intrinsic linewidth is 3kHz) can reach 2.5×10^{-17}@1s and 5×10^{-19}@10000s after 30km optical fiber link. The transmission stability of EMCORE laser (intrinsic linewidth is 300kHz) will degrade to 1.3×10^{-15}@1s and 2.8×10^{-17}@10000s. The correspondence between the laser linewidth and the coherence length is shown in Tab.1. Because the length of transmission link is within the coherence length of NKT-X15 and RIO, There is no deterioration in the stability performance of the optical frequency transmission, but the transfer stability of EMCORE laser is badly deteriorated for the length of fiber link exceeds its coherence length.

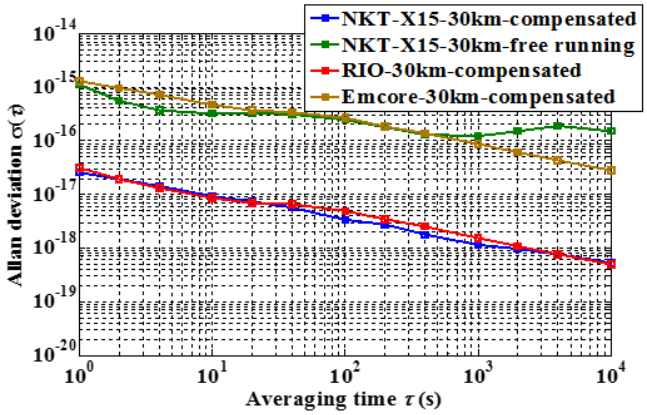

Fig.4. Frequency stability of 30km fiber link. Blue, NKT X15 after 30km with compensation;Green, NKT X15 after 30km without compensation; Red, RIO after 30km with compensation; Brown, EMCORE after 30km with compensation.

TABLE 1. The correspondence between the laser linewidth and the coherence length

(Laser) Linewidth	(NKT-X15) 100 Hz	(RIO) 3 kHz	(EMCORE) 300 kHz
Coherent length	2000 km	66 km	660 m

III. CONCLUSION

We used our proposed laser phase and frequency noise measurement system based on the 120 degree difference interferometer to study the variation trend of the frequency noise characteristics of commercial narrow linewidth lasers, including RIO, NKT-X15 and EMCORE. The results show that the frequency noise characteristics of the laser is degraded after the transmission. Meanwhile, the ANC experiment also reveals that the laser linewidth has little effect on the transmission stability if the link length is less than the coherence length of the laser. Next, we will study more complete relations by use of the Hz and sub-Hz linewidth laser and longer optical fiber.

REFERENCES

[1] Droste S, Ozimek F, Udem T, et al. Optical-frequency transfer over a single-span 1840 km fiber link[J]. Physical review letters, 2013, 111(11): 110801.

[2] H. Lee, M.G. Suh, T. Chen, J. Li, S. A. Diddams, and K. J. Vahala, “Spiral resonators for on-chip laser frequency stabilization,” Nat. Commun. 4, 1-6 (2013)..

[3] T. Okoshi, K. Kikuchi, and A. Nakayama, “Novel method for high resolution measurement of laser output spectrum,” Electron. Lett. 16(16), 630-631 (1980).

[4] S. Piazzolla, P. Spano, and M. Tamburrini, “Characterization of phase noise in semiconductor lasers,” Appl. Phys. Lett. 41(8), 695-696 (1982).

[5] H. Tsuchida, “Laser frequency modulation noise measurement by recirculating delayed self-heterodyne method,” Opt. Lett. 36(5), 681-683 (2011).

[6] Xu D, Yang F, Chen D, et al. Laser phase and frequency noise measurement by Michelson interferometer composed of a 3× 3 optical fiber coupler [J]. Optics express, 2015, 23(17): 22386-22393.

[7] Ma L S, Jungner P, Ye J, et al. Delivering the same optical frequency at two places: accurate cancellation of phase noise introduced by an optical fiber or other time-varying path[J]. Optics letters, 1994, 19(21): 1777-1779

Stabilized optical-frequency transfer using optical injection locking amplifier

Feng Zitong [1,3*], Yang Fei[1*], Zhang Xi[1,3], Chen Dijun[1], Cheng Nan[2], Gui YouZhen[2] and Cai Haiwen[1*]
[1]Key Laboratory of All Solid-State Laser and Applied Techniques, Shanghai Institute of Optics and Fine Mechanics, Chinese Academy of Science, Shanghai 201800, China;
[2]Key Laboratory for Quantum Optics, Shanghai Institute of Optics and Fine Mechanics, Chinese Academy of Science, Shanghai 201800, China;
[3]University of Chinese Academy of Sciences, Beijing 100049
Email: ztfeng@siom.ac.cn fyang@siom.ac.cn hwcai@siom.ac.cn

***Abstract*—We present a novel optical injection locking-based regenerative amplifier for optical frequency transfer applications. This amplifier can provide more than 50dB gain and ensure that the input carrier frequency fractional stability is better than 2×10^{-19}@10000s.The amplifier was tested for the transfer of commercial narrow linewidth laser carrier over 100km optical fiber link and reached the stability of 2.2×10^{-16}@1s and 2.6×10^{-19}@10000s.**

Keywords—optical frequency transfer; optical injection locking; regenerative amplifier

I. INTRODUCTION

With the progress in the development of optical atomic clocks, it is necessary to develop a way for its precise transfer. The traditional satellite-based frequency transfer is far from meeting the requirements for its stability is only 10^{-16} level in an entire day. Therefore, optical fiber-based high-precision optical frequency transmission technology has emerged and the distances of transmission up to 1840km has been demonstrated[1]. In order to transmit such a long distance, not only the noise introduced by the optical fiber link should be eliminated, but also the power loss caused by long-distance transmission should be compensated for significantly improving the signal-to-noise ratio of the detected signal.

Erbium-doped fiber amplifiers (EDFA) is the most commonly used method for optical fiber link amplification. However, the bidirectional nature of the frequency transfer system pose a limit on its gain and also deteriorate the stability of transmission due to the fact that point reflections and Rayleigh scattering existing in the fiber link will feedback into the EDFAs to trigger the stimulated effect[2]. Brillouin amplification has the advantage of a small gain bandwidth, so it can hardly be affected by Rayleigh scattering in an optical frequency transmission system, but in order to achieve a narrow gain bandwidth, it is necessary for the pump laser frequency to be locked at the signal laser frequency which increases the complexity of the system[3]. Joonyoung Kim et al's[4] has proposed an optical injection locking-based amplification scheme which provides high gain within a narrow bandwidth and can preserve the frequency stability to 10^{-18}@1000s.

We propose a novel regenerative amplification scheme based on laser injection locking technology. Optical injection locking is a non-linear process. The output frequency from the laser is "locked" to the injected optical frequency when the optical frequency difference between the "Master" laser and the "Slave" laser is within a certain frequency range. When the injection power of light is much less than the power of output, the "Slave" laser can be regarded as an optical amplifier. Our amplifier can provide more than 50dB gain and preserve frequency stability better than 2×10^{-19}@10000s.

II. EXPERIMENTS SETUP

The amplifier scheme we implement is shown in fig.1. It is a combination of optical injection locking and optical phase-locked loop technology. The input port inputs a weak optical carrier, which is divided into two parts at point A, one part is used as a reference and the other part is injected into a DFB laser to be amplified. The amplified signal is also divided into two parts at point E, one part is beat with the reference in PD to create error signal to feedback to AOM to achieve optical phase lock so that the output signal is phase locked to the input carrier.

There are two advantages when Compared with previous scheme[4]: First, The bandwidth of the feedback loop is greater than 200kHz by using the AOM to realize the optical phase-locked loop. It is a great progress because the bandwidth of the

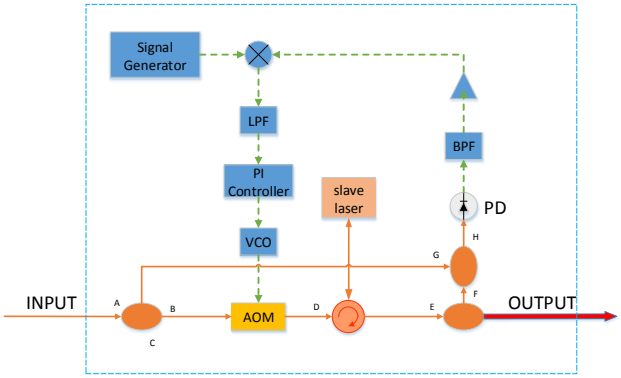

Fig.1. optical injection locking-based amplifier (PD, photodiode; BPF, bandpass filter; LPF, lowpass filter; VCO, voltage controlled oscillator; AOM, acousto-optic modulator)

previous scheme is less than 1kHz; Second, we use the single sideband coherent detection to detect the optical phase rather than the previous Intensity modulation direct detection (IMDD) scheme, so it has higher signal to noise ratio. Both of these make the loop lock easier and more stable.

We tested the performance of this amplifier. As shown in Fig.2, we can see when the injection ratio is -51dB (the injection ratio means the ratio of output optical power to the injected optical power of "Slave" laser or EDFA), the stability of the amplifier can reach 1.7×10^{-19}@10000s. When the injection ratio is -60dB, the stability will degrade to 4.9×10^{-19}@10000s but still superior to commercial EDFA which stability is 2.4×10^{-18}@10000s at -35dB injection ratio.

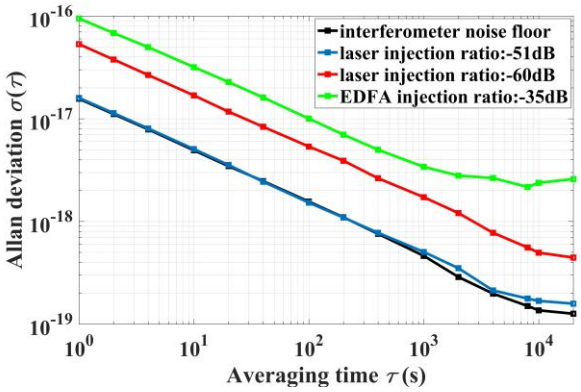

Fig.2. Frequency stability of optical injection locking-based amplifier and commercial EDFA. Black, interferometer noise floor; Blue, laser injection ratio:-51dB; Red, laser injection ratio:-60dB; Green: EDFA injection ratio: -35dB.

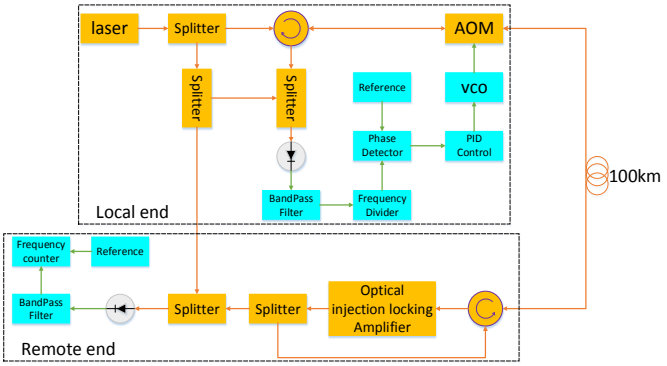

Fig.3. Schematic diagram of 100km fiber link with optical injection locking-based amplifier (PD, photodiode; BPF, bandpass filter; LPF, lowpass filter; VCO, voltage controlled oscillator; AOM, acousto-optic modulator)

Further, we tested this amplifier in a system of optical frequency transmission[5]. Experimental system schematic shown in Fig.3. The laser is NKT-E15 commercial narrow linewidth laser. The 100-km fiber link is connected by a 65-km and a 35-km fiber spool. The overall optical power attenuation is approximately -35 dBm. The optical injection locking amplifier is placed at the far end of the link and the power of the signal can be amplified to 15dBm. Since the amplifier includes an AOM for phase-locking, it can also function as a frequency shifter. Therefore, the remote end does not need to place an additional AOM for frequency-shifting. Experimental results shown in Fig. 4, the stability of transfer is 2.2×10^{-16}@1s and 2.6×10^{-19}@10000s which is worse than the stability of optical injection locking amplifier at -51dB injection ratio, so we can conclude that this amplifier does not degrade the stability of the transfer.

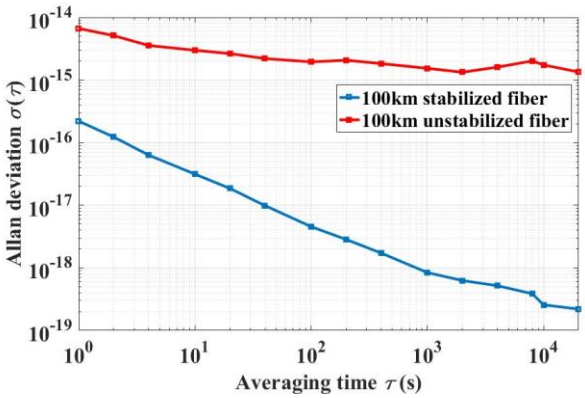

Fig.4. Frequency stability of 100km fiber link with the optical injection locking-based amplifier. Blue, 100km stabilized fiber; Red, 100km unstabilized fiber.

III. CONCLUSION

We propose an optical injection-locking amplifier that can be used for optical frequency transmission which provides high gain amplification of greater than 50 dB and still maintains the stability of input carrier better than 2×10^{-19}@10000s. Further, experiments on the optical frequency transmission of the 100km optical fiber link in the laboratory have tested this amplifier and obtained the transfer stability of 2.2×10^{-16}@1s and 2.6×10^{-19}@10000s. In the next step, we will use a cave-stable laser to do experiment on urban fiber link to further extend the length of the transfer, and we will make the polarization control for the optical injection locking amplifier to further improve its stability.

REFERENCES

[1] Droste S, Ozimek F, Udem T, et al. Optical-frequency transfer over a single-span 1840 km fiber link[J]. Physical review letters, 2013, 111(11): 110801.

[2] Grosche G, Terra O, Predehl K, et al. Optical frequency transfer via 146 km fiber link with 10− 19 relative accuracy[J]. Optics letters, 2009, 34(15): 2270-2272.

[3] Terra O, Grosche G, Schnatz H. Brillouin amplification in phase coherent transfer of optical frequencies over 480 km fiber[J]. Optics express, 2010, 18(15): 16102-16111.

[4] Kim J, Schnatz H, Wu D S, et al. Optical injection locking-based amplification in phase-coherent transfer of optical frequencies[J]. Optics letters, 2015, 40(18): 4198-4201.

[5] Ma L S, Jungner P, Ye J, et al. Delivering the same optical frequency at two places: accurate cancellation of phase noise introduced by an optical fiber or other time-varying path[J]. Optics letters, 1994, 19(21): 1777-1779.

Microwave Acoustic Properties of Diamond Based HBAR at Low Temperatures

Boris P. Sorokin[1,2], Gennady M. Kvashnin[1], Andrey S. Novoselov[1,2], Anton B. Shipilov[1,2]

[1] Diamond electronics department, Technological Institute for Superhard and Novel Carbon Materials, Troitsk, Moscow, Russian Federation

[2] Moscow Institute of Physics and Technology (State University), Dolgoprudny, Moscow region, Russian Federation

Email: bpsorokin1953@yandex.ru

Original technique for low-temperature microwave acoustic investigations of single crystalline diamond by HBAR operating on bulk acoustic wave (BAW) has been developed for the first time. Study of the temperature dependences for the BAW phase velocities as well as HBAR's quality factor *Q* in experimental samples as Al/AlN/Mo/diamond and Al/(Al, Sc)N/Mo/diamond was carried out in a wide frequency range 0.5-10 GHz and temperatures of 2-400 K. Measured value of the phase velocity (17542 m/s) of longitudinal wave propagating along [100] direction in diamond at room temperature was in close accordance with earlier published one [1]. It was found that the BAW phase velocities and the elastic moduli of the diamond change with the temperature decreasing in accordance with the Debye-Grüneisen theory and tend to a constant value at temperatures below 110 K (Fig.1). Character of the *Q* temperature dependences depends essentially on the frequency at which the measurements were performed. Considering the operational HBAR frequencies below 1 GHz measured with different orientations of a diamond substrate, a similar behavior of $Q(T)$ in those cases was observed as a weak monotonic dependence. Note that at higher frequencies and low temperatures the significant increasing in *Q* value about 2 - 3 times compared with its value at room temperature was obtained.

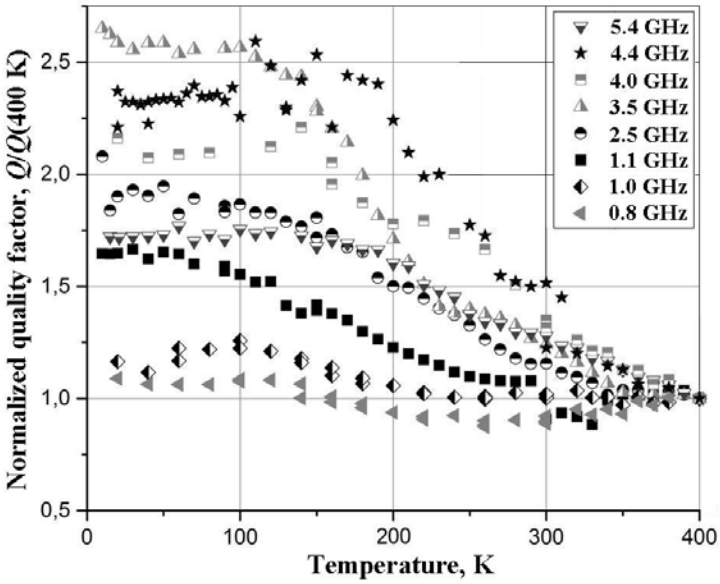

Fig. 1: Temperature and frequency dependences of the normalized *Q*-factor in diamond-based HBARs, in which the longitudinal acoustic wave propagates along the [100] direction.

Authors assume that such change could be associated with the transition from the Akhiezer's mechanism of UHF acoustic attenuation in diamond to the Landau-Rumer's one.

This work was supported by a grant of Russian Science Foundation (project #16-12-10293).

References

[1] B. P. Sorokin, G. M. Kvashnin, A. V. Telichko, et al. //In: Proc. of 2012 IEEE Int. Ultrason. Symp. (Dresden, Germany), p. 763–766, 2012.

1.14 um clock transition in Tm

Artem Golovizin[1,2], Elena Kalganova[1,2], Dmitry Tregubov[1], Ksenia Khabarova[1,2], Vadim Sorokin[1,2], Nikolai Kolachevsky[1,2]

[1]P. N. Lebedev Physical Institute of RAS, Leninsky prosp. 53, Moscow 119991, Russia
[2]Russian Quantum Center, Novaya st. 100, Skolkovo, Moscow region, 143025, Russia

Email: artem.golovizin@gmail.com

We report on the first thorough experimental study of the properties of the magneto-dipole clock transition $4f^{13}(^2F^o)6s^2$ (J = 7/2, F = 4) → $4f^{13}(^2F^o)6s^2$ (J = 5/2, F = 3) at 1.14 um in ultracold thulium (Tm) atoms trapped in a 1D optical lattice. Our recent calculations [1] have shown that this clock transition is very insensitive to the BBR shift and it is possible to reach 10^{-18} uncertainty level. We've also predicted existence of an optical lattice magic wavelength near 807 nm owing to the weak transitions from the clock level.

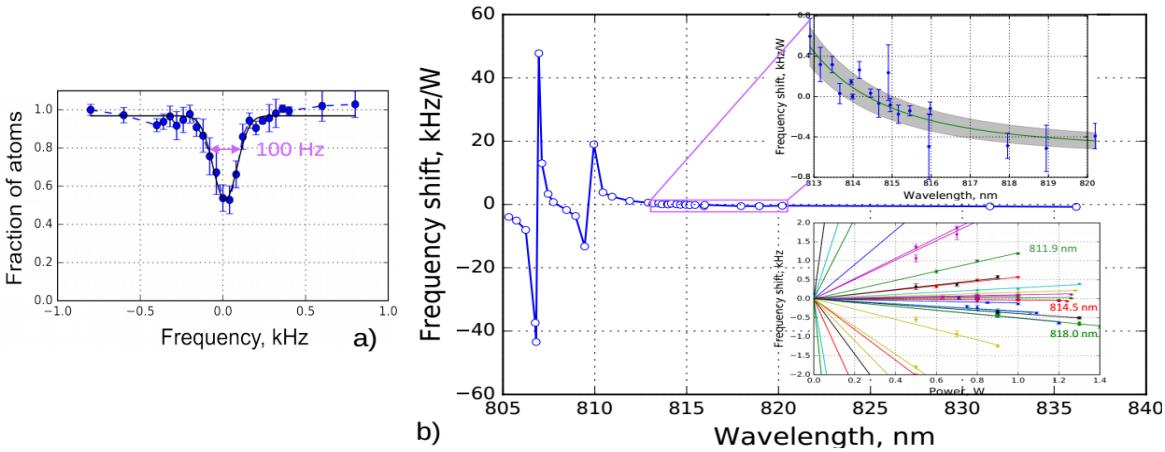

Fig. 1: a) Clock transition spectral line recorded at lattice wavelength 814.4 nm. b) Clock transition frequency shift per 1W optical lattice power vs. lattice wavelength. Inserts: top – detailed region around the magic wavelength at 814.4(3) nm, bottom – measured line center shifts vs. lattice power for different lattice wavelengths.

We have measured clock transition frequency shift vs. lattice wavelength in the range 805-837 nm (fig. 1b) and experimentally determined positions of two magic wavelength. The measurements are fulfilled in 1D optical lattice produced with Ti:Sa laser with ~1W output power. We have built an out-of-chamber enhancement cavity with finesse ~10 to increase both lattice depth and number of trapped atom. With this setup we can reload about 50% (few 100k atoms) from second stage MOT to the optical trap with the waist radius 110 um. Figure 1a shows clock transition spectral line with FWHM=100 Hz at a wavelength 814.4 nm (close to the magic wavelength).

The dependence of the transition shift on the wavelength has two features at 807 nm and 809.5 nm which correspond to the transitions from the clock level. For lattice wavelengths larger than 820 nm it levels off to very small value that confirms our theoretical prediction of small (<2 a.u.) differential static polarizability of the clock levels.

References

[1] Sukachev, D., et al. "Inner-shell magnetic dipole transition in Tm atoms: A candidate for optical lattice clocks." Physical Review A 94.2 (2016): 022512.

Effect of Dipping in Liquids on the Resonance Characteristics of a Backward-Wave-Type Trapped-Energy Resonator

Ken Yamada and Koji Ito

Department of Electronic Engineering
Tohoku Gakuin University
Tagajo 985-8537, Japan

Email: k-yamada@mail.tohoku-gakuin.ac.jp

The authors' group proposed a new method for detecting a small-scale variation in liquid level by using a piezoelectric thickness vibrator operating in a trapped-energy mode [1]-[5]. When the evanescent-wave region of the trapped-energy resonator is dipped in a liquid, a small leakage of vibration energy occurs. Therefore, small variations in liquid level are detected by observing the changes in, for example, the electric conductance G at resonance.

In this paper, a new attempt is presented to detect the liquid level in a few-millimeter range using a trapped-energy resonator operating in a backward-wave-type thickness-extensional mode. Because the thickness mode of this type has the cutoff regime above the cutoff frequency, energy-trapping works when the outer regions of the plate are covered with short-circuited electrodes and a capacitance is connected in series to the central excitation electrodes [6]. In this trapped-energy resonator, inharmonic spurious modes do not appear irrespective of the size of the central excitation electrodes. This is a quite unique phenomenon.

Experimental examinations were carried out using a thickness-poled $PbTiO_3$ plate of 30 mm in length, 20 mm in width and 1 mm in thickness. The central electrode and the two isolation gaps were spanned from one end to the other, and their width were 3 mm and 1 mm, respectively. The ratio of the central-electrode capacitance C_0 to the series capacitance C_A was 2.4. The admittance characteristic of the resonator is shown in Fig. 1. The resonator was supported vertically by clamping its top corners, and the whole part of the resonator, i.e., the central trapping region as well as the evanescent-wave region, was dipped in liquids from its lower end, as shown in Fig. 2. The test liquids were water, glycerin, olive oil, and honey. The variations in G against the dipping depth d were measured at the resonance point using an impedance analyzer. Depth dependent gradual variations such as shown in Fig. 3 have been observed, and the feasibility of liquid-level sensing by this method has been confirmed.

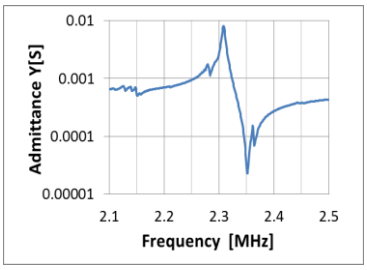

Fig. 1 Admittance characteristic of the trapped-energy resonator.

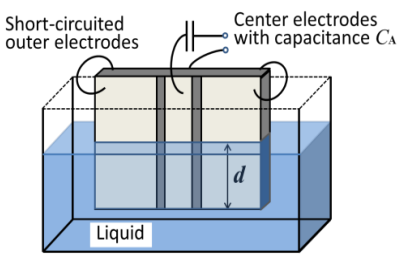

Fig. 2 Resonator configuration and measurement setup.

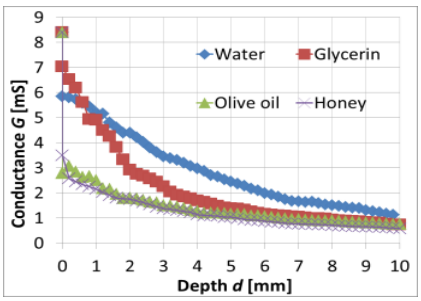

Fig. 3 Variations in G on the depth d.

[1] K. Yamada, S. Horiuchi, H. Honda, and T. Kinai: Proc. 2009 IEEE Ultrassonic Symp., p.2508.

[2] K. Yamada and S. Seto: Proc. 2010 IEEE Ultrassonic Symp., p.1439

[3] K. Yamada, S. Seto, and S. Horiuchi: Proc. 2011 IEEE Ultrasonic Symp., p.1522.

[4] K. Yamada, T. Ishioka, and N. Aita: Proc. 2013 Joint UFFC, EFTF and PFM Symp., p.282.

[5] K. Yamada and Y. Kunii: Proc. 2016 IEEE Frequency Control Symp.

[6] K. Yamada and H. Shimizu: Proc. 1984 IEEE Ultrasonic Symp., p.383.

GNSS Time Scales Analysis

Petr Bogdanov, Andrei Druzhin, Arkadii Tiuliakov, Tatiana Primakina

Russian Institute of Radionavigation and Time, Saint-Petersburg, Russia

Email: bogdanov_pp@rirt.ru

In all GNSS Satellite Time scales are referenced to GNSS Time and GNSS Time is referenced/synchronized to UTC(k) which is a local implementation of UTC. GNSS Time accuracy parameters influence the accuracy of positioning and timing as well as the accuracy of calculating and predicting GNSS-GNSS Time Offsets for GNSS interoperability.

GNSS Time accuracy parameters are specified in GNSS Interface Control Documents and Interface Specifications. GPS Time is a composite time scale referenced to UTC(USNO) [1]. The specified GPS Time offset of UTC is within 1 microsecond (modulo 1 s). GLONASS Time is based on GLONASS Central Synchronizers and is referenced to UTC(SU) [2]. The specified GLONASS Time offset of UTC(SU) is within 1 microsecond (modulo 1 s). Galileo Time is physically implemented by Precise Timing Facility and steered to UTC [3]. The specified Galileo Time offset of UTC is within 50 ns (95%). Beidou Time is based on Master Control Station and Monitoring Stations time scales and referenced to UTC(NTSC) [4]. The specified Beidou Time offset of UTC(NTSC) is within 100 ns (modulo 1 s). QZSS Time is based on the time scale of the receiver located at Koganei station [5]. QZSS Time is synchronized to GPS Time and referenced to UTC(NICT). The specified QZSS Time offset of UTC(NICT) is within 1 microsecond.

Thus, most of GNSS Time scales are mathematical and can be analyzed only indirectly by using either broadcast corrections to convert from GNSS System Time to Reference Time UTC(k) or the values of GNSS Time–Reference Time offsets calculated from measurements of the receivers located at UTC(k) Timing Laboratories. By means of both approaches GNSS Time Scales were analyzed. For all operational GNSS the plots of System Time scales were obtained with using broadcast corrections to convert from GNSS Time to Reference Time UTC(k) (Fig 1).

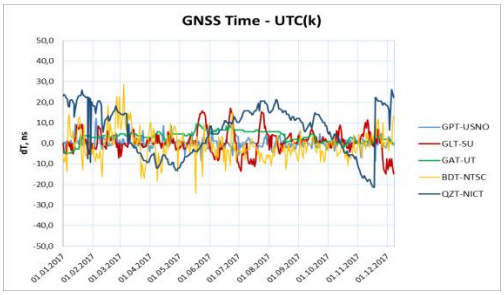

Fig. 1: GNSS Time Offsets of UTC(k)

The results show that the practical values of GNSS-Reference Time offsets are much smaller than the specified ones: in GPS and Galileo the value of System Time offset off Reference Time is maintained within ±10 нс, in GLONASS, Beidou and QZSS – within ±20 нс.

References

[1] Interface Specification IS-GPS-200, 2013

[2] GLONASS Interface Control Document, Release 5.1, 2008.

[3] GNSS Timescale Description. Galileo. Definition of System, www.unoosa/pdf/icg/2016/gst2016.pdf.

[4] Beidou Timescale Description. Definition of time system, www.unoosa/pdf/icg/2016/Beidou-Timescale2016.pdf.

[5] GNSS Timescale Description. QZSS. Definition of System, www.unoosa/pdf/icg/2016/QZSS-Timescale2016.pdf.

Characterization of a Reference Cavity for a Transportable Strontium Optical Clock

Sofia Herbers[1], Sebastian Häfner[1], Erik Benkler[1], Uwe Sterr[1], Christian Lisdat[1]

[1]Physikalisch-Technische Bundesanstalt, Bundesallee 100, 38116 Braunschweig, Germany

Email: sofia.herbers@ptb.de

Ultra-stable high-finesse cavities are used, inter alia, to pre-stabilize interrogation lasers of optical clocks, that are employed for relativistic geodesy or tests of fundamental physics. The ultra-stable high-finesse cavity discussed here is designed to improve the performance of PTB's transportable optical Sr clock [1].

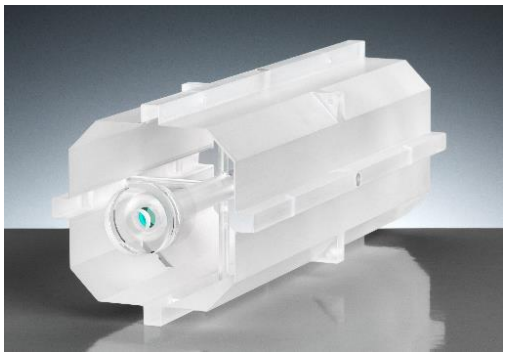

Fig. 1: Reference cavity designed for a transportable optical Sr clock.

One limiting factor of ultra-stable high-finesse cavities is the Brownian noise of the mirror coatings. This noise is reduced for state-of-the-art cavities by using single-crystalline mirror coatings [2]. For a Sr optical lattice clock the ideal wavelength for the clock transition is 698 nm. Since GaAs-based crystalline coatings are highly absorbing for visible light, we choose to operate the cavity at twice the interrogation wavelength (1396 nm) and a second-harmonic generation (SHG) module is used for frequency conversion to 698 nm. To enable transportability, the cavity requires isolation from seismic noise, pressure, and temperature fluctuations beyond lab requirements. Hence, a special mounting different form the usually employed loose mounting is needed. Thus, solutions must be found that do not degrade the cavity performance. We choose a cylindrical cavity design (see figure 1) similar to [1,3].

Here, we present the characteristics of a transportable 20 cm long reference resonator for a transportable Sr lattice clock with the potential for a fractional frequency instability of 1×10^{-16}. We will discuss the vibration sensitivity and thermal decoupling from the environment. Additionally, we have investigated phase noise accumulated in a periodically poled lithium niobate (PPLN) waveguide SHG module (see figure 2), and compare it to previous results [4].

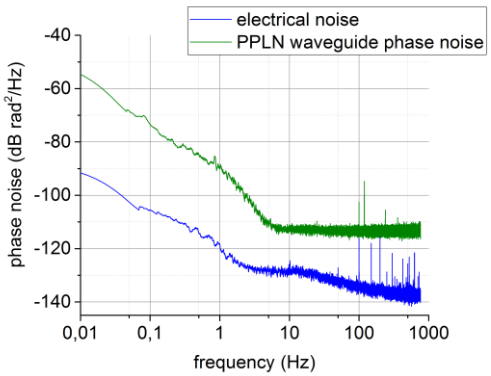

Fig. 2: Measured phase noise of a PPLN waveguide using a frequency comb (green line) and electronic detection noise (blue line).

This work is supported by QUEST and DFG (CRC 1129 (A03)). We thank Garrett Cole and colleagues from Crystalline Mirror Solutions (CMS) for supplying the crystalline coatings used in this work.

References

[1] S.B. Koller et al., Phys. Rev. Lett., vol. 118, p. 073601, 2017

[2] G.D. Cole et al, Nature Photonics, vol. 7, p. 644 – 650, 2013

[3] Q.-F. Chen et al, Rev. Sci. Instrum., vol 85, p. 113107, 2014

[4] M. Delehaye et al, IEEE Photonics Technol. Lett., vol. 29, p. 1639 – 1642, 2017

Practical Approach to the Use of Linear Quadratic Gaussian Control for Time Scale Signals

Konstantin Mishagin[1,2], Vladimir Lysenko[1,2], Svetlana Podogova[1], Sergey Medvedev[1]

[1]Department of IT, Vremya-CH JSC, Nizhniy Novgorod, Russia
[2]Department of Radiophysics, University of Nizhniy Novgorod, Nizhniy Novgorod, Russia

Email: mishagin@vremya-ch.com

Linear quadratic Gaussian (LQG) control is one of effective techniques used for steering of atomic clocks to external references [1]. Complexity of the use of LQG method is caused by uncertainty in selection of the weight coefficients of the cost function. Therefore, modeling of the steering algorithm for particular noises of master and slave signals (or some experimental parameter selection) is required. In this report, we propose the algorithm, which allows to calculate weight coefficients, and consequently gain coefficients of the control loop without modeling, using initial information about steering problem only. Expected Allan deviation of master and slave signals is known, therefore the crossing point τ_x of ADEV plots is also known. Using τ_x the appropriate time constant T of the control loop is calculated. Time constant T is related to pole positions of the control loop transfer function, which are determined by gain coefficients (g_x, g_y) and steering interval Δt. To choose gain coefficients for particular time constant LQG approach is used. It turned out, that dependence of LQG weight W_R on time constant T and steering interval Δt can be approximated by simple analytical expression (Fig. 1), if $T >> \Delta t$. For known W_R and fixed weight matrix $\mathbf{W_Q}$, gain coefficients are calculated by means of standard LQG procedure.

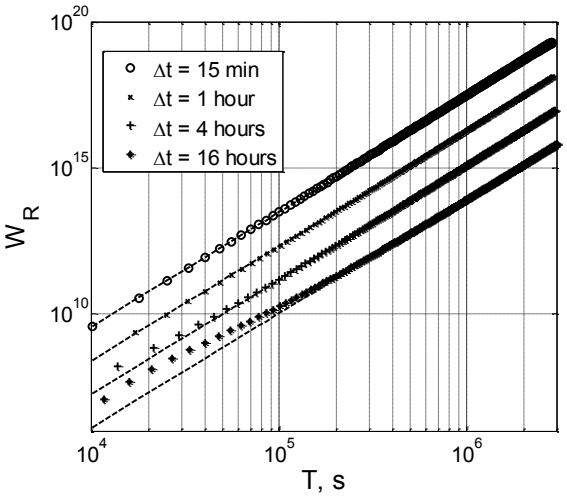

Fig. 1: Dependence of LQG cost function parameter on time constant of the control loop. Dashed lines correspond to the analytical approximation

Details of the algorithm are described in the report. Significant simplification of practical use of LQG technique is demonstrated by several examples.

Implementation of steering and ensembling algorithms in time scale systems developed in Vremya-CH is also discussed.

References

[1] P. Koppang, R. Leland “Linear quadratic stochastic control of atomic hydrogen masers”, Ultrasonics, Ferroelectrics, and Frequency Control, IEEE Transactions, vol. 46(3), p. 517-522, 1999.

Optimal traceability to the SI second through TAI

Gérard Petit[1], Gianna Panfilo[1]

[1]Bureau International des Poids et Mesures, 92312 Sèvres France

Email: gpetit@bipm.org

It is well known that frequency standards based on optical transitions surpass the present realization of the SI second by Cs fountains primary frequency standards (PFS) and numerous laboratories worldwide develop such new frequency standards. Some of these optical transitions are recognized as secondary representations of the second (SRS) by a joint body of the Consultative Committees for Length (CCL) and for Time and Frequency (CCTF). For these SRS, the frequency of the clock transition must be documented with an uncertainty budget of all systematic effects and it must be referenced to the frequency of the Cs transition.

When a new frequency standard can be operated with an operating PFS, its transition frequency can be directly determined. In this paper we study how a clock transition frequency can be compared to the SI second through TAI without direct comparison to a PFS. We study how the corresponding uncertainty can be estimated and propose an optimal scheme in this purpose. Such a scheme is essential when no PFS is directly available but it is also useful to ensure the consistency of the local determination of the transition frequency when a PFS is available.

A first, readily available, method is to use the duration of the scale interval of TAI (d), estimated each month and published in Circular T, as an access to the SI second. However this is available only over a monthly interval and requires either to operate the frequency standard under study over one month or to account for dead time. The same algorithm use to estimate d may be applied over any interval for which TAI is published (i.e. 5 days and multiples) Given the present (2017) availability of about 4-5 fountain evaluations per month, and the reported uncertainties of these evaluations, the standard uncertainty of the d value varies with the length of the estimation interval, from about 7-8x10^{-16} for 5 days to about 2x10^{-16} for 30 days. This ad-hoc estimation of d may be implemented as a new service in the future.

One limiting factor is the uncertainty in frequency transfer from UTC(k) to UTC, presently estimated at ~9x10^{-16} for 5 days to ~1.6x10^{-16} for 30 days. These values are based on the performance of the time and frequency transfer techniques presently used in TAI and on the present algorithm to compute them. Significant progress is expected: First new satellite-based frequency transfer methods should reach ~1x10^{-16} at 5-day averaging, not to mention fiber links for which the transfer noise is close to negligible. In addition we present different schemes to optimize the uncertainty in accessing the SI second through UTC(k) or other reference time scales.

Such a method has been put into operation e.g. for the determination of ^{87}Sr [1] and has been provided for a few other frequency standards. A review of the results is presented.

References

[1] H. Hachisu, et al., “SI-traceable measurement of an optical frequency at the low 10^{-16} level without a local primary standard”, Opt. Express 25, 8511-8523, 2017.

GNSS Antenna Group Delay Characterization at the ESTEC Compact Test Range

Esteban Garbin[1], Piotr Krystek[1], Ricardo Piriz[1], Pierre Waller[2], Damiano Trenta[2], Luis Rolo[2], Pascale Defraigne[3], Bruno Bertrand[3]

[1]GMV, Madrid, Spain
[2]ESTEC, ESA, Noordwijk, The Netherlands
[3]Royal Observatory of Belgium, Brussels, Belgium

Email: egarbin@gmv.com

Traditionally, group delay characterizations of GNSS antennas have been performed either by means of a portable anechoic chamber or by means of real GNSS signals measurements and a short baseline setup with post-processing. For the results presented in this paper, the characterization of antennas inside anechoic chambers will be further investigated. A key parameter to consider for the correct measurement of the antenna characteristics, is the assumption of measuring the antennas in far field conditions. Based on the dimensions of the anechoic chamber and on the antennas to be used, the minimum distance required for the far field conditions to be met, can be challenging to achieve in small laboratories. In addition, not meeting far-field criteria will yield an erroneous measurement due to the non-uniform phase illumination of the antenna under test. Aiming at minimizing the sources of uncertainty, the tests performed took place in Antenna Laboratories at ESA/ESTEC, benefiting from large anechoic chambers and ESA/ESTEC's experience in the measurement of antenna characteristics and uncertainty estimation in antenna measurements.

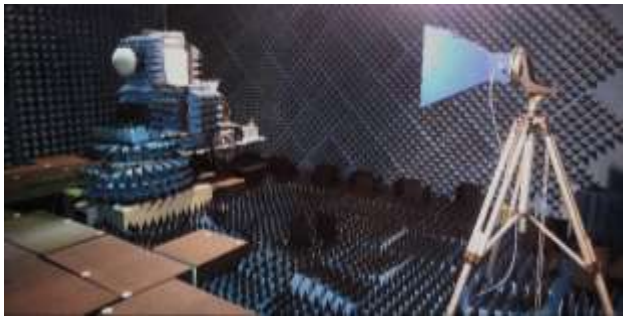

Fig. 1. GNSS antenna group delay characterization versus azimuth and elevation, inside anechoic chamber present at ESTEC.

The GNSS antenna, in our case a Leica AR20, is calibrated inside the anechoic chamber over elevation and azimuth using a Standard Gain Horn as a transmitting antenna as can be seen in Figure 1. An accurate measurement of the distance between the two antenna reference points is done, in order to remove the delay introduced by the free space propagation.

This paper builds up on the results presented in [1], and expands the procedures for group delay calibration of GNSS. The advantages of using a professional antenna test facility are highlighted, aiming at obtaining precise results for all frequencies in the evolving GNSS world. The transformation required for the group delay with respect to reference point and the phase center is also introduced in the paper, in order to comply with CGGTTS standard computation procedures.

The work reported in this paper has been supported under a contract of the European Space Agency in the frame of the European GNSS Evolutions Programme. The views presented in the paper represent solely the opinion of the authors and should be considered as R&D results not necessarily impacting the present EGNOS and Galileo system design.

References

[1] E. Garbin Manfredini, P. Krystek, R. Piriz, P. Waller, D. Trenta and L. Rolo. "Absolute group delay characterization of GNSS antennas for reference receiver chains", *to be presented in ITM/PTTI 2018.* Reston, VA. January 2018.

Enhanced Techniques for Absolute Calibration of GNSS Receiver Chains

Esteban Garbin[1], Piotr Krystek[1], Ricardo Piriz[1], Pierre Waller[2], Pascale Defraigne[3],Bruno Bertrand[3]

[1]GMV, Madrid, Spain
[2]ESTEC, ESA, Noordwijk, The Netherlands
[3]Royal Observatory of Belgium, Brussels, Belgium

Email: egarbin@gmv.com

In this paper we present enhanced techniques for the absolute calibration of receiver chains as used in timing reference stations. The elements of the GNSS chain (antenna, receiver and cable) are each calibrated individually and with careful considerations regarding the uncertainty level assigned to them. This paper is presented in the framework of the "Accurate calibration of multi-system/multi-frequency GNSS receiver chain" (AKAL) project.

The absolute GNSS antenna calibration have been historically done in small and so-called "portable" anechoic chambers, that could give a good approximation of the group delay of the antenna for signals at elevation 90 degrees, but cannot be used if an analysis versus azimuth and elevation is required. During this work we extract absolute delays of the GNSS antenna, using the Antenna Laboratories at ESA/ESTEC. We benefited from large anechoic chambers and ESA/ESTEC's experience in the measurement of antenna characteristics and uncertainty estimation in antenna measurements. Additionally to using large anechoic chambers, which helps reducing the uncertainty of the measurements, we developed a novel calibration technique considering a physical reference point of the antenna. This allows for ultra-precise determination of the distance between the two antennae and produce a very low uncertainty related to scenario characterization, not having to rely on phase center calculations. We also present the proper transformation between the used reference point and the phase center of the GNSS antenna, to comply with CGGTTS standard computation procedure.

Absolute delay calibration of GNSS receivers has been gaining interest inside the timing community due to the low uncertainty level that can be achieved, and also due to the need of having a reference calibrated receiver for the relative calibrations, especially in a multi-GNSS context. In this paper we present the calibration of two timing receivers, a brand new PolaRx5TR and a GTR51. The calibration is done for GPS signals L1 and L2, GLONASS L1 and L2 and all the available signals in the Galileo system. The focus of the enhanced calibration was exploring different sources of uncertainty and selecting the best possible configuration to reduce them to the minimum. Different considerations where taken, like the PRN number, the satellite configuration, output power level, Automatic Gain Control of the receiver and thermal sensitivity. Additionally, the simulator calibration is performed by means of a newly developed correlation software, and the impact of the power, the position of the simulated satellite and the bandwidth of the filter used were all thoroughly analyzed. Finally, all these different aspects are either fully mitigated or decreased to a minimum, while adding the corresponding uncertainty level to the final budget of the receiver calibration. This type of combined in depth analysis, to the best of our knowledge, have not been presented before and the final uncertainty budget is below the 1 ns level.

The work reported in this paper has been supported under a contract of the European Space Agency in the frame of the European GNSS Evolutions Programme. The views presented in the paper represent solely the opinion of the authors and should be considered as R&D results not necessarily impacting the present EGNOS and Galileo system design.

Towards a single-ion compact optical clock: experimental apparatus and current status

Marion Delehaye[1], Lucas Groult[1], Maël Souidi[1], Pierre-Yves Bourgeois[1], Jacques Millo[1], Emmanuel Bigler[1], Yann Kersalé[1], Clément Lacroûte[1]

[1]FEMTO-ST institute, univ. Bourgogne Franche-Comté, CNRS, ENSMM Time and frequency dept. 26 Rue de l'Épitaphe, 25030 Besançon cedex, France.

Email: clement.lacroute@femto-st.fr

Outstanding performances have been obtained by optical atomic clocks: fractional frequency instabilities and accuracies of single-ion optical clocks are now as low as $3\times10^{-15}\ \tau^{-1/2}$ for the former [1] and $3\times10^{-18}\ \tau^{-1/2}$ for the latter [2], while optical lattice clocks have reached instabilities and inaccuracies as low as $6\times10^{-17}\ \tau^{-1/2}$ [3] and $2\times10^{-18}\ \tau^{-1/2}$ [4] respectively. Optical clocks are exquisite measuring tools, useful to various domains of precision science, and many proposals require to bring optical clocks into the field. For this purpose, a number of laboratories worldwide are now building transportable optical clocks. The first operational setups have been reported recently, for both a strontium lattice clock [5], [6] and a single-ion calcium clock [7].

Optical lattice clocks can reach lower fractional instability, thanks to the high atom number, but the frequent reloading required induces an increased susceptibility to the Dick effect [8]. They also require a complex loading scheme into the optical lattice trap, starting with a 2D magneto-optical trap (MOT) or a Zeeman slower. On the other hand, single-ion optical clocks involve a simpler loading scheme and lower optical powers, leading to potentially more compact and less power-consuming systems.

We are developing a compact optical atomic clock based on trapped Yb^+ single ions [9]. The clock should reach a fractional frequency instability around $10^{-14}\ \tau^{-1/2}$ in an overall volume below 500 L. This clock would therefore exhibit a stability 10 times better than an active Hydrogen Maser in a similar volume. We will present the details of our experimental apparatus, which includes a miniature single ion-trap based on surface-electrodes (SE) [10].

References

[1] C. W. Chou, D. B. Hume, J. C. J. Koelemeij, D. J. Wineland, and T. Rosenband, "Frequency Comparison of Two High-Accuracy Al^+ Optical Clocks," *Phys. Rev. Lett.*, vol. 104 (7), p. 070802, 2010.

[2] N. Huntemann, C. Sanner, B. Lipphardt, C. Tamm, and E. Peik, "Single-Ion Atomic Clock with 3 10^{-18} Systematic Uncertainty," *Phys. Rev. Lett.*, vol. 116 (6), p. 063001, 2016.

[3] M. Schioppo *et al.*, "Ultrastable optical clock with two cold-atom ensembles," *Nat. Photonics*, vol. 11 (1), p. 48–52, Jan. 2017.

[4] T. L. Nicholson *et al.*, "Systematic evaluation of an atomic clock at 2×10^{-18} total uncertainty," *Nat. Commun.*, vol. 6, 2015.

[5] N. Poli *et al.*, "A transportable strontium optical lattice clock," *Appl. Phys. B*, vol. 117 (4), p. 1107–1116, 2014.

[6] S. B. Koller *et al.*, "Transportable Optical Lattice Clock with 7 10^{-17} Uncertainty," *Phys. Rev. Lett.*, vol. 118 (7), p. 073601, 2017.

[7] J. Cao *et al.*, "A compact, transportable single-ion optical clock with 7.8×10^{-17} systematic uncertainty," *Appl. Phys. B*, vol. 123 (4), p. 112, 2017.

[8] A. Quessada, R. P. Kovacich, I. Courtillot, A. Clairon, G. Santarelli, and P. Lemonde, "The Dick effect for an optical frequency standard," *J. Opt. B Quantum Semiclassical Opt.*, vol. 5 (2), p. S150, 2003.

[9] C. Lacroûte *et al.*, "Compact Yb^+ optical atomic clock project: design principle and current status," *J. Phys. Conf. Ser.*, vol. 723 (1), p. 012025, 2016.

[10] S. Seidelin *et al.*, "Microfabricated Surface-Electrode Ion Trap for Scalable Quantum Information Processing," *Phys. Rev. Lett.*, vol. 96 (25), p. 253003, 2006.

A model for detection of topological dark matter using GNSS networks

Bertrand Bruno[1], Defraigne Pascale[1]

[1]Royal Observatory of Belgium, Brussels, Belgium

Email: bruno.bertrand@oma.be

It can be inferred from cosmological observations that 23 % of the mass-energy budget of the Universe consists of dark matter while our ordinary baryonic matter is reduced to 4 %. However, the lack of evidence for dark matter at the level of particle physics leads to the conclusion that if it exists, dark matter hardly interacts with ordinary matter, except gravitationally. Hence an impressive panoply of models have been developed this last decade to account for the microscopic nature of dark matter. Despite the observations at the scales of cosmology and particle physics, there is a crucial need to bring further constraints on these models in order to reduce drastically the ocean of possibilities.

Within this context, A. Derevianko et al [1] proposed to use the large network of atomic clocks and GPS satellite as a gigantic detector with an aperture of 50000km. They focused on a particular type of dark matter arising from ultralight hypothetical quantum fields that condensate into spatially extended object. These latter are allowed to reach a size similar to that of the Earth. The appearance of these structures, called topological defects, should be related to phase transition in the early universe, in a way similar to what occurs in condensed matter. The topological defect cores' can cover various spatial dimentionalities: point-like (0d monopoles), string-like (1d vortex stings) or planar (2d domain walls). When the trajectory of the Earth in the Galactic halo intercepts such topological defects, a coherent succession of glitches should appear at the level of atomic clock and would propagate through the GPS constellation and the Earth.

In this poster we introduce a new effective theoretical model from which all the basic types of topological defects (monopole, vortex string and domain wall) can be described at low energy scale. Along with this model a series of parameters are initially let free but are further constrained by observational data coming from GNSS networks. Using this model, we show that when Earth sweeps through topological defects, these latter act as a homogeneous electric and magnetic medium. Disturbances are thus induced in the GNSS signals from satellites to the Earth's surface. This formulation paves the way towards a new method of detection of topological defects using GNSS signal measurements.

References

[1] A. Derevianko and M. Pospelov, Nature Phys., vol. 10, p. 933, 2014 [arXiv:1311.1244].

Effect of pulse duration fluctuation on the photodetection of a train of pulses from an optical frequency comb

Xiaopeng Xie[1], Romain Bouchand[1], Michele Giunta[2,3], Wolfgang Hänsel[2], Matthias Lezius[2], Ronald Holzwarth[2,3], Giorgio Santarelli[4], Yann Le Coq[1*]

[1] LNE-SYRTE, Observatoire de Paris, PSL Research University, CNRS, Sorbonne Universités, UPMC Univ. Paris 06, 61 avenue de I'Observatoire, 75014 Paris, France
[2] Menlo Systems GmbH, Am Klopferspitz 19a, D-82152 Martinsried, Germany
[3] Max-Planck-Institut für Quantenoptik, 85748 Garching, Germany
[4] LP2N, IOGS-CNRS-Université de Bordeaux 1, rue F. Mitterand, 33400 Talence, France

*Email: yann.lecoq@obspm.fr

Microwave signals with unprecedented ultra-low phase noise can be generated by photodetecting stabilized optical pulse trains from femtosecond laser [1, 2]. However, excess noise introduced by photodetection limits the phase noise performance of generated microwave signals. In this contribution, we will report on a new limitation that arises from the pulse duration fluctuation of ultra-short optical pulses. Such fluctuations, although minute compared to the pulse duration itself, convert to phase fluctuations in the microwave electrical waveforms generated by photodetection in a fast InGaAS pin photodiode, due to nonlinear processes. By using a spatial light modulator wave-shaper, we quantitatively characterize the pulse duration to phase conversion coefficient under various experimental configurations (bias voltage, optical power, etc…). Furthermore, by combining this quantitative characterization with experimental microwave phase noise measurement under conditions where this new effect is the dominant source of noise, we have characterized quantitatively, to our knowledge for the first time, the pulse duration noise that is present at the output of an Erbium doped fiber based femtosecond laser and its optical amplification chain.

Figure 1 displays the experiment set-up. An L+C band wave-shaper in used in the phase locked loop to modify the optical pulse duration by setting different group delay dispersion. The 12 GHz signal, harmonic of repetition rate frequency, is isolated after the photodiode. We observe the phase evolution of 12 GHz signal is sensitive to the optical pulse duration being detected. Note that the well-known amplitude to phase noise conversion needs to be carefully excluded during this measurement process [3]. In such conditions where the pulse-duration fluctuations effect is dominant, a microwave phase noise measurement can therefore allow probing of the power spectral density of the optical pulse duration noise in our system (measured below $\Delta\tau/\tau \approx 3\times10^{-7}$).

References

[1] X. Xie, R. Bouchand, et al., Y. Le Coq, "Photonic microwave signals with zeptosecond-level absolute timing noise", Nat. Photonics, vol. 11, p. 41-47, 2017.

[2] T. Fortier, et al., "Generation of ultrastable microwaves via optical frequency divison", Nat. Photonics, vol. 5, p.425-429, 2011.

[3] R. Bouchand, et al., "Accurate control of optoelectronic amplitude to phase noise conversion in photodetection of ultra-fast optical pulses", Opt. Express, vol. 25, p. 12268, 2017.

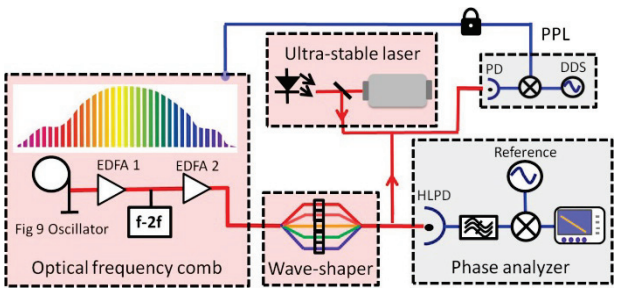

Fig. 1: Experimental set-up for exploring the nonlinearity of photodetection of ultra-short optical pulse trains. EDFA, Erbium-doped fiber amplifier; HLPD, High-linear photodiode; PD, Photodiode; DDS, direct digital synthesizer; PPL, Phase lock loop.

Improvements on the UTC(IT) timescale at INRIM

Marco Sellone[1], Roberto Costa[1], Alberto Mura[1], Giancarlo Cerretto[1], Marco Siccardi[2] and Filippo Levi[1]

[1]Time and Frequency Laboratory, INRIM – Istituto Nazionale di Ricerca Metrologica, Torino, Italy
[2]SKK Electronics, Cuneo, Italy

Email: m.sellone@inrim.it

INRIM realization of UTC, namely UTC(IT), is currently generated by means of an Hydrogen Maser conceived as a master clock supported by an Atomic Caesium Fountain, as well as by an ensemble of 10 other commercial clocks (Ceasium Beam Clocks and H-Maser). The master clock signal drives a microstepper device, hereafter indicated as Auxialiary Output Generator (AOG), used to correct the clock frequency offset and drifts, in order to keep UTC(IT) as much as possible aligned to UTC. The AOG's 1PPS and 5 MHz signals, are then distributed to all the Time and Frequency Laboratory equipment and services [1], by means of a cascade 1PPS/10 MHz distribution system. UTC(IT) generation system is then duplicated, in order to have a backup time scale ready to be used in case failures of the first one. The primary and the backup time scales (called UTC(IT)_1 and UTC(IT)_2), are kept aligned at the highest level of accuracy, in order to prevent possible time jumps when switch among them. To fulfill this requirement we continuously monitor the time difference between the two scales, keeping their time offset within few ns. The switching process from the primary time scale to the backup one, both for maintenance purposes or for emergency reasons, is not a trivial aspect, since it is mandatory to guarantee signals continuity during the commutation.

To achieve this goal, a new device has been procured and will be introduced in the UTC(IT) generation chain. This new device, specifically designed for the purpose, is an automatic switch that accepts as input the 5 MHz signals generated by two independent AOGs, generating 1PPS, 10 MHz and 100 MHz output signals. When the new switching device will be permanently installed at the laboratory, the two inputs will come directly from UTC(IT)_1 and UTC(IT)_2 time scales. The device will allow switching from one time scale, to the other, transparently (if the two scales are properly aligned), simplifying the commutation process and making UTC(IT) generation more robust and reliable. At the conference a complete description of the new device will be presented, as well as its full characterization, and an overview of the whole new system for the generation of UTC(IT). The new scale generation will become operative most likely in 2018.

References

[1] Cerretto, G., Costa, R., Fantino, G., Cantoni, E., Sesia, I., Signorile, G., Tavella, P., "INRIM Time and Frequency Laboratory: An Update on the Status and on the Ongoing Enhancement Activities," Proceedings of the 46th Annual Precise Time and Time Interval Systems and Applications Meeting, Boston, Massachusetts, December 2014, pp. 33-40.

Phase Synchronization for 5G Using Mass Market GNSS Receivers

Zdenek Chaloupka, Lionel Ries, Andrea Samperi, Pierre Waller, Massimo Crisci

European Space Agency/European Space Research and Technology Centre, Noordwijk, Netherlands

Email: z.c.nl@ieee.org

Industry and academia have been quite active in defining the next generation telecommunication technology (5G) and its requirements for quite some time now. The unwavering effort (from industry) is fueled mainly by the expected revenues, but also by the need to have the first technology standard in place before 2020 to follow the schedule laid out by ITU in IMT-2020 [1]. Even though the standard definition is progressing quite quickly now, it is not clear yet what are the key requirements of the 5G technology with respect to time, phase or frequency synchronization accuracy and precision.

However, looking at the requirements of already published standards for 4G, one could conclude that the telecommunication technology synchronization shifts from frequency synchronization (for LTE) to phase synchronization (for LTE-A) due to advantages that the latter offers for MIMO techniques. Indeed, the document [2] clearly states that a time alignment error for MIMO transmissions shall not exceed 65ns at the base station transmitter port. It is more than evident that in order to enable a smooth roll out of 5G technology, industry and academia should look for an affordable technology capable to deliver such accuracy. Quite possibly, even more accurate one to allow for more future proof solutions.

Our paper contributes toward that goal by evaluating relative time (phase) synchronization of mass market Global Navigation Satellite System (GNSS) receivers and hence giving an overview of what is possible to achieve with the current technology. The evaluation is performed in rather idealistic conditions, i.e. by feeding multiple receivers from the same antenna, however, this will help to understand a lower bound of relative synchronization accuracy achievable by commercial-off-the-shelf receivers.

The measurement test bed is designed as follows. Multiple GNSS receivers (mostly single frequency, multiple-constellation) from different manufacturers (u-blox NEO-M8T, Telit SL869-DR, Swift navigation) are fed with GNSS signal from a single antenna through eight-way splitter (GPS Networking ALDCBS1X8). The output of the 1PPS port of the receivers is connected to an oscilloscope with eight channels, allowing to truly capture relative synchronization performance at every epoch. In order to create even more favorable conditions for phase synchronization, multiple receivers (six u-blox NEO-M8T) are tested simultaneously to demonstrate how difficult it is to maintain tight phase synchronization required by future 5G technology.

The receivers are evaluated in a rover mode (computing Position, Velocity and Time), timing mode with fixed position (if the receiver permits it) and using single (GPS/Galileo) and multi-constellation (GPS/Galileo/GLONASS/BeiDou) operation of the receiver.

References

[1] IMT Vision - Framework and Overall Objectives of the Future Development of IMT for 2020 and Beyond Recommendation ITU-R M. 2083-0, Sept. 2015.

[2] ETSI TS 136 104, LTE; Evolved Universal Terrestrial Radio Access (E-UTRA); Base Station (BS) radio transmission and reception, October 2016.

The research of UTC(NTSC) and UTC(SU) joint time scale algorithm

BAI Shanshan[1,2,3], DONG Shaowu[1,2], ZHAO Shuhong[1,2], QU lili[1,2], LI Wei[1,2]
1 National Time Service Center, Chinese Academy of Sciences, Xi'an, China
2 Key Laboratory of Time and Frequency Primary Standards, National Time Service Center, CAS, Xi'an, China
3 University of Chinese Academy of Sciences, Beijing, China

Email: xfydy5@163.com

Russian-Chinese Cooperation Committee on Satellite Navigation was established by the two sides of China and Russia under the regular meeting mechanism, In order to effectively promote the cooperation between China and Russia in the field of satellite navigation. The technical communication of existing and future compatibility, interoperability and time system interoperability, etc was convoked by the committee. Russian-Chinese joint time keeping lab was established by the two sides of China and Russia. Chinese responsible institute is National Time Service Center, Chinese Academy of Sciences(NTSC), UTC(NTSC) was maintained by NTSC, UTC(NTSC) is the traceability reference of BDT. Russian responsible institute is Institute of Metrology for Time and Space(RIRT), UTC(SU) was maintained by RIRT, UTC(SU) is the traceability reference of GLONASST. UTC(NTSC) and UTC(SU) joint time scale is a unified reference for compatibility and interoperability of GLONASS and BeiDou navigation system step by step. The unified reference can build the foundation for further work and promote GNSS time interoperability.

In this paper, prediction of cesium atomic clock with linear model, and prediction of hydrogen atomic clock with quadratic model by the atomic clock stability analysis. To Calculate the weight of atomic clock based on "predictability". MJD from 57814 to 57894, UTC(NTSC) and UTC(SU) joint time scale was calculated by NTSC and SU atomic clock, NTSC time scale was calculated by NTSC atomic clock only. Figure 1 shows the deviation of TA_{joint} between UTC,the deviation of TA_{NTSC} between UTC, the deviation of UTC(SU) between UTC. Figure 2 shows the stability of TA_{joint} and TA_{NTSC}. As shown in the figure, the joint time scale have a better stability than the time scale calculated using only NTSC laboratory atomic clocks.

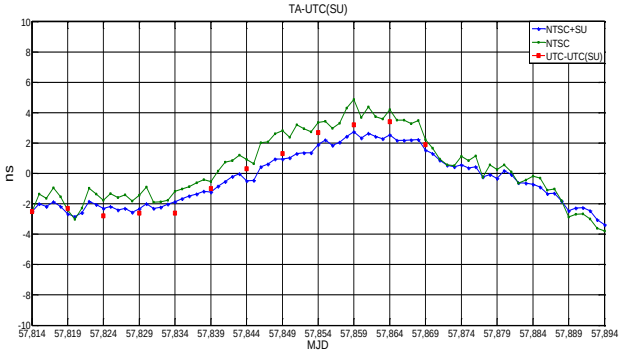

Figure 1

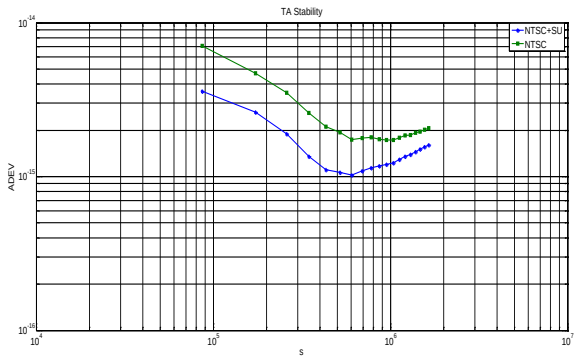

Figure 2

References

[1] Panfilo G, Harmegnies A , Tisserand L, "A new prediction algorithm for the generation of International Atomic Time", J. Metrologia., vol. 49(1), p. 49-56, 2012.

[2] GreenhallCA, "A Kalman Filter Clock Ensemble Algorithm that Admits MeasurementNoise", J. Metrologia., vol. 43, p. 311-321, 2006.

Towards a Quantum-Enhanced Atomic Clock on a Chip

Tommaso Mazzoni[1], Meng-Zi Huang[2], Théo Laudat[2], Carlos L. Garrido Alzar[1], Jakob Reichel[2]

[1]LNE-SYRTE, Observatoire De Paris, PSL, CNRS, UPMC, 61 Av De l'Observatoire, 75014 Paris, France

[2]Laboratoire Kastler Brossel, Unité mixte CNRS, UPMC, ENS, CdF, 24 Rue Lhomond, 75005 Paris, France

Email: tommaso.mazzoni@obspm.fr

The Dick effect and quantum projection noise are among the most stringent limiting factors for state-of-the-art atomic frequency standards, both primary standards and compact clocks. A possible solution to the Dick effect relies on Quantum Non-Destructive (QND) detection, which allows multiples interrogations with weak measurement of the same atomic ensemble. Spin-squeezed states, which can also be prepared by QND detection, have the potential to enable metrology beyond the standard quantum limit, by employing quantum correlations. Both mechanisms have been demonstrated in proof-of-principle experiments [1-5], but the stability of these experiments did not reach any metrologically relevant level.

Our Trapped Atom Clock on a Chip (TACC) is a compact microwave atomic clock with a demonstrated stability of 5.8×10^{-13} $s^{-1/2}$ [6]. It uses an atom chip as a robust, miniature platform. TACC has recently allowed us to demonstrate that spin squeezing can be generated spontaneously in a rubidium BEC [7]. In the new experiment, we target on a quantum-enhanced version of TACC, by using QND detection and spin-squeezed ultra-cold thermal atoms generated by cavity-QED interactions. To reach this goal, we have integrated two fiber Fabry-Perot cavities [8] on the clock chip (Fig. 1), realizing a platform for cavity-QED in the strong-coupling and weak-coupling regime. We will report on the current status and perspectives of this project.

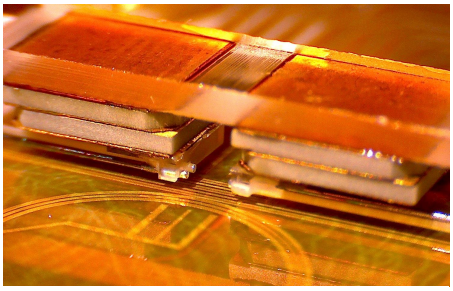

Fig. 1: A pair of optical fiber cavities integrated on the clock atom chip.

References

[1] T. Vanderbruggen et al. "Feedback Control of Trapped Coherent Atomic Ensembles", Phys. Rev. Lett. 110, p. 210503, 2013.

[2] G. Vallet et al. "A noise-immune cavity-assisted non-destructive detection for an optical lattice clock in the quantum regime", New J. Phys. 19, p. 083002, 2017.

[3] J. Appel et al. "Mesoscopic atomic entanglement for precision measurements beyond the standard quantum limit", PNAS 106(27), pp. 10960-10965, 2009.

[4] I. Leroux et al. "Implementation of Cavity Squeezing of a Collective Atomic Spin", Phys. 4ev. Lett. 104, p. 073602, 2010.

[5] O. Hosten et al. "Measurement noise 100 times lower than the quantum-projection limit using entangled atoms", Nature 529, pp. 505–508, 2016.

[6] R. Szmuk et al. "Stability of a trapped-atom clock on a chip", Phys. Rev. A 92, p. 012106, 2015.

[7] T. Laudat et al., in preparation.

[8] K. Ott et al. "Millimeter-long fiber Fabry-Perot cavities", Optics Express 24(9), pp. 9839-9853, 2016.

Comparison of highly-stable optical frequency transfer in a single bidirectional and double unidirectional fibers

P. Włodarczyk[1], P. Krehlik[1], Ł. Śliwczyński[1]
[1]Faculty of Computer Science, Electronics and Telecommunications
AGH University of Science and Technology, Krakow, Poland
Email: pwl@agh.edu.pl

Due to the growing interest in the distribution of time and frequency signals, several fiber optic systems designed for this purpose have been built in the recent years. It is known that best results for this type of systems are obtained by using so called dark fiber operated bidirectionally to ensure the highest symmetry of phase fluctuation in transmission in both directions. However, in many practical situations the only possibility for fiber-optic frequency transfer is to use a channel in a DWDM telecom network, which as a rule uses two parallel fibers for both directions. Therefore, it is advisable to compare the stability of the transmitted optical frequency in a single bidirectionally operated fiber with a link consisting of two separate unidirectional fibers, to determine the stability limit for such a link. This kind of experiments were carried out previously [1, 2], but the results were not consistent. Thus, we have decided to conduct more research based on similar approach to enrich the experimental data for future analysis and discussions. We performed measurements in a standard closed-loop system canceling the fiber induced phase noise [3]. Frequency transfer stability was evaluated both, in a single-fiber configuration and in two parallel optical fibers. In both cases a real, 60 km long fiber optic link, running through urban areas of Krakow, was used. The transmission stability was also measured in non-stabilized (open loop) link. Based on the results shown in Fig. 1, it was found that phase fluctuations in the band up to some tens of hertz (acoustic noise) are well suppressed. The long-term drifts however are not fully compensated, but still about two orders of magnitude noise reduction was observed in comparison with a one way, not compensated transfer. This work will not only focus on an analysis of the results obtained, but will also gather more data from longer observation periods.

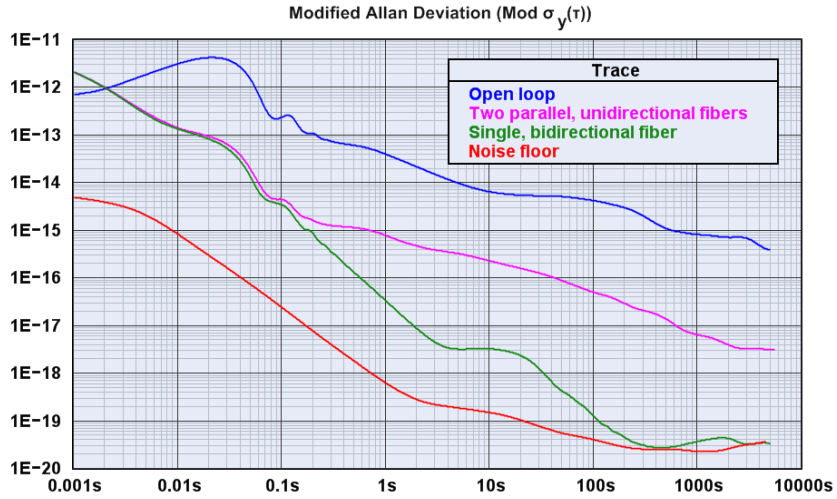

Fig. 1. Stability of optical frequency transfer through the investigated optical links.

Acknowledgment: This work was supported by the EMPIR initiative co-funded by the European Union's Horizon 2020 research and innovation programme and the Participating States via project 15SIB05.

References

[1] P. A. Williams, W. C. Swann, N. R. Newbury, "High-stability transfer of an optical frequency over long fiber-optic links", J. Opt. Soc. Am. B, Vol. 25, Issue 8, pp. 1284-1293

[2] A. Bercy et al., "Two-way optical frequency comparisons at $5 \cdot 10^{-21}$ relative stability over 100-km telecommunication network fibers", Phys. Rev. A 90, 061802(R)

[3] L.S. Ma, P. Jungner, J. Ye, J.L. Hall, Delivering the same optical frequency at two places: accurate cancellation of phase noise introduced by an optical fiber or other time-varying path, Opt Lett. 1994 Nov 1;19(21):1777-9.

Timing jitter characterization of dual-comb system via TWTFT method

Honglei Yang, Shengkang Zhang, Huan Zhao, Hongbo Wang, Xueyun Wang, Haifeng Wang, Hang Yi, Wenzhe Yang, Shuwei Wang

Beijing Institute of Radio Metrology and Measurement, Beijing China
Science and Technology on Metrology and Calibration Laboratory, Beijing China

Email: yhlpc@163.com

In dual-comb system, timing jitter is of utmost crucial for promoting diverse scientific applications, such as high-precision ranging [1,2], high-speed and high-resolution molecular spectroscopy [3], time and frequency distribution [2,4,5], to name a few. Characterization of timing jitter of dual-comb system could also give a general performance evaluation [6].

Here we propose a method of timing jitter characterization for dual-comb system. The concept of two-way time and frequency transfer is adopted for cancelling path drift. The repetition rate of one comb is detuned to the other in order to achieve linear optical sampling. Type-II second order correlation signals, which are generated by the orthogonal-polarized pulses from individual combs when overlapping in time domain, give the timing jitter information. The arrival time of the correlation signals in both sites, is recorded by a time-to-digital converter. The timing jitter is obtained by directly subtracting the arrival time of the correlation signals, which is retrieved by fitting, from expected time. This avoids calibration in balanced optical cross-correlation.

For verification, we conducted a numerical simulation, where dual-comb system is configured in one-way transfer if in the assumption of no path drift due to environmental variation. In practice, two-way reciprocal transfer configuration, which has been adopted in optical two-way time and frequency transfer(TWTFT) is set to cancel the path drift caused by refractive index change due to environmental variation. Note that the simulation does not take detection noise into consideration. The simulation being in well agreement with presetting timing jitter verifies the proposed characterization method. Based on simulation, we investigated the effect on the precision from the number of fitting points, and the effect from quantizing noise as well. The simulation could enhance the understanding of timing jitter characterization of dual-comb system, and dual-comb time and frequency transfer. The proposed method could significantly reduce the environmental variation when confronting with remote combs.

References

[1] I. Coddington, W. Swann, L. Nenadovic, and N. Newbury, "Rapid and precise absolute distance measurements at long range," Nat. Photonics 3, 351-356 (2009).
[2] H. Zhang, H. Wei, X. Wu, H. Yang, and Y. Li, "Absolute distance measurement by dual-comb nonlinear asynchronous optical sampling," Opt. Express 22, 6597-6604 (2014).
[3] I. Coddington, W. Swan, and N. Newbury, "Coherent multiheterodyne spectroscopy using stabilized optical frequency combs," Phys. Rev. Lett. 100, 013902 (2008).
[4] F. Giorgetta, W. Swan, L. Sinclair, E. Baumann, I. Coddington, and N. Newbury. "Optical two-way time and frequency transfer over free space," Nature Photonics, 7(6): 434-438 (2013).
[5] J. Deschênes, L. Sinclair, F. Giorgetta, W. Swan, E. Baumann, H. Bergeron, M. Cermak, I. Coddington, and N. Newbury. "Synchronization of distant optical clocks at the femtosecond level," Physical Review X, 6, 021016 (2016).
[6] H. Yang, H. Wei, H. Zhang, K. Chen, Y. Li, V. Smolski, and K. Vodopyanov, "Performance estimation of dual-comb spectroscopy in different frequency-control schemes," Appl. Opt. 55, 6321-6330 (2016).

Towards a Cryogenic Silicon Resonator with Low Thermal Noise Crystalline Mirrors

Thomas Legero[1], Dan G. Matei[1], Robin Weyrich[1], Sebastian Häfner[1], Fritz Riehle[1], Lindsay Sonderhouse[2], John M. Robinson[2], Eric Oelker[2], Wei Zhang[2], Jun Ye[2], Paula Heu[3], David Follman[3], Christoph Deutsch[3], Garrett Cole[3], Uwe Sterr[1]

[1]Physikalisch-Technische Bundesanstalt, Bundesallee 100, 38116 Braunschweig, Germany
[2]JILA, National Institute of Standards and Technology and University of Colorado, 440 UCB, Boulder, CO 80309-0440, USA
[3]Crystalline Mirror Solutions LLC and GmbH, Santa Barbara, CA 93101, USA and 1010 Vienna, Austria

Email: thomas.legero@ptb.de

Single-crystal materials have proven to be an ideal choice for ultra-stable optical resonators. Among them, cryogenic silicon-based cavities have demonstrated stabilized lasers with an unprecedented fractional frequency instability down to mod $\sigma_y = 4 \cdot 10^{-17}$ and linewidths below 10 mHz [1,2]. The coherence properties and the frequency instability of the laser systems are limited by the Brownian thermal noise of the resonator. The dominant contribution of the thermal noise arises from the dielectric Ta_2O_5/SiO_2 mirror coatings.

Crystalline mirror coatings based on AlGaAs multilayers have previously demonstrated a ten-fold reduction in Brownian thermal noise at room temperature [3]. Combining these coatings with a 21-cm long silicon cavity at 124 K leads to the potential for a thermal noise limited frequency instability of $1 \cdot 10^{-17}$.

We have characterized a pair of crystalline mirror coatings on silicon substrates at temperatures down to 100 K with a finesse of up to 390 000. The new mirrors will be used to construct a 21-cm long silicon cavity operated at 124 K. To benefit from the reduced thermal noise, we must further decrease the impact of technical noise such as seismic or acoustic vibrations, etalon effects and temperature fluctuations [4].

We will report on the current setup and discuss measures to reduce technical noise to below $1 \cdot 10^{-17}$.

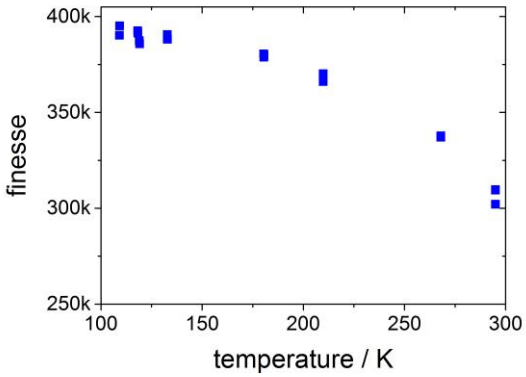

Fig. 1: Finesse of a silicon test cavity with crystalline coatings. The coating parameters are optimized for a temperature around 120 K. The 10-cm long test cavity shows a finesse of around 390 000.

References

[1] D. G. Matei et al., "1.5 µm lasers with sub-10 mHz linewidth", Phys. Rev. Lett, vol. 118, pp. 263202, 2017
[2] W. Zhang et al., "Ultrastable Silicon Cavity in a Continuously Operating Closed-Cycle Cryostat at 4K", Phys. Rev. Lett., vol. 119, pp. 243601, 2017.
[3] G. D. Cole et al., "Tenfold reduction of Brownian noise in high-reflectivity optical coatings", Nature Photonics, vol. 7, pp. 644, 2013.
[4] D. G. Matei et al., "A second generation of low thermal noise cryogenic silicon resonators", J. Phys.: Conf. Ser., vol. 723, pp. 012031, 2016

Development of an ytterbium optical lattice clock at NMIJ

Takumi Kobayashi[1], Daisuke Akamatsu[1], Yusuke Hisai[2,1], Takehiko Tanabe[1], Hajime Inaba[1], Tomonari Suzuyama[1], Feng-Lei Hong[2], Kazumoto Hosaka[1], and Masami Yasuda[1]

[1]National Metrology Institute of Japan (NMIJ), National Institute of Advanced Industrial Science and Technology (AIST), 1-1-1 Umezono, Tsukuba, Ibaraki 305-8563, Japan
[2]Department of Physics, Graduate School of Engineering, Yokohama National University, 79-5 Tokiwadai, Hodogaya-ku, Yokohama 240-8501, Japan

Email: takumi-kobayashi@aist.go.jp

Optical lattice clocks (OLCs) have demonstrated fractional uncertainties and stabilities at the 10^{-18} level [1] and are expected to contribute to the redefinition of the SI second. Ytterbium (Yb) is one of important atomic species that are used to realize OLCs, since the $^1S_0$-$^1P_0$ clock transition of ^{171}Yb at 578 nm is adopted as one of the secondary representations of the second. At National Metrology Institue of Japan (NMIJ), we have previously developed an Yb OLC, and determined the absolute frequency of the clock transition [2].

In the present work, we report our second Yb OLC. This clock is intended for use in calibrating our time scale: the Coordinated Universal Time (UTC) of NMIJ. For this purpose, it is essential to operate the OLC with a large uptime. We are therefore attempting to develop a reliable and low maintenance OLC. We installed all the parts of the OLC, which consists of a vacuum chamber for preparing atoms and laser systems, in a well temperature-controlled room. Compact laser systems were realized using half-inch optical components. A multi-branch fiber-based frequency comb was used to stabilize frequencies of light sources for laser cooling, trapping, and interrogation of the clock transition. This eliminates the need for a hollow-cathode lamp or an atomic vapor for laser frequency stabilization. The comb transfers the linewidth of a stable master laser stabilized on an ultra-low expansion cavity to the other lasers [3], which allows preparation of only one cavity.

Figure 1 shows the observed spectrum of one Zeeman component (m_F = 1/2) of the $^1S_0$-$^1P_0$ transition with spin-polarized atoms, which was obtained by applying a 55-ms-long π pulse. We are now measuring the absolute frequency of the clock transition and systematic frequency shifts. So far, the clock operation lasts for 3-6 hours par day with little human effort.

This work was supported by Japan Society for the Promotion of Science (JSPS) KAKENHI Grant Number 17H01151, 15K05238, and 17K14367.

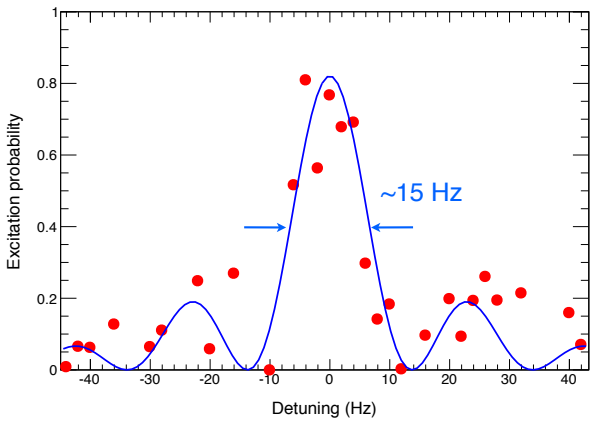

Fig. 1: Spectrum of one Zeeman component (m_F = 1/2) of the $^1S_0$-$^1P_0$ clock transition with spin-polarized ^{171}Yb atoms. The solid blue line indicates the best fit of a Rabi excitation profile.

References

[1] I. Ushijima *et al.*, "Cryogenic optical lattice clocks", Nat. Photonics, vol. 6, p. 185-189, 2015.

[2] M. Yasuda *et al.*, "Improved Absolute Frequency Measurement of the 171Yb Optical Lattice Clock towards a Candidate for the Redefinition of the Second", Appl. Phys. Express, vol. 5, p. 102401, 2012.

[3] H. Inaba *et al.*, "Spectroscopy of ^{171}Yb in an optical lattice based on laser linewidth transfer using a narrow linewidth frequency comb", Opt. Express, vol. 21, p. 7891-7896, 2013.

An alignment technique for optimal atomic trajectory of an atomic fountain clock

Sangmin Lee[1, 2], Hyun-Gue Hong[1], Myoung-Sun Heo[1], Taeg Yong Kwon[1], Sang-Bum Lee[1], Sang Eon Park[1, 2]

[1]Korea Research Institute of Standards and Science, Daejeon 34113, South Korea
[2]University of Science and Technology, Daejeon 34113, South Korea

Email: parkse@kriss.re.kr

To improve the performance of the atomic fountain clock, it is necessary to optimize the initial position of the atom, the launch angle, and the fountain tilt angle. These parameters have a direct effect on the short-term stability in relation to the number of detected atoms and the contrast of Ramsey signal. The atomic trajectory is also a key factor in analyzing the DCP (distributed cavity phase) errors of the fountain clocks [1]. A study using a hyperfine transition with a $\Delta m_f = \pm 1$ to predict atomic trajectories has been done [2]. Here we use variation of transition probabilities of atomic ensemble for Rabi and Ramsey interrogations to find optimum atomic trajectories with respect to microwave cavity.

We numerically analyzed the detected atom number and the amplitude of the Rabi, Ramsey signals according to the initial position and launch angle of the atom and the fountain tilt angle [3]. We solved the Bloch equation by matching the trajectory of the atoms obtained using the Monte Carlo method and the field profile within the microwave cavity obtained through the COMSOL finite element solver. Figure 1 shows the detected atom number and the Rabi and Ramsey signals according to fountain tilt angle when the launch angle is -2 mrad, 0 mrad, and 2 mrad. In fountain clocks, atoms interact with the microwave field inside the cavity twice as they go up and down. When the atom cloud passes through the center of the cavity, the loss of atom number is smallest and interacts with the microwave of the most optimized intensity. As shown in Figure 1, the optimal condition is when the peak of the atom number matches the peak of the Rabi signal. The above results can be used as a method for correct align of atomic fountain clocks and launching angle of atomic cloud, experimentally.

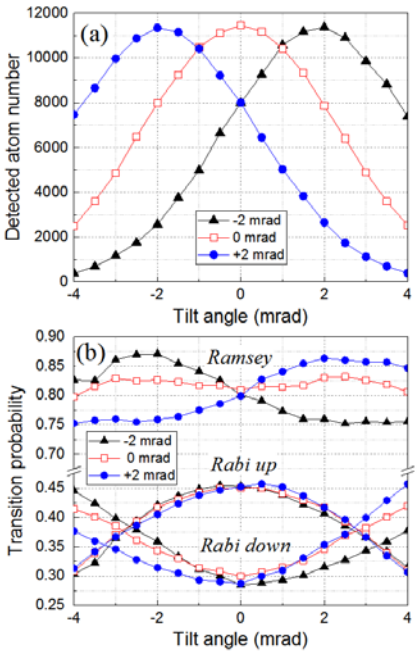

Fig. 1: Calculated results: (a) Detected atom number as a function of fountain tilt angle relative to the vertical z-axis for launch angles of -2, 0, 2 mrad relative to the central axis of the cavity. (b) The variation of transition probabilities for Ramsey, Rabi up, and Rabi down. Rabi up (Rabi down): Microwave field is applied only when atom goes up (down). Microwave amplitude is set to 4.9 times of normal operation (two π/2 pulses) to amplify deviation of transition probability.

References

[1] R. Li and K. Gibble, "Evaluating and minimizing distributed cavity phase errors in atomic clocks", Metrologia, Vol. 47, p. 534-551, 2010.

[2] N. Nemitz, V. Gerginov, R. Wynands and S. Weyers, "Atomic trajectory characterization in a fountain clock based on the spectrum of a hyperfine transition", Metrologia, vol. 49, p. 468-78, 2012.

[3] C. J. Foot, "Atomic Physics", Oxford University Press, New York, p. 123-150, 2005.

Lattice induced decoherence in an optical lattice clock

Roman Schwarz[1], Sören Dörscher[1], Ali Al-Masoudi[1], Marcin Bober[2], Richard Hobson[3], Stephan Falke[1*], Uwe Sterr[1] and Christian Lisdat[1]

[1]Physikalisch-Technische Bundesanstalt, Bundesallee 100, 38116 Braunschweig, Germany
[1*]Now with TOPTICA Photonics AG, Munich Germany
[2]Institute of Physics, Faculty of Physics, Astronomy and Informatics, Nicolaus Copernicus University, Grudziadzka 5, 87-100 Torun, Poland
[3]National Physical Laboratory, Hampton Road, Teddington, Middlesex, UK, TW11 0LW

Email: roman.4.schwarz@ptb.de

Atomic clocks for frequency metrology are continuously improving and have reached systematic uncertainty of few parts in 10^{18} [1,2] and frequency instability below $10^{-16}\,\tau^{-1/2}$ [3], where τ is the averaging time in seconds. In principle, the performance of optical clocks benefits from increasing interrogation time, and Ramsey interrogation with free evolution times of up to 15 s has been demonstrated [4]. Scattering of lattice photons becomes relevant at such interrogation times and may cause atomic decoherence as well as frequency shifts of the clock. In our ^{87}Sr clock, we have investigated this effect and its impact on clock operation.

At the lattice wavelength of about 813 nm, elastic scattering and inelastic scattering $^3P_0 \rightarrow {}^3P_J$ where $J \neq 0$ are the processes that occur at relevant rates. In particular, scattering $^3P_0 \rightarrow {}^3P_1$ effectively induces decay of the excited state to the ground state due to subsequent radiative decay of the state $^3P_1$. We calculate the rates of these scattering processes and investigate lattice-induced decay experimentally by measuring the population dynamics. Moreover, we study their effect on clock operation. From our measurements, we derive the lattice-induced decay rate, which agrees with our calculations, and the natural lifetime of the excited state $^3P_0$.

For long interrogation times as discussed above, the coherence time of the clock laser becomes another limiting factor. Technical progress of narrow-linewidth laser systems does not allow resolving the natural linewidth of the clock transition, yet. Here we present a novel interrogation method [5], which allows interrogation times beyond the coherence time of the laser. An optimized interrogation sequence improves the performance of the method. We discuss limitations caused by the finite length of the Ramsey pulses.

References:

[1] T. L. Nicholson, et. al., “Systematic evaluation of an atomic clock at 2×10^{-18} total uncertainty,” Nature Com., vol. 6, p. 6896, 2015

[2] N. Huntemann, et. al., “Single ion atomic clock with 3×10^{-18} systematic uncertainty,” Phys. Rev. Lett., vol. 116, p. 063001, 2016

[3] Schioppo, et. al, “Ultra-stable optical clock with two cold-atom ensembles”, Nature Photonics, vol. 11, p. 48-52, 2017.

[4] G. E. Marti, et. al., “Imaging optical frequencies with 100 μHz precision and 1.1 μm resolution, 2017” arXiv:1711.08540

[5] Proceedings of the European Frequency and Time Forum held 4-7 April 2016, York, United Kingdom

GNSS antenna multipath effects

G. D. Rovera[1], M. Abgrall[1], P. Uhrich[1], P. Defraigne[2], B. Bertrand[2]

[1]LNE-SYRTE, Observatoire de Paris, PSL Research University, CNRS, Sorbonne universités, UPMC, Univ. Paris 06, Paris, France
[2]Royal Observatory of Belgium, Brussels, Belgium

Email: Daniele.Rovera@obspm.fr

For a better organization of the network of laboratories contributing to the Temps Atomique International (TAI), the Bureau International des Poids et Mesures (BIPM) has built a document aiming at homogenizing GNSS link calibrations called "BIPM guidelines for GNSS calibration" [1]. The Working Group on Global Navigation Satellite Systems (GNSS) of the Consultative Committee on Time and Frequency (CCTF) approved these guidelines in 2017. Among other elements inside this document, BIPM is providing a comprehensive model of uncertainty budget for GNSS link calibration, where there are some lines devoted to the uncertainties related to multipaths of the satellite signals. But there are only scarce published works on such effects, and the quantization of such uncertainties remains to be estimated more precisely.

In this paper, we propose a series of tests between two GNSS receiving chains in common-clock set-up, with one of the antennas placed either in a normal environment, or in an environment where metallic plates are extensively used in order to generate multipaths at close range. In addition, clear offsets already observed on GNSS data after a change in an antenna environment at larger range will be documented.

The first goal of this experiment is an attempt to define experimentally what a perturbing environment around such a GNSS receiving chain would be about from multipath point of view. The second goal is to provide a quantitative analysis of the results, in order to compute some upper limit of multipath effects on GNSS antennas. Such results would certainly prove to be useful for any GNSS link calibration implementation and computation. This should eventually lead to a better estimate of the uncertainties to be used in a GNSS calibration link uncertainty budget.

These tests will however remain limited to existing available equipment in both our laboratories. We do not pretend to consider all types of GNSS antennas and receivers comprehensively.

References

[1] Bureau International des Poids et Mesures, "BIPM guidelines for GNSS calibration", v3.2, 15/02/2016.

DWDM stabilized optics for White Rabbit

Paul Boven[1]

[1]Joint Institute for VLBI ERIC (JIVE), Dwingeloo, the Netherlands.

Email: boven@jive.eu

The Square Kilometre Array (SKA) is a future radio telescope to be built in South Africa and Australia, with an unprecedented sensitivity due to its large collecting area. Each site will host numerous receptors (parabolic dishes for the SKA1-Mid and arrays of logperiodic antennas for SKA1-Low) that will act as interferometers. Phasing up these receptors requires the distribution of accurate timing signals over fiber distances of up to 175km, with the fiber and some of the equipment exposed to the semi-desert environment. Meeting the SKA scientific objectives requires a timing distribution accuracy of better than 2ns.

White Rabbit (WR) is an extension of the IEEE1588v2 protocol that allows for sub-ns accuracy in timing distribution over fiber for distances of up to 10km. We have extended the reach, stability and accuracy of White Rabbit by using Dense Wavelength Division Multiplexing (DWDM) optics and filters, instead of the 10km reach BiDirectional optics that are part of the WR standard.

Chromatic dispersion, in combination with the long distances required, converts any variations of the laser wavelength into large changes in propagation delay which are not compensated for by the WR system. The laser wavelength itself is sensitive to temperature, and has an intrinsic spread of a few nm in the BiDi optics. The use of DWDM optics eliminates both issues.

This paper describes the design of WR with DWDM optics for the SKA. It includes accuracy estimates (accounting for temperature, dispersion, calibration, attenuation, wavelength uncertainty and the Sagnac effect) and experimental results on long distance links.

Portable atomic clock based on a single Ca+

Callan Jobson, Nathan Gemmell, Matthias Keller

ITCM Group, University of Sussex, Brighton, UK

Email: C.Jobson@sussex.ac.uk

We present our recent advances in developing a portable atomic clock based on a single trapped Ca+. Atomic clocks based on optical transitions have been shown to be the most stable and most precise measures of time [1]. However, current optical clock systems have large spatial footprints, high power consumption, and complex operational procedures. For this reason they have yet to find applications outside of the scientific community.

We aim to build a portable atomic reference based on a single trapped calcium ion. With all required wavelengths available either directly from, or through frequency doubling of diode lasers, making calcium a good candidate for compact, portable system.

We have developed an all-fibre coupled laser system to provide a rugged source of laser light for cooling, re-pumping and generating trapped calcium ions. Along with an ion trap design which utilizes fully fibre integrated systems for both fluorescence detection [2] and laser light delivery to the ion [3], allowing for a compact ion trapping structure without the need for any free space optical elements. Combining the laser system and fibre integrated ion trap, a highly compact system with minimal free space beam propagation and thus vastly reduced vibration sensitivity becomes possible. Based on these developments, with a volume of a few litres and a weight of a few kilograms we aim to realise a truly portable optical clock.

References

[1] N. Huntemann, et al, “Single-Ion Atomic Clock with 3*10^-18 Systematic Uncertainty”, Phys. Rev. Lett. , vol. 116, p. 063001, 2016.

[2] H. Takahashi et al, “An integrated fiber trap for single-ion photonics”, New Journal of Physics, vol. 15, p. 053011, 2013.

[3] D. Lorenser, “Accurate Modeling and Design of Graded-Index Fiber Probes for Optical Coherence Tomography Using the Beam Propagation Method”, IEEE Photonics Journal, vol. 5, p. 3900015-3900015, 2013.

Development of cryogenic silicon cavity stabilized laser

B. Marechal, S. F. Tetsing, J. Millo, C. Rocher, C. Lacroûte, E. Rubiola, Y. Kersalé

FEMTO-ST, UBFC, CNRS, ENSMM
26 Rue de l'Épitaphe, 25030 Besançon cedex, France

Email: baptiste.marechal@femto-st.fr

Abstract

We present the development of a cavity stabilized laser at 1550 nm. The expected thermal noise limit of the silicon Fabry-Pérot cavity is 3×10^{-17} in terms of fractional frequency instability. We cooled it to its thermal expansion turning point, measured at 18.1 K, with a pulse-tube based cryocooler. The second order thermal sensitivity has been measured at -3.9×10^{-10} K^{-2}. Thanks to the thermal filtering and the temperature control of the cavity, the induced fractional frequency instability is below the thermal noise up to 1000 s of integration time. The cavity sensitivity to the laser power is about 7.8×10^{-9} W^{-1}. Without power stabilization of the laser source, we are limited at the level of 3×10^{-16} at 1 s with a 0.3 mW of incident power. We also discuss the vibration induced limitations, the thermal characterization of the cryocooler and the digital servo implementation and performances.

References

[1] D. G. Matei et al. "1.5 μm lasers with sub 10 mHz linewidth". In: *Phys. Rev. Lett.* 118 (26 2017), p. 263202.

[2] A. D. Ludlow et al. "Optical atomic clocks". In: *Reviews of Modern Physics* 87.2 (2015), pp. 637–701.

[3] T. Kessler et al. "A sub-40-mHz-linewidth laser based on a silicon single-crystal optical cavity". en. In: *Nature Photonics* 6.10 (2012), pp. 687–692.

[4] K. G. Lyon et al. "Linear thermal expansion measurements on silicon from 6 to 340 K". In: *Journal of Applied Physics* 48.3 (1977), pp. 865–868.

[5] E. D. Black. "An introduction to Pound–Drever–Hall laser frequency stabilization". In: *American Journal of Physics* 69.1 (2001), p. 79.

[6] E. Wiens et al. "Silicon single-crystal cryogenic optical resonator". In: *Opt. Lett.* 39.11 (2014), pp. 3242–3245.

Towards laser excitation of the Th-229 nuclear clock isomer

D.-M. Meier, J. Thielking, P. Glowacki, M. Okhapkin, E. Peik

Physikalisch-Technische Bundesanstalt, Braunschweig, Germany

Email: ekkehard.peik@ptb.de

The recent success of hyperfine structure measurements of $^{229m}Th^{2+}$ in a cooperation of PTB, LMU Munich and GSI has provided values for the nuclear magnetic dipole and electric quadrupole moments of the ^{229m}Th low-energy isomer and for the change in nuclear charge radius relative to the ground state [1]. Using this information, analyses of expected systematic uncertainties of ^{229}Th nuclear clocks can be stated more precisely [2]. In a clock based on ^{229}Th-doped crystals the nuclear quadrupole moment interacts with crystal field gradients, which may lead to a significant frequency shift. In the trapped ion clock the field-induced shifts will only make minor contributions to the uncertainty budget. The determination of the isomer's nuclear properties allows one to calculate the hyperfine structure of ^{229m}Th for any electronic transition when the frequencies of ^{229}Th and another isotope with measured nuclear radius are known. For the future, this makes it possible to apply a sensitive electronic-nuclear double resonance detection of the isomer in the search for nuclear laser excitation and in nuclear clock operation with trapped ions. This is particularly important when the long radiative lifetime of the isomer makes it difficult to detect photons emitted in isomer decay.

Experimental attempts at a direct laser excitation of the nuclear clock transition have not been successful so far, hampered by the large uncertainty in the transition wavelength, combined with a small transition strength and the difficulties associated with work in the VUV spectral region. We will present the status of our search via electronic bridge excitation of the nucleus in Th^+ and Th^{2+}. In Th^+, we recently expanded our search range to higher energies and have observed more than 100 previously unknown electronic energy levels in the range from 7.8 eV to 9.8 eV. The level density in Th^{2+} is lower, but a few states with the leading electronic configuration 5f8s are known around 9 eV excitation energy that can provide an efficient isomer excitation because the wave function of the s-electron has the greatest overlap with the nucleus.

This work is supported by the European Union's Horizon 2020 Research and Innovation Programme under Grant Agreement No. 664732 (nuClock) and by DFG through CRC 1227 (DQ-mat, project B04).

References

[1] J. Thielking, M. V. Okhapkin, P. Głowacki, D.-M. Meier, L. von der Wense, B. Seiferle, C. E. Düllmann, P. G. Thirolf, E. Peik, arXiv 1709.05325

[2] E. Peik, M. Okhapkin, C. R. Physique **16**, 516 (2015)

Dark matter searches within the intercontinental optical atomic clock network

P. Wcisło[1], P. Ablewski[1], K. Beloy[2], S. Bilicki[1,3], M. Bober[1], R. Brown[2], R. Fasano[2], R. Ciuryło[1], H. Hachisu[4], T. Ido[4], J.Lodewyck[2], A. Ludlow[2], W. McGrew[2], P. Morzyński[1,4], D. Nicolodi[2], M. Schioppo[2], M. Sekido[4], R. Le Targat[3], P. Wolf[3], X. Zhang[2], B. Zjawin[1], and M. Zawada[1]

[1]Institute of Physics, Faculty of Physics, Astronomy and Informatics, Nicolaus Copernicus University, Grudziadzka 5, 87-100 Torun, Poland
[2]National Institute of Standards and Technology, 325 Broadway, Boulder, CO 80305, USA
[3]SYRTE, Observatoire de Paris, PSL Research University, CNRS, Sorbonne Universités, UPMC Univ. Paris 06, LNE, 61 avenue de l'Observatoire, 75014 Paris, France
[4]National Institute of Information and Communications Technology 4-2-1 Nukuikitamachi, Koganei, 184-8795 Tokyo, Japan

Email: zawada@fizyka.umk.pl

We report preliminary results of dark mater searches within the worldwide network made of our laboratories. We demonstrate that data routinely collected by our currently operating optical atomic clocks without any further developments of the experimental set-ups may be used to run a global program aimed on searches of dark matter.

Optical atomic clocks are the most precise scientific instruments available to humanity. Their accuracy and stability reach eighteen significant digits. Therefore, optical atomic clocks are one of those experiments that push the boundaries of knowledge and metrology. The cost of their construction and maintenance, however, is many times lower and the needed research team is smaller in comparison to other great experiments that enlarge our knowledge on structure and history of our Universe, and as a consequence, bring new emerging technologies into our lives. The unique properties of these sensors are direct consequences of a typical optical atomic clock set-up. A standard optical atomic clock consists of two state-of-the-art components: an ultra-stable high-Q optical cavity which transfers stability of the length into stability of the frequency, and an atomic sample which transfers accuracy of the energy of the ultra-precise atomic clock transition into accuracy of the frequency. These two components have different susceptibilities to the external perturbations such as electric and magnetic fields, and to the possible changes of fundamental physical constants.

In this paper, we use this property to derive new constraints for oscillating massive scalar fields [1] and topological defects in the scalar fields [2] couplings to standard matter exceeding previously reported limits [3] by several orders of magnitude. These constraints were obtained by tracking the imprint of these effects in the frequency difference between cavities and atoms of several clocks distributed worldwide and running simultaneously. In this network of clocks, the technical noises (thermal noise, drift of cavities) is uncorrelated, while the effects we probe would yield correlations in remote measurements. As a consequence the optical clocks within our network do not have to be linked via phase-noise-compensated optical fibre links but only via a standard internet connection.

References

[1] A. Arvanitaki, J. Huang, K. Van Tilburg, Phys. Rev. D, vol. 91, p. 015015, 2015

[2] A. Derevianko, M. Pospelov, Nat. Phys, vol. 10, p. 933, 2014

[3] P. Wcisło, et al, Nat. Astron., vol 1, p. 0009, 2016; K. Van Tilburg, et al, Phys. Rev. Lett., vol. 115, p. 011802, 2015; B. M. Roberts, et al, Nat. Commun., vol 8, p. 1195, 2017; A. Hees, et al, Phys. Rev. Lett., vol. 117, p. 061301, 2016; T. Kalaydzhyan, N. Yu, Phys. Rev. D, vol. 96 p. 075007, 2017

A compact optical iodine frequency reference for a sounding rocket mission

Franz B. Gutsch[1], Klaus Döringshoff[1], Vladimir Schkolnik[1], Evgeny V. Kovalchuk[1], Markus Oswald[2], Christian Kürbis[3], Thilo Schuldt[2,4], Benjamin Pröbster[5], Matthias Lezius[5], Ronald Holzwarth[5], Andreas Wicht[3], Claus Braxmaier[2,4], Markus Krutzik[1], Achim Peters[1]

[1]Insitut für Physik, Humboldt-Universität zu Berlin, Berlin, Germany
[2]Zentrum für angewandte Raumfahrttechnologie und Mikrogravitation (ZARM), Universität Bremen, Bremen, Germany
[3]Ferdinand-Braun-Institut, Leibniz-Institut für Höchstfrequenztechnik, Berlin, Germany
[4]Deutsches Zentrum für Luft- und Raumfahrt (DLR), Institut für Raumfahrtsysteme, Bremen, Germany
[5]Menlo Systems GmbH, Martinsried, Germany

Email: klaus.doeringshoff@physik.hu-berlin.de

Ongoing development of optical technologies, such as miniaturized laser systems and optical frequency combs, enables the realization of compact optical frequency references. These are mandatory for future space missions based on laser ranging, such as LISA or NGGM, and experiments dedicated to tests of fundamental physics. A convenient way to take first steps towards routine application of such optical frequency references in space are sounding rocket missions [1, 2].

With JOKARUS, we have realized an autonomous, absolute optical frequency reference based on hyperfine transitions in molecular iodine at 532 nm [3]. We apply modulation transfer spectroscopy on a quasi-monolithic spectroscopy module with an unsaturated iodine cell, using a micro-integrated ECDL MOPA at 1064 nm as a compact high power light source and a fiber coupled laser system. The complete setup was readily qualified with 8.8 g_{rms} random vibration. With an anticipated stability of $3 \cdot 10^{-14} / \sqrt{\tau}$, this system provides an optical reference that is compatible with the requirements of LISA or NGGM [4]. During a rocket flight, planned for April 2018, the frequency stability of JOKARUS will be compared to a vacuum compatible, dual frequency comb developed by Menlo Systems, which is already qualified for the mission.

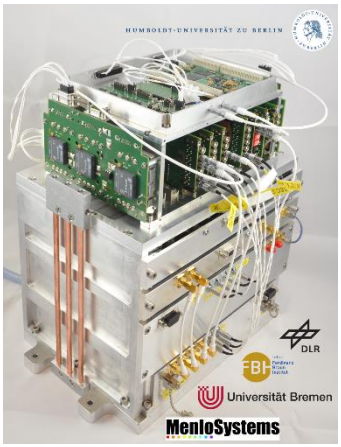

Fig. 1: JOKARUS Payload. (36 x 34 x 25 cm^3, 25 kg)

We will report in detail on the design of the JOKARUS payload, on its frequency stability and autonomous operation during flight.

This work is supported by the DLR with funds provided by the Federal Ministry for Economic Affairs and Energy under grant number DLR 50WM 1646.

References

[1] M. Lezius, et al. "Space-borne frequency comb metrology", Optica 3, 1381-1387, 2016.
[2] A. Dinkelaker, et al. „Autonomous frequency stabilization of two extended-cavity diode lasers at the potassium wavelength on a sounding rocket“, Appl. Opt. 56, 1388-1396, 2017.
[3] V. Schkolnik, K. Döringshoff, F. B. Gutsch, et al. „JOKARUS - design of a compact optical iodine frequency reference for a sounding rocket mission“, EPJ Quantum Technol. 4: 9, 2017.
[4] K. Döringshoff, T. Schuldt, E.V. Kovalchuk, et al. „A flight-like absolute optical frequency reference based on iodine for laser systems at 1064 nm“, Appl. Phys. B 123: 183, 2017.

Frequency Comb Stabilization of a 4 W, 50-fs Thin-Disk Laser Oscillator

Norbert Modsching[1], Clément Paradis[1], Pierre Brochard[1], Nayara Jornod[1], Kutan Gürel[1], Christian Kränkel[2,3], Stéphane Schilt[1], Valentin J. Wittwer[1], and Thomas Südmeyer[1]

[1]Laboratoire Temps-Fréquence, Université de Neuchâtel, Neuchâtel, Switzerland
[2]Center for Laser Materials, Leibniz Institute for Crystal Growth, Berlin, Germany
[3]Institute of Laser-Physics, University of Hamburg, Hamburg, Germany

Email: norbert.modsching@unine.ch

Ultrafast thin-disk lasers (TDLs) are a simple approach to generate powerful ultrashort pulse trains directly out of the oscillator [1] and are highly attractive for intracavity nonlinear optics. Recently, we demonstrated a compact XUV source by driving high-harmonic generation (HHG) inside the cavity of a mode-locked TDL oscillator [2]. Kerr lens mode-locked (KLM) TDLs can operate with nearly transform-limited soliton pulses as short as 30 fs [3] and intracavity peak power levels of currently up to 70 MW in 35 fs pulses [4]. These sources are highly attractive for power-scaling of intra-cavity HHG. The latter is a coherent process, thus driving sources with stabilized carrier-envelope offset frequency (f_{CEO}) and repetition rate frequency (f_{rep}) directly yield to powerful XUV frequency combs. However, a full stabilization of a TDL has never been demonstrated yet.

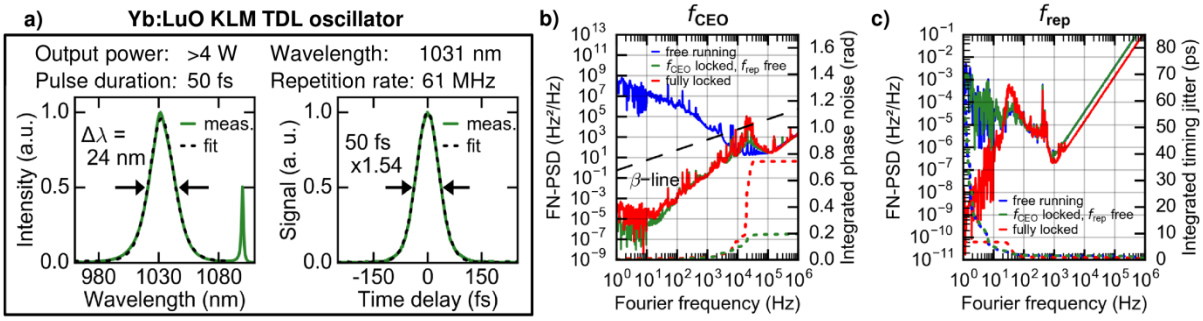

Fig. 1: Optical frequency comb based on a KLM TDL a) Laser parameters, intensity autocorrelation trace and optical spectrum; b) Frequency noise power spectral density (FN-PSD) of the CEO beat and integrated phase noise (upper cut-off frequency); c) FN-PSD of the repetition rate frequency and integrated timing jitter (lower cut-off frequency).

Here, we demonstrate the first self-referenced fully-stabilized optical frequency comb based on a TDL. The oscillator is described in more detail in Ref. [4]. Its ultra-short laser pulses allowed for CEO detection without any external compression. A tight phase lock of the CEO frequency is achieved with an active feedback to the pump-diode current leading to a residual in-loop phase noise of 200 mrad [1 Hz-1 MHz]. Besides, we present initial experiments on the full stabilization of the TDL comb. The repetition rate frequency is stabilized via a cavity mirror mounted onto a piezo-electric actuator, which resulted in a residual timing jitter of 7 ps [1 Hz-1 MHz]. Due to cross talk between the two stabilization loops the f_{CEO} phase noise increased to 745 mrad [1 Hz-1 MHz] for the fully-stabilized optical frequency comb. We believe that this approach of KLM TDL-based frequency combs will open doors to numerous experiments in the areas of metrology and broadband high-resolution spectroscopy, especially for future short-pulse intra-cavity HHG-based XUV frequency combs.

References

[1] C. J. Saraceno et al., "275 W average output power from a femtosecond thin disk oscillator operated in a vacuum environment," Opt. Express **20**, 23535 (2012).
[2] F. Labaye et al., "Extreme ultraviolet light source at a megahertz repetition rate based on high-harmonic generation inside a mode-locked thin-disk laser oscillator," Opt. Lett. **42**, 5170 (2017).
[3] C. Paradis et al., "Sub-50-fs Kerr Lens Mode-Locked Thin-Disk Lasers," in *CLEO Europe - EQEC 2017* (Optical Society of America, 2017), paper PD-1.4.
[4] C. Paradis et al., "Generation of 35-fs pulses from a Kerr lens mode-locked Yb:Lu_2O_3 thin-disk laser," Opt. Express **25**, 14918 (2017).

Utilising Grating Chip Technology for Raman-Ramsey CPT

Rachel Elvin[1], James P. McGilligan[1], Gregory W. Hoth[1], Michael W. Wright[1], Aidan S. Arnold[1], Paul F. Griffin[1], and Erling Riis[1]

[1]Experimental Quantum Optics and Photonics Group, University of Strathclyde, Glasgow, G4 0NG, UK

Email: rachel.elvin@strath.ac.uk

The development of laser cooling has led to atomic frequency standards with excellent stability and accuracy [1]. However, the complexity of these systems has largely confined laser-cooled atoms to laboratories. In order to bring the benefits of cold atoms to a wider range of applications, it is desirable to reduce the size and complexity of sensors based on cold atoms [2,3]. Working towards this goal, we are developing a microwave atomic clock based on a Grating Magneto-Optical Trap (GMOT) [4]. With the GMOT, we are able to prepare 10^7 laser-cooled ^{87}Rb atoms by use of a single laser beam incident on a micro fabricated diffractive optic [5]. The relative simplicity of the GMOT makes this system a strong candidate to realize a cold-atom clock that can operate outside of a laboratory environment.

The clock signal is produced by use of Coherent Population Trapping (CPT) on the D1 line in ^{87}Rb with the lin ⊥ lin polarization configuration [6]. We have achieved 70% contrast on the magnetically insensitive clock transition. In order to enable long interrogation times and suppress light shifts, we have implemented a two-pulse Raman-Ramsey CPT sequence [6]. We have realized CPT Ramsey fringes with a free evolution time of T=10 ms.

We will discuss the ongoing work to characterize and optimize our system. We plan to develop a portable, compact cold-atom clock utilizing the GMOT and Raman-Ramsey CPT interrogation.

References

[1] A. D. Ludlow, M. M. Boyd, and J. Ye, “Optical Atomic Clocks”, Rev. Mod. Phys., vol. 87, p. 637-701, 2015.

[2] X. Liu, E. Ivanov, V. I. Yudin, J. Kitching, and E. A. Donley, “Low-Drift Coherent Population Trapping Clock Based on Laser-Cooled Atoms and High-Coherence Excitation Fields”, Phys. Rev. Appl., vol. 8, p. 054001, 2017.

[3] S. B. Koller, J. Grotti, St. Vogt, A. Al-Masoudi, S. Dörscher, S. Häfner, U. Sterr, and Ch. Lisdat, “Transportable Optical Lattice Clock with 7×10^{-17} Uncertainty”, Phys. Rev. Lett., vol. 118**,** p. 073601, 2017.

[4] J. P. McGilligan, R. Elvin, P. F. Griffin, E. Riis, and A. S. Arnold, “Utilising diffractive optics towards a compact cold atom clock” 2016 European Time and Frequency Forum (EFTF), York, p. 1-2, 2016.

[5] J. P. McGilligan, P. F. Griffin, E. Riis, and A. S. Arnold, “Phase-space Properties of Magneto-optical Traps Utilising Micro-Fabricated Gratings”, Opt. Express, vol. 23**,** p. 008948**,** 2015.

[6] T. Zanon, S. Guerandel, E. de Clercq, D. Holleville, N. Dimarcq, and A. Clairon, “High Contrast Ramsey Fringes with Coherent-Population-Trapping Pulses in a Double Lambda Atomic System”, Phys. Rev. Lett., vol. 20, p. 193002, 2005.

Preliminary progress in the development of an operational calcium thermal beam clock at the U. S. Naval Observatory

Jennifer Taylor, Bryan Hemingway, Thomas Swanson, and Steven Peil
US Naval Observatory

The US Naval Observatory is developing a new generation of clocks for future incorporation into its master clock ensemble. Similar to the rubidium fountains developed at USNO, the ultimate goal is for these clocks to run continuously in an operational environment, without user intervention. Our initial approach is to investigate the possibility of building an operational clock based on a thermal calcium atomic beam, while future efforts may incorporate laser cooling.

Characterization of the frequency stability of an optical clock can be carried out directly at optical frequencies by comparing to a second system. This method postpones the need for a frequency comb, and by using a common interrogation laser, it can mitigate the contribution of local oscillator (LO) noise. We have built two calcium atomic beams at USNO, and we will present our preliminary progress on calcium spectroscopy in these systems.

In related work, we have demonstrated that we can use a tellurium (Te_2) vapor cell as a frequency reference for blue transitions in calcium. We have characterized the spectrum of Te_2 in the vicinity of the calcium $^1S_0$-$^1P_1$ transition at 423nm and the $^3P_1$–$^3P_0$ transition at 431nm. The 423nm transition can be used for characterizing the atomic beam and for (future) laser cooling, while the 431nm transition can be used to improve detection efficiency. We will discuss plans to use Te_2 as a reference at 423nm for a measurement of the instability in a thermal beam caused by the second-order Doppler shift, which is expected to be one of the limiting factors to long-term performance, and we will discuss the improvement in detection of the clock transition from using 431nm light.

Microsemi Chip Scale Atomic Clock (CSAC)

Technical Status, Applications and Future Plans

Peter Cash [1], Will Krzewick[1], Paul Machado[1], Dr. K. Richard Overstreet[1], Mike Silveira[1], Dwayne Taylor[1], Dr. Xianli Zhang[1]

[1]Microsemi Incorporated, Beverly, Massachusetts USA

Email: peter.cash@microsemi.com

Microsemi's CSAC was developed from 2001 to 2011 and represented revolutionary technology for atomic clocks. The use of Coherent Population Trapping, pioneered at NIST, enabled a significant reduction in size, weight, and power compared to conventional gas cell clocks. Last year, Microsemi released an updated version of CSAC that improved the operating temperature range and reliability. Development of the technology continues at Microsemi to meet the current and future applications. This paper provides some historical background, design description, a detailed technical status of CSAC including performance data from production testing. Also, the paper will contain a description of both the original and future applications. Finally, a description of the future development plans with the goals of increased performance, further reliability improvements, and wider environmental tolerances. The improvements include wider temperature range from -40°C to 80 °C, improved drift and temperature stability, radiation tolerance and RoHS 6/6 compliance.

Photoassociation measurements to evaluate collisional shifts in strontium

Marcin Bober, Piotr Morzyński, Sławomir Bilicki, Mateusz Borkowski, Piotr Ablewski, Roman Ciuryło, and Michał Zawada

Institute of Physics, Faculty of Physics, Astronomy and Informatics,
Nicolaus Copernicus University, Grudziądzka 5, 87-100 Toruń, Poland

Email: bober@fizyka.umk.pl

Although higher number of atoms in optical atomic clock may lead to a better signal-to-noise ratio, the effect of cold collisions may limits the accuracy. It is especially important for optical clocks with atoms trapped in one dimensional optical lattice.

We report a photoassociation approach which will allow determination of scattering length for $^1S_0$-$^3P_0$ and $^3P_0$-$^3P_0$ cold collisions. Positions of molecular states, connected with asymptotes of $^1S_0$+$^3S_1$ and $^3P_0$+$^3S_1$ states could be determined using a tunable 679 nm laser and with atoms trapped in an optical lattice in $^1S_0$ and $^3P_0$ states mixture. Information about those molecular states yields asymptotic molecular potentials and radial wave functions. Together with the information about photoassociation losses, they can be used to determine the scattering length for $^1S_0$-$^3P_0$ and $^3P_0$-$^3P_0$ collisions. This approach allows an indirect calculation (without direct probing of $^1S_0$-$^3P_0$ molecular state) of the effect of cold collisions on an optical atomic clock operation. Preliminary results for ^{88}Sr will be presented. This indirect approach may be also used for ytterbium atoms, where direct measurements of $^1S_0$-$^3P_0$ molecular states near the clock transition is not only hard to observe because of the extremely small dipole moment of the transition but also due to the small Frank-Condon factors [1].

References

[1] M. Borkowski, prepared for publication

Accuracy Evaluation of the NRC-FCs2 Atomic Fountain Clock at the National Research Council of Canada

Bin Jian[1], Scott Beattie[1], A. John Alcock[1], Marina Gertsvolf[1], Rich Hendricks[2], Filip Ozimek[2], Krzysztof Szymaniec[2], and Kurt Gibble[3]

[1]National Research Council, Ottawa, Ontario, Canada
[2]National Physical Laboratory, Hampton Road, Teddington, UK
[2]Department of Physics, Pennsylvania State University, University Park, USA

Email: Bin.Jian@nrc-cnrc.gc.ca

At the National Research Council of Canada, we are developing an atomic fountain clock, NRC-FCs2, to serve as Canada's primary frequency standard. The evaluation of the systematic shifts of NRC-FCs2, as well as the associated uncertainties, is currently in progress and nearing completion.

The physics package of NRC-FCs2 was built at the National Physical Laboratory (NPL) UK, based on the proven design of the NPL-CsF2 atomic fountain clock with a Ramsey cavity designed to minimize the distributed cavity phase (DCP) shift [1, 2]. With a measured signal to noise ratio of > 2000, the short term stability of NRC-FCs2 is now $\sigma_y(\tau=1s)=1\times10^{-13}$ thanks to the high stability of a recently installed Vremya-CH active hydrogen maser, which is used to servo a frequency synthesizer. The short term stability of the fountain clock is limited by the stability of the local oscillator.

NRC-FCs2 is operated with a magneto-optical trap (MOT) atom cloud loaded directly from the background caesium atomic vapour. The well-known large collisional frequency shift with MOT-based Cs fountain clocks has been overcome by operating atomic fountain clocks at the collisional shift cancellation point [3]. By varying the experimental parameters, mainly the initial size of the MOT atom cloud, and adjusting the Ramsey microwave amplitude, we reduced the collisional frequency shift significantly and obtained a type-B uncertainty due to collisions of under 10^{-16}. Other systematic shifts have also been evaluated such as the AC Stark shift, 2nd order Zeeman shift, blackbody radiation shift, gravitational red shift, and Rabi and Ramsey pulling, all with uncertainties of less than 10^{-16}.

The evaluation of the DCP shift of the Ramsey cavity relies on both numerical simulation of the field distribution inside the microwave cavity and experiment. Specifically, the m=0 and m=2 components of the DCP shift of our cavity, as well as the microwave lensing effect, have been computed with relative uncertainties of less than 10^{-16} for our typical experimental parameters. The evaluation of the m=1 component of the DCP shift is currently being evaluated experimentally by differential measurements of the frequency shift between opposite microwave feeds for various fountain tilt angles.

References

[1] K. Szymaniec, S. E. Park, G. Marra, and W. Chalupczak, "First accuracy evaluation of the NPL-CsF2 primary frequency standard," Metrologia, vol. 47, p. 363-376, 2010.
[2] R. Li and K. Gibble, "Evaluating and minimizing distributed cavity phase errors in atomic clocks," Metrologia, vol. 47, p. 534-551, 2010.
[3] K. Szymaniec *et al*, "Cancellation of the Collisional Frequency Shift in Caesium Fountain Clocks," Phys. Rev. Lett., vol. 98, p. 153002-1-4, 2007.

Electronic instrumentation for experiments with ultracold atoms and ions

Marco Pomponio[1], Carlo Sias[2,3], Claudio Eligio Calosso[2]

[1]DET, Polytechnic of Turin, Turin, Italy
[2]Division of Physics Metrology, INRIM, Turin, Italy
[3]European Laboratory for Nonlinear Spectroscopy (LENS), Sesto Fiorentino, Italy

Email: s224761@studenti.polito.it

In most physics experiments, the electronic equipment plays a main role for managing the apparatus and performing measurements. The equipment typically includes oscilloscopes, waveform generators, data acquisition cards and PID controllers, the actions of which must be coordinated. However, the presence of many different parts may cause synchronization and managing issues. Moreover, most of the instruments in the market do not allow the user to modify and reconfigure some of their outputs, especially in short timescales, therefore imposing limitations on the experiments that can be performed with the apparatus.
In order to lift these limitations, it is crucial to develop a system that is able to acquire and generate signals, with the properties of being highly adaptable, reconfigurable, scalable and expandable, and that is able also to elaborate data in real time [1]. The thesis tackles this problem by designing and partially realizing a novel electronic system with the aim of controlling an experiment, currently under development at LENS, with ultracold ions and atoms [2]. A modular architecture was chosen, and two main parts were identified: the Master module – with management and communication purposes – and the Slave modules, which have analog to digital and digital to analog converters, DDSs and an FPGA for interfacing and data elaboration. This approach ensures the realization of a single electronic system with an expandable number of inputs and outputs that are precisely synchronized. The high-speed communication between Master and Slave modules is committed to the 3.125 Gbps transceivers embedded into the FPGA chosen, a Cyclone V GX.
A Slave module was successfully realized. To this end, all the electronic specifications were derived and all the components chosen. The schematic includes the generation of all the required voltage rails starting from ±12V, all the front-ends for the signal conditioning, and all the parts that guarantee the proper operation of the FPGA and all the other integrated circuits. The board is powered by a combination of DC-DC converters and low dropout linear regulators, ensuring an adequate power efficiency together with low noise power rails.
During the design of the Printed Circuit Board (PCB) many considerations were made to guarantee the signal integrity and to reduce the switching noise caused by the DC-DC converters and by the digital circuitry. The PCB design turned out to be challenging because of the high number of components, the relatively small dimensions of the Eurocard 10x16 cm standard, and the managing of the heat.
Finally, the FPGA was configured with the goals of being as general as possible and of holding the conditions of flexibility, adaptability and fast operation: the component drivers were designed to fully exploit the hardware. Each part was successfully tested by comparing the measured performances with the ones reported in the technical documentation.

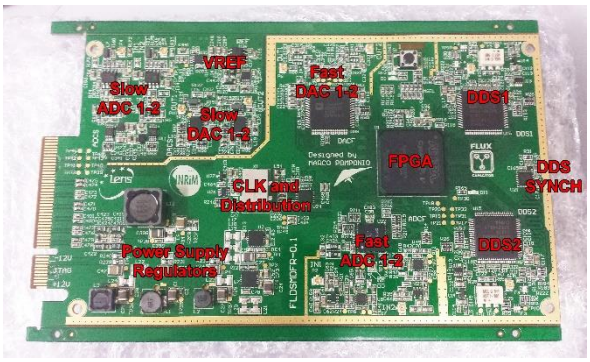

Fig.1: Slave module

[1] C. E. Calosso et al., Generalized electronics for compact atomic clocks, Proceedings IFCS-EFTF2017, Besançon (2017).
[2] C. Sias, M. Köhl “Hybrid quantum systems of ions and atoms”, Chapter 12 in "Quantum gas experiments - exploring many-body states", edited by P. Törmä and K. Sengstock, Imperial College Press, 2014, arXiv:1401.3188

Two-Photon Spectroscopy of Hydrogen Molecular Ions for Precision Measurements of Fundamental Constants

Florin Lucian Constantin[1]

[1]Laboratoire PhLAM, CNRS UMR 8523, 59655 Villeneuve d'Ascq, France

Email: FL.Constantin@univ-lille1.fr

Spectroscopy of hydrogen molecular ions and molecular theory can be exploited for a determination of the proton-to-electron mass ratio [1]. Two-photon spectroscopy with trapped and sympathetically cooled HD^+ ions allows an increase of the experimental accuracy [2]. This contribution presents a prospect for an improved determination of fundamental constants based on two-photon spectroscopy of rotational and rovibrational transitions of HD^+ [3].

A closed set of HD^+ energy levels is addressed with the two-photon transitions (v,L)=(0,1) →(0,3) at 3.268 THz and (v,L)=(0,3)→(9,3) at 207.637 THz, and the photodissociation of the (v,J)=(9,3) level with 532 nm laser radiation. Blackbody radiation recycles continuously HD^+ ions in the (v,L)=(0,0)-(0,5) levels. The two-photon transition rates are calculated with the two-photon operator formalism. Temporal dependences of the populations of trapped HD^+ ions are described by a set of coupled rate equations, and the lineshapes of the two-photon transitions are derived (Fig. 1). The resolution with this Doppler-free scheme is pushed at better than the 10^{-12} level. The dynamic polarizabilities of HD^+ hyperfine structure energy levels are calculated with the two-photon operator formalism. Some hyperfine components of the rotational transition have lightshifts at the 10^{-15} level for a THz-wave intensity of 1 mW/mm^2 and Zeeman shifts at the 10^{-14} level for a residual magnetic field of 20 mG. Different schemes for reduction of these systematic frequency shifts are discussed. Experimental frequencies of two-photon transitions from isotopic hydrogen molecular ions, with accuracies assumed at the 10^{-12} level, may be compared with theoretical calculations to determine the Rydberg constant, the proton-to-electron and deuteron-to-proton mass ratios, the proton and deuteron radii independently on previous results. This data has to be compared with the values of the proton and deuteron radius determined in atomic spectroscopy. Depending on possible issues of the proton radius puzzle, two-photon spectroscopy of hydrogen molecular ions may improve the determination of the proton-to-electron and deuteron-to-proton mass ratios beyond the 10^{-11} level.

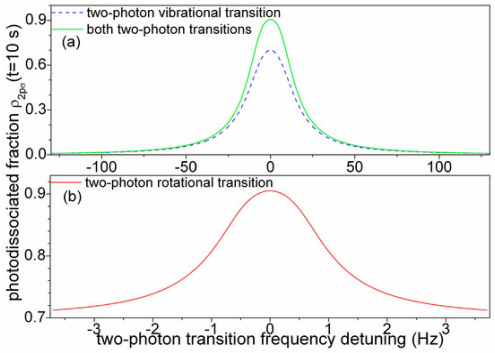

Fig. 1: (a) Spectra of the two-photon rovibrational transition calculated with or without THz-wave at the two-photon rotational resonance. (b) Spectrum of the two-photon rotational transition calculated at the two-photon rovibrational resonance. Transition rate at resonance for the two-photon rotational transition $\Gamma_{2ph,r}$=2000 s^{-1}, for the two-photon rovibrational transition $\Gamma_{2ph,v}$=10 s^{-1}, for the dissociation Γ_{diss} = 200 s^{-1}, respectively.

References

[1] W. H. Wing, G. A. Ruff, W. E. Lamb Jr., J. J. Spezeski, "Observation of the infrared spectrum of the hydrogen molecular ion HD^+", Phys. Rev. Lett., vol. 36, p. 1488–1491, 1976.

[2] V. Q. Tran, J.-Ph. Karr, A. Douillet, *et al*, "Two-photon spectroscopy of trapped HD^+ ions in the Lamb-Dicke regime", Phys. Rev. A, vol. 88, p. 033421, 2013.

[3] F. L. Constantin, "THz/infrared double resonance two-photon spectroscopy of HD^+ for determination of fundamental constants", Atoms, vol. 5, p. 38, 2017.

Improvements of Fibre Brillouin Amplifier Modules for Optical Frequency Dissemination

Alexander Kuhl[1], Thomas Waterholter[1], Sebastian Koke[1], and Gesine Grosche[1]

[1]Physikalisch-Technische Bundesanstalt, Bundesallee 100, 38116 Braunschweig, Germany

Email: alexander.kuhl@ptb.de

Bidirectional phase-stabilized optical fiber links [1] require bidirectional amplification to compensate optical losses of about 20 dB/100km. Several techniques are possible and demonstrated to compensate the losses, such as bidirectional erbium doped amplifiers (biEDFA), repeater laser stations [2] or fiber Brillouin amplifier modules (FBAM) [3].

FBAMs are based on stimulated Brillouin scattering (SBS). Here, an optical pump power below 10 dBm is injected into the link counter-propagating to the signal [4], which enable a gain of more than 45 dB [3] in a bandwidth of about 10 MHz in the optical domain. Gain and SNR are sensitive to the relative polarization between pump and signal light. The polarization of the light is not static and changes due to environmental effects. To date [3], the polarization of the pump light was adjusted by maximizing the total power after amplification, which is imprecise, complicated and very difficult to automate.

We designed and tested an improved injection concept which allows a precise polarization alignment between signal and pump light. In contrast to the previous design, we now implemented a polarization alignment that solves a minimization problem instead of searching for a (possibly fluctuating) global maximum of optical power. Additionally, this setup simultaneously reduces the overall optical losses of the amplifier itself: the injection efficiency increases by about 3 dB and the signal losses are reduced by more than 2 dB.

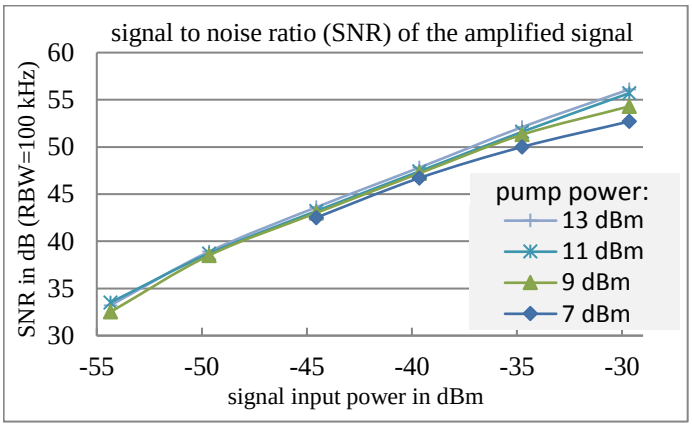

Fig. 1: Measured SNR of the amplified signal with the improved injection system of the FBAM.

Due to an approximately linear scaling of the SNR with the signal power (see Fig. 1), a higher SNR is expected for a cascaded link with the improved injection setup compared to the previous setup.

An additional development is an optical add-on module to monitor the signal characteristics by beating part of the signal with part of the pump laser. This allows remote evaluation of the SNR of the signal at the FBA locations along the fibre link. Further, the temperature-dependent Brillouin frequency shift can easily be measured and can subsequently be corrected if necessary.

The authors would like to thank the DFG Sonderforschungsbereich (SFB) 1128 Relativistic Geodesy and Gravimetry with Quantum Sensors (geo-Q) for financial support.

References:

[1] Williams P. A., Swann W. C., and Newbury N. R, J. Opt. Soc. Am. B 25.8, pp. 1284–1293, 2008
[2] Chiodo N., Quintin N., Stefani F. et al., Opt. Express 23.26, pp. 33927–33937, 2015
[3] Raupach S., Koczwara A., and Grosche G., Phys. Rev. A 92.2, p. 021801, 2015
[4] Souidi Y., Taleb F., Zheng J. et al., Appl. Opt. 55, 248-253, 2016

Clock Anomaly Detection Using l_1 Norm Optimization

Masato Hirano[1], Kazumune Hashimoto[1],

Fumimaru Nakagawa[2], Tetsuya Ido[2], Yuko Hanado[2],

Shuichi Adachi[1]

[1]Keio University, Yokohama, Kanagawa, Japan
[2]National Institute of Information and Communications Technology, Koganei, Tokyo, Japan

Email: mhirano@keio.jp

In time scale generation, it is important to accurately estimate a phase difference between the Coordinated Universal Time (UTC) and an atomic clock. Recently, some methods to estimate this phase difference have been proposed that use a state space model of atomic clocks, enabling estimation by using Kalman filter [1][2][3]. When the system is observable, it is guaranteed that the variance of the estimation error by Kalman filtering converges to a constant value, and the estimate becomes asymptotically stable. However, the system is unobservable in this case since only relative phase differences among clocks are locally available. In addition phase and frequency jumps often occur in atomic clocks, which deteriorates the estimation considerably for the case using l_2 norm minimization like Kalman filter.

In this paper, we propose a new method to solve the unobservability problem as well as the anomaly detection problem. For the former problem, we use the information on the past phase difference between atomic clocks and UTC, which are released by BIPM every month. As a result, the system becomes observable in the sense that the true value of the state can be estimated intermittently, and the increase of the estimation error can be suppressed. For the latter problem, we propose formulating l_1 norm optimization problem, which allows us to simultaneously estimate the phase difference and to detect occasional phase (frequency) jumps. The l_1 norm minimization method is used in the field such as compressed sensing and has attracted attention recently as a powerful method for obtaining a sparse estimate. By assuming that phase and frequency jumps rarely occur in atomic clocks, it is possible to keep a high estimation accuracy by minimizing the l_1 norm, where the jumps are effectively considered as sparse disturbances. The usefulness of the proposed approach was validated through a numerical simulation using actual clock data.

References

[1] Galleani, Lorenzo, and Patrizia Tavella. "Time and the Kalman filter." IEEE Control Systems 30.2, 2010: 44-65.
[2] Greenhall, Charles A. "Forming stable timescales from the Jones–Tryon Kalman filter." Metrologia 40.3, 2003: S335

[3] Greenhall, Charles A. "A Kalman filter clock ensemble algorithm that admits measurement noise." Metrologia 43.4, 2006: S311.

Systematic uncertainty evaluation of an $^{27}Al^{+}$ quantum-logic clock

Samuel M. Brewer[1], Jwo-Sy Chen[1,2], David B. Hume[1], Aaron M. Hankin[1], Ethan R. Clements[1,2], Chin-Wen Chou[1], David J. Wineland[1,2], and David R. Leibrandt[1,2]

[1]Time and Frequency Division, National Institute of Standards and Technology, Boulder, CO 80305, USA

[2]Department of Physics, University of Colorado, Boulder, CO 80309, USA

Email: samuel.brewer@nist.gov

A previous optical atomic clock based on quantum-logic spectroscopy of the $^{1}S_0 \leftrightarrow {}^{3}P_0$ transition of $^{27}Al^{+}$ reached a systematic uncertainty of 8.0×10^{-18} [1,2]. This uncertainty was dominated by environmental effects related to the traps used to confine the ions; i.e. time-dilation shifts due to motion of the ions in the trap and the blackbody radiation (BBR) shift due to elevated trap temperature. Improvements in a new trap have reduced excess micromotion and secular heating, making it possible to operate the clock near the three-dimensional motional ground state [3], and leading to a reduced time-dilation shift uncertainty. In addition, the operating temperature of the system has been lowered to reduce the BBR shift uncertainty. Here we present the systematic uncertainty evaluation of a new $^{27}Al^{+}$ quantum-logic clock based on this improved trap design. In addition, we present preliminary results from recent optical frequency comparisons between this $^{27}Al^{+}$ clock and the Yb and Sr optical lattice clocks at NIST/JILA.

References

[1] C. W. Chou, D. B. Hume, J. C. J. Koelemeij, D. J. Wineland, and T. Rosenband, "Frequency Comparison of Two High-Accuracy Al^{+} Optical Clocks" Phys. Rev. Lett. 104, 070802 (2010).

[2] C. W. Chou, *et. al.*, private communication.

[3] J.-S. Chen, S. M. Brewer, C. W. Chou, D. J. Wineland, D. R. Leibrandt, and D. B. Hume, "Sympathetic Ground State Cooing and Time-Dilation Shifts in an $^{27}Al^{+}$ Optical Clock" Phys. Rev. Lett. 118, 053002 (2017).

This work was supported by NIST, ONR, and DARPA QuASAR. S.M.B. acknowledges support from the ARO through MURI grant number W911NF-11-1-0400.

Investigation and study on combination of multiple GNSS techniques using a new GNSS time transfer receiver developed at NIM

Kun Liang[1] , Aimin Zhang[1], Zhiqiang Yang[1], Ye Wang[2]

[1]Time and Frequency Metrology Division, National Institute of Metrology, Beijing, China
[2]School of Electronic and Information Engineering, Beijing Jiaotong University, Beijing, China

Email: liangk@nim.ac.cn

A new multi-GNSS (Global Navigation Satellite System) version of GNSS time transfer receiver NIM-TF-GNSS-3, has been under development by NIM (National Institute of Metrology, Beijing, China) since 2016. It is the third generation of GNSS time transfer receiver developed by NIM following NIM-TF-GNSS-1[1] and NIM-TF-GNSS-2[2]. The receiver provides the code and carrier phase measurements from BDS (BeiDou Navigation Satellite System), GPS (Global Positioning System), GLONASS (GLObal NAvigation Satellite System) and Galileo for precise time transfer. The receiver core parts including the receiver engine board and time interval counter(TIC) for raw measurements are located in a temperature chamber so that its ambient temperature stability can be controlled within 0.3(1 sigma) degrees, which would improve the measurement precision related to the variation of the ambient temperature. The stability of the internal reference delay has been investigated and studied. The automatic measurement for the internal reference delay has been involved in the receiver routine operation. The receiver can generate measurement data of both single frequency and dual frequencies in CGGTTS (CCTF Group on GNSS Time Transfer Standards) V2E, RINEX (Receiver Independent Exchange Format) V3 files. Using the web-based user interface of the receiver, the comparisons can be provided and displayed in real-time, between the local reference time and GNSS time in 30-s and 16-min, and between the local reference time and UTC(NIM) in 16-min, through the ground network and BDS short message communication. The method and data of GNSS time monitoring have been discussed and one type of modified CGGTTS file could be set to be generated for GNSS time monitoring by the receiver. The measurement noise (standard deviation, *std*) has been evaluated as about 1 ns by CCD results. The experiments on the long baseline, have been implemented for the long-term stability and accuracy.

The weighted average combination method of multiple GNSS techniques for time transfer based on time stability has been studied and validated using these types of receivers. The improved stability from the combination of two or more GNSS systems could be observed.

References

[1] LIANG Kun, ZHANG Aimin, GAO Xiaoxun, WANG Weibo, NING Dayu，ZHANG Side, Study and Development of a New GNSS Receiver for Time and Frequency Transfer, EFTF 2012.

[2] Liang K, Zhang A, Yang Z, et al. Developing of one time link calibrator with GNSS at NIM[C]//Frequency Control Symposium & the European Frequency and Time Forum (FCS), 2015 Joint Conference of the IEEE International. IEEE, 2015: 545-548.

Measurement of the Infrared Magic Wavelengths for the $^{40}Ca^{+}$ Ion Clock Transition

Y. Huang[1], H. Zhang[1], B. Zhang[1], M. Zeng[1], H. Guan[1], K. Gao[1]

[1]Wuhan Institute of Physics and Mathematics, Chinese Academy of Sciences, Wuhan 430071, China

Email: klgao@wipm.ac.cn

One of the infrared magic wavelengths for $^{40}Ca^{+}$ ion is measured with high precision. Lambrecht et al shows that the ions can be all-optical trapped for longer time with infrared lasers because of the lower heating rates [1]. Promisingly, the measurement of these magic wavelengths paves the way to building all-optical trapped ion clocks. Furthermore, the measured wavelength agrees well with the theoretical calculations but has higher accuracy. The related oscillator strengths can be determined with higher accuracy by using the measured magic wavelength.

The magic wavelength for an atomic transition is a wavelength for which the AC Stark shift vanishes. It has provided extensive applications in quantum state engineering and precision frequency metrology, especially in the optical lattice clocks. Until now, the stabilities of the best optical lattice clocks are more than 1 order of magnitude better than that of the best ion optical clocks. The technique of effective trapping multiple ions with small systematic frequency shift uncertainties need to be developed for building ion optical clocks with stability comparable to the optical lattice clocks.

Table 1: The uncertainty budget of the magic wavelength measurement.

Sources of uncertainty	Uncertainty (nm)
Broadband light	0.02
Light polarization grade	0.05
Angel between the magnetic field and the laser propagation direction	0.05
Laser wavelength	<0.001
Clock uncertainty	<0.001
Statistical	0.02
Total	0.08

The magic wavelengths for $^{40}Ca^{+}$ at ~ 395 nm have been measured a few years ago [2]. However, for the all-optical trapping of the ions, the 395 nm laser will produce relatively high heating rate for the small frequency detuning. It is theoretically predicted that $^{40}Ca^{+}$ has magic wavelength at the infrared regime. Here after the stability and uncertainty of our optical clocks are much improved [3], the infrared magic wavelength is measured, which can be potentially used to all-optical trapping the ions with small Ac Stark shift. Compared to the measured magic wavelength at ~395 nm, the inferred magic wavelength is found to be more sensitive to the polarization grade and the angel between the magnetic field and the laser propagation direction. The evaluated uncertainty budget of the magic wavelength measurement is shown in Table 1.

References

[1] A. Lambrecht, et al, "Long lifetimes and effective isolation of ions in optical and electrostatic traps", Nature Photonics, vol. 11, p. 704–707, 2017.

[2] P. Liu, et al, "Measurement of Magic Wavelengths for the $^{40}Ca^{+}$ Clock Transition", Physical Review Letter, vol. 114, p. 223001, 2015.

[3] Y. Huang, H. Guan, P. Liu, W. Bian, L. Ma, K. Liang, T. Li, K. Gao, "Frequency Comparison of Two $^{40}Ca^{+}$ Optical Clocks with an Uncertainty at the 10^{-17} Level", Physical Review Letter, vol. 116, p. 013001, 2016.

REFIMEVE+ : towards a wide optical fiber network for optical frequency standard dissemination

Etienne Cantin[1,2], Olivier Lopez[1], Nicolas Quintin[1,3], Emilie Camisard[3], Christian Chardonnet[1], Giorgio Santarelli[4], Anne Amy-Klein[1], and Paul-Eric Pottie[2]

[1] Laboratoire de Physique des Lasers, Université Paris 13, CNRS, Villetaneuse, France
[2] Laboratoire National de Métrologie et d'Essais–Système de Références Temps-Espace, Observatoire de Paris, CNRS, UPMC, Paris, France
[3] RENATER, Paris, France
[4] Laboratoire Photonique, Numérique et Nanosciences, Institut d'Optique d'Aquitaine, Université de Bordeaux, CNRS, Talence, France

Email: etienne.cantin@obspm.fr

Coherent optical fiber links were established over ranges of 1000 km, enabling unprecedented resolution for clock comparisons. By opening a new era of optical metrology, these fiber links create opportunities for a wide range of high precision measurements in any physics laboratories. Such development however requires that the techniques are extended beyond the current point-to-point architecture and some effective fiber network architecture is implemented in order to disseminate an ultrastable frequency standard to a large number of laboratories.

The REFIMEVE+ project aims to build such a wide scale fiber network, highly reliable and robust, capable at the same time of comparing the best optical clocks and of disseminating an optical frequency standard. To that aim, our groups have explored several dissemination techniques and network building blocks, and the way to combine them and to improve their reliability in terms of uptime and cycle-slip free operation [1-3].

In view of multi-user dissemination, we introduce a generalization of the repeater laser station (RLS), based on an ultra-low sensitivity multi-branch Michelson interferometer. This Super-RLS enables us to feed five links at once and acts as a metrological node. As a first step, we will show that an optical frequency can be disseminated at two places simultaneously with the same performance that obtained with RLSs [4]. We will also show how to combine Super-RLS, RLS and two-way techniques for a wide and versatile optical metrological network.

We will also present the latest experimental results we obtained over several months for the 1400-km long optical fiber link between Syrte and Université of Strasbourg. We improved the robustness of the link, which instability is in the 10^{-20} range at long-term. The reliability of this technology has also been demonstrated in the frame of the knowledge transfer achieved with SME, where most of the metrological network equipments are now commercially available.

References

[1] A. Bercy et al, "Ultrastable optical frequency dis-semination on a multi-access fibre network", Appl. Phys. B, 122 : 189, 2016.
[2] A. Bercy et al, "Two-way optical frequency comparisons at $5x10^{-21}$ relative stability over 100-km telecommunication network fibers", Phys. Rev. A, vol. 90, p. 061802, 2014.
[3] W.-K. Lee et al, "Hybrid fiber links for accurate optical frequency comparison", Appl. Phys. B, 123 : 161, 2017.
[4] N. Chiodo et al., "Cascaded optical fiber link using the internet network for remote clocks comparison", Opt. Express, vol. 23, p. 33927-33937, 2015.

Study on time scale algorithm of hydrogen maser based on minimum error theory

Meng Jiang[1,3], ShaoWu Dong[1,2,4], WenJun Wu[1,2], Huijie Song[1,2,3], LiLi Qu[1,2], WeiXiong Wang[1,3]

[1] National Time Service Center， Chinese Academy of Sciences, Xi'an, China
[2] Key Laboratory of Time and Frequency Primary Standards, National Time Service Center, CAS, Xi'an, China
[3] University of Chinese Academy of Science, Beijing, China
[4] School of Astronomy and Space Sciences, University of Chinese Academy of Science, Beijing 100049

Email: m13259460281@163.com

Abstract—With the rapid development of science and technology, the demand for time is getting higher and higher by users in various fields. The high performance cesium clock has a better long-term stability than the hydrogen maser, but the short term stability is poor. Most of the world's time laboratories use high performance cesium clocks and hydrogen masers for timekeeping in order to ensure the accuracy and stability of their atomic time scale. However, the hydrogen maser has frequency drift, and the inaccurate deduction of the frequency drift of the maser will affect the accuracy of the atomic time calculation directly. Therefore, in this paper, a method based on the minimum error theory is used to estimate the frequency drift parameter of masers in a certain time interval. Taking the clock difference data of three hydrogen masers as the research object, this method determines the frequency drift parameter. After removing hydrogen maser frequency drift, we use exponential filtering method to calculate the time scale of the ensemble of hydrogen masers. At the same time, according to the frequency drift parameters of the hydrogen atom clock published by BIPM, the frequency drift is deducted and the time scale is calculated, then the comparative analysis is made at the end. The results show that the method based on minimum error theory can accurately estimate the parameters of hydrogen maser frequency drift, and the accuracy of this time scale is significantly higher than that of the atomic time scale which employs the frequency drift parameter published by BIPM, and the maximum deviation in 13.93ns. Preliminary results of the algorithm were showed in figure1 and table 1.

Keywords—minimum error, hydrogen maser, time scale, frequency drift estimation

Table 1: the deviation of time scales calculated by two methods to estimate the frequency drift parameters

MJD	57883-57884	57885-57886	57887-57888	57889-57890	57891-57892
Maximum deviation (ns)	1.23	3.33	6.20	9.87	13.93
Minimum deviation (ns)	0.05	1.37	3.53	6.48	10.22

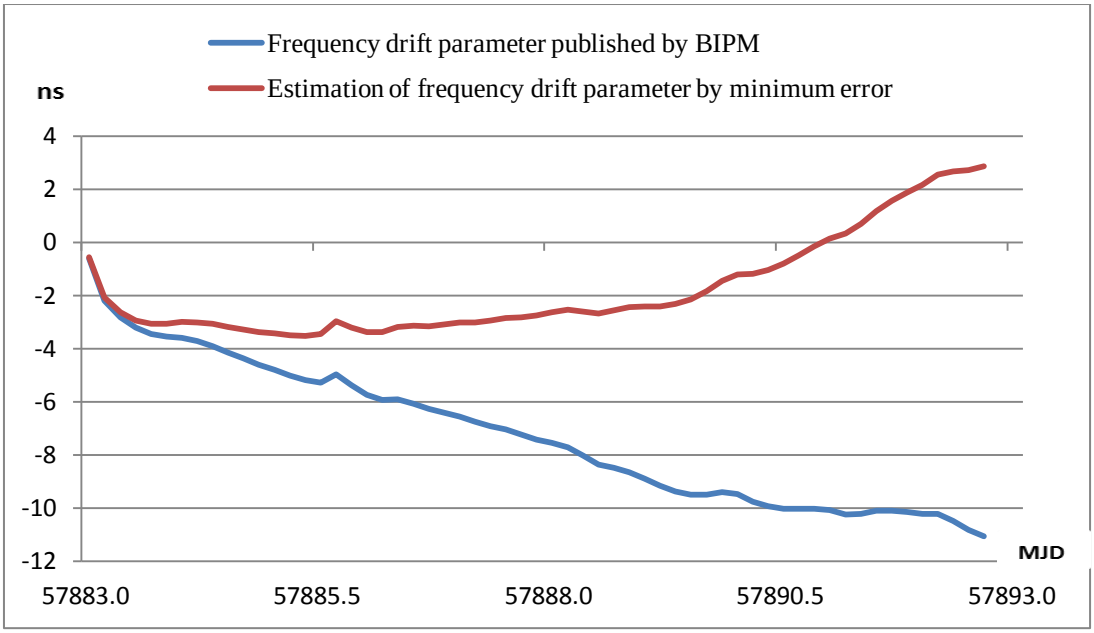

Fig 1: The difference between calculated time scale and TA(NTSC) which used two methods to estimate the frequency drift parameters

References

[1] SONG Hui-jie, DONG Shao-wu, WANG Zheng-ming. An Analysis of NTSC's Time-keeping Hydrogen Masers[J]. Chinese Astronomy and Astrophysics 40(2016) 569-577

Comparision of Two Methods of Time-Interval Measurement Based on SAWF and SAWDDL

Haifeng WANG, Xueyun WANG, Hongbo WANG, Hang YI, Honglei YANG, Wenzhe YANG, Shuwei WANG, Yong Xie, Shengkang ZHANG

Science and Technology on Metrology and Calibration Laboratory,
Beijing Institute of Radio Metrology and Measurement, Beijing, China, 100854

Email: haifengwang203@163.com

With the higher performance of the Time-Interval Counter technology that people are looking for, researchers have done large numbers of work to achieve it, most of these are based on time interpolation. Traditional time interpolation methods are usually utilize interval-to-voltage increment conversion, different variants of the vernier principle, or pulse propagation through tapped delay lines[1]. At the present time, two methods of Time-Interval Measurement with 1ps precision and stability are realized based on Surface Acoustic Wave Filter (SAWF) and Surface Acoustic Wave Dispersive Delay Line (SAWDDL) which are used as the time interpolator.

In this paper, I demonstrate my work details on these two interpolation methods to compare which one is easy and precise to be implemented. The two methods are all based on the fact that a transversal SAW component excited by a short pulse can generate a finite signal with highly suppressed spectra outside a narrow frequency band. As can be seen from Fig.1, the shape of the output signal envelop from SAW filter is as sinc function, and the output signal from SAW delay line is a chirp signal which is commonly use in radar systems. If the two band limit signals are sampled at clock ticks, they can be approximately reconstructed from a finite number of samples according to the Shannon sampling theory[2] and then compared to determine the interval between the two pulses.

We all know that the peak shape of the self-correlation function (SCF) determine the precision of the time interval measured. As can be seen from Fig.2, the SCF of SAWDDL is shaper than the SCF of SAWF with the same bandwidth and duration time of response. So if we use the SAWDDL as the time interpolator, the result must be better than the SAWF in theory. But when we take it in practice, the result is cross to our expectation because of Gibbs Phenomena when using sinc interpolation to reconstruct the original signal on the steep boundary. Steeper boundary of samples envelope will increase the reconstruction error. Obviously, the response envelope of SAWF is gradually approaching to zero on the boundary, it can be easily and precisely to reconstruct from samples with small interpolation error.

We have done a simulation using SAWF as the time interpolator in Time-Interval Measurement with low frequency sampling clock which can be implemented easily on hardware platform and the result shows that the time interval measurement is about 1ps precision and stability.

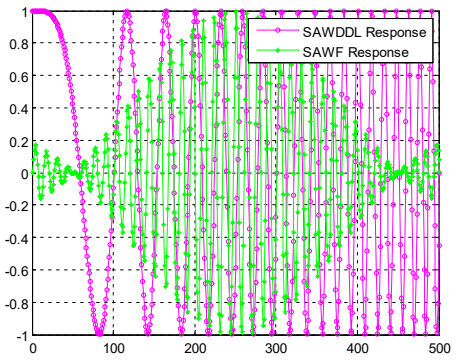

Fig.1 The Response of Two Methods

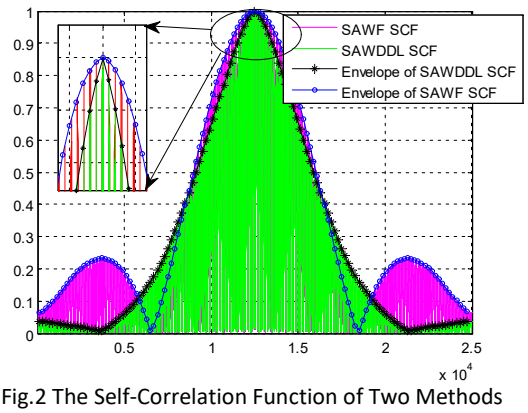

Fig.2 The Self-Correlation Function of Two Methods

References

[1] P. Pánek, “Random errors in time interval measurement based on SAW filter excitation,” IEEE Trans. Instrum. Meas., vol. 57, no. 6, pp. 1244–1250, Jun. 2008.

[2] F. Candocia and J. C. Principe, “Comments on “Sinc interpolation of discrete periodic signals”,” IEEE Trans. Signal Processing, vol. 46, pp. 2044–2047, July 1998.

Simple Analytical Expressions and Experimental Verifications for the Dark Resonance Amplitude in a Vacuum Vapour Cell

Denis Brazhnikov[1,2], Stepan Ignatovich[1], Vladislav Vishnyakov[1], Mikhail Skvortsov[1], Christophe Gorecki[3] and Rodolphe Boudot[3]

[1]Institute of Laser Physics SB RAS, Novosibirsk, Russia
[2]Novosibirsk State University, Novosibirsk, Russia
[3]FEMTO-ST, CNRS, Université de Bourgogne Franche-Comté, Besançon, France

Email: brazhnikov@laser.nsc.ru

Coherent population trapping (CPT) is one of the brightest representatives of nonlinear interference effects occurring in resonant light-matter interactions. Since its first observation in 1976 [1], it has already found numerous interesting applications. Perhaps, the most relevant and marketable direction of its use lies in the field of quantum metrology and sensing (atomic clocks and magnetometers). Often CPT manifests itself as a narrow resonance in light wave transmission through a vapour cell. This resonance is known as “dark resonance”. It is frequently observed using two frequency components of the light field with intensities I_1 and I_2.

Despite of a large number of theoretical papers devoted to the dark resonance properties, still there is some lack of analytical results. At the same time, to know explicit analytical laws of the resonance parameters is quite important for fundamental physics as well as for real applications. For instance, analytical expressions can help to estimate the resonance properties (amplitude, contrast, etc.) before carrying out any experiment and prompt how to achieve desirable results.

Many applications of the dark resonance exploit buffer-gas-filled or antirelaxation-coated vapour miniature cells (Ø << 1 cm) to achieve good resonance properties together with a chip-scale implementation. These methods have their advantages and disadvantages. The latest trends in this area are related to buffer-gas-free technologies. One of them consists in using cold atoms prepared in a magneto-optical trap. The other way is much simpler and deals with “hot” atoms in a regular vacuum cm-size cell. Surprisingly, the latter case is much worse studied in the sense of derivation of necessary analytical expressions. It is due to some difficulties in analytical calculations when motion of atoms should be taken into account in full. For the case of vacuum vapor cell, only numerical calculations are widely presented in the literature for arbitrary light intensities, while analytical results have been obtained only for the pump-probe regime ($I_1 \ll I_2$). The important regime $I_1 \approx I_2$ has not been analytically studied well enough.

Our research is aimed on derivation of analytical results, which would adequately describe experimental data for a vacuum vapor cell. The explicit and simple analytical expressions obtained will be demonstrated during the conference as well as results of experimental verifications in microfabricated as well as cm-size thermal vapour cells. The comparisons show quite acceptable agreement between our theory and experiments in wide range of light intensities, so that the derived expression for the resonance amplitude can be used in practice.

Russian group thanks Russian Science Foundation (pr. no. 17-72-20089). Ch. Gorecki and R. Boudot were supported by LabeX FIRST-TF, Région de Franche-Comté and EquipX OSCIMP.

References

[1] G. Alzetta et al., Nuovo Cimento B, vol. 36, pp. 5–20, 1976.

CANCELLED

Electromagnetically induced Tansparency Ramsey sequence interference

Zhengfeng Hu[1], Chengpu Liu[2], Yuzhu Wang[1]

[1]The Key Laboratory of Quantum Optics, Shanghai Institute of Optics and Fine Mechanics, Chinese Academy of Science, Shanghai P.O.Box 201800, China

[2]State Key Laboratory of High Field Laser Physics, Shanghai Institute of Optics and Fine Mechanics, Chinese Academy of Science, Shanghai P.O.Box 201800, China

Email: zfhu@siom.ac.cn

Reducing light shift in an atomic frequency standards is important for obtaining its higher long time stability. We proposed an atomic frequency standards scheme based on an electromagnetically induced transparency Ramsey (EIT-Ramsey) sequence interference which is the lasers interacting with a three-level Λ-type atomic medium as shown in Fig. 1(a). $|1\rangle$, $|2\rangle$ are the two ground states of ^{87}Rb atom belonging to different hyperfine states, which can be the clock states with $m_F=0$ or magnetically insensitive states with $|m_F=\pm 1\rangle$. $|3\rangle$ is an excited state which belongs to the excited hyperfine state. For the preparation of the ground state coherence, the two EIT-type lasers are applied to atomic ensemble. The one laser is relative intense coupling laser driving the transition between the states $|2\rangle$ and $|3\rangle$. The other is the weak probe laser driving the transition of the states $|1\rangle$ and $|3\rangle$. In order to produce Ramsey interference [1, 2], these two lasers can be applied to atomic ensemble separated in time and in a two-photon resonant way. A dark state which is the coherent superposition of the two ground states is formed. The time sequence of the atomic clock operation is shown in Fig. 1(b). The interacting time of the EIT pulse with atoms τ is long enough to allow the atomic prepared into the dark state superposition. Then atoms are freely evolution with the time duration of T. A short query pulse is used to detect the Ramsey interference in order to avoid the optical repumping process. It has advantages of smaller atomic dipole interaction which may cause frequency shift. By using the density matrix approach for a three-level system and considering various the relaxation processes, we studied the properties of the EIT-Ramsey fringe and the relations with the various atomic and lasers' parameters.

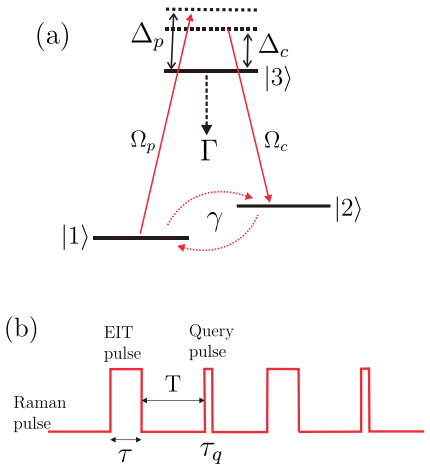

Fig. 1: (a) Raman excitation in a three-level Λ-type system. (b) EIT-Ramsey pulse sequence considered in the computational model for generating Raman Ramsey interference.

References

[1] J. E. Thomas, P. R. Hemmer, S. Ezekiel, C. C. Leiby Jr., R. H. Picard, and C. R. Willis, "Observation of Ramsey Fringes Using a Stimulated, Resonance Raman Transition in a Sodium Atomic Beam", Phys. Rev. Lett. vol. 48, p. 867-870, 1982.

[2] T. Zanon, S. Guerandel, E. De Clercq, D. Holleville, N. Dimarcq, A. Clairon, "High Contrast Ramsey Fringes with Coherent-Population-Trapping Pulses in a Double Lambda Atomic System", Phys. Rev. Lett. vol. 94, p.193002-1-5, 2005.

Status report on two ^{171}Yb optical lattice clocks at KRISS

Huidong Kim, Myoung-Sun Heo, Won-Kyu Lee, Dai-Hyuk Yu, Sang Eon Park, Chang Yong Park

Korea Research Institute of Standards and Science, Daejeon 34113, Korea

Email: cypark@kriss.re.kr

The first Yb optical lattice clock (Yb1) at KRISS recently reached the total systematic uncertainty of 8.3×10^{-17} and the absolute frequency measurement is under way using a Cs fountain clock with expected uncertainty of low 10^{-16}. We expect its accuracy will be limited eventually by a BBR shift due to lack of isolation from inhomogeneous thermal environments. Therefore the second Yb clock (Yb2) that has a specially designed BBR chamber (Fig.1) has been under construction. The chamber has eleven 16-mm-daiameter apertures closed by BK7 windows (4.5 mm thickness) or BK7 lenses (10 mm edge thickness), two open apertures with 10 mm diameter, and two smaller open apertures with 4 mm diameter. Because the temperature of the BBR chamber is controlled actively slightly higher than those of surroundings, there can exist temperature gradient on it. In addition, there are other heat sources such as an atomic beam oven, a Zeeman slower, and a heated window for a Zeeman slowing laser. Hence the performance of the BBR chamber were verified by using a 10-mm-diameter black copper ball with a platinum resistance thermometer (black ball PRT) as a radiation detector at the center of the BBR chamber as is shown in Fig. 1. The black ball PRT was coated by a black material with absorptivity of 90 % over wavelengths of 1~30 μm. Temperatures of other parts of the chamber were measured using ten calibrated PRT's. The radiation on the surface of the ball was a dominant source of the energy flux on the black ball PRT over the conduction via wires and the self-heating of the PRT. With an energy rate equation and the specific heat of copper, the temperature of the black ball PRT could be calculated. Fig.2 shows the measured temperature of the black ball PRT (red-line) by the radiation from the heated window for the Zeeman slowing laser, and its fitted curve (black-line) by the simulation model equation. Using parameters fitted to experimental data, the radiation intensity at the position of the atom trap was evaluated with equivalent accuracy of 40 mK for the blackbody temperature which corresponded to 1.3×10^{-18} uncertainty for the clock transition of ^{171}Yb.

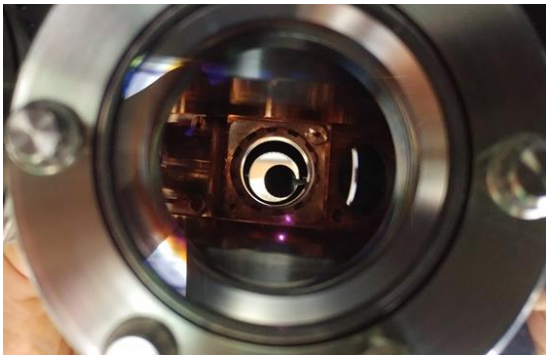

Fig. 1: Black ball PRT installed in the BBR chamber.

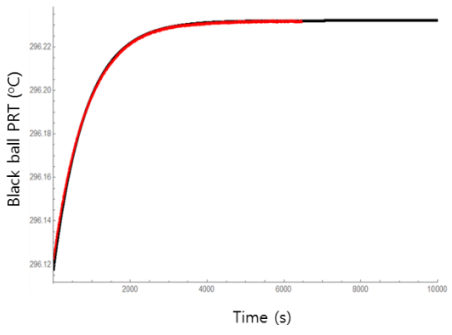

Fig. 2: Temperature increase of black ball PRT (red-line) and simulation result (black-line).

Hysteresis in Phononic Frequency Combs

Adarsh Ganesan[1] and Ashwin Seshia[1]

[1]The Nanoscience Centre, University of Cambridge, Cambridge, UK

Email: ag815@cam.ac.uk

Hysteresis is a common feature evidenced in many nonlinear mechanisms. Particularly, in this paper, we present experimental evidence of hysteresis observed in a recently discovered non-linear process leading to the formation of phononic frequency combs. The phononic frequency comb is an array of precisely positioned equidistant frequencies and is generated through the interactions among phonon modes and drive frequency [1-2]. Such underlying interactions related to the generation of phononic frequency combs are only existent under specific drive conditions (cf. Fig. 4A of [1] and Fig. 3A of [2]). However, when hysteresis is also operative, the existence and uniqueness of such frequency combs at a nominally favorable drive condition is lost. This paper demonstrates this specific aspect through the systematic control of drive

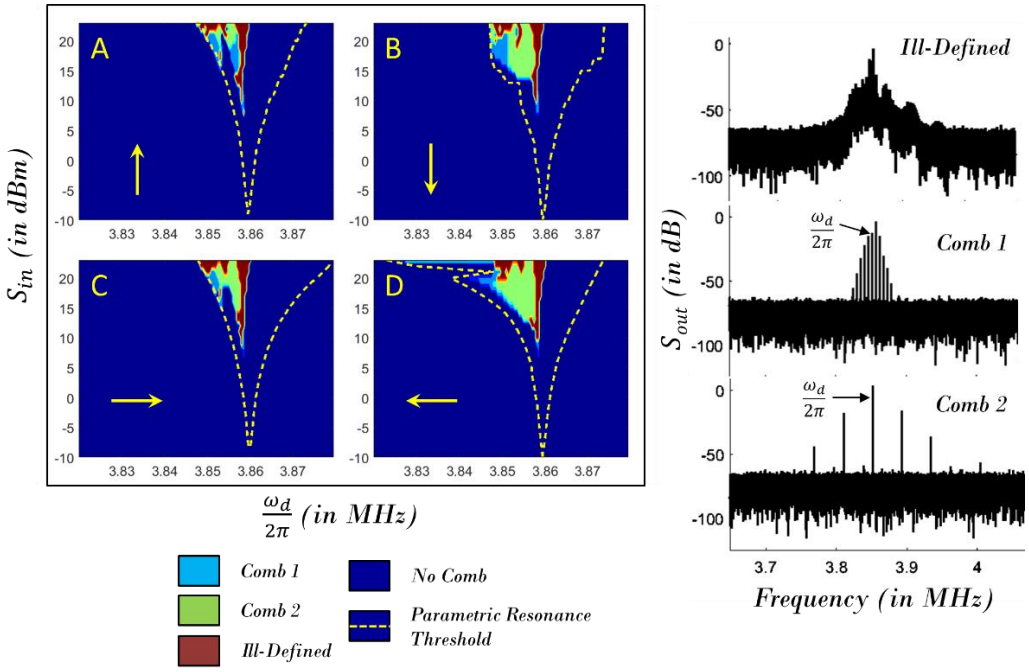

Fig. 1: Evidence for Hysteresis in Phononic Frequency Combs. The operational regimes of frequency combs when the electrical drive level S_{in} and drive frequency ω_d are varied along different paths – A: S_{in} is increased from $-10\ dBm$ to $23\ dBm$ for each ω_d; B: S_{in} is decreased from $23\ dBm$ to $-10\ dBm$ for each ω_d; C: ω_d is increased from $3.82\ MHz$ to $3.88\ MHz$ for each S_{in}; D: ω_d is decreased from $3.88\ MHz$ to $3.82\ MHz$ for each S_{in}.

conditions along different paths. For this study, an experimental device of two mechanically coupled micromechanical resonators is considered (cf. Fig. 1A of [2]). The existence proof of frequency combs in such a device model is experimentally validated in [2]. Now, owing to the operative hysteresis, the uniqueness of frequency comb regimes (cf. Fig. 3A of [2]) is lost and is dependent on the hysteretic path. Fig. 1 showcases this behavior. This paper thus elaborates on this specific feature of phononic frequency combs.

References

[1] Adarsh Ganesan, Cuong Do and Ashwin Seshia, "Phononic Frequency Comb via Intrinsic Three-Wave Mixing," Physical Review Letters, vol. 118, p. 033903, 2017.

[2] Adarsh Ganesan, Cuong Do and Ashwin Seshia, "Excitation of Coupled Phononic Frequency Combs via Two-Mode Parametric Three-Wave Mixing," arXiv:1708.07563, 2017.

Thermal noise further reduced ultrastable laser with frequency instability of 5×10^{-16}

Lulu Yan[1,2], Zhaoyang Tai[1,2], Yanyan Zhang[1,2], Pan Zhang[1], Wenyu Zhao[1], Xiaofei Zhang[1,2], Wenge Guo[1], Shougang Zhang[1], Haifeng Jiang[1,2,*]

[1] Key Laboratory of Time and Frequency Primary Standards, National Time Service Center, Chinese Academy of Sciences, Xi'an, China
[2] School of Astronomy and Space Science, University of Chinese Academy of Sciences, Beijing, China

Email: haifeng.jiang@ntsc.ac.cn

Ultrastable lasers play key roles in accurate modern measurement systems, such as optical clock[1], ultra-low phase noise microwave generation[2], and gravitational wave detection[3]. Their frequency instability is mainly attributed to mirror surface fluctuation introduced by thermal noise. Usually, we improve the performance by using longer cavity; however, longer cavity is sensitive to mechanical noise, and faces more difficulties in space application. In this paper, we report on a new approach to reduce the thermal noise limitation by enlarging the equivalent beam size without increasing the cavity length.

We have reported our previous ultrastable lasers, which are referenced to 10-cm ULE Fabry-Pérot (F-P) cavities. Frequency instability of ultrastable laser is 7×10^{-16} [4] limited by the thermal noise. In this experiment, we synthesize these lasers to produce a more stable laser signal with frequency instability of $\sim5\times10^{-16}$ @ 1s. Fig. 1 shows preliminary result that the improvement factor of instability is square root of 2 over the full measurement range. With this technique, we believe that relative instability can be achieved with 10-cm length cavity under room temperature. The experiment is ongoing, we will demonstrate the details later.

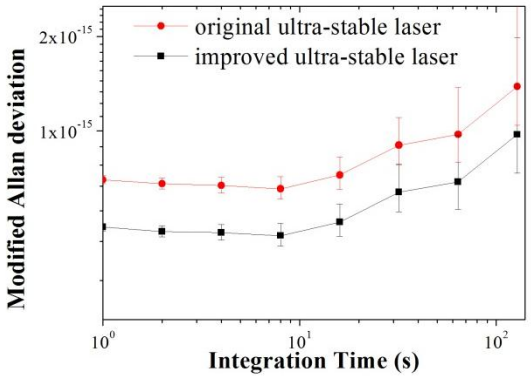

Fig. 1: The red circles: fractional frequency instability of ultrastable laser without using this improved method (characterized by the modified Allan deviation). The black squares: fractional frequency instability of the new ultrastable laser using this beam size enlarging method.

References

[1] Y. Y. Jiang, A. D. Ludlow, N. D. Lemke. R. W. Fox, J. A. Sherman, L. S. Ma and C. W. Oates, "Making optical atomic clocks more stable with 10^{-16}-level laser stabilization", Nat. Photon., vol.5, p. 158-161, 2011.

[2] T. M. Fortier, M. S. Kirchner, F. Quinlan, J. Taylor, J. C. Bergquist, T. Rosenband, N. Lemke, A. Ludlow, Y. Jiang, C. W. Oates and S. A. Diddams, "Generation of ultrastable microwaves via optical frequency division," Nat. Photon., vol. 5, p. 425-429, 2011.

[3] Abbott B. P. et al., "Prospects for observing and localizing gravitational-wave transients with advanced LIGO and advanced Virgo," Phys. Rev. Lett., vol. 116, p.061102,2016.

[4] Z. Y. Tai, L. L. Yan, Y. Y. Zhang, X. F. Zhang, W. G. Guo, S. G. Zhang and H. F. Jiang, "Transportable 1555-nm ultrastable laser with sub-0.185-Hz linewidth," Chin. Phys. Lett., vol. 34, p. 090602, 2017.

Study of the phase noise of Langatate crystal resonators

A. Pokharel[1], E. Vaillant[1], J. Imbaud[1], J.J. Boy[1], F. X. Esnault[2], G. Cibiel[2] and F. Sthal[1],

[1] FEMTO-ST Institute, Besançon, France
[2] Centre National d'Etudes Spatiales (CNES), Toulouse, France

Email: fsthal@ens2m.fr

Among the crystals belonging to the langasite family, the langatate one ($La_3Ga_{5.5}Ta_{0.5}O_{14}$ also called LGT) seems the best candidate to substitute to the quartz crystal for frequency and time applications [1]. Its electromechanical coupling coefficients, quality factor-frequency product are higher than in quartz whereas the amplitude-frequency effect and the force-frequency coefficient (named Kf) are lower. Up to now, only the frequency-temperature behavior is not advantageous, compared to the SC cut quartz resonators.

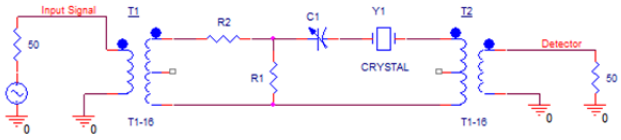

Fig. 1: Resonator impedance adapter.

High quality LGT crystal resonators prototypes working at 10 MHz have been measured on an advanced phase noise measurement system set up in collaboration with the Centre National d'Etudes Spatiales (CNES) [2]. This bench uses carrier suppression technique and allows to made passive characterizations of resonators pairs with near Fourier frequencies, typically few Hertz. Due to the very small impedance of the resonators (The motional resistance is in the order of ten ohms), special adapters using transformers have been studied in order to maximize the loaded Q in the measurement system. The impedance bridge have been simulated by Pspice analyzes using optimization process (Fig. 1).

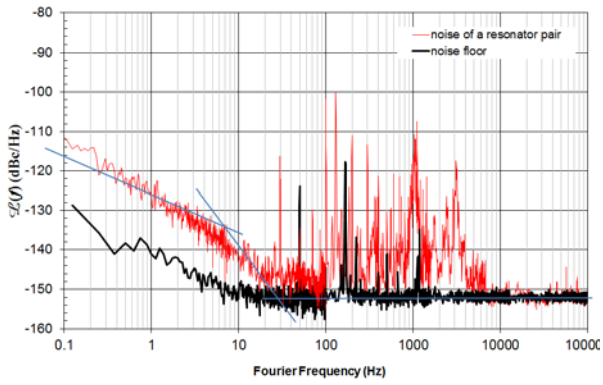

Fig. 2: Noise spectrum of one LGT resonator pair.

The resonators have been characterized in terms of impedance, turn-over temperature, amplitude-frequency effect and noise. The LGT crystal resonators noise has been measured (Fig. 2). The order of magnitude of the resulting flicker floor in Allan standard deviation is about $4 \cdot 10^{-13}$ for this respecting pair. Large spurious frequencies outside the resonator bandwidth have been observed. Discussion about the difficulties to obtain the results will be presented in the final paper.

References

[1] J. Imbaud, J. J. Boy, F. Sthal, "LGT alternative quartz materials for Ultra-Stable Oscillators", Proc. IEEE Int. Freq. Cont. Symp., Taipei, Taiwan, 19-22 May, pp. 32-39, (2014).

[2] F. Sthal, M. Devel, J. Imbaud, R. Bourquin, S. Ghosh, G. Cibiel, "Study on the origin of 1/f noise in quartz resonators", J. Stat. Mech., n° 6, May, 054025, (2016).

Progress on development of optical frequency combs at NTSC

Yanyan Zhang[1,2], Lulu Yan[1,2], Pan Zhang[1], Songtao Fan[1,2], Bingjie Rao[1], Xiaofei Zhang[1,2], Wenge Guo[1], Shougang Zhang[1,2]and Haifeng Jiang[1,2,*]

[1]Key Laboratory of Time and Frequency Primary Standards, National Time Service Center, Chinese Academy of Sciences, Xi'an, China
[2]School of Astronomy and Space Science, University of Chinese Academy of Sciences, Beijing, China

Email: haifeng.jiang@ntsc.ac.cn

Optical frequency comb is a frequency-controlled femtosecond laser, which has been widely used in many applications[1, 2]. Robust mode-locked laser and capability of its frequency control are critical in some cases. In this paper, we demonstrate two techniques to improve performance of Er:fiber frequency combs at NTSC[3, 4].

The first technique is to obtain a low noise and robust mode-locked laser. As we know, thenonlinear polarization evolution (NPE) mode-locked laser is the most widely employed type of the erbium fiber lasers for its low noise andnarrow pulse width. However, the drawback of the NPE laser is sensitivity to temperature and difficultto start mode locking.On the other hand, polarization-maintaining lasers based on nonlinearamplifier loop mirrors (NALM) can self-starting by introducing a nonreciprocal phase bias in the cavity and insensitive to the environmental perturbation**.** To obtain self-start and low noise mode-locked laser, we design a hybrid laser incorporatingNPE and NALM mechanisms. The system can self-start and work normally after being unpowered six months, and the noise level is similar to thepure NPE.

The second technique is to control mode-locked laser frequency with broad bandwidth and large range. Usually, combining control techniques have to be used for this[5], because high bandwidth control technique has insufficient dynamic control range to conquer long term frequency drift. We propose a method that rotates of a NPR mode-locked laser the polarization state to steer laser`s frequencies. By taking advantage of birefringence of thewhole laser cavity, this approach can tune frequencies in a broadbandwidth and over a large dynamic range. Compared with other high bandwidth frequency control techniques, the control range of this approach is at least 10 times larger.

References

1. J. Kim,*et. al.*,"Ultralow-noise mode-locked fiber lasers and frequency combs:principles, status, and applications," Advances in Optics and Photonics8(3), 465-540, 2016.
2. M. Lexius, *et. al.*,"Space-borne frequency comb metrology,"Optica3(12), 1381-1388, 2016.
3. Y. Zhang, *et. al.*,"Robust optical-frequency-comb based on the hybrid mode-locked Er:fiber femtosecond laser,"Optics Express 25(18), 21719-21725, 2017.
4. Y. Zhang, *et. al.*,"Steering optical comb frequencies by rotating the polarization state," Optics Letters 42(24), 5145-5148, 2017.
5. S. Droste, *et. al.*,"Optical frequency comb generation based on erbium fiber lasers,"Nanophotonics 5(2), 196-213, 2016.

Towards compact transportable optical clock based on $^{171}Yb^{+}$

Zalivako Ilia[1], Khabarova Ksenia[1], Semerikov Ilia[1], Borisenko Alexander[1], Sherstov Ivan[2], Bagaev Sergei[3], Lugovoy Alexey[3], Taichenachev Alexey[3], Chepurov Sergei[3], Kolachevsky Nikolay[1]

[1] P.N. Lebedev Physical Institute of Russian Academy of Sciences, Moscow, Russia

[2]Skolkovo Institute of Science and Technology, Moscow, Russia

[3] Institute of Laser Physics, Siberian Branch, Russian Academy of Sciences, Novosibirsk, Russia

Email: zalivako.ilya@yandex.ru

Compact and robust transportable optical clocks are required in wide range of applications like navigation, time and frequency metrology, geodesy etc. Transportable optical clocks based on neutral Sr atoms [1], single Ca+ [2] and Yb+ [3] ions are under development by different groups all over the world. Here we present a new project aimed for development of a transportable, compact and relatively low mass optical clock based on a single ^{171}Yb+ ion. The project was started at LPI in 2017th and joined leading Russian scientific companies and physics institutes. A concept of the clock will be discussed as well as suggested solutions for design of compact, robust and stable diode lasers necessary for the clock.

References

[1] S. B. Koller et al., “Transportable Optical Lattice Clock with 7×10^{-17} Uncertainty”, Phys. Rev. Lett., vol. 118, no. 7, p. 73601, 2017.

[2] J. Cao et al., “A compact, transportable single-ion optical clock with 7.8×10^{-17} systematic uncertainty”, Appl. Phys. B Lasers Opt., vol. 123, no. 4, pp. 1–9, 2017.

[3] Opticlock.de, “German Quantum Initiative QUTEGA starts with optical single ion clock”, 2017. [Online]. Available: https://www.opticlock.de/en/info/. [Accessed: 21- Dec- 2017].

Long term simulations for bi-static radar and test bench design

Ricardo Granados[1], Alain Herique[1], Sylvain Rochat[1], Etienne Le-Coarer[1]

[1]Univ. Grenoble Alpes, CNRS, IPAG, F-38000 Grenoble, France

Email: alain.herique@univ-grenoble-alpes.fr

Nowadays the internal structure knowledge of asteroids comes from remote sensing and theoretical modeling. This approach cannot give enough details to completely unveil the evolution of the body. Direct study can give information of the formation of the body, therefore giving insight in the history of Solar System [1]. Also internal structure study can give valuable information for planetary defense against hazardous bodies and for future exploration [2].

Bi-static radar is a technology capable of sounding asteroids to characterize the internal structure. We present a Low Frequency Radar (LFR) that inherits the measurement concept from the bi-static radar CONSERT on-board Rosetta mission, which studied the comet 67P/Churyumov-Gerasimenko [3]. The measurement consists to send radio waves through the asteroid from an Orbiter, orbiting the asteroid, and a Lander placed in the surface Fig.1[4]. The principal objective is to measure the propagation delay from which is possible to deduce the dielectric permittivity of the material. This relates to the porosity and mineralogy of the body [5].

Two separated electronics means two clocks, and two calendars. Frequency and calendar drift impose design and operational constraints. Planetary mission constraints limits mass and power, and there was no compliant clock to preserve synchronization for the whole experiment. An in-time transponder was implemented. First transmission gives time reference, the second transmission is the science signal Fig.1. With this structure, frequency and time requirements are reduced and split into 4 different time scales. Calendar drift acts different for each time scale inducing different requirements, while the corresponding errors are correlated. This makes difficult to have an idea on how the phase and the time errors impact in the measurement and its correlations in long term.

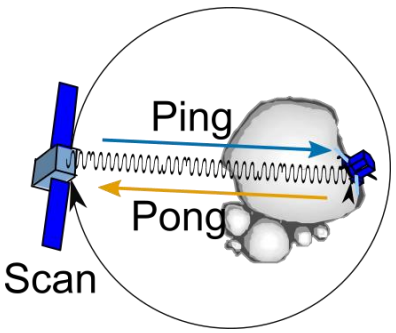

Fig. 1: LFR operational concept. Transmission Orbiter-Lander. Ping gives time reference, Pong is science signal.

Increasing the accuracy of time measurement is a way to improve science return and possibly to relax electronic constraints. Therefore we developed, first a simulator to estimate long term effects and secondly we improve time and phase in post processing. We built a Kalman filter estimator and we proposed a modification of the transponder structure to improve this estimation. To validate this approach, a Test Bench (TB) is under development to measure real clocks.

References

[1] A. Herique *et al.*, "Direct observations of asteroid interior and regolith structure: Science measurement requirements," *Adv. Space Res.*, Oct. 2017.

[2] P. Michel *et al.*, "Science case for the Asteroid Impact Mission (AIM)" *ASR*, vol. 57, no. 12, pp. 2529–2547, Jun. 2016.

[3] W. Kofman *et al.*, "The Comet Nucleus Sounding Experiment by Radiowave Transmission (CONSERT)" *Space Sci. Rev.*, vol. 128, no. 1–4, pp. 413–432, Feb. 2007.

[4] W. Kofman *et al.*, "Comet nucleus sounding experiment by radiowave transmission," *Adv. Space Res.*, vol. 21, no. 11, pp. 1589–1598, Jan. 1998.

[5] W. Kofman *et al.*, "Properties of the 67P/Churyumov-Gerasimenko interior revealed by CONSERT radar," *Science*, vol. 349, no. 6247, p. aab0639, Jul. 2015.

Design status of the Rb POP space clock for GNSS applications

P. Arpesi[1], J. Belfi[2], M. Gioia[1], N. Marzoli[3], R. Romani[1], A. Sapia[1],
M. Gozzelino[4], C. Calosso[4], F. Levi[4] and S. Micalizio[4],
A. Tuozzi, [5]
M. Belloni[6]
[1] Atomic Clocks, Leonardo SpA, Milan, Italy
[2] Leonardo consultant (Altran, Milan, Italy)
[3] Leonardo consultant (Positech s.r.l., Alten group, Milan, Italy)
[4] Physic Metrology Division , INRIM, Torino, Italy
[5]Agenzia Spaziale Italiana, Rome, Italy
[6]European Space Research and Technology Centre – Noordwijk, NL

Email: marina.gioia@leonardocompany.com

The ^{87}Rb Pulsed Optically Pumped (POP) clock is a vapor cell clock based on a Ramsey interrogation scheme.inside a microwave cavity resonating at 6834 MHz. The clock transition is excited by means of microwaves pulses while pulsed optical radiation at 780 nm is used to prepare the atomic sample polarization and to detect the ground state population.
Since the atomic sample is never interacting simultaneously with microwave and optical radiation, a strong reduction of light shift effect is obtained with respect to other vapour cell frequency standards. A frequency stability of 1.7×10^{-13} at 1s and 5×10^{-15} up to 50000 s, (drift $<10^{-14}$/day) has been demonstrated [1]. This result is fully compliant to the Galileo Second Generation specifications, with better stability performance of the Passive Hydrogen Maser (PHM) and the possibility to implement a compact device, with reduced mass (< 10 kg), power consumption (< 40 W) and maintenance needs.
Leonardo Finmeccanica, in collaboration with INRIM, is developing a space version of the POP for next generation Global Navigation Satellite Systems. Such kind of application demands for clocks with high frequency stability, low failure rate over 15 years mission time, low sensitivity to environmental characteristics, low mass and power consumption.
This paper presents the latest results from the industrialization activity of the physics package of the Rb POP designed to meet space environment and life time requirements.
Leonardo completed the design phase of the Physics Package (PP) of the clock, including thermal, mechanical and magnetic analyses. PP manufacturing will start in the beginning of 2018 with vibration test on a first prototype of the full microwave cavity assembly including the Rb cell in the first half of the year.

This work is funded by GSTP 6.2 Contract N. 4000118182/16/NL/GLC/fk for Rubidium POP Atomic Clock – Physic Package and by Leonardo and INRIM.
In addition it was supported by the European Metrology EM Model Unit Layout Research Program (EMRP project IND55-Mclocks). The EMRP is jointly funded by the EMRP participating countries within EURAMET and the European Union.

[1] S. Micalizio et al., Metrological characterisation of the pulsed Rb clock with optical detection, Metrologia vol. 49, pp.425-436,

Noise Characterization of Red Pitaya Internal PLL

A. C. Cardenas-Olaya[1,2], C. E. Calosso[1], J.-M. Friedt[2], S. Micalizio[1], E. Rubiola[2]

[1]Istituto Nazionale di Ricerca Metrologica (INRiM), Physics Metrology Division, Turin, Italy
[2]Femto-ST Institute, Time and Frequency Department, Besancon, France

Email: carolina.cardenas@femto-st.fr

Increasing development on electronic technology has resulted in embedded platforms capable of performing digital processing on rapidly sampled signals allowing the use of Software Defined Radio [1] in time and frequency metrology. As consequence, new methods have been proposed based on digital systems [2], taking advantage of the reconfiguration flexibility and compactness, reducing complex calibration procedures and unwanted environmental noise. Currently, commercially available platforms provide the main components for research on this field and they have been demonstrated to be suitable tools for the implementation of time and frequency metrology [3].
In general, for time and frequency applications it is important to refer the system timebase and the Device Under Test (DUT) to a common oscillator. Most commercial platforms based on FPGA are clocked by quartz oscillators whose accuracy and frequency stability are not suitable for many of these applications being at the level of $10^{-10} - 10^{-9}$ in the short term, $10^{-8} - 10^{-7}$ in the medium term and with an uncertainty of tens of ppm. Standard low noise oscillators are available at 5 MHz, 10 MHz and 100 MHz, but generally digital systems are clocked at higher frequencies (such as 125 MHz, 250 MHz); therefore a frequency synthesizer is necessary for generating the proper system clock. Since external commercial synthesizers are expensive and bulky, in these cases it is possible to take advantage of the internal PLL provided by the FPGA to generate the internal clock from an external frequency reference. However, the PLL phase noise could degrade the oscillator stability thereby limiting the entire system performance becoming a critical component for digital instrumentation.

In this paper we report the noise characterization of the internal PLL of Red Pitaya platform, an open source embedded system architectured around a Zynq 7010 System on Chip that integrates a dual-channel 14-bit 125 MSps Analog to Digital Converter (ADC) and a dual-channel 14-bit 125MSps Digital to Analog Convert (DAC). Through experimental data we obtain that this PLL exhibits a residual frequency stability of 1.2×10^{-12} at 1 s and 1.3×10^{-15} at 4000 s for a 10 MHz carrier frequency in a 5 Hz measurement bandwidth. The results of the characterization lead to the noise limitations of the platform as a function of the reference power and frequency and this allows predicting its contribution to the performance of a specific time and frequency application in a wide range of the PLL operating conditions giving a guideline for instrumentation design techniques.

References

[1] Mitola III, J.: “Software Radio Architecture: Object-Oriented Approaches to Wireless Systems Engineering”, John Wiley & Sons, Inc., New York, NY, USA, 2000.
[2] Calosso, C. E.: “Tracking DDS in Time and Frequency Metrology”, In Proc. of Joint European Frequency and Time Forum and International Frequency Control Symposium, Prague, Czech Republic, 21-25 July, 2013.
[3] Sherman, J.A. and Jördens, R.: “Oscillator metrology with software defined radio”, Review of Scientific Instruments, 2016, 87.

Final characterization of InLambda delay standards for Supplementary Time Interval Comparison

Albin Czubla[1], Piotr Szterk[1], Roman Osmyk[1], Borut Pinter[2], Rado Lapuh[3], Uros Dragonja[4], Jurij Tratnik[4]

[1] Time and Frequency Laboratory, Central Office of Measures (GUM), Warsaw, Poland
[2] Metrology Department, Slovenian Institute of Quality and Metrology (SIQ), Ljubljana, Slovenia
[3]Metrology Institute of the Republic of Slovenia (MIRS), Ljubljana, Slovenia
[4] InLambda Company, Ljubljana, Slovenia

Email: a.czubla@gum.gov.pl

In this paper we present the final results of characterization of three time interval standards developed and produced by InLambda Company within the EURAMET Project #1288, coordinated by MIRS/SIQ, as a part of preparation for a new Inter-Laboratory Comparison planned as a Supplementary Comparison in the KCDB. Our purpose was to assess the real accuracy of the generated time intervals, covering short- and long-term stability and possible influence of systematic factors, so to define/ verify required repeatability and reproducibility conditions giving reduction of systematic effects to a single picoseconds (≤ 10 ps) level.

The previous experience with a cable delay measurements within the EUROMET Project #828 showed that a cable delay is not well-defined measured quantity and its value is significantly dependent on the shape of signals used for cable delay measurements and the selected trigger levels. For the cable delay of about 175 ns (the cable length of about 35 m), the values of obtained results (final estimates) were scattered even within the range of about ± 1 ns.

The tested InLambda standards (Fig. 1) are based on stabilized optical delay lines (by heating chamber with stabilization of fibers temperature at approximately 35 °C) and complete the set of time interval standards prepared within the Project #1288 (next to the electronic based Time Interval Generator (TIGen) developed by AGH and GUM, characterized before – poster presentation during EFTF 2016, not yet published). The InLambda standards use external input pulses to generate Start and Stop pulses. Precise matching Start and Stop outputs provides very close shape of the rising slopes of the output signals and short rising time (< 500 ps) which allow to minimize trigger level errors.

Fig.1. Three InLambda time interval standards of about 20 ns, 100 ns and 300 ns.

The obtained results for InLambda standards confirm the stability of generated time intervals at the single picoseconds level. However, there was observed a slight dependence of the delay value of the input pulse parameters (about 9 ps by 1 ns change of the rising time) and small influence of temperature changes (0,6 ps/ K, 1,4 ps/ K and 2,5 ps/ K accordingly). The first problem was solved by the usage of the output signal of the other InLambda standard as the input signal of the currently measured standard which resulted in the disappearance of the effect for the original input signal up to rising time ≤ 10 ns and about 20-times less sensitivity than before for the input signal with rising time > 10 ns. The second problem, with temperature sensitivity, requires fixed value of the reference temperature and, if need be, recalculation results relatively to temperature offset and temperature coefficient of the standard.

Finally, the designed InLambda delay standards are also ready to Supplementary Time Interval Comparison. The next step is to prepare the technical protocol of comparison.

Generalized auto-balanced Ramsey spectroscopy of clock transitions

V. I. Yudin[1,2], A. V. Taichenachev[1,2], M. Yu. Basalaev[1,2], T. Zanon-Willette[3], J. W. Pollock[4], M. Shuker[4], E. A. Donley[4], and J. Kitching[4]

[1]Novosibirsk State University, Novosibirsk, Russia
[2]Institute of Laser Physics SB RAS, Novosibirsk, Russia
[3]LERMA, Observatoire de Paris, PSL Research University, Paris, France
[4]National Institute of Standards and Technology, Boulder, Colorado, USA

Email: viyudin@mail.ru

When performing precision measurements, the quantity being measured is often perturbed by the measurement process itself. This includes precision frequency measurements for atomic clock applications carried out with Ramsey spectroscopy. With the aim of eliminating probe-induced perturbations, a method and rigorous substantiation of generalized auto-balanced Ramsey spectroscopy (GABRS) are developed and presented. Note that the intuitive approach proposed and experimentally realized in [1] can be considered as a particular case of GABRS.

For GABRS the usual local oscillator frequency control loop is augmented with a second control loop derived from secondary Ramsey sequences interspersed with the primary sequences and with a different Ramsey period. This second loop feeds back to a secondary clock variable and ultimately compensates for the perturbation of the clock frequency caused by the measurements in the first loop. We show that such a two-loop scheme can lead to perfect compensation of measurement-induced light shifts and does not suffer from the effects of relaxation, time-dependent pulse fluctuations and phase-jump modulation errors that are typical of other hyper-Ramsey schemes. Several variants of GABRS are explored based on different secondary variables including added relative phase shifts between Ramsey pulses, external frequency-step compensation, and variable second-pulse duration. We demonstrate that a universal anti-symmetric error signal, and hence perfect compensation at finite modulation amplitude, is generated only if an additional frequency-step applied during both Ramsey pulses is used as the concomitant variable parameter. This universal technique can be applied to the fields of atomic clocks, high-resolution molecular spectroscopy, magnetically induced and two-photon probing schemes, Ramsey-type mass spectrometry, and to the field of precision measurements. Some variants of GABRS can also be applied for rf atomic clocks using CPT-based Ramsey spectroscopy of the two-photon dark resonance.

This work was supported by the Russian Scientific Foundation (Project No. 16-12-10147).

References

[1] Ch. Sanner, N. Huntemann, R. Lange, Ch. Tamm, and E. Peik, arXiv:1707.02630 [physics.atom-ph] (2017).

Exploiting coherent fiber links with a Hg optical lattice clock

L. De Sarlo[1], M. Favier[1], V. Cambier[1], J. Calvert[1], C. Guo[1], J. Lodewyck[1], H. Alvarez-Martinez[5], Y. Le Coq[1], R. Le Targat[1], E. Cantin[1], D. Xu[1], O. Lopez[2], A. Amy-Klein[2], G. Santarelli[3], Ch. Chardonnet[2], P. –E. Pottie[1], N. Huntemann[4], C. Sanner[4], R. Lange[4], B. Lipphardt[4], Chr. Tamm[4], E. Peik[4], R. Schwarz[4], A. Al-Masoudi[4], S. Dörscher[4], Ch. Lisdat[4], E. Benkler[4], S. Koke[4], A. Kuhl[4], T. Waterholter[4], G. Grosche[4], and S. Bize[1]

[1]SYRTE, Observatoire de Paris, PSL Research University, CNRS, Sorbonne Université, LNE, Paris, France
[2]LPL, Université Paris 13, Sorbonne Paris Cité, CNRS, Villetaneuse, France
[3]LP2N, UMR 5298 Institut d'Optique Graduate School, CNRS, and Université de Bordeaux, Talence, France
[4]Physikalisch-Technische Bundesanstalt, Braunschweig, Germany
[5]Sección de Hora, Real Instituto y Observatorio de la Armada, San Fernando, Spain

Email: luigi.de-sarlo@obspm.fr

Coherent optical fiber links enable comparisons of remote optical frequency standards over distances of thousands of kilometers, as if they were located in the same room. This technology opens the possibility of greatly enhancing the number and the diversity of optical frequency standard comparisons. In turn, this contributes advancing optical frequency metrology and its applications [1,2].

We will report on experiments exploiting a coherent optical fiber link in conjunction with a Hg optical lattice clock which exemplifies these possibilities. We will describe a remote comparison between a Hg optical lattice clock (operated at LNE-SYRTE) and a single ion optical clock based on the Yb^+ octupole transition [5] (operated at PTB) and Sr lattice clock [2] (also operated at PTB). The remote comparison enables the first direct determination of the $Hg/Yb^+(E3)$ optical frequency ratio and yields Hg/Sr measurements that can be compared to earlier determinations [3,4].

For these long distance optical clock comparisons, we will report stabilities reaching the 1×10^{-17} level. We will present an updated uncertainty budget for the mercury optical lattice clock. In particular, together with differential measurements, the comparison with the more accurate Yb^+ [5] and Sr clocks [2], allowed us to investigate the lattice light shift in mercury with an improved resolution. The knowledge of this effect, predicted to play a significant role in mercury [6,7], is particularly important as otherwise mercury is only weakly impacted by many other systematic effects, such as sensitivity to thermal radiation and stray electric fields.

[1] A. Ludlow *et. al.*, Rev. Mod. Phys. **87**, 637, 2015. https://doi.org/10.1103/RevModPhys.87.637

[2] C. Lisdat *et al.*, Nat. Comm. **7**, 12443, 2016. https://doi.org/10.1038/ncomms12443

[3] T. Yamanaka *et al.*, PRL **114**, 230801, 2015. https://doi.org/10.1103/PhysRevLett.114.230801

[4] R. Tyumenev *et al.*, New J. of Phys. **18**, 113002 2016. https://doi.org/10.1088/1367-2630/18/11/113002

[5] N. Huntemann *et al.*, PRL **116**, 063001, 2016. https://doi.org/10.1103/PhysRevLett.116.063001

[6] H. Katori *et al.*, Phys. Rev. A **91**, 052503, 2015. https://doi.org/10.1103/PhysRevA.91.052503

[7] V. D. Ovsiannikov *et al.,* PRA **93**, 043420, 2016. https://doi.org/10.1103/PhysRevA.93.043420

Preprocessing for fast synchronization of high-stability oscillators disciplined by GNSS 1PPS signal

Paweł Kubczak, Michał Kasznia, Mieczysław Jessa

Faculty of Electronics and Telecommunications,
Poznan University of Technology, Poznań, Poland

Email: pawel.w.kubczak@doctorate.put.poznan.pl

The rubidium oscillators are commonly used as time and frequency sources for many purposes. Their good properties, combined with disciplining by 1 Pulse Per Second (PPS) signal from generally available Global Navigation Satellite Systems (GNSS), give excellent globally available tool for synchronization of many sources. The precise time and frequency are used in many different areas, such as telecommunications, networking, monitoring, navigation, electricity, measurement and control systems.

The goal of this paper is to present a novel algorithm for preprocessing of pulses coming from GNSS and signals produced locally by a rubidium oscillator to reduce synchronization time without changing the main algorithm of the control loop. The characteristic feature of the proposed preprocessing is simultaneous processing of 1 PPS pulses from a GNSS and 10 MHz signal synchronized in the loop.

The preprocessing of 1 PPS pulses includes the outliers rejection procedure, moving average with averaging time adequate to the phase characteristic of 1 PPS pulses provided by a GNSS receiver, and Kalman filtering. We reset also the phase of the feedback signal using FPGA resources and predict the control word based on the knowledge obtained during power-on self-test of the device.

The paper contains the description of the proposed solutions, simulation results performed with MATLAB and the experimental results for three rubidium oscillators with different parameters, coming from different manufactures. The experimental servo-loop consists of a phase detector implemented using FPGA technology, microcontroller realizing control algorithm and providing communication with PC, and rubidium oscillator. The experiments were performed for compact size as well as for chip scale size rubidium oscillators. The influence of the proposed solutions on the synchronization time and the quality parameters MTIE and TDEV were also examined and discussed. A synchronization time of less than three minutes was obtained, after which the signal met the PRC standards. The proposed algorithm is considered a new, effective and simple hardware defined time and frequency source upgrade that addresses the challenges of modern synchronization.

Geometric scale factor stabilization of a large frame Ring Laser Gyroscope

F. Stefani[1,2], N. Beverini[1,2], G. Carelli[1,2], A. Di Virgilio[2], U. Giacomelli[1,2], E. Maccioni[1,2]

[1]Dipartimento di Fisica, Università di Pisa, Pisa, Italy
[2]INFN, Sezione di Pisa, Pisa, Italy

Email: fabio.stefani@unipi.it

Large frame ring laser gyroscopes (RLG), are the most sensitive devices for detecting angular motion, in a very large range of frequency extending from some tens Hz down to μHz. A square RLG (GINGERino) with side of 3.60 m has been installed in the underground Gran Sasso INFN laboratories [1]. In spite of the absence of active control of the geometry, the system shows an excellent long-term stability. In particular, the daily Fourier component, probably related to the tides, is well evident (Fig.1). A second smaller square RLG (GP2, 1.60x1.60 m^2) is operating in the INFN laboratory in Pisa in order to test the long-term stabilization technique of the ring geometry. Indeed, the fluctuation of the geometrical scale factor of the ring resonator is the ultimate limit to the long-term stability for application to Geodesy and Geophysics. In our case (square cavity), the environmental parameters effect on the ring laser beam path stability can be strongly reduced if the two diagonals of the square are constrained to a constant length [2]. Moreover, the knowledge of their absolute values allows the definition of the scale factor that relates rotation speed and Sagnac frequency. The RLG diagonals constitute two Fabry-Perot linear cavities (finesse about 1000, length about 2264 mm), whose resonances are exploited by an external laser diode, stabilized by a He-Ne/I_2 reference laser via injection-locking technique. As shown in fig. 2, we used a double stage locking technique to stabilize the length of the diagonals and to measure their absolute values with an accuracy better than 1 ppm (standard deviation <2μm). The first locking stage cancels out any high-frequency noise by using AOM actuators and slow temperature driven deformations by means of PZT actuators acting on the cavity mirrors. The second locking stage, via EOM devices, allows simultaneous laser frequency f_L locking at an integer n number of FSR (n=3 in the experiment) to perform the absolute length measurement, $L = \frac{C}{2(f_L/3)}$.

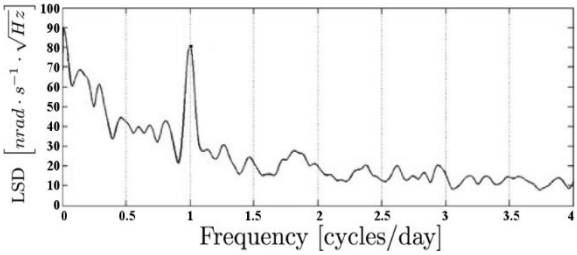

Fig. 1: Power Spectral Density of "GINGERino"

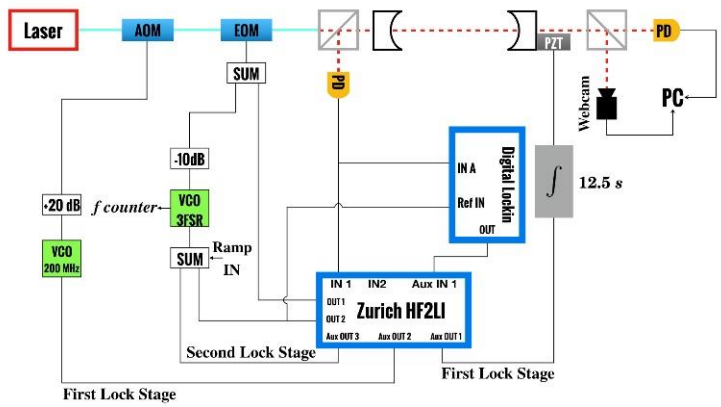

Fig. 2: Locking scheme for one diagonal

References

[1] J. Belfi, et al.: Deep underground rotation measurements: GINGERino ring laser gyroscope in Gran Sasso, Rev Sci Instrum 88, 034502 (2017).

[2] R Santagata, et al.: Optimization of the geometrical stability in square ring laser gyroscopes Class. Quantum Grav. 32 055013 (2015).

High precision test of gravity with the MIGA large scale Atom Interferometer

B. Canuel[1], for the MIGA consortium

[1]LP2N, Laboratoire de Photonique Numérique et Nanosciences, Université Bordeaux-IOGS-CNRS:UMR 5298, rue F. Mitterrand, 33400 Talence, France.

Email: benjamin.canuel@institutoptique.fr

We are building a new, hybrid detector that couples laser and matter-wave interferometry to study sub Hertz variations of the strain tensor of space-time and gravitation [1]. Using a novel approach exploiting a set of atomic interferometers simultaneously manipulated by the resonant optical field of a 200 m cavity, this instrument will allow at the same time a better understanding of the evolution of the gravitational field and a new tool for gravitational waves (GW) detection. This new infrastructure will be embedded into the LSBB underground laboratory, ideally located away from major anthropogenic disturbances and benefitting from very low background noise.

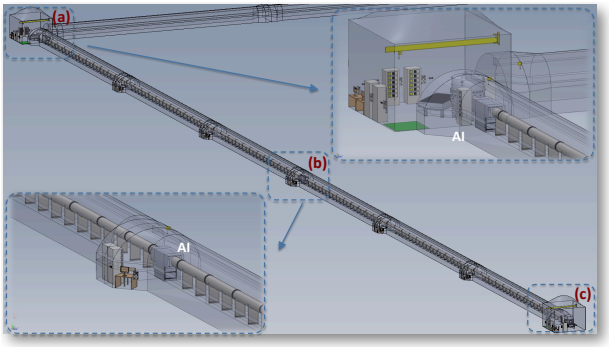

Fig. 1: Scheme of the MIGA antenna at the LSBB laboratory.

Each atomic ensemble of the antenna will be manipulated by cavity enhanced Bragg pulses to create an atom interferometer (AI) that will simultaneously read out motion of the cavity, GW and inertial effects. The use of the spatial resolution offered by the different AIs placed along the cavity will permit to discriminate between these contributions [2]. This will bring to unprecedented sensitivities to gravity gradients fluctuations and open new perspectives for sub Hertz GW detection.

The project is carried out by a consortium that gathers 17 expert French laboratories and companies in atomic physics, metrology, optics, geosciences and gravitational physics, with the aim to build the MIGA infrastructure by 2019. We will present the main objectives of the project, the status of the construction of the instrument and the motivation for the applications of MIGA in GW physics.

References

[1] B. Canuel, S. Pelisson, L. Amand, A. Bertoldi, E. Cormier, B. Fang, S. Gaffet, R. Geiger, J. Harms, D. Holleville, A. Landragin, G. Lefèvre, J. Lhermite, N. Mielec, M. Prevedelli, I. Riou, and P Bouyer, “MIGA: combining laser and matter wave interferometry for mass distribution monitoring and advanced geodesy,” Proceedings of SPIE 9900, Quantum Optics, 990008 (2016)

[2] W. Chaibi, R. Geiger, B. Canuel, A. Bertoldi, A. Landragin, and P. Bouyer, “Low frequency Gravitational Wave detection with ground based Atom Interferometer arrays,” Phys. Rev. D 93, 021101(R) (2016)

Stability analysis and continuous operation of Rb fountains for timescale generation

L. Lorini[1], K. Pavlenko[3], S. Bize[1], B. Desruelle[2], G. Stern[2], I. Doronin[3], Yu. Pavlenko[3], I. Blinov [4]

[1]LNE-SYRTE, Observatoire de Paris, PSL Research University, CNRS, Sorbonne Université, 61 avenue de l'Observatoire, 75014 Paris, France
[2]MUQUANS, Institut d'Optique d'Aquitaine, rue F. Mitterrand, 33400 Talence, France
[3]JSC Vremya-CH, Russia, 603105, Nizhny Novgorod, Osharskaya str., 67
[4]FSUE VNIIFTRI, Russia, 141570, Moscow oblast, Solnechnogorski district, Mendeleevo

Email: lorini@obspm.fr

Two cold rubidium fountains for timekeeping have been realized on request of the FSUE VNIIFTRI. Installed in 2016 [1], they have been optimized for short and long term stability and during 2017 they cumulated several months of continuous, unattended operation.
The design and realization of the two fountains has been the result of a scientific and commercial collaboration among Vremya-CH, MuQuans and SYRTE. They use frequency-doubled fiber telecom lasers for robustness and reliability. The two fountains only differ by the cold atomic source: molasses capture from Rb hot vapor in VerA, molasses capture from a slow beam of cold atoms generated by a 2D-MOT in VerB.
At VNIIFTRI, fountains measure the frequency of an active Hydrogen maser with a built-in extra low noise quartz (model VCH-1003M opt. L from Vremya-CH). As described in [1], the fountain cycles have been optimized for the best short term stability, trading off between detection noise and local oscillator aliased noise.
As the fountains have very low detection noise, the optimized molasses loading times are quite short (150-250 ms). VerB has better short term stability than VerA, taking advantage of the higher molasses loading rate provided by the 2D-MOT cold atom source. The short term performance obtained with VerB ($9.5 \cdot 10^{-14}$ at 1 s) is the state-of-the-art for a fountain using a quartz-filtered H-maser as a local oscillator. In the medium term the stability goes down to $4 \cdot 10^{-16}$ at 1 day. Fountains are running completely unattended, remotely monitored by Vremya-CH, which also takes care of the data management and analysis.

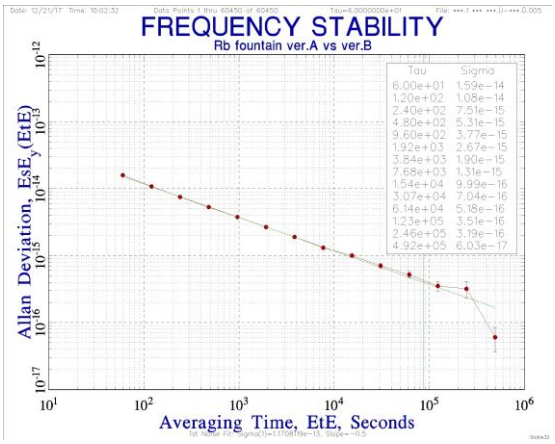

Fig. 1: Stability of VerB vs. VerA frequency difference data, divided by $\sqrt{2}$

During 2017, VerA cumulated several months of operation time while VerB is running continuously since last May. Since last November both the fountains are running at their best performances, measuring the same local oscillator. No statistically relevant frequency drift between the two fountains has been detected. At the epoch of the conference, we expect to have enough data to allow fountain characterization for integration times larger than 10^6, with a potential stability of $1 \cdot 10^{-16}$ at 16 days.

References

[1] L. Lorini, K. Pavlenko, S. Bize, B. Desruelle, G. Stern, I. Doronin, Yu. Pavlenko and S. Donchenko, "Preliminary stability analysis of Rb fountains for timescale generation", in 2017 Joint Conference of the European Frequency and Time Forum and International Frequency Control Symposium (EFTF/IFCS), 2017, pp. 317-321.

Novel Methods for CEO Stabilization in Fiber Laser Frequency Combs

K. Gürel, S. Hakobyan, V. J. Wittwer, N. Jornod, S. Schilt, T. Südmeyer

Laboratoire Temps-Fréquence, Université de Neuchâtel, CH-2000 Neuchâtel, Switzerland

Email: kutan.guerel@unine.ch

Combining compactness, low-cost and ease of construction, fiber lasers have become the prominent choice of optical frequency combs in many applications. They have shown remarkable improvement of their noise properties by combining a low-noise oscillator with high bandwidth actuators for frequency stabilization. Here we present two novel techniques for the phase stabilization of the carrier envelope offset (CEO) frequency of fiber lasers.

Our proof-of-principle demonstrations are based on an Yb-doped fiber laser mode-locked by nonlinear polarization rotation (NPR). It operates at a repetition rate above 125 MHz and produces pulses with a spectral width of more than 26 nm. The output is amplified in an Yb-doped fiber and sent to a grating compressor. The amplified and compressed signal has up to 500-mW average power in sub-100-fs pulses. The pulses are sent to a photonic-crystal fiber for supercontinuum generation followed by an *f*-to-2*f* interferometer for CEO detection.

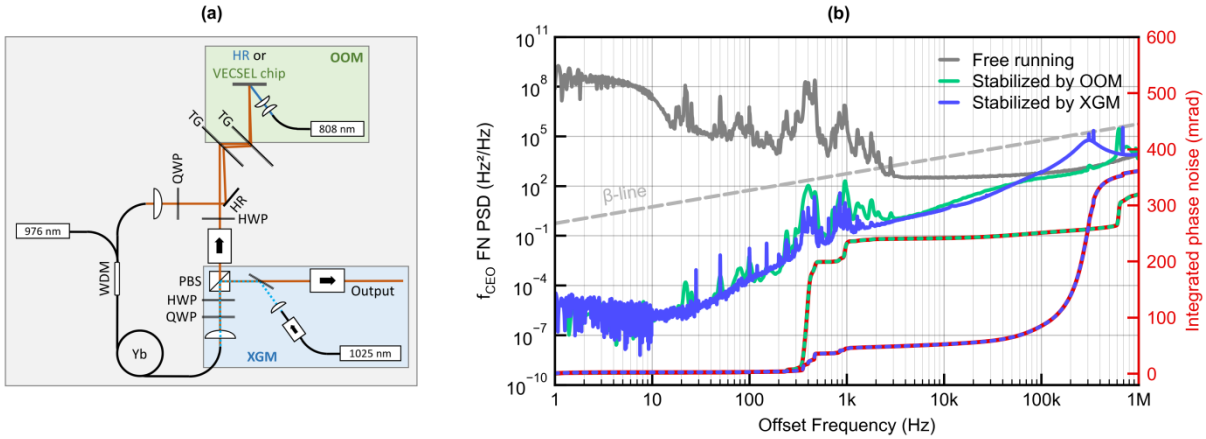

Fig. 1: (a) Schematic figure of the NPR mode-locked fiber laser implemented with either OOM (green box) or XGM (blue box) with an HR at the VECSEL chip position. (WDM: wavelength division multiplexer, QWP: quarter waveplate, HWP: half waveplate, PBS: polarization beam splitter, TG: transmission gratings, HR: highly reflective mirror). (b) Single sideband frequency noise (FN) power spectral density (PSD) of the CEO beat while free running (gray), stabilized by OOM (green), stabilized by XGM (blue) and corresponding integrated phase noise as a function of the upper cut-off frequency.

The detected CEO frequency is stabilized by either of the two methods as depicted in Fig. 1 (a). The first method is through opto-optical modulation (OOM) [1] of a vertical external-cavity surface-emitting laser (VECSEL) chip by a laser diode at 808 nm, optionally inserted in the cavity as a folding mirror. The second method modulates the intra-cavity power of the laser by cross gain modulation (XGM) [2] using a laser diode emitting at 1025 nm. The CEO frequency is tightly locked by both methods, reaching feedback bandwidths of up to 600 kHz [Fig. 1 (b)]. In both cases, we achieved a residual integrated phase noise of the CEO frequency of less than 360 mrad (integrated from 1 Hz to 1 MHz), which originates to a significant extend from mechanical noise in the range of tens of Hz to a few kHz in the laser.

We will present the properties and discuss the high potential of the two new methods for stabilizing fiber laser frequency combs.

References

[1] M. Hoffmann, S. Schilt, and T. Südmeyer, Opt. Express **21**, 30054–30064, (2013).
[2] K. Obermann, S. Kindt, D. Breuer, and K. Petermann, J. Lightwave Tech. **16**, 78-, (1998).

Analysis of Intersatellite Frequency Transfer

Bethany Kroese[1], Gabriele Giorgi, and Christoph Günther

German Aerospace Center, Institute of Communications and Navigation, Oberpfaffenhofen, Germany

Email: Bethany.Kroese@dlr.de

Highly accurate time and frequency synchronization is crucial for the advancement of a variety of research fields including navigation, geodesy, and relativity. The ever-increasing improvements in clock technology enable more precise investigations in each of these fields. These opportunities in turn place stricter demands on coordination and dissemination of timescales. Within the field of space-based time and frequency transfer, intersatellite links are of high interest for GNSS clock synchronization [1]. In addition to synchronizing clocks, these links can also improve orbit determination through precise ranging and diversification of spatial observations. Transmissions resolve time and frequency information (i.e. clock offsets and drifts) by modeling orbit and relativistic delays. In order to fully capitalize on the stability of next-generation space clocks, relativity corrections must be described to a high level of precision and orbital positions must be accurately known. Specifically, relativistic models must consider contributions up to order $1/c^3$ [2].

The frequency of a received signal is influenced by the location of the transmitter and receiver as well as by its propagation path. The goal of this study is to quantify the impact of various relativistic terms on such a scheme. A set of links are simulated using relativistic models and stochastic clock noise [3,4]. The aim is to determine which relativistic corrections must be included to reach a desired accuracy. Recent proposals for space clocks, such as DLR's molecular Iodine frequency standard (6×10^{-15} at 1 s), establish the baseline for stability requirements [5]. As a case study, bidirectional links are generated using the nominal Galileo orbit between adjacent satellites in the same orbital plane. Relativity corrections with increasing levels of fidelity are applied to each transmission. Each relativistic correction requires specific knowledge of the satellites' orbital parameters (i.e. position, velocity, etc.). The influence of each parameter on the accuracy of the recovered clock offsets is analyzed. Since satellites' positions and velocities are themselves uncertain, they are subjected to a set of errors in order to perform a sensitivity analysis.

References

[1] F. A. Fernández, "Inter-satellite ranging and inter-satellite communication links for enhancing GNSS satellite broadcast navigation data", Advances In Space Research, vol. 47, p. 786-801, 2011.

[2] L. Blanchet, C. Salomon, P. Teyssandier and P. W. Daly, "Relativistic theory of time and frequency transfer to order c-3", Astron. Astrophys, vol. 370, p. 320-329, 2001.

[3] C. Zucca and P. Tavella, "The Clock Model and Its Relationship with the Allan and Related Variances", IEEE Transactions on Ultrasonics, Ferroelectrics, and Frequency Control-vol. 52, p. 289-296, 2005.

[4] N. Ashby, "Relativity in GNSS", In: Ashtekar A., Petkov V. (eds) Springer Handbook of Spacetime, Springer, Berlin, Heidelberg, 2014.

[5] T. Schuldt, K. Döringshoff, E. V. Kovalchuk, A. Keetman, J. Pahl, A. Peters, and C. Braxmaier, "Development of a compact optical absolute frequency reference for space with 10−15 instability," Appl. Opt. vol. 56, p. 1101-1106, 2017.

A Recursive Clock Anomalies Detector with Double Exponential Smoothing

Valerio Formichella[1], Patrizia Tavella[1,2]

[1]Department of Physical Metrology, INRiM, Turin, Italy
[2]Time Department, BIPM, Sèvres, France

Email: v.formichella@inrim.it

Space qualified atomic clocks are one of the fundamental components of Global Navigation Satellites Systems. It is well known that such clocks suffer from different types of anomalies [1], like phase and frequency jumps, frequency drift changes and variance changes. These anomalies can affect the quality of the navigation message and the eventual navigation performance, unless they are rapidly corrected or at least notified to the users.

Therefore, the automated on-board detection of clock anomalies is a topic of great interest and different solutions have been proposed, e.g. in [2], [3] and [4]. In particular, the frequency jump detector proposed in [5] is based on a recursive exponential filter, which is particularly useful for on-board applications since it has softer requirements in terms of memory and computational power. Indeed, most of the detectors are based on the processing of a batch of past data, requiring a certain effort in terms of CPU and memory consumption which is not always possible on board of a spacecraft, whereas a recursive detector needs much less data and operations. Here, we propose a generalization of the recursive detector presented in [5], based on double exponential smoothing [6], which properly takes into account the frequency drift and also detects drift and variance changes. We also test the detector on simulated an real data: Fig. 1 shows an example of the detector performance, where a frequency jump, a drift change and a variance change have been properly detected.

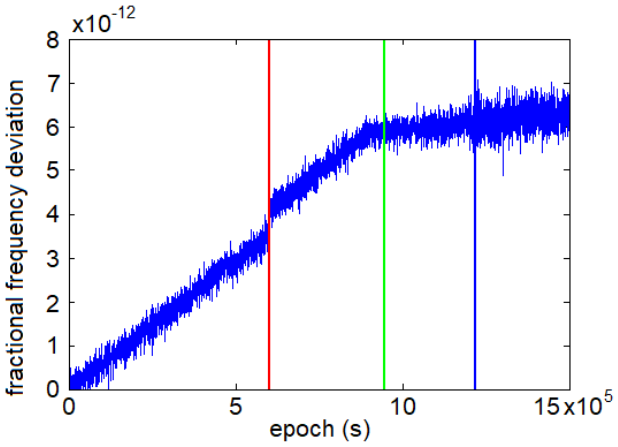

Fig. 1: An example of detected frequency jump (red line), drift change (green line) and variance change (blue line), on simulated frequency data.

References

[1] A. Cernigliaro, G. Fantino, I. Sesia, P. Tavella, L. Galleani, "Non-stationarities in space clocks: investigations on experimental data", in Proc. EFTF 2014.

[2] L. Galleani, P. Tavella, "Robust detection of fast and slow frequency jumps of atomic clocks", IEEE Trans. Ultrason., Ferroelect., Freq. Control, 64, 2 (2017), pp. 475-485.

[3] Q. Wang, P. Rochat, "An anomaly clock detection algorithm for a robust clock ensemble", in Proc. 41st PTTI.

[4] X. Huang, H. Gong, G. Ou, "Detection of weak frequency jumps for GNSS onboard clocks", IEEE Trans. Ultrason., Ferroelect., Freq. Control, 61, 5 (2014), pp. 747-755.

[5] Q. Wang, F. Droz, P. Rochat, "Robust clock ensemble for time and frequency reference system", in Proc. 2015 EFTF-IFCS.

[6] R. G. Brown, "Exponential smoothing for predicting demand", Arthur D. Little, Inc., 1956.

The important phase phenomena in quantum frequency standard

Wei Zhou, Qianqian Guo,Shen Zhang,Wei Shang,Shihao Zhao

Dept. of Measurement and Instrument, Xidian University, Xi'an, 710071, China

Abstract

Phase is a very important parameter in frequency signal. Atomic clock and optical frequency standard as the important frequency standard, clarifying and dealing with the phase phenomena in them is very important for ensuring and improving the performance of the clock. But due to the lack of understanding for the complex clock phase relationship, much phase information is not fully used. Only the frequency processing can be used. Its result makes the FM white noise be introduced in the clock output and the important technology index of clock --frequency stability changing with time be transformed into a typical rules of $1/\sqrt{\tau}$. Therefore, it is of great value to analyze the law of phase change in the atomic clock. In the typical passive atomic clock, there are frequency and phase of locked VCOCXO, the frequency and phase of low frequency modulation signal of excitation signal, the periodic variation of transition probability of atomic energy level transition under the action of excitation signal in the physical part as well as the phenomenon in the variation. In the background of these interlaced frequencies, especially the phase relation, we realize the phase control of the output frequency of quantum frequency standard, the frequency of VCOCXO with the reference frequency of physical transition. What we can use here is: 1. On the phase problems such as the updating of concepts and processing methods. 2. Phase processing can be achieved on the basis of frequency processing with phase continuum conforming to certain conditions. 3. In passive atomic clock the occurrence of the atomic energy level transition in an interval, such as the maximum probability phenomenon can express the accurate frequency deviation of VCOCXO. 4. The phase change recovery of output signal and the control information are realized on the basis of the three-dimensional frequency difference--occurrence time--voltage (current). 5. The degree of accuracy of the transition. 6. How to use the stability of the physical frequency discrimination curve to obtain the higher precision of the maximum probability point of the atomic energy level transition--frequency difference information.

The comprehensive understanding of the complex phase relationship in the passive atomic clock is conducive to the realization of the control of the clock output in the minimum processing noise and high resolution. With the aid of the above analysis, the new phase control can be realized and the development of new atomic clock technology will also appear.

Reference:

[1] China Patent: 201710718224.X, A new method regarding digital phase locking to passive atomic frequency standard.

High accuracy continuous time transfer with GPS IPPP and T2L2

Julia Leute[1,2], Gérard Petit[1], Pierre Exertier[3], Etienne Samain[3], Daniele Rovera[2], Pierre Uhrich[2]

[1]Bureau International des Poids et Mesures, 92312 Sèvres, France
[2] LNE-SYRTE, Observatoire de Paris, PSL Research University, CNRS, Sorbonne Universités, UPMC Univ. Paris 06, 75014 Paris, France
[3] University Nice Sophia Antipolis, CNRS, IRD, Observatoire de la Côte d'Azur, Géoazur UMR 7329, 06560 Valbonne, France

Email: julia.leute@bipm.org

We present a comparison of time transfer results over European baselines obtained with two space-based techniques: Precise Point Positioning with integer ambiguity resolution (IPPP) using GPS satellites [1] and Time Transfer by Laser Link (T2L2) using the low orbiting satellite Jason-2. The data was obtained in a 2-month experiment in 2013 for baselines between Paris, Herstmonceux and Grasse. Previously, a sub-nanosecond consistency between GPS dual frequency code and T2L2 Common View (CV) was reported for these baselines [2]. In this analysis GPS IPPP time transfer is compared to high-rate T2L2 data.

The IPPP technique is based on dual-frequency GPS phase measurements and therefore does not provide the absolute value of the time comparison. However, it provides a continuous time link as long as the GPS stations at both sites are continuously operating. It has a time transfer stability of a few tens of picoseconds up to several weeks of averaging time.

The T2L2 technique is based on laser telemetry technology and dedicated space instruments. The uncertainty for CV time transfer between remote sites is below 140 ps [3], an order of magnitude improvement over GPS code-based methods. A drawback of the T2L2 technique is its dependence on weather conditions which does not allow for a continuous time transfer.

We find that the comparison of 30-s IPPP link results to the closest 1-s T2L2 data points has a standard deviation below 100 ps for all three baselines. The good agreement between both methods allows for the identification of outlier passes in the T2L2 data, which could help to improve the handling of the raw T2L2 data.

These results provide the basis for a continuous time transfer technique with accuracy at the 100 ps level for baselines over which T2L2 can operate in CV as envisioned in [4]. Occasional T2L2 measurements provide the absolute time difference with a high accuracy and a continuous IPPP link maintains the accuracy for weeks or months between calibrations.

References

[1] G. Petit et al., "1×10^{-16} frequency transfer by GPS PPP with integer ambiguity resolution", Metrologia, 52, 301-309, 2015.

[2] P. Exertier et al., "Sub-ns time transfer consistency: a direct comparison between GPS CV and T2L2", Metrologia 53, 1395-1401, 2016.

[3] E. Samain et al., "Time transfer by laser link: a complete analysis of the uncertainty budget", Metrologia, 52, 423-432, 2015.

[4] P. Guillemot et al., "Combination of T2L2 and GPS-CP Data: Towards an improvement of Time Transfer accuracy", Proceedings of the IFCS/EFTF 2013, 372-375, 2013.

Fiber-based Traceability Chain for Molecular Spectrosopy at 5.8 µm

C. Clivati[1], S. Borri[2,3], D. Calonico[1], P. Cancio Pastor[2], D. D'Ambrosio[2,4], P. De Natale[2,3], G. Insero[2,3], M. Inguscio[2], F. Levi[1], G. Santambrogio[1,2,3]

[1]Time and Frequency Programme, Istituto Nazionale di Ricerca Metrologica, Turin, Italy
[2]Istituto Nazionale di Ottica-CNR, dip. Fisica e Astronomia Università di Firenze, European Laboratory for Non-Linear Spectroscopy LENS, Sesto Fiorentino, Italy
[3]Istituto Nazionale di Fisica Nucleare, Sez. di Firenze, Sesto Fiorentino, Italy
[4]Politecnico di Torino, Torino, Italy

Email: c.clivati@inrim.it

Mid-infrared is the typical absorption range of fundamental rovibrational transitions in molecules. Thanks to their rich internal structure and to the strength of intermolecular fields, molecular spectroscopy is an extremely powerful tool for a number of fundamental physics tests. The probing of transitions at these wavelengths is performed with Quantum Cascade Lasers (QCLs), which cover the full 3-25 µm range providing considerable power up to several hundreds of mW; however, their intrinsic linewidth does not allow precision spectroscopy. Frequency referencing of such lasers is hence obtained by nonlinear conversion techniques to bridge the gap with the near-infrared domain, where absolute traceability is provided by optical combs, and narrow linewidth optical references are available [1].

We report on the development of a metrological chain that provides absolute traceability to primary frequency standards for precision spectroscopy at the laboratories of the National Institute of Optics (INO), Sesto Fiorentino, Italy. The cryogenic Cs fountain ITCsF2, maintained at the Italian National Metrology Institute (INRIM), is disseminated to INO using a 642-km long phase-stabilized optical fiber link, delivering an ultrastable, absolutely-referenced optical carrier at 1.5 µm. In turns, the radiation is used at INO as a reference for a near-IR optical comb, to which two lasers at 1064 nm and 1301 nm are locked using the transfer-oscillator scheme. A quantum cascade laser at 5.8 µm is then locked to the difference frequency signal generated by the two IR lasers on an orientation-patterned GaP crystal.

In this approach, only a small part of the available QCL power is used for referencing, leaving most of it available for spectroscopy; in addition, the high band edge of orientation-patterned GaP makes it suitable for pumping with 1 µm lasers, with considerable advantages in terms of efficiency and spectral purity. The resulting scheme can be easily adapted to cover the full range up to 10 µm. This chain was exploited for spectroscopy of a vibrational transition on a beam of highly-excited, metastable CO molecules. The $6 \cdot 10^{-11}$ relative uncertainty on the line center determination was mainly due to systematic effects on the molecular sample, while the QCL frequency uncertainty was less than $2 \cdot 10^{-14}$ [2]. At the conference, we will report on the detailed realization of this metrological chain, and review the experimental results we obtained on CO spectroscopy.

This work was supported by INFN under the SUPREMO project, and by EMPIR-15SIB05-OFTEN, which has received funding from the EMPIR programme co-financed by the Participating States and from the European Union's Horizon 2020 research and innovation programme.

References

[1] B. Argence et al. "Quantum cascade laser frequency stabilization at the sub-Hz level," Nature Phot. Vol. 9, p. 456, 2015.

[2] G. Insero et al., "Measuring molecular frequencies in the 1–10µm range at 11-digits accuracy," Sci. Rep. Vol. 7, 12780, 2017.

First frequency comparison of a bosonic magnesium lattice clock based on the $^1S_0 - {}^3P_0$ transition

Dominika Fim[1], *Steffen Rühmann*[1], *Klaus Zipfel*[1], *Nandan Jha*[1], *Steffen Sauer*[1], *Waldemar Friesen-Piepenbrink*[1], *Wolfgang Ertmer*[1], *Ernst M. Rasel*[1], *Thomas Waterholter*[2], *Alexander Kuhl*[2], *Sebastian Koke*[2], *Gesine Grosche*[2], *Ali Al-Masoudi*[2], *Sören Dörscher*[2], and *Christian Lisdat*[2]

[1]Institut für Quantenoptik, Leibniz Universität Hannover, Germany

[2]Physikalisch- Technische Bundesanstalt Braunschweig, Germany

Email: fim@iqo.uni-hannover.de

We present the first frequency measurement of a lattice clock based on magnesium atoms. The most important characteristics of magnesium related to clock operation are the low black body radiation sensitivity and its low mass. The low mass allows us to investigate tunnelling effects in shallow lattices which will be a crucial topic for lattice clock operation in space. So far, the shallow lattice depth caused a spectral broadening of or to clock transition to a linewidth in the kHz scale, limiting the clock‘s accuracy and stability.

After implementing a new lattice laser system, we were able to perform spectroscopy in a 50 E_r deep lattice resulting in a clock transition linewidth of 50 Hz reaching the highest Q value for magnesium until now. With the reduced linewidth, we characterized all relevant effects influencing a lattice clock based on bosonic atoms like for example the 2nd order Zeeman shift caused by the magnetic field required for mixing $^3P_0$ and $^3P_1$ [1] resulting in a frequency shift uncertainty in 10^{-15} regime. After the error analysis a frequency comparison between the stationary Sr lattice clock [2] of the group of C. Lisdat at the PTB via a fiber link was done. The stabilization of the 73 km link between Hannover and Braunschweig as well as parts of the transfer beat measurement setup was provided by the group of G. Grosche [2,3,4].

This work was supported in part by Deutsche Forschungsgemeinschaft (DFG) within QUEST, Center for Quantum Engineering and Space-Time Research and by DFG through CRC 1128 geo-Q (project A03). Moreover, we acknowledge financial support from DFG Research Training Group (Graduiertenkolleg) 1729, the Marie Curie Initial Training Network FACT (ITN-FACT) Program, call FP7-PEOPLE-2013-ITN and the DLR BOOST project and A. Bauch for providing the passive H-Maser.

References

[1] A. V. Taichenachev et al., PRL 96, 083001 (2006).

[2] S. Falke et al., New J. Phys. 16, 073023 (2014).

[3] G. Grosche, Opt. Lett. **39**, 2545 (2014).

[4] T. Waterholter et al. „Regional Multipoint Frequency Dissemination for the Optical Fiber Link PTB – Hannover“, EFTF-IFCS2017

Analysis and compensation of polarization in an optical frequency transfer through a fiber communication network

P. O. Hedekvist, L. Weddig and S-C. Ebenhag

Department of Measurement Science, Research Institutes of Sweden, Borås, Sweden
E-mail: per.olof.hedekvist@ri.se

The time and frequency laboratory at RISE in Borås, Sweden, which are realizing the UTC(SP) timescale, is connected to the fiber optics research laboratory at Chalmers University of Technology through an active WDM communication network. It is the Swedish University Network (SUNET) and is a modern network, where the connected sites have access to 100 Gbit/s on a single wavelength through multi-level amplitude and phase modulation in combination with utilization of both polarizations. The link between the two laboratories is implemented mainly as a designated wavelength in the WDM network, with a few km of dark fiber on each side, with a total distance of approximately 60 km. As it all operates in an active data communication network with amplifiers, the transfer must be implemented in duplex fiber, meaning that the light runs in separate parallel fibers to the university lab and back.

The present analysis is performed on the output of the returned signal at RISE, where the light have been transmitted 120 km, and it has been previously observed that the polarization of the light varies with the 50 Hz frequency harmonics of the power grid[1], and that the variation during one 20 ms period is substantial. With an optical interrogation of heterodyne beating with a local oscillator laser, this polarization variation will deteriorate the detection of the frequency difference.

This extended analysis evaluates the polarization variation using two different polarization analyzers, with different sampling frequencies. The fastest analyzer is also utilized as the detection unit for a digital polarization tracker, where the output polarization is steered to be at a linear state. The purpose of the polarization tracking, and the parameters it will be evaluated against, are the applicability of compensating the polarization variations in optical frequency tracking through deployed and active WDM networks.

[1] S.C. Ebenhag, M. Zelan, P.O. Hedekvist, M. Karlsson and B. Josefsson, “Coherent Optical Two-Way Fre-quency Transfer in a Commercial DWDM Network”, The Institute of Navigation Precise Time and Time Interval (PTTI) Systems and Applications Meeting, pp. 1116–120 2016

Reducing blackbody radiation shift uncertainty in optical lattice clocks

Piotr Ablewski, Marcin Bober, Michał Zawada

Institute of Physics, Faculty of Physics, Astronomy and Informatics,
Nicolaus Copernicus University, Grudziądzka 5, 87-100 Toruń, Poland

Email: piotra@fizyka.umk.pl

Blackbody radiation shift uncertainty is one of the most significant contribution in accuracy budgets of modern optical atomic clocks [1, 2]. Known approaches to the reduction of this contribution assumes shielding atoms from the hot environment by storing them in cryogenically cooled cold-fingers [3], covering the internal parts of vacuum chamber with ultra-high emissivity coatings [4] or directly measuring the temperatures visible for atoms [2,5].

Our approach is to simulate the conductive heat transfer in optical clock system and calculate the radiative heat transfer between vacuum parts and atoms stored in optical lattice. By measuring the temperatures of external surfaces of parts we are able to simulate the temperature gradients and estimate the temperatures of the interior of the clock's chamber. With the knowledge of the emissivity coefficients of the materials used in the construction of optical clocks' set-ups [6] we are able to calculate the radiative heat transfer from the clock's chamber surfaces to the atoms. Calculations can be performed in two complementary ways: using finite element method (FEM) numerical simulation or analytically. Analytical solutions are much more complicated and can be performed only for limited number of geometries, but in case of possibility of high accuracy uncertainty estimations, they are much more desirable than the numerical ones. We present recent results of the calculations of blackbody radiation shift in strontium optical lattice clock performed analytically, supported by numerical FEM simulation.

References:

[1] B. J. Bloom et al., "An optical lattice clock with accuracy and stability at the 10^{-18} level", Nat., vol. 506, p. 71-75, 2014.

[2] T. L. Nicholson et al., "Systematic evaluation of an atomic clock at 2×10^{-18} total uncertainty", Nat. Comm., vol. 6, 2015.

[3] M. Ushijima et al., "Cryogenic optical lattice clocks", Nat. Photon. Vol. 9, p. 185-189, 2015.

[4] K. Beloy et al., "Atomic Clock with 1×10^{-18} Room-Temperature Blackbody Stark Uncertainty", Phys. Rev. Lett., vol. 113, 2014.

[5] M. Doležal et al., "Analysis of thermal radiation in ion traps for optical frequency standards", Metrologia, vol. 52, 2015.

[6] P. Ablewski et al., "Emissivities of vacuum compatible materials: towards minimizing blackbody radiation shift uncertainty in optical atomic clocks at room temperatures", in preparation

Analysis of optical atomic clocks readouts aimed on searches for dark-matter signatures

B. Zjawin[1], P. Ablewski[1], K. Beloy[2], S. Bilicki[1,3], M. Bober[1], R. Brown[2], R. Ciuryło[1], R. Fasano[2], H. Hachisu[4], T. Ido[4], J. Lodewyck[2], A. Ludlow[2], W. McGrew[2], P. Morzyński[1,4], D. Nicolodi[2], M. Schioppo[2], M. Sekido[4], R. Le Targat[3], P. Wcisło[1], P. Wolf[3], X. Zhang[2] and M. Zawada[1]

[1]Institute of Physics, Faculty of Physics, Astronomy and Informatics, Nicolaus Copernicus University, Grudziadzka 5, 87-100 Torun, Poland
[2]National Institute of Standards and Technology, 325 Broadway, Boulder, CO 80305, USA
[3]SYRTE, Observatoire de Paris, PSL Research University, CNRS, Sorbonne Universités, UPMC Univ. Paris 06, LNE, 61 avenue de l'Observatoire, 75014 Paris, France
[4]National Institute of Information and Communications Technology 4-2-1 Nukuikitamachi, Koganei, 184-8795 Tokyo, Japan

Email: 279076@fizyka.umk.pl

Astrophysical observations indicate that the Universe contains five times more dark matter than standard matter, however its nature still remains an unsolved mystery. Dark matter candidates like topological defects and oscillating massive scalar fields can be searched for by a single optical atomic clock [1, 2]. We describe the optical atomic clocks readouts analysis and provide a recipe for analysing data from transcontinental network made of already existing optical atomic clocks. We describe, basing on Very-Long-Baseline Interferometry (VLBI) procedures [3], how to correlate the data obtained from already operating optical atomic clocks. We discuss methods of computing cross-correlation of more than two readouts. We present how to obtain topological defect velocity space distribution from the data (Fig. 1). Furthermore, we discuss how to filter the readouts in order to restrict desirable frequency range and improve already existing limits on oscillating massive scalar fields couplings to standard matter. We also show how to analyse the data from a network of many clocks to exceed previously reported limits on such couplings.

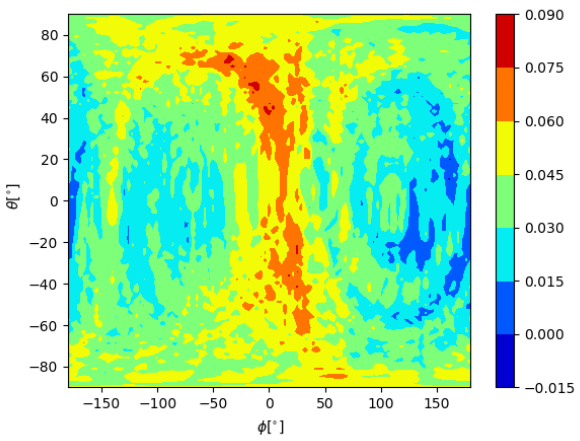

Fig. 1: Expected distribution of averaged cross--correlation values of signals from eight clocks placed on different continents. When a velocity of a defect is assumed, its direction can be estimated (here shown in spherical coordinates).

References

[1] A. Arvanitaki, J. Huang, and K. Van Tilburg, "Searching for dilaton dark matter with atomic clocks", Phys. Rev. D, vol. 91, p. 015015, 2015.
[2] P. Wcisło, P. Morzyński, M. Bober, A. Cygan, D. Lisak, R. Ciuryło, and M. Zawada, "Experimental constraint on dark matter detection with optical atomic clocks", Nat. Astro., vol. 1, p. 0009, 2016.
[3] A. Whitney, "Precision geodesy and astrometry via Very-Long-Baseline Interferometry", Ph.D. thesis, Massachusetts Institute of Technology, 1974.

Self-controlled Offset-free Er:Fiber Frequency Combs

A. Liehl[1], D. Fehrenbacher[1], P. Sulzer[1], A. Leitenstorfer[1], and D. V. Seletskiy[1,2]

[1]Department of Physics and Center for Applied Photonics, University of Konstanz, 78457 Konstanz, Germany

[2]Department of Engineering Physics, Polytechnique Montréal, Quebec H3T 1J4, Canada

Email: andreas.liehl@uni-konstanz.de

Amplitude-to-phase noise coupling within nonlinear optical media complicates the stabilization of fiber-based frequency combs, i.e., of its repetition rate f_{rep} and carrier-envelope offset (CEO) frequency [1]. In contrast to active electronic feedback schemes, passive CEO elimination based on ultrabroadband difference frequency generation (DFG) has recently been demonstrated in Er:fiber frequency combs [2]. Since only f_{rep} remains to be stabilized, this method substantially increases the simplicity and long-term reliability of the system. The drawback is a broadened optical linewidth owing to intra-cavity Gordon-Haus jitter [3] which coherently multiplies during the nonlinear frequency conversion [2]. In this work, we address this issue by transferring the outstanding noise properties of the Er:fiber master oscillator to the DFG comb. Due to the unique nature of phase noise conversion in DFG combs, this task can be straightforwardly accomplished via feedback from a free-running CEO beat note. This strategy also eliminates the need for ultralow-noise external optical single-line references (SLRs).

Fig. 1a outlines the scheme for the self-controlled stabilization of our DFG comb. Out-of-loop (OOL) detection is obtained via superposition of a comb mode with an SLR. The optical phase noise is dramatically suppressed (Fig. 1b) by feedback to the pump power of the master oscillator and an extra-cavity electro-optic modulator (EOM), leading to strong narrowing of the optical linewidth to < 15 kHz (Fig. 1c). The present linewidth of this self-controlled comb is largely limited by the noise of the SLR (grey), as determined from its low-frequency overlap with the stabilized DFG comb (blue), while remaining above the β-separation line (pink dashed) [4]. Slow drifts of f_{rep} are additionally corrected by means of a slow control loop (Fig. 1a), suitable for direct Doppler-free locking to an optical two-photon transition in ^{85}Rb [2].

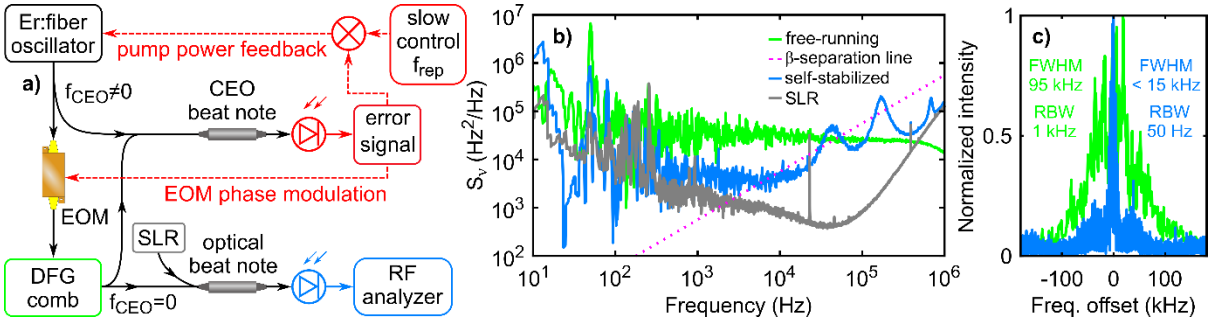

Fig. 1: a) Setup for self-controlled optical linewidth narrowing. Black: fiber connections; red: feedback electronics; blue: analysis. b) Frequency noise of free-running (green) and narrowed (blue) optical mode; SLR noise (grey) and β-separation line (pink). c) RF power spectra of optical beat notes.

References

[1] J. Kim and Y. Song, "Ultralow-noise mode-locked fiber lasers and frequency combs: principles, status, and applications", Adv. Opt. Photon., vol. 8, p. 465-540, 2016, and refs. therein.

[2] D. Fehrenbacher, et al., "Free-running performance and full control of a passively phase-stable Er:fiber frequency comb", Optica, vol. 2, 917-923, 2015.

[3] J. P. Gordon and H. A. Haus, "Random walk of coherently amplified solitons in optical fiber transmission", Opt. Lett., vol. 11, p. 665-667, 1986.

[4] G. Di Domenico, et al., "Simple approach to the relation between laser frequency noise and laser line shape", Appl. Opt., vol. 49, p. 4801-4807, 2010.

First Experiments on Application of Rb Fountain Frequency Standards for TA(SU) Time Scale Maintenance

Blinov I., Boiko A., Kosheliaevskii N. and Kupalova O.
Department of Metrology for Time and Space, VNIIFTRI
Mendeleevo, Moscow region, Russia

At last PTTI meeting, PTTI'17, we mentioned that VNIIFTRI has got four Rb fountain frequency standards [1], which run as frequency standards, not clocks. These instruments are not intended for secondary presentation of time unit the second SI. These are indeed very stable frequency reference without frequency drift inherent, for example, to H-masers. During last year output frequency of these standards has been calibrated against operational CsF02 primary fountain frequency standard and now one may use these instruments as time and frequency unit keepers.

This report will present very preliminary results of the first experiments on application of Rb fountain frequency standards for maintenance the national atomic time scale TA(SU). According internal regulation TA(SU) is independent atomic time scale with the unit of time the second SU, reproduced by operational primary Cs fountain frequency standards. This time scale by-turn is maintained by ensemble of continuously operating high stable hydrogen masers. On other hand, each H-maser demonstrate more or less predictable frequency drift the value of which may be quite comparable to daily H-maser frequency stability. That is why one has times to times re-evaluate H-maser output frequency parameters. The more often one will re-evaluate H-maser output frequency parameters the more stable and accurate (in sense unit of time the second SU) time scale will be produced.

The key problem is interruptible Cs primary fountain frequency standard mode of operation. Typically, Cs primary fountain frequency standard produces two or three sessions per month, but sometimes happens gaps for a some months. In such cases availability of more or less continuously operating stable and none drifting frequency reference such as Rb fountain frequency standards may be a solution of the problem.

The paper will present comparisons of some scenarios of TA(SU) maintenance: a. purely based on H-maser ensemble and primary Cs fountain frequency standards data and b. based on H-maser ensemble and single/ensemble of Rb fountain frequency standards data.

References

[1] Blinov I., Domnin Yu., Donchenko S., Goncharov A., Kosheliaevskii N., Naumov A., Slyusarev S., Russian State Time and Frequency Standard Laboratory Activities and Updates, Proceedings of the 48th Annual Precise Time and Time Interval Systems and Applications Meeting, (PTTI 2017), January 30-February 02, 2017, Hyatt Regency Monterey, Monterey, California, USA.

Beyond the first frequency measurement of the Magnesium lattice clock at the IQ Hannover

Waldemar Friesen-Piepenbrink[1], Steffen Rühmann[1], Dominika Fim[1], Klaus Zipfel[1], Nandan Jha[1], Steffen Sauer[1], Sebastian Häfner[2], Thomas Legero[2], Wolfgang Ertmer[1], Uwe Sterr[2], and Ernst Rasel[1]

[1]Institut für Quantenoptik, Leibniz Universität Hannover, Hannover, Germany
[2]Physikalisch-Technische Bundesanstalt, Braunschweig, Germany

Email: friesen@iqo.uni-hannover.de

Magnesium has turned out to be a promising candidate for an atomic clock due to its small black body radiation shift. Deploying the strongly forbidden $^1S_0 \rightarrow {}^3P_0$ transition, made accessible by magnetic field induced spectroscopy, we have set up an optical lattice clock based on bosonic ^{24}Mg.

Due to its low mass, high laser intensities are required to achieve trap depth to sufficiently suppress tunnelling between adjacent lattice sites. Improvements in the lattice setup have led to trap depth up to 50 E_R, which enabled us to perform spectroscopy of a 50 Hz linewidth and characterize the systematics of the clock with an uncertainty in the 10^{-15} regime. In this context it has shown that we are mainly limited due to tunneling and therefore the lattice power and clock laser inhomogeneity.

Here we report on our efforts to further reduce the linewidth of the magnesium clock transition primarily addressing the limitations mentioned above. Particularly we are working on increasing the lattice power and reducing the inhomogeneity of the probe laser field. To go to lower linewidth as well as to further reduce the probe laser AC Stark shift, it is important to increase the spectroscopy time which requires a laser with a longer coherence time. For this purpose, we are setting up a resonator of 48 cm length with crystalline mirror coatings in cooperation with the PTB at 1560 nm. After characterizing the resonator at the PTB, it will be used as an ultra-stable reference for our clock laser in IQ Hannover by transferring the frequency stability to it via a frequency comb. In this contribution we will report on our ongoing work on these lines.

This work was supported in part by Deutsche Forschungsgemeinschaft (DFG) within QUEST, Center for Quantum Engineering and Space-Time Research. Moreover we acknowledge financial support from DFG Research Training Group (Graduiertenkolleg) 1729, the Marie Curie Initial Training Network FACT (ITN-FACT) Program, call FP7-PEOPLE-2013-ITN and the DLR BOOST project.

Operation of the fibre links PTB–UoS and NPL–LPL in the first trinational fibre link clock-comparison campaign

S. Koke[1], J. Kronjäger[2], E. Cantin[3], O. Lopez[3], A. Kuhl[1], T. Waterholter[1], E. Benkler[1], A. Amy-Klein[3], P.-E. Pottie[4], and G. Grosche[1]

[1] Physikalisch-Technische Bundesanstalt, Bundesallee 100, 38116 Braunschweig, Germany
[2] National Physical Laboratory, Hampton Road, Teddington, Middlesex, TW11 0LW, UK
[3] Laboratoire de Physique des Lasers, Université Paris 13, CNRS, Villetaneuse, France
[4] LNE-SYRTE, Observatoire de Paris, PSL Research University, CNRS, Sorbonne Universités, UPMC Univ. Paris 06, 61 avenue de l'Observatoire, 75014 Paris, France
Email: sebastian.koke@ptb.de

Comparing optical clocks built by different national metrology institutes (NMIs) at the level of their uncertainty is an important step towards the redefinition of the SI second. After the first international comparisons between two NMIs [1,2], the joint fibre link NPL–SYRTE–PTB via LPL and University of Strasbourg (UoS) has been created. The first fibre-based clock comparison including seven optical clocks from all three connected NMIs was carried out in June 2017. Complementing a separate contribution on the LPL–SYRTE–UoS link, we here report the status and performance of the sublinks NPL–LPL and PTB–UoS during the 5-week campaign and elucidate the clock-data sharing framework based on the transfer oscillator concept [3].

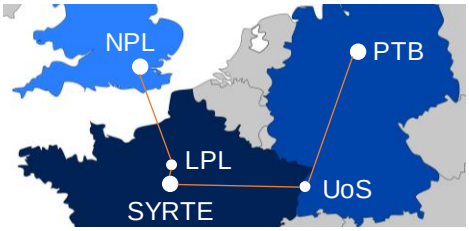

Fig. 1: Schematic of the joint fibre link

The 760 km long link NPL–LPL, consisting of a pair of dark fibres, employs a hybrid two-way layout [4] and shows a 1 s-instability of $<2\times10^{-15}$. Unfortunately, an inaccessible source of back reflections on one of the fibres limits the maximum achievable integration time in out-of-loop characterizations. The uptime of the phase-stabilization was 84% within this campaign. Out-of-loop characterization in the 700 km long dark-fibre link PTB–UoS is achieved via the cascaded, individually stabilized up- and downlink [5]. In this campaign, 72% of all possible data points were validated to contribute a statistical and systematic uncertainty $<6\times10^{-18}$, resulting in ~2 million valid 1 s-data points.

With the new capability to perform multi-NMI comparisons, we are confident that the fibre links PTB–UoS and NPL–LPL will serve to further pursue the path towards a redefinition of the SI second.

This work was supported by the EU program EMPIR in project 15SIB05 (OFTEN), the French Equipex REFIMEVE (ANR-11-EQPX-0039) and CNRS with Action Spécifique Gravitation, Réferences, Astronomie, Métrologie (GRAM), and by DFG through CRC 1128 geo-Q (project A03)

References:

[1] C. Lisdat *et al.*, "A clock network for geodesy and fundamental science," Nat. Commun. 7, 12443, 2016.
[2] P. Delva *et al.*, "Test of Special Relativity Using a Fiber Network of Optical Clocks", Phys. Rev. Lett. 118, 221102, 2017.
[3] H. Telle, B. Lipphardt, J. Stenger, "Kerr-lens, mode-locked lasers as transfer oscillators for optical frequency measurements", Appl. Phys. B 74, 1, 2002.
[4] J. Kronjäger *et al.*, "Towards an International Optical Clock Comparison Between NPL and SYRTE Using an Optical Fiber Network", EFTF 2016
[5] S. Koke *et al.*, "Performance of a Fibre Link Combining Fibre Brillouin Amplification with a Repeater Laser Station", EFTF-IFCS 2017

Operational transfer of spectral purity at LNE-SYRTE

H. Álvarez-Martínez[1], Y. Le Coq[2], R. Le Targat[2]

[1]Sección de Hora, Real Instituto y Observatorio de la Armada, San Fernando, Spain
[2]SYRTE, Observatoire de Paris, PSL Research University, CNRS, Sorbonne Université, LNE, Paris, France

Email: Hector.Alvarez-Martinez@obspm.fr

Optical frequency combs and ultra-stable lasers are key elements opening the way to optical clocks at the 10^{-18} level. The spectral purity of ultra-stable lasers built at convenient wavelengths, e.g. in the telecom domain, can be transferred to target metrological wavelengths via the Transfer Oscillator Technique [1]. The noise introduced needs to be assessed in order to ensure both the stability and the accuracy of the process.

Here we present a scheme transferring the 5×10^{-16} fractional frequency stability from a 1542 nm ultra-stable master laser to 698 nm and 1062 nm slave lasers which correspond to the clock transitions for the optical lattice clocks with Sr and Hg (after frequency quadrupling) at SYRTE [2]. To this end, we use an Er-doped fiber comb locked in the optical domain to the 1542 nm laser in order to reach the "narrow-linewidth regime". It performs the Transfer Oscillator Method, with dedicated branches (independent optical amplifiers) both for the Sr and the Hg clock lasers. We will report on preliminary results on the single branch approach (beats with the master and with the slave lasers formed with the same EDFA), and compare them to the multi-branch approach (beats formed with independent EDFAs).

We will also evaluate the accuracy of comb-based measurements by performing synchronous frequency measurements of the metrological lasers (698 nm and 1062 nm) with the Er-doped fiber laser comb on one hand, and with a Titanium-Sapphire laser based comb on the other hand. We will describe the principle of the operation, quantify the noise sources and discuss the difficulties to circumvent in order to reach the 10^{-17} range.

Finally, we will present a study of the global accuracy of the frequency chain, with a focus on the possible bias introduced by counters from different manufacturers, or by digital synthesizers used for phase-lock loops or for demodulating signals.

References

[1] H. R. Telle, B. Lipphardt and J. Stenger, "Kerr-lens, mode-locked lasers as transfer oscillators for optical frequency measurements", Appl. Phys., vol. B74, p. 1-6, 2002.

[2] D. Nicolodi, B. Argence, W. Zhang, R. Le Targat, G. Santarelli and Y. Le Coq, "Spectral purity transfer between optical wavelengths at the 10^{-18} level", Nature Photonics, vol. 8, p. 219-223, 2014.

Passive Utilization of the TWSTFT Technique

Carsten Rieck[1], Per Jarlemark[1], Kenneth Jaldehag[1]

[1]Measurement Science and Technology, RISE Research Institutes of Sweden, Borås, Sweden

Email: carsten.rieck@ri.se

Two Way Satellite Time and Frequency Transfer (TWSTFT) is an established time transfer method for both continental and inter-continental baselines. Despite the current performance problems, TWSTFT is the most accurate of the long distance methods used today and can be considered the backbone of international time keeping as it links more than half of all the clock weight in TAI. However, only a few nations deploy the technique for national links.

TWSTFT is an active technique with transmission at both ends of a link [1]. It can be passively exploited by orbit determination of the used satellite. In a passive configuration a receiver observes, possibly multiple, codes sent by the active users of a TWSTFT-network. Common view observations of the same signals by a pair of observers can be used to compare their local clocks. Similar to GNSS, the users need to know their local coordinates and the orbit of the satellite in order to reduce the measurements by the geometry. As the orbit is usually poorly known, it is essential to establish an infrastructure that provides the users with satellite ephemerides and appropriate correction models. A passive use of TWSTFT will for example enable us to increase the number of measurements without increasing the noise level on the transponder and thus improve the current poor bandwidth utilization in the scheduled peer-to-peer measurement configuration. It will also reach out to a new group of users, both commercial and scientific, which will benefit from current and future developments of TWSTFT. NMIs will be able to offer an independent method for robust and resilient distribution of their national time scales.

In this paper we report the advances in methodology achieved since the initial study present in [2]. Now the orbit determination allows the concurrent assimilation of both ranging and regular measurements in a single step and detects orbit maneuvers close the steering events. We also exploit inter-transponder measurements, as available in the bi-transponder configuration between the US and the European network using TELSTAR 11N. This dramatically improves the observational geometry and increases the east-west accuracy of the orbit. The real-time capable calculations result in extended Kepler descriptions of the satellite orbit, which can be used to estimate ranges from the satellite to a passive user at arbitrary station positions and arbitrary epochs. Residual ranges of the position estimates are well below 1 m allowing potential time transfer with a few nanoseconds uncertainty (u_a). For the PTB-SP baseline, using the full potential of the European network for orbit determination, we observe typical standard deviations of about 700 ps in bias-removed differences to the filtered active TW link.

The paper also suggests a design of a passive ground station based on software defined receivers.

References

[1]: D. Piester et al., ”Time transfer with nanosecond accuracy for the realization of International Atomic Time”, Metrologia 45 (2008) 185–198 doi:10.1088/0026-1394/45/2/008
[2]: Rieck et al. “Utilizing TWSTFT in a Passive Configuration”
Precise Time and Time Interval Meeting 2017 (PTTI), Monterey, CA, USA, 2017

Ramsey-mode Rb cell clock demonstration with a 3D-printed microwave cavity

William Moreno[1], Christoph Affolderbach[1], Anton E. Ivanov[2], Tomislav Debogovic[3], Matthieu Pellaton[1], Anja K. Skrivervik[2], Emile de Rijk[3], and Gaetano Mileti[2]

[1] Laboratoire Temps-Fréquence (LTF), Institut de Physique, University of Neuchâtel, 2000 Neuchâtel, Switzerland

[2] Microwave and Antenna Group (MAG), École Polytechnique Fédérale de Lausanne, 1015 Lausanne, Switzerland

[3] SWISSto12 SA, EPFL Innovation Park Building L, 1024 Ecublens, Switzerland

Email: christoph.affolderbach@unine.ch

During the past years, significant progress has been made in the development of compact and high-performance Rb-type atomic frequency standards, notably using the Pulsed Optically Pumped (POP) scheme [1]. Recently our teams showed that state-of-the-art clock stabilities can also be achieved with POP clocks based on highly compact microwave cavities using a loop-gap-type electrode configuration [2, 3]. Here we exploit one further step towards the simplification of compact and high-performance atomic clocks, by demonstrating clock operation using a microwave cavity manufactured by 3D-printing (additive manufacturing).

The 3D-printed microwave cavity, based on the design presented in [2], is manufactured by stereolithography of a polymer, followed by a proprietary metal coating process [4]. The critical six-electrode configuration is 3D-printed in one single monolithic block, which greatly simplifies the cavity assembly. The polymer material used allows a significant reduction in the cavity mass, which is advantageous in view of mobile or space applications.

We report on the evaluation of the 3D-printed cavity. From the full Zeeman spectrum measured we find a field orientation factor [3] of 0.98, showing an excellent uniformity of the microwave field, slightly superior to our conventional cavities [2]. Clear Rabi oscillations and high-contrast Ramsey fringes (Fig. 1) observed indicate a good homogeneity of the longitudinal field component H_z. The suitability of the cavity for POP clock operation is demonstrated by a measured clock short-term stability of $2.2\times10^{-13}\ \tau^{-1/2}$, on the same level as with a conventional cavity [2]. Stability limits for the clock will be discussed.

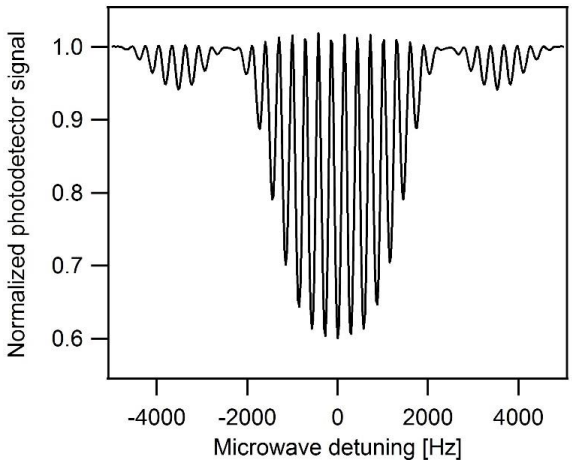

Fig. 1: Ramsey signal of the clock transition observed with the 3D-printed cavity prototype.

References

[1] S. Micalizio, C.E. Calosso, A. Godone, F. Levi, Metrologia, 49, pp. 425-436 (2012).
[2] S. Kang, M. Gharavipour, C. Affolderbach, F. Gruet, G. Mileti, J. Appl. Physics 117, 104510 (2015).
[3] C. Stefanucci, T. Bandi, F. Merli, M. Pellaton, C. Affolderbach, G. Mileti, A. K. Skrivervik, Rev. Sci. Instrum. 83, 104706 (2012).
[4] A.I. Dimitriadis, T. Debogovic, M. Favre, M. Billod, L. Barloggio, J.P. Ansermet, E. de Rijk, Proc. IEEE 105 (4), pp. 668–676 (2017).

Microwave field amplitude stabilization using Ramsey spectroscopy signal

Michele Gozzelino[1,2], Salvatore Micalizio[2], Filippo Levi[2], Aldo Godone[2], Claudio E. Calosso[2]

[1]Departmento of Electronics and Communication, Politecnico di Torino, Torino, Italy
[2]INRIM, Istituto Nazionale di Ricerca Metrologica, Torino, Italy

Email: michele.gozzelino@polito.it

We present a method to actively stabilize the amplitude of the microwave field which constitutes the probe for many state-of-the-art compact atomic clocks. The method applies to clocks working in pulsed operation, specifically with a Ramsey scheme [1].

The proposed technique relies on information directly extracted from the clock atomic signal, as it computes the gradient in the two variables (amplitude and frequency) of the probe field, instead of differentiating solely the frequency response, as in usual operation. Indeed, as shown in Fig. 1, the atomic signal coming from the Ramsey technique presents a local minimum for zero frequency detuning from the atomic resonance but also for an offset of the field amplitude with respect to the desired set point ($\pi/2$ pulse area). This approach provides confidence in the knowledge of the true field-amplitude level at atoms location, comparing to other method involving the measurement of the power before the coupling circuit or of the power reflected by the cavity. Notably this method does not require additional hardware and very few modification in the configuration of the apparatus.

Furthermore, we demonstrate the need or advantage in stabilizing the microwave field amplitude in order to reach 10^{-15} stability with compact clocks. Particular focus is given to the cavity-pulling effect as it is often the main contributor to the sensitivity of such devices to microwave field amplitude fluctuations. Within this frame, the proposed method is proven to be resilient also against detrimental aging of the experimental setup, which again can turn into long-term instability.

Measurements and experimental implementation mainly refer to the Pulsed Optically Pumped clock developed at INRIM [2], but the technique can be straightforwardly applied to cold-atom compact clocks.

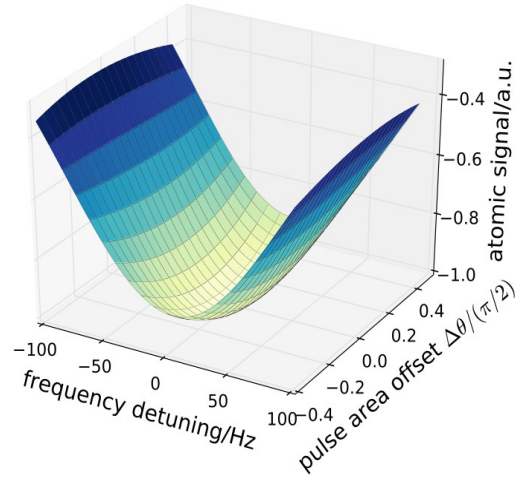

Fig. 1: Atomic signal as a function of the two variables: 1) frequency offset from the hyperfine transition. 2) Rabi pulse area (amplitude times duration) offset from pi/2. Experimentally and in the calculations the duration is fixed and only the amplitude is modulated.

References

[1] J. Vanier and C. Audoin, *The Quantum Physics of Atomic Frequency Standards*, vol. 2. Philadelphia: Adam Hilger, 1989.

[2] S. Micalizio, C. E. Calosso, A. Godone, and F. Levi, *"Metrological characterization of the pulsed Rb clock with optical detection,"* Metrologia, vol. 49, no. 4, p. 425, 2012.

Optical frequency transfer across the sea: two case studies

Cecilia Clivati[1], Filippo Levi[1], Giuseppe Marra[2], Alberto Mura[1], Anna Tampellini[2,3], André Xuereb[4], Davide Calonico[1]

[1]Time and Frequency Programme, Istituto Nazionale di Ricerca Metrologica, Turin, Italy
[2]National Physical Laboratory, Teddington, UK
[3]Department of Electronics and Communications, Politecnico di Torino, Turin, Italy
[4]Department of Physics, University of Malta, Msida, Malta

Email: c.clivati@inrim.it

Optical frequency transfer over optical fibers has proved to exceed the performances of satellite techniques by several orders of magnitude over thousands of kilometers [1]. However, these techniques require bi-directional propagation of the light and cannot be used when unidirectional optical amplifiers, normally placed every 70-80 km along the link, cannot be by-passed, such as in intercontinental links.

Frequency transfer techniques over fiber are based on the transmission of an ultrastable optical carrier over a standard telecommunication cable. Any changes in the fiber length due to temperature variations and acoustic noise must be detected and actively canceled. This is done through an interferometric scheme, where the round-trip radiation is compared to that injected into the fiber [2]. Unidirectional amplifiers are by-passed and bidirectional amplifiers are used instead. An alternative approach consists in sending two coherent lasers signals in opposite directions, so that the fiber-induced phase noise on the two is passively rejected in a synchronous comparison [3]. In both approaches, the ultimate link performances depend on the intrinsic fiber noise and on its length.

We report, for the first time to our knowledge, on the realization of optical frequency transfer over submarine telecommunication cables and on the characterization of the fiber-induced noise in such system. We performed the experiment on two different testbeds located in the Mediterranean Sea of lengths 98 km and 116 km, making use of a transportable high-finesse cavity system at 1542 nm. Peculiar effects were identified in one of the testbeds, which simultaneously carries high-voltage electricity. Nevertheless, and in both cases, the observed phase noise is several orders of magnitude lower than in terrestrial links, potentially making them suitable for the implementation of ultra-long-haul optical links. We show that the low level of environmental noise measured on submarine fiber cables could enable the comparison of optical clocks over submarine links without requiring bidirectional propagation of light.

INRIM acknowledges for funding the Italian Ministry of Education, University and Research (MIUR) through the Progetti Premiali 2015 program (LABMED projects). We acknowledge funding by the Research, Innovation and Development Trust of the University of Malta and by the Department for Business, Energy and Industrial Strategy (BEIS) as part of the UK National Measurement System programme.

References

[1] Ch. Lisdat et al., “A clock network for geodesy and fundamental science,” Nat. Comm. Vol. **7,** 12443, 2016.

[2]W-K. Lee et al., “Hybrid fiber links for accurate optical frequency comparison,” Appl. Phys. B vol. 123:161, 2017.

[3] A. Tampellini et al., “Effect of a timebase mismatch in two-way optical frequency transfer,” Metrologia Vol. 54, 805, 2017

Telecomm laser standard for time and frequency transfer

Hrabina Jan, Pravdova Lenka, Cizek Martin, Cip Ondrej

Department of Coherence Optics, Institute of Scientific Instruments,
Czech Academy of Sciences, Kralovopolska 147, 61264 Brno, Czech Republic

Email: hrabina@isibrno.cz

The technology development of dissemination of accurate time and high-stable frequencies over optical fiber links allows not only to realize precise measurements between scientific institutes and metrological laboratoires, but it also opens new posibilities and applications for using of novel specialized sensors in industry. The remote calibration of interrogators of Fiber Bragg Grating strain sensors networks is one of important examples. A 306 km long optical fiber link operated between ISI CAS Brno and CESNET Prague [1] uses an internet communication fiber where a DWDM window of 1540-1546 nm is dedicated for the coherent transfer and 1PPS signal. This contribution describes the development and resulted parameters of the optical frequency standard operated at 1540.6 nm wavelength, which will serve as the laser source for demanded coherent transfer and communication [2].

The erbium doped fiber laser source with very narrow linewidth (below 100 Hz) and output optical power of ~20 mW is equipped with external erbium doped fiber amplifier (EDFA, P_{out} ~100 mW) and easy to operate frequency stabilization setup based on method of saturated spectroscopy in isotopically pure acetylene gas ($^{13}C_2H_2$, its absorption spectrum overlaps the dedicated transfer band). The detection of hyperfine lines of the absorption gas (filled in 50 cm long fused silica made absorption cell) is done by simple third harmonic technique. Thanks to its simple opto-mechanical setup, the system is very robust and can be independtly operated without any adjustment for several months.

The relative frequency stability of the stabilized system was tested by frequency beat-note measurement between the developed laser source and H-maser referenced optical frequency comb. The resulted frequency stability exhibits 1e-12 level / 1 s integration time, with minimum of 8e-14 for 512 s integration time. Potential improvement represented by prelocking of the laser to ultra-stable optical cavity (short-term) and better environmental influences protection (long-term), is in actual progress. The subject of presented work also covers measurement of the stability of the stabilized optical fiber link between both facilities (ISI-CESNET).

Acknowledgement
The research was supported by Grant Agency CR, project GA15-18430S. The infrastructure for the research was funded by Ministry of Education, Youth and Sports CR, projects LO1212, CZ.1.05/2.1.00/01.0017, and by Academy of Sciences CR, project RVO:68081731.

References

[1] J. Vojtech et al., “Joint accurate time and stable frequency distribution infrastructure sharing fiber footprint with research network”, Opt. Eng., vol. 56(2), 027101, 2017.

[2] M. Cizek et al., “Transfer of Stable Optical Frequency for Sensors Networks via 306 km Optical Fiber Link”, EFTF2016 Conference, York, UK, 2016.

Two-branch fiber links for international clock networks

Dan Xu[1], Etienne Cantin[1,2], Florian Frank[1], Nicolas Quintin[2], Frédéric Meynadier[1], Philip Tuckey[1], Anne Amy-Klein[2], Olivier Lopez[2], and Paul-Eric Pottie[1]

[1] LNE-SYRTE, Observatoire de Paris, PSL Research University, CNRS, Sorbonne Universités, UPMC Univ. Paris 06, 61 avenue de l'Observatoire, 75014 Paris, France
[2] Laboratoire de Physique des Lasers, Université Paris 13, CNRS, Villetaneuse, France
Email: paul-eric.pottie@obspm.fr

Comparisons of clocks through fiber links at the continental scale have become a reality in Europe [1-3]. The challenge is now to combine several coherent fiber links to build a clock network, with the means of comparison making a negligible contribution to the uncertainty compared to the resolution of the clocks. This is a key step towards a new definition of the SI second based on optical frequency standards and opens novel opportunities for stringent tests of fundamental physics [3-5].

These prospects rely on the ability to realize a multi-branch fiber network. This requires delicate control of many experimental aspects. In this contribution, we will report on the specific problems encountered and the solutions developed when implementing a two-branch fiber link, as part of a wider concatenation of links between NMIs in Europe.

We will focus our contribution to the frame of the recent campaign of comparisons between NPL, SYRTE and PTB, for which we used only one laser source as a seed for two links. We will describe our experimental arrangement and discuss the optical phase relationship between a reference plane and the stabilized points of the two links. We will also describe how the connections to international links are implemented at LPL and at University of Strasbourg. We will report at the conference on more than one month of simultaneous operation of our dual links, with a combined uptime of more than 90%, and a stability and accuracy at the level of 5×10^{-20} or below.

We will also discuss the need for synchronization and RF services, both to meet the high accuracy goal of international clock comparisons and the needs of non-NMI sites. We will present solutions based on White-Rabbit and/or GPS disciplined local oscillators that we have implemented, opening new opportunities for time and RF standard dissemination.

This work represents a decisive step towards the realization of a robust fiber network for clock comparisons, contributing to progress along the roadmap towards the redefinition of the SI second.

References

[1] C. Lisdat *et al.*, "A clock network for geodesy and fundamental science" Nat. Commun. 7, 12443, 2016
[2] P. Delva *et al.*, "Test of Special Relativity Using a Fiber Network of Optical Clocks", Phys. Rev. Lett. **118**, 221102, 2017
[3] J. Guéna *et al.*, "First international comparison of fountain primary frequency standards via a long distance optical fiber link", Metrologia 54 (3), 2017
[4] A. Hees *et al.*, Phys. Rev. Lett. **117**, 061301, 2016
[5] N. Huntemann *et al.*, "Improved Limit on a Temporal Variation of *mp*/*me* from Comparisons of Yb+ and Cs Atomic Clocks", Phys. Rev. Lett. **113**, 210802 , 2014

A Simple High-Performance Remote-Maser Concept

Thomas Fordell, Anders Wallin

VTT Technical Research Centre of Finland Ltd, Centre for Metrology MIKES, Espoo, Finland
Email: thomas.fordell@vtt.fi

Due to their low phase noise and predictable long term behavior, active hydrogen masers are widely used in very-long baseline interferometry and in time keeping. Unfortunately, masers are expensive, bulky and their environment needs to be actively controlled in order to reach ultimate performance; therefore, stable means of time and frequency distribution are needed.

PTP White Rabbit [1] is finding wide-spread usage in time and frequency dissemination. Currently the best performance WR-devices reach 2E-12 at 1 s being limited by the internal phase meter and transceiver interfacing implemented on commonly available FPGAs. Maser-like performance can be achieved, e.g., using the ELSTAB technique [2], which uses a pair of dedicated, matched delay lines for phase compensation. Unfortunately, due to the limited range of phase compensation, fiber spools with fixed delays are needed to be switched in and out, complicating the system in long-haul links.

Unlimited phase compensation suitable for long-haul frequency transfer can be obtained using RF frequency mixers [e.g. 3-6]. Here we report on a simple RF mixing scheme to be used for distributing the 100 MHz signal from a hydrogen maser to the nearby Metsähovi Geodetic Research Station and Radio Observatory. The test setup uses 40 km of spooled fiber and standard telecom SFP DWDM transceivers for the electrical-to-optical and optical-to-electrical conversion.

Preliminary results are shown in Fig. 1 where the signals have been divided down to 10 MHz in order to be compatible with the used Symmetricom 3120A phase meter. Note that the shown result includes not only the link but also noise from the measurement setup. Extension to simultaneous data and time transfer will also be discussed.

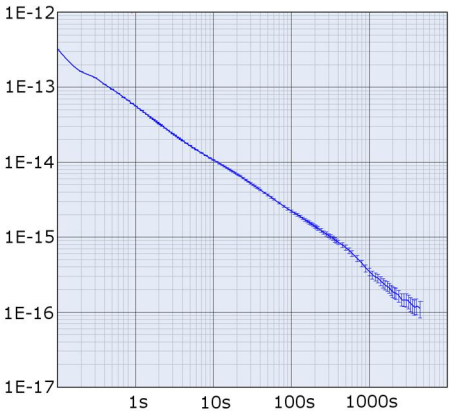

Fig. 1: Allan deviation for frequency transfer over 40-km of spooled fiber (5 Hz bandwidth). The result includes contributions from the reference and the measurement setup.

References

[1] M. Lipinski, et al., “White rabbit: A PTP application for robust sub-nanosecond synchronization,” in Proc. IEEE Int. Symp. Precis. Clock Synchronizat. Meas. Control Commun. (ISPCS), 2011, pp. 25–30
[2] P. Krehlik et al., "ELSTAB - Fiber-Optic Time and Frequency Distribution Technology: A General Characterization and Fundamental Limits", IEEE Trans. Instrum. Meas. 63, 993 (2016).
[3] L. E. Primas et al., “Stabilized fiber-optic frequency distribution system,” The Telecommunications and Data Acquisition Progress Report TDA PR 42-97, 88-97 (1989).
[4] F. Narbonneau et al., “High resolution frequency standard dissemination via optical fiber metropolitan network”, Rev. Sci. Instrum. 77, 064701 (2006).
[5] Y. He et al., Stable radio-frequency transfer over optical fiber by phase-conjugate frequency mixing”, Opt. Express 21, 18754 (2013).
[6] B. Wang et al., “Square Kilometre Array Telescope—Precision Reference Frequency Synchronisation via 1f-2f Dissemination”, Sci. Reports 5, 13851 (2015).

Micro-integrated ultra-narrow linewidth diode laser module with resonant optical feedback from a monolithic cavity

Max Schiemangk[1], Bassem Arar[1], Ahmad Bawamia[1], Heike Christopher[1], Mandy Krüger[1], Christian Kürbis[1], Wojciech Lewoczko-Adamczyk[1,2], Christoph Pyrlik[1], Robert Smol[1], Andreas Wicht[1], Achim Peters[1,3], Günther Tränkle[1]

[1] Joint Lab Laser Metrology, Ferdinand-Braun-Institut (FBH), Leibniz-Institut für Höchstfrequenztechnik, Berlin, Germany

[2] *present address:* Abt. SIIT/Optical Interconnection Technology, Fraunhofer-Institut für Zuverlässigkeit und Mikrointegration (IZM), Berlin, Germany

[3] Optical Metrology Group, Department of Physics, Humboldt-Universität zu Berlin, Berlin, Germany

Email: max.schiemangk@fbh-berlin.de

Semiconductor laser technology is a promising alternative to other laser technologies, e.g. solid state lasers, for employment in coherent optical communication [1] as well as in fundamental physics applications [2]. Being compact, robust, energy-, and cost-efficient these lasers fulfill the key requirements for deployment in the field. At the Ferdinand-Braun-Institut we have developed a versatile technology platform for micro-integration of semiconductor chips and optics [3].

However, monolithic diode lasers typically suffer from poor spectral stability. Different concepts have been developed to overcome this issue, i.e. to reduce the diode laser's frequency noise. Here, we present the employment of our technology platform for micro-integration of a diode laser with an external cavity for resonant optical feedback. In this setup a distributed feedback (DFB) diode laser is coupled to a monolithic confocal cavity [4]. The resonant feedback leads to a significant reduction of the frequency noise by more than 4 orders of magnitude (see Fig. 1).

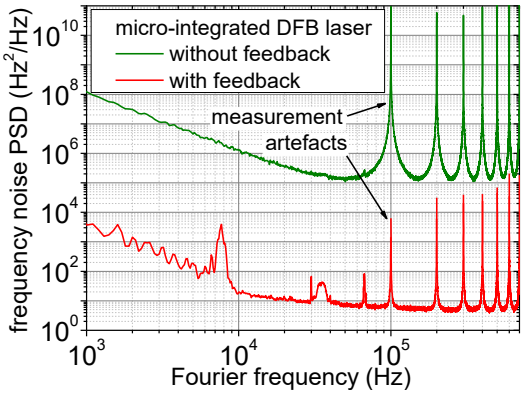

Fig. 1: Frequency noise PSD of DFB laser and ultra-narrow linewidth laser module.

Furthermore, we give an outlook on the transfer of this external cavity laser concept to an extended cavity diode laser module, which in addition to the resonant cavity utilizes an external grating in order to suppress coupling of roundtrip phase and frequency-selective element.

References

[1] S. Spießberger *et al.*, "Micro-integrated 1 Watt semiconductor laser system with a linewidth of 3.6 kHz," Opt. Express 19, 7077, 2011.

[2] V. Schkolnik *et al.*, "A compact and robust diode laser system for atom interferometry on a sounding rocket," Appl. Phys. B Lasers Opt. 122, 217, 2016.

[3] A. Wicht *et al.*, "Narrow linewidth diode laser modules for quantum optical sensor applications in the field and in space," in Proc. SPIE, Components and Packaging for Laser Systems III 10085, 100850F, 2017.

[4] W. Lewoczko-Adamczyk *et al.*, "Ultra-narrow linewidth DFB-laser with optical feedback from a monolithic confocal Fabry-Perot cavity," Opt. Express 23, 9705–9709, 2015.

Optical-to-RF Frequency Division for Ultra-low Noise Microwave Generation Using a Transfer Oscillator Method

Pierre Brochard, Stéphane Schilt, Thomas Südmeyer

Laboratoire Temps-Fréquence, Université de Neuchâtel, CH-2000 Neuchâtel, Switzerland

Email: pierre.brochard@unine.ch

Microwave signals with the lowest phase noise and highest relative frequency stability have been generated to-date by frequency division of an ultra-stable laser (USL) using an optical frequency comb (OFC). The traditional method consists in tightly locking one mode of the OFC to the USL, leading to a low phase noise of the comb repetition rate f_{rep} that essentially corresponds to the down-scaled laser noise. This approach requires a fast actuator for the optical lock of the OFC, which makes the system fairly complex and more costly. Furthermore, the achieved performance directly depends on the properties of this lock.

Here, we show a proof-of-principle experiment of ultra-low noise microwave generation realized in a different approach. Optical-to-RF frequency division is achieved with an OFC used as a transfer oscillator, which circumvents the demanding optical lock. This attractive method can be implemented with any type of frequency comb (free-running or only weakly locked) without stringent requirement on fast actuators and high bandwidth stabilization loops. The implemented scheme was inspired by a method that we previously developed to characterize the noise properties of the carrier-envelop offset frequency f_{CEO} in an OFC without directly detecting it by traditional *f*-to-2*f* interferometry [1]. We performed an electronic division of the USL frequency down to 15 GHz by using an appropriate combination of beat signals with the OFC [see Fig.1(a)], in which the comb noise (from both f_{CEO} and f_{rep}) is eliminated to a high degree in the final output signal. Our proof-of-principle demonstration was implemented using a 1557-nm USL and a commercial Er:fiber comb that has only a slow piezo-electrical transducer (PZT) as actuator for the stabilization of $f_{rep} \approx 250$ MHz. Some preliminary results are shown in Fig. 1(b). The achieved phase noise perfectly overlaps the noise obtained with an optical lock of the OFC (implemented here via the PZT) at low Fourier frequencies, while it is reduced by orders of magnitude at higher frequencies (out of the PZT bandwidth). So far we have only one ultra-low-noise microwave signal available, so that its noise characterization is limited by the instrumental noise floor, despite the use of long cross-correlation times. We are currently building a second similar RF chain to produce a distinct ultra-low noise signal to enable direct comparison. With this method that does not require an optical lock of the OFC, a single comb can be used for the independent generation of the two signals (from two different USLs), which is not feasible by the traditional method with an optical lock.

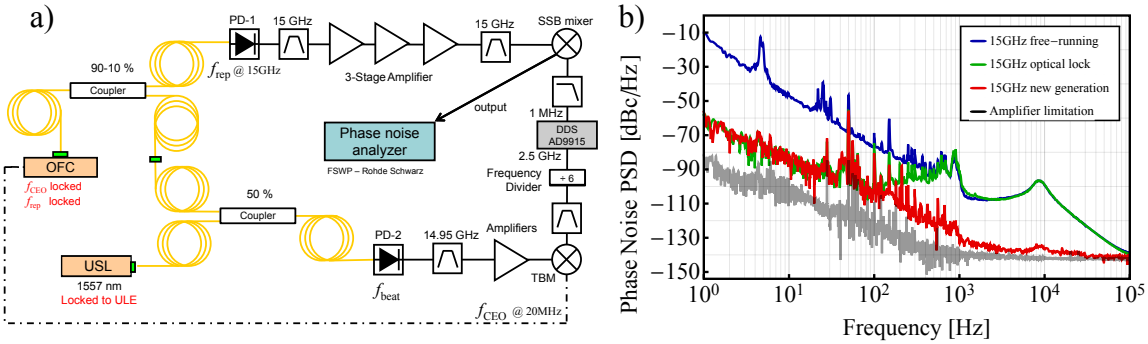

Fig. 1: (a) Schematic setup for frequency division of the USL using a comb as a transfer oscillator. (b) Phase noise power spectral density (PSD) of the generated ultra-stable signal at 15 GHz (red), compared to the 60th harmonic of f_{rep} in free-running mode (blue) and with a comb line locked to the USL (green). The grey curve shows the noise floor resulting from the RF amplifiers used in the setup.

[1] P. Brochard, S. Schilt, V. J. Wittwer, T. Südmeyer, *Opt. Lett.* 40, 5522–5525, 2015.

Development and research of the system for long time continues frequency measurements based on Sr87 clock transition

O. Berdasov, A. Gribov, S. Strelkin, D. Sutyrin, G. Belotelov, E. Stelmashenko, S. Slusarev

FSUE VNIIFTRI/Mendeleevo,Moscow/Russia

Email: berd_7@mail.ru

We report on the next stage of the Sr optical clock development in FSUE VNIIFTRI [1]. Optical clocks ^{87}Sr have outstanding characteristics of frequency stability and accuracy but it's practice implementation is limited due to short operation time.

We use a CDD camera for the spectroscopy signal detection to decrease noise level of background fluctuations. We apply not classical lock to atoms based on probabilities of 2 points, instead we use Lorenz fit. Such fit procedure demands several points (minimum 4), that increase time of clock frequency correction by several times. To avoid such problem, we implemented point-to-point correction. This scheme makes our lock to clock transition very robust. It was tested on bosonic and fermionic strontium isotopes.

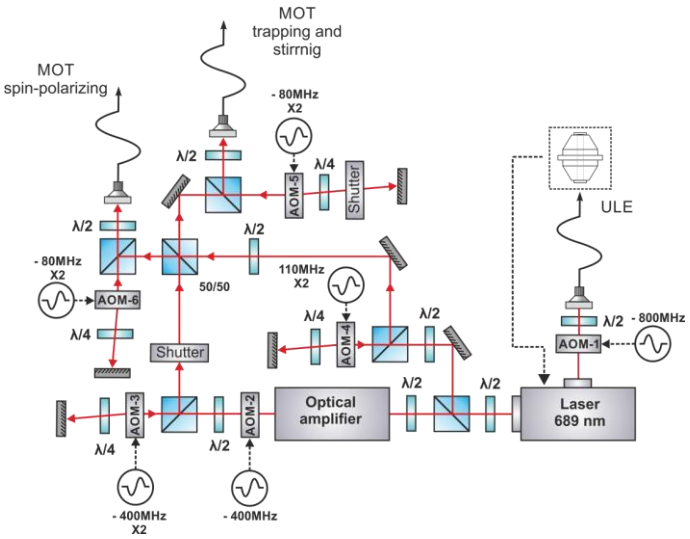

Fig. 1. Optical scheme for the second stage cooling

The cooling process for the 87Sr demands many lasers that decrease system long term operation. The standard way to realize a 1.4 GHz offset between a stirring and trapping lasers of the second stage cooling is to use a phase-lock between 2 different lasers. Our way to avoid this is to use one laser source and several AOMs to tune the frequency. The optical scheme realization is demonstrated on the Fig. 1. This approach requires more optical power at 689 nm, but commercial lasers and optical amplifiers are easy available now. It's also bulky, but it's not a problem for stationary system. The main advantage is that this scheme works several month without any realignment and allows us to create robust optical clock.

All this improvements have allowed us to consider ^{87}Sr clock as a part of Russian National Time Scale. As part of this process, we present results of comparisons our optical clock against hydrogen and Cs fountain standards.

We performed continues comparisons (except one relock of the femtosecond comb) between our optical standard and H-maser referenced to Cs fountain standard. The achieved frequency stability is about 9e-16 at 20000 s. It's limited by the link between two standards and frequency measurement scheme.

References

[1] Berdasov,O I et al "Ultrastable laser system for spectroscopy of the $^1S_0 - {}^3P_0$ clock transition in Sr atoms", Quantum Electronics, 47 (5):400, 2017.

a-Si:H Thin-Film MEMS Resonators: Towards Mass Sensing Applications

Rui MR Pinto[1], Pedro Brito[1], Virginia Chu[1], João Pedro Conde[1, 2]

[1] Instituto de Engenharia de Sistemas e Computadores – Microsistemas e Nanotecnologias (INESC MN) and IN – Institute of Nanoscience and Nanotechnology, Portugal
[2] Department of Bioengineering, Instituto Superior Técnico, University of Lisbon, Portugal

Email: rmpinto@inesc-mn.pt

Hydrogenated amorphous silicon (a-Si:H) thin films can be deposited over large areas and at low temperatures, allowing the use of a variety of substrates, including glass, polymers and silicon integrated circuits. The Young's modulus and density of a-Si:H are similar to crystalline silicon (E ~ 130 GPa, ρ ~ 2330 kg m^{-3}) and the residual stress of the films, which is important for MEMS fabrication, can be tuned from tensile to compressive.

Here, we fabricated clamped-clamped (bridge) and clamped-free beam (cantilever) resonators, using n-type a-Si:H as the structural layer on glass substrates. This surface-micromachining process employed an aluminium sacrificial layer and TiW as electrodes. The bridge (cantilever) dimensions were between 40 µm and 120 µm of length (20-40 µm) (l), 10 µm of width (w) and 1 µm of thickness. To study the mass sensitivity of our resonators, in the same process, we also fabricated structures with a mass added to the beam. This added mass consisted of two sputtered films: 10 nm of Cr + 20 nm of Au. The added mass was confined to a 4 µm x 4 µm square in the center of the bridges and the tip of the cantilevers. Resonators with the added mass (loaded) were compared to the resonators without the added mass (bare).

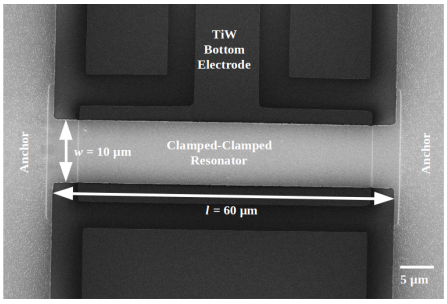

Fig. 1 – SEM Micrograph of a bare 60 µm-long bridge. The characteristic dimensions (l and w) are shown and the anchoring regions of the beam identified.

The resonators were excited electrostatically into the fundamental flexural mode (out-of-plane) using a bottom electrode. The vibration was detected optically, and the fundamental resonance frequency (f_{res}) and quality factor (Q) were extracted. The f_{res} of the resonators without added mass ranged from 250 kHz to 2.7 MHz and the Q was in the range of 1000 to 3000 in vacuum. When comparing the loaded resonators to the bare resonators, there is a f_{res} shift which is a result of the stiffness change and the mass change of the system. For the thicknesses of Cr and Au films that we added to the resonators, the effect of the stiffness increase dominated over the mass increase, resulting in the rise of the f_{res} (see Fig. 2). For thicker added films, we expect the mass effect to dominate, taking f_{res} to lower values (work in progress).

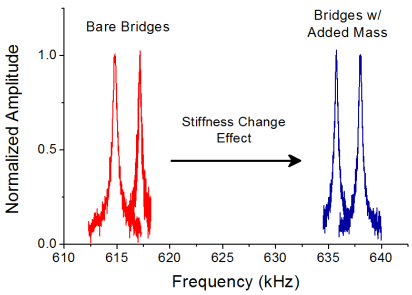

Fig. 2 – Resonance specta of 80 µm-long bridges with and without added mass (10 nm of Cr + 20 nm of Au). Two replicates of each condition are depicted. An increase in f_{res} was observed due to the increase of the stiffness of the system.

The use of the added Cr+Au films is a model that allows to study the mass sensitivity of MEMS resonating systems, aiming at applications such as gas sensing and biomolecular detection. The resonators will also be characterized electronically to extract the equivalent RLC parameters. The frequency stability of the thin-film a-Si:H resonators will also be presented.

CPT Atomic Clock Based on an Antirelaxation-Coated Cell and Quadrature-Signal Method of the Light Shift Cancellation

S.M. Ignatovich[1], V.I. Vishnyakov[1], A.O. Makarov[1], M.N. Skvortsov[1], N.L. Kvashnin[1], V.A. Vasiliev[1], S.N. Atutov[1,3], D.V. Brazhnikov[1,2], V.I. Yudin[1,2,4], A.V. Taichenachev[1,2] and S.N. Bagayev[1,2]

[1]Institute of Laser Physics SB RAS, Novosibirsk, Russia
[2]Novosibirsk State University, Novosibirsk, Russia
[3]Institute of Automation and Electrometry SB RAS, Novosibirsk, Russia

Email: skv@laser.nsc.ru

High-stability and compact clocks are in great demand for many applications, for example, such as global navigation satellite systems (GNSS), broadband communication and high-secret lines, smart electricity grids, etc. Several crucial applications require small size and weight ($V < 50$ cm^3, $m < 30$ g), low power consumption ($P_\Sigma << 1$ W) and high long-term frequency stability ($\sigma_y \leq 5\times10^{-12}$ per a day). The most promising technology involves approach based on the coherent populations trapping (CPT) phenomenon, because it can combine all the features listed.

Usually, the buffer-gas-filled vapour cells are used to achieve narrow CPT signals required for obtaining the good error signals for feedback frequency stabilization loop. However, the buffer-gas approach leads to very strict requirements to thermostabilization system and other problems. Another serious issue that should be solved to reach the high long-term stability consists in the light-induced shift of "clock" transition in an atom. The cells with antirelaxation coating of walls are less sensitive to temperature variations than the buffer-gas-filled ones. Moreover, the coated cells can be also made pretty small by means of glass-blown as well as MEMS technologies.

Since CPT atom clock represents an all-optical technology, the microwave frequency is produced by frequency modulation of laser radiation. The frequency of modulation is stabilized by means of the dark resonance in an alkali-metal vapour cell. To create required feedback stabilizing loop, the error signal is generated. To generate the signal, the carrier microwave frequency is also modulated at a rate typically from a hundred of Hz and up to 15 kHz (Pound-Drever-Hall technique). The first harmonic component of this modulation is detected synchronously with a lock-in amplifier and can be used as an error signal for the stabilization loop. It is essential that, in general, the error signal significantly depends on the lock-in amplifier phase [1]. And only if the laser is tuned to a zero-shift frequency, there is no phase sensitivity. This means that one can use "in-phase" and "out-of-phase" (quadrature) signals to suppress the light shift of the atomic microwave transition by means of electronics [1].

Novelty of our work consists in combining the antirelaxation-coated-cell approach and the quadrature-signal method of the light shift suppression. We used a glass-blown compact ^{87}Rb vapour cell with antirelaxation coating of walls. The Pound-Drever-Hall technique was engaged for microwave frequency stabilization. Our preliminary tests showed a medium-term stability $\sigma_y \leq 5\times10^{-11}$ at $\tau=10^3$ s and it continued go down with τ increase. After realization of the physical package evacuation, we anticipate achieving the long-term stability better than 5×10^{-12}.

The authors thank the Russian Science Foundation (grant no. 17-72-20089).

References

[1] B.H. McGuyer et al., Appl. Phys. Lett., vol. 94, 251110, 2009.

Nonlinear Dynamics in MEMS Resonators

Steven W. Shaw[1,2]

[1]Department of Mechanical and Aerospace Engineering, Florida Institute of Technology, Melbourne, FL 32903 USA
[2]Departments of Mechanical Engineering and Physics and Astronomy, Michigan State University, East Lansing, MI 48824 USA

Email: sshaw@fit.edu

This presentation will provide an overview of nonlinear dynamic behavior in MEMS and its potential for applications. Many micro-scale systems utilize resonator elements that respond in a classical linear manner that can be characterized by natural frequency and quality factor. These components have well-understood input/output characteristics and noise properties that facilitate device design. However, there are situations where nonlinear response is required or has the potential to offer improved performance. Nonlinearities can arise in stiffness from mechanical and electrostatic effects and in damping from many sources, and these can affect individual vibration modes and also lead to nonlinear mode coupling. In addition, noise and nonlinearity have some fundamental connections that have implications for device design [1]. Canonical models that account for these properties will be described, as will methods for characterizing nonlinearities and accounting for them in design. The discussion will pay particular attention to nonlinear mode coupling, including its underlying physics, its effects on open and closed loop operation, and recently described potential applications that include frequency conversion [2], frequency stabilization [3], self-induced parametric amplification in sensors [4], free (ringdown) response with anomalous and potentially advantageous behavior [5,6], and frequency comb generation [7]. These examples will offer a sampling of the rich and potentially useful dynamic behavior that is possible when devices are operated in the nonlinear domain.

References

[1] Atalaya, Juan, Thomas W. Kenny, M. L. Roukes, and M. I. Dykman. "Nonlinear damping and dephasing in nanomechanical systems." *Physical Review B* 94, no. 19 (2016): 195440.
[2] Qalandar, Kamala, Brian S. Strachan, Brian Gibson, Mrigank Sharma, Alice Ma, Steven Shaw, and Kimberly Turner. "Frequency division using a micromechanical resonance cascade." *Applied Physics Letters* 105, no. 24 (2014): 244103.
[3] Antonio, Dario, Damián H. Zanette, and Daniel López. "Frequency stabilization in nonlinear micromechanical oscillators." *Nature Communications* 3 (2012): 806.
[4] Nitzan, Sarah H., Valentina Zega, Mo Li, Chae H. Ahn, Alberto Corigliano, Thomas W. Kenny, and David A. Horsley. "Self-induced parametric amplification arising from nonlinear elastic coupling in a micromechanical resonating disk gyroscope." *Scientific Reports* 5 (2015).
[5] Chen, Changyao, Damián H. Zanette, David Czaplewski, Steven Shaw, and Daniel López. "Direct observation of coherent energy transfer in nonlinear micro-mechanical oscillators." *Nature Communications* 8 (2017): 15523
[6] Shoshani, Oriel, Steven Shaw, and Mark Dykman. "Anomalous dissipation of nanomechanical modes going through nonlinear resonance." arXiv preprint arXiv:1702.00769, revised version to appear in *Scientific* Reports (2017).
[7] Ganesan, Adarsh, Cuong Do, and Ashwin Seshia. "Phononic Frequency Comb via Intrinsic Three-Wave Mixing." *Physical Review Letters* 118.3 (2017): 033903.

Relativistic geodesy with a transportable optical clock

J. Grotti[1], S. B. Koller[1], S. Herbers[1], S. Vogt[1], A. Al-Masoudi[1], S. Dörscher[1], R. Schwarz[1], S. Häfner[1], U. Sterr[1], E. Benkler[1], S. Koke[1], A. Kuhl[1], T. Waterholter[1], G. Grosche[1], R. Le Targat[2], J. Lodewyck[2], H. Á. Martinez[2], M. Abgrall[2], E. Cantin[3], D. Xu[2], O. Lopez[3], A. Amy-Klein[3], P.-E. Pottie[2], H. Denker[4] and C. Lisdat[1]

[1]Physikalisch-Technische Bundesanstalt, 100 Bundesallee 38116 Braunschweig Germany
[2]Observatoire de Paris, 61 Avenue de l'Observatoire 75014 Paris France
[3]Laboratoire de Physique des Laser, 93 Avenue J. B. Clément 430 Villetaneuse France
[4]Institut für Erdmessung, Leibniz Un. Hannover, Schneiderberg 50 30167 Hannover Germany

Email: jacopo.grotti@ptb.de

With optical clocks reaching low 10^{-18} fractional uncertainties in relatively short averaging time and with the development of fibre links for optical frequency transfer [1], relativistic geodesy is becoming feasible [2,3,4,5]. Here we present the new accuracy evaluation of the PTB transportable optical lattice clock based on ^{87}Sr [6] to a fractional uncertainty of 3×10^{-17} and its application in a new measurement campaign.

The transportable clock has been used to resolve the geopotential difference between PTB (Braunschweig, Germany) and Observatoire de Paris (France) through the measured difference between a remote, employing a 1400 km optical fiber link between the two institutes [3], and a local comparison to PTB stationary ^{87}Sr lattice clock. Both comparisons have been performed at the low 10^{-17} fractional uncertainty. Technical improvements on the transportable clock increased the availability of the system (about 90 000 s of measurement time in two weeks of clock operation) and allowed a measurement uncertainty reduction by one order of magnitude with respect to the previous campaign [5]. However, in the last week of the campaign the data showed jumps in the frequency ratio of the optical clocks at the 10^{-16} level. The identification of the origin of this problem is still ongoing.

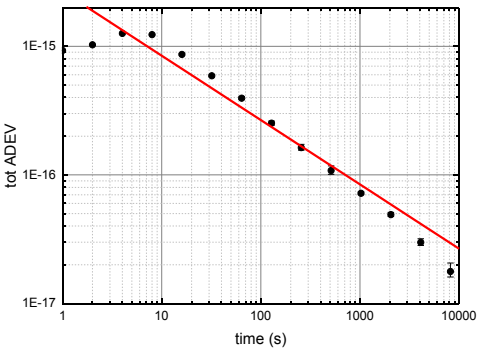

Remote comparison instability ($2.7\times10^{-15}/\sqrt{\tau}$)

This campaign shows that after further improvements, transportable clock comparisons by optical fibre can be applied in geodesy with an accuracy comparable to standard methods. New campaigns are planned for the near future, together with improvements for the measurement stability via the development of a new transportable interrogation laser system.

This work was supported by QUEST, DFG trough the RTG 1729 and CRC 1128 geo-Q (projects A03, A04, and C04). the Marie-Curie Action ITN FACT and the EMPIR project 15SIB05 OFTEN. This project has received funding from the EMPIR program co-financed by the Participating States and from the European Union's Horizon 2020 research and innovation program.

References:

[1] F. Riehle, Nature Photonics, vol. 11, no. 1, pp. 25-31, 2017
[2] M. Vermeer, ser. Reports of the Finnish Geodetic Institute, 1983
[3] C. Lisdat et al., Nature Communications, vol. 7, p. 12443, 2016
[4] T. Takano et al., Nature Photonics, vol. 10, pp. 662-666, 2016
[5] J. Grotti et al., arXiv:1705.04089, 2017
[6] S.B. Koller et al., Phys. Rev. Lett., vol. 118, p. 073601, 2017

Two-way optical frequency transfer on in-field long-haul fiber link

Anna Tampellini[1,2], Cecilia Clivati[1], Filippo Levi[1], Alberto Mura[1] and Davide Calonico[1]

[1]Physical Metrology Division, Istituto Nazionale di Ricerca Metrologica-INRIM, Turin, Italy
[2]Department of Electronics and Telecommunications, Politecnico di Torino, Turin, Italy

Email: a.tampellini@inrim.it

Two-way frequency transfer (TWFT) on optical fibers is a powerful technique for the comparison of remote optical clocks at their intrinsic level of accuracy [1-3]. In contrast to active noise cancellation schemes that require a double pass of light into to the fiber, it is based on the simultaneous transmission of an ultrastable laser in counterpropagating directions; at both ends, the received signal is compared to the local laser, and by subtracting the measurements at both sites, the fiber noise is rejected. Because of the single pass, TWFT is less affected by optical attenuation, with respect to the Doppler noise cancellation technique [4-7]. This mitigates the need of optical amplification and regeneration, reducing the complexity of the experimental setup and making it especially suitable for ultra-long-hauls link.

We present the implementation of a TWFT on a multiplexed fiber haul of 300 km, with the aim of investigating the ultimate performances of this technique in its most simple implementation on a realistic testbed. We used two completely independent experimental setups at the link ends, i.e. two transfer lasers and separate acquisition systems, to fully resemble a frequency comparison between remote laboratories. In particular, we studied the effect of synchronization on the ultimate comparison performances. We derive a theoretical model, confirmed by experimental results, describing the performance deterioration when data interpolation is used on un-synchronised data to compensate for a timebase mismatch. We stress that the ultimate stability of the two-way technique can be achieved only by hardware-synchronizing the measurements at the same level as propagation time of light into the fiber, which is usually of the order of milliseconds.

We demonstrate that, in hardware-synchronization conditions, the link contribution to instability can be rejected at the level of 10^{-19}, which makes this technique suitable for the comparison of the state-of-art optical clocks.

This work has been funded by the European Metrology Program for Innovation and Research (EMPIR) project 15SIB05 OFTEN.

References

[1] Calosso C E et al., “Frequency transfer via a two-way optical phase comparison on a multiplexed fiber network”, Opt. Lett., Vol. 39, 11771180, 2014.
[2] Bercy A et al., “Two-way optical frequency comparisons at 5 × 10−21 relative stability over 100 km telecommunication network fibers” Phys. Rev. A, Vol. 90, 15, 2014.
[3] Tampellini A et al., “Effect of a timebase mismatch in two-way optical frequency transfer” Metrologia, Vol. 54, 805, 2017.
[4] Calonico D et al., “High-accuracy coherent optical frequency transfer over a doubled 642 km fiber link”, Appl. Phys. B, Vol. 117, 979–86, 2014.
[5] Raupach S M F et al., “Brillouin amplification supports 1×10^{-20} uncertainty in optical frequency transfer over 1400 km of underground fiber”, Phys. Rev. A, Vol. 92, 021801, 2015.
[6] Chiodo N et al., “Cascaded optical fiber link using the internet network for remote clocks comparison”, Opt. Express, Vol. 23, 33927–37, 2015.
[7] Fujieda M et al., “All-optical link for direct comparison of distant optical clocks” Opt. Express, Vol. 19, 16498–507, 2011

Cryogenic Yb lattice clock below 10^{-17} uncertainty

N. Nemitz[1,2], F. Bregolin[1,3,4], R. Yanagimoto[1,5], R. Mizushima[1,5] and H. Katori[1,5]

[1]Quantum Metrology Laboratory, RIKEN, Wako-shi, Saitama, Japan
[2]Space-Time Standards Laboratory, National Institute of Information and Communications Technology (NICT), Koganei, Tokyo, Japan
[3] Physical Metrology Division, Istituto Nazionale di Ricerca Metrologica (INRIM), Torino, Italy
[4] Dep. of Electronics and Telecommunications, Politecnico di Torino, Torino, Italy
[5] Dep. of Applied Physics, The University of Tokyo, Bunkyo-ku, Tokyo, Japan

Email: f.bregolin@inrim.it

Optical atomic clocks have now demonstrated accuracies of few parts in 10^{18} [1–4]. Among these, optical lattice clocks offer the advantage of being able to perform measurements to full accuracy within a few hours of operation, thanks also to continuous advances in the development of ultra-stable optical local oscillators [5]. These results make lattice clocks a powerful tool for fundamental science experiments, such as general relativity tests [6]. In addition, these achievements are important steps towards the redefinition of the SI second on an optical atomic transition, and fuel the interest in developing and comparing optical clocks based on different atomic species.

We present an updated uncertainty budget for the cryogenic Yb clock operated at RIKEN, with overall fractional uncertainty below 10^{-17}, significantly improved from previous results [7] thanks to a new evaluation of the frequency shifts limiting the clock accuracy. The lattice light shift has been re-characterized through new measurements evaluated with an extended model, which provides similar results than a different available model [8]. The probe-induced light shift and 2^{nd} order Zeeman shift have been measured to reduce their uncertainty contributions to below 10^{-18}. Our evaluations remain limited by the statistical uncertainties of the characterizing measurements and promise even better accuracy with improved clock laser stability.

We will also report on the progress of a renewed measurement of the Yb/Sr frequency ratio taking advantage of the improved uncertainty budget.

References

[1] T. Nicholson et al., Nature Communications 6, 6896 (2015).

[2] I. Ushijima et al., Nature Photonics 9, 185–189 (2015).

[3] C. W. Chou et al., Phys. Rev. Lett. 104, 070802 (2010).

[4] N. Huntemann et al., Phys. Rev. Lett. 116, 063001 (2016).

[5] D. G. Matei et al., Phys. Rev. Lett. 118, 263202 (2017).

[6] T. Takano et al., Nature Photonics 10, 662–666 (2016).

[7] N. Nemitz et al., Nature Photonics 10, 258–261 (2016).

[8] R. C. Brown et al., arXiv:1708.08829 (2017).

Kinetics of atoms cooled on clock transitions: the behavior of energy and momentum

R.Y. Ilenkov[1,2], O.N. Prudnikov[1,2], A.V. Taichenachev[1,2], V.I. Yudin[1-3]

[1]Institute of Laser Physics SB RAS, Novosibirsk, Russia
[2] Novosibirsk State University, Novosibirsk, Russia
[3] Novosibirsk State Technical University, Novosibirsk, Russia

Email: ilenkov.roman@gmail.com

The theoretical description of the kinetics of neutral atoms in the polarized light fields with all the atomic levels, the coherence, the recoil effect is both important and challenging problem. The first step toward understanding mechanisms of interaction between atoms and light was called quasi-classical approach. [1,2] It lies in the fact that the equations for the density matrix can be reduced to the Fokker-Planck equation for the Wigner function in the phase space. But the semiclassical approximation is inapplicable for investigating the cooling of atoms at clock transitions, because the quasiclassical parameter (the recoil frequency) is not small (in comparison with the natural line width). Later quantum methods were developed [3], for example, the secular approach which describes cooling and localization of atoms in the optical potential. Secular approximation fails high vibrational levels and for atoms in high vibrational states.

We have developed an own quantum method [4] to obtaining the stationary distribution of two-level atoms in a standing wave of arbitrary intensity, allowing full account the recoil effect.

The adoption of the method to the problem of cooling at clock transition has yielded the following interesting results: a bimodal and multi-peaks (manifestation of VSCPT) impulse distribution of atoms was detected, a non-monotonicity of the energy distribution of the total energy of the atoms was observed.

Most of the atoms are not collected at zero oscillation level (Fig. 1). Non-Gaussian impulse distributions are interesting for obtaining a greater number of cold atoms, and energy distributions have not previously been studied in detail by scientists.

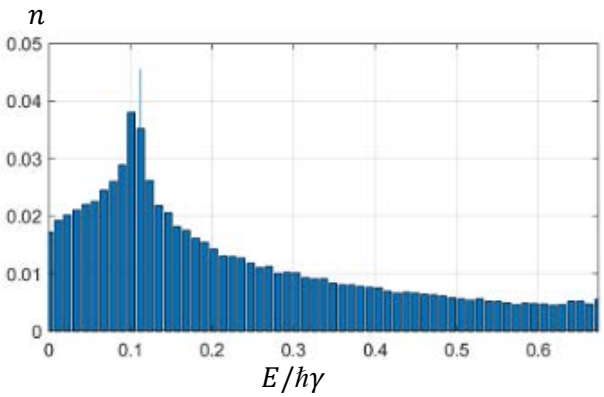

Fig. 1: None-Boltzmann's energy distribution of atoms. Blue vertical line is optical potential depth.

The work was personally supported by Russian Science Foundation (project № 17-72-10139)

References

[1] V.G. Minogin, V.S. Letokhov, Laser Light Pressure on Atoms, Gordon and Breach, New York, 1987.

[2] A. P. Kazantsev, G. I. Surdutovich, and V. P. Yakovlev, Mechanical Action of Light on Atoms, World Scientific, Singapore, 1990.

[3] A. Aspect, E. Arimondo, R. Kaiser, N. Vansteenkiste, and C. Cohen-Tannoudji, Phys. Rev. Lett. vol 61, pp.826 (1988).

[4] O. N. Prudnikov, R. Ya. Il'enkov, A. V. Taichenachev, A. M. Tumaikin, V. I. Yudin, JETP, Volume 112, pp.939-945 (2011).

Real-time detection of frequency jumps in GNSS satellite clocks using stand-alone receiver

Wei Huang[1], Patrizia Tavella[1], Pascale Defraigne[2]

[1]Politecnico di Torino and Istituto nazionale di ricerca metrologica, Torino, Italy
[2]Royal Observatory of Belgium, Brussels, Belgium

Email: wei.huang@polito.it

The Global Navigation Satellite Systems (GNSS) provides positioning and timing services to the users from the ground to the low earth orbit, knowing the time of flight of signals from the GNSS satellites to the receiver. However, the satellite clocks in space may have some anomalies, due to different reasons. These anomalies will cause errors in the GNSS solutions, especially the frequency jump, if not corrected, may cause the errors to accumulate up to tens of meters in one day, which is the update rate of GPS navigation message.

We present a method to detect the satellite clock frequency jump in real time, using stand-alone receiver. The satellite clocks are compared with the ground atomic clock in the time laboratory, and the algorithms in [1] is used to determine the jumps. The results show that, by only receiving the satellite navigation signals, a frequency jump of moderate size can be already fast detected. Then the effects of the detected frequency jumps on user positioning errors are demonstrated, and two strategies to get rid of the jumps are then proposed and compared.

In the next section, some other methods are also studied and presented in case some external products are available (e.g. IGS products), they are suggested to be used in different circumstance.

In the last section, the possibility of global real-time detection of the frequency jump in satellite clock is studied, using the proposed method.

References

[1] Lorenzo Galleani, Patrizia Tavella ,“Robust Detection of Fast and Slow Frequency Jumps of Atomic Clocks”, IEEE TUFFC VOL. 64, NO. 2, FEBRUARY 2017.

Optimization of low-power oscillator topology for frequency modulated MEMS inertial sensors

Cristiano R. Marra[1], Alessia M. Ruggieri[1], Paolo Minotti[1], Giorgio Mussi[1], Andrea G. Bonfanti[1], Andrea L. Lacaita[1], and Giacomo Langfelder[1]

[1]Dipartimento di Elettronica, Informazione e Bioingegneria, Politecnico di Milano, Italy

Email: cristianorocco.marra@polimi.it

Recent implementations of MEMS inertial sensors for high-stability applications (augmented reality, pedestrian navigation…) are based on topologies where a frequency-modulated (FM) signal sees a further amplitude-modulation (AM) at about 100-200 Hz from the carrier frequency, which usually falls in the 20-50 kHz range [1, 2]. Therefore, phase noise in the oscillator forming the basic electronic building block in these sensors needs to be analyzed at the mentioned split from the carrier. This work investigates the optimum oscillator topology in terms of power-noise trade-off, showing how an analog phase shifter in the loop provides better performance than a phase-locked-loop (PLL) approach.

Due to the need for amplitude controlling circuits, feedback oscillators are the preferred choice for the described scenario. With a charge-amplifier (C2V) based frontend, which optimizes noise at the operating frequency, the need for a 90-deg shifter arises to properly close the loop. This need is often accomplished by combining a comparator after the C2V and a PLL. Its output provides the 90-deg shifted signal which, after proper conditioning, is used to electrostatically drive the MEMS resonant sensor. In view of a low-noise, low-power design, such a topology however shows a drawback associated to the fact that the comparator receives at its input a wide-band-noise signal, and thus the noise fold penalty [3] becomes as large as about 10 dB.

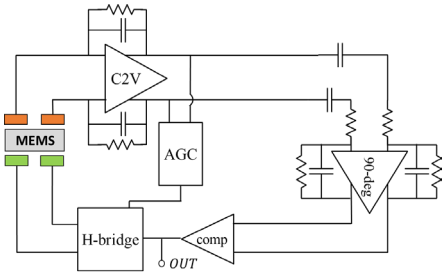

Fig. 1: proposed feedback oscillator topology for MEMS FM sensors, based on an analog shifter, instead of a PLL, for optimum performance in terms of noise-power trade-off.

The proposed solution (see Fig. 1), exploits an analog 90-deg shifter, behaving as an integrator at the operating frequency. This serves both purposes of providing the needed shift and limiting the noise band at the comparator input. With such a limitation of folding penalties, the same output phase noise can be obtained with a 65% lower consumption in the oscillator.

To verify predictions, both circuits (with a PLL and with the analog shifter) are fabricated (AMS 0.35 µm process) and connected to a FM MEMS accelerometer (with a Q~1000). Results (Fig. 2) demonstrate slightly better noise performance for the analog-shifter solution, which furthermore operates at a much lower current.

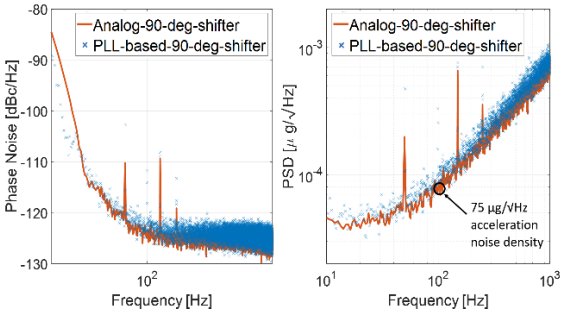

Fig. 2: measured phase noise (left) and equivalent acceleration density (right), for the analog-shifter and for the PLL based circuits. Comparable noise performance is obtained with a 27 µA current consumption for the analog shifter, instead of a 45 µA current in the PLL-based implementation.

References

[1] I. I. Izyumin et al., "A 7ppm, 6 deg/hr frequency-output MEMS gyroscope," proc. IEEE MEMS 2015, Estoril, Portugal, pp. 33–36, 2015.

[2] S. A. Zotov et al., "High Quality Factor Resonant MEMS Accelerometer with Continuous Thermal Compensation", IEEE Sensors Journal, vol. 15, no. 9, pp. 5045-5052, Sept. 2015.

[3] C. Samori et al., "Spectrum folding and phase noise in LC tuned oscillators," IEEE Trans. Circ. Syst. II: Analog and Digital Signal Processing, vol. 45, no. 7, pp. 781-790, Jul 1998.

Milliradian Phase Comparison Between Optical Oscillators Across Turbulent Air

Laura C. Sinclair[1], Hugo Bergeron[2], William C. Swann[1], Esther Baumann[1], Jean-Daniel Deschênes[2], and Nathan R. Newbury[1]

[1]National Institute of Standards and Technology, Boulder, Colorado
[2] Université Laval, Québec, Canada

Email: laura.sinclair@nist.gov

Work of the U.S. government. Not subject to copyright.

Future optical clock networks will require optical links to achieve their full potential and will include some nodes connected not by fiber but by free-space paths. While the straightforward transfer of fiber-based approaches to free-space links is possible; it is limited by the presence of atmospheric turbulence. The alternate approach of optical two-way time-frequency transfer (O-TWTFT) based on the two-way exchange of frequency comb pulses exploits the reciprocity in the time-of-flight across a link to achieve residual instabilities of ~$4x10^{-16}$ at 1-second averaging time [1] and to enable femtosecond-level time synchronization [2]. Here, we demonstrate that carrier-phase O-TWTFT can exploit the carrier phase of the frequency comb pulses to achieve a 10-20 times improvement in performance over this envelope-only O-TWTFT. [3]

The presence of atmospheric turbulence causes fades (signal loss) at random times, with random durations and random separations, making the tracking of the optical phase between measurements complicated as the duration between measurements can exceed the mutual phase coherence time between the two oscillators. We combine the timing information from both the pulse's carrier-phase and envelope and implement a Kalman-filter-based algorithm to extend the coherence across these fades. The two optical oscillators were separated by 4 km of air in a folded geometry to allow for the acquisition of truth data. The difference between the carrier-phase O-TWTFT measurements and the truth data are shown for one run with ~1% fades in Fig. 1(a).

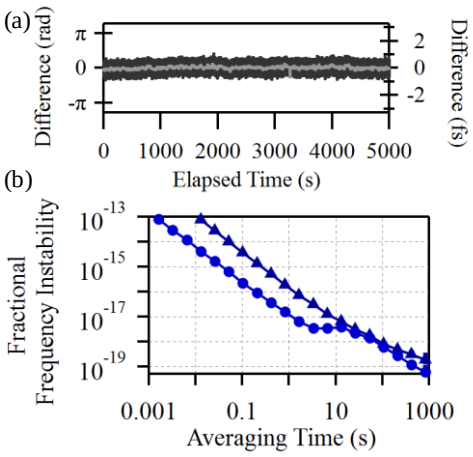

Fig. 1: (a) Difference between the carrier-phase O-TWTFT and truth data at 400-μs sampling (black) and at 1-second averaging (gray). (b) Residual fractional frequency instability (modified Allan deviation) for carrier-phase O-TWTFT (blue circles) compared to the corresponding envelope-only O-TWTFT (blue triangles).

Through carrier-phase O-TWTFT, we track the frequency difference between two optical oscillators separated by 4 km of air to tens of milliradians despite the presence of strong random frequency walk noise and the accumulation of a 300 million radian difference in phase. We achieve a fractional stability of 1.2 x 10^{-17} at a 1-second averaging time, corresponding to a time deviation of 7 attoseconds, despite the presence of turbulence-induced fades.

References

[1] F. R. Giorgetta, W. C. Swann, L. C. Sinclair, E. Baumann, I. Coddington, and N. R. Newbury, "Optical two-way time and frequency transfer over free space", Nat. Photonics, vol 7, 434, 2013.

[2] J.-D. Deschênes, L. C. Sinclair, F. R. Giorgetta, W. C. Swann, E. Baumann, H. Bergeron, M. Cermak, I. Coddington, and N. R. Newbury, "Synchronization of Distant Optical Clocks at the Femtosecond Level", Phys. Rev. X, vol 6, 021016, 2016.

[3] L. C. Sinclair, H. Bergeron, W. C. Swann, E. Baumann, J.-D. Deschênes, and N. R. Newbury, "Comparing optical oscillators across the air to milliradians in phase and 10^{-17} in frequency", ArXiv171004063 Phys., 2017.

High-precision mid-IR molecular spectroscopy with traceability to primary standards

D.B.A. Tran[1], R. Santagata[1,2], O. Lopez[1], S. K. Tokunaga[1], M. Abgrall[2], Y. Le Coq[2], R. Le Targat[2], W. K Lee[2], D. Xu[2], P.-E. Pottie[2], B. Darquié[1], A. Amy-Klein[1]

[1]Laboratoire de Physique des Lasers, Université Paris 13, CNRS, Villetaneuse, France
[2]LNE-SYRTE, Observatoire de Paris, CNRS, UPMC, Paris, France

Email: amy@univ-paris13.fr

The optical frequency comb (OFC) is a unique tool for high accuracy measurements. It allows the spectral properties from one laser source to be transferred to another, which opens perspectives for precision tests in several fields of physics. Ultra-high resolution molecular spectroscopy can strongly benefit from using OFCs, as significant improvements in precision and sensitivity can be obtained, especially in the mid-infrared (MIR) "fingerprint" region which exhibits intense and narrow rovibrational molecular transitions.

This has prompted us to develop a new setup for controlling the frequency of MIR quantum cascade lasers (QCLs) with the highest stability and accuracy [1]. A QCL emitting at 10.3 µm is stabilized to an OFC itself stabilized to an ultra-stable near-infrared reference signal at 1.5 µm transferred from SYRTE to LPL using an optical link [2]. The reference stability is copied to the QCL, which therefore exhibits relative frequency stability lower than 2×10^{-15} between 1 and 100 s. Moreover its absolute frequency is known with an uncertainty below 10^{-14} for averaging time around 100 s thanks to the traceability to the primary standards of SYRTE [3]. By scanning the near-IR reference laser using an electro-optic modulator, the setup allows us to scan the QCL over at least a few hundreds of MHz.

We use this ultrastable spectrometer to carry out saturated absorption spectroscopy of methanol in a multipass cell at pressures around 1 Pa. The statistical uncertainty obtained in determining the central frequency of the transitions is below 1 kHz. The main systematic effect arises from the analysis of the line shape which is affected by fluctuations in the baseline. It is expected to be below 10 kHz, improving on the literature by one to two orders of magnitude [4]. A detailed analysis of the frequency measurement uncertainty will be presented.

By combining wide tunability, high sensitivity and resolution, this setup constitutes a key technology for precise spectroscopic tests with molecules. It is a crucial element for our ongoing project of measuring the tiny energy difference between enantiomers of a chiral molecule induced by electroweak interactions, a signature of parity violation [5].

References

[1] B. Argence et al., "Quantum cascade laser frequency stabilization at the sub-Hz level", Nature Photon., vol. 9, 2015.

[2] W.-K. Lee et al., "Hybrid fiber links for accurate optical frequency comparisons", Appl. Phys. B 123, P. 161-172, 2017.

[3] J. Guéna et al., "Progress in atomic fountains at LNE-SYRTE", IEEE. Trans. Ultrason. Ferroelec. Freq. Control 59, p. 391-409, 2012.

[4] L.-H. Xu et al., "New assignments, line intensities, and HITRAN database for CH_3OH at 10 µm", J. Mol. Spectros. 228, p. 453-470, 2004; Z.-D. Sun, R. M. Lees, and L.-H. Xu, "Saturation-dip measurements for the ν_8 C–O stretching band of CH_3OH with a CO_2-laser–microwave-sideband spectrometer", J. Opt. Soc. Am. B, vol. 23, 2398, 2006.

[5] S. Tokunaga et al., "Probing weak force-induced parity violation by high-resolution mid-infrared molecular spectroscopy", Mol. Phys. 111, p. 2363-2373, 2013.

Injection Locking of Dissipative Kerr Solitons

Wenle Weng[1], Erwan Lucas[1], Hairun Guo[1], Grigory Lihachev[2,3], Valery E. Lobanov[2], Michael L. Gorodetsky[2,3], Tobias J. Kippenberg[1]

[1] École polytechnique fédérale de Lausanne (EPFL), CH-1015 Lausanne, Switzerland
[2] Russian Quantum Center, Skolkovo 143025, Russia
[3] Faculty of Physics, M.V. Lomonosov Moscow State University, 119991 Moscow, Russia

Email: wenle.weng@epfl.ch

Recently frequency combs based on dissipative Kerr solitons (DKS) [1] have been used in applications such as ultrafast ranging [2] and terabit optical communication [3] owing to their high coherence and smooth spectrum profiles. To realize a fully stabilized soliton comb, the repetition rate (f_{rep}) needs to be stabilized. Past efforts towards this purpose mostly focused on feedback control techniques, which not only increase complexity of the systems but also have limited control bandwidths. On the other hand, an injection locking technique was used to stabilize microresonator-based-combs operating at the modulational-instability (MI) state [4]. In this work we demonstrate the injection locking of f_{rep} of a soliton microcomb by amplitude-modulating the pump laser.

A Mach-Zehnder modulator is used to modulate the pump laser with a modulation frequency f_m. As we tune f_m across f_{rep} we observe frequency pulling effect and injection locking. Measurement of locking ranges shows that the locking range increases as the modulation index rises. In the case of injection locking, f_{rep} is phase locked to the modulation signal, and the long-term stability of f_{rep} is remarkably improved. Phase noise measurement shows that at low frequency offsets (1 - 20 Hz) the injection-locked f_{rep} exhibits a noise level lower than that of the unlocked f_{rep}. However, it is interesting to note that at higher frequency offsets (1 kHz - 3 MHz) the *phase noise level* of injection-locked f_{rep} is *much lower* than that of the injected RF signal. Such filtering behavior is due to the soliton dynamics and high quality-factor of the resonator: the trapping potential of the soliton decrease at high frequency, thus leading to a reduced transduction of the drive noise.

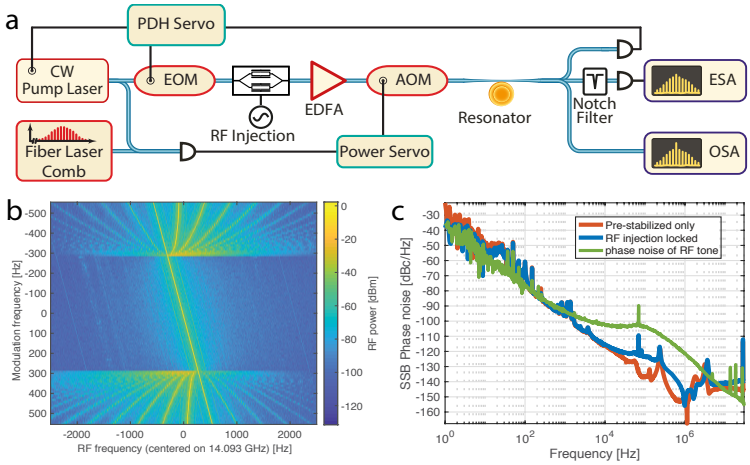

Fig. 1: (a) Experimental setup. (b) Evolution of the RF spectrum of solitons around f_{rep}. (c) Single-sideband phase noise spectra of f_{rep} with and without injection locking.

References

[1] T. Herr et al., "Temporal solitons in optical microresonators," Nature Photonics 8, 145–152 (2014).
[2] P. Trocha et al., "Ultrafast optical ranging using microresonator soliton frequency combs," arXiv preprint arXiv:1707.05969 (2017).
[3] P. Marin-Palomo et al., "Microresonator-based solitons for massively parallel coherent optical communications," Nature 546, 274–279 (2017).
[4] S. B. Papp et al., "Microresonator frequency combs optical clock," Optica 1, 10 (2014).
[5] J. Li et al., "Low-pump-power, low-phase-noise, and microwave to millimeter-wave repetition rate operation in microcombs," Physical Review Letters 109, 233,901 (2012).

Ytterbium optical lattice clocks at NIST: stability, accuracy, and agreement at low 10^{-18}

K. Beloy[1], W. F. McGrew[1,2], X. Zhang[1,3], R. J. Fasano[1,2], D. Nicolodi[1], S. A. Schäffer[1,4], R. C. Brown[1], R. W. Fox[1], N. Hinkley[1], T. H. Yoon[1], A. D. Ludlow[1]

[1]National Institute of Standards and Technology, Boulder, Colorado, USA
[2]Department of Physics, University of Colorado, Boulder, Colorado, USA
[3]State Key Laboratory of Advanced Optical Communication Systems and Networks, School of Electronics Engineering and Computer Science, Peking University, Beijing, China
[4]Niels Bohr Institute, University of Copenhagen, Copenhagen, Denmark

Email: kyle.beloy@nist.gov

Over the past few years, optical lattice clocks have begun to realize their promise [1] of stability and accuracy below the 10^{-17} fractional level [2,3,4]. Here we highlight our two ytterbium optical lattice clocks at NIST, which have previously demonstrated 1×10^{-18} instability. We have recently completed an accuracy evaluation for both clocks, including all known systematic effects. Each clock now boasts an inaccuracy of better than a few 10^{-18}. By directly comparing the two clocks, agreement is also found at this level, providing valuable corroboration for the evaluated accuracies.

We will discuss our assessment of the various line items in the uncertainty budget. This includes clock shifts due to lattice laser light, probe laser light, blackbody radiation, stray and applied static fields (electric and magnetic), cold-collisions, background gas collisions, and residual motion. We will also discuss frequency comparisons between the two Yb systems, as well as with other optical clocks at NIST.

Our group is also in the initial stages of constructing a portable Yb optical lattice clock. Key design features, which must inevitably strike a compromise between accuracy/stability and fieldability, will also be briefly highlighted.

References

[1] H. Katori, M. Takamoto, V. G. Pal'chikov, and V. D. Ovsiannikov, "Ultrastable Optical Clock with Neutral Atoms in an Engineered Light Shift Trap", Physical Review Letters, vol. 91, pp. 173005(1-4), 2003.

[2] N. Hinkley, J. A. Sherman, N. B. Phillips, M. Schioppo, N. D. Lemke, K. Beloy, M. Pizzocaro, C. W. Oates, and A. D. Ludlow, "An Atomic Clock with 10^{-18} Instability", Science, vol. 341, pp. 1215-1218, 2013.

[3] T. L. Nicholson, S. L. Campbell, R. B. Hutson, G. E. Marti, B. J. Bloom, R. L. McNally, W. Zhang, M. D. Barrett, M. S. Safronova, G. F. Strouse, W. L. Tew, and J. Ye, "Systematic evaluation of an atomic clock at 2×10^{-18} total uncertainty", Nature Communications, vol. 6, pp. 6896(1-8), 2015

[4] I. Ushijima, M. Takamoto, M. Das, T. Ohkubo, and H. Katori, "Cryogenic optical lattice clocks", Nature Photonics, vol. 9, pp. 185-189, 2015

Improved systematic and random errors for long-distance time-transfer using PTP White Rabbit

Anders E. Wallin[1], Mattia Rizzi[2], Guifré Molera Calvés[3], Thomas Fordell[1], Jyri Näränen[3]

[1] Centre for Metrology MIKES, VTT Technical Research Centre of Finland Ltd, Espoo, Finland
[2]Universita degli Studi di Brescia, Brescia, Italy
[3]Finnish Geospatial Research Institute, National Land Survey, Masala, Finland

Email: anders.wallin@vtt.fi

The IEEE1588-2018 High Accuracy profile, also known as PTP White Rabbit (WR), is a leading technology candidate for low-uncertainty long-distance time-transfer and for large synchronization networks. PTP-WR links have been established over distances up to 1000 km with < 2 ns uncertainty after calibration [1], while laboratory experiments have shown ~2e-12 @ 1 s random uncertainty using the Low Jitter Daughterboard (LJD) modification [2] to the WR-Switch (WRS) [3]. Reduced systematic errors due to lower chromatic dispersion in the optical fiber were recently also demonstrated [4].

We report on a 50-km low-jitter, low-asymmetry, PTP-WR link between laboratories operating active hydrogen masers at VTT MIKES Metrology and Metsähovi Observatory. We show that the recently developed LJD modification together with a low-asymmetry fiber-link can be used for time-transfer over 50 km with ~2e-12 @ 1s (0.5 Hz BW) random error. The link is realized using optical DWDM transceivers on adjacent ITU DWDM channels (optical carrier spacing 100 GHz). This limits the systematic error due to chromatic dispersion to <700 ps - without any calibration. We investigate how a measurement of the asymmetry can further reduce this error. The results of PTP-WR time-transfer were verified using a dual-frequency GNSS timing-receiver and Precise Point Positioning post-processing.

Our results show that use of the WRS LJD together with a low-asymmetry optical link significantly reduces the expected systematic and random errors for PTP-WR time transfer. Random errors at the 1e-12 level (at 1s, with 0.5 Hz BW), are below the resolution of typical time-interval/frequency counters, and sufficient for all but the most demanding applications. A future challenge for PTP-WR is to reduce random errors to the 1e-13 level - that of active H-masers used worldwide for continuous timekeeping. The demonstrated bidirectional optical link using adjacent 100 GHz DWDM channels is an economical and simple solution for reducing systematic errors on long links below 1 ns. An evaluation of the long-term drift of our link, relevant for time-scale maintenance and clock modeling/steering, is ongoing with initial promising results.

References

[1] E. F. Dierikx et al., "White Rabbit Precision Time Protocol on Long-Distance Fiber Links," TUFFC, vol. 63, no. 7, pp. 945-952, July 2016. doi: 10.1109/TUFFC.2016.2518122

[2] M. Rizzi et al., “WRS Low Jitter Daughterboard”, Open Hardware repository, https://www.ohwr.org/projects/wrs-low-jitter

[3] C. van Tour and J. Koelemeij, “Sub-Nanosecond Time Accuracy and Frequency Distribution through White Rabbit Ethernet”, ngVLA Memo #22, https://library.nrao.edu/public/memos/ngvla/NGVLA_22.pdf

[4] X. Yuan and B. Wang, “A Novel Synchronization Method for WR System”, EFTF-IFCS 2017, Besancon, France.

Frequency stability transfer with a fully stabilized and a transfer-oscillator optical frequency comb

Erik Benkler[1], Michele Giunta[2,3], Sofia Herbers[1], Thomas Legero[1], Dan Matei[1], Wolfgang Hänsel[2], Ronald Holzwarth[2,3], Uwe Sterr[1]

[1]Physikalisch-Technische Bundesanstalt, Bundesallee 100, 38116 Braunschweig, Germany
[2]Menlo Systems GmbH, Am Klopferspitz 19a, 82152 Martinsried, Germany
[3]Max-Planck-Institut für Quantenoptik, 85748 Garching, Germany

Email: erik.benkler@ptb.de

Currently, the best stabilized lasers have instabilities in the low 10^{-17} at 1s averaging time [1], with prospects to reach < 10^{-17} at 1s with crystalline mirrors at T = 4 K. Optical frequency combs can transfer frequency stability to interrogation lasers of optical atomic clocks. The comb and associated optics and electronics should not limit the stability transfer at the targeted levels. We employ two different combs to investigate the frequency stability transfer from a Si-cavity stabilized laser at 1542 nm (modified Allan deviation mod$\sigma = 4\times10^{-17}$ at 1s) to a clock laser at 1397 nm for a Sr lattice clock. In an out-of-loop measurement, we find an excess contribution from the combs, optics and electronics to the stability transfer with mod$\sigma < 7\times10^{-18}$ at 1s (20 kHz pre-filter BW). In an independent measurement, we show that excess noise during frequency doubling to the 698 nm Sr clock transition wavelength is negligible.

The first comb (Menlo Systems FC1500-250-ULN) has tightly locked (BW ~1.5 MHz) CEO frequency by self-referencing and an intra-cavity electro-optic modulator (EOM) as fast actuator [3]. With a second intra-cavity EOM as fast repetition rate actuator, a comb line was phase-locked also with high bandwidth (~2 MHz) to the Si cavity stabilized laser light field. An external cavity diode laser (TOPTICA Photonics DL-Pro) at 1397 nm, later to be frequency-doubled in a waveguide-PPLN for interrogation of a Sr lattice clock, is phase-locked to one of the stabilized comb lines (BW ~500 kHz). Thus, the stability of the Si cavity is transferred to all comb lines and to the clock laser.

For an out-of-loop check of the stability transfer to the clock laser, a second comb (Menlo Systems FC1550 with nonlinear polarization evolution mode-locking) and DDS-based RF-electronics is used as transfer oscillator [3] to generate a physical transfer beat between the diode laser and Si cavity laser fields. The transfer beat thus provides the out-of-loop information about excess instability contributions added during the stability transfer, including uncompensated optical path length fluctuations as well as excess noise from the frequency combs and electronics. All beat frequencies including the physical transfer beat frequency are counted with deadtime-free counters in Lambda averaging mode (K&K FXE with 20 kHz pre-filter BW) and then further processed offline for the data analysis. In a related contribution by some of us, an upper limit set by the fully stabilized ultra-low noise comb is reported as modσ < 2×10^{-18} at 1s (1 MHz pre-filter BW).

To minimize uncompensated paths, all fiber links are stabilized and the beat notes of the cw fields with the combs are generated in a single amplifier (EDFA) branch at each comb. Furthermore, at the ULN comb the fibers in the beat detection units are well isolated, with ~2 m uncompensated fiber length. At the second comb, a novel common-path free-space optics beat detection setup is employed, which at first order circumvents any differential uncompensated paths and hence eliminates the main obstacle for high spectral purity stability transfer.

[1] D.G. Matei et al., “1.5 µm lasers with sub-10 mHz linewidth”, Phys. Rev. Lett. 118, pp. 263202, 2017.
[2] W. Hänsel et al., “Rapid electro-optic control of the carrier-envelope-offset frequency for ultra-low noise frequency combs”, in *2017 Joint Conference of the EFTF and IEEE IFCS* 128–129 (IEEE, 2017).
[3] H.R. Telle et al., “Kerr-lens, mode-locked lasers as transfer oscillators for optical frequency measurements”, Appl. Phys. B 74, pp. 1, 2002.

The Features of Collective Level Shift and Line Broadening in a Fabry-Perot Microcavity and Near the Conducting Surface

Alexey S. Kuraptsev, Igor M. Sokolov

Department of Theoretical Physics, Peter the Great St.-Petersburg Polytechnic University, St.-Petersburg, 195251, Russia

Email: ims@is12093.spb.edu

Dipole–dipole interatomic interaction that arises from the exchange of virtual photon may play an important role in different physical systems. One of such system is cold atomic gas in special atomic trap. Here this interaction is responsible both for collective level shifts and atomic line broadening. These effects can limit the accuracy of an optical lattice clock [1]. The influence of dipole–dipole interaction on level shift and broadening has recently been observed experimentally [2, 3].

Another system which may be used in quantum metrology and where dipole-dipole interaction may be important is ensemble of impurity centers (atoms) embedded in a transparent dielectric matrix. The main goal of the present work is theoretical analysis of the influence of dipole-dipole interaction on spectral properties of such systems in the case when they are located in Fabry-Perot cavity or near the conducting surface.

For this purpose, we generalize the theoretical approach developed previously for atomic ensembles in free space on the case of considered atomic system in the cavity. Our approach is based on the Schrodinger equation for joint system consisting of N motionless atoms inside a Fabry-Perot cavity and the electromagnetic field including the vacuum reservoir. We take into account the peculiarities of the field modes of a cavity, the Zeeman structure of atomic levels as well as the possible shifts of the transition frequency caused by internal fields of the dielectric medium.

On the basis of the general theory we calculate the spontaneous decay dynamics of an excited atom as well as the shape of the transition spectrum. Obtained results are compared with the case of the system in free space. We show that the cavity or conducting surface can essentially modify dipole-dipole interaction and consequently spectral properties of studied atomic ensembles. This modification is explained by the peculiarities of the structure of modes of electromagnetic field in these cases.

This work was supported by the Russian Science Foundation, project no. 17-12-01085.

References

[1] D. E. Chang, J. Ye, M. D. Lukin, “Controlling dipole-dipole frequency shifts in a lattice-based optical atomic clock”, Phys. Rev. A vol. 69, 023810, 2004.

[2] S. J. Roof, K. J. Kemp, M. D. Havey, and I. M. Sokolov, “Observation of single-photon superradiance and the cooperative Lamb shift in an extended sample of cold atoms”, Phys. Rev. Lett. Vol. 117, 073003 (2016).

[3] S. L. Bromley, B. Zhu, M. Bishof, X. Zhang, T. Bothwell, J. Schachenmayer, T. L. Nicholson, R. Kaiser, S. F. Yelin, M. D. Lukin, A.M. Rey, J. Ye “Collective atomic scattering and motional effects in a dense coherent medium”, Nature Communications vol. 7, 11039, 2016.

Influence of an optical dense medium at the Ramsey method of CPT resonance detection

Konstantin Barantsev, Igor Sokolov, Gavriil Voloshin, Andrey Litvinov, Evgeniy Popov

Department of Theoretical Physics, Peter the Great St. Petersburg Polytechnic University, St. Petersburg, Russia

Email: kostmann@yandex.ru

The Ramsey method [1] of detection the resonance of a physical system allows us to significantly narrow down the line width of this resonance. So this method can be used in the metrological areas, such as frequency standards, magnetometers, high-resolution spectroscopy. The main idea of this method for detecting atomic resonance by an external coherent electromagnetic wave is use two separated interaction regions between which an atomic beam flies.

On the other hand, one of the effects providing a narrow resonance line is the coherent population trapping (CPT) [2,3] effect. The idea of using two-frequency optical radiation to stabilize the frequency of microwave range was expressed. The idea's value lies in the fact that there is no need to use bulky waveguides and microwave cavities, which can significantly reduce the size and power consumption of the device.

Detection of the CPT resonance by the Ramsey method was realized in the beam of sodium atoms in [4]. In [5] it is proposed the Ramsey method of registration with separation of the interaction regions of atoms with field not in space, as in original Ramsey method, but in time domain, that is, the use of pulse pumping. In this variant it is not necessary to create a collimated atomic beam and fly-through base, which makes it possible to significantly reduce the dimensions of the device. This method allows to narrow the resonance and suppress the light shifts.

This work is devoted to investigation of the CPT resonance which is excited by the pulsed radiation in an optically dense cold atomic cloud and detected by Ramsey method. Despite the large number of modern works on the investigation of Ramsey detection method, there remain some open questions related to the influence of an optical density of the medium at the shape of Ramsey fringes, which is the main subject of our work. We compared the signal of radiation passed through the medium and fluorescence signal. Also we analyzed dependence of the Ramsey fringes on intensities and durations of the pulses, direction of the detecting pulse, duration of the dark pause. This results can be applied in frequency standards, magnetometers and high-resolution spectroscopy.

The work was done under financial support of Ministry of Education and Science of the Russian Federation in terms of FTP "Research and development on priority trends of Russian scientific-technological complex evolvement in 2014-2020 years (agreement 14.578.21.0211, agreement unique identifier RFMEFI57816X0211)".

References

[1] N. F. Ramsey, Phys. Rev., vol. 78, p. 695-699, 1950.

[2] G. Alzetta, A. Gozzini, L. Moi, et al., Nuovo Cimento B, vol. 36, no.5, 1976.

[3] E. Arimondo, G. Orriols, Nuovo Cimento Lett., vol. 17, p. 333–338, 1976.

[4] J. E. Thomas, P. R. Hemmer, S. Ezekiel, et al., Phys. Rev. Lett., vol. 48, p. 867, 1982.

[5] G. Pati, K. Salit, R. Tripathi, et al., Opt. Commun., vol. 281, p. 4676, 2008.

Gold micro-discs as alkali preferential condensation spots for cell clock long-term frequency improvement

Sylvain Karlen, Thomas Overstolz, Jean Gobet, Jacques Haesler, Fabien Droz and Steve Lecomte

Time & Frequency, Systems, CSEM SA Neuchâtel, Switzerland

Email: sylvain.karlen@csem.ch

One of the main source of long-term frequency instabilities in cell clocks is the light-shift induced by changes of optical intensity. These variations, among other effects, can be due to the presence of condensed alkali droplets within the light-path of the interrogation laser, at the input window of the cell, and changes in their size, shape or location. A common solution to avoid this issue is to use a thermal gradient in order to create a cold spot and thus condensate the alkali on a preferential zone outside of the light-path. This solution is however hard to implement in MEMS cells due to their small dimensions and does not prevent alkali migration during storage of the clock in off mode. As an alternative, we report here on the use of CSEM patent pending gold micro-discs as alkali preferential condensation spots.

Fig. 1: MEMS atomic vapor cell with Au micro-discs

At low gold concentration, rubidium is known to form an intermetallic alloy (AuRb), the free Gibbs energy of which is large, negative and V-shaped [1]. The so-formed AuRb + Rb liquidus phase is thus expected to be energetically favorable with respect to pure Rb. By structuring gold micro-discs inside the cell cavity, the alkali metal is therefore expected to preferably condense on these gold-covered surface.

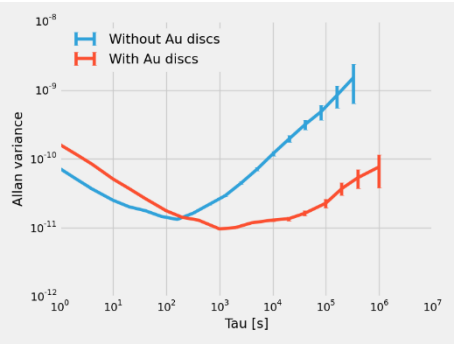

Fig. 2: Frequency stability comparison between cells with and without Au micro-discs. The short-term frequency stability difference is due to the use of different Rb isotopes between the two cells.

To test this principle, MEMS alkali vapor cells with such Au micro-discs, filled with rubidium dispensing micro-pills and an Ar-Ne buffer gas mixture [2], sealed by anodic bonding (see Fig. 1), were produced. Microscope imaging showed an effective preferential condensation of Rb on the Au micro-discs after cell activation. Moreover, a cell was tested in a CPT long-term clock setup and the results were compared with those of a cell without Au micro-discs. A significant improvement of the long-term frequency stability (see Fig. 2) was observed which shows the potential of this technology for MEMS cells long-term frequency stability improvement.

Last results on that subject as well as a detailed estimation of the effect of all the frequency shifts on the clock frequency stability will be presented at the conference.

References

[1] A. Pelton, “The Au-Rb (Gold-Rubidium) system,” *Bull. Alloy Phase Diagrams*, vol. 7, no. 2, pp. 139–142, 1986.

[2] S. Karlen, J. Haesler, T. Overstolz, G. Bergonzi, and S. Lecomte, “MEMS atomic vapor cells sealed by Cu-Cu thermocompression bonding,” in *International Frequency Control Symposium (IFCS), Joint with the 31st European Frequency and Time Forum (EFTF)*, 2017.

Elastic strain engineering for exceptional mechanical coherence

Amir H. Ghadimi[1], Sergey A. Fedorov[1], Nils J. Engelsen[1], Mohammad J. Bereyhi[1], Ryan Schilling[1], Dalziel J. Wilson[2,*], Tobias J. Kippenberg[1,†]

[1]IPHYS, École Polytechnique Fédérale de Lausanne, 1015 Lausanne, Switzerland
[2]IBM Research — Zurich, Saümerstrasse 4, 8803 Rüschlikon, Switzerland
[*]daw@zurich.ibm.com, [†]tobias.kippenberg@epfl.ch

Elastic strain engineering utilizes stress to realize unusual material properties [1]. For instance, strain is used to enhance the electron mobility in semiconductor thin films. In the context of nanomechanics, the pursuit of ultra-coherent resonators has led to intense study of "dissipation dilution", a technique where the stiffness of a material is effectively increased without added loss [2]. Dissipation dilution causes the anomalously high quality factor of thin-film Si_3N_4 nanomechanical resonators including recently-developed "soft-clamped" resonators [3]; however, the paradigm has so far relied only on the weak strain produced during material deposition. Geometric strain engineering techniques—capable of producing local stresses near the material yield strength—remain largely unexplored. Here, we will present a spatially non-uniform phononic crystal pattern, used to co-localize the strain and flexural motion of a Si_3N_4 nanobeam, while increasing the former to near the yield strength. This combined approach produces string-like modes with **Qf products approaching 10^{15} Hz**, exceeding previous values for a room-temperature mechanical oscillator of any size. The devices we have realized can have force sensitivities of $aN/\sqrt{Hz}$, perform hundreds of quantum coherent cycles at room temperature, and attain **Q>400 million** at megahertz frequencies.

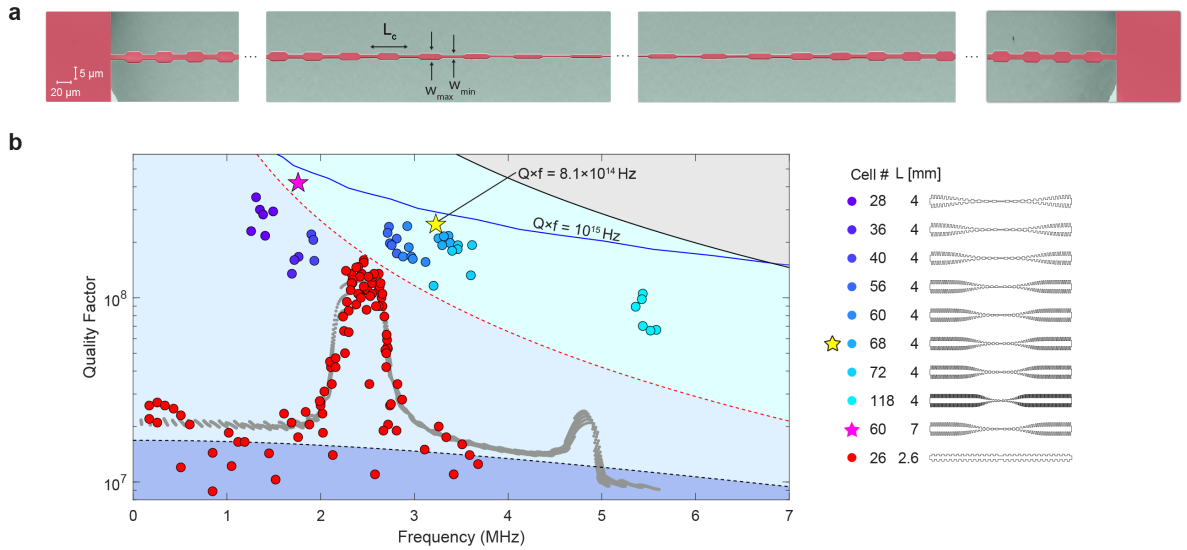

Figure 1: Enhancing the quality factor a soft-clamped nanobeam by strain-engineering (a) False colored scanning electron micrograph (SEM) of a typical device, vertically scaled for perspective. (b) The plot shows Q vs. frequency for nanobeams of different geometries. Red circles are from 2:6-mm, soft-clamped beams with 26 unit cells (model in gray). Blue shaded points are from strain-engineered nanobeams with varying numbers of unit cells, and correspondingly varied taper lengths (blue line is a numerical model). The magenta star displays Q of 420 million at a mode frequency of 1.76MHz. The yellow star shows $\boldsymbol{Q \times f = 8.1 \times 10^{14}}$ Hz. All quality factors were measured using ringdown spectroscopy. The red dashed line shows the limit for an idealized clamp-free beam (the limit of a soft-clamped resonator). Finally, the gray area delineated by solid black line is forbidden by the material yield strength of 6GPa.

References:

[1] J. Li, Z. Shan, and E. Ma, MRS Bulletin 39, 108 (2014).
[2] G. I. Gonzalez and P. R. Saulson, J. Acoust. Soc. Am. 96, 207 (1994).
[3] Y. Tsaturyan, A. Barg, E. S. Polzik, and A. Schliesser, Nat. Nano. 12, 776 (2017).
[4] A. H. Ghadimi et al., arXiv:1711.06247 [physics:quant-ph] (2017).

Inkjet printing of thin electrodes for quartz resonators

Amina Saadani[1], Pierre Lavenus[1], Gilgueng Hwang[2], Fabrice Sthal[3], Olivier Le Traon[1]

[1]Physics, Instrumentation, Environment, Space Department, ONERA, Châtillon, France
[2]Department of Microsystems and Nanobiofluidics, C2N, Orsay, France
[3]Time and Frequency Department, FEMTO-ST/ENSMM, Besançon, France

Email: amina.saadani@onera.fr

Microelectromechanical systems (MEMS) are used to develop different kinds of sensors: accelerometers, gyrometers, gas sensors… They can be actuated by three means: optically, electrostatically and piezoelectrically. For the piezoelectric actuation, electrodes are deposited on a piezoelectric material, as quartz. In response to an applied force, the vibrating part of the resonator deflects, and vice versa. Conventional electrodes are made of evaporated gold, with a thickness of about 200 nm to assure a good electrical conductivity and charge collect. However, for resonators with small dimensions and a very high intrinsic quality factor, these gold electrodes spoil the quality factor because of the viscous dissipation of the energy contained in the gold layers [1]. The viscoelastic losses are proportional to the electrode thickness, suggesting that ideal electrodes have to be very thin but still conductive. Thus, metallic nanoparticles seem suitable for reducing the electrode thickness below 200 nm.

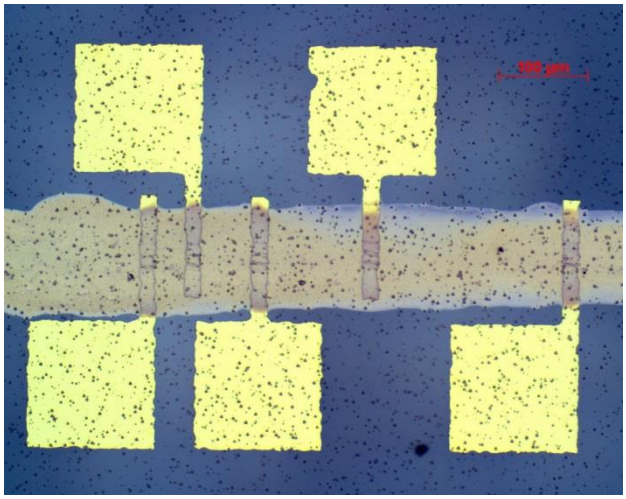

Fig. 1: A TLM device. Gold pads are made by e-beam evaporation and gold nanoparticles are deposited by an inkjet printing technique.

In this work, gold nanoparticles, with a diameter between 2 and 4 nm, dispersed in toluene are deposited by inkjet printing [2] on Transmission Line Measurement (TLM) devices (Fig. 1).The resistance of the gold nanoparticles can be characterized according the number of passes or the speed of printing. The first measurements show that the bands are conductive with a sheet resistance between 1.55 and 4.67 Ω/□. Then gold nanoparticles have also been deposited on a vibrating inertial gyrometer in order to create electrodes. Electrical and laser vibrometric measurements are in progress on the gyrometer to characterize the viscoelastic losses of the nanoparticles layer. Discussion about the resulting Q-factor and the frequency changes will be given.

References

[1] O. Le Traon, S. Masson, C. Chartier and D. Janiaud, “LGS and $GaPO_4$ piezoelectric crystals: New results”, Solid State Sciences 12 (2010) 318–324.

[2] G. Hwang, S. Haliyo, S. Régnier, “Infrared-photovoltaic properties of graphene revealed by electro-osmotic spray direct patterning of electrodes”, Micro & Nano Letters, 2010, Vol. 5, Iss. 2, pp. 140–145.

Interleaved cold atom gyroscope

D. Savoie, M. Altorio, B. Fang, L. Sidorenkov, R. Geiger and A. Landragin

LNE-SYRTE, Observatoire de Paris, PSL Research University, CNRS, Sorbonne Université, Paris, France

Email: arnaud.landragin@obspm.fr

We report the operation of a cold-atom gyroscope based on a four-Raman-pulse configuration [1], which enables a very large Sagnac area of 11 cm^2. In such cold-atom inertial sensors, the main limit to the sensitivity comes from aliasing effect linked to the sequential nature of the cold-atom experiments, leading to fluctuations of the inertial phase shift to more than a fringe from shot to shot. In order to resolve this problem and to achieve the intrinsic sensitivity of such sensors, we have demonstrated the possibility of continuous measurement of the rotation signal [2], i.e. without dead time between successive measurement, and the filtering of the vibration in real time so as to remain at the mid-fringe, where the sensitivity is maximal [3]. Moreover, we have setup a three time interleaved measurement mode [4] allowing both high sensitivity with the 800 ms total interrogation time and a 4 Hz effective sampling frequency.

The short-term sensitivity of the gyroscope has been improved by more than a factor three compared to our previous record [2], illustrated in Fig. 1 with a rotation sensitivity of 30 $nrad.s^{-1}.Hz^{-1/2}$. Moreover, the fast averaging of the rotation noise, as $1/\tau$ up to 10 s, is a clear signature of the gain of the continuous measurement. The long term sensitivity has also been improved to below 0.3 $nrad.s^{-1}$ at 10^4 s.

We have carried out a preliminary study of the systematic effects associated to these specific methods. We have shown that the continuous operation does not lead to any systematic effect at the level of 2. $nrad.s^{-1}$. Moreover, we have shown that the misalignment between the Raman pairs needs to be at the µrad level in order to achieve long term stability below 0.1 $nrad.s^{-1}$.

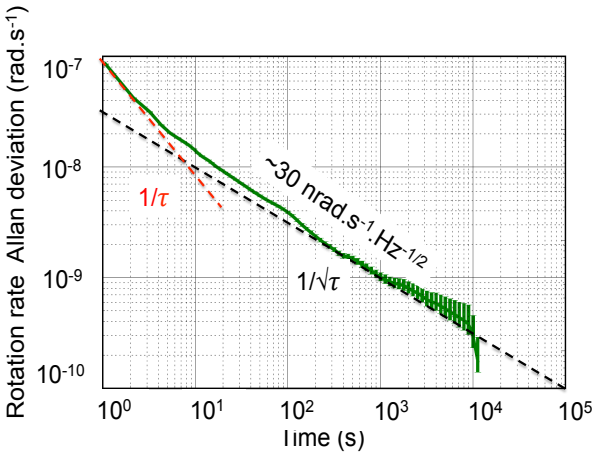

Fig. 1: Allan standard deviation of the rotation rate sensitivity.

Acknowledgment

We acknowledge the financial support from Direction Générale de l'Armement (DGA Contract No. 2010.34.0005), Centre National d'Etudes Spatiales (CNES), Institut Francilien de Recherche sur les Atomes Froids (IFRAF), the Action Spécifique du CNRS Gravitation, Références, Astronomie et Métrologie (GRAM), and Ville de Paris (project HSENS-MWGRAV). D. S. is supported by DGA.

References

[1] B. Canuel, et al., Phys. Rev. Lett. 97, 2006, 010402.

[2] I. Dutta, et al., Phys. Rev. Lett. 116, 2016, 183003.

[3] J. Lautier, et al., Applied Physics Letters 105, 2014, 14410.

[4] M. Meunier, et al., Phys. Rev. A 90, 063633 (2014).

Atom interferometry from Earth to space

Waldemar Herr

Institut für Quantenoptik, Leibniz Universität Hannover, Germany

Email: herr@iqo.uni-hannover.de

Atom interferometry is widely used for measuring rotations and accelerations with applications in navigation, geophysics/geodesy, and fundamental physics. In our group, a cold atom gyroscope [1] measured earth's rotation at the percent level, a dual species cold atom gravimeter performed a test of the universality of free fall at parts in 10^7 [2,3], and we investigate novel techniques for ground based and spaceborne implementations.

Today's inertial sensitive atom interferometry devices operate mostly with sources of laser cooled atoms. The finite temperature and size of these sources limit the efficiency of employed beam splitters and the analysis of systematic uncertainties. These limits can be overcome by the use of ultra-cold sources such as a Bose-Einstein condensates (BEC) or in addition magnetically lensed atomic ensembles with extremely narrow velocity distributions. Usually the creation of BECs is time-consuming, but our demonstration of a compact high-flux source for the generation of BEC [4] has led to a paradigm shift in atom interferometry. BECs open up the use of high-contrast single and double Bragg diffraction, the transfer of more than 1000 $\hbar k$ by multi-photon transitions, and the utilization of matter-wave lenses to collimate the atomic ensemble in 3D equivalent to 50 pK. These methods enabled the demonstration of our quantum tilt meter [5] and our ultra-compact atom chip fountain gravimeter [6]. Currently a transportable atom-chip based Quantum Gravimeter is being set up, promising unprecedented accuracy for the determination of local gravity for studies in geodesy.

As the sensitivity in these kinds of experiments depends on the square of the free evolution time of the atomic ensemble, the extension of this time is investigated in our new facility for Very Long Baseline Atom Interferometry, in the QUANTUS experiments in the drop tower Bremen [7,8] and in the MAIUS sounding rocket experiment, which demonstrated the first BEC in space in January, 2017.

These experiments are opening the era of maturity of transportable precision quantum interferometers and for future space borne applications [9]. This talk will focus on our work on BEC interferometry on earth and in space.

[1] Berg et al., Phys. Rev. Lett. **114**, 063002 (2015).
[2] N. Gaaloul et al., Precision interferometry with Bose-Einstein condensates, in: Atom Interferometry, edited by G. M. Tino and M. A. Kasevich, Amsterdam: IOS (2014).
[3] D. Schlippert, et al., Phys. Rev. Lett. **112**, 203002 (2014).
[4] J. Rudolph et al., New J. Phys. **17**, 079601 (2015).
[5] H. Ahlers, et al., Phys. Rev. Lett. **116**, 173601 (2016).
[6] S. Abend et al. Phys. Rev. Lett. **117**, 203003 (2016).
[7] H. Müntinga et al., Phys. Rev. Lett. **110**, 093602 (2013).
[8] J. Rudolph et al. Microgravity Sci. Technol. **23**, 287 (2011).
[9] D. N. Aguilera et al., Class. Quantum Grav. **31**, 115010 (2014).

Effects of atmospheric turbulence on optical two-way time-frequency transfer across partially reciprocal free-space links

Martha I. Bodine[1], William C. Swann[1], Isaac H. Khader[1], Laura C. Sinclair[1], Esther Baumann[1], Jean-Daniel Deschenes[2], Nathan R. Newbury[1]

[1]National Institute of Standards and Technology, Boulder, Colorado
[2] Université Laval, Québec, Canada

Email: martha.bodine@nist.gov
Work of the U.S. government. Not subject to copyright.

Despite picosecond-level or greater timing fluctuations caused by atmospheric turbulence, optical two-way time-frequency transfer (OTWTFT) enables femtosecond-level synchronization of optical clocks across free-space links, and phase comparisons at the 10^{-18} level [1]. To achieve this level of performance, OTWTFT relies on the reciprocity of a bi-directional single-spatial mode free-space link. Over link distances of a few kilometers, optical transit times are on the order of microseconds, and the turbulent features of the atmosphere are effectively frozen in time. Consequently, the reciprocity of the bi-directional link is nearly perfect. However, as uplink and downlink paths become physically separated due to relative motion of the two clock sites, e.g. in ground-satellite links, link reciprocity begins to break down, degrading the precision of OTWTFT.

Here, we explore the effects of partial reciprocity on OTWTFT. We quantify the effects of reciprocity breakdown by measuring jitter in time-of-flight measurements across a 2 km free-space link. Additionally, we investigate the accuracy of models that predict timing jitter using Taylor's frozen turbulence hypothesis and a transfer function determined by measurement geometry [2]. By varying the spatial separation between two counterpropagating beams in the bi-directional link, we control the reciprocity of the link and thereby measure the dependence of time-of-flight variance on link reciprocity.

Our initial results are shown in Fig. 1. Below Fourier frequencies of approximately 10 Hz, timing jitter across non-reciprocal links shows excellent agreement with modeled piston-mode variation caused by Kolmogorov atmospheric turbulence [2]. Across partially reciprocal links, timing jitter is reduced, but remains above the fully reciprocal noise floor. At frequencies between 10 Hz and 100 Hz, the departure of the timing jitter from piston-mode predictions, as well as near-total reciprocity breakdown in the partially reciprocal link, indicates that existing timing variation models must be expanded to include higher-order turbulence effects such as angle-of-arrival fluctuations.

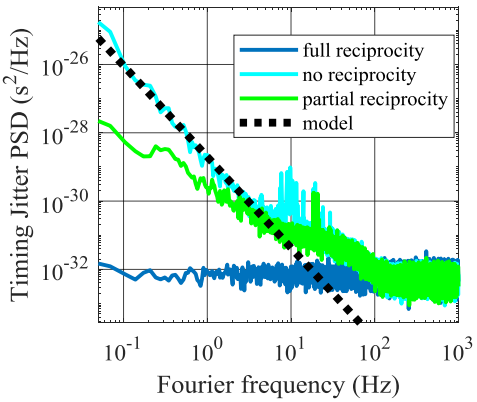

Figure 1. Timing jitter power spectral density (PSD) in optical time-of-flight across a 2 km free-space link.

References

[1] L. C. Sinclair, H. Bergeron, W. C. Swann, E. Baumann, J.-D. Deschênes, and N. R. Newbury, "Comparing optical oscillators across the air to milliradians in phase and 10-17 in frequency", ArXiv171004063 Phys., 2017.

[2] A. Belmonte, M. Taylor, L. Hollberg, and J. Kahn, "Effect of atmospheric anisoplanatism on earth-to-satellite time transfer over laser communication links," Opt. Express, 25, 15676-15686, 2017.

Development of the Strontium Optical Lattice Clock at National Time Service Center

Mojuan Yin[1], Qinfang Xu[1], Yebing Wang[1,2], Jie Ren[1], Yang Guo[1,2], Hong Chang[1]

[1]CAS Key Laboratory of Time and Frequency Primary Standards, National Time Service Center, Chinese Academy of Sciences, Xi'an 710600, China
[2]School of Astronomy and Space Science, University of Chinese Academy of Sciences, Beijing 100049, China

Email: changhong@ntsc.ac.cn

In past decades, atomic optical lattice clock based on neutral atoms and single ions have made remarkable development on instability and uncertainty achieving 10^{-18} level.[1,2] The application of optical lattice clock covers lots of field, such as the fundamental constant precision measurement, gravitational wave detection, and clock-based geodesy. Recently, a measurement precision of 5×10^{-19} in 1 hour of averaging time based on ^{87}Sr three-dimensional optical lattice clock was reported.[3] Since the ^{87}Sr optical lattice clock became one of the most promising candidates for redefinition of the second of the SI.

The work presented in this paper is based on a ^{87}Sr one-dimensional optical lattice clock at National Time Service Center in China. In our experiment, a closed-loop operation of a ^{87}Sr optical lattice clock is demonstrated. A two-stage three-dimensional magneto-optical trap (MOT) combined with a slowed beam and a Zeeman slower is employed to efficiently cooling and trapping the atoms. After the second-stage cooling, the number of atoms in the red MOT is around 3.5×10^6 and the logitudinal temperature of the red MOT is 3.9 μK. Then we apply a 813 nm diode laser to form a one-dimensional optical lattice for loading the atoms of the red MOT, and a 1/e lifetime of 1.6 s of the lattice is obtained. The normalized shelving detection method is adopted to detect the clock transition with a narrow linewidth 698 nm clock laser system (Hz level). Finally, a spin-polarized spectrum of transitions $^1S_0(m_F=+9/2)$-$^3P_0(m_F=+9/2)$ with a linewidth of 3.9 Hz is measured at the detecting pulse duration of 300 ms. And an in-loop fractional frequency Allan deviation is achieved to $5\times10^{-15}/\tau^{1/2}$ at an average time of 3000 s. Furthermore, we will improve the instability and measure the accuracy of ^{87}Sr optical lattice clock.

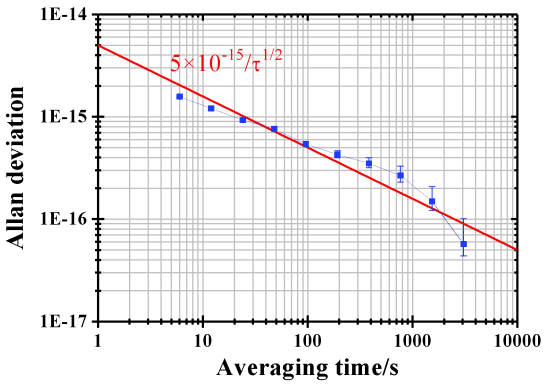

Fig. 1: An in-loop fractional frequency Allan deviation.

References

[1] T. L. Nicholson, et al., "Systematic evaluation of an atomic clock at 2×10^{-18} total uncertainty", Nat. Commun., vol. 6, p. 6896-6903, 2015.

[2] N.Hinkley, et al., "An atomic clock with 10^{-18} instability", Science, vol 341, p. 1215-1217, 2013.

[3] S. L.Campbell, et al., "A Fermi-degenerate three-dimensional optical lattice clock", Science, vol 358, p. 90-94, 2017.

Multi-GNSS Time Transfer with CGGTTS-V2E

Pascale Defraigne[1], Katrijn Verhasselt[1]

[1]Royal Observatory of Belgium, Brussels, Belgium

Email: p.defraigne@oma.be

GNSS Time transfer is based on code pseudorange measurements collected by GNSS receivers. When using only the code observations, the Common GNSS Generic Time Transfer Standard (CGGTTS) is commonly used. The CGGTTS is a format for delivering time solutions computed with a standard computation procedure using pseudorange observations. The latest version of the CGGTTS is the V2-Extended (V2E), and includes timing solutions for satellites from five GNSS constellations: GPS, GLONASS, Galileo, BeiDou, and QZSS.

The R2CGGTTS software has been developed since more than 15 years to allow time transfer in the CGGTTS standard when using geodetic receivers providing raw observation files in the RINEX format. The goal was also to have a full control of the procedure from the raw observations to the time products available in the CGGTTS files. A completely new version of the software has been built, named R2CGGTTSV8, and provides the CGGTTS-V2E files for the four global GNSS constellations, as well as 30-second clock solutions for all the code signals of each constellations, which is needed for the computation of relative calibration. Both versions 2 and 3 of the RINEX format are supported.

After a brief presentation of the new SW different results of time transfer solutions based on the different constellations for continental and inter-continental links will be presented. As a second step, different options for the combination of the different constellations into a single combined solution will be discussed and tested. The first one is a combination at the observation level, which requires combined satellite clock products having the same reference for all the constellations. In that case the IGS products of the Multi-GNSS Experiment (MGEX) products will be used here. The second option is a combination of the time transfers solutions, where a weighted average of the solutions for each constellation can be done. The important issue in these combinations is the calibration of the equipment for the different signals of the different constellations. A particular attention will therefore be given to the consistency between the calibration results that can be achieved for the different constellations.

Cross-spectrum approach to absolute timing jitter measurement of mode-locked lasers

Alexis Casanova[1,2] , Benoît Trophème[1], Antoine Courjaud[1] and Giorgio Santarelli[2]
[1]Amplitude-Systèmes, 11 Avenue de Canteranne, 33600 Pessac, France.
[2]LP2N, IOGS, CNRS, Univ. de Bordeaux, 33400 Talence, France.
Email: giorgio.santarelli@institutoptique.fr

Ultralow timing jitter femtosecond mode-locked lasers can be used for timing synchronization, optical sampling and analog-to-digital conversion, low-noise microwave generation, photonic radars and metrology. It is well known that mode-locked lasers can inherently generate optical pulse trains with extremely low timing jitter. The theoretically predicted quantum-limited timing jitter from a soliton solid state laser well below 1 fs above 100 kHz offset frequency. Record low timing jitter of less than 13 as have been demonstrated from a 10 fs pulse duration Ti:Sapphire laser [1]. The measurement of such low timing jitter level is a fantastic challenge. The balanced optical cross-correlator (BOC) introduced in 2003 [2] allows to evaluate residual timing jitter with a resolution approaching a few 10^{-13}fs²/Hz. More recently, the use of an optical heterodyne technique allowed a record noise floor of 10^{-13}fs²/Hz [3]. The BOC approach allows only residual jitter measurement and the measurement floor is strongly dependent on pulse duration and pulse energy. For the first time we implement cross-spectrum techniques extensively used in phase noise measurements to a dual BOC system with three independent mode-locked lasers, enabling absolute timing jitter measurement with unprecedented noise floor. For this experiment we use Ytterbium passively mode-locked solid-state lasers with a semiconductor saturable absorber mirror (SESAM). This configuration allows self-starting, robust and stable laser operation with 200fs output pulse duration at 1030nm. The lasers are multimode diode-pumped with 500mW output power with a repetition rate of 62MHz. Each balanced optical cross-correlator exhibits a shot-noise-limited measurement floor of 2 10^{-12} fs²/Hz for input pulses peak powers of 13kW and 26kW from the master laser and the slave lasers, respectively. After 70000 averages, the timing jitter measurement resolution is 10^{-14}fs²/Hz, one order of magnitude better than the state-of-the-art. The integrated residual timing jitter is estimated to 73as from 10kHz to 31MHz offset frequency [Fig1]. The timing jitter performance is limited by intra-cavity amplitude-noise-to-timing-noise conversion, mostly attributed to the SESAM.

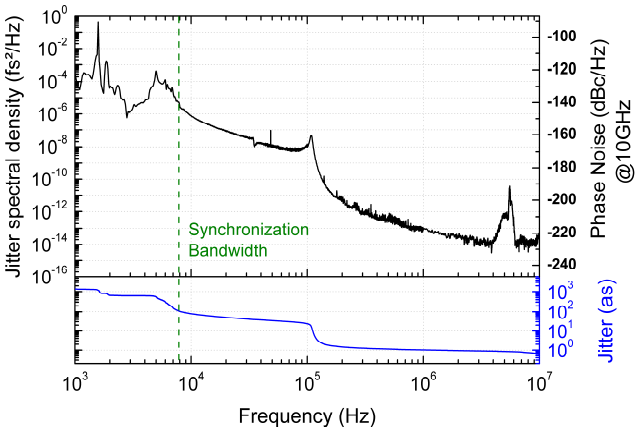

Fig. 1: Absolute timing jitter of a diode pumped SESAM mode locked solid-state Ytterbium laser.

References

[1] A. J. Benedick, J. G. Fujimoto & F. X. Kärtner, "Optical flywheels with attosecond jitter" *Nature Photonics* , vol., 9 p.7–100, 2012.
[2] T. R. Schibli et al, "Attosecond active synchronization of passively mode-locked lasers by balanced cross correlation," *Opt. Lett.* , vol. 28, p. 947-949, 2003.
[3] D. Hou et al., "Timing jitter characterization of mode-locked lasers with <1 zs/√Hz resolution using a simple optical heterodyne technique," *Opt. Lett*. vol.40, p. 2985-2988, 2013.

Watt level narrow linewidth transportable laser source at 852 nm for laser cooling of cesium atoms

Laura Antoni-Micollier[1], Baptiste Battelier[1], Daniel Comparat[2], Bruno Desruelle[3], Matthieu Viteau[4], Giorgio Santarelli[1]
[1]LP2N, IOGS,CNRS Université de Bordeaux, 33400 Talence, France
[2]Laboratoire Aimé Cotton, , 91405 Orsay Cedex, France
[3]Muquans, Institut d'Optique d'Aquitaine, 33400 Talence, France
[4]Orsay Physics, 13710 Fuveau, France
Email: giorgio.santarelli@institutoptique.fr

Cooling atoms of cesium is a process with high interest for metrology, fundamental physics, space and industrial applications. The laser technology used to perform this process is usually free space external cavity laser diode (ECDL) at 852 nm [1] with tapered semiconductor amplifiers, which can present misalignments with vibrations and temperature fluctuations.

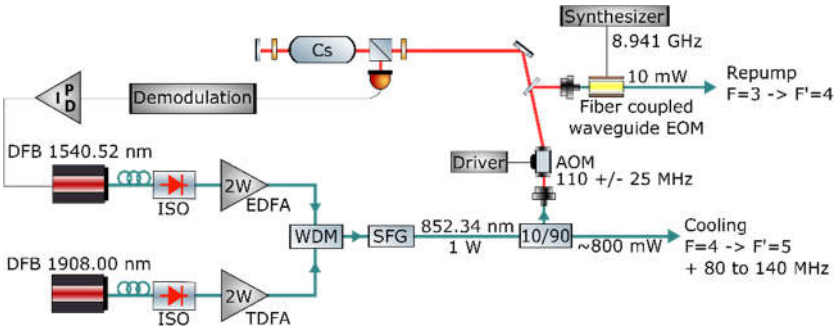

Fig. 1: Scheme of the laser architecture. DFB: Distributed Feedback Laser diode, EDFA: Erbium-doped fiber amplifier, TDFA: Thulium-doped fiber amplifier, WDM: Wavelength Division Multiplexing, SFG: Sum-frequency generation.

In this context, we are developing a stable and robust all fiber architecture (fig. 1), based on a sum-frequency generation (SFG), to produce a watt level MHz linewidth laser at 852 nm. This type of architecture to generate 852 nm has already been recently tested independently from our work by C. Diboune et al. [2], with different seed wavelengths. In our experiment, the SFG is realized through a fiber periodically poled lithium niobate (PPLN) waveguide, from the combination of a laser at 1540 nm and a laser at 1908 nm. With this method, we benefit from off-the-shelf fiber components in the telecom domain, which present the advantage to be efficient, compact and robust, and fiber components at 2 µm, which are highly developed since several years.

In order to reach about one Watt at the output of the SFG, each wavelength is amplified up to 2W before the combination in a wavelength division multiplexing (WDM). An efficiency of 40% has been obtained in the PPLN leading to a total power of more than 800mW. About 5% of the 852nm laser is then used for frequency stabilization on a saturated absorption spectroscopy scheme, and the feedback signal is applied on the 1540 nm laser diode current (see Fig. 1). We also use a fiber pigtailed waveguide phase modulator to generate the repumping signal at 9GHz offset from the cooling transition. We are currently working towards linewidth reduction by a custom 1908nm fiber laser.

References

[1] T. Lévèque et al, "PHARAO laser source flight model: Design and performances" *Review of Scientific Instruments*, vol. 86, p.033104, 2015.
[2] C. Diboune et al., " Multi-line fiber laser system for cesium and rubidium atom interferometry," *Optics Express* vol 25, p. 16898-16906, 2017.

RF/MW Signal Generations Aiming SDR & IoT Applications

Ulrich L. Rohde[1,2], Ajay K. Poddar[1,2], Alexandru M. Silaghi[2]

[1]Synergy Microwave Corp., 201 McLean Boulevard, Paterson, NJ, USA
[2]University of Oradea, Faculty of EE and IT, Oradea, Romania

Email: akpoddar@synergymwave.com

The Internet of Things (IoT) encompasses a range of emerging wireless network technologies for sensing and control on a massive and unprecedented scale. The disposition of IoT will eventually necessitate improvements in RF/MW signal generation technologies, integration of sensor technologies, improved energy storage and recovery technologies, massive data mining, security, and network protocol improvements. Wireless communication system is the essential part for IoT infrastructure, which acts as the bridge for dual directional communication for data collection and control message delivery. Figure (1) depicts the typical IoT architecture. Low cost small size RF/MW signal sources generation, signal processing, and synthesis are ubiquitous in IoT architecture. Classical synthesis and synchronization circuits, like DDS, PLLs etc., depend heavily on the performance of their analog and mixed-signal blocks to produce spectrally pure and jitter-free signals. SDR (Software defined radios) inspired digitally intensified RF/MW Signal sources and synthesizers architecture play important role in targeting IoT (internet of things) to support the optimized communication from the senor network to the wide area radio network. Figure (2) shows the typical block diagram of SDR based radio monitoring receiver for IoT applications. As depicted in Figures (1) and (2), IoT and SDR architectures mandate for multi-band/multi-mode signal generating electronics. In this paper, metamaterial Möbius strips based RF/MW components discussed for the realization of signal generation and signal processing electronics for SDR and IoT applications. Figure (3) depicts the typical Möbius-Strips formed by Graphene nanoribbons; possess topology-induced electromagnetic and thermal properties. It is found that nonzero magnetic moment and excellent energy storing properties of Möbius Loop formed by Graphene nanoribbons shown in Figure (3) is extraordinarily stable. As shown in Figure (3), cylindrical closed ring strips structures formed by Graphene-nanoribbons possess 2-edges, exhibit anti-ferromagnetic (Zero-magnetic moment, whereas Mobius closed ring strips structure formed by Graphene-nanoribbons possess single-edge, exhibit ferromagnetism (nonzero magnetic moment). Graphene nanoribbons with 'zigzag' edge structure exhibit magnetism at their edges; most stable configuration of these ribbons is anti-ferromagnetic, so that magnetic moments at opposite edges point in opposite directions, reducing the total magnetic moment of the ribbons to zero. However, Graphene Möbius strip shown in Figure (1), possess only one continuous edge, hence no magnetic cancellation between the opposite edges, resulting in a nonzero magnetic moment. These unique properties allow possibility of quantum clock and spintronic devices for IoT applications. The detail description and measured result will be discussed in full length paper. The potential impact of widespread deployment of IoT technology over the next forty years is comparable to the impact wireless cellular technology has had over the last forty years. Improvements in RFIC technology, micro-power signal sources, and integrated sensors will be required in order to fully exploit the possibilities.

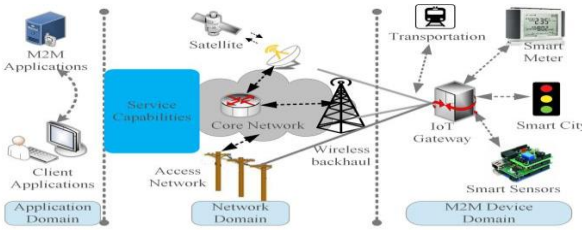

Fig. 1: shows the typical IoT architecture

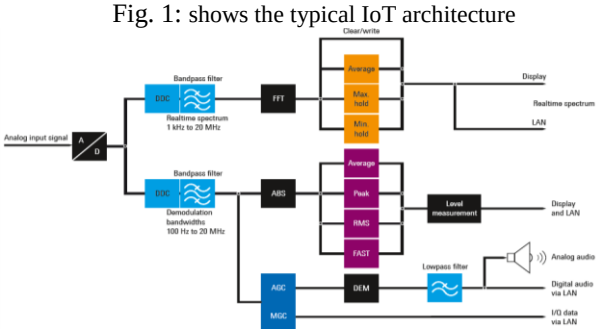

Fig. 2: SDR inspired monitoring receiver for IoT applications

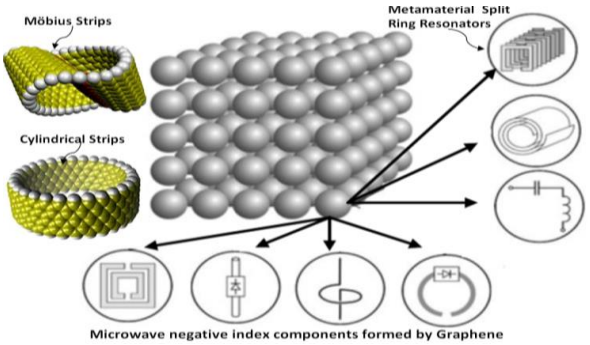

Fig. 3: Möbius-Strips formed by Graphene nanoribbons suitable for high quality factor microwave frequency components

Galileo and GNSS Time Offsets

G. Signorile[1], I. Sesia[1], P. Defraigne[2], P. Tavella[1,3]

[1] Istituto Nazionale di Ricerca Metrologica (INRIM), Turin, Italy
[2] Royal Observatory of Belgium, Brussels, Belgium
[3] Bureau International des Poids et Mesures, Sevres - since November 2017

Email: g.signorile@inrim.it

Since April 2013, Galileo started to disseminate the GPS to Galileo Time Offset (GGTO), by transmitting the conversion parameters through the navigation message.

This broadcast offset is allowing the user of a combined GSP/Galileo receiver to achieve a unique navigation solution by using measurements from both GPS and Galileo satellites, thus allowing interoperability between the two navigation satellite systems.

Nowadays, many positioning systems are available, the topic of interoperability is therefore crucial to provide better capabilities at user level than the ones that would be achieved by relying solely on one system. The time offsets between the different systems should therefore be made available to the multi-GNSS users. An alternative would be that each constellation broadcast only the time offset between its time scale and a reference common to all GNSS.

In this paper, we investigate this scenario. We propose, as reference common to all GNSS, either a combination of the predictions of the GNSS time scales of the different systems, or directly the UTC predictions broadcast by the different systems. From these approaches, we present a first assessment of the performances that can be achieved by a single user equipped with a multi-GNSS receiver when estimating the offset between Galileo and other GNSS time scales, therefore addressing the interoperability of Galileo with other GNSS.

Air pressure dependence and compensation of a passive hydrogen maser

Harald Hauglin[1,2], Tim Dunker[1]

[1]Justervesenet - Norwegian Metrology Service, Kjeller, Norway
[2]Department of Technology Systems, University of Oslo, Oslo, Norway

Email: hha@justervesenet.no

We use daily clock offsets with respect to UTCr to characterize the frequency shift of a passive H-maser due to changes in atmospheric air pressure. We find evidence of linear dependence on air pressure (no hysteresis) with a sensitivity coefficient of magnitude $+5.6 \times 10^{-16}$ $(\mathrm{hPa})^{-1}$.

Passive hydrogen masers offer superior short-term stability compared to industrial Cesium beam standards and low frequency drift (typically $< 10^{-15}$/d) makes them potentially suitable for time scale generation if systematic influences due to environmental factors can be controlled. Temperature and humidity can routinely be controlled to within +- 0.1 K and a few %RH, while lab air pressure is unregulated and follows the overall local atmospheric variations. By contributing clock- and time transfer data to the CCTF-K001.UTC, JV gets daily clock offsets referenced to UTCr. Analysis of clock performance with respect to UTCr (figure 1) reveals that air pressure variations has a substantial systematic influence on clock performance and directly impacts the stability of the generation of the UTC(JV) timescale.

Our analysis indicates that real time pressure compensation of the passive H-maser frequency may offer improved timescale generation and predictability.

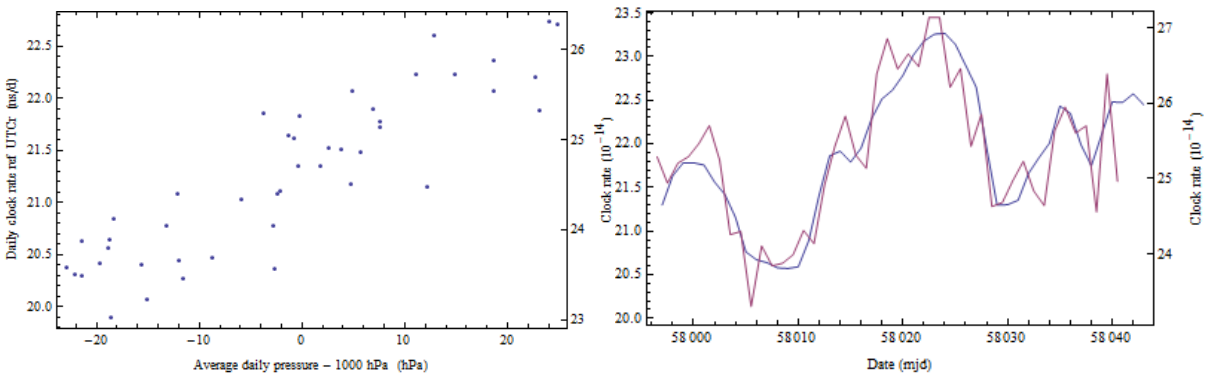

Figure 1. Air pressure dependence of a passive H-maser (Vremya-Ch VCH-1008). The left panel shows daily clock rate plotted against local daily averaged air pressure. The right panel shows time series of daily clock rate with respect to UTCr (jagged line) and fit to the clock rate using a model with linear frequency drift and air pressure dependence.

The INRIM Timing Performance Monitoring Facility

I. Sesia[1], G. Signorile[1], F. Fiasca[2], V. Formichella[1], P. Tavella[1]

[1] Istituto Nazionale di Ricerca Matrologica (INRIM), Turin, Italy
[2] AizoOn, Turin, Italy

Email: i.sesia@inrim.it

During the past twenty years, the Italian National Metrology Institute (INRIM) has been involved in the research, development and monitoring of the European Global Navigation Satellite System Galileo, in collaboration with the European Space Agency (ESA), some of the major European space industries, Politecnico di Torino, and the European metrological time laboratories.

Based on the experience gained in this context, recently INRIM developed a Timing Performance Monitoring Facility (TPMF) to carry out a close monitoring of the timing performances of the Global Navigation Satellite Systems, such as Galileo, GPS, GLONASS and BEIDOU as well as the European Geostationary Navigation Overlay Service EGNOS.

This paper shows the architecture and main functionalities of the TPMF, as well as examples of the key products which are generated by the facility and regularly used for monitoring and validation of GNSS and EGNOS timing aspects, including space clocks and the time dissemination through the navigation message.

The Galileo Time Service Provider: Design and Operational Key Elements

I. Sesia[1], G. Signorile[1], T. T. Thai[1], E. Cantoni[1], C. De Stefano[1], P. Tavella[1]
M. Gandara[2], P.L. Puech[2]
V. Hamoniaux[3], V. Jacquard[3], S. Capou[3], T. Deboschere[3], V. Lafon[3]
G. C. Rodi[4], F. Fiasca[4], A. Cernigliaro[4], R. Affinito[4] , F. Arico[4],
G. Pantalone[4], A. Perucca[4], M. Raimondi[4]

[1] Istituto Nazionale di Ricerca Metrologica (INRIM), Turin, Italy
[2] Thales Alenia Space France (TAS-F), Toulouse, France
[3] SII, Toulouse, France
[4] AizoOn, Turin, Italy

Email: i.sesia@inrim.it

The Galileo Time Service Provider (TSP) is the definitive operational timing facility with service oriented perspective of the European Global Navigation Satellite System Galileo. In 2016, the Galileo Service Operator (GSOp) contract managed by the European GNSS Agency (GSA) on behalf of the European Commission and funded by the European Union has been awarded to Spaceopal GmbH, a joint venture between the German Aerospace Agency (DLR) and Italy's Telespazio. In the same year, Spacecopal selected the Project of the TSP consortium, led by Thales Alenia Space France (TAS-F) and the Italian National Metrology Institute (INRIM), with the collaboration of European space industries, Politecnico di Torino and the European metrological time laboratories. In 2017 the TSP has been designed, developed and put in operation following a challenging timeline schedule.

The main TSP tasks are:

- ✓ to allow the Galileo Mission Segment (GMS) to steer the Galileo System Time (GST) to the international reference time UTC
- ✓ to predict the difference of GST versus UTC, which is then transmitted in the Galileo navigation message to fulfill the Galileo time dissemination service
- ✓ to validate the Galileo timing infrastructure, including space and ground clocks and the GST behavior.

This paper presents the TSP main mission, its fundamental role in the Galileo time keeping and in the assessment of the system performances from the timing point of view.

The activity described in this presentation is carried out under a contract managed by GSA on behalf of the European Commission and funded by the European Union.

Time-Frequency Analysis of Atomic Clock Anomalies

Lorenzo Galleani[1]

[1]Department of Electronics and Telecommunications, Politecnico di Torino, Torino, Italy

Email: galleani@polito.it

Atomic clocks are fundamental elements of global navigation satellite systems (GNSS), such as GPS and Galileo. In a GNSS, in fact, the user position is estimated from the time of flight of the signals travelling from the system satellites to the receiver. An error in time implies therefore an error in position, and hence atomic clocks are used both on-board the system satellites, as well as in the ground stations. In addition to satellite navigation, atomic clocks are becoming fundamental in many other applications, such as, for instance, time stamping of bank transactions, and tests of fundamental physics.

Monitoring and analyzing the performances of the atomic clocks involved in these applications is hence essential. Anomalous behaviors can in fact generate nonstationarities in the signals corresponding to the clock time and frequency deviations, resulting in a temporary degradation of the clock performances.

An effective way to study nonstationary signals is to analyze their time-varying spectrum by using time-frequency analysis [1], a body of techniques for the description of signals whose frequency content changes with time.

By using the time-frequency method developed in [2], we analyze the time-varying spectrum of the most common atomic clock anomalies, such as frequency jumps and short-duration sinusoidal terms. Our results show that time-frequency analysis can be used to reveal the anomalies of atomic clocks, and hence to analyze and monitor their performances.

References

[1] L. Cohen, Time-Frequency Analysis, Prentice-Hall, 1995.
[2] L. Galleani, “Detection of changes in clock noise using the time-frequency spectrum,” Metrologia, vol. 45, pp. 143-153, December 2008.

Poling conditions for PZT thin film-based resonators

Alexandre Reinhardt[1], Guillaume Tochou[1], Selimen Benahmed[1], Amy N'Hari[2], Marie Bousquet[1], Henri Sibuet[1]

[1] Univ. Grenoble Alpes, Grenoble, France
CEA, LETI, MINATEC-Campus, Grenoble, France
[2] ST Microelectronics, Tours, France

Email: alexandre.reinhardt@cea.fr

$PbZr_xTi_{1-x}O_3$ (PZT) is the prime material for micro-actuators, owing to its large piezoelectric coefficients. Therefore, it has also been investigated for resonators, sensors or piezoelectric transformers applications, that are expected to take benefit from its large electromechanical coupling factor (close to 40% for bulk ceramics). However, unlike polar materials such as AlN or ZnO, PZT is also ferroelectric and exhibits ferroelectric domains with possibly opposite orientations. As such, in order to obtain optimum piezoelectric properties without applying an electric bias during operation, a poling step is required to align a majority of domains along the same direction. This polarization state has then to survive over the lifetime of the device.

In this work, we fabricated film bulk acoustic resonators (FBAR) made of 2 µm-thick sol-gel $PbZr_{0.52}Ti_{0.48}O_3$ films with (100) preferential orientation, sandwiched between a platinum bottom electrode and a ruthenium top electrode [1]. These resonators were used as test structures for investigating the impact of poling conditions on the elastic, dielectric and more importantly piezoelectric properties of the PZT film. Devices were poled under various conditions, by heating the sample to a given temperature (up to 150°C, i.e. close to half the Curie temperature of the PZT thin film) for a given time (between 30 and 90 min) and applying a bias voltage up to ±6 times the coercive voltage, maintaining it until the heating stopped and the devices were fully cooled down. Devices poled this way were regularly measured and in the most interesting case did not exhibit significant aging (i.e. loss of piezoelectric properties) over the course of more than one year.

Poling conditions proved to affect significantly electromechanical coupling factors. Best performances were obtained, as expected, when the highest temperature was applied during poling, due to improved domain mobility, and for the longest poling duration, which offered more time for domains to properly align. More interestingly, as shown in Fig. 1, the poling direction proved to be the major factor influencing piezoelectric properties and aging behavior owing to the existence of an internal field (or imprint) favoring the stability of the poling in a preferential direction.

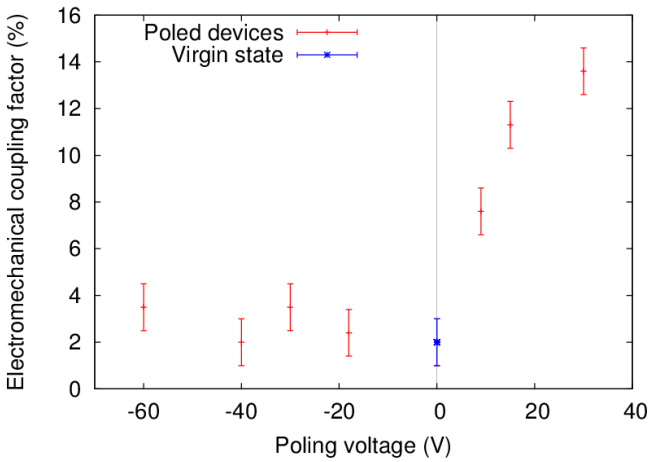

Fig. 1: Influence of the voltage applied during poling (60 min at 150°C) on the effective electromechanical coupling factor of FBAR resonators.

Reactive sputtering of AlScN thin films with variable Sc content on 200 mm wafers

Clement M.+, Felmetsger V.*, and Iborra E.+
+GMME-CEMDATIC ETSI de Telecomunicación. Universidad Politécnica de Madrid, Spain
*OEM Group LLC. Gilbert, AZ, USA
E-mail: eiborra@etsit.upm.es

Sc-doped AlN polycrystalline films are attractive active layers for high frequency (GHz range) acoustic resonators owing to the significant enlargement of the AlN piezoelectric activity with the increasing Sc content. Although a dramatic drop in the elastic constants is observed at high Sc concentrations, low Sc doping levels can offer the advantage of considerably increasing the electromechanical coupling factors while keeping the elastic constants relatively high. To sputter homogenously doped AlScN films on 200 mm production wafers, alloyed Al-Sc targets would be desirable. However, Sc/Al alloys with Sc contents greater than 10-12 at. % are hardly achievable, which together with the high cost of Sc suggests that a configurable cathode based on a variable, non-homogeneous Sc content could be a better solution to fine tuning the Sc content for each particular application. We propose here a method based on the versatile co-sputtering technique, commonly used at research levels, for mass production of $Al_xSc_yN_z$ films on 200 mm wafers with enough uniformity and quality to be competitive. The method was implemented in an Endeavor -AT™ cluster tool from OEM Group, adapted for sputtering on 200 mm wafers.

The sputtering module is equipped with a dual-cathode S-gun magnetron. AC (40 kHz) power is applied between two pure Al targets containing embedded 12 mm in-diameter Sc pellets (see figure 1), the number of which can be varied to achieve the desired composition in the deposited film. The 180 mm inner target can contain up to 20 Sc pellets, whereas the 280 mm outer target can accommodate up to 14 pellets. The theoretical Sc sputter flux is calculated taking into account the ratio of the Al to Sc exposed areas and the respective sputtering yields of Al and Sc, which gives a value of around 6% for 10 pellets in the inner target. The real concentration may be higher since the eroded region may be overestimated in the calculation.

AlScN films were sputtered on 200 mm bare Si wafers and on oxidized Si wafers covered with non-optimized Al/Mo-based acoustic mirrors intended for fabricating test resonators to characterize the piezoelectric activity of the films. The composition of the films assessed by RBS measurements, giving Sc contents around 6% at. with reasonably good homogeneity across the wafers. The electrical characterization of the resonators yielded material coupling factors (k^2) around 7%. XRD measurements revealed that AlScN films are highly *c*-axis oriented, with plane spacing (from Bragg angle of the (00·2) reflection) of 5.00 Å ±0.005 Å and FWHM of the rocking curve around the (00·2) reflection ranging from 1.6˚to 2˚ across the wafers. We also present a method for assessing the compositional changes by using a non-destructive technique based on IR reflectance measurements.

In conclusion, AlScN films with uniform Sc content (around 6% atomic), high crystal quality and good piezoelectric response were sputtered on 200 mm production-level wafers using an anisotropic Al/Sc cathode with composition tunable by varying the number of embedded Sc pellets.

Comparisons of single-ion Yb^+ and Cs fountain clocks for searches for new physics

N. Huntemann, C. Sanner, R. Lange, B. Lipphardt, J. M. Rahm, S. Weyers, Chr. Tamm, E. Peik

Physikalisch-Technische Bundesanstalt, Bundesallee 100, 38116 Braunschweig, Germany

Email: nils.huntemann@ptb.de

Investigations of the invariability of transition frequencies realized by atomic clocks can be used for searches for new physics phenomena that might point to a unified model of the fundamental forces which manifest in the quantum regime and on the cosmological scale. These phenomena might cause a temporal variation of fundamental constants, a violation of Lorentz symmetry or indicate light dark matter [1].

We employ two $^{171}Yb^+$ single-ion optical frequency standards that differ significantly with respect to trap geometry, control software and interrogation sequence [2]. The clock frequency is determined by the $^2S_{1/2} \rightarrow {}^2F_{7/2}$ electric octupole (E3) transition. The relative systematic uncertainty of the clocks has been evaluated to less than 4×10^{-18} [3]. In a long-term comparison of the two clocks for a period of seven months with a duty cycle of up to 95 % per day, we found an agreement of the Yb^+ clock frequencies within the systematic uncertainty. Due to the electronic structure of the $^2F_{7/2}$ state, the E3 transition frequency is very sensitive to violations of Local Lorentz Invariance (LLI) [4]. The orientation of the magnetic field in each trap was chosen such that a violation of LLI would cause a modulation of the clocks' frequency difference resulting from the rotation of the earth in space. Analyzing our long-term data with millihertz resolution, we improve the current limits of violations of LLI in the electron sector by a factor of 100.

To investigate perturbations of the trapped ions by external fields on a magnified scale, the frequency ratio of the E3 transition and the $^2S_{1/2} \rightarrow {}^2D_{3/2}$ electric quadrupole that is significantly more sensitive was determined over the course of the long-term measurement. Furthermore, over a significant part of the measurement period, the Yb^+ clocks were compared to the Cs fountain clocks of PTB. These data can be used to improve knowledge on the absolute frequency of the E3 transition. In addition, due to the sensitivity of the Cs transition frequency to the proton-to-electron mass ratio μ, they improve present limits on the temporal variation of μ [5] and can also be used for searches for light dark matter.

References

[1] M. S. Safronova, D. Budker, D. DeMille, D. F. Jackson Kimball, A. Derevianko and C. W. Clark, "Search for New Physics with Atoms and Molecules," arXiv:1710.01833 (2017).

[2] C. Sanner, N. Huntemann, R. Lange, Chr. Tamm, E. Peik, "Auto-balanced Ramsey spectroscopy," arXiv:1707.02630 (2017), Phys. Rev. Lett. in press.

[3] V. A. Dzuba, V. V. Flambaum, M. S. Safronova, S. G. Porsev, T. Pruttivarasin, M. A. Hohensee, and H. Häffner, "Strongly enhanced effects of Lorentz symmetry violation in entangled Yb^+ ions," Nature Physics **12**, 465 (2016).

[4] N. Huntemann, C. Sanner, B. Lipphardt, Chr. Tamm, and E. Peik, "Single-Ion Atomic Clock with 3×10^{-18} Systematic Uncertainty," Phys. Rev. Lett. **116**, 063001 (2016).

[5] N. Huntemann, B. Lipphardt, Chr. Tamm, V. Gerginov, S. Weyers, and E. Peik, "Improved Limit on a Temporal Variation of m_p/m_e from Comparisons of Yb^+ and Cs Atomic Clocks," Phys. Rev. Lett. **116,** 210802 (2014).

Operation of the world's first industrial autonomous long-haul optical fiber link at a 10^{-20} level of frequency stability

Bruno Desruelle[1], Fabiola Guillou-Camargo[1], Mathieu Corradini[1], Vincent Ménoret[1], Etienne Cantin[2], Anne Amy-Klein[2], Paul-Eric Pottie[3], Olivier Lopez[2], Emilie Camisard[4], Giorgio Santarelli[5], Christian Chardonnet[2]

[1]Muquans, Institut d'Optique d'Aquitaine, rue François Mitterrand, 33400, Talence, France
[2]Laboratoire de Physique des Lasers, LPL Université Paris 13, CNRS, Villetaneuse, France
[3]LNE-SYRTE, Observatoire de Paris, PSL Research University, CNRS, Sorbonne Universités, UPMC, Paris, France
[4]RENATER, Paris, France
[5]Laboratoire Photonique, Numérique et Nanoscience, LP2N Institut d'Optique d'Aquitaine, Université de Bordeaux, Talence, France
Email: bruno.desruelle@muquans.com

This paper reports on the operation of the world's first optical frequency transfer link deployed at an industry level in the frame of the REFIMEVE+ project supported in France by LPL (University of Paris 13) and SYRTE (Observatory of Paris) laboratories [1], [2]. We will present our work to produce the equipment, set up and operate a link by focusing on the development and the status of the optical link between the French cities Paris and Lille - distant of 311 km. The Paris-to-Lille link is based on the active compensation of the phase noise accumulated by the optical reference signal when conveyed on a dark channel of the DWDM spectrum over an existing optical fiber, in parallel of internet data traffic [2]. We report on a stability of the frequency transfer at the 10^{-20} level in a real field environment. We also describe this segment of network in terms of operational features such as accessibility, reliability and flexibility. The link between Paris and Lille is operational since October 2017 and we will comment on the latest measurement campaigns and comparisons. These have in particular validated the repeatability of the optical frequency transfer, the ease of use and the robustness of such technology. The optical fiber link between Paris and Lille today meets the objective to provide a long-haul optical frequency transfer solution as a turn-key and autonomous platform. It is also an example of a successful partnership between academic laboratories and a consortium of companies reaching state-of-the-art metrological performances. This paper will also be the occasion to describe in more details the maturity of several key technologies such as intelligent integrated laser systems and remote monitoring protocols that can sustain Time and Frequency transfers at a continent scale.

Industry-grade Regeneration Laser Station successfully developed by Muquans in collaboration with laboratories LPL and SYRTE.

References

[1] http://www.refimeve.fr/index.php/en/
[2] E. Cantin et al, "Progress on the REFIMEVE+ Project for Optical Frequency Standard Dissemination", 2017 Joint Conference of the EFTF and IEEE IFCS
[3] N. Chiodo et al, "Cascaded optical fiber link using the Internet network for remote clocks comparison", Optics Express 23, 33927-33937, 2015

A low phase noise microwave frequency synthesizer based on parameters optimized NLTL for Cs fountain clocks

Wenbing Li[1], Yuanbo Du[1], Hui Li[1], Zehuang Lu[1]

[1]MOE Key Laboratory of Fundamental Physical Quantities Measurement, Hubei Key Laboratory of Gravitation and Quantum Physics, School of Physics, Huazhong University of Science and Technology, 1037 Luoyu Road, Wuhan, People's Republic of China

Email: zehuanglu@hust.edu.cn

The short-term frequency stability of a Cs fountain clock is mainly limited by quantum projection noise and phase noise of the local oscillator through the Dick effect [1, 2]. To reduce the phase noise contribution and improve the frequency stability, a microwave frequency synthesizer based on an ultralow phase noise 5 MHz Oven Controlled Crystal Oscillator (OCXO) and a non-linear transmission-line (NLTL) used as a substitution for frequency comb generator is developed. The input power, the input and output impedances of the NLTL are all carefully optimized to suppress the residual phase noise of the synthesizer. The absolute phase noise of the 9.192 GHz output signal are measured to be -64 dBc/Hz, -83 dBc/Hz, -92 dBc/Hz and -117 dBc/Hz at 1 Hz, 10Hz, 100Hz and 1 kHz offset frequencies, respectively, while the measured residual phase noise of the synthesizer reaches -82 dBc/Hz at 1 Hz offset frequency. It is calculated that the Cs fountain frequency stability contributed by the absolute phase noise through the Dick effect is $7.0\times10^{-14}\ \tau^{-1/2}$, which may render the total frequency stability of our Cs atomic fountain clock being built less than $1\times10^{-13}\ \tau^{-1/2}$. In addition, to further push the atomic fountain clock frequency stability to the quantum projection limit, a ultra-low phase noise synthesizer scheme based on the laboratory ultra-stable laser is being investigated [3].

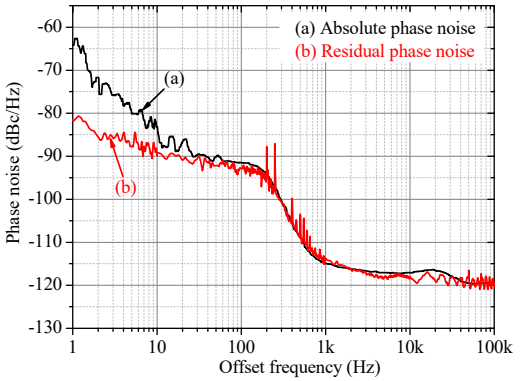

Fig. 1. The absolute and residual phase noise of the microwave frequency synthesizer at 9.192GHz.

References

[1] G. Santarelli, P. Laurent, P. Lemonde, A. Clairon, A. G. Mann, S. Chang, et al., "Quantum Projection Noise in an Atomic Fountain: A High Stability Cesium Frequency Standard," Phys. Rev. Lett., vol. 82, p. 4619-4622, 1999.

[2] R. Wynands and S. Weyers, "Atomic fountain clocks," Metrologia, vol. 42, p. S64, 2005.

[3] J. Zhang, X. H. Shi, X. Y. Zeng, X. L. Lü, K. Deng, and Z. H. Lu, "Characterization of electrical noise limits in ultra-stable laser systems," Rev. Sci. Instrum., vol. 87, p. 123105, 2016.

Progress report of an $^{27}Al^+$ ion optical clock

Ke Deng[1], Zetian Xu[1], Huang Che[1], Wenhao Yuan[1], Hongli Liu[1], Jie Zhang[1], Zehuang Lu[1]

[1]MOE Key Laboratory of Fundamental Quantities Measurement, School of Physics, Huazhong University of Science and Technology, Wuhan, People's Republic of China

Email: zehuanglu@hust.edu.cn

The $^1S_0$-$^3P_0$ transition of $^{27}Al^+$ at 267.4 nm has long been recognized as an excellent optical clock transition candidate. Here we give a progress report of our project to build an $^{27}Al^+$ ion optical clock based on the quantum logic spectroscopy technique.

In our experiment $^{25}Mg^+$ had been chosen to be the logic ion. Raman sideband cooling of $^{25}Mg^+$ ion to its vibration ground state is necessary before applying quantum logic technique. We investigate both numerically and experimentally the optimization of Raman sideband cooling strategies and propose an efficient one. The simulation result shows that the fixed-width pulses and varied-width pulses have almost the same efficiency for both the first-order and the second-order Raman sideband cooling. Then a single $^{25}Mg^+$ ion is trapped in a linear Paul trap and Raman sideband cooled, and the achieved average vibrational quantum numbers are evaluated. A good agreement between the experimental result and the simulation result is obtained [1].

To compensate the magnetic field and evaluate the Zeeman shift of the clock, both the DC and AC magnetic field need to be measured. We measured the frequency of $|S_{1/2}, F = 2, m = 2\rangle$ to $|S_{1/2}, F = 3, m = 3\rangle$ transition ("magnetic sensitive" transition) by RF resonant method for compensating the magnetic field. We also measured the frequency of $|S_{1/2}, F = 2, m = 0\rangle$ to $|S_{1/2}, F = 3, m = 0\rangle$ transition (0-0 transition). For the 0-0 transition, different frequency shifts and uncertainties are evaluated [2]. The main effect is quadratic Zeeman shift caused by the AC magnetic field. Precision measurement of this AC magnetic field can help evaluating the related uncertainty when a single-ion optical clock is established on the trap.

In our experiment a single $^{25}Mg^+$ ion ion and a single $^{27}Al^+$ ion are loaded efficiently through laser ablation in a linear Paul trap. For laser ablation a frequency-doubled Nd:YAG laser at 532 nm with a pulse duration of 2 ns and a maximum pulse energy of 150 μJ is used. A lens on a motor stage help the 532 nm laser beam selectively hit the Mg or Al targets. To improve the loading efficiency, magnesium and aluminum ions are loaded into the trap with help of 285 nm and 396 nm photon-ionization lasers, respectively.

We also proposed a next-generation $^{27}Al^+$ ion optical clock [3] where a direct laser cooling scheme is used and both the stability and accuracy of the clocks can be greatly improved. In the proposed scheme, two $^{27}Al^+$ traps are utilized. The first trap is used to trap a large number of Al^+ ions to improve the stability of the clock laser, while the second trap is used to trap a single $^{27}Al^+$ ion to provide the ultimate accuracy. Both traps are cooled with a continuous wave 167 nm laser. Feasibility study of this proposal will be presented.

References

[1] H. Che, K. Deng, Z. T. Xu, W. H. Yuan, J. Zhang, and Z. H. Lu, "Efficient Raman sideband cooling of trapped ions to their motional ground state", Phys. Rev. A, vol. 96, p. 013417, 2017.

[2] Z. T. Xu, K. Deng, H. Che, W. H. Yuan, J. Zhang, and Z. H. Lu, "Precision measurement of the $^{25}Mg^+$ ground-state hyperfine constant", Phys. Rev. A, vol. 96, p. 052507, 2017.

[3] Jie Zhang, Ke Deng, Jun Luo, and Ze-Huang Lu, "Direct laser cooling Al^+ ion optical clocks", Chin. Phys. Lett., Vol. 34, p. 050601, 2017.

Reduction of thermal noise limit for ultra-stable lasers with a higher-order Hermit-Gaussian mode

Yanxia Ye, Xiaoyi Zeng, Xiaohui Shi, Zhiyuan Wang, Jie Zhang* and Zehuang Lu

MOE Key Laboratory of Fundamental Physical Quantities Measurement, Hubei Key Laboratory of Gravitation and Quantum Physics, School of Physics, Huazhong University of Science and Technology, Wuhan 430074, P. R. China

*Email: jie.zhang@mail.hust.edu.cn

Thermal noise, a major limitation of the frequency stability of ultra-stable lasers based on Fabry-Perot (FP) cavities, depends on the parameters of the FP cavity, the temperature, and the strain energy distribution of the laser beam stored in the mirrors [1, 2]. Thus, there are various methods to reduce the thermal noise limit of an FP cavity including choosing a high Q cavity, cooling down the surrounding temperature, and enlarging the laser beam radius, etc.

We study a simple way to reduce the thermal noise limit of an FP cavity by locking the incident laser onto a higher-order Hermit-Gaussian (HG) mode of the cavity. The cavity we used is a 10 cm long all-ULE cavity, with a notched cylindrical spacer and a pair of plano-concave mirrors. The absolute frequency stabilities are obtained by a three-cornered-hat (TCH) measurement with another two similar performance laser systems. As presented in Fig. 1, the thermal noise limit performance is achieved not only for the HG_{00} mode locking, but also for the HG_{02} mode locking. The frequency instability is reduced from a modified Allan deviation of 5.9×10^{-16} to 5.1×10^{-16} at 0.4 s. Therefore, we obtain a very high level frequency stability in the experiment among all similar designed 10 cm long all ULE cavities. It is expected that further reduction of the thermal noise limit can be achieved by reshaping the incident laser beam to a higher-order mode using a spatial light modulator to improve the coupling efficiency.

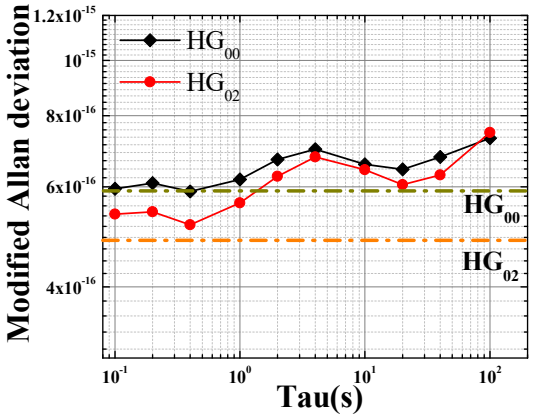

Fig. 1: Modified Allan deviation of a 10 cm long all ULE FP cavity with the HG_{00} mode locking and the HG_{02} mode locking. The black and red dot-lines show the TCH measurement results, while two dash-dot lines are the theoretical thermal noise limits of the two modes.

References

[1] K. Numata, A. Kemery, and J. Camp, "Thermal-noise limit in the frequency stabilization of lasers with rigid cavities", Phys. Rev. Lett., vol. 93, p. 250602, 2004.

[2] J.-Y. Vinet, "Thermal noise in advanced gravitational wave interferometric antennas: A comparison between arbitrary order Hermite and Laguerre Gaussian modes", Phys. Rev. D, vol. 82, p. 042003, 2010.

An atomic clock with a measurement stability at 10^{-18} level

Qiang Wang[1], Yige Lin[1], Ye Li[1, 2], Zhen Sun[2], Baike Lin[1, 2], Tao Yang[1], Tianchu Li[1] and Zhanjun Fang[1]

[1] Division of Time and Frequency, National Institute of Metrology, Beijing, P. R. China
[2] Department of Precision Instruments, Tsinghua University, Beijing, P. R. China

Email: Wangqiang@nim.ac.cn

Optical atomic clocks have shown lower systematic uncertainties and better stabilities than microwave clocks. They are possible candidates to redefine the SI (International System of Units) second in the near future.

The stability quantified by the Allan deviation is a key property of an atomic clock. The systemic uncertainty is constrained by its long term stability [1]. At the same time, better measurement stability allows for faster evaluations of systematic uncertainties [2]. Neutral atom lattice clock based on strontium keeps the record of the stability and uncertainty [2, 3]. Its best measurement stability has reached to 5×10^{-19} in 1 hour of averaging time [3].

An atomic clock based on strontium has been developing at National Institute of Metrology (NIM) of China. In 2015, the systemic uncertainty of the clock has evaluated to be 2.3×10-16 and the measurement stability was about $6\times10^{-15}/\tau 1/2$ with a clock laser based on a 10-cm-long reference cavity.

A new clock laser referenced to a 30-cm-long ultrahigh finesse cavity was developed to improve the stability of the optical clock. Atoms are selected according to the temperature by an energy filter procedure [4]. The atoms temperature in the lattice is ~2.5 μK in the longitudinal axis and ~3.8 μK in the radial direction. Owing to better performance of the clock laser and lower temperature of atoms, the narrowest 2-Hz Rabi linewidth of the clock transition is obtained with a 500 ms interrogation time. For the robust operation, a linewidth of 4 Hz with a clock cycle of 0.77 s is chosen in daily experiments. A self-comparison method is used to measure systematic shift of the optical clock [2]. More than 150,000 points (equivalent measurement time of 450 000 s) are recorded in 8 days. The measurement stability is $\sim2\times10^{-15}/\tau^{1/2}$ and reaches to 10^{-18} in an averaging time of ~40,000 s.

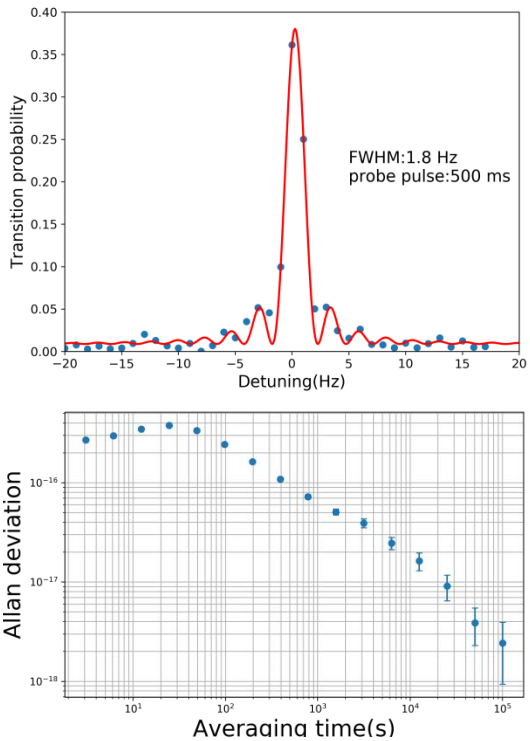

Fig. 1: The narrowest linewidth (upper) and the measurement stability measured with self-comparison method (lower).

References

[1] N. Hinkley, *et al.*, "An optical clock with 10^{-18} instability", Science, vol. 341, p. 1215-1218, 2013.

[2] T. L. Nicholson, *et al.*, "Systematic evaluation of an optical clock at 2×10^{-18} total uncertainty", Nat. Commun., vol. 6, p. 6896/1-8, 2015.

[3] S. L. Campbell, *et al.*, "A Fermi-degenerate three-dimensional optical lattice clock", Science, vol. 358, p. 90-94, 2017

[4] S. Falke, *et al.*, "A strontium lattice clock with 3×10^{-17} inaccuracy and its frequency", New J. Phys. vol. 16, p. 073023, 2014

Finding the upper mass limit until which gravimetric sensors preserve their original TCF and sensitivity

Teona Mirea, Marta Clement, Jimena Olivares, Enrique Iborra

GMME-CEMDATIC-ETSIT, Universidad Politécnica de Madrid, Spain

Email: teona@etsit.upm.es

The resonant frequency of thin film bulk acoustic wave resonators (FBARs) experience shifts upon mass deposition on their surface. To accurately use FBARs as gravimetric sensors, either in liquid or gaseous media, other factors influencing their sensitivity need to be considered, such as the temperature coefficient of frequency (TCF) that accounts for the influence of the ambient temperature on the sensor frequency shifts. If the TCF value is well-known, it can be used to correct measurements. Numerous studies on the TCF analysis of FBARs have been carried out, most particularly on their zero TCF compensation, which can be achieved by adding an SiO_2 film to the device structure [1]. Most of them investigate the appropriate SiO_2 thickness to get the full compensation, however none of them discuss the maximum SiO_2 (or other material) thickness up to which the initial TCF does not vary. Another important issue is the variation of the device sensitivity due to the energy trapping effect, i.e. the sensitivity variation with the increased deposited material [2]. Both effects need to be considered in biosensors with complex functionalization or in mass sensors that do not recover the initial state (mass accumulation).

In this work we study the TCF and mass sensitivity evolution of shear mode solidly mounted resonators (SMRs) based on piezoelectric metal/AlN/metal stacks over fully-insulating AlN/SiO_2 acoustic reflectors with frequencies ranging between 1.3 GHz and 2 GHz. Since we intend to use the SMRs as gravimetric sensors, we aim at finding the thickness limit of a given film deposited on top of the device, up to which the initial TCF and sensitivity values of the device are still preserved in a given range. We do so by sequentially depositing 30 nm of SiO_2 up to 110 nm, and assessing the TCF and frequency shifts after each cycle. Fig. 1 shows the Mason's simulation and experimental values of TCF and mass sensitivity of the same device. We observe that the TCF keeps a steady value of around -14.5 ± 1 ppm/°C up to 150 nm of SiO_2, after which a linear increasing behavior is observed. Likewise, the sensitivity starts to significantly vary after 100 nm, in both simulation and experimental, although a discrepancy between theory and measurement is observed for greater values. Subsequent studies with larger thicknesses and different deposited materials follow to be performed.

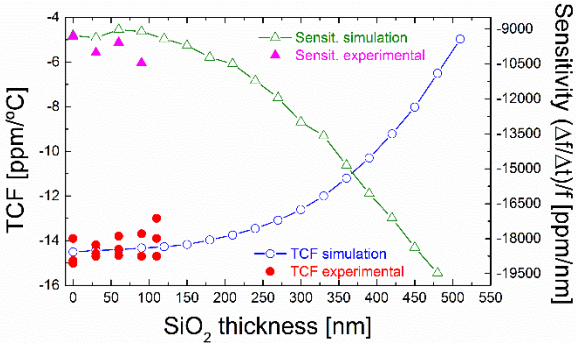

Fig. 1: TCF and sensitivity values of AlN based SMRs after the sequential deposition of SiO_2 layers on their surface. The TCFs are calculated in the range from 20°C to 100°C.

References

[1] B. Ivira, P. Benech, R. Fillit, F. Ndagijimana, P. Ancey, and G. Parat, "Modeling for temperature compensation and temperature characterizations of BAW resonators at GHz frequencies," *IEEE Trans. Ultrason. Ferroelectr. Freq. Control*, vol. 55, no. 2, pp. 421–430, Feb. 2008.

[2] G. Wingqvist, V. Yantchev, and I. Katardjiev, "Mass sensitivity of multilayer thin film resonant BAW sensors," *Sensors Actuators, A Phys.*, vol. 148, no. 1, pp. 88–95, 2008.

Ultra-Stable Cryogenic Optical Resonator Composed of Sapphire and Silicon

Yunlong Sun, Xiaohui Shi, Yanxia Ye, Chunjie Yan, Jie Zhang*, and Zehuang Lu

MOE Key Laboratory of Fundamental Physical Quantities Measurement, Hubei Key Laboratory of Gravitation and Quantum Physics, School of Physics, Huazhong University of Science and Technology, Wuhan 430074, P. R. China

*Email: jie.zhang@mail.hust.edu.cn

Ultra-stable lasers have many applications in optical clocks, precision measurement and gravitational wave detection, etc. The stability of ultra-stable lasers at room temperature is limited by the thermal noise of optical cavities. To reach lower frequency stability and slower drift rate, new ultra-stable optical resonators in the cryogenic temperature are preferred [1].

We design an ultra-stable cryogenic hybrid cavity composed with a monocrystalline silicon spacer and two sapphire mirrors operating at cryogenic temperature, with a thermal noise limit of 2×10^{-17}. The advantage of the hybrid cavity is that the effective coefficient of the thermal expansion (CTE) reaches zero at 17.7 K, and the slope of the CTE is around $6.7\times10^{-10}/K^2$. To make a vibration insensitive design, the cavity structure is optimized with finite element analysis.

In order to make the bonding of the two materials strong enough, and survive the cooling cycle from room temperature to 4 K, we use the hydroxide catalysis bonding (HCD) technique [2]. Figure 1 shows a hybrid cavity realized with the HCD technique. Some preliminary tests of hydroxide catalysis bonding of the two materials are performed, and the bonding strengths are measured.

A low vibration pulse tube cryogenic system is built for the experiment. The temperature stability is around 2 mK peak to peak at the 4 K cold plate. We will present details on the design of this ultra-stable cavity as well as frequency stability measurements under cryogenic temperature.

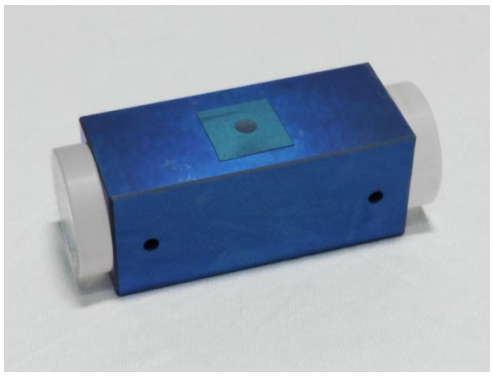

Fig. 1: A picture of the hybrid cavity.

References

[1] W. Zhang, J. M. Robinson, L. Sonderhouse, E. Oelker, C. Benko, J. L. Hall, T. Legero, D. G. Matei, F. Riehle, U. Sterr, and J. Ye, “Ultrastable silicon cavity in a continuously operating closed-cycle cryostat at 4 K”, Phys. Rev. Lett., vol. 119, p. 24601, 2017.

[2] A. M. A. van Veggel and C. J. Killow, “Hydroxide catalysis bonding for astronomical instruments”, Adv. Opt. Techn., vol. 3, p. 293–307, 2014.

Influence of the acoustic energy distribution on the in-liquid sensitivity of thin film electroacoustic resonators

Teona Mirea, Jimena Olivares, Marta Clement, Enrique Iborra

GMME-CEMDATIC-ETSIT, Universidad Politécnica de Madrid, Spain

Email: teona@etsit.upm.es

In a first approach, the sensitivity of electroacoustic resonators like QCMs to liquid properties (density and viscosity) or to mass attachment can be derived from Sauerbrey's [1] or Kanazawa and Gordon's [2] equations, being in both cases directly dependent on the resonant frequency. However, in high frequency thin film resonators other factors affect the sensitivity, such as the distribution of the acoustic energy within the resonant cavity. In thin film bulk acoustic wave resonators (FBARs) operating in air it has been proved that the addition of a low impedance material (e.g. SiO_2) on the sensing surface can increase their mass sensitivity [3], which can also be achieved by using low impedance electrodes of appropriate thicknesses [4].

In this work we investigate if the in-liquid sensitivity of shear-mode AlN-based solidly mounted resonators (SMRs) displays a similar dependence on the device configuration (top electrode thickness and material). We use the finite element method (FEM) and an experimental validation to demonstrate that the variations in sensitivity, at constant frequency, are mostly dependent on the energy distribution within the resonant cavity, which depends on the type and thickness of the materials used. We use different structures operating at resonant frequencies around ~ 2 GHz. The FEM results from Fig. 1 show how the sensitivity towards density and viscosity can be increased by reducing the thickness of the Mo top electrode (sensing interface), or by using an Al electrode of lower acoustic impedance. Likewise, the in-liquid pure mass sensitivity is increased as proved by the shifts in frequency after adding a 50 nm-thick SiO_2 layer on top of the resonators. Therefore, it can be derived that the energy trapping effect that enhances the pure mass sensitivity in air also occurs in liquid media. Experimental results corroborate these findings.

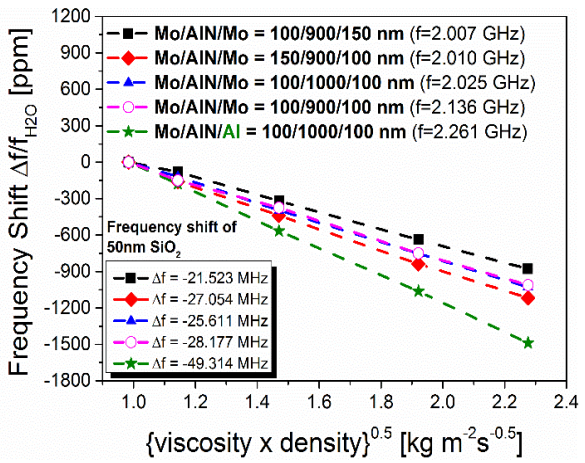

Fig. 1: FEM normalized frequency shifts vs. density and viscosity variations, for the different device configurations. The resonant frequencies values correspond to the pure-water ones. The inset shows frequency shifts due to the mass addition of 50 nm of SiO_2 (working in pure-water). The fully-insulating acoustic reflectors are composed of seven alternating layers of SiO_2/AlN centered at 2 GHz.

References

[1] G. Sauerbrey, "Verwendung von Schwingquarzen zur Wagungdiinner Schichten und zur Mikrowagung," *Zeitschrift fur Phys.*, vol. 155, pp. 206–222, 1959.

[2] K. K. Kanazawa and J. G. Gordon, "Frequency of a quartz microbalance in contact with liquid," *Anal. Chem.*, vol. 57, no. 8, pp. 1770–1771, Jul. 1985.

[3] G. Wingqvist, V. Yantchev, and I. Katardjiev, "Mass sensitivity of multilayer thin film resonant BAW sensors," *Sensors Actuators A Phys.*, vol. 148, no. 1, pp. 88–95, 2008.

[4] H. Liu, S. Ma, H. Wang, Q. Wang, and L. Qin, "Electrode effects on mass sensitivity of GaN thin film bulk acoustic wave resonator sensors," in *2015 Symposium on Piezoelectricity, Acoustic Waves, and Device Applications (SPAWDA)*, 2015, pp. 179–183.

Investigation of Methane Based Microwave Reference Oscillator for Cs/Rb Fountains

A.S. Shelkovnikov[1], A.I. Boiko[2], A.N. Kireev[1], D.A. Tyurikov[1,3], A.V. Tausenev[1,4], A.V. Konyashchenko[1,4], M.A. Gubin[1,3]

[1]P.N. Lebedev Physical Institute, Russian Academy of Sciences, Moscow, Russia
[2]VNIIFTRI, Mendeleevo, Russia
[3]N.E. Bauman Moscow State Technical University, Moscow, Russia
[4]Avesta, Ltd., Moscow, Russia
Email: shelkov@x4u.lebedev.ru

At present the Cs/Rb fountains included in the Russian State Service of Time and Frequency use active H-masers as interrogative oscillators. Their stability at averaging time $\tau = 1$ s is ADEV = $(6\text{-}7)\times10^{-14}$. Due to the Dick effect [1] it results in averaging time of 2-3 weeks to reach fountain's accuracy of $(1\text{-}2)\times10^{-16}$. Present work is directed at substituting the H-maser for a more stable interrogative oscillator - Methane Based Microwave Local Oscillator ("CH_4 LO"). The CH_4 LO consists of an optical frequency standard (He-Ne/CH_4 OFS, $\lambda = 3.39$ μm) and an optical frequency divider (OFD) based on a femtosecond Er^{3+} fiber laser ($\lambda = 1.55$ μm). The short term stability of CH_4 LO was demonstrated at the level ADEV $\leq 1\times10^{-14}$ at 1 s (in the range of output frequencies 0.8 - 1.5 GHz) [2]. This level of stability is enough for effective decreasing of the Cs/Rb fountains averaging time [3, and references therein].

Here we developed and tested a scheme of frequency transfer from a microwave comb to H-masers and Cs/Rb fountains. The experimental scheme is presented in Fig.1. 100 MHz output frequency is used to slow lock the CH_4 LO to H-maser. The typical time constant of a phase lock loop is 50 s, lock error is 2×10^{-15}.

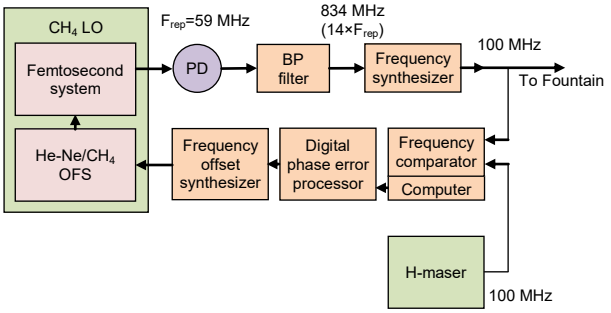

Fig. 1: Frequency locking scheme of the CH_4 LO to the H-maser. PD – photo detector.

Instability of the interrogating frequency was measured by the phase comparator (VCH-314) at 100 MHz by comparison of two H-masers and CH_4 LO ("3 corner hat" method). We obtained ADEV = 3×10^{-14} ($\tau = 1$s) for CH_4 LO at 100 MHz. That is ~ 2 times below the instability of H-masers but 3 times worse than the intrinsic instability of CH_4 LO [2]. We clarified that the lack of stability resulted from the noise of the frequency synthesizer used. Developing of a better RF - synthesizer for CH_4 LO and testing it in fountains is planned by the time of the Conference.

References

[1] C. Audoin, G. Santarelli, A. Makdissi, P. Laurent, G.J. Dick and A. Clairon, "Frequency Stability Degradation of an Oscillator Slaved to a Periodically Interrogated Atomic Resonator", IEEE Trans. Ultrason., Ferroelect., Freq. Control, vol. **45**, p. 877-894, 1998.

[2] M.A. Gubin, A.N. Kireev, D.A. Tyurikov, et al. "Methane Based Microwave Reference Oscillator", in Proceedings EFTF/IFCS, July 9–13, 2017, Besançon, France, p. 452-455.

[3] B. Lipphardt, V. Gerginov, S. Weyers, "Optical stabilization of a microwave oscillator for fountain clock interrogation", IEEE Trans. Ultrason., Ferroelect., Freq. Control, vol. **64** (4), p. 761-766, 2017.

This work was supported by the Russian Science Foundation (Project No. 16-19-10694).

Direct Measurement of Cryogenic Sapphire Oscillators with Tracking DDSs and Two-Sample Covariance

C. E. Calosso[1], F. Vernotte[2], V. Giordano[3], C. Fluhr[4], B. Dubois[4], E. Rubiola[3]

[1] INRIM, Strada delle Cacce 91, 10135 Torino, Italy
[2] Besancon Observatory, 41 Avenue de l'Observatoire, 25030 Besançon, France
[3] FEMTO-ST Institute, TF Dept, 23 rue de l'Epitaphe, 25000 Besançon, France
[4] FEMTO Engineering, 15B Avenue des Montboucons, 25030 Besançon, France

Email: c.calosso@inrim.it

Cryogenic Sapphire Oscillators (CSOs) provide microwave signals, and also HF-VHF signals via dedicated frequency synthesis, with short-term stability of parts in 10^{-16} [1]. This exceeds by two orders of magnitude the stability of masers and other commercial atomic standards. The measurement of such CSOs is possible only by comparing three similar units, and the task is challenging because the short-term instability it significantly lower than the background noise of commercial phasemeters and counters. For this reason, the measurement was until now done by beating the microwave outputs of the bare CSOs, with no synthesizer [2]. The beat notes of a few MHz provide a leverage factor of >60 dB. In this work we remove the limitation of the beat note method, and we demonstrate the direct ADEV measurement of each CSO at 100 MHz. We use a 6-channel tracking DDS which exhibits $2 \times 10^{-14}/\tau$ background noise in single channel mode [3]. Each CSO output is split into two channels. Thus, we collect two data streams per CSO, with statistically independent background noise. We use the two-sample covariance [4], which is superior to the classical three-cornered hat method in that the contribution of the instrument background converges to zero for large averaging size.

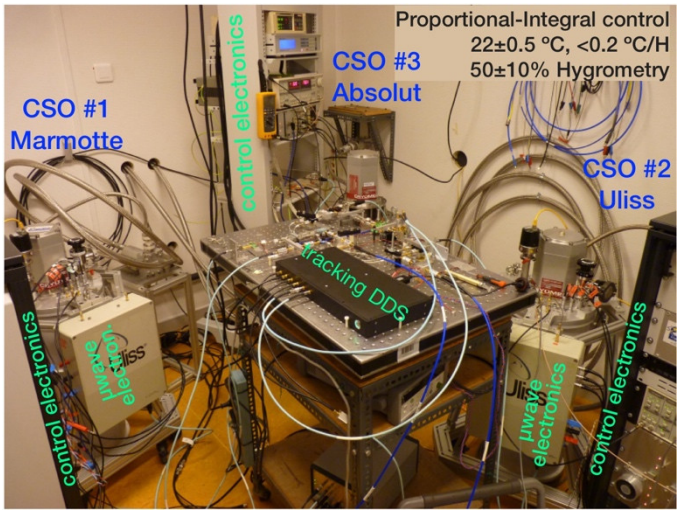

Fig. 1: Photo of the complete experiment.

The experiment produces six values of phase-time data, one per channel, at a rate of 10 samples per second. Setting the synthesizers at three different frequencies slightly off the nominal value of 100 MHz helps in reducing crosstalk and spurs. Processing a few days of data, we calculate the ADEV of the three CSOs for $\tau = 1 \ldots 2 \times 10^4$ s, free from the instrument background noise. The result is 2×10^{-15} at $\tau = 1s$ limited by the frequency divider implemented in the CSO frequency synthesis. The best CSO presents a flicker floor of 3×10^{-16}.

References

[1] V. Giordano, S. Grop, C. Fluhr, B. Dubois, Y. Kersale, E Rubiola, *J. Physics: Conf. Series* 723 (2016), article no. 012030.
[2] C. Fluhr, S. Grop, B. Dubois, Y. Kersale, E. Rubiola, V. Giordano, *IEEE Transact UFFC* 63(6) pp. 915-921, June 2016.
[2] M. Caligaris, G. Costanzo, C. E. Calosso, *Proc. 2015 IFCS-EFTF* pp. 681-683.
[3] F. Vernotte, C. E. Calosso, E. Rubiola, *Proc. 2016 IFCS*, pp. 282-287.

Measuring Small Propagation Frequency Shifts and Fluctuations by Phase to Avoid Cross-Correlation Errors

Michael J Underhill
Underhill Research Limited, Lingfield, UK
Email: mike@underhill.co.uk

Keywords. Frequency Measurement by Phase, SDR, Gravity Frequency Errors

Research continues into the measurement of propagation frequency shifts and fluctuations of off-air frequency standards at frequencies from 25MHz now down to 162kHz. The ionospheric frequency shifts down to about 1.5MHz can easily be observed and measured on the spectrum displays of an SDR receiver supplied with a high-quality reference source. Measurements so far have been made on the RFSpace SDR-IP clocked at 10MHz by a SpectraTime LCR 900 Rubidium Source [1-2]. (These references are based on the fundamental physics of reference [3]).

Ionospheric frequency shifts vary from about 50mH to 1Hz and can be multi-path with several components. All these can be seen and measured on a SpectraView display on an SDR receiver with a resolution of <10 mHz. However, the absolute accuracy of these measurements depends on accurate calibration and setting of the Rubidium Clock for the SDR. For this the SDR Kits GPS phase locked 10MHz source is used. Although the GPS signal is not phase stable when switching from one satellite to another calibration can easily be obtained over one or two hours on a single satellite source. This paper shows that the final measurement accuracy is improved by up to two orders by measuring phase to $\pm 1.8^0$ rather than frequency differences over this time. A 1000s measurement can thereby give a10μHz accuracy on a 10MHz comparison, corresponding to an accuracy of 1 in 10^{12}.

The present research focus is the measurement of standard frequency sources available by groundwave propagation at LF. The two successful measurements so far at Lingfield, 30km south of the Thames in London, are (a) from the 198kHz signal from the BBC Radio 4 500kW transmitter at Wychbold, near Droitwich at a distance of 190 km and 312^0 bearing, and (b) the 2MW 162 kHz RTF standard frequency transmission at Allouis, France at a distance of 475 km and 160^0 bearing.

The first measurements shown in figures 1 and 2 respectively that both transmitters have small frequency errors relative to the local LCR-900 rubidium source which has been phase synchronised to the GPS derived SDR-kits source during an observed time of GPS frequency/phase stability.

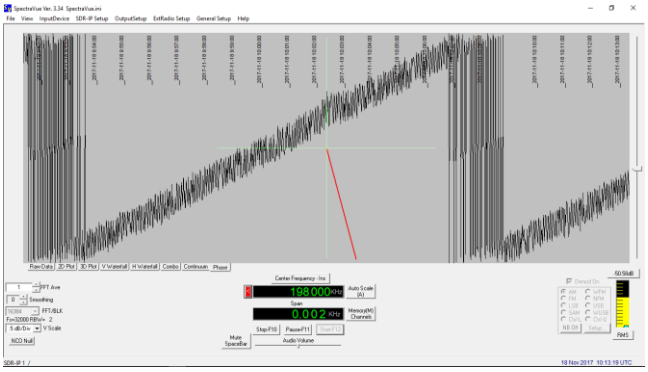

Figure 1. Measurement of phase of BBC R4 Droitwich transmitter at 190 km. One cycle in 930s is 1.075mHz or 1/(930×198000) =5.43 parts in 10^9 frequency error.

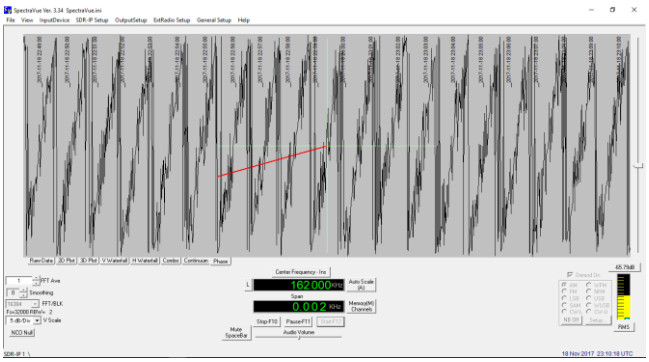

Figure 2. Measurement of phase of Allouis RTF transmitter at 475 km. 18 cycles in 20min 45s =14 46mHz which in 162kHz is 89 parts in 10^9.

More explanation and theory for these and further results will be presented at the conference.

Some additional advantages of measuring frequency and phase noise by phase were pointed out by S. Stein in [4]. Spectrum collapse and unwanted spurs do not occur. There are no 'mixers' as a cause of these.

References

[1] M. J. Underhill, "The two-edge anti-jitter circuit for phase noise reduction on received frequency standards", Joint Conf. EFTF/IFCS 2017, Besancon, France, pp. 117 - 120.
[2] M. J. Underhill "Observed propagation-phase/frequency-shift theory with impact on time/frequency transfer and GNSS", Joint Conf. EFTF/IFCS 20177, Besancon, France, pp. 733 – 735.
[3] M. J Underhill, "A Physical Model of Electro-magnetism for a Theory of Everything", *PIERS Online*, Vol.7, No. 2, 2011, pp. 196 -200. Also in *Proc. PIERS 2011*, March 20-23, Marrakesh, Morocco, pp. 1665 – 1669.
[4] S. Stein; slide showing that "Phase Measurements of Oscillator Noise Avoid Spectrum Collapse and Unwanted Spurs" presented in Cross Spectrum Workshop, Joint Conf. EFTF/IFCS 2017, Besancon, France.

A high Q Length-Extension Mode Quartz Resonator for MEMS Oscillator and Time-Frequency Applications

Chapellier Paul[1], Pierre Lavenus[1], Bernard Dulmet[2], Olivier Le Traon[1]

[1]Physics, Instrumentation, Environment, Space Department, ONERA, Châtillon, France
[2]Time and Frequency Department, FEMTO-ST, Besançon, France

Email: paul.chapellier@onera.fr

A two dimensional length-extension mode (LEM) quartz resonator vibrating at few MHz and showing a high quality factor (Q) up to 250 000 is presented in this paper. Based on a previous bulky resonator [1] this smaller version consists of a vibrating beam in compression extension, the resonant frequency is directly inversely proportional to the length of the beam, one can adjust the resonant frequency depending on the targeted applications.

Because of its high anisotropy and faceting, wet etching using hydrofluoric acid is not suited hence the development of the Deep Reactive Ionic Etching (DRIE) of quartz using fluorocarbon gaz. Nearly vertical sidewalls can be obtained with a depth of 200 µm. Our process uses two DRIE steps: first the patterns of the resonators made with a thick nickel mask are etched, then the wafer is flipped and cavities are etched until the full liberation of the vibrating structures. A resonator vibrating at f=2.2 MHz fabricated with this process is shown in Fig. 1, gold electrodes are only deposited on the top face. The resonators have shown very promising mechanical parameters with a quality factor up to 250 000 for a fundamental mode at 2.2 MHz and a first partial mode at 6.6 MHz, leading to a figure of merit, i.e. the Qxf product of $1.7*10^{12}$ Hz and improving previous works on similar resonators [2][3]. However, Q is less than expected by simulations: the possible mechanisms of dissipation of the energy are viscosity of the layers of the electrodes or a less effective trapping of the energy inside the resonator due to the not perfect verticality of the flanks or even surface losses.

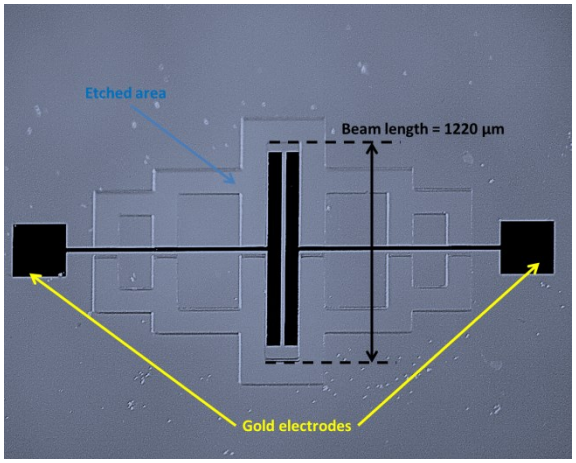

Fig. 1: A LEM resonator vibrating at 2.2 MHz fabricated with the two DRIE steps.

Future work will be focused on understanding and evaluating the predominant losses mechanisms and correcting them in order to increase the quality factor while increasing the resonant frequency through the use of higher partial modes.

References

[1] O. Le Traon, M. Bahriz, O. Ducloux, S. Masson, and D. Janiaud, “A Micro-Resonator for Fundamental Physics Experiments and its Possible Interest for Time and Frequency Applications.”

[2] R. J. Dinger, “A minature quartz resonator vibrating at 1 MHz,” *Proc. 35th Ann. Freq Control Symposium*, p. 144–148, 1981.

[3] H. Kawashima and M. Nakazato, “Variational analysis of new shape length extensional mode quartz crystal resonator taking account of lateral motion.” *Proc. 44th Ann. Freq Control Symposium*, p. 378–.386, 1990.

Dual-Comb Spectroscopy

Nathalie Picqué[1],

[1] Max-Planck Institute of Quantum Optics, Hans-Kopfermann-Strasse 1, 85748 Garching, Germany

Email: Nathalie.picque@mpq/mpg.de

Almost two decades ago, laser frequency combs have revolutionized time and frequency measurements. Frequency combs are now finding applications far beyond the original purpose. In particular, laser combs are becoming powerful instruments for broadband molecular sensing and they create new opportunities for multiplex nonlinear spectroscopy.

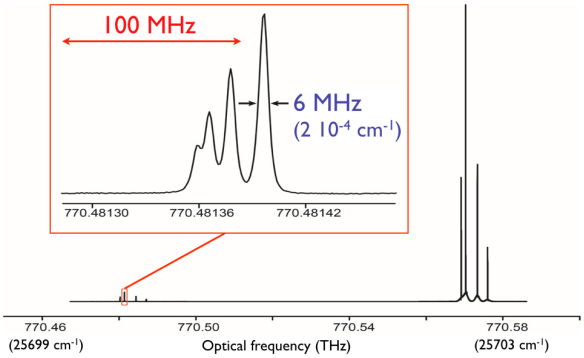

Fig. 1: Doppler-free dual-comb two-photon spectrum of the 5S-5D transitions of Rubidium around 770 THz.

Multi-heterodyne dual-comb spectroscopy, a comb-enabled technique of Fourier transform spectroscopy, demonstrates that the precisely spaced spectral lines of a laser frequency comb can be harnessed for broadband absorption spectroscopy, with much improved acquisition speed, precision and accuracy. One of main instrumental difficulties of this technique which measures the time domain interference between two combs of slightly different repetition frequencies, has been keep the two combs mutually coherent over the measurement time; it is now entirely overcome [1].Ongoing developments will expand the range of applications of this new spectroscopy for new approaches to sensing [2] of gaseous, liquid and solid-state samples. Mid-infrared frequency combs interrogate [3] the fundamental vibrational transitions of molecules, resulting in improved sensitivity to trace gases. Miniaturized frequency comb generators might even lead to chip-scale sensors [4]. Moreover, since femtosecond frequency combs involve intense ultra-short laser pulses, new schemes of nonlinear spectroscopy may be explored. With coherent Raman effects [5], real-time multiplex accessing of hyperspectral images may expand the range of applications of nonlinear microscopy. Doppler-free two-photon dual-comb spectroscopy [6] may eventually (Figure 1) make the most of the frequency precision offered by the combs and may open up intriguing opportunities for broad spectral bandwidth spectroscopy of molecules with high precision.

References

[1] Z. Chen, M. Yan, T. W. Hänsch, and N. Picqué, "A phase-stable dual-comb interferometer," arXiv:1705.04214 (2017).

[2] G. Millot, S. Pitois, M. Yan, T. Hovannysyan, A. Bendahmane, T.W. Hänsch, N. Picqué, Frequency-agile dual-comb spectroscopy, Nature Photonics 10, 27-30 (2016).

[3] M. Yan, P.-L. Luo, K. Iwakuni, G. Millot, T.W. Hänsch, N. Picqué, Mid-infrared dual-comb spectroscopy with electro-optic modulators, Light: Science and Applications 6, e17076, (2017).

[4] M. Yu, Y. Okawachi, A.G. Griffith, N. Picqué, M. Lipson, A.L. Gaeta, Silicon-chip-based mid-infrared dual-comb spectroscopy, arXiv:1610.01121 (2016).

[5] T. Ideguchi, S. Holzner, B. Bernhardt, G. Guelachvili, N. Picqué, T.W. Hänsch, Coherent Raman spectro-imaging with laser frequency combs, Nature 502, 355-358 (2013).

[6] S.A. Meek, A. Hipke, G. Guelachvili, T.W. Hänsch, N. Picqué, Doppler-free Fourier transform spectroscopy, Optics Letters 43, 162-165 (2018).

Towards an $^{27}Al^{+}$ based optical clock

Khabarova Ksenia[1,2], Zalivako Ilia[1,2], Semerikov Ilia[1,2], Borisenko Alexander[1,2], Kolachevsky Nikolay[1,2]

[1] P.N. Lebedev Physical Institute of Russian Academy of Sciences, Moscow, Russia

[2]Russian Quantum Centre, Skolkovo, Russia

Email: kseniakhabarova@gmail.com

Today optical frequency standards based on single trapped ions as well as neutral atoms in optical lattices demonstrate unsurpassed accuracy and stability reaching level of several units in 18th digit [1, 2]. Combining quantum logic spectroscopy and sympathetic cooling methods also allowed usage for optical clocks of ions with remarkable clock transitions but lacking achievable cooling transitions [3]. Here we present current status of a project aimed for development of an optical clock based on $^{27}Al+$ ion and auxiliary $^{25}Mg+$ ion started at LPI. Results on Mg+ ions trapping and cooling are presented. A new photoionization method of Mg atoms is suggested. Numerical modeling of Mg+ ions behavior in a trap including estimations of sensitivity to external fields is discussed.

References

[1] N. Huntemann, C. Sanner, B. Lipphardt, C. Tamm, and E. Peik, “Single-Ion Atomic Clock with 3×10^{-18} Systematic Uncertainty”, Phys. Rev. Lett., vol. 116, no. 6, p. 63001, 2016.

[2] T. L. Nicholson et al., “Systematic evaluation of an atomic clock at 2×10^{-18} total uncertainty”, Nat. Commun., vol. 6, p. 6896, 2015.

[3] C. W. Chou, D. B. Hume, J. C. J. Koelemeij, D. J. Wineland, and T. Rosenband, “Frequency comparison of two high-accuracy Al+ optical clocks”, Phys. Rev. Lett., vol. 104, no. 7, pp. 8–11, 2010.

Tool kit for a portable optical clock

Sruthi Viswam, Jonathan Bass, Marco Menchetti, Qasim Obaid, Jonthan Jones, David Morris, Peter Molony, Matthew Aldous, Markus Gellesch, Kai Bongs and Yeshpal Singh

Department of Physics and Astronomy, University of Birmingham, Edgbaston Park Road, Birmingham B15 2TT, UK

Email: y.singh.1@bham.ac.uk

There is a great emphasis on making optical clock portable for outside lab applications. We have been working on modules that are potential enablers for such efforts. Here we report on a novel atom source and compact frequency stabilisation unit. The specific feature of our atom source is the small size, which together with being free from Black Body Radiation systematic shifts allows the construction of much smaller and more accurate optical lattice clocks. Our "cold" method allows fast and controlled emission of strontium atomic vapour from a bulk material irradiated by a low power and low cost diode laser. Our results demonstrate that millions of strontium atoms from the vapour can be captured in a magneto-optical trap (MOT) both in a fully controlled manner and with several Hz repetition rate.

Additionally, we have developed compact optical resonator, which could be used for multiple lasers stabilisation. The unit is compact, portable and low power consuming. We will report on the up to date progress on it.

The parameters for these units are aligned with current optical Sr lattice clocks and are thus relevant to developments in metrology institutions and laboratories around the world.

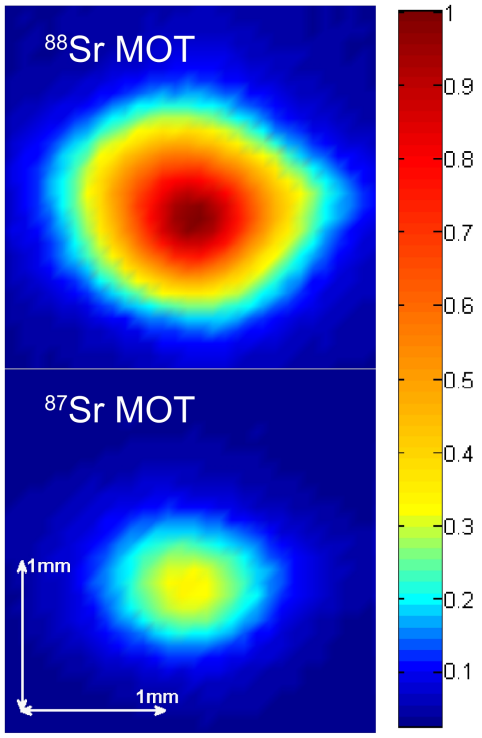

Fig. 1: Typical photographs of a ^{88}Sr (top) and ^{87}Sr (bottom) MOT, consisting of ~4 M atoms and ~1M atoms, respectively.

References

[1] Ole Kock, et. al., , "Laser controlled atom source for optical clocks",Nat Scientific Report, vol. 6, 37321, 2016.

CO_2-filled Hollow-Core Fiber Reference Gas Cells for Laser Frequency Stabilization at 2 μm

Renaud Matthey[1], Benoît Debord[2], Kenny Hey-Tow[3], Fan Yang[3], Stéphane Schilt[1], Fetah Benabid[2], Luc Thévenaz[3], Thomas Südmeyer[1]

[1]Laboratoire Temps-Fréquence, Université de Neuchâtel, Neuchâtel, Switzerland
[2]GPPMM Group, Xlim Research Institute, CNRS UMR 7252, University of Limoges, France
[3]EPFL Swiss Federal Institute of Technology, Group for Fibre Optics, Lausanne, Switzerland
Email: renaud.matthey-de-lendroit@unine.ch

Hollow-core photonic crystal fibers (HC-PCF) filled with a controlled gas pressure enable light-gas interaction over a long path in a very confined volume. As a result, they constitute an attractive solution for the realization of reference gas cells for laser stabilization onto molecular transitions that combine compactness and light weight in an all-fibered architecture that is particularly attractive for space applications. In the development of a frequency-stabilized seed laser at 2051 nm for a space-borne differential absorption lidar instrument, we have implemented a versatile modulation sideband locking scheme enabling a laser to be directly locked at an adjustable frequency detuning from the center of a CO_2 transition [1] in an all-fibered reference cell built around an HC-PCF.

Different configurations for the realization of tightly-sealed low-pressure CO_2 HC-PCF cells were investigated. The fabrication process relies on the permeation of gaseous helium through the walls of the silica fiber [2] to seal low pressure cells without contamination by ambient air. First cells were fabricated using a commercial hollow-core photonic bandgap fiber (HC-PBF) at 2 μm. To reduce the impact of interferometric noise, which was consequent with this fiber due to its multimode nature, a configuration made of a single-mode polarization-maintaining fiber spliced at the input of the HC-PCF and a multimode fiber at the output was adopted. An improved transmission profile was obtained using Kagomé HC-PCFs recently developed by Xlim and Glophotonics that operate with a different guiding mechanism based on inhibited coupling [3]. They typically provide quasi-single-mode propagation that leads to a smoother error signal for laser stabilization with strongly reduced interferometric noise (see Fig. 1). Different sealing approaches were considered with these large core (>50 μm) HC-PCFs, such as the use of an intermediate large mode fiber as well as end-caps. The different fabricated CO_2 cell configurations will be reviewed and their optical properties will be compared and discussed. Results of frequency stability of a 2051-nm laser obtained by modulation sideband locking with these different HC-PCF cells will be presented.

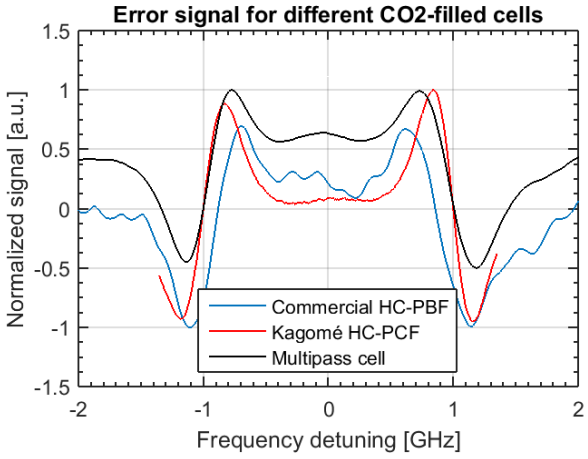

Fig. 1: Error signal of the modulation sideband locking method for laser stabilization at 1-GHz detuning from the center of the CO_2 R30 transition at 2051 nm obtained with different reference gas cells: a commercial HC-PBF (blue), a Kagomé HC-PCF (red), and a bulk multipass cell for comparison (black). A balanced detection was used with the two HC-PCF cells.

[1] S. Schilt, R. Matthey, K. Hey-Tow, L. Thévenaz, T. Südmeyer, *CEAS Space Journal* 9, 493–505 (2017).
[2] P. S. Light, F. Couny, F. Benabid, *Opt. Lett*. 31, 2538–2540 (2006).
[3] B. Debord, M. Alharbi, T. Bradley, C. Fourcade-Dutin, Y. Y. Wang, L. Vincetti, F. Gérôme, F. Benabid, *Opt. Expres*s 21, 28597-28608 (2013).

Pushing forward the stability and accuracy of Sr optical lattice clocks

G Vallet[1], E Bookjans[1], S Bilicki[1], R Le Targat[1], J Lodewyck[1]

[1] SYRTE, Observatoire de Paris, PSL Research University, CNRS, Sorbonne Universités, UPMC Univ. Paris 06, LNE, Paris, France

Email: Gregoire.vallet@obspm.fr

Recently we demonstrated a cavity-assisted non-destructive detection of an atomic ensemble on an operational Sr lattice clock that offers a 1st order rejection of the technical noise sources, a homogeneous atom-cavity coupling, is optimal with respect to the photon shot noise limit and which resolution is on the order of a few atoms, giving a signal to noise ratio of more than 100. The number of photons scattered per atom over the detection time is low enough to keep the atoms trapped after detection. This calssical non-destructivity enables cycle-to-cycle atoms recycling, allowing a strong Dick effect reduction, the current main limititation of optical lattice clocks staibility. However, this scheme did not permit us to reach a photon scattering rate lower than one per atom during the detection pulse, a key condition to enter the quantum non-desctructivity regime. We present here new ideas and improvements of our previous setup that allow us to reach this regime, which is expected to enable cavity spin-squeezing, a key ingredient to beat the quantum projection noise limit which is the next frequency stability limitation after the Dick effect.

Moreover we shed some light on new systematic effects degrading the clock accuracy we observed with our two strontium clocks. This effects stem from perturbations induced on the frequency of the clock laser by our second strontium clock. In our two clocks the atoms are probed by a clock laser referenced to the same ultra-stable cavity. The clock cycle of the second clock produces spikes on the ultra-stable cavity PDH error signal, leading to frequency fluctuations on the clock laser randomly sampled by the first clock, whose cycles are not synchronized with the second one. This effect led to a discrepancy between the two clocks at the level of 10^{-15} in fractional unit, two orders of magnitude higher than the clock accuracy. We could explore by varying the timing pattern of one clock with respect to the other. When the two are synchronized, the effect is minimal whereas it reaches a maximum for a particular delay. We established a simple model that enabled us to reproduce theoretically the effect considering the sensitivity function of the atomic ensemble and the measured fluctuations of the ultra-stable cavity error signal. Based on this model we could correct retrospectively the effect and recover the expected level of fractional accuracy of 10-17 for the second clock.

References

G Vallet, E Bookjans, U Eismann[1], S Bilicki, R Le Targat and J Lodewyck, “A noise-immune cavity-assisted non-destructive”, New Journal of Physics, vol. 19, 7 August 2017.

The H2020 European Project CLONETS: clock services over optical-fibre networks in Europe

Davide Calonico[1], Cecilia Clivati[1], Filippo Levi[1], Przemysław Krehlik[2], Łukasz Śliwczyński[2], Jiri Dostal[3], Jan Radil[3], Vladimir Smotlacha[3], Radek Velc[3], Josef Vojtěch[3], Mauro Campanella[4], Ondřej Číp[5], Simon Rerucha[5], Ronald Holzwarth[6], Maurice Lessing[6], Sarah Saint-Jalm[6], Fabiola Camargo[7], Bruno Desruelle[7], Jean Lautier-Gaud[7], Elizabeth Laier English[8], Jochen Kronjäger[8], Peter Whibberley[8], Fratišek John[9], Milan Šnajder[9], Jiří Štefl[9], Paweł Nogaś[10], Robert Urbaniak[10], Artur Binczewski[11], Wojbor Bogacki[11], Krzysztof Turza[11], Gesine Grosche[12], Harald Schnatz[12], Emilie Camisard[13], Nicolas Quintin[13], Javier Diaz[14], Trinidad García[14], Eduardo Ros[14], Alessandro Galardini[15], Alwyn Seeds[16], Zhen Yang[16], Anne Amy-Klein[17] , Eva Bookjans[18], Paul-Eric Pottie[18], and Philip Tuckey[18]

[1] Istituto Nazionale di Ricerca Metrologica, Turin, Italy
[2]AGH University of Science and Technology Cracow, Poland
[3]CESNET, Prague, Czech Republic
[4]Consortium GARR, Rome, Italy
[5]Institute of Scientific Instruments of the ASCR, v.v.i. (ISI) Brno, Czech Republic
[6]Menlo Systems GmbH, Martinsried, Germany
[7]Muquans, Talence, France
[8]National Physical Laboratory, Teddington, United Kingdom
[9]OPTOKON a.s. Jihlava, Czech Republic
[10]Piktime Systems sp. z o.o. Poznan, Poland
[11]Poznan Supercomputing and Networking Center, Poznan, Poland
[12]Physikalisch-Technische Bundesanstalt Braunschweig, Germany
[13]GIP-Renater, Paris, France
[14]Seven Solutions S.L. Granada, Spain
[15]Conzorzio ToP-IX, Turin, Italy
[16]University College London, London, United Kingdom
[17]LPL, Université Paris 13, CNRS Villetaneuse, France
[18]LNE-SYRTE, Observatoire de Paris, PSL Research University, CNRS, Sorbonne Université, Paris, France

Email: d.calonico@inrim.it

Time and frequency transfer based on optical fibre links techniques have demonstrated excellent performances. They are a key technology for very demanding application in metrology and science, e.g. optical clock comparisons, and also for applications in industry and society. They are complementary and/or alternative to radio- and satellite-based transfer.

The H2020 project CLONETS (www.clonets.eu) is a coordination and support action started in January 2017, and it aims at accelerating the take-up of the fibre link technology by industry, research and society. One of the main target is to prepare the deployment of a permanent pan-European fibre network, providing high performance clock services to European research, and supporting wider services to industry and society.
CLONETS brings together National Metrology Institutes (NMIs), academic research groups, National Research and Education Network providers (NRENs), an internet exchange and small and medium-sized high-technology companies.

The main objectives include collecting information on needs, studying industrial and societal applications, defining strategies to support future work, training, focusing on contractual aspects.

At the conference, we will present the advances on the different objectives. In particular, there will be (i) the first outcomes from two surveys of needs and applications for time and frequency transfer over optical fibre, one aimed at research infrastructures and the second for a wide range of other application areas including government, industry, societal, etc. (ii) the presentation of a university master program (post-graduate level) and the short training courses. The survey activity will allow a better decision process about the future infrastructure. The training activity is intended to train new competences useful for optical T/F metrology over fibre and to offer to scientists, metrologists, industry, society and research the opportunity of focusing on needs and possibilities presently available.

References

[1] A. A. Klein et al., “CLONETS – Clock Network Services: Strategy and Innovation for Clock Services Over Optical-Fibre Networks”, Proc. of the 2017 Joint Conference of the European Frequency and Time Forum and IEEE International Frequency Control Symposium, July 9 –13, 2017 Besançon, France, p 697, 2017

CLONETS receives funding from the European Union’s Horizon 2020 research and innovation programme under grant agreement no. 731107.

Recent Progress of Development of Cesium Fountain Primary Frequency Standard NMIJ-F2

Akifumi Takamizawa, Shinya Yanagimachi, Ken Hagimoto, Iku Hirano, Takeshi Ikegami

National Metrology Institute of Japan, AIST, 1-1-1 Umezono, Tsukuba, Ibaraki, Japan

Email: akifumi.takamizawa@aist.go.jp

Our second cesium fountain, NMIJ-F2, has been developed, aiming at an uncertainty of < 1×10^{-15}. Together with very high frequency stability $7\times10^{-14}\ \tau^{-1/2}$ (τ: averaging time (s)) by taking optical pumping to the Zeeman sublevel $m_F = 0$ and employing a cryocooled sapphire oscillator with very high short-term stability [1], systematic uncertainty has been evaluated for most of the effects resulting in frequency shifts. In this presentation, uncertainty evaluations which have been conducted so far as well as remaining evaluations will be described.

The well-known large frequency shifts such as the second-order Zeeman shift, the Blackbody radiation shift, and the shift due to cold-atom collision were evaluated to be typically -165.5±0.10, +16.7±0.06, and +2.0±0.20 in 10^{-15}, respectively, in terms of frequency corrections by the conventional methods. The first one was derived from the first-order Zeeman shift of $m_F = +1$ experimentally measured by Ramsey interrogation. The second one was calculated from the temperature of the interrogation region. Then, the third one was estimated by extrapolation to zero density taking alternation operation between high and low atomic densities. On the other hand, the distributed cavity phase shift was evaluated to be $(0\pm0.5)\times10^{-15}$ by our own calculation with Monte Carlo simulation [2].

As for the microwave power dependence shift, we found a problem probably only for us; the shift reached $+5\times10^{-15}$ when the Ramsey cavity was continuously fed with microwave. The shift was largely reduced as shown in Fig. 1, when the microwave was turned off with a common voltage controlled attenuator while atoms going downward passed through the state-selection cavity (only < 10 ms). The large shift at the continuous feed should attribute to so-called the after-Ramsey interaction in the state-selection cavity; because the two cavities are combined in our apparatus, the microwave leaked from the Ramsey cavity is relatively easy to go into the state-selection cavity. The correction for the shift in the case of using the switch was estimated to be $(-0.1\pm0.10)\times10^{-15}$ by frequency measurement at pulse areas of $n\pi/2$ (n: odd integer) and fitting to the function $A\sin(n\pi/2)$. While the shift was sufficiently decreased, the phase-transient by the switching must be checked and remains as an unevaluated effect. We will also show the status of the phase-transient measurement in the presentation.

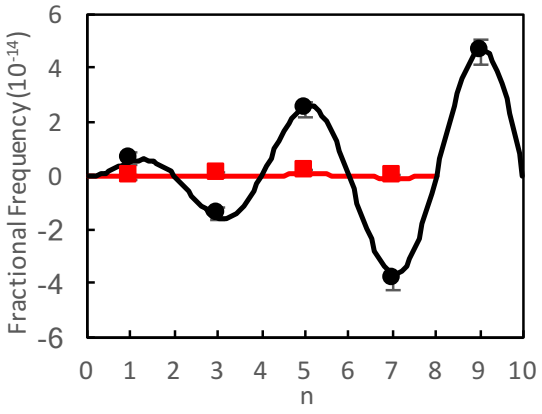

Fig. 1 Fractional frequency as a function of pulse areas $n\pi/2$ of microwave. Here, black dots: cw, red squares: using the switch.

References

[1] A. Takamizawa et al., "Atomic fountain clock with very high frequency stability employing a pulse-tube-cryocooled sapphire oscillator", IEEE Trans. Ultrason. Ferroelectr. Freq. Control, vol. 61, pp. 1463-1469, 2014.

[2] S. Yanagimachi et al., "Numerical simulation of distributed cavity phase shift in atomic fountain frequency standard", Jpn. J. Appl. Phys., vol. 44, pp. 1468-1475, 2005.

Two-way optical phase comparison at 10^{-21} level

Zang Qi[1], Cao Qun[1], Deng Xue[1,2], Liu Jie[1], Jiao Dongdong[1,2], Gao Jing[1], Zhang Xiang[1], Wang Dan[1], Xu Guanjun[1], Dong Ruifang[1,2] Liu Tao[1,2], Zhang Shougang[1,2]

[1]National Time Service Center, Chinese Academy of Sciences, Xi'an, China
[2] University of Chinese Academy of Sciences, Beijing, China

Email: zangqi@ntsc.ac.cn

High-precision frequency comparison between remote atomic clocks over fiber links has become increasingly important in many research fields including metrology [1], fundamental physics [2], time keeping, and relativistic geodesy [3]. To realize such a frequency comparison, a two-way optical phase comparison technique has been previously reported [4]. In their method, the frequency difference was measured by beating between the local laser and the remote one at each end of the fiber link. Assuming that the propagation noise is equal for the two directions, one can efficiently reject the extra noise by synchronizing and post processing the data. However, under an insufficient synchronization, the short-term laser noise could degrade the precision.

In this letter, we demonstrate an improved optical phase comparison method without the requirement of synchronization. In this method, the remote signal at one end of the fiber link is sent back. At the other end of the fiber link, the beatings between the local laser and the remote laser as well as the laser after the round-trip propagation are simultaneously measured by a single photodetector and a multi-channel phase recorder. Since the single-trip propagation noise can be directly subtracted, no post processing is needed and therefore a real-time frequency comparison can be achieved. Furthermore, as the beating measurements are based on the same setup, the effect of common-mode noise suppression can be more efficient compared with previous method [4].

Based on this scheme, we implement a real-time frequency comparison over a bi-directional 50-km fiber spool. The achieved relative frequency stability is 1.2E-16 at 1 s integration time and reaches 1.3E-21 at 40,000 s. Recently, we extended the experiment to a fiber link of 200-km together with a bidirectional EDFA for fiber loss compensation. The preliminary measurement shows that the relative stability at 10000-s scales down to 2E-21, which is twice better than that of the previous results.

These results show that our method is an alternative and more accurate approach for frequency comparison of optical clocks over fiber links.

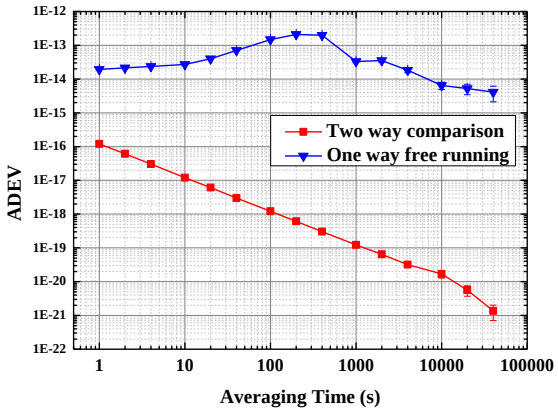

Fig. 1: Allan deviation (ADEV) of one-way fiber noise (blue line) and of two-way phase comparison (red line) over 50-km fiber spool.

References

[1] M. Fujieda, "All-optical link for direct comparison of distant optical clocks," Opt. Express, vol. 19, p.16498, 2011.

[2] C.W. Chou, "Optical clocks and relativity," Science, vol. 329, p. 1630, 2010.

[3] P. Delva, "Atomic clocks: New prospects in metrology and geodesy," Acta Futura, vol. 7, 2013.

[4] C. E. Calosso, "Frequency transfer via a two-way optical phase comparison on a multiplexed fiber network." Opt. Lett, vol. 39, p. 1177-1180, 2014.

Spatially-Multiplexed Solitons in Optical Microresonators

Erwan Lucas[1], **Grigory Lihachev**[2,3] **Michael L. Gorodetsky**[2,3], **Tobias J. Kippenberg**[1]

[1]*Institute of Physics (IPHYS), Ecole Polytechnique Federale de Lausanne (EPFL), 1015 Lausanne, Switzerland*
[2]*Russian Quantum Center, 143025 Skolkovo, Russia*
[3]*Faculty of Physics, M.V. Lomonosov Moscow State University, 119991 Moscow, Russia*
**tobias.kippenberg@epfl.ch*

Spatial multiplexing is widely used in optical telecommunication to accommodate multiple wavelengths within spatially distinct fiber modes. Here, we demonstrate multiplexing of dissipative Kerr solitons (DKS) [1] in multiple spatial mode families of a single optical microresonator, pumped simultaneously via electro-optical modulation. DKSs are self-localized pulses of light that can be excited in coherently-driven passive nonlinear optical resonators [1]. We spatially multiplex DKSs for dual comb generation in both co- or counter-propagating configurations and demonstrate amplitude- and phase-resolved spectroscopy with the latter. We then combine these two schemes to generate *three combs* simultaneously. The soliton combs have a high degree of mutual coherence, which is desirable for many dual comb schemes [2].

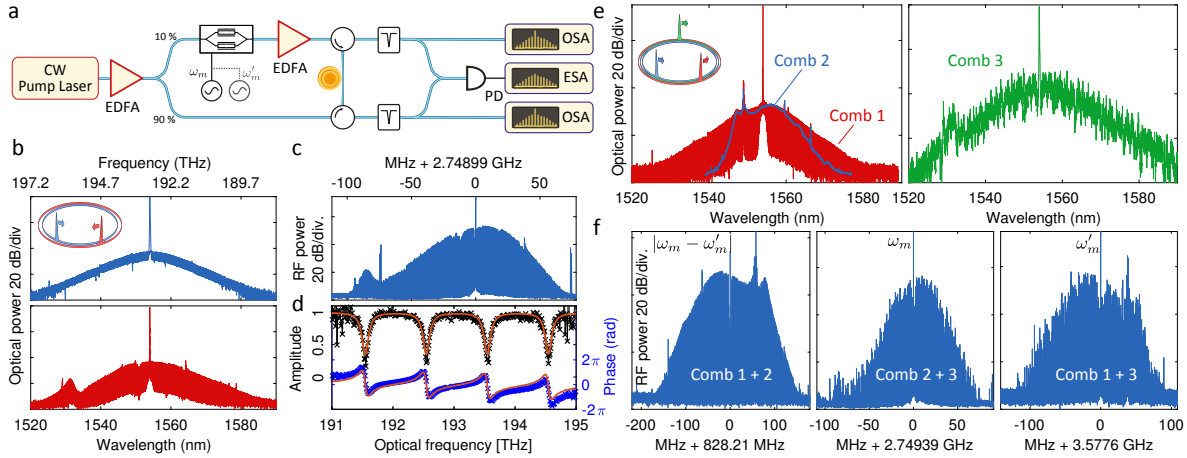

Fig. 1: **(a)** Setup for counter-propagating dual and triple DKS-comb generation. **(b)** Optical spectra of two counter-propagating combs. **(c)** Resulting dual comb beatnote (rbw 3 kHz). **(d)** Retrieved amplitude and phase of interferogram produced by coupling the dual-soliton pulse trains through a Waveshaper (not shown) with synthetic absorption features (100 GHz FWHM). The orange lines display the programmed functions. **(e)** Triple comb generation. Comb 1 and 2 are generated in the CW direction, while Comb 3 is obtained in the CCW direction. **(f)** Heterodyning the three pulse trains leads to the formation of three RF combs (rbw 3 kHz).

We take advantage of the multimode nature of a crystalline MgF_2 whispering gallery mode cavity [3] (FSR $\sim$ 12 GHz), in which DKSs can be formed in several spatial mode families. In the co-propagating scheme, an IQ-modulator generates a single sideband, without full suppression of the initial carrier, such that pump and sideband reach the same power level and can act as coherent drive to generate DKS in two mode families. Both combs are generated in the same resonator and derived from the same laser, resulting in a high level of mutual coherence. Alternatively, the two mode families can be excited in a counter-propagating way, analogous to prior implementations [4, 5] (see Fig. 1a). The two generated single-soliton combs are shown in Fig. 1b, together with the corresponding RF comb (Fig. 1c). As a proof of concept spectroscopy experiment, one comb is sent through a waveshaper before interfering with the second comb. The beating is recorded on a fast oscilloscope and compared with a reference signal without the waveshaper. Figure 1d shows that the retrieved amplitude and phase closely match the programmed profiles over a span of 4 THz. The co- and counter-propagating approaches can be combined. Adding an additional tone on the modulator enable the creation of two combs in one direction, while one comb is generated in the opposite direction (Fig. 1e). Heterodyning all the comb together creates a set of three RF combs (Fig. 1f). Such a triple comb configuration, with two co-propagating combs, could find applications in two-dimensional spectroscopy, where pump and probe pulse trains are mixed in a sample and the mixing result is heterodyned with a third local oscillator comb [6].

Acknowledgments: This work was supported by funding from the Swiss National Science Foundation under grant agreement 163864, by the AFOSR, Air Force Material Command, USAF under Award No. FA9550-15-1-0099, and by the Ministry of Education and Science of the Russian Federation under project RFMEFI58516X0005.

References

[1] T. Herr et al. “Temporal solitons in optical microresonators”. *Nat. Photon.* 8.2 (2013).
[2] I. Coddington, N. Newbury, and W. Swann. “Dual-comb spectroscopy”. *Optica* 3.4 (2016).
[3] T. Herr et al. “Mode spectrum and temporal soliton formation in optical microresonators”. *Phys. Rev. Lett.* 113.12 (2014).
[4] C. Joshi et al. “Counter-rotating cavity solitons in a silicon nitride microresonator” (2017). arXiv: 1711.04849.
[5] Q. F. Yang et al. “Counter-propagating solitons in microresonators”. *Nat. Photon.* 11.9 (2017).
[6] B. Lomsadze and S. T. Cundiff. “Frequency combs enable rapid and high-resolution multidimensional coherent spectroscopy.” *Science* 357.6358 (2017).

High-precision Long-haul Time Transfer between Multi Stations Over Field Fiber Link

Chen Faxi[1,3], Zhao Kan[1,3], ZhouXu[1,2,3],Liu Tao[1,3],Zhang Shougang[1,3]

[1]National Time Service Centre, Chinese Academy of Science, Xi'an, China
[2]University of Chinese Academy of Science, Beijing, China
[3]Key Laboratory of Time and Frequency Standards, Chinese Academy of Science, Xi'an, China

Email: cfx2006xd@163.com

To achieve high-precision fiber-optic time transfer, the method of two-way transmission is usually used. On this basis, this paper further proposes that, by simultaneously transferring the 1PPS signal, time code signal and 10MHz frequency signal over single fiber with the same wavelength, and adopting time division multi address (TDMA) as well as the purification and regeneration method at individual station, high-precision long-haul fiber-optic time transfer between multi stations can be achieved. With the self-developed engineering prototypes, the experimental verifications are subsequently made . A field fiber link of 871.6km long was utilized, along which 11 self-developed time-frequency transceivers were set at the cascaded fiber-optic stations. Since only the 11th remote stations co-located with the local station, the performance the time transfer between the 11th remote station and the local station are measured accurately. The time transfer is experimentally demonstrated with the time standard deviation of 29.8ps and the time deviations of 3.85ps/1000s. The timing uncertainty on the field fiber link is also checked and gives a value of 25.4ps. To further improve the long-term stability of time transfer, more accurate thermal control of the lasers used in the system should be adopted to reduce the optical wavelength drift. By compressing the bandwidth of the PLL modules in every remote device, the short-term stability of time synchronization can also be better. This proposal can also be extended to applications in fiber networks with star-shaped and chain-shaped connections. Therefore time synchronization in even larger areas and more stations can be realized.

References

[1] Guiling Wu, "High-precision two-way optic-fiber time transfer using an improved time code", J.Science Letter, vol. 85, 114701 , 2015.

[2] S.C. Ebenhag, "Measurement and Error Sources in Time Transfer Using Asynchronous Fiber Network", IEEE transactions on instrumentation and measurement, in press, 2010.

[3] O. Terra, "Phase-coherent comparison of two optical frequency standards over 146 km using a telecommunication fiber link", Applied Physics B, Laser and Optics, vol. 97, pp. 541-551, 2009.

ACES Mission Status

L. Cacciapuoti[1], R. Much[1], C. Moratto[1], J. Kehrer[2], M.P. Hess[2], A. Helm[2], T. Niedermaier[2], F.X. Esnault[3], D. Massonnet[3], W. Schaefer[4], J. Pittet[5], D. Goujon[5], P. Rochat[5], P. Laurent[6], P. Wolf[6], F. Meynadier[6], I. Prochazka[7], A. Schlicht[8], U. Schreiber[8], C. Salomon[9]

[1]European Space Agency, ESTEC, Noordwijk, The Netherlands
[2]Airbus Defence and Space, Friedrichshafen, Germany
[3]CNES, Toulouse, France
[4]Timetech, Stuttgart, Germany
[5]Spectratime, Neuchâtel, Switzerland
[6]SYRTE, Observatoire de Paris, CNRS, UPMC, LNE, Paris, France
[7]Czech Technical University in Prague, Prague, Czech Republic
[8]Technical University of Munich, Munich, Germany
[9]Laboratoire Kastler Brossel, ENS, Paris, France

Email: Luigi.Cacciapuoti@esa.int

Atomic Clock Ensemble in Space (ACES) is developing high performance clocks and links to test Einstein's theory of general relativity. From the International Space Station, the ACES payload will distribute a clock signal with fractional frequency instability and inaccuracy of $1 \cdot 10^{-16}$ establishing a global network to compare clocks in space and on the ground.

The ACES mission is close to completion. The flight model of the PHARAO clock has been delivered and integrated in the ACES payload. The performance of the active H-maser SHM have been established and the clock is now completing its environmental test campaign. The on-board frequency comparator has recently been tested showing correct operation of the phase locked loop stabilizing the PHARAO oscillator on the SHM clock signal. The single-photon avalanche detector for the ACES optical link ELT (European Laser Timing) has been tested and it is now waiting to be integrated on the ACES payload. The microwave link (MWL) flight model is on its way.

In preparation for the final acceptance of the payload, system tests involving the flight models of PHARAO, FCDP and the onboard computer as well as the SHM engineering model have been completed to demonstrate the main functions of ACES. The accuracy of the ACES clock signal has been checked by performing an absolute frequency measurement with respect to the SYRTE clocks via a GPS link.

The recent test results will be presented together with the major milestones that will lead us to the ACES launch.

Low thermal noise Fabry-Perot cavities for ultrastable lasers

Nikita Zhadnov[1,2], Konstantin Kydeyarov[1,2], Ilia Semerikov[1,2], Ksenia Khabarova[1,2], Nikolay Kolachevsky[1,2]

[1]*P.N. Lebedev Physical Institute of the Russian Academy of Sciences, 53 Leninskiy Prospekt, Moscow, 119991, Russia*

[2]*Russian Quantum Center, Business-center "Ural", 100A, Novaya street, Skolkovo, Moscow, 143025, Russia*

e-mail: nik.zhadnov@yandex.ru

Ultrastable lasers play an important role in many experiments with high precision as one of targets. Optical atomic clocks, precision optical spectroscopy, quantum states manipulations etc. require extremely narrow spectral linewidth light with the lowest possible relative frequency instability.

Locking the laser's frequency to a TEM00 mode of a very high finesse reference optical cavity with active temperature and vibration isolation allows to reach an instability level that corresponds to the thermal noise limit of the cavity. Today the state of the art ultrastable lasers demonstrate fractional frequency instabilities on the level of $4 \cdot 10^{-17}$ at τ=1-1000 s [1]. This value is fundamentally limited mostly by thermal noise of the cavity's mirrors, that causes fluctuations of the cavity length. The level of thermal noise for cavities, made up of different materials and of different size and shape can be calculated using the Levin's formulation of fluctuation-dissipation theorem [2]. We've applied this method to different types of cavities in order to select the most perspective configuration; some results are shown in Table 1. The cavity design is described in [3].

№	Spacer/substrate	Mirror coating	$\sigma_{Y,\,10^{-17}}$
1	ULE/SiO_2	SiO_2/Ta_2O_5	100
2	Si/Si	SiO_2/Ta_2O_5	30
3	Si/Si	AlGaAs (crystalline)	6
4	GaAs/GaAs	AlGaAs (crystalline)	5

Table 1. Here, σ_Y is the thermal noise-limited fractional frequency instability at τ=1 s.

A very promising way to decrease thermal noise is to increase length of the cavity. The 0.5 m long ULE cavity were used to achieve fractional instability lower than 1E-16 [4]. Our group is working on development of different design ultrastable cavities: cryogenic silicon cavities with dielectric or crystalline mirrors and 0.5 m long ULE cavities in vertical and horizontal orientation. The features and difficulties one meets will be discussed.

[1] Matei D.G. et al., Phys. Rev. Lett. 118, 263202 (2017)
[2] Yu. Levin, Phys. Rev. D 57, 659 (1998)
[3] Zhadnov N.O. et al., Quantum Electronics, 47 (5):421 (2017)
[4] Hafner S. et al., Opt. Lett. 40, 2112-2115 (2015)

LNE-SYRTE (Ultra) Cold Atom Gravimeter

Romain Karcher[1], Almazbek Imanaliev[1], Sébastien Merlet[1], Franck Pereira Dos Santos[1]

[1]LNE-SYRTE, Observatoire de Paris, PSL Research University, CNRS, Sorbonne Université, UPMC Univ Paris 06, 61 avenue de l'Observatoire 75014 Paris France

Email: romain.karcher@obspm.fr

The LNE-SYRTE Cold Atom Gravimeter (CAG) is an inertial sensor which operates since 2009. It performs 3 gravity measurements per second with laser cooled Rubidium-87 atoms using two-photon Raman transitions to realize an atomic interferometer. Its design makes it movable, able to perform on field measurements and to participate to international comparisons. Since the first Key Comparison CCM.G-K1 at BIPM (ICAG-2009) [1], its capabilities have been regularly compared to other technologies and its gravity measurements agree with the Key Reference Values of ICAG-2009, ECAG-2011 [2] and ICAG-2013 [3].
The CAG is a state of the art instrument which has demonstrated a short term sensitivity of 5.6µGal in 1s measurement time [4] and 0.06µGal in 40 000s (1µGal = 10^{-8}m.s^{-2} ~10^{-9}g). The total accuracy budget is 4.3µGal, dominated by the uncertainty on the effect of wavefront aberrations of 4 µGal.

The wavefront aberration bias is due to distortions of the interferometer laser phase fronts, arising from reflection and transmission trough imperfectly flat optics. This leads to phase shifts sampled by the atoms at the interferometer pulses, which depend on their expansion across the laser beams, and thus on their temperature. This is today one of the major limits to the accuracy of atomic gravimeters. To tackle this problem and reduce the uncertainty on the evaluation of this effect below the µGal level, we have modified the CAG to perform gravity measurement with ultra cold atoms. For that purpose, we implemented a crossed dipole trap using a high power (30W) laser at 1.55µm. Using evaporative cooling we can cool down the atomic source from 100µK to a few hundreds of nK which reduces its expansion in the laser beams. We measure significant variations of g with respect to the atomic temperature, irrespective of the orientation of the setup, and thus of Coriolis acceleration (Figure 1). With such measurements we hope to better extrapolate the gravity value to zero temperature [5] and thus reduce its uncertainty.

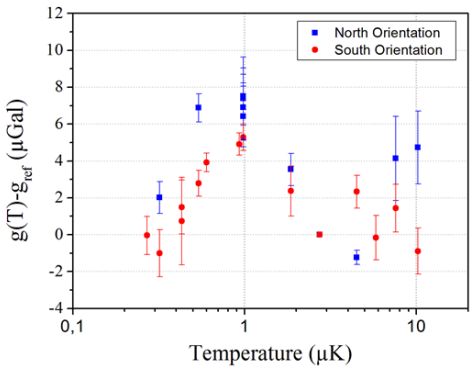

Figure 1 Measured gravity value as a function of the atomic source temperature, for two opposite orientation of the instrument, with the reference measurement performed at a temperature of 2.7µK

I will present the instrument, the principle of the gravity acceleration measurement and its performances. I will then discuss the development of the optical trap and the optimization of the evaporation sequence, before focusing on recent gravity measurements with ultra cold atoms. With a rework of the global uncertainty budget, we expect to be able to reach accuracy below 1µGal.

References

[1] Z.Jiang et al, *Metrologia* 49 (2012)

[2] O.Francis et al, *Metrologia* 50 (2013)

[3] O.Francis et al, *Metrologia* 52 Tech.Suppl (2015)

[4] P.Gillot et al, *Metrologia* 51 (2014)

[5] A.Louchet-Chauvet et al, *New Journal of Physics* 13 (2011)

Evaluation of Optical Frequency Transfer via 500 km Fiber Links

Xue Deng[1,2,3], Zang Qi[1,3], Liu Jie[1,3], Jiao Dongdong[1,2,3], Zhang Xiang[1,3], Wang Dan[1,3], Dong Ruifang[1,2,3,] Liu Tao[1,2,3*]

[1]National Time Service Center, Chinese Academy of Sciences, Xi'an, China
[2] University of Chinese Academy of Sciences, Beijing, China
[3] Key Laboratory of Time and Frequency Standards, Chinese Academy of Sciences, Xi'an, China

Email: dengxue@ntsc.ac.cn

Frequency transfer through fiber links shows a great potential in many applications such as remote atomic clock comparison, metrology and high precision measurement [1]. In 2016, a phase-coherent frequency link connecting Paris and Braunschweig using 1415 km of telecom fibre was established for the comparison of two Sr optical clocks at an uncertainty of 5E-17 [2]. In China, a high-precision time and frequency transfer network based on a ten-thousands kilometers dedicate optical fiber was proposed and under discussion. As a part of the investigation on the possible long-distance optical frequency transfer techniques, we demonstrate an optical frequency transfer over 500km spooled fiber link with EDFA scheme and cascaded scheme respectively.

In the first test of so called EDFA scheme, four bi-EDFAs are implemented to amplify the optical signal, and the whole-loop phase noise is compensated at the sender site. In the so called cascaded scheme, a repeater station is applied between the first 300 km fiber segment and the second 200km fiber segment. A 1kHz narrow-linewidth laser is applied as the source of the repeater and locking fidelity can be ignored compared with the transfer instability of the two fiber links. The phase noise of the two fiber segments are compensated separately with individual control loop. The transfer instability is measured with beating the transferred laser and the local laser. The measurement results are shown in the Fig. 1.

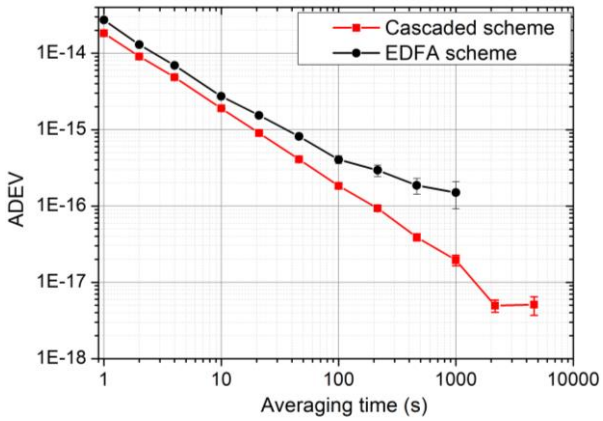

Fig. 1: Allan deviation (ADEV) of one-way fiber noise (blue line) and of two-way phase comparison (red line) over 50-km fiber spool.

With the cascaded scheme, we achieve an optical frequency transfer instability of 1.8×10^{-14} at 1s and scale down to 5×10^{-18} at 2000s. In contrast with this result, frequency transfer instability of the 2.6×10^{-14} at 1s is achieved for the EDFA scheme. The transfer instability of the cascaded scheme is roughly two times superior than the EDFA scheme for 1s averaging time, which agrees almost with the theoretical prediction.

Since we all know, the transfer instability follows an $L^{3/2}$ rule which leads to a worse transfer instability for a long-haul link. From this test, the cascaded scheme shows a great advantage on the transfer instability, when multi-segment fiber link are applied instead of a single span.

References

[1] C.W. Chou, D.B. Hume, T. Rosenband and D. J. Wineland, “Optical clocks and relativity,” Science, vol. 329, p. 1630, 2010.

[2]. Lisdat, C. et al. A clock network for geodesy and fundamental science. Nat. Commun. 7:12443 doi: 10.1038/ncomms12443 (2016).

Phase-Coherent Transfer of Optical Frequency Between ISI CAS and CESNET

Martin Cizek[1], Lenka Pravdova[1], Vaclav Hucl[1], Simon Rerucha[1], Jan Hrabina[1], Michal Jelinek[1], Bretislav Mikel[1], Vladimir Smotlacha[2], Ondrej Havlis[2], Josef Vojtech[2], Josef Lazar[1], Ondrej Cip[1]

[1]Department of Coherence Optics, Institute of Scientific Instruments of the CAS, Brno, CZ
[2] CESNET, z. s. p. o., Prague, CZ

Email: cizek@isibrno.cz

The contribution reports on the current state of the fibre link for phase-coherent transfer of optical frequency between ISI CAS (Brno, CZ) and CESNET (Prague, CZ). The 306 km long link is operated on an internet communication fibre in a dedicated 1540-1546 nm DWDM window. The narrow linewidth laser Kohereas ADJUSTIK working at 1540.5 nm locked to the nearest tooth of the stabilized optical frequency comb referenced by the H-Maser serves as the optical frequency standard at the transmitting side.

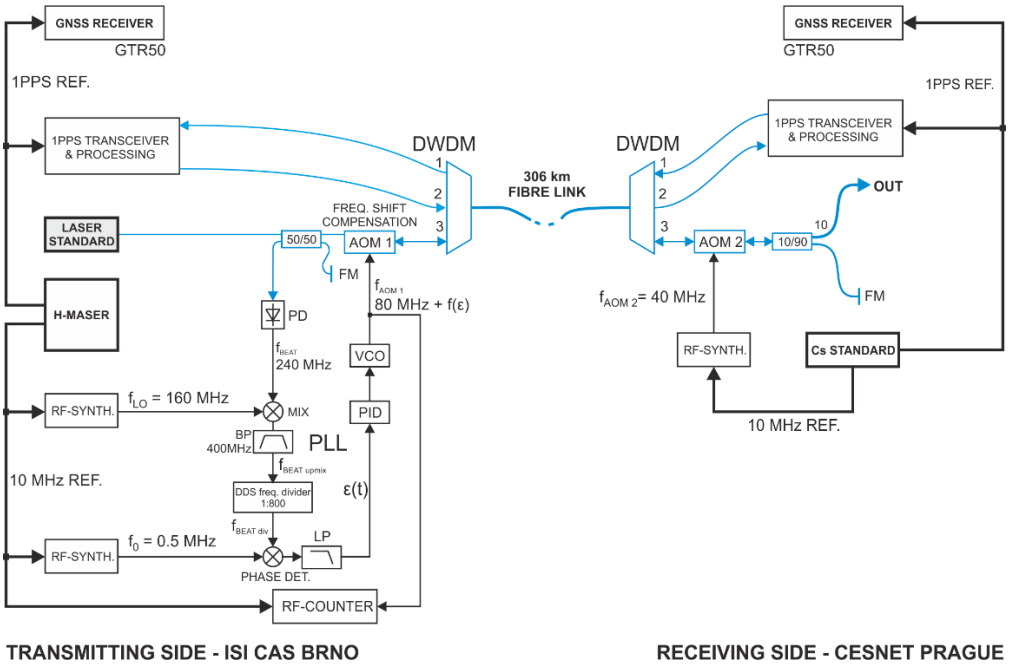

Fig.1: Setup for phase-coherent optical frequency transfer. Legend: AOM – acousto-optic modulator, BP – RF band-pass filter, DWDM – DWDM mux/demux, FM – Faraday mirror, LP – low-pass filter, PD – photodetector, PID – P-I-D controller, VCO – voltage-controlled oscillator; f_{LO} – local oscillator frequency used for up mixing the beat note before frequency division, f_0 – reference frequency of the phase detector, $\varepsilon(t)$ – phase error signal.

As seen in Fig. 1, electronics for active compensation of optical frequency shifts induced by the fibre link optical path fluctuations works on the principle of the phase-locked loop. The frequency of the signal driving AOM1 (control action) is continuously recorded to compute fluctuations of transport delay of the link. At both sides, the link is equipped with 1-PPS signal transceivers connected to the same DWDM mux/demux. The measured intrinsic relative stability of the transfer over the fibre link in uncompensated state is better than 10^{-13} for 1s integration time and 10^{-14} for 1 000s integration time.

The authors acknowledge the support from Technology Agency of CR (project TH01011254) for establishing long-haul fibre link. The issues with optical frequency shift compensation have been supported by Czech Science Foundation (project GB14-36681G).

Optical Iodine Frequency References for Space

Markus Oswald[1,5], Thilo Schuldt[1,2], Klaus Döringshoff[3],
Vladimir Schkolnik[3], Tobias D. Schmidt[4], Johann Furthner[4], Markus Krutzik[3],
Ulrich Johann[5], Achim Peters[3], Claus Braxmaier[1,2]

[1]University of Bremen, Center of Applied Space Technology and Microgravity (ZARM), 28359 Bremen, Germany
[2]German Aerospace Center (DLR), Institute of Space Systems, 28359 Bremen, Germany
[3]Institute of Physics, Humboldt-University of Berlin, 12489 Berlin, Germany
[4]German Aerospace Center (DLR), Institute of Communications and Navigation, 82234 Wessling, Germany
[5]Airbus Defence and Space GmbH, 88090 Immenstaad, Germany

Email: markus.oswald@zarm.uni-bremen.de

Highly stable optical frequency references are a key element for future space missions related to navigation (GNSS), geodesy, Earth observation and fundamental physics tests such as gravitational waves detection. In this regard, absolute frequency references based on hyperfine transitions in molecular iodine at 532 nm using modulation transfer spectroscopy are promising candidates due to their high long-term stability and low complexity.

We present our recent work of developing and realizing frequency references based on iodine spectroscopy with emphasis towards space compatibility. This includes a setup on elegant breadboard level (EBB) realized on a 55 x 25 cm² thermally and mechanically stable glass-ceramic base plate using a 30 cm long iodine cell in triple pass configuration [1], and a more compact system on engineering model level (EM) utilizing a squared iodine cell in 9-pass configuration on a 38 x 18 cm² fused silica base plate [2]. Both setups show similar frequency stabilities in the 10^{-15} domain at integration times between 10 s and 1000 s. The EM setup was subjected to thermal cycling and vibrations. As the most recent development, a spectroscopy unit optimized in terms of compactness and ruggedness for the JOKARUS sounding rocket mission has been developed and integrated [3]. Moreover, first long-term stability measurement results of the EBB setup to a H_2-maser over a frequency comb are presented.

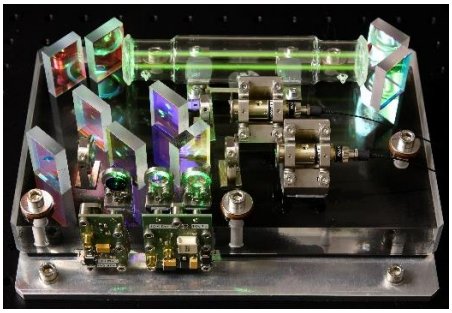

Fig. 1: Spectroscopy unit for the JOKARUS sounding rocket mission using a 15 cm long tube cell in double pass configuration. Components are integrated on a fused silica base plate with a footprint of 24.6 x 14.5 cm².

References

[1] T. Schuldt, K. Döringshoff, E. Kovalchuk, A. Keetman, J. Pahl, A. Peters, C. Braxmaier, "Development of a compact optical absolute frequency reference for space with 10^{-15} instability", Applied Optics, vol. 56, p. 1101-1106, 2017.

[2] K. Döringshoff, T. Schuldt, E.V. Kovalchuk, et. al., „A flight-like absolute optical frequency reference based on iodine for laser systems at 1064 nm", Appl. Phys. B 123: 183, 2017.

[3] V. Schkolnik, K. Döringshoff, F.B. Gutsch, et al. „JOKARUS – design of a compact optical iodine frequency reference for a sounding rocket mission", EPJ Quantum Technol. 4: 9, 2017.

Kalman filter simulation and characterization of BDS satellite clock

Bin Wang[1], Junping Chen[2], Binghao Wang[3]

[1] Shanghai Astronomical Observatory, CAS, Shanghai, China
[2] Shanghai Astronomical Observatory, CAS, Shanghai, China
[3] Information Engineering University, Zhengzhou, China

Email: binw@shao.ac.cn

An accurate and correct characterization of satellite clock in orbit is of great importance for clock prediction, and the prerequisite and basis for the production of time scale in GNSS systems. In this paper, an Kalman filter algorithm for the simulation and characterization of BDS satellite clock that fits the real oscillator behavior is presented.

Study of BDS satellite clock in orbit [1] indicated the presence of periodic variation that are not accounted by the three-state model (with states corresponding to time-offset, fractional frequency offset and frequency drift). Besides the periodic variation, flicker noise processes (flicker phase modulation (FLPM) and flicker frequency modulation (FLFM)) can also observed the in the BDS satellite clock time-offset data. There are three different models of clock periodic states in Kalman filter [2], and the first one is chosen, i.e., adding the periodic variation to only the phase state. The flicker noise processes over some time span can be modelled approximately by a linear combination of several independent Gauss-Markov processes [3]. Each Markov process can be included in the Kalman filter and contributes an additional component to the state vector.

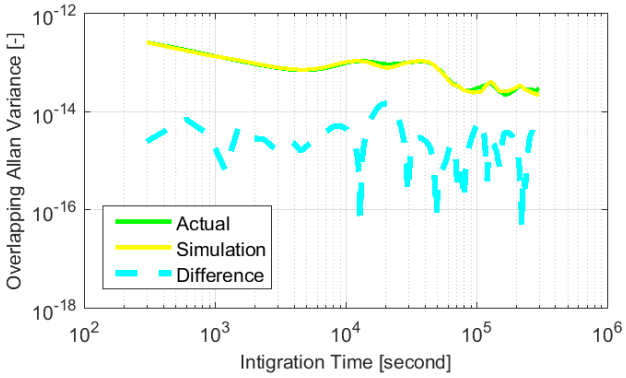

Fig. 1: Comparison of frequency stability between simulation data and real data of BDS satellite clock. Frequency stability analysis result of the simulation data is plotted as yellow line, while that of the actual data is plotted as green line, and the difference between them is plotted as blue-dot line.

Analysis results show that simulation data can fit the real oscillator behavior of BDS satellite clock well. The difference between the simulation clock and the real clock data is within 20ns in the two weeks period. Comparison of frequency stability analysis results between them is shown in Fig. 1. It is found that the difference is below 10^{-14}, which is approximately ten percent of the actual stability performance.

References

[1]. Bin Wang, Yidong Lou, Jingnan Liu, et al., Analysis of BDS satellite clocks in orbit. GPS Solutions, 2016. 20(4): p. 783-794.

[2]. Michael J. Coleman and Ken Senior. A comparison of GPS clock models for the next generation GPS system timescale. Proceedings of the 43rd annual precise time and time interval systems and applications meeting. 2011. Long Beach, CA.

[3]. J. A. Davis, C.A. Greenhall, and P.W. Stacey, A Kalman filter clock algorithm for use in the presence of flicker frequency modulation noise. Metrologia, 2005. 42(1): p. 1-10.

Breaking Lorentz Reciprocity with Spatio-Temporal Modulation

Andrea Alù[1,2], Dimitrios L. Sounas[2], Ahmed Kord[2]

[1]Advanced Science Research Center, City University of New York, New York, NY, USA
[2]Department of Electrical and Computer Engineering, The University of Texas at Austin, Austin, TX, USA

Email: aalu@gc.cuny.edu

In this talk, we will provide an overview of our recent efforts in the realization of magnet-free non-reciprocal devices and metamaterials based on spatio-temporal modulation. Lorentz reciprocity is a fundamental principle in electromagnetics, stipulating the fact that signal transmission between two points in space is the same for both transmission directions. Breaking this symmetry is important in various practical instances, for instance for the protection of lasers from spurious back-reflections and the design of circulators for full-duplex communication systems. Nonreciprocity is conventionally achieved through magnetic biasing, but the challenges related to integration on chip have recently raised a lot of interest in developing magnet-free non-reciprocal devices. In this context, our group has introduced the concept of angular momentum biasing, according to which strong nonreciprocal response as in conventional nonreciprocal devices can be obtained if the static magnetic biasing is replaced with angular momentum biasing effectively generated in a circuit through spatiotemporal modulation, e.g., modulation of three symmetrically resonators with signals of equal amplitude and phases 0, 120 and 240 deg [1-3]. In this talk, we will present our recent progress in this direction and show how spatio-temporal modulation can largely break reciprocity and realize magnet-less isolators, circulators and metamaterials with metrics satisfying the requirements of practical applications. We will show how we can eliminate intermodulation products by employing a differential architecture based on two circulators with 180 deg phase shifted modulation, allowing to improve insertion loss and reduce the modulation parameters. We will also discuss the problem of matching and show how bandwidth can be significantly extended by adding passive networks at the circulator ports. We will show results for other practically important metrics, including linearity, noise and power consumption, and discuss how they can be improved. Furthermore, we will present an analytical theory for the proposed devices, which is useful for their efficient design, and show experimental results of different implementations of the proposed circuits on printed circuit boards. Our results will demonstrate that angular-momentum biasing is a practically attractive approach for various applications, including full-duplex systems, RFIDs and radars, and also amenable to different implementations, including PCB, integrated circuit and MEMS, creating exciting opportunities for fundamental and applied research.

References

[1] N. Estep, D. Sounas, J. Soric, and A. Alù, “Magnetic-Free Non-Reciprocity Based on Parametrically Modulated Coupled-Resonator Loops,” Nature Physics, Vol. 10, No. 12, pp. 923-927, December 1, 2014

[2] N. A. Estep, D. L. Sounas, and A. Alù, “Magnetless Microwave Circulators Based on Spatiotemporally Modulated Rings of Coupled Resonators,” IEEE Transactions on Microwave Theory and Techniques, Vol. 64, No. 2, pp. 502-518, February 1, 2016.

[3] D. Sounas, and A. Alù, “Non-Reciprocal Photonics Based on Time Modulation,” Nature Photonics, Vol. 11, No. 12, pp. 774-783, November 30, 2017.

Transportable Ultra-Low Noise Photonic Microwave Synthesizer

M. Giunta[1,2], X. Xie[3], W. Hänsel[1], M. Lessing[1], M. Lezius[1], M. Fischer[1], R. Bouchand[3], D. Nicolodi[3], P.-A. Tremblin[4], A. Joshi[5], S. Datta[5], G. Santarelli[4], Y. Le Coq[3] and R. Holzwarth[1,2]

[1]Menlo Systems GmbH, D-82152 Martinsried, Germany
[2]Max-Planck-Institut für Quantenoptik, 85748 Garching, Germany
[3]LNE-SYRTE, Observatoire de Paris, 75014 Paris, France
[4]LP2N, Université de Bordeaux 1, 33400 Talance, France
[5]Discovery Semiconductors Inc., New Jersey, USA
Email: m.giunta@menlosystems.com

With the unceasing progress in the development of ultra-stable Fabry-Pérot cavities, the linewidth of continuous wave lasers can now be stabilized down to the millihertz level. By optically phase-referencing an ultra-low noise optical frequency combs (OFC) with such ultra-stable laser (USL) source, this stability can be transferred to all comb modes. With appropriate optical and photo-detection techniques, the resulting OFC can be used to generate exceptional ultra-low noise microwave signals, employing the comb as an optical frequency divider. Here we present the progress towards a fieldable photonic microwave synthesizer, which could serve numerous applications, ranging from coherent radar systems to deep-space communication.

The system consists of two rack-mountable sub-units. A USL source serves as the reference flywheel and a compact ultra-low noise Er:fiber femtosecond frequency comb serves as an optical-to-microwave divider. The fractional frequency stability of the USL corresponds to 1.5×10^{-15} at 1 s, assessed with a PI-mode frequency counter (100 ms gate time and 1 MHz measurement bandwidth). The core of the OFC is a compact mode-locked fiber laser with a repetition rate of 250 MHz [1]. The output of the oscillator is amplified in a short Erbium-doped fiber amplifier (EDFA) then split in two different branches. The first one is used for the detection of the CEO frequency via an f-2f interferometer. The second output is further amplified in an ultra-low relative intensity noise (RIN) EDFA followed by a 4-stage pulse interleaver for repetition rate multiplication to 4 GHz. State-of-the-art highly-linear photodetectors (HLPD) are used to extract microwave signals at 4 GHz and overtones. The 12 GHz harmonic has a power above 0 dBm. It is analyzed by digital cross-correlation as described in [2] and the results are shown in Figure 1.

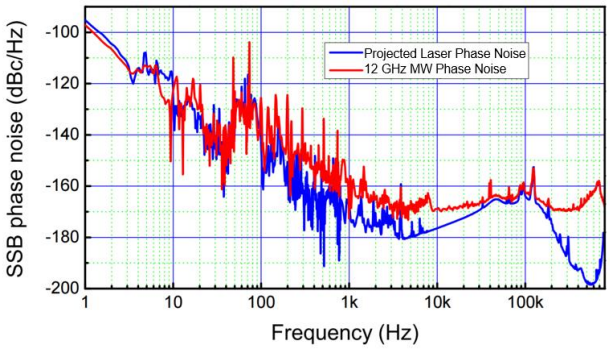

Fig. 1: Single side-band phase noise power spectral density of a 12 GHz signal synthesized from the ultra-stable laser (red trace). Its optical phase noise is projected (blue trace), being scaled down to the 12 GHz signal. This data have been produced with a table-top OFC prototype soon to be integrated in the compact transportable microwave synthesizer.

References

[1] W. Hänsel, *et. al.*, "All polarization-maintaining fiber laser architecture for robust femtosecond pulse generation," *Appl. Phys. B*, vol. 123, no. 1, p. 41, Jan. 2017.

[2] X. Xie, *et. al.*, "Photonic microwave signals with zeptosecond-level absolute timing noise," *Nat. Photonics*, vol. 11, no. 1, pp. 44–47, Nov. 2016.

The ACES-PHARAO test of the gravitational redshift: Refined performance estimates

C. Guerlin[1,2] E. Savalle[1], F. Meynadier[1], P. Delva[1], C. Le Poncin-Lafitte[1] ,P. Laurent[1]
P. Wolf[1]

[1]SYRTE , Observatoire de Paris, PSL Reseach University, CNRS, Sorbonne Universités, UPMC Univ. Paris 06, LNE
[2]Laboratoire Kastler Brossel, ENS-PSL Research University, CNRS, UPMC-Sorbonne University, Collège de France

Email: Etienne.Savalle@obspm.fr

The ACES-PHARAO space mission will install the first cold Cs atom clock on the International Space Station. It will enable scientific projects in many fields such as tests of fundamental physics, international clock comparison or ionosphere studies.

The SYRTE laboratory is implementing a specific Data Analysis Center consisting of theoretical modeling, numerical simulation and the data analysis software itself. The simulation and analysis includes all realistic effects known to be present (atmospheric delay, Doppler effect, fundamental measurement noise…), and all tests are in agreement with the mission specifications [1].

In this contribution we focus on one of the primary mission objectives: the test of the gravitational redshift. We use a simple parametrized theoretical framework for a possible deviation from GR, and numerically determine the uncertainty that can be obtained by ACES on the redshift parameter α. The numerical simulations are carried out using real ISS orbit data over 12 days. We assume up to 8 ground stations located at different metrological institutes around the world, with the dominating noise sources being the onboard clock and the ACES microwave link (MWL). Using different statistical methods to analyze the data we present the results on the redshift test for different configurations and analysis methods.

Finally we use degraded ISS orbit determination to study the effect of orbit errors on the performance of the test of the gravitational redshift. We show that the expected orbit errors are negligible, and that the ISS orbit determination is not going to be a limiting factor for the ACES-PHARAO test of the gravitational redshift.

References

[1] F. Meynadier et al. *Atomic Clock Ensemble in Space (ACES) data analysis*, Classical and Quantum Gravity, accepted. arXiv: 1709.06491, (2017).

Photonic Damascene process with reflow step for ultra-smooth Si_3N_4 waveguides

Martin H. P. Pfeiffer, Junqiu Liu, Tiago Morais, Bahareh Ghadiani, Tobias J. Kippenberg

IPHYS-LPQM, Ecole Polytechnique Fédéral de Lausanne, Lausanne, Switzerland

Email: martin.pfeiffer@epfl.ch

Low loss, planar optical waveguides have been actively investigated because of their wide application range, including nonlinear photonic devices such as microresonator based frequency comb generators [1]. For the latter low loss waveguides with highly confining geometries that allow for anomalous group velocity dispersion (GVD) at telecom wavelengths are of particular interest. The combination of low propagation losses and high effective nonlinearity lowers the parametric threshold for broadband nonlinear wavelength conversion to practical values and enables photonic chip based precision metrology, based e.g. on direct optical synthesis [2]. Silicon nitride (Si_3N_4) waveguides embedded in a silicon dioxide cladding (SiO_2) are an increasingly used photonic integration platform, especially for nonlinear photonic devices [3]. Resonator Q factor of up to $8x10^7$ have been demonstrated [4], but only using waveguide core geometries providing low confinement. Similar Q factors in dispersion engineered microresonators for nonlinear photonics has remained elusive, as the tightly confining waveguide geometries increase their scattering losses.

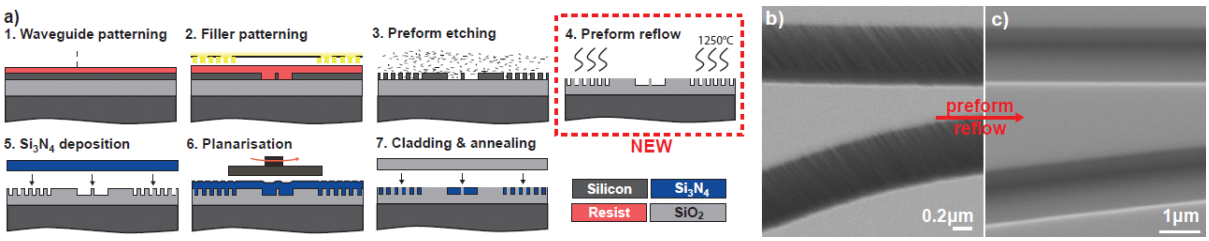

Fig. 1: Ultra-smooth waveguide fabrication. a) Photonic Damascene process with new preform reflow step. In order to smooth the recess sidewalls in the SiO_2 bottom cladding, the wafer is heated to 1250C for 18h. b-c) Ring recess structure before and after reflow process. Significant roughness reduction is observed.

Here, we add a novel reflow step to the recently introduced photonic Damascene process [5] in order to achieve ultra-smooth waveguide sidewalls and high Q factors for tightly confining geometries. Heating the glass cladding above its glass transition temperature leads to a surface tension driven reorganization which reduces the surface roughness drastically. We achieve *mean* Q factors above $3x10^6$ in devices with anomalous GVD. Moreover, a systematic study reveals the dominant loss factors. Our results pave the way for power efficient, compact precision metrology devices based on nonlinear processes in integrated microresonators with unprecedented finesse.

References

[1] T. J. Kippenberg et al., "Microresonator-based optical frequency combs," Science 332, 555–559 (2011).
[2] D. Spencer et al, "An Integrated-Photonics Optical-Frequency Synthesizer", Arxiv, 1708.05228 (2017).
[3] D. J. Moss et al., "New CMOS-compatible platforms based on silicon nitride and Hydex for nonlinear optics," Nat Phot 7, 597–607 (2013).
[4] D. Spencer et al., "Integrated waveguide coupled Si3N4 resonators in the ultrahigh-Q regime," Optica 1, 153–157 (2014).
[5] M. H. P. Pfeiffer et al., "Photonic Damascene process for integrated high-Q microresonator based nonlinear photonics," Optica 3, 20–25 (2016).

Atom interferometry on narrow intercombination transitions of alkali-earth atoms

Nicola Poli, Leonardo Salvi, Liang Hu, Guglielmo M. Tino

Dipartimento di Fisica e Astronomia and LENS - Università di Firenze, INFN - Sezione di Firenze, Via Sansone 1, I-50019 Sesto Fiorentino, Italy

Email: poli@lens.unifi.it

Today, matter-wave interferometers as clocks and gravimeters allow for precision measurements of time and gravity at an unprecedented level.

In all these sensors, indeed, the exquisite control of both internal (electronic) and external (center of mass motion) degrees of freedom of ultra-cold atomic samples, enable us to study interactions at their most basic, quantum level, paving the way for new tests of fundamental physics [1,2].

In this talk, I'll review some of the most recent results obtained by our group in this field, presenting also a novel approach to atom interferometry, based on ultra-narrow intercombination transitions of strontium atoms (^{88}Sr) [3,4]. Novel spin-squeezing techniques with direct application to strontium atom interferometers will also be discussed [5].

References:

[1] N. Poli, F.-Y. Wang, M. G. Tarallo, A. Alberti, M. Prevedelli and G. M. Tino "Precision measurement of gravity with cold atoms in an optical lattice and comparison with a classical gravimeter", Phys. Rev. Lett. 106, 038501 (2011)

[2] M. G. Tarallo, T. Mazzoni, N. Poli, D. V. Sutyrin, X. Zhang, and G. M. Tino, "Test of Einstein Equivalence Principle for 0-spin and half-integer-spin atoms: Search for spin-gravity coupling effects", Phys. Rev. Lett. 113, 023005 (2014)

[3] L. Hu, N. Poli, L. Salvi and G. M. Tino, "Atom interferometry with the Sr optical clock transition", Phys. Rev. Lett. 119, 263601 (2017)

[4] R. P. del Aguila, T. Mazzoni, L. Hu, L. Salvi, G. M. Tino and N. Poli, "Bragg gravity-gradiometer using the 1S0-3P1 intercombination transition of 88Sr", arXiv:1712.01388 (2017)

[5] L.Salvi, N. Poli, V. Vuletic and G. M. Tino, "Squeezing on momentum states for atom interferometry", arXiv:1708.05112 (2017)

Real Like Transmission Lines for Sagnac Correction Study

Martin Šlapák[1], Josef Vojtěch[1]

[1]Department of Optical networks, CESNET, Prague, Czech Republic

Email: slapak@cesnet.cz

The highly accurate time and frequency transfers need the stable underlying line and knowledge of its parameters. The relativistic effects must be considered – especially at one-way transfers the Sagnac correction must be evaluated. In our previous work [1] we proposed automated method for estimation of Sagnac correction for links with unknown or uncertain paths. The method was validated on four artificial lines and two real lines. There are similar works [2, 3] aiming to the estimation of Sagnac correction and its bounds based on limited knowledge of the lines.

The mentioned works [1-3] differs in the estimation of the lower and upper bounds. Fig. 1 illustrates a partial step of algorithm proposed in [1] for a search of upper bound of correction. The bound is defined by an area which is enclosed by the line segment of length l_x and length of the arc L_x. The comparison of these approaches is a logical step. The major problem is the fact that no fiber line operator is willing to share even approximate path of the line. The comparison will be made on artificial paths with parameters of existing lines and real-like tracing. The real like tracing is an approach when the artificial path is projected and drawn into the map according to the practice of projecting a real optical infrastructure – e.g. the link uses the linear infrastructure objects like cable collectors along the railways.

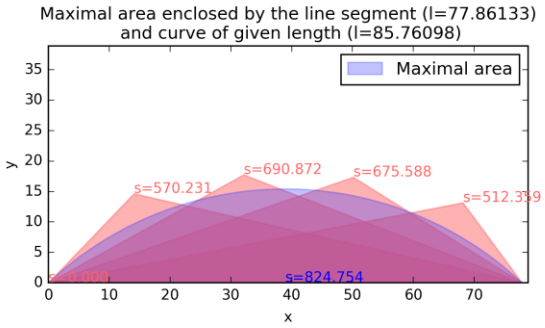

Fig. 1: Examples of maximal area enclosed by line segment (l_x =77.86133) and semicircle defined by length of arc (L_x =85.76098) and few triangles with length of legs equal to L_x and hypotenuse of length l_x.

The concept of real like transmission lines brings us the ability to assemble the validation dataset of optical paths with properties similar to the existing optical lines. Such dataset can be used for the comparison and validation of distinct approaches which cannot be compared directly on paths on which are developed.

References:

[1] M. Šlapák, J. Vojtěch, R. Velc, "Automated numerical calculation of Sagnac correction for photonic paths", Optics Communications, vol. 389, p. 230-233, 2017.

[2] J. Gersl, P. Delva, P. Wolf, Relativistic corrections for time and frequency transfer in optical fibres, in: Metrologia, Volume 52, Number 4, 2015, pp. 552–264.doi:10.1088/0026-1394/52/4/552.552–564, http://dx.doi.org/10.1088/0026-1394/52/4/552

[3] Czubla, Albin, et al. "Some approximated methods of calculation Sagnac correction for optical fiber time transfer." Frequency and Time Forum and IEEE International Frequency Control Symposium (EFTF/IFC), 2017 Joint Conference of the European. IEEE, 2017.

Two-stage stabilization setup of the laser working on 729 nm for spectroscopy with cold $^{40}Ca^{+}$ ion.

Tuan Minh Pham[1], Martin Cizek[1], Adam Lesundak[1], Vaclav Hucl[1], Lukas Slodicka[2], Petr Obsil[2], Radim Filip[2], Josef Lazar[1], Ondrej Cip[1]

[1]Department of Coherence Optics, Institute of Scientific Instruments of the CAS, Brno, CZ
[2]Department of Optic, Palacký University, Olomouc, CZ

Email: tuan@isibrno.cz

The experiments with trapped ions, such as precision spectroscopy techniques or experiments with quantum mechanical interaction and quantum computing experiments, demand a narrow-linewidth excitation laser. This requirement comes from the physical properties of the forbidden transitions of ultra-cold ions trapped into an electrical trap. To be able to coherently transfer population into dipole forbidden transition one need laser working with Hz or sub-Hz linewidth. The spectral linewidth of the external cavity laser diode (ECLD) chosen for this purpose is 300 kHz approx. for the integration time 1 s. Because this relatively broader linewidth doesn't fulfil the requirement for the efficient pumping of the long live forbidden transition, an implementation of a linewidth narrowing technique is necessary. We have considered two stage setup for laser linewidth narrowing. Firstly the ECDL laser optical frequency is phase locked to a selected component of an optical frequency comb. The following stage is the suppression of the frequency noise with the high-finesse optical resonator which serves as a frequency discriminator allowing the further linewidth suppression.

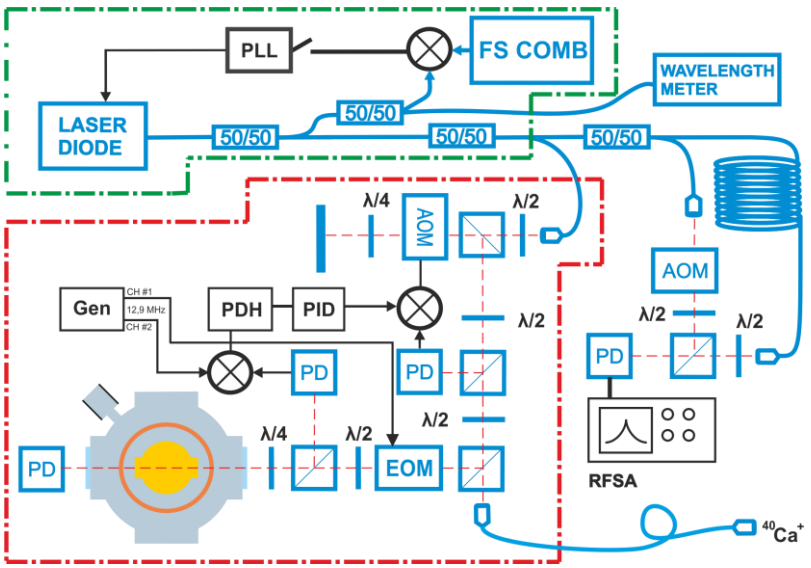

Figure 1. The setup for the ECDL laser linewidth narrowing and the frequency noise properties analysis. The green section includes the ECDL laser and a phase locked loop to the selected spectral component of the optical frequency comb – FS COMB. The red section represents the second stage of the linewidth narrowing using the spectroscopy with a high-finesse optical resonator: 50/50 - fibre couplers, λ/2 and λ/4 - wave plates, Gen – frequency generator, PD - photodetector, AOM - acousto-optic modulator, EOM - electro-optic modulator, PID - fast regulator, PDH - module for the Pound-Drever-Hall detection technique, RFSA - spectral analyser, HF-cavity – High finesse optical cavity.

The work includes the description and design of the housing with the acoustic and thermal isolation of the cavity setup and examples of spectroscopy measurements on the dipole forbidden transition.

The authors acknowledge the support from Czech Science Foundation (project GB14-36681G).

Mid-infrared Optical Frequency Comb via Coherent Supercontinuum Processes in Nano-photonic Waveguides

Hairun Guo, Wenle Weng, Martin. H. P. Pfeiffer, and Tobias J. Kippenberg

École Polytechnique Fédérale de Lausanne (EPFL), CH-1015 Lausanne, Switzerland

Email: tobias.kippenberg@epfl.ch

Mid-infrared (Mid-IR) optical frequency combs [1] are of significant interest for molecular spectroscopy, due to the fact that many molecules have strong vibrational transitions in this spectral region. Triggered by a significant number of applications such as pharmaceutical, environmental or medical breath analysis, mid-IR spectroscopy has attracted substantial attention in the past decade. A variety of methods have been developed to generate mid-IR frequency combs, such as nonlinear frequency conversion including both optical parametric oscillators (OPOs) and difference frequency generation (DFG), phase-locked states in quantum cascade lasers, microresonator Kerr frequency combs or using mid-IR mode-locked lasers. Recent work has also highlighted the potential to generate mid-IR optical frequency combs from coherent supercontinuum process [2]. When applying this process in chip-based nano-photonic waveguides, the pulse energy can be substantially reduced owing to the large Kerr nonlinearity and tight confinement. Today, nano-photonic waveguide-based SCG has been extensively studied in the visible and near-infrared (near-IR), particularly those made from silicon and Si_3N_4, and has enabled carrier-envelope frequency detection, full phase stabilization of frequency combs, as well as offset-free frequency comb generation by DFG. For accessing the mid-IR, dispersion engineering plays the key role in extending the long wavelength portion of the supercontinuum. Dispersive wave generation can induce a coherent and efficient light conversion over a large frequency span, and facilitate ultra-broadband SCG beyond the self-phase modulation (SPM) regime.

Here we demonstrate the ability to synthesize mid-IR frequency combs in the range $2.5-4\,\mu$m [3], directly from an erbium-fiber based femtosecond laser in the telecom-band (at $1.55\,\mu$m), based on mid-IR dispersive wave generation, and using Si_3N_4 nano-photonic waveguides. One example is shown in Fig. 1, where by means of dispersion engineering, soliton and dispersive waves will find phase matching such that in both visible and mid-IR range, dispersive waves can be generated through the supercontinuum process (Fig. 1(a)). In large-cross-section Si_3N_4 waveguides, one supercontinuum spectrum is shown in Fig. 1(b) in which the dispersive wave in the mid-IR spans $2.9-3.6\,\mu$m. This mid-IR wave was then filtered by a long-pass edge-filter and its comb structure was assessed in two aspects: the repetition beatnote of the mid-IR wave alone (Fig. 1(c)), and the heterodyne beatnote with respect to a CW reference laser (Fig. 1(d)). Compared to the pump laser in the telecom-band, no obvious degradation was observed on both beatnote signals, implying that the generated mid-IR wave inherits the phase coherence of the pump laser. Our investigation therefore demonstrates a coherent regime of mid-IR frequency comb generation.

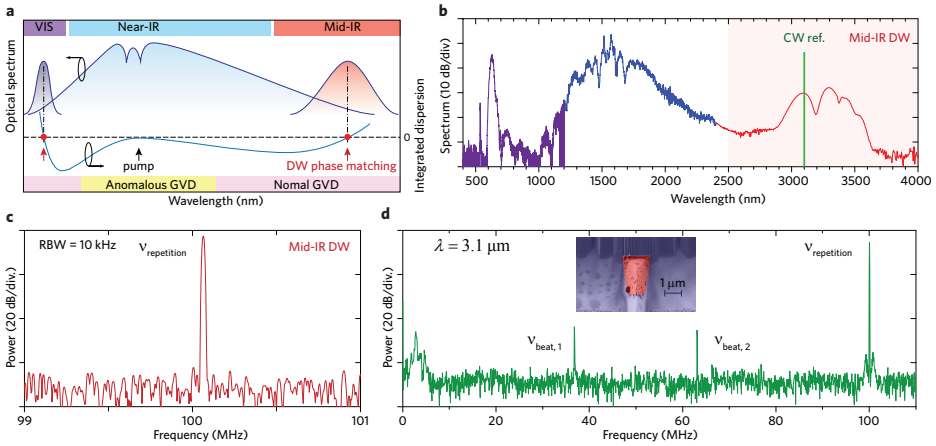

Fig. 1. (a) Schematic representation of soliton induced dispersive wave generation; (b) Spectrum of the generated supercontinuum in a large-cross-section Si_3N_4 waveguide, in which the mid-IR wave spans $2.9-3.6\,\mu$m; (c) The repetition beatnote of the mid-IR wave which is filtered by a long-pass edge-filter (cut-on wavelength at $2.5\,\mu$m), resolution bandwidth 10 kHz; (d) The heterodyne beatnote of the mid-IR wave with a CW reference laser (wavelength at $\sim 3.1\,\mu$m; inset shows the corss-section SEM picture of Si_3N_4 waveguides, in which the height of the waveguide is as large as $\sim 2.3\,\mu$m.

This work is supported by DARPA (SCOUT: W31P4Q-16-1-0002); Air Force (No. FA9550-15-1-0099); Marie Sklodowska-Curie IF grant (No. 709249); European Research Council (ERC-2012- StG 306630-MATISSE).

References

1. A. Schliesser, N. Picqué, and T. W. Hänsch, "Mid-infrared frequency combs," Nat. Photonics **6**, 440–449 (2012).
2. J. M. Dudley, G. Genty, and S. Coen, "Supercontinuum generation in photonic crystal fiber," Rev. Mod. Phys. **78**, 1135–1184 (2006).
3. C. Herkommer, A. Billat, D. Grassani, H. Guo, M. H. P. Pfeiffer, C.-S. Bres, and T. J. Kippenberg, "Mid-infrared dispersive wave generation in silicon nitride nano-photonic waveguides," arXiv:1704.02478 (2017).

Modified primary time and frequency standard of VNIIFTRI

S.I. Donchenko[1], A.N. Schipunov[1], I.Yu. Blinov[1], N.B. Koshelyaevsky[1], I.B.Noretz[1],

Yu.F. Smirnov[1], V.G. Palchikov[1]

[1]FGUP "VNIIFTRI", 141570 Mendeleevo, Moscow Region, Russia

Email: vitpal@mail.ru

The National time scale of the Russian Federation is reproduced and maintained based on the use the primary State standard of time and frequency operated at a facility located in Mendeleevo, Moscow Region, Russia. The main purpose of the VNIIFTRI system of primary frequency standards, comprising two caesium fountains, is to perform regular calibrations of the international time-scale TAI/UTC at the highest accuracy and to provide a stable reference for the construction and steering of UTC(SU), as well as the local representation of UTC in Russia. In the present time, the system of primary frequency standard can be use for absolute frequency measurements of optical frequency standards using femto-second Comb techniques developed at VNIIFTRI. It is important to note, that VNIIFTRI is involved in the implementation of the Federal special-purpose programme GLONASS, and it is the principal metrological Institution of Russia, concerned with creation of new and upgrading of existing standard means of timing, positioning and navigation support with the aim of achieving the prescribed accuracy characteristics of GLONASS.

The UTC(SU) time scale is currently transmitted to the GLONASS Ground Control Segment using signal receivers. The UTC(SU) time scale is a representation of UTC in accordance with the BIPM requirements.

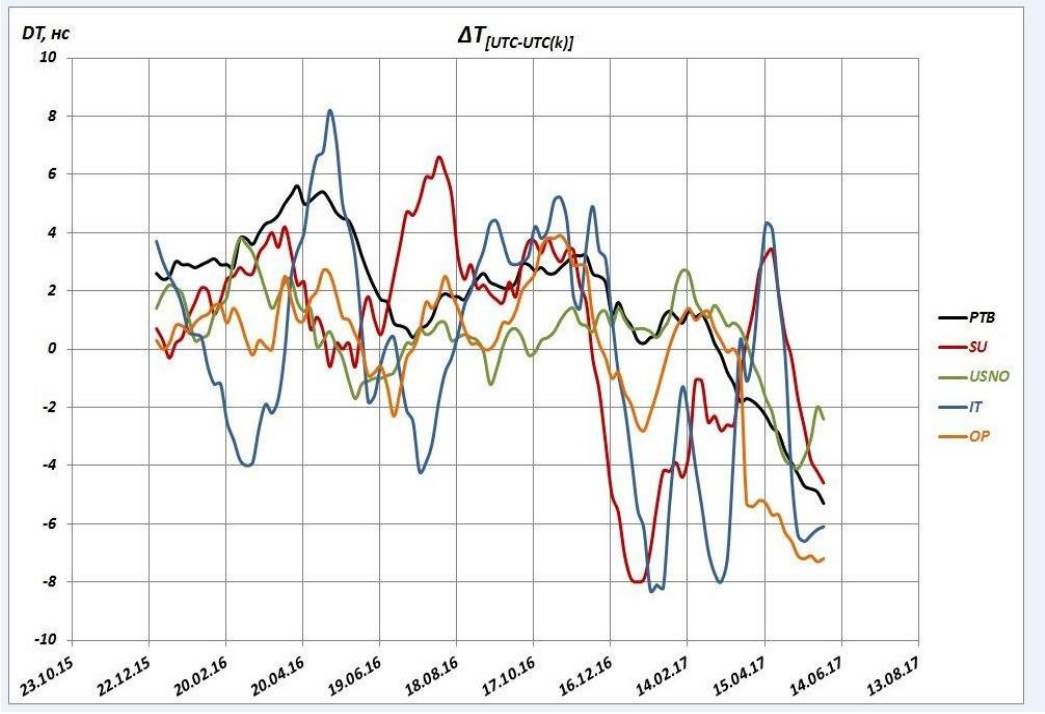

Figure 1. National local representations of UTC (k).

As follows from the BIPM Circular T, the UTC(SU) time offset from UTC has not exceeded 10 ns in the last years (see, for example, Fig.1)

Oscillator with electrostrictive resonator

Thomas Baron[1], William Daniau[1,2], Gilles Martin[1], Valérie Soumann[1], Roland Salut[1,2], Sylvain Ballandras[2]

[1]FEMTO-ST, Besançon, France
[2]frec|n|sys, Besançon, France

Email: thomas.baron@femto-st.fr

Few works have already described electrostrictive actuation to generate surface acoustic waves. Some of them propose different uses of resonator structures, such as switch on-off [1] or modulation of the signal [2] or 180° phase changing [1]. Therefore, electrostrictive effect can be used for tunable acoustic wave devices [3]. One of our previous work [3] has demonstrated the feasibility of SAW resonators on perovskites single crystals like $SrTiO_3$. The agility of such a resonator can be used for instance to compensate thermal effects by DC voltage control.

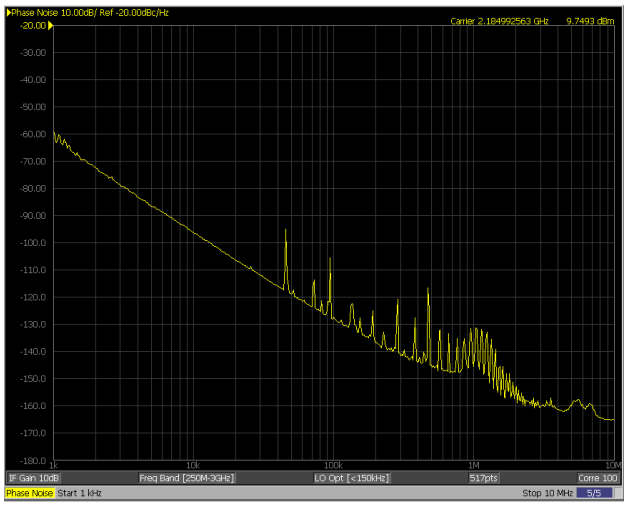

Fig. 1: Phase Noise of hybrid oscillator based on electrostrictive resonator with 30V.

Based on this previous work, new resonators have been fabricated using e-beam-lithography-based techniques and an hybrid oscillator has been developed using these resonators to stabilize the device frequency. Due to the breakdown voltage, DC actuation is limited to 40V. For such voltage, the product $Q \times f$ of the resonator at 2 GHz is about 2×10^{12} Hz. One oscillator has been fabricated with the resonator under probe allowing for phase noise measurement as shown in Fig. 1. A value of -95dBc/Hz has been measured at 10kHz of the carrier.

References

[1] K.Iamsaku, W. Elder, C.D.W. Wilkinson, R.M. De la Rue, “Surface acoustic wave devices using electrostrictive transduction”, J. Appl. Phys., vol. 8, p. 266-282, 1975.

[2] G.R. Laguna, P.F. Delval, B.A. Auld, “Electronic control of SAW transduction in electrostrictive ceramics”, Ultrasonics Symposium, p.207-211, 1985

[3] S. Alzuaga, W. Daniau, T. Baron, G. Martin, R. Salut, E. Defaÿ, S. Ballandras, “SAW resonator using electrostrictive effect”, Joint UFFC, EFTF, PFM Symposium, p.749-752, 2013

Design Optimization for Surface Acoustic Wave devices considering simultaneously apodization and transverse modes effects in Mixed Matrix Approach

Thierry Laroche [1] , Sylvain Ballandras [1] , Marianne Sagnard [1] , William Daniau [2]

[1]Department R&D, frec|n|sys, Besançon, France
[2]Department Time & frequency, Institut Femto-ST, Besançon, France

Email: thierry.laroche@frecnsys.fr

New area in Radio Frequency telecommunications (RF) and Internet Of Things (IOT) require additional efforts to achieve Surface Acoustic Waves components (SAW) able to match with extra targets.

Early in SAW design history, several numerical tools have been achieved to allow the knowledge of their behaviour under numerous parameter variations [1,2]. To consider an entire SAW device, one of the most popular tools is the mixed matrix approach [3]. Classical approach does not take into account lateral effects. However, one of the most important sources of spurious is the transverse mode effect. They are well known and numerical tools already exist to consider them [4]. Some technical paths have also been developed, as transducer apodization [5]. Nevertheless, the mix between transverse modes and apodization effects in SAW has never been numerically consider.

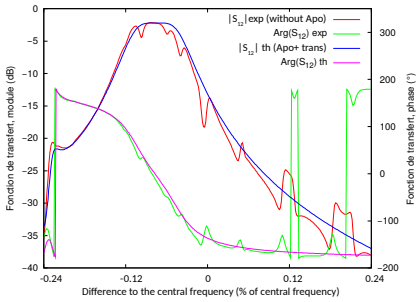

Figure 1: Module and phase of S_{12} parameter for DMS filter on quartz AT. The experimental results show transverse modes whereas theoretical ones are obtained with apodization.

In this work, we first present the classic numerical method to achieve SAW design. Therefore, we briefly introduce the finite element method and the mixed matrix approach. Next, one define the way to consider transverse mode and apodization in the mixed matrix approach and particularly how to mix both of them. This method is applied to real SAW filters on several bulk piezoelectric materials as Quartz (AT cut), lithium tantalate (YXl/42, 112, 130). We then demonstrate the effects of apodization on the spurious modes due to transverse modes (see Figure 1). At last, an extension of these applications is also dedicated to composite wafers with thin piezoelectric layer.

References:

[1] P. Ventura, “Numerical methods for SAW propagation characterization”, IEEE Ultrasonics Symposium, 1998, pp175-186.
[2] S. Ballandras, Wilm, “Finite-element analysis of periodic piezoelectric transducers”, Journal of Applied Physics 93(1), pp702-711, 2003
[3] Tobolka, G.: Mixed matrix representation of SAW transducers, IEEE Transactions on Sonics and Ultrasonics 26(6), pp426-428, 1979.
[4] CK Campbell, “Modelling the transverse-mode response of a two-port SAW resonator”, IEEE Trans Ultr Ferroelectr Freq Control, 1991;38(3):237-42.
[5] M. Solal et al., "Transverse modes suppression and loss reduction for buried electrodes SAW devices," 2010 IEEE International Ultrasonics Symposium, San Diego, CA, 2010, pp. 624-628.

Consideration and implementation of inherent losses in SAW devices design

Marianne Sagnard[1], Thierry Laroche[1], Sylvain Ballandras[1]

[1]Department R&D, frec|n|sys, Besançon, France

Email: marianne.sagnard@frecnsys.fr

Surface acoustic wave (SAW) devices are often used in various industry sectors, such as defense, aeronautics, telecommunications. Actually, highly reliable sensors and filters can be manufactured using SAW technologies [1]. Among the numerous advantages they provide, we can notice their small sizes, their sustainability in harsh environments due to the absence of batteries and wires and to the remote monitoring of physical quantities such as pressure, temperature or strain. In the past decades, numerical simulation tools have been improved to allow more efficient designs of SAW devices [2]. Indeed, many phenomena can now be considered such as the electrical resistance due to the device probing, the electrode resistivity, the transverse modes [3] to most closely evaluate the behaviour of the system in actual environment.

In keeping with these previous works, this paper is dedicated to the raising of two current approximations: the first one considers the wave propagation without losses; the second one assesses that piezoelectric materials are perfectly dielectric and their polarization is performed without losses (the effective permittivity ε is real). These two statements involve imprecisions in the computations. In this study, one uses a physical model (Kelvin-Voigt internal damping [4]) to describe the internal behaviour of the material under stress or strain. The strain is imposed by the passing of the SAW. Furthermore, losses related to the polarization of the material and to the residual conductivity in the piezoelectric are no more considered as null. Then, numerical simulations are conducted and calculation/test correlations based on a very well known piezoelectric material, Quartz, are carried out (see figure 1). We also consider other materials to build their non-linear tensors as lithium tantalate in standard cut.

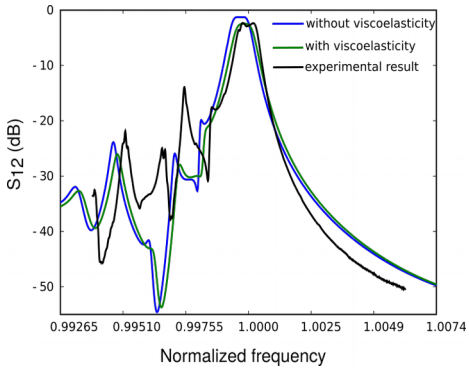

Figure 1: Transfer function of a manufactured SAW device (black curve) whose frequency response was simulated first with (green) and without (blue) taking account the viscoelasticity phenomenon

References:

[1] G. Bruckner, J. Bardong, M. Postl, and A. Klug. Experimental investigations of the acousto-electric effect in high temperature SAW gas sensing. In 2016 IEEE International Ultrasonics Symposium (IUS), pages 1–4, Sept 2016.

[2] V. Laude, A. Reinhardt, M. Wilm, A. Khelif, and S. Ballandras. Fast FEM/BEM simulation of SAW devices via asymptotic waveform evaluation. IEEE Transactions on Ultrasonics, Ferroelectrics, and Frequency Control, 51(3):359–363, March 2004.

[3] CK Campbell, “Modelling the transverse-mode response of a two-port SAW resonator”, IEEE Trans Ultr Ferroelectr Freq Control, 1991;38(3):237-42.

[4] Krzystof Marynowski and Tomasz Kapitaniak. Kelvin-Voigt versus Bürgers internal damping in modeling of axially moving viscoelastic web. International journal of non-lienar mechanics, 37:1147–1161, 2002.

Bidirectional optical amplifier delivering high gain

Josef Vojtech[1], Ondrej Havlis[1], Martin Slapak[1], Miloslav Hula[1], Vladimir Smotlacha [2], Martin Kolbe [2], Jan Radil[1]

[1]Department of Optical Networks, CESNET, Prague, Czech Republic
[2]Department of Technology for network applications, CESNET, Prague, Czech Republic

Email: josef.vojtech@cesnet.cz

For long distance transmission of highly accurate time or stable frequency it is important to keep the reciprocal propagation path. It allows us to improve transmission stability (slow effect will cancel in first order) and also to establish active compensation of propagation fluctuations. Unfortunately, single fiber transmission introduces necessity of bidirectional symmetrical amplifiers in order not to lose advantage of a reciprocal path. In case of time transfer, quasi-bidirectional amplification might be acceptable [1]. It means that amplifiers contain short nonreciprocal path, e.g. wavelength routers or even active fibers. But the ultra-stable frequency transfer requires truly single path optical amplifiers that are considered further.

Design of described amplifier was motivated by our experience with system for time and frequency transfer utilizing reserved bandwidth in shared optical network with data transmission. Among available technologies, we can mention discrete amplifiers: rare earth doped fiber amplifiers (namely Erbium Doped Fiber Amplifiers (EDFAs) suitable for wavelengths range from 1530 to 1610nm), Semiconductor Optical Amplifiers (SOA) and distributed amplifiers based on scattering, namely Raman or Brillouin amplifiers. Natural request on high and broadband gain together with multi-channel operation unfortunately exclude SOAs (as they have limited possibility of multichannel operation [2]), Raman amplifiers (as they provide only moderate gains in common telecommunication fibers due to low gain coefficient [3]) and also Brillouin amplifiers (as their gain bandwidth is very limited [4]). Remaining EDFAs can deliver high small signal gains (e.g. over 30 dB) but are very sensitive to unwanted oscillations. It is very difficult to avoid these oscillations as they are caused by feedback provided from two sources: Rayleigh backscattering and reflection from fiber splices, connectors and passive components.

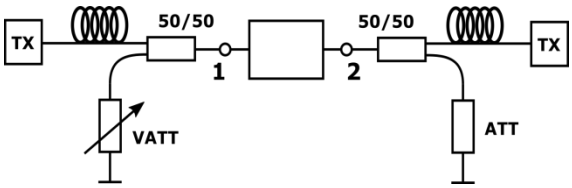

Fig. 1: Setup for device evaluation by reflection level control

We propose bidirectional EDFA equipped with detector of unwanted oscillations. Such EDFA allows us to achieve higher gain compared with legacy approach which keeps safe low gain. For evaluation of the device, we propose setup with controlled level of reflections, see Fig. 1. In the poster, we will report on achieved efficiency of oscillation detection and its avoidance.

References

[1] X. Chen et al., “Simultaneously precise frequency transfer and time synchronization using feed-forward compensation technique via 120 km fiber link,” Sci. Rep. 5, 18343 (2015).

[2] Vojtech, J., Radil, J., and Smotlacha, V., "Semiconductor Optical Amplifier with Holding Beam Injection for Single Path Accurate Time Transmission," Proc. CLEO, JTh2A.78 (2015).

[3] Clivati, C., "Distributed Raman Amplification for long-haul optical frequency dissemination," Proc. IFCS-EFTF-SPC, 184 (2013).

[4] Droste, S. et al., "Optical Frequency Transfer over a Single-span 1840 km Fiber Link," Proc. IFCS-EFTF-SPC, 183 (2013).

Study on the effect of ULE rings on the vibration sensitivity of ultra-stable optical reference cavities

G. Xu[1,2], L. Zhang[2,3], L. Chen[2,3], J. Liu[2], D. Jiao[2,3], C. Jiang[2,3], X. Zhang[2,3], R. Dong[2], T. Liu[2]

[1]School of Mechanical Engineering, Northwestern Polytechnical University, Xi'an , China
[2] National Time Service Center, Chinese Academy of Science, Xi'an , China
[3] Graduate University of Chinese Academy of Science, Beijing, China

Email: xuguanjun@ntsc.ac.cn

Email: taoliu@ntsc.ac.cn

The state-of-the-art narrow linewidth laser plays an important role in many domains, such as optical atomic clocks, high-precision laser spectroscopy, gravitational wave detection and tests of fundamental physics. The ultra-stable optical reference cavity is a core component for the state-of -the-art narrow linewidth laser. The stability of the ultra-narrow linewidth laser mainly depends on the stability of optical length of ultra-stable optical reference cavity. One of fundamental factors leading to the change of optical reference cavity length is the Brownian thermal noise from their constituents including mirror substrates, mirror coatings and space, in which the biggest contributions are mirror coatings and substrates. At present, for 698nm ultra-narrow linewidth lasers, to reduce the noise, the most effective way is to increase the space length and use the fused silica (FS) as the mirror substrate with ultra-low expansion glass (ULE) rings, which is used to decrease the effect of the differential thermal expansion between the fused silica substrate and the ULE glass spacer.

However, the use of long cylindrical and heavier cavities makes it much more difficult to reach the required suppression of optical length changes through forces induced by seismic vibrations and through thermal expansion caused by temperature fluctuations.

Under the condition of vibration sensitivity with 10^{-11}/g to realize the 10^{-17} stability at 1 second, this raises a higher demand for the design of vibration sensitivity of the optical reference cavity, and any changes in the cavity's components are likely to lead to design failure.

In this paper, we focus on the effect of ULE rings on the vibration sensitivity of ultra-stable optical reference cavities.

Firstly, the elastic deformation of optical reference cavities with low frequency vibration is analyzed by using the theory of elasticity and vibration. We derive the analytical formula that the length variation of cavity along the optical axis is induced by ULE rings. In order to verify the correctness of the analytical formula, finite element analysis (FEA) is applied. The results show that the length varication calculated by the analytical formula is basically identical with FEA. However, there are still small differences between the analytical formula and FEA, and the main reason may be that the Poisson's ratio of cavity's material is not considered by analytical.

Secondly, the mass vibration sensitivities are calculated by using FEA under a variety of variables including cavity's length, supporting position, supporting way (vertical or horizontal), the area of the support pad, shape of cross section of cavity. The simulation results for the vertical vibration sensitivity of the three lengths cavities as a function of the support points distance from mirror is shown in Fig.1. The calculation results show that the effect of ULE rings on the vibration sensitivity is greater with increasing the cavity's length in the case of other variables unchanged. For longer cavities, as the distance between supporting position and ULE rings increases, the length variation induced by ULE rings is obvious, eventually leading to change the position of zero vibration sensitivity. With the area of the supporting

pad increasing, the variation of vibration sensitivity caused by ULE rings is smaller. Based on the same cross section of cavity, the length variation induced by ULE rings is negligible for three kinds of shape of cross section.

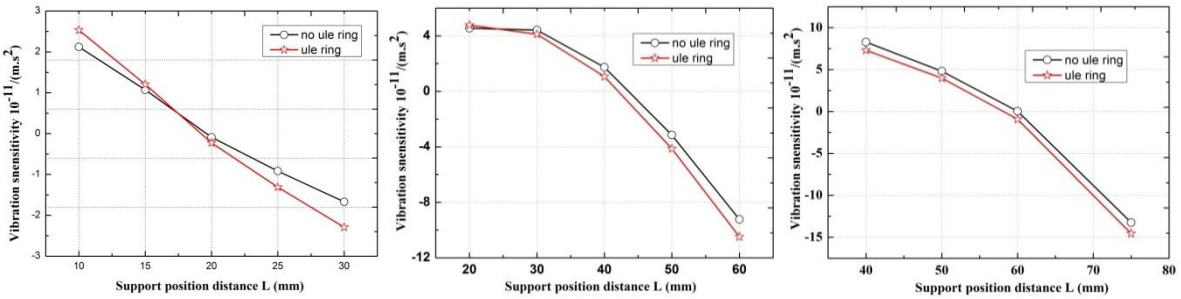

(a) 100mm (b) 200mm (c) 300mm

Fig. 1: The simulation results for the vertical vibration sensitivity of the three lengths cavities as a function of the support points distance from mirror. In all FEA simulations, the contact plane for supporting cavities is square, and the contact areas 4 mm^2 is used to calculate for conveniently comparing with each other in the three lengths cavities. The diameter of all three spacers is 50 mm. (a) The length of cavity is 100mm. (b) The length of cavity is 200mm, (c) The length of cavity is 300mm.

In conclusion, the analysis results about the effect of ULE rings on the vibration sensitivity in this paper are helpful to optimization design of vibration sensitivity of ultra-stable optical reference cavities, specifically longer and thinner optical reference cavities.

References

[1] J. Millo, *et. al.*, "Ultrastable lasers based on vibration insensitive cavities," Phys. Rev. A vol. 79, p. 053829, 2009.

[2] S. A. Webster, *et. al.*, "Thermal-noise-limited optical cavity", Phys. Rev. A, vol.75, p.1-6, 2008.

[3] T. Legero, *et. al.*, "Tuning the thermal expansion properties of optical reference cavities with fused silica mirrors", J. Opt. Soc. Am. B., vol.5, p. 914-919, 2010.

Remote atomic clock contribution to UTC(TP)

Vladimir Smotlacha[1], Alexander Kuna[2]

[1]CESNET z.s.p.o., Prague, Czech Republic,
[2]Institute of Photonics and Electronics, Academy of Sciences, Czech Republic

Email: vs@cesnet.cz

The Laboratory of the National Time and Frequency Standard (LNTFS) in the Institute of Photonics and Electronics (UFE) is responsible for generating the national time scale denoted as UTC(TP). Along with a pair of the atomic clocks operated in the Laboratory, five atomic clocks in possession of the partnering institutes are continuously linked to the UTC(TP) and reported to the BIPM for contributing to the calculation of the UTC. All these clocks are connected using optical time transfer.

The paper is focused on one part of the national optical time and frequency infrastructure used for joining four partnering institutes utilizing bidirectional time transfer over a single fiber as shown in the figure below. Here, the timescales generated from the atomic clocks in CESNET – the Czech NREN, in the Geodetical Observatory VUGTK, and in the Czech Technical University (CTU FEE) are transferred to the Laboratory in UFE and further reported to BIPM.

At the conference, we are going to present our long term experience with the described optical time transfer, the link parameters and the time transfer properties.

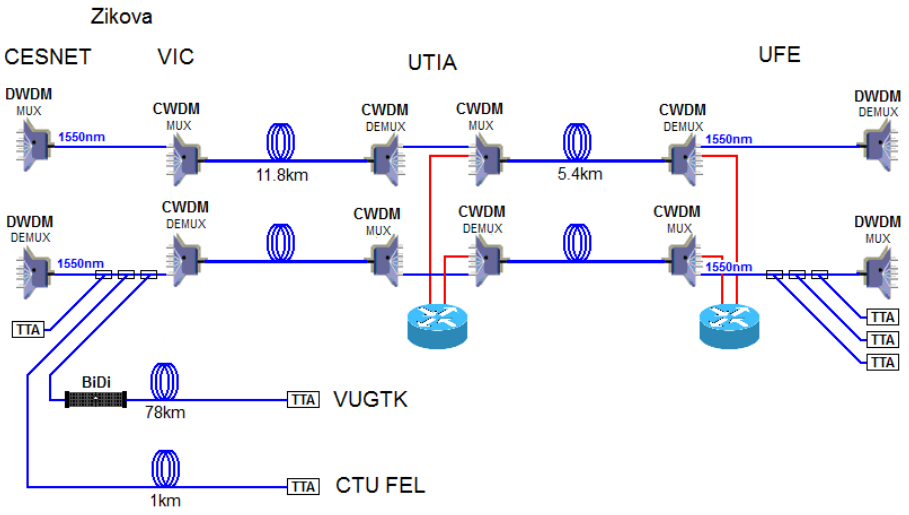

Fig. 1: Schematics of optical path VUGTK – CESNET – UFE

The compact setup for laser cooling and high-resolution spectroscopy with cold $^{40}Ca^{+}$ ions

Ondrej Cip[1], Adam Lesundak[1], Tuan Minh Pham[1], Vaclav Hucl[1], Martin Cizek[1], Jan Hrabina[1], Simon Rerucha[1], Petr Obsil[2], Radim Filip[2], Lukas Slodicka[2], Josef Lazar[1]

[1]Department of Coherence Optics, Institute of Scientific Instruments of the CAS, Brno, CZ
[2]Department of Optics, Palacký University, Olomouc, CZ

Email: ocip@isibrno.cz

Trends in ultimate optical frequency standards initiated an effort to establishing a joined laboratory in the Czech Republic where a research of quantum mechanical interactions of trapped ions with highly-coherent laser lights would be realized. The Institute of Scientific Instruments Brno and Palacky University Olomouc have put together an experimental research infrastructure for $^{40}Ca^{+}$ ion trapping, cooling, experiments of quantum mechanics and spectroscopy in joined laboratory in Brno.

We report on the working scheme of the experimental infrastructure for $^{40}Ca^{+}$ ion trapping and cooling, vacuum chamber, Paul trap, trap radiofrequency control, magnetic field control and monitoring of many parameters in the real-time.

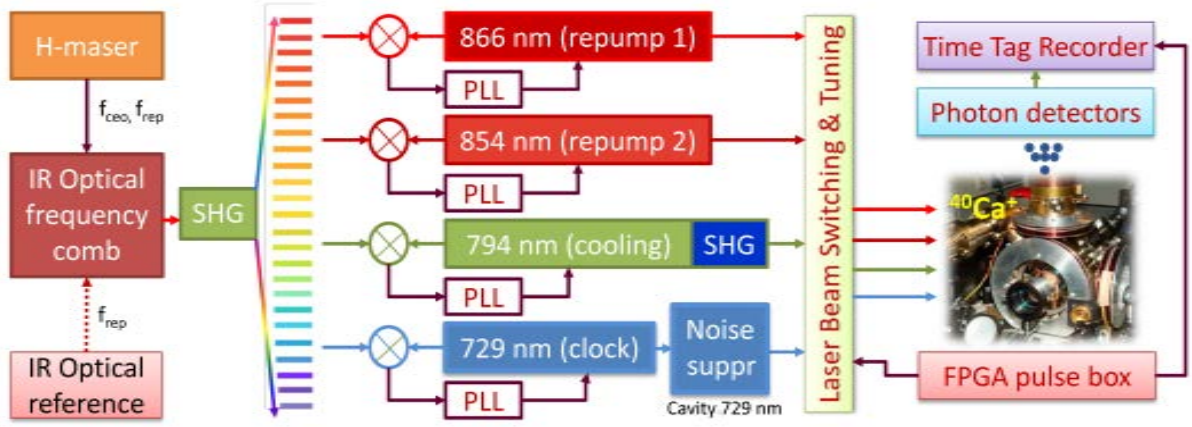

Fig. 1: The principle of the frequency control of excitation lasers for the $^{40}Ca^{+}$ ion trapping and cooling where the optical frequency comb is used as an optical reference. The beat-notes of particular lasers are used as the control values for the appropriate phase locked loops (PLL) and servo-loop controllers locking laser frequencies to the comb.

The important effort is put on the excitation lasers control and their referencing to an optical frequency comb disciplined by an active H-maser as is shown in Fig. 1. The principle of other instruments control necessary for the trapping and laser cooling setup is presented as well. The work also reports the records of spectroscopic measurements of multi-level electronic structure of the ion i.e. the occurrence of dark resonances in the fluorescence signal on the dipole transition and the forbidden transition spectrum of trapped single $^{40}Ca^{+}$ ion.

The research was supported by Czech Science Foundation (project GB14-36681G), Ministry of Education, Youth and Sports of the Czech Republic (projects LO1212 and CZ.1.05/2.1.00/01.0017) and by Czech Academy of Sciences (project RVO:68081731).

Stabilized Time Transfer between CESNET and UFE

Vladimir Smotlacha, Josef Vojtěch

CESNET z.s.p.o., Prague, Czech Republic,

Email: vs@cesnet.cz

CESNET, the Czech NREN (National Research and Education network), operates own optical network. On top of it runs an optical infrastructure for time and frequency transfer (TF Infrastructure) in the Czech Republic. It is a joint activity of several research institutes including national time and frequency laboratory. The total length of utilized transmission lines is over 1600 km. One of main goals of TF infrastructure is time comparison between atomic clocks located in distant places.

We recently started experimental evaluation of a new delay stabilization system on the optical link between CESNET and the national time and frequency laboratory in the Institute of Photonics and Electronics (UFE). This link is 17.2 km long and serves for transfer of CESNET atomic time scale (generated by Cesium clock 5071A) to UFE. We designed method of electric delay stabilization based on phase shift of the 10 MHz clock output. The frequency phase is affected by a pair of analog shifters with 360° range. Shifters are controlled by an output of phase comparator keeping 10 MHz clock output in phase with returning signal from the far end. This way we can compensate optical path delay variations up to 100 ns. According to our long term experience, that will allow us to stabilize typical annual delay variation of up to 150 km long buried fiber.

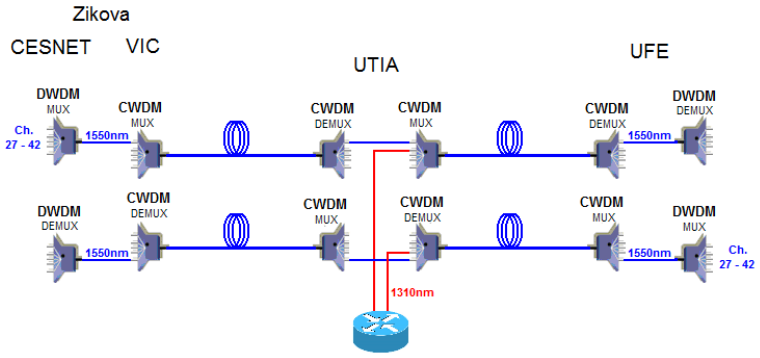

Fig. 1 The transmission path utilize unique dark channel. It runs as a DWDM channel over roughly 12.8 nm wide band in CWDM rented channel provided by the Prague metropolitan network.

The delay stabilization system is now under evaluations and we are going to present first results at the conference.

Nonlinear optoelectronic down-conversion and phase locking of mm-wave and THz signals – Invited

M. Alouini[1], A. Rolland[1], M. Brunel[1], M. Vallet[1], G. Kervella[2], F. Van Dijk[2], G. Ducournau[3], J-F. Lampin[3], G. Loas[1], L. Frein[1], C. Hamel[1]

[1]Institut Foton, UMR 6082, Université de Rennes 1, CNRS, Rennes, France
[2]III-V Lab, Thales, Alcatel-Lucent Bell Labs and CEA LETI, Palaiseau, France
[3]IEMN, UMR 8520, Université de Lille 1, CNRS, Villeneuve d'Ascq, France

Email: mehdi.alouini@univ-rennes1.fr

Bridging the gap between microwave and optical domains is an exciting challenge that is counted one. Technological spin-offs are expected in numerous applications such as coherent communications, mm-wave and THz metrology, ultra-high resolution THz spectroscopy and THz radio-astronomy, where tunable high spectral purity sources are mandatory. In addition to providing narrow linewidth emission, such sources might be integrated, as a local oscillator, in mm-wave and THz detectors offering a high signal-to-noise ratio at room temperature. Among the promising approaches, frequency multiplication is today widely used. Nevertheless, this approach forbids wide frequency tunability. Conversely, heterodyning two continuous optical waves enables, in principle, to cover the whole electromagnetic spectrum of interest from microwave to THz. However, the spectral purity of the generated beat note is limited by that of the feed lasers leading to a linewidth of few tens of kHz at best [1].

In this framework, we have been investigating a new paradigm in view of bringing the tunability offered by optics to the microwave domain on the one hand, and bringing the spectral purity offered by microwave to the optical domain on the other hand [2]. In this respect, an important step was taken few years ago through the development of nonlinear optoelectronic down-conversion principle and up-converted phase-locking technique [3]. In practice, two optical lines separated by the mm-wave or THz targeted frequency are simultaneously modulated at a microwave frequency using a phase or amplitude modulator with a nonlinear response. Optical combs are thus generated around each optical line. Their interleaving gives rise to an intermediate beatnote which can be detected in the microwave domain and exploited either to measure the phase stability of a THz source or to demodulate a given signal around a THz carrier. Achieving such a dual comb in the optical domain presents several advantages among which possible spectral extension through four-wave-mixing in highly nonlinear fibers [4], micro ring resonators [5] or even in photonic crystal membranes. On the other hand, once detected, the intermediate microwave frequency can be easily used to control one of the two laser optical lines and consequently to steer the mm-wave or THz carrier, i.e. to up-convert a low frequency signal in the mm-wave or THz domain.

Ultimately, when the two techniques are combined, mm-wave or THz optoelectronic loops can be realized where the nonlinear optoelectronic down conversion process feeds the up-conversion process [6]. Accordingly, we have been able to phase lock tunable THz beat notes to linewidths below 1 Hz; that is well below the laser linewidth itself, using only low frequency electronic circuits. We are currently extending this paradigm to monolithically integrated dual frequency semiconductor lasers whose optical linewidths are intrinsically too

large to be compliant with standard phase locking electronics. To overcome this drawback, an alternative nonlinear optoelectronic down conversion scheme has been demonstrated where the generated dual combs are delayed and directly re-injected into the laser. The combined effect of self-injection and mutual cross-injection is shown to lead to robust phase locking [7] opening the way to fully integrated devices.

References

[1] A. Rolland, G. Ducournau , G. Danion, G. Loas, M. Brunel, A. Beck, F. Pavanello, E. Peytavite, T. Alkin, M. Zaknoune, J-F. Lampin, F. Bondu, M. Vallet, P. Szriftgiser, D. Bacquet, and M. Alouini, "Narrow linewidth tunable terahertz radiation by photomixing without servo-locking", *IEEE trans. Terahertz Science and Tech.* **99**, 1 (2014).

[2] M. Alouini, A. Rolland, L. Pouget, M. Brunel, M. Vallet, L. Frein, G. Loas, J-F. Lampin, and G. Ducournau, “Bridging the gap between THz and microwave photonics through optoelectronic generation of interleaved combs, Invited paper,” *2014 International Topical Meeting on Microwave Photonics* 350-358 (2014).

[3] M. Alouini, G. Loas, F. Bondu, M. Vallet, M. Brunel, M. Romanelli, "Oscillateur générant un signal comportant une fréquence de l’ordre du térahertz", Patent, FR2961042 (2010), EP2577864 (2013), US20130141174A1 (2013).

[4] A. Rolland, L. Pouget, M. Brunel, and M. Alouini, “Terahertz Optoelectronic Down-Conversion and Phase-Locking Through Four-Wave Mixing,” *Photon. Technol. Lett.* **26**, 1944 (2014).

[5] J. Li, X. Yi1, H. Lee, S.A. Diddams, and K.J. Vahala, “Electro-optical frequency division and stable microwave synthesis,” *Science* **345**, 309 (2014).

[6] A. Rolland, G. Loas, M. Brunel, L. Frein, M. Vallet, and M. Alouini, "Non-linear optoelectronic phase-locked loop for stabilization of opto-millimeter waves: towards a narrow linewidth tunable THz source", *Opt. Express 19*, **17944** (2011).

[7] G. Kervella, F. Van Dijk, G. Pillet, M. Lamponi, M. Chtioui, L. Morvan, and M. Alouini, "Optoelectronic cross-injection locking of a dual-wavelength photonic integrated circuit for low-phase-noise millimeter-wave generation," *Opt. Lett.* **40**, 3655 (2015).

Spectroscopy of trapped antihydrogen in the ALPHA experiment

Stefan Eriksson[1]

[1]Department of Physics, College of Science, Swansea University, Swansea, UK

Email: s.j.eriksson@swansea.ac.uk

Antihydrogen offers a unique way to test matter/antimatter symmetry. Antihydrogen can reproducibly be synthesized and trapped in the ALPHA-experiment at CERN for extended periods of time [1, 2] offering an opportunity to study the properties of antimatter with high precision. New techniques to study antihydrogen have emerged; the ALPHA-collaboration can now interrogate the bound state energy structure with resonant microwaves [3], determine the gravitational mass to inertial mass ratio [4] and measure charge neutrality [5.6]. Very recently, the two-photon optical transition to the first excited state in antihydrogen has been observed with a relative frequency precision of 200 parts in a trillion [7]. The development of antihydrogen accumulation [8] allows larger antihydrogen samples and as a consequence more precise measurements as first demonstrated by the observation of the hyperfine spectrum [9] in the microwave domain with a relative frequency precision of 400 parts in a million. Both the optical and microwave experiments yield results which are consistent with CPT invariance within the precision of the measurements.

Here, I present an overview of antihydrogen synthesis and trapping in the ALPHA-experiment, together with the latest results on spectroscopy of the ground and first excited state in trapped antihydrogen. I present an outlook on the future of probing fundamental symmetry with antihydrogen including work in the era of CERN's new extra-low-energy antiproton source ELENA.

References

[1] G. B. Andresen et al. Nature vol. 468, p. 673, 2010.

[2] G. B. Andresen et al. Nature Physics vol. 7, p. 558, 2011.

[3] C. Amole et al. Nature vol. 483, p. 439, 2012.

[4] A. E. Charman et al. Nature Communications vol. 4, p. 1785, 2013.

[5] C. Amole et al. 2014 Nature Communications vol. 5, p. 3955, 2014.

[6] M. Ahmadi et al. Nature vol. 529 p. 373, 2016.

[7] M. Ahmadi et al. Nature vol. 541 p. 506, 2017.

[8] M. Ahmadi et al. Nature Communications vol. 8, p. 681, 2017.

[9] M. Ahmadi et al. Nature vol. 548 p. 66, 2017.

Ro-vibrational fine structure of CF_3H by frequency-comb-assisted saturated spectroscopy at 8.6 μm

Edoardo Vicentini[1], Alessio Gambetta[1,2], Nicola Coluccelli[1,2], Eugenio Fasci[3], Antonio Castrillo[3], Livio Gianfrani[3], Valentina Di Sarno[4], Pasquale Maddaloni[4,5], Adina Ceausu-Velcescu[6], Paolo De Natale[4], Yuchen Wang[1,2], Toney T. Fernandez[2], Paolo Laporta[1,2], and Gianluca Galzerano[1,2]

[1]Dipartimento di Fisica - Politecnico di Milano, Milano, Italy
[2]Istituto di Fotonica e Nanotecnologie - CNR, Milano, Italy
[3]Dipartimento di Matematica e Fisica - Universita degli Studi della Campania, Caserta, Italy
[4]Istituto Nazionale di Ottica - CNR, Via Campi Flegrei 34, 80078 Pozzuoli (NA), Italy
[5]INFN Istituto Nazionale di Fisica Nucleare, Sez. di Napoli, Napoli, Italy
[6]Laboratoire de Mathématiques et Physique, Université de Perpignan, Perpignan, France

Email: gianluca.galzerano@polimi.it

We report on metrology-grade roto-vibrational fine structure spectroscopy of room-temperature trifluoromethane with a saturated absorption method using a quantum cascade laser (QCL) at around 8.6 μm phase-locked to a self-reference mid-infrared optical frequency comb synthesizer. With respect to our previous sub-Doppler experiment [1], in the current approach the comb repetition frequency is finely tuned to fully access the saturated absorption profiles of several transitions enabling a quantitative study of effects related to collisions, transit-time, saturation, and sub-Doppler line-shapes instead of measuring the line-center frequencies with the highest accuracy. A comprehensive analysis of the Lamb-dip profiles using both direct pump-probe spectroscopy method and wavelength modulation technique is performed for two selected components, $^rR_{41}(61)$ and $^rR_{36}(38)$, as a function of either the gas pressure or the pump beam power. This allows for the first time the measurements of the saturation intensity, the transition electric dipole moment, the lightshift coefficient, as well as the self pressure broadening and shifting coefficients. Moreover, overall, the absolute line center frequency is measured for 36 lines, with a best fractional uncertainty of 2×10^{-9} in a single scan acquisition from 34.7426 to 34.7443 THz; assignment of vibration-rotation quantum numbers is also provided for 14 transitions belonging to the ν_5 band.

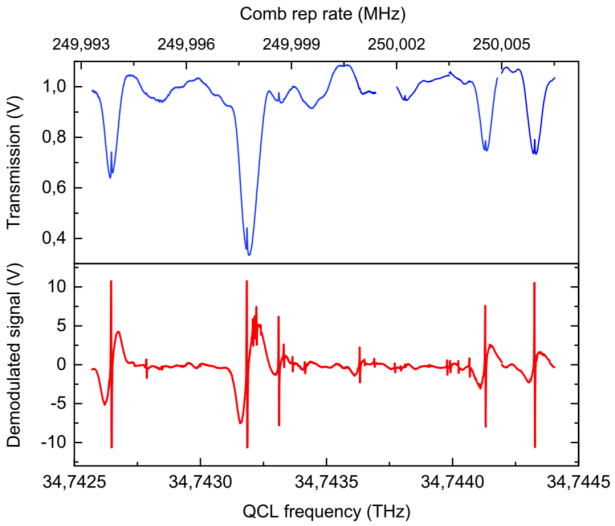

Fig. 1: (a) Direct Lamb-dip absorption signal and (b) corresponding dispersion-like first-harmonic demodulated signal (10 kHz modulation frequency, 320 kHz modulation depth, and 300-ms lock-in integration time) for a pump beam power of 5 mW and a CF_3H pressure of 6 Pa.

References

[1] A. Gambetta, E. Vicentini, Y. Wang, N. Coluccelli, E. Fasci, L. Gianfrani, A. Castrillo, V. Di Sarno, L. Santamaria, P. Maddaloni, P. De Natale, P. Laporta, and G. Galzerano "Absolute frequency measurements of CHF_3 Doppler-free ro-vibrational transitions at 8.6 μm" Opt. Lett., vol. 42 p. 1911-1914, 2017

Mid-term contributions to the frequency noise of the Pulsed CPT clock at SYRTE

F. Tricot, E. De Clercq, S. Guerandel

SYRTE, Observatoire de Paris, PSL Research University, CNRS,

Sorbonne Universités, UPMC Univ. Paris 06, LNE

61 avenue de l'Observatoire, 75014 Paris, France

Email: francois.tricot@obspm.fr

We report on the mid-term contributions of the pulsed CPT clock operating on the Cs D1 line, using a double Λ scheme and a Ramsey interrogation technique. Previous work has been focussed on the two main frequency noise sources which are the local oscillator noise and the laser intensity noise [1], leading to a short-term frequency stability at the level of $2.3\times10^{-13}\tau^{-1/2}$ up to 100 s [2].

Recently, we have investigated the mid-term noise contributions which give rise to a drift of the clock frequency. The laser power fluctuations are one of the main contributions estimated at 8×10^{-14} at 1 000 s, close to the frequency stability measured at about 1×10^{-13}. Further work led to understand that the residual power fluctuations were induced by polarisation fluctuations at the output of the AOM in the laser power lock system. Indeed, we have demonstrated that the fluctuations of the AOM crystal temperature are responsible for most of the laser power drift.

During this conference, we will show how the temperature and light effects can be reduced. The latest investigations and results about the mid-term frequency stability will be presented.

References

[1] J.-M. Danet et al., IEEE Trans. UFFC, vol. **61**(4): 567-574, 2014.

[2] F. Tricot et al., Proceedings of IFCS-EFTF2017, Besançon (2017).

Nanomechanical resonators: frequency stability and Mass Spectrometry applications

Sébastien Hentz[1,2], Marc Sansa[1,2], Shawn Fostner[1,2], Sergio Dominguez Medina[3,4,5], Martial Defoort[1,2], Marc Gély[1,2], Thomas Alava[1,2], Guillaume Jourdan[1,2], Christophe Masselon[3,4,5]

1. Univ. Grenoble Alpes, F-38000 Grenoble, France
2. CEA, LETI, Minatec Campus, F-38054 Grenoble, France
3. CEA, IRTSV, Biologie à Grande Echelle, F-38054 Grenoble, France
4. INSERM, U1038, F-38054 Grenoble, France
5. Université Joseph Fourier, Grenoble 1, F-38000, France

Email: sebastien.hentz@cea.fr

After two decades of pioneering work, Nano Electro Mechanical Systems (NEMS) are only starting to fulfil (some) of their huge promises, in particular for sensing. A few start-up companies have been created in the last few years, in particular for chemical sensing. Mass sensing using nanomechanical resonators has been performed for the last fifteen years with a variety of devices. In an effort to compete with conventional, ionization-based Mass Spectrometry, researchers have started a long quest towards the lowest mass limit of detection, eventually reaching a few Daltons using a carbon nanotube[1]. Firstly, we will discuss how the frequency stability –and resolution- of NEMS are far from the commonly accepted limits and depend on poorly-understood noise sources in the mechanical domain[2], even with semiconductor-grade monocrystalline silicon resonators. Secondly, NEMS operate best in the MDa to GDa range, a mass range where conventional MS instruments struggle to perform. Important milestones have been reached recently[3] in this range. Nevertheless, one of the main challenges preventing NEMS-MS analysis in a practical time frame stems from the detection efficiency of the overall system. We will present a new system architecture, circumventing issues associated with ionization of species, allowing for reasonable analysis time and potentially making NEMS-MS a viable analytical technique for biological or environmental applications.

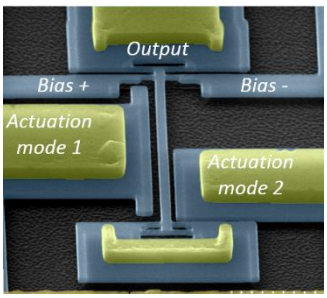

Fig. 1: Monocrystalline silicon nanoresonator with piezoresistive transduction

References

(1) Chaste, J.; Eichler, A.; Moser, J.; Ceballos, G.; Rurali, R.; Bachtold, A. *Nat. Nanotechnol.* **2012**, *7* (5), 301–304.

(2) Sansa, M.; Sage, E.; Bullard, E. C.; Gély, M.; Alava, T.; Colinet, E.; Naik, A. K.; Villanueva, L. G.; Duraffourg, L.; Roukes, M. L.; Jourdan, G.; Hentz, S. *Nat. Nanotechnol.* **2016**, *11* (June), 552–559.

(3) Sage, E.; Brenac, A.; Alava, T.; Morel, R.; Dupré, C.; Hanay, M. S.; Roukes, M. L.; Duraffourg, L.; Masselon, C.; Hentz, S. *Nat. Commun.* **2015**, *6*, 6482.

Active Isolator Development of Ultra-stable Narrow Linewidth Laser of Atomic Clock

Qing Li[1], Min Xiong[1], Lei Liu[1] Guanjun Xu[2]
[1]School of Astronautics, Northwestern Polytechnical University, Xi'an, China
[2]National Time Service Center Chinese Academy of Sciences

Email: leiliu@nwpu.edu.cn, xuguanjun@ntsc.ac.cn

China will launch a space station system around 2021 and carry out the high-precision time-frequency experiments in space applications. The ultra-stable narrow linewidth laser, one key component of the time-frequency science experiment, is extremely sensitive to micro-vibration of the space station, and requires μg micro-vibration level. Due to the existence of various disturbance sources such as astronauts' activities, fans, refrigeration and so on, the problem of micro-vibration environment of the space station is serious. From the result of micro-vibration environment test in the International Space Station, the level of micro-vibration level can achieve mg order. To realize ultra-quiet environment of the ultra-stable narrow linewidth laser, it is necessary to develop a high performance active vibration isolator for the narrow linewidth laser. The active isolator will provide the micro-gravity level of μg, and has a long time continuous working ability to meet the technology requirements of the narrow linewidth laser. Figure 1 shows the designed active isolator for the ultra-stable narrow linewidth laser. Figure 2 shows the control scheme of the active vibration isolator, which uses the acceleration feedback and position feedback. Figure 3 shows the performance of the active vibration unit. The space station disturbance is set to 4 mg. By using the control of the proposed active isolator, the residual micro-vibration of the active vibration isolation platform is less than 5μg.

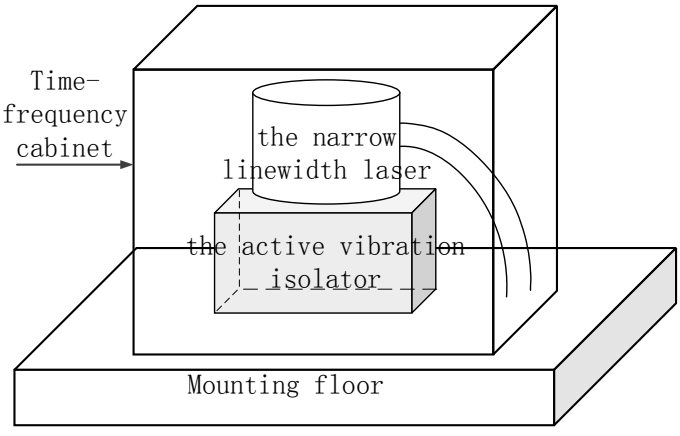

Fig 1 Designed active isolator

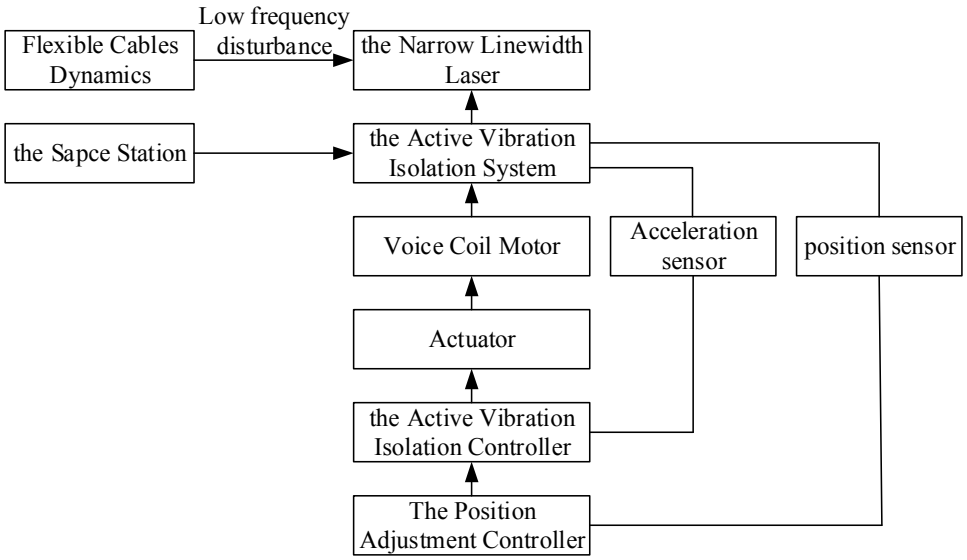

Fig 2 Control scheme of the active vibration isolator

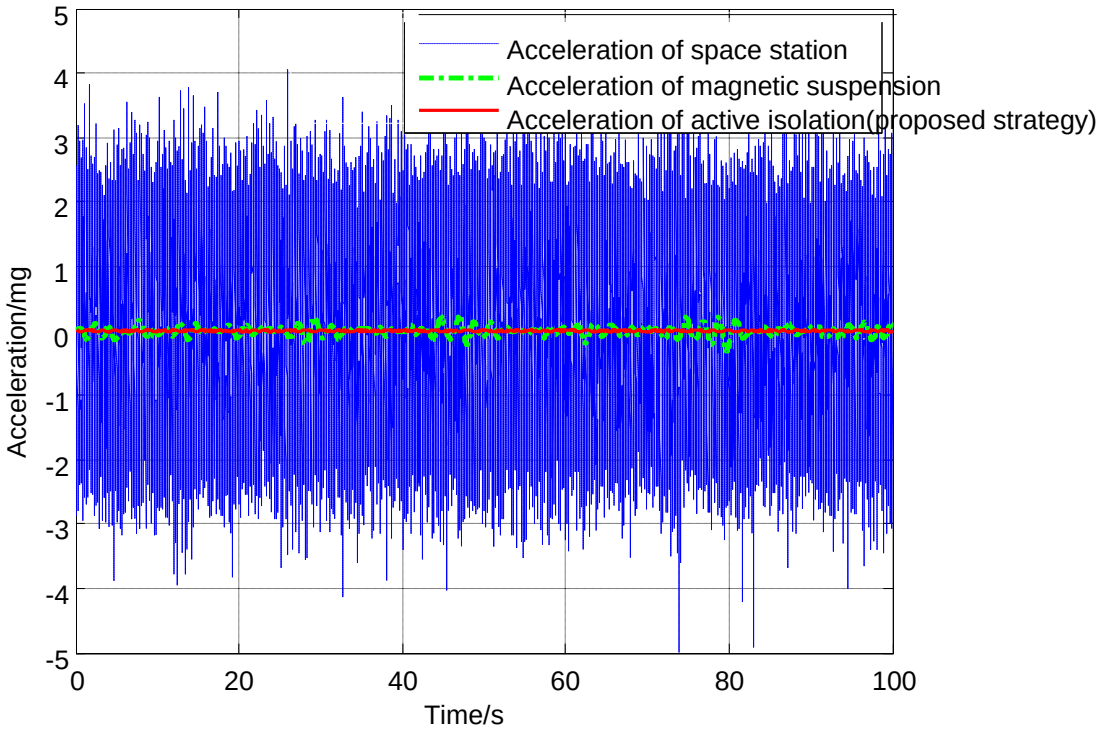

Fig 3 Performance of the active vibration unit

Galileo gravitational Redshift test with Eccentric sATellites: the GREAT experiment

Pacôme Delva, N. Puchades

SYRTE, Observatoire de Paris, Paris, France

Email: pacome.delva@obspm.fr

We are going to present the results of the analysis of the GREAT (Galileo gravitational Redshift test with Eccentric sATellites) experiment from SYRTE (Observatoire de Paris), funded by the European Space Agency. The General Relativity (GR) predicts that time flows differently for two clocks that have a relative speed and are placed in different gravitational potentials. It is therefore possible to test GR by comparing the frequencies of two clocks, in a so-called gravitational redshift test. The best test to date was performed with the Gravity Probe A (GP-A) experiment in 1976 with an uncertainty of 1.4 × 10^(−4).

An elliptic orbit induces a periodic modulation of the fractional frequency difference between a ground clock and the satellite clock, while the good stability of Galileo clocks allows to test this periodic modulation to a high level of accuracy. Galileo 201 and 202, with their large eccentricity and on-board H-maser clocks, are perfect candidates to perform this test. However, the accuracy of the gravitational redshift test is limited by the systematic uncertainty due to orbital errors, and Satellite Laser Ranging (SLR) measurements are crucial to understand them. SLR data allows us to reduce the effect of the systematics, in particular to partly decorrelate the orbit perturbations from the clock errors. By analyzing several years of Galileo satellites data we have been able to improve on the GP-A test of the gravitational redshift.

Low-power optical frequency standard based on a cavity-enhanced two-photon transition in a Rb microfabricated vapor cell

Vincent Maurice[1], Zach Newman[1], Matt Hummon[1], Liron Stern[1], Leo Hollberg[2], John Kitching[1]

[1]National Institute of Standards and Technology, Boulder, CO, 80305, USA
[2]Department of Physics, Stanford University, 452 Lomita Mall, Stanford, CA, 94305, USA

Email: vincent.maurice@nist.gov

Miniature optical atomic clocks could become an attractive alternative to chip-scale atomic clocks (CSACs). Indeed, frequency combs generated from microfabricated optical ring resonators could soon become sufficiently efficient to divide optical frequencies down to the microwave domain within battery-powered devices [1]. Combined with a low-power, miniature optical frequency standard, such a device could eventually meet the stringent power budget of a portable device while improving over the frequency stability of current CSACs [2].

We report on the developments towards a low-power miniature optical atomic frequency standard. This standard is based on the 778 nm $5S_{1/2}$-$5D_{5/2}$ two-photon transition in rubidium-87, which has long been identified as a promising option [3,4]. The atoms are contained in a microfabricated vapor cell composed of a 3-mm thick silicon frame enclosed between two glass windows. A plano-concave Fabry-Perot cavity is used to increase the two-photon transition excitation rate to allow operation at low optical power. The planar reflector of the cavity consists of a high-reflectivity coating directly deposited on the back window of the cell. The curved mirror placed in front of the cell features a 5-m radius of curvature yielding a cavity mode waist of 280 µm. The 420-nm fluorescence is detected with a photodiode instead of a photomultiplier tube, reducing further the overall power consumption. With a power build-up factor of 7, the cavity allows to reduce the input optical power from an external cavity diode laser down to ≈2 mW, while maintaining a short-term fractional frequency stability of $2 \cdot 10^{-12}\ \tau^{-1/2}$.

This stability, shown in Fig. 1, is essentially limited by the intermodulation effect [5]. We investigate the long-term limitations of the system and discuss its potential use in a miniature optical atomic clock.

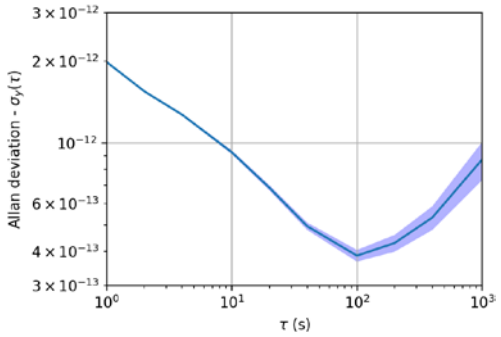

Fig. 1: Fractional frequency stability of the optical frequency standard.

References

[1] T. C. Briles, *et al.*, "Kerr-microresonator solitons for accurate carrier-envelope-frequency stabilization", arXiv:1711.06251, 2017.
[2] R. Lutwak, *et al.*, "The miniature atomic clock-Pre-production results", Frequency Control Symposium and 21st European Frequency and Time Forum, 2007.
[3] L. Hilico *et al.*, "Metrological features of the rubidium two-photon standards of the BNM-LPTF and Kastler Brossel Laboratories", The Eur. Phys. J. Appl. Phys., vol. 4, p. 219-225, 1998.
[4] J. H. Burke, *et al.*, "A compact, high-performance all optical atomic clock based on telecom lasers", Proc. SPIE 9763, Slow Light, Fast Light, and Opto-Atomic Precision Metrology IX, 976304, 2016.
[5] C. Audoin, *et al.*, "A limit to the frequency stability of passive frequency standards due to an intermodulation effect", IEEE Transactions on Instr. and Meas., vol. 40, p. 121, 1991.
This research was developed with funding from the Defense Advanced Research Projects Agency (DARPA). The views, opinions and/or findings expressed are those of the author and should not be interpreted as representing the official views or policies of the Department of Defense or the U.S. Government.

The operation and performance of Galileo on-board clocks

Pierre Waller, Marco Belloni

European Space Research and Technology Centre – ESA/ESTEC
Noordwijk, The Netherlands

Email: pierre.waller@esa.int

Since the declaration of Initial Services in December 2016, the Galileo system has been operating continuously, providing users globally with Open (OS) and Search and Rescue (SAR) services with performance exceeding the committed minimum performance levels targets [1]. The system currently includes 14 nominal operational satellites in service, making it the GNSS with the higher number of satellites providing publicly available dual frequency signals (E1-E5). While the system is reaching its final deployment, several activities are being conducted to define its evolution towards the second generation of Galileo satellites.

The Galileo on-board clocks represent a key contributor to the system performance, both in terms of ranging/time dissemination accuracies and in terms of availability. While their frequency stability shall guarantee a good predictability over extended period of time, they shall also survive the mechanical/thermal stress of the launch and operate flawlessly over prolonged duration in a harsh environment.

All Galileo satellites embark two types of on-board clock technologies. The primary reference is the Passive Hydrogen Maser (PHM) and the secondary reference is the Rubidium Atomic Frequency Standard (RAFS). Dual technology has been planned from the onset to guarantee redundancy in both technology and supply chain. Since the first launch of the Galileo constellation satellite, both technologies have cumulated in-orbit operation in excess of 40 years.

The paper will present the current status of Galileo on-board clocks, based on data collected from in-orbit performance estimation using the Galileo ground infrastructure. The analysis of clock in-orbit operation and performance will be presented, together with lessons learnt. Finally, an overview of the on-going technology developments in preparation for the Galileo second generation will be outlined.

[1] GSA, Galileo Initial Services Open Service Quarterly Performance Report, available at https://www.gsc-europa.eu/electronic-library/performance-reports